Giorgio Lollino
Andrea Manconi
John Clague
Wei Shan
Marta Chiarle
Editors

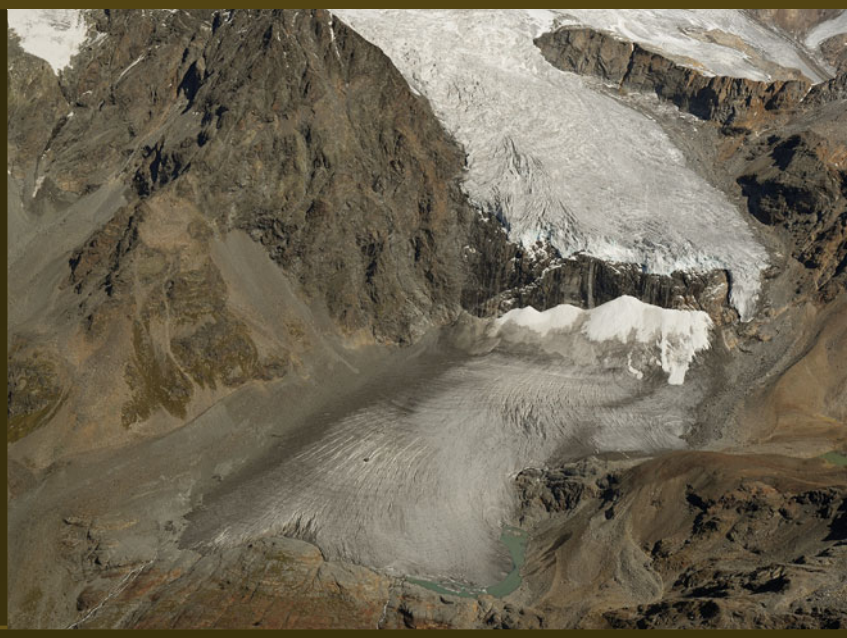

Engineering Geology for Society and Territory – Volume 1

Climate Change and Engineering Geology

Springer

Engineering Geology for Society and Territory – Volume 1

Giorgio Lollino • Andrea Manconi
John Clague • Wei Shan
Marta Chiarle
Editors

Engineering Geology for Society and Territory – Volume 1

Climate Change and Engineering Geology

Springer

Editors
Giorgio Lollino
Andrea Manconi
Marta Chiarle
Institute for Geo-hydrological Protection
National Research Council (CNR)
Turin
Italy

John Clague
Department of Earth Sciences
Simon Fraser University
Burnaby, BC
Canada

Wei Shan
Institute of Engineering Geology
Northeast Forestry University
Harbin
China

ISBN 978-3-319-09299-7 ISBN 978-3-319-09300-0 (eBook)
DOI 10.1007/978-3-319-09300-0
Springer Cham Heidelberg New York Dordrecht London

Library of Congress Control Number: 2014946956

Cover Illustration: The Fellaria Glacier (Bernina Massif, Central Italian Alps). The lowest part of the Fellaria glacier tongue, more than 1 km long, was cut in 2006 from the upper glacier mass in correspondence to a rock cliff. Glaciers are among the best indicators of climate change, thanks also to their clear visibility to the public. *Photo Courtesy*: Giovanni Kappenberger.

Printed on acid-free paper

Springer is part of Springer Science+Business Media (www.springer.com)

Foreword

It is our pleasure to present this volume as part of the book series of the Proceedings of the XII International IAEG Congress, Torino 2014.

For the 50th Anniversary, the Congress collected contributions relevant to all themes where the IAEG members have been involved, both in the research field and in professional activities.

Each volume is related to a specific topic, including:

1. Climate Change and Engineering Geology;
2. Landslide Processes;
3. River Basins, Reservoir Sedimentation and Water Resources;
4. Marine and Coastal Processes;
5. Urban Geology, Sustainable Planning and Landscape Exploitation;
6. Applied Geology for Major Engineering Projects;
7. Education, Professional Ethics and Public Recognition of Engineering Geology;
8. Preservation of Cultural Heritage.

The book series aims at constituting a milestone for our association, and a bridge for the development and challenges of Engineering Geology towards the future.

This ambition stimulated numerous conveners, who committed themselves to collect a large number of contributions from all parts of the world, and to select the best papers through two review stages. To highlight the work done by the conveners, the table of contents of the volumes maintains the structure of the sessions of the Congress.

The lectures delivered by prominent scientists, as well as the contributions of authors, have explored several questions ranging from scientific to economic aspects, from professional applications to ethical issues, which all have a possible impact on society and territory.

This volume testifies the evolution of engineering geology during the last 50 years, and summarizes the recent results. We hope that you will be able to find stimulating contributions which will support your research or professional activities.

Giorgio Lollino

Carlos Delgado

Preface

Many natural phenomena occur over a wide range of magnitudes. Typically, small events occur more frequently than large ones. For example, small earthquakes occur frequently, while large earthquakes are rare. Sixty years ago, earthquake scientists developed a relationship, known as the 'magnitude–cumulative frequency' (MCF) relationship, to characterize earthquake hazards.

MCF relationships are widely used today in engineering geology to evaluate hazard and risk to people and property, specifically the likelihood or probability of earthquakes, floods, severe storms and landslides of different sizes. For example, an MCF relationship for floods can be constructed for any watershed if a continuous and lengthy record of river discharge is available. If the observed peak discharge each year over a period of N years is ranked in the order of decreasing magnitude, from the largest to the smallest, the largest flood has an annual probability of occurrence of 1/N, because only one such event was observed in N years. The cumulative frequency of the second largest event or larger is 2/N, because two such events occurred in N years. Similarly, the cumulative frequency of any given rank 'x' or larger is x/N. When such MCF data are graphed using logarithmic scales, they commonly plot on a reasonably straight line.

When compiling lists of events for MCF relationship analysis, only events of similar type, nature or process should be used. Such events are referred to as a 'population'. In the case of landslides, for example, the events in each population must be similar in type, character, materials and mechanics of failure and movement. Two populations that are not similar in these characteristics may exhibit different MCF relationships.

The construction and use of MCF relationships assume stationarity in the conditions controlling the process that is being modelled. It is reasonable to assume stationarity in earthquake occurrence over time, as long as the monitoring period is sufficiently long, typically more than two centuries. This assumption, however, is almost certainly invalid for atmospheric and hydrological phenomena, such as cyclones, debris flows and floods, because climate is continually changing.

Climate Change and Hazardous Processes

Climate change, which can be defined as long-term weather patterns that deviate from historical ranges, can have an effect on the volume and/or frequency of landslides, floods and other hydrometeorological hazards. Over the past two decades, successive reports by the Intergovernmental Panel on Climate Change (IPCC) have expressed increased confidence that climate is changing around the world and will continue to do so in the foreseeable future. The physical processes driving climate change are complex and the models on which the forecasts of climate change are based are simplifications and subject to uncertainty and error. Global climate models are downscaled to regional and local levels by comparing output from the models with historical, regional and local weather station data. By doing so, climate

scientists attempt to forecast annual and seasonal climate changes at scales that are pertinent to government decision-makers, land-use planners, engineering geologists and engineers.

Even more difficult to predict are changes in (1) volumes, frequencies and even types of landslides, (2) peak discharges of floods and (3) the severity and frequencies of extreme weather events. Such changes can be regarded as second-, third- or even fourth-order effects of climate change.

Climate change affects the entire hydrologic system by changing temperature; type, amount and intensity of precipitation; evaporation; balance between water storage as ice, snow or liquid forms; and levels of soil moisture. By the end of this century, mean global temperatures at Earth's surface are likely to be 2–4 °C warmer than today, but there will be pronounced spatial and seasonal differences on our planet. For example, warming will be greater at high latitudes and in high mountains than elsewhere. Projected temperatures for an average year will be warmer than almost all of the warmest years in the recent past.

Changes in precipitation are more difficult to forecast, with many areas experiencing an overall increase in rainfall and others likely to see a reduction in precipitation. Many models suggest that extreme rainfall events will become more common with warming, although this is by no means certain. An increase in surface water runoff is expected during the winter months over large areas of North America and Northern Europe due to a greater proportion of precipitation falling as rain. An earlier spring freshet due to warmer spring temperatures is also expected. Drier conditions are expected during the summer.

Although the above-described conditions are expected to produce characteristically lower spring freshets and summer stream flows, years with severe stream floods are likely to occur in the future. For smaller watersheds with a hybrid (snowmelt and rainfall-dominated) runoff regime, a trend towards purely rain-dominated stream floods is expected. Increased temperatures are also expected to influence the intensity of summer convective rainstorms and the frequency of intense, long duration winter rainfall in areas with temperate climate. These changes have a potential bearing on the timing and magnitude of winter storms, rain-on-snow events, spring freshets, the soil–water balance and effects of antecedent moisture on landslides.

Warmer winters will raise winter freezing levels and decrease snow cover. This effect, in combination with warmer summers, will cause glaciers in high mountains to continue to thin and retreat, as they have over the past century.

As noted above, changes in landslide activity are third- or fourth-order effects of climate change; they are at least one step removed from changes in precipitation and surface water runoff. Therefore, the uncertainties associated with forecasting the effects of climate change on landslide size and frequencies on a regional, much less local, scale are large. Nevertheless, any increase in the amount and intensity of winter precipitation will likely increase the number and frequency of small and perhaps medium-sized landslides, specifically debris flows and debris floods. Although individual rainstorms are not expected to have an effect on stability of rock slopes, increased long-term saturation of the ground could reduce the stability of steep slopes, leading to major rockslides.

Because of the large uncertainties in estimates of landslides and floods in a changing climate, possible climate change effects must be dealt with by selecting suitably conservative parameters during the design of any mitigation, and by selecting solutions that have certain flexibility with respect to the magnitude of potential effects.

Incorporating Climate Change into Professional Practice?

The primary duties of professional engineers and geoscientists are to (1) hold paramount the safety, health and welfare of the public, (2) protect the environment and (3) promote health and safety within the workplace. Changing climate conditions, particularly weather patterns

that deviate from historical ranges, may adversely affect engineered systems. It is the geoscientist's responsibility to ensure that possible impacts of climate change on hazardous natural processes are articulated in the hazard or risk studies they perform. It is the engineer's duty to take all reasonable measures to ensure that engineered systems are designed and built to properly function under new climatic conditions. This understanding imposes a responsibility of due diligence on professionals to address the issue of climate change in their activities. This responsibility plays out in two ways. First, engineering geologists and engineers must consider climate change in their work to ensure public safety. Second, given the level of awareness of this issue and high visibility of impacts arising from more intense and severe weather events, engineers may ultimately be held personally or jointly liable for failures or damages arising from failure to anticipate climate impacts on engineered systems. The scientific literature indicates that significant departures from historical climate averages are happening and will continue to occur, thus planning and engineering design must take into account these departures.

Professional engineers and engineering geologists have a higher standard of care than a layperson. They have more years of training and experience with geoscience and engineering matters, and are uniquely qualified to identify and respond to issues that may compromise public health and safety through their work. This standard of care is currently poorly defined and is constantly being reviewed both by professional associations and the legal profession. The concept of 'reasonable level of care' will continue to evolve over time, and climate change imposes a new and evolving pressure on this standard.

Contents

The Istituto di Ricerca per la Protezione Idrogeologica (IRPI), of the Italian Consiglio Nazionale delle Ricerche (CNR), designs and executes research, technical and development activities in the vast and variegated field of natural hazards, vulnerability assessment and geo-risk mitigation. We study all geo-hydrological hazards, including floods, landslides, erosion processes, subsidence, droughts, and hazards in coastal and mountain areas. We investigate the availability and quality of water, the exploitation of geo-resources, and the disposal of wastes. We research the expected impact of climatic and environmental changes on geo-hazards and geo-resources, and we contribute to the design of sustainable adaptation strategies. Our outreach activities contribute to educate and inform on geo-hazards and their consequences in Italy.

We conduct our research and technical activities at various geographical and temporal scales, and in different physiographic and climatic regions, in Italy, in Europe, and in the World. Our scientific objective is the production of new knowledge about potentially dangerous natural phenomena, and their interactions with the natural and the human environment. We develop products, services, technologies and tools for the advanced, timely and accurate detection and monitoring of geo-hazards, for the assessment of geo-risks, and for the design and the implementation of sustainable strategies for risk reduction and adaptation. We are 100 dedicated scientists, technicians and administrative staff operating in five centres located in Perugia (headquarter), Bari, Cosenza, Padova and Torino. Our network of labs and expertizes is a recognized Centre of Competence on geo-hydrological hazards and risks for the Italian Civil Protection Department, an Office of the Prime Minister.

Assessing Climate Change Risks Under Uncertain Conditions

1

Antonello Provenzale and Elisa Palazzi

Abstract
Climate and environmental change is expected to affect hydrometeorological hazard and ecosystem functioning, with possible threats to human societies due to increased probability of extreme events and loss of ecosystem services. In mountain regions, the environmental response could be even larger. For this reason, it is important to obtain estimates of the expected modifications in natural hazards associated with climate and environmental change, to develop appropriate adaptation and risk mitigation strategies. This goal, however, is made difficult by the scale mismatch between climate model projections and land surface response, which requires the use of appropriate climate downscaling procedures. To complicate the picture, one should also cope with the chain of uncertainties which affect climate and risk projections, from the wide range of global climate model estimates for the water cycle variables, to the uncertainties in regional climate response, to the uncertainties in the hydrological and/or ecosystem models themselves. Precipitation data used to validate the models, on the other hand, are also affected by severe uncertainties, especially in mountain regions. This leads to the general problem of assessing natural hazards for different climate and environmental change scenarios under uncertain conditions.

Keywords
Climate change • Risk • Uncertainty assessment

1.1 Introduction

Global warming should not be intended as a slow, continuous and homogeneous temperature rise. Temporally, the warming of the last 80 years has manifested itself in a sequence of steps, alternating periods of rapid change with times of slowly changing temperatures (as in the last 10 years). Spatially, the temperature increase is widely varying, with geographical areas where the warming has been up to three times the global mean (as in the Arctic and in several mountain chains such as the Alps), and other regions where warming has been more modest (IPCC 2013).

Even more importantly, the effect of global warming is not solely a temperature increase. The largest energy of the atmospheric motions and the potentially larger amount of moisture in the atmosphere can lead to an intensification of the hydrological cycle, with more intense precipitation events and more prolonged dry periods. Evidence of this behaviour is now available, and these effects are expected to become even more relevant in coming decades (Giorgi et al. 2011).

In turn, stronger intensity of the hydrological cycle is associated with potential modifications in the hydrometeorological risk. For this reason, assessing the impact of climate change on the statistics of precipitation extremes,

A. Provenzale (✉) · E. Palazzi
ISAC-CNR, Torino, Italy
e-mail: a.provenzale@isac.cnr.it

G. Lollino et al. (eds.), *Engineering Geology for Society and Territory – Volume 1*,
DOI: 10.1007/978-3-319-09300-0_1,

and the associated surface effects such as flooding and landslides, is a much needed step in order to develop adequate risk mitigation and adaptations strategies. Of course, science can help in suggesting the proper avenues, but it is then in the hands of administrators and politicians to assure that the proper actions are taken.

1.2 Climate Downscaling and Surface Processes

To estimate the impact of future climate change on surface geo-hydrological and ecosystem processes, we have to face a difficult problem: information on climate projections is usually provided on relatively large spatial scales (50–100 km for global climate models and 10–50 km for most regional climate models), while the hydrological response takes place at much smaller spatial scales, particularly in mountain areas and small coastal basins. Thus, a climate downscaling procedure is needed, especially for highly intermittent (but crucial) fields such as precipitation.

In recent years, various ways to bridge the scale gap between climate change scenarios and the small scales needed for impact studies have been proposed. One option is provided by statistical and/or stochastic downscaling methods. Statistical downscaling maps large-scale deterministic predictors to variables at small scales (Maraun et al. 2010), to produce realizations of the expected small-scale climate variability. Stochastic rainfall downscaling (Rebora et al. 2006; D'Onofrio et al. 2014) aims at generating synthetic spatial-temporal precipitation fields whose statistical properties are consistent with the small-scale statistics of observed precipitation, based only on the knowledge of the large-scale precipitation field. Stochastic downscaling also holds the potential of estimating uncertainties in rainfall scenarios, by generating ensembles of small-scale precipitation fields which can be compared with measured data (Brussolo et al. 2008).

Clearly, stochastic downscaling is not a substitute for physically-based models, and it is just a way to introduce realistic rainfall variability on the scales which are not resolved by physical models. Dynamical downscaling, on the other hand, attempts at nesting high-resolution, non-hydrostatic convective models in larger-scale global or regional climate models, producing a small-scale zoom of the relevant dynamical fields. Of course, such approach is much more powerful and interesting, but the computational burden (in terms of CPU and storage) of these simulations often limits the possibility of having large ensembles of realizations or long time slices, thus reducing the ability to estimate climate statistics.

Thus, at the time of writing, the standard "climate impact" chain is to start with large-scale global climate models (or reanalysis products if one wants to verify current conditions), go through a nested (hydrostatic or non-hydrostatic) regional climate model, then through a statistical/stochastic downscaling procedure, to finally drive eco-hydrological and geo-hydrological models for risk assessment. Such chain is illustrated in Fig. 1.1.

1.3 The Chain of Uncertainties

Parallel to the downscaling chain, we should consider another important element of the story: the chain of uncertainties propagating from the global climate models through the downscaling procedures, to the final risk estimate. This aspect is far less studied, and it can potentially affect our ability to assess the impact of climate change on surface processes.

First, we have to take into account the uncertainties arising from global climate simulations. These are generated by the uncertainty in the emission scenario which will be followed—and for this reason we should always consider different scenarios, such as the currently utilized RCP4.5, RCP8.5 and so on—but also by the natural variability of climate and of its numerical representations for a given scenario (see for example Provenzale 2014).

Figure 1.2 shows the time series of surface mean winter temperature, spatially-averaged over the Hindu-Kush Karakoram area in Asia, as simulated by an ensemble of global climate models from the CMIP5 initiative (http://cmip-pcmdi.llnl.gov/cmip5/). The black line represents the average over all model results for the historical period, the blue and red lines represent the average over all models for the RCP4.5 and RCP8.5 future scenarios respectively, and the pink and green lines represent the data from CRU and GHCN respectively. The pale grey lines represent the outputs of the individual models, and their spread indicates the range of model responses.

From this figure, some interesting facts emerge: (1) there is not much agreement between the two observational datasets (even though they do measure exactly the same quantity: surface temperature for CRU and 2 m air temperature for GHCN); (2) most models predict a cooler climate than observed today (the so-called "cold bias"), and (3) the average winter temperature displays a difference of up to 10° between the different models. Clearly, both issues are serious, and require further work on climate models—something that most workers in this field are aware of. On the other hand, even the validation of model results on measured data is difficult, especially in the case of precipitation, since

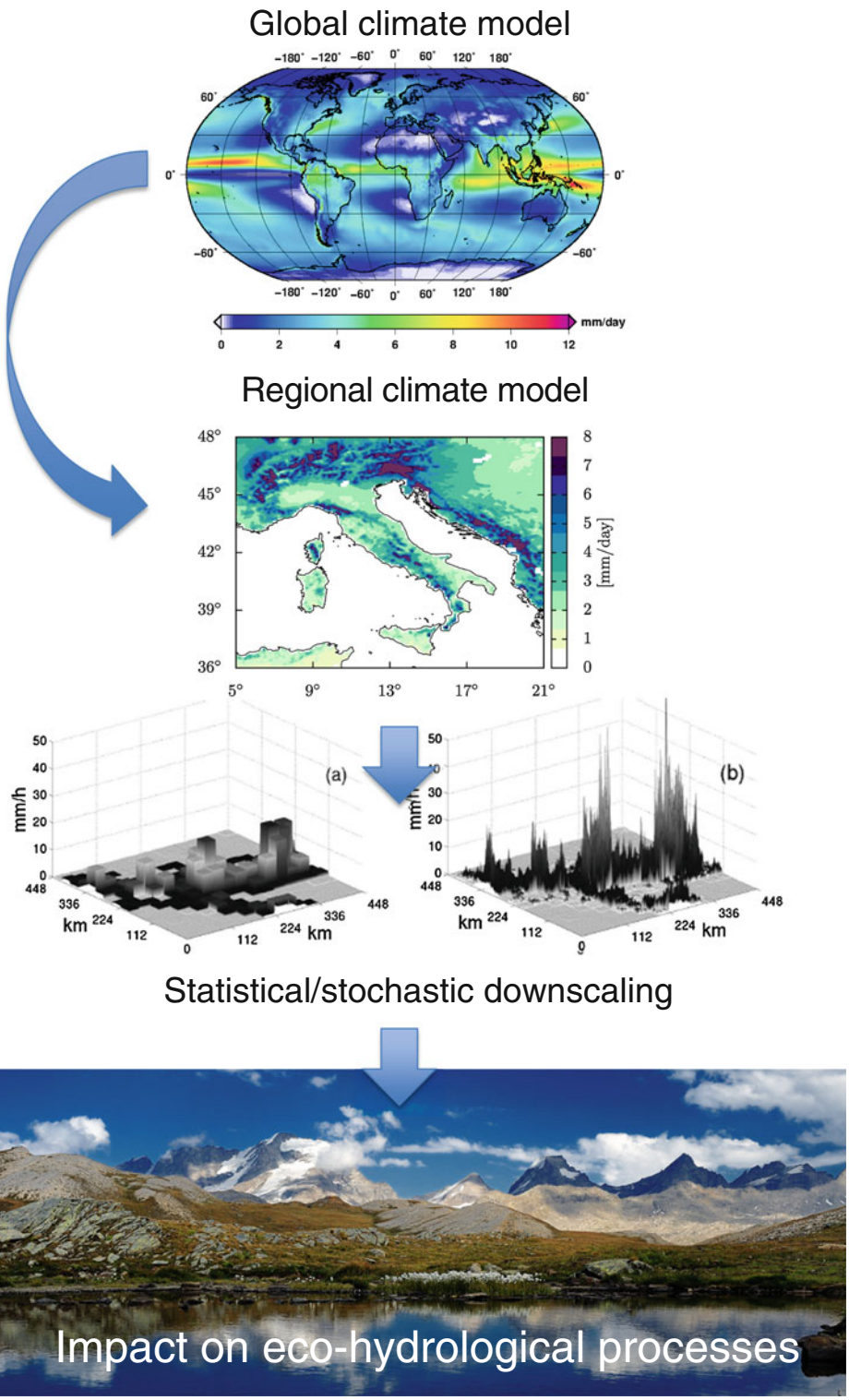

Fig. 1.1 The climate downscaling chain for precipitation

in certain regions such as the Karakoram-Himalayan chain the different datasets provide rather different views and a definite "ground truth" is not available (Palazzi et al. 2013).

But if we are interested in driving a downscaling/impact chain with such models, what should we do? Often, what is done is to use some form of "bias correction": we normalize the model output to the currently observed values

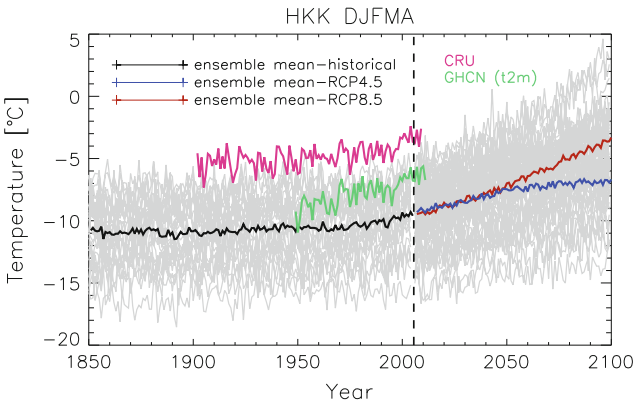

Fig. 1.2 Average winter temperature, as a function of time, for the area of the Hindu-Kush Karakoram (HKK) in Asia, as simulated by a suite of global climate models from the CMIP5 initiative. The meaning of the different *lines* is discussed in the text

(of temperature or precipitation), and then we simply look at the anomaly, that is, at the difference between the model-generated values for the future and those for today. This procedure is simple, and widely used, but it is not devoid of danger. For example, a cold bias affects the saturation water vapour pressure in the atmosphere (where temperature enters nonlinearly and not as an anomaly), with possibly serious consequences for the correct reproduction of the hydrological cycle. For this reason, we cannot take climate model outputs at face value and simply bias-correct them, but we should be aware of the spread in model behaviours and of its potential implications.

When nesting a regional model for a specific area in the output of a global climate simulation, one drives the regional model by the boundary conditions provided by the global model. But then, what is the effect of uncertainties in such boundary values and how such uncertainties propagate in the regional model? That is, what is the sensitivity of the regional model to changes in boundary conditions? Such issue has been explored for specific cases (see for example the Arctic case considered by Rinke and Dethloff 2000), and should not be forgotten when working with nested regional models. In addition, regional models themselves can add their own uncertainty and unpredictability, which is often difficult to quantify.

The statistical/stochastic downscaling adds its own uncertainties, mainly related to the fact that statistical relationships and stochastic realizations do not provide a single time series of temperature or precipitation in the location of interest, but rather give an ensemble of possible time histories, all compatible with the constraints imposed by the climate models at the larger scales. An interesting point is to determine how the uncertainty range introduced by the downscaling compares with that associated with the ensemble of climate models. The question is not simple and must be carefully disentangled, see for example von Hardenberg at al. (2007) for a similar problem in a meteorological framework.

Finally, we have the uncertainty coming from the imperfect knowledge of the model for surface processes, such as the form and parameter values for a semi-distributed hydrological model, or the soil and vegetation parameters in an eco-hydrological model. The relevance of such uncertainty varies with the model and the processes considered, and it could either be larger or smaller than the uncertainty propagated through the chain till this point. In such conditions, one should also consider the sensitivity of a given surface process model to variations in the driving factors. An example of the assessment of the sensitivity of a hydrological model to variations in the parameters of the stochastic downscaling procedure is discussed in Gabellani et al. (2007).

1.4 Final Remarks

Assessing the effects of climate change on surface geo-eco-hydrological processes, and estimating the associated risks, is currently one of the most important challenges for the Geosciences. This challenge involves important conceptual aspects, such as cross-scale interactions and downscaling methods, and it has crucial societal implications. However, several sources of uncertainty contribute to make this endeavour rather complex. In particular, we cannot provide useful estimates of the surface response and of the potential risks if we do not include a quantitative assessment of the uncertainty on the estimates. As seen above, the different sources of uncertainty all potentially contribute to affect the final result, and they should be carefully quantified and weighted. Most current impact assessments include the use of different scenarios, and many take into account model variability by considering an ensemble of model behaviours. However, this is often not enough, as other uncertainty sources are at play. On the other hand, it can be difficult from a practical point of view to build ensembles of ensembles of ensembles of realizations taking into account all possible uncertainties and their propagation across scales, and new, more refined, ingenious and synthetic approaches should be developed.

For these reasons, the assessment of climate change impacts on surface processes is not just an automated procedure based on the blind applications of models driven by other models, but it is, in all respect, an intriguing, challenging and difficult scientific endeavour. It is, in addition, a topic having extremely important practical implications, as it is at the base of the development of knowledge-based risk

mitigation and adaptation strategies. Such topic deserves the establishment of national and international programs devoted to provide risk assessments in an uncertain future.

References

IPCC (2013) Fifth Assessment Report (AR5), Approved Summary for Policymakers. Intergovernmental Panel on Climate Change. http://www.ipcc.ch

Brussolo E, von Hardenberg J, Ferraris L, Rebora N, Provenzale A (2008) Verification of quantitative precipitation forecasts via stochastic downscaling. J Hydrometeorology 9:1084–1094

D'Onofrio D, Palazzi E, von Hardenberg J, Provenzale A, Calmanti S (2014) Stochastic rainfall downscaling of climate models. J Hydrometeorology. http://dx.doi.org/10.1175/JHM-D-13-096.1

Gabellani S, Boni G, Ferraris L, von Hardenberg J, Provenzale A (2007) Propagation of uncertainty from rainfall to runoff: a case study with a stochastic rainfall generator. Adv Water Resour 30:2061–2071

Giorgi F, Im E-S, Coppola E, Diffenbaugh NS, Gao XJ, Mariotti L, Shi Y (2011) Higher hydroclimatic intensity with global warming. J Climate 24:5309–5324

von Hardenberg J, Ferraris L, Rebora N, Provenzale A (2007) Meteorological uncertainty and rainfall downscaling. Nonlinear Processes Geophys 14:193–199

Maraun D et al (2010) Precipitation downscaling under climate change: recent developments to bridge the gap between dynamical models and the end user. Rev Geophys 48:RG3003. doi:10.1029/2009RG000314

Palazzi E, von Hardenberg J, Provenzale A (2013) Precipitation in the Hindu-Kush Karakoram Himalaya: observations and future scenarios. J. Geophys Res Atmos 118:85–100. doi:10.1029/2012JD018697

Provenzale A (2014) Climate models. Rend Lincei 25:49–58

Rebora N, Ferraris L, von Hardenberg J, Provenzale A (2006) RainFARM: rainfall downscaling by a filtered autoregressive model. J Hydrometeorology 7:724–738

Rinke A, Dethloff K (2000) On the sensitivity of a regional Arctic climate model to initial and boundary conditions. Clim Res 14:101–113

Part I

Climate Change and the Mountain Environment

Convener: Dr Antonello Provenzale—*Co-conveners*: Elisa Vuillermoz

Mountains are "sentinels of climate change" because they respond rapidly and intensely to climatic and environmental modifications. Mountain areas are the "water towers" of entire regions: climatic and environmental alterations in the hydrological cycle in high mountains can significantly affect the availability of water resources for energy production, agriculture, economy, urban settlements and societies in the surrounding regions. It is therefore essential to increase our knowledge of the current and expected modifications in high mountains, and use this knowledge to assess possible changes in hydrogeological hazard, to develop sustainable adaptation strategies and to improve the quality of life of the people living in the mountains. We welcome contributions on all aspects of climate change impacts in mountain regions, with special attention to those papers that deal with engineering geology, risk assessment and the management of infrastructures in high-elevation areas.

Assessing Climate Impacts on Hydropower Production of Toce Alpine Basin

2

Giovanni Ravazzani, Francesco Dalla Valle, Thomas Mendlik, Giorgio Galeati, Andreas Gobiet and Marco Mancini

Abstract

The aim of the presented study is to assess the impacts of climate change on hydropower production of the Toce alpine river basin, in Italy. A model of the hydropower system was driven by discharge time series at hourly scale with the simulation goal of defining the reservoirs management rule that maximize the economic value of the hydropower production. To this purpose, current energy price was assumed for the future. Assessment of hydropower production of future climate (2041–2050) respect to current climate (2001–2010) showed an increment of production in Autumn, Winter and Spring, and a reduction in June and July. Significant change in the reservoirs management policy is expected due to anticipation of the date when the maximum volume of stored water has to be reached and an increase of reservoir drawdown during August and September to prepare storage capacity for autumn inflows.

Keywords

Alpine basin • Climate change • Hydrological impact • Hydropower production

2.1 Introduction

Climate change has significant implications for environment, water resources and human life in general (Beniston 2004). Changes in temperatures and changes in precipitation patterns can have profound effects on river systems and cause important changes in the management of water, particularly on uses highly dependent on the hydrological regime, such as hydropower production. In several European countries, this source of energy represents an important part of the electric mixt. The hydropower plants with reservoirs deserve a mention because indirectly they allow storing electricity at a relatively low price. Thanks to their flexibility, they significantly contribute to the stability of the international network; to the follow-up of the daily and seasonal load fluctuations; and to the integration of the intermittent energy sources, notably solar and wind energy. Hydropower also represents an important source of revenue for their owners and in particular for the mountain regions.

Although predictions vary depending on the model, in general water availability is likely to increase across northern Europe and decrease in southern and southeastern Europe over the next several decades (Lehner et al. 2005). How these widespread trends will effect hydropower production depends on specific changes in flow regime and characteristics of existing hydropower development.

G. Ravazzani (✉) · M. Mancini
Department of Civil and Environmental Engineering, Politecnico Di Milano, Piazza Leonardo Da Vinci 32, Milan, Italy
e-mail: giovanni.ravazzani@polimi.it

F. Dalla Valle · G. Galeati
Divisione Generazione Ed Energia Management, ENEL S.p.A., Via Torino 105/E, 30172 Mestre, Italy

T. Mendlik · A. Gobiet
Wegener Center for Climate and Global Change and Institute for Geophysics, Astrophysics, and Meteorology, University of Graz, Graz, Austria

G. Lollino et al. (eds.), *Engineering Geology for Society and Territory – Volume 1*,
DOI: 10.1007/978-3-319-09300-0_2,

The present study aims at quantifying the climate change impacts on hydropower production of the Toce alpine river basin, in Italy, where 18 plants (total installed capacity $\approx$ 470 MW) and 10 reservoirs with a total storage capacity of about 139 million m^3 were analyzed.

2.2 The Toce River Case Study

The Toce watershed is a typical glacial basin with steep hillslopes bounding a narrow valley located mainly in the north Piedmont region of Italy, and partially in Switzerland (10 % of the total area) with a total drainage area of about 1,800 km^2. A total of 14 major dams are located within the Toce watershed, with a total effective storage capacity of about 151 $\times$ 10^6 m^3 (Montaldo et al. 2004).

The hydrographic area involved in the case study represents the upper part of the Toce river catchment. The drainage surface sums up to 691.7 km^2. The altitude ranges from 300 to 4,100 m a.s.l., with an average value of about 1,900 m a.s.l. and 52 % of the catchment area located above 2,000 m a.s.l.. In the considered hydrographic catchment irrigation is not present and drinking water uses are negligible; it follows that reservoirs management can be simulated as completely oriented to hydropower production.

2.2.1 At Site Bias Corrected Climate Scenario Forcings

For meteorological forcing of future scenarios, two different regional climate models (RCMs) are used, namely a REMO (Jacob 2001) and a RegCM3 (Pal et al. 2007) simulation. Both models cover Europe on a 25 $\times$ 25 km^2 grid, cover the same simulation period (1951–2100) and are driven by the same global ocean-atmosphere-coupled model ECHAM5 (Roeckner et at. 2003) using observed greenhouse gas concentrations between 1951 and 2000 and IPCC's greenhouse gas emission scenario A1B between 2001 and 2100. A quantile based error correction approach was used in order to downscale the RCM simulations to point scale as well as to reduce its error characteristics (Themeßl et al. 2012).

2.2.2 The Model of the Hydropower System

The hydropower system has been represented by a network made up with 27 nodes and 64 arcs. Nodes represent intakes and reservoirs; arcs represent rivers, channels, hydropower plants and water volume stored into the reservoirs. Each node is characterized by an inflow time series that describe natural discharges produced by the upstream sub-catchment. The model is a simplified representation of the real hydropower system and not all the existing intakes are represented as a single node; to keep computational burden within acceptable limits, minor intakes have been grouped in a single node.

2.2.3 The Model of the Hydrologic System

In order to simulate continuous streamflow, FEST-WB, a distributed physically based hydrological model was used (Rabuffetti et al. 2008; Corbari et al. 2011; Ravazzani 2013). FEST-WB computes the main processes of the hydrological cycle: evapotranspiration, infiltration, surface runoff, flow routing, subsurface flow and snow and glaciers dynamics. The computation domain is discretized with a mesh of regular square cells (200 m in this application) in each of which water fluxes are calculated at hourly time step.

The FEST-WB model was subjected to a process of calibration and validation by comparison of daily simulated and observed discharge at Candoglia (basin area 1534 km^2) where discharge observations are available from 2000 to 2008. FEST-WB was used to simulate hourly discharge time series scenarios from 2001 to 2050 in 36 sections representative of the hydropower system.

2.3 Results and Discussion

Impacts of climate changes on hydrological processes are assessed by comparing FEST-WB results driven by REMO and RegCM3 for the decade 2041–2050 respect to decade 2001–2010. REMO and RegCM3 simulate increase of temperature equals to 1.3 K and 1.1 K, respectively and increase of mean annual precipitation equals to 13 % and 25 %, respectively. This reflects an increase of evapotranspiration and discharges for all durations of flow duration curves.

Once the model of the hydropower system has been set up, natural inflows to the nodes and energy value index time series have been properly defined, the simulation goal is the definition of the reservoirs management rule that maximize the economic value of the hydropower production using BPMPD solver (http://www.sztaki.hu/~meszaros/bpmpd).

Two groups of simulations were performed at bihourly time step: the first one using 6 h averaged discharge data from 2001 to 2050 evaluated on the basis of the REMO regional climate model outputs, the second group employing discharge data modelled starting from the RegCM3 regional climate scenarios.

To evaluate the impact of climate change on hydropower production and on the operational management of the system a comparison of the simulation results for 3 different periods was carried out:

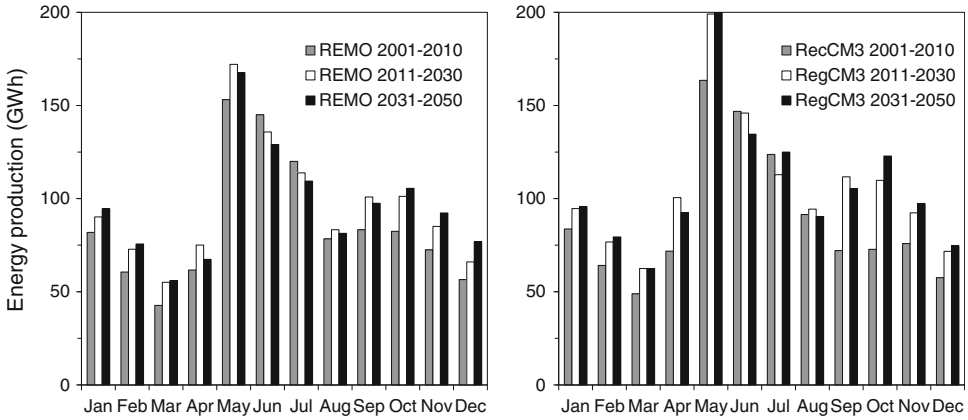

Fig. 2.1 Average Monthly hydropower production evaluated by the simulation model using the discharge dataset built starting from REMO and RegCM3 climatic scenarios

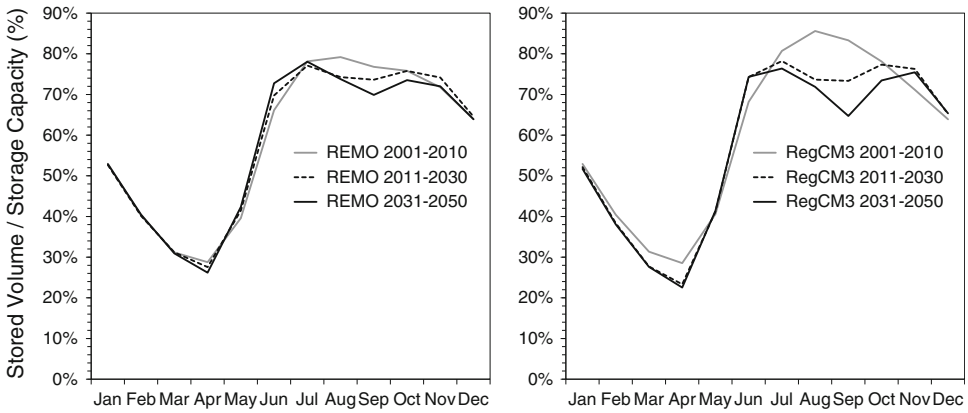

Fig. 2.2 Average monthly stored water volume evaluated by the simulation model using the discharge dataset built starting from REMO and RegCM3 climatic scenarios

- Period A: years from 2001 to 2010 (hereafter "reference period");
- Period B: years from 2011 to 2030;
- Period C: years from 2031 to 2050.

Total hydropower production and water volume stored in reservoirs were compared. Figure 2.1 presents a comparison between the monthly total hydropower system production. Both climatic scenarios highlight a relevant increase in hydropower production: +11 % for REMO dataset and +19 % for RegCM3 dataset. Production increase is expected to be observed in autumn, winter and spring; in summer, expecially in June and July, simulation outputs show a decrease up to −11 % (REMO dataset, June 2031–2050). Analysis of total volume stored in reservoirs allows to investigate possible change in reservoirs management policy (Fig. 2.2). Simulation results show a trend, for both the periods 2011–2030 and 2031–2050, to anticipate the date when the maximum volume of stored water stored has to be reached, which moves from August (reference period) to July (2031–2050). A reduction of maximum water stored may be observed too, as well an increase of reservoir draw down during August and September to prepare empty storage capacity for autumn inflows, which are expected to evidence a relevant increase.

2.4 Conclusions

Assessment of hydropower production of future climate (2031–2050) respect to current climate (2001–2010) showed an increment of production in Autumn, Winter and Spring, and a reduction in June and July.

Significant change in the reservoirs management policy is expected due to anticipation of the date when the maximum volume of stored water has to be reached and an increase of reservoir drawdown during August and September to prepare storage capacity for autumn inflows.

Results of this analysis depend on shift in temperature and precipitation patterns and amount expected for the Toce river case study and cannot be generalized to the whole Alpine region.

Acknowledgements This work was supported by ACQWA EU/FP7 project (grant number 212250) "Assessing Climate impacts on the Quantity and quality of WAter" [link:http://www.acqwa.ch]. We thank ARPA Piemonte for providing meteorological and discharge observations used to calibrate the hydrological model.

References

Beniston M (2004) Climatic change and its impacts. An overview focusing on Switzerland. Kluwer Academic Publishers, Dordrecht/The Netherlands and Boston/USA (now Springer Publishers)

Corbari C, Ravazzani G, Mancini M (2011) A distributed thermodynamic model for energy and mass balance computation: FEST–EWB. Hydrol Process 25(9):1443–1452

Jacob D (2001) A note to the simulation of the annual and inter-annual variability of the water budget over the Baltic Sea drainage basin. Meteorol Atmos Phys 77:61–73

Lehner B, Czisch G, Vassolo S (2005) The impact of global change on the hydropower potential of Europe: a model-based analysis. Energy Policy 33(7):839–855

Montaldo N, Mancini M, Rosso R (2004) Flood hydrograph attenuation induced by a reservoir system: analysis with a distributed rainfall-runoff model. Hydrol Process 18(3):545–563

Pal J.S, Giorgi F, Bi X, Elguindi N, Solmon F, Gao X.J, Francisco R, Zakey A, Winter J, Ashfaq M, Syed F, Bell J, Diffenbaugh N, Karmacharya J, Konare A, Martinez-Castro D, Porfirio da Rocha R, Sloan L, Steiner A (2007) Regional climate modeling for the developing world: the ICTP RegCM3 and RegCNET. Bull Am Meteorol Soc 88:1395–1409

Rabuffetti D, Ravazzani G, Corbari C, Mancini M (2008) Verification of operational quantitative discharge forecast (QDF) for a regional warning system—the AMPHORE case studies in the upper Po River. Nat Hazards Earth Syst Sci 8:161–163

Ravazzani G (2013) MOSAICO, a library for raster based hydrological applications. Comput Geosci 51:1–6

Roeckner E, Baeuml G, Bonaventura L, Brokopf R, Esch M, Giorgetta M, Hagemann S, Kirchner I, Kornblueh L, Manzini E, Rhodin A, Schlese U, Schulzweida U, Tompkins A (2003) The Atmospheric General Circulation Model ECHAM5. Part 1: Model Description, Report 349, Max Planck Institute for Meteorology (MPI), Hamburg

Themeßl MJ, Gobiet A, Heinrich G (2012) Empirical-statistical downscaling and error correction of regional climate models and its impact on the climate change signal. Clim Change 112(2):449–468

Proposal for Climate Change Impact Research in Western Central Andes of Peru

3

Sandra Villacorta, Jose Ubeda, Lucile Tatard and Andrés Diez

Abstract

In this paper an initiative of the Peruvian Geological Survey, INGEMMET, is shown to promote the research on geomorphology and climate change in Peru. The plan is to elaborate geomorphological maps of the Lima Metropolitan Area and iťs watershed headers (Chillon, Rimac and Lurin rivers), in order to generate analytical instruments to achieve the following objectives: (1) Decode the record of climatic changes in landforms. (2) Delimit water reserves stored as ice masses (cryosphere). (3) Recognize the relationship between the geomorphology and the geological hazards which may affect people and their economic activities. (4) Design a methodology that can be extrapolated to others Peruvian regions. To reach this objective, geomorphological mapping will be integrated into a GIS, so the morphoclimatic units and the related genetic processes will be identified. Also, their relative chronologies will be proposed. Then, the absolute dating of key units will be established, to confirm or correct the relative chronologies. The information will be compiled into databases, to be contrasted with other evidences and paleoclimatic proxies. This is intended to produce models of climate evolution, to contribute to the assessment of geological hazards, and the knowledge of current state of cryosphere, including recent trends and future forecasts.

Keywords

Climate change • Glacial geomorphology • Fluvial geomorphology • Lima metropolitan area

3.1 Introduction

Climate change and exceptional phenomena, such as El Niño—Southern Oscillation, ENSO, have been recorded in geomorphological processes related to temperature and precipitation (Ubeda and Palacios 2009). The research of these processes is useful for understanding the geological risks, while their evolution can be evidenced by geoindicators (permafrost, pollen, moraines, river terraces or landslides, etc.). On scales between decades up to a century, these studies provide information of the current impact of climate change and are the basis to develop forecasts on its future evolution (Ubeda 2012). In Western Central Peruvian Andes these researches have great socio-economic implications; because 55 % of Peruvians live on the Pacific slope

S. Villacorta (✉)
Department of Environmental Geology and Geological Hazard, Geological, Mining and Metallurgical Institute, Lima, Peru
e-mail: svillacorta@ingemmet.gob.pe

J. Ubeda
Grupo de Investigación en Geografía Física de Alta Montaña, Madrid, Spain

L. Tatard
ISTerre - OSUG – Universidad de Grenoble, Grenoble, Francia

L. Tatard
Institut pour la Recherche et le Développement (IRD), Montpellier, Francia

A. Diez
Instituto Geológico y Minero de España, Madrid, Spain

G. Lollino et al. (eds.), *Engineering Geology for Society and Territory – Volume 1*,
DOI: 10.1007/978-3-319-09300-0_3,

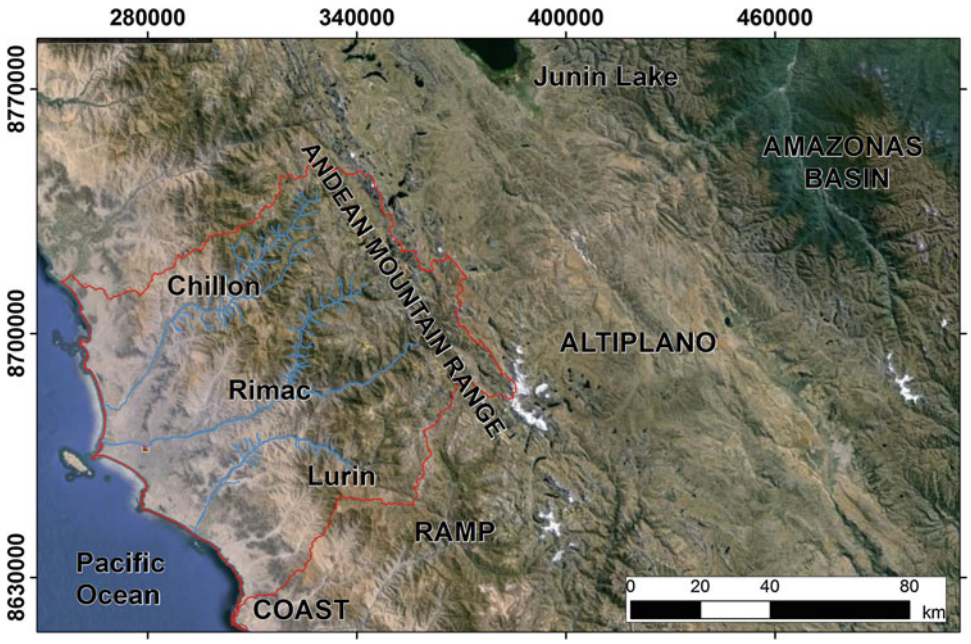

Fig. 3.1 Delimitation of the study area, indicating the location of the macro-geomorphic units, watersheds and the city of Lima

(INEI 2008) and much of its water reserves are stored as ice in the glaciers of the Andes (IPCC 2007). During the last century there has been a strong process of deglatiation, accelerated for the last 30 years (IPCC 2007). It is therefore imperative that the Peruvian authorities take action to mitigate their effects, which should be based on research to design and prioritize policies to be implemented.

In this context the INGEMMET is leading a joint initiative between INGEMMET, the Research Group of High Mountain Physical Geography of the Complutense University of Madrid (GFAM-UCM; Spain), the Institut pour la Recherche et le Développement (IRD, France) and the Geological Survey of Spain (IGME), which seeks to collaborate with the problem explained and promote research on geomorphology and climate change in Peru.

3.2 Background

This research proposal is the sequel to the work begun by INGEMMET between 2008 and 2012 to develop and create the geomorphological map of Peru. During the year 2013 INGEMMET has accorded a strategic alliance with GFAM, the IRD and the IGME to incorporate studies on the evolution of climate during geological past times, as well as research on floods in Peru related to extreme events, such as ENSO.

The Western Central Peruvian Andes have been chosen as the pilot area to test the research methodology to be applied thereafter throughout all the country.

3.3 Pilot Project Area

The study area (Fig. 3.1) is a band trending SW-NE with an area of approximately 100×100 km^2, where the three macro-geomorphic units of the western facade of the Central Andes are represented: the Andean Mountain Range and Altiplano (the Puna plateau), the steep ramp leading down to the ocean (with height differences over 5,000 m) and the Pacific coast.

The landforms present in these macro-geomorphic units allow differentiating, at different scales, five morphoclimatic areas: glacial, periglacial, temperate forest, semi-arid and hyper-arid (Ubeda and Palacios 2009; Ubeda 2011, 2012).

The ramp between the Pacific coast and the Puna plateau is deeply dissected by the drainage network, which may have been regularly fed by the glacial melting of the range for most of the Pleistocene. This has generated a wide range of landforms (Fig. 3.2) related to erosion and river sedimentation, fans, floodplains, river terraces and gullies.

3.4 Methodology

Geomorphological and paleo-hydrological techniques will be used for this purpose, as they have the advantage of extending the periods of observation, measurement and recording of geological past events. Applied to floods, provide information on hydrologic variability and extraordinary floods in time intervals between 100 and 10,000 years (Benito et al. 2004). It is planned to develop

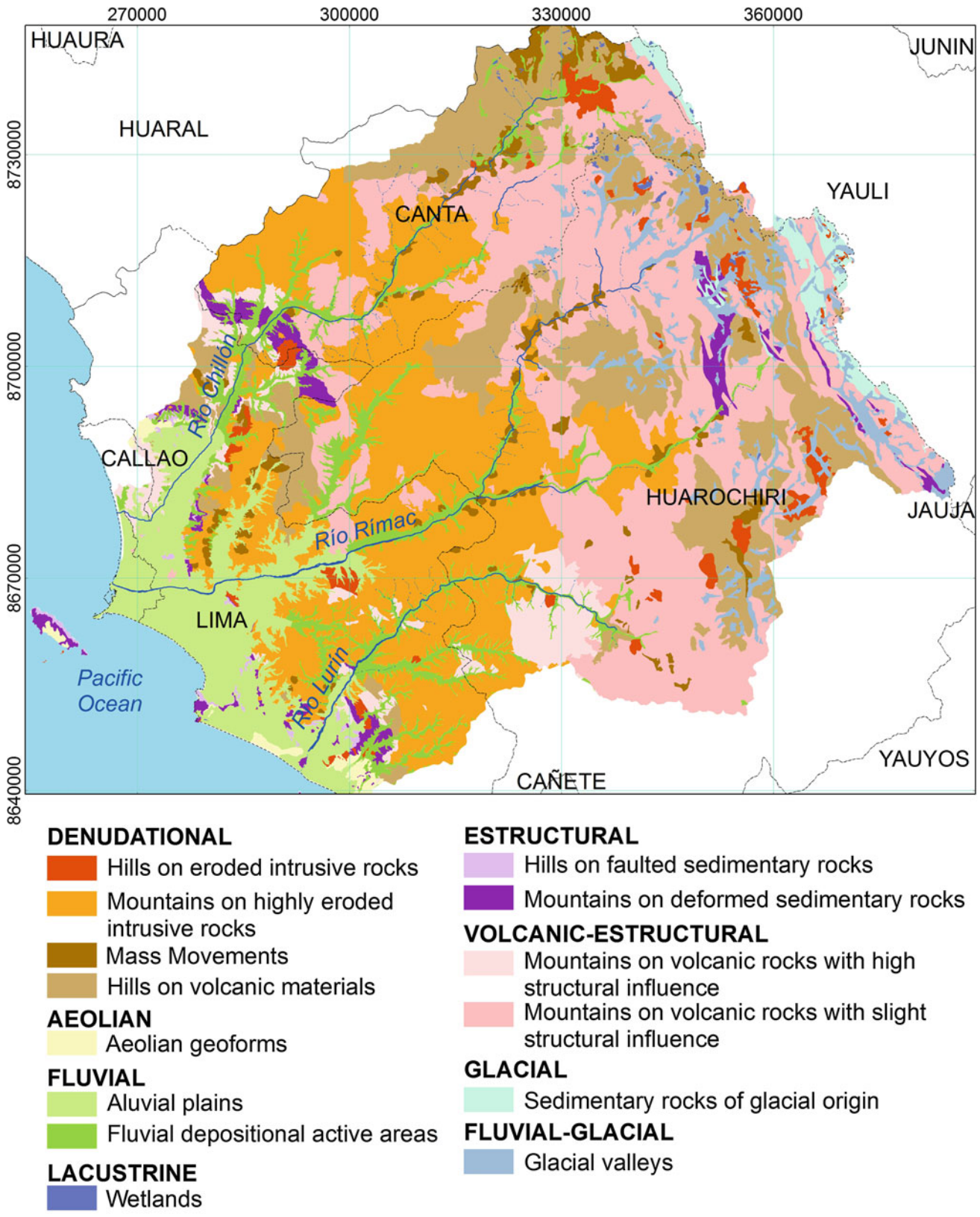

Fig. 3.2 Landforms of the study area (Villacorta et al. 2014)

the following fieldwork: (1) Making of stratigraphic columns, (2) Characterization of landforms and their constituent materials, (3) Sampling for isotopic dating and thermoluminescence, and (4) Installation of data loggers. Whilst the laboratory work will be: (1) Dating of fluvial units by aminoacid racemization (in the Polytechnical University of Madrid), (2) Paleohydrology and dendrogeomorphology (in IGME), and (3) Dating of glacial and periglacial units measuring the isotopic abundance of chlorine-36 on the surface of rocks (in laboratories of the Complutense University of Madrid).

3.5 Expected Results

3.5.1 Geomorphology and Climate Change

- A standardized methodology that can be used in other regions of Peru.
- Geomorphological maps of glacial and fluvial units in the Central Andes of Peru West, with their absolute datings and paleo-climate correlations.
- Forecasts of the evolution during the XXI century of water reserves stored in the mountain cryosphere, testable with the predictions of the expertś group of the Intergovernmental Panel on Climate Change (IPCC 2007).

3.5.2 Geological Hazards

- Flood risk analysis in the Rimac River basin (Lima), with periods of relapse and numerical simulations of avenues calibrated with geomorphological evidence of actual events.
- Scientific based recommendations to apply in planning policies to mitigate the effects of a more than expected reduction in water availability and the risks related to floods and landslides.

3.6 Conclusions

The project aims to encourage research on Geomorphology and Climate Change in Peru, as well as to contribute to the investigation of climate change scenarios related to the occurrence of disasters, a subject which has not yet been analyzed conveniently in Peru.

The geomorphological map availability will more effectively address the assessment and modeling of geological hazards affecting population and their economic activities.

Although the initiative is still in its early stages of development, these interagency joint efforts have begun to generate useful tools for planning, disaster prevention and investigation of the impact of Climate Change on the cryosphere. The expected final products are geomorphological maps and numerical modeling of geological hazards that will contribute to the management and territorial planning in Peru. It is expected to obtain these results by the year 2015.

Finally, it is important to note that the assessment of geological hazards, not only involves analyzing threats, but also the causes of the increase of the vulnerability of populations. Therefore, an interdisciplinary effort is completely needed to articulate the different actors. For this reason the proposal is opened for cooperation to any institution wishing to participate and work together towards the fulfillment of the objectives of this project.

References

Benito G, Díez-Herrero A, Fernández de Villalta M (2004) Flood response to NAO and solar activity in the Tagus Basin (Cental Spain) over the last millennium. Climatic Change 66:27–28

INEI (2008) National surveys 2007: XI for population and VI for housing. Growth Population Distrib 2007, p 44 (First results. Peru)

IPCC (2007) Contribution of working groups I, II and III to the fourth assessment report of the intergovernmental panel on climate change. In: Pachauri RK, Reisinger A (eds) Geneva, Switzerland, p 104

Ubeda J, Palacios D (2009) The climate of the pacific slope of the central andes and its geomorphic implications, vol 20. Space and Development, Center for Applied Geography Research, Pontifical Catholic University of Peru, pp 31–58

Ubeda J (2011) The impact of climate change in the glaciers of nevado coropuna volcanic complex (western cordillera of the Andes, Southern Peru), Universidad Complutense de Madrid, Madrid. p 558

Ubeda J (2012) Climate change and the glaciers of Nevado Coropuna (southern Peru). Spanish Academic Publisher, p 576

Villacorta S, Núñez S, Úbeda J, Tatard L, Pari W, Fidel L (2014) Geological hazard of the area of lima and callao region, in edn. Boletin Serie C. INGEMMET, Lima (Perú), p 108 (In press)

Response of Alpine Glaciers in North-Western Italian Alps to Different Climate Change Scenarios

4

Riccardo Bonanno, Christian Ronchi, Barbara Cagnazzi and Antonello Provenzale

Abstract

We analyse long time series of annual snout positions of several valley glaciers in the northwestern Italian Alps, together with a high-resolution gridded dataset of temperature and precipitation available for the last 50 years. Glacier snout fluctuations are on average negative during this time span, albeit with a period of glacier advance between about 1970 and 1990. To determine which climatic variables best correlate with glacier snout fluctuations, we consider a large set of seasonal predictors, based on our climatic dataset, and determine the most significant drivers by a stepwise regression technique. This in-depth screening indicates that the average glacier snout fluctuations strongly respond to summer temperature and winter precipitation variations, with a delay of 5 and 10 years respectively. Snout fluctuations display also a significant (albeit weak) response to concurrent (same year) spring temperature and precipitation conditions. A linear regressive model based on these four climatic variables explains up to 93 % of the variance. When employed for out-of-sample projections, the empirical model displays high prediction skill, and it is thus used to estimate the average glacier response to different climate change scenarios (RCP4.5, RCP8.5, A1B), using both global and regional climate models. In all cases, our linear regressive model display an accelerated retreat for the glaciers of this region. By 2050, the retreat is estimated to be between about 300 and 400 m with respect to the current position. Glacier regression is more intense for the RCP8.5 and A1B scenarios, as it could be expected from the higher severity of these emission pathways.

Keywords

Glacier retreat • Climate change • Water resources • Future scenarios • EC earth

4.1 Introduction

In the densely populated Alpine regions, glaciers represent an important source of freshwater and a significant component of tourism economy and hydro-electric power production. The shrinking of glaciers inevitably leads to a reduction of the frozen water supply they are able to store. This is one of the reasons why it is important to model and quantify, over time, the response of Alpine glaciers to different climate change scenarios.

The aim of this work is the study of the average response of a set of 14 glaciers in the north-western Italian Alps to climate variability during the last 50 years and to future climate change scenarios.

The method adopted here consists in the use of a lagged-linear empirical stochastic model, in which glacier snout variations depend on the fluctuations in temperature and precipitation. Annual fluctuations of glacier snout positions are used as a substitute for the quantitative measurement of glacier mass balance (proxy data) whereas temperature and

R. Bonanno (✉) · C. Ronchi · B. Cagnazzi
Arpa Piemonte, Via Pio VII No 9, 10135 Turin, Italy
e-mail: r.bonanno@arpa.piemonte.it

A. Provenzale
Institute of Atmospheric Sciences and Climate - CNR, 10133 Turin, Italy

G. Lollino et al. (eds.), *Engineering Geology for Society and Territory – Volume 1*,
DOI: 10.1007/978-3-319-09300-0_4,

precipitation are used as proxies of the whole set of climate parameters which can influence glacier dynamics.

The model is then used to estimate the average response of Alpine glaciers in different climate change scenarios, assuming that the selected predictors are suitable also for future climate conditions.

4.2 Available Data: Snout Position and Climatic Data

Glacier snout data are collected by the Comitato Glaciologico Italiano—Consiglio Nazionale delle Ricerche (GCI) and regularly published in the GCI Bulletin (http://www.glaciologia.it/). All snout fluctuation data considered here cover the period 1958–2009, while the starting date varies with the individual glaciers. Almost all values of average snout fluctuation for the glaciers considered are negative, confirming the overall retreat of Alpine glaciers in this area and the homogeneity of the regional behavior of large glaciers in the northwestern Italian Alps (Calmanti et al. 2007). This homogeneity allows for averaging the standardized time series of the individual glaciers, to obtain a signal describing the regional glacier behavior in the period 1958–2009.

As regards the records of temperature and precipitation, they are available in the study area in the period 1958–2009. The observations have been distributed over a predefined regular grid by means of an Optimal Interpolation technique (Ronchi et al. 2008).

4.3 Construction of an Empirical Model for the Average Glacier Response

From the precipitation and temperature data, we calculated the standardized monthly averages over the area that includes Piedmont and Valle d'Aosta. The averages were then grouped in periods of varying duration, resulting in seasonal values. Using precipitation as an example, we considered $P(1–3)$, $P(1–4)$, $P(1–5)$, $P(1–6)$, $P(2–4)$, $P(2–5)$, $P(2–6)$, $P(2–7)$, $P(3–5)$ and so on.

Glacier snout variations respond to climatic fluctuations with a time delay from years to tens of years (Oerlemans 2001). We estimate the value of the time lag between climatic variables and glacier snout response by systematically examining the lagged cross-correlations between individual climatic variables and snout fluctuations. For each predictors, we thus calculated the cross-correlation with the series of average snout fluctuations, determining for each variable the time delay (in years) that maximizes the correlation between the glacial snout and the meteorological variables. Snout fluctuations turn out to be positively correlated with precipitation and negatively with temperature.

Table 4.1 Model parameter estimates obtained from the screening of the precipitation and temperature variables

Parameter	Estimated value a	95 % prediction bounds	$P(a^r > \|a\|)$
a_0	0.1018	(0.0651, 0.1384)	0.0
$a_{P(10–3)}$	0.5714	(0.0651, 0.7728)	0.0
$a_{P(3–5)}$	0.1835	(−0.0035, 0.3707)	0.002
$a_{T(2–5)}$	−0.2732	(−0.4946, −0.0518)	0.0
$a_{T(6–8)}$	−0.4828	(−0.6633, −0.3023)	0.0
$R^2 = 0.93$	*Adjusted* $R^2 = 0.93$	AIC = −185	$\sigma_r = RMSE = 0.093$

The first column indicates the predictor, the second column reports the value of the parameter obtained by fitting the linear model to the whole data set, the third column reports the 95 % prediction bounds and the fourth column reports the probability that the parameter estimate from a random reordering of the data is larger, in absolute value, than the original parameter. Probabilities have been estimated from a total of 1000 random reorderings of the time series. In the bottom of the table, R^2 , Adjusted R^2 , AIC and RMSE $= \sigma_r$ are shown

By screening the predictors with appropriate statistical techniques (such as backward stepwise regression and cross-validation for out of sample prediction), we obtained a simple lagged-linear empirical stochastic model that is able to reproduce past snout fluctuations. Moreover, the cross-validation shows that the model is reliable for estimating glacier retreat in north-western Italy also in the near future.

The selected model depends only on four predictors: summer temperature $T_5(6–8)$ and winter precipitation $P_{10}(10–3)$ with time delay of 5 and 10 years respectively, and spring temperature and precipitation $P_0(3–5)$, $T_0(2–5)$ in the year of the snout fluctuation. These predictors are meaningful in terms of glacier physics: summer temperature and winter precipitation correspond to the ablation period and to the accumulation period respectively, whereas spring temperature and precipitation can change the surface glacier albedo in summer ablation period accelerating/slowing down the ice melting. The parameter values for this model are reported in Table 4.1.

4.4 Impact of Climate Change on the Glaciers of North-Western Alps: RCPs and SRES A1B Scenarios

The global climate change scenarios considered here are produced by the EC-Earth model, a recent Earth System model developed by a Consortium of European research Institutions (Hazeleger 2012, see also http://ecearth.knmi.nl/).

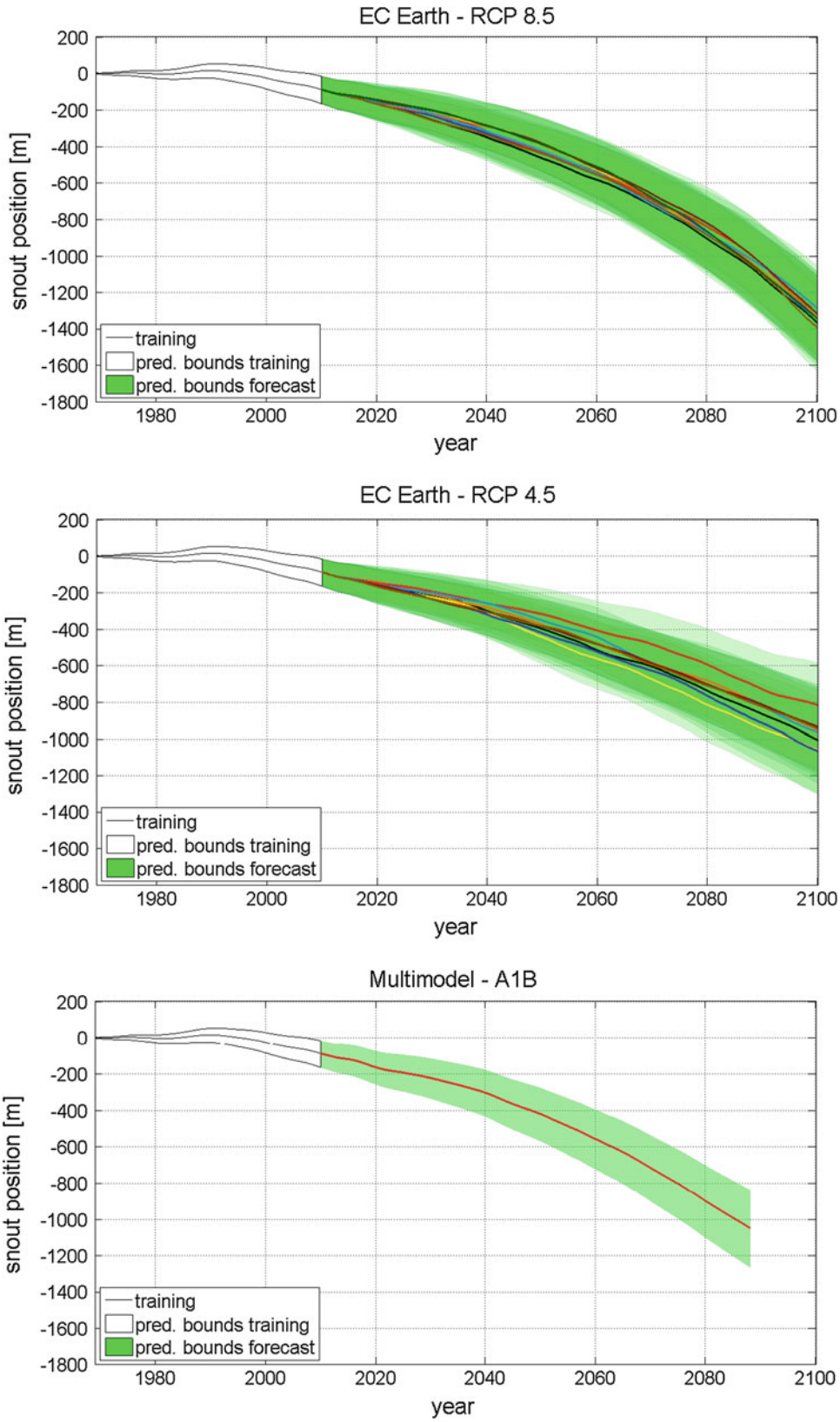

Fig. 4.1 Cumulated snout positions over the period 1958–2100. For each climate run, 1,000 realizations of the glacier models were generated to provide an estimate of the uncertainty bands, defined by the 5th and 95th percentiles of the distribution of values produced by the glacier model. The first portion with white uncertainty bounds refers to the training period 1958–2009 used to determine the parameters of the glacier model, the second portion with *green* uncertainty bounds refers to the simulation of the snout variations over the period 2010–2100 (or 2088) from the climate scenarios. *Upper panel*: EC-Earth for RCP8.5; *middle panel*: EC-Earth for RCP4.5; *lower panel*: Multimodel SuperEnsemble for A1B. The *colored curves* refer to the average of the glacier model runs; for each EC-Earth scenario, eight different climate simulations with the same model are used

For EC-Earth, climate change scenarios have been simulated using the recently developed Representative Concentration Pathways (RCP), see Moss et al. (2010). For this work, we considered the RCP4.5 and RCP8.5 scenarios. One advantage of the EC-Earth Consortium is that, in the framework of the international program CMIP5, several members of an ensemble of climatic simulations have been made available.

For our study, we also used the outputs of several Regional Climate Models from the ENSEMBLES project for the SRES A1B scenario runs which are individually weighted by an adequate set of weights determined by comparison with observations during a suitably defined training period. For more details about the Multimodel SuperEnsemble technique used to aggregate the RCM outputs see Cane et al. (2012).

For the time series of temperature and precipitation obtained by this technique, bias correction is not necessary as the weights applied to the individual model outputs are determined explicitly to reproduce the observations in the training period 1961–2009 and the model average is imposed to be equal to that of the observations. In the case of EC Earth runs, bias correction was necessary only for temperature and not for precipitation. Figure 4.1 shows an estimate of the cumulated snout positions in the period 1958–2100 for the three scenarios.

In all cases, the glacier model indicates a strong retreat of the glacier snouts in the northwestern Italian Alps, with retreats between about 300 and 400 m with respect to the current position by 2050. In general, the RCP8.5 and A1B Multimodel scenarios indicate slightly larger retreats than RCP4.5, as could be expected from the different severity of these emission pathways.

As a word of caution, we note that for strong glaciers retreat the assumption of linear response to climate forcing may be invalid and when the glaciers shrink to smaller lengths, the model is not applicable, so it cannot be used to copy glaciers behavior while they are disappearing.

References

Calmanti S, Motta L, Turco M, Provenzale A (2007) Impact of climate variability on Alpine glaciers in Northwestern Italy. Int J Climatol 27:2041–2053

Cane D, Barbarino S, Renier LA, Ronchi C (2012) Regional climate models downscaling in the Alpine area with multimodel superensemble. Hydrol Earth Syst Sci Discuss 9:9425–9454

Hazeleger W (2012) EC-Earth v2.2: description and validation of a new seamless earth system prediction model. Clim Dyn 39: 2611–2629

Moss RH et al (2010) The next generation of scenarios for climate change research and assessment. Nature 463:747–756

Oerlemans J (2001) Glaciers and climate change. Balkema Publishers, Lisse

Ronchi C, De Luigi C, Ciccarelli N, Loglisci N (2008) Development of a daily gridded climatological air temperature dataset based on a optimal interpolation of ERA-40 reanalysis downscaling and a local high resolution thermometers network. Dissertation, 8th EMS Annual Meeting and 7th European Conference on Applied Climatology, 2008, Amsterdam, The Netherlands

Metamorphic CO_2 Degassing in the Active Himalayan Orogen: Exploring the Influence of Orogenic Activity on the Long-Term Global Climate Changes

5

Franco Rolfo, Chiara Groppo, Pietro Mosca, Simona Ferrando, Emanuele Costa and Krishna P. Kaphle

Abstract

A number of studies suggest that mountain ranges have strong impact on the global carbon cycle; metamorphic degassing from active collisional orogens supplies a significant fraction of the global solid-Earth derived CO_2 to the atmosphere, thus playing a fundamental role even in today's Earth carbon cycle. The Himalayan belt, a major collisional orogen still active today, is a likely candidate for the production of a large amount of metamorphic CO_2 that may have caused changes in long-term climate of the past, present and near future. Large metamorphic CO_2 fluxes are facilitated by rapid prograde metamorphism of big volumes of impure carbonate rocks coupled with facile escape of CO_2 to the Earth's surface. So far, the incomplete knowledge of the nature, magnitude and distribution of the CO_2-producing processes hampered a reliable quantitative modeling of metamorphic CO_2 fluxes from the Himalayan belt. This study, integrated in the framework of the Ev-K2-CNR SHARE (Stations at High Altitude for Research on the Environment) Project, focuses on the metamorphic decarbonation processes occurring during the Himalayan collision. We hereby present preliminary results focusing on the distribution of different types of metacarbonate rocks in the Eastern Himalaya, their petrographic description and the first reported petrological data about the nature of the CO_2-producing reactions in garnet-bearing calc-silicate rocks. These results represent a contribution toward a better understanding of the influence exerted by orogenic processes on climatic changes at global scale.

Keywords

Orogenic CO_2 • Climate changes • Decarbonation processes • Himalaya • Metacarbonate rocks

5.1 Introduction and Aim of the Study

Metamorphic degassing from active collisional orogens supplies a significant amount of CO_2 to the atmosphere, playing a fundamental role in the long-term (>1 Ma) global carbon cycle (e.g. Kerrick and Caldeira 1993; Selverstone and Gutzler 1993; Bickle 1996; Berner 1999; Gaillardet and Galy 2008; Evans 2011). The Himalaya is the most prominent collisional orogen on Earth, where tectonic and erosional processes are still active today. Therefore, it is a likely candidate for the production of a large amount of metamorphic CO_2 that may have caused changes in long-term climate of the past and that may still influence the

F. Rolfo (✉) · C. Groppo · S. Ferrando · E. Costa
Department of Earth Sciences, University of Torino, 10125 Turin, Italy
e-mail: franco.rolfo@unito.it

F. Rolfo · P. Mosca
IGG – CNR, 10125 Turin, Italy

K.P. Kaphle
Nepal Geological Society, Kathmandu, Nepal

G. Lollino et al. (eds.), *Engineering Geology for Society and Territory – Volume 1*,
DOI: 10.1007/978-3-319-09300-0_5,

atmospheric composition in the near future (Gaillardet and Galy 2008). Large metamorphic CO_2 fluxes should have been (and should be) facilitated by rapid metamorphism of large volumes of metacarbonate rocks, coupled with facile escape of CO_2 to the Earth's surface. The nature and magnitude of the metamorphic CO_2 cycle in Himalaya, however, is still poorly known. This study, integrated since 2012 in the framework of the Ev-K2-CNR SHARE (Stations at High Altitude for Research on the Environment) Project, focuses on the metamorphic decarbonation processes occurring during the Himalayan collision. Fieldwork activity is combined with petrographic, petrologic, structural, geochronological, geochemical and fluid inclusion studies with the aims of clarifying: (i) abundance and types of CO_2-source rocks, (ii) nature and rate of CO_2-producing reactions, (iii) nature and composition of the released CO_2-rich fluids, (iv) nature and distribution of the CO_2 escape-paths toward the Earth's surface, and (v) chronology of metamorphic CO_2-producing reactions occurred in the Himalayas at different structural levels and at different times. We hereby present a preliminary sketch map reporting the distribution of the different types of metacarbonate rocks in the Eastern Himalaya. The first petrological results on the nature of the CO_2-producing reactions in garnet-bearing calc-silicate rocks are summarized and discussed in the global perspective of the orogenic CO_2-cycle. These results represent a contribution toward a better understanding of the influence exerted by the orogenic processes on climatic changes at global scale.

5.2 Metacarbonate Rocks in Eastern Himalaya

5.2.1 Field Occurrences

In the eastern Himalaya, calc-silicate rocks are widespread in the lower and upper structural levels of the Greater Himalayan Sequence (GHS) (e.g. Goscombe et al. 2006), but they have received so far little notice. Field data acquired in more than 10 years in central-eastern Nepal and Sikkim allowed us to distinguish two different modes of occurrence (Fig. 5.1): (i) in the lower portion of the GHS (GHS-L), calc-silicate rocks generally occur as decimetre to metre-thick levels or boudins (Fig. 5.2a, b) within medium- to high-grade, locally anatectic, staurolite- and/or kyanite-bearing metapelites (e.g. Groppo et al. 2009; Mosca et al. 2012); (ii) structurally upward (GHS-U), calc-silicate rocks are hosted in anatectic kyanite-sillimanite- bearing gneisses (i.e. Barun Gneiss, see Groppo et al. 2012) and often occur as tens to hundreds of meter thick, folded or boudinated, levels occasionally associated to layers of impure marbles (Fig. 5.2c, d). The transition between the hosting paragneiss and the calc-silicate granofels is generally gradual and is characterized by the progressive disappearance of biotite, the appearance of clinopyroxene and the modal increase of plagioclase. A banded structure is locally observed in the calc-silicate rocks, defined by the different modal proportion of the rock-forming minerals in adjacent layers. This suggest that calc-silicate rocks derive from former marly intercalations within a thick sedimentary sequence.

5.2.2 Petrography

The studied samples have granofelsic structure, and sometimes show evidence of a brittle- to ductile deformation resulting in a local grain size reduction. Mineral assemblages are systematically different in the GHS-L and GHS-U, respectively.

5.2.2.1 Garnet-Bearing Assemblages (GHS-L)

The equilibrium assemblage consists of plagioclase + clinopyroxene + quartz + garnet ± zoisite. Garnet is locally very abundant and it is often intergrown with quartz (Fig. 5.3a, b). Microstructural evidence suggest that garnet grew at the expense of zoisite, clinopyroxene and calcite, the latter being only locally observed as inclusion in garnet. Coarse-grained graphite is locally very abundant and it has been interpreted as precipitated from a H_2O-CO_2 fluid released through decarbonation reactions during prograde and/or early retrograde metamorphic evolution (Groppo et al. 2013). Titanite and apatite are ubiquitous. Thin layers of phlogopite + white mica impure marbles are only occasionally associated to these calc-silicate rocks.

5.2.2.2 K-Feldspar + Scapolite Assemblages (GHS-U)

Calc-silicate rocks from the GHS-U consist of K-feldspar + clinopyroxene + quartz ± scapolite ± calcite, and later plagioclase, epidote, green amphibole and interstitial carbonates (Fig. 5.3c, d). Relict biotite often occurs within clinopyroxene and/or is replaced by K-feldspar. Clinopyroxene is often partially replaced by later green Ca-amphibole ± epidote ± calcite, whereas scapolite is locally partially replaced by fine-grained dusty aggregates of plagioclase + calcite and/or it is overgrown by coarse-grained epidote. In addition to the ubiquitous titanite, a strongly pleochroic allanite and a bluish to colorless tourmaline locally occur, whereas graphite is always absent. The decimetric to metric levels of marbles often intercalated with these calc-silicate granofels are characterized by the same mineral assemblage, but in different modal proportions.

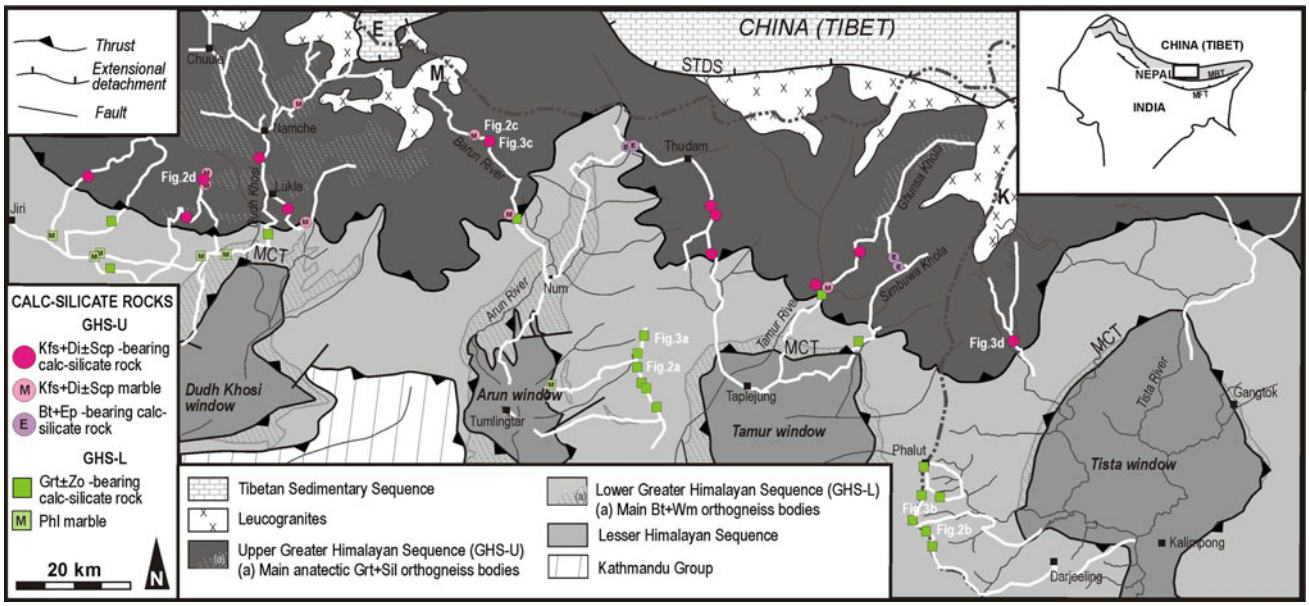

Fig. 5.1 Simplified geological map of the central-eastern sector of the Himalayan belt (modified from Goscombe et al. 2006; Dasgupta et al. 2004; Mosca et al. 2012, 2013) showing sample locations (*squares*: Grt + Zo calc-silicate assemblages and Phl marbles of the GHS-L; *circles*: Kfs + Di + Scp calc-silicate rocks and marbles of the GHS-U). *White lines* are the geotraverses investigated since 2004. The *double-dashed grey line* is the approximate political boundary between Nepal to the south, west, China (Tibet) to the north, India (Sikkim) to the east. MCT: Main Central Thrust; STDS: South Tibetan Detachment System; E: Everest, K: Kangchenjunga, M: Makalu. Inset shows the location of the study area (*black rectangle*) in the framework of the Himalayan chain. The *grey* shaded belt approximates the location of the Higher Himalayan Crystallines. MFT: Main Frontal Thrust; MBT: Main Boundary Thrust

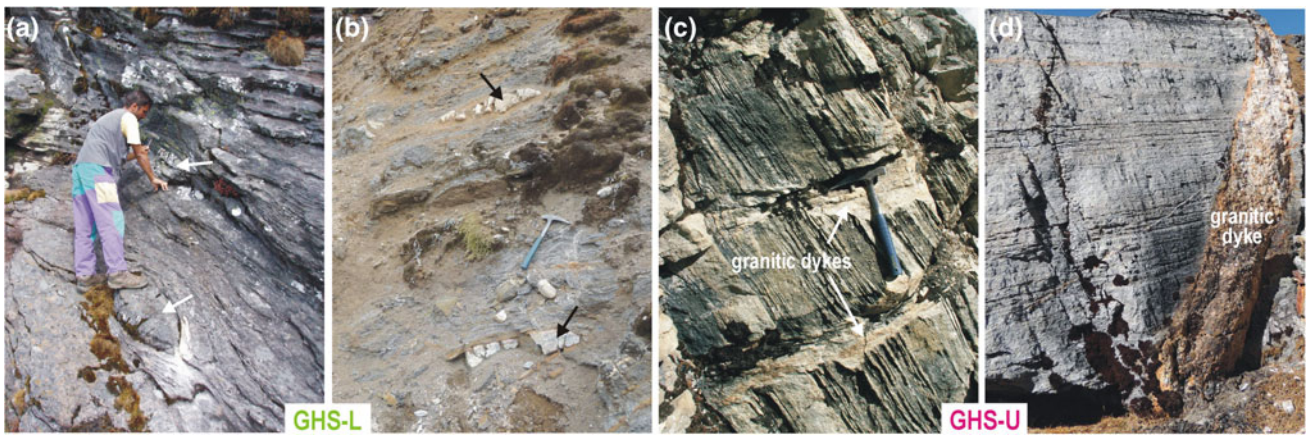

Fig. 5.2 Field occurrence of calc-silicate rocks from the GHS-L (**a, b**) and GHS-U (**c, d**). The *arrows* in **a** and **b** indicate the calc-silicate boudins

5.3 CO_2-Producing Processes in Garnet-Bearing Assemblages

The nature of the CO_2-producing reactions in the garnet-bearing calc-silicate rocks from the GHS-L has been petrologically investigated in the CFAS-CO_2-H_2O system using activity-corrected P-T phase diagrams at fixed fluid composition, isobaric T-X(CO_2) phase diagram sections, and phase diagram projections in which fluid composition is not explicitly constrained (Groppo et al. 2013).

The petrological results allowed to define the P-T-X_{fluid} regime during the metamorphic evolution of the studied calc-silicate rocks. A prograde heating up to peak-T of ca. 800° C (at about 10–11 kbar) involved the growth of grossular-rich garnet ($Grs_{67–81}$) in equilibrium with quartz at the expenses of zoisite, clinopyroxene and calcite; this

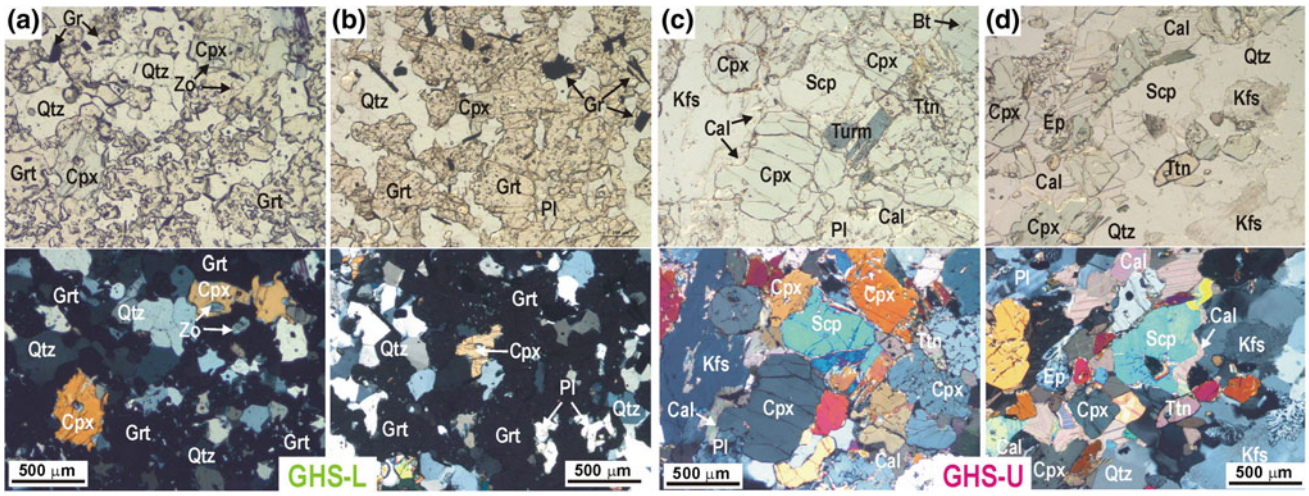

Fig. 5.3 Representative microstructures of calc-silicate granofels from the GHS-L (**a, b**) and GHS-U (**c, d**). *Top*: plane polarized light. *Bottom*: crossed polarized light

reaction released a CO_2-rich fluid ($XCO_2 = 0.20–0.44$). A grossular-rich garnet ($Grs_{67–76}$) additionally grew in equilibrium with plagioclase and quartz during either prograde heating or early decompression. Also this second reaction released a CO_2-rich fluid, with approximately the same composition ($XCO_2 = 0.30–0.44$) as that released through the first reaction. It follows that the amount of CO_2 released during garnet growth increases with the increase in grossular component of garnet (Groppo et al. 2013). The study of primary and secondary carbonic and aqueo-carbonic fluid inclusions occurring in quartz, plagioclase, clinopyroxene and, possibly, garnet and calcite will provide direct constrains on nature and composition of the involved CO_2-rich fluids.

Our results also demonstrate that the studied calc-silicate rocks behaved as a closed-system during their prograde and early retrograde evolution, although their volume abundance within the hosting paragneiss is low. In such a closed system, the CO_2-rich fluid released during prograde and early retrograde evolution induced the hydration of the adjacent silicates (mainly plagioclase and clinopyroxene); these hydration reactions, depleting the fluid in H_2O (i.e. enriching the fluid in carbon) triggered the precipitation of graphite.

5.4 Conclusions

In the eastern Himalaya, calc-silicate rocks are widespread in the lower and upper structural levels of the GHS. From field data and petrographic observations, two main calc-silicate assemblages have been recognized, reflecting differences in the protolith composition: garnet + zoisite assemblages in the GHS-L, and K-feldspar + scapolite assemblages in the GHS-U. Our preliminary petrologic study (Groppo et al. 2013) demonstrates that calc-silicate rocks of appropriate composition may act as CO_2-source during prograde heating and/or early decompression, releasing internal-derived CO_2-rich fluids through garnet-forming reactions. However, if the system remains closed, fluid-rock interactions may induce hydration of the calc-silicate assemblages and the "in situ" graphite precipitation, thereby removing carbon from the fluid. The interplay between these two contrasting processes—i.e. production of metamorphic CO_2-rich fluids versus carbon sequestration through graphite precipitation—must be taken in account when dealing with a global estimate of the role exerted by decarbonation processes on the orogenic CO_2-cycle.

References

Berner RA (1999) A new look at the long-term carbon cycle. GSA Today 9(11):1–6

Bickle MJ (1996) Metamorphic decarbonation, silicate weathering and the long-term carbon cycle. Terra Nova 8:270–276

Dasgupta S, Ganguly J, Neogi S (2004) Inverted metamorphic sequence in the Sikkim Himalayas: crystallization history, P–T gradient and implications. J metamorphic Geol 22:395–412

Evans KA (2011) Metamorphic carbon fluxes: how much and how fast? Geology 39:95–96

Gaillardet J, Galy A (2008) Himalaya-carbon sink or source? Science 320:1727–1728

Goscombe B, Gray D, Hand M (2006) Crustal architecture of the Himalayan metamorphic front in eastern Nepal. Gondwana Res 10:232–255

Groppo C, Rolfo F, Lombardo B (2009) P-T evolution across the Main Central Thrust Zone (Eastern Nepal): hidden discontinuities revealed by petrology. J Petrol 50:1149–1180

Groppo C, Rolfo F, Indares A (2012) Partial melting in the Higher Himalayan Crystallines of Eastern Nepal: the effect of decompression and implications for the "channel flow" model. J Petrol 53:1057–1088

Groppo C, Rolfo F, Castelli D, Connolly JAD (2013) Metamorphic CO_2 production from calc-silicate rocks via garnet-forming reactions in the CFAS-H_2O-CO_2 system. Contrib Mineral Petrol 166:1655–1675

Kerrick DM, Caldeira K (1993) Paleoatmospheric consequences of CO_2 released during early Cenozoic regional metamorphism in the Tethyan orogen. Chem Geol 108:201–230

Mosca P, Groppo C, Rolfo F (2012) Structural and metamorphic features of the Main Central Thrust Zone and its contiguous domains in the eastern Nepalese Himalaya. J Virtual Expl Electronic Edition 41, paper 2

Mosca P, Groppo C, Rolfo F (2013) Main geological features of the Rolwaling-Khumbu Himal between the Khimti Khola and Dudh Khosi valleys (eastern-central Nepal Himalaya). Rend Online Soc Geol It 29:112–115

Selverstone J, Gutzler DS (1993) Post-125 Ma carbon storage associated with continent-continent collision. Geology 21:885–888

Effects of Dust Deposition on Glacier Ablation and Runoff at the Pascua-Lama Mining Project, Chile and Argentina

6

Lukas U. Arenson, Matthias Jakob and Pablo Wainstein

Abstract

Dust deposition on surficial ice bodies is common in many areas around the world. In the high and arid northern Chilean and Argentine Andes, the public fears the dust generated by mining activities would increase ice ablation and thus decrease downstream water availability. This fear is based on a poor understanding of the complex and non-linear interaction between dust and glacier ablation as well as the uncertainties about relative contribution of glacier containing watersheds to total runoff at the point of water use. The focus of this contribution is to assess impacts to down gradient water users resulting from increases in ablation due to dust. Depending on the thickness, type, frequency of deposition and concentration of the dust on the ice surface, a net increase or decrease in ice ablation may occur. While a thin dust cover reduces the surface albedo and hence increases ablation, a thicker cover increasingly acts as thermal insulation, thus reducing ice ablation and increasing the glacier's longevity. Data from literature indicate that at less than 1 mm dust thickness ablation rates peak, resulting in ablation increases between 20 and 400 %. Field ablation tests and numerical dust distribution models for three different scenarios demonstrate that for the Andean site investigated, the downstream hydrological effects of mining-generated dust on glaciers and glacierets, at the first point of agricultural water use, are likely less than half a percent of the annual average river flow. This is largely due to the very small percent of glacial coverage upstream of the first water use point and is well below the local hydrological natural variability that is primarily driven by El Niño events.

Keywords

Andean glacier • Ablation • Dust • Environmental impact

6.1 Introduction

Fine mineral particles, or dust and soot, have long been identified as an agent to alter glacial ablation rates via changes in albedo and the thermal conductivity of snow and ice (Kulkarni et al. 2013). The layering of dust in ice cores has been observed worldwide, and depending on the seasonality of strong winds, eolian dust deposits can be used to date glacier ice (Vimeux et al. 2009). In tropical and subtropical glaciers such as those in the high and arid Andes of South America, dust further affects the glacier surface as it

L.U. Arenson (✉) · M. Jakob
BGC Engineering Inc., Vancouver, BC, Canada
e-mail: larenson@bgcengineering.ca

M. Jakob
e-mail: mjakob@bgcengineering.ca

P. Wainstein
BGC Engineering Inc., Calgary, AB, Canada
e-mail: pwainstein@bgcengineering.ca

G. Lollino et al. (eds.), *Engineering Geology for Society and Territory – Volume 1*,
DOI: 10.1007/978-3-319-09300-0_6,

Fig. 6.1 Penitentes and dust collector at Toro 1 Glaciaret (*left*), and eolian dust deposition observed for Esperanza Glaciaret (*right*). Photos provided by Barrick

changes the growth of so-called penitentes or pilgrim's snow (Rabatel et al. 2011). Figure 6.1 shows the natural, eaolian dust deposition and the formation of penitentes on the glacier surface at two tropical glaciers located in the area used for this study.

In this study, the prime motivation for determining the effects of dust on ablation and ultimately runoff, is to investigate the perception that mining operations create dust, which are thought to always augment natural ablation rates and therefore, lead to a decrease in the quantity and a change in the seasonality of runoff.

6.2 Background

Dust on glaciers can reduce the surface albedo, resulting in increased surface temperatures and melt rates above those without dust. However, melt rates strongly depend on the thermal conductivity of the ice or snow and the thickness of the dust cover as it may also thermally insulate the ice. At a critical thickness, the dust layer begins to protect the underlying ice or snow, leading to reductions in ablation (e.g., Mattson et al. 1993). Changes in dust layer thickness also herald changes in sublimation rates, principally due to the reduction of wind-enhanced sublimation. The effects of dust have been summarized in Fig. 6.2 from a global literature search and allow the broad background conclusion that the critical dust thickness, which is the thickness of a dust layer at which the ablation is similar to one of the uncovered glacier, varies between 4 and 40 mm and that the maximum possible ablation changes vary between 20 and 400 %. The majority of studies on the effects of ablation changes on glaciers have focused on thicker debris covers rather than thin dust layers. Despite this limitation, lessons learned from such studies can be applied to thin dust layers on ice.

6.3 Methods and Study Area

6.3.1 Study Area

Barrick Gold Corporation is currently developing their open pit gold mining project at Pascua Lama, located in the central Andes straddling the international border between Chile and Argentina. Because of the proximity of the project to glaciers and glacierets, the impact of dust generated by the mine development and operation on the ice ablation behavior is a concern. As part of a comprehensive glacier monitoring program, several studies have been and are currently being conducted to investigate the potential changes in ablation due to dust deposition. The project is located in the Atacama Region at about 29.3 °S/70.13 °W with ice bodies located at elevations between 4,800 and 5,400 masl. Glaciers are within an area underlain by permafrost and are thus cold-based, i.e. frozen at their base. Vegetation cover is virtually absent above 3,800 masl. Precipitation almost exclusively occurs as snow mainly in winter. The El Niño Southern Oscillation (ENSO) strongly affects the inter-annual variability in snowfall. Further, low relative humidity, high solar radiation and strong winds result in very high sublimation rates; a major component of the snow and ice mass balance (Ginot et al. 2006; Gascoin et al. 2013).

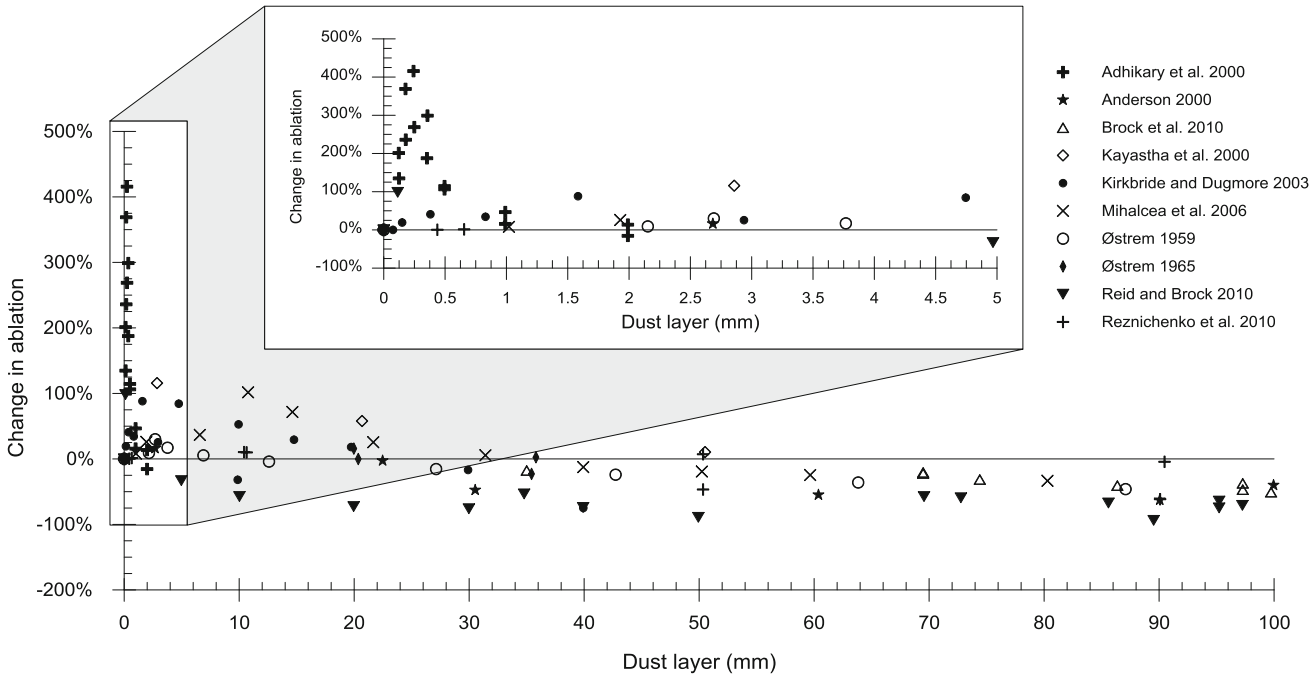

Fig. 6.2 Compilation of ice ablation data as a function of dust layer thickness available from published research

6.3.2 Field Experiments

During 2008 and since 2011 the Centro de Estudios Avanzados en Zonas Áridas (CEAZA) and the Centro de Estudios Científicos (CECs), on behalf of Barrick, have conducted a number of experiments to measure changes in ablation rates as a function of debris cover. These experiments were carried out using test plots of different sizes and lysimeters that were treated with different dust concentrations. The resulting changes in ablation rates and surface albedo were recorded.

Between December 2012 and March 2013, ablation experiments were carried out by CECs on a number of research plots with a size of 3 × 3 m on top of glacial ice (Fig. 6.3). Different dust thicknesses between 1 and 50 mm were applied during these various tests.

Several simple dust traps (ASTM D-1739-98, V. 2004) were installed by the project owner in April 2008 to measure particle accumulation near the glaciers (Fig. 6.1). The representativeness of these dust traps is, however, limited as they may not accurately collect particles that are redistributed by saltation close to the ground surface, nor are they likely to measure the extreme fine fraction of dust that may travel for hundreds of kilometres. The latter, however, are of lesser importance since this fraction hardly deposits on proximal ice bodies, while the former will.

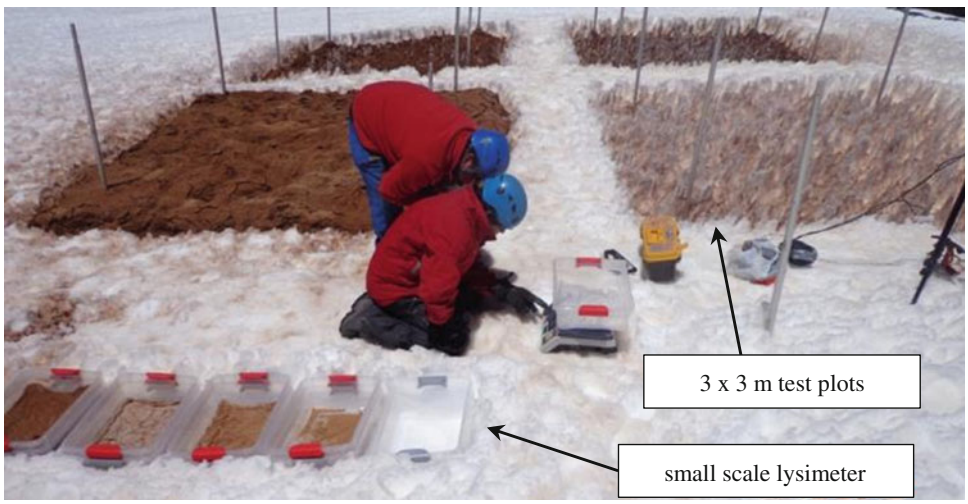

Fig. 6.3 3 × 3 m ablation test plots and small scale lysimeter ablation test setup used by CECs, located on Guanaco Glacier. Photo provided by Barrick

6.3.3 Runoff Simulations

Konovalov (2000) presented a model to estimate changes in glacier ablation as a function of a dust cover. The lysimeter tests conducted at Pascua Lama were used to determine the local parameters for the Konovalov model. In addition to the Konovalov model, ablation of an uncovered, i.e., white, glacier was estimated using a multivariate regression between the ablation and key meteorological parameters, such as wind, air temperature, precipitation and solar radiation. The assessment indicated that of all the climate variables included in the regressions, the two with the highest influence on daily glacier melting rates are the average daily temperature and the average wind speed. By applying the multivariate regression and the calibrated Konovalov model it was possible to estimate glacier ablation and runoff for a series of dust accumulation scenarios. The increased runoff from glacier ablation then allowed an impact assessment on the river runoff downstream from the glaciers where the water is used for agricultural, domestic and industrial purposes.

To account for the inherent limitations of the dust trap measurements in capturing the full extent of dust transport, three scenarios were used to estimate the effect of glacier dust accumulation on runoff. Scenario 1 assumed an increase in ablation of 20 %, Scenario 2 an increase of 50 and 250 % for Scenario 3. Dust distribution modelling has indicated very little dust for the glaciers due to mining activity. Therefore, it is not expected that the critical thickness is reached at this site and the increase in ablation is limited to the dust thicknesses below the maximum change in ablation. These scenarios correspond to potential average and sustained dust accumulations of about 0.1, 0.2 and 1 mm, respectively. Hence, Scenario 1 is considered realistic, Scenario 2 as a high upper scenario, whereas Scenario 3 is included only as a theoretical maximum.

6.4 Results

The lysimeter field experiments demonstrate a broad range of ablation rates consistent with values reported in the literature. The modelling exercise also re-emphasizes that the changes in ablation are highly dependent on meteorological variables and are thus site-specific. Figure 6.4 shows an estimated upper and lower bound of the observed values.

The measurements of dust plots indicate that for a 1 mm dust cover, the ablation rates are minimally increased. The critical thickness occurs at approximately between 15 and 50 mm. The upper value is considerably higher than those reported in the literature (Fig. 6.2) demonstrating the wide variability in dust affected ablation caused by local meteorological conditions. Some of the most recent field tests showed a minimum increase in ablation due to a layer of dust below 3 mm. The maximum increase in ablation ($\sim$50 %) was reached at a 5 mm layer, which for most other tests corresponds to the critical thickness. The data points are shown in Fig. 6.4, but have not been considered in the estimation of a possible range in the change of ablation.

Dust measurements from the six dust traps in the project area show a maximum dust concentration of 10.2 g/(m^2 · 30 days). Assuming a dust density of 500 kg/m^3 this maximum dust deposition measured results in a thickness accumulation of 0.0002 mm/day or less than 0.1 mm/year. As indicated above, the representativeness of these dust traps is uncertain, however, the measurements indicate that extensive dust deposition of fine particles is comparatively low.

Using all three scenarios, the increase in glacier ablation was applied to all glaciers in two sub-basins called Rio de Transito and Rio del Carmen. The ratio between the non-covered ablation and the contribution from the dust cover on the stream flow is presented as a function of the distance

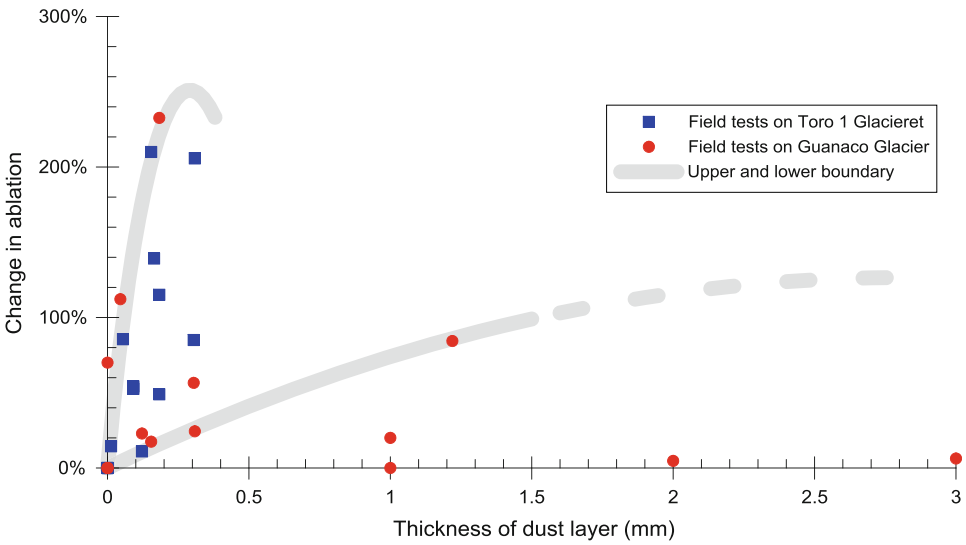

Fig. 6.4 Results of various lysimeter tests showing the change in ablation as a function of the dust cover thickness. The upper and lower boundaries are estimates using the Konovalov model

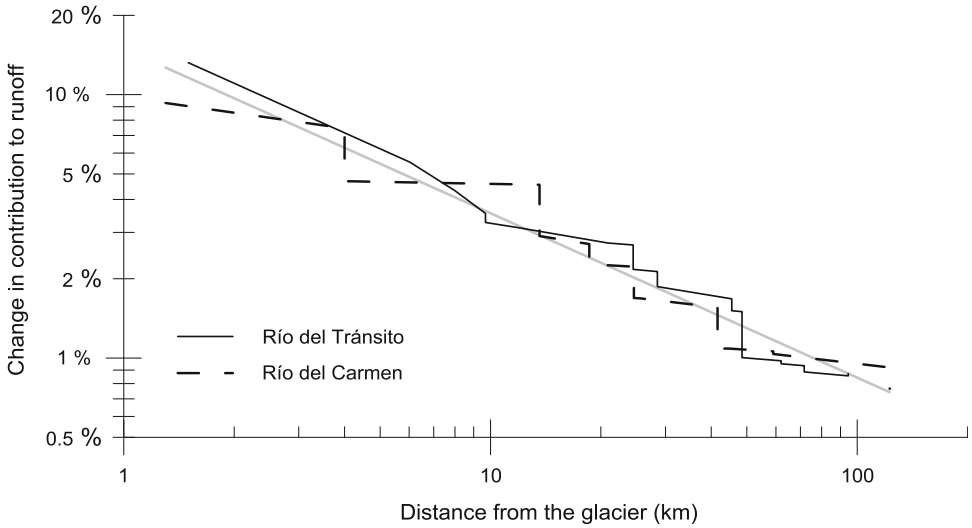

Fig. 6.5 Change in additional contribution to runoff due to 20 % increase in ablation (Scenario 1) caused by the presence of dust on ice, as a function of the distance to the glacier. The gray line shows the best regression for both rivers together. *Note* the scale of the y-axes is logarithmic

from the glaciated areas in Fig. 6.5. With increasing distance from the glaciers, the contribution from glacier runoff decreases exponentially (note that this is a log-log plot). For Scenario 1, the difference in runoff, 80 km downstream from the glaciers due to a dust layer on the ice surface is less than 1 %. Such a change in stream flow is well within the range of the natural variability and would be unnoticeable.

6.5 Discussion and Conclusions

This paper presents the results from a study on dust accumulation on northern Andean glaciers and examined the potential effects on changes in ablation and runoff. A review of data available from literature and local ablation experiments indicate that the critical dust thickness is likely around 15 to 50 mm, although further experiments are under way to better constrain this number and provide improved estimates of its variability. The local peak increase in ablation due to dust cover is estimated to be 2.5 times the uncovered ablation.

With respect to changes in runoff, the ablation scenarios were reviewed using a model developed by Konovalov. The maximum effect of glacial dust on runoff as measured at the bottom of the Rio del Carmen and Rio de Transito watersheds, some 80 km downstream of the mine, were estimated to amount to less than 1 % of its annual runoff for the conservative dust deposition scenario (Fig. 6.6). A maximum of 20–40 % of that percentage could possibly be attributed to mine-generated dust which reduces the total

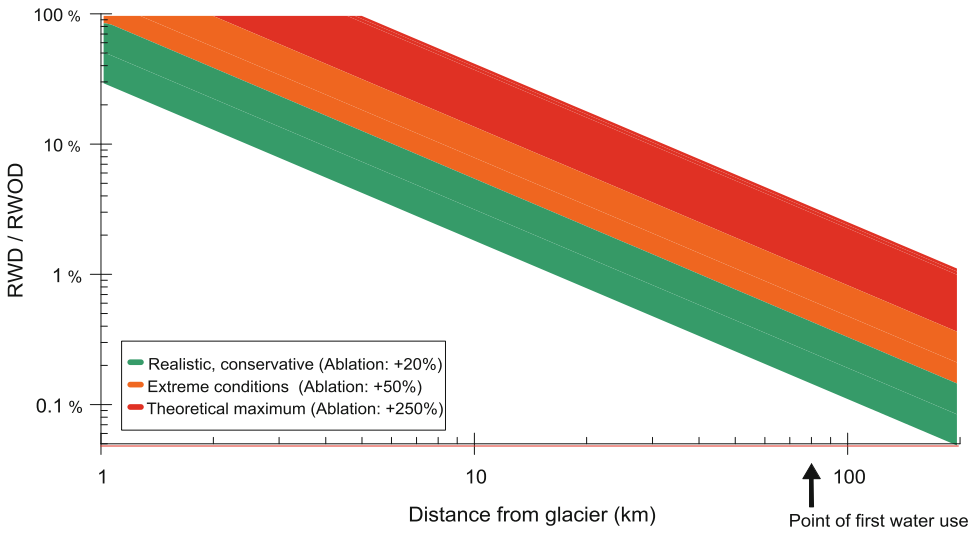

Fig. 6.6 Generalized diagram showing the effect of a dust layer on the glacial runoff with distance from the glacier based on three different ablation scenarios. RWOD: Runoff without dust; RWD: Runoff with dust

runoff contribution from mine-related dust to 0.2–0.4 % of the mean annual runoff. Such small changes are impossible to detect given the pronounced natural variability in these rivers whose seasonal discharge varies by more than 100 %. Variations in river discharge are principally controlled by precipitation which in turn is heavily influenced by El Niño Southern Oscillation events.

The majority of runoff in the high and dry northern Andes is generated by rainfall and snowmelt at higher elevations. Glacial melt is only important at the small (<10 km^2) watershed scale but diminishes exponentially with distance downstream and the proportional increase in watershed area. Since the area and mass of ice bodies in the upper watersheds have declined dramatically over the past 60 years due to progressive climate change (Rabatel et al. 2013), the proportion of glacial water contribution will continue to decrease even if precipitation amounts were to remain stationary.

In summary, the impact of mining-related dust on glaciers and glacierets on the downstream water availability in the Central Andes is considered negligible and well within the natural variability of river discharge. This is largely due to the very small proportions of contributing watersheds that are glacierized.

Acknowledgement The authors would like to thank Barrick Gold Corporation, and in particular Ms. Susan Henry of Compañía Minera Nevada, for the permission to present these data. We also acknowledge the input from Virginia Cullen on an earlier version of this manuscript.

References

Adhikary S (2000) Dust influence on the melting process of glacier ice: experimental results from Lirung Glacier, Nepal Himalayas. IAHS Publ 264:43–52

Anderson RS (2000) A model of ablation-dominated medial moraines and the generation of debris-mantled glacier snouts. J Glaciol 46(154):459–469

Brock BW, Mihalcea C, Kirkbride M, Diolaiuti G, Cutler M, Smiraglia C (2010) Meteorology and surface energy fluxes in the 2005–2007 ablation seasons at the Miage debris-covered glacier, Mont Blanc Massif, Italian Alps. J Geophys Res 115(D9):1–16

Gascoin S, Lhermitte S, Kinnard C, Bortels K, Liston GE (2013) Wind effects on snow cover in Pascua-Lama, Dry Andes of Chile. Adv Water Resour 55:25–39

Ginot P, Schotterer U, Kull C, Schwikowski M, Gäggeler HW (2006) Glacier mass balance reconstruction by sublimation induced enrichment of chemical species on Cerro Tapado (Chilean Andes). Clim Past 2:21–30

Kayastha R, Takeuchi Y, Nakawo M, Ageta Y (2000) Practical prediction of ice melting beneath various thickness of debris cover on Khumbu Glacier, Nepal using a positive degree- day factor. IAHS Publ 264:71–81

Kirkbride M, Dugmore A (2003) Glaciological response to distal tephra fallout from the 1947 eruption of Hekla, south Iceland. J Glaciol 49(166):420–428

Konovalov V (2000) Computations of melting under moraine as a part of regional modelling of glacier runoff. IAHS Publ 26:109–118

Kulkarni AV, Vinay Kumar G, Negi HS, Srinivasan J, Satheesh SK (2013) The effect of black carbon on reflectance of snow in the accumulation area of glaciers in the Baspa basin, Himachal Pradesh. Cryosphere discuss 7:1359–1382

Mattson LE, Gardner JS, Young GJ (1993) Ablation on debris covered glaciers: an example from the Rakhiot Glacier, Punjab, Snow and Glacier Hydrology. In: Proceedings of the Kathmandu symposium, Nov 1992, pp 289–296

Mihalcea C, Mayer C, Diolaiuti G, Lambrecht A, Smiraglia C, Tartari G (2006) Ice ablation and meteorological conditions on the debris-covered area of Baltoro glacier, Karakoram, Pakistan. Ann Glaciol 43(1):292–300

Østrem G (1965) Problems of dating ice-cored moraines. Geogr Ann A Phys Geogr 47(1):1–38

Rabatel A, Castebrunet H, Favier V, Nicholson L, Kinnard C (2011) Glacier changes in the Pascua-Lama region, Chilean Andes (29° S): recent mass balance and 50 yr surface area variations. Cryosphere 5:1029–1041

Rabatel A, Letréguilly A, Dedieu, J-P, Eckert N (2013) Changes in glacier equilibrium-line altitude in the western Alps from 1984 to 2010: evaluation by remote sensing and modeling of the morpho-topographic and climate controls. Cryosphere 7(5):1455–1471

Reid T, Brock B (2010) An energy-balance model for debris-covered glaciers including heat conduction through the debris layer. J Glaciol 56(199):903–916

Reznichenko N, Davies T, Shulmeister J, Mcsaveney M (2010) Effects of debris on ice-surface melting rates: an experimental study. J Glaciol 56(197):384–394

Vimeux F, Ginot P, Schwikowski M, Vuille M, Hoffmann G, Thompson LG, Schotterer U (2009) Climate variability during the last 1000 years inferred from Andean ice cores: a review of methodology and recent results. Palaeogeogr Palaeoclimatol Palaeoecol 281:229–241

Climatic Characterization of Baltoro Glacier (Karakoram) and Northern Pakistan from In-situ Stations

7

Palazzi Elisa, Tahir Adnan Ahmad, Cristofanelli Paolo, Vuillermoz Elisa and Provenzale Antonello

Abstract
In this study we analyze the temperature and precipitation data collected by sixteen in-situ stations located in the high-elevated regions of northern Pakistan to provide a climatic characterization of the Karakoram mountains. We focus our attention on the analysis of the precipitation annual cycle at the various stations and on the investigation of the vertical variability of both precipitation and temperature, averaged over the Upper Indus Basin (UIB) area. The precipitation annual cycle at the individual stations generally shows higher precipitation amounts in winter (December to April) than in summer (June to September), confirming that northern Pakistan is not under the prevailing influence of the Indian monsoon. The spatially-averaged temperature and precipitation vertical gradients show that the temperature lapse rate is consistent with the moist adiabatic lapse rate of the atmosphere. The vertical precipitation gradient indicates an increase with elevation until about 3,000 m and then a decrease that can be attributed to the strong underestimate of solid precipitation by rain gauges at high-altitudes.

Keywords
Karakoram • Precipitation climatology • Precipitation gradient • Western disturbances • Monsoon

7.1 Introduction

In the Karakoram and Upper Indus Basin (UIB) region, climatic variables are strongly influenced by the orography and exhibit both horizontal and vertical variability. In this paper we explore the elevation dependence of precipitation and temperature, averaged over the UIB region, by exploiting the availability of data from 16 in-situ stations located at different altitudes and managed by different agencies: the Italian Ev-K2-CNR, the Pakistan Meteorological Department (PMD) and the Water and Power Development Authority (WAPDA) of Pakistan. The mean precipitation annual cycle at each individual station is also analyzed to quantify the winter and summer contribution to the annual precipitation amount. Unlike central-eastern Himalayas, in fact, the Karakoram mountains are only weakly affected by the summer monsoon rainfall, but receive important precipitation amounts during winter and early spring owing to the arrival of western weather patterns originating from the Mediterranean/North-Atlantic regions (WWP Singh et al. 1995; Syed et al. 2006).

P. Elisa (✉) · P. Antonello
ISAC-CNR, Torino, Italy
e-mail: epalazzi@isac.cnr.it

T.A. Ahmad
COMSATS Institute of Information Technology, Abbottabad, Pakistan

C. Paolo
ISAC-CNR, Bologna, Italy

V. Elisa
EV-K2-CNR, Bergamo, Italy

G. Lollino et al. (eds.), *Engineering Geology for Society and Territory – Volume 1*,
DOI: 10.1007/978-3-319-09300-0_7,

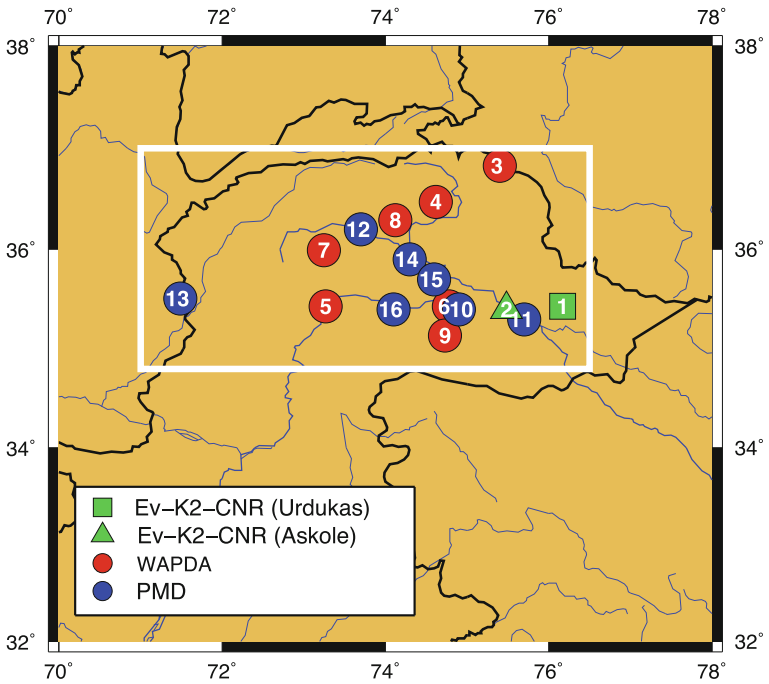

Fig. 7.1 Geographical distribution of the 16 in-situ stations employed in this study: Ev-K2-CNR (*green*), WAPDA (*red*) and PMD (*blue*) (refer to Table 7.1 for station numbering)

After introducing the characteristics of the in-situ stations employed in this study (Sect. 7.2), in Sect. 7.3 we discuss the vertical gradients of temperature and precipitation in UIB region, while the seasonality of precipitation is dealt with in Sect. 7.4. Final considerations are discussed in the Conclusions.

7.2 Meteorological Station Data

This study analyses the data collected at 16 in-situ stations spread over northern Pakistan (see Fig. 7.1) and located at different altitudes, ranging from 1,250 to 4,710 m a.s.l. The principal characteristics of the stations—altitude and spatial coordinates, temporal resolution of the data and managing agency—are resumed in Table 7.1. Two stations among those included in our study are located on the Baltoro glacier, at the Urdukas campsite (3,962 m a.s.l.) and in the Askole village (3,015 m a.s.l.), about 45 km away from each other. They were installed by Ev-K2-CNR in collaboration with PMD in June 2004 and August 2005, respectively, in the framework of the SHARE (Stations at High Altitude for Research on the Environment, http://www.evk2cnr.org/cms/en/share/project/intro) project promoted by Ev-K2-CNR and the Italian National Research Council (CNR). In this study we analyze hourly measurements of precipitation and air temperature provided by the two AWS. The precipitation time series show important data gaps during winter and early spring months, when the collection efficiency lowers considerably owing to the difficulty in measuring precipitation in solid form (e.g., Winiger et al. 2005; Rasmussen et al. 2012). PMD maintains other in-situ stations, mainly located at relatively low elevations, providing standard meteorological measurements since the 1950s. Here we consider about 50-years of monthly-mean maximum and minimum temperature and monthly-accumulated precipitation from seven PMD stations (blue circles in Fig. 7.1) located at altitudes between 1,250 m a.s.l. and 2,394 m a.s.l. A network of meteorological and hydrological stations in the ablation zone of the UIB is also managed and maintained by WAPDA. In this study, we use ten years (1999–2008) of daily-mean maximum and minimum temperature and daily-accumulated precipitation from seven WAPDA stations located between 2,570 m and 4,710 m altitude.

7.3 Precipitation and Temperature Vertical Gradients

The vertical gradient of precipitation over mountain terrains is still a poorly understood phenomenon (e.g., Barry 2012; Rangwala et al. 2012). Studies on precipitation gradients in the mountain regions of northern Pakistan, in particular, are scarce, mainly owing to the limited availability of high-elevation data. Our results for summer (JJAS) and winter (DJFMA) vertical gradients of temperature and precipitation in northern Pakistan are shown in Fig. 7.2; each point represents the multiannual-mean value of temperature (a, b) or

Table 7.1 Elevation, latitude and longitude coordinates of the in-situ stations considered in this study, along with the temporal resolution of the measured data and the managing agency

Stations	Height (m a.s.l.)	Lat (°N)	Lon (°E)	Time resolution	Agency
1. Urdukas	3,962	35.43	76.17	Hourly	Ev-K2-CNR
2. Askole	3,015	35.40	75.48	Hourly	Ev-K2-CNR
3.Khujerab	4,710	36.83	75.40	Daily	WAPDA
4. Ziarat	3,669	36.47	74.62	Daily	WAPDA
5. Yasin	3,150	35.43	73.27	Daily	WAPDA
6. Rama	3,000	35.43	74.79	Daily	WAPDA
7. Ushkore	2,970	35.99	73.25	Daily	WAPDA
8. Naltar	2,810	36.29	74.12	Daily	WAPDA
9. Rattu	2,570	35.14	74.73	Daily	WAPDA
10. Astore	2,394	35.4	74.9	Monthly	PMD
11. Skardu	2,210	35.3	75.7	Monthly	PMD
12. Gupis	2,156	36.2	73.7	Monthly	PMD
13. Chitral	1,498	35.51	71.49	Monthly	PMD
14. Gilgit	1,460	35.9	74.3	Monthly	PMD
15. Bunji	1,372	35.7	74.6	Monthly	PMD
16. Chilas	1,250	35.4	74.1	Monthly	PMD

precipitation (c, d) plotted against the nominal station altitude. Blue and red symbols indicate the Askole and Urdukas stations, respectively, while filled and empty diamond symbols refer to WAPDA and PMD data, respectively. At Askole and Urdukas, the multiannual winter averages of precipitation were not calculated due to the low statistics available in winter months. As indicated in Fig. 7.2a, b, the linear fit of the data gives a temperature lapse rate of −6.8 °C/(100 m) and −7.7 °C/(100 m) in winter and summer, respectively, averaged over the UIB region. The winter value, in particular, is very close to the standard moist adiabatic lapse rate for the atmosphere (−6.5 °C/(100 m), as defined by the International Civil Aviation Organization (ICAO). This is consistent with the fact that seasonal temperatures exhibit also high horizontal coherence across the UIB region (as seen in the analysis of the temperature

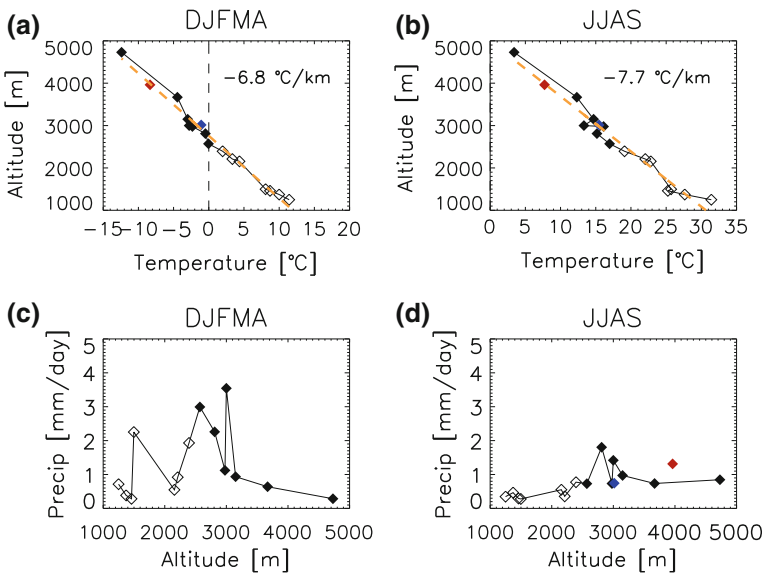

Fig. 7.2 Winter and summer temperature (**a**, **b**) and precipitation (**c**, **d**) vertical gradients derived from the measurements at the Askole (*blue*), Urdukas (*red*), PMD (*empty diamond symbols*), and WAPDA (*filled symbols*) stations

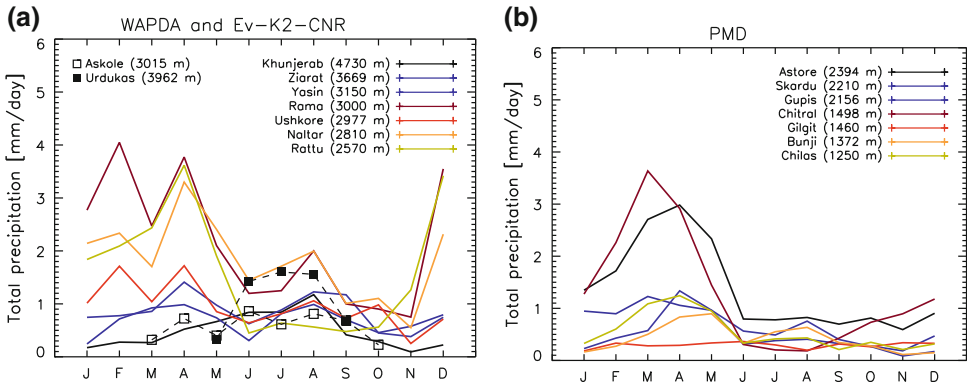

Fig. 7.3 Mean annual cycle of precipitation inferred from **a** WAPDA and Ev-K2-CNR data, **b** PMD data

correlation coefficient between each station pair, not discussed here), suggesting that the different stations provide a coherent regional characterization of the vertical gradient of mean temperatures. The seasonal vertical gradients of precipitation, shown in Fig. 7.2c, d, seem to indicate that precipitation increases with altitude until about 3,000 m, while it decreases beyond that altitude. On the other hand, we expect an underestimation of precipitation measured at the highest elevations, due to the strong under catch of solid precipitation by rain gauges. For summer precipitation (Fig. 7.2d), the situation is more complicated. There is a weak trend of increasing precipitation with elevation (especially evident from the two Ev-K2-CNR stations), onto which an apparent intensification between about 2,500 m and 3,500 m is superposed. This could either be a real signature, with the largest precipitation occurring in that elevation range owing to orographic effects and convective processes, or the true behavior at higher altitudes could be again underestimated owing to a non-negligible summer snowfall contribution at high-elevation.

7.4 Precipitation Annual Cycle

The mean annual cycle of precipitation for the WAPDA and Ev-K2-CNR stations, and for the seven PMD stations is shown in Fig. 7.3 (panels a and b, respectively). It is worth underlying that these averages are estimated on different time intervals for the various stations: 10 years for all WAPDA stations (1999–2008), ~5 years for the Askole (2005–2009) and Urdukas (2004–2008) stations, and 42 (1965–2007) to 63 (1945–2007) years for the PMD stations. Even though monthly precipitation amounts display clear differences at different stations, owing to geo-graphical position, altitude and wind exposure, all stations indicate the importance of December to April precipitation in this region.

7.5 Conclusions

Precipitation is one of the most important climatic parameters but it is probably the most critical one to measure, owing to technical difficulties in measuring the snowfall contribution accurately (Winiger at al. 2005; Rasmussen et al. 2012). This situation is encountered also in the Karakoram area, though the number of research and monitoring programmes focused on this region has recently increased. In this paper, we have analyzed the precipitation and temperature data from 16 in-situ stations in the upper Indus basin, managed by the Ev-K2-CNR Committee, the PMD and WAPDA agencies of Pakistan. We have investigated the dependence of temperature and precipitation on the elevation and found that the average temperature lapse rate in the UIB, inferred from all station data, is consistent with the moist adiabatic lapse rate for the atmosphere, while winter precipitation is observed to increase until about 3,000 m and to decrease thereafter. Summer precipitation, on the other hand, seems to increase weakly with elevation, with an intensification at elevations between about 2,500 m and 3,500 m. It remains to be seen whether this behavior is a real feature of summer precipitation in the UIB or it is generated by underestimating summer solid precipitation at higher elevations. Our analysis of the precipitation annual cycle confirms that the Karakoram area is not under the main influence of the monsoon, as the higher precipitation values in winter than in summer, as found at most stations in the UIB, indicate.

References

Barry RG (2012) Recent advances in mountain climate research. Theoret Appl Climatol 110:549–553. doi:10.1007/s00704-012-0695-x

Rangwala I, Miller J, Xu M (2009) Warming in the Tibetan Plateau: possible in-fluences of the changes in surface water vapor. Geophys Res Lett 36:L06703

Rasmussen R, Baker B, Kochendorfer J, Meyers T, Landolt S, Fischer AP, Black J, Thériault JM, Kucera P, Gochis D, Smith C, Nitu R, Hall M, Ikeda K, Gutmann E (2012) How well are we measuring snow? Bull Am Meteorol Soc 93:811–829. doi: http://dx.doi.org/10.1175/BAMS-D-11-00052.1

Singh P, Ramasastri KS, Kumar N (1995) Topographical influence on precipitation distribution in different ranges of Western Himalayas. Nord Hydrol 26(4–5):259–284. doi:10.2166/nh.1995.015

Syed FS, Giorgi F, Pal JS, King MP (2006) Effect of remote forcings on the winter precipitation of central southwest Asia part 1: observations. Theoret Appl Climatol 86:147–160. doi:10.1007/s00704-005-0217-1

Winiger M, Gumpert M, Yamout H (2005) Karakorum-Hindukush-western Hima-laya: assessing high altitude water resources. Hydrol Process 19:2329–2338. doi:10.1002/hyp.5887

Current Status and Future Projections of the Snow Depth in the Third Pole from CMIP5 Global Climate Models

8

Terzago Silvia, Von Hardenberg Jost, Palazzi Elisa and Provenzale Antonello

Abstract

The Tibetan plateau and the Hindu-Kush Karakoram Himalaya mountains, with mean elevation above 4,000 m a.s.l., are the world's largest snow and ice reservoir outside the polar regions and they are often referred to as the "Third Pole". These mountains provide water to about 1.5 billion people in Afghanistan, Bangladesh, Bhutan, China, India, Myanmar, Nepal and Pakistan, and changes in snow dynamics would impact on water availability for downstream populations. Despite its importance, the knowledge on the snow dynamics in the Third Pole region is still incomplete, due to difficult and sporadic surface observations. In this work we investigate how CMIP5 Global Climate Model (GCM) simulations represent the snowpack in the Third Pole environment and we compare the results to the ERA-Interim/Land reanalysis. Then we discuss the historical snow depth trends and the projections for the XXI century under RCP8.5 scenario.

Keywords

Snow depth • Climate change • CMIP5 global climate models • Third pole • Hindu-Kush Karakorum Himalaya

8.1 Introduction

With their 5 million Km^2 extension the Hindu-Kush Karakoram Himalaya and the Tibetan Plateau are the largest mountain range in the world, including the 14 world's highest peaks above 8,000 m. This area hosts the largest reservoir of snow and ice mass outside the polar regions and it is often referred to as the "Third Pole" (Qiu 2008) to point out its relevance in the Earth's cryosphere. The snow melting from the mountains feeds all of Asia's major river systems, providing water to about 1.5 billion people living downstream (Yao et al. 2012). The contribution of the snow and glacier melt to the stream flow may vary in the region and it becomes more and more important in the areas that do not receive monsoonal summer precipitation, such as the Hindu-Kush Karakoram and Western Himalaya. Here summer precipitation is relatively scarce and the contribution of meltwater is the major source for the river flow (Liniger et al. 1998). This feature makes the Third Pole Environment crucial for both local economies and socio-economical activities in the bordering countries.

Despite its relevance, some current climatic features of the Third Pole, such as precipitation and in particular snow, are still poorly known, mainly due to the difficulties in performing regular meteorological observations in high elevation areas. The highest density of surface snow depth observations is in the Eastern Tibetan Plateau, which currently represents also the most studied area of the Third Pole (Qian et al. 2003). Concerning the Karakoram, Winiger et al. (2005) analyzed 10-year time series of snow depth and water equivalent measurements derived from several

T. Silvia (✉) · V.H. Jost · P. Elisa · P. Antonello
ISAC-Institute of Atmospheric Sciences and Climate, CNR, Torino, Italy
e-mail: s.terzago@isac.cnr.it

G. Lollino et al. (eds.), *Engineering Geology for Society and Territory – Volume 1*,
DOI: 10.1007/978-3-319-09300-0_8,

automatic weather stations at elevations between 1,500 and 4,700 m a.s.l.. Several studies have been performed on the Hindu-Kush Karakoram Himalaya glaciers (i.e. Hewitt (2005); Gardelle et al. (2012)) and a review is offered in Bolch et al. (2012). In that paper the authors point out the existing gaps in the present knowledge: the spatial variability of mountain snow and ice, the annual melting and its contribution to the total discharge are all uncertain mainly owing to the insufficient number of surface observations, only partly balanced by satellite measurements.

Given the strong limitations associated with scarce availability of observations, in these work we investigate the large scale features of the snowpack in the Third Pole region using the Global Climate Models simulations included in the CMIP5 experiment (Taylor et al. 2012). In particular we explore how different GCMs represent the snow depth characteristics in the Third Pole region. The results are compared to the ERA-Interim/Land reanalysis (Balsamo et al. 2012) considered here as the best approximation of the ground truth. Finally we dicuss the historical snow depth trends and the future projections under the RCP8.5 scenario.

8.2 Data and Methods

The area of study includes the Tibetan Plateau and the Hindu-Kush Karakoram Himalaya mountains. We considered all CMIP5 GCMs providing the snow depth variable, including the EC-Earth model run at ISAC-CNR (Hazeleger et al. 2012).

The spatial resolution of CMIP5 models varies in a wide range, from 0.75 up to 2.8125°. We excluded from our analysis the model with too coarse spatial resolution and we considered only those with a maximum gridsize of 1.25° (Table 8.1).

For each model we selected the first ensemble member of the historical runs and we generated seasonal maps of the average winter (December-January-February-March-April) snow depth. The models climatology has been compared to the ERA-Interim/Land snow depth reanalysis in the overlapping period 1980–2005. Finally we considered the full GCMs time series in order to evaluate the snow depth trends during the historical period 1850–2005 and the expected changes from 2006 to 2100 assuming the conditions prescribed in the RCP8.5 scenario.

8.3 Results

We analyzed the spatial distribution of the winter (DJFMA) mean snow depth obtained from the CMIP5 GCM historical simulations averaged over the period 1980–2005. The ERA-Interim/Land snow field can be considered as an approximation of the ground truth. It presents a fictitious peak of about 10 m of snow water equivalent in correspondence of the Baltoro glacier: since this value is not intended to be representative of the real conditions the Baltoro area has been excluded from the analysis below.

Table 8.1 The dataset used in this study includes the high resolution (not coarser than 1.25°) CMIP5 Global Climate Models providing the snow depth variable and the ERA-Interim/Land Reanalysis

Dataset	Spatial resolution [°lon]	DJFMA SD Q2	DJFMA SD IQR = Q3 − Q1
ERA-Interim/Land	0.75	0.07	0.02
CMCC-CM	0.75	0.11	0.05
EC-Earth	1.125	0.10	0.03
BCC-CSM1.1m	1.125	0.23	0.07
MRI-CGCM3	1.125	0.19	0.04
CESM1-BGC	1.25	0.15	0.06

The median (Q2) and the Inter Quartile Range (IQR) of the DJFMA snow depth spatially averaged over HKKH mountains with elevation above 1,000 m a.s.l. (excluded the Baltoro area) during the period 1980–2005 are reported for comparison

All GCMs identify a similar spatial pattern with a snow depth peak over the Hindu-Kush Karakoram and Western Himalaya mountains and decreasing values moving toward the Himalaya in South-East direction. Another snow depth peak is found in the South-Eastern part of the Tibetan plateau, at the border with India.

For each GCM we analyzed the winter snow depth spatially averaged over HKKH mountains with elevation above 1,000 m a.s.l. (excluding the Baltoro area) in the period 1980–2005 and we compared the results to the ERA-Interim/Land Reanalysis. The models are in fairly good agreement with the reanalysis but they generally represent a thicker snow depth throughout the region. This behavior is confirmed by the statistics reported in Table 8.1: the median of the average winter snow depth above 1,000 m a.s.l. is higher in GCMs than in the reanalysis.

A remarkable difference among the GCMs is found over the Tibetan plateau: while BCC-CSM1.1m, MRI-CGCM3 and CESM1-BGC models identify continuous and locally deep winter snowpack, the other models show a shallower (EC-Earth, CMCC-CM) snow depth. The surface observation data available from Chinese stations confirm the presence of thick snow-pack in the Eastern and South-Eastern Tibetan Plateau, where winter average snow depth is locally above 40 cm (Qian et al 2003). For the rest of the region it is very difficult to make a comparison with the ground-truth due the lack of surface observations.

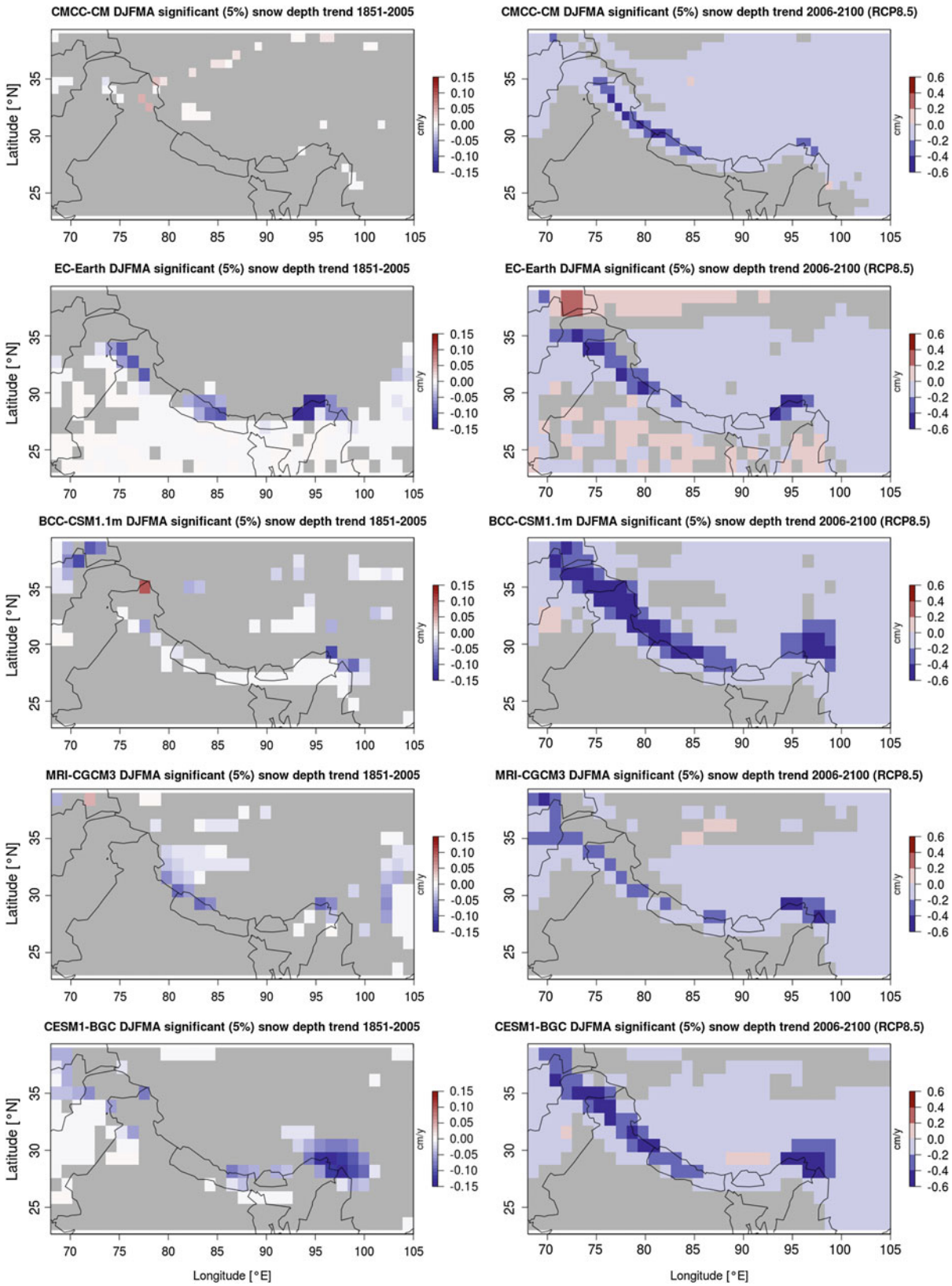

Fig. 8.1 GCMs DJFMA snow depth trends (significant at 95 % confidence level) referring to the historical period 1851–2005 (*left*) and to the future projections (2006–2100) under the RCP8.5 scenario

8.3.1 Historical Snow Depth Trends and Future Projections

For each GCM we explored and compared the snow depth trends during the historical period (1850–2005) and in the future simulations (2006–2100) under the scenario RCP8.5. Figure 8.1 reports the statistically significant trends (0.05 significance level) obtained performing the Mann-Kendall test.

During the historical period the GCMs show stable snow depth conditions except for some spotted areas in the Eastern Himalaya where snow depth slightly decreased. BCC-CSM1.1m model identifies a slightly positive trend at the border between India, Pakistan and China.

The future projections under the RCP8.5 scenario show a clear signal common to all the models. The GCMs indicate a decrease in snow depth up to −0.8 cm/y all along all the Hindu-Kush Karakoram Himalaya mountain range (please note the different scale with respect to the historical period). In the Pamir mountains EC-Earth model identifies an increase of the snow depth, probably due to the increase in the solid precipitation fraction.

8.4 Conclusions

The definition of the snow characteristics in the mountains of the Third Pole region is extremely difficult owing to insufficient surface observations. We considered high resolution (not coarser than 1.25° longitude) GCMs datasets provided by the CMIP5 experiment and we investigated how they represent the winter snow-pack distribution. The GCMs intercomparison shows an overall agreement in the representation of the spatial patterns of snow depth. The high resolution GCMs tend to overestimate snow depth over the Third Pole region in comparison to the ERA-Interim/Land reanalysis, anyway it is difficult to establish what model performs best in such a poorly instrumented area.

While during the historical period GCMs identify significant snow depth trends only in sparse areas along the mountain range, the future projections under the RCP8.5 scenario indicate a clear decrease in snow depth along all the Hindu-Kush Karakoram Himalaya chain by the end of the XXI century.

Acknowledgments This work was funded by the Ev-K2-CNR SHARE-PAPRIKA-Karakoram project and by the NextData project of the Italian Ministry of Education, University and Research (http://www.nextdataproject.it).

References

Balsamo G, Albergel C, Beljaars A, Boussetta S, Brun E, Cloke H, Dee D, Dutra E, Pappenberger F, de Rosnay P, Sabater JM, Stockdale T, Vitart F (2012) ERA Report Series 13, p 25

Bolch T, Kulkarni A, Kääb A, Huggel C, Paul F, Cogley JG, Frey H, Kargel JS, Fujita K, Scheel M, Bajracharya S, Stoel M (2012) Science 336(6079):310–314

Gardelle J, Berthier E, Arnaud Y (2012) Nat Geosci 5:322–325

Hazeleger et al. W (2012) Clim Dynam 39:1–19

Hewitt K (2005) Mt Res Dev 25(4):332–340

Liniger H, Weingartner R, Grosjean M (1998) Mountains of the world: water towers for the 21st century (Mountain Agenda for the Commission on Sustainable Development (CSD), BO12: Berne, 1998), pp 32

Qian YF, Zheng YQ, Zhang Y, Miao MQ (2003) Int J Climatol 23:593–613

Qiu J (2008) Nature 454:393–396

Taylor KE, Stouer RJ, Meehl GA (2012) Bull Amer Meteor Soc 93:485–498

Winiger M, Gumpert M, Yamout H (2005) Hydrol Process 19:2329–2338. *Special issue: mountain hydrology ed. by de Jong C, Whelan F, Messerli* B, 2329–2338 (2005)

Yao T et al (2012) Env Dev 3:52–64

Hydrology of the Upper Indus Basin Under Potential Climate Change Scenarios

9

Andrea Soncini, Daniele Bocchiola, G. Confortola, E. Nana, A. Bianchi, R. Rosso, G. Diolaiuti, C. Smiraglia, J. von Hardenberg, E. Palazzi, A. Provenzale and E. Vuillermoz

Abstract

The mountain regions of the Hindu Kush, Karakoram and Himalaya (HKKH) are the "third pole" of our planet, and the glaciers in this area are "water towers" of Asia. Recent studies postulated the existence of a "Karakoram anomaly", i.e. with substantially unchanged ice cover during the last decade, against noticeable area loss worldwide. Yet, recent major floods occurring in Pakistan and the Karakoram area, may represent an effect of modified climate in the area, carrying heavier precipitation in the Monsoon season, and possibly faster ice melting. We present here the results of the SHARE-Paprika project of the EvK2CNR Committee of Italy, aiming at evaluating the impact of climate change on the hydrology of the upper Indus river. We focus here on a particular watershed, the Shigar river closed in Shigar, with an area of about 7,000 km^2 and fed by seasonal melt from two major glaciers (Baltoro and Biafo). Based upon data gathered during three field campaigns we set up a semi-distributed, altitude belt based hydrological model, providing acceptable depiction of in stream flows, and snow and ice cover dynamics. We then project the future (until 2,100) hydrological cycle in the area by feeding the hydrological model with future precipitation and temperature (plus downscaling, whenever necessary) from a number of climate models, under different RCP scenarios.

Keywords

Karakoram • Hydrological models • Climate models • Future water resources

A. Soncini · D. Bocchiola (✉) · G. Confortola · E. Nana · A. Bianchi · R. Rosso
Department of Hydrologic, Environmental, Roads and Surveying Engineering, Politecnico Di Milano, L. Da Vinci, 32, 20133 Milan, Italy
e-mail: daniele.bocchiola@polimi.it

G. Diolaiuti · C. Smiraglia
Earth Sciences Department, University Milano, Mangiagalli, 32, Milan, Italy

J. von Hardenberg · E. Palazzi · A. Provenzale
CNR—Institute of Atmospheric Sciences and Climate, Corso Fiume 4, Turin, Italy

D. Bocchiola · G. Diolaiuti · E. Vuillermoz
EVK2CNR Committee of Italy, S. Bernardino 145, Bergamo, Italy

9.1 Introduction

The mountain range of the Hindu Kush, Karakoram and Himalaya (HKKH) contains a large amount of glacier ice, and it is the *third pole* of our planet (e.g. Smiraglia et al. 2007; Kehrwald et al. 2008). There are estimates indicating that more than 50 % of the water flowing in the upper Indus basin UIB in Pakistan is due to snow and glacier melt (Immerzeel et al. 2010). Economy of Himalayan regions is relying upon agriculture, and thus is highly dependent on water availability and irrigation systems (e.g. Akhtar et al. 2008). While southern Himalaya is strongly influenced by the monsoon climate and by abundant seasonal precipitation therein, meteo-climatic conditions of Karakoram suggest a stricter dependence of water resources upon snow and ice

G. Lollino et al. (eds.), *Engineering Geology for Society and Territory – Volume 1*,
DOI: 10.1007/978-3-319-09300-0_9,

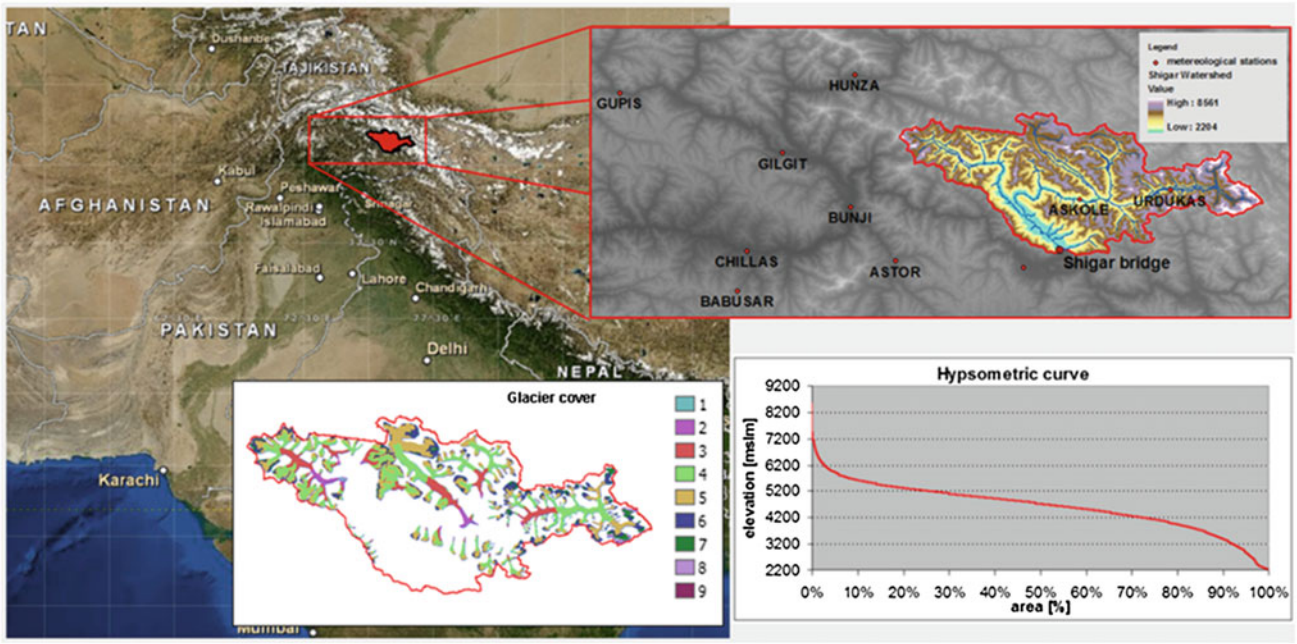

Fig. 9.1 The study area: Shigar river basin in the HKH region. Dots are the weather stations. We report hypsometric curve and glacier cover

ablation, and therefore the needs of its believable projection for the future (Mayer et al. 2010). In high altitude glacierized catchments such as Shigar river here simple hydrological modeling based upon scarce data amount is necessary for water budget estimation, and prediction under climate change conditions (e.g. Chalise et al. 2003; Konz et al. 2007; Bocchiola et al. 2010). Here we present an updated study, based upon former results (Bocchiola et al. 2011), plus data from recent field activities, aimed to improve our knowledge of physical processes underlying hydrology of the area, and we carry out hydrological projections based upon updated climatological tools.

9.2 Case Study Area

The Shigar river flows within the Hindu Kush, Karakoram and Himalaya (HKH) region in the northern of Pakistan, ranging ca. from 74.5 to 76.5 °E in Longitude, and from 35.2 to 37 °N in Latitude. This study focuses upon the Shigar river watershed, closed in Shigar (ca 7,000 km^2), nested within the upper Indus basin, and fed mainly by seasonal melt from major glaciers.

The whole catchment is laid within Pakistan in the region called Gilgit-Baltistan, the highest altitude is reached by K2 mountain (8,611 masl) and the lower in the control section at Shigar bridge (2,204 masl). The average altitude is 4,613 masl. In Shigar catchment there are many glaciers, covering a total area of 1,164 km^2, among which the most renowned are the Biafo glacier and the Baltoro glacier, at the toe of K2 (see Fig. 9.1).

The climate in the area falls in the BWK region of the Köppen-Geiger climate classification (Peel et al. 2007), that displays dry climate with little precipitation and large daily temperature range (Bocchiola and Diolaiuti 2013). Precipitation is concentrated in two main periods, Winter (JFM) and summer (JAS), i.e. Monsoon and Westerlies, the latter providing the dominant nourishment for the glacier systems of the HKH. High altitude snowfall is poorly measured, and it is still rather unknown (Bocchiola et al. 2011).

9.3 Database

9.3.1 Observed Data

Within the Shigar river catchment there are two meteorological stations available with measurements during 2005–2012, at Askole (3,015 masl) and Urdukas (3,926 masl), and one from 2011 at Concordia (4,690 masl), all property of the EvK2-CNR committee. For the three stations there are available daily values of rainfall, air temperature and some other meteorological parameters, with some missing data, due to extreme conditions at this altitude, especially during the winter season. Out of the basin there are available monthly meteorological data for the period 1980–2009 from some stations belonging to Pakistan Meteorological Department (PMD), all below 2,500 masl.

Table 9.1 Properties of the adopted GCM models

Model	Research centre	Nation	Grid size [°]	No. layers [.]
EC-EARTH	Europe-wide consortium	E.U.	1.125 × 1.125	62
ECHAM6	Max Planck Institute for Meteorology	GER	1.9 × 1.9	47
CCSM4	National Center for Atmospheric Research	U.S.A.	1.4 × 1.4	26

Only hydrometric data available are the average values of monthly mean discharge during 1985–1997 from Water Power Development Agency (WAPDA), plus daily discharge data since 2011 from a new hydrometric station installed by the authors. Concerning ice ablation, for summer 2011 there are available measurements from 17 ablation stakes deployed along the main flow line of Baltoro glacier, from 3,600 masl to 4,600 masl.

9.3.2 GCM Data

We used in this study climate data from three General Circulation Models (GCM) chosen from among those used by IPCC for the Fifth Assessment Report (AR5), namely EC-Earth, EcHam6 and CCSM4 models. Typically, GCMs provide a poor representation of local precipitation. Therefore, a downscaling is necessary (e.g. Groppelli et al. 2011). Still, *GCMs* carry considerable information concerning large scale forcing to local climate, so their use is appropriate for projections of climate change impact. For the future scenario simulation we used IPCC's Representative Concentration Pathways (RCPs) from AR5, particularly RCP26, RCP45 and RCP85, during 2012 to 2100 (see Table 10.1).

9.4 Methodology

9.4.1 Weather Data

Temperature, and expectedly precipitation increase with altitude. To evaluate their vertical gradients we used monthly meteorological data from PMD (1980–2009) and data of the Ev-K2 CNR stations at high altitudes as reported. We evaluated monthly temperature gradients. Assessment of vertical gradients of precipitation is more difficult, given that there is less information at high altitudes, and our approach was to use a power law (Winiger et al. 2005), to estimate precipitation vertical lapse rate. At high elevation, this may lead to an overestimation of precipitation, but this may have a little impact on the hydrologic balance, because with increasing altitude contributing area decreases significantly. However, comparison against accumulation data from high altitude (ca. 6,000 masl) snow pits carried out in 2011 (the authors of this study, not shown for shortness) displayed an acceptable performance of the model in depicting precipitation at increasing elevations. Our daily meteorological data did not cover the same period as that of the monthly mean discharge value, see we used a downscaling approach to convert monthly precipitation in Astore to a daily scale. We used a random cascade approach (e.g. Groppelli et al. 2011), slightly modified to deal with monthly precipitation.

9.4.2 Ice and Snow Ablation

Shigar watershed includes glaciers spread over a considerable area, several of which displaying debris cover. Mihalcea et al. (2006) and Mayer et al. (2006) evaluated ice melt factors for both ice covered and ice free glacier based upon field ablation data from the Baltoro glacier. Based on 17 ice ablation stakes measured during the 2011 field campaign located between 3,600 and 4,600 masl, we built a relationship between the degree-day factor for ice DD_i, altitude and debris depth. In this way it was possible to estimate the DD_i value at every altitude. As a rough average value on the area we found a melt factor for ice $DD_i = 5.65$ mm °C^{-1}d^{-1}, that is comparable with expected values for this region. In addition, from a GPS survey of the ablation stakes position we also estimated the surface velocity of the glacier, ranging from 10 to 120 m y^{-1} along the main flow line.

Snow melt was tackled using degree day approach and melt factor. For this study, we used degree day factor for snow melt (DD_s) estimated from MODIS snow cover images, starting from $DD_s = 1.5$ mm °C^{-1} day^{-1} in April (start of the snowmelt season at the lowest altitudes), and approximately linearly increasing by the month until $DD_s = 5$ mm °C^{-1} day^{-1} in August, and then decreasing again until $DD_s = 1.5$ mm °C^{-1} day^{-1} in October. Overall, an average value was obtained of $DD_s = 2.5$ mm °C^{-1} day^{-1}.

9.4.3 The Glacio-Hydrological Model

In this study, we used a semi-distributed altitude belts based model, able to reproduce ice and snow dynamics, evapotranspiration, recharge of groundwater reservoir, discharge formation and routing to the control section (Bocchiola

et al. 2011). This simple model needs a few input data, i.e. a DEM, daily values of precipitation and temperature, information about soil use, vertical gradient of temperature and precipitation and some others parameters. In this model are considered two mechanism of flow formation: superficial and groundwater. The model is based on mass conservation equation and evaluates for each time step the variation of the soil water content in the ground layer. Soil water content S in two consecutive time steps (t, $t + \Delta t$), is

$$S^{t+\Delta t} = S^t + R + M_s + M_i - ET_{eff} - Q_g, \tag{9.1}$$

with R the liquid rain, M_s snowmelt, M_i glacial ablation, ET_{eff} the effective evapotranspiration, and Q_g groundwater discharge. Snowmelt M_s and glacial ablation M_i are estimated according to a degree day method. Ice melt occurs upon glacier covered area within each belt, after snow depletion is complete.

The superficial flow Q_s occurs only for saturated soil

$$\begin{aligned} Q_s &= S^{t+\Delta t} - S_{Max} \quad \text{if } S^{t+\Delta t} > S_{Max} \\ Q_s &= 0 \qquad\qquad\quad \text{if } S^{t+\Delta t} \leq S_{Max}, \end{aligned} \tag{9.2}$$

with S_{Max} greatest potential soil storage [mm]. Potential evapotranspiration is calculated using Hargreaves equation, only requiring temperature data and monthly mean temperature excursion.

The model take into account also the glacier gravity flow. Every year at the end of the ablation season the model moves a quantity of ice from an altitude belt to the lower one. The quantity of ice is evaluated using an ice velocity value estimated with a power law calibrated on the observed velocity values.

$$V_{ice,\,i} = V_0 \cdot h_{ice,i}^{\alpha} \tag{9.3}$$

With $h_{ice,i}$ the ice water equivalent in the belt i and V_0 and α two calibration parameters.

$$\begin{aligned} h_{ice,i}(t + \Delta t) = h_{ice,i}(t) \; - \; & F_{i\to i-1}(t) + F_{i+1\to i}(t) \\ & F_{i\to i-1} \propto V_{ice,\,i} \end{aligned} \tag{9.4}$$

With $h_{ice,i}$ the ice water equivalent in the belt i at time t and $F_{i\to i-1}$ or $F_{i\to i+1}$ the ice depth passing from a belt to the lower or from the upper proportional to the velocity by the ratio between the ice covered area in the belt i and the one in the belt $i-1$ or $i + 1$. Equations (9.1)–(9.4) are solved using fifty equally spaced elevation belts inside the basin. The flow discharges from the belts are routed to the outlet section through a semi-distributed flow routing algorithm. For calculation of the in stream discharge we hypothesize two (parallel) systems (groundwater, overland) of linear reservoirs (in series) each one with a given number of reservoirs (n_g and n_s). The hydrological model uses a daily series of precipitation and temperature from one representative station, here Askole, and the estimated vertical gradients to project those variables at each altitude belt. Topography is here represented by a DTM model, with 30 m spatial resolution, derived from ASTER (2006) mission, used to define altitude belts and local weather variables against altitude.

9.4.4 GCMs Downscaling

To evaluate future hydrological scenarios we downscaled three GCM models output of precipitation and temperature. Again we use a random cascade approach (e.g. Groppelli et al. 2011) to obtain ground precipitation and temperature. The random cascade parameters are been calibrated using the observed data at Askole and the control run series for each model. With the parameters we disaggregate the three future RCPs scenarios for every model, in total we obtained 9 precipitation and temperature series for the next century (2012–2100). Downscaling of temperature is also carried out using data at Askole station. We used in practice a monthly averaged DT approach and vertical lapse rate as estimated before to project temperature at each belt.

9.5 Results

9.5.1 Model Performance

We run a 33 years simulation (1980–2012) obtaining daily estimation of in channel discharge at Shigar bridge. Then we compare this results with the monthly mean discharge observed during the period 1985–1997 and with the 2012 daily discharge data (Fig. 9.2). We tuned some parameters in a fixed range reproducing the yearly average discharge, the best fitting of the observed monthly and daily values and the Nash–Sutcliffe Efficiency coefficient (NSE). Concerning the ice flow model, velocity has its maximum at Concordia, which is associated with the confluence of the two major tributary glaciers, the Godwin Austen Glacier and the Baltoro South Glacier. Mean velocity estimated using remote sensing techniques (Quincey et al. 2011) is 107 m y^{-1}, while the one estimate by the model is 99 m y^{-1}. The mean velocity calculate from the ablation stakes GPS survey is 83 m y^{-1}, which is lower respect the remote sensing analysis, likely because the ablation stakes cover only the lowest part of the glacier (the highest is at Concordia). However, mean ice velocity from remote sensing in the same altitude range is 90 m y^{-1}, that is comparable. Concerning instream flow, the model for the year 1985–1997 estimated a mean annual discharge value of 203.73 m^3 s^{-1}, against an

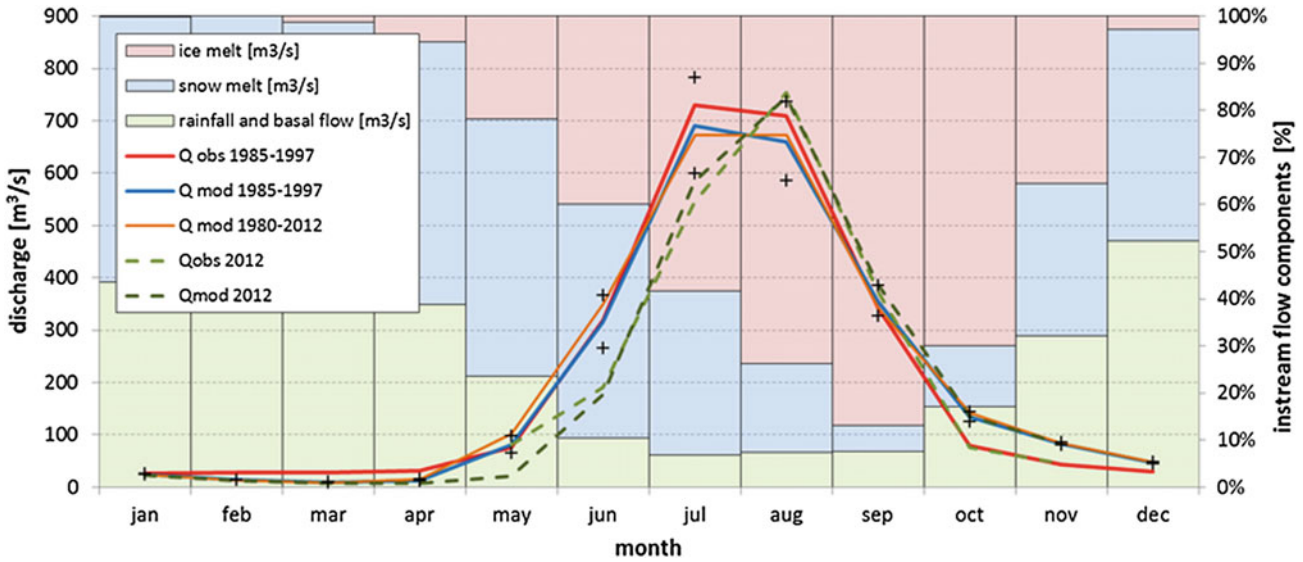

Fig. 9.2 Hydrological model calibration, and flow components (rainfall, ice melt, snow melt) as estimated by the model

observed value of 202.12 $m^3\ s^{-1}$ (bias = −0.79 %), while for 2012 the values are respectively 294.95 $m^3\ s^{-1}$ from the model and 305.03 $m^3\ s^{-1}$ from the observation (bias = −3.3 %), and obtained NSE = 0.941. During the peak months (July and August) the model reproduce quite well the observations, also the increasing months (April, May and June) are well represented, while there are some criticalities in Fall, in fact October and November discharges are slightly overestimated by the model. Looking at monthly discharge components in percentage is possible to see how snow melting represents half of the total discharge until May and then decreases its percentage in favor of ice melting that in August and September represent about the 80 % of the total instream flow (respectively 74 and 87 %).

9.5.2 Future Projections

A reported above we used 3 GCMs (EC-Earth, CCSM4 and ECHAM6) under 3 different climate scenarios (RCP26, RCP45 and RCP85), properly downscaled based upon local climate observation, for a total of 9 different simulations. We simulated daily flow during 2012–2099, and we present here two representative decades, 2040–2049, and 2090–2099. Potential future climate variations may have impacts on the hydrologic cycle modifying instream flows, ice and snow contribution and accumulation within the Shigar catchment. In Fig. 9.3 the annual mean discharge percentage variations are reported. In the first half of the century all scenarios show a significant increase, i.e. 13–20 % for RCP26, 20–35 % for RCP45, and 24–33 % for RCP85. Towards the end of the century, the situation is similar for RCP45 and RCP85, but RCP26 displays variations nearby 10 % for all models. Concerning snow contribution (not shown for shortness) it will decrease in all cases, with a largest variation of −11 % for the EC-earth RCP85 and a smallest one of −5.98 % for Echam6 RCP26. Water from ice melt will increase. In the first half of the century ice melt change against 1980–2012 would be 6–12 %, but decreasing towards the end of the century, with values in the range 1–8 % (against 1980–2012), due large depletion of ice bodies, as displayed by the model (not shown).

9.6 Discussion

Ice in our catchment is laid for 78 % between 3,470 masl and 5,375 masl, and for approximately 65 % within 4,105 masl and 5,375 masl. During control period, continuous snow cover at relatively low altitude (ca. 5,200 masl) provides shield to the underlying ice. However, under the future scenario with increasing temperature and decreasing snowfall amount, the permanent snowline altitude would increase (until 5,500 masl or so), causing ice melting higher up. Initially, such ice ablation would provide a significant increase of water flows. However, when glaciers would down waste largely, a decrease in stream flows would be seen. At 2099 the ice melt contributing areas should in practice be limited below 6,000 masl. Our model, explicitly developed for poorly gauged basins, suffer from some lacks. The melt factor approach is considerably simple in view of the complex dynamics of snow and ice melts, including debris cover. Energy based model are nowadays available

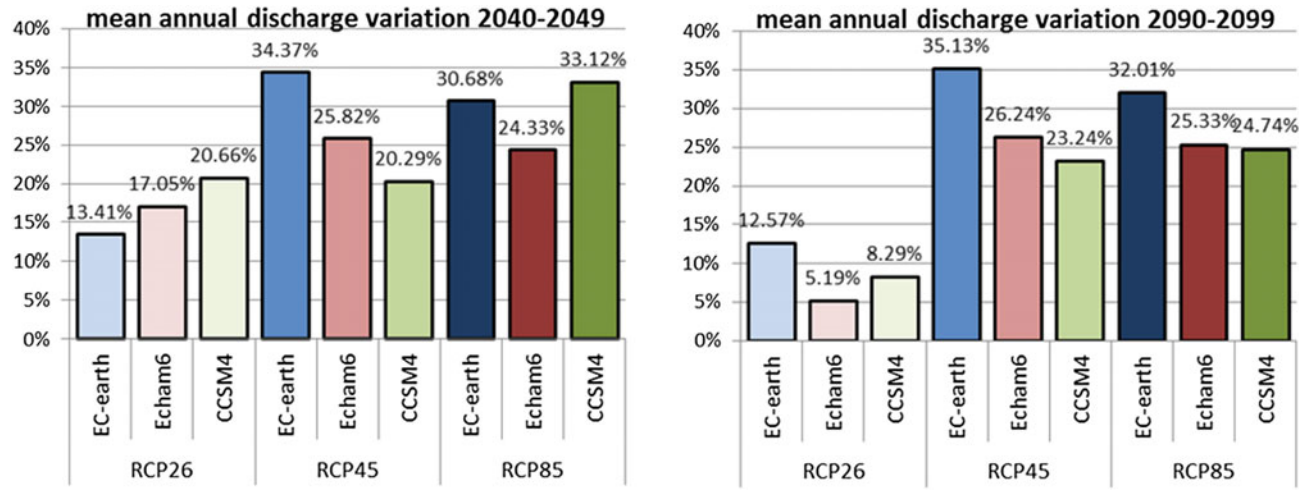

Fig. 9.3 Mean annual discharge variations from the control period (1980–2012)

for snow and ice melt (Lehning et al. 2002), but they may require more information, unavailable here. The use of extrapolated rather than measured temperatures and precipitation may affect the performance of the model, especially during Spring and melt season. Initial conditions concerning ice thickness (i.e. volume) are also uncertain. Future work may be devoted to better estimate ice volume.

9.7 Conclusions

We investigated here future instream flows, snow and ice dynamics from watershed within HKH mountain. We gathered information from available meteorological and hydrological data, we used data from three field campaigns to evaluate ice ablation, and we then coupled glaciological concepts to hydrological modeling theory, to obtain a reasonable synthesis of the hydrological patterns from this glacierized area. We then projected hydrological cycle one century ahead from now, and we tried to highlight the possible consequences of a changing climate, as expected according to the present literature, upon water resources down slope. The proposed approach profits of sparse data from several sources, and is simple enough that portability to other catchments nearby should be reasonably feasible, for large scale water resources assessment in this very sensitive area water wise.

Acknowledgments The present work was carried in the frame of the SHARE-Paprika project, funded by the EVK2CNR committee of Italy, aiming at evaluating the impact of climate change upon hydrology of the UIB region. We hereby acknowledge EVK2CNR committee for providing also weather data from their stations, and PMD for providing monthly data of their stations.

References

Akhtar M, Ahmad N, Booij MJ (2008) The impact of climate change on the water resources of Hindukush–Karakoram–Himalaya region under different glacier coverage scenario. J Hydrol 355:148–163

Bocchiola D, Groppelli B (2010) Spatial estimation of Snow Water Equivalent at different dates within the Adamello Park of Italy. Cold Reg Sci Technol 63(3):97–109

Bocchiola D, Mihalcea C, Diolaiuti G, Mosconi B, Smiraglia C, Rosso R (2010) Flow prediction in high altitude ungauged catchments: a case study in the Italian Alps (Pantano Basin, Adamello Group). Adv Water Resour 33(10):1224–1234

Bocchiola D, Diolaiuti G, Soncini A, Mihalcea C, D'Agata C, Mayer C, Lambrecht A, Rosso R, Smiraglia C (2011) Prediction of future hydrological regimes in poorly gauged high altitude basins: the case study of the upper Indus, Pakistan. Hydrol Earth Syst Sci 15:2059–2075

Bocchiola D, Diolaiuti G (2013) Recent (1980–2009) evidence of climate change in the upper Karakoram. Pakistan Theor Appl Climatol 113(3–4):611–641

Chalise SR, Kansakar SR, Rees G, Croker K, Zaidman M (2003) Management of water resources and low flow estimation for the Himalayan basins of Nepal. J Hydrol 282:25–35

Groppelli B, Bocchiola D, Rosso R (2011) Spatial downscaling of precipitation from GCMs for climate change projections using random cascades: a case study in Italy. Water Resour Res 47:W03519. doi:10.1029/2010WR009437

Immerzeel WW, van Beek LPH, Bierkens MFP (2010) Climate change will affect the Asian water towers. Science 328:1382–1385

Kehrwald NM, Thompson LG, Tandong Y, Mosley-Thompson E, Schotterer U, Alfimov V, Beer J, Eikenberg J, Davis ME (2008) Mass loss on Himalayan glacier endangers water resources. Geophys Res Lett 35:L22503. doi:10.1029/2008GL035556

Konz M, Uhlenbrook S, Braun L, Shrestha A, Demuth S (2007) Implementation of a process-based catchment model in a poorly gauged, highly glacierized Himalayan headwater. Hydrol Earth Syst Sci 11(4):1323–1339

Lehning M, Bartelt P, Brown B, Fierz C (2002) A physical SNOWPACK model for the Swiss avalanche warning Part III:

meteorological forcing, thin layer formation and evaluation. Cold Reg Sci Technol 35:169–184

Mayer C, Lambrecht A, Belo‘ M, Smiraglia C, Diolaiuti G (2006) Glaciological characteristics of the ablation zone of Baltoro Glacier, Karakoram. Ann Glaciol 43:123–131

Mayer C, Lambrecht A, Mihalcea C, Belò M, Diolaiuti G, Smiraglia C, Bashir F (2010) Analysis of glacial meltwater in Bagrot Valley, Karakoram based on short-term Ablation and debris cover observations on Hinarche Glacier. Mt Res Dev 30(2):169–177

Mihalcea C, Mayer C, Diolaiuti G, Lambrecht A, Smiraglia C, Tartari G (2006) Ice ablation and meteorological conditions on the debris covered area of Baltoro Glacier (Karakoram, Pakistan). Ann Glaciol 43:292–300

Peel MC, Finlayson BL, McMahon TA (2007) Updated world map of the Köppen-Geiger climate classification. Hydrol Earth Syst Sci 11:1633–1644

Quincey DJ, Glasser NF, Braun M, Bishop MP, Hewitt K, Luckman A (2011) Karakoram glacier surge dynamics. Geophys Res Lett 38. doi: 10.1029/2011GL049004

Smiraglia C, Mayer C, Mihalcea C, Diolaiuti G, Belo‘ M, Vassena G (2007) Ongoing variations of Himalayan and Karakoram glaciers as witnesses of global changes: recent studies of selected glaciers. Dev Earth Surf Process 10:235–248

Winiger M, Gumpert M, Yamout H (2005) Karakoram–Hindukush–western Himalaya: assessing high-altitude water resources. Hydrol Process 19:2329–2338

Assessing Impacts of Climate Change, Ski Slope, Snow and Hydraulic Engineering on Slope Stability in Ski Resorts (French and Italian Alps)

10

Carmen de Jong, Gloria Carletti and Franco Previtali

Abstract
Climate change and increased skier density is increasing ski run reworking, use of artificial snow and snow grooming. Few studies are available on these engineering impacts on slope stability. Therefore, the soil properties, compaction and infiltration characteristics were investigated on ski slopes and compared to natural sites for three different ski resorts (Les Menuires, La Rosière and Foppolo) in the French and Italian Alps. The results show that soil properties differ substantially, with lower nitrogen and carbon content and higher pH on ski runs. Soil compaction is up to three times higher and infiltration takes up to four times longer on ski slopes compared to natural sites. Some new ski slopes were even 100 % impermeable. This explains why ski slopes are more prone to landslides, sheet, rill and gully erosion and have a distinct vegetation cover.

Keywords
Artificial snow • Infiltration • Permeability • Soil properties • Ski slope stability

10.1 Introduction

Slope stability in winter tourism resorts in the Alps is affected by climate change as well as human impacts related to ski resort management such as ski run engineering, artificial snow production and snow grooming (Previtali 2011; de Jong 2014; de Jong 2012; de Jong 2011). Climate change impacts such as increased temperature and decreased snowfall cause more pronounced low flows and floods (Alexander 1998; Chardon 1990). In combination with anthropogenic impacts on ski runs such as soil and vegetation removal, reduced soil permeability, increased surface runoff, changes in vegetation cover, changes in surface roughness and large-scale water transfers mountain ecosystems are under increasing pressure (Lovato and Montagna 2011; Buisson 2011). This study compares soil infiltration and compaction measurements carried out with infiltrometers and penetrometres on different sections of ski runs and adjacent, natural sites with differing gradients and contrasting geological settings in Les Menuires and La Rosière (northern French Alps) and Foppolo (central Italian Alps). In addition, chemical, bio-chemical and soil physical properties were studied for the French sites. It also examines potential natural and anthropogenic triggers of erosion and mass movements on ski runs with natural and artificial snow.

C. de Jong (✉)
Mountain Centre, University of Savoy, Savoie Technolac, 73376 Le Bourget du Lac, France
e-mail: dejong.carmen@neuf.fr

G. Carletti
Mountain University/University of Milan, Via Morino 8, 25048 Edolo, BS, Italy

F. Previtali
Department of Earth and Environmental Sciences, University of Milan Bicocca, Piazza della Scienza 1, 20126 Milano, Italy

G. Lollino et al. (eds.), *Engineering Geology for Society and Territory – Volume 1*,
DOI: 10.1007/978-3-319-09300-0_10,

Fig. 10.1 Study sites in **a** Les Menuires (1,860–2,160 m), **b** La Rosière (1,850–2,090 m) and **c** Foppolo (1,820–2,000 m)

10.2 Study Areas

Three test sites in small and large ski resorts with different geology, geomorphology and climatology were studied in the French and Italian Alps (Fig. 10.1). The ski slopes in Les Menuires (Trois Vallées) and La Rosière (San Bernardo, France) are situated in carbonic limestone and schist of the "Briançonnaise zone". The ski slopes in Foppolo (Brembana Valley, Italy) are situated in para- and orthogneiss of the internal crystalline massif. Les Menuries and La Rosière have a semi-humid climate with approx. 1,000 mm of rainfall and 400 mm of snow water equivalent (SWE) annually. Foppolo receives approx. 2,400 mm of rainfall and 1,000 mm of SWE. 50, 5 and 20% of ski slopes are covered by artificial snow in Les Menuires, La Rosière and Foppolo respectively. Les Menuires has a natural vegetation of shrub and grass. The ski slopes are susceptible to mass movements. In La Rosière, the lower ski slopes have been deforested. In Foppolo, the natural vegetation is forest. Due to the persistent artificial snow cover and frequent ski run reworking, the ski slopes in all sites are devoid of vegetation except for grass during the short growing season.

10.3 Methodology

This study compares soil properties and permeability of ski runs and adjacent natural sites for field campaigns in May, July and August 2013. Biochemical soil properties such as pH, carbon and nitrogen content were defined from soil samples at 0–5, 5–25 and 25–50 cm depth for the French sites. The depth was limited due to the absence of soil development on ski runs. Soil infiltration and compaction measurements were carried out with infiltrometers and penetrometres. The top, middle and bottom sections of ski runs and natural slopes were sampled for Les Menuires (2,160, 2,050 and 1,860 m), La Rosière (2,090, 1,960, and 1,850 m) and Foppolo (2,000, 1,940 and 1,820 m) with average slope gradients of 22–55, 21–39 and 30–55% respectively.

10.4 Results and Discussion

Soil properties (pH, N and organic C), soil permeability and soil compaction were compared on different ski slopes with natural sites.

10.4.1 Soil Properties

The pH and nitrogen (Fig. 10.2) and carbon content of soils on ski slopes differs substantially versus natural sites. The pH of ski slopes (4.9–5.3) is generally higher than for natural sites (4.4–4.6). The distribution of nitrogen and carbon content is nearly identical and it is generally lower on the ski slopes (up to threefold lower in the top soil layers). The results are corroborated by studies on ski runs in the Sierra Nevada (Delgado et al. 2007).

10.4.2 Soil Permeability

The differences in soil permeability between ski runs and natural sites are substantial (see Figs. 10.3 and 10.4).

The infiltration on ski slopes is less than half that of natural sites. Similar results were found on ski runs in Scotland and Austria (Greenop 2013).

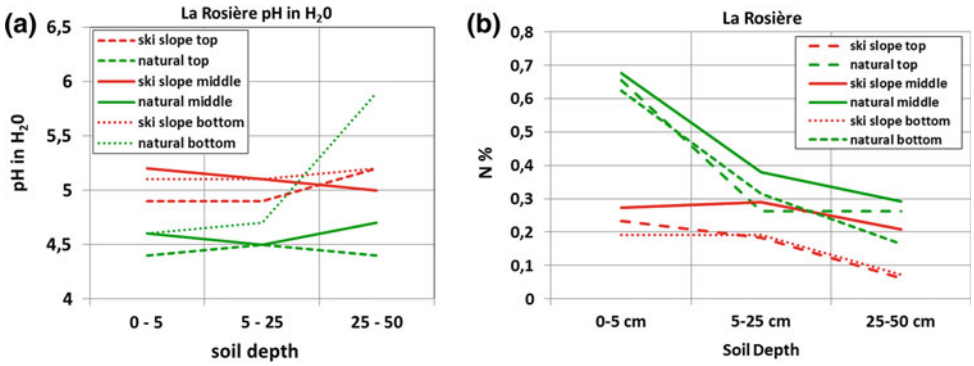

Fig. 10.2 **a** pH content and **b** nitrogen content for soil samples in La Rosière

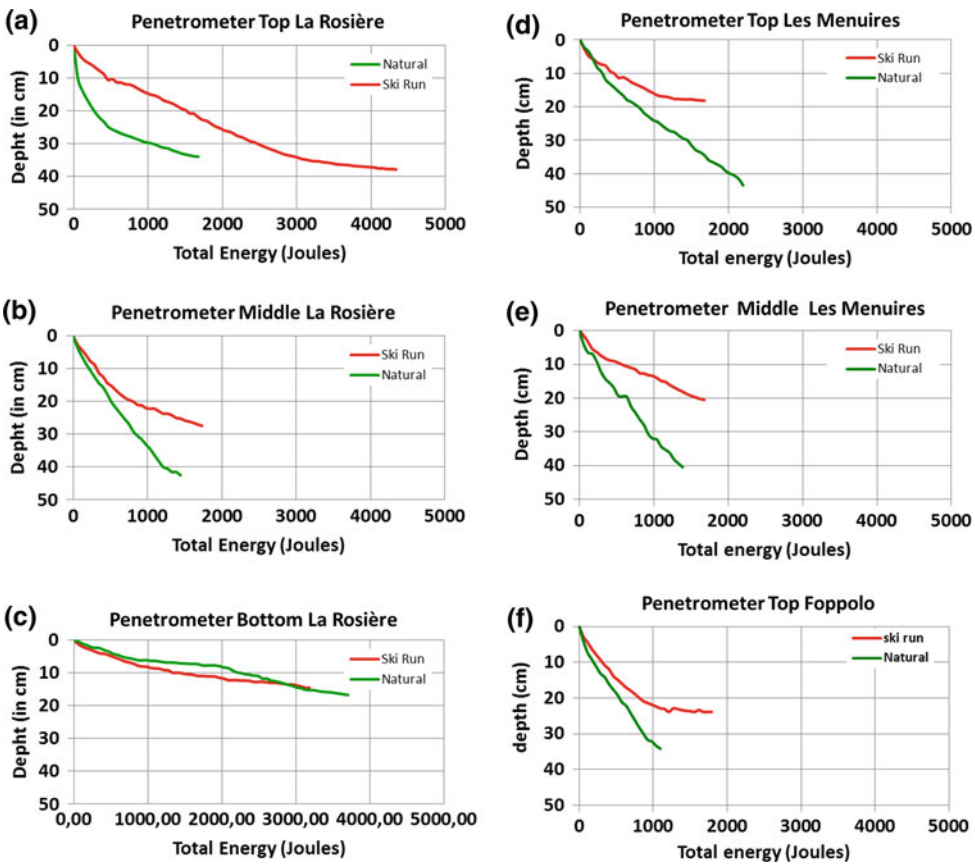

Fig. 10.3 Soil compaction at top, middle and bottom sites on ski run with natural comparison at **a**–**c** La Rosière, **d**–**e** Les Menuires, **f** Foppolo

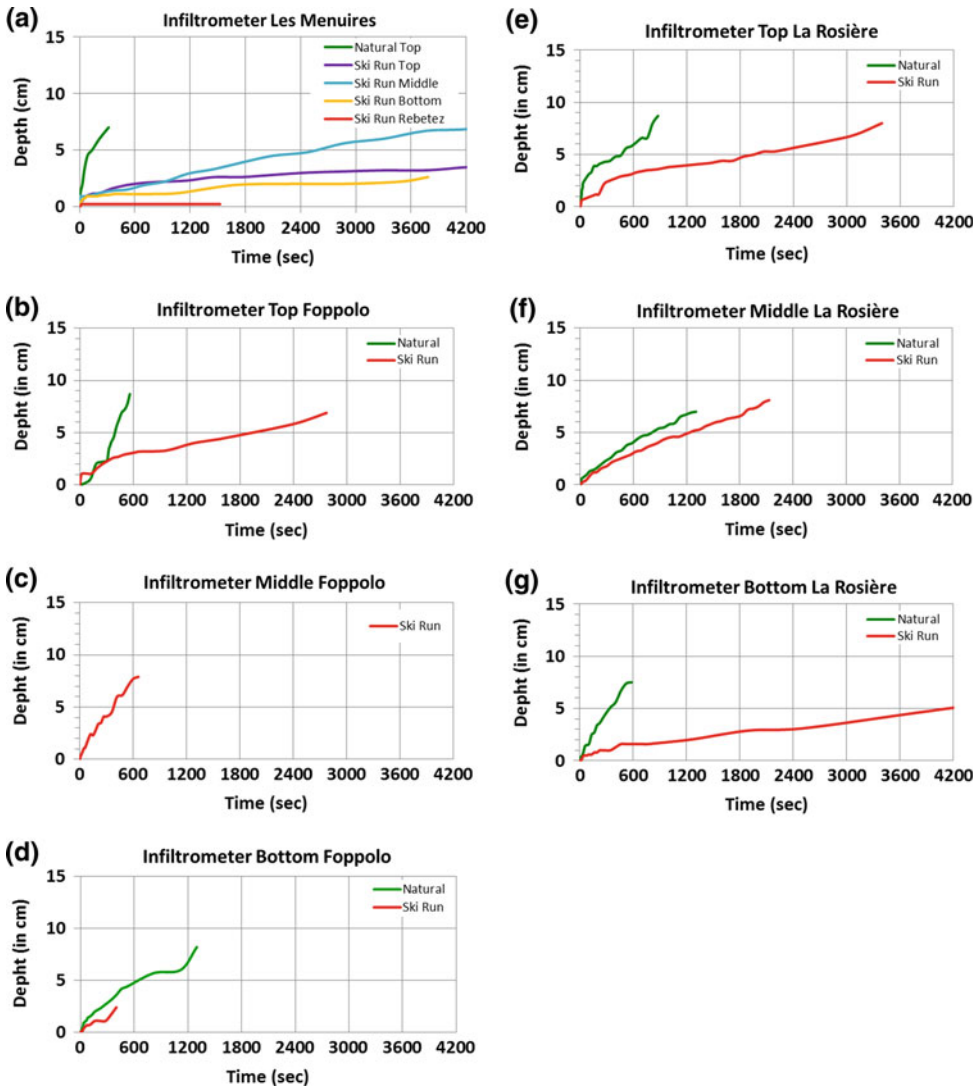

Fig. 10.4 Infiltration rates at top, middle and bottom sites on ski run with natural comparison at **a** Les Menuires, **b–d** Foppolo and **e–g** La Rosière

10.5 Conclusions

The results show that there are substantial differences between ski runs and their surrounding environment in terms of soil development, physical and biochemical soil properties, permeability and compactness, runoff and vegetation type. Differences in soil and vegetation retention capacity are related to modifications of slope gradient, ski run width and aspect due to leveling. In addition, snow grooms have major impacts on snow cover as well as vegetation and soil structure, since the entire surface of ski runs are reworked on a daily basis. The overall recovery time for vegetation is reduced by several weeks on ski runs due to the long persisting modified snow cover, sealing effects of snow grooms on soils, as well as large surplus input of water from artificial snow on the ski runs. Drainage on ski runs and relocation of natural streams accelerates flow. During extreme precipitation events, which are likely to increase with climate change especially in summer, such diversions can trigger slope movements and increase flood intensity.

Acknowledgements We thank Dr. Fabio Moia for his help with the soil analyses in the Geopedology laboratory of the University of Milan Bicocca. Meteorological data was provided by ARPA Lombardia.

References

Alexander D (1998) Valtellina landslide and flood emergency, Northern Italy, 1987. Disasters 12(3):212–222

Buisson C (2011) Gestion des zones humides du Domaine skiable des Ménuires, Mémoire fin d'étude, ISARA-Lyon, pp 84

Chardon M (1990) Les catastrophes naturelles de l'été 1987 en Lombardie: crues, inondations, écroulement de Val Pola, Revue de géographie alpine. Tome 78(1–3):59–87

de Jong C (2011) Artificial production of snow, encyclopedia of snow, ice and glaciers. In: Singh VP, Singh P, Haritashya UK (eds) Encyclopedia of earth science series, Springer, Dordrecht, p 61–66

de Jong C (2012) Artificial snow and winter sports. Environmental change and winter sports : Lessons learned from the Alps. Univ Sports Mag 83:72–79

de Jong C (2014) A White Decay of Winter Tourism. Climate Change Adaptation Manual. In: Prutsch A, Grothmann T, McCallum S, Schauser I, Swart R (eds) Lessons learned from European and other industrialized countries. Routledge, p 226–253

Delgado R, Sanchez-Maranon M, Martin-Garcia JM, Aranda V, Serrano-Bernardo F, Rosua JL (2007) Impact of ski pistes on soil properties: a case study from a mountainous area in the Mediterranean region, Soil Use Manage 23:269–277

Greenop CAB (2013) How do processes of ski resort management affect the alpine environment and the local catchment hydrology? Under-graduate Dissertation. School of Geography, The University of Leeds, BSc Geography and Geology, pp 88

Lovato E, Montagna E (2011) Turismo montano tra crisi e prospettive. Il caso del compendio sciistico si Malga San Giorgio, Verona. Politecnico di Milano, Sede di Mantova, Facoltà di Architettura e Società, Corso di Laurea Magistrale in Architettura, pp 269

Previtali F (2011) Mountain anthroscapes. The case of the Italian Alps. In: Kapur S, Eswaran H, Blum WEH (eds) Sustainable land management. Learning from the past for the future. Springer, Berlin, p 143–161

How Snow and Its Physical Properties Change in a Changing Climate Alpine Context?

11

Fratianni Simona, Terzago Silvia, Acquaotta Fiorella, Faletto Mattia, Garzena Diego, Prola Maria Cristina and Barbero Secondo

Abstract

In this study we will present the preliminary results of an activity of the Italian MIUR Project NextData, research project NextSnow (national coordinator V. Levizzani). This is the analysis of snow depth and snowfalls data in the western Italian Alps during the period 1961–2010. These series were available until now, only on paper: we performed the recovery and digitization of daily data. We carried out the historical research and data quality control which allowed a complete climate analysis, with the identification of trends and their statistical significance. The increase of maximum and minimum temperatures are considered as a consequence of significant snow depth reduction. Moreover, in the last period (2001–2010) the study has been enhanced by data provided by 46 automatic snow-gauge stations of ARPA Piemonte in order to obtain more detailed informations on climatic features from a larger altitude range.

Keywords

Snow • Temperatures • Climate change • Italian Alps

11.1 Introduction

This study analyzes the theme of snow in Piedmont with particular reference to the fifty years 1961–2010 with a focus for the years since 1933. The work is the result of a scientific collaboration between Arpa Piemonte and the Department of Earth Sciences, University of Turin. The main aim is to promote and continue the recovery activities of long term snow data, to develop complete sets, consistent, reliable and high quality making it possible to have a great deal of information about climate change. The datasets recovered not only have scientific value, but have an impact in the economic development of the territory. The knowledge of the distribution and variability of snowfall and duration of snow cover is fundamental that given their strong impact on the hydrological balance with direct consequences on the availability of water in agriculture, industry and energy production, and also on winter tourism during the ski season (Fazzini et al. 2004).

F. Simona (✉) · T. Silvia · A. Fiorella · G. Diego
Dipartimento di Scienze Della Terra, Università di Torino, Via Valperga Caluso 35, 10125 Turin, Italy
e-mail: simona.fratianni@unito.it

F. Simona
Natrisk, Via Leonardo da Vinci 44, 10095 Grugliasco, TO, Italy

F. Mattia · P.M. Cristina · B. Secondo
Dipartimento Sistemi Previsionali, Arpa Piemonte, Via Pio VII 9, 10135 Turin, Italy

11.2 Study Area and Stations Measurement

The area of the Piedmont region is characterized by a very large mountainous zone (42 % of the total) that surrounds it to the south, west and north. The topographic location, sea distance and close interactions with near French Alpine region, define and regulate the climatic peculiarities of the Piedmont. This is an area where continental air masses in

G. Lollino et al. (eds.), *Engineering Geology for Society and Territory – Volume 1*,
DOI: 10.1007/978-3-319-09300-0_11,

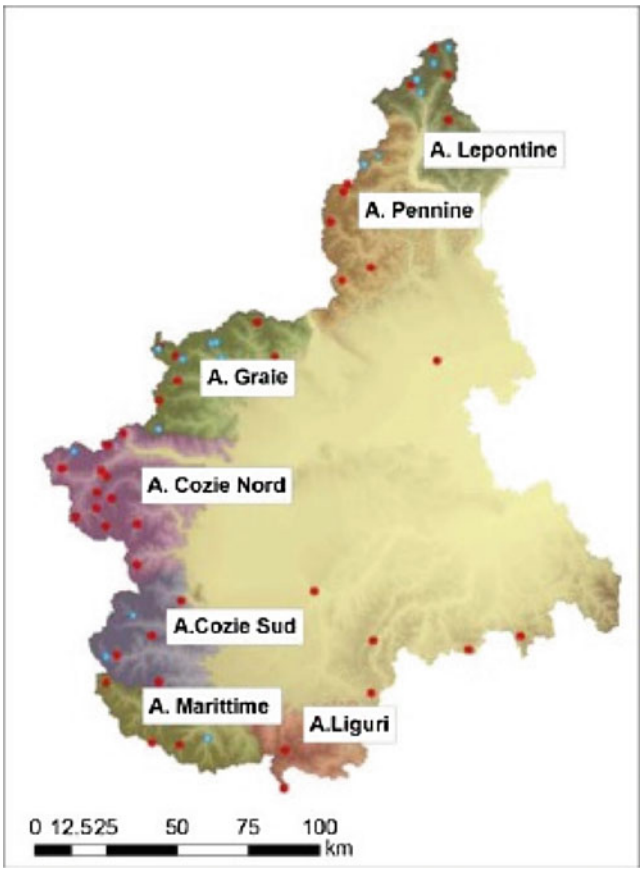

Fig. 11.1 Snow stations network and sector names of Piedmont Alps. TSS (ASS) stations are represented in *red* (*blue*)

coming from the plains collide with warm wet air masses from the Mediterranean and the Atlantic north-western fresher that interact with topography triggering frequent local circulations.

The snow data analyzed in this study are derived from the regional measurements network which includes manual and automatic stations. Currently there are 109 snow measuring points of which 32 traditional snow stations—TSS—and 77 are automatic snow station—ASS—(Fig. 11.1).

The method of collecting data from the TSS are carried out according to the technical specifications applied in the AINEVA (Modello 1).

16 TSS were chosen for the study. These are distributed uniformly throughout the Piedmont Alps, at altitudes between 700 and 2,412 m a.s.l., are representative of all alpine zones, with the exception of the Ligurian Alps.

The ASS are 46 out of which 39 are located above 1,000 m a.s.l. and distributed almost uniformly in all alpine areas. The 7 ASS located below 1,000 m a.s.l. are representative of the hills (Appennino) and the plains as low as Vercelli station at 155 m a.s.l. 3 stations are located above 2,500 m a.s.l., the highest one is Passo Moro—Macugnaga at 2,820 m a.s.l. TSS stations data are available since 1930, thus allow to analyze the snow depth variations over long period. ASS stations data are available since 2001 and allow to analyze in more detail the altitudinal variation of snow parameters, from 155 to 2,820 m a.s.l.

11.3 Data Processing

The historical time series used in this study have been recovered from the paper archives of the Ufficio Idrografico del Bacino del Po (Po basin Hydrographic Office) now hosted by the Agenzia Regionale per la Protezione Ambientale (Regional Agency for Environmental Protection) of Piemonte and Lombardia.

The original bulletins report daily maximum and minimum temperatures, rainfall, snow depth and occasionally fresh snow data acquired by observers. A parallel in-depth historical research has been carried out in order to acquire stations metadata, i.e. information on the geographical position, elevation, exposure and any other characteristics of the measurement site, as its instrumentation and operational period. Particular attention has been addressed to possible relocations or changes occurred during the stations lifetime, which could reflect in relevant changes in the data not related to climatic factors (Aguilar et al. 2003; Acquaotta et al. 2009; Venema et al. 2012). All the historical time series have been quality controlled in order to identify and eventually correct errors due to the observers and to the process of digitization. A procedure for the identification of the data outlying prefixed thresholds is applied to the snow accumulation a(t) and snow depletion d(t) time series. Values of a(t) and d(t) exceeding a given threshold (95th percentile calculated on non-zero values) are highlighted and the corresponding HS is (i) checked with original value reported on the paper bulletins, (ii) evaluated in relation to temperatures and precipitation and finally (iii) compared with corresponding values registered in the neighboring stations, in order to test the reliability of abrupt changes in snow thickness.

For the TSS the snow data is acquired by ultrasonic snow gauge every 30 min and transmitted to the Functional Centre to ARPA Piedmont, where it is stored in a relational database RBDMS. These data are then daily subjected to a quality semi-automatic control to detect any anomalies, also through the use of a algorithm (Terzago et al. 2013a) that identifies and correct anomalous data.

11.4 Climatological Features

Several snow parameters were considered in order to describe the average climatological features of snow precipitation at seasonal (November–May) scale. The statistics over the 1961–2010 period have been calculated. In summary:

- snow precipitation (HN) median is about 62 cm at 700 m a.s.l., 300–400 cm at about 1,500 m a.s.l. and 600 cm at about 2,000 m a.s.l.;
- snow depth (HS) median is about few centimeters at 700 m a.s.l., about 50 cm at about 1,500 m a.s.l. and 100–150 cm at 2,000 m a.s.l.;
- days with snow precipitation (SD) median is about 9 days/season at 700 m a.s.l., 30 days at about 1,500 m a.s.l. and 46 days at about 2,200 m a.s.l.;
- days with snow cover (HS0) median is <100 days per season until 1,000 m a.s.l., between 130 and 180 days at 1500–2000 m a.s.l. and >200 days at >2,000 m a.s.l.

The analysis of the results of the ASS agrees with the values of TSS. The seasonal distribution of snow precipitation is mainly dependent on the elevation:

- below 2,000 m it is unimodal, with an absolute maximum in winter (January);
- between 2,000 and 2,200 m January is still the month with maximum snow precipitation but a sensible amount of snow fall in March/April;
- above 2,200 m the distribution is unimodal with a maximum in spring (April).

We have correlate snow data with altitude of all stations by a weighted regression: weight 5 for manual station (1961–2010), weight 1 for automatic stations (2001–2010). The results are:

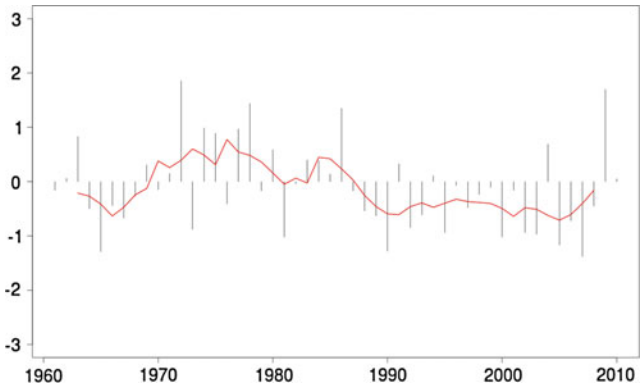

Fig. 11.2 Snowfall SAI, reference period 1971–2000. *Red line*: 5 years moving average

- seasonal snowfall average (∑HN) increases of 30 cm/100 m;
- days number average with snow cover (HSD) increases of 9 days/100 m;
- days number average with snowfalls (SD) increases of 2 days/100 m;
- the logarithm of snow cover (Log10(HS)) increases of 0.09 cm/100 m.

Table 11.1 Trend of seasonal snowfall (HN) and annual minimum temperature (TN) and maximum temperature (TX) from 1961 to 2010

Stations	ASL (m)	HN		TN		TX	
		b	ϐb	b	ϐb	b	ϐb
Valsoera	2,412	−1.83	1.92	**0.06**	**0.01**	**0.08**	**0.01**
Camposecco	2,316	−1.46	1.65	**0.07**	**0.01**	0.00	0.01
Serrù	2,283	−1.22	2.10	**0.03**	**0.01**	−0.01	0.01
Vannino	2,177	−1.29	1.31	**0.04**	**0.01**	**0.04**	**0.01**
Toggia	2,165	0.11	1.46	0.02	0.01	**0.04**	**0.01**
Rochemolles	1,950	**−3.72**	1.11	0.02	0.01	**0.08**	**0.01**
Telessio	1,940	−2.70	2.48	**0.03**	**0.01**	**0.02**	**0.01**
Malciaussia	1,800	**−2.68**	1.63	**0.06**	**0.01**	0.02	0.01
Devero	1,634	−1.44	1.36	0.01	0.01	0.00	0.01
Agaro	1,600	**−2.89**	1.21	**0.04**	**0.01**	**0.05**	**0.02**
Castello	1,589	−0.50	1.00	**−0.03**	**0.01**	0.01	0.01
Ceresole	1,573	−1.72	1.35	**−0.03**	**0.01**	0.00	0.01
Saretto	1,540	−1.71	1.09	**0.02**	**0.01**	**0.02**	**0.01**
Cavalli	1,500	−1.48	1.32	**0.02**	**0.01**	0.02	0.01
Piastra	960	−1.88	1.19	0.03	0.01	0.00	0.00
Rosone	701	0.10	0.52	0.01	0.01	**−0.04**	**0.01**

We report the slope (b) and the absolute error associated to the slope (b). Statistical significance was indicated in bold (95 %)

11.5 Temporal Evolution

For each station, the seasonal snow depth standardized anomalies have also been considered. All the stations time series have been averaged to get the regional Standardized Anomaly Index, which express the anomaly of the studied parameter respect to the mean value over a reference 30-year period, in this case 1971-2000. During the last 25 years almost all seasons were characterized by negative anomalies. The SAI calculated on snow precipitation shows the same phases of positive snow depth anomalies. The snow precipitation has been below average along the 1940 till the mid 50s, during the 1960s and from the mid 80s up to 2008. In the last 25 years only 6 seasons present positive anomalies, all the others had below average snow precipitation (Fig. 11.2). This evolution is in opposite accordance with the maximum and minimum temperatures SAI series index that are both negative from 1961 to 1986 and positive from 1987 to 2010. The analysis of trends has been conducted over the complete snow season November–May. To assess the significance of trends was used the nonparametric Mann-Kendall test. The seasonal snowfall has negative trends in 14 stations out of 16 and in 3 cases are statistically significant: Rochemolles, Malciaussia and Agaro. This decrease was higher at medium—low altitude, in fact, especially below 2,000, they receive less snow today than in the past (Terzago et al. 2013b). In the station of Rochemolles the seasonal average of snowfall during the period 1990–2010 decreased by 26 % compared to the period 1961–1990. In most of the stations considered (10 of 16) the seasonal trend in the number of snowy days show significant changes in the values of −0.10 days/year. Trend analysis shows a general decrease of the average thickness of the seasonal snowpack. The trends are negative in all the stations considered, with the exception of the station situated at an altitude lower (Rosone, 701 m).

For the minimum and maximum temperature the trends are increasing and statistically significant in most locations analyzed. For the mean maximum temperature the highest slopes are calculated in the stations with elevation greater than 1,600 m a.s.l. Valsoera and Rochemolles shows the maximum value (0.08 °C/season) followed by Camposecco with 0.07 °C/season (Table 11.1).

11.6 Conclusions

The present study gives a contribution to the assessment of the temporal and spatial variability of the climatic conditions at high elevation sites in Western Italian Alps. The analysis on the maximum and minimum temperature highlights an increasing of the variables in the last 50 year, from 1961 to 2010.

The investigation on temporal evolution of snow precipitation shows snow precipitation fluctuations with an irregular period of about one decade, with relative maxima around 1940, 1950, 1960, and the absolute maximum in the 70s. Snow was abundant till the early 80s, then a sequence of poor snow winters leads to the absolute minimum of the record in the 1990s. This study outlines a significant decrease of snow depth in all the stations over seasonal (November–May) time scale in the period 1961–2010. The northern stations suffer an higher significant decrease, so North Piedmontese Alps result the most sensitive to climate change. The results will provide useful information to the prediction and adaptation of climate risks.

References

Acquaotta F, Fratianni S, Cassardo C, Cremonini R (2009) On the continuity and climatic variability of the meteorological stations in Torino, Asti, Vercelli and Oropa. Meteorol Atmos Phys 103:279–287. doi:10.1007/s00703-008-0333-4

Aguilar E, Auer I, Brunet M, Peterson TC, Wieringa J (2003) Guidance on metadata and homogenization. WMO-TD No. 1186

Fazzini M, Fratianni S, Biancotti A, Billi P (2004) Skiability conditions in several skiing complexes on Piedmontese and Dolomitic Alps. Meteorol Z 13(3):253–258

Terzago S, Faletto M, Prola MC, Fratianni S, Cremonini R, Barbero S (2013a) An innovative algorithm for unmanned validation of automatic snow depth measurements. ISSW Proceeding, pp 989–993

Terzago S, Fratianni S, Cremonini R (2013b) Winter precipitation in Western Italian Alps (1926–2010): trends and connections with the North Atlantic/Arctic Oscillation. Meteorol Atmos Phys 119:125–136

Venema V, Mestre O, Aguilar E, Auer I, Guijarro J, Domonkos P, Vertacnik G, Szentimrey T, Stepanek P, Zahradnicek P, Viarre J, Müller-Westermeier G, Lakatos M, Williams CN, Menne MJ, Lindau R, Rasol D, Rustemeier E, Kolokythas K, Marinova T, Andresen L, Acquaotta F, Fratianni S, Cheval S, Klancar M, Brunetti M, Gruber C, Prohom Duran M, Likso T, Esteban P, Brandsma T (2012) Benchmarking homogenization algorithms for monthly data. Clim Past 8:89–115. doi:10.5194/cp-8-89-2012

12 Air Temperature Thresholds to Assess Snow Melt at the Forni Glacier Surface (Italian Alps) in the April–June Period: A Contribution to the Application of Temperature Index Models

Senese Antonella, Vuillermoz Elisa, Azzoni Roberto Sergio, Verza Gian Pietro, Smiraglia Claudio and Diolaiuti Guglielmina

Abstract

Glacier melt occurs whenever the surface temperature is null (273.15 K) and the net energy budget is positive. These conditions can be assessed by analysing meteorological and energy data acquired by a supraglacial Automatic Weather Station (AWS). In the case this latter is not present at the glacier surface the assessment of actual melting conditions and the evaluation of the melt amount is difficult and simple methods based on Temperature index (T-index) or degree days models are generally applied. These models require the choice of a correct temperature threshold. In fact, melt does not necessarily occur at air temperatures higher than 273.15 K, since it is determined by the surface energy budget which in turn is only indirectly affected by air temperature. This is particularly the case of the late spring period when ablation processes start at the glacier surface thus progressively reducing snow accumulation. In this paper, to detect the most indicative air temperature threshold witnessing snow or ice melting in the April–June period, we analysed air temperature data recorded from 2006 to 2012 by a supraglacial AWS set up on the ablation tongue of Forni Glacier (Italian Alps). Moreover we also evaluated the glacier energy budget and the Snow Water Equivalent (SWE) value during this time-frame. We also analysed air temperature data from a station located outside the studied glacier. Then the ablation amount is estimated both from the surface energy balance (from supraglacial AWS data) and from T-index method (from daily air temperature measured outside the glacier) and the results were compared.

Keywords

Snow melt • Glacier energy-budget • Temperature-index model • Temperature threshold

12.1 Introduction and Study Aims

Melt conditions generally are estimated considering both positive energy budget and surface temperature equal to 273.15 K (e.g. Hock 2005; Senese et al. 2012a, b). Whenever a supraglacial Automatic Weather Station (AWS) is not present, simple methods based on Temperature index (T-index) or degree days models, which assume an empirical relationship between air temperatures and melt rates, are applied (e.g. Braithwaite 1985; Cazorzi and Dalla Fontana 1996; Hock 1999; Pellicciotti et al. 2005). Without a supraglacial AWS only the amount of energy available for melting (by applying appropriate lapse rate to data from

S. Antonella (✉) · V. Elisa · A.R. Sergio · S. Claudio · D. Guglielmina
"A. Desio" Department of Earth Sciences, University of Milan, Via Mangiagalli 34, 20131 Milan, Italy
e-mail: antonella.senese@unimi.it

D. Guglielmina
e-mail: guglielmina.diolaiuti@unimi.it

V. Elisa · V.G. Pietro · S. Claudio · D. Guglielmina
Ev-K2-CNR Commitee, Via San Bernardino 145, 24126 Bergamo, Italy

G. Lollino et al. (eds.), *Engineering Geology for Society and Territory – Volume 1*,
DOI: 10.1007/978-3-319-09300-0_12,

AWSs nearby) can be quantified, but no information about presence and features of snow or ice at the glacier surface can be assessed. This is particularly the case of late spring time (April–June) at the glacier ablation zone where we cannot establish in detail if snow is at the melting point and how long this phenomenon occurs. Generally, in the most applied degree-day models a temperature threshold of 273.15 K is used to evaluate snow ablation from temperature data (Braithwaite 1985; Hock 2003; Bocchiola et al. 2010) acquired by AWSs located outside the glacier area and shifted to the glacier elevation by applying a lapse rate. This assumption neglected the fact that melt does not necessarily occur at air temperatures >273.15 K, since it is determined by the surface energy balance and this latter is only indirectly affected by air temperature (Kuhn 1987). Then the choice of an appropriate air temperature threshold is fundamental to detect the actual melting days and to evaluate the melt amount.

To assess the most suitable air temperature threshold for applying T-index models it is necessary to analyse air temperature data with respect to glacier energy budget data and surface temperature data. In this way it is possible to detect the actual melting days (those ones featuring both surface temperature of 273.15 K and positive energy budget) and to evaluate the air thermal conditions they feature. This analysis can be performed on glaciers where AWSs have been installed thus permitting the availability of meteorological and energy data sets acquired at the glacier surface. This is the case of the Forni Glacier (Italian Alps) where an AWS has been running since September 2005 (Citterio et al. 2007; Senese et al. 2012a, b). In this paper we present results from an analysis of meteo and energy data of the April–June period acquired by the Forni Glacier AWS in the 2006–2012 time window to evaluate an actual air temperature threshold suitable for applying T-index models. Moreover we also compared and discussed the ablation amount derived from snow melt which we calculated both from glacier energy budget and T-index models.

The Forni Glacier is the largest Italian glacier (Fig. 12.1). It is widely debris-free, even if darkening phenomena are shown (Diolaiuti and Smiraglia 2010; Diolaiuti et al. 2012).

12.2 Methods

At Forni Glacier the available meteorological dataset recorded by an automatic weather station (AWS1 Forni, Fig. 12.1) set up on the ablation tongue starts from 26th September 2005. The AWS1 Forni was developed in the framework of the SHARE (Stations at High Altitude for Research on the Environment) program and data are quality checked and validated according to the SHARE protocol and available to all the scientific community upon request. This dataset is quite uninterrupted (from 26/09/2005 up to now) with very few gaps (3.05 % of the total period). In this study the time frame from 1st October 2005 to 31st December 2012 is analysed.

The melting is assessed both by energy budget (M_{EB}, from AWS1 Forni data) and by T-index (also named degree days) model ($M_{T\text{-}INDEX}$). The input data of this latter are temperatures measured at Bormio (1,225 m a.s.l.), a village nearby (Fig. 12.1) by a Weather Station (WS) managed by the Lombardy Regional Agency for Environmental Protection (ARPA Lombardia). ARPA takes care data validation and availability through a dedicated web site. The net energy (Rs) available for heating the surface and melting snow and/or ice is calculated following Senese et al. (2012a). Then whenever the surface temperature is at 273.15 K and Rs is positive, the ablation amount (M_{EB}, kg m^{-2} or mm w.e.) is quantified.

The daily snow melting rate through a degree days (or T-index) model is estimated following Hock (1999) from daily air temperature measured at Bormio and shifted to the AWS1 Forni elevation ($T_{from\text{-}Bormio}$ from here) by applying a general lapse rate (-6.5 K km^{-1}).

The snow Degree-Days Factor (sDDF) is found considering the Snow Water Equivalent (SWE) values estimated from snow pits performed nearby the AWS1 Forni. These pits have been provided by personnel from the Centro Nivometeorologico di Bormio of ARPA Lombardia according to the AINEVA protocol. The pits were annually dug at the end of the accumulation period (April–May), only in 2007 no surveys were performed. From albedo data the presence of snow or bare ice is deducted and then the length of the snow coverage period. In fact, the SWE was considered completely melted when the albedo becomes lower than 0.4. Finally the sDDF is calculated as:

$$sDDF = \frac{SWE}{DD_{glacier}} \tag{12.1}$$

where $DD_{glacier}$ is the sum of Degree-Days (calculated from $T_{from\text{-}Bormio}$ and considering different air temperature thresholds) in the time frame between a snow pit survey and the occurrence of ice albedo.

To detect the most suitable daily temperature threshold witnessing a glacier melting surface in the April–June period we started analysing melt conditions at the glacier surface. We considered hourly M_{EB} values (obtained from AWS1 Forni data) to detect if ablation occurs and how long this phenomenon takes (number of hours per day). Then we sorted

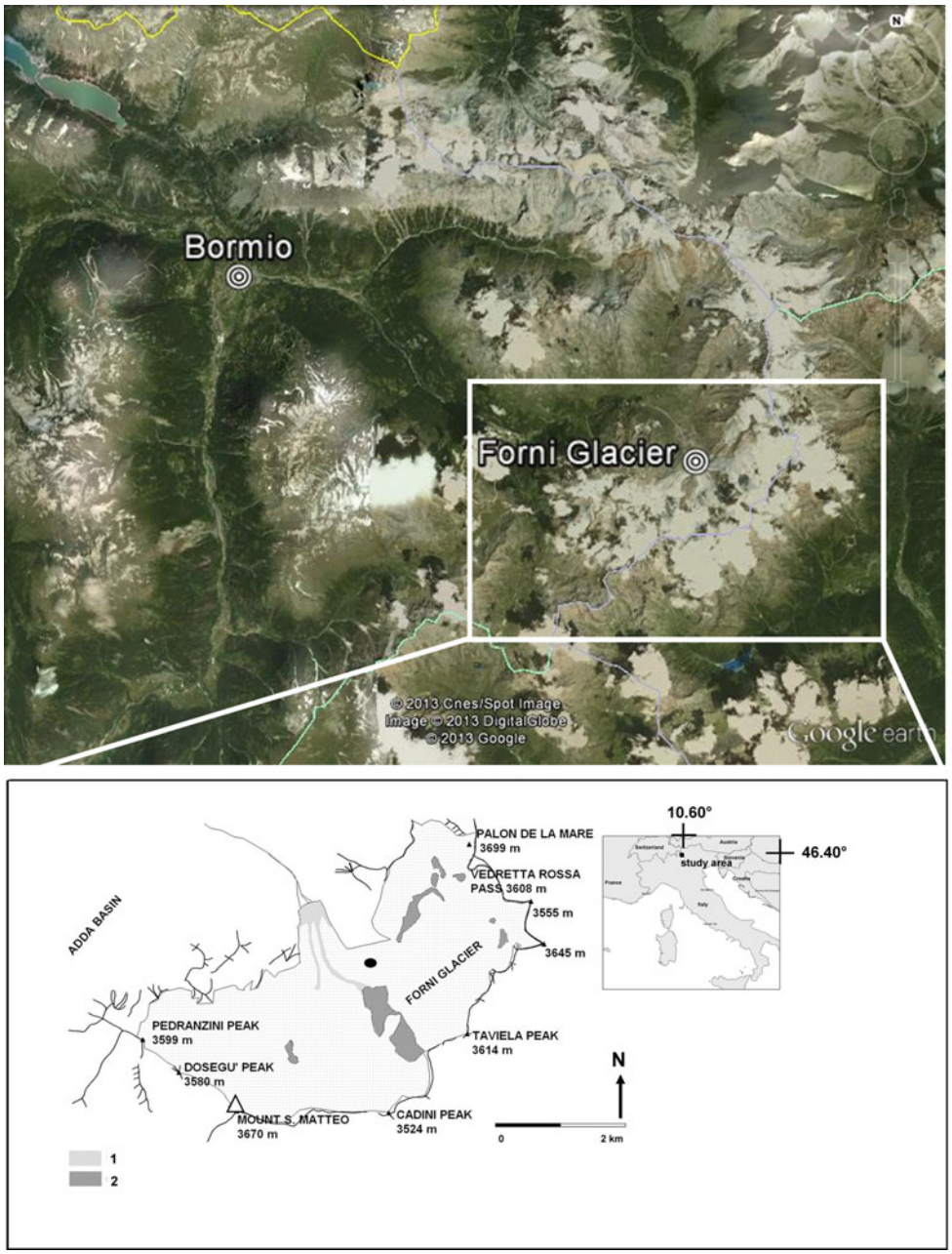

Fig. 12.1 On the *top* the location of Bormio and Forni Glacier (Google Earth © raster base) and in the *lower* picture the location of the AWS1 Forni (*black dot*, WGS84 coordinates 46°23′56.0″ N and 10°35′25.2″ E, 2,631 m a.s.l.). In the map the *light grey* areas (1) are used to mark supraglacial debris coverage and the *dark grey* zones (2) indicate rock exposures and nunataks

these data according to temporal length classes (0, 4, 6, 12 and 24 melting hours per day). For each class we calculated the maximum, minimum and mean value of daily average air temperature from both AWS1 Forni data and $T_{\text{from-Bormio}}$ data. These temperature data represent possible thresholds to be applied to calculate degree days driving snow melt. We performed several attempts of running the degree days model by applying the different temperature threshold values and the obtained melt amounts are compared with the one from energy budget computation (M_{EB}) thus permitting to select the most suitable and performing threshold values.

12.3 Results

12.3.1 Melting from Energy Balance

Regarding M_{EB}, it was estimated considering only hours characterized by null (273.15 K) surface temperature and positive energy budget. The time window of our analysis is scheduled according to the hydrological year (i.e. from 1st October of the year x to 30th September of the year x + 1) and it results a total M_{EB} of −37.5 m w.e. over a seven year long period. Supraglacial albedo data permit to detect snow

cover presence (albedo >0.4) during days featuring both positive energy balance and surface temperature of 273.15 K. The occurrence of these three criteria (ranging from 69 to 108 days per year) allows calculation of M_{3C} (light grey bars in Fig. 12.2) which is found not negligible with a melt amount from 17.61 to 29.17 % of the total annual value. In general the melting ice period results longer (with an average value of 100 days per hydrological year) than the M_{3C} time frame (89 days per year mean value) with the unique exception of the hydrological year 2009/2010 (88 and 101 days for ice and snow respectively).

Moreover we performed a test calculating ablation (M_{PEB}) only from positive energy balance data during April–June period (91 days long) and not considering glacier surface temperature and conditions (snow presence or not). The results were compared with the M_{3C} and M_{EB} values (Table 12.1). Totally a M_{EB} for the April–June period over the time window 2006–2012 of −12.72 m w.e. is calculated. This value differs both from the M_{PEB} which results equal to −13.43 m w.e. and from the M_{3C} which is found equal to −8.47 m w.e. The quite wide range of variability of our results suggests further analyses. Moreover, the April–June melt corresponds to ca. 1/3rd of the total M_{EB}.

Focusing on the April–June M_{EB} values we found the most intense ablation occurred in 2011 (−2.26 m w.e. contributing for 43.5 % with respect to the total M_{EB} for that year) and the minimum was found in 2008 (−1.55 m w.e., 31.0 % of the annual value).

12.3.2 Daily Air Temperature Thresholds Witnessing Glacier Melting in the April–June Period

To choose the most suitable daily air temperature threshold to detect melting days and to evaluate melt amount by degree days model we analysed both AWS1 Forni and $T_{from\text{-}Bormio}$ data in the April–June period (see Table 12.2).

Days without melting (0 M_{EB} hours per day, 3rd column in Table 12.2) resulted occurring over 4.87 % of the total time frame (April–June over a 7 year long period). On the other hand, days featuring continuous and uninterrupted melt (24 M_{EB} hours per day, 8th column in Table 12.2) cover 3.30 % of the total time. These days are characterized by daily air temperature at AWS1 Forni always positive with a daily mean value of 278.60 K, the maximum of daily average data equal to 282.06 K and the minimum of daily average values of 275.48 K. $T_{from\text{-}Bormio}$ data are characterized by minimum daily temperature of 274.73 K, a mean daily average of 279.75 K and a maximum of daily average of 284.61 K. The cumulative melt occurred over these 21 days of continuous and uninterrupted ablation is equal to −0.77 m w.e. and it represents only the 6.04 % of the total loss.

Days with 12 M_{EB} hours (7th column tab 3.2) occurred on the 47.25 % of the total analysed time and they represent the 73.15 % of the whole ablation (cumulative M_{EB}: −9.30 m w.e.).

Days with 6 M_{EB} hours (6th column tab 3.2) occurred on the 83.83 % of the total analysed time and they represent

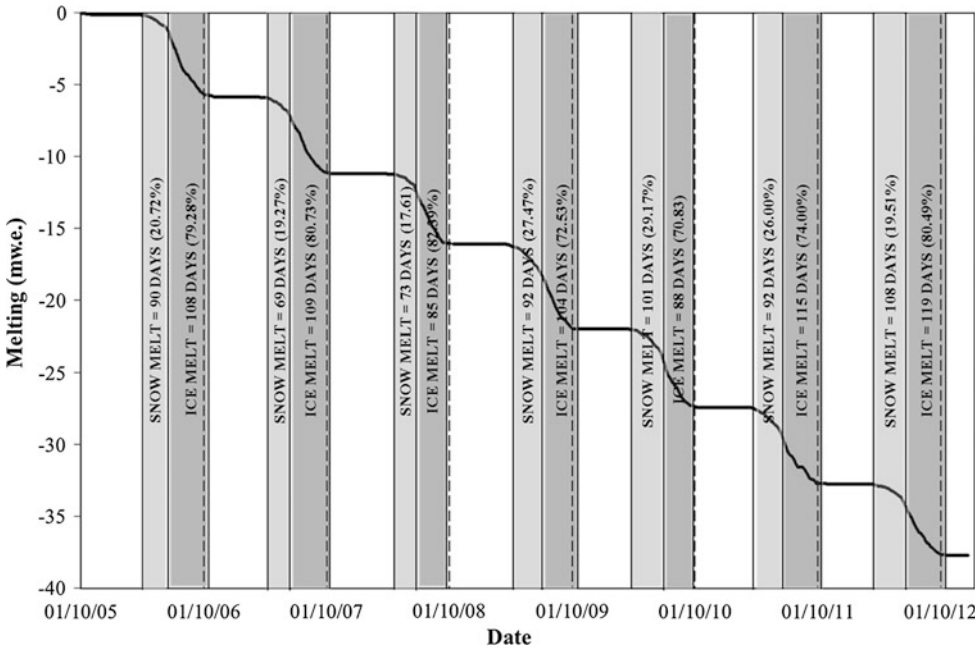

Fig. 12.2 Cumulative melting amount (M_{EB}) over the 7-year period from October 2005 to December 2012. The *dotted lines* mark the beginning of the hydrological year (1st October). In some cases ablation continues also in a few days of October and albedo values remain lower than 0.4. In *light grey* the time frames with snow melting (M_{3C}) and in *dark grey* the ice melting periods are shown

Table 12.1 For each hydrological year the following data are shown: cumulative M_{3C} during the snow melting period (2nd column), cumulative M_{EB} during April–June (4th column), cumulative M_{PEB} during April–June (6th column), annual M_{EB} value (8th column) and percentages with respect to the annual M_{EB} value (3rd, 5th and 7th column respectively)

Hydrological year	M_{3C}	M_{3C} % with respect to the annual M_{EB}	Apr–June M_{EB}	April–June M_{EB} % with respect to the annual M_{EB}	April–June M_{PEB} ($Rs > 0$)	April–June M_{PEB} % with respect to the annual M_{EB}	Annual M_{EB}
2005/2006	−1.15	20.54 %	−1.91	34.07 %	−1.98	35.41 %	−5.6
2006/2007	−1.00	18.18 %	−2.08	37.74 %	−2.11	38.35 %	−5.5
2007/2008	−0.84	16.80 %	−1.55	31.00 %	−1.85	36.91 %	−5.0
2008/2009	−1.61	28.75 %	−1.68	29.93 %	−1.73	30.89 %	−5.6
2009/2010	−1.54	27.50 %	−1.62	28.96 %	−1.74	31.05 %	−5.6
2010/2011	−1.37	26.35 %	−2.26	43.50 %	−2.33	44.81 %	−5.2
2011/2012	−0.96	19.20 %	−1.63	32.52 %	−1.69	33.87 %	−5.0
TOT	**−8.47**	**22.59 %**	**−12.72**	**33.92 %**	**−13.43**	**35.81 %**	**−37.5**
MEAN	**−1.21**	**22.47 %**	**−1.82**	**33.92 %**	**−1.92**	**35.81 %**	**−5.4**

Table 12.2 Number of days and daily temperature values (mean, minimum and maximum of the average data) in the April–June period considering different temporal length classes of M_{EB} hours

	M_{EB} hours						
	All	0	<4	≥4	≥6	≥12	24
Number of days	637	31	32	574	534	301	21
% with respect to the total studied period	100.00 %	4.87 %	5.02 %	90.11 %	83.83 %	47.25 %	3.30 %
Mean average Daily Ta AWS1 Forni (K)	274.74	265.95	268.76	275.55	275.93	277.75	278.60
Max of average Daily Ta AWS1 Forni (K)	284.28	269.09	275.00	284.28	284.28	284.28	282.06
Min of average Daily Ta AWS1 Forni (K)	262.53	262.53	265.76	265.95	268.57	271.96	275.48
Mean average Daily $T_{from\text{-}Bormio}$ (K)	276.43	267.68	270.19	277.21	277.59	279.41	279.75
Max of average Daily $T_{from\text{-}Bormio}$ (K)	286.88	275.74	276.94	286.88	286.88	286.88	284.61
Min of average Daily $T_{from\text{-}Bormio}$ (K)	264.13	264.13	266.84	267.51	268.11	268.88	274.73

The air temperature data are recorded by AWS1 Forni and from Bormio WS. These latter data are shifted to the glacier elevation by applying a general lapse rate (−6.5 K/km)

the 97.71 % of the whole ablation (cumulative M_{EB}: −12.43 m w.e.).

Then the largest part of the melt resulted occurring on days with at least 6 M_{EB} hours thus suggesting to consider temperature data calculated for this class as suitable temperature thresholds. In particular the minimum value of the average daily temperature calculated with more than 6 M_{EB} hours per day (268.57 K and 268.11 K considering the AWS1 Forni and $T_{from\text{-}Bormio}$ data respectively) were applied to detect the actual melting days. The first threshold was applied to air temperature data from AWS1 Forni and permitted to select 586 melting days describing the 99.38 % (−12.64 m w.e.) of the total M_{EB}. Considering $T_{from\text{-}Bormio}$ data, the threshold of 268.11 K permitted to detect 601 melting days giving a cumulative M_{EB} of −12.66 m w.e. equal to 99.54 % of the total.

From our results it is also clear that the use of the 273.15 K as temperature threshold drives an underestimation of ablation. In fact, this value applied to the AWS1 Forni temperature data allows to detect 421 melting days (66.09 % with respect to the total time frame) equal to a cumulative M_{EB} of −11.39 m w.e. (89.54 % with respect to the total melt). The same threshold applied to the $T_{from\ Bormio}$ data allowed to select 481 melting days giving a M_{EB} of −12.00 m w.e. (94.34 % with respect to the total value). In both the cases the application of 273.15 K threshold does not represent the most suitable and exhaustive solution and an underestimation up to 10 % of the total M_{EB} in the April–June period can occur.

12.3.3 Melt Calculation from Degree Days Model

Secondly the melt rate is calculated by applying a degree days model. $T_{from\text{-}Bormio}$ data represent the input values to

calculate the degree days sum driving snow ablation. We focused on melt in the April–June period. Different temperature thresholds are used: the most common and applied value (273.15 K), the minimum of daily average temperature calculated for days featuring at least 6 M_{EB} hours (268.11 K) and the minimum daily average temperature calculated for days featuring 24 M_{EB} hours (274.73 K).

By comparing the cumulative $M_{T\text{-}INDEX}$ curves (Fig. 12.3) a similar trend is evident but the total amount of snow melting over the 7 year long period results quite different depending on the applied temperature threshold: from −6.81 m w.e. (threshold 274.73 K) to −8.23 m w.e. (threshold 268.11 K). The cumulative M_{EB} in the same period results −8.23 m w.e. thus underlying that the temperature threshold that better explains magnitude and variability of snow melting is 268.11 K (Fig. 12.3b).

12.4 Discussions and Conclusions

In this study by applying a point energy balance model (following Senese et al. 2012a) we found that a not negligible annual snow melt amount (M_{3C}) occurred from 1st October 2005 to 30th September 2012 on the tongue of the Forni Glacier (Italian Alps).

The snow melt resulted ranging from 17.61 to 29.17 % of the total annual M_{EB} (totally −37.5 m w.e. from snow and ice melt over the 7 year long analysed period).

Our data also indicate that during April–June all the snow coverage present at the glacier ablation tongue disappears due to melting processes; in fact from 2006 to 2012 the M_{3C} over the April–June time frame is found −8.47 m w.e. that corresponds to the 66.59 % of the April–June M_{EB}. This latter results equal to −12.72 m w.e., representing to ca. 1/3rd of the total M_{EB} calculated over the 7 hydrological years. Moreover we also computed the April–June mass loss without considering the glacier surface temperature and conditions; this ablation, M_{PEB}, results equal to −13.43 m w.e. thus underlining an overestimation (+5.56 % with respect to the M_{EB} over the same period). Then whenever a supraglacial AWS is available, the most accurate evaluation of snow melt is given by M_{3C} computation.

On the other hand supraglacial AWSs have been running only on a small number of glaciers thus suggesting to look for different strategies to assess the snow melt amount. The most diffuse and simple method is the degree days approach. The major uncertainty in applying such method is the choice of an appropriate air temperature threshold. In fact ablation does not occur only with air temperature higher than 273.15 K since it is determined by the surface energy balance and this latter is only indirectly affected by air temperature (Kuhn 1987). Then, to assess the most suitable temperature threshold, we firstly analysed hourly M_{EB} values (obtained from AWS1 Forni data) in the April–June period to detect if ablation occurs and how long this phenomenon takes (number of hours per day). Then we sorted these data according to temporal length classes (0, 4, 6, 12 and 24 melting hours per day). For each class we calculated the maximum, minimum and mean value of daily average air temperature from both AWS1 Forni and $T_{from\text{-}Bormio}$ data. Moreover we also evaluated the cumulative M_{EB} for each temporal length class to evaluate its weight with respect to the total ablation. The largest part of the melt (97.71 % of the whole ablation) resulted occurring on days with at least 6 M_{EB} hours thus suggesting to consider temperature data calculated for this class as suitable temperature thresholds. In particular the minimum value of the daily average temperature calculated with more than 6 M_{EB} hours per day (268.57 K and 268.11 K considering the AWS1 Forni and $T_{from\text{-}Bormio}$ data respectively) were applied to detect the actual melting days. The first threshold was applied to air temperature data from AWS1 Forni and permitted to select 586 melting days describing the 99.38 % (−12.64 m w.e.) of the total M_{EB}. Considering $T_{from\text{-}Bormio}$ data, the threshold of 268.11 K permitted to detect 601 melting days giving a cumulative M_{EB} of −12.66 m w.e. equal to 99.54 % of the total.

Then we ran a simple degree days model using as input data $T_{from\ Bormio}$ and varying the temperature threshold (273.15 K, 268.11 K and 274.73 K). The cumulative $M_{T\text{-}INDEX}$ curves we obtained (Fig. 12.3) show a similar trend but the total amount of snow melting over the 7 year long period results quite different. The cumulative M_{EB} in the same period results −8.23 m w.e. and this values is also obtained applying as threshold 268.11 K thus suggesting to use this temperature value to better explain magnitude and variability of snow melting (Fig. 12.3b).

As regards the threshold 273.15 K, which has been largely used in the literature dealing with degree days model (Braithwaite 1985; Hock 2003), our tests indicate that it drives an underestimation of snow melt (−19.86 % with respect to the M_{EB} value). Moreover also in the case the main purpose should be only the detection of the melting days and not the assessing of the melt amount, the application of the 273.15 K threshold drives an underestimation (481 melting days detected with this threshold against 601 melting days selected by applying the 268.11 K threshold).

Summarizing it results that using a 4.58 K lower threshold value (with respect to the largely applied 273.15 K) avoids most of the sampling problem in the application of the positive degree-day models. Moreover our air temperature threshold analysis on an Alpine glacier results in agreement with findings by van den Broeke et al. (2010) in Greenland ice sheet. They found an about 5 K lower threshold value by observing the cumulative distribution of daily average temperature for days with melt at three AWSs.

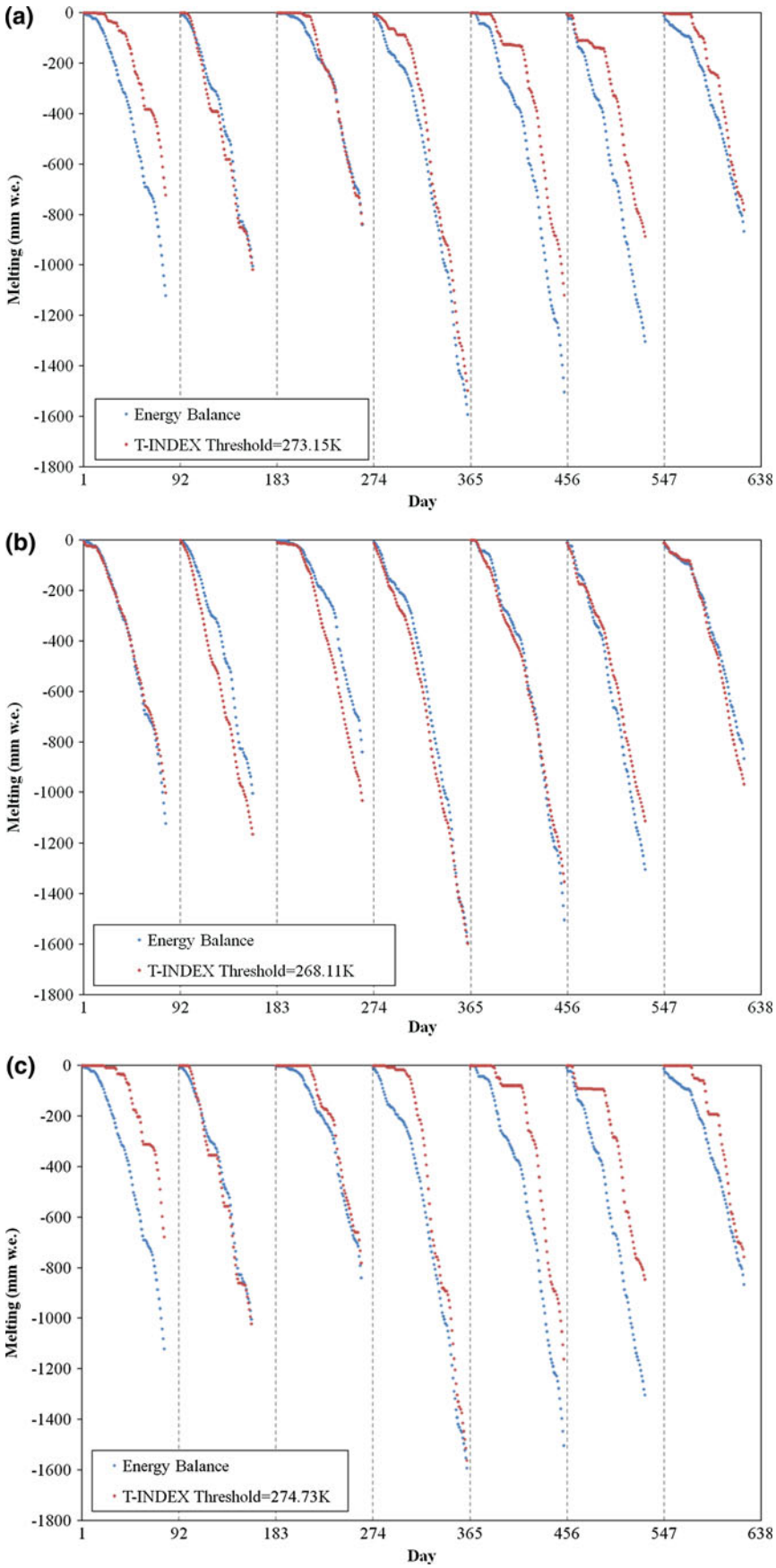

Fig. 12.3 From April to June 2006–2012 snow melting amount. With *blue dots* are shown the results from the energy balance. *Red dots* represent the results from degree days applying different temperature thresholds: 273.15 K (panel **a**), 268.11 K (panel **b**) and 274.73 K (panel **c**)

Acknowledgments The AWS1 Forni project is developed under the umbrella of the SHARE Program. SHARE (Stations at High Altitude for Research on the Environment) is an international program developed and managed by the Ev-K2-CNR Committee. This work was conducted in the framework of SHARE Stelvio project, promoted and funded by Ev-K2-CNR and Fondazione Lombardia per l'Ambiente. The data analysis was performed in the framework of the PRIN 2010/2011 (2010AYKTAB_006). We thank the Stelvio National Park, the Commune of Valfurva, the Valfurva section of the Italian Alpine Club (CAI) and the ARPA Lombardia for their kind help and support. We are also grateful to Eraldo Meraldi and Roberto Chillemi for their fundamental technical assistance on the field.

References

AINEVA: www.aineva.it

Ahlmann HW (1924) Le niveau de glaciation comme fonction de l'accumulation d'humidité sous forme solide (The level of glaciation as the function of the accumulation of solid precipitation). Geogr Ann 6:223–272

Bocchiola D, Mihalcea C, Diolaiuti G, Mosconi B, Smiraglia C, Rosso R (2010) Flow prediction in high altitude ungauged catchments: a case study in the Italian Alps (Pantano Basin, Adamello Group). Adv Water Resour 33:1224–1234

Braithwaite RJ (1985) Calculation of degree-days for glacier-climate *research*. Zeitschrift fue Gletscherkunde und Glazialgeologie 20(1984):1–8

Cazorzi F, Dalla Fontana G (1996) Snowmelt modelling by combining air temperature and a distributed radiation index. J Hydrol 181(1–4):169–187

Citterio M, Diolaiuti G, Smiraglia C, Verza G, Meraldi E (2007) Initial results from the automatic weather station (AWS) on the ablation tongue of Forni Glacier (Upper Valtellina, Italy). Geografia Fisica e Dinamica Quaternaria 30:141–151

Diolaiuti G, Bocchiola D, D'Agata C, Smiraglia C (2012) Evidence of climate change impact upon glaciers' recession within the Italian Alps: the case of Lombardy glaciers. Theoret Appl Climatol 109(3–4):429–445. doi:10.1007/s00704-012-0589-y

Diolaiuti G, Smiraglia C (2010) Changing glaciers in a changing climate: how vanishing geomorphosites have been driving deep changes in mountain landscapes and environments. Géomorphol Relief Processus Environ 2:131–152

Finsterwalder S, Schunk H (1887) Der Suldenferner. Zeitschrift des Deutschen und Oesterreichischen Alpenvereins 18:72–89

Hann J (1908) Handbuch der Klimatologie (Handbook of Climatology). Verlag von J Engelhorn, New York 394

Hock R (1999) A distributed temperature-index ice- and snowmelt model including potential direct solar radiation. J Glaciol 45(149):101–111

Hock R (2003) Temperature index melt modelling in mountain areas. J Hydrol 282(1–4):104–115

Hock R (2005) Glacier melt: a review of processes and their modeling. Prog Phys Geogr 29(3):362–391

Krenke AN, Khodakov VG (1966) O svyazi poverkhnostnogc tayaniya lednikov s temperaturoy vozdukha (On the relationship of surface melt of glaciers with air temperature.) Materialy glyatsiologicheskikh issledovaniy (Data of glaciological studies). Khoronika obsuzhdeniya (Chronicle Discussions) 12:153–164

Kuhn M (1987) Micro-meteorological conditions for snow melt. J Glaciol 33(113):263–272

Kuusisto E (1980) On the values and variability of degree-day melting factors in Finland. Nord Hydrol 11:235–242

Lang H (1968) Relations between glacier runoff and meteorological factors observed on and outside the glacier. IAHS Publ 79:429–439

Oerlemans J, Giesen RH, Van Den Broeke MR (2009) Retreating alpine glaciers: increased melt rates due to accumulation of dust (Vadret da Morteratsch, Switzerland). J Glaciol 55(192):729–736

Pellicciotti F, Brock BW, Strasser U, Burlando P, Funk M, Corripio JG (2005) An enhanced temperature-index glacier melt model including shortwave radiation balance: development and testing for Haut Glacier d'Arolla, Switzerland. J Glaciol 51(175):573–587

Senese A, Diolaiuti G, Mihalcea C, Smiraglia C (2012a) Energy and mass balance of Forni Glacier (Stelvio National Park, Italian Alps) from a 4-year meteorological data record. Arct Antarct Alp Res 44(1):122–134

Senese A, Diolaiuti G, Verza GP, Smiraglia C (2012b) Surface energy budget and melt amount for the years 2009 and 2010 at the Forni Glacier (Italian Alps, Lombardy). Geografia Fisica e Dinamica Quaternaria 35(1):69–77

van den Broeke M, Bus C, Ettema J, Smeets P (2010) Temperature thresholds for degree-day modeling of Greenland ice sheet melt rates. Geophys Res Lett 37:L18501

A System for Assessing the Past, Present and Future of Glacial Resources

13

Marta Chiarle, Guido Nigrelli and Antonello Provenzale

Abstract

The cryosphere is especially sensitive to the fluctuations of climatic parameters, and specifically to ongoing global warming. Mountain glaciers, in particular, are good indicators of climatic trends, as they have response times to climate forcing which are intermediate between snow (which responds mainly to short-term climate forcing) and permafrost/ground ice, whose response is delayed in time and conditioned by a complex ensemble of factors. When studying glacier response to climate change, the main objectives are: (i) understand the terrestrial, local impacts of global climatic changes, (ii) develop scenarios of the future evolution of glaciated areas, according to the available global climatic projections. This two objectives have both scientific and applied merits. The latter are related to the importance of glaciers in the water cycle, in sediment fluxes, and as a source of natural hazards. The combination of historical and geomorphological information with numerical models of climate systems and glacier response to climate forcing is one of the most robust approaches to address the study of glacier evolution in response to climate fluctuations and change. In order to be promptly available for use, historical and geomorphological data (including climatic ones) need to be properly organized in information management systems, which guarantee the preservation and standardization of data, along with their easy processing and retrieval. The present contribution aims at illustrating the experience gained through the application of this multidisciplinary approach to glaciers of the western Italian Alps.

Keywords

Glaciers • Climate change • Italian Alps

13.1 Introduction

Glaciers are one of the best terrestrial indicators of climate change (IPCC 2013), as they react promptly to changes of the climatic variables, and their response is easily detected and monitored. The study of glacier response to climate change has two main objectives: (i) understand the terrestrial, local impacts of global climatic changes, (ii) develop scenarios of the future evolution of the glaciated areas, according to the available climatic projections. These two objectives have both scientific and applied relevance. The latter is related to the importance of glaciers in the water cycle (Braun et al. 2000), in sediment fluxes (Stott and Mount 2007), and in affecting natural hazards (Chiarle and Mortara 2008).

M. Chiarle (✉) · G. Nigrelli
Consiglio Nazionale delle Ricerche, Istituto di Ricerca per la Protezione Idrogeologica, GeoClimAlp Research Group, Strada delle Cacce 73, 10135 Turin, Italy
e-mail: marta.chiarle@irpi.cnr.it

G. Nigrelli
e-mail: guido.nigrelli@irpi.cnr.it

A. Provenzale
Consiglio Nazionale delle Ricerche, Istituto di Scienze dell'Atmosfera e del Clima, Corso Fiume 4, 10133 Turin, Italy
e-mail: A.Proventale@isac.cnr.it

G. Lollino et al. (eds.), *Engineering Geology for Society and Territory – Volume 1*,
DOI: 10.1007/978-3-319-09300-0_13,

To properly address these issues, it is crucial to know the location, extent and characteristics of present glacial resources, and model their response to climate change. Modeling glacier dynamics, though, requires the knowledge of glacier changes over time as a result of climatic forcing. The collection and analysis of historical/geomorphological information, its storage and cataloguing in a specific database, and the development of glacier dynamics models, are components of an integrated approach which has been tested on some of the glaciers in the western Italian Alps. The experience gained by the authors on this topic is the focus of the present contribution.

13.2 Data Availability on Alpine Glaciers and Climate

Global glacier inventories are a quite recent reality: the World Glacier Monitoring Service (WGMS) published the first World Glacier Inventory in 1989, and since then annually collects data of about 130.000 glaciers through a scientific collaboration network extending in over 30 countries around the world. After year 2000, the GLIMS (Global Land Ice Measurements from Space) project attempted to fill the numerous gaps on world-wide glacier distribution and extent with the use of satellite imagery. Before these initiatives, the documentation of glacier evolution in the European Alps has been carried out on a local scale, with the production of a very heterogeneous historical documentation. The history of Italian glaciers over the past century is remarkably well documented thanks to the efforts of the Italian Glaciological Committee (Comitato Glaciologico Italiano; CGI 2013). Every year since 1914, volunteer surveyors visit the glaciers, measure the terminus position and take pictures from fixed points (Fig. 13.1); in addition, they write reports on the general conditions of the glaciers and the main changes observed, as well as the occurrence of relevant phenomena (e.g., rockfall, lake growth). The results of the surveys are annually published on the CGI journal (Bollettino del Comitato Glaciologico Italiano, until 1977; Geografia Fisica e Dinamica Quaternaria, since 1978), and are available online. Besides the data from annual surveys, the CGI archives also contain aerial and terrestrial photos, topographic surveys and maps, thematic maps, mass balance reports, journals, books, and unpublished studies. Additional (mainly iconographic) documentation can be found in other archives (e.g. archives of the "Istituto Geografico Militare-IGM", "Club Alpino Italiano-CAI").

Unfortunately, geographical information on Italian glaciers is much more rare and often outdated. In recent years, local initiatives (e.g. Regione Autonoma Valle d'Aosta 2013; Bonardi et al. 2012; Glariskalp Project 2013) provided updated information, which nevertheless is inhomogeneous, from a spatial, temporal, and methodological point of view.

Geomorphological investigation is a valid tool for integrating the spatial information on present and past glacier extent, available from the documentary sources. Rapid technological improvements in recent decades made this tool more reliable and precise. Traditional field surveys have been integrated by remote sensing techniques based on aerial photo interpretation since 1950s, and by satellite imagery analysis since 1970s. In recent years, accurate DEMs became available thanks to terrestrial and aerial LIDAR surveys: the integration of these data with orthophotos opens new opportunities for remote-based geomorphological analysis. In addition, orthophotos of good quality of the entire Earth surface have become freely available online through engines like Google Earth/Maps and Bing Maps, which also provide prospective views of the landscape.

Another valid tool for assessing past, present and future conditions of glacial resources is the use of information from climate variables. The climate of the European Alps is highly complex, governed by the interaction between mountain range systems and the general atmospheric circulation. In this context, the interactions between climate

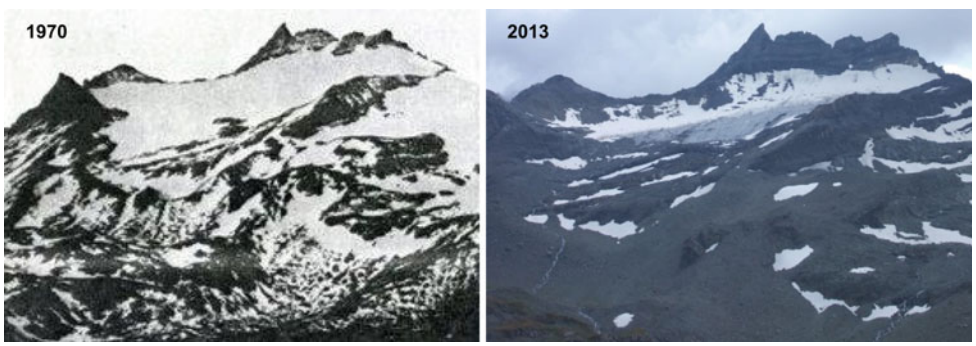

Fig. 13.1 The Arguerey Meridionale Glacier (Aosta Valley, NW Italy): two pictures taken from a fixed point of observation show the strong retreat of the glacier. (*Sources*: 1970 photo by C. Clerici; 2013 photo by G. Nigrelli)

variability and glacier response are difficult to study. For some purposes, such as the detailed analysis of local dynamics, it is necessary to adopt a local scale approach and use data from meteorological stations located in glacial and periglacial areas. However, for climatological studies, where the important climatic variables are needed only in terms of seasonal averages, also larger-scale spatial (regional) averages can be satisfactorily used (Calmanti et al. 2007, Bonanno et al. 2014).

13.3 Methods and Tools for Data Storage, Distribution and Analysis

In order to be promptly available for use, historical, geomorphological and climatic data need to be properly organized in information management systems, which guarantee preservation and standardization of data, along with their easy processing, retrieval, and distribution.

For these purposes, the development of server-side databases is a necessary step towards integrated information management. These tools should also be made easy to use, through the development of user-friendly web interfaces, in the spirit of international programmes such as GEO/GEOSS and national projects such as NextData (www.nextdataproject.it). The main features that these systems should have are: (i) archive and store a huge amount of historical, geomorphological and climatic information; (ii) manage different types of formats assuring interoperability; (iii) share the collected data, making them accessible and useful for various purposes; (iv) to meet the above-mentioned demands with low-cost solutions (Nigrelli et al. 2013). For all cases with large amounts of diverse data, the speed and accuracy in information retrieval are main strategic success factors. In order to improve these aspects, it is necessary to include a system of meta-databases, able to simultaneously query various databases located in different web servers. An example of this approach is the SHARE GeoNetwork developed for different national Italian projects such as SHARE, NextData and I-AMICA.

To evaluate past, present and future of glacial resource is important to archive and manage also geospatial information on each glacier (e.g. total area). This is possible through the use of GIS technologies. To meet these needs, the world of free open source provides powerful and reliable solutions at very low cost. Softwares like PostgreSQL, PostGIS and QGIS can be a valuable starting point for achieving these objectives. To make available the information stored by these systems, the web is the best solution, and even for these needs the free and open source world can help; in this direction, the choice of technological solutions such as GeoNetwork Opensource provides a high level of reliability (Fig. 13.2).

13.4 Numerical Modeling

Estimating the glacier response to climatic fluctuations requires the development and use of appropriate models of the glacier dynamics, which should be driven by the climatic variables produced by numerical simulations of future climate conditions. In this framework, it is important to decide the level of detail in the description of glacier response, which can range from simple statistical models to full three-dimensional integrations of ice flow.

Empirical models relate, through the statistical analysis of available historical data, some of the glacier characteristics (such as fluctuations in the snout position) to the appropriate climatic variables. Not surprisingly, the work of Calmanti et al. (2007) and Bonanno et al. (2014) have indicated that the most relevant climatic variables driving glacier snout fluctuations in the western Italian Alps are the average summer temperature and the cumulated winter precipitation, with a delay varying between about 5 and

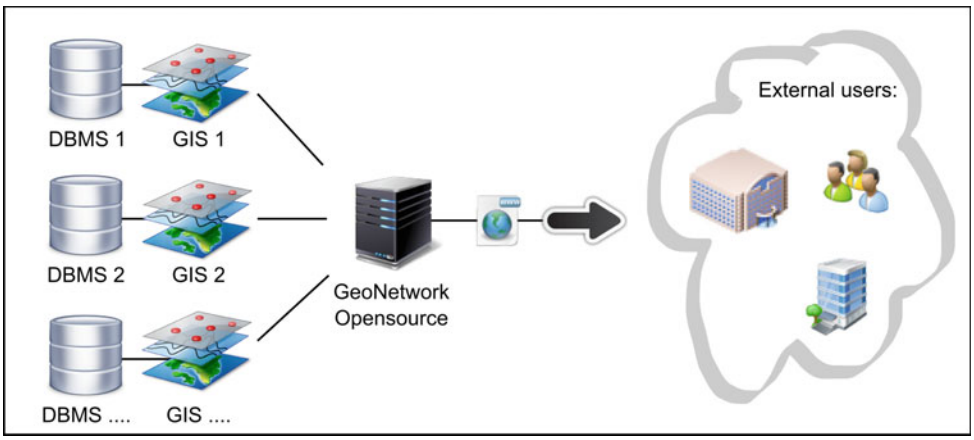

Fig. 13.2 Schematic structure of an information management system based on free open source technologies applied to the web

10 years. Such approach is quite successful in describing the average response of an ensemble of glaciers with similar characteristics, but could fail when applied to individual glaciers.

Another approach, which is more appropriate for the study of individual glaciers, is based on developing physical-based models of the glacier dynamics. The simplest are the so-called "minimal" models, where the glacier is assumed to have a very simple and fixed geometry, glacier length and depth are strictly related to each other and time is the only independent variable (Oerlemans 2011). From these, one can complicate the picture and use flow-line models, which assume the glacier width and depth and the ice flow to be functions of time and of a spatial coordinate running along the glacier. Further, one can get to full 3D models, based on the fluid dynamical equations with appropriate rheology, where all dynamical variables are function of time and of (three-dimensional) space.

Clearly, the more detailed the picture, the larger is the information needed to build a reliable model. When the information is incomplete (as for most mountain glaciers), it is probably better to be content with a rougher description. In all cases, before being used for future projections, the models must be validated on the historical period, by a quantitative comparison between model outputs and measured data. Once again, models and data cannot live independently, if the goal is to obtain relevant information on the future conditions of the mountain cryosphere.

13.5 Final Remarks

The combination of historical and geomorphological information with numerical models of the climate systems and of glacier dynamics, is one of the most robust approaches to address the study of glacier response to climate fluctuations and change.

In order to be promptly available for use, historical, geomorphological and climatic data need to be organized in information management systems, which guarantee the preservation and standardization of data, along with their easy processing and retrieval. Modern open-source, web-based solutions allow to build efficient information systems for the storage, analysis, query and distribution of data.

References

Bonanno R, Ronchi C, Cagnazzi B, Provenzale A (2014) Glacier response to current climate change and future scenarios in the northwestern Italian Alps. Reg Environ Change 14: 633–643

Bonardi L, Rovelli E, Scotti R, Toffaletti A, Urso M, Villa F (2012) I ghiacciai della Lombardia. Evoluzione e attualità. Hoepli, Milano, p 328

Braun LN, Weber M, Schulz M (2000) Consequences of climate change for runoff from Alpine regions. Ann Glaciol 31:19–25

Calmanti S, Motta L, Turco M, Provenzale A (2007) Impact of climate variability on Alpine glaciers in northwestern Italy. Int J Climat 27:2041–2053

Chiarle M, Mortara G (2008) Geomorphological impact of climate change on alpine glacial and periglacial areas. In: Examples of processes and description of research needs. Interpraevent 2008, Dornbirn, 26-30 maggio 2008, II/111-122

CGI (2013) Italian Glaciological Committee. http://www.glaciologia.it. Accessed 22 Oct 2013

GlaRiskAlp (2013) Glacial risks in Western Alps. ALCoTra, Italian transborder Alpine cooperation program 2007-2013. http://www.glariskalp.eu. Accessed 27 Sept 2013

IPCC (2013) Fifth assessment report (AR5), approved summary for policymakers. In: Intergovernmental panel on climate change. http://www.ipcc.ch. Accessed 22 Oct 2013

Nigrelli G, Chiarle M, Nuzzi A, Perotti L, Torta G, Giardino M (2013) A web-based, relational database for studying glaciers in the Italian Alps. Comput Geosci 51:101–107

Oerlemans, J (2011) Minimal glacier models. http://www.staff.science.uu.nl/~oerle102/MM2011-all.pdf

Regione Autonoma Valle d'Aosta (2013) http://catastoghiacciai.regione.vda.it/Ghiacciai/MainGhiacciai.html. Accessed 7 Nov 2013

Stott TA, Mount NJ (2007) Alpine proglacial suspended sediment dynamics in warm and cool ablation seasons: Implications for global warming. J Hydrol 332(3–4):259–270

The Case Study of the Changri Nup Glacier (Nepal, Himalaya) to Understand Atmospheric Dynamics and Ongoing Cryosphere Variations

14

Vuillermoz Elisa, Senese Antonella, Diolaiuti Guglielmina, Smiraglia Claudio, Cristofanelli Paolo, Marinoni Angela, Gian Pietro Verza and Bonasoni Paolo

Abstract

Surface energy fluxes estimated at the debris free surface of Changri Nup Glacier (5,700 m a.s.l.—Nepal Himalayas) since 2010 allow to determine glacier ablation rate and high resolution analysis of glacier albedo. Energy and meteorological data are measured from a supraglacial Automatic Weather Station (AWS). Moreover the impact of atmospheric absorbing aerosol (e.g. Black Carbon, BC) deposition on snow albedo variability has been analyzed. In fact the energy data (from the AWS) were coupled with BC concentration (in snow) values, estimated from the BC atmospheric concentration continuously measured at the Nepal Climate Observatory at Pyramid Station (5,079 m a.s.l.), thus making possible to investigate the relationship between BC deposition in snow and the percentage of albedo reduction at the glacier. Experimental results could improve glacier melt modelling also considering BC impacts on snow albedo variability and then on snow melt rates.

Keywords

Himalaya • Glacier energy-budget • Albedo • Black carbon

14.1 Introduction

Recent studies on Himalayan glacier witnessed overall degradation of these glaciers, moreover global warming should intensify the summer monsoon. The analysis of atmospheric and cryospheric recent variations (last decade and present) allow to identify the connections between the two systems, contributing to the comprehension of recent atmospheric dynamics and their effects on glacier and water resources at local scale. The southern slope of the Himalaya is directly exposed to Indian emissions and more likely to be impacted by BC than the northern slope (Yasunari at al. 2010). Changri Nup is one of the tributaries of the larger Khumbu Glacier, located in the Sagarmatha National Park, in the Nepal Himalaya. It is oriented E-W and it is partially debris covered from the terminus until it reaches an altitude of about 5,350 ma.s.l. The debris cover on the glacier tongue varies in thickness between a few cm to 1–2 m. The glacier terminus is at an elevation of about 5,200 m a.s.l. The glacier area is about 8 km^2, whereas the mean glacier width is approximately 800 m. The accumulation area starts at an elevation of around 5,400 m which leads to two separate accumulation basins. Only the north one resulted nowadays still contribution to the glacier flow.

V. Elisa (✉) · G.P. Verza
Ev-K2-CNR Committee, Via San Bernardino 145,
24126 Bergamo, Italy
e-mail: elisa.vuillermoz@evk2cnr.org

S. Antonella · D. Guglielmina · S. Claudio
University of Milan – A. Desio, Department of Earth Sciences,
Via Mangiagalli 34, 20133 Milan, Italy

C. Paolo · M. Angela · B. Paolo
CNR-Institute of Atmospheric Sciences and Climate-ISAC,
Via Gobetti 101, 40129 Bologna, Italy

G. Lollino et al. (eds.), *Engineering Geology for Society and Territory – Volume 1*,
DOI: 10.1007/978-3-319-09300-0_14,

14.2 Materials and Methods

For the determination of the albedo and surface energy balance it has been used the method reported in Senese et al. (2012), while for the calculation of the Black Carbon (BC) concentration in snow, the method by Yasunari et al. (2010). Meteorological and radiative parameters have been continuously monitored since 2010 through the Automatic Weather Station (AWS) installed on the debris-free surface of the glacier, at 5,700 m a.s.l. (N 27°58'54.5"; E 86°45'53,8"). AWS data are sampled at 60-s intervals and averaged over a 30-min time period. Pressure sensor was not available, thus atmospheric pressure data have been derived from Kala Patther AWS, located at 5.600 m a.s.l. according to the ipsometric formula of Wallace and Hobbs (2006). Energy fluxes have been measured by a Kipp and Zonen CNR1 Net radiometer that measure incoming and outgoing longwave and shortwave radiation. To calculate surface reflectivity (or albedo, α) the following relation was applied:

$$\alpha = \mathrm{SWout} * \mathrm{SWin}^{-1}$$

The energy balance at the glacier surface (RS) determines the net energy available for heating and melting. RS was calculated, by considering the hourly meteorological values, as:

$$\mathrm{RS} = \mathrm{SWnet} + \mathrm{LWnet} + \mathrm{SH} + \mathrm{LE} + \mathrm{G}$$

where SWnet is the net short wave flux, LWnet is the net long wave flux, SH is the sensible heat component, LE is the latent heat contribution and G is the conductive heat flux at the surface. All the fluxes (W m^{-2}) were defined positive when directed towards the surface. The conductive heat flux at the surface, G, was neglected since no temperature sensors were located in the snowpack and in the ice surface layer. Further details on the applied methods in Senese et al. (2012). BC atmospheric concentration is monitored continuously at NCO-P (Nepal Climate Observatory at Pyramid) station since February 2006 through the Multi Angle Absorption Photometer (MAAP), Bonasoni et al. (2010).

14.3 Results and Discussion

Meteorological and energy balance data measured at Changri Nup in the period 2010–2012 are reported in Table 14.1. The 3-year mean albedo was found equal to 0.65 (Fig. 14.1). During the three accumulation seasons the mean albedo was 0.75 while during the three ablation periods resulted 0.26. This shows a marked seasonal cycle related to the different surface reflectivity between ice and snow. Snowfall implies higher albedo, increasing outgoing radiation, and then less energy is available for melting. The snow albedo tends to decrease for larger values of the incoming radiation. This mainly occurs when incoming radiation is large, air temperatures are high and snowfall rarely occurs. In this case the snow structure has been transformed into large grain sand there is normally some accumulation of dust on the surface that reducing the reflectivity, Oerlemans (2010). The four components of energy budget (SWnet, LWnet, SH and LE) show a comparable trend of the annual cycle in the period, consistently with the ablation seasons. During the transition from snow to ice, the lowering of the albedo occurs when the flux of SWin is large, determining a very steep increase in the net solar radiation. LWnet increases up to values close to 0 W m^{-2} during monsoon season, confirming the higher presence of cloudy days (which features more absorption of the infrared radiation and consequently more emission towards the surface). Negative values, up to −85 W m^{-2}, are constantly present in the whole period. Generally LWnet values up to −100 W m^{-2} are due to the 0°C glacier surface temperature (Oerlemans 2001). During the ablation season, the latent heat flux (LE) is generally positive or close to zero, while in the other part of the year, the negative values correspond to low humidity combined with a minimal temperature difference between the glacier surface and the air. Consequently sensible heat flux is higher in correspondence of negative LE values and lower or close to zero during the ablation season. Cumulative daily melt in the 3 year long period is reported in Fig. 14.2, showing that glacier melting has been higher in 2010/2012 than in 2011. Daily mean albedo values have been compared with daily mean value of atmospheric Black Carbon concentrations

Table 14.1 Site characteristics, meteorology and energy balance data

Coordinates	28° 00° N; 86° 48'E
Elevation range (m a.s.l.)	5.000–5.700
Length (km)	3
Area (km^2)	7 (65 % debriscovered)
AWS elevation (m a.s.l.)	5.700
net SW (W m^{-2})	84
net LW (W m^{-2})	−39
SH (W m^{-2})	7
LE (W m^{-2})	−2
RS (W m^{-2})	40
SW In (W m^{-2})	220
SW out (W m^{-2})	136
SW In extra (W m^{-2})	465
Air temperature °C	−4.6
Snow albedo	0.75
Ice albedo	0.26

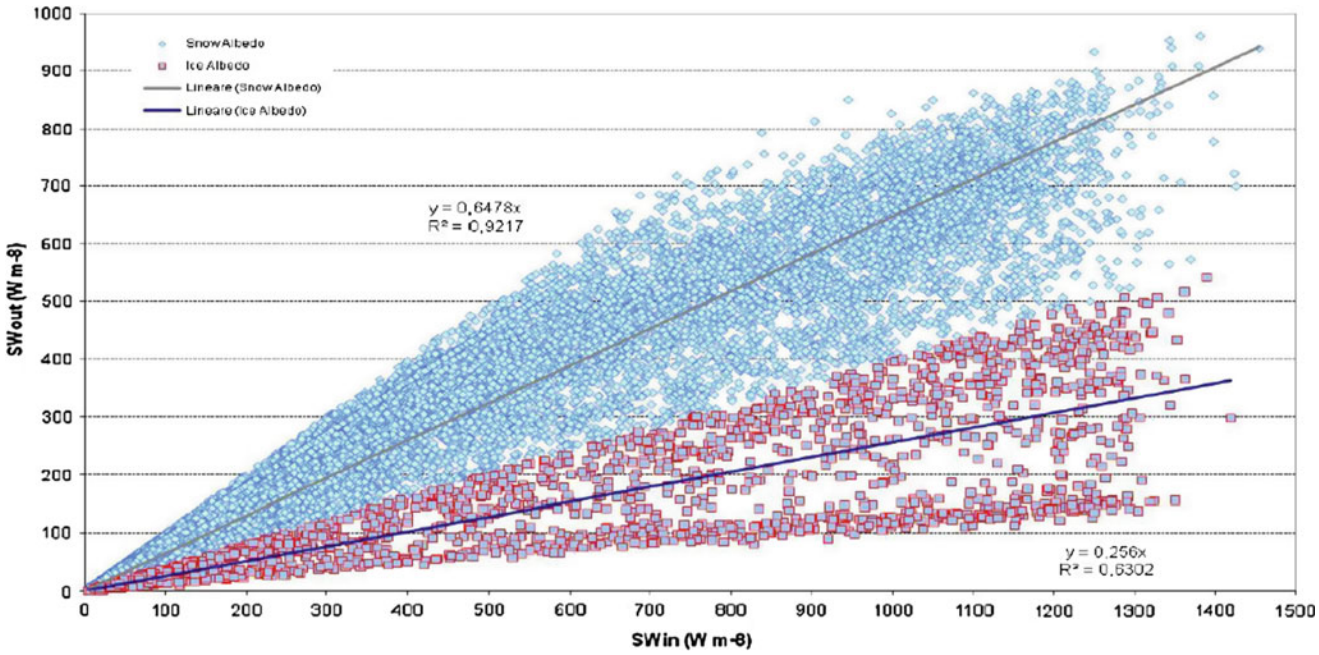

Fig. 14.1 Daily albedo characterizing exposed ice and snow cover surface in 2010–2012

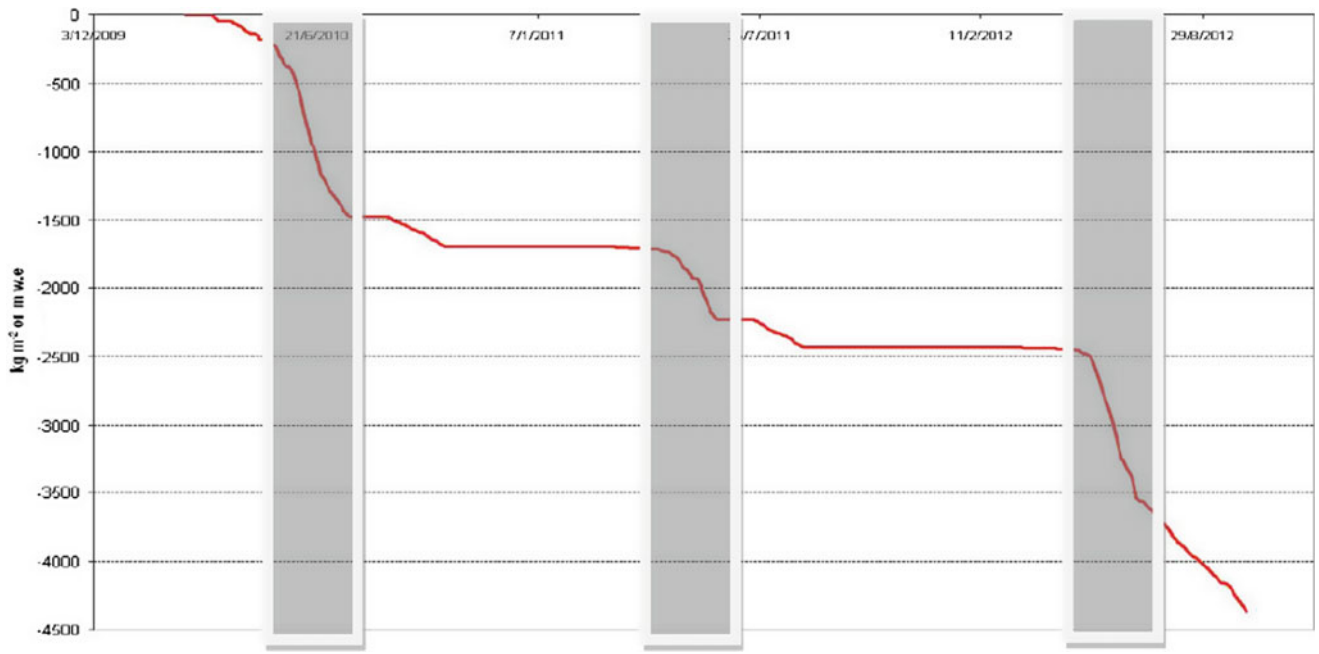

Fig. 14.2 Cumulative daily melt at Changri Nup AWS in the period 2010–2012. Ice ablation is highlighted in *grey*

(BCC) continuously monitored at NCO-P station. Data have been correlated calculating their respective weekly moving average (Fig. 14.3) during April 2010 (premonsoon season). Usually, on a glacier, the 2 cm top layer of snow surface is more contaminated than the deeper part because the snow impurities are derived from dry depositions of atmospheric aerosols, thus the top snow layer is considered the key to assess albedo reductions. For this reason, assuming that the atmospheric BC (average: 394 μg m^{-3}), is deposited on 2 cm of thickness of pure snow for March-April 2010, we calculated a 49 μg kg^{-1} BC concentration in snow surface, considering a measured snow density of 400 kg m^{-3}, as. This result is consistent with literature data. The percentage of the albedo reduction corresponded to the peak of

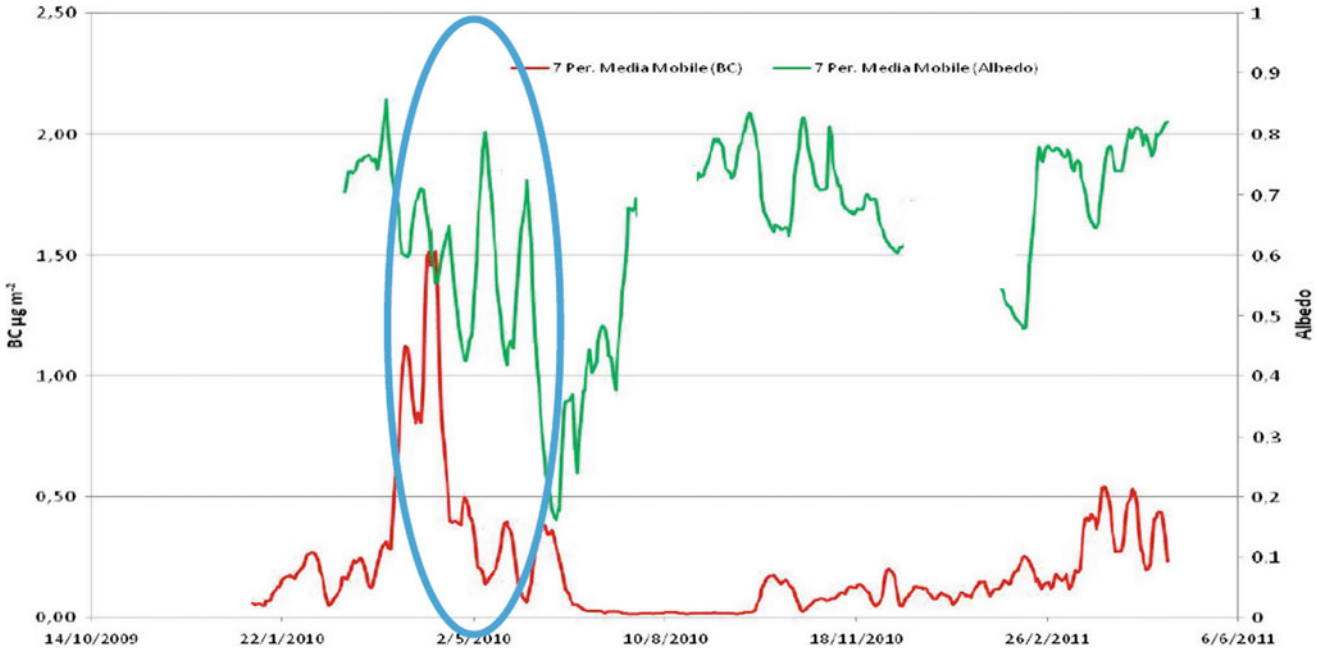

Fig. 14.3 Moving average (7 Per) of daily mean albedo measured at Changri Nup glacier and daily mean atmospheric BCC measured at NCO-P station

atmospheric BC concentration (BCC) deposited and measured at Changri Nup results equal to 4.29.

14.4 Conclusion

Himalayan debris free glaciers are subjected to the impact of climate variations which in the last decades are driving stronger melting processes thus impacting future water availability. The quantification of this melting amount is difficult due to the lack of permanent monitoring sites and long term reliable data. It has been recently put in evidence that the factors driving ablation, are not only related to the radiative forcing at glacier surface an climate conditions, but also to the effect of deposition of absorbing aerosol and dust at the glacier surface, varying the albedo and thus accelerating melting. The analysis of BC deposition in snow calculated from atmospheric data and the % of the albedo reduction has been consistent with the estimation available in literature for Changri Nup site, where the highest amount of BC in the atmosphere during premonsoon season allows a consistent correlation with the % of albedo reduction measured and calculated. The next project step will be to consider BC impacts on ice albedo variability and with this specific aim an experimental protocol to measure ice albedo and to measure and describe fine sparse debris and soot has been developed and is currently under test at the Chagri Glacier surface.

Acknowledgments This study was carried out in the framework of Ev-K2-CNR/SHARE and the Project of National Interest MIUR-NextData Projects.

References

Bonasoni P, Laj P, Marinoni A, Sprenger M, Angelini F, Arduini J, Bonafè U, Calzolari F, Colombo T, Decesari S, Di Biagio C, di Sarra AG, Evangelisti F, Duchi R, Facchini MC, Fuzzi S, Gobbi GP, Maione M, Panday A, Roccato F, Sellegri K, Venzac H, Verza GP, Villani P, Vuillermoz E, Cristofanelli P (2010) Atmospheric brown clouds in the himalayas: first two years of continuous observations at the nepal climate observatory at pyramid (5079 m). In: Special issuēatmospheric brown clouds in the himalayas‖ atmospheric chemistry and physics, vol 10, pp 7515–7531

Oerlemans J (2001) Glaciers and climate change. Balkema, Lisse, p 115

Oerlemans J (2010) The microclimate of valley glaciers. Institute for Marine and Atmospheric Research Utrecth, Utrecth University, The Netherlands, p 138

Senese A, Diolaiuti D, Mihalcea C, Smiraglia C (2012) Energy and mass balance of Forni Glacier (Stelvio National Park, Italian Alps) from a 4-year meteorological data record. Arctic Antarctic Alpine Res 44(1):122–134

Wallace JM, Hobbs PV (2006) Atmospheric science: an introductory survey, 2nd edn. Academic Press, San Diego

Yasunari TJ, Bonasoni P, Laj P, Fujita K, Vuillermoz E, Marinoni A, Cristofanelli P, Duchi R, Tartari G, Lau KM (2010) Estimated impact of black carbon deposition during pre-monsoon season from Nepal Climate Observatory-Pyramid data and snow albedo changes over Himalayan glaciers. In: Special issue ¯atmospheric brown cloud in the Himalayas‖ atmospheric chemistry and physics, vol 10, p 660

Temperature Analysis on the North-Western Italian Alps Through the Use of Satellite Images and Ground-Based Meteorological Stations

15

Diego Garzena, Simona Fratianni and Fiorella Acquaotta

Abstract

In the present study we have analyzed the temperature data of the stations of high altitude on the north-western Italian Alps. The data used are the daily series of temperature over the last 51 years. The data were digitized and subjected to quality control and finally to homogenization. To improve the quantity of the ground-data, we decided to use the remote sensing data. The availability of large scale reliable and consistent spatial data as those of the MODIS "land surface temperature" datasets from the satellites "Terra" and "Aqua" allows to evaluate the variation of temperature extent over Alps even where there are no stations on the ground. Finally for the ground-base data the climatic indices were calculated. The analysis of the series showed a positive trend in temperature that coincide on the rise in altitude. In fact, the stations located above 1,600 m asl show a rise in temperatures and a decrease in cold periods. For maximum temperatures were observed greater increases in trends spring and winter, minimum temperatures in summer trends. The trends confirm climate change in an environment is particularly sensitive to temperature changes especially during the season of snow accumulation and vegetative growth.

Keywords

Climate change • Nord-West alps • Climate series • Climate indices • MODIS

15.1 Introduction

Global climatic changes have different impacts on the different environments according to their characteristics. Several studies are in agreement in identifying the alpine environment among the most sensitive environments to climate change (Knoche 2011). Since 1996 IPCC underlines the needing to understand and predict the effects of climate change in mountain regions (IPCC 1996. Indeed, changes in alpine climate regimes affect winter precipitation (Valt et al. 2006) and the snow cover duration, causing impacts of sizeable magnitude (Ronchi and Loglisci 2008) on river systems and on socio-economic structures (Fazzini et al. 2004) of the population that living in mountain (Beniston et al. 1997). The sensitivity of the alpine environment is observable both climate variability that in the effects that this entails, including the occurrence of extreme events likely to have a major impact on local and national economies.

The north-western Italian Alps are within the administrative boundaries of Piedmont and Valle d'Aosta regions (approximately 28,700 km^2). The main factor of the climate control over this area is due by the reliefs shape, the mountains cover about 15,500 km^2 including the highest mountains of Italy and Europe.

D. Garzena (✉) · S. Fratianni · F. Acquaotta
Dipartimento di Scienze della Terra, Università di Torino, via Valperga Caluso 35, 10125 Torino, Italia
e-mail: diego.garzena@unito.it

S. Fratianni
e-mail: simona.fratianni@unito.it

F. Acquaotta
e-mail: fiorella.acquaotta@unito.it

S. Fratianni
Natrisk, Via Leonardo da Vinci 44, 10095 Grugliasco (TO), Italia

G. Lollino et al. (eds.), *Engineering Geology for Society and Territory – Volume 1*,
DOI: 10.1007/978-3-319-09300-0_15,

This research was supported by the Italian MIUR Project (PRIN 2010–2011): "Response of morphoclimatic system dynamics to global changes and related geomorphological hazards" (national coordinator C. Baroni).

15.2 Historical Series

In this study we analyze the observed climate change on temperature series and evaluate the climate indices of the temperatures measured in the high altitude meteorological stations. The data used are from stations located on north-western Italian Alps, from Piedmont and Aosta Valley regions, at altitudes between about 600 and 2,500 m, representative of all Alpine sectors, with the exception of the Ligurian Alps (Fig. 15.1).

Many stations are located near artificial basins, made for exploiting electricity, by the National Energy Authority (ENEL). For each meteorological station we have recovered the paper registers, now hosted at the environmental agency of Piedmont or at the regional institution of Aosta Valley. Where necessary we have been digitized the data from the paper registers. Finally, was selected a common period of activity, from 1961 to 2010.

15.3 Methodology

To make a thermometric characterization is necessary to have a reliable dataset and possibly distributed throughout the study area. For this purpose, data from high-altitude stations of north-western Italian Alps in Piedmont and Valle d'Aosta regions are used for the climatic analysis.

Fig. 15.1 Location of the monitoring stations

The parameters chosen for the analysis are the daily values of maximum and minimum air temperature (°C). To achieve the climatic analysis is necessary to use the data of manual and automatic stations and subject them to a process of quality control. This is done using the software RClimDex (Zhang and Yang 2004). The software RClimdex allows to identify data transcription errors for example maximum temperature minor of minimum temperature and any outliers identified as the values that fall in the tail of the distribution (Acquaotta et al. 2009).

In order to reach the analysis stage has been necessary subject the temperature data to a homogenization process. To homogenize the variables we have employed the SPLIDHOM test (Mestre et al. 2011; Venema et al. 2012).

The variations of temperature data were identified by the trends and the climate indices (Table 15.1) for monthly, seasonal and annual values. The trends were calculated using simple linear regression and the level of significance, 90, 95 and 99 %, has been assessed using Mann Kendall test (Sneyers 1990; dos Santos 2011). The change in the alpine climate regimes, it is able to influence winter precipitation and duration of snow cover, this can have a significant impact on river systems and the socio-economic structures of the populations living in mountain and valley (Beniston et al. 1997).

In order to evaluate the climate variations in the analyzed area, and to highlight the years with major anomalies we have calculated the SAI (Standardized Anomaly Index) using as reference period the 1971–2000.

In order to assess climate change even in areas where there are no measuring stations on the ground it was decided to use the satellite data. These data, freely downloadable from the official website of the project, were subjected to verification of the measure for understanding the validity and the possible use of the same data. The data used are those of the sensors MODIS (MODerate resolution Imaging Spectroradiometer) of NASA satellite "Terra" and "Aqua" created for the program EOS (Earth Observing System), which has as main objective to improve the knowledge on global change land through the continuous observation of the planet. The satellite images used are the land surface temperature with 1 km definition, already prepared and properly positioned by NASA (level 2) of the collection 5. From the pictures we have been extracted the values of temperature and time of passage of the satellites to be able to compare with the values measured at the same time by ground stations.

15.4 Results

15.4.1 Temperature

The climatic and trend analysis have shown different tendency in temperature between the different stations

Table 15.1 List of climatic indices used

ID	Indicator name	Indicator definitions	Units
CSDI	Cold spell duration indicator	Annual count when at least six consecutive days of min temperature <10th percentile	days
TN90p	Warm nights	Percentage of time when daily min temperature >90th percentile	%
TX90p	Warm days	Percentage of time when daily max temperature >90th percentile	%
TN10p	Cool nights	Percentage of time when daily min temperature <10th percentile	%
TX10p	Cool days	Percentage of time when daily max temperature <10th percentile	%
WSDI	Warm spell duration indicator	Annual count when at least six consecutive days of max temperature >90th percentile	days

according to the altitudes of detection. It can be observed a positive trend by the temperature at which generally corresponds to an increase in altitude. In particular, the stations located above 1,600 m asl show a rise in temperatures and a decrease in cold periods. For these stations the higher trends were calculated on minimum temperature but for both variables, maximum and minimum temperature, the maximum trends were estimated in the locations with elevations upper to 2,000 m asl.

The analysis of seasonal temperatures show, for the high-altitude stations, that the seasons, which recorded the biggest changes, are different between minimum and maximum temperatures. For maximum temperatures the greatest changes are in spring and winter, for minimum temperatures in summer.

The analysis of climate indices has also allowed to highlight how the temperatures were increasing. In all stations we have calculated an increase of extreme temperature. The warm days (TX90P) and warm nights (TN90P) show increasing trends, while the cold days (TX10P) and cold nights (TN10P) highlight decreasing trends. Also for these indices the greater values were estimated in the stations with elevations upper 1,600 m asl.

In order to evaluate the commune performance of temperatures in the western Alps over the last 50 years, from 1961 to 2010, we calculated the SAI. The Standardized Anomaly Index (SAI) provides an immediate idea of the degree of anomaly of the behaviour of a variable recorded in a given year compared to the behaviour of the same variable in the 30 years of reference, 1971–2000.

The SAI series of maximum and minimum temperatures (Fig. 15.2) have two very similar trends. For both variables, the index is negative until the beginning of the 80 s and positive at the end of the same decade.

15.4.2 Satellite Data Information

The comparison between the detected temperature data from meteorological stations on the ground and those detected by the satellite sensor MODIS is the subject of numerous studies (Franklin 2001; Quattrochi and Luvall 2004; Quattrochi and Luvall 2009) that have identified a lot of problems related to the inhomogeneity of the quadrants.

In order to verify the possibility of using of the data acquired from the satellites "Terra" and "Aqua", in addition of the measurements of temperature, even the times of the steps are used to be able to put the data in correlation with measurements of ground stations. The verification phase of the available data began with a control on homogeneous dials (plain), which show a general correlation between the ground and satellite data.

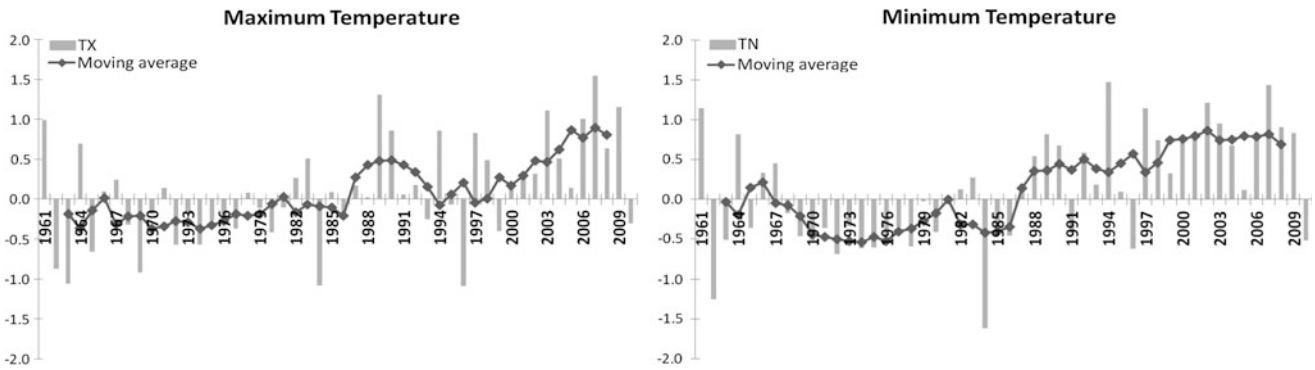

Fig. 15.2 *Left* annual SAI calculated for the maximum temperatures from 1961 to 2010, the reference period 1971–2000, *right* SAI index calculated annual minimum temperatures from 1961 to 2010, the reference period 1971–2000. The *line* represents the moving average on 5 years

Currently in mountainous areas the tests are still in progress, the image resolution (1 km) could hide local climatic variations caused by morphological appearance of the area.

15.5 Discussion and Conclusions

In this study we have analyzed the temperature data series of high-altitude regions of Piedmont and Valle d'Aosta. For the analysis of data has been identified a common period of operation of the stations, 1961–2010.

The data collected by the original series, have been digitized and were subjected to a quality control and homogenization in order to minimize possible errors in recording. The series thus obtained were then used for climatological investigations. We evaluated the trend, climatic indices and assessed the SAI. Finally, the data were compared with the data obtained from the satellite images obtained via the sensor MODIS.

This first analysis shows that the temperature increase is greater in areas of high altitude and in particular the major changes are measurable at altitudes above 1,600 m asl.

Although further studies are needed, the satellite data even if with different values show results comparable to those obtained with ground stations.

References

Acquaotta F, Fratianni S, Cassardo C, Cremonini R (2009) On the continuity and climatic variability of the meteorological stations in Torino, Asti, Vercelli and Oropa. Meteorol Atmos Phys 103:279–287. doi:10.1007/s00703-008-0333-4

Beniston M, Diaz HF, Bradley RS (1997) Climatic Change at High Elevation Sites: An Overview. Clim Change 36:233–251. doi:10.1023/A:1005380714349

Dos Santos CAC (2011) Trends in indices for extremes in daily temperature and precipitation over Utah, USA. Rev Bras Meteorologia 26:19–28

Fazzini M, Fratianni S, Biancotti A, Billi P (2004) Skiability conditions in several skiing complexes on Piedmontese and Dolomitic Alps. Meteorol Z 13(3):253–258

Franklin SE (2001) Remote sensing for sustainable forest management, 1st edn. CRC, Boca Raton

Knoche HR (2011) Ripercussioni dei cambiamenti climatici nella dorsale alpina settentrionale. Segnali Alpini n.6 (Ministero Sloveno dell'Ambiente e della Pianificazione del Territorio, Segratariato permanente della Convenzione delle Alpi, Innsbruck, 2011) p 9–14

Mestre O, Gruber C, Prieur C, Caussinus H, Jourdain S (2011) SPLIDHOM: A Method for Homogenization of Daily Temperature Observations. J Appl Meteorol Climatol 50:2343–2358

Quattrochi DA, Luvall JC (2004) Thermal remote sensing in land surface processes, 1st edn. CRC Press, Boca Raton

Quattrochi DA, Luvall JC (2009) Thermal remote sensing in Earth science research. In: Warner TA, Nellis MD, Foody GM The SAGE handbook of remote sensing. SAGE, London, pp 64–78

Ronchi C, Loglisci N (2008) Il clima tra passato, presente e futuro, Neve e Valanghe, AINEVA, 63, 11–19, http://www.aineva.it/pubblica/neve63/1_ronchi.html. Accessed 29 April 2014

Sneyers R (1990) On the statistical analysis of series of observations. Secretariat of the World Meteorological Organization, Geneva

Valt M, Cagnati A, Crepaz A, Marigo G (2006) Neve sulle Alpi italiane—L'andamento delle precipitazioni nevose sul versante meridionale delle Alpi. Neve e Valanghe, AINEVA, 56, 24–31 (2006), http://www.aineva.it/pubblica/neve56/3_valt.html. Accessed 29 April 2014

Venema V, Mestre O, Aguilar E, Auer I, Guijarro J, Domonkos P, Vertacnik G, Szentimrey T, Stepanek P, Zahradnicek P, Viarre J, Müller-Westermeier G, Lakatos M, Williams CN, Menne MJ, Lindau R, Rasol D, Rustemeier E, Kolokythas K, Marinova T, Andresen L, Acquaotta F, Fratianni S, Cheval S, Klancar M, Brunetti M, Gruber C, Prohom Duran M, Likso T, Esteban P, Brandsma T (2012) Benchmarking homogenization algorithms for monthly data. Clim Past 8:89–115. doi:10.5194/cp-8-89-2012

IPCC (1996) Climate change, 1995: impacts, adaptations, and mitigation of climate change: scientific-technical analyses. In: Watson RT, Zinyowera MC, Moss RH(eds) Contribution of working group II to the second assessment report of the intergovernmental panel on climate change, Cambridge University Press, Cambridge, New York, p 880

Zhang X, Yang F (2004) RClimDex (1.0) User guide. Climate Research Branch Environment Canada, Downsview, pp 22

Preliminary Study to Define a Distributed Hydrogeological Model Based on Snow Melt for Groundwater Recharge

16

Muriel Lavy, Marina De Maio and Enrico Suozzi

Abstract
This study aims to analyze data acquired by an experimental meteorological station in conjunction with data continuously measured in springs in order to evaluate the groundwater recharge deriving from snow melt process in a mountain basin. An experimental meteorological station was installed by DIATI of Politecnico di Torino in Mascognaz (Ayas) in the Aosta Valley, as part of a project with the Regional government. It is equipped with advanced sensors for the measure of snow parameters. The site also has two springs, used for drinking purposes, situated at the end of the mountain basin and equipped with probes for monitoring. The purpose is to define the correct response to meteorological inputs in an alpine basin in order to define an appropriate hydrological cycle and to monitor climate change in a mountain environment. The study shows how much snow contributes to groundwater recharge and how the resource fluctuates according to climate change over time.

Keywords
Snow-melt • Snow water equivalent • Groundwater • Spring • Climate change

16.1 Introduction

Climate change is the main factor that induces alterations in the hydrological cycle, whose effects on water resources need to be quantified in order to plan appropriate management measures. In this context mountains represent the first indicators of climate change, because they respond rapidly and intensely to climatic and environmental modifications. Climatic and environmental alterations in the hydrological cycle in high mountains can significantly affect the availability of water resources; snowfall and the resulting seasonal snow cover represent an important source of both surface and subsurface water flows.

M. Lavy (✉) · M. De Maio · E. Suozzi
Politecnico Di Torino - DIATI, Corso Duca Degli Abruzzi, 24, Turin, Italy
e-mail: muriel.lavy@polito.it

It is clear that groundwater resources and meteorological sources of water need to be carefully monitored.

For these reasons the Politecnico di Torino installed an advanced meteorological station in Mascognaz Valley, a small lateral valley, extending from 1830 m to 3030 m asl, in the Ayas municipality, thanks to a collaboration with Regione Au- tonoma Valle d'Aosta. Moreover this is an excellent test site due to the proximity to two monitored springs, 100 m apart, located at the closing section of the Mascognaz basin (about 10 km^2) (Fig. 16.1).

16.2 Instrumentation

The Meteorological station, located at 1935 m asl, is constituted by two different stations equipped with specific advanced sensors: Corr-Tek Hydrometry S.r.l. Station:

- Thermometer, hygrometer, barometer and anemometer-protractor (CWS, OTT company)
- Solar Irradiation (OTT company)
- Pluviograph (Pluvio2, OTT company)

G. Lollino et al. (eds.), *Engineering Geology for Society and Territory – Volume 1*,
DOI: 10.1007/978-3-319-09300-0_16,

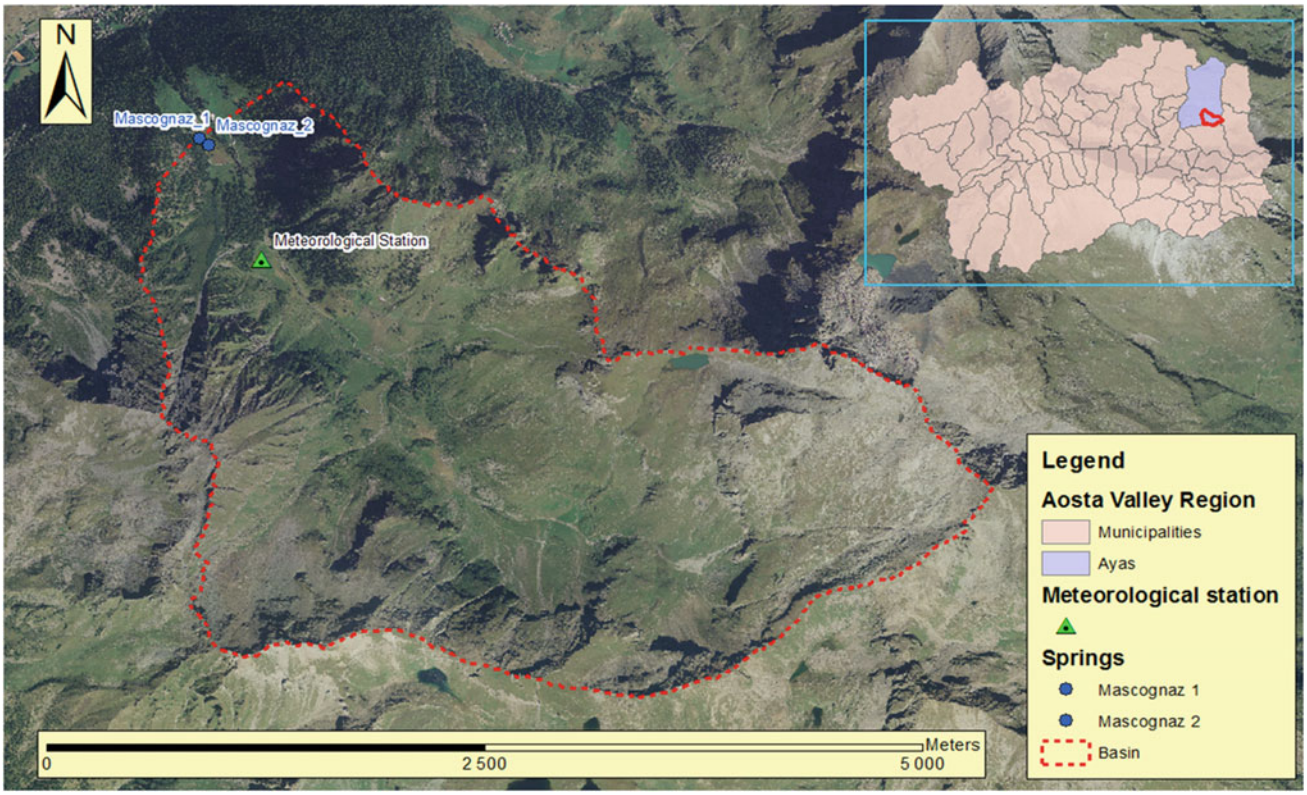

Fig. 16.1 Geographical framework of test site

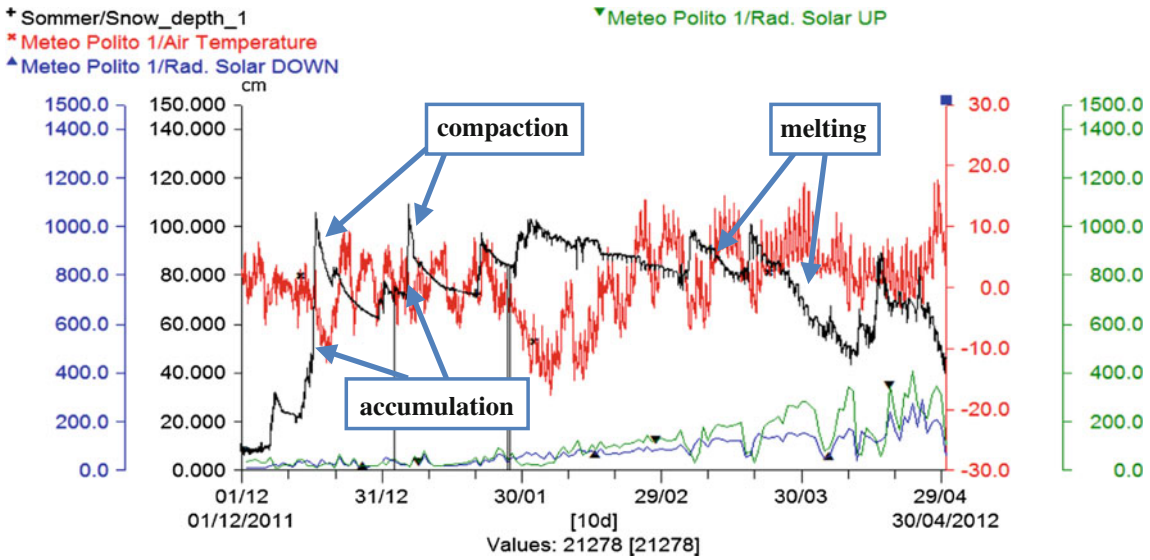

Fig. 16.2 Snow depth and energy parameters (winter 2011–2012)

GmbH & Co. KG Station:

- Snow Depth (Sommer company)
- Snow Scale (Sommer company)
- Snow Pack Analyser (Sommer company)

Each springs was equipped with a probe, the first to measure the water level, temperature and conductivity, the second for water level and temperature.

16.3 The Study

In many regions of the Alps, snowfall and the resulting seasonal snow cover represent an important source of water. When the snow-packs melt, they recharge the groundwater and replenish surface water storage (Vigna et al. 2011).

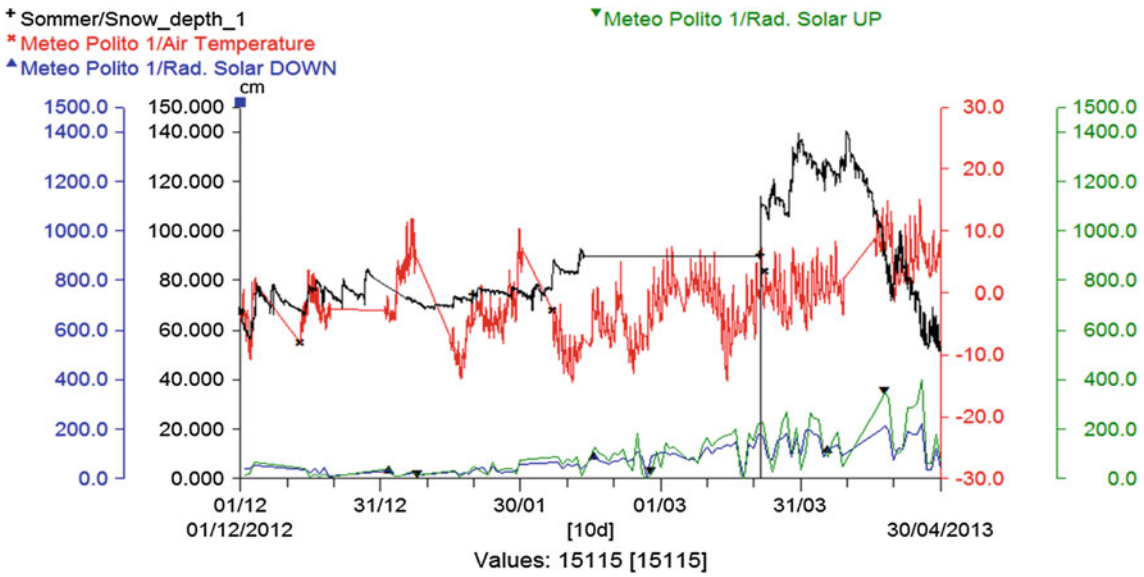

Fig. 16.3 Snow depth and energy parameters (winter 2012–2013)

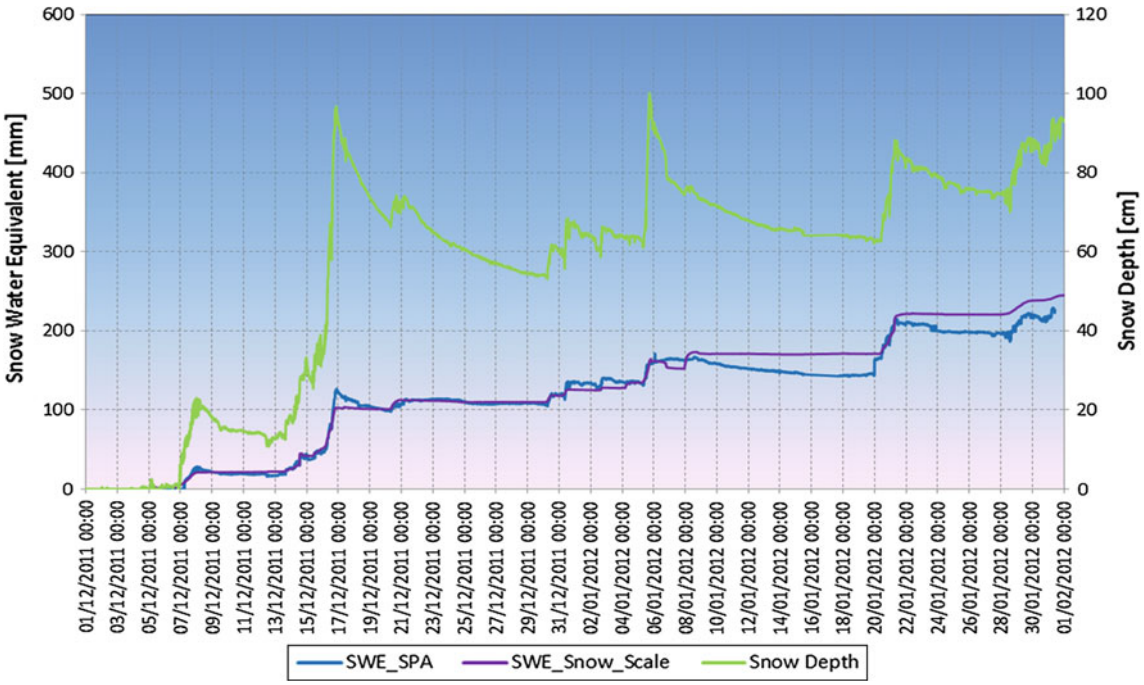

Fig. 16.4 SWE and snow depth comparison (winter 2011–2012)

The study takes into account two aspects of the main physical phenomena, which are closely related to each other: the snow melt process, strongly influenced by energy fluxes, and the groundwater recharge connected to the snow water equivalent.

Data analysis shows that snow-depth can be identified in three different parts: the accumulation process, the compaction process and the melting process, each linked to the external temperature condition and to radiation fluxes (Figs. 16.2, 16.3).

The accumulation process is typical of the winter month (December–January) when the temperature range varies between −1 and 0 °C. The compaction process takes place in the first few days following a snowfall and it is evident in

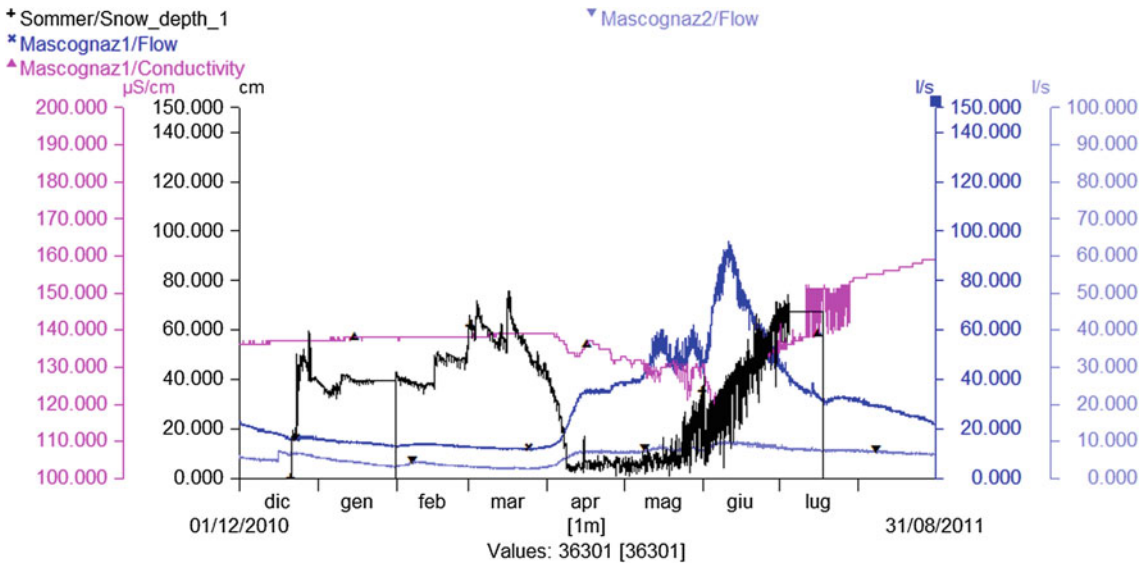

Fig. 16.5 Snow-depth and springs comparison (2010–2011)

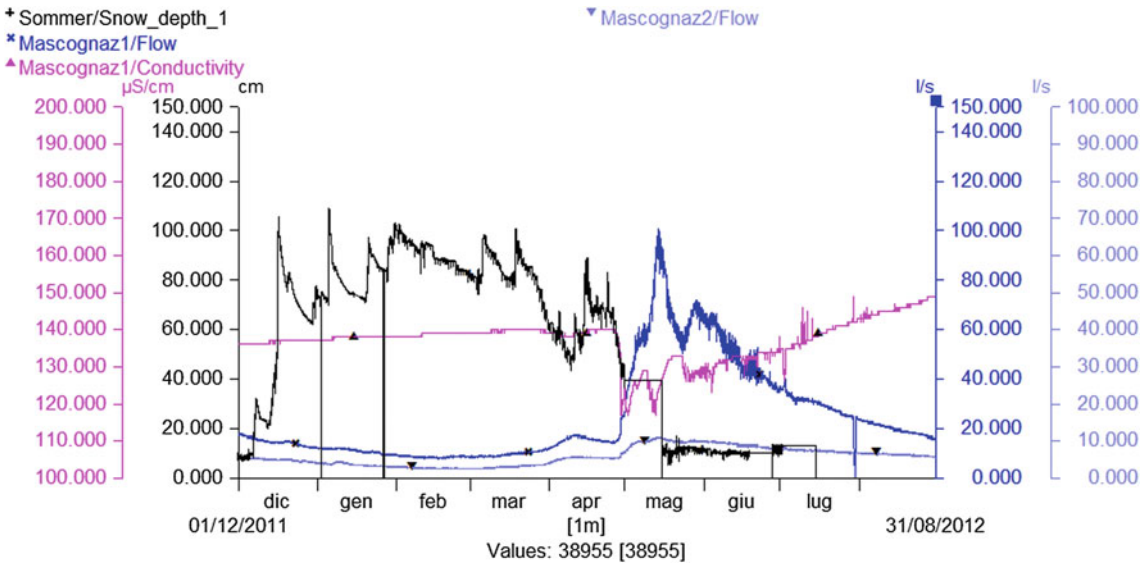

Fig. 16.6 Snow-depth and springs comparison (2011–2012)

winter months at low temperatures (under −2 °C). The melting process starts when the temperature is over 1 °C and its trend is less steep than that of compaction. Finally, this process is characterized by a solar radiation of over than 100 w/m^2 (average daily).

The groundwater recharge deriving from the snowmelt process is evaluated by the snow water equivalent (S.W.E.). The quantity of water is measured by sensors installed in the meteorological station:

- The Snow Scale measures the weight of snow and converts it to mm of water
- The SPA multiplies the value of correct density by the height of the cover band

The graph represented in Fig. 16.4 shows the increment of the SWE according with the contribution snow during the winter 2011–2012.

For December 2011 and January 2012 a contribution variable of between 250 mm (SWE SPA) and 270 mm (SWE Snow Scale) was obtained.

Combining the station data with data measured in the spring it is possible to quantify the water supply deriving from snowmelt (Figs. 16.5, 16.6, 16.7).

The analysis show that the springs respond to snow inputs in about 10–15 days; This is important both to determine the recharge and to evaluate the vulnerability of the springs.

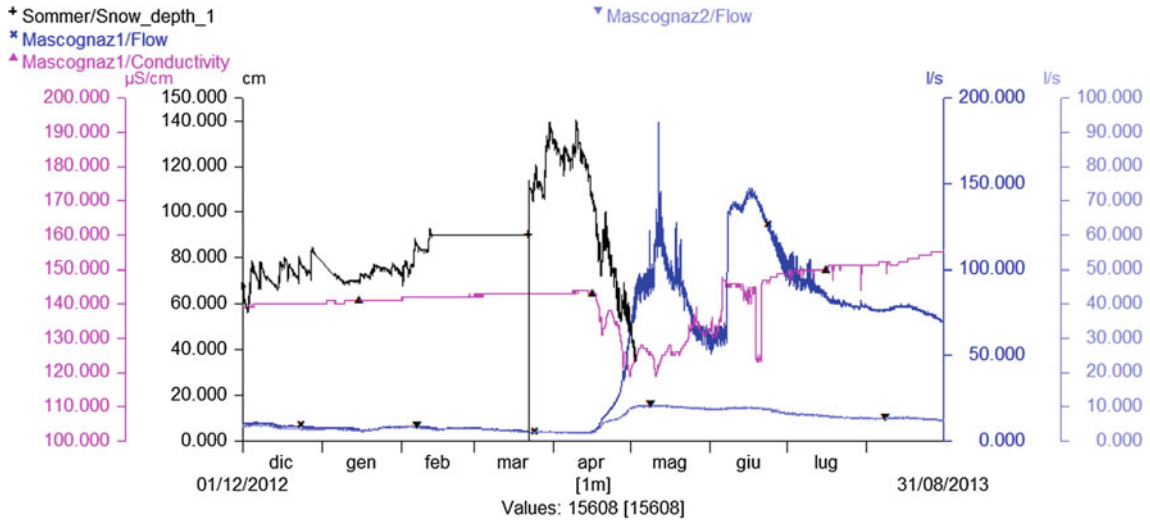

Fig. 16.7 Snow-depth and springs comparison (2012–2013)

Monitoring made it possible to observe the increase of snow precipitation dur-ing the last 3 years in the Mascognaz site. This aspect affects directly the in-crease of water availability as measured in the springs rate.

16.4 Conclusions

This study has allowed us to identify key parameters involved in the snow melt process and groundwater recharge in order to implement a spatial analysis on an alpine basin. The response-recharge mechanism identified will allow us to improve the project in order to better estimate the hydrogeological cycle.

Furthermore the characterization of the snow melt process in mountain environments is an important step both for the quantification of groundwater recharge and for the monitoring of climate change over time.

References

Bloschrl G, Kirnbauearn R, Gutknecht D (1991) Distributed Snowmelt Simulations in an Alpine Catchment, 1 and 2. Water Resour Res 27(12):3171–3179, 3181–3188

Cazorzi F, Dalla Fontana G (1995) Snowmelt modelling by combining air temperature and a distributed radiation index. J Hydrol 181(1996):169–187

Garen DC, Marks D (2005) Spatially distributed energy balance snowmelt modeling in a mountainous river basin: estimation of meteorological inputs and verification of model results. J Hydrol 315:126–153. doi:10.1016/j.jhydrol.2005.03.026

Luce CH, Tarboton DG, Cooley KR (1998) The influence of the spatial distribution of snow on basin-averaged snowmelt. Hydrol Process 12(10–11):1671–1683

Tarboton DG, Chowdhury TG, Jackson TH (1994) A spatially distributed energy balance snowmelt model. Utah State University, report, paper 60

U.S. Army Corps Of Engineers (1998) Runoff from snowmelt. University Press of Pacific, Honolulu (HI; F-14)

Vigna B, Suozzi E, (2009) The importance of the nival melting process on the recharging of acquifers. In: EPITOME, Geoitalia 2009, Rimini, Italy 9–11 Settembre, 41 (1) (ISSN: 1972-1552)

Part II

Climate Change and Water Resources

Convener: Prof. Alberto Bellin—*Co-conveners*: Elisa Palazzi, Ralf Ludwig

Climate change is expected to induce alterations in the hydrological cycle, whose effects on water resources should be quantified in view of the possible adverse consequences on society and ecosystems. Obtaining reliable scenarios on water resources availability is a necessary prerequisite to planning mitigation measures as required in the last IPCC report. To achieve these goals, state-of-the-art hydrological models operating at the catchment scale should be combined with regional climate models. This calls for new approaches and a careful evaluation of the cascade of uncertainty emerging when the climate signal is transformed into hydrological surface and subsurface flows. We welcome contributions on all aspects of the multifaceted interactions between climate change and water resources, including basic research studies, data measurements, modelling results, management and adaptation strategies and policy issues.

Seasonal Hydrochemical Changes of Water from Alluvium Aquifers: Drean-Annaba Aquifer Case Study (NE Algeria)

17

L. Djabri, Ch. Fehdi, A. Hani, S. Bouhsina, I. Nouiri, M.C. Djouamaa, A.P Boch and F. Baali

Abstract

Water quality is subject to frequent changes in the Drean-Annaba alluvium aquifer. Water-rock interaction can not be the only process that produces the observed modification, but dryness that the country knew during the last two decades has highly contributed to the water quality changes. During this period, irregularities in the distribution of rainfalls, in time and space, have been observed. As a result, a periodicity in hydrochemical changes in water of wells and rivers is noticed. Statistical, the Principals components analysis (PCA) tools and Tickel diagram have been used to show, through chemical presentation, these effects. The results show, indeed, seasonal changes of water quality for the period 1999–2000. From a cationic point of view, a competition between alkaline and alkaline earths is shown. On the other hand, from an anionic point of view, there is a transition from chlorides to sulphates and may be to bicarbonates. The present work was carried out in a relatively small area and this was useful to show the relationship that exists between dryness and water quality of both the aquiferous system and surface water.

Keywords

Annaba • Seasonal • Pollution • Variations • Aquifer

17.1 Introduction

Some countries bordering the Mediterranean had many problems with water quantity and quality. This situation has constrained the scientists to look at this problem. In Algeria, the work carried out by Djabri (2013) highlights the salinity of water in two aquifers with different climates and geology: alluvial aquifer of Tebessa (semi-arid zone) and superficial aquifer of Annaba-Bouchegouf-Guelma. Zenati (2009) and Habes (2013) showed that the presence of highly salted water lake (Fetzara lake) could influence the salinity of groundwater by bringing in mineralised waters. The water flows from the lake towards the aquifer passing Oued Meboudja. Debieche (2002), Hani (2003) and Aoun Sebaiti (2010) underline a salinity of Annaba deep aquifer waters, which its origin is not well defined. Aoun Sebaïti (2010) demonstrated the existence of seawater intrusion through the South-North oriented periphery. We present the influence of the seasonal climate on groundwater. The physicochemical

L. Djabri (✉) · A. Hani
Laboratory of Water Ressources and Sustainable Development, Badji Mokhtar University, Annaba, Algeria
e-mail: djabri_larbi@yayoo.fr

Ch. Fehdi · F. Baali
University of Larbi Tebessi, Tébessa, Algeria

S. Bouhsina
Department of Chemistry, Littoral Dunkerque University, Dunkirk, France

I. Nouiri
INAT Tunis, Tunis, Tunisia

M.C.Djouamaa
Laboratory LM2PM, Badji Mokhtar University, Annaba, Algeria

A.P. Boch
Universiy of Almeria, Almería, Spain

G. Lollino et al. (eds.), *Engineering Geology for Society and Territory – Volume 1*,
DOI: 10.1007/978-3-319-09300-0_17,

analyses of the Oued-Lake-Sea aquifer system confirm again this relationship. This work is based on the above mentioned research studies.

The objectives of this research are to identify and describe the impact of the seasonal climate on the water quality and its distribution among different hydraulically linked zones.

17.2 Materials and Methods

To realize this work, water samples were collected each month. 148 samples were taken through the zone of study. The withdrawal concerned the domestic wells of the unconfined groundwater located in Annaba-Dréan zone (65), the groundwater surrounding Fedzara lake (42), the Seybouse (25) and Meboudja stream (16). The proportioning of strontium was realized on 23 samples only.

The physicochemical parameters (pH, T°C and conductivity) were measured in situ using a WTW multi-parameter device (Multi-line P3 PH/LF-SET) and a SEBA KLL type probe for the measurement of the piezometric level. The chemical analysis was carried out by flame atomic absorption (PerkinElmer 11005) for cations. Anions and trace elements were measured using a spectrophotometer "PhotoLab WTW".

17.3 Geographic Location and Geological Framework of the Studied Zone

The studied region is located in the North-East of Algeria (Fig. 17.1). It is bound by the Mediterranean Sea to the North, by Drean town to the South, by Oued Mafragh to the East and by Fetzara Lake to the West. The plain is supplied at the West by the streams water coming from the Edough mount, and at the South by the upstream supplies.

17.4 Geological Framework

The studies realized in the region show that there are two types of formations: metamorphic and sedimentary (Fig. 17.2). The geological formation dates back from the Palaeozoic to the Quaternary period.

The Quaternary is represented by dunar and alluvial formations. We distinguish Old Quaternary (high terraces) containing the alluvia aquifer of which the material is composed of sands, clays and gravels; Recent Quaternary corresponding to low and medium terraces; and Current Quaternary including the alluvia of the current riverbeds, constituted by sands and gravels.

17.5 Regional Climate

The average annual precipitation on the whole Seybouse basin varied between 700 and 400 mm, with a monthly maximum between 90 and 120 mm, in December–January. As far as the temperatures are concerned, the extremes are observed in winter and summer. The minima are observed in December–January (less than 10 °C, and the maxima in July or August (between 25 and 30 °C). The contrast between winter and summer is highly important far from the Mediterranean sea. The potential evapotranspiration is closely linked to the temperatures. The annual average of the evapotranspiration range from 1000 to 2000 mm. The Seybouse climate is mediterranean but changing from the north to the south. Along the coast, the annual rainfall varies between 700 and 900 mm.

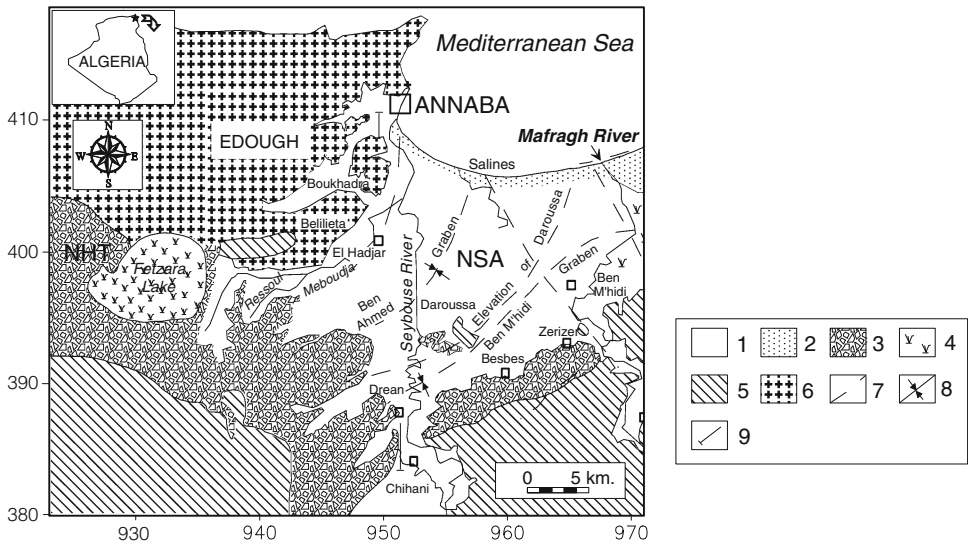

Fig. 17.1 Geographic location and geological frame of the studied zone. *1* Undifferentiated Quaternary, *2* dunes, *3* Ancient alluvium, *4* lake or swamp, *5* Numidian sandstone or clay, *6* Metamorphic formation, *7* Border of the graben, *8* Graben axis, *9* Cross section, *NSA* Superficial aquifer, *NHT* Ancient alluvium aquifer

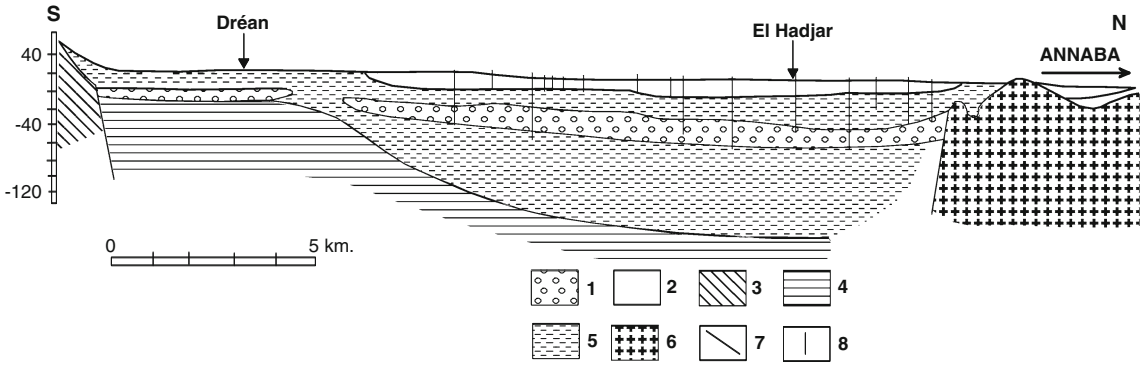

Fig. 17.2 Cross-section through the plain of Annaba and Aquifers dispositions. Key: *1* pebbles and gravels, *2* sand, *3* Numidian clay, *4* Cenomanian marl and marly limestone, *5* Plio-Quaternary detrital clays, *6* metamorphic formations, *7* fault, *8* drilling

17.6 Hydrogeology

The disposal of these formations highlighted two aquifers (Fig. 17.2) communicating between them principally by Oued Meboudja, the superficial aquifer of Annaba and Alluvial aquifer of high terraces.

The piezometric map realized (Fig. 17.3) shows, in general, that the flow follows the topographic form of the studied zone in the South-North direction. However, at the level of the Daghoussa elevation, we notice a change of the flow direction, which is from the sea towards the continent. Zenati (2009).

This predisposition sited on the Northern part of the map indicates a possible supply of the aquifer by the sea. Furthermore, the presence of depression highlights the influence of pumping which can contribute to the advance of saltwater wedge.

The second aquifer is the alluvial aquifer of high terraces (NHT).

The piezometric map shows the existence of an interaction between the various elements of the system (lake, Oued, aquifer) Aoun Sebaiti (2010). The excessive number of pumping (more than 150 installations between well and drillings) in the studied zone affects the two aquifers (superficial and deep) and generates a disturbance of the direction of the water flow.

This results in an imbalance of the salt-fresh water interface. This state deteriorates the quality of water (increase in the salinity). The water chemistry indicates the state of the aquifer according to other constituent parameters of the system.

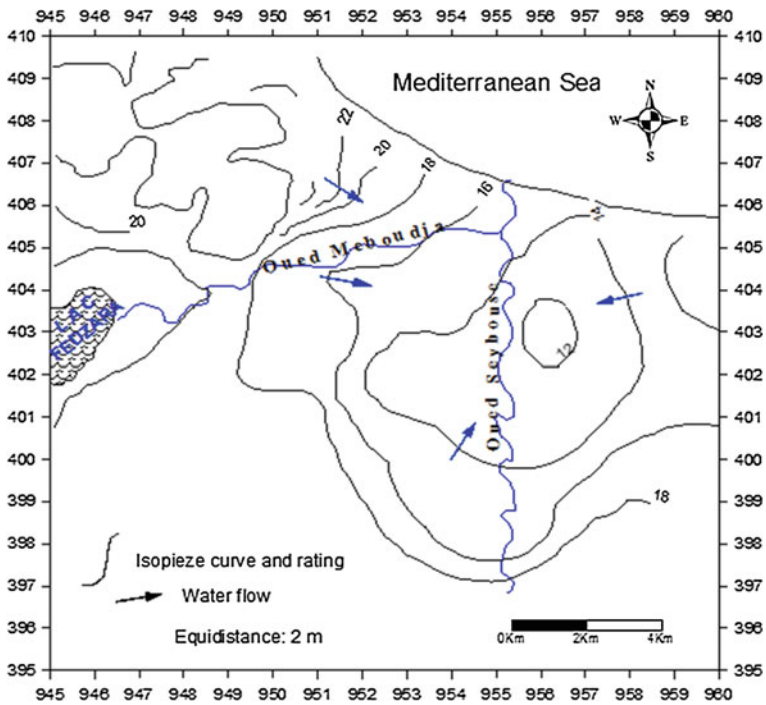

Fig. 17.3 Piezometric map of superficial aquifer of Annaba

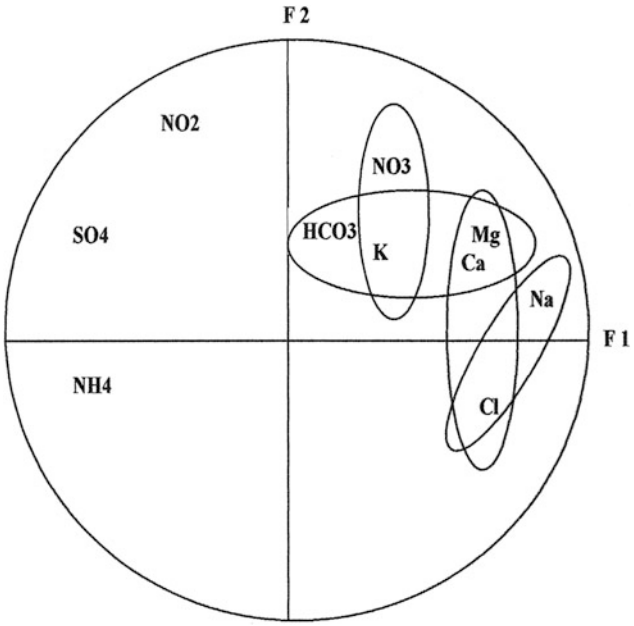

Fig. 17.4 PCA circle of superficial aquifer

17.7 Results

The chemical analyses carried out have enabled us to highlight the cause and effect relationship, which appear to exist between the sea and the aquifer, between the lake and the aquifer, and between the Oueds and the aquifer. Relaying on the representations, the following tools will be developed: analyses in principal components, Piper diagrams and Tickel diagrams. Habes (2013).

17.7.1 Principals components analysis

The PCA realized refers to the four periods where each one corresponds to one season. The number of samples taken into account were 149, and 9 chemical elements was analyzed.

The axes F1, F2 and F3 provide 68 % of the total information.

The observation of the circle (Fig. 17.4) formed by F1 and F2 shows, along the axis F1, an opposition between strongly mineral bearing water and water slightly mineral bearing.

The axis F2 indicates an opposition between chlorinated water and the remainder of water. While looking on a seasonal scale we notice a variation of the quality of water. This variation remains dependent on the following parameters:

- piezometric proximity of the level compared to the surface of the ground,
- its geology (change rather frequent of the quality),
- the effective infiltration which conditions the refill of the aquifer. Hani (2003)

This interpretation gives some idea for the variation of water quality but do not explain the variation observed. So, now we use the second method using the Tickel diagrams.

17.8 The Piper Diagrams

The Piper diagram of the superficial aquifer of Annaba (Fig. 17.5a and b) shows that, in general, the samples concentrate on the sodic and chlorinated poles showing a sodic chlorinated facies domination. We notice that some samples are rich in calcium and chlorides showing the presence of a second calcic chlorinated water type. In the aquifer of the Fetzara lake, three families seem to exist (Fig. 17.5a and b): water rich in chlorides and calcium, showing a calcic chlorinated type; water rich in sulphates and calcium originating from the calcic sulphated type; and water rich in bicarbonates and calcium, producing a hydro carbonated calcic type. The presence of these three facies is related to the sources of supply of the lake (Oued Mellah, Oued El Hout and Oued Zied) Debieche (2002).

The Piper diagrams show a variability of the chemical facies of the distributed water on three principal poles:

1. A saliferous pole characterizing the sodic chlorinated facies produced either by marine water or by the presence of evaporated formations, in deep geological layers.
2. A gypsiferous pole at the origin of the calcic sulphated facies, generated by the gypsiferous formations which undergo dissolution.
3. A carbonated pole at the origin of the calcic bicarbonate facies due to the scrubbing and the dissolution of metamorphic limestone (cipolin marbles) of the near Edough complex. The interpretation of the Piper diagrams shows the presence of two poles. This enables us to seek the origin of these elements and their contribution to the gain of water salinity.

To assess the element evolution between two periods, we used the Tickel diagram and we compared the results obtained.

17.9 Tickel Diagrams

We notice some variations between chemical analyses. The Tickel diagram (Fig. 17.6) confirms the result obtained by Piper diagram. So, we notice a seasonal variation of water quality. In summer, the salinity is very high because the evaporation is more important. In winter, we observe the contrary because the precipitations are important and the

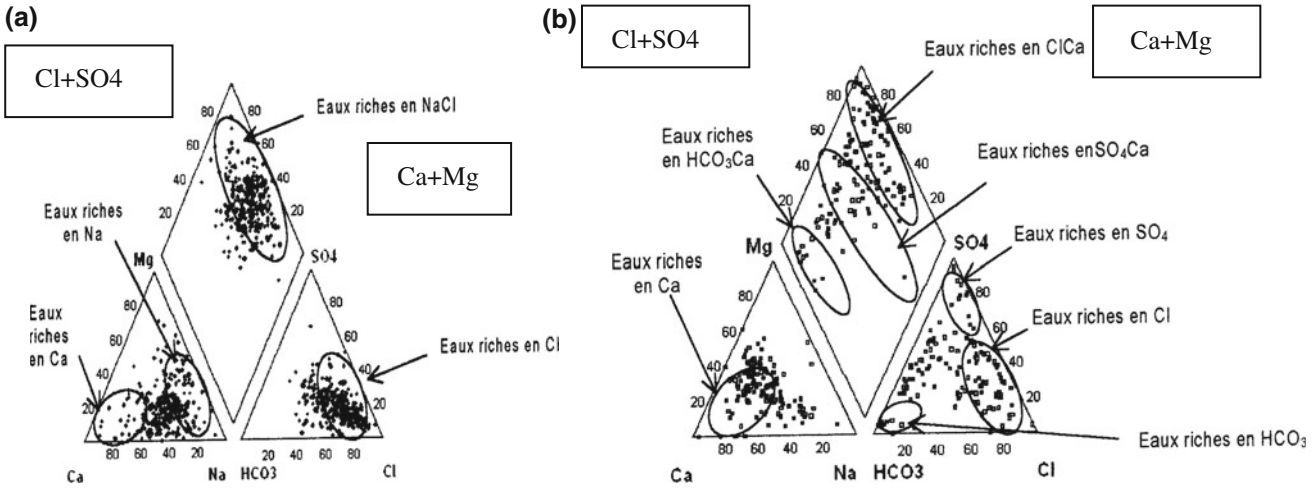

Fig. 17.5 **a** Piper diagram of the superficial aquifer of Annaba, **b** Piper diagram of the superficial aquifer of lake Fetzara

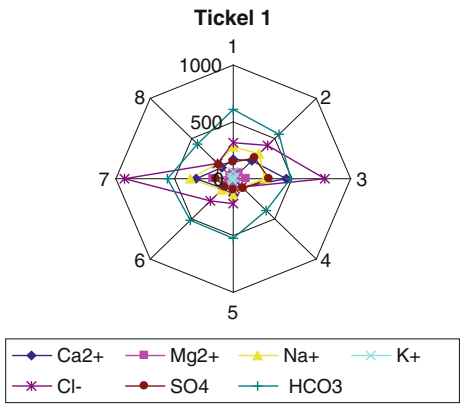

Fig. 17.6 Tickel diagram

dilutions generate low salinity Djabri (2013). In the last years, we observed a decrease of the precipitation in winter. This situation emphasizes the salinity of water because the exchange between rocks and water is weak and the dilution is not important. The dominant facies are chloride and sodium. This repartition is caused by geological formations. The dilution is the principal factor causing this quality.

17.10 Conclusion

This work is realised in a region characterized by a Mediterranean climate. In the last 10 years, we noticed an elevation of the temperatures which caused a salinity of water. In the superficial aquifer, the salinity is more important because of the low water depth. Between two seasons, the water quality changes: in the first season, the sodium and chloride are present; in the second one, the calcium and carbonate dominate. The heterogeneity of the formations explains the variations of water quality in the deep aquifer.

References

Aoun Sebaiti B (2010) Study of the water's salinity and modelization of the aquifer system of Annaba. Doctorate thesis. University of Annaba, (p 85, 2003)

Debieche H (2002) Evolution of the water's quality (salt levels, azotes and heavy metals) influenced by industrial, agricultural and salt pollution: application for the lower plains of Seybouse, Algerian NE. Doctorate thesis, University of FRANCHE-COMTE, (p 200, 2002)

Djabri L (2013) Mechanism of seybouse water pollution and venerability-geological, industrial, agricultural and urban origins. Doctorate thesis, University of Annaba, (p 176, 1996)

Habes S (2013): Chemical characteristics of a lake belonging to wetland ecosystems in northern Algeria; Case: Lake Fetzara, North - East Algerian. Doctorate thesis, University of Annaba, (p 211, 2013)

Hani A (2003) Methodological examination of anthropological structure and process, application for Mediterranean coastal basin water sources. Doctorate thesis, University of Annaba, (p 213, 2003)

Zenati N (2009) Aquifer-lake relation, hydrochemistry confirmation. West plain of El-Hadjar Superficial aquifer case, Fetzara Lake, Algerian NE. Master Degree thesis, University of Annaba, (p 148, 1999)

Groundwater Protection and Climate Change Predictions of a Complex Dinaric Karst Catchment. A Case Study of the Bokanjac-Poličnik Area, Croatia

18

Josip Terzić, Jasmina Lukač Reberski and Josip Rubinić

Abstract

The paper deals with two main issues: climate change impact on water supply and sanitary protection zones of a very sensitive Dinaric karst catchment "Bokanjac-Poličnik" in Zadar area, northern Dalmatia, Croatia. Within this complex hydrogeological system there are five public extraction sites (Bokanjac wells, Jezerce estavelle, Oko well, Golubinka spring, and Boljkovac well). Their catchments (subcatchments of the Bokanjac-Poličnik system) are interwoven and share common areas—at this moment there is no possibility of their delineation and they should be treated as one hydrogeological karst system. Since this area is close to the Adriatic Sea coast, some of these water supply sites are subjected to the underground seawater influence. In the paper it is discussed how changes (decreases of recharge) of water balance will cause decrease of extracted quantities and possible deterioration of water quality (increase of salinity). Therefore, sanitary protection zones should be established and further research of this karst system corroborated by the continuous water quality monitoring is needed, with the special regard to climate changes.

Keywords

Karst hydrogeology • Water balances • Climate changes • Groundwater quality • Sanitary protection

18.1 Introduction and Physical Setting

The research area is situated in northern Dalmatia, a hinterland of Zadar city. The terrain is built of karstified carbonate rocks and represents a typical Dinaric karst environment. This hydrogeological system, called "Bokanjac-Poličnik", is a complex karst system that consists of a few subcatchments which cannot be precisely delineated according to current knowledge. This catchment's groundwater is being extracted for the public water supply of the Zadar city and whole region. There are five extraction sites within this area (Fig. 18.1):

- Bokanjac wells: five pit wells at the boundary of karst polje; two working—17–19 m deep. Minimal capacity 30 L/s, total (maximal) 500 L/s;
- Jezerce estavelle: a pit well in karst polje, constructed at the position of estavelle. Total capacity 500 L/s, minimum 90 L/s;
- Oko well: 12 m deep pit well, constructed at the position of periodical spring, total capacity 60 L/s, minimal 20 L/s;
- Golubinka coastal spring: typical karst spring situated at the coast, brackish during the dry season (chlorides

J. Terzić (✉) · J.L. Reberski
Croatian Geological Survey, Sachsova 2, 10000 Zagreb, Croatia
e-mail: terzic@hgi-cgs.hr

J.L. Reberski
e-mail: jlukac@hgi-cg.hr

J. Rubinić
Faculty of Civil Engineering, Radmile Matejčić 3, 51000 Rijeka, Croatia
e-mail: jrubinic@gradri.hr

G. Lollino et al. (eds.), *Engineering Geology for Society and Territory – Volume 1*,
DOI: 10.1007/978-3-319-09300-0_18,

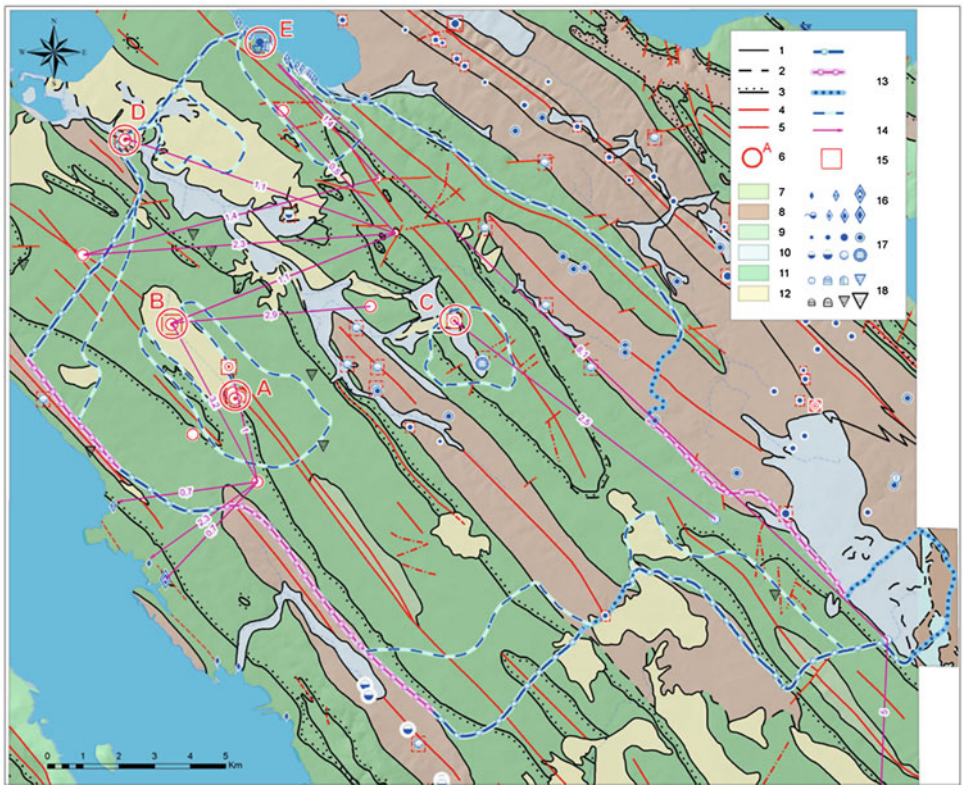

Fig. 18.1 Hydrogeological map of the "Bokanjac-Poličnik" karst system. *1* geological boundary; *2* presumed geological boundary; *3* transressive geological boundary; *4* faults; *5* structural axes; *6* main extraction sites (*A* Bokanjac wells, *B* Jezerce, *C* Oko, *D* Boljkovac, *E* Golubinka); *7* low permeable carbonate; *8* flysch; *9* mediocre permeable carbonate; *10* permeable quaternary soils; *11* highly permeable carbonate; *12* low permeable quaternary soils; *13* groundwater divides; *14* connections proven by tracer tests; *15* extraction site; *16* coastal and submarine springs; *17* springs; *18* speleological objects

reach close to 6,000 mg/L). Total capacity 300 L/s (for extraction, spring discharge is much higher), minimal quantities approximately 50 L/s;

- Boljkovac well: 6 m deep pit well situated 2 km from the cost, but under significant influence of the seawater intrusion. Chlorides usually higher than allowed, sometimes reach over 1,500 mg/L. Total capacity 100, minimal 40 L/s.

Since this is coastal area, in some of these extraction sites there is a significant influence of seawater intrusions on groundwater quality, what makes hydrogeological setting extremely complex. During the researches that took place in 2012–2013 (Terzić and Lukač Reberski 2013), previous researches (Fritz et al. 1994) have been revised according to new knowledge (new mappings, new quality measurements and results of climate change studies: Rubinić et al. 2011; Simonffy 2011). Existing published works were also referred (Pavičić et al. 2006).

Whole investigated area is 235 km^2 large. This hydrogeological system, which can hardly be called a catchment because of the fact that it is a complex network of interrelated catchments, subcatchments and preferential karst flow paths; was studied as a whole. The authors used geological and hydrogeological maps of different scale (from 1:1,000 to 1:100,000), hydrochemical researches of few year-long datasets, former tracer test results, and climate /climate change analyses of the region. All these methods were analyzed and reinterpreted to establish the new sanitary protection zones and to propose further directions of management and research of this sensitive karst system.

18.2 Climate Change Issues

Climate changes of the area were studied within the CC-WaterS project (TC SEE, EU). Three climatic models were applied to predict climate until the end of century (2100): Aladin, RegCM3 and Promes (Promes only until 2050) (Gajić-Čapka et al. 2010). These predictions were used to calculate water balances under such climatic conditions (Rubinić et al. 2011; Simonffy 2011). The evaluation was made for the chosen 30 years long periods, based on results of climatological models. Yearly discretization has been chosen for these balance calculations, because of insufficient hydrological data for more detailed approach. Using Langbein's method for effective precipitation estimation (Langbein 1962), annual time series of Bokanjačko Blato inflow were generated based on average annual air temperature and precipitation data. Average annual inflow was estimated using spatial distribution of specific runoff and compared with discharge data estimated using point input data—average annual precipitation and air temperatures for the referent 30 years time period at climatological gauging station Zadar.

Table 18.1 Changes in percentages of the main balance parameters: mean annual and minimum mean monthly discharges for the Bokanjačko Blato test area and for selected time periods

	Mean annual discharges (%)					Minimum mean monthly discharges (%)				
	Mean	St. dev.	Cv	Min	Max	Mean	St. dev.	Cv	Min	Max
2021–2050										
RegCM3	−8.1	−35.7	−28.3	52.2	−30.0	−7.2	−35.3	−30.2	47.7	−28.3
Aladin	−11.2	−25.8	−15.2	−0.9	−29.6	−10.2	−25.1	−16.3	−1.0	−27.9
Promes	−20.0	−45.7	−30.4	−11.7	−49.6	−18.5	−44.3	−30.2	−10.9	−47.2
2071–2100										
RegCM3	−32.0	−46.8	−21.7	−24.2	−47.9	−39.6	−36.6	7.0	−65.3	−45.4
Aladin	−38.5	−41.9	−4.3	−26.1	−39.2	−46.8	−30.6	32.6	−67.4	−35.1

As evaluating parameter for the critical intraannual drought periods a minimum mean monthly discharge was selected. In Table 18.1 there are achieved differences of these results, compared to the historical referent climatic data set 1961–1990.

Although these are just predictions, they shouldn't be neglected by the decision makers now or in the future, because water supply of Zadar and its surroundings has already reached its maximal capacities. In the period 2071–2100 drastic deterioration of the water balance is expected. There will be decrease of mean annual discharges between 32 and 38.5 %. The changes in minimum mean monthly discharges are even more emphasized: from 39.6 to 46.8 %. Higher changes are predicted by Aladin, and somewhat smaller by RegCM3 model. Decrease of recharge will cause drop of groundwater level, and as one of the most important consequences, that will cause seawater intrusions much deeper into the catchments. In that case, extraction sites that are under the seawater influence now will increase their salinity (possibly much higher than allowed what can cause their abandoning), and other sites that are completely potable now could become brackish to a certain extent.

18.3 Sanitary Protection and Concluding Discussion

According to Croatian legislation, a sanitary protection zones in karst areas consist of four zones delineated according to two main criteria: (1) apparent groundwater velocity achieved by tracing experiments, and (2) time (days) that water spends in the aquifer until it reaches the spring or well. Five extraction sites have their own 1st zone each, while 2nd zone is common for Bokanjac wells and Jezerce estavelle (well) (both sites are in Bokanjačko blato karst polje). The 3rd and 4th zone cover larger areas and they are common for whole hydrogeological system. Nevertheless, the Bokanjac-Poličnik system can be divided into subcatchment areas, and areas that are common to different parts of terrain.

Expected decrease of water balance recharge that will probably happen within the following decades emphasize a need for continuation of hydrogeological and hydrological research, because such decrease of recharge components can cause (among other, mostly minor, influences): (1) decrease of pumping quantities (followed by higher water demand), (2) stronger seawater intrusion that can significantly deteriorate groundwater quality, or (3) changes in land use that could cause further groundwater pollution (such as agricultural or touristic use). Therefore, a monitoring and continuous research should be established to evaluate every change of groundwater levels (indicator of quantity) or quality. Neglect of such approach could even cause a loss of this valuable karst aquifer.

According to all presented data, results, analyses and interpretation of three different projects that took place in the last few years (together with all previous knowledge), the Bokanjac-Poličnik hydrogeological system can be protected, and its water resources management can be improved. There is a need of establishing a monitoring network and to perform a few tracing experiments, so that subcatchments could be differed more precisely.

Acknowledgements The authors wish to express their gratitude to the research investors and project within which the research was performed. These are: (1) Zadarska County, local authority (thanks to Mr. Olivio Meštrović); (2) CC-WaterS project (a Transnational cooperation SEE project funded by EU); and (3) Basic hydrogeological map of Croatia project, funded by Croatian Ministry of science, education and Sports. We would also like to acknowledge a friendly help of colleagues from Zadar water supply Company (Vodovod d.o.o. Zadar).

References

Fritz F, Pavičić A, Renić A (1994) Vodovod d.o.o. Zadar extraction sites. Hydrogeological investigations for sanitary protection. Unpublished, technical report, archive HGI-CGS 70/94, Zagreb

Gajić-Čapka M, Güttler I, Branković Č (2010) Contribution to CC-WaterS project: a study of climate and climate change for three test beds in Croatia. Meteorological and hydrological service, Zagreb

Langbein WB (1962) The water supply of arid valleys in intermountain regions in relation to climate. IAHS Bull 7(1):34–39

Pavičić A, Terzić J, Berović N (2006) Hydrogeological relations of the Golubinka karst spring in Ljubač Bay, Dalmatia, Croatia. Geol Croat 59:123–135

Rubinić J, Terzić J, Marković T, Horvat B (2011) WP4: availability of water resources. Test area Bokanjačko Blato, North Dalmatia, Croatia. CC-WaterS—Climate change and impacts on water supply, TC SEE Project

Simonffy Z (2011) WP4: availability of water resources. Final Report. CC-WaterS—Climate change and impacts on water supply, TC SEE Project

Terzić J, Lukač Reberski J (2013) Hydrogeological elaborate for establishment of sanitary protection zones of the Vodovod d.o.o. Zadar water extraction sites (Bokanjac wells B-4 and B-5, Jezerce, Oko, Boljkovac and Golubinka) within the hydrogeological system Bokanjac-Poličnik. Unpublished, technical report, archive HGI-CGS 07/13, Zagreb

Preliminary Chemical and Isotopic Characterization of High-Altitude Spring Waters from Eastern Nepal Himalaya

19

Emanuele Costa, Enrico Destefanis, Chiara Groppo, Pietro Mosca, Krishna P. Kaphle and Franco Rolfo

Abstract

Metamorphic degassing from active collisional orogens supplies a significant fraction of CO_2 to the atmosphere, thus playing a fundamental role even in today's Earth carbon cycle. Appealing clues for a contemporary metamorphic CO_2 production in active orogens are represented by the widespread occurrence, along the whole Himalayan belt, of CO_2 rich hot-springs mainly localized along major tectonic discontinuities. In contrast to these well-studied hot-springs, almost no chemical and isotopic data are actually available for cold-springs, especially for those located at high-altitude and in remote areas of the Himalayas. In the framework of the Ev-K2-CNR SHARE (Stations at High Altitude for Research on the Environment) Project, we have started a preliminary chemical and isotopic study on high-altitude cold-springs located at different structural levels in the eastern Nepal Himalayas. Chemical and isotopic data obtained from the high-altitude cold-springs are compared with those obtained by previous authors from hot-springs located along the MCT. The isotopic signature of stable isotopes of hydrogen and oxygen could help to identify the waters sources in the investigated Himalayan sectors, to individuate mixing phenomena between waters of different provenience and possible connection with different circulation nets. These first measurements on high-altitude springs from remote areas of eastern Nepal represent a first step towards a better definition of a reliable scenario of water resources availability and will contribute to the understanding of the water cycle in the studied area.

Keywords

High-altitude springs • Chemical and isotopic study • Eastern himalayas • Hydrological cycle • Global carbon cycle

19.1 Introduction and Aim of the Study

Mountain ranges have strong impact on the global carbon cycle: metamorphic degassing from active collisional orogens, in fact, supplies a significant fraction of the global solid-Earth derived CO_2 to the atmosphere, thus playing a fundamental role even in today's Earth carbon cycle (Evans 2011; Rolfo et al. 2014). Appealing clues for a contemporary metamorphic CO_2 production in active orogens are represented by the widespread occurrence, along the whole Himalayan belt, of CO_2 rich hot-springs mainly localized along the major tectonic discontinuities, such as the Main Central Thrust (Becker et al. 2008; Perrier et al. 2009). Peak

E. Costa (✉) · E. Destefanis · C. Groppo · F. Rolfo
Department of Earth Sciences, University of Torino, 10125 Turin, Italy
e-mail: emanuele.costa@unito.it

F. Rolfo
e-mail: franco.rolfo@unito.it

P. Mosca · F. Rolfo
IGG – CNR, 10125 Turin, Italy

K.P. Kaphle
Nepal Geological Society, Kathmandu, Nepal

G. Lollino et al. (eds.), *Engineering Geology for Society and Territory – Volume 1*,
DOI: 10.1007/978-3-319-09300-0_19,

values of the measured CO_2 flux at these gas discharges are exceptionally high and similar to values reported on volcanoes (19,000 g m^{-2} day^{-1}; Perrier et al. 2009). In contrast to these well-studied hot-springs, almost no chemical and isotopic data are actually available for cold-springs, especially for those located at high-altitude and in remote areas of the Himalayas.

In the framework of the Ev-K2-CNR SHARE (Stations at High Altitude for Research on the Environment) Project, we have started a preliminary chemical and isotopic study on high-altitude cold-springs located at different structural levels in the eastern Nepal Himalayas (Khimti Khola, Likhu Khola and Dudhkund Khola catchments). Preliminary chemical and isotopic data obtained from these high-altitude cold-springs are hereby compared with those obtained by previous authors from hot-springs located along the Main Central Thrust.

These first measurements on high-altitude springs represent a first step towards a better definition of a reliable scenario of water resources availability and will contribute to the understanding of the water cycle in the studied area.

19.2 Sampling and Analytical Methods

19.2.1 Sampling

Eleven spring water samples were collected in the Numbur and Dudh Khunda region of eastern Nepal Himalayas in the post-monsoon season, November 2012. The investigated springs are located in the Khimti Khola, Likhu Khola and Dudhkhund Khola catchments (tributaries of the Sun Khosi river), at an altitude between 1,800 and 4,500 m a.s.l. (Fig. 19.1). Most of the springs are located in remote areas, far from villages and accessible through poorly known trails. Water sampling was further complicated by the high altitude environment and by the fact that, due to logistic reasons, the amount of collected water had to be minimized.

Temperature and pH were measured *in situ* at the source vents using an HANNA HI2211 pH meter, calibrated every morning with pH standards. Conductivity was measured with an HANNA HI8820 N. Water samples for chemical and isotopic analysis were collected in two polyethylene bottles of 250 ml, capped without head space to minimize degassing. The water samples to be used for DIC isotopic analysis were added with $SrNO_3$ and NaOH to precipitate all the dissolved inorganic carbon as $SrCO_3$, as suggested in

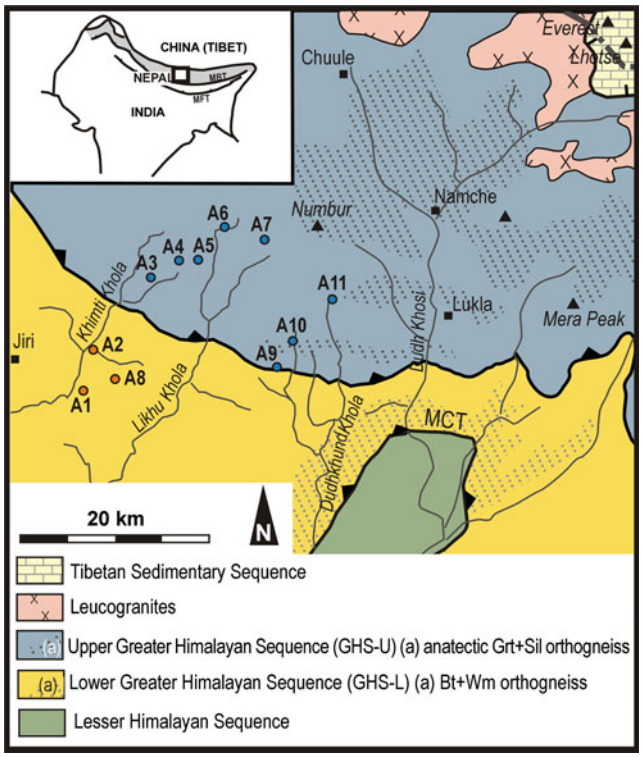

Fig. 19.1 Simplified geological map of the central-eastern sector of the Numbur and Dudh Khunda area, eastern Nepal Himalaya (modified from Mosca et al. 2013) showing sample locations. *MCT* Main central thrust. *Inset* shows the location of the study area (*black rectangle*) in the framework of the Himalayan chain. The *grey* shaded belt approximates the location of the Greater Himalayan Sequence. *MFT* Main frontal thrust; *MBT* Main boundary thrust

De Groot (2004). A subsequent filtration of the samples that would have precipitated enough carbonate could have led to isotopic measurement of the Dissolved Inorganic Carbon.

19.2.2 Geological Setting

The Khimti Khola, Likhu Khola and Dudhkhund Khola rivers cross the main tectonostratigraphic units of eastern Nepal Himalaya, flowing across the Greater Himalayan Sequence (GHS) and the Lesser Himalayan Sequence and crossing the Main Central Thrust Zone (MCTZ). Three of the investigated springs are located in the structurally lower GHS domain (GHS-L) (i.e. within the MCTZ), and seven are located in the upper GHS domain (GHS-U) (Fig. 19.1).

The GHS-L mainly consists of a metasedimentary sequence (mostly metapelites and minor calc-silicate rocks

and impure marbles) recording an increase in metamorphic grade upward, passing from the staurolite zone to the sillimanite zone and, locally, to anatexis (Groppo et al. 2009; Mosca et al. 2013). The GHS-U is characterized by high-grade metamorphic rocks (metapelites, metacarbonate rocks and orthogneiss), often anatectic, recording a progressive decrease in peak-pressure structurally upward (Groppo et al. 2012, 2013). Most of the analyzed springs are hosted in silicate rocks, except springs A1 and A11 that are hosted in metasedimentary rocks including impure marbles and calc-silicate levels.

19.2.3 Analytical Methods

Samples for chemical analysis were collected in pre-cleaned HDPE 250 ml bottles, without any addition of acid substances, because the same sample has to be suitable for both cations and anions determinations. Analysis were done at the Dept. Earth Sciences (Univ. Torino), using a Metrohm IC 732 Ion Cromatography System for anions quantification, and a Spectro Iris Advantage II ICP-AES for cations evaluation. Isotopic analysis were performed on five representative samples from different structural levels at ISO4 Laboratories in Turin, using a Picarro L2120-i Isotope Analyzer, with a precision of $\pm 3\ \delta‰(3\sigma)$ for deuterium and $\pm 0.6\ \delta‰(3\sigma)$ for ^{18}O. So far, none of the samples was submitted to DIC isotope analysis for the evaluation of $\delta^{13}C$; only sample A1 is rich enough in DIC to ensure the necessary amount of carbonate suitable for the determination.

19.3 Results

19.3.1 Geochemical Features

The analyzed springs are characterized by low discharge temperature varying between 3 and 16 °C, with a negative correlation between temperature and altitude (Table 19.1). They are characterized by a very low salinity (TDS < 150 mg/L) and a correspondent very low conductivity (<200 µS/cm). The pH varies between 6.5 and 7.3 and the samples are Ca–Mg–HCO^{3-} in composition (Fig. 19.2a). No significant compositional variations are observed between the GHS-L and the GHS-U springs; the springs hosted in metacarbonate rocks show the highest TDS.

Overall the characteristics of the analyzed cold-springs are coherent with those described by previous authors in other areas of central Nepal Himalaya (e.g. cold-springs of the Marsyandi Valley: Evans et al. 2001; Becker et al. 2008). Cold-springs composition is significantly different from that of the well-known hot-springs located along the MCT, which are typically Na–Cl to Na–Ca–Cl type waters with high total dissolved solids (TDS up to 8,500 mg/L), vary in temperature between 20 and 60 °C and have a pH in the range 5.5–7 (e.g. Evans et al. 2004; Becker et al. 2008; Perrier et al. 2009).

19.3.2 Isotopical Features

The very low total dissolved solids of the measured samples hampered the possibility of analyzing their carbon isotopic composition. Five of the water samples were submitted to isotopic determination to measure hydrogen and oxygen values. These are typical of meteoric waters and show a very good correlation with the Global Meteoric Water Line (GMWL) of precipitation (IAEA 1970, 2005), lying directly upon or very near the GMWL (Fig. 19.2b). A difference is clearly visible between samples collected at minor altitude (A1 and A2) and those collected at higher altitude. The close correlation suggests the absence of any evaporation process prior of the infiltration of rain runoff, or exchange reactions between the infiltrated water and the host rocks. Topography and altimetry indicate that a short distance could be traveled through the hosting geological formation between recharge area and spring location; therefore, the short residence time, combined with the low water temperature, prevented reactions with silicates.

19.4 Conclusions and Further Studies

Our preliminary data obtained from Himalayan high-altitude cold-springs show waters with low salinity contents and an isotopic signature that clearly indicates a provenience from meteoric rain-fall. Low temperature of the waters, as well as the low content in chloride and other ions, suggest that these springs are unrelated to geothermal activity. Overall, chemical and isotopic data are in good agreement with the few data on Himalayan cold-springs already available in the literature.

Since the isotopic determinations are related to a single sampling campaign, they do not allow further hypothesis about water circulation and seasonal change, or variations in the hydrological cycle. However, these are amongst the first δD and $\delta^{18}O$ data for high-altitude cold-springs from remote areas of eastern Nepal Himalaya. New sampling

Table 19.1 Location, field observations

Sample	Altitude (m a.s.l.)	GPS coordinates	Host rocks	Estimated discharge rate (l/sec) and field observations	T °C	pH	Conductivity (μS cm^{-1})	TDS	Na^{+} (mg/l)	K^{+} (mg/l)	Ca^{++} (mg/l)	Mg^{++} (mg/l)	NH^{++} (mg/l)	F^{-} (mg/l)
A1	1805	N27°36′27.0″ E86°17′47.4″	Wm+Chl filladic schist and Phl+Wm impure marble	10–20 l/sec; several discharge points in the alluvial sediments	16.1	7.3	172	134.4	0.83	1.57	12.70	4.50		0.02
A2	I960	N27°38′32.9″ E86°19′08.0″	Fine-grained two-micas Grt-bearing gneiss	<1 l/sec and discontinuous; few discharge points at at the base of an alluvial fan	15.0	7.1	28	25.15	1.44	0.61	1.71	0.42	0.08	
A3	3930	N27°42′57.0″ E86°23′4.8″	Two-micas, Grt- and Ky-bearing gneiss	<0.1 l/sec, single discharge point in the alluvial sediments	6.0	6.8	18	14.51	0.68	0.92	0.85	0.31		
A4	4510	N27°43′57.3″ E86°25′21.6″	Bt+Grt+Sil anatectic gneiss	01–0.2 l/sec. few discharge points from (the rock outcrop	3.0	6.9	21	17.11	0.5	0.32	2.22	0.29		0.01
A5	4370	N27°43′54.9″ E86°26′15.4″	Bt+Grt+Sil anatectic gneiss	2 l/sec, few discharge points at the base of an alluvial fan	5.1	7.2	7	8.27	0.14	0.3	0.81	0.28		0.00
A6	4140	N27°45′48.0″ E86°28′03.4″	Fine-grained Bt gneiss with Sil+Qtz nodules	1 l/sec: single discharge point in the alluvial sediments	5.6	7	15	14.39	0.39	0.44	1.80	0.32		0.01
A7	4380	N27°45′11.0″ E86°30′37.5″	Bt + Grt + Sil anatectc gneiss	0.1–0.2 l/sec; single discharge point from from the rock outcrop	3.6	7	25	23.66	0.24	0.39	2.74	0.46		0.01
A8	3090	N27°36′43.2″ E86°20′47.8″	Two-micas Grt-bearing quartzitic micaschist	0.1–0.2 l/sec; single discharge point from the colluvial sediments	9.2	6.8	8	10.29	0.04	0.47	0.60	0.42		
A9	3700	N27°38′00.1″ E86°32′04.6″	Bt+Grt+Sil anatectic augen-gneiss	0.1–0.2 l/sec; single discharge point from the colluvial sediments	6.9	6.9	16	15.97	0.64	0.57	1.28	0.46	0.13	0.00
A10	3870	N27°39′23.1″ E86°33′04.7″	Bt+Grt+Sil anatectic augen-gneiss	0.1–0.3 l/sec, single discharge point in the alluvial sediments	7.9	6.3	15	14.28	0.55	0.68	1.40	0.42		
A11	4465	N27°41′44.6″ E86°35′4I.9″	Calc-silicate granofels and impure marble	50–100 l/sec; few discharge points from the rock outcrop	3.6	6.5	55	43.06	0.49	0.63	6.29	0.33		0.02

Sample	Altitude (m a.s.l.)	GPS coordinates	Host rocks	Estimated discharge rale (l/sec) and field observations	Cl^{-} (mg/l)	HCO^{3-} (mg/l)	CO^{3-} (mg/l)	NO^{2-} (mg/l)	SO_4^{2-} (mg/l)	PO_4^{3-} (mg/l)	NO_3^{-} (mg/l)	$\delta^{18}O$ (‰ VSMOW)	δD (‰ VSMOW)
A1	1805	N27°36′27.0″ E86°17′47.4″	Wm+Chl filladic schist and Phl+Wm impure marble	10–20 l/sec; several discharge points in the alluvial sediments	0.82	111.1	0.00	0.22	0.87	0.00	1.84	−8.74	−60.01
A2	I960	N27°38′32.9″ E86°19′08.0″	Fine-grained two-micas Grt-bearing gneiss	<1 l/sec and discontinuous; few discharge points at at the base of an alluvial fan	0.21	19.53	0.00		0.42	0.00	0.73	−9.13	−61 78
A3	3930	N27°42′57.0″ E86°23′4.8″	Two-micas, Grt- and Ky-bearing gneiss	<0.1 l/sec, single discharge point in the alluvial sediments	0.97	6.10	0.00		0.21	0.17	4.30		
A4	4510	N27°43′57.3″ E86°25′21.6″	Bt+Grt+Sil anatectic gneiss	01–0.2 l/sec. few discharge points from (the rock outcrop	0.10	9.75	0.00		3.40	0.00	0.51	−14.40	−102.46
A5	4370	N27°43′54.9″ E86°26′15.4″	Bt+Grt+Sil anatectic gneiss	2 l/sec, few discharge points at the base of an alluvial fan	0.09	4.88	0.00		1.19	0.00	0.58		
A6	4140	N27°45′48.0″ E86°28′03.4″	Fine-grained Bt gneiss with Sil+Qtz nodules	1 l/sec: single discharge point in the alluvial sediments	0.23	9.76	0.00	0.01	0.90	0.00	0.52		

(continued)

Table 19.1 (continued)

Sample	Altitude (m a.s.l.)	GPS coordinates	Host rocks	Estimated discharge rale (l/sec) and field observations	Cl^{-} (mg/l)	HCO^{3-} (mg/l)	CO^{3-} (mg/l)	NO^{2-} (mg/l)	SO_4^{2-} (mg/l)	PO_4^{3-} (mg/l)	NO_3^{-} (mg/l)	$\delta^{18}O$ (‰ VSMOW)	δD (‰ VSMOW)
A7	4380	N27°45′11.0″ E86°30′37.5″	Bt+Grt+Sil anatectic gneiss	0.1–0.2 l/sec; single discharge point from from the rock outcrop	0.09	17.09	0.00		2.30	0.00	0.35		
A8	3090	N27°36′43.2″ E86°20′47.8″	Two-micas Grt-bearing quartzitic micaschist	0.1–0.2 l/sec; single discharge point from the colluvial sediments	0.28	7.32	0.00		0.15	0.00	1.00		
A9	3700	N27°38′00.1″ E86°32′04.6″	Bt+Grt+Sil anatectic augen-gneiss	0.1–0.2 l/sec; single discharge point from Vie colluvial sediments	0.20	12.20	0.00		0.13	0.04	0.29		
A10	3870	N27°39′23.1″ E86°33′04.7″	Bt+Grt+Sil anatectic augen-gneiss	0.1–0.3 l/sec, single discharge point in the alluvial sediments	0.36	9.76	0.00		0.89	0.00	0.22	-12.92	−93.27
A11	4465	N27°41′44.6″ E86°35′4I.9″	Calc-silicate granofels and impure marble	50–100 l/sec; few discharge points from the rock outcrop	0.16	29.29	0.00		5.40	0.00	0.45	−15.52	−113.24

Stable Isotope, and chemical data for the cold-spring of the Numbur and Dudh Khund area

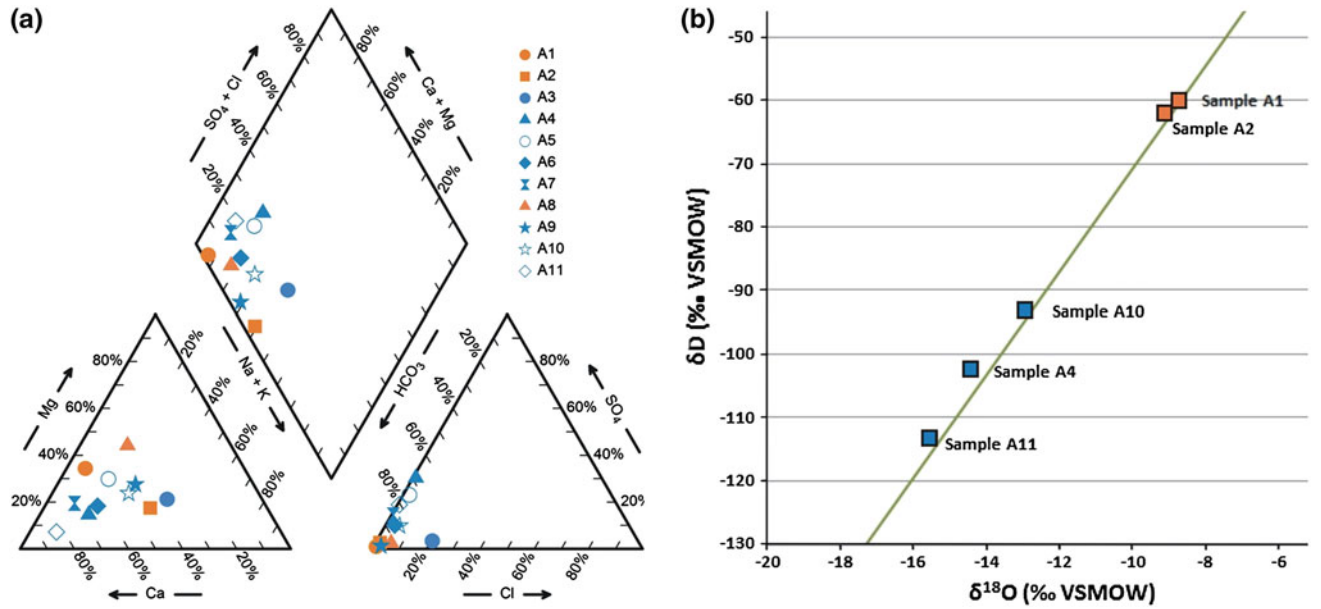

Fig. 19.2 **a** Piper diagram of the investigated water samples, showing their Ca–Mg–HCO_3 composition. **b** Projection of the isotopic data of the studied Himalayan cold-spring along with a projection of the Global Meteoric Water Line (in *green*). The studied samples are in good agreement (within the instrumental uncertainty) with rain waters with no (or very few) evaporation and/or exchange with the mineralogical assembly of the host rock. In both the diagrams, *orange symbols* GHS-L springs; *blue symbols* GHS-U springs

campaigns, planned for the next future, will increase the sampling density of both cold- and hot- springs thus allowing to achieve a better understanding of the hydrological cycle in the area.

References

Becker JA, Bickle MJ, Galy A, Holland TJB (2008) Himalayan metamorphic CO_2 fluxes: quantitative constraints from hydrothermal springs. Earth Planet Sci Lett 265:616–629

De Groot PA (2004) Handbook of stable isotope analytical techniques. Elsevier, Amsterdam

Evans KA (2011) Metamorphic carbon fluxes: how much and how fast? Geology 39:95–96

Evans MJ, Derry LA, Anderson SP, France-Lanord C (2001) Hydrothermal source of radiogenic Sr to Himalayan rivers. Geology 29:803–806

Evans MJ, Derry LA, France-Lanord C (2004) Geothermal fluxes of alkalinity in the Narayani river system of central Nepal. Geochem Geophys Geosyst 5:Q08011

Groppo C, Rolfo F, Lombardo B (2009) P-T evolution across the main central thrust zone (Eastern Nepal): hidden discontinuities revealed by petrology. J Petrol 50:1149–1180

Groppo C, Rolfo F, Indares A (2012) Partial melting in the Higher Himalayan Crystallines of Eastern Nepal: the effect of decompression and implications for the ''channel flow'' model. J Petrol 53:1057–1088

Groppo C, Rolfo F, Mosca P (2013) The cordierite-bearing anatectic rocks of the Higher Himalayan Crystallines (eastern Nepal): low-pressure anatexis, melt-productivity, melt loss and the preservation of cordierite. J Metamorph Geol 31:187–204

IAEA (1970) Technical report IAEA-116, Interpretation of environmental isotope data in hydrology. International Atomic Energy Agency, Vienna

IAEA (2005) Isotopes in the water cycle: past, present and future of a developing science. International Atomic Energy Agency, Vienna

Mosca P, Groppo C, Rolfo F (2013) Main geological features of the Rolwaling-Khumbu Himal between the Khimti Khola and Dudh Khosi valleys (eastern-central Nepal Himalaya). Rend Online Soc Geol It 29:112–115

Perrier F, Richon P et al (2009) A direct evidence for high carbon dioxide and radon-222 discharge in Central Nepal. Earth Planet Sci Lett 278:198–207

Rolfo F, Groppo C, Mosca P, Ferrando S, Costa E, Kaphle KP (2014) Metamorphic CO_2 degassing in the active Himalayan orogen: exploring the influence of orogenic activity on the long-term global climate changes. In: G. Lollino et al. (eds.), Engineering Geology for Society and Territory - Volume 1. Springer International Publishing Switzerland

Study of Climatic Variations and Its Influence on Erosive Processes in Recent Decades in One Location of Central Spain

20

A. García-Díaz, R. Bienes and B. Sastre

Abstract

Erosion is one of the main problems of agricultural soils in Spain. Climate change is causing increasingly severe erosive episodes. This paper analyzes the reduction of annual rainfall in the periods 1933–1969 and 1995–2012 in the town of Aranjuez (Central Spain). The second period data came from an automatic weather station with recordings every 10 min, which allowed to study the evolution of rainfall intensities for different time intervals and the determination of R Factor. The results showed an increase in aridity in the study area. The annual average rainfall has decreased from 425 mm (1933–1969 period) to 263 mm (1995–2012 period), which represents the 40 %. The 1995–2012 period showed a cyclic behavior approximately 5 years each and not an increase or decrease. We found significant correlations ($p < 0.05$) between annual rainfall and the following variables: annual R Factor, maximum R Factor value in one event each year, and annual maximum rainfall intensity in 30 and 60 min of events above 5 mm·h^{-1}. Throughout the 1995–2012 period the regression models obtained show an increase in annual maximum rainfall intensity in 60 min and the maximum annual R factor per event of 60 and 47 % respectively.

Keywords

Climate change • Climate aggressiveness • Central Spain • Erosion • Rainfall • R-factor

20.1 Introduction

The current context of climate change threats to the quantity and quality of water resources all over the world. Based on IPCC (2007) forecasts Climate Change will influence the magnitude and frequency of floods and drought in Europe. Moreover, the population and water demand will increase in all models considered (IPPC 2007).

The Mediterranean Basin is one of the "Hot-Spots" in terms of global climate change due to a large expected decrease in mean precipitation and an increase in precipitation variability, especially in summer (Giorgi 2006).

Most of climate studies developed in Centre and Southern Spain have reported a decrease in mean precipitation and runoff. De Luis et al. (2009) observed a decrease in mean precipitation in the 90 % of total surface of Mediterranean side in Spain. These authors observed a decrease between 15 and 25 mm·decade^{-1} in Mediterranean side of Iberian Range. Arnell (1999) proposed some projection models that set between 0 and 25 mm·year^{-1} the decrease in runoff in Spain.

A. García-Díaz (✉) · R. Bienes
Departamento de Investigación Aplicada, IMIDRA, Finca Experimental El Encín, A-2 km 38.2, 28800 Alcalá de Henares (Madrid), Spain
e-mail: andres.garcia.diaz@madrig.org

B. Sastre
Departamento de Agroalimentación, IMIDRA, Finca Experimental El Encín, A-2 km 38.2, 28800 Alcalá de Henares (Madrid), Spain

G. Lollino et al. (eds.), *Engineering Geology for Society and Territory – Volume 1*,
DOI: 10.1007/978-3-319-09300-0_20,

Climate Change research under Mediterranean conditions is often associated with decrease of mean annual precipitation and with an increase in rainfall intensity. Though, in Centre Spain, Rodrigo and Trigo (2007) detected a negative trend in precipitation intensity from 1951 to 2002.

Variations of major climatic patterns are observed not only in center plateau and Southern Spain. Reduction in snow accumulation have been recorded in Pyrenees (López-Moreno 2005).

Erosive and runoff events are linked with rainfall intensities rather than total rainfall (Merz et al. 2006). Nearing et al. (2005) found that both runoff and soil lost are related to the intensity of the rain, but erosion is more affected by rainfall intensity changes that runoff. On the other hand, Hoyos et al. (2005) measured R Factor and found that low intensity rainfall explain 61–70 % of the variability of the R Factor.

The available weather information usually consists on daily rainfall data, which does not allow knowing the amount of precipitation falling at different time intervals. As a result, it is not possible to calculate the maximum rainfall intensity in 15, 30 and 60 min. This parameters are needed to calculate the erosivity of the rain.

Therefore, it is necessary a higher knowledge of the evolution of rainfall erosivity in this region. Hence, a comparative study has been performed regarding the climate data from 1933 to 1969 and from 1995 to 2011. These data were taken from the town of Aranjuez, located 50 km south of Madrid, in Central Spain. The aim of the work is to verify if a climate change has happened and how this can affect the erosive processes.

20.2 Materials and Methods

It has been considered the annual and monthly mean rainfall from 1933 to 1969 (Elías Castillo y Ruiz Beltrán 1977), while for the period 1995–2012 data were recorded from an automatic meteorological station every 10 min located on the same place. Therefore, the first problem that arises is the disparity in the type of data to manage. While for the first period the data available are averages obtained from daily data, for the second period (1995–2012) the intensities of different events throughout the eighteen years can be calculated.

Consequently, this work includes two parts. The first focuses on comparing monthly and annual average data of rainfall for the mentioned periods (1933–1969 and 1995–2012). The second part of the study focuses on analyzing the evolution of the main climatic variables over the period 1995–2012. The considered variables are: maximum intensities in 15, 30 y 60 min (both averages and extreme values); maximum rainfall per event; annual and per event R Factor values (both the average value as the corresponding to more erosive event. R Factor was calculated based on Wischmeier and Smith (1978) with use of Eq. 20.1.

$$\sum \mathrm{R}\left(\frac{\mathrm{MJ}\cdot\mathrm{mm}}{\mathrm{ha}\cdot\mathrm{h}}\right) = \mathrm{E}\cdot\mathrm{I30} \qquad (20.1)$$

where E = kinetic energy of the event ($\mathrm{MJ\cdot ha^{-1}}$) and I30 = maximum rainfall intensity in 30 min ($\mathrm{mm\cdot h^{-1}}$). Kinetic energy can be calculated as: $\mathrm{E}\left(\frac{\mathrm{MJ}}{\mathrm{ha}}\right) = 0.119 + 0.0873 \times \mathrm{Log}_{10}\mathrm{I60}$ where I60 = maximum rainfall intensity in 60 min.

20.3 Results and Discussion

20.3.1 Annual and Monthly Rainfall

The average annual rainfall was 425 mm between 1933 and 1969, while data from 1995 to 2011 show an average of 263 mm. Thus, it can be observed a decrease of 40 % in mean annual rainfall. Regarding to monthly data, there was a rainfall general decrease in all months (Fig. 20.1). The month with the most important reduction on average was September (72 %), and the month with the most similar precipitation was may (1 % less).

This results are consistent with those previously cited. The observed annual rainfall decreased, and the fact that years with less than 300 $\mathrm{mm\cdot year^{-1}}$ happens more often, indicate a progressive desertification of this Centre Spain location, whose climate is becoming arid from semi-arid.

20.3.2 Evolution of Climatic Variables 1995–2012

Also we have observed that the evolution of the parameters considered over the period 1995–2012 has shown a cyclic behavior and not an increase or decrease (Fig. 20.2). There are three clearly marked periods of the series available. These cycles are approximately 5 years each, and correspond to the periods 1995–2000 (wet and very erosive), 2001–2005 (dry and little erosive) and 2006–2011 (wet and very erosive). Average rainfalls each period, in chronological order, are 316, 156 and 339 $\mathrm{mm\cdot year^{-1}}$. In the same way, the averages of rainfall erosivity (R factor) for each of the cycles are 349, 114 and 344 $\mathrm{MJ\cdot mm\cdot ha^{-1}\cdot h^{-1}}$ respectively. However, the available period is just 18 years, therefore it does not allow to make any definitive conclusions.

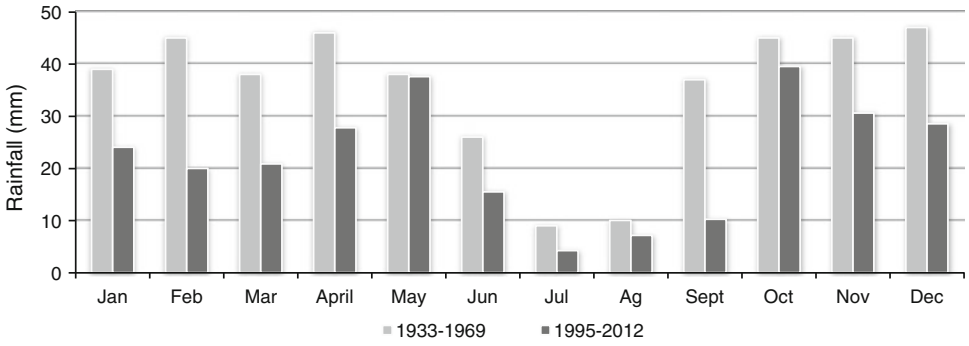

Fig. 20.1 Average monthly rainfall in the two periods considered

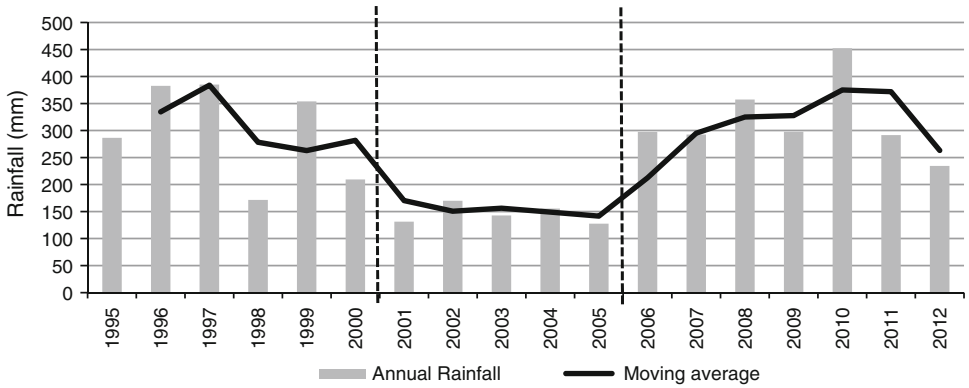

Fig. 20.2 Annual rainfall in Aranjuez between 1995 and 2012. It can be observed rainfall cycles

The data analysis from the period 1995–2012 shows positive significant correlations between annual precipitation and R factor, both annual and per event. Unlike it could be expected, it has been observed that in this area of Central Spain the most erosive rainfall and more violent events do not occur in the driest years, but in the most humid ones. This fact is only observed when we exclude the low intensity events (<5 mm·h^{-1}). The events with intensity >5 mm·h^{-1} trend to appear in rainy years (Table 20.1). Maximum R Factor values obtained in one event are also positively correlated with total rainfall.

Average annual intensities between I15 and I30 did not show an evolution along the study period. Nevertheless, maximum R Factor and I60 maximum intensity values

Table 20.1 2 Spearman correlations between studied variables

	RF	R	R max	I15 max	I30 max	I15 Avg	I15 5 mm·h^{-1}	I30 Avg	I30 5 mm·h^{-1}	I60 max
RF	1									
R	0.75*	1								
R max	0.63*	0.77*	1							
I15 max	0.40	0.57*	0.73*	1						
I30 max	0.46	0.60*	0.81*	0.91*	1					
I15 Avg	0.15	0.45	0.58*	0.45	0.53*	1				
I15 > 5 mm·h^{-1}	0.26	0.39	0.52*	0.57*	0.50*	0.39	1			
I30 Avg	0.02	0.14	0.05	−0.17	−0.24	0.38	0.06	1		
I30 > 5 mm·h^{-1}	0.74*	0.83*	0.76*	0.61*	0.62*	0.45	0.69*	−0.32	1	
I60 max	0.49*	0.60*	0.74*	0.86*	0.86*	0.31	0.55*	−0.02	0.65*	1

*significant differences to $p < 0.05$

RF: Annual Rainfall; *R*: Annual R Factor; *R* max: maximum annual R Factor value in one event per year; I15 max: maximum I15 value; I30 max: maximum I30 value; I15 *Avg*: annual average value; I15 5 mm·h^{-1} : I15 annual average of events above 5 mm·h^{-1} ; I30 *Avg*: annual average I30 value; I30 5 mm·h^{-1} : I30 annual average of events above 5 mm·h^{-1} ; I60 max: maximum annual I60 value

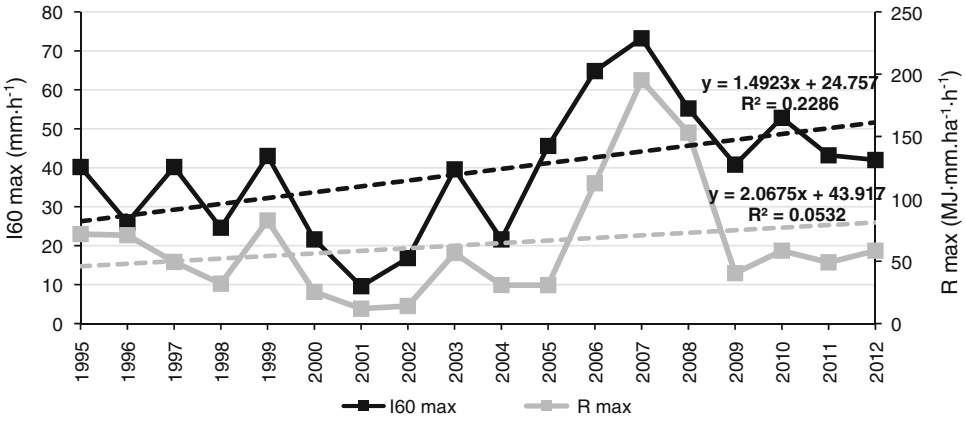

Fig. 20.3 Interannual evolution of I60 max (maximum annual I60 value) and R max (maximum R Factor value per event)

showed an increase. We have obtained two regression equations for the evolution of these variables (Fig. 20.3). The maximum I60 proportionally increases more than the maximum R factor. Annual maximum intensity in 60 min (I60) has increased an average of 14.9 $mm \cdot h^{-1}$ (60 %) per decade, while maximum annual R Factor value per event increases in 20.67 $MJ \cdot mm \cdot ha^{-1} \cdot h^{-1}$ (47 %) per decade.

It can be observed the cyclic behavior of annual rainfall and its correlation with climatic aggressiveness parameters (maximum annual R Factor value per event, annual maximum I60 value and annual I30 average of events above 5 $mm \cdot h^{-1}$). Besides, maximum R Factor value per event and annual maximum I60 value showed an increase in the period studied which lead to a growing climatic aggressiveness in this region. But 18 years is a very short period to study climatic variables. More research and data are needed to validate the observed trends.

20.4 Conclusions

Annual average rainfall between the two considered periods decreases 40 %. This could indicate a change from semi-arid to arid climate in this Centre Spain location.

There is not a variation of mean annual rainfall between 1995 and 2012, and everything points to a cyclic behavior of 5 years each. Unlike it could be expected, the most erosive events happen in the most wet years and not in the driest ones.

Despite 18 years is not enough to set conclusions about climatic variables, it can be observed an important increase of maximum R Factor value and maximum I60 value between 1995 and 2012, which is leading to a growing climatic aggressiveness.

References

Arnell NW (1999) Climate change and global water resources. Glob Environ Change 9:S31–S49. http://dx.doi.org/10.1016/S0959-3780(99)00017-5

De Luis M, González-Hidalgo JC, Longares LA, Stepanek P (2009) Seasonal precipitation trends in the Mediterranean Iberian Peninsula in second half of 20th century. Int J Climatol 29:1312–1323. doi:10.1002/joc.1778

Elías F, Ruiz Beltrán L (1977) In: Ministerio de Agricultura (ed) *Agroclimatología de España*. Cuaderno INIA, vol 7. Instituto Nacional de Investigaciones Agrarias. (Madrid, España)

Giorgi F (2006) Climate change hot-spots. Geophys Res Lett 33:L08707. doi:10.1029/2006GL025734

Hoyos N, Waylen PR, Jaramillo A (2005) Seasonal and spatial patterns of erosivity in a tropical watershed of the Colombian Andes. J Hydrol 314:177–191. doi: 10.1016/j.jhydrol.2005.03.014

López-Moreno JI, Beniston M, García-Ruiz JM (2008) Environmental change and water management in the Pyrenees: facts and future perspectives for Mediterranean mountains. Global Planet Change 61:300–312. http://dx.doi.org/10.1016/j.gloplacha.2007.10.004

Merz J, Dangol PM, Dhakal MP, Dongol BS, Nakarmi G, Weingartner R (2006) Rainfall-runoff events in a middle mountain catchment of Nepal. J Hydrol 331:446–458. http://dx.doi.org/10.1016/j.jhydrol.2006.05.030

Nearing MA, Jetten V, Baffaut C, Cerdan O, Couturier A, Hernandez M, Le Bissonnais Y, Nichols MH, Nunes JP, Renschler CS, Souchère V, van Oost K (2005) Modeling response of soil erosion and runoff to changes in precipitation and cover. Catena 61:131–154. http://dx.doi.org/10.1016/j.catena.2005.03.007

Parry ML, Canziani OF, Palutikof JP, van der Linden PJ, Hanson CE (eds) (2007) Impacts, adaptation and vulnerability. Contribution of working group II to the fourth assessment report of the IPCC. Cambridge University Press, Cambridge, UK, p 976

Rodrigo FS, Trigo RM (2007) Trends in daily rainfall in the Iberian Peninsula from1951 to 2002. Int J Climatol 27:513–529. doi:10.1002/joc.1409

Wischmeier WH, Smith DD (1978) Predicting rainfall erosion losses: a guide to conservation planning. In: USDA-Science and Education Administration Agric (ed) Hanbdbook vol. 537. U.S.Goverment. Print. Office, Washington, D.C.

Preliminary Study on the Snow-Melt for the Groundwater Recharge Estimated by an Advanced Meteorological Station

21

Stefano Crepaldi, Marina De Maio and Enrico Suozzi

Abstract

In this study a preliminary procedure was analyzed in order to evaluate the Snow Water Equivalent through data derived from the sensors installed in the metereological station located upstream of the locality of Mascognaz—Ayas—Valle d'Aosta. The meteorological station has been developed within a research project covering various fields concerning climate change and space-time meteorological variability. Specifically we purpose to thoroughly study the transformations occurring inside the snowpack during the winter period and how it affects the groundwater recharge. Through the analysis of the parameters of humidity, temperature, precipitation and manual data, performed at least 3 days after the event, we have developed a methodology for the estimation of water availability before the melting process.

Keywords

Snow-melt • Groundwater • Spring • Snow water equivalent • Hydrogeological balance

21.1 Introduction

In the hydrogeology field, understanding groundwater recharge is essential for many purposes such as the successful management of water resources, the modeling fluid and contaminant transport within the subsurface.

Groundwater is a critical source of freshwater throughout the world.

In many regions of the Alps, snowfall and the resulting seasonal snow cover represent an important source of water. When the snowpack melts, it recharges the groundwater and replenishes surface water storage.

Excessive snowmelt runoff can cause flooding, while inadequate snowmelt is often the prelude to later drought. In this preliminary study about the snow-melt process we have tried to understand how to measure the snow water equivalent (SWE).

Thanks to a collaboration project between Politecnico di Torino and Regione Autonoma Valle d'Aosta, corporate sponsor, one of the most advanced meteorological stations (comparison numbers of sensors from different companies to snow- pack evaluation) in Italy has been built (Fig. 21.1).

It is located in the Mascognaz Valley, a little lateral valley in the Ayas Municipality. This site is crucial for its proximity to two springs (1 km), allowing the comparison between the snow-melt and the flow rate, in order to define the time of travel from the infiltration point to the springs. In each springs a probe has been installed, the first to measure the water level and temperature, the second, situated below, water level, temperature and also conductivity. In the advanced meteorological station is installed the best available technologies (BAT) to study the snowmelt process, chosen from many factories around the world have been installed.

S. Crepaldi (✉) · M. De Maio · E. Suozzi
Politecnico Di Torino (DIATI) Department of Environment, Land and Infrastructure Engineering, Torino, Italy
e-mail: stefano.crepaldi@polito.it

G. Lollino et al. (eds.), *Engineering Geology for Society and Territory – Volume 1*,
DOI: 10.1007/978-3-319-09300-0_21,

Fig. 21.1 Advanced meteorological stations site

21.2 Installed Equipment

The station consists of the different instruments described below:

Corr-Tek Hydrometry S.r.l. Station

- Thermometer, hygrometer, barometer and anemometer-protractor (CWS, company OTT)
- Pluviograph (Pluvio2, OTT company) GmbH & Co. KG Station
- Snow Scale (Sommer company)
- Snow depth sensor (Sommer company).

To measure the SWE, the instruments used are: snow scale which is the evolution of Snow Pillow, Pluvio 2 which is a new generation of rain gauge, and is defined as the evolution of the weighing precipitation gauge and, lastly, the buried rain gauge, modified for this installation (Vigna and Suozzi 2009). Then a Natural Resources Conservation Service (NRCS) methodology to calculate the SWE modified after a long study on Alpine snow density has been used.

21.3 Preliminary Study

After studying (Alexeev et al. (1972); Anderson (1973); Gray and Male (1981); U.S. Army Corps of Engineers (1998)) we have assumed that in mountainous areas the hydrologic year can be divided into two parts, the first part relating to the period when the snow depth sensor registers the first data while the second one relates to the remaining period.

In the first case using a new empirical relationship (21.1) created by Authors:

$$P(mm) = \begin{cases} if\ T\ < 1\,^{\circ}\mathrm{C};\ P[mm] = h_{f\,all}\frac{Density(AINEVA)}{Density_w} \\ if\ T\ > 1\,^{\circ}\mathrm{C}\ and\ h_{f\,all} = 0;\ P[mm] = Pluviograph[mm] \end{cases} \quad (21.1)$$

To define the content of SWE, resulting from snowfall in high mountain stations, you can easily calculate it (21.1) in the case where the temperature is less than one degree, the value which was taken as the limit of the change of state from rain to snow, the quantity of water is estimated with the snow depth sensor data (the variation of height in metres snow after snow precipitation) and those mediated by AINEVA (Ass. Italiana Neve e Valanghe) observing places. If there is no sampling density, as a result of precipitation near the station, into account also those relating to other adjoining valleys have to be takes.

In the case where the temperature is higher than one degree and a variation of the height of snow is not recorded but the pluviograph registers a variation, two situations are possible:

The amount of water measured comes from the melting of snowfall a few days earlier;

The change actually records the occurrence of a liquid precipitation (autumn and spring). In this case the average temperature of the previous days should be checked. The possibility that a liquid precipitation occur following a snowfall during the winter period is rare. Consequently, the errors caused by an incorrect interpretation of meteorological data is very low. In the second case:

$$if\ T\ > 1\,^{\circ}\mathrm{C};\ P[mm] = Pluviograph\ [mm] \quad (21.2)$$

The situation shown in (21.2) is the one that occurs whenever during the spring-summer-autumn the snow depth sensor does not record a change in the height of snow and therefore only the data relating to the pluviograph are considered.

21.3.1 Results 3.1

Graphs 21.1 and 21.2 shows how the trends of the data are comparable, so there is a good correlation between the data collected by each of the four sensor (Table 21.1).

The buried rain gauge is the most reliable because it gives data about quantity and the time when the snowmelt process starts. There was an increase in the flow rate, measured by the buried rain gauge, 8 days after the data shown by the snow depth sensor started to decrease (Graph 21.3).

The time lag between the start of acquisition of the two instruments last named depends on several environmental condition.

Graph 21.1 2010–2011 season SWE Comparison Snow Scale: 108 mm; Metodologia Empirica: 112 mm; SPA: 101 mm

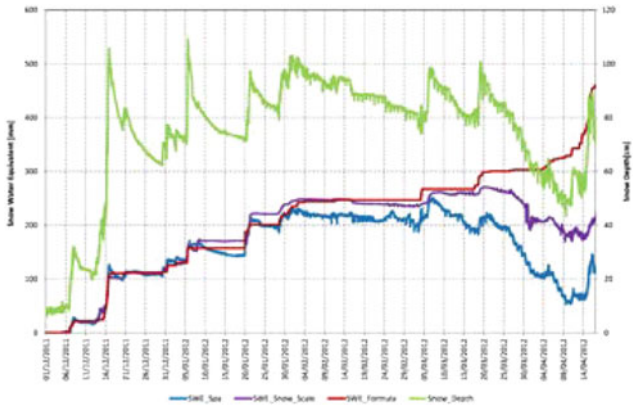

Graph 21.2 2011–2012 season SWE Comparison Snow Scale: 270 mm.; Empirical Methodology : 279 mm; SPA: 252 mm

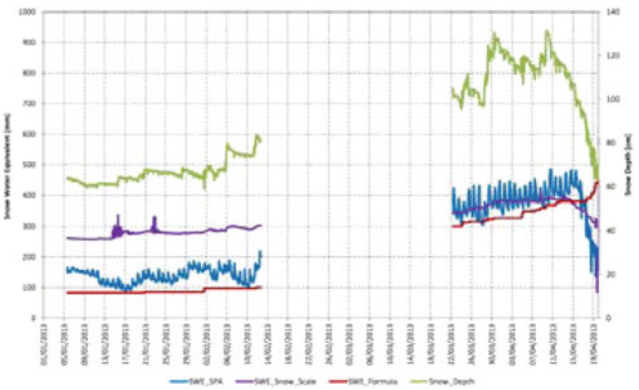

Graph 21.3 2012–2013 season SWE Comparison Snow Scale: 412 mm.; Empirical Methodology 443: mm; SPA: 484 mm

The empirical methodology is the result of a careful evaluation of the phenomena that lead to the formation of atmospheric precipitation. The rainfall that characterizes the Mascognaz valley comes from the Mediterranean (humid with higher intakes) or the Atlantic (dry with low rainfall) (Baker 1982).

Table 21.1 SWE measured in Mascognaz from different instruments

Instruments	2010–2011 (mm)	2011–2012 (mm)	2012–2013
Snow scale	108	270	412
Empirical methodology	112	279	443
SPA	101	252	484
Buried rain gauge	103	–	–

Through the study of humidity, temperature, source of the precipitation and field measurements carried out up to 3 days after the event, a methodology for the estimation of the quantity of water available before the fusion has been developed.

- The Snow scales measure the weight of snow and converts it to mm of water;
- The empirical methodology multiplies the snow fall to an average value which takes into account the origin of the precipitation and density measured within 3 days of precipitation;
- The SPA multiplies the value of correct density by the height of the cover band.

Note (Graphs 21.1 and 21.2) how the data are in agreement in all the years of measurement.

21.4 Conclusions

The results of this project provide an improved knowledge about the snow-melt phenomena, allowing, a better estimation of groundwater recharge and runoff. The comparison between the snow-melt and the flow rate, is crucial to define the time of travel from the infiltration point to the monitored springs. The analysis of collected data in different hydrogeologic year also permitted to evaluate how the climate change (in mountain basin) significantly influence the recharge of mountain springs. For these reason, the management of drip pans and water supply become crucial in order to provide a proportional service to the request and without waste.

The weather station project should be continue in the coming years as it currently appears to be one of the most modern stations in the Alps. Moreover, the conclusions to which this research project has come will be validated through further study thanks to the increasing amount of data that will come from the various sensors installed and the addition of spatial snowpack data from laser scanner sensor. The improvement of this study is aim to obtain a

mountain basin test site for developing multidisciplinary approaches also permit the integration of all these data (spatial and temporal data).

References

Alexeev GA, Kaljuzhny IJ, Kulik VY, Pavlova KK, Romanov VV (1972) Infiltration of snowmelt water into frozen soil. The role of snow and ice in hydrology. Symposia in Banff, Canada, pp 313–325

Anderson EA (1973) National weather service river forecast system—snow accumulation and ablation model. NOAA Technical Memorandum NWS HYDRO-17, U. S. Department of Commerce, Silver Spring, Md., 217

Baker D (1982) Hydrological aspects of Alpine and high mountain areas. Int Assoc Hydrogeol Sci Publ 138:103–112

Gray DM, Male DH (1981) Handbook of snow principles, processes, management and use. Pergamon Press, Toronto, p 776

Healy RW (2010) Estimating groundwater recharge. University Press, Cambridge, p 245

McCuen R (1985) Statistical methods for engineers. Prentice-Hall, Inc., New York, p. 439

U.S. Army Corps of Engineers (1998) Runoff from snowmelt. University Press of Pacific, Honolulu, HI; F-14

Vigna B, Suozzi E (2009) The importance of the nival melting process on the recharging of acquifers, EPITOME, Geoitalia 2009, Rimini, Italy 9–11 Settembre, pp 1, 41., ISSN: 1972-1552

Preliminary Results of a Comparison Study Between Two Independent Snow Networks in North-Western Italian Alps (Piemonte Region)

22

Fiorella Acquaotta, Nicola Colombo, Simona Fratianni, Vincenzo Romeo and Secondo Barbero

Abstract
The snow represents a fundamental resource for hydro-power generation, irrigation, domestic and industrial water supply. The knowledge of behaviour and trends of this meteorological variable is very important for the human society and mountain system. Thus, climatologists are increasingly interested in studying changes in the intensity, frequency, duration and spatial distribution of snowfall and snow depth. Unfortunately, long instrumental climate records are usually affected by non-climatic changes (inhomogeneities), which compromise the quality of these studies. In order to analyse non-climatic biases, such as the influence of position or instrument changes due, for example, to the transition from manual to automatic measurements, we have compared the parallel measurements. The presence of two independent climate networks offers the opportunity to study the data inhomogeneity of snow records. The analyses highlight higher measured values in manned gauges respect to automatic stations. The major differences have been recorded at the beginning of the winter season, in October and April.

Keywords
Snow series • Parallel measurements • Inhomogeneities • NW alps

22.1 Introduction

The Alps are one of the major mountain ranges in Europe. Their significance for the regional water cycle is commonly expressed in the notion "water tower of Europe", which hints to their climatic characteristics with abundant liquid and solid precipitations, and the role of snow and ice in storing freshwater.

The long term climate dataset are essential to analyse and monitor the climate change. The quality of these measurements is governed by the accuracy of the instruments used in the national networks.

The Italian networks have experienced many technological, economical and organizational changes, which may affect the homogeneity of the record (Acquaotta et al. 2009; Venema et al. 2012). Consequently, identifying inhomogeneities in meteorological time series is necessary to achieve a comprehensive assessment of climatic changes (Parker 1994). Therefore, it is necessary to apply a literature data review and rigorous data analysis procedures to search and detect steps due to stations relocation. In Europe the inhomogeneity problem of meteorological series has been often addressed on daily or monthly temperature and rainy

F. Acquaotta (✉) · N. Colombo · S. Fratianni
Department of Earth Sciences, University of Turin, via Valperga Caluso 35, 25100, Turin, Italy
e-mail: fiorella.acquaotta@unito.it

V. Romeo
Corpo Forestale dello Stato - Servizio Meteomont, Rome, Italy

S. Barbero
Agenzia Regionale per la Protezione Ambientale (ARPA) Piemonte - Sistemi Previsionali, Turin, Italy

G. Lollino et al. (eds.), *Engineering Geology for Society and Territory – Volume 1*,
DOI: 10.1007/978-3-319-09300-0_22,

series (Burauskaite-Harju et al. 2012), but for the snow series this problem has been frequently neglected.

With this study we would like to integrate the scientific literature and contribute to a better understanding of the processes of non-climatic changes (inhomogeneities) and their effects on daily records of snow, through the analysis of the recent transition from manned to automatic precipitation measurements in Piemonte, Italy. Mekis and Vincent (2011) have shown, for the transition process of Canadian network, how the magnitude of the inhomogeneity brake strongly differed per station; some stations showed no difference, whereas others highlighted a clear inhomogeneity.

The analysis of several pairs of nearby high-quality stations has allowed us to study the variability of the inhomogeneity from station to station, detecting the artificial discontinuities that affect the trends. In the future we will carry out analyses on other weather stations of Piemonte Region in order to extend the present preliminary local results to a wider scale.

22.2 Dataset

The first network analyzed is composed by manual stations characterised by a long period of activity (Table 22.1). This work has allowed to recover the daily data of fresh snow and snow depth for 16 locations across Piemonte Region. The stations belong to different Institutes (Meteomont, Servizio Idrografico Mareografico Nazionale and National Energy Authority-ENEL). The stations are located at high altitude (Table 22.1) and they have always been managed by Institutes that have recorded all changes and upgrades realizing an extensive metadata archive. In addition, the surrounding environment of the stations has not changed over time.

For each meteorological station we have recovered the paper register and we have digitized all daily data. The examination of the register has allowed to carry out an accurate historical research for each station, identifying any potential breaks (metadata) in the data homogeneity, due to location or instrument changes.

Later, for every station we have created a metadata file showing: meteorological station's location, geographical area (basin), latitude, longitude, altitude, instrumentation type, location/instrument changes.

The second network was created in Piemonte in 1986. It is managed by the Regional Agency for Environmental Protection of Piemonte (ARPA Piemonte) and it is currently composed by 400 automatic stations. Therefore, in Piemonte there are snow series from two different meteorological networks. This gives us a good overlapping period, from 1990 to 2012, to study the difference of measurements between manual and automatic instruments.

Table 22.1 Activity period and elevation of the 6 analyzed manual stations (see details in the text)

Station	Activity period	Elevation (m a.s.l.)
Alpe Cavalli	1924—present	1500
Lago Serrù	1961—present	2,283
Ceresole Reale	1931—present	1,573
Pontechianale Castello	1943—present	1,586
Malciaussia	1936—present	1,815
Acceglio Saretto	1925—present	1,540

Snow depth (HS) and fresh snow (HN) are the parameters analyzed in this study. HS indicates the vertical distance measured between the soil surface and the surface of the snow. HN indicates the vertical measurement of snowfall falling in a certain time-frame, by convention the last 24 h. The measurement unit is cm for both variables.

In the manual stations HS is measured using a graduated fixed bar. HN is measured by using a wood tablet (size 40 × 40 cm) set up with a wood stick. After a measurement the snow is removed from the tablet. For both the variables the reading of instrumentations is done every 24 h, at 8:00 a.m.

The sensor for the measurement of HS in the automatic station is an ultrasonic snow gauge. The ultrasonic snow gauge is constituted by a pair of ultrasonic transducers in air which measure the travel time of the pulse from transmission to reception, after being reflected from the surface of the snowpack. The sensor measures the HS every 30 min. HN must be calculated by difference of HS in the time of interest, usually from 8.00 a.m. compared to the previous 24 h.

22.3 Methodology

We have selected locations with pairs of stations belonging to both networks, with an overlapping period greater than 5 years (Vincent and Mekis 2009). A further selection criterion is the difference in elevation and the distance between two stations. This selection has been based on the results of the work done by Isotta et al. (2013), in which a spatial consistency check, depending on the elevation difference, less than 300 m, and distance below 20 km, is estimated. The pairs of stations that satisfied these parameters have been compared without artificial data changes.

After the spatial consistency check, a manual quality control has been carried out. We have highlighted wrong precipitation data (e.g. negative values) and we have realized plots to identify the outliers. To obtain uniform and comparable dataset between automatic and manual stations, we have also recalculated the daily HN values as the difference from values of HS between two consecutive days.

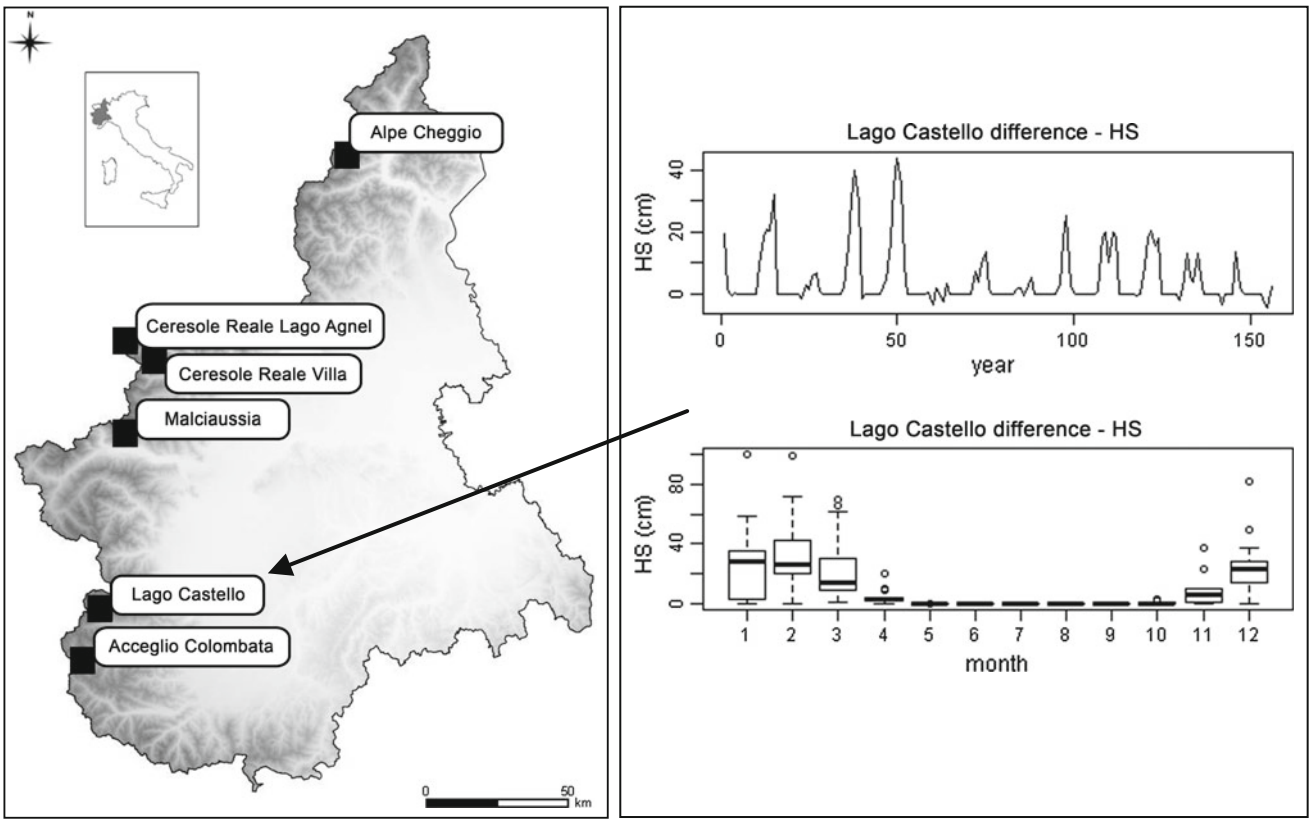

Fig. 22.1 *Left* locations of the six investigated stations (toponym refers to current denomination—automatic stations). *Right* difference series and monthly box plot of snow depth (HS) recorded in the meteorological stations of Lago Castello

In order to achieve a direct comparison between the daily snow series, missing values in one series have been also set to missing in its counterpart before computing monthly statistics. We have calculated the mean monthly value for the daily HS series and the monthly sum for the daily HN series. A statistical analysis has been carried out on the monthly series. We have evaluated the mean value, the median, the standard deviation, the first and third quartile and the maximum and minimum values.

For the parallel series we have calculated the correlation coefficient and we have applied the Kolmogorov-Smirnov non-parametric test to evaluate the presence of the same distribution between the two investigated series (Sneyers 1990). The series have been also compared using graphics: scatter plots, q-q plot and box plot.

Finally, from the monthly series of HS and HN two new monthly series have been created; for the HS the difference series (22.1) and for the HN the ratio series (22.2) between the parallel series have been calculated:

$$DS_{i,j} = HS_{m,ij} - HS_{a,ij} \tag{22.1}$$

and

$$RN_{i,j} = HN_{m,ij}/HN_{a,ij} \tag{22.2}$$

where $DS_{i,j}$ is the difference between the monthly series of snow depth recorded in the manual station ($HS_{m,ij}$) and the monthly series of snow depth recorded in the automatic station ($HS_{a,ij}$); $RN_{i,j}$ is the ratio between the monthly series of fresh snow recorded in the manual station ($HN_{m,ij}$) and the monthly series of fresh snow recorded in the automatic station ($HN_{a,ij}$); i indicates the month and j the year. On the new series ($DS_{i,j}$ and $RN_{i,j}$) a statistical analysis has been carried out.

22.4 Results

The parallel meteorological stations selected are six (Table 22.1, Fig. 22.1) with a good continuity in the recorded daily data, an adequate overlapping period (from 2000 to 2012) and a limited difference in elevation (Table 22.2). For these pairs of series all rank correlations are greater than 0.9 except for the month of October where in all locations the correlation coefficient admits values near zero. The Kolmogorov-Smirnov test detects in the parallel

Table 22.2 The six analysed stations with parallel measurements of snow (the toponym identifies the current automatic station's denomination; for the previous denomination, see Table 22.1)

Station	UTM_X	UTM_Y	Period	Elev	Corr_HS	KS_HS	Corr_HN	KS_HN
Alpe Cheggio	431,711	5,104,080	2000–2012	40	0.97	0.99	0.96	0.99
Ceresole Reale Lago	354,620	5,036,811	2000–2012	21	0.97	0.85	0.92	0.04
Ceresole Reale Villa	360,163	5,033,606	2000–2012	8	0.97	0.41	0.93	0.92
Malciaussia	354,672	5,007,898	2000–2012	15	0.94	0.99	0.83	0.64
Castello	345,555	4,941,889	2000–2012	11	0.96	0.41	0.96	0.99
Acceglio Colombata	339,567	4,927,939	2000–2012	70	0.97	0.41	0.93	0.92

Difference of elevation between pair of stations [m]; Corr, correlation coefficient; KS, p-value of Kolmogorov-Smirmov non parametric test (statistically significant $\geq$0.05), calculated on monthly fresh snow (HN) and monthly snow depth (HS)

series the same distributions except for the HN series of Ceresole Reale Lago Agnel (Table 22.2).

The analysis of the difference shows that in four locations, Alpe Cheggio, Ceresole Reale Villa, Malciaussia and Lago Castello (Fig. 22.1), the higher amount of fresh snow and snow depth has been measured by the manual stations. In these sites the maximum difference for HS and HN has been calculated for the winter season 2008/2009. The average difference between monthly fresh snow is 155 cm and monthly snow depth is 59 cm.

In two locations, Ceresole Reale Lago Agnel and Acceglio Colombata, automatic stations have measured a greater amount of fresh snow and snow depth. For Ceresole Reale Lago Agnel the maximum difference of monthly HS (78 cm) has been calculated in May 2004, while for Acceglio Colombata in March 2009 (33 cm).

In all locations the greatest differences have been individuated in October and April, the months that open and close the winter season. In the middle of the season only in the years 2008 and 2009 we have calculated great difference in fresh snow and snow depth; in 2008/2009 all stations have recorded the maximum value of snow difference for the investigated time-frame.

22.5 Conclusions

In the Piemonte Region we have analyzed an archive with parallel snow series. The database contains many daily precipitation series characterized by a long-time data acquisition. The meteorological observations have been recorded continuously since 1924 by the first meteorological network. In 2000 this network was replaced by a new automatic network in the Region. Then, in six locations two meteorological stations are simultaneously present, manual and automatic types, with overlapping measures for approx. 13 years. Thus, an unique dataset with independent and simultaneous measures (parallel observations) is available.

This preliminary analysis highlights that in manual stations a greater amount of solid precipitation is recorded in all winter seasons, in particular in October and April. Moreover, the present study has clearly highlighted the importance of analyzing parallel measurements for the study of non climatic changes in the climate record to identify the real variation of the meteorological variable.

Finally, further analyses will be conducted on other manual and automatic stations, in order to quantify the inhomogeneities at regional scale.

References

Acquaotta F, Fratianni S, Cassardo C, Cremonini R (2009) On the continuity and climatic variability of meteorological stations in Torino, Asti, Vercelli and Oropa. Meteorol Atmos Phys 103:279–287. doi:10.1007/s00703-008-0333-4

Burauskaite-Harju A, Grimvail A, von Bromssen C (2012) A test for network-wide trends in rainfall extremes. Int J Climatol 32:86–94. doi:10.1002/joc.2263

Isotta F, Frei C, Weilguni V, Perčec Tadić M, Lassègues P, Rudolf B, Pavan V, Cac-ciamani C, Antolini G, Ratto SM, Munari M, Micheletti S, Bonati V, Lussana C, Ron-chi C, Panettieri E, Marigo G, Vertačnik G (2013) The climate of daily precipitation in the Alps: development and analysis of a high-resolution grid dataset from pan-Alpine rain-gauge data. Int J Climatol. doi:10.1002/joc.3794

Mekis E, Vincent L (2011) An overview of the second generation adjusted daily precipitation dataset for trend analysis in Canada. Atmos Ocean 2:163–177

Parker DE (1994) Effects of changing exposure of thermometers at land stations. Int J Climatol 14:1–31

Sneyers R (1990) On statistical analysis of series of observations. Technical note N° 143, World Meteorological Organization, pp 192

Venema V, Mestre O, Aguilar E, Auer I, Guijarro JA, Domonkos P, Vertacnik G, Szentimrey T, Stèpànek P, Zahradnicek P, Viarre J, Müller-Westermeier G, Lakatos M, Williams CN, Menne MJ, Lindau R, Rasol D, Rustemeier E, Kolokythas K, Marinova T, Andresen L, Acquaotta F, Fratianni S, Cheval S, Klancar M, Brunetti M, Gruber C, Prohom Duran M, Likso T, Esteban P, Brandsma T (2012) Benchmarking homogenization algorithms for monthly data. Clim Past 8:89–115. doi:10.5194/cp-8-89-2012

Vincent L, Mekis E (2009) Discontinuities due to joining precipitation station observations in Canada. J Appl Meteorol Climatol 48:156–166. doi:10.1175/2008JAMC2031.1

Improving the MSGMPE Accuracy for the Northern of Tunisia by the Multispectral Analysis of the Cloud Field from MSG SEVIRI

23

Saoussen Dhib, Chris Mannaerts and Zoubeida Bargaoui

23.1 Introduction

The advanced Spinning Enhanced Visible Infra-Red Imager (SEVIRI) radiometer onboard the Meteosat Seconde Generation (MSG) series has a temporal resolution of 15 min. It has the ability to scan the Earth in 12 spectral channels from visible to thermal infrared. The spatial resolution of the SEVIRI instrument is 3 km for 11 of the 12 channels, and 1 km for the High Resolution Visible (HVR) channel (Govaerts et al. 2007). Several MSG SEVIRI bands provide a powerful tool in detecting convective activities (Barbosa et al. 2011). Images of cloud analysis (CLA-MSG) are made available by the European Organisation for the development and management of weather satellites EUMETSAT through both a global network of a satellite based data dissemination system called GEONETCast, and the Unified Meteorological Archive and Retrieval Facility and Services (UMARF) archive, which is online accessible through the internet. The products that are disseminated and archived, are described in accompanying documentation, the so-called Product Navigator, which is transmitted along with the data and products. All data and products can be received in real-time by anyone that wishes to do so, with a low-cost ground receiving station, consisting of a satellite receiving dish, and a computer with DVB decoding hardware. In non-real-time the data and products can be downloaded from the UMARF archive through the internet (Maathuis et al. 2011).

The MPE algorithm is based on a combination of the advantages of the high spatiotemporal resolution of the MSG images and the instantaneous rain rates estimated from the Special Sensor Microwave Imager SSM/I (Heinemann et al. 2002).

In previous work (Dhib et al. 2012), the MPE algorithm was applied to northern Tunisia. A severe underestimation was noticed for some events occurring almost during the wet season (Dhib et al. 2012).

Two main objectives were assigned to this study. The first is to review the lack of the MSGMPE accuracy by highlighting some of the limitations of the SSM/I satellite-derived rain rate estimations. The second is to see if this new analysis method will help us to provide an adequate spatial and temporal assessment specially for risk events which can be beneficial to take early the adequate precautions like emptying the dams and preventing people from being in risk areas.

This paper is organized in four sections: Sect. 23.1 includes methodology. Section 23.2 presents data. Section 23.3 reports the results and visual analysis. The final part draws conclusions and perspectives.

23.2 Methodology

The comparison between precipitation and cloud microphysical characteristics was achieved by comparing the SEVIRI cloud products and the in situ daily rain data registered by the General Direction of Water Resources in Tunisia (DGRE). The moving average method (Mav) under ILWIS was adopted to interpolate the ground data. The weight function which was selected for this interpolation is

S. Dhib (✉) · Z. Bargaoui
Université Tunis El Manar Ecole Nationale d'ingénieurs de Tunis, Rue Béchir Salem Belkhiria Campus Universitaire, BP 37, 1002 Le Bélvédère, Tunis, Tunisia
e-mail: dhib_saoussen@hotmail.fr

Z. Bargaoui
e-mail: zoubeida.bargaoui@laposte.net

C. Mannaerts
Faculty of Geo-Information Science and Earth Observation, University of Twente, Hengelosestraat 99, 7514 AE Enschede, The Netherlands
e-mail: c.m.m.mannaerts@utwente.nl

G. Lollino et al. (eds.), *Engineering Geology for Society and Territory – Volume 1*,
DOI: 10.1007/978-3-319-09300-0_23,

the inverse distance method. It implements a weighted averaging on point values and returns as output a raster map. It is appropriate to use this method when the measured point values are very accurate (Ilwis Help 1999).

Estimates were performed using the visible *VIS0.6* channel, the infrared *IR3.9* channel, the infrared *IR10.8* window channel and the brightness temperatures difference (BTD) between the Water Vapor (*WV6.2*) and the Infra Red (IR10.8) bands. The approximation of cloud top likelihood precipitating increase if the BTD (WV6.2-IR10.8) is less than 11 K (Kidder et al. 2005).

High Rate Information Transmission (HRIT) data files were extracted and archived at the Faculty of Geo-information Science and Earth Observation (ITC FTP). The ILWIS extension Geonetcast-Toolbox was used to read and write geographic data formats, among others the HRIT data. This data can be extracted and converted into a known raster-GIS or raster image file format by the "*MSG Data Retriever*" option in the GEONETCast-Toolbox.

The Red-Green-Blue (RGB) composition is a widely used method to analyze the cloud-top SEVIRI data (Kerkmann et al. 2004). To create the satellite images we have to specify the data source, the satellite, channels, date, series, conversion, output and the study area.

It is proposed to analyze the structure of clouds with the extension of the ILWIS 'GEONETCast toolbox' (Maathuis et al. 2011). On the other hand, evaluation assessment is based on the BTD between the IR temperature at 10.8 μm and the WV temperature channel 6.2 μm.

23.3 The Study Area and Observation Period

Tunisia lies between latitudes 35 and 38 °N, and longitudes 8 and 11 °E. Despite its relatively small size, Tunisia has great environmental diversity due to the sharply decreasing rainfall and increasing solar radiation southward. The study area is focused on the northern part where the climate is sub-humid with mild rainy winters and dry summers. The terrain is mountainous exceeding in some area 800 m in its south western part. The study period is from January 2007 to June 2009. Observations from up to 318 stations covering an area of 36,000 Km^2 were analyzed (Dhib et al. 2012). It was found that most of undetected heavy precipitation events using the MSGMPE method occurred during the wet season: 23/02/2007, 11/03/2007, 13/01/2009, 06/03/2009, and 09/04/2009. Two other events that occurred during the dry season (on 25/09/2007 and 13/09/2008) were also undetected. According to ground observations, the number of stations with heavy rainfall (rainfall greater than 50 mm/d) exceeded 15 for each event.

23.4 Results and Visual Analysis

The analysis of the seven interpolated images (Figs. 23.1 and 23.2) highlighted two image types: the first type corresponds to large rainy areas with a maximum rainfall greater than 20 mm/day (the 13/09/2008, 11/03/2007, 06/03/2009 and 09/04/2009 events). The second type is related to high precipitation values exceeding 80 mm/day but on limited surfaces (the 25/09/2007 and 23/02/2007 events).

The event of the wet season 13/01/2009 is selected for deeper analysis. The maximum ground rainfall reached 109 mm and the average spatial rainfall was estimated to 18 mm.

The 25 September 2007 event is also selected for deeper analysis. It is characterized by very high rainfalls greater than 100 mm/d in a very limited surface. We think that it will be interesting to see the potential of the SEVIRI data to detect this specific case.

23.4.1 13/01/2009 Event

The sequence of the daytime Microphysical color scheme composite (DMP) (Fig. 23.2) summarizes the properties of clouds in the *VIS 0.06*, *IR 3.9* and *IR 10.8* μm. The optical thickness, the quantity of the cloud water and the ice of the clouds are given by the VIS0.06 channel reflectance in red. The particle size and the phase of the clouds are derived by the IR_039 solar channel reflectance in green. The cloud top temperature is reported by the IR_108 channel modulates in the blue (Torricella et al. 2008).

In the RGB color scheme (Fig. 23.3) white color indicates small cloud drops which is not precipitated, whereas pink color reflects the presence of large drops that are typical for precipitating clouds; the blue color reflects warm top clouds and the red color indicates cold and thick clouds with tops composed of wide ice particles (Maathuis and Mannaerts 2012).

The visual analysis shows the presence of the red color at several times during the studied event (10:30, 11:15, 00:00) which indicates the dominance of convective rainy clouds in these areas. The occurrence of this red color (Fig. 23.3) confirms the good correlation between the microphysical display RGB and the ground rainfall (Figs. 4.1 and 23.2).

Evaluation assessment based on the BTD between the IR temperature at 10.8 μm and the WV temperature channel 6.2 μm has as output a Boolean response: the pink color indicates rain and blue color the lack of rain.

Based on the colors reported in Fig. 23.4, we note the presence of pink color at several times during the studied day. Thus results obtained by the BTD algorithm confirm the results obtained by the color composite RGB.

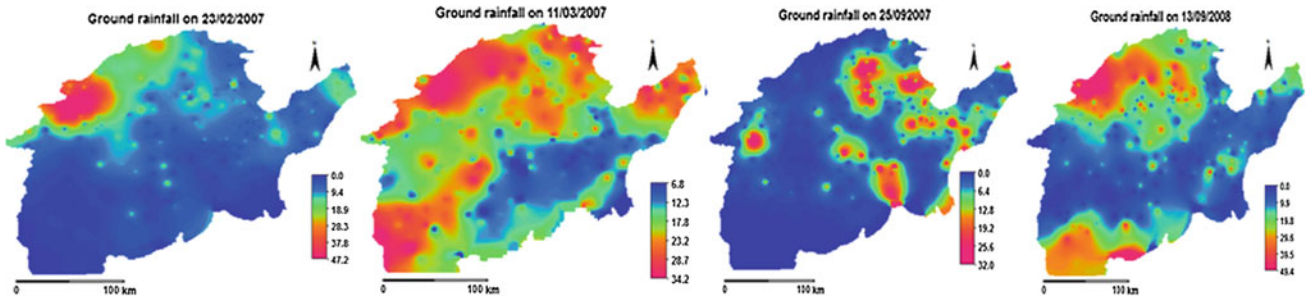

Fig. 23.1 Interpolation of 4 studied events

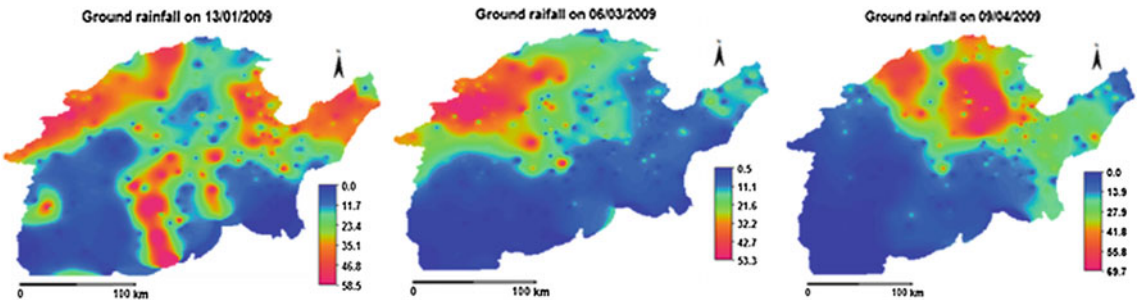

Fig. 23.2 Interpolation of 3 studied events

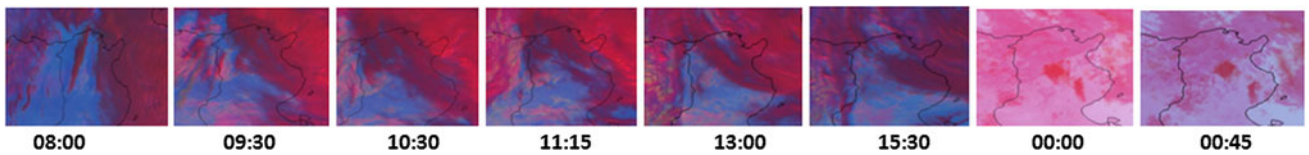

Fig. 23.3 DMP Sequence on 13/01/2009 respectively at 8, 9:30, 10:30, 11:15, 13, 00:00, 00:45 h on 14/01/2009

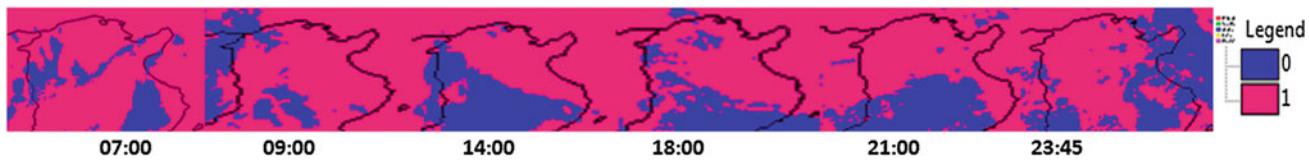

Fig. 23.4 Identification sequence of precipitations at 7, 9, 14 h; 18, 21 and 23:45 h on 13/01/2009

23.5 September 2007 Event

We notice the presence of the pink color at several times during that day (Fig. 23.5) which indicates the presence of wide drops that are typical to precipitating clouds.

On the other hand, for each pixel, the difference (WV6.2–IR10.8 μm) is used as a proxy for deep convection, reported the presence of rain during several hours of the day (Fig. 23.6). We notice the high ability of the SEVERI data to detect convective clouds even in limited surfaces (image of 25/09/2007 Fig. 23.1).

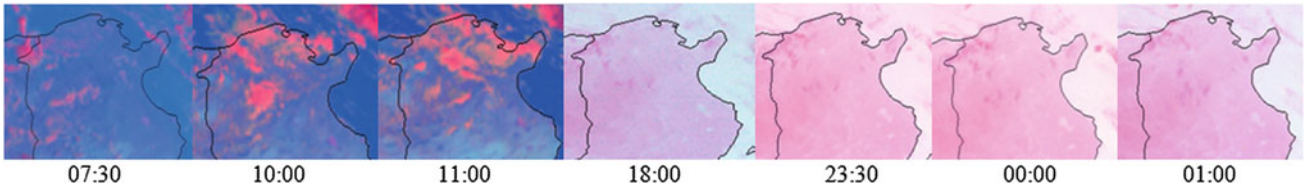

Fig. 23.5 Identification sequence of precipitation RGB on 25/09/2007

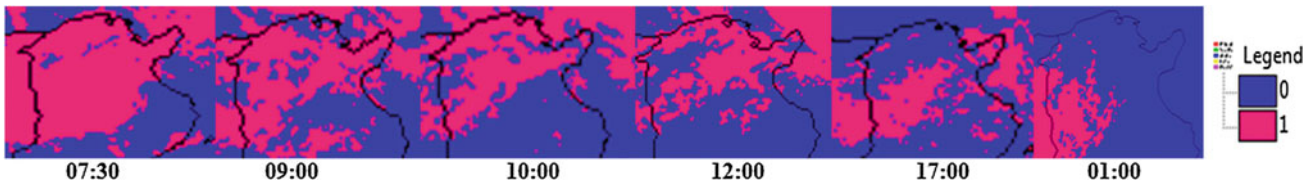

Fig. 23.6 Identification sequence of precipitation BTD method on 25/09/2007

23.6 Conclusion

In this paper, we described a new way of analysis for undetected rain events by the MSGMPE approach using the data SEVERI radiances (MSG-2). The characterization of cloudy and potentially precipitating pixel areas was realized using RGB composite and BTD method. The ILWIS extension GEONETCast-Toolbox was used to process this data.

For the seven events analyzed, the interpretation of the results showed that SEVERI data correspond well with the deep convective storms registered at the ground: in wet season, in orographic area and in low geographic extent. The seven events of the study period were registered as rainy by the microphysic method.

The MSGMPE approach combines the brightness temperature from MSG and the rain rates from SSM/I. According to the microphysical clouds analysis performed here for seven events we can conclude that the inaccuracy of MSGMPE was generally caused by the SSM/I data.

The present study has demonstrated the great potential offered by the multispectral analysis of the cloud method which shows interesting and encouraging performance in Northern Tunisia during the dry and the wet season. Because the MSG SEVIRI data is a near real time product (temporal resolution of 15 min), it can be quite useful for early forecast for subsequent water hazards such as flooding and inundation and accurate estimation of heavy rainfall occurrences.

As a final remark, and recommended for future work, in order to get more reliable extreme rainfall estimates, it is proposed to use the informative SEVERI channel data to create an improved algorithm which will give us the rain rates directly from the cloud analysis.

References

Barbosa HA, Junior IWdS, Ertük AG, Prieto J (2011) The cloud-top SEVIRI data for monitoring convective storms. Anais XV Simpósio Brasileiro de Sensoriamento Remoto—SBSR, Curitiba, PR, Brasil, 30 de abril a 05 de maio de 2011, INPE p.2179

Dhib S, Bargaoui Z, Mannaerts C (2012) Investigation on extreme daily rainfall estimation using MPE approach for North Tunisia. In: Plinius and MEDEX conference 2012

Govaerts Y, Wagner S, Clerici M (2007) SEVIRI native format preprocessing toolbox user's guide. Issue: SPT VERSION 3.0 Doc No: EUM/OPS MSG/ TEN/ 03/0011.EUMETSAT. p 82

Heinemann T, Lattanzio A, Roveda F (2002) The EUMETSAT multisensor precipitation estimate (MPE), EUMETSAT Am Kavalleries and 31, 64295 Darmstadt, Germany, p 8

Ilwis Help (1999) ILWIS version 2.22. http://www.itc.nl/ilwis. Accessed on July 1999

Kerkmann J, Rosenfeld D, Bridge G (2004) MSG interpretation guide. RGB IMAGES: PART IV, RGB Composites with channels 01-11 and their interpretation. http://oiswww.eumetsat.org/WEBOPS/msginterpretation/index.html

Kidder S, Kankiewicz JA, Eis K (2005) Meteosat Second Generation cloud algorithms for use in AFWA. In: BACIMO 2005, Monterey, CA

Maathuis B, Mannaerts C (2012) Water and food security-ethiopia toolbox, p 127

Maathuis BPM, Mannaerts CM, Schouwenburg M, Retsios B, Lemmens R (2011) GEONETCast Toolbox: installation, configuration and user guide for the GNC Toolbox Plug-in for Ilwis 3.7. Faculty of Geo-information Science & Earth Observation (ITC), University of Twente, Enschede, The Netherlands. http://www.itc.nl

Torricella F, Cattani E, Levizzani V (2008) Rain area delineation by means of multispectral cloud characterization from satellite. Natl Res Coun Adv Geosci 17:43–47

Part III

Climate Change: Impacts on Natural Resources and Hazards

Convener: Dr. Maurizio Polemio—*Co-conveners*: Marta Chiarle, Marco Turco

Relevant temperature and rainfall modifications have been observed worldwide during recent decades. As differences exist in the observed trends, if variable durations and/or different regions and climatic parameters are considered, it is extremely complex to assess the combined, resulting effects of climate change on the hydrological cycle, mainly in terms of runoff and infiltration, on glacier volume and extent, and on snow cover extent and duration. All these variations and trends can modify natural hazards occurrence, create relevant difficulties in terms of water resources availability and hit ecological balance. These variations require efforts upgrading technological approaches, improving design and planning criteria, and adopting strategies to manage modifications of natural hazards and water resources availability. Study cases of climate change and damage effects, technical solution reports and scientific research results are suitable for the session purposes.

Role of Climate and Land Use Variations on the Occurrence of Damaging Hydrogeological Events in Apulia (Southern Italy)

24

Teresa Lonigro and Maurizio Polemio

Abstract

The aim of this work is to present a methodology, based on the use of correlation, cross-correlation and trend analysis, which analyses monthly climatic data (rainfall, wet days, rainfall intensity, and temperature) from 1877 to 2008, in order to characterise the climate variations, particularly in terms of rainfall, and the effects on the occurrence trend of Damaging Hydrogeological Events (DHEs), floods and landslides. The proposed methodology consists of four phases. The first two phases concern the data collection and the creation of the climate and DHE databases, the third phase of work involves the analysis of data previously collected and the last part, not yet finished, is relative to the study of land use variations. This methodology was applied to a southern Italian region (Apulia) frequently hit by flood and landslide events. Despite the decreasing trend of rainfall and rainfall intensity and the increasing trend of temperatures and wet days, there is an increasing trend of DHE occurrence, which might related to the negative effect of anthropogenic activities in landslide-prone areas. The preliminary analysis on land use variations confirmed the increase of urban areas in the Apulia region from the 1959 to the 2006.

Keywords

Climate change • Land use • Landslides • Floods • Apulia

24.1 Introduction

Recent international research has underlined the evidence of climate change throughout the world, which is evident in the gradual, but constant, rise of temperatures and in the variation in the distribution of rainfall, which are concentrated in certain periods of time, often assuming exceptional intensities (EEA 2008). Among the consequences of these climate conditions there is the increase in the frequency and magnitude of natural disasters, such as droughts, windstorms, heat waves, landslides, floods and secondary floods (i.e. rapid accumulation or pounding of surface water with very low flow velocity). The Damaging Hydrogeological Events (DHEs) can be defined as the occurrence of one or more simultaneous aforementioned phenomena causing damages (Petrucci and Polemio 2002). They represent a serious problem, especially in DHE-prone areas with growing urbanisation. In these areas the increasing frequency of extreme hydrological events could be related to climate variations and/or urban development. The historical analysis of DHEs can support decision making and land-use planning, ultimately reducing natural risks.

The research was realized at CNR-IRPI in the context of PhD school in "Plant sciences and environmental technologies", specializing in "Management and engineering of biosystems agroforestry" of the University of Bari "A. Moro".

T. Lonigro (✉) · M. Polemio
CNR-IRPI, Bari, Italy
e-mail: t.lonigro@ba.irpi.cnr.it

M. Polemio
e-mail: m.polemio@ba.irpi.cnr.it

G. Lollino et al. (eds.), *Engineering Geology for Society and Territory – Volume 1*,
DOI: 10.1007/978-3-319-09300-0_24,

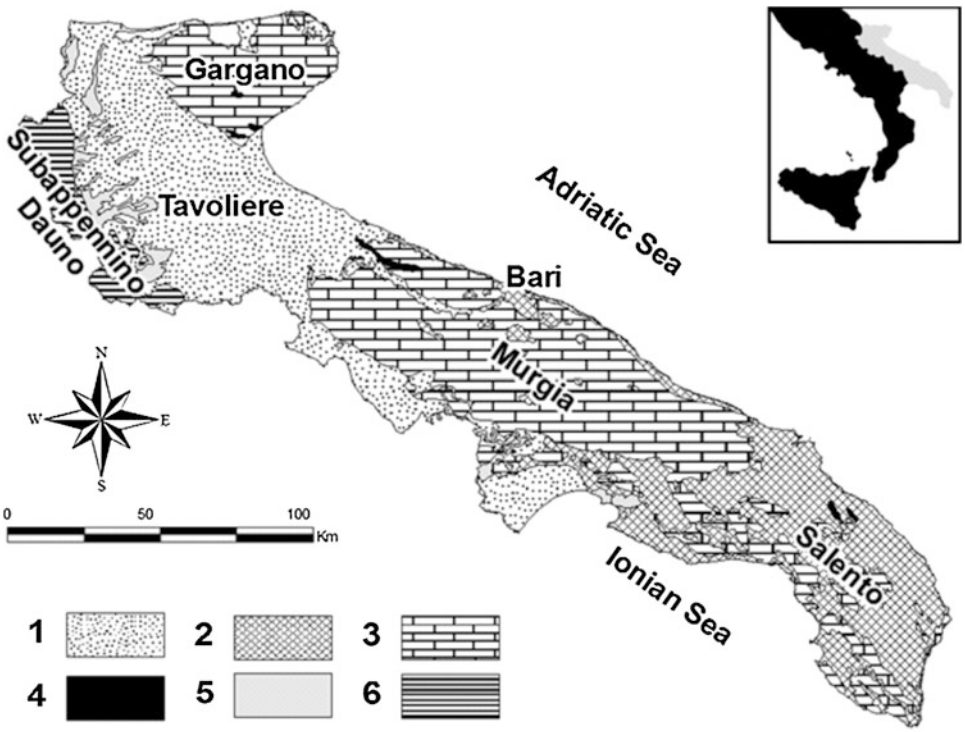

Fig. 24.1 Apulian geological-technical map. *1* Sandy clay, clayey sand, sand and gravel; *2* Sand, silt, calcareous sandstone, limestone and dolomite; *3* Limestone and dolomite; *4* Calcareous sandstone and sandstone; *5* Marly clay; *6* Flysch

The paper proposes a methodology, based on both historical and time series approaches, used for describing the influence of climatic variability on the number of phenomena observed. The historical approach is finalised to collect phenomenon historical data, very important for the comprehension of the evolution of a study area, especially in DHE-prone areas (Petrucci and Polemio 2002). Phenomenon historical data is useful for expanding the historical period of investigation in order to assess the occurrence trend of DHEs. The time series approach includes the collection and the statistical analysis of climatic data (monthly rainfall, wet days, rainfall intensity, and temperature), which are also used as a proxy data for floods and landslides. The climatic data are useful to characterise the climate variations and trends and to roughly assess the effects of these trends on river discharge and on the triggering of landslides. The time series approach is completed by tools to analyse simultaneously all data types. The study of land use variations is important to understand how the modifications occurred in the territory, especially in terms of vulnerability, could influence the occurrence of DHEs (Palmieri et al. 2011). The methodology can be applied simultaneously to floods and landslides and was tested considering a selected Italian region (Apulia, southern Italy), particularly affected by climate changes, enduring significant effects in terms of the decreasing trends of water availability (Polemio and Casarano 2004; Polemio et al. 2011).

24.2 The Apulian Case Study

The Apulia region can be divided into five physiographic units: Gargano, Tavoliere, Subappennino Dauno, Murgia, and Salento (Fig. 24.1). From east to west, it is possible to recognise three different geological domains related to Apennine orogenic phase, the foreland, the foredeep and the chain. The foreland is made primarily of the carbonate platform sediments deposited during the Upper Jurassic—Cretaceous (Cotecchia et al. 2005); it is composed of micritic limestones, with a fairly high fossil content. Moving westward, there are Plio—Pleistocene units in transgression on the carbonate platform units; the entire cycle of sedimentation includes limestones, clays, sands and conglomerates. In the Subappennino Dauno, there are units belonging to the Apennine chain; they consist primarily of carbonate silicoclastic and marine deposits, which settled in different pre-orogenic sedimentary basins. The tectonic forces then stacked these sediments, which, at present, are chaotic and strongly tectonised. As a consequence, these sediments present poor geotechnical properties, characterising the Subappennino Dauno as the landslide-prone Apulian physiographic unit.

The main source of records of DHEs for Apulia was the AVI database (CNR-GNDCI 1999), which was useful for the period 1918–1996. This source was integrated up to 2006 by consulting newspapers, publications and technical reports kept by the authors' Institute. In Apulia, 251

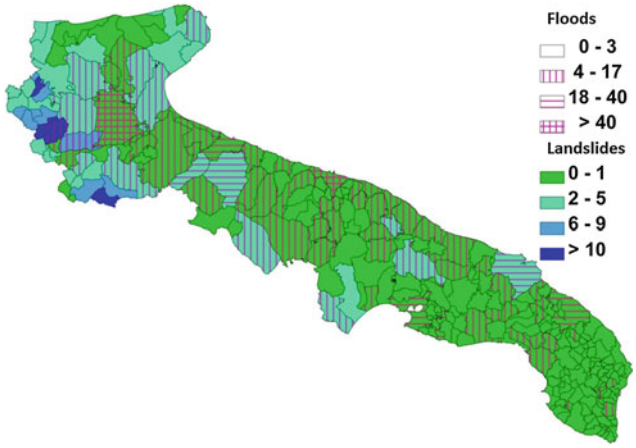

Fig. 24.2 Recurrence of DHEs (1918–2006)

landslides (the first recorded landslide was in 1928) and 935 floods were documented. Landslide and floods monthly time series were defined both for each municipality and for the entire region. The whole dataset was implemented in a GIS environment (Fig. 24.2).

The spatial distribution of floods indicated that floods were not rare where karstic outcropping features are observed (Polemio 2010). The two highest occurrence classes (>18 floods) were typical of the municipalities of Tavoliere, Salento, and Murgia, where the main regional towns are located. The regional distribution of landslides underlined the high concentration of these events in the area of the Subappennino Dauno, where the two highest occurrence classes were observed. This could be justified considering the geological, morphological, and geotechnical features for which Subappennino Dauno could be a landslide-prone area.

The climate database was realised by collecting monthly data on rainfall R, temperature T and wet days WD (days in which precipitation is equal to or greater than 1 mm) from the Annali Idrologici (annual publication of the national hydrological service), published from 1919 to 1996. This database has been integrated with historical data from 1877. The most recent data (until 2008) were provided by the Centre of Functional Service of Civil Protection of Regione Puglia. For each month and rain gauge, the monthly-mean rainfall intensity of wet days (following rainfall intensity or I) was calculated as the ratio between the monthly rainfall R and the monthly number of wet days WD. The following text always refers to the hydrological year, which runs from September to August. Sixty rainfall gauges/time series were selected, 47 of which were also thermometric. The selection was optimised by maximising time series length, minimising time series gaps and pursuing a sufficient gauge density.

To simplify the complexities of the spatial-temporal analysis of changes in the climate, the damaging landslide and flood occurrences and the relationship between these variables, monthly (RI, WDI, II, TI, LI, and FI) and annual indices (Ry, WDy, Iy, Ty, Ly, and Fy) were defined by reducing the discussion to a discussion of time series (see Polemio and Petrucci 2010 for more details).

Table 24. 1 Trend and correlation coefficient between annual indices

	Fy	Ly	Ry	WDy	Iy	Ty	Trend
Fy	1.00						I
Ly	0.12	1.00					I
Ry	0.36	0.14	1.00				D
WDy	0.36	0.18	0.80	1.00			I
Iy	0.17	−0.02	0.56	0.12	1.00		D
Ty	0.04	0.26	−0.32	−0.42	−0.02	1.00	I

Fy, *Ly*, *Ry*, *WDy*, *Iy*, *Ty* are respectively flood, landslide, rainfall, wet days, rainfall intensity, and temperature indices; *I* increasing, *D* decreasing

24.3 Results and Conclusions

The correlation analysis between annual indices underlined a positive and direct correlation between landslides from a side and rainfall, wet days, and temperature from the other side, while an indirect and very low correlation was noticed between landslides and rainfall intensity. The correlation between the flood indices and annual climate indices was always direct, with higher values compared to those obtained in the case of landslides (Table 24.1). The trend analysis showed a decreasing trend of rainfall and rainfall intensity and an increasing trend of wet days and temperatures, in agreement with what is known for all of southern Italy (EEA 2008; Polemio and Casarano 2004).

The climate trend, overall, does not show favourable conditions for the increase of the annual DHEs number. Nevertheless, the trend of the annual number of damaging landslides and floods is positive or increasing (Fig. 24.3).

If there is not an evident relationship between climate variability and the increasing trend in the occurrence of DHEs, the role of anthropogenic modifications and the mismanagement of risk-prone areas should be considered to justify the increasing occurrences of floods and landslides.

To reduce the uncertainty in the results described above, the research is being expanded with two approaches: the improvement of DHEs database and the study of land use modifications.

For the improvement of DHEs dataset further data were collected searching in the archives of regional libraries. About 700 useful news from 17 different local newspapers were found from 1876 to 1951. From a critical analysis of the 700 news collected since 1876–1952 only 437 were useful for the implementation of the Apulia DHEs database. The screening of the selected sources is still in progress and the expansion of the database is not concluded yet.

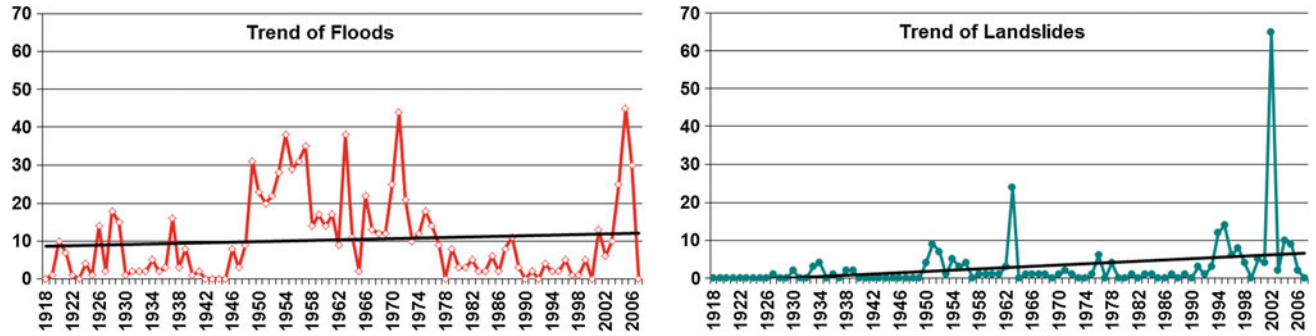

Fig. 24.3 Time series of annual flood and landslide number and trend

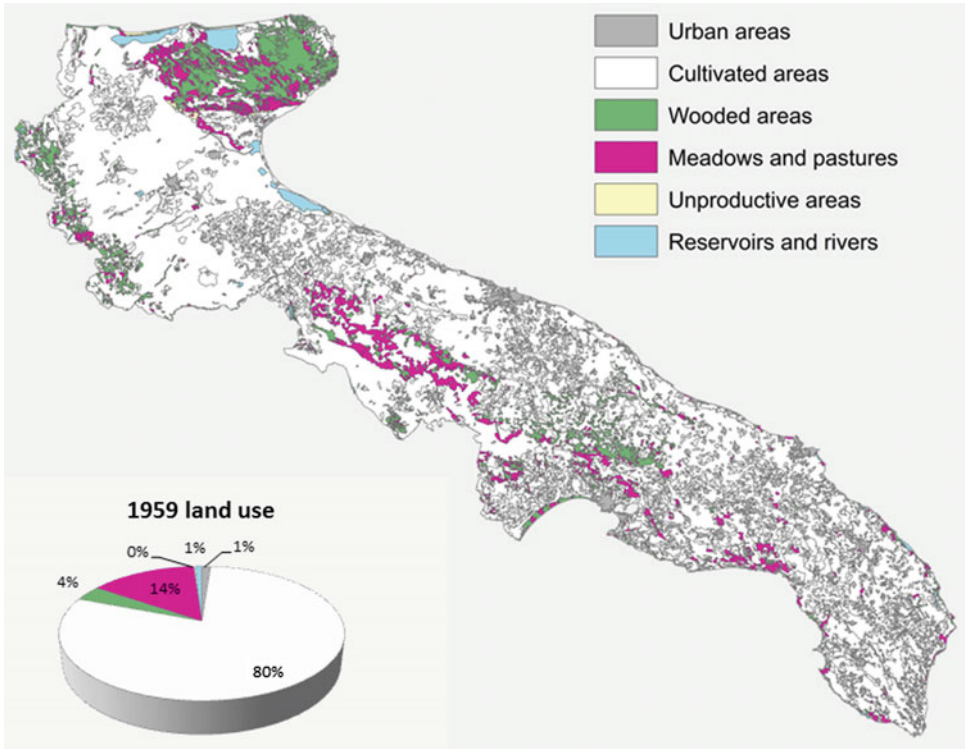

Fig. 24.4 2006 Apulian land use map and land use diagram of 1959

For the comprehension of land use modifications the available data were represented by the "Corine Land Cover" programme for the years 2006, 1999 and 1990 and the "Land use Map" edited by CNR-TCI of the 1959, which was acquired in digital format, loaded in a GIS environment, georeferenced and digitalized.

It was necessary to create a legend that was useful both for Corine Land Cover levels and for the Land use Map. A new legend was created; it was composed by six fields, representing the principal uses of land (Fig. 24.4). A preliminary analysis showed, starting from 1959 to 2006, a significant increase in urban areas (from 231 to 898 km^2), cultivated areas (from 15,392 to 15,576 km^2), and wooded areas (from 716 to 1,429 km^2), and a decrease in the meadows and pastures (from 2,772 to 1,168 km^2).

Notwithstanding the increase of wooded areas, the increasing vulnerability due to the expansion of urban areas and anthropogenic activities could justify the increasing occurrence of the DHEs on the Apulian territory. This phase of the study is not yet completed and the above considerations have to be validated with higher accuracy.

References

CNR-GNDCI (1999) Database AVI degli eventi alluvionali occorsi su tutto il territorio nazionale dal 1930 al 1999. http://avi.gndci.cnr.it/

Cotecchia V, Grassi D, Polemio M (2005) Carbonate aquifers in Apulia and seawater intrusion. G Geol Appl 1:219–231

EEA (2008) Impacts of Europe's changing climate—An indicator-based assessment. European environment agency report, 4. http://www.eea.europa.eu/publications/eea_report_2008_4/

Palmieri W, Petrucci O, Versace P (2011) La difesa del suolo nell'Ottocento nel mezzogiorno d'Italia. IV Quaderno dell'Osservatorio di Documentazione Ambientale, UNICAL, 183 p

Petrucci O, Polemio M (2002) Hydrogeological multiple hazard: a characterisation based on the use of historical data. In: Rybar J, Stemberk J, Wagner P (eds) Landslides. Balkema Publishers, Prague, pp 269–274

Polemio M (2010) Historical floods and a recent extreme rainfall event in the Murgia karstic environment (Southern Italy). Z Geomorphol 54:195–219

Polemio M, Casarano D (2004) Rainfall and drought in southern Italy (1821–2001). In: Rodda JC, Ubertini L (eds) The basis of civilization—water science? vol 286, IAHS, Roma, Italy, pp 217–227

Polemio M, Petrucci O (2010) Occurrence of landslide events and the role of climate in the twentieth century in Calabria, southern Italy. Q J Eng Geol Hydrogeol 43:1–14

Polemio M, Dragone V, Casarano D, Basso A, Brunetti M, Maugeri M, Nanni T, Simolo C (2011) Cambiamenti climatici e disponibilità di acque superficiali e sotterranee: trend in atto e previsioni. In: Polemio M (ed) Le modificazioni climatiche e i rischi naturali. CNR IRPI, Bari, pp 213–216

An Assessment of the Water Resources Availability and of the Flood Hazard in a Climate Change Scenario in Tuscany

25

Campo Lorenzo and Caparrini Francesca

Abstract

The effects of the global climate change on the hydrological balance at regional scale received a growing attention in the last decade. While this issue affects all the components of the hydrological cycle, the most studied aspects refer the extreme events like floods and droughts, increasing the concerns about the water resource availability in such scenarios. Given a particular set of climate evolution forecasts, one of the available tools for the study of these topics is given by the distributed hydrological models. In this work a long-term simulation was performed on the Tuscany territory (Central Italy) with the hydrological distributed model MOdello di BIlancio Distribuito e Continuo (MOBIDIC) developed by the Department of Civil and Environmental Engineering of the University of Florence. The daily meteorological forcing (rainfall height, air temperature) used in the simulations were obtained by a meteorological simulation at 4-km horizontal resolution performed by a Limited Area Meteorological Model (LAM) based on the IPCC A2 scenario of climatological forecast for the 2070–2099 period. The MOBIDIC model was previously calibrated on the 1997–2007 period basing on the observations of the ground network of sensors of Tuscany Region. Analyses and comparisons of the results of the hydrological simulations between the two periods (current and climatic change scenario) are provided in terms of a statistics characterization of the extreme events and modifications in the rainfall regimes. A discussion of the results is provided.

Keywords

Climate change • Floods • Hydrological modeling

25.1 Introduction

The importance of a correct estimation of water resources is largely recognized not only in the developing countries, but also at global scale. The issue of the availability of adequate water amounts affects several fields of human activities like agriculture, industry, sanitary aspects, etc. but the attention on the ecohydrological dynamics has also grown in the last decades.

Strictly tied with these concerns are the problems related to the extreme events that involve the water availability (or its scarcity): the floods, that affects a large portion of the inhabitated areas of the world (Milly et al. 2002;

C. Lorenzo (✉)
Department of Civil and Environmental Engineering, University of Florence, Via S. Marta 3, 50139 Florence, Italy
e-mail: lcampo24@gmail.com

C. Francesca
Eumechanos, Via La Marmora 22, 50121 Florence, Italy

C. Lorenzo
CIMA Research Foundation, Via A. Magliotto 2, 17100 Savona, Italy

G. Lollino et al. (eds.), *Engineering Geology for Society and Territory – Volume 1*,
DOI: 10.1007/978-3-319-09300-0_25,

Lehner et al. 2006; Morita 2011) and can have also effects on the public health (Ahern et al. 2005) and the droughts, defined as a medium-long period of scarcity or absence of precipitation (Dai at al. 2004).

Given the increasing complexity of the challenges to be faced, a number of tools are used by the scientific community to assess, forecast and, in some measure, contain the consequences of these extreme events. Among these tools we can name the remote sensing techniques, the continuous direct monitoring of the hydrosphere, both at the ground (hydrological measurements, discharge flows) and in the atmosphere (sondages, etc.) and the numerical modeling. With reference to the latter, the distributed hydrological modeling constitutes a valuable tool for a quantitative assessment of the various components of the hydrological balance at watershed or regional scale.

The above considerations have to deal with the several applications of the hydrological modeling: from the assessment of the current or past state of a watershed (soil moisture, flow regimes) to the short or long-term forecast at the purpose of flood monitoring and management. In the framework of the Climate Change, the horizon of the forecast becomes even longer, up to cover until the end of the 21st century.

In this work a distributed hydrological model, MOdello di BIlancio Distribuito e Continuo (MOBIDIC), was employed in order to assess a forecast of the hydrological balance at regional scale until the end of the period considered for the Intergovernmental Panel on Climate Change (IPCC) long-term scenarios of climate change forecast (IPCC 2007).

The model employed, as input, the meteorological forecasts in terms of rainfall and surface air temperature of the A2 IPCC forecast scenario (IPCC 2007). More specifically, a Limited Area Model (LAM) atmospheric model was employed in order to downscale the original IPCC data. The model was used in order to produce daily states in terms of river discharge flows, soil moisture maps, etc. at regional scale. The domain of the study was Tuscany Region (Fig. 25.1), in Central Italy, and the period of simulation was 2070–2099.

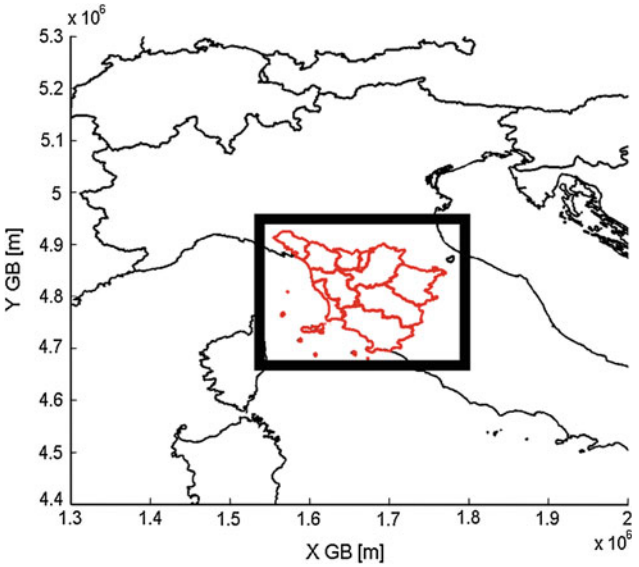

Fig. 25.1 Tuscany, Central Italy. Administrative divisions: Tuscany is divided into ten provinces. The area represents the domain of the LAM simulation at 4 km of horizontal resolution

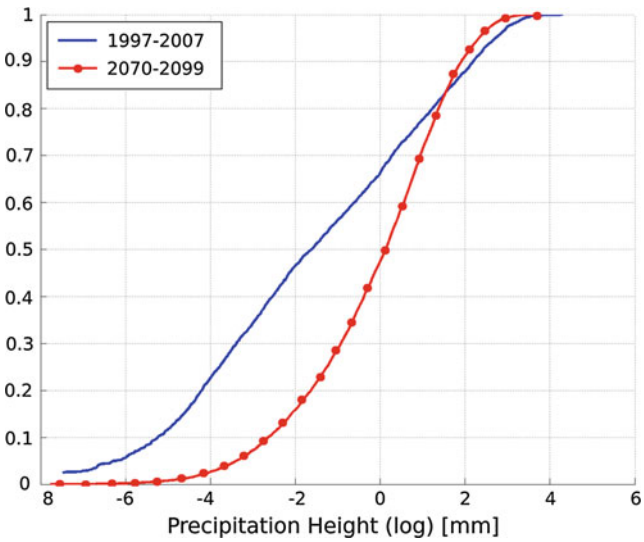

Fig. 25.2 Comparison of the cumulated distribution functions of the spatially-averaged precipitation height (*blue line* 1997–2007, *red line* 2070–2099)

25.2 Methodology

MOBIDIC is a distributed hydrologic model developed at the Civil and Environmental Engineering Department, University of Florence (Castelli et al. 2009). It simulates all the main processes of the hydrologic balance: network channels flow, evapotranspiration, infiltration, adsorption, percolation, hypodermic flow, base flow, hillslope flow, etc. The model is able to simulate either a single rainfall-runoff event and the hydrologic balance for a period of several years. The distributed approach allows to represent a river basin by discrete cells with assigned hydraulic and geomorphological properties, while the drainage network is modeled as a set of elementary branches.

It is able to simulate the presence of various kind of anthropic withdrawals distributed on the territory and evaluate the percentage of satisfaction of each one in the different flow conditions of the network.

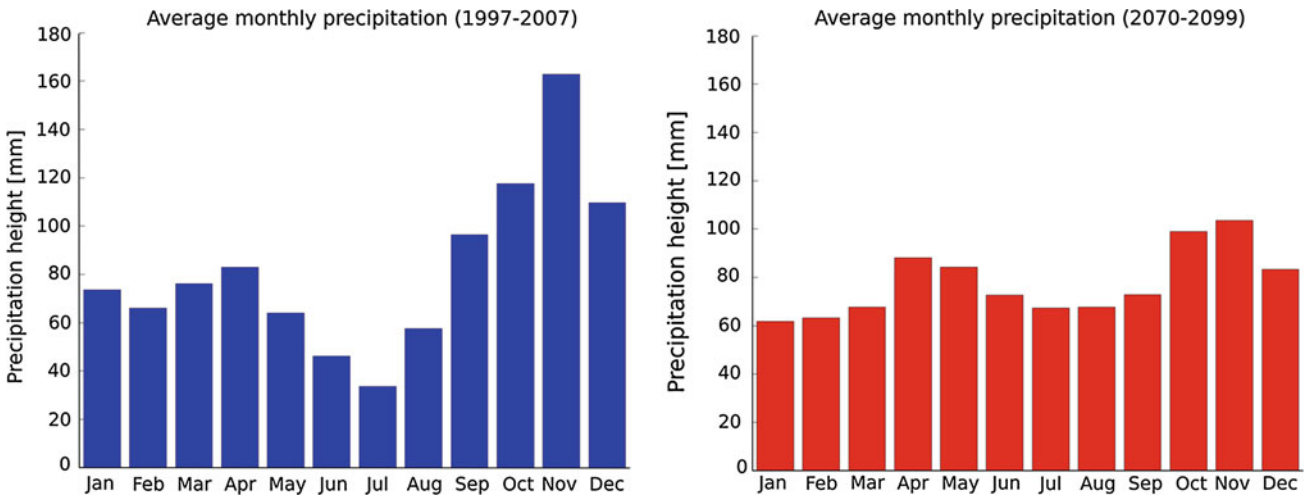

Fig. 25.3 Average monthly rainfall in the average year. *Left* 1997–2007, *right* 2070–2099

The model requires at least daily values of precipitation and temperature of the air in distributed maps. The domain of the simulation was Tuscany Region, in Central Italy, with a total area of approximately 23,000 km^2, and the simulation was performed with a daily timestep and a 500 m horizontal resolution.

The input maps of rainfall and temperature were obtained by a downscaling of the original, coarse resolution, IPCC meteorological fields relative to the A2 scenario (IPCC 2007). The downscaling was performed with a Limited Area atmospheric Model, and the resulting data were daily maps at 4 km of horizontal resolution, that were then interpolated at the hydrological simulation resolution (the Inverse Distance Weight method was employed).

In order to give an assessment of the future scenarios of withdrawals, the current database of the Tuscany region withdrawals for agriculture, industry and civil use was employed.

The hydrological model was previously calibrated using the meteorological and discharge flows time series of the first decade of the century, namely the data from 1997 to 2007.

25.3 Results

The simulation was performed for the whole 2070–2099 period, showing significant differences in the hydrological regimes with respect to the current period (1997–2007). In Fig. 25.2 a comparison between the cumulated distribution of the area-averaged rainfall is shown. As it is possible to see, the prediction for the 2070–2099 period shows a less uniform distribution of the rainfall events intensity, with a major concentration around the mid-intensity events.

This reflected in a more uniform behavior during the year with a less evident season cycle, as it is possible to see in Fig. 25.3.

From the point of view of the flood hazard, this led to an increasing of the extreme hydrological events, due to a major concentrations of the precipitation volumes in more intense events. More specifically, the average intensity of the hydrological events increased, and their distribution along the year became more uniform, leading to an increase in terms of flood risk (infrastructure damages, etc.) and, at the same time, reducing the droughts periods.

In Figs. 25.4 and 25.5 the results in terms of hydrological balance are shown. In Fig. 25.4 the maps of the average soil saturation are compared for the current and the future scenarios: while in time the trend tended to disappear, for what concerns the spatial patterns an enhancement of the spatial features is observed in the future scenario, showing a stronger dependence of the soil moisture from the elevation (this reflects an analogous change in the main spatial patterns of the rainfall).

In Fig. 25.5 the withdrawals scenarios are taken in consideration. In each map the average (on the territory of the main basins) percentage of satisfaction of the withdrawals is represented. The total of the civil, industrial and agricultural water amount are considered. As it is possible to see, the changes in the temporal trends of the rainfall and flows events reflected in a higher satisfaction of the withdrawals, that are always above the 70 %. In the current scenario, on the opposite, there are regions below 60 %. However, approximately the same spatial pattern is observed. It is important to highlight that, in a scenario of increasing temperatures, and consequent increase of potential evapotranspiration, according to the simulation, the availability of

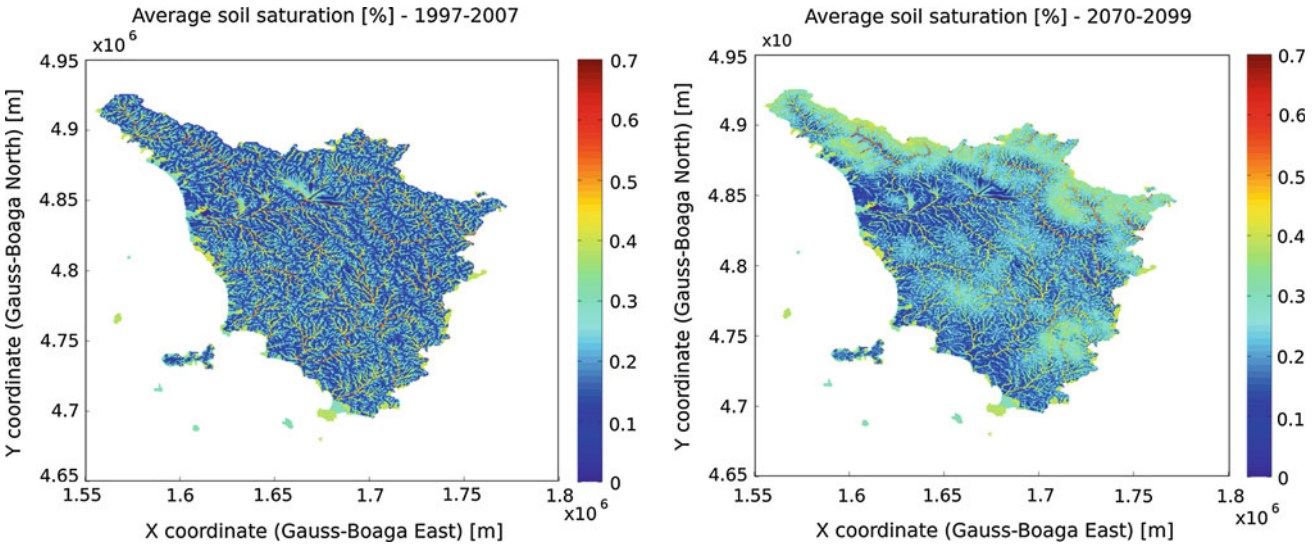

Fig. 25.4 Map of the average soil saturation [%] of small and large pore soil, period: 1997–2007 (*left*), 2070–2099 (*right*)

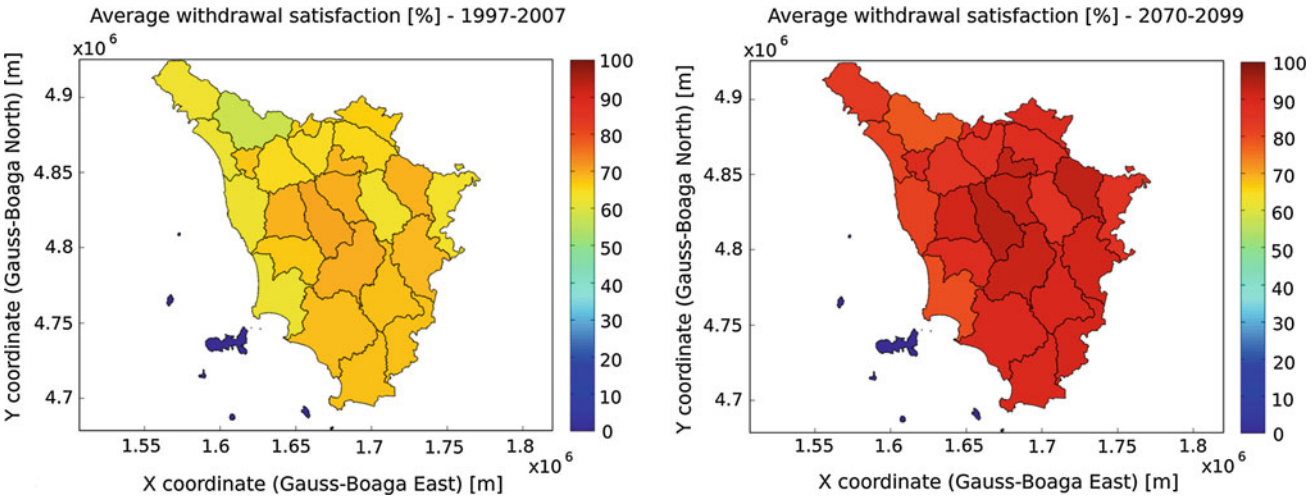

Fig. 25.5 Maps of the average satisfaction percentage of the total water withdrawals (all uses: agricultural, civil, industrial) aggregated on the main watersheds, period: 1997–2007 (*left*), 2070–2099 (*right*)

water resources improves. This is due primarily to the more homogeneous temporal distribution of the rainfall along the seasonal cycle, that avoid the concurrence of high temperature (and potential evapotranspiration) and shortage of water resources due to lower rainfall totals.

In conclusion, the investigation about the far future hydrological states in the A2 IPCC scenario of climate change showed, as a result of a 30-years long hydrological simulation, a significant change in the hydrological regimes, and an attenuation of the seasonal cycle. This, causing a more uniform distribution of the precipitation in the year, led to a better satisfaction of the human demand of water for the various destined uses. Further investigations, thought, are required in order to assess these issues in different scenarios and for the whole period of IPCC forecast.

References

Ahern M, Kovats RS, Wilkinson P, Few R, Matthies F (2005) Global health impacts of floods: epidemiologic evidence. Epidemiol Rev 27(1):36–46. doi:10.1093/epirev/mxi004

Castelli F, Menduni G, Mazzanti B (2009) A distributed package for sustainable water management: a case study in the Arno basin. IAHS Publ. 327

Dai A, Trenberth KE, Qian T (2004) A global dataset of palmer drought severity index for 1870–2002: relationship with soil moisture and effects of surface warming. Am Meteorol Soc J 5:6

IPCC (2007) Climate change 2007: synthesis report. Geneva, Switzerland, p 104

Lehner B, Döll P, Alcamo J, Henrichs T, Kaspar F (2006) Estimating the impact of global change on flood and drought risks in Europe: a continental, integrated analysis. Clim Change 75(3):273–299. doi:10.1007/s10584-006-6338-4

Milly PCD, Wetherald RT, Dunne KA, Delworth TL (2002) Increasing risk of great floods in a changing climate. Nature 415:514–517. doi:10.1038/415514a

Morita M (2011) Quantification of increased flood risk due to global climate change for urban river management planning. Water Sci Technol 63(12):2967–2974

Climate Change Impacts on Soil Erosion: A High-Resolution Projection on Catchment Scale Until 2100

26

A. Routschek, J. Schmidt and F. Kreienkamp

Abstract

The aim of this study was to quantify the impact of climate change on soil loss at catchment scale at high temporal and spatial resolution. Simulations are performed for three example catchments in West, North and East Saxony/Germany. The study is based on the A1B IPCC-scenario and model outputs of four models: ECHAM4-OPYC3 (general circulation model), WETTREG (statistical downscaling climate model), METVER (hydrological model for calculating daily initial soil moisture) and EROSION 3D as a process-based soil erosion model. Simulations were run for measured and projected single rainstorm events at a temporal resolution of 5 min. Soil loss was simulated for two future periods from 2041 to 2050 and 2091 to 2100. Results were compared to simulated soil loss based on 10 years of measured climate data from 1989 to 2007. Expected changes in land use, soil management due to changed crop rotation and shifted harvest date are taken into account in scenario studies. The results of the simulations with EROSION 3D allow to quantify the impacts of climate change on erosion rates. The impact of the expected increase of precipitation intensities leads to a significant increase of soil loss by 2050 and a partly decrease by 2100. The impacts of land use, soil management and soil properties on soil loss are higher than the effects of changed precipitation patterns.

Keywords

Climate change • Soil erosion • Soil erosion model • Regional climate modeling

26.1 Introduction

The increase of global temperature influences, among others, regional weather circulation patterns and leads to a modified frequency and intensity of heavy rainstorms. Because soil erosion is mostly the result of extreme but short rainfall events, changes in frequency and intensity of precipitation should affect soil erosion processes. Furthermore climate changes influence a variety of physical and chemical soil properties which interact on infiltration and soil erosion processes. Climate change forces land use changes. New crops, crop rotations and management practices will be implemented to accommodate the new climate regime.

To consider all these processes, predicting climate and soil erosion models have become indispensably tools for assessing the response of soil erosion to a future climate (Lal 1998; Toy et al. 2002). In this study the scenario-based approach was applied to incorporate future land-use and management changes with the aim to quantify the impact of

A. Routschek (✉) · J. Schmidt
Technical University Freiberg, Soil and Water Conservation Unit, Agricolastrasse 22, 09599 Freiberg, Germany
e-mail: amichael@ioez.tu-freiberg.de

F. Kreienkamp
Deutscher Wetterdienst, Michendorfer Chaussee 23, 14473 Potsdam, Germany
e-mail: frank.kreienkamp@dwd.de

G. Lollino et al. (eds.), *Engineering Geology for Society and Territory – Volume 1*,
DOI: 10.1007/978-3-319-09300-0_26,

climate change on soil loss at catchment scale at high temporal and spatial resolution.

26.2 Material and Methods

26.2.1 Climate Simulation

Peaks of rainfall intensity mostly persist from several minutes till only a few hours. A daily or even hourly resolution of precipitation data cannot record the nature of heavy rainfall events which are setting off erosion processes. A previous limitation of simulated climate data was the temporal resolution of available outputs: predicted precipitation primary consists of monthly or daily data. Weather generators within downscaling models are used to disaggregate monthly data into finer resolved data. The highest temporal resolutions of precipitation data (daily and sub-daily data on basis of a sensitivity analyses respectively) for the prediction of future soil loss were used by Klik and Eitzinger (2010) and Mullan et al. (2012) running the WEPP-Model (Water Erosion Prediction Project). Michael et al. (2005) tested the approach used in this study on two single slopes.

The application of the WETTREG-Model allows to project future climate data in high temporal resolution for local climate stations, if long-term measurements in the same high temporal resolution are available. In this study, a five-minute-resolution of precipitation was used for measured and simulated precipitation data. WETTREG (weather situation-based regression method) is an empirical statistical downscaling method that links large-scale features of the atmosphere to locally measured climate data. The model was developed and described in detail by Enke (Enke et al. 2005; Enke and Spekat 1997; Spekat et al. 2007, 2010; Kreienkamp et al. 2008, 2010, 2011). The application was performed on the base of ECHAM5-OPYC3 (general circulation model) and the A1B IPCC scenario. The model is conditioned to reproduce the climate of 1971–2000 with an accuracy of −0.1 K (mean temperature 2 m above ground) and 5 % (precipitation) for each season.

26.2.2 Simulation of Soil Erosion

EROSION 3D, developed by Schmidt (1990), is a field-tested and widely validated, process-based computer model for prediction of surface runoff and soil erosion by water in catchments. A broad overview about model physics, its validation and the state of the art of the existing 3D soil erosion models is given among others by Schmidt (2000), Schmidt et al. (1999a, b), Michael (2000), Klik et al. (1998), Schindewolf and Schmidt (2012) and Arévalo and Schmidt (2011). The model EROSION 3D, as applied in this study, was developed with the intention to provide an easy-to-use tool for erosion prediction in soil and water conservation planning and assessment (Schmidt 1996; Schmidt et al. 1999a, b; Von Werner 1995).

The EROSION 3D model is predominantly based on physical principles. For each single rainfall a soil file describing the actual soil conditions has to be created. EROSION 3D is able to provide long-term simulations by connecting soil-data-files with precipitation-data-files in a batch routine.

Simulations were performed on basis of an official data base provided by the state agencies of Saxony (DEM and land-use distribution, soil reference map 1:200000). Spatial resolution was adjusted to a 10 × 10 m-Raster ASCII-format by GIS. Soil erosion rates at the outlets of the watersheds were calculated for every single rainfall event.

26.2.3 Simulation of Soil Moisture

METVER is a meteorological evaporation model, developed by Mueller (1987). METVER is a one-layer-model based on the approach of Turc (1961) and its modification by Wendling et al. (1991).

Three types of input data were needed: climate data, soil-hydrological data and land use parameter. Climate data were provided by the National German Weather Service for the reference-period from 1998–2007 for the climate stations Chemnitz, Oschatz and Goerlitz. Climate data for the projected periods from 2041–2050 and 2091–2100 were calculated by WETTREG (Kreienkamp et al. 2010). Out of ten equally likely WETTREG-simulations the runs with the highest (MAX) and the lowest medium precipitation intensity (MIN) were chosen for the calculation of the soil moisture.

Results were the daily water contents [Vol.-%] in the upper layer of the topsoil (0–10 cm) for the described soils and crops within the three catchments for the time periods from 1998–2007, 2041–2050 (MIN and MAX) and 2091–2100 (MIN and MAX).

26.2.4 Site Description

Three small hydrological catchments were chosen near the climate stations Chemnitz, Oschatz and Görlitz in The Federal State of Saxony/Germany. Each catchment represents a natural region of Saxony: catchment “Dittersdorf” the lower and middle Erzgebirge mountain region in the Southwest, catchment “Rasslitz” the Saxon loess belt in the North and catchment “Viebig” the Lusatia loess belt in the

Table 26.1 Catchment properties

Catchment	Size [km^2]	Altitude [mNN]	Arable land [%]	Texture [%]: Clay/Silt/Sand
Dittersdorf	1.01	465–628	56	12/45/43
Rasslitz	2.32	134–213	88	14/76/10
Viebig	2.69	185–365	74	14/76/10

East of Saxony. Typical crops and crop rotations for these sites were provided by the Saxon State Agency. Table 26.1 shows the catchment characteristics.

26.2.5 Model-Chain and Scenarios

The general circulation model ECHAM4-OPYC3 drives the statistical downscaling model WETTREG. In addition, WETTREG is fed with long term measured high resolved data of the selected climate stations. WETTREG delivers as well simulated daily temperature, radiation and precipitation to the METVER-Model as high resolved simulated precipitation data until 2100 to EROSION 3D. METVER determines daily soil moisture for the different soils and crops within the selected catchments. The calculated soil moistures are transferred to EROSION 3D as model input (Fig. 26.1).

Table 26.2 gives an overview about computed scenarios. Soil parameters were derived from a parameter catalogue (Michael 2000) in dependence of soil texture, soil cover, tillage practice and season accordingly to the date of precipitation (measured and simulated).

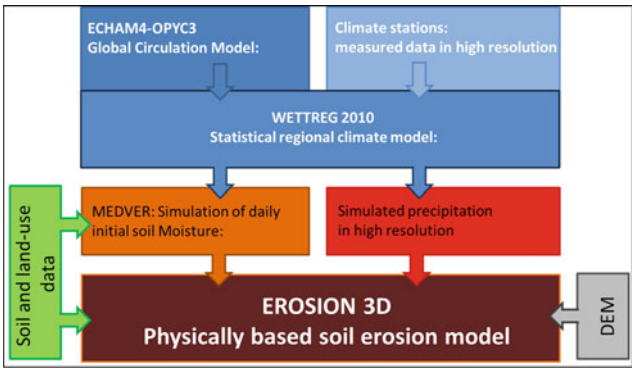

Fig. 26.1 Model-chain

26.3 Results

26.3.1 Impacts of Climate Change on Heavy Rainstorms

The output of WETTREG is a set of ten equally probable continuous time series until 2100 for the selected climate stations. This approach ensures that future climate variability is assessed to the greatest possible extent and adds to the variation of the predicted variables. Out of these ten simulations the runs with the highest (MAX) and the lowest medium precipitation intensity (MIN) and two future periods (2041–2050 and 2091–2100) were selected. All single rainfall events with intensity ≥0.1 mm/min (±60 min) were selected out of the MAX and the MIN runs within the two future periods. This intensity matches the lowest infiltration rates measured during rainfall experiments in Saxony (Michael 2000; Schindewolf and Schmidt 2012). Simulated rainstorms for both future periods (runs MIN and MAX) have been interpreted with regard to frequency and intensity in comparison with measured rainstorms for the reference period.

While the total amount of precipitation by heavy rainstorms will slightly increase in future, the number of heavy rainstorms with intensities ≥0.1 mm/min will decrease for the tree climate stations. Differentiation from West to East (higher number of rainstorms in West, lower in East) is maintained. However, the distribution of heavy rainstorms within the year will clearly change: The number of extreme events will decrease from May until September and increase from October until April. This trend will aggravate until the end of the century.

The number of rainstorms with lower intensities (>0.15 mm and <0.5 mm/min) will decline compared to the present state. In contrast to that trend, the frequency of rainstorms with high and very high intensities (>1.0 mm/min) will increase.

26.3.2 Impacts of Climate Change on Soil Moisture

While the total amount of precipitation is decreasing and the duration of sunshine is strongly increasing, soils becomes more dry under predicted climate conditions.

Soil moisture values calculated with METVER were assigned to following categories: “dry”, “low moist”, “moist” and “very moist” (Bundesanstalt für Geowissenschaften und Rohstoffe 2005) in order to visualize any changes in the allocation of soil humidity. Afterwards the frequency distribution of moisture categories was determined.

For all three locations a change in moisture regime is obvious. At all climate stations the number of “very moist” days is decreasing, while the number of “low moist” days is increasing.

Table 26.2 Scenarios

	Scenario name	Period	Land use
0	Reference-scenario	1998–2007	*Conventional tillage*
	Future-scenarios	2041–2050	
1b 1a 1c	"conservation tillage" "conventional tillage" "no tillage"	2091–2100	(1a) *Conventional tillage*, no plant residues (2a) *Conservation tillage*, 20 % plant residues (2b) *Direct seeding*, 70 % plant residues
2	Future-scenario "decreasing TOC"	2091–2100 2041–2050	Conventional tillage, TOC until 2050: −0.1 % TOC until 2100: −0.2 %
3	Future-scenario "changed phenology"	August/ September	Conventional tillage, earlier harvest
4	"Monoculture" Future-scenario	2041–2050	Conventional tillage, monoculture corn

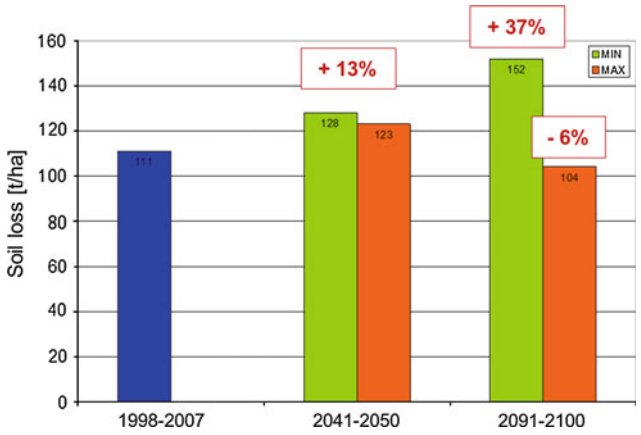

Fig. 26.2 Future soil loss for catchment Rasslitz (Oschatz) in comparison with the reference period

26.3.3 Impacts of Climate Change on Soil Erosion

26.3.3.1 Reference Scenario 1998–2007 (0)

In a first step, the soil loss during the reference period from 1998 to 2007 was calculated. Conventional tillage and typical crop rotation were assumed. A total soil loss of 22 t/ha was calculated for the reference period in the catchment Dittersdorf (Chemnitz), 111 t/ha in Rasslitz and 160 t/ha in Viebig. The differences in soil loss between the three sites can be explained by the various soils.

26.3.3.2 Future Scenarios "Conventional Tillage" (1a), "Conservation Tillage" (1b) and "No Tillage" (1c)

Scenario "conventional tillage" (1a): Secondly, soil loss for the two future periods from 2041–2050 and 2091–2100 was calculated. Only initial soil moisture has been changed to be comparable to the reference scenario (0). Model results show the direct impact of climate change—inclusive an altered soil moisture regime—on soil loss.

Catchment Dittersdorf (climate station Chemnitz): The soil loss will triple until 2050. The months from June till September will be most affected by erosion with a peak in July and August. Until the end of the century the computed soil loss for the catchment will rise again to the present level.

Catchment Rasslitz (climate station Oschatz): Soil loss will increase by approximately 13 % until 2050. The projection for the second future period is not clear. For the MIN-run a moderate increase (+37 %) was calculated. On the contrary, for the MAX-run a slight decrease (−6 %) was calculated due to low initial soil moistures, calculated with METVER. The soil erosion risk remains at a very high level (Fig. 26.2).

Catchment Viebig (climate station Goerlitz): Comparing the reference period with the MIN-run, a higher (+23 %) soil loss was simulated, while for the MAX-run a lower soil loss (−66 %) was determined. Likewise in Rasslitz, the future soil erosion risk remains at a high level until the mid of the century. Yet, it does not increase clearly. Until the end of the century the soil erosion risk drops markedly down (−56 to −92 %) due to much lower initial soil moistures. Nevertheless, 84 % (58 t/ha) of the soil loss of the whole period (MAX-run) were generated by a short sequence of four extreme rainfall events in March 2098.

Scenarios "conservation tillage" (1b) and "no-tillage" (1c): The changeover from conventional tillage to profitable conservation tillage by cultivator or no-tillage can take many years, depending on the initial conditions. For the parameterization of these scenarios this form of management was assumed to be well established. Plant residues are responsible for the protection of the soil surface and contribute to an enrichment of organic carbon in the upper centimeters of the soil. Twenty percent soil cover by plant residues (what is estimated as too low for an enrichment of organic carbon) were assumed for the scenario "conservation tillage". For the scenario "no tillage" 70 % of plant residues and an enrichment of 1 % of organic carbon for both periods were considered.

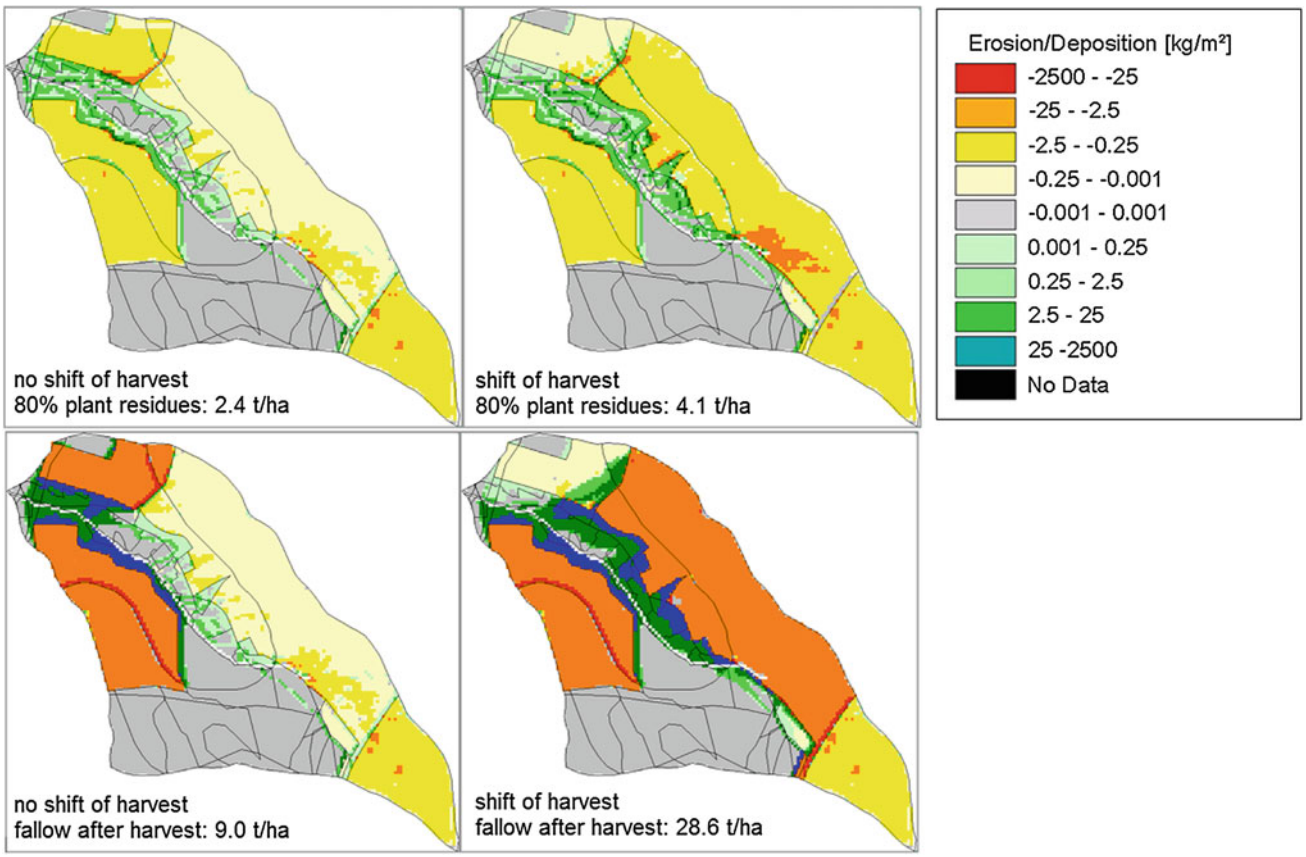

Fig. 26.3 Climate change and shifted harvest with different managements in August 2043 (MAX-run)—catchment Ditterdorf—in comparison with present harvest dates

The scenario "conservation tillage" resulted in a reduction of soil loss by 75 % compared to the future scenario "conventional tillage". Even 91 % were calculated for the scenario "no-tillage".

The probability of soil erosion processes declines during summer and increases during spring and autumn. This applies to all three catchments.

26.3.3.3 Future Scenarios "Decreasing Total Organic Carbon" (2)

The review of recent literature implies a moderate decrease of organic carbon content in soils through the faster residue decomposition from increased microbial activity. The speed of this process depends on various physical, chemical and management factors. Kolbe (2009) listed the projected development of the contents of organic carbon in top-soils of Saxony. Based on these data, an average decrease of 0.1 % until 2050 and 0.2 % until 2100 were assumed for the future scenario "decreasing TOC".

Incorporating this assumption, it results in an additional increase of soil loss of about 2–4 % until 2050 and of about 5–14 % until 2100.

26.3.3.4 Future Scenarios "Changed Phenology" (3)

Chmielewski et al. (2004) and Estrella (2007) investigated the trends of the future phenology of crops. While the shift of the date of sowing will be only minor, the harvesting date of many crops will be shifted notably.

For the investigated time period only four heavy rainstorms fell into the timeslot between former and future harvest date. For these few cases, the shift of phenology causes a significant increase in soil loss. Certainly the amount of soil loss depends on the soil conditions after harvest (Fig. 26.3).

26.3.3.5 Future Scenarios "Monoculture Corn" (4)

The future scenario "monoculture corn" was modeled for the period 2041–2050 (Max-run) for the catchment Rasslitz only. This simulation was conducted with two different assumptions: (1) stubbles after harvest, 20 % plant residues, (2) fallow after harvest.

(1) An increase of 47 % compared to the mixed crop rotation will be observed, if stubbles remain on the field after harvest. The poor soil cover implicates a fast

silting. High soil losses were calculated for spring (March and April) and late autumn (October, November and December).

(2) Soil loss decreases in comparison to a mixed crop rotation (−32 %), due to the high roughness of the fallow. The soil erosion risk rises in early spring because of the decreasing surface roughness after imposed load of snow layers and snow melt.

26.4 Discussion and Implications

The predicted change of the regional weather circulation patterns will lead to increased or unchanged soil erosion rates until 2050 in Saxony/Germany. Until the end of the century, decreases of soil erosion rates are generally projected. Precipitation intensities of extreme events will accelerate, although the total number of such events is dropping down. Additionally the occurrence of rainstorms within the year will change: The number of rainstorms will decrease during summer and increase during the winter half-year. This trend will intensify until the end of the century.

The main reason for the decrease of soil erosion rates in the second half of the century are lower initial soil moistures due higher temperatures, radiation and a decline of total precipitation amount.

Contemporary climate change induces land use changes. This study confirms the results of Mullan et al. (2012) and Nunes et al. (2013): Soil management affects soil erosion rates much more than the impact of the predicted climate change. Permanent conservation tillage and no-tillage proves to preserve soil best with respect to climate change. A stable soil structure due to minimal soil disturbance and a high soil cover all year round are of prime importance. Current soil protection measures are suitable for soil conservation at conditions of a changing climate.

The statistical downscaling model WETTREG turned out to be a robust method according to state of the art. Its major advantage, unlike previous studies, is the reproduction of rainstorms at a very fine scale (resolution of 5 min). This fine scale is necessary to drive event based soil erosion models in order to simulate soil erosion processes as precise as possible.

Further analysis of the impacts of climate change on soil loss should consider the variation of social and economic conditions and potential adaptation strategies. Adaptation strategies are unavoidable taking the probability of climate change into account. Adaption strategies cover changes in land use and land-use structure, soil management and related to that soil structure, cover, roughness, porosity, content of organic carbon, etc.

This study was conducted as a first approximation of the impact of climate and land-use changes on soil loss at a fine temporary scale. With progressing climate research and improvement of model concepts of regionalisation, the projections will become more detailed, faster and robust.

References

Arévalo SA, Schmidt J (2011) Modelling mud deposition patterns due to flash floods in urban areas. Z dt Ges Geowiss 162(4):443–451

Bundesanstalt für Geowissenschaften und Rohstoffe (2005) Bodenkundliche Kartieranleitung. 5. Auflage, Hannover, 438 p

Chmielewski F-M, Müller A, Bruns E (2004) Climate changes and trends in phenology of fruit trees and field crops in Germany 1961–2000. Agric Forest Meteorol 121:69–78

Enke W, Spekat A (1997) Downscaling climate model outputs into local and regional weather elements by classification and regression. Clim Res 8:195–207

Enke W, Deutschlaender Th, Schneider F, Küchler W (2005) Results of five regional climate studies applying a weather pattern based downscaling method to ECHAM4 climate simulations. Meteorol Z 14:247–257

Estrella N (2007) Räumliche und zeitliche Variabilität von phänologischen Phasen und Reaktionen im Zuge von Klimaveränderungen. (Spatial and temporal variability of phenological events and responses due to climate change). Dissertation, TU München

Klik A, Zartl AS, Hebel B, Schmidt J (1998) Comparing RUSLE, EROSION 2D/3D, and WEPP soil loss calculations with four years of observed data. ASAE Paper No. 982055

Klik A, Eitzinger J (2010) Impact of climate change on soil erosion and the efficiency of soil conservation practices in Austria. J Agric Sci 148:529–541

Kreienkamp F, Spekat A, Lahmer G, Orlowski B, Gerstengarbe F-W, Schaller E, Jacob D (2008) Evaluierung und Synopse beobachteter und projizierter Klimate für Sachsen und Umgebung auf der Basis deutscher statistischer und dynamischer Regionalmodelle (REGKLIM). Abschlussbericht Im Auftrag des Sächsischen Landesamts für Umwelt, Landwirtschaft und Geologie AZ 13-8802.26/10/3

Kreienkamp F, Spekat A, Enke W (2010) Erstellung von zeitlich hoch aufgelösten Szenarien. Im Auftrag der TU Bergakademie Freiberg, Bereich Boden- und Gewässerschutz, Auftragsnummer 1260-10

Kreienkamp F, Baumgart S, Spekat A, Enke W (2011) Climate signals on the regional scale derived with a statistical method: relevance of the driving model's resolution. Atmosphere 2:129–145

Lal R (ed) (1998) Soil quality and soil erosion. CRC Press, Boca Raton, FL

Michael A (2000) Anwendung des physikalisch begründeten Erosionsprognosemodells EROSION 2D/3DEmpirische Ansaetze zur Ableitung der Modellparameter. Dissertation TU Bergakademie Freiberg, Freiberger Forschungshefte, Reihe Geowissenschaften

Michael A, Schmidt J, Enke W, Deutschlaender Th, Malitz G (2005) Impact of expected increase in precipitation intensities on soil loss—results of comparative model simulations. Catena 61:155–164

Müller J (1987) Verdunstung landwirtschaftlicher Produktionsgebiete in ausgewählten Vegetationsabschnitten und deren statistische, modellmäßige und kulturbezogene Bewertung. Dissertation Martin-Luther-Universität Halle-Wittenberg

Mullan D, Favis-Mortlock D, Fealy R (2012) Addressing key limitations associated with medelling soil erosion under the impacts of future climate change. Agric Forest Meteorol 156(2012):18–30

Runoff to changes in precipitation and cover. Catena 61:131–154

Nunes JP, Seixa J, Keizer JJ (2013) Modeling the response of within-storm runoff and erosion dynamics to climate change in two Metiterranean watersheds: a multi-model, multi-scale approach to scenario design and analyses. Catena 102:27–39

Schindewolf M, Schmidt J (2012) Parameterization of the EROSION 2D/3D soil erosion model using a small-scale rainfall simulator and upstream runoff simulation. Catena 91:47–55

Schmidt J (ed) (2000) Soil erosion—application of physically based soil erosion models. Springer, New York

Schmidt J (1990) A mathematical model to simulate rainfall erosion. Catena (Suppl 19), 101–109

Schmidt J (1996) Entwicklung und Anwendung eines physikalisch begründeten Simulationsmodells für die Erosion geneigter landwirtschaftlicher Nutzflaechen. In: Berliner Geographische Abhandlungen, Heft 61

Schmidt JV, Werner M, Michael A (1999a) Application of the EROSION 3D model to the Catsop watershed, The Netherlands. Catena 418:449–456

Schmidt JV, Werner M, Michael A (1999b) Application of the EROSION 3D Model to the Catsop Watershed, The Netherlands. Catena 37:449–456

Spekat A, Enke W, Kreienkamp F (2007) Neuentwicklung von regional hoch aufgelösten Wetterlagen für Deutschland und Bereitstellung regionaler Klimaszenarios auf der Basis von globalen Klimasimulationen mit dem Regionalisierungsmodell WETTREG auf der Basis von globalen Klimasimulationen mit ECHAM5/MPI-OM T63L31 2010 bis 2100 für die SRES-Szenarios B1, A1B und A2. Forschungsprojekt im Auftrag des Umweltbundesamtes FuE-Vorhaben Förderkennzeichen 204 41 138

Spekat A, Kreienkamp F, Enke W (2010) An impact-oriented classification method for atmospheric patterns. Phys Chem Earth 35(2010):352–359

Toy TJ, Foster GR, Renard KG (2002) Soil erosion: processes, prediction, measurement and control. Wiley, New York

Turc L (1961) Estimation of irrigation water requirements, potential evapotranspiration: a simple climatic formula evolved up to date. Ann Agron 12:13–49 (in French)

Von Werner M (1995) GIS-orientierte Methoden der digitalen Reliefanalyse zur Modellierung von Bodenerosion in kleinen Einzugsgebieten. Dissertation am Fachbereich Geowissenschaften der Freien Universitaet Berlin

Wendling U, Schellin H-G, Thomae M (1991) Bereitstellung von täglichen Informationen zum Wasserhaushalt des Bodens für die Zwecke der agrarmeteorologischen Beratung. Z Meteorol 41:468–475

Prediction of Climate Change Forced Mass Movement Processes Induced in Periglacial Areas

27

Daniel Tobler, Peter Mani, Rachel Riner, Nils Haehlen and Hugo Raetzo

Abstract

Based on glacier retreat and degrading permafrost in high alpine regions across the Bernese Oberland (Central Switzerland), several new hazardous source areas for processes became evident within the last years. The evaluation of susceptible periglacial areas and the assignment of resulting processes by modelling will be one of the major tasks to be solved in near future. The prediction of those processes and their consequences is an interdisciplinary question. Meteorological scenarios for the next 50 years derived from climate change scenarios stand at the beginning of the decision chain. Based on those, susceptible periglacial areas which act as starting zones for massmovements (rockfall, landslides, debris flows) or new sediment sources can be calculated through sophisticated permafrost and glacier retreat models. A vast basic monitoring of the permafrost by BTS measurements helps understanding on-going processes and is fundamental for the bedload calculation in the periglacial area, which is measured by monitoring systems at representative and characteristic locations within the study area (e.g. Spreitgraben near Guttannen, Switzerland). Dealing with large investigation areas of several 100 km^2 it is important to use adequate models. Well established simulation tools have been used within the project. The result is a so called periglacial hazard indication map visualizing endangered areas in the year of 2060 for massmovement processes as well as other natural hazards like floods, glacial ice avalanche or subglacial lake outburst.

Keywords

Process chains • Permafrost • Mass movements • Climate change • Process modelling

D. Tobler (✉) · R. Riner
GEOTEST AG, 3052 Zollikofen, Switzerland
e-mail: daniel.tobler@geotest.ch

R. Riner
e-mail: rachel.riner@geotest.ch

P. Mani
geo7 AG, 3012 Berne, Switzerland
e-mail: peter.mani@geo7.ch

N. Haehlen
Abt. Naturgefahren, Tiefbauamt Kt. Bern, 3800 Interlaken, Switzerland
e-mail: nils.haehlen@vol.be.ch

H. Raetzo
Federal Office for the Environment FOE, 3003 Bern, Switzerland
e-mail: hugo.raetzo@bafu.admin.ch

27.1 Introduction

The study area is situated in the center of the Swiss Alps in the Bernese Oberland (Fig. 27.1). The main damage potential is an important mountain pass road connecting two districts. Over the past several years, an increase in the number of large mass movements occurred—in the form of debris flows, landslides and rockfalls (Tobler et al. 2012). In a number of locations, these processes are meanwhile posing a threat to the continued existence of the road as well as the villages. In the period 2005–2012, up to 1 million cubic meters of material were carried downhill along two debris flow channels, with volumes in individual events amounting to approximately 200,000 m^3. At least part of the events

G. Lollino et al. (eds.), *Engineering Geology for Society and Territory – Volume 1*,
DOI: 10.1007/978-3-319-09300-0_27,

Fig. 27.1 Investigation area in the central Swiss Alps (*red dot*) and debris flow deposition of 2011 at Guttannen, the main village along the mountain pass road

were due to processes arising in the periglacial area. In connection with climate change, such processes may become more intensified, more frequent and more extensive in the near future.

From the geological point of view the whole valley belongs to the Aaremassiv, where crystalline rocktypes dominate the landscape. The rock formations of the Ritzlihorn, the highest peak along the road and the debris flows origin, consist essentially of highly foliated gneisses (crystalline rock of the Aare Massif, Gwinner 1978). The rock shows ductile and brittle shear-zones with well-educated clusters of steep parallel joints. The steep foliation of the mountain together with the well-educated ductile and brittle shear-zones and a high proportion of phyllosilicates make the rock mass especially vulnerable to weathering. This is a major factor producing high loads of sediment in the catchment area of debris flows.

27.2 Climate Scenarios

Meteorological scenarios for the next 50 years derived from climate change scenarios stand at the beginning of the decision chain. Using the results of regional climate models for the Swiss Alps the frequency of warm extremes in future can be analyzed (Rajczak et al. 2013; Huggel et al. 2013). The models show an increase in the frequency of high-temperature events for the period 2001–2050 compared with the 1951–2000 reference period. The 5-, 10- and 30-day warm events are projected to increase about 1.17–4 times by 2075, and in some models by up to 10 times. Warm extremes can trigger large landslides or rockfalls in temperature-sensitive, high mountain environments by increasing occurrence of liquid water due to melt of snow and ice, and by rapid thaw of permafrost.

Regional scenarios for 2060 were defined according to Swiss climate scenarios CH2011 (Appenzeller et al. 2011). These ones show a rise in summer temperature of up to almost 3 °C for 2060 (Fig. 27.2), and an increase in the number of very hot days from 5 currently to 27 in 2060. As regards precipitation, the development is not clear-cut, which complicates forecasting. Monthly precipitation in summer is likely to decline by as much as 10%, with summertime daily precipitation showing a similar trend. However, in this respect there is a high degree of uncertainty in the CH2011 model data. At lower altitudes, there is likely to be an intensification of convective heavy precipitation, which is an important factor in triggering debris flows. The temperature controls their spatial occurrence while the precipitation defines the magnitude and the frequency of events.

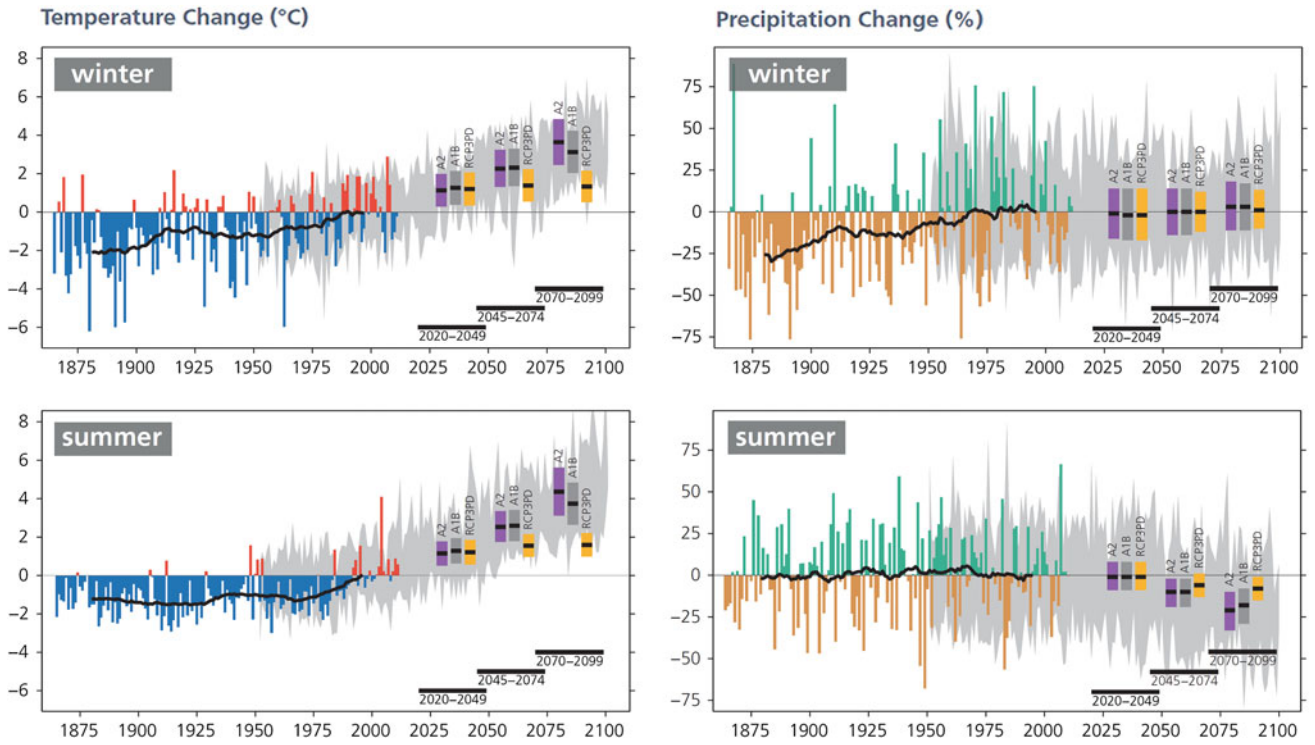

Fig. 27.2 Past and future changes in seasonal temperature and precipitation over northern Switzerland relative to the reference period 1980–2009. The *thin colored bars* display the year-to-year differences with respect to the average. The *black lines* are the corresponding smoothed 30-year average (Appenzeller et al. 2011)

27.3 Impact of Climate on Glaciers and Permafrost

The impact of climate change on glaciation and permafrost was quantified using empirical model approaches (IPCC 2001; Nötzli et al. 2012).

The calculations show, on the one hand, that glacial retreat opens up new debris deposits for erosion processes that form a substantial additional debris input into the further process examinations (Linsbauer et al. 2013; Fischer et al. 2012). On the other hand, relief of the slope stands at the beginning of the process chain of major rockfalls and rock avalanches (Fischer et al. 2012). Here, however, the maturation is in principle a lengthy process, which can occur right at the present time or only decades later.

In permafrost regions, climate change will lead to a gradual disappearance of areas with permanently frozen ground over the next 40 years (Hasler 2011). In regions where permafrost exists, the impact of climate change will be similar to the case of glaciers. The stabilizing effect of permafrost leads to reduced erosion, whereby bodies of permafrost served as a kind of debris deposit (Nötzli et al. 2012). As a result of general warming, permafrost shrinkage increases, which may in turn have the result of making previously frozen material deposits easily mobile.

27.4 Process Chains and Mass Movements

Taking these new boundary conditions into account (moderate climate scenario), the processes likely to cause conflicts and their extent have been simulated using tried-and-tested models: Geotest+Zinggeler for rockfall (Tobler et al. 2009), SLIDISP^{+} (Riner 2009; Liener 2000) and SLIDEPOT (Tobler et al. 2011) for landslides, df-walk (Gamma 2000) and RAMMS for debris flow processes (WSL 2011). In this respect, the following processes and process chains play a key role (Fischer et al. 2012): permafrost degradation and resultant increased availability of debris from moraines, scree and glacier forelands. This results in major material displacements, primarily through debris flows or fluvial transport. Permafrost degradation will further increases rockfall and -avalanches activity (Smith and Burgess 2011) as well as slides of all kinds; all

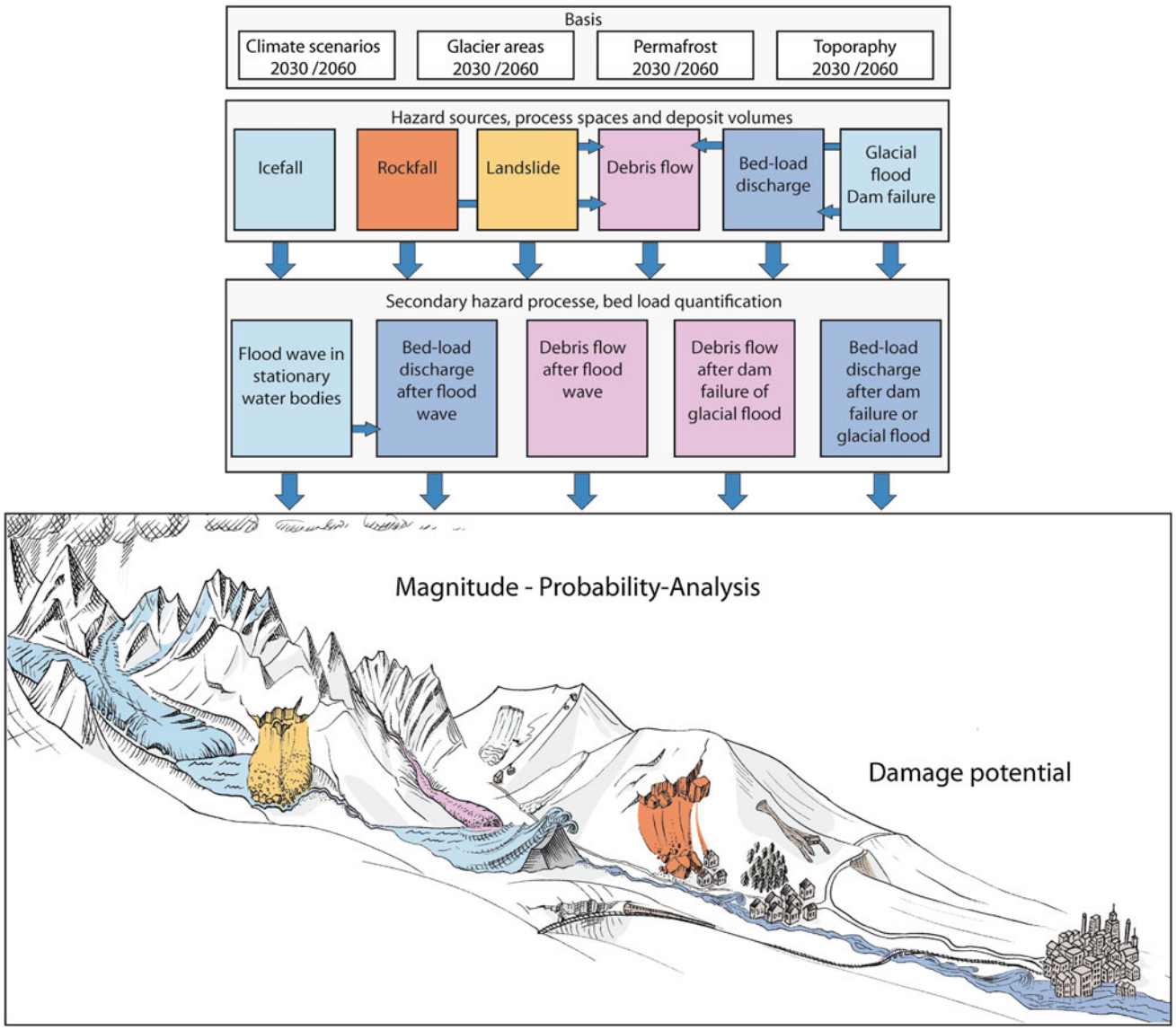

Fig. 27.3 Different primary and secondary processes and their connection induced through climate change in high alpine regions

of them lead to a further increase in debris input (Fig. 27.3).

The process simulations for the year 2060 have been realized with three different probabilities (high, medium, low, Fig. 27.4). The probability classes represent the range of a certain process based on the defined moderate climate scenario. The potential deposition volumes (rockfall and landslide) respectively the maximal flow height (flood wave) and the bedload discharges (debris flow) have been calculated for all processes. At this stage a full uncertainty analysis describes the quality of every single parameter and its importance in the work flow as well as the relevance of all of them.

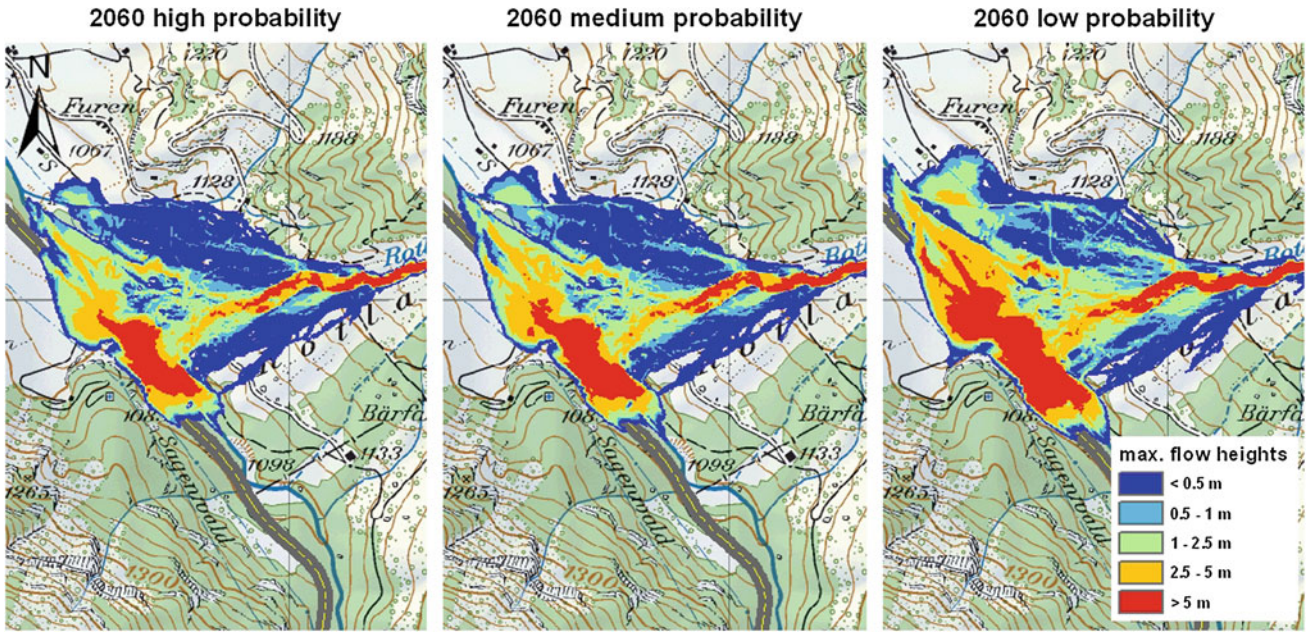

Fig. 27.4 Debris flow modelling results for 2060 for different probabilities

27.5 Conclusion and Outlook

The study provides a basis for answering further-reaching planning, policy and financial questions regarding the evolution of natural hazards in the study area. The results are based on a newly developed methodology calibrated to the well-known events in a small area. The methodology is currently being refined in a further follow-up study, supplemented by glacier lake outburst, flood wave and overbank sedimentation processes, and extended to cover entire Switzerland.

References

Appenzeller C, Bey I, Croci-Maspoli M, Fuhrer J, Knutti R, Kull C et al (2011) Swiss climate change scenarios CH2011. Zurich

Fischer L, Purves RS, Huggel C, Noetzli J, Haeberli W (2012) On the influence of topographic, geological and cryoshperic factors on rock avalanches and rockfalls in high-mountain areas. Nat Hazards Earth Syst Sci 12:241–254

Gamma P (2000) Df-walk—Ein Murgang-Simulationsprogramm zur Gefahrhenzonierung. Bern: Geographica Bernensia G66, Geogr. Inst. Univ. Bern

Gwinner MP (1978) Geologie der Alpen, 2nd edn. Schweizerbart, Stuttgart

Hasler A (2011) Thermal conditions and kinematics of steep bedrock permafrost. Disseration der Universität Zürich, Zürich

Huggel C, Salzmann N, Allen S (2013) High-mountain slope failures and recent and future warm extreme events. In: McGuire B, Maslin M (eds) Climate forcing of geological hazards, 1st edn. Wiley, Chichester

IPCC (2001) Climate change 2001: the scientific basis. Contribution of Working Group I to the third assessment report of the intergovernmental panel on climate change. Cambridge University Press, United Kingdom, New York

Liener S (2000) Zur Feststofflieferung in Wildbächen. Dissertation. Bern: Geographica Bernensia G64, Verlag des Geogr. Instistuts der Universität Bern

Linsbauer A, Paul F, Machguth H, Haeberli W (2013) Comparing three different methods of modelling scenarios of future glacier change in the Swiss Alps. Ann Glaciol 54:241–253

Nötzli J, Gruber S, Böckli L (2012) Permafrostabschätzung im Raum Innertkirchen—Grimselpass: Glaciology, Geomorphodynamics & Geochronology. Departement of Geography, University of Zurich, Switzerland

Rajczak J, Pall P, Schär C (2013) Projections of extreme precipitation events in regional climate simulations for Europe and the Alpine Region. J Geophys Res Atmos 118(9):3610–3626. doi:10.1002/jgrd.50297

Riner R (2009) Geotechnische Analysen von Lockergesteinen zur Modellierung von Rutschdipositionen. Masterarbeit der Universität Bern, Bern

Smith S, Burgess M (2011) Permafrost and climate interactions. An encyclopedia of snow, ice and glaciers. Springer, UK

Tobler D, Graf K, Krummenacher B (2009) Rockfall assessment of natural hazards by 3D-simulation potential. Geophys Res Abs 11, EGU General Assembly 2009

Tobler D, Riner R, Pfeifer R (2011) Runout modelling over large areas with SliDepot. In: Proceedings of 2nd world landslide forum, Rome

Tober D, Kull I, Haehlen N (2012) Hazard management in a Debris flow affected area—the Spreitgraben in Central Switzerland. Extended abstract, GRF/IDRC, Davos

WSL (2011) Klimaänderung und Wasserkraft, Fallstudie KWO, Birmensdorf

Adaptation to Climate Change-Induced Geodisasters in Coastal Zones of the Asia-Pacific Region

28

Do Minh Duc, Kazuya Yasuhara, Mai Trong Nhuan and Nguyen Ngoc Truc

Abstract

Results of recent investigations suggest that climate change tends to accelerate geodisasters. Therefore, adaptation to climate change has rapidly become and urgent issue. In comparison to those examining water disasters, few studies have examined climate change-induced geodisasters. This study aims to focus on climate change-induced geodisasters in various countries of the Asia-Pacific region, especially in Japan and Vietnam. Sea level rise is accounted for about 2 mm/y on average in the region. This amount is much larger in some places due to groundwater extraction. Moreover, we should prepare for the worst case in which climate-induced severe rainfall, wave attacks, storm surges and a great earthquake might take place simultaneously or almost simultaneously with each other in the coastal zone, although this worst case might be very rare. As a possible compound geohazard caused by climate change, we propose solutions with emphasizes on using geosynthetics and ecological engineering measures.

Keywords

Climate change • Geodisaster • Geosynthetics • Ecological engineering • Asia-Pacific region

28.1 Introduction

The Asia-Pacific region includes a series of coastal megacities (Fig. 28.1). Nowadays, the Asia-Pacific's share of global gross domestic production (GDP) predicted to rise from 28 % in 2010 to 44 % in 2035 (Lee and Park 2013). However, Asia has been seriously affected by a number of large-scale natural disasters over the past decades (Natural Disasters Data Book 2011).

D.M. Duc (✉) · M.T. Nhuan · N. Ngoc Truc
Faculty of Geology, VNU University of Science, Vietnam National University, 334 Nguyen Trai, Hanoi, Thanh Xuan, Vietnam
e-mail: ducdm@vnu.edu.vn

K. Yasuhara
Institute for Global Change Adaptation Science, Ibaraki University, Mito, Japan

The paper aims to investigate climate change-induced geodisasters in coastal zones of Asian countries in the Pacific Ocean, excluding small islands and propose adaptation measures through case studies in Vietnam and Japan.

28.2 Climate Change-Induced Geodisasters in the Asia-Pacific Region

Disasters occurring in Asia comprise 39 % of the worldwide total (Kaku and Held 2013). Several geodisasters in the Asia-Pacific region are strongly impacted by climate change.

Sea level rise (SLR) IPCC (2007) indicated a clear trend of SLR worldwide with the average rate of 1.8 mm/y over 1961–2003. In a potential scenario that sea level is rising 1 m in 50 years 10.8 % of Vietnam population will be directly affected (Susmita et al. 2007). The present annual cost of protecting the coasts of Singapore ranges from 0.17 to 3.08 million US$ depending on the SLR scenario. It

G. Lollino et al. (eds.), *Engineering Geology for Society and Territory – Volume 1*,
DOI: 10.1007/978-3-319-09300-0_28,

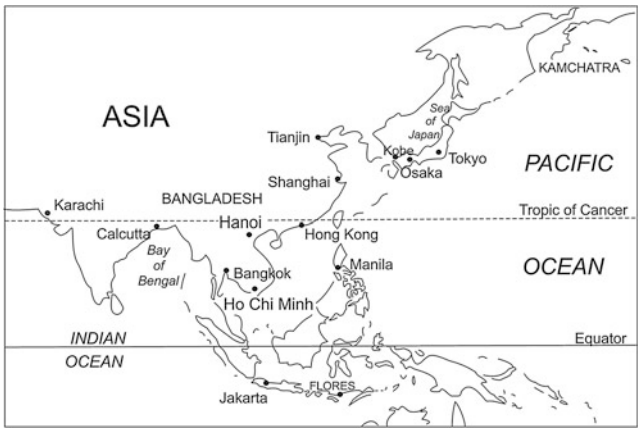

Fig. 28.1 Location of the Asia-Pacific region

will rise to 0.9–16.8 million US$ by 2100 (Ng and Mendelsohn 2005).

Land subsidence Most of the major Asian deltas are now sinking faster than global SLR (Syvitski et al. 2009). Land subsidence was found in more than 90 cities in China by 2005 with the total area of about 90,000 km^2 (Xu et al. 2008). Bangkok city has been seriously subsidized. The rate reached to 120 mm/year in the early 1980s (Phien-weij et al. 2006). Land subsidence in conjunction with a rise in sea level, greatly increases the inundation.

Coastal erosion It be a significant hazard in the region such as in Bangladesh, China, and the Southeast Asia. The increase of erosion rate due to SLR can reach to 0.14–0.31 m/y in the coast of the Red River delta, Vietnam (Duc et al. 2012). Coastal erosion occurs irregularly along the coast of Thailand but an intensification of erosion has been noticed during the past decade (Thampanya et al. 2006).

Saltwater intrusion It is now common problem in deltas and coastal urban areas (Haq and Milliiman 1996). It is as a consequence of one or more of the following factors: relative sea level rise, the excessive pumped abstraction of groundwater from coastal aquifers and impeded flows in rivers due to human activities (Arthurton 1998).

Storm surge and coastal flooding The areas below high tide level and storm surge level (i.e. inundated and flooded areas) are 0.48 and 0.94 % of the total land area of the Asia and Pacific region, respectively (Hay and Mimura 2006). Surges are normally associated with tropical cyclones, thus the incidence of this hazard varies greatly within the Asia-Pacific region. A severe typhoon and flood in 1991 killed 140,000 people in the coastal lowlands of Bangladesh (Arthurton 1998).

Slope disasters Extreme weather events induced by climate changes can cause torrential rainfalls and cloudbursts more flash floods, debris flows and landslides. During 2005–2010, the number of dead and missing was 189, and the economic loss totaled more than 2.8×10^8 yuan (US$4.379 x 10^7) in Southeastern China (Huang and Cheng 2013). The increase in slope disaster risk in Fukuoka by 2050 posed by global warming is 70.6 %, which will reach to 61.43 billion yen/year (Yasuhara et al. 2012a).

Liquefaction Variation of rainfall resulting from climate change raises groundwater levels in inland regions, where rainfall increases. Consequently, liquefaction risk posed by rising groundwater levels increases. Climate change will extend the prone areas to liquefaction risks in the case of an earthquake in the Tokyo Bay coastal zone (Yasuhara et al. 2012a).

28.3 Adaptation Using Conventional Techniques and Locally Available Materials in Vietnam

Instead of conventionally used adaptation against climate change (such as dyke, revetment, groynes, and mangrove forest), use of geosynthetics was proposed and adopted in Vietnam around 1970 (Yasuhara et al. 2012b). From a perspective of cost savings, several measures are useful for reinforcement dykes and embankments, including the usage of locally available materials such as bamboo tree fiber, granular solid waste. Sandwich structure dykes are suitable for construction of dykes using cohesive soils. Therefore, locally available granular materials are promising for the formation of sandwich layers among cohesive soil layers.

The use of only a single countermeasure such as the seadyke is insufficient for long-term protection, particularly against severe weather conditions following storm surges or typhoons. Multiple protection can be proposed as one solution, as presented in Fig. 28.2, which depicts a combination of three countermeasures: an off-shore wave-eating facility, near-shore measures (mangrove forest), and a reinforced dyke using locally available techniques and materials.

28.4 Coastal Protection: Lessons Learned From the Great East Japan Earthquake

Lessons learned from experience with the Great East Japan earthquake are upmost useful to prepare for future severe climate change-induced storm surge. The Great East Japan Earthquake of 2011 posed significant land subsidence along coastal areas triggered by crustal movement. In addition to land subsidence, marked SLR has affected the area. Therefore, this situation is useful for land use planning if we draw variations of land subsidence and SLR over time. Establishment of a long-term monitoring system is necessary. Another necessary issue is construction of

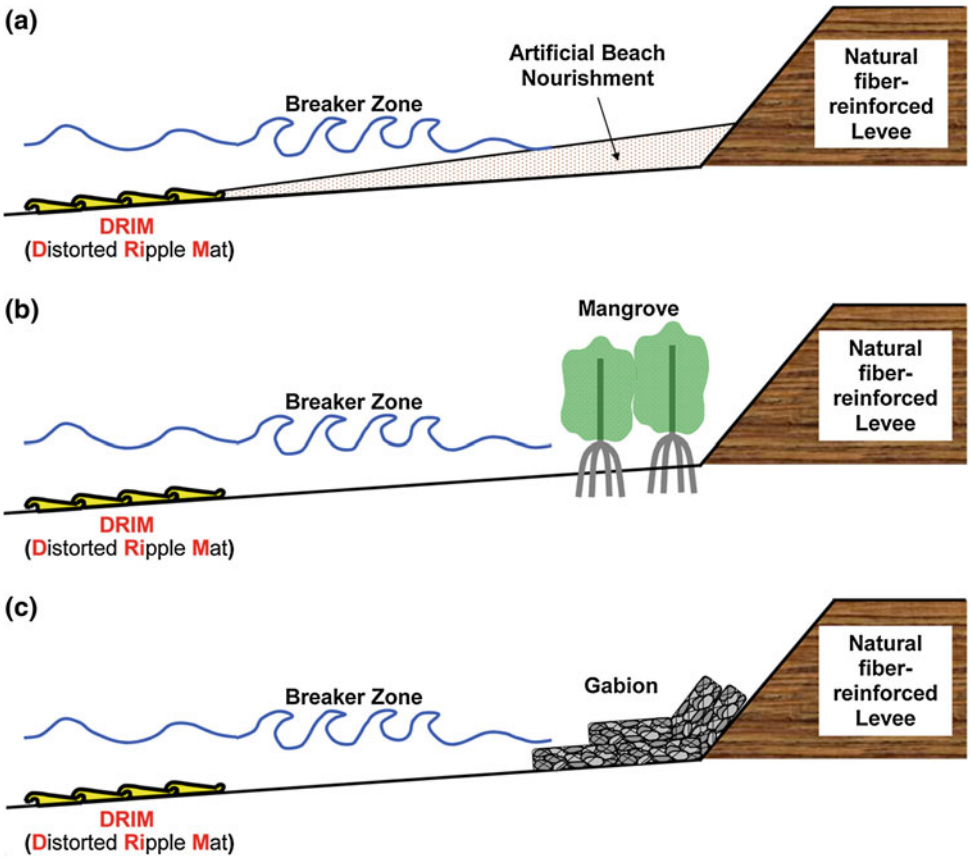

Fig. 28.2 Multiple protection including levees reinforced with naturally available materials **a** Combination with artificial beach nourishment **b** Combination with mongrove plantation **c** Combination with gabion

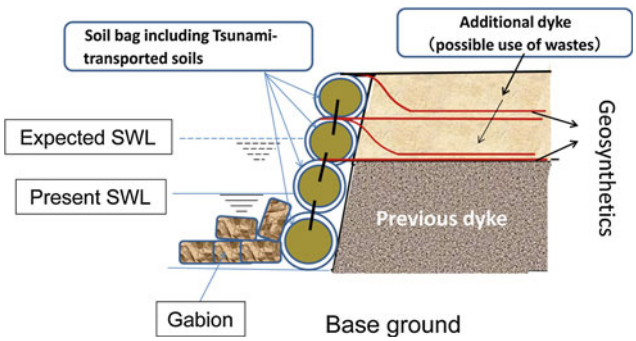

Fig. 28.3 Reinforced seawall using soil bags and geosynthetics

countermeasures against inundation caused by the combined effects of land subsidence and SLR. For successful execution of countermeasures, the authors propose reinforcement techniques combining soil bags with geosynthetics, as presented in Fig. 28.3. The seawalls are reinforced with geosynthetics or other work such as injection of concrete into soil bags. These techniques have been proved in laboratory tests as countermeasures against severe storms (Yasuhara et al. 2012b). They should be combined with other techniques, particularly for use against strong earthquake motions and tsunamis.

28.5 Conclusions

Climate change tends to accelerate geodisasters in coastal zones of the Asia-Pacific region. They are classified as long-term (sea level rise, land subsidence, coastal erosion, saline intrusion) and extreme events (storm surge and coastal flood, slope disasters, liquefaction). Locally available materials can be used as artificial geosynthetics against increasing coastal erosion and inundation attributable to SLR. A combination of hard structures and ecological measures (such as mangrove) can enhance coastal protection in the context of climate change. As lessons from the Great East Japan earthquake and tsunami 2011, geosynthetics combined with soil improvement using cement can be used as adaptive measures against future severe waves and storm surges.

References

Arthurton RS (1998) Marine-related physical natural hazards affecting coastal megacities of the Asia-Pacific region—awareness and mitigation. Ocean Coastal Manage 40(1998):65–85

Duc DM, Nhuan MT, Ngoi CV (2012) An analysis of coastal erosion in the tropical rapid accretion delta of the Red River, Vietnam. J Asian Earth Sci 43:98–109

Haq BU, Milliman JD (1996) Coastal vulnerability: hazards and strategies. In: Milliman JD, Haq BU (eds) Sea level rise and coastal subsidence. Kluwer Academic Publishers, Dordrecht, pp 357–364

Hay J, Mimura N (2006) Supporting climate change vulnerability and adaptation assessments in the Asia-Pacific region: an example of sustainability science. Sustainability Sci 1:23–35

Huang Y, Cheng H (2013) The impact of climate change on coastal geological disasters in Southeastern China. Natural Hazards 65(1):377–390

IPCC (2007) Climate change 2007: synthesis report

Kaku K, Held A (2013) A space-based disaster management support system in the Asia-Pacific region. Int J Dis Risk Red (2013). http://dx.doi.org/10.1016/j.ijdrr.2013.08.004

Lee M, Park D (2013) Asia's energy challenge. Asian development outlook 2013. Manilla Asian Development Bank, pp 53–116

Natural Disasters Data Book (2011) Analyzed by Asian disaster reduction center by CREDEM-DAT database, July 2012. http://www.adrcasia/publications/databook/DB2011_e.html

Ng WS, Mendelsohn R (2005) The impact of sea level rise on Singapore. Environ Develop Econom 10:201–215

Phien-wej N, Giao PH, Nutalaya P (2006) Land subsidence in Bangkok, Thailand. Eng Geol 82(2006):187–201

Susmita D, Laplante B, Meisner C, Wheeler D, Yan J (2007) The impact of sea level rise on developing countries: a comparative analysis. World Bank Policy Research Working Paper 4136, February 2007

Syvitski JPM, Kettner AJ, Overeem I, Hutton EWH, Hannon MT, Brakenridge GR, Day J, Vorosmarty C, Saito Y, Giosan L, Nicholls RJ (2009) Sinking deltas due to human activities. Nat Geosci 2(10):681–686

Thampanya U, Vermaat JE, Sinsakul S, Panapitukkul N (2006) Coastal erosion and mangrove progradation of Southern Thailand. Estuarine, Coastal and Shelf Sci 68(2006):75–85

Xu YS, Shen SL, Cai ZY, Zhou GY (2008) The state of land subsidence and prediction approaches due to groundwater withdrawal in China. Natural Hazards 45(1):123–135

Yasuhara K, Komine H, Murakami S, Chen G, Mitani Y, Duc DM (2012a) Effects of climate change on geo-disasters in coastal zones and their adaptation. Geotextiles Geomembranes 30(2012):24–34

Yasuhara K, Van TC, Duc DM (2012b) Geosynthetics-aided adaptation against coastal instability caused by sea-level rise. Proc. Geosynthetics Asia 2012, Bangkok, Thailand, December 2012

The Alluvial Fan Risk Assessment in Piedmont (NW, Italy)

29

Dario Fontan, Antonia Impedovo, Claudio Costa, Walter Giulietto, Davide Marchisio and Ilaria Stringa

Abstract

The alluvial fans risk assessment is a very important step for territorial planning of mountainous areas that allows to design preventive protection works and identify actions of civil protection. This work represents an action of the Strategic project Risknat performed by the Piedmont Region to focus on the development of new methods and operational tools to estimate the risk assessment on alluvial fans in Piedmont (NW Italy). Based on geomorphological and geological data, land cover, historical information and climatic factors (all deriving from 1:100,000 to 1:25,000 scale GIS maps and alphanumerical database), the hazard of 893 alluvial fans has been calculated by applying the method proposed by the "Autorità di bacino del fiume Po", implemented with the catchments basin hazard index (HIcb) calculated with the Alluvial Fan Hazard Evaluation procedure (AFHE). The risk has been evaluated considering the value of human systems and environmental themes, all deriving from 1:10,000 scale GIS maps. AFHE methodology permits the evaluation of the Disequilibrium Index (DI), a useful parameter for the understanding of the debris supply, the rainfall threshold, the channel recharge rate and the catchments mostly influenced by the climate changes. The results are useful to identify the most hazardous situations and to provide additional information for land management. Finally, results need to be verified on a local scale through further study that takes in account in detail the characteristics of each catchment-alluvial fan system.

Keywords

Alluvial fans • Hazard risk • Climate change • Land management

29.1 Introduction

The alluvial fan risk assessment is necessary to bring out risky situations that need mitigation works and civil protection interventions in the urban and spatial policy design of the alpine valleys.

D. Fontan (✉) · W. Giulietto · D. Marchisio · I. Stringa
SEA Consulting S.R.L., C.so Bolzano, 14, 10121 Turin, Italy
e-mail: fontan@seaconsult.eu

A. Impedovo · C. Costa
Regione Piemonte, Direzione Opere pubbliche, difesa del suolo, economia montana e foreste, C.so Bolzano, 44, 10121 Turin, Italy

The complexity of the expected natural processes and of the human system makes it difficult to choose the tools to define the hazard, namely the probability of occurrence, within a specific period of time in a given area, of a potentially damaging natural process, the vulnerability, that is the degree of a loss to a given element at risk, or set of such elements resulting from the occurrence of a flood with a given intensity", and the elements at risk (exposure), or receptors, that is people, properties and goods that can be lost, injured or damaged during an event (UNDRO 1980).

These tools are a function of the scale of study, of the quality and detail of spatial information available, and especially of the type of risk assessment objectives (urban planning, insurance, civil protection, etc.).

G. Lollino et al. (eds.), *Engineering Geology for Society and Territory – Volume 1*,
DOI: 10.1007/978-3-319-09300-0_29,

An experimental method using the available GIS territorial data of the public administration has been developed for the quick assessment of the risk of alluvial fans in Piedmont (Fig. 29.1), as part of the Strategic RiskNat project (Volet B, Action 4.1) of the "Alcotra EU Program".

The risk on 893 alluvial fan, chosen from the ARPA Piemonte catalogue (http://www.dati.piemonte.it/catalogodati/dato/100506-.html), was calculated with the method proposed by "Autorità di bacino del fiume Po" (hereafter AdbPo) with some changes that consider the GIS data available. The hazard assessment is done by defining some variables, depending on the geology, geomorphology, vegetation of the catchment-basin, type, magnitude and energy of the expected process on the alluvial fan, the flood occurrences and the presence and functionality of any mitigation work. The methodology takes in account the hazard index of the catchment-basin (HIcb) and the Total Probability Index—TPI) defined using the Alluvial Fan Hazard Evaluation (hereafter AFHE) (Fontan et al. 2004; Fontan and Murgese 2007) (Fig. 29.2).

In the AFHE method the catchment-basin is considered as a "dynamic system" resulting from natural and human-related processes. The hazard index of the catchment-basin (HIcb) is the product between the Total Probability Index,

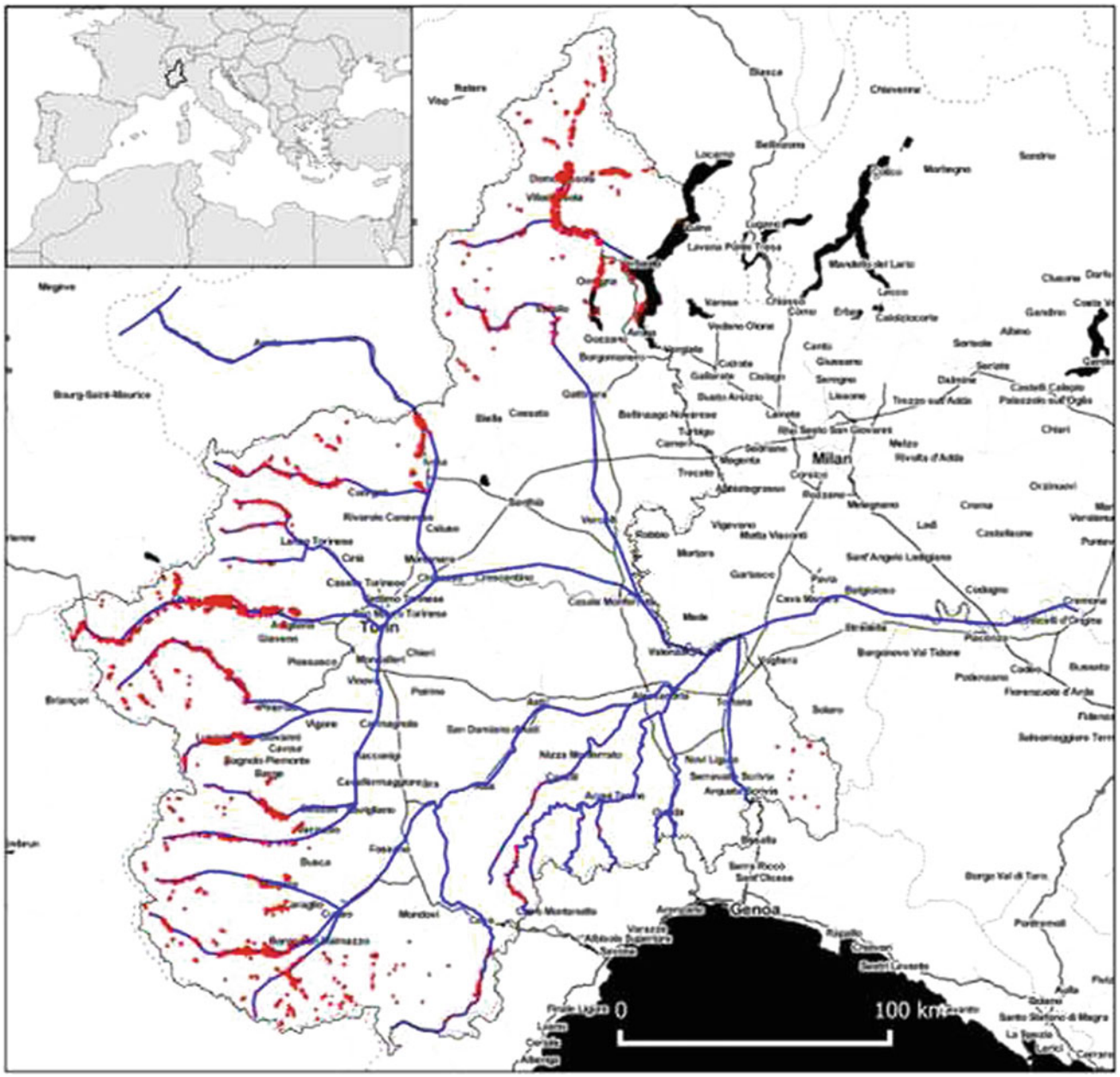

Fig. 29.1 Distribution of the 893 studied alluvial fans

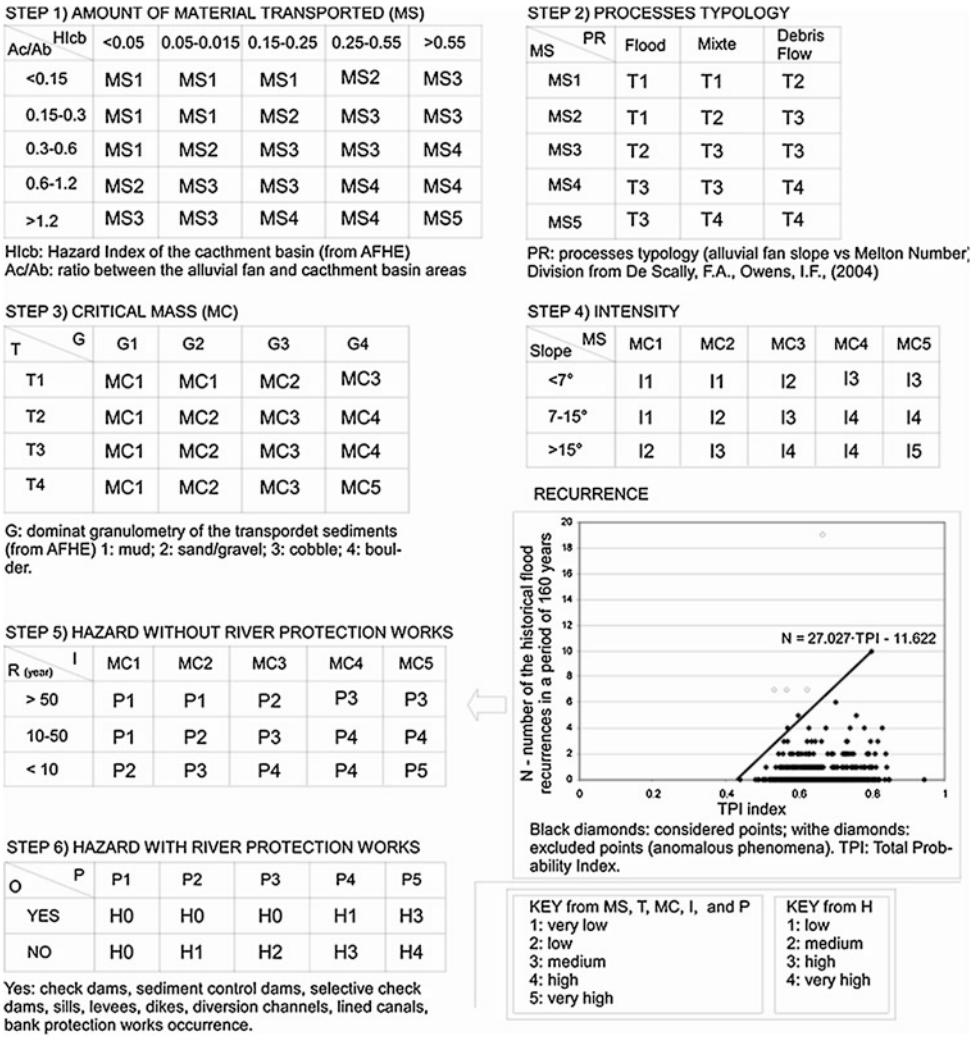

Fig. 29.2 Matrices for the hazard (H) calculation. Steps 1–6

the mean value of the hill-slope tendency to deliver sediments to the channels (PIslo index) and their capability to transfer this material to the alluvial-fan apex (PIch index), and the average of available sediments (Mm), normalized to 10 m (Mmax). These indexes derive from the combination of weighted GIS thematic maps related to geomorphological, geological and environmental factors (land use, land cover), climate and the amount of available sediments.

$$HI_{cb} = \left(\frac{\mathrm{PI_{slo}} + \mathrm{PI_{ch}}}{2}\right) \cdot \left(\frac{\mathrm{M_m}}{\mathrm{M_{max}}}\right)$$

$$TPI = \left(\frac{\mathrm{PI_{slo}} + \mathrm{PI_{ch}}}{2}\right)$$

HIcb values range between 0 and 1.

PIslo and PIch permit to calculate the disequilibrium index DI (which ranges from 0 to 1). The disequilibrium index (DI) allows determining the relationship between the propensity of the slope to produce material and the one of the channels to remove it.

29.2 Hazard Evaluation

The hazard evaluation is done through the estimation of some parameters about the amount of material that might be transported, energy transport, physiographic characteristics of the catchment, the event recurrence rate and the presence of mitigation works. The hazard is assessed by means of double entry tables and consists in six steps (Fig. 2.1).

The relation involving the HIcb index and the ratio between the fan and basin area (Ac/Ab) allows the evaluation of the amount of transported material (MS) (step 1). The ratio Ac/Ab simply expresses the propensity of the basin to mobilize and transport debris to the alluvial fan.

The magnitude of the prevailing process, (T) is defined by the relation between MS and the type of transport resulting from the diagram "Melton index—slope of the fan" that allows to discriminate flood, debris-flow and mixed flow (De Scally and Owens 2004) (step 2).

Table 29.1 List of territorial information (Economic, Environmental and Social) and the related weights assigned (0: no weight; 0.25: low; 0.50: medium; 0.75: high; 1: very high) and the final value normalized to the maximum value (3.00)

Themes	Economic	Environment	Social	Normalized values
Highways	1	0	0.75	0.583
National and regional roads	0.75	0	0.75	0.500
Local roads	0.5	0	0.5	0.333
Minor roads	0.25	0	0	0.083
Rails	1	0	0.75	0.583
Bridges	1	0	0.5	0.500
Houses, inhabitants, schools	1	0	1	0.667
Police, military buildings, hospitals	1	0	1	0.667
Environmental and architectural heritages, archaeological sites	0.5	0.75	0.25	0.500
Natural parks	0.5	1	0.25	0.583
Water supply network, water wells Water springs	0.5	0	0.25	0.250
Sewerage, sewage treatment plants	0.5	0.75	0.25	0.500
Pipelines (oil and CH_4)	0.5	0.75	0.25	0.500

The critical mass (MC), that provides a first estimate of the expected composition of transported material, is calculated by crossing the type of movement (T) and the estimated soil classification (G) of the dominant process, depending on the lithology of the basin (step 3). The intensity of the dominant process (I) is given by the combination of the critical mass (MC) and the fan slope (S) (step 4).

The relationship between the recurrence (R) and the intensity (I) determines an index which expresses the probability of occurrence (P) (step 5). The recurrence derives from the flood frequencies (on 160 year) of 405 alluvial fans of the historical database of the EU project Interreg IIIA "Prinat". The frequency of occurrence of the others 488 fans has been deduced from the relation between the number of events and the TPI index (Total Probability Index, the mean value of the propensity indexes of the channel and the slope).

Finally, the relationship between the danger of occurrence (P) and the presence of mitigation works sets the final hazard (H) (step 6).

29.3 Climate Change

Many works that develop the climate models at regional and global scale in order to obtain long term prediction have been realizing for 40 years (IPCC 2013). Nevertheless, the large net grid used in the Global Climate Models (GCM) doesn't permit a good compliance with local scale. The statistical downscaling methodology (Pal et al. 2007) permits to improve the global model to regional scale (Regional Climate Models). The RCM models have a good correspondence with the observation data and a greater ability to predict the extreme events. In the alpine area, all the RCM models referred to the 1990–2010 forecast indicate an increase of the average annual temperature of 3–4°, a reduction of the mean annual rainfall (Faggian and Giorgi 2009), with an increase of the periods without rainfall of 20–50 % with an intensification of extreme rainfalls (Allamano et al. 2010; Ferrara 2002 in Murgese et al. 2011).

The AFHE disequilibrium index (DI) permits to evaluate the catchments that display a certain degree of sensitivity concerning the increase of extreme rain falls, due to the climate change. An high DI indicates severe erosion in basins with high rainfall thresholds that involves a long recurrence time (few events with high magnitude); the hazard depends on the increase of extreme events. Low DI indicates basins with weak erosive trend, low rainfall thresholds and hydrographic network frequently cleaned by many events of low magnitude; the catchment basin is not very sensitive to climate change.

Calculations indicate that about two-thirds of the basins studied were found to be sensitive to climate change.

29.4 Risk Calculation

According to Italian laws, the risk (R) of the alluvial fan is given by the product of the hazard (H), the value of elements at risk (E) and their vulnerability (V) (Decree of the President of the Council of Ministers—DPCM—29.09.1998 (http://www.protezionecivile.gov.it/cms/attach/editor/dpcm_29_09_98.pdf Accessed 06 may 2014).

Table 29.2 Results and risk classes (from PAI—hydrogeological master plan of the Po River). The classes range is determinate by the method of Jenks (1967). *n* class population over 893

Classes	Values (H·E)	Results		Description
		n	%	
R1 low	<0.0447	613	68.6	Possible social and economical damages
R2 medium	≤0.153	241	27.0	Possible minor damages to buildings and infrastructures that do not affect the people safety, the practicability of buildings and the development of social-economic activities
R3 high	≤0.440	32	3.6	Possible problems for people safety, functional damages to buildings and infrastructures, their consequently unavailability and the interruption of social-economic activities, cultural heritage damages
R4 very high	>0.440	7	0.8	Possible deaths and severe injuries for people, severe damage for buildings, infrastructures, cultural heritage and the lost of social-economic activities

The evaluation of the elements at risk considers many elements relevant to human life and activities, indicated in Table 29.1. The index of each theme is given by the normalized value of the weights assigned to the economic, social and environmental components multiplied by the respective quantity (number, m, m^2) in the alluvial fan. The available spatial data did not allow an easy calculation of vulnerability, which always needs a unit value. The results of the risk analysis are reported in Table 29.2.

29.5 Conclusion

The alluvial fan risk calculation methodology is the first attempt that uses a re-traceable and defined algorithm on the base of the available data on a regional scale. The results are available on the website http://www.risknet-alcotra.org/rna/index.cfm/b-4.html and are useful to identify risk situations and to provide the general government, local authorities and freelancers with additional information for regional and provincial spatial planning and also for the preparation of urban and spatial policy design or emergency plan.

The methods that consider the number of inhabitants in the sparsely populated alluvial fans, can lead to the underestimation of risk. This is best seen in the Garin alluvial fan (Villar Pellice, Pellice Valley) that, despite a high hazard, has a low risk (R1) because the elements at risk are low. The calculated risk level is not the same risk perceived from the local population and mass media because of the debris-flow that occurred in May 2008 and resulted in 4 deaths, the destruction of three buildings and the interruption of the main road (Arattano et al. 2010).

The disequilibrium index (DI) let us to understand that the hazards (H) of two-thirds of the studied basins are sensitive to climate change. This remark must be considered in the future urban and spatial policy design of the alluvial fans.

The disequilibrium index (DI) let us to understand that the hazards (H) of two-thirds of the studied basins are sensitive to climate change. This remark must be considered in the future urban and spatial policy design of the alluvial fans.

References

Allamano P, Bartolini E, Claps P, Laio F (2010) In: XXXII Convegno Nazionale di Idraulica e Costruzioni Idrauliche. Palermo, 14–17 settembre 2010

Arattano M, Conte R, Franzi L, Giordan D, Lazzari A, Luino F (2010) Nat Hazards Earth Syst Sci 10:999

De Scally FA, Owens IF (2004) Earth Surf Proc Land 29(3):311

DPCM 29 settembre 1998—Atto di indirizzo e coordinamento per l'individuazione dei criteri relativi agli adempimenti di cui all'art. 1, commi 1 e 2, del decreto-legge 11 giugno 1998, n.180 (G. U. 5 gennaio 1999 n.3). http://www.protezionecivile.gov.it/cms/attach/editor/dpcm_29_09_98.pdf. Accessed 06 may 2014

Faggian P, Giorgi F (2009) Clim Change 96(1–2):239

Fontan D, Murgese DS (2007) In: 4th international conference on debris flow hazard and mitigation, Chengdu, China

Fontan D, Stringa I, Dematteis A (2004) In: La Difesa del territorio abitato da piene, colate detritiche, valanghe e frane. Riva del Garda, Trento, Italy, IX, pp 55–66

IPCC Climate Change (2013) In: Stocker TF, Qin D, Plattner GK, Tignor M, Allen SK, Boschung J, Nauels A, Xia Y, Bex V, Midgley PM (eds) The physical science basis. Contribution of working group I to the fifth assessment report of the intergovernmental panel on climate change. Cambridge University Press, p 1535

Jenks GF (1967) Int Yearbook Cartography 7:186

Jiao Y, Hudson JA (1995) Int J Rock Mech Miner Sci Geomech 32:491

Murgese DS, Fontan D, Dematteis N, Filippi ML, Dematteis A (2011) In: Polemio M (ed) Le modificazioni climatiche e i rischi naturali, Bari

Pal JS, Giorgi F, Bi X, Elguindi N, Solmon F, Grimm A, Sloan L, Syed F, Zakey A (2007) Bull Amer Meteor Soc 88:1395

Office of the United Nations Disaster relief Co-ordinator (UNDRO) (1980) Natural disasters and vulnerability analysis, report of expert group meeting (1980). http://www.preventionweb.net/files/resolutions/NL800388.pdf. Accessed 05 may 2014

Effects of Soil Management on Long-Term Runoff and Soil Erosion Rates in Sloping Vineyards

30

Marcella Biddoccu, Stefano Ferraris, Francesca Opsi and Eugenio Cavallo

Abstract

Runoff and soil losses caused by natural rainfall events were monitored over a 12-year period in an experimental vineyard located in Alto Monferrato, a vine-growing area of Piedmont (NW Italy). The measurements were carried out on three plots, each of which was managed with a different inter-row soil management practice: conventional tillage (CT), reduced tillage (RT) and controlled grass cover (GC), respectively. The annual average runoff coefficients were 17.4 % in CT and 15.3 % in RT, while in the GC plot it was limited to 10.3 %. The highest soil losses were observed for the tilled plots, with average yearly erosion rates of 10.4 and 24.8 Mg $ha^{-1}year^{-1}$ in the CT and RT plots. Only 2.3 Mg $ha^{-1}year^{-1}$ were recorded for GC treatment. The protective role of grass cover will be more and more relevant, taking in account climate changes that predict increase in rainfall intensity and erosivity. The evaluation of the effect of different conservation measures on the runoff and soil erosion, in relation with future climate scenarios, would be a useful to support soil management decisions in vineyards.

Keywords

Soil erosion • Runoff • Soil management • Vineyard

30.1 Introduction

Soil erosion is one of the eight soil degradation processes identified by the European Commission in the "Thematic Strategy for Soil Protection" (CEC 2006). Although this process occurs naturally, agriculture has increased soil erosion around the world with greater extent until today, with conventional and mechanized agricultural practices that have gradually compromised the soil quality and fertility (Montgomery 2007). Soil erosion directly causes fertility decrease, producing nutrient losses and reducing organic carbon stock. It is frequently related to other degradation processes like soil compaction and low soil water storage capacity. Furthermore the off-site impacts of soil erosion are relevant: water-courses pollution from fertilizers and pesticides, supply of sediments into rivers and reservoirs, and muddy floods (Boardman 2010) represent the undesirable consequences of the soil erosion process, which role is underestimated among natural hazards.

Cerdan et al. (2010) estimated a mean erosion rate of 2.3 t ha^{-1} $year^{-1}$ for Italy, corresponding to 12.5 % of the total European erosion. Measured data showed that in the Mediterranean region the highest runoff rates are related to vineyard land use (Maetens et al. 2012). The soil management practices adopted in hilly vineyards (such as land leveling works during the vineyard plantation, orientation of the vine-rows along the slope, tillage and maintenance of

M. Biddoccu (✉) · F. Opsi · E. Cavallo
Institute for Agricultural and Earthmoving Machines, Italian National Research Council, Strada delle Cacce 73, 10135 Turin, Italy
e-mail: m.biddoccu@ima.to.cnr.it

M. Biddoccu · S. Ferraris
Interuniversity Department of Regional and Urban Studies and Planning, Politecnico e Università di Torino, Viale Mattioli 39, 10125 Turin, Italy

G. Lollino et al. (eds.), *Engineering Geology for Society and Territory – Volume 1*,
DOI: 10.1007/978-3-319-09300-0_30,

bare soil in the inter-rows) play a primary role in determining high runoff and soil erosion rates (Tropeano 1984; Ramos and Martinez-Casasnovas 2007; Blavet et al. 2009). The runoff and soil erosion processes are deeply related to climate, especially to rainfall intensity and precipitation pattern, and the antecedent soil moisture content and soil surface conditions (Biddoccu et al. 2013, 2014).

Evaluation of actual and future erosion rates under a changing climate and land use conditions is a fundamental step in soil and water conservation and environmental planning and assessment. Direct measurements and modeling represent the essential tools available in drawing the present and future soil erosion scenarios. In this paper results obtained from a 12-year monitoring period are presented. Data includes direct measurements of rainfall, runoff and soil erosion in three vineyard plots with different inter-row soil management.

30.2 Materials and Methods

30.2.1 Description of the Experimental Site

The monitored vineyard is part of the "Tenuta Cannona" Experimental Vine and Wine Centre of Regione Piemonte, which is located in the "Alto Monferrato" vine-growing region (Piedmont, NW Italy), at an average elevation of 290 m asl. The pluviometric pattern is alpine sublitoranean, with an average annual precipitation of 965 mm at the Ovada weather station (1951–1990). The mean annual temperature measured at Alessandria during the same period of observation was 12.6 °C (Biancotti et al. 1998).

The three experimental vineyard plots lie adjacent to each other on a hillslope with SE aspect and average slope of 15 %. Soil is classified as *typic Ustorthents, fine-loamy, mixed, calcareous, mesic* (Soil Survey Staff 2010), with a loam texture (33.1%, 44.4%, 22.5% for sand, silt and clay fraction, respectively) at time of vines plantation, in 1998.

Each plot is 1,221 m^2 (74 m long and 16,5 m wide), with rows aligned along the slope. During the period of observation, a different cultivation technique was adopted on the soil between the vine rows of each plot: conventional tillage (CT), which was carried out with a chisel at a depth of about 0.25 m; reduced tillage (RT), with a rotary cultivator to a depth of 0.15 m; controlled grass cover (GC), with spontaneous grass controlled by mowing during the year. Tillage and mowing were usually carried out twice a year, in spring and autumn, or in spring and summer. Under the vine-rows of all the three plots, grass was controlled by chemical weeding in spring.

Each plot was hydraulically bounded. Runoff and sediments were collected at the bottom of each plot by a channel. Each drain was connected to a sedimentation trap and then to a tipping bucket device to measure the runoff discharge. A portion of the runoff-sediment mixture was sent to a sampling tank. From 2000 to 2011, after each rainfall event producing runoff higher than 0.01 mm in every plot, runoff volumes were recorded. A 1.5 L sample of runoff-sediment mixture was collected from each sampling tank, then oven-dried and weighted in order to determine the mean sediment concentration and thus the amount of sediment transported by overland flow. Sediments deposited along drains and in the sedimentation traps were collected to obtain the total soil losses due to each event. Resulting precision of the measurements was 0.1 Mg $ha^{-1}year^{-1}$. Hourly rainfall measurements were recorded by a rain-gauge station placed at about 200 m from the plots. Rainfall characteristics were calculated from the data recorded by the rain-gauge for each rainfall event. Detailed information about climate, topography, soil characteristics, cropping, soil management are also available for the experimental plots.

Table 30.1 Mean annual values for runoff (RO_{mean}), runoff rates (RC_{mean}, obtained from the ratio between runoff and rainfall), soil losses calculated from the dataset for the three plots (CT, RT and GC)

	CT	RT	GC
RO_{mean} (mm $year^{-1}$)	167.32	143.19	99.09
RC_{mean} (%)	17.4	15.3	10.3
SL_{mean} (Mg $ha^{-1}year^{-1}$)	10.4	24.8	2.3

30.3 Results and Discussions

30.3.1 Runoff

The dataset includes 219 rainfall events that produced runoff in the period 2000–2011. The mean annual runoff rates were respectively 17.4 and 15.3 % for the CT and RT plots, meanwhile it was reduced to 10.3 % with the adoption of permanent grass cover in the inter-rows (Table 30.1).

The RT treatment resulted in a slight reduction of runoff with respect to CT. The presence of herbaceous cover limited the runoff from the GC plot during the entire period of observation, with greater efficiency from the fourth year onwards (Fig. 30.1). Blavet et al. (2009) also observed lack of efficacy of green cover during first years of installation, with unexpected high runoff in grassed vine.

The 12-year average runoff coefficients measured in the three plots were higher than the mean value of 7.4 %, which was calculated from 123 plot-year measurements in European vineyards managed with different techniques by Maetens et al. (2012). Higher runoff rates measured in the Cannona vineyard are likely due to specific soil properties, topography (especially slope gradient) and vineyard management (rows along the slope, mechanization). However,

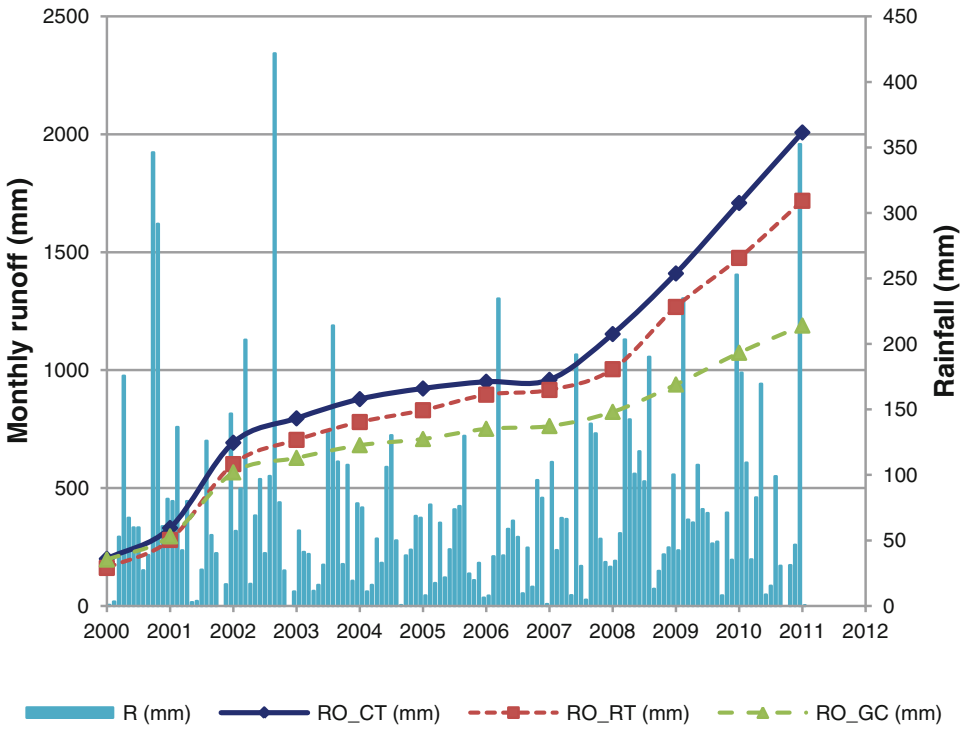

Fig. 30.1 Monthly rainfall (*R*) and cumulative annual runoff (*RO*) for the three vineyard plots (*CT*, *RT* and *GC*), measured in the period 2000–2011

GC assured a 41 % total reduction of water losses during the observation period, with respect to CT.

30.3.2 Soil Losses

The protective role of grass cover is even more evident considering mean annual soil losses (Table 30.1), that ranged from 2.3 Mg ha^{-1} year^{-1} for the GC vineyard to 24.8 Mg ha^{-1} year^{-1} for the RT plot. The yearly soil loss rate was 10.4 Mg ha^{-1} year^{-1} for CT. The soil losses recorded in each plot were higher than the tolerable soil erosion rates proposed for Europe by Verheijen et al. (2009), ranging from 0.30 to 1.4 Mg ha^{-1} year^{-1}. The erosion rate observed in the CT plot was slight lower than the mean weighted erosion rate of 12.2 Mg ha^{-1} year^{-1}, that was calculated from a European data-base including 1,350 plot-months measures in vineyards without conservation techniques (Cerdan et al. 2010). The use of RT caused an increase of soil losses, especially from 2005 onwards (Fig. 30.2). Rotary cultivator tends to break up soil clods into smaller sizes, more susceptible to breakdown with respect to soil treated with chisel. After some years, the use of rotary cultivator in RT likely resulted in changes of the soil properties, with a decrease of aggregate stability and organic content in the topsoil, as Hajabbasi and Hemmat (2000) observed in a clay-loam soil. Thus, the observed increase in soil losses is consistent with results obtained from Bharthès and Roose (2002): they reported that runoff rate and soil loss were negatively correlated with topsoil aggregate stability, especially on vineyard hillsides.

The adoption of grass cover in the vineyard reduced by 78 and 91 % the amount of soil lost during 12 years with respect to the CT and RT soil managements. The grass cover showed the best effectiveness in reducing soil losses in summer, especially during high-intensity (and high-erosive) storms. An example was the highest erosion event, which was the storm that occurred in August 2002, when 63.4 mm fell in 5.3 h, with a maximum 30-min rainfall intensity of about 75 mm h^{-1}. It occurred just 6 days after the execution of tillage operations, producing soil loss higher than 20 Mg ha^{-1} in the tilled plots, while in the GC plot the soil loss was 1.1 Mg ha^{-1}.

As reported by Giorgi and Lionello (2008), climate change projections suggest that the Mediterranean will be subjected to increasingly warmer conditions, with a pronounced decrease in precipitation, especially in the warm season, except for the northern Mediterranean areas in winter. In the future precipitation scenario the overall substantial decrease in the summer mean precipitation will be not accompanied by a corresponding decrease in the intensity of events, but rather a decrease in their frequency. In particular, the frequency of extreme summer precipitation events will increase over large regions of the Mediterranean. On a yearly basis, a prevailing increase in precipitation extremes over the Mediterranean was found by the cited authors, particularly over and around the Alpine region. Rainfall erosivity is strongly related to rainfall intensity, and it is usually

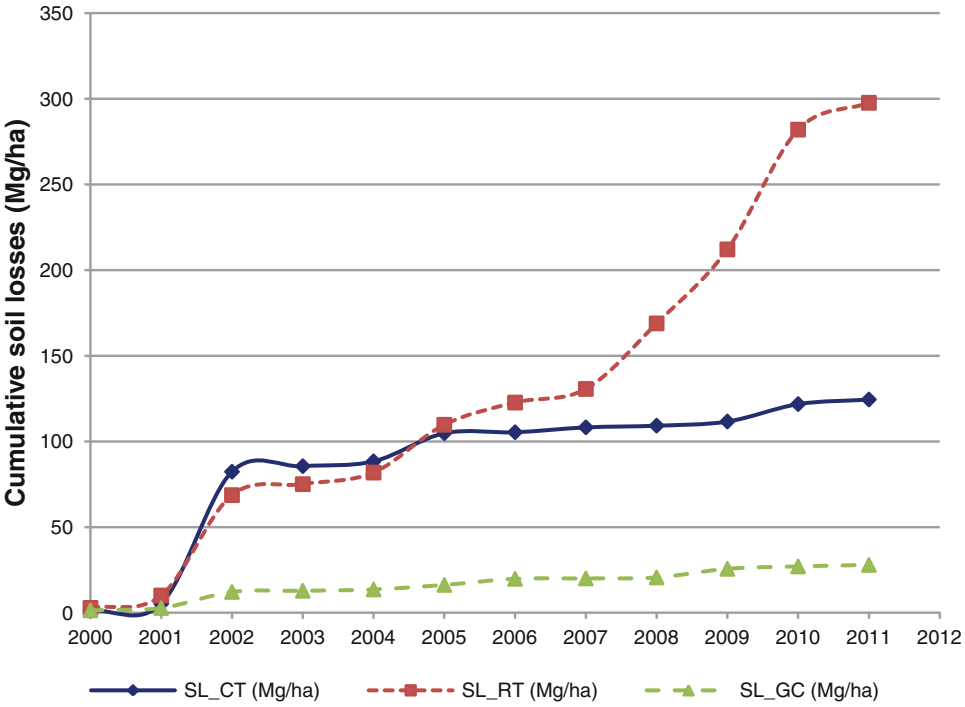

Fig. 30.2 Cumulative annual soil losses (*SL*) measured in the period 2000–2011 from the three vineyard plots (*CT*, *RT* and *GC*)

expressed by means of the USLE/RUSLE R factor, which is calculated from the EI_{30} index (Wischmeier 1959). The adoption of cover crop in vineyards will have a fundamental role in soil protection against erosion, in consequence of the predicted increase of rainfall intensity and erosivity. On the other side, as shown by Celette and Gary (2013), the use of permanent cover crop in vineyards in a water-limited environment generates both water and nitrogen stress to grapevine. In the vineyard numerous planting and management decisions have the potential to provide adaptive capacity to the predicted climate changes (Keller 2010), as it will impact not only on temperature and rainfall distribution. Moriondo et al. (2013) showed that a progressive increase in temperature and dryness for the future periods outlines a potentially radical change in the area that is suitable for cultivating grapevines, with a progressive shift of existing grapevine cultivated area to north–northwest.

30.4 Conclusions

The data collected over a 12-year period in the "Tenuta Cannona" experimental vineyard showed that the use of permanent grass cover in the inter-rows reduces runoff and especially soil losses. The role of grass cover in protecting will be more and more relevant, taking in account climate changes that predict increase in rainfall intensity and erosivity. Nevertheless, cover crops also compete with grapevine for soil resources.

The evaluation of the effect of different conservation measures on the runoff and soil erosion, in relation with future climate scenarios, would support soil management decisions in vineyards. The "Tenuta Cannona" dataset will be useful in the calibration of model for runoff and erosion estimation. The validation and application of the WEPP model (Nearing 1989) at plot scale is currently in progress by means of the available measurements related to climate, slope, soil and cropping/management. Then the WEPP model could be effectively applied in order to evaluate the in-site and off-site effects of soil management on the runoff and soil erosion in sloping vineyards, in relation with different conservation measures and future climate scenarios.

Acknowledgments This research was funded by the "Centro Sperimentale Vitivinicolo Regionale Tenuta Cannona" and the Regione Piemonte—Office for Agricultural Development (research projects titled "Erosione del suolo: confronto tra inerbimento e diverse modalità di lavorazione del terreno, a rittochino e di traverso" and "Tutela del suolo e delle acque superficiali").

References

Bharthès B, Roose E (2002) Aggregate stability as an indicator of soil susceptibility to runoff and erosion; validation at several levels. Catena 47:133–149

Biancotti A, Bellardone G, Bovo S, Cagnazzi B, Giacomelli L, Marchisio C (1998) Distribuzione Regionale di Piogge e Temperature. Collana Studi Climatologici del Piemonte, vol 1. Regione Piemonte, Torino

Biddoccu M, Ferraris S, Cavallo E, Opsi F, Canone D, Previati M (2013) Hillslope Vineyard rainfall-runoff measurements in relation to soil infiltration and water content. Procedia Environ Sci 19:351–360

Biddoccu M, Opsi F, Cavallo E (2014) Relationships between runoff and soil losses with rainfall characteristics and a long-term soil management practices in a hilly vineyard (Piedmont, NW Italy). Soil Sci Plant Nutr. doi:10.1080/00380768.2013.862488

Blavet D, De Noni G, Le Bissonnais Y et al (2009) Effect of land use and management on the early stages of soil water erosion in French Mediterranean vineyards. Soil Till Res 106:124–136

Boardman J (2010) A short history of muddy floods. Land Degrad Dev 21:303–309

Celette F, Gary C (2013) Dynamics of water and nitrogen stress along the grapevine cycle as affected by cover cropping. Eur J Agron 45:142–152

Cerdan O, Govers G, Le Bissonnais Y et al (2010) Rates and spatial variations of soil erosion in Europe: a study based on erosion plot data. Geomorphology 122:167–177

CEC (2006) Communication from the commission to the council, the European Parliament, the European economic and social committee and the committee of the regions. Thematic Strategy for Soil Protection. Brussels, 22.9.2006, COM(2006) 231 final

Hajabbasi MA, Hemmat A (2000) Tillage impacts on aggregate stability and crop productivity in a clay-loam soil in central Iran. Soil Till Res 56:205–212

Keller M (2010) Managing grapevines to optimize fruit development in a challenging environment: a climate change primer for viticulturists. Aust J Grape Wine R.16:56–69

Giorgi F, Lionello P (2008) Climate change projections for the Mediterranean region. Global Planet Change 63:90–104

Maetens W, Vamaercke M, Poesen J et al (2012) Effect of land use on annual runoff and soil loss in Europe and the Mediterranean: a meta-anlysis of plot data. Progr Phys Geog 36(5):599–653

Montgomery DR (2007) Soil erosion and agricultural sustainability. PNAS 104(33):13268–13272

Moriondo M, Jones GV, Bois B, Dibari C, Ferrise R, Trombi G, Bindi M (2013) Projected shifts of wine regions in response to climate change. Clim Change 119:825–839

Nearing MA, Foster GR, Lane LJ et al (1989) A process-based soil erosion model for USDA-Water Erosion Prediction Project. Trans ASAE 32(5):1587–1593

Ramos MC, Martínez-Casasnovas JA (2007) Soil loss and soil water content affected by land leveling in Penedès vineyards. Catena 71:210–217

Soil Survey Staff (2010) Keys to soil taxonomy, 11th edn. USDA-natural resources conservation service, Washington

Tropeano D (1984) Rate of soil erosion processes on vineyards in Central Piedmont (NW Italy). Earth Surf Proc Land 9:253–266

Verheijen FGA, Jones RJA, Rickson RJ et al (2009) Tolerable versus actual soil erosion rates in Europe. Earth-Sci Rev 94:23–38

Wischmeier WH (1959) A rainfall erosion index for a universal soil-loss equation. Soil Sci Soc Am Proc 23:246–249

Success of Reclamation Works and Effects of Climatic Changes in Taranto Area: South Italy

31

Annalisa Galeandro, Angelo Doglioni and Vincenzo Simeone

Abstract

The paper presents some considerations on the potential influence of climatic changes on the effectiveness and the success of reclamation works made between the 19th and the 20th century in some areas of the west bound of Taranto (South Italy), characterized by large swamps for centuries. Historical documents underline the difficulty to make effective and successful reclamation works in the area of Taranto, as in other areas of the Mediterranean basin because swamps were continuously supplied by upward groundwater flow from the powerful deep karst aquifer. Success were obtained during Thirties thanks to improvement in technical knowledge and design technics, but these successes were obtained in a period characterized by rainfall decreasing. This paper aims at emphasizing that successes in reclamation works were obtained during a period of rainfall decreasing that affected Taranto area and all southern Italy between the 19th and the 20th century. Rainfall decreasing induced a lowering of groundwater table and a reduction of swamp supply, favoring the success of reclamation works.

Keywords

Climatic changes • Reclamation works • Swamps • Taranto • Tara springs

31.1 Introduction

Climatic changes may have relevant impacts on risk assessment, on territory management as well as on the impacts on the performance and the effectiveness of reclamation work systems. This work introduces some considerations on the potential effects of climatic changes on the effectiveness and success of reclamation works.

Several historical maps showed that the entire territory of the western side of Taranto city in Apulia region was characterized by large swamps area (Perrone 1992; Canora et al. 2012). Reclamation works started at the end of the 19th century, but they were ineffective and unsuccessful due to manifold reasons (Perrone 1992), especially because swamps were continuously supplied by upward groundwater flow from a powerful deep aquifer. Successes in reclamation works were obtained during Thirties thanks to a better technical knowledge and development of design and technology. The present work aims at introducing among the causes of that success also climatic changes due to the decrease of rainfall precipitations that severely affected Taranto area between the 19th and the 20th century (Simeone 2001) inducing a lowering of groundwater table and then a reduction of swamp supply.

31.2 Geological Climatic and Hydrogeological Features of the Investigated Area

The investigated area (Fig. 31.1) is located in the coastal flat area on west of Taranto (south Italy). The study area is characterized by a Cretaceous carbonatic platform overlaid by Quaternary formations such as sandstones, clays and

A. Galeandro (✉) · A. Doglioni · V. Simeone
Department of Civil Engineering and Architecture, Technical University of Bari, via Orabona, n. 4, 70125 Bari, Italy
e-mail: a.galeandro@email.it

G. Lollino et al. (eds.), *Engineering Geology for Society and Territory – Volume 1*,
DOI: 10.1007/978-3-319-09300-0_31,

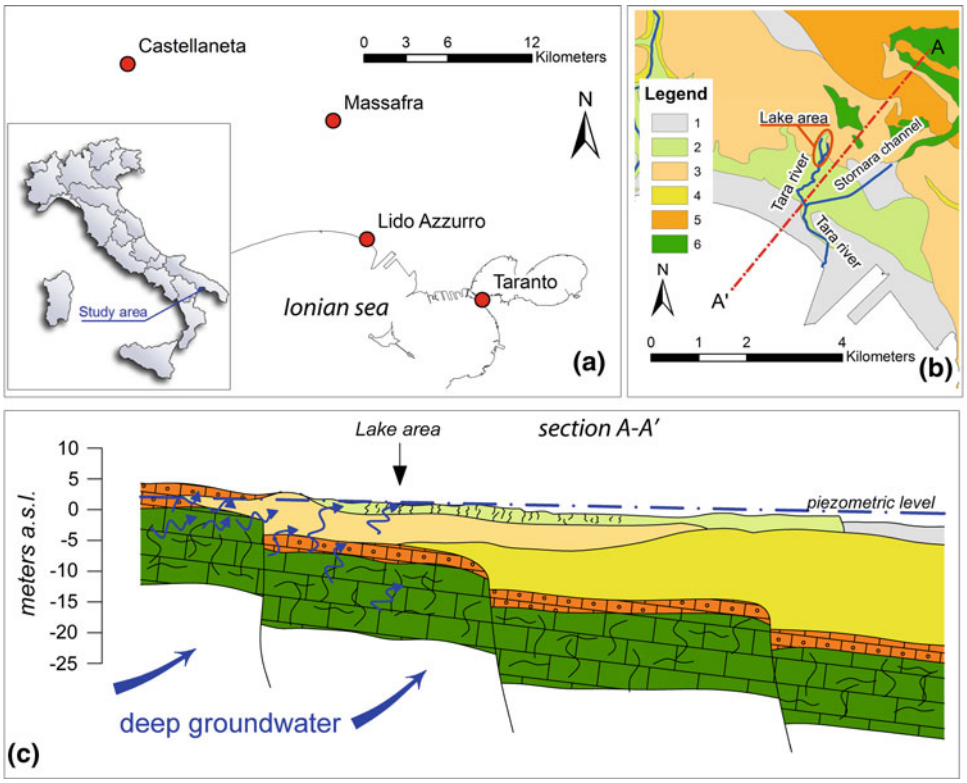

Fig. 31.1 **a** Location; **b** Schematic geological map and **c** Cross-section of the investigated area (after Bergamin et al. 1980, modified): *1* coastal dunes and recent sands (Holocene); *2* sandy and loamy-clayey palustrine and alluvial deposits (Holocene-Pleistocene); *3* sands, gravels and coarse sandstones (Holocene-Pleistocene); *4* Sub-Apennine clays (Pleistocene); *5* Gravina Sandstone (*upper* Pliocene-Pleistocene); *6* Altamura Limestones (Cretaceous)

topped by sands, loams, palustrine deposits, clays and sandstone (Federico et al. 1996). Limestones host an important karst aquifer which is supplied by rainfall water infiltration across Murgia calcareous platform (Cotecchia et al. 2005) while runoff is rare (Doglioni et al. 2012) and the infiltration is related to rainfall amount and intensity (Galeandro and Simeone 2012). Near the coastline, groundwater flows under pressure, due to the presence of Quaternary sub-Apennine clayey layers, overlaying the limestone hosting the aquifer and confining groundwater (Bergamin et al. 1980; Tadolini and Spizzico 1996). Locally Quaternary clayey deposits are thin, thus the upward groundwater flow from the karst aquifer may create swamps. Springs can be originated by the break-through of very thin clay layers due to upward groundwater, thus creating a lake. It is the case of Tara Springs where there is a swamp area with a lake supplied by several upward flow points, where groundwater naturally reaches the surface. The lake originates a small river flowing toward its outlet into the Ionian Sea.

The climate of the studied area is typically Mediterranean with quite hot dry summer and temperate rainy autumn and winter. The average yearly rainfall amount is about 500 mm/year along the coast and about 600 mm/years for

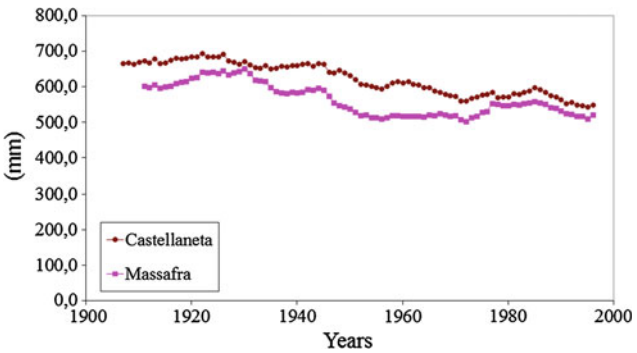

Fig. 31.2 30-year moving average of total annual precipitation at the rain gauge stations of Massafra and Castellaneta (Taranto, Italy)

the inland rain gauge stations. An analysis of rainfall amount variation in Taranto area (Simeone 2001) showed a quite severe decrease of rainfall amount since the mid-19th century. The rain gauge stations relevant for the springs catchment showed a decrease of about 25 % of the total yearly rainfall amount in the 20th century (Fig. 31.2). This decrease is actually concentrated during the autumn and winter periods, when groundwater supply occurs and this is subsequently affected by a decrease of more than 35 %.

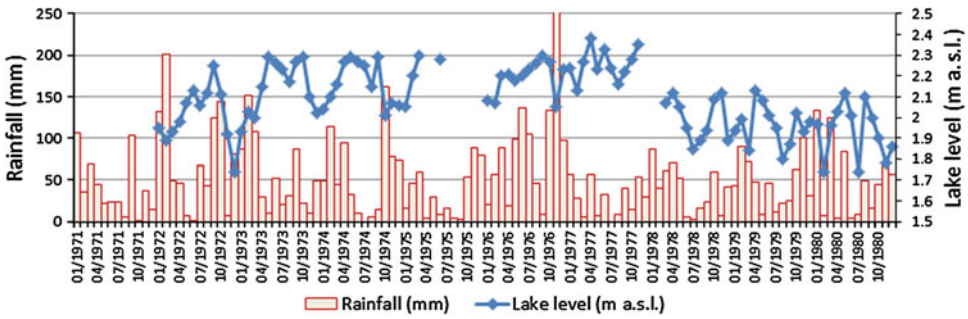

Fig. 31.3 Monthly rainfall measured at the rain gauge station of Massafra and monthly water level at the Tara lake

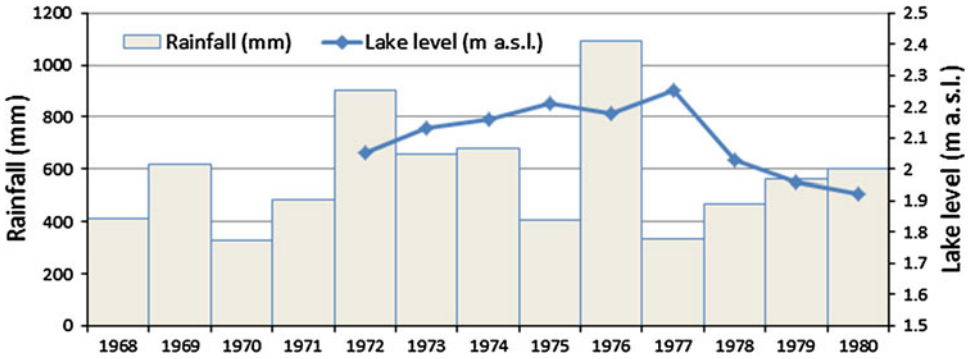

Fig. 31.4 Annual rainfall measured in Massafra rain gauge station and mean annual level of Tara Spring lake

Water level surface measurements of the Tara Spring lake developed between February 1972 and December 1980 (Santovito 1981) showed relevant variations of the water level in that period, from a minimum value of 1.74 m AMSL to a maximum of 2.35 m AMSL, with an average value of 2.10 m AMSL. Variations in lake water level, even if far from having a clear mathematical model (Doglioni et al. 2010), are in good agreement with rainy periods with a delay of peaks of water level of some months with respect to rain (Fig. 31.3). During the years, variations in the lake level range from a maximum of 51 cm in 1972 to a minimum in of 25 cm in 1975, 1976, 1977 after a sequence of quite rainy years. The maximum mean annual level in the lake was 2.26 m AMSL in 1977 after 1976 that was a very rainy year (more than 1,000 mm of rainfall), while the minimum was 1.93 m AMSL in 1980 after several quite dry years (Fig. 31.4).

These data showed how groundwater level in the lake is sensible to rainy or dry periods (Figs. 31.3 and 31.4). Water level variations in the lake were up to some tens of centimeters, even if there was not a sequence of rainy or dry years. Then, as consequence of large scale rainfall amount variation, groundwater level variations could be higher than those measured in the studied period. Therefore it is reasonable to assume that during the 19th century, when rain where more severe than in the studied period (Fig. 31.2), groundwater level was higher than today, favoring swampy phenomena in the area.

31.3 Effectiveness of Reclamation Works in the Studied Area

Several maps of 19th century (Perrone 1992) show that large swamps characterized the entire area of the western side of Taranto city. This was before the reclamation works developed between the 19th and the 20th century. Perrone (1992) indicates the existence of documents referred to reclamation work proposals for this area dated 1858–1894 and 1902–1927. These documents underline the main features of these zones and the difficulty to make effective reclamation works, which should involve an irregular shallow hydrography and an area where basic infrastructures were completely missing. Reclamation works were ineffective and unsuccessful due to manifold reasons, but particularly because swamps were continuously supplied by upward groundwater flow from the powerful deep karst aquifer.

Successes in reclamation works were obtained during Thirties, thanks to an enhanced technical knowledge and improving in design technics (Perrone 1992; Greco 1992). Anyway here it is assumed that the success of those works was likely supported by climatic changes due to the decrease of rainfall precipitations that severely affected Taranto area between the 19th and the 20th century.

Since the mid-19th century to the mid-20th century, there was a relevant rainfall decrease (Fig. 31.2) and the analysis of Tara Spring lake levels (Figs. 31.3 and 31.4) shows a close relation between rainfall amount and

groundwater level. The rainfall amount decrease (Fig. 31.2) may have caused a decrease of groundwater level in the lake as observed in the studied period (Figs. 31.3 and 31.4), fostering the success of reclamation works.

31.4 Conclusions

This work analyzed the role of climatic changes on the effectiveness of reclamation works in some areas of the west bound of Taranto (South Italy), historically affected by large swamps. Attempts at reclamation works for this area started unsuccessfully since the mid-19th century. Successes in reclamation works were obtained only during Thirties.

The analysis of the level of Tara Spring Lake, located in the area that was affected by swamps, shows relevant variations of groundwater level very close to ground level, related to rainfall amount. Rainfall variations may induce oscillations of several tens of centimeters, which may favor reclamation works. Relevant rainfall amount variations occurred since the end of the mid-19th century and during the whole 20th century. About 25 % of the average yearly rainfall amount was lost during the 20th century, particularly concentrated during autumn and winter periods when rainfall are more effective in groundwater supply.

The effectiveness of reclamation works in the swampy area of Tara Spring in Thirties (Perrone 1992) was surely due to improvement in design and technology, but probably it was supported also by climatic changes related to rainfall decreasing. In fact rainfall amount decreasing measured since the end of the 19th century may have induced variation of some tens of centimeters in groundwater levels, favoring the effectiveness of reclamation works.

References

Bergamin G, Scorcia M, Trimigliozzi A (1980) Prime risultanze di recenti studi sulle sorgenti Tara in Puglia. Annali 1980 (printed 1983), Ente per lo sviluppo dell'irrigazione e la trasformazione fondiaria in Puglia e Lucania, Bari

Canora F, Rossi CA, Spilotro G, La Piccola Età Glaciale nell'area di Taranto (Puglia, Italia). Rend Online Soc Geol It 18:12–18. doi:10.3301/ROL.2011.59

Cotecchia V, Grassi D, Polemio M (2005) Carbonate aquifers in Apulia and seawater intrusion. Giornale di Geologia Applicata 1:219–231

Doglioni A, Mancarella D, Simeone V, Giustolisi O (2010) Inferring groundwater system dynamics from time series data. Hydrolog Sci J 55(4):593–608

Doglioni A, Simeone V, Giustolisi O (2012) The activation of ephemeral streams in karst catchments of semi-arid regions. Catena 99:54–65. doi:10.1016/j.catena.2012.07.008

Federico A, De Filo F, Gelato G, Simeone V (1996) Vulnerabilità idrogeologica della fascia costiera ad ovest di Taranto—Nota preliminare. Geologia Applicata e Idrogeologia 31:289–296

Galeandro A, Simeone V (2012) Infiltration processes in fractured and swelling soils and their influence on the stability of surficial covers. Rend Online Soc Geol It 21(1):518–520

Greco AV (1992) Le bonifiche nella storia del paesaggio del tarantino sud orientale. Umanesimo della Pietra, Martina Franca (TA) 7:109–140

Perrone R (1992) Le paludi del tarantino occidentale prima delle bonifiche. Umanesimo della Pietra, Martina Franca (TA) 7:103–109

Santovito D (1981) L'andamento delle caratteristiche delle acque delle sorgenti Tara in un decennio di utilizzazione promiscua. Annali 1981, Ente per lo Sviluppo dell'Irrigazione e la Trasformazione Fondiaria in Puglia e Lucania, Bari

Simeone V (2001) Variazioni climatiche e rischi di depauperamento delle falde e di desertificazione in provincia di Taranto. Geologia Tecnica Ambientale 2:23–32

Tadolini T, Spizzico M (1996) Caratterizzazione idrogeologica della zona delle sorgenti Tara (Taranto). Mem Soc Geol It 51:793–802

Stability Monitoring of High Alpine Infrastructure by Terrestrial Laser Scanning

32

Ludovic Ravanel, Philip Deline, Christophe Lambiel and Pierre-Allain Duvillard

Abstract

Rock mass movements are dominant in the morphodynamics of high Alpine rock slopes and are at the origin of significant risks for people who attend these areas and for infrastructures that are built on (e.g. huts, cable cars). These risks are increasing because of permafrost degradation and glacier retreat as consequences of the global warming. These two factors may affect slope stability by changing mechanical properties of the interstitial ice and modifying the mechanical constraints in these rock slopes. The monitoring of rock slopes is thus an essential element for risk management. Our study focuses on two particularly active areas of the Western Alps: the lower Arête des Cosmiques (3613 m a.s.l., Mont Blanc massif, France) on which is located the very popular Refuge des Cosmiques, and the Col des Gentianes (2894 m a.s.l., Valais, Switzerland) where is located a cable car station. Discussed on the basis of geophysical and glaciological data, the evolutions monitored by terrestrial laser scanning probably result from the combination between permafrost activity/degradation and glacier shrinkage.

Keywords

High alpine infrastructure • Landslides • Permafrost • Glacier • Hazards

32.1 Introduction

High mountain environments became true markers of the climate warming, particularly through the glacier retreat and the permafrost degradation (Harris et al. 2009) i.e. the warming of any lithospheric materials that remain at or below 0 °C for at least two years. Both processes—and combination -, are often pointed out to explain the current upsurge of gravitational hazards (rockfalls, landslides) in high mountains (Ravanel and Deline 2011) by changing mechanical properties of the interstitial ice and modifying the mechanical constraints in the rock slopes.

Such instabilities are becoming of increasing concern (Haeberli et al. 1997). It is especially true since high alpine mountains are more and more visited (tourist flows) and well endowed with infrastructure (refuges, railways cable cars and associated buildings). In the recent years, an increasing number of damage occurred on structures, both in context of bedrock and sedimentary formations.

Our study focuses on the case of two highly anthropised areas (Fig. 32.1). The first one is the lower Arête des Cosmiques (LAC hereafter, 3613 m a.s.l., Mont Blanc massif, France) on which is located the very popular Cosmiques hut. Since 1998, when a rockfall threatened a part of the refuge, observations allowed to identify several detachments. Since 2009, this area is yearly surveyed by terrestrial laserscanning (TLS) to obtain high-resolution 3D

L. Ravanel (✉) · P. Deline · P.-A. Duvillard
EDYTEM Lab, University of Savoie CNRS, Le Bourget-du-Lac, Chambéry, France
e-mail: Ludovic.Ravanel@univ-savoie.fr

L. Ravanel · C. Lambiel
Institute of Geography and Durability, University of Lausanne, Lausanne, Switzerland

G. Lollino et al. (eds.), *Engineering Geology for Society and Territory – Volume 1*,
DOI: 10.1007/978-3-319-09300-0_32,

Fig. 32.1 **a** The lower Arête des Cosmiques with the Cosmiques hut (3613 m a.s.l.) on it; **b** the inner side of the Gentianes moraine (2894 m a.s.l.) with its lower Mont Fort cable-car station

models. Their diachronic comparison shows few important rock detachments between 2009 and 2011. The second one is the Col des Gentianes (2894 m a.s.l., Valais, Switzerland) where is located a cable-car station. Since the early 1980s the moraine is unstable: its inner slope has retreated for several meters. Since 2007, the moraine is monitored by TLS: 8 campaigns were conducted between July 2007 and October 2011. The comparison of the high resolution 3D models obtained allowed the detection and quantification of mass movements that have affected the moraine over this period.

32.2 The TLS Method

In the case of the LAC, the presence of refuge keepers attentive to the mountain evolution has yielded a quasi-complete data collection of rockfalls since 2003 (Ravanel et al. 2013). Prior this date, a rockfall in 1998 had however attracted the attention of keepers and risk managers in Chamonix. It affected the slope immediately under the refuge, requiring closure of the refuge and important works of consolidation. These observations were then completed in 2011 by TLS measurements in order to characterize the affected areas and to compute the fallen volumes.

These topographic measurements have been carried out using a terrestrial laser scanner. This is an active acquisition device that emits electromagnetic energy in the form of laser beams and records back the amount of energy that is reflected by the object being scanned. The high degree of accuracy of the measurement of the time-of-flight and of the angle attitude of each pulse provides quickly high resolution point clouds (Oppikofer et al. 2008; Ravanel et al. 2010).

The first TLS campaign at the LAC was carried out in October 2009. Two others were carried out the two following years (Oct. 2010, Sept. 2011). The first TLS measurements at the Gentianes moraine were carried out in July 2007 (Ravanel and Lambiel 2013). Since this date, the moraine has been scanned one (2009), two (2007 and 2008) or three times (2011) a year, with a break in 2010. The device used is an *Optech* ILRIS 3D (wavelength: 1500 nm; acquisition speed: 2000 pts. per sec.; effective range: 600 m). According to the manufacturer, the acquisition accuracy of a point at 100 m is 7 mm in distance and 8 mm in position. Initialization and setup of the scanner are controlled by a driver. After the determination of shooting windows and the point spacing, the acquisition is automatic.

The obtained point clouds are assembled in the software *InnovMetric* PolyWorks to get a full single high resolution 3D model of the rockwall (Rabatel et al. 2008). The comparison of 3D models allows measuring morphological changes. As result of this comparison is a difference map where each point of the 3D model "data" is coloured depending on its distance from the nearest point on the 3D model "reference". The operator can then identify rockfalls or landslides using this difference map and the corresponding colour scale—once remove the differences resulting from changes in ice/snow cover and shifts in measuring stations. Then, the volume of identified rockfalls can be computed.

32.3 Results

32.3.1 A Very Active Cosmiques Rock Ridge

The first important collapse occurred in 1998, immediately below the refuge (600 m^3). No evidence of instability has been collected for the following 5 years. In 2003, a rockfall (140 m^3) occurred a hundred meters SW of the refuge. In 2004, two rockfalls occurred. One mobilized a rock volume of 200 m^3 in the immediate vicinity of the scar of 2003, whereas the second one (20 m^3) reshaped the SW margin of the 1998 scar. A new deposit was formed on the Glacier du Géant due to a rockfall of 85 m^3 that occurred in July 2006 on the crest line, just above the 2003 scar. Another rockfall detached in the same area in July 2007 (180 m^3), reshaping the crest line. Another rockfall (40 m^3) affected again the ridge. No significant destabilization occurred until August 2009 when a rockfall (200 m^3) detached, mobilizing blocks that formed the crest of the LAC.

The first TLS comparison (Oct. 2009–2010; Fig. 32.2) shows two unstable areas. The first, fairly recurrent, was the most active area between 2003 and 2009. Three new ones affected it in 2010: a fractured block of 256.2 m^3, a block of 0.7 m^3 and a pile of blocks of 52 m^3. The second unstable area recognized during the period is a couloir. A minimal volume of 111.7 m^3 of rock detached in the lower part of the couloir. Two unstable areas were identified for the second period (Oct. 2010–Sept. 2011). A massive block of 40.1 m^3 detached about 10 m downstream the most active area. A second unstable area is the couloir. In its lower part, three events occurred: the instability documented in 2010 continued mobilizing 48.7 m^3, a column slightly tilted, and another detachment (4.4 m^3).

32.3.2 Evolution of the Gentianes Moraine

TLS data acquired between 2007 and 2011 have provided opportunities for 7 diachronic comparisons (Ravanel and Lambiel 2013). The first comparison (July–Oct. 2007) reveals several evolutions. The most directly visible one is a landslide of 198 ± 6 m^3. Positive volume changes appear on both sides of this landslide, related to deposits of anthropogenic origin. Finally, about twenty meters downstream from the cable-car station, a 40-m-wide and 15-m-high area is characterized by gravitational movements of blocks. Between Oct. 2007 and July 2008, morphodynamics is reduced. The third comparison (July-Oct. 2008) is evidencing a new landslide occurred just south of the 2007 one, mobilizing 111 ± 6 m^3 of material. Two other areas were affected by movements of blocks. The following comparison (Oct. 2008–Sept. 2009) reveals new deposits probably of anthropogenic origin. Three areas have been affected by movements of blocks. Two juxtaposed landslides occurred,

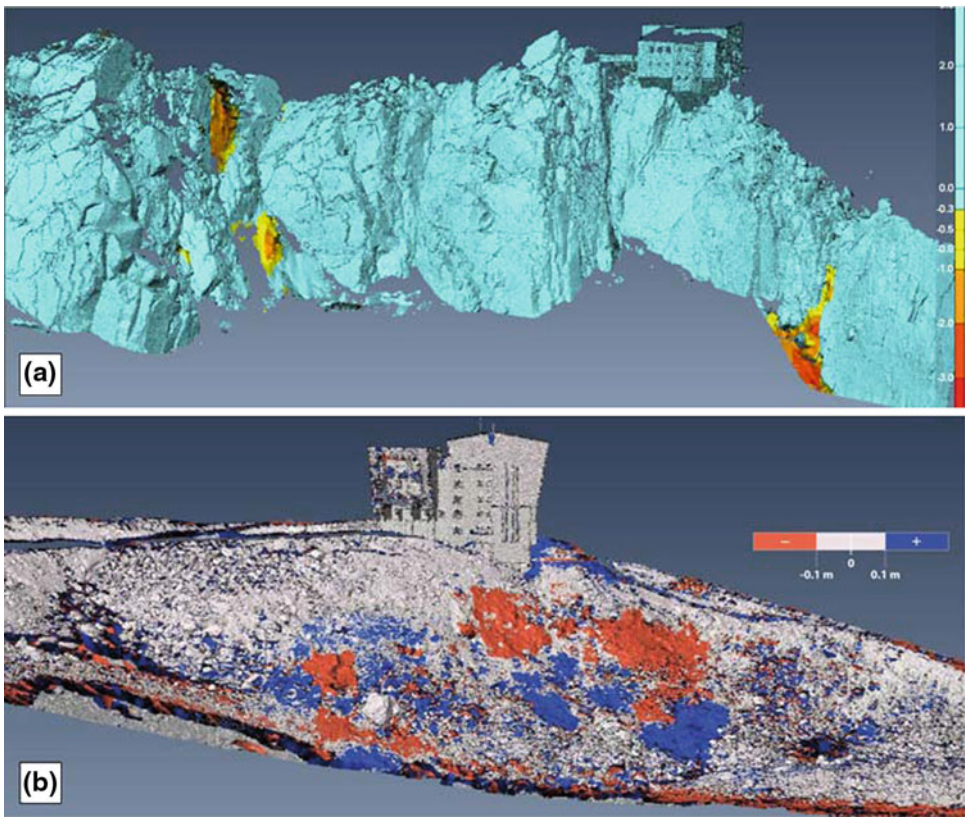

Fig. 32.2 **a** 3D model comparison of Oct. 2009 and Oct. 2010 of the LAC (4 identified rock detachments; scale is in m); **b** comparison of July 2011 and Aug. 2011 of the Gentianes area

with a total volume of 1138 ± 47 m^3. The following comparison (Sept. 2009–July 2011) indicates that the two main areas of individual movements of blocks continued to evolve. Between these two sectors, a significant loss of volume was recorded (874 ± 61 m^3). The absence of deposit at the foot of the moraine suggests that this loss is due to ice melting. The activity of the summer 2011 (early July–late Aug.) is arguably the most important of the study period (Fig. 32.2). Beyond the anthropogenic establishment of a small deposit and the continuation of the movements of blocks, three landslides have affected the moraine (270 ± 12 m^3, 217 ± 14 m^3 and 546 ± 20 m^3). The last comparison (Aug.–Oct. 2011) shows that three areas continued to be affected by block movements. A new landslide, whose volume is estimated around 115 m^3 finally affected the area.

32.4 Discussion and Conclusions

At the LAC, rock temperature data suggest the presence of temperate permafrost from the first meters to depth in the SE face, and cold permafrost in the NW face. The presence of permafrost has been corroborated by the observation of massive ice in several rockfall scars, emphasizing the role of ice in the slope stability. As suggested by the occurrence of rockfalls mainly during or at the end of hot periods in summer, degradation of the ice has likely participated in the triggering of a large part of these rockfalls (see: Gruber and Haeberli 2007).

The evolution of the glacier also directly interferes with the stability of the LAC. It is indeed striking to note that the rockfall of 1998 has affected a slab whose base was located under the ice until that year. The glacier mass balance of the hydrological year 1997–1998 is the lowest of the 8 years that have been measured, which caused a strong lowering of the glacier and the snow cover below the refuge. Similarly, 2010 and 2011 rockfalls in the couloir located east of the refuge were possible because of the lowering of the glacier in the recent years. Before, the glacier exerted a stop-effect prone to stabilize the potential instability determined by the geological structure.

The diachronic comparisons of 3D models at the very probably ice-cored Gentianes moraine also showed a significant general instability trend that can be mainly explained by the combination of the loss of glacier thickness and the permafrost activity/degradation, both allowed by a series of hot summers. The annual thaw of the active layer (measured) seems to promote rearrangements of rock material (block movements) and, when this active layer reaches the ice present in a part of the moraine, landslides are initiated. Two main scenarios are then possible: (i) the buttress exerted by the sediment located just below is sufficient to stop the phenomenon, or (ii) a landslide occurs. The latter scenario, which has been reproduced 7 times over the study period, is largely induced by the loss of thickness of the glacier (locally reaching 11.3 m, which corresponds to a local ablation in the order of 2.25 m per year) and certainly by the increase of the slope angle.

Given those results, the TLS method appears as a very relevant method for monitoring the evolution of those highly anthropised and vulnerable area.

References

Gruber S, Haeberli W (2007) Permafrost in steep bedrock slopes and its temperature-related destabilization following climate change. J Geophys Res 112:F02S18

Haeberli W, Wegmann M, Mühll Vonder D (1997) Slope stability problems related to glacier shrinkage and permafrost degradation in the Alps. Eclogae Geologicae Helvetiae 90:407–414

Harris C et al (2009) Permafrost and climate in Europe. Earth-Sci Rev 92:117–171

Oppikofer T, Jaboyedoff M, Keusen HR (2008) Collapse at the eastern Eiger flank in the Swiss Alps. Nature Geosci 1:531–535

Rabatel A, Deline P, Jaillet S, Ravanel L (2008) Rock falls in high-alpine rock walls quantified by terrestrial LiDAR measurements: a case study in the Mont-Blanc area. Geophys Res Lett 35:L10502

Ravanel L, Deline P (2011) Climate influence on rockfalls in high-Alpine steep rockwalls: the North side of the Aiguilles de Chamonix (Mont Blanc massif) since the end of the Little Ice Age. The Holocene 21:357–365

Ravanel L, Allignol F, Deline P, Gruber S, Ravello M (2010) Rock falls in the Mont Blanc Massif in 2007 and 2008. Landslides 7:493–501

Ravanel L, Lambiel C (2013) Evolution récente de la moraine des Gentianes: un cas de réajustement paraglaciaire? Environnements Périgl, p18–19, 8

Ravanel L, Deline P, Lambiel L, Vincent C (2013) Instability of a highly vulnerable high alpine rock ridge: the lower arête des Cosmiques (Mont Blanc massif. Geografiska Annaler A, France. doi:10.1111/geoa.12000

Integrated Geomatic Techniques for Assessing Morphodynamic Processes and Related Hazards in Glacial and Periglacial Areas (Western Italian Alps) in a Context of Climate Change

33

Stefania Bertotto, Luigi Perotti, Marco Bacenetti, Elisa Damiano, Chiarle Marta and Marco Giardino

Abstract

High elevation environments proved to be particularly sensitive to climate changes, in relation to an increase in instability especially in areas where the cryosphere is present. The purpose of this work is to present the geomatic methodologies that have been applied to study dynamical areas, such as glacial and periglacial ones, in order to detect morphological changes that can be ascribed to climatic changes. The working group has been composed by members of the University of Torino (GeoSitLab laboratory) and of the CNR-IRPI Torino, in the framework of the Alcotra 2007–2013 project n.56 GlaRiskAlp (Glacial Risks in the Western Alps). Remote sensing techniques, necessary for large or remote areas, have been integrated, for the purposes of this study, by GNSS campaigns in the field, using a fixed GPS station, and a kinematical one. In order to identify landscape changes over the tens of years, it is particularly useful the digital aerial photogrammetry which exploits historical aerial photos that are orthorectified, to extract themes for a topographical and geomorphological characterization of landscape at regional scale. For the specific purposes of our work, the DEM extraction, at a local scale, from flights of different years, is useful to make comparisons of glacier surface. All data have been implemented in a GIS.

Keywords

Glaciers • Natural hazard • Periglacial • GNSS • Photogrammetry

33.1 Introduction

Western alpine glaciers are responding rapidly to the ongoing climate change (IPCC 2013). Thus periglacial areas can develop instability phenomena (Dutto and Mortara 1992; Chiarle and Mortara 2008; Mortara and Chiarle 2005). Considering the importance of locating and identifying that kind of phenomena in the Western Alps (Didier and Gay 2003; Bertotto et al. 2011), the Alcotra 2007–2013 project n.56 GlaRiskAlp was set up. The purpose of the project was to study natural hazards using innovative methodologies, thanks to the contribution of different partners,

S. Bertotto (✉) · L. Perotti (✉) · M. Bacenetti (✉) · M. Giardino
GeoSITLab, Università degli Studi di Torino, Via Valperga Caluso, 35, Turin, Italy
e-mail: stefania.bertotto@unito.it; stefania.bertotto@irpi.cnr.it

L. Perotti
e-mail: luigi.perotti@unito.it

M. Bacenetti
e-mail: marco.bacenetti@unito.it

S. Bertotto · E. Damiano · C. Marta
CNR-IRPI Torino, Strada delle Cacce 73, Turin, Italy

G. Lollino et al. (eds.), *Engineering Geology for Society and Territory – Volume 1*,
DOI: 10.1007/978-3-319-09300-0_33,

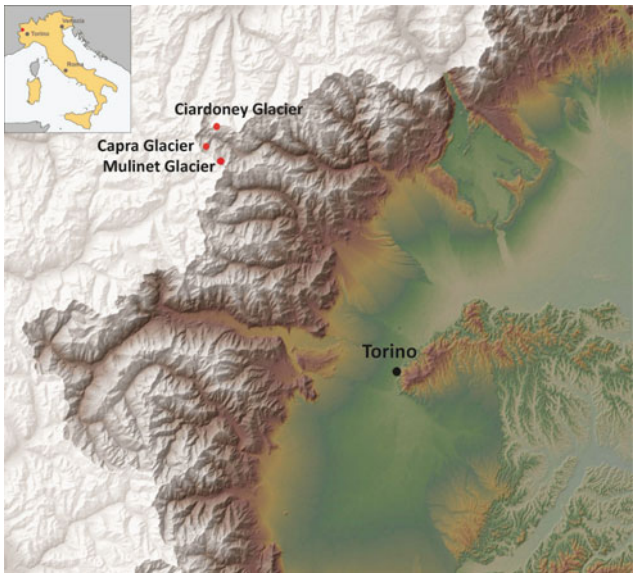

Fig. 33.1 Study area. *Red dots* show the location of the test site glaciers

including Universities and Research centers (http://www.glariskalp.eu).

Any attempt to cope with the effects of climate change, and related impacts down valley, has to rely on accurate and up-to-date information about glacier location and characteristics, and about extent and properties of recently deglaciated areas. That information can be obtained by means of remote sensing techniques, which are particularly suitable for large glacial areas or remote ones.

The authors tested a manifold geomatic approach in three test sites set in the Graian Alps (Western Italian Alps), not very far from the city of Turin: the Capra Glacier (Ceresole Reale, Orco Valley), the Ciardoney Glacier (Ronco Canavese, Soana Valley), and the Mulinet Glacier (Forno Alpi Graie, Lanzo Valley). The Fig. 33.1 shows the location of the test sites.

33.2 Data and Methods

To pursue the general aim of the project, an ESRI ArcMap document was created, to visualize the different layers of information, as carthographical data, aerophotographical data and satellite archive images, available for each test site (Table 33.1).

Remote sensing techniques allow to handle a large amount of data and a multitemporal approach to phenomena (Kääb et al. 2005), useful in glaciology and for the analysis of processes related to deglaciation. In accessible areas, field survey techniques (GNSS, terrestrial photogrammetry and Lidar) were used to monitor specific situations: to realize topographical profiles (Capra Glacier), to allow the reconstruction of the glacial surface (Ciardoney Glacier) and the analysis of the variations of its snout position (Ciardoney and Capra glaciers).

Table 33.1 Date of surveys and archive data available for each glacier

Methodologies/Year	Capra glacier	Mulinet glacier	Ciardoney glacier
GNSS	2011–2012–2013	2012	2012
Terrestrial photogrammetry	2011–2012–2013		2012
Aerial photogrammetry	1954–1983–1988–2000–2005	1954–1983–1988–2000	1954–1975–1983–1988–2000–2001–2005
Lidar	2010		2012
Satellite images	2010	2010	2010
Ortophotos	1989–200–2006–2010	1989–2000–2006–2010	1989–2000–2006–2010
Digital terrain model	2000–2010	2000–2010	2000–2010

33.2.1 Aerial Photogrammetry Applied to the Ciardoney Glacier

Aerial photogrammetry represents an immediate and reliable tool for acquire metrical and thematical data, through the acquisition, the processing and the analysis of analogical or digital aerial photographs.

In the framework of this project, this technique has been used in order to reconstruct historical evolution of glaciers from a quantitative point of view, both from the planimetric point of view (surface extent in relation with specific time steps) and from the volumetric point of view. The evaluation of changes in glacier front position or in its mass is only possible for the last 50–60 years, which is time interval for which aerial photogrammetric frames are available. For the planimetric reconstruction, orthophotos have been obtained from stereo pairs and have been successively entered in a GIS for quantitative evaluations, such as the detection of glacial limits and planimetric variations of other geomorphological elements (Fig. 33.2b). All the extracted data have been used to realize cartographical products whose scale of representation is between 1:5,000 and 1:25,000.

For 3D analysis, instead, digital models of the ground surface (DEM) had to be obtained from stereoscopic frames. This process was finalized to the detection of volumetric changes in glacial masses by comparing 3D models (Fig. 33.2a) referred to different periods (Schiefer and Gilbert 2007). Moreover, the so obtained stereoscopic digital models can be used for the visualization, and the editing of objects in a 3D environment.

For this project, the Leica Photogrammetry Suite (LPS) and Z-Map by Menci software have been used. LPS has

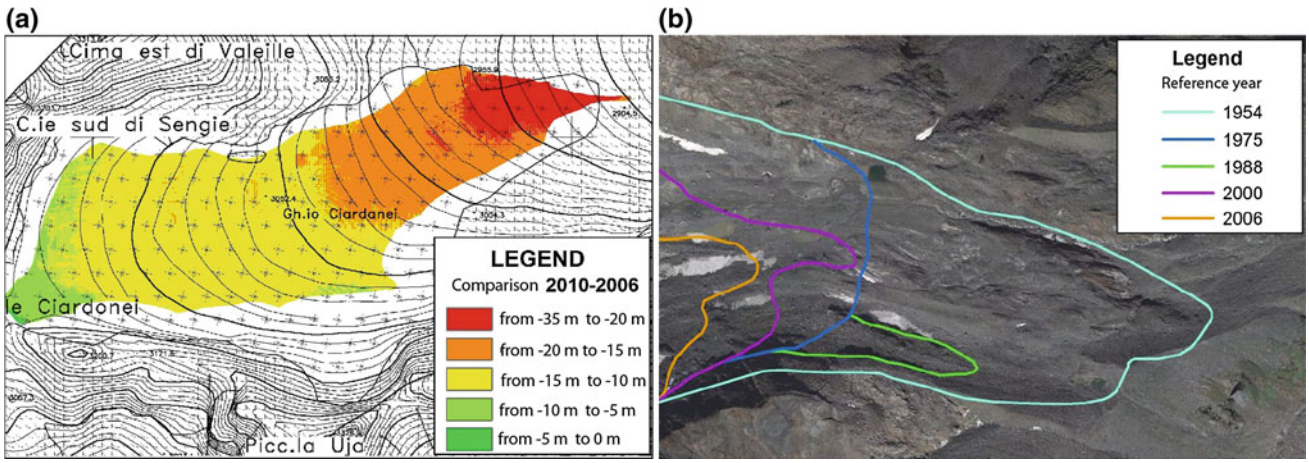

Fig. 33.2 Example of carthographical products from aerial photogrammetry on the Ciardoney Glacier. **a** Map obtained from the comparison of two DTMs (2010–2006) showing increasing ice thickness loss from the head (*green area*) to the front (*red area*) of the glacier, approximate scale 1:35,000. **b** Glacier snout extent at several time steps, scale 1:5,000

been already used in orientation process with remarkable results. Z-Map is indeed very convenient as a 3D visualizer.

The time required for the whole procedure depends on the amount of data, on their initial quality and on the required quality for the data extracted.

Consequently, the number of considered frames, their format, availability and quality are parameters affecting the processing. For example, more time is necessary if ad hoc acquisitions are necessary and the time required for the editing of glacial limits and for the evaluation of volumetric variations depends on the amount of images considered and on the accuracy required for the final data. For the DEM extraction the time required depends on the characteristics of the considered area (in particular the availability of clearly identifiable points of reference) and on the distribution of the GCP; the time of processing also depends on the modality chosen for the points localization: manual or semiautomatic.

Regarding the uncertainty of the method, it is necessary to take into account that output data come from a succession of previous elaborations. For this reason, the uncertainty of the final data is in relation to: (1) the technique of the data acquisition and resolution of the extracted data; (2) the quality of the starting data (regarding the archival images); (3) the variable accuracy and the subjectivity of the manual restitution procedures, for example taking ground control points.

The overall planimetric accuracy of data is between 2.5 and 5 m and between 3 and 7 m in elevation.

Another limitation refers to an intrinsic characteristic of the process of comparison of DEMs: the procedure is particularly effective only if the variations are chiefly vertical, and if the changes are greater than the accuracy expected for the final data. Finally, the precision of the method is mainly related to the basic parameters of the photogrammetrical process (Gomarasca 2004).

33.2.2 GNSS Technique Applied to the Capra Glacier

The Global Navigation Satellite System (GNSS) is based on the satellite technology and allows to detect the Earth's surface and to obtain the position of points over it with a high accuracy. The advantages of a GNSS system are the high accuracy, the ability to operate in any point of the Earth at any instant, its functionality in every weather conditions, and equipment transportability.

In this specific project, this technique was applied to detect modifications in recently deglaciated areas, to find initial instability processes that could not be easily recognized naked eye or with other photogrammetrical techniques.

To study topographical variations of proglacial areas, cross-section profiles were realized (Fig. 33.3).

The GNSS profiles were made with kynematical mode: it consists of keeping in a fixed position one of the receiver (base) and to carry the second one (rover) along a path moving continuously (Hofmann-Wellenhof 2001). The profiles were made during summer 2011, 2012, 2013 to do comparisons.

The post-processing was made using the Topcon Tools software. The errors for each survey theoretically are less than one meter: because of the presence of boulders and steep walls, that value is commonly higher. This characteristics make the GNSS a useful system in dynamical environments, and when we want to evaluate variations of the surface in decimeters or meters: in this conditions, aerial photogrammetry can be applied with more difficulties, due

Fig. 33.3 The GPS kinematical traces made during 2011–2012–2013 in the snout position of Capra Glacier. The *red dot* shows the positioning of fixed position. Scale 1:10,000

to the absence of reference points stable/easily recognizable, and for the attended minor precision. In this cases, its reasonable costs, compared with other techniques with similar precision (es. LIDAR o georadar), make the GNSS a more advisable method.

33.3 Final Remarks

In the Italian Alps, glaciers are often accessible, small, and debris covered. In these cases, an integrated methodology, combining different geomatic methodologies (remote sensing, photogrammetry, GNSS and GIS) might give the most accurate results, and perhaps be the less expensive. Our work focused on problems that have been faced, and on solutions that have been envisaged, in a ongoing study on glaciers and periglacial areas of the Piemonte Region (NW Italy), with the aim of identifying debris sources, slopes prone to instability, and present geomorphologic dynamics in glaciated and recently deglaciated areas. The analysis of data obtained from remote sensing and field surveys is still in progress: the outcomes of the different techniques will be compared with each other, with historical documents and literature, in order to draw a final picture of glaciers evolution and of the suitability and accuracy of the different used techniques for studying geomorphological dynamics in glacial and periglacial areas.

References

Bertotto S, Fioraso G, Giardino M, Nigrelli G, Perotti L (2011) Effetti del cambiamento climatico sui ghiacciai delle alpi occidentali. Rischi associati e nuove metodologie d'indagine. Atti, vol Le modificazioni climatiche e i rischi naturali. Polemio M (ed). CNR IRPI, pp 109–112

Chiarle M, Mortara G (2008) Geomorphological impact of climate change on alpine glacial and periglacial areas. Examples of processes and description of research needs. Interpraevent 2008, Dornbirn, 26–30 maggio 2008, II/111–122

Didier R, Gay M (eds) (2003) Survey and prevention of extreme glaciological hazards in European mountainous regions, Glaciorisk report. http://glaciorisk.granoble.cemagref.fr. Pdf edition; 470 p

Dutto F, Mortara G (1992) Glacial hazards in Italian Alps. Geogr Fis Din Quat 15:85–99

Gomarasca M (2004) Basis of Geomatics. Springer, New York. ISBN 978-1-4020-9013-4

Hofmann-Wellenhof (2001) GPS: theory and practice. Springer, New York

IPCC (2013), Inter-governmental panel on climate change, summary for policymakers. Twelfth session of working group. www.ipcc.ch [last visit: 4 Nov 2013]

Kääb A, Huggel C, Fischer L, Guex S, Paul F, Roer I, Salzmann N, Schlaefli S, Schmutz K, Schneider D, Strozzi T, Weidmann Y (2005) Remote sensing of glacier- and permafrost-related hazards in high mountains: an overview. Nat Hazards Earth Syst Sci 5:527–554

Mortara G, Chiarle M (2005) Instability of recent moraines in the Italian Alps. Effects of natural processes and human intervention having environmental and hazard implications. Giornale di Geologia Applicata 1:139–146

Schiefer E, Gilbert R (2007) Reconstructing morphometric change in a proglacial landscape using historical aerial photography and automated DEM generation. Geomorphology 88(1–2):167–178

Climate Change Impacts on Groundwater Active Recharge in Coastal Plain of Dar es Salaam (Tanzania)

34

Giuseppe Sappa, Antonio Trotta and Stefania Vitale

Abstract

This paper presents some early results of the ACC Dar Project (Adapting to Climate Change in Coastal Dar es Salaam), a three-year project co-funded by the European Commission that aims to improve the effectiveness of municipal initiatives for supporting coastal peri-urban populations in their efforts to adapt to the impacts of Climate Change (CC). The present study is focused on changes in groundwater active recharge in Dar es Salaam's coastal aquifer, which are attributable to two factors: the decrease in precipitation recorded over the last 10 years, and the change in land cover during the same period. To assess the impacts that these factors have had on active groundwater recharge, the hydrogeological inverse budget was applied, introducing new values for the potential infiltration factor. Temporal analysis of climatic and land cover data for the last 10 years reveal a decreasing trend in groundwater availability. Study results therefore indicate that aquifer recharge is directly related to the amount of precipitation that can infiltrate into the soil, which in turn depends on precipitation and land cover.

Keywords

Dar es salam • Climate change • Groundwater recharge • Coastal aquifers • Land cover

34.1 The Area Under Study

The study area is located in the Dar es Salaam coastal plain, between latitudes 6°36′ and 7°0′ South and longitudes 39°0′ and 33°33′ East. It lies in the eastern part of the United Republic of Tanzania, and is divided in the three municipalities of Kinondoni, Ilala, and Temeke. It covers a surface of approximately 260 km^2, extending from the Nyakasangwe River in the north to the Mzinga River in the south, and bisected by the Msimbazi River, which flows NE into the Indian Ocean. The eastern boundary is formed by the Indian Ocean (Fig. 34.1).

G. Sappa (✉) · A. Trotta (✉) · S. Vitale (✉)
DICEA, Department of Civil, Building and Environmental Engineering – Sapienza, University of Rome, Via Eudossiana 18, 00186 Rome, Italy
e-mail: giuseppe.sappa@uniroma1.it

A. Trotta
e-mail: trottanto@yahoo.it

S. Vitale
e-mail: stefania.vitale@speingegneria.com

34.2 Geological and Hydrogeological Settings

The geological setting of the Tanzanian coastal area can be divided into different regions, depending on their distinctive tectonic development (Kent et al. 1971).

In the area of concern, two main geological units are recognized: Quaternary and Neogene. Quaternary sediments lie predominantly beneath the coastal plain, while

G. Lollino et al. (eds.), *Engineering Geology for Society and Territory – Volume 1*,
DOI: 10.1007/978-3-319-09300-0_34,

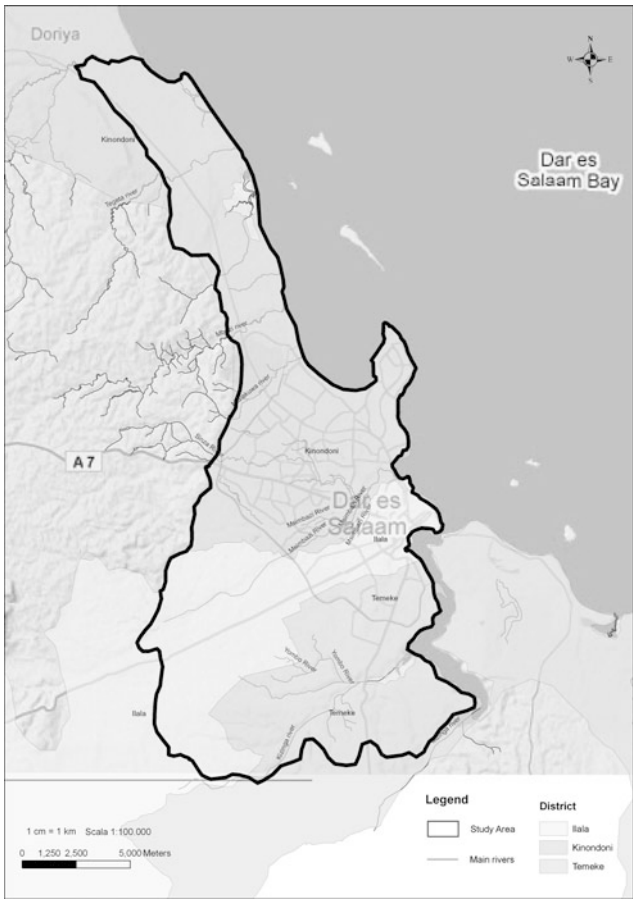

Fig. 34.1 The study area

Quaternary terrace sandstones are more widespread in the central and southern parts of Dar es Salaam Region. The Quaternary deposits also include coral reef limestone nearer the coast (Fig. 34.2).

Neogene sandstone formations, interbedded with siltstones and mudstones, occupy the upland zone south and west of the city centre. Within Neogene formations, several distinct varieties are recognizable. Various types of sandstone occupy over three-quarters of the region (Msindai 2002).

The aquifer system in the study area includes two main aquifers, both from the Quaternary: an upper unconfined sand aquifer and a lower semi-confined sand aquifer, separated by a clay aquitard. The sediment type for both aquifers consists of Quaternary deposits from Pleistocene to the recent age.

A recent hydrogeological assessment of this area (Mjemah 2007) reports that the groundwater active recharge of the aquifer is produced, in large part, by coastal plain infiltration. However, part of the recharge may also uplift from deep troughs from the Miocene geological formations of the inland hills, beyond the fault dividing the Pugu Hills from the coastal plain aquifer. The analyses and results regarding the groundwater active recharge presented below address only the contributions from direct infiltration in the area under study. These values may therefore represent only a part of the total groundwater active recharge of the area.

34.3 Evolution of Active Groundwater Recharge

34.3.1 Methodological Approach

Fifty-year monthly precipitation measurements were available, collected in three meteorological stations in Dar es Salaam: JNIA, Wazohill, and Ocean. The hydrogeological inverse budget (Civita et al. 1999) was applied to the JNIA

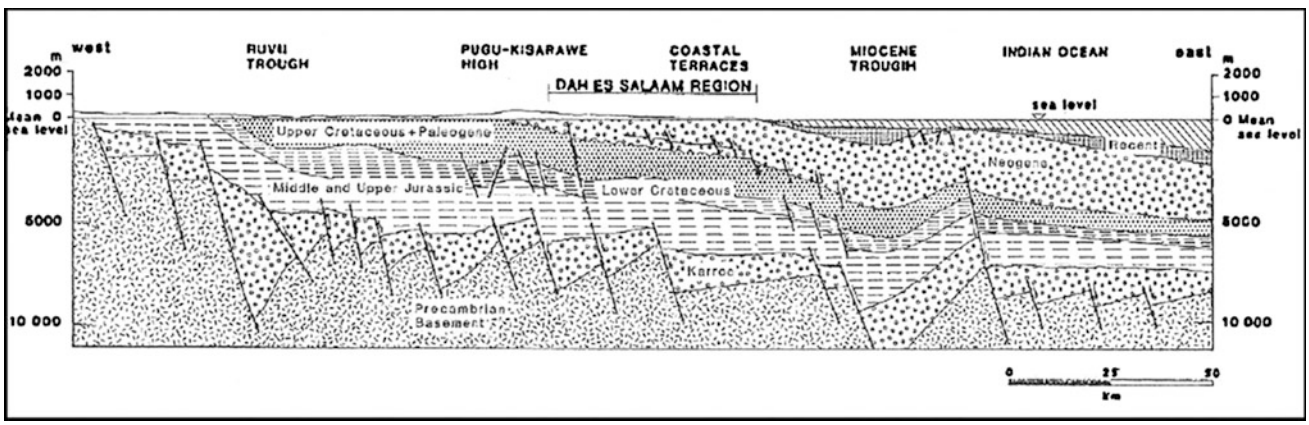

Fig. 34.2 A geological cross section of the study area (Msindai 1988)

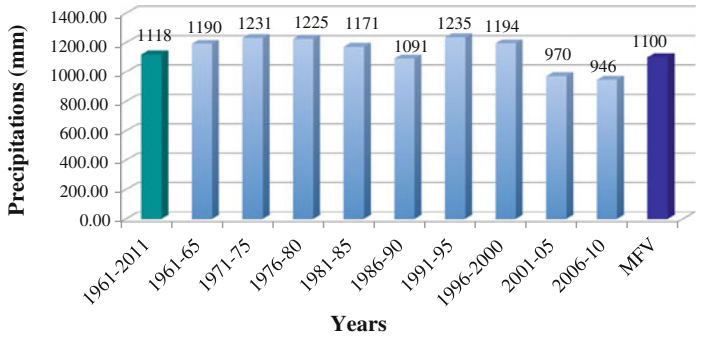

Fig. 34.3 Average 5-yearly precipitation, 1961–2010

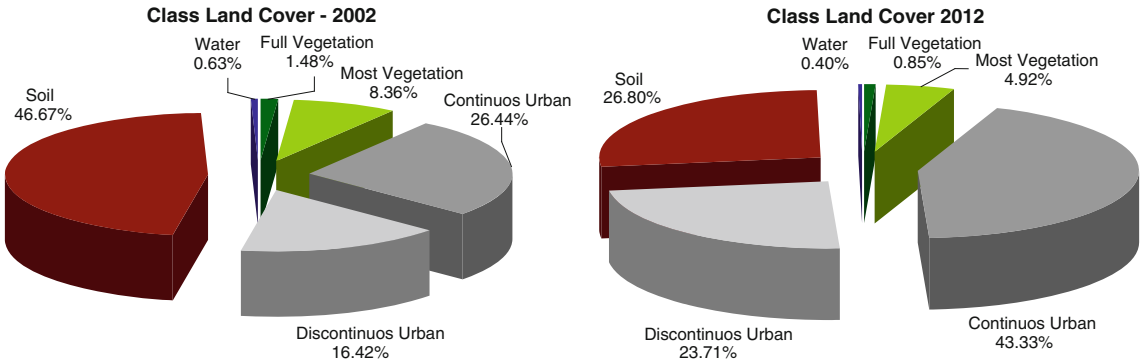

Fig. 34.4 Land cover distribution in 2002 and 2012

station measurements, as they were the most complete. This methodology has been tested in over more 500 sites around the world.

In order to analyse the impacts of climate change on groundwater active recharge in the area under study, we first considered the average precipitation data for all 50 years. The data was then divided into 5-year sets, and the average annual precipitation was calculated for each (Fig. 34.3), finally it was considered the Most Frequent Value, MFV.

The evaluation of the impact of climate change on groundwater active recharge considered land cover as the second most important factor affecting infiltration. Land cover data for 5 sample years was considered (Sappa et al. 2013), 2002, 2004, 2007, 2009 and 2012.

Changes in land cover influence the infiltration capacity of the soil and are a consequence of people's adaptation to climate change. In the last 10 years, soil, which is land cover type with the maximum Potential Infiltration Factor (PIF) value (Sappa et al. 2002), decreased from 46.7 % in 2002 to 26.7 % in 2012 in the area under study (Fig. 34.4).

Table 34.1 Potential infiltration factor, referred to the different land cover class (modified from Civita et al. 1999)

Land cover class	Potential infiltration factor
Full vegetation	0.3
Most vegetation	0.4
Continuous urban	0.1
Discontinuous urban	0.2
Soil	0.3
Water	0.6

34.3.2 Results and Discussion

Specific PIF values were assigned to each land cover class (Table 34.1).

In order to evaluate infiltration in the study area, the following scenarios were considered. First, the Most Frequent Annual Precipitation Value (MFPV) was calculated for the 5 available historical land cover scenarios

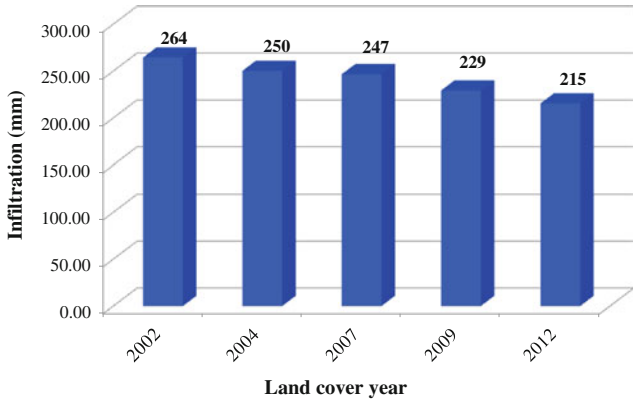

Fig. 34.5 Infiltration trend according to land cover and MFPV

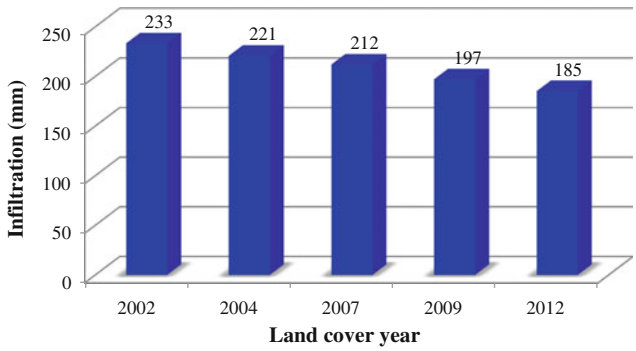

Fig. 34.6 Infiltration trend according to land cover distributions

(Fig. 34.5). Results indicate a continuous decrease in infiltration of 18.6 % over the last ten years, with a consequent decrease in groundwater active recharge.

For the purpose of comparison, the Average Annual Precipitation (AAP) for 2001–2005 was correlated to land cover distribution for the years 2002 and 2004, and the same correlation was applied to the AAP for 2006–2010 and the land cover data for years 2007, 2009, and 2012.

The results (Fig. 34.6) of this deterministic method for infiltration evaluation show that in the last 10 years the loss of infiltration, due to both land cover changes and to decreases in precipitation, was 20.6 %, with an average annual loss of 2 %. The application of the two methods produced very similar results, with a difference between the two of less than 10 %.

Both sets of results indicate a considerable decrease in groundwater active recharge in the last 10 years. This constitutes an alarming warning of the downward trend that will continue to occur in this area in the near future as a direct and indirect consequence of climate change.

References

Civita et al (1999) Una metodologia per la valutazione della ricarica attiva degli acquiferi. Quaderni di Geologia applicata—vol 1 Pitagora Editrice Bologna

Kent PE, Hunt JA, Johnstone DW (1971) The geology and geophysics of coastal Tanzania. Geophysical paper No. 6, National Environment Research Council, Institute of Geological Sciences, London, 101 p

Mjemah IC (2007) Hydrogeological and hydrogeochemical investigation of a Coastal Aquifer in Dar es Salaam, Tanzania. PhD Thesis, Ghent University, Ghent, 222 p

Mpanda (1997) Geological development of the East African coastal basin of Tanzania. Stockholm Contrib Geol 45(10):121 p

Msindai (2002) Engineering geological mapping of Dar Es Salaam City, Tanzania. Tanz J Sci 28(2):83–96

Sappa et al (2002) Groundwater budget of Maiella (Italy). In: Proceedings of the balancing the groundwater budget, Darwin (Australia)

Sappa et al (2013) Evaluation of the groundwater active recharge trend in the coastal plain of Dar es Salaam (Tanzania). J Chem Pharm Res 5(12):548–552

Part IV

Downscaling Climate Information for Impact Studies

Convener: Dr Marco Turco—*Co-conveners*: Maria del Carmen LLasat Botija, Jost von Hardenberg

Developing regional climate scenarios is a key problem for climate change impact/adaptation studies, especially for geographically complex and heterogeneous regions that are sensible to climate change. Despite the considerable effort to bridge the gap between dynamical models and the end user, this task is still representing a research challenge. This session aims at bringing together researchers working on downscaling climate change scenarios. The session will focus on new methodologies of dynamical and/or statistical downscaling, but also state-of-the-art applications of downscaling methods, including bias correction methods, are welcome.

A GIS-Based Tool for Regional Adaptation Decision-Making for Depopulated Communities in Japan

35

Yingjiu Bai, Ikuyo Kaneko, Hikaru Kobayashi, Hidetaka Sasaki, Mizuki Hanafusa, Kazuo Kurihara, Izuru Takayabu and Akihiko Murata

Abstract

Expert knowledge using high-resolution projection is a growing need and is particularly useful for local climate change adaptation. However, the inability to access and apply these scientifically-based climate data becomes a significant hurdle, especially in the poorest and most marginalized communities. Poor countries and depopulated communities in developed countries are more vulnerable to climate change because they tend to be in geographically weather-sensitive areas. This paper aims to: (1) develop an approach based on Geographic Information Systems (GIS) to cost-effectively and easily integrate observed and projected data into decision-making processes; (2) document how to adjust bias of projections, to provide accurate climate predictions for local decision makers; and (3) assist local decision makers in clarifying regional complex priorities for marginalized communities, with a wide array of adaptation options through efficient use of a GIS database. Kurihara (population 74,149; area 804.93 km^2) in Miyagi Prefecture, Japan was chosen for a pilot study. The city comprises 10 depopulated communities within an active volcanic mountain and seismogenic area that is topographically complex, with the highest peak at 1,627.4 m. Post-disaster power shortages have renewed attention toward territorial planning and infrastructure, particularly in extreme climate regions. Our discussion focuses on how to transform the most recent regional climate projections (5 km resolution) into understandable and useful form for local policy makers to meet regional demands and to produce new forms of collective action via GIS. This method can be transferred to developing countries for potential climate change adaptation and mitigation plans.

Keywords

Bias adjustment • Climate projection • Depopulated communities • Geographic information system (GIS) • Regional adaptation

35.1 Introduction

The period 2001–2010 was the warmest decade on record since modern meteorological records began in the 1850s (WMO 2013). In 2007, Japan attained a new national record of absolute maximum temperature at 40.9 °C. Furthermore, in 2007, 2010 and 2011, the death toll from heat waves was 904, 1,731 and 948, respectively (Ministry of Health, Labour and Welfare 2011).

Y. Bai (✉) · I. Kaneko · H. Kobayashi
Graduate School of Media and Governance, Keio University, 5322 Endo, Fujisawa, Kanagawa 252-8520, Japan
e-mail: bai@sfc.keio.ac.jp

H. Sasaki · M. Hanafusa · K. Kurihara · I. Takayabu · A. Murata
Meteorological Research Institute, Tsukuba, Ibaraki 305-0052, Japan

G. Lollino et al. (eds.), *Engineering Geology for Society and Territory – Volume 1*,
DOI: 10.1007/978-3-319-09300-0_35,

Reducing vulnerability by adapting to climate change is a logical endeavor (Furlow et al. 2011). There is mounting evidence related to the need for providing "high-resolution reliable, timely, accurate and appropriate" regional climate change data and local information, as part of local decision-making processes for adaptation planning at the local (community) scale. This especially includes building and generation of databases that reveal which areas are most vulnerable to climate change (Reid et al. 2010).

For decades, many international meteorological organizations have promoted wide-ranging international cooperation frameworks. These were designed to facilitate sharing of data, products and services, and to make these data freely available to the research community. These databases are a particularly useful resource for research, but are not in understandable form for non-expert users. Moreover, poor countries and depopulated communities in developed countries are more vulnerable to climate change because they tend to be in geographically sensitive areas, such as drought-prone Sudan, cyclone-prone Bangladesh, and other vulnerable locations (Reid et al. 2010). The most important reason such areas adapt poorly to climate change is the lack of a support framework or social learning program, for providing local communities with basic and cost-effective tools to access expert knowledge databases and cope with a changing climate.

The objectives of this paper are to: (1) provide a cost-effective, user-friendly tool that allows the exchange of climatic data (observed and projected) in an easily understandable form for local policy-makers to meet regional demands; (2) document how to adjust the bias of projections, using observations effectively; and (3) develop GIS-based databases designed to aid evidence-based decision-making processes. The city of Kurihara (area 804.93 km^2) in Miyagi Prefecture, Japan was chosen for a pilot study; it comprises 10 depopulated communities. All GIS mapping output can be formatted and displayed by Google Earth or other browser programs. These capabilities greatly aid local governments in undeveloped areas and depopulated communities to obtain information via the Internet. The GIS-based approach can be achieved in both developed and developing countries.

35.2 Depopulated Community in Miyagi Prefecture

Kurihara (population 74,149 as of 31 August 2013) consisted of 10 depopulated communities in 2005. The region is in northwestern Japan and is topographically complex, with the highest peak at 1,627.4 m. The city has the largest area (804.93 km^2; Fig. 35.1a) in Miyagi Prefecture, and is an active volcanic mountain and seismogenic area (the 2008 Iwate-Miyagi Nairiku Earthquake and the 11 March 2011 Great East Japan Earthquake both affected Kurihara). Population density in this mountain area is 0-50 people per square kilometer. The complex topography and poor transportation make Kurihara a geographically isolated region in Japan. Kurihara has 24,412 people aged 65 or older (including 40 aged 100 or older), making up 32.9 % of the total population as of 31 August 2013.

Geographic factors make mountain communities around the world vulnerable to the direct effects of climate change. Kurihara is an agricultural village society with marginalized communities; approximately 70 % of people involved in agriculture are elderly. Significantly, these elderly people live alone, because poor transportation and terrain obstacles limit employment opportunities. This is a distinctive trend in regional towns and cities in Japan. Such elderly populations in mountain areas are expected to suffer greatly from climate change, and are most vulnerable because few people have adequate information. Figure 35.1b, c indicate that annual maximum temperatures in the mountain area (Komanoyu Station; location ② in the right panel of Fig. 35.1a) and low-lying area (Tsukidate Station; location ① in the same panel) rose by more than 1 °C during 1978–2012. Additionally, hourly maximum precipitation in July 2001–2013 rose by more than the average of 1980–2000. This could have potentially substantial negative impacts on this isolated community, such as loss of biodiversity and declining tourism, owing to sediment disasters and landslides triggered by torrential rain. These are related to the fact that warm air can hold more moisture, which affects the occurrence and intensity of extreme precipitation events.

35.3 Methods and Data

We used a high-quality daily dataset of JMA observations (Japan Meteorological Agency 2013) and projections (5 km resolution) developed by the JMA Meteorological Research Institute (MRI). Projections were on a 5 km mesh from a non-hydrostatic regional climate model (NHRCM-5 km), following the Special Report on Emissions Scenarios A1B scenario developed by the MRI. These were dynamically downscaled results from the MRI-AGCM3.2S (grid spacing 20 km), an atmospheric general circulation model (AGCM) driven by the ensemble mean sea surface temperature of all Coupled Model Intercomparison Project 3 coupled GCMs (CMIP3 climate Model Documentation, Reference and Link 2007). MRI-AGCM3.2S output is successful in simulating features characteristic of the seasonal cycle of the East Asian summer monsoon and topography-regulated precipitation data.

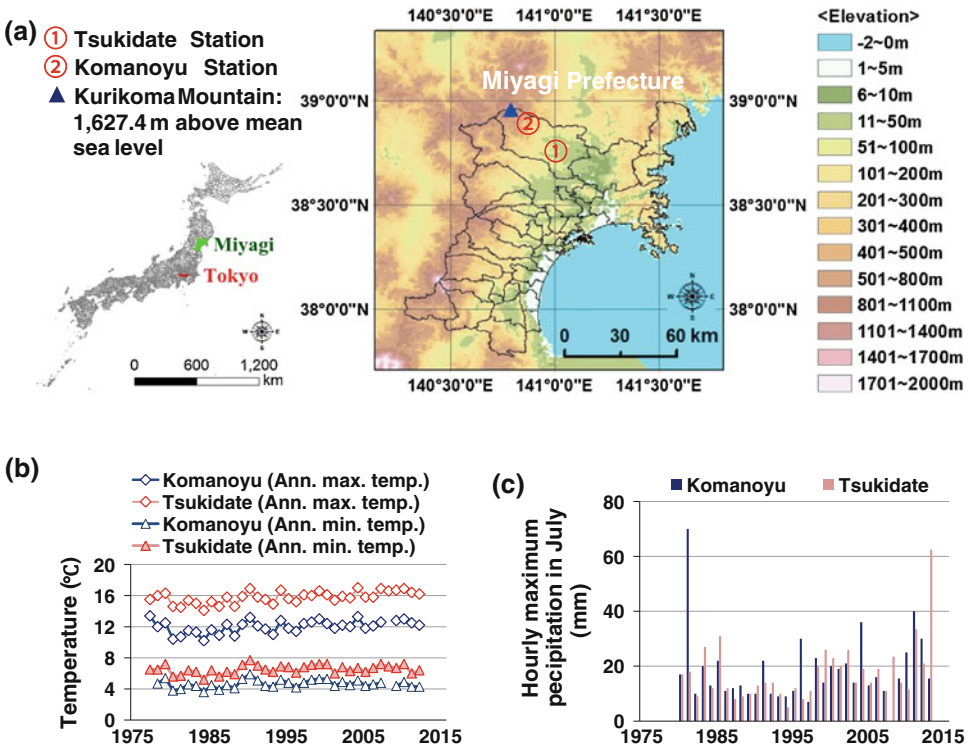

Fig. 35.1 Location and elevation of Kurihara, Miyagi Prefecture in Japan (**a**); observed annual maximum temperature during 1978–2012 (**b**) and observed maximum precipitation in 1 hour in July during 1980–2013 (**c**) in Kurihara based on average records from Tsukidate (town center, low-lying area, location ①) and Komanoyu (mountain area, location ②) stations (**c**). Tsukidate station (38°44.1′ N, 141°00.3′ E; elevation 25 m above mean sea level); Komanoyu Station (38°54.8′ N, 140°49.7′ E; elevation 525 m above mean sea level). *Data source* Japan Meteorological Agency (2013)

We developed a mapping tool for managing an integrated spatial and attribute database, with a suite of climate change indices, regional statistics and regional vulnerability indices focused on extreme climatic events. The study involved four main steps, namely, climate change mapping (climate change information with geographic scale and location information), regional statistical GIS, vulnerability assessment by GIS and local (community) adaptation identification, and analysis. After the 1990s, GIS statistical analysis was conducted stepwise for local governments in Japan. GIS-based datasets are available for re-editing and visualization in Google Earth as needed. GIS represents a mapping approach designed to present a regional development snapshot of governmental statistical information. The mapping tool uses GIS to easily present observed (station) and projected (grid) data together. Mapping these observed and projected data in the same GIS domain allows the user to directly link other GIS data, such as societal statistical databases and climate change data. Climate change mapping is a vehicle for readily depicting special distribution changes and trends across temporal and geographic scales. Vulnerability assessment by GIS includes analysis of natural, social and economic vulnerabilities. All data are computed and analyzed for regional tasks in the GIS domain, and output is saved in a GIS database. Moreover, the user can easily transform all output into a Keyhole Markup Language (KML)/Keyhole Markup Language Zip (KMZ) file, which can easily be presented in Google Earth or Internet browser programs. This method brings policy makers and citizens together and facilitates policy analysis at national and local levels.

35.4 Regional Climate Change and Adjusting Bias of Projections

The climate informatics module consists of the spatial distribution of projected climatic indices and their change, using daily, monthly and annual weather data (focusing on temperature and precipitation) from three study periods. These are present period (September 1980–August 2000), near-future period (September 2016–August 2036), and future period (September 2076–August 2096). Comparing near-future and future conditions, temperatures in Kurihara will increase more than 0.7–1.7 °C and 0.7–2.3 °C (summertime), and 2.5–3.3 °C and 2.8–4.3 °C (wintertime), respectively. Percentage changes of monthly precipitation in summer and winter are −15 to 23 % and 9–2 % in the future period, respectively. June monthly precipitation will decrease 0–9 % in mountain areas and 10–15 % in plains areas. July and August monthly precipitation will increase 5–28 % in plains areas and the area between the mountains. The rainy season (Baiu front) will shift from the end of June to July and August, and have longer duration. For the near-future period, percentage change for June and July monthly precipitation will decrease 0–16 %, and for August will increase 10–29 % in mountain areas. For winter, percentage change for December monthly precipitation will not

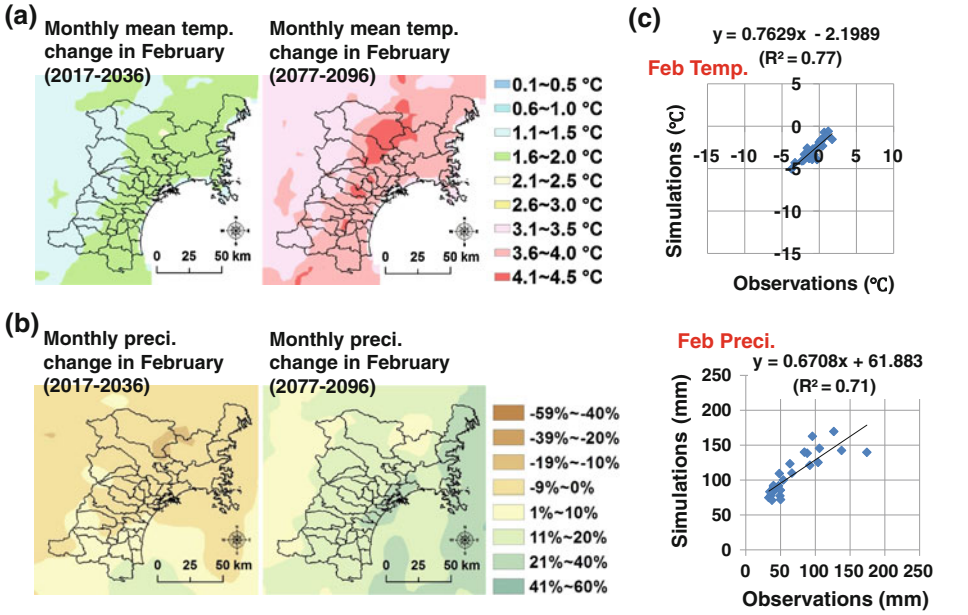

Fig. 35.2 Monthly Mean temperature changes (**a**) and percentage changes in monthly precipitation (**b**) in February over Miyagi Prefecture in the near-future (2017–2036) and future (2077–2096) periods based on the NHRCM-5 km output; samples of good correlation between observations and NHRCM-5 km outputs of monthly mean temperature ($R^2 = 0.77$) and monthly precipitation ($R^2 = 0.71$) in February during the present period (**c**, 520 samples)

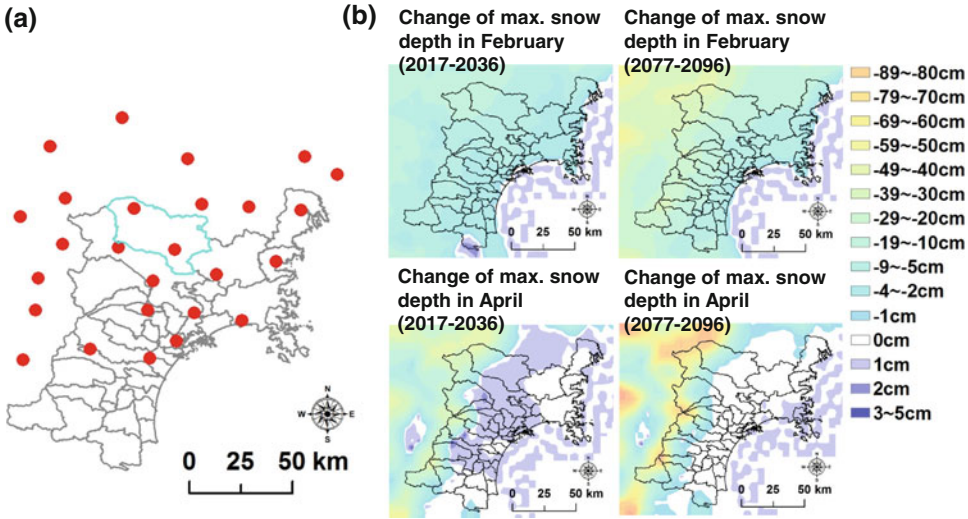

Fig. 35.3 Locations of 26 observing stations (*red points* in **a**); changes of maximum snow depth in February and April during near-future (2017–2036) and future (2077–2096) periods from NHRCM-5 km output (**b**)

change; January will increase more than 10–19 % and February will decrease 7–10 % (Fig. 35.2a, b). Maximum snow depth in February will decrease 6–16 cm and 12–45 cm during the near-future and future periods, respectively. However, that depth in April will increase little in the near-future period (Fig. 35.3b).

Recent regional climate model (RCM) improvements have enhanced the ability to simulate many aspects of climate variability. However, the RCMs and computer technology are not sufficient to provide credible probabilistic projections of changes in daily climate, such as extremely hot days or spells of sustained heavy rainfall. The database with a GIS-based tool provides projected changes associated with monthly, seasonal and annual climate for 20-year periods (for example, change in August temperature or in wintertime). So the climatic changes are provided as probabilistic projections, for example, changes to seasonal extremes such as the warmest day of summer or wettest day of winter. Downscaling uncertainty and systematic limitations in accurately simulating regional climate conditions persist. To estimate and reduce possible structural modelling uncertainty, root mean square (RMS) errors and bias of monthly mean temperature and monthly precipitation were calculated. Observed data were available from 26 observation stations covering Kurihara (Fig. 35.3a).

Twenty years of data in the present period were analyzed. Table 35.1 shows RMS errors and bias of monthly mean temperature and monthly precipitation between model simulations and observations (for each month, there are 520

Table 35.1 RMS errors and bias of monthly mean temperature and monthly precipitation between model simulations and observations during the present period

	Jan	Feb	Mar	Apr	May	Jun	Jul	Aug	Sep	Oct	Nov	Dec
Temperature												
RMS (°C)	2.47	2.13	0.91	0.53	0.66	1.37	0.67	0.63	0.67	0.70	1.51	2.51
Bias (°C)	–2.33	–2.03	–0.78	–0.11	0.49	1.31	0.55	0.46	0.45	0.37	–1.40	–2.41
Precipitation												
RMS (%)	140.73	87.70	70.29	6.36	13.84	27.16	14.96	19.78	10.61	17.10	19.92	157.39
Bias (%)	121.66	76.98	67.75	−1.16	−12.06	−26.52	−13.16	−13.67	8.14	2.50	10.16	133.00

26 observation stations; for each month there are 520 samples

samples). In addition, statistical analyses of correspondence were estimated between model simulations and observations during the present period. Both monthly mean temperature and monthly precipitation indicate a significant correlation between model simulations and observations ($r = 0.78$ to 0.95; 520 samples). As an example, Fig. 35.2c indicates spatially strong correlation between observations and NHRCM-5 km outputs of monthly mean temperature ($R^2 = 0.77$) and monthly precipitation ($R^2 = 0.71$) in February, demonstrating the model experiments' ability to obtain probabilistic projections in the present period.

35.5 Conclusions

Archie (2013) cited three stages of the local adaptation process. These are "understanding and detecting the problem," "gathering and using information," and "(re)defining the problem." Here, we validated the integration of observed and projected data into decision-making processes at community levels, and then provided a user-friendly GIS approach to a local adaptation plan. Communities can thereby take appropriate and effective actions by understanding the risks they face. Our findings clearly illustrate the importance of measuring the bias of projections, particularly a valid and feasible means for characterizing and adjusting projection uncertainty that can facilitate effective decision making.

Of 3,233 cities, towns and villages in Japan, 1,208 are currently classified as depopulated areas, comprising 48 % of the total national area (Ministry of International Affairs and Communications 2013). By providing conceptually valid and practically robust information regarding areas that are most vulnerable to climate change through efficient use of a GIS database, this study effectively guides researchers' future endeavors in helping marginalized local people and communities cope with a changing climate.

Acknowledgments The authors would like to thank the Meteorological Research Institute of the Japan Meteorological Agency for supporting this research. This study was conducted under the Green Society ICT (Information and Communication Technology) Life Infrastructure Project conducted by Keio University, and was supported by Funds for Integrated Promotion of Social System Reform and Research and Development, sponsored by the Ministry of Education, Culture, Sports, Science and Technology of Japan.

References

Archie KM (2013) Mountain communities and climate change adaptation: barriers to planning and hurdles to implementation in the Southern Rocky Mountain Region of North America. Mitig Adapt Strateg Glob Change. doi:10.1007/s11027-013-9449-z

CMIP3 Climate Model Documentation, References, and Links (2007) http://wwwpcmdi.llnl.gov/ipcc/model_documentation/ipcc_model_documentation.php. Accessed 25 Sept 2013

Furlow J, Smith JB, Anderson G, Breed W, Padgham J (2011) Building resilience to climate change through development assistance: USAID's climate adaptation program. Clim Change 108:411–421. doi:10.1007/s10584-011-0127-4

Japan Meteorological Agency (2013) Metrological data. http://www.data.jma.go.jp/obd/stats/etrn/index.php. Accessed 26 Sept 2013 (in Japanese)

Ministry of Health, Labour and Welfare (2011) Press release. http://www.mhlw.go.jp/stf/houdou/2r9852000001g7ag-att/2r9852000001g7fo.pdf. Accessed 25 Sept 2013 (in Japanese)

Ministry of International Affairs and Communications (2013) Statistics bureau: population census. http://www.stat.go.jp/english/data/kokusei/index.htm. Accessed 25 Sept 2013

Reid H, Huq S, Murray L (2010) Community champions: adapting to climate challenges. International Institute for Environment and Development, London. http://www.rockefellerfoundation.org/news/publications/community-champions-adapting-climate

WMO (2013) The global climate 2001–2010, a decade of climate extreme summary report. http://library.wmo.int/pmb_ged/wmo_1119_en.pdf. Accessed 25 Sept 2013

Extension of the SIM Reanalysis by Combination of Observations and Statistical Downscaling

36

Minvielle Marie, Pagé Christian, Céron Jean-Pierre and Besson François

In the framework of climate change, it appears necessary to better understand the natural variability over the 20th century of hydrometeorological variables at very fine spatial scales over France. The study of long climate datasets is also required to isolate the contribution of natural decadal variability from that of anthropogenic forcing to climate variations. The aim of this work is the extension of the SIM reanalysis over the entire 20th century, especially focusing on temperature and rainfall over France, but also soil wetness and river flows. The available surface observations of the Météo-France database appear insufficient to force the hydrometeorological chain of models and produce a good reanalysis. To overcome that fact, a new methodology is developed, combining the use of a statistical downscaling algorithm and the available surface observations to better constrain the statistical downscaling reconstruction and produce the more realistic as possible hydrometeorological dataset over France over the entire 20th century.

36.1 Introduction

The scientific understanding of climate change is now sufficiently clear to show that anthropogenic global warming is already upon us. Uncertainties remain, however, especially regarding how climate will change in the next decades, in particular at regional and local scales for which natural variability is large and resolution of models too coarse. Long climate data sets at very fine spatial scales provide crucial information and are required for evaluation and verification of climate hindcasts/forecasts at sub-regional scale. Furthermore, their study is necessary to isolate the contribution of natural decadal variability from that of anthropogenic forcing to climate variations.

The aim of this work is the extension of the fine-mesh SIM (SAFRAN-ISBA-MODCOU) hydrometeorological reanalysis to the entire 20th century, especially focusing on temperature and rainfall over France, but also soil wetness and river flows. This extension will first allow a detailed investigation of the influence of decadal variability on France temperature and precipitation at very fine spatial scales. This new dataset will also provide crucial information for climate model evaluation at local scales and for the study of the past decadal climate variability of both near surface atmospheric parameters and water resources over France.

Here, we try to develop a methodology to extend the SIM hydrometeorological reanalysis. Two approaches are possible and explored in this work. The first is to use the available daily observations over France over the past decades along with NOAA 20th Century Reanalysis to directly force the SIM hydrometeorological suite of models. If the available surface observations prove to be insufficient, the second approach is the use of a statistical downscaling methodology. After having estimated the biases and strengths of the two methods, a novel methodology combining these two approaches and including past observations in the statistical downscaling algorithm is discussed.

36.2 Data and Models

36.2.1 SAFRAN and the SIM Hydrometeorological Chain

The SIM system is a combination of three different components: an atmospheric analysis system SAFRAN (Durand et al. 1993) providing the atmospheric forcing for the land surface model ISBA (Noilhan and Planton 1989) that computes surface water and energy budgets and the hydrological model MODCOU (Ledoux et al. 1989) that

M. Marie · C. Jean-Pierre · B. François
Direction de La Climatologie/Météo-France, 42 Avenue G. Coriolis, 31057 Toulouse, France

P. Christian (✉)
SUC au CERFACS, URA CERFACS/CNRS No1875, Toulouse, France
e-mail: christian.page@cerfacs.fr

G. Lollino et al. (eds.), *Engineering Geology for Society and Territory – Volume 1*,
DOI: 10.1007/978-3-319-09300-0_36,

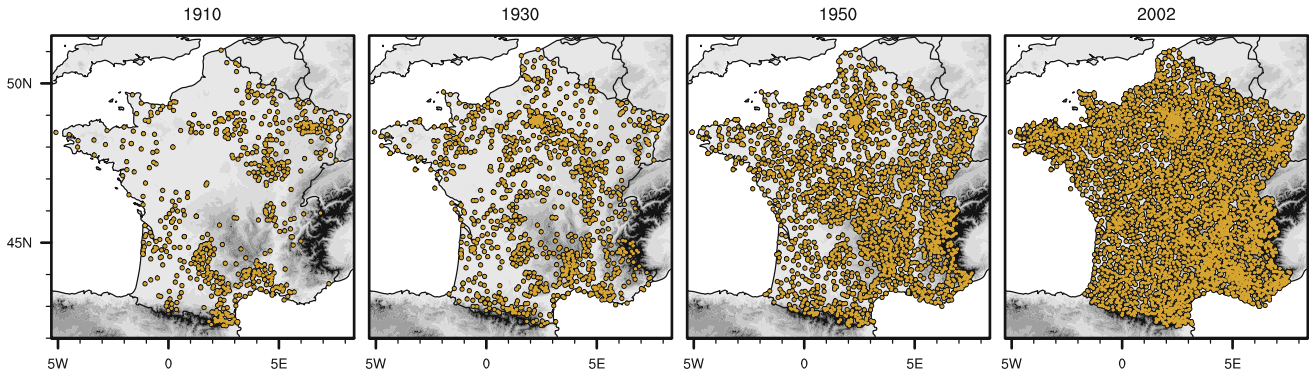

Fig. 36.1 Example of the density of daily rainfall observations over France respectively in 2002, 1950, 1930 and 1910

provides river flows and level of several aquifers. Initially designed to provide atmospheric forcing data in mountainous areas for avalanche hazard forecasting, the SAFRAN analysis system was extended over all of France, and the SIM system has been used operationally at Météo-France since 2003 in order to monitor the water resources in France in near-real time. All these atmospheric and hydrological variables generated by the SIM system constitute the SIM reanalysis. The current version only covers the 1958–2012 period (Vidal et al. 2010; Quintana-Seguí et al. 2008). The objective of this work is to extend this reanalysis to the entire 20th century. SAFRAN produces hourly atmospheric analysis by combining surface observations at station locations with a first-guess field from model outputs from ECMWF archives, or in our case the NOAA 20th Century Reanalysis data (Compo et al. 2011). The analysis consists of 8 parameters, used to force ISBA-MODCOU: the 10 m wind speed, 2 m relative humidity, 2 m air temperature, cloudiness, incoming solar and atmospheric radiations, snowfall and rainfall. All analyzed values are interpolated at the hourly time step, and ultimately projected on an 8-km regular grid.

36.2.2 Surface Observations

All surface observations of wind speed, relative humidity, air temperature, cloudiness, radiations, snowfall and rainfall available in the Météo-France database are considered here. Figure 36.1 shows the evolution of the number of available precipitation observations throughout the 20th century. However the number of observations dramatically decreases in the past. A non-negligible number of rainfall observations are available over the past decades, but the density of observations for temperature, wind, cloudiness and humidity before 1958 is greatly reduced. As it will be discussed in Sect. 36.3, the number of observations at the beginning of the 20th century is insufficient to produce a suitable SAFRAN atmospheric analysis, which results in biases in the SIM hydrometeorological reanalysis.

36.2.3 The Statistical Downscaling Software DSCLIM

To overcome the coarse resolution of models or the absence of data, several downscaling techniques have been developed to obtain surface variables at very fine scale. To extend the SIM reanalysis, a statistical downscaling approach is used to reconstruct the surface atmospheric variables and overcome the lack of observations at the beginning of the 20th century. The chosen methodology is the DSCLIM software package implemented by the CERFACS, a weather typing based statistical methodology (Pagé et al. 2010 for more details about the DSCLIM algorithm). The principle is first to establish a statistical relationship between a large-scale atmospheric variable (from NOAA 20CR reanalysis) and surface atmospheric variables (the existing SIM reanalysis) over France for the present climate (1958–2008). Once this transfer function obtained, it can be applied to the past decades using the NOAA 20CR reanalysis as predictor since 1871 and resample the existing 1958–2008 SIM reanalysis to reconstruct the atmospheric surface conditions over the entire 20th century.

36.3 Comparison of the Two Methods

The first step of this work was to compare the biases and strengths of both DSCLIM and SAFRAN forced only by the available observations and estimate their ability to

reconstruct the atmospheric surface conditions over France during the past decades. If the number of observations is sufficient in the past, it could be possible to realize a reconstruction only using observations as inputs to the SIM chain. However, as shown in Fig. 36.1, the decrease of the density of observations at the beginning of the 20th century is important and it is first necessary to estimate the consequence on the quality of the SAFRAN analysis. In this sense, SIM hydrometeorological experiments were performed for some recent years, with a number of observations artificially reduced to what is available in years 1910, 1930 and 1950. For example, for the 2002–2003 hydrological year, the SIM chain has been forced only by the observations of 2002–2003 comparable in number and distribution to 1910, 1930 and 1950. Concurrently, the same recent years have been downscaled by DSCLIM and used to force ISBA-MODCOU. Additionally, a improved version of the DSCLIM algorithm have been developed, more adapted to the present study case.

The comparison of these experiments with the original SIM years has pointed out the weaknesses and strengths of each approach (Fig. 36.2). It has been particularly shown that observations are not enough at the beginning of the century to reproduce with SAFRAN a correct mean state, which is on the other hand better reconstructed with DSCLIM. As expected, biases are especially stronger in the 1910 experiment than in the 1950 one, and clearly localized in areas with a low density of observations. On the other hand, the DSCLIM methodology does not appear efficient to generate an appropriate daily temporal correlation. Furthermore, DSCLIM exhibits significant biases (not shown) especially during summer and near the Mediterranean region.

36.4 Application to the Entire 20th Century and Combination of the Two Approaches

DSCLIM is able to reproduce a very good mean state and interannual variability (Fig. 36.3, left) as shown by the correlation of 0.78 between the reconstructed and original annual precipitation accumulation over the 1958–2008 period. By comparison with the observations, the application of the DSCLIM algorithm over the 1871–1957 period using the NOAA 20CR reanalysis as large scale predictor, has shown its ability to reconstruct a good interannual variability in the past (Fig. 36.3, right). Furthermore, observed trends and decadal variability over the entire 20th century are also very correctly captured by DSCLIM. But as discussed in Sect. 36.3, DSCLIM also exhibits biases: an underestimation of variance and its difficulty to reproduce the daily variability.

Given these results, it was decides to combine DSCLIM with the available observations over the past decades in order to keep the reconstruction of the atmospheric variables as close as possible to the observations. The suggested methodology is to modify the actual DSCLIM algorithm by

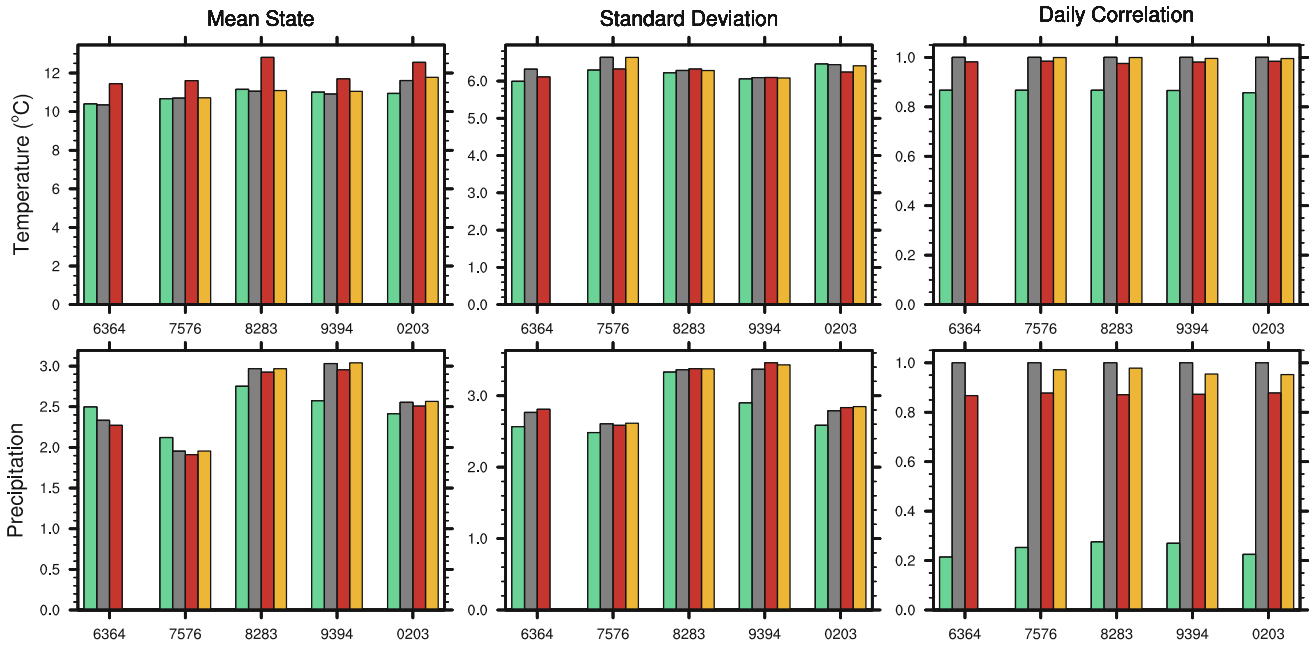

Fig. 36.2 Comparison of mean state (*left*), standard deviation (*center*) and daily correlation (*right*) for 5 recent years reconstructed by DSCLIM (*green*), or by SAFRAN using a reduced number of observations similar to 1910 (*red*) and 1950 (*yellow*), and compared to the original SIM dataset (*grey*) for temperature (*top*) and precipitation (*bottom*)

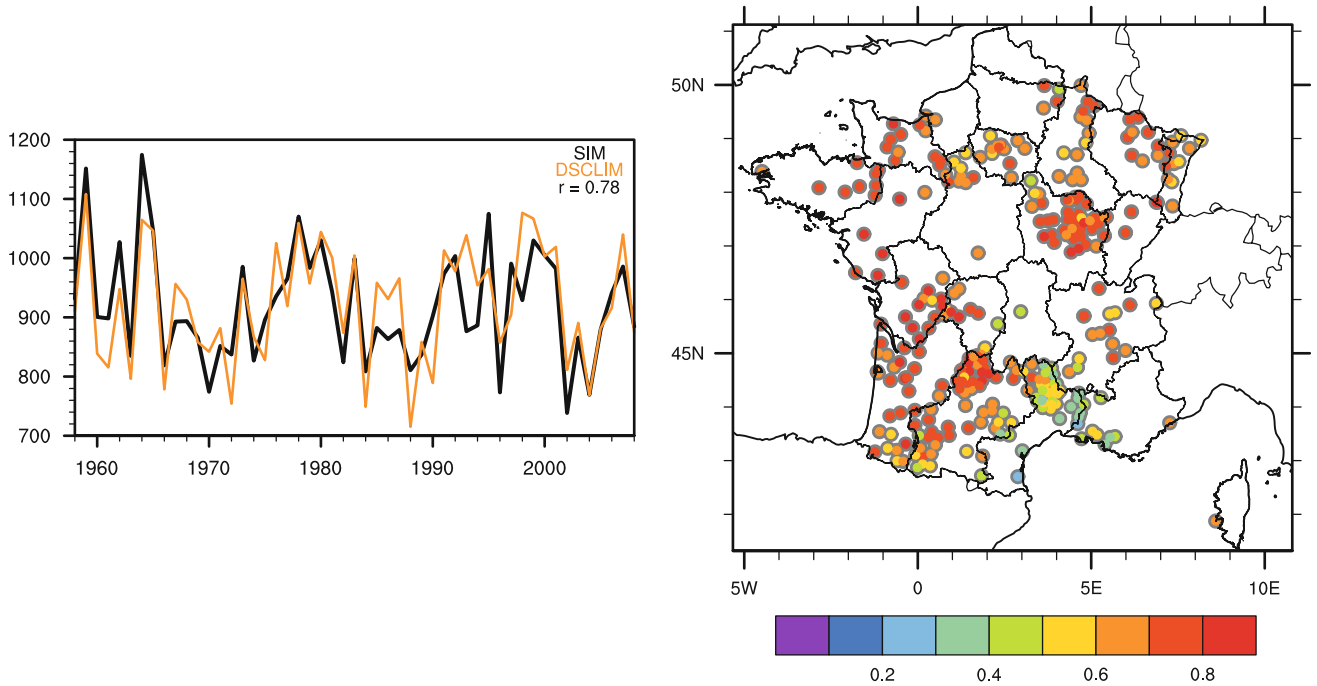

Fig. 36.3 *Left* Annual precipitation accumulation averaged over France over the 1958–2008 period from SIM reanalysis (*black*) and DSCLIM (*orange*). *Right* Correlation of the annual DJF precipitation accumulation over the 1871–1957 period between observations and DSCLIM

forcing the final choice of the analog day by the available observations for this day. Even if the number of observations is reduced as in 1910, a simple analog method applied to precipitation shows a better estimation of the daily correlation than DSCLIM. That's why, an improvement of the DSCLIM reconstruction is expected by the direct use of observations in the algorithm. This approach constitutes an alternative method to the SAFRAN analysis, biased when few observations are available, as before 1950.

36.5 Conclusions and Perspectives

A new methodology has been developed to extend the hydrometeorological SIM reanalysis over the entire 20th century. The reduced number of observations over the past decades does not allow the simple use of the SAFRAN-ISBA-MODCOU system to produce this dataset. On the other hand, the statistical downscaling algorithm DSCLIM is able to produce a surface atmospheric dataset with a correct mean state and interannual variability. However this approach has biases, which are stronger in the summer or in some areas as the Mediterranean region, and presents a weakness in the estimation of the daily variability. The suggested methodology is thus to combine the DSCLIM algorithm (using the NOAA 20CR reanalysis as large scale predictor) to the available observations in order to circumvent these biases and produce an hydrometeorological dataset over France for the entire 20th century which a much better quality.

References

Compo G et al (2011) The twentieth century reanalysis project. Q J R Meteorol Soc 137:1–28. doi:10.1002/qj.776

Durand Y, Brun E, Merindol L, Guyomarc'h G, Lesaffre B, Martin E (1993) A meterological estimation of relevant parameters for snow models. Ann Geophys 18:65–71

Ledoux E, Girard G, de Marsily G, Deschenes J (1989) Spatially distributed modeling: conceptual approach, coupling surface water and ground-water. In: Morel-Seytoux HJ (ed) Unsaturate flow hydrologic modeling: theory and practice. NATO Sciences Service, pp 435–454

Noilhan J, Planton S (1989) A simple parameterization of land surface processes for meteorological models. Mon Weather Rev 117:536–549

Pagé C, Terray L, Boé J (2010) dsclim, a software package to downscale climate scenarios at regional scale using a weather-typing based statistical methodology. Technical report TR/CMGC/09/21, CERFACS, Toulouse, France

Quintana-Seguí P, Le Moigne P, Durand Y, Martin E, Habets F, Baillon M, Canellas C, Franchisteguy L, Morel S (2008) Analysis of near-surface atmospheric variables: validation of the SAFRAN analysis over France. J Appl Meteor Climatol 47:92–107

Vidal J-P, Martin E, Franchistéguy L, Baillon M, Soubeyroux J-M (2010) A 50-year high-resolution atmospheric reanalysis over France with the Safran system. Int J Climatol 30(11):1627–1644. doi:10.1002/joc.2003

Assessment of Hybrid Downscaling Techniques for Precipitation Over the Po River Basin

37

Alessandra Lucia Zollo, Marco Turco and Paola Mercogliano

Abstract

Although regional climate models (RCMs) are powerful tools for describing small scale climate conditions, their direct use in impact studies is still challenging since they are commonly biased. In order to provide "corrected" climate scenarios, here we propose and compare three different hybrid downscaling methods for precipitation, that merge dynamical and statistical approaches, using in cascade the COSMO-CLM RCM and three post-processing techniques: linear-scaling, quantile mapping and MOS analogs. Comparison results over the Po river basin indicate that these approaches generally improve the direct outputs of the COSMO-CLM model, and, among the methods, better results have been obtained with the quantile mapping technique. Finally, the application of these methods to future scenarios is also discussed.

Keywords

Climate change • Precipitation • Regional scenarios • Hybrid downscaling

37.1 Introduction

Global Climate Models (GCMs) are useful tools to produce future climate scenarios required for impact assessments of climate change. However, the direct use of their outputs is often not possible due to their coarse resolution. In order to bridge the gap between the information necessary for the impacts research community and the climate available data, downscaling methods are required. The downscaling of GCM scenarios is usually performed with two different methods: statistical downscaling or dynamical downscaling (see Maraun et al. (2010) and references therein). Traditionally, these two methods have been considered as an alternative to each other. However, the use of the two kinds of downscaling approaches together consents, at least to some extent, to combine their advantages. The idea is to apply the statistical post-processing directly to the RCM outputs following the Model Output Statistics (MOS) approach (Maraun et al. 2010). Here we test three different hybrid downscaling methods for precipitation over the Po river basin. This area is a challenging domain to study the impact of climate change on the hydrogeological risk, since it is characterized by a complex and heterogeneous orography and by a great variability of precipitation regimes. The dynamical downscaling is performed using the non-hydrostatic regional climate model COSMO-CLM, while the statistical post-processing of the RCM outputs is carried

A.L. Zollo (✉) · P. Mercogliano
Impacts on Soil and Coasts Division, Centro Euro-Mediterraneo Sui Cambiamenti Climatici (CMCC), Via Maiorise s.n.c., 81043 Capua, CE, Italy
e-mail: a.zollo@cira.it

P. Mercogliano
e-mail: p.mercogliano@cira.it

A.L. Zollo · P. Mercogliano
Meteo System & Instrumentation Laboratory, Italian Aerospace Research Center (CIRA), Via Maiorise s.n.c., 81043 Capua, CE, Italy

M. Turco
ISAC-CNR, Corso Fiume 4, 10133 Turin, Italy
e-mail: m.turco@isac.cnr.it

G. Lollino et al. (eds.), *Engineering Geology for Society and Territory – Volume 1*,
DOI: 10.1007/978-3-319-09300-0_37,

out using three different methods: linear scaling (LS), quantile mapping (QM) and MOS analogs (MA).

37.2 Data and Methods

The observed data of daily precipitation are provided by the high-resolution (≃8 km) gridded dataset *EMR* (Turco et al. 2013b), which covers the period 1971–2000. In order to develop regional climate scenarios a needed preliminary step is the assessment of uncertainties of the observed datasets (Turco et al. 2013a); to this aim, Turco et al. (2013b) gave some evidences that this dataset could be considered suitable for climate studies.

The dynamical downscaling considered in this study is performed using the COSMO-CLM regional climate model (Rockel et al. 2008). In order to test the regional model capabilities in reproducing the present climate, two simulations have been performed on the control period 1971–2000: one forced by ERA40 Reanalysis and one driven by CMCC-CM global climate model (Scoccimarro et al. 2011). The two COSMO-CLM simulations adopted in this work have been carried out over Italy at a horizontal resolution of 0.0715° (about 8 km), 40 vertical levels and 7 soil levels.

The three considered post-processing methods are: (i) linear-scaling (LS), (ii) quantile mapping (QM), and (iii) MOS Analog method. Linear-scaling is the simplest approach: it consists in scaling the model data using a corrective factor calculated as the ratio of observed and simulated monthly mean precipitations. The quantile mapping correction, instead, tries to correct the probability distribution function (PDF) of the RCM climate data to agree with the observed PDF. We applied the quantile mapping assuming that both observed and simulated monthly distributions are well approximated by a Gamma distribution (Teutschbein and Seibert 2012). Finally, the MOS analog method is based on the hypothesis that "analogue" weather patterns (predictors, e.g. 500 mb geopotential) should cause "analogue" local effects (predictands, e.g. precipitation at a given location). Here a different implementation of the standard analogs method is considered, which uses the same algorithm of the standard method, but employs the daily RCM precipitation as predictor instead of circulation variables (Turco et al. 2011). More details on the implementation of the methods are available in Turco et al. (2013c).

We evaluate the performance of the three MOS methods by means of a leave-one-out cross-validation, in which a moving window of 1 year is used as the validation data, and the remaining observations as the training data. The performance of these methods are assessed, at seasonal scale, in terms of spatial similarity between observed and downscaled climatologies of three ETCCDI (Expert Team on Climate Change Detection and Indices) indices characterizing total precipitation amount PRCPTOT, number of rainy days R1 (with precipitation greater than 1 mm) and maximum precipitation over 1 day RX1DAY (for more details see: http://eca.knmi.nl/indicesextremes/indicesdictionary.php). The comparison between the simulated and observed climatologies is shown through the Taylor diagram (Taylor 2001), which summarizes three metrics of spatial similarity (correlation, standard deviation and centred root-mean-square-error) in a single bidimensional plot.

37.3 Results

37.3.1 Control Scenarios

The three proposed hybrid downscaling techniques are evaluated both in "perfect boundary conditions", that is, considering the ERA40-driven simulation, to minimize the error relate to the GCM model, and in "suboptimal conditions", that is, using the CMCC-CM global model as forcing, in order to test these methods applied to the entire GCM-RCM model chain.

The Taylor diagrams in Fig. 37.1 provide, for both simulations, a summary of the performance of the COSMO-CLM model and the three MOS methods, in terms of the ETCCDI indices considered (PRCPTOT, R1 and RX1DAY). For the sake of brevity, only the Taylor diagrams for winter and autumn are shown; similar results have been obtained in the other seasons (not shown). These diagrams indicate that the direct model output has poor performances, especially the CMCC-CM driven simulation in winter. The linear-scaling method improves the representation of the PRCPTOT index, as expected, and also of the other two indices, although to a lesser extent. The MOS analog method shows a higher agreement with the observations and clearly outperforms the uncalibrated RCM outputs, but it is not able to reduce the autumn bias of the RCM. Finally, the quantile mapping method has the best scores for most indices and it clearly improves the direct output of the COSMO-CLM model.

Once the spatial similarity has been analysed, we test the temporal agreement with observations of ERA40 driven simulation and QM values, which is the method with best performances. This analysis is possible only for the reanalysis driven simulation, thanks to its day-to-day correspondence with observations. The Spearman correlation (CORR) and relative mean absolute error (MAEr) between the simulated and observed series have been calculated at each grid box (not shown for the sake of brevity). Generally the QM has slightly greater values of CORR (from 62 to 65 %) and lower of MAEr (from 1.07 to 1.04).

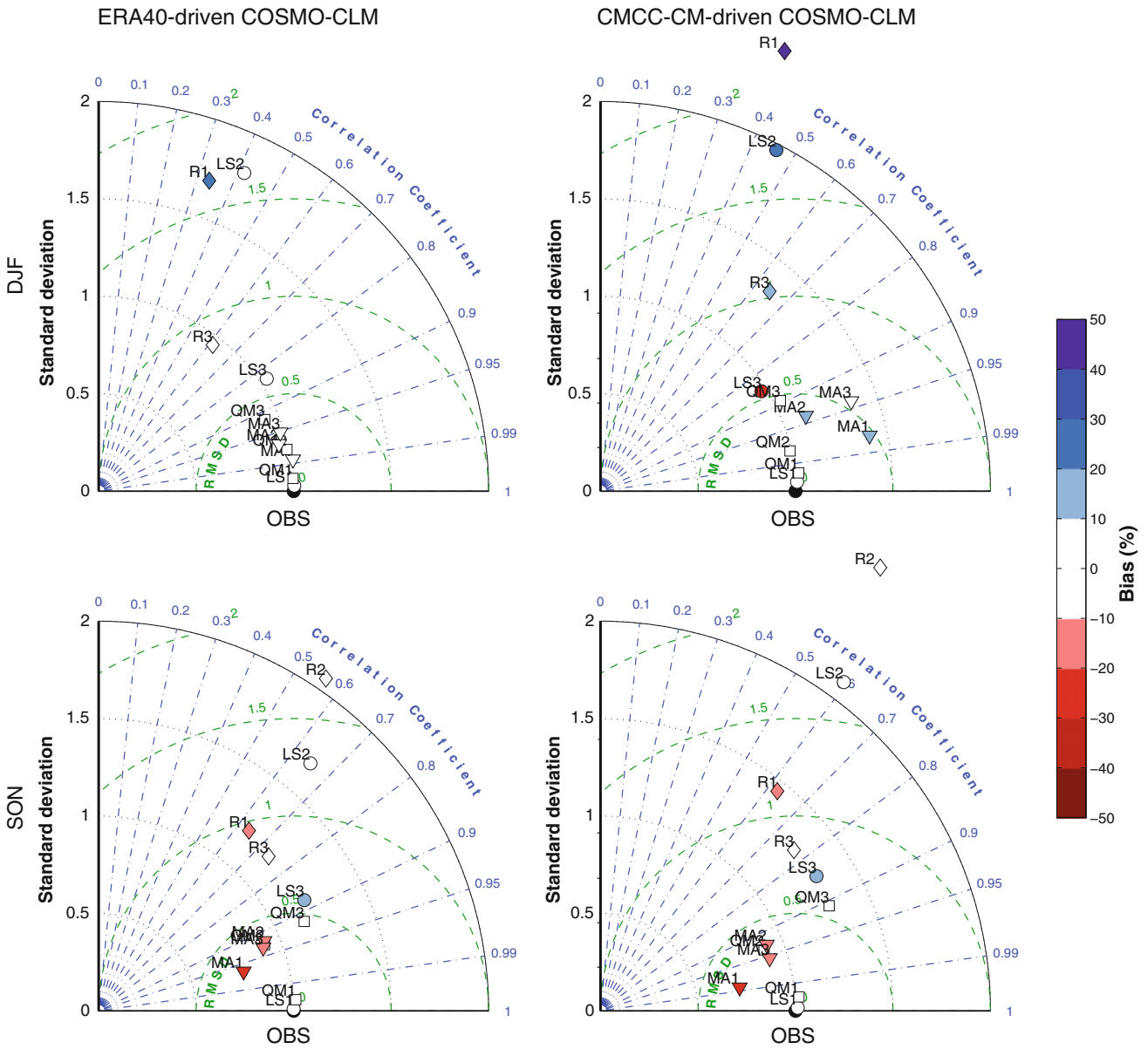

Fig. 37.1 Taylor diagrams for the seasonal precipitation climatology, considering the ERA40 and CMCC-CM driven simulations. Better results are closer to observation (OBS). The *circles*, *squares*, *triangles* and *diamonds* are used for the linear-scaling (LS), the quantile mapping (QM), the MOS analog (MA) and the RCM, respectively, while the *colours* and the *numbers* indicate the bias (in percentage w.r.t. the observed mean) and the indices (1 = PRCPTOT; 2 = R1; 3 = RX1DAY)

37.3.2 Future Scenarios

In order to use these techniques to downscale future scenarios it is also important to assess their robustness in climate change conditions. To this aim, as a first test of the stationarity of these methods, we analyse the consistency of their climate change signals with that of the RCM. Indeed the climate change signals of the MOS methods should be similar to the original RCM ones.

Figure 37.2 reports the comparison between seasonal climate change signals of the RCM and all the three proposed methods, both for the RCP4.5 scenario and for the RCP8.5 scenario, for the three considered indices. The mean change is calculated between control (1971–2000) and future (2071–2100) periods. These results show that the change signal obtained using LS, QM and MA methods is generally comparable to that obtained by the COSMO-CLM model for both the scenarios, indicating the capability of these post-processing techniques to preserve the climate change signal of the RCM. The only more evident discrepancies are a slight overestimation of the QM method for the change of the PRCPTOT and RX1DAY indices in

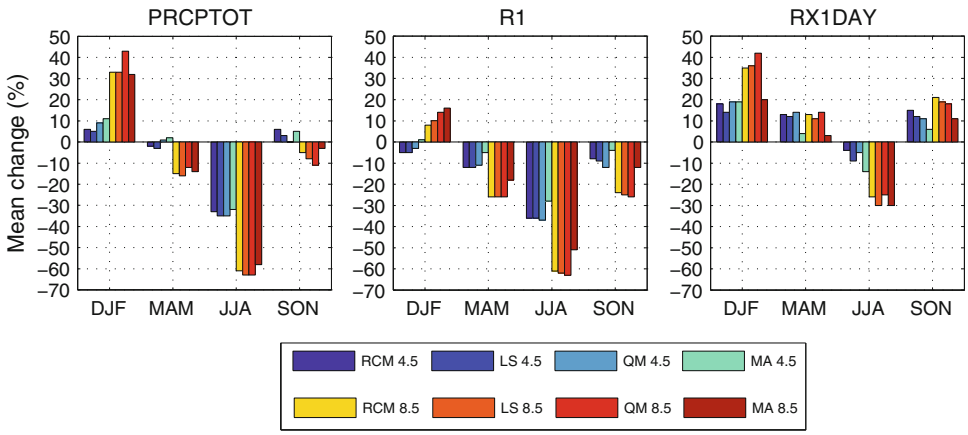

Fig. 37.2 Seasonal mean changes (%) for the three indices PRCPTOT, R1 and RX1DAY, both for the RCP4.5 (*blue tones*) and for the RCP8.5 (*red tones*) scenarios. The mean change in percentage is calculated between control (1971–2000) and future (2071–2100) periods

winter and a slight underestimation of the MA method for the RX1DAY index, probably due to the likely presence of unprecedented values in future scenarios, not observed in the baseline period used for the analog research.

The climate change signal projected by RCP4.5 scenario for the RCPTOT index shows a strong decrease in summer months (around 30 %) and a substantial steady (or slight increasing) signal in the other seasons. A decrease in the number of rainy days is projected in all seasons, more pronounced in summer. Finally the scenarios indicate a slight increase in the RX1DAY index in all seasons except in summer. The comparison between the RCP4.5 and RCP8.5 scenarios indicates that for almost all the cases (except for PRCPTOT in autumn and R1 in winter) the sign of the climate change signal remains the same for both scenarios, but the magnitude of the change is much greater for the RCP8.5. In particular, the slight increment of PRCPTOT (6 %) projected in winter by RCP4.5, becomes a large increase (33 %) following the RCP8.5 scenario, and the decrease of all indices in summer is more pronounced, with a reduction of about 60 % for PRCPTOT and R1, and about 25 % for RX1DAY.

37.4 Conclusions

In this study we have investigated the applicability of hybrid downscaling techniques using the COSMO-CLM model along with three different statistical post-processing methods: linear scaling, quantile mapping and MOS analog. These post-processing techniques have been evaluated over the Po river basin, both in "perfect boundary conditions" and in "suboptimal conditions", using as forcings, respectively, ERA40 reanalysis and CMCC-CM global model. The validation against the observed data shows that the post-processed values clearly outperform the uncalibrated RCM outputs for both simulations. In most of the cases better performances are achieved using the quantile mapping method.

These techniques have been applied to future RCM scenarios in order to evaluate the consistency among direct model and post-processed climate change signals. We have found that generally the climate change signal is similar among the dynamical model outputs and the statistical ones, indicating the capability of these post-processing techniques to preserve the signal of the RCM.

These results suggest that the proposed hybrid downscaling techniques may be very useful tools for climate change impact studies, where users require high-resolution data where systematic errors are reduced.

Acknowledgments This work was funded by the Projects "GEMINA" and "NextData" of the Italian Ministry for Education, University and Research, and the Italian Ministry of Environment, Land and Sea. The authors thank ARPA Emilia Romagna for the EMR dataset kindly provided for this work.

References

Maraun D, Wetterhall F, Ireson A et al (2010) Precipitation downscaling under climate change: recent developments to bridge the gap between dynamical downscaling models and the end user. Rev Geophy 48:RG3003

Rockel B, Will A, Hense A (2008) The regional climate model COSMO-CLM (CCLM). Meteorol Z 17(4):347–348

Scoccimarro E, Gualdi S, Bellucci A et al (2011) Effects of tropical cyclones on ocean heat transport in a high resolution coupled general circulation model. J Clim 24:4368–4384

Taylor K (2001) Summarizing multiple aspects of model performance in a single diagram. J Geophys Res 106(D7):7183–7192

Teutschbein C, Seibert J (2012) Bias correction of regional climate model simulations for hydrological climate-change impact studies: review and evaluation of different methods. J Hydrol 456–457:12–29

Turco M, Quintana-Seguí P, Llasat MC et al (2011) Testing MOS precipitation downscaling for ENSEMBLES regional climate models over Spain. J Geophys Res 116(D18):1–14

Turco M, Zollo AL, Ronchi C et al (2013a) Assessing gridded observations for daily precipitation extremes in the Alps with a focus on northwest Italy. Nat Hazards Earth Syst Sci 13:1457–1468

Turco M, Zollo AL, Vezzoli R et al (2013b) Daily precipitation statistics over the Po Basin: observation and post-processed RCM results. In: Climate change and its implications on ecosystem and society (Proceedings of first SISC Conference). Lecce, 23–24 September 2013, pp 222–234 (2013b)

Turco M, Zollo AL, Rianna G et al (2013c) Post-processing methods for COSMO-CLM precipitation over Italy. Technical report, CMCC. http://www.cmcc.it/wp-content/uploads/2013/05/rp0171-isc-04-2013.pdf

Evaluation of the ENSEMBLES Transient RCM Simulations Over Spain: Present Climate Performance and Future Projections

38

Marco Turco, Antonella Sanna, Sixto Herrera, Maria-Carmen Llasat and José Manuel Gutiérrez

Abstract

We analyzed the state-of-the-art ensemble of RCMs produced in the ENSEMBLES project, focusing on daily maximum temperature and precipitation over Spain. We found that the best GCM-RCM couplings show a relatively good agreement with observed climate. The projected changes up to 2050 (A1B scenario) are quite consistent among the RCMs, generally indicating a decrease in precipitation (between −5 and −25 %) and an increase in maximum temperature (between 1 and 2.5 °C, depending on the season/area). These results suggest the urgency to develop and apply adaptation and mitigation strategies, also considering that, already at present, many areas in Spain suffer from problems related to climate change.

Keywords

Regional climate model • Climate change projections

38.1 Introduction

Global climate models (GCMs) are an important tool to study the climate. However, due to the limitations of the current computers performance, the equations can be solved only on a grid of generally few hundred kilometres. One possible approach (here analyzed) to bridge the gap between the GCMs solved scales and the ones required by the regional climate change impact/adaptation studies is the *dynamical downscaling*. This tool permits to downscale GCM simulations over a region of interest (e.g. Europe) using high resolution (e.g. 25 km) Regional Climate Models (RCMs), which are driven at the boundaries by the GCM outputs (see Maraun et al. 2010, and references therein).

The state-of-the-art ENSEMBLES database (van der Linden and Mitchell 2009) provides the largest available transient simulations over Europe, with more than ten RCMs initialized and driven by the ERA40 reanalysis and by several GCM simulations (considering both the control 20C3M and transient A1B scenario runs). An evaluation of the ERA40-driven RCMs has been already performed over Spain (Herrera et al. 2010) both for mean and extreme spatial precipitation regimes, and the spatially averaged

M. Turco (✉)
ISAC-CNR, Corso Fiume 4, 10133 Turin, Italy
e-mail: m.turco@isac.cnr.it

A. Sanna
CMCC (Euro-Mediterranean Centre on Climate Change), Viale Aldo Moro 44, 40127 Bologna, Italy
e-mail: antonella.sanna@cmcc.it

S. Herrera · J.M. Gutiérrez
Grupo de Meteorología, Department of Applied Mathematics and Computer Science, Universidad de Cantabria (UC), Av. de los Castros s/n, 39005 Santander, Spain
e-mail: herreras@unican.es

J.M. Gutiérrez
e-mail: manuel.gutierrez@unican.es

M.-C. Llasat
University of Barcelona, Av. Diagonal 647, 08028 Barcelona, Spain
e-mail: carmell@am.ub.es

G. Lollino et al. (eds.), *Engineering Geology for Society and Territory – Volume 1*,
DOI: 10.1007/978-3-319-09300-0_38,

Table 38.1 RCM-GCM couplings from the ENSEMBLES project used in this study. The acronyms correspond to that ones in the ensemble web page http://ensemblesrt3.dmi.dk

Number-Acronym	RCM	Driving GCM
1-C4I	RCA3	HadCM3Q16
2-CNRM	ALADIN	ARPEGE
3-DMI	HIRHAM	ARPEGE
4-DMI-BCM	HIRHAM	BCM
5-DMI-ECHAM5	HIRHAM	ECHAM5-r3
6-ETHZ	CLM	HadCM3Q0
7-HC	HadRM3Q0	HadCM3Q0
8-ICTP	RegCM3	ECHAM5-r3
9-KNMI	RACMO	ECHAM5-r3
10-MPI	M-REMO	ECHAM5-r3
11-OURANOS	MRCC4.2.1	CGCM3
12-SMHI-BCM	RCA	BCM
13-SMHI-ECHAM5	RCA	ECHAM5-r3
14-SMHI-HCQ3	RCA	HadCM3Q3
15-UCLM	PROMES	HadCM3Q0

The acronyms marked in bold correspond to the GCM-driven RCMs with a very large bias in reproducing the seasonal precipitation climatology (Turco et al. 2013)

annual cycle. Afterwards, Turco et al. (2013) compared the performance of the GCM-driven control runs (20C3M scenario) with the ERA40-driven ones and found large biases for some RCM-GCM combinations (acronyms marked in bold in Table 38.1) attributable to RCM in-house problems with the particular GCM coupling. These biases are shown to distort the corresponding climate change signal in the last decades of the 21st century.

In this work, we extend such studies considering the maximum temperature (*Tmax*) and precipitation (*Prec*), two key variables for many impact sectors (tourism, agriculture, hydrology, etc.), over Spain, and evaluating (i) the performance of the control (1961–2000) simulations and (ii) their future (2021–2050) scenarios.

38.2 Data

The observed data of daily *Tmax* and *Prec* used in this study, are provided by the high-resolution (≃20 km) gridded dataset *Spain02* (Herrera et al. 2012), covering the Spanish Iberian Peninsula and the Balearic Islands over the period 1950–2008.

The simulation data are based on an ensemble of the state-of-the-art RCMs (see Table 38.1), produced in the EU-funded project ENSEMBLES (van der Linden and Mitchell 2009). The dataset includes ERA-40 reanalysis-driven simulations and GCM-driven simulations for the 20C3M scenario (1961–2000) as well as for the A1B scenario (2001–2050). For practical reasons, the outputs of the RCMs were bilinearly interpolated from their original resolution (≃25 km) to the *Spain02* grid (≃20 km). While this process may introduce a small additional uncertainty, we considered it negligible.

38.3 RCMs Evaluation in Present Climate Conditions (1961–2000)

In order to evaluate the RCMs' performance in present climate conditions we consider the ensemble mean of the fifteen GCM-driven RCMs members—ENS1—, and the eleven best performing RCMs members according to Turco et al. (2013), that is, without the models 4, 5, 12 and 14, —ENS2—. Besides, in order to compare the GCM-driven RCMs with the ERA40-driven ones, also the ensemble mean of the eleven ERA40-driven RCMs members are considered — ENS —.

Figure 38.1 shows the seasonal climatology observed and the mean bias of the three ensembles ENS, ENS1 and ENS2, for *Tmax*. Generally, the ensemble bias is representative of the majority of the models bias (not shown). Over most of the domain, the three ensembles are generally colder than the observed pattern. The most relevant exception is in the south, in summer, probably due to model overestimation of the highest temperature (Boberg and Christensen 2012). Generally, ENS2 reduces the BIAS of ENS1 and has comparable (as in MAM and SON) or less BIAS compared to the ENS (as in DJF and JJA) one.

A detailed analysis of the RCMs evaluation in representing the *Prec* in present climate conditions has been given in Turco et al. (2013). Table 38.2 confirms their main results: all the three ensembles overestimate the seasonal average *Prec* and, except for JJA, the GCM-driven RCMs (ENS1 and ENS2) have stronger bias than the ERA40-driven (ENS). In all of the seasons, ENS2 reduces the bias of ENS1.

38.4 RCMs Analysis of Future Climate Conditions (2021–2050)

To show the uncertainty of the *Prec* scenarios we adopted the technique used by Hemming et al. (2010). This technique allows to represent in only one plot the direction of the mean climate change signal (expressed by different colours) and the agreement in the direction of change among different ensemble members (expressed with

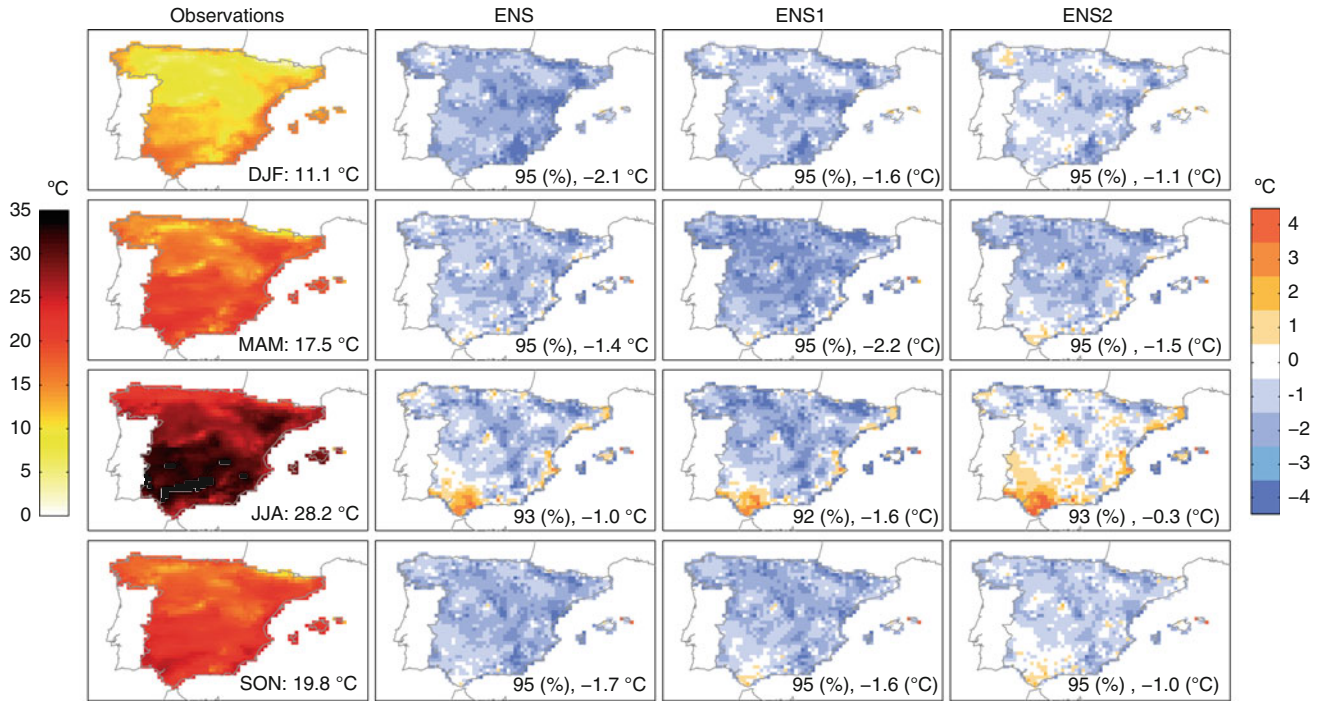

Fig. 38.1 Seasonal *Tmax* climatology of the *Spain02* grid (observed, *left*), the ensemble of ERA40-driven RCMs (ENS, second column), the ensemble of the GCM-driven RCMs (ENS1, third column) and the ensemble of the best GCM-driven RCMs (ENS2, fourth column). The numbers on the maps indicate the spatial correlation (in percentage) between the ensemble mean climatology and the observations, and the spatial mean of the map, respectively. In the case of the observations, only the spatial mean is shown

Table 38.2 Comparison of the seasonal *Prec* climatology of the *Spain02* and the three ensembles (ENS, ENS1 and ENS2)

Season	OBS	ENS	ENS1	ENS2
	mean (mm/day)	*corr* (%)—*bias* (%)	*corr* (%)—*bias* (%)	*corr* (%)—*bias* (%)
DJF	2.2	87–19	82–52	87–34
MAM	1.8	82–33	82–44	87–30
JJA	0.8	84–92	84–38	88–18
SON	2.0	85–11	80–30	86–19

mean spatial mean; *corr* spatial correlation between the ensemble mean climatology and the observations; *bias* mean error of the ensemble wrt observations

different intensity of colour). Figure 38.2 shows the mean change in seasonal *Prec* (DJF, MAM, JJA and SON, from left to right) between the baseline (1971–2000) and future (2021–2050) periods for ENS1 (top) and ENS2 (bottom). In DJF, most of the domain shows no agreement in the direction of change, both considering ENS1 and ENS2. In the other seasons, there is a greater agreement (higher in the western part of the region) among the members of both ensembles, toward a decreased rainfall between −5 and −25%. No substantial differences are observed between ENS1 and ENS2 except in summer, when the ensemble ENS2 shows generally a higher level of agreement and higher values of change, with −25% decreasing *Prec* over the western part of the domain.

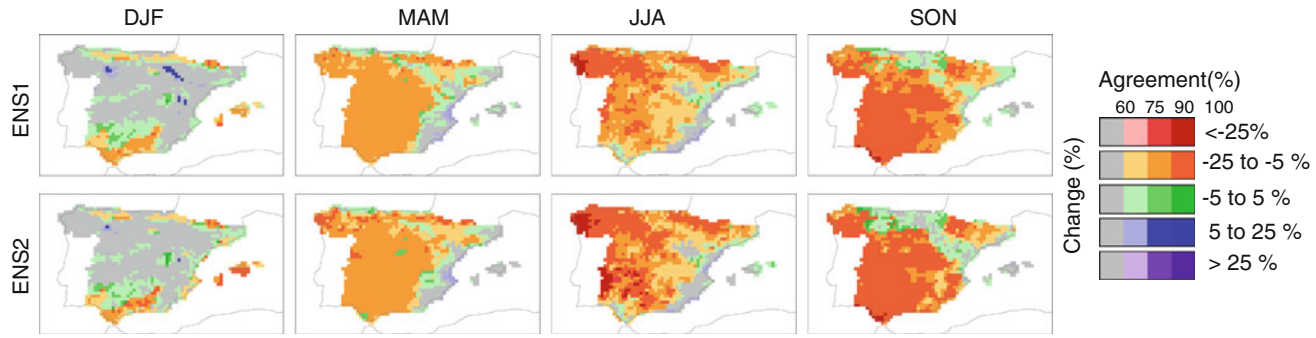

Fig. 38.2 Mean change in seasonal (DJF, MAM, JJA and SON, from *left* to *right*) *Prec* between 1971–2000 and 2021–2050 for (*top*) the ensemble of all the available RCMs and (*bottom*) the ensemble of the best RCMs. The colour saturation level shows the percentage agreement in the direction of change among the ensemble RCMs

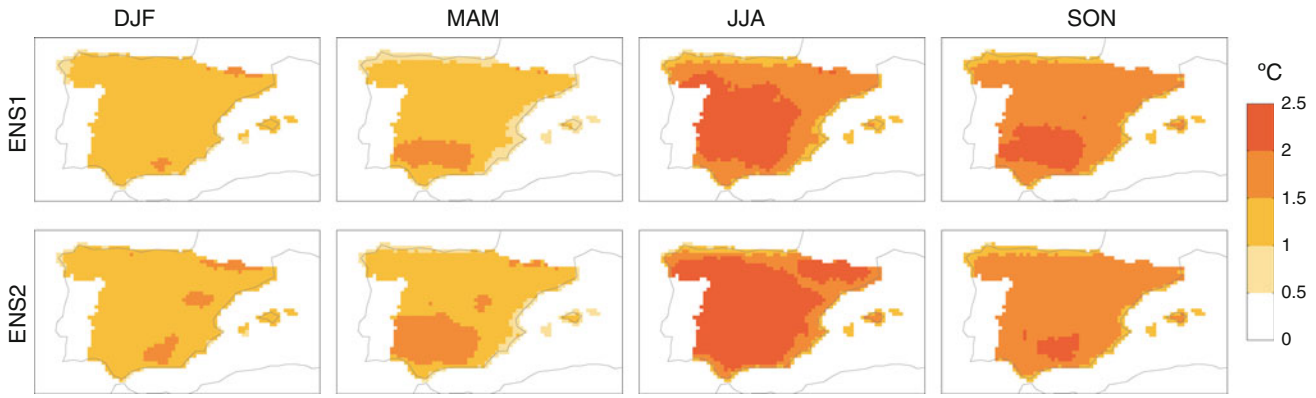

Fig. 38.3 Mean difference in seasonal (DJF, MAM, JJA and SON, from *left* to *right*) *Tmax* between 2021–2050 and 1971–2000 for (*top*) the ensemble of all the available RCMs and (*bottom*) the ensemble of the best RCMs

Figure 38.3 shows the mean difference in seasonal (DJF, MAM, JJA and SON, from left to tight) *Tmax* between the future (2021–2050) and the baseline (1971–2000) periods for (top) ENS1 and (bottom) ENS2. The ensemble agreement in the direction of change is very high (the standard deviation of the ensemble members is always around 0.5 °C), that is, all the RCMs indicate an increase in *Tmax*. The scenario indicates an increase of *Tmax* between 1 and 2 °C in DJF and MAM, and between 1.5 and 2.5 °C in JJA and SON. Besides, in JJA, the ENS2 indicates higher change in *Tmax* w.r.t. ENS1.

38.5 Conclusion

We analysed the state-of-the-art ENSEMBLES RCMs, focusing on *Prec* and *Tmax* over Spain and evaluating (i) the performance of the control (1961–2000) simulations and (ii) the possible future changes up to 2050.

The validation against *Spain02* shows that the ensemble of the best GCM-RCM couplings is able to reasonably reproduce the observed features of present climate.

Under the A1B scenario, over most of the domain, winter *Prec* shows no agreement in the direction of climate change among the RCMs. Instead, in other seasons, a greater agreement among the members is found, with decreasing rainfall, between –5 and –25%. The RCM scenarios agree on a general increase in *Tmax*, higher in summer and autumn.

These scenarios indicate the urgency to apply adaptation and mitigation strategies, according to the Spanish National Climate Change Adaptation Plan.[1]

Acknowledgments This work was supported by esTcena (Exp. 200800050084078), EXTREMBLES (CGL2010-21869) Spanish projects, from Plan Nacional de I+D+i 2008–2011 and by the Project of Interest ''NextData'' of the Italian Ministry for Education, University and Research. For the RCM data used in this study, we acknowledge the ENSEMBLES project, funded by the European Commission's 6th Framework Programme through contract GOCE-CT-2003-505539. The authors thank AEMET and UC for the *Spain02* dataset provided for this work.

[1] http://www.magrama.gob.es/es/cambio-climatico/temas/impactos-vulnerabilidad-y-adaptacion/.

References

Boberg F, Christensen JH (2012) Overestimation of mediterranean summer temperature projections due to model deficiencies. Nat Clim Change 2(6):433–436

Hemming D, Buontempo C, Burke E, Collins M, Kaye N (2010) How uncertain are climate model projections of water availability indicators across the Middle East? Philosophical transactions. Ser A Math Phys Eng Sci 368(1931):5117–5135

Herrera S, Fita L, Fernández J, Gutiérrez JM (2010) Evaluation of the mean and extreme precipitation regimes from the ENSEMBLES regional climate multimodel simulations over Spain. J Geophys Res 115:1–13

Herrera S, Gutiérrez JM, Ancell R, Pons MR, Fras MD, Fernández J (2012) Development and analysis of a 50-year high-resolution daily gridded precipitation dataset over Spain (Spain02). Int J Climatol 32(1):74–85

van der Linden P, Mitchell J (eds) (2009) ENSEMBLES: climate change and its impacts: summary of research and results from the ENSEMBLES project. Met Office Hadley Centre, FitzRoy Road, Exeter EX1 3PB, UK

Maraun D, Wetterhall F, Ireson AM et al. (2010) Precipitation downscaling under climate change: recent developments to bridge the gap between dynamical downscaling models and the end user. Rev Geophys 48:RG3003

Turco M, Sanna A, Herrera S, Llasat MC, Gutiérrez JM (2013) Large biases and inconsistent climate change signals in ENSEMBLES regional projections. Clim Change 120(4):859–869

Application of Climate Downscaled Data for the Design of Micro-Hydroelectric Power Plants

39

Niccolò Dematteis, Murgese Davide and Claudio Cassardo

Abstract

In this paper, changes in annual average precipitation levels from the statistical downscaling (multi linear regression) of RegCM3 data for the meteorological station of Aymaville (Aosta Valley Region, NW Italy) are applied to assess the effect of climate change on stream discharge in presence of a micro-hydroelectric power plant. Impacts were assessed by comparing minimum stream discharge for present days condition with the required water withdrawn under future annual precipitation scenarios (A2 and B2). Equations used to calculate monthly and minimum stream discharge are those provided by the Valle d'Aosta Region Water quality management plan. Modifications in annual average precipitation levels are useful to assess future impacts for months from October to May. Water discharge for the period from June to October, is solely or partially a function of catchment mean altitude (=snowmelt contribution), thus an assessment of climate change effects is not possible. Taking into account the effects of climate change on snow precipitation level and snow accumulation, we suggest that catchment mean altitude is not a suitable parameter for depicting climate change effects on stream discharge during months characterised by prevalent snowmelt contribution.

Keywords

Climate change • Environmental impact assessment • Statistical downscaling • Micro-hydroelectric power plants • Stream minimum discharge

39.1 Introduction and Aims of the Study

The need for reducing greenhouse gasses emissions and fossil fuel dependency, together with the availability of public funds for the construction of power plant based on renewable energy, has prompted the demand for micro-hydroelectric power plants (MHPP) over the Alpine Region. For these plants, principal aspects defining the amount of producible energy are two: (1) difference in altitude between the intake weir and the power house, (2) the average stream discharge that can be withdrawn. Alpine catchments are characterised by relevant altitude difference and significant streams water discharge during the year: these elements result in a significant energy production level. According to Italy laws, MHPPs water withdrawn have to be defined assuring a water flow after the intake higher than the minimum stream water discharge (MSD), to prevent damages to

N. Dematteis · C. Cassardo
Department of Physics, University of Turin, Turin, Italy

M. Davide (✉)
SEA Consulting srl, Turin, Italy
e-mail: murgese@4e-arth.eu

M. Davide
4e-arth (for environment, for ecology, for education for earth our planet), Turin, Italy

C. Cassardo
CINFAI, National Inter/University Consortium for Physics of the Atmosphere and Hydrosphere, Turin, Italy

C. Cassardo
NatRisk Center, University of Torino "Alma Universitas Taurinorum", Turin, Italy

G. Lollino et al. (eds.), *Engineering Geology for Society and Territory – Volume 1*,
DOI: 10.1007/978-3-319-09300-0_39,

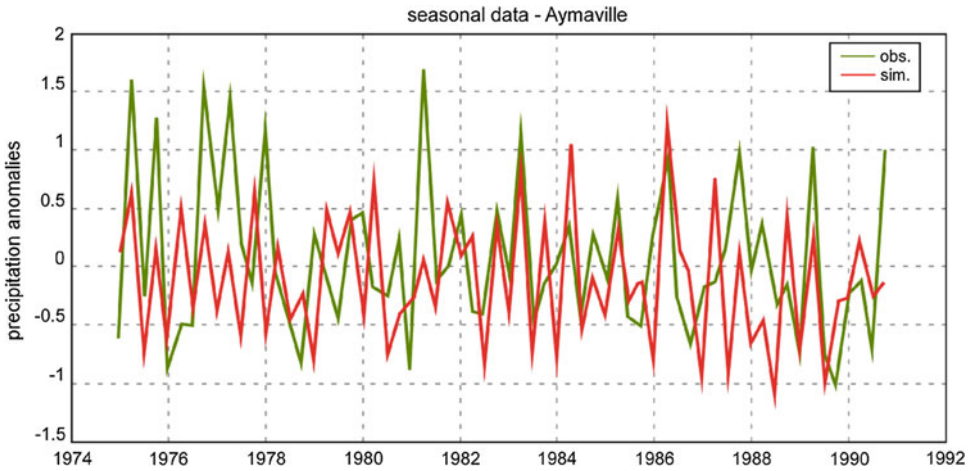

Fig. 39.1 Comparison between observed precipitation anomalies (*green line*) and regression model results (*red line*) for the period 1976–1990

the ecosystems. MSD is calculated according to statistical formulae that are function of annual average precipitation, catchment area and catchment mean altitude. Water quality management plan of Valle d'Aosta Region provides average annual precipitation levels and water discharge equations. Knowing that changes in precipitation levels predicted by climate models will certainly affect streams water discharge, it is important to examine how actual procedures followed by environmental impact assessment (EIA) of MHPPs are taking into account this new information. Also, climate models results are often provided at global or regional scale, whereas hydrological and hydraulic analyses are conducted at local scale. In this view, the availability of downscaled data is an important requirement, in order to include climate model predictions into the EIA of micro-hydroelectric power plants. Following environmental impact assessment procedure, results of statistical downscaling (multi linear regression) of regional climate model data (RegCM3) were applied to the equations used for the calculation of minimum stream discharge related to a hypothetic MHPP. Potential and limitations of this method are discussed.

39.2 Downscaling: Methods and Results

The first step of this study was the statistical downscaling of regional model data, for a meteorological station of Valle d'Aosta Region (NW Italy) (Dematteis 2011). RegCM3 output was chosen as it is one of the existing datasets with the highest resolution currently available (20 km) and since it was also used in other studies (Giorgi et al. 2004; Gao et al. 2006), allowing a useful check of procedures and results. In order to define statistical relationships between regional model output and local climate conditions, precipitation levels (predictand) from 1961 to 1990 recorded at Aymaville station (1,130 m a.s.l.) were analysed. According to criteria proposed by Benestad (2004) and by Benestad et al. (2007), chosen predictors from the regional model were the following: ground pressure, specific humidity, 2 m-temperature. The statistical downscaling was based on a multi-linear regression model (MLR), as it can be applied to a single data series. Exploratory data analysis of precipitation levels recorded at Aymaville station (AMS) indicated a normal distribution for seasonal means of precipitation levels therefore MLR was applied to define a statistical relationship between predictors values and observed seasonal means during the 1961–1975 period. Results were then compared with the observed data of AMS series between 1976 and 1990. Linear regression methods show a low-skill in determining the variances of results; for this reason variances of observed data was related to regression results according to Storch (1999) equation. Validation process showed an acceptable correlation between observed predictands and inflated results ($p = 0.07$; $R = 0.36$) (Fig. 39.1). Based on RegCM3 predictor values for the period 2070-2099, the statistical relationship was used to calculate changes in seasonal average precipitation levels at AMS (Table 39.1) under A2 and B2 scenarios (IPCC AR4 SYR 2007).

Table 39.1 Changes in precipitation levels at AMS for the period 2070–2099 (under A2 and B2 scenarios), compared to precipitation levels recorded between 1961–1990

	A2 scenario	B2 scenario
Annual average precipitation level	−7 %	−5 %
DJF	−12 %	−3 %
MAM	−6 %	−4 %
JJA	−11 %	−10 %
SON	+1 %	−1 %

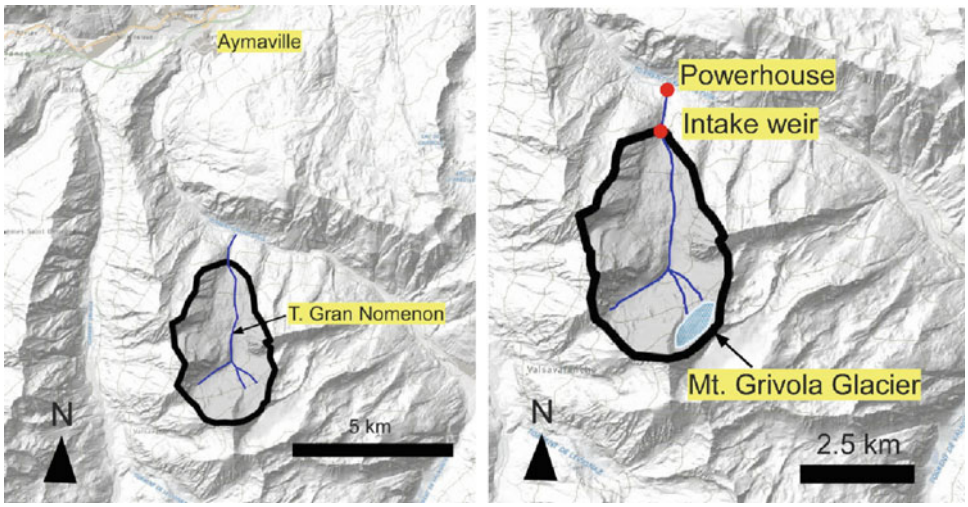

Fig. 39.2 *Left* Aymaville station and Gran Nomenon catchment. *Right* Gran Nomenon catchment; MHPP intake weir and powerhouse location

39.3 Stream Minimum Discharge: Present Day—Future Scenarios

Downscaled data were then applied to assess the effect of a hypothetic MHPP along the Gran Nomenon Stream (Cogne Valley, Valle d'Aosta, NW Italy). The stream is located in the vicinity of AMS, allowing a reliable use of downscaled results (Fig. 39.1). With regard to stream discharge of Gran Nomenon, an important catchment feature is represented by the Mt. Grivola Glacier, which is located along the SE limit of the basin (Fig. 39.2). The main features of MHPP and Gran Nomenon catchment are indicated in (Table 39.2).

Based on the difference of the intake weir and power house altitudes, together with catchment features, expected MHPP nominal power is 425 kW, requiring an average monthly withdrawn of 130 l/s. Average annual discharge (321 l/s), average monthly discharge and monthly minimum stream discharge (MSD) at intake weir, were calculated according to the equations provided by the Water Quality Management plan of Valle d'Aosta Region—Annex G (Table 39.3).

Equations in Table 39.3 results from statistical correlation between observed stream discharge values, catchment features and annual average precipitation levels. These are the equations that have to be used when assessing environmental impacts of MHPPs according to Valle d'Aosta Region guide lines. For the period from November to May, monthly discharge depends only on average annual precipitation level. During both June and September it depends both on precipitation levels and snowmelt (expressed by catchment average altitude). During July and August, water discharge depends only on the snowmelt. According to obtained results, for present days condition, monthly stream discharges are sufficiently large to allow the required withdrawn and the release of an amount of water always higher than the calculated MSD for all considered months

Table 39.2 MHPP characteristics (left) and Gran Nomenon catchment features (right)

MHPP		Gran Nomenon catchment	
ΔH	334 m	Area	11.2 km^2
Average water withdrawn	130 l/s	Average altitude	2,726.5 m
	0.13 m^3/s	Minimum altitude (intake weir)	1,485 m
Nominal power	425 kW	Maximum altitude	3,968 m
Yearly average production	3,402 MWh	Average annual precipitation level	750 mm/yr

(Fig. 39.2). This condition occurs also when considering the reduction in annual average precipitation levels according to downscaling results (Table 39.1), under both scenario A2 and scenario B2 (Fig. 39.3). For present days condition, desired MHPP production rate are obtained with water withdrawn limited to 57 % of total stream discharge, but it has to be increased up to 60 % under A2 and B2 scenarios. It is important to notice that, according to Water Quality Management Plan equations, in July and August stream discharge is mainly a function of catchment mean altitude, indicating that for these months the only contributor to stream flow is the snowmelt. Discharges values are almost the same for present days and for A2 and B2 scenarios (Fig. 39.3), as the equations for these months approximate a climate element (snow cover and melting process) to a morphological parameter (altitude), whose modification-rate and dynamics are significantly different from snow accumulation ones. In our view, this phenomenon should be differently expressed in discharge equations, as it is known that climate change will significantly affect glaciers and snow cover in the future (Bonanno et al. 2014).

Table 39.3 Stream discharge equations according to Valle d'Aosta region water quality management plan—Annex G

Specific discharge (l/s/km^2)	
A: annual average precipitation level (mm)	
H: catchment average altitude (m)	
S: catchment area (km^2)	
q_{meda} (annual specific average stream discharge) = 0.004204856 H + 0.02302933 A	
q_{jan} = 0.231656449 q_{meda}	q_{jul} = 0.034169591 H*
q_{feb} = 0.211382342 q_{meda}	q_{aug} = 0.025126331 H*
q_{mar} = 0.245702885 q_{meda}	q_{sep} = 0.01019068 H + 0.380281169 q_{meda}
q_{apr} = 0.457959942 q_{meda}	q_{oct} = 0.703911596 q_{meda}
q_{may} = 1.478190999 q_{meda}	q_{nov} = 0.434878021 q_{meda}
q_{jun} = 0.012059623 H + 1.92348292 q_{meda}	q_{dec} = 0.286993259 q_{meda}
MSD_{month} = q_{month} S 0.4 (l/s)	Q_{month} = q_{month} S (l/s)

* specific monthly average discharge depends only on average catchment altitude (≈ snowmelt)

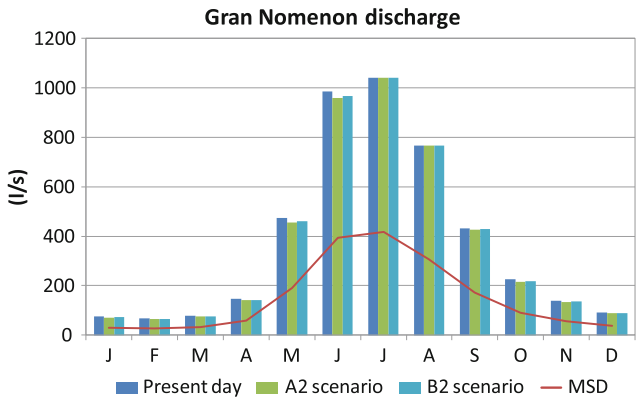

Fig. 39.3 Gran Nomenon monthly discharge: present days, A2 and B2 scenarios. The *red line* indicates the MSD

39.4 Conclusions

This study presents a preliminary application of downscaled climate data for the assessment of impacts on stream ecosystems related to the presence of a MHPP along the Gran Nomenon stream (Valle d'Aosta Region). According to the reduction in annual average precipitation levels calculated for A2 and B2 scenarios, expected impacts on ecosystems from October to May and from are similar to those estimated during present days conditions. From June to September, discharge equations are totally or partially function of catchment average altitude and no reliable indications of climate change impacts on stream flow can be obtained. In this view, we suggest that stream discharge equations defined regional water quality management plans should be revised to better depict climate parameters controlling streams flow and to allow a more reliable assessment of expected changes in precipitation levels under future climate scenarios.

References

Benestad R et al (2007) An evaluation of statistical models for downscaling precipitation and their ability to capture long-term trends. Int J Climatol 27:649–665

Benestad R (2004) Empirical-statistical downscaling in climate modeling. Eos 85:42

Bonanno R, Ronchi C, Cagnazzi B, Provenzale A (2014) Glacier response to current climate change and future scenarios in the northwestern Italian Alps. Reg Env Change 14:633–643

Dematteis N (2011) Modello di precipitazione con tecniche di downscaling statistico, Bachelor Thesis, Deptartment of Physics, University of Turin, Italy

Gao XJ, Pal JS, Giorgi F (2006) Projected changes in mean and extreme precipitation over the Mediterranean region from a high resolution double nested RCM simulation. Geophys Res Lett 33:1–4

Giorgi F, Bi X, Pal JS (2004) Mean, interannual variability and trends in a regional climate change experiment over Europe. II: climate change scenarios (2071–2100). Clim Dynam 23:839–858

IPCC AR4 SYR (2007) Core writing team. In: Pachauri RK, Reisinger A (ed) Climate change 2007: synthesis report, contribution of working groups i, ii and iii to the fourth assessment report of the intergovernmental panel on climate change, IPCC

Storch H (1999) On the use of infaltion in statistical downscaling. J Clim 12:3505–3506

Impact of Microphysics and Convective Parameterizations on Dynamical Downscaling for the European Domain

40

Jost von Hardenberg, Antonio Parodi, Alexandre B. Pieri and Antonello Provenzale

Abstract

In what follows, we present the study of different configurations of the Weather Research and Forecast model restricted to the EURO-CORDEX area at different spatial resolutions from 0.44° × 0.44° down to 0.04° × 0.04°. Our numerical model is forced at the boundaries by ERA-interim re-analysis data. Monthly and daily statistics for the year 1979 are compared in order to set the best configuration for rainfall predictions. Precipitation climatologies are then derived and particular attention is paid to the Alpine region. Our results show that local precipitation patterns are well reproduced by the regional model while highlighting the need of grid-resolved convection to avoid artificial additive precipitation and to reduce the rainfall rate bias especially of regions with complex orography.

Keywords

Dynamical downscaling • Microphysics • WRF • Explicit convection

40.1 Introduction

The Coordinated Regional Climate Downscaling Experiment (CORDEX) aims at providing an ensemble of numerical simulations at the regional scale in order to better characterise climate change. The project involves several numerical models and forcing datasets. In this paper we are interested in simulating climate variation over the European CORDEX domain on a high resolution grid.

Previous studies of climate variability over Europe using global models (GCMs) (e.g. Wilson and Mitchell (1987)) have shown that they are not well suited to reproduce climate variability at the local scale. This is mainly due to the fact that global models have inner parametrizations well suited to the coarse, large scale resolution. The alternative is to introduce regional models able to capture the physics from medium scale down to the smallest scales if the horizontal resolution is high enough. The underlying idea is to assume that regional climate is essentially driven at the boundaries by the largest scales which act and persist on larger time scale than meteorological events occuring at the regional level. The use of such regional models to provide dynamical downscaling is of capital interest in a view of climate change analysis (Giorgi (1990)). In particular, a sharp quantification of the precipitation rate at the local scale is of major importance not only in tracking extreme events and floods but also to have a good estimate of water runoff when further hydrological post-processing is needed.

Some attempts toward regional dynamical downscaling over Europe has been done in the past decades, see e.g. (Giorgi (1990); Wilson and Mitchell (1987)). Recently, endeavour to achieve fine scale climate prediction over Europe is being done under the Euro-CORDEX experiment (Gobiet et al. (2012)). The main advantage of using such dynamical downscaling is to avoid statistical modeling and

J. von Hardenberg (✉) · A.B. Pieri · A. Provenzale
ISAC-CNR, Corso Fiume, 4, 10133 Turin, Italy
e-mail: j.vonhardenberg@isac.cnr.it

A. Parodi
CIMA Foundation, Via Armando Magliotto, 2,
17100 Savona, Italy

G. Lollino et al. (eds.), *Engineering Geology for Society and Territory – Volume 1*,
DOI: 10.1007/978-3-319-09300-0_40,

hence to preserve the physical correlation between all the different variables without introducing ad hoc statistical laws. For a discussion on downscaling over Europe, see (Murphy et al. (2000)).

The numerical model of interest is the Weather Research and Forecast model (WRF) in its 3.4.1 version that is a non-hydrostatic atmospheric model driven by prescribing the ocean surface temperature. The model is forced at the boundaries by ERA-interim dataset (Dee et al. (2011)) that is a 0.75° re-analysis which came to replace ERA-40. Such methods are called 'one-way' nesting, in that the high resolution model cannot feedback the global model at the boundaries. Investigations on the limits of such methods are found in (Vannitsem and Chomé (2005)). Recent applications of the WRF model as a nested RCM for dynamical downscaling can be found in (Bukovsky and Karoly (2009)). While the resolution of regional climate models (RCMs) has increased, using nested RCMs still presents some issues such has choosing the size of the nested domains and parametrizing the model. Therefore, a careful analysis of the sensitivity of the model to different parametrizations—e.g. resolution, microphysics and convective schemes—is essential. In this context, retrospective climate analysis is useful to check the behaviour of the model and compare its own climatology with available datasets. This aspect is addressed in the next section.

40.2 Experimental Setup

While large scale phenomena are quite well accounted for in modern models, modeling the processes acting at the smallest scales is unavoidable. Essentially, subgrid scale processes such as rain, ice or snow formation, cloud formation and turbulent mixing are still parametrized in both global models and RCMs. The Weather Research and Forecast model then allows the use of a wide range of parametrizations. By configuring the model we essentially mean choosing the microphysics scheme, the cumulus convection scheme and to assess the best compromise for the horizontal resolution.

First, we focus on three recently developed microphysics schemes, namely (Thompson et al. (2004); Morrison and Gettelman (2008)) and WSM6 (Hong and Lim (2006)) microphysics. Second, we investigate the sensitivity of the model to the convection scheme. Our study is centered on (Kain and Fritsch (1990); Betts (1986)) schemes. In addition, a run with explicit convection at a resolution of $\approx$4 km is done and compared to the previous runs with parametrized convection. Vertical resolution is kept fixed with 56 vertical pressure levels. The analysis is pushed further by adjusting some well chosen parameters in the microphysics and cumulus schemes. Different representations of the physical processes acting in the atmosphere dynamics are thus compared. Lastly, a simulation at a lower resolution is done to complete our analysis on the effect of the resolution. Table 40.1 gathers the nomenclature of all the aforementioned simulations.

Table 40.1 Nomenclature of the different parametrizations used in WRF

Nameme	Grid	Microphysics	Convective scheme
c1ei	0.11°	Thompson	Kain-Fritsch
c2ei	0.11°	Morrison	Kain-Fritsch
c3ei	0.11°	WSM6	Kain-Fritsch
c4ei	0.11°	Thompson	Betts-Miller-Janjic
c1fi	0.11°	Thompson-Ntc = 3×10^8	Kain-Fritsch
c1gi	0.11°	Thompson	Kain-Fritsch-TIMEC = 3600
c1hi	0.11°	Thompson-Ntc = 3×10^8	Kain-Fritsch-TIMEC = 3600
c1di	0.44°	Thompson	Kain-Fritsch
c1li	0.11°	Thompson	Kain-Fritsch (60 %)
h1e4	0.04°	Thompson	Explicit

Table 40.2 Nomenclature and characteristics of datasets that serve as reference datasets in this study

Name	Grid	Institution	Data type
ERAI	0.75° × 0.75°	ECMWF	Re-analysis
MERRA	0.67° × 0.5°	NASA-EOS	Re-analysis
GPCP	2.5° × 2.5°	GEWEX	Observation
GPCC	0.5° × 0.5°	GEWEX	Observation
CFSR	T382 (0.31°)	NCEP-UCAR	Re-analysis
EOBS	0.25°	E-OBS	Observation
CRU	0.5°	Climate research unit	Observation
HISTALP	0.083°	ZAMG	Observation

In Thompson microphysics, the Ntc parameter corresponds to the prescribed number of cloud droplets. In WRF it is set according to known data. For maritime cases it is set to 10^8 m^{-3} and to 3×10^8 m^{-3} for continental cases. It has direct consequences on the Gamma shape parameter which is calculated based on Ntc and is of capital importance in the autoconversion scheme and consequently on the efficiency of collision-coalescence processes.

In the Kain-Fritsch cumulus scheme, the parameter TIMEC is responsible for the convective time scale.

It is computed as TIMEX = DX/VCONV, where DX is the zonal grid spacing and VCONV is the averaged horizontal wind speed between the horizontal wind speed at the LCL (lifted condensation level) and the wind speed at 500 mb (wind at the middle troposphere). If this average results to be equal to zero, the default value TIMEC = 3,600s is imposed (Table 40.2).

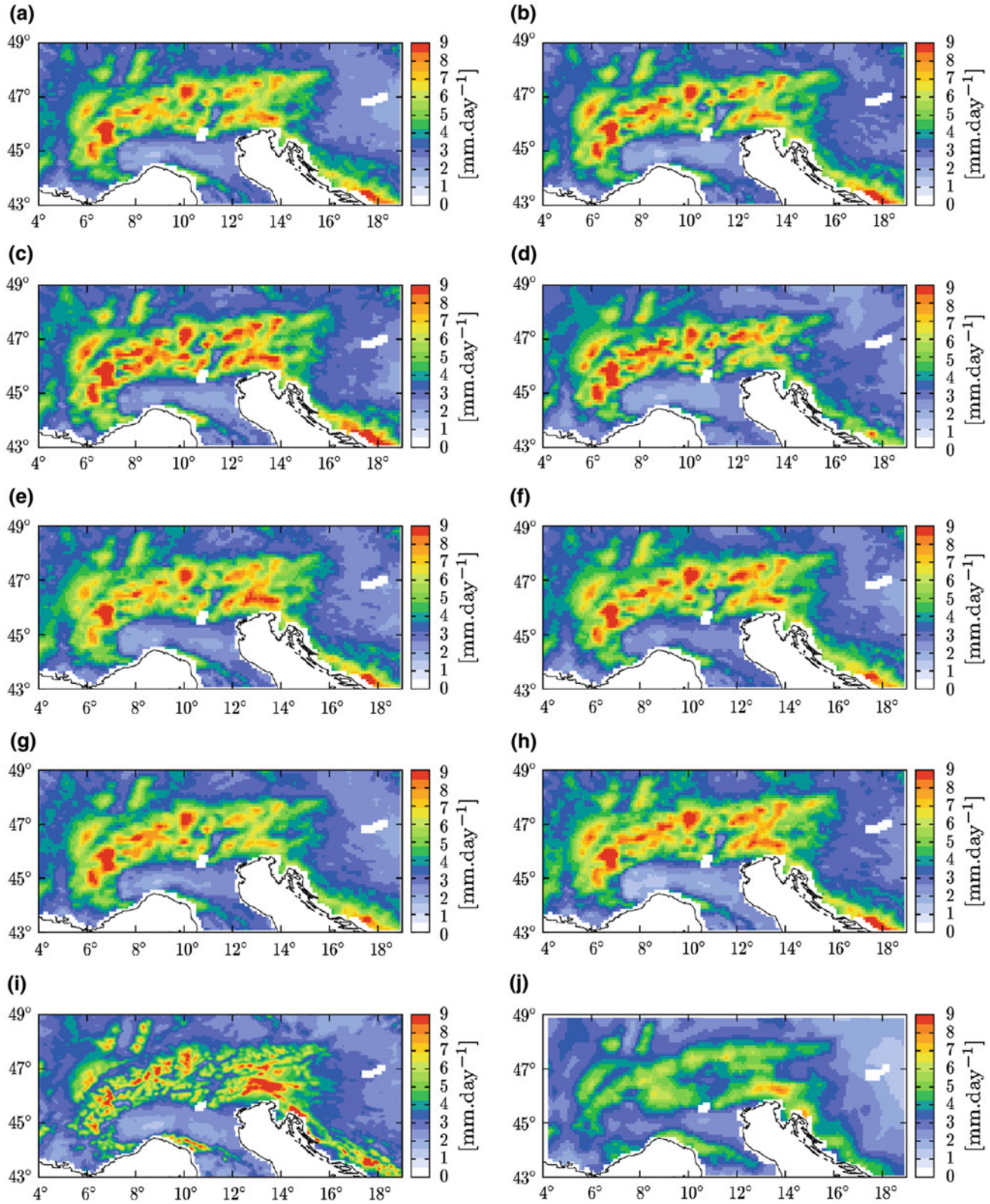

Fig. 40.1 Annual mean precipitation over the Great Alpine Region (GAR) for run **a** c1ei; **b** c2ei; **c** c3ei; **d** c4ei; **e** c1fi; **f** c1gi; **g** c1hi; **h** c1li; **i** h1e4; **j** histalp (observed)

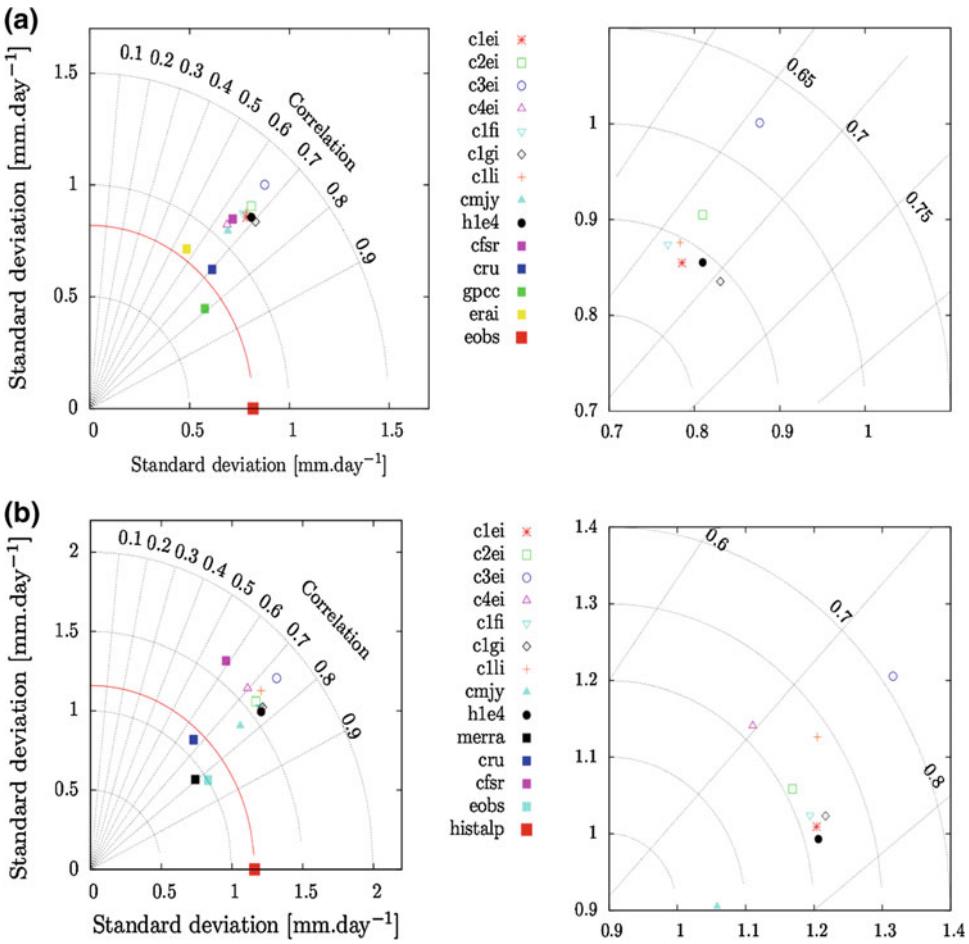

Fig. 40.2 Taylor diagrams showing the correlations between the annual precipitation between numerical experiments and: **a** E-obs dataset over the nested EURO-CORDEX domain; **b** HISTALP over the GAR

Increasing the resolution allows to take into account smaller scale physics. The finer grid spacing ranges between 1–5 km, and it should make the model able to resolve explicitly, albeit crudely, many convective processes (Kain et al. (2006, 2008)). More studies have investigated numerical simulations at the so-called grey-zone resolution to understand if convective parameterization is still able to work correctly on those scales (Gerard (2007)). In the next section we compare three different spatial resolutions: from coarse (44 km) to intermediate (11 km) and fine (3.5 km).

40.3 Results and Conclusions

Our results show that explicit convection—run h1e4, 4 km resolution—presents a better spatial distribution of precipitation over regions with complex orography, see Fig. 40.1 i. Run c4ei (10 km, parametrized convection) with Betts-Miller-Janjic convective scheme also shows a slight improvement in estimating the precipitation especially over the eastern part of the Alps and Croatia, Fig. 40.1d. Focusing on the variance of the rainfall field, Fig. 40.2b shows that our simulations provide better correlation coefficients than other datasets, e.g. CRU or CFSR, over the Alpine region. Considering the whole nested region, the results do not testify a clear improvement in estimating the rainfall rate variance, Fig. 40.2a. Future work will be devoted to high resolution climate predictions over Europe using configuration h1e4 (explicit convection, 4 km resolution).

References

Betts AK (1986) A new convective adjustment scheme. Part I: observational and theoretical basis. Q J Royal Meteor Soc 112 (473):677–691

Bukovsky MS, Karoly DJ (2009) Precipitation simulations using WRF as a nested regional climate model. J Appl Meteorol Climatol 48(10):2152–2159

Dee DP et al (2011) The ERA-Interim reanalysis: configuration and performance of the data assimilation system. Q J Royal Meteor Soc 137(656):553–597

Gerard L (2007) An integrated package for subgrid convection, clouds and precipitation compatible with meso-gamma scales. Q J Roy Meteor Soc 133(624):711–730

Giorgi F (1990) Simulation of regional climate using a limited area model nested in a general circulation model. J. Clim 3(9):941–963

Gobiet A, Jacob D et al. (2012) A new generation of regional climate simulations for Europe: the Euro-CORDEX initiative. In: EGU general assembly conference, vol 14, p 211

Hong S-Y, Lim J-OJ (2006) The WRF single-moment 6-class microphysics scheme (WSM6). J Korean Meteor Soc 42(2):129–151

Kain JS, Fritsch JM (1990) A one-dimensional entraining/detraining plume model and its application in convective parameterization. J Atm Sci 47(23):2784–2802

Kain JS, Weiss SJ, Levit JJ, Baldwin ME, Bright DR (2006) Examination of convection-allowing configurations of the WRF model for the prediction of severe convective weather: the spc/nssl spring program 2004. Weather Forecast 21(2):167–181

Morrison H, Gettelman A (2008) A new two-moment bulk stratiform cloud microphysics scheme in the community atmosphere model, version 3 (CAM3). Part I: description and numerical tests. J Clim 21 (15):3642–3659

Murphy J et al (2000) Predictions of climate change over Europe using statistical and dynamical downscaling techniques. Int J Climatol 20(5):489–501

Thompson G, Rasmussen RM, Manning K (2004) Explicit forecasts of winter precipitation using an improved bulk microphysics scheme. Part I: description and sensitivity analysis. Mon Weather Rev 132(2):519–542

Vannitsem S, Chomé F (2005) One-way nested regional climate simulations and domain size. J Clim 18(1):229–233

Wilson CA, Mitchell JFB (1987) Simulated climate and co_2 induced climate change over western Europe. Clim Change 10(1):11–42

Part V

Environmental and Engineering Geological Problems in Permafrost Regions in the Context of a Warming Climate

Convener: Prof. Wei Shan—*Co-conveners*: Tonglu Li, Marina Leibman, Marta Chiarle, Ying Guo

For nearly a century, global climate warming has impacted high latitude and high altitude regions of the earth. The warming trend continues. Boundaries of high-latitude permafrost regions continue to move northward and high-altitude permafrost retreats up slope. At the same time glaciers are receding at alarming rates, and extreme weather phenomena are becoming more common. Issues arising from warming in permafrost regions include thaw (permafrost degradation), cryogenesis, landslides, differential settlement of ground, and changes in vegetation and ecosystems. Our session is organized as follows: (a) Global distribution of permafrost and its evolution; (b) The environmental effects of permafrost degradation; (c) The effect of climate and environment change on permafrost degradation; (d) The effect of permafrost degradation on slope stability; (e) Monitoring and forecasting as well as countermeasures for permafrost degradation and its related problems.

The Landslides Induced by the Released Inclusion Water of the Frozen Soil in the Side of the Heifangtai Loess Platform, Gansu Province, China

41

Tonglu Li, Xianli Xing and Ping Li

Abstract
The Heifangtai loess platform is a highland which is the forth terrace of the Yellow River. The top of the platform is a cultivated irrigation farmland for setting up the migrants from Yanguoxia, Bapanxia and Liujiaxia reservoir submerged areas. The irrigation water are pumped up from the Yellow River aside the east side of the platform. It has induced a large number of landslides and collapses around the side of the platform since the irrigation system built up in 1967. Investigation suggests that the groundwater level at the centre of the platform has risen up to 20 m in the past decades and the annual rising rate is about 0.27 m. Because most of the landslides occurred in spring, release of the inclusion grounder by frozen soil may deteriorate the slope stability. Observation shows that frozen soil in a winter can cause the groundwater level to rise more than 3 m and extends backward to a range of more than 30 m. As the water released in spring, both high static pore water pressure and steep water gradient are the significant agents for the slope failure. The countermeasures for the slope failure mitigation are the reasonable irrigation method, such as dropping or sprinkling irrigation, to control the irrigation water quantity. In addition, the present grounder water should be drained by vertical or horizontal drilling holes to draw down the water level.

Keywords
Irrigation • Landslide • Loess • Inclusion water • Slope stability

41.1 Introduction

Seasonal freeze and thaw have different mechanism on aggravating slope deformation and failure. Freezing can prevent groundwater from discharging in soil, resulting in accumulation of water in slope, which is called Frozen Water Barred Effect (Wu 1997). The effect may cause a rise of static pore water pressure, coincidently decreasing the slope stability. Inversely, thawing may suddenly release the enclosed water as the climate is warming up, which will produce a high water gradient and also trigger landslides. The slope stability may be improved by draining in the summer season. However, the actions repeats year by year, finally make the slope conditions worse and worse.

The landslides at the side of Heifangtai loess platform, Gansu Province, China are generally attributed to seasonal freeze-thaw actions. The platform is located in the left bank of the Yellow River, the convergence of the Yellow River and the Huangshui River. The north boundary of the platform is a gully with the depth of 30–110 m and the gradient of 13°–40°, the east and the south boundary is adjacent to the second terrace of the Yellow River. The slope of the platform side has the height of 60–131 m and the gradient of 20°–50°, and distributes a series of landslides as shown in Fig. 41.1. The top of the platform is 1.7 km long east-west,

T. Li (✉) · X. Xing · P. Li
Department of Geological Engineering, School of Geological Engineering and Surveying, Chang'an University, Xi'an 710054, China
e-mail: dcdgx08@chd.edu.cn

G. Lollino et al. (eds.), *Engineering Geology for Society and Territory – Volume 1*,
DOI: 10.1007/978-3-319-09300-0_41,

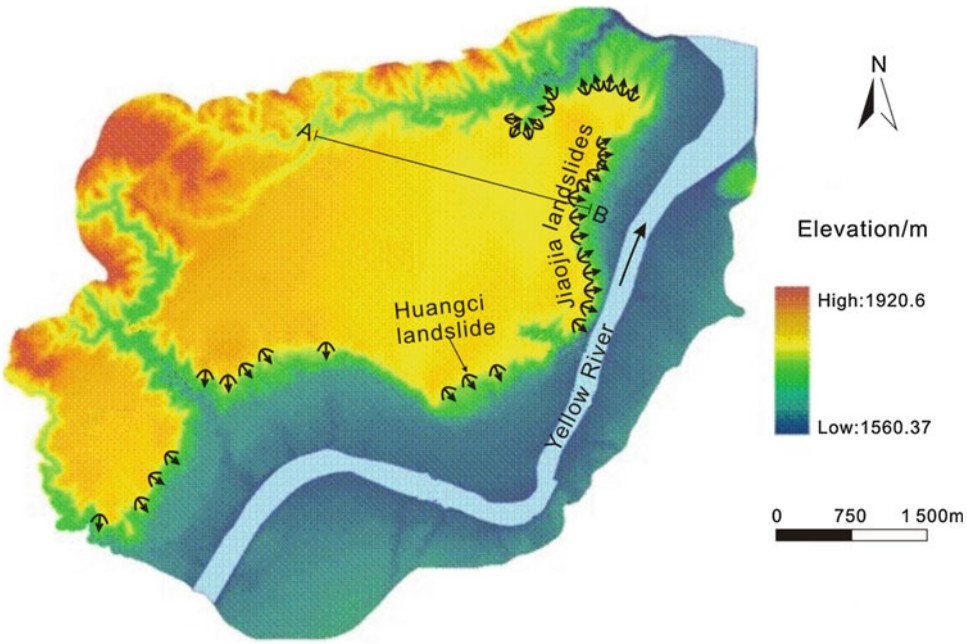

Fig. 41.1 DEM diagram and the landslides in the Heifangtai platform (After Zhang et al. 2013)

1.3 km wide south-north and has the total area of 13.7 km^2. It used to be an arid platform without resident originally. However, in the early 1960s, due to construction of the Liujiaxia, Yanguoxia and Bapanshan reservoirs, people lived in the submerged areas were immigrated on the platform. For exploiting the barren land for the immigrant living, the Yellow River pumping irrigation project was begun to build since 1966. From July 1966 to June 1969, three high-lift pumping station were put into use, which has the total water supply of 2.115 m^3/s for 11,340 acres of farmland irrigation. In recent years, the average annual irrigation amount keeps in 5.91 million m^3 (Zhang 2013).

Since irrigating on the top of the platform, landslides began to occur at the side of the platform frequently. The landslides had caused more than 400 million of economic loss and 38 causalities, more than 100 people injured, about 500 acres of farmland destroyed, 3,000 acres of arable land in the margin of the platform abandoned. According to our investigation in August 2010, 37 sites of landslide at the side of Heifangtai platform were confirmed. The real number of landslide events is more than this figure because the same place may have occurred several times of failure.

The strata of the Heifangtai platform is composed of aeolian loess deposit, alluvium of the Yellow River terrace and bedrock from top to bottom (Fig. 41.2). Aeolian loess (Q_{2-3}^{eol}) has grayish yellow color, loose texture and uniform structure, with macro-porous, silt component and well vertical joints. The loess bed is 21–50 m thick lying on the alluvium bed of the fourth terrace. The upper alluvium bed (Q_2^{al}) is of the 0.3–2.0 m thick lamina light brown silty clay with horizontal bedding and is interbedded with yellowish fine sand; the lower bed is pebbles consisting of quartzite, granite and metamorphic rocks. The pebbles are round to sub-round shape, well sorting, 3–10 cm in grain size, silt filled, no cementation, which outcrops 2–5 m thick along the side of the platform. The bedrock is Cretaceous interbedded sand-mudstone (K_1^{hk}) with the attitude 185°∠12° and outcrops about 70 m thick on the lower of the slope.

The hydrogeological condition was entirely changed by the long-term and massive irrigation. Perched water table was formed in the loess bed over the whole area. Before irrigation, phreatic water was distributed discontinuously. The bedrock base dips from the west to east in the platform, so the west almost had no groundwater before, and the east only had a very thin layer. Since extensive irrigation started in 1968, perched water table was formed on the relative impermeable alluvial silty clay and the water level increases at the rate of 0.27 m each year. The water level at the center of the platform has risen by 20 m high. Figure 41.3 shows that on the upper of the slope, groundwater has been leaking along the top of the silty clay. Undoubtedly, continuous rising of the groundwater level with irrigation was the main cause of landslides at the side of Heifangtai platform. However, the landslides occurred at the side of Heifangtai platform with clear time records are counted by month as shown in Fig. 41.4, it suggests that March and July are two peak numbers (Wang and Yao 2008). The peak in July is closely related to irrigation in May, while the peak in March was apparently related to freeze-thaw.

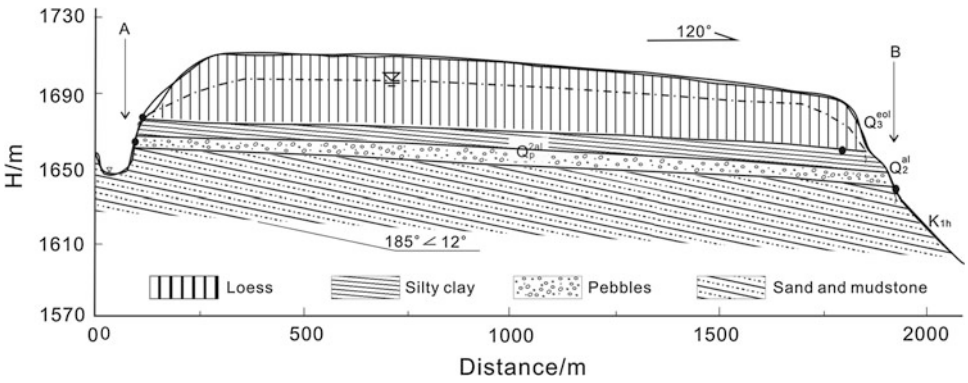

Fig. 41.2 Geological profile of the Heifangtai platform (The line AB in Fig. 41.1, after Zhang et al. 2013)

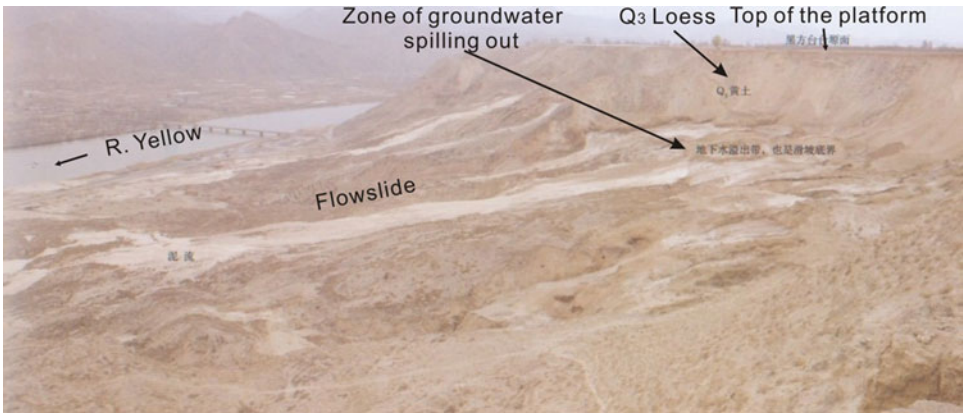

Fig. 41.3 Jiaojia Landslide group (The location seeing Fig. 41.1, photo by Yin)

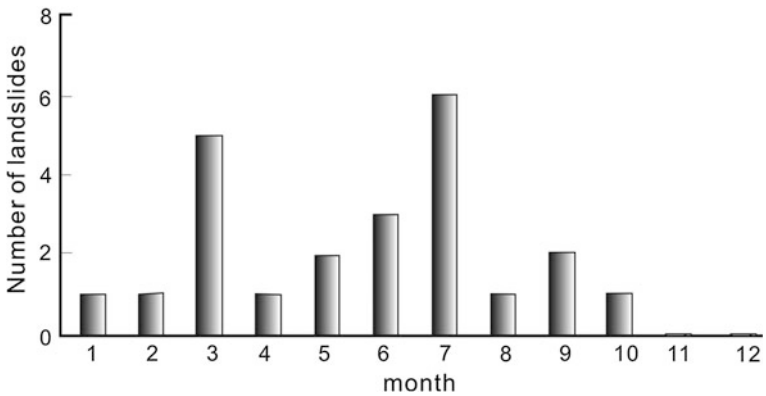

Fig. 41.4 Relation between the number of landslides and months on the side of Heifangtai loess platform (After Wang and Yao 2008)

41.2 The Mechanism of the Landslide Triggered by Seasonal Freeze-Thaw Actions

Loess landslide occurred in the loess bed lying on the alluvial silty clay. A thick perched water was generated on the top of alluvial clay because of relative impermeability. Heifangtai platform tilts from south-west to north-east, groundwater flows to north-east and spills along the top of the silty clay on the northeast side of the platform near Jiaojia village, so a series of landslides were triggered and distributes side-by-side as shown in Fig. 41.1. The earliest case occurred on March 15th, 1989, which is located to the south of Jiajia village and next to the bank of the Yellow River. There were 60 thousand m^3 sliding mass slipped into the Yellow River, the water was flooded on to the opposite bank and inundated 1.6 acres farmland. Another loess landslide with the volume of 400 thousand m^3 was occurred along the slope behind the Silicon-Carbide Factory to south of Jiaojia village on March 12th, 1999, sliding mass proceeded 500 m in 30s. In recent years, landslides often occurred in this area. A length of only 3 km slope of platform has 15 loess landslides occurred. Loess landslides show the characters of high shear outlet and quick sliding speed. The height of the shear outlet relative to the toe of the slope is 60–80 m. As the landslide started to slip, the

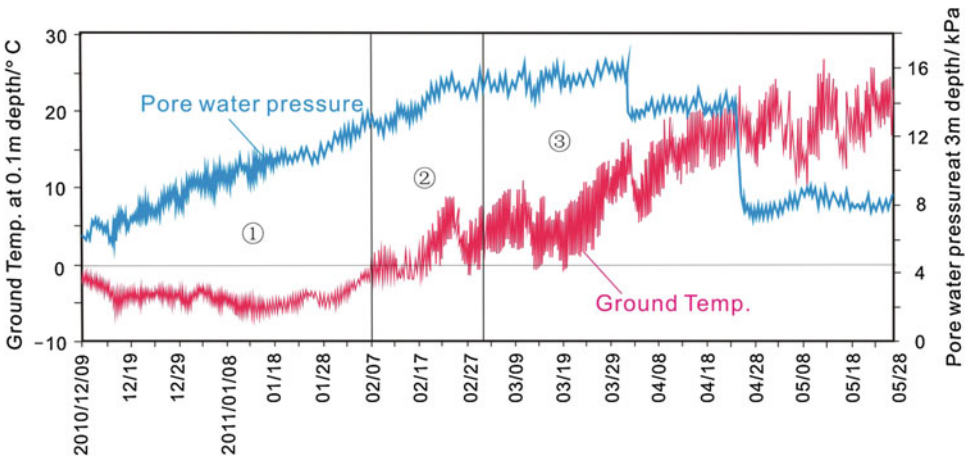

Fig. 41.5 Pore water pressure and ground temperature variation with time in JH9 landslide (After Zhang et al. 2013)

loose saturated loess in the base changed from solid to fluid rapidly, then flowed down on the slope. They belong to rapid flow slides.

From more than 30-years record of the landslides on the side of Heifangtai platform, it is found that the landslides occurred at the winter and the early spring were apparently concentrated. The reason is generally attributed to freeze-thaw action. In order to obtain the data of ground temperature and pore water pressure, monitoring devices were buried in the front of a largest landslide in Jiaojia village by Xi'an Geological Survey Center (Zhang et al. 2013). Figure 41.5 shows the data of ground temperature at the depth of 10 cm and pore water pressure at the depth of 3 m in the period from December 9th, 2010 to May 26th, 2011. From the results, The freeze-thaw process can be divided into three episodes, namely freezing, freezing-thawing and thawing. Freezing episode began at the end of November and ended in the beginning of the next February, the ground temperature was below 0 °C. Therefore, the groundwater drainage paths were closed, which resulted in a continuous rising of pore water pressure in the slope. Freezing-thawing period started in the early February and ended in the early March. Temperature fluctuated between day and night, which may resulted in alternative freezing and thawing between day and night, but the groundwater drainage paths were still blocked, so pore water pressure still increased steadily. The thawing period started from the early March to the end of April, spring water began to discharge as normal, and the pore water pressure does not rise any more, but had a tendency of decrease with some sudden falls.

The above monitoring results show that groundwater level in the slope could increase because the frozen water closed the water drainage outlet. The range of water lifting on the slope could be 2 m by once frozen season, then it is estimated that the affected horizontal distance might be more than 30 m according to the loess permeability. The rise of groundwater level could lead to the rise of static pore water pressure and reduce soil strength. For investigating

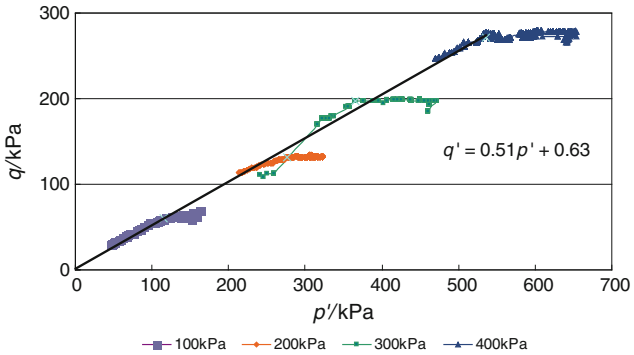

Fig. 41.6 Stress path of triaxial CU shear test under the conditions of giving confining axial pressure and by increasing pore water pressure

the loess strength under increasing of pore water pressure, intact loess samples near shear outlet the monitored landslide were taken. The specimens were saturated in laboratory and consolidated under definite confining pressure and axial pressure, then pore water pressure was increased by exerting counter pressure to make the specimen fail. The results are expressed as stress path as in Fig. 41.6. Effective cohesion and internal friction angle may be calculated through parameters of K_f line. The effective cohesion was near to 0 and the internal friction angle was 30.0°. Gradients of the loess slopes at the side of Heifangtai platform were generally 30°–35°. It may be concluded that increase of groundwater level and pore water pressure by freezing caused that the loess cohesion almost lost and the effective internal friction angle is even below the slope gradient, so the slope failure could be occurred naturally.

Once the landslide occurred, loess in the disturbed shear zone converted into flow state immediately because of its loose structure, and then rapid mudflow along the slope surface was generated as shown in Fig. 41.3. Even during the thawing period, high hydraulic gradient would be generated due to the sudden release of groundwater, which would cause the stability of the slope in much worse state.

41.3 Conclusion

Landslides on the side of Heifangtai platform, Gansu province, are the most typical cases triggering by farmland irrigation and freeze-thaw action. According to investigation, monitoring and triaxial test for the landslide in this area, it can be concluded that groundwater discharge outlet was barred by freezing action, which resulted in accumulation of groundwater within the slope, then increased pore water pressure and reduced soil strength consequently caused the slope failure. High hydraulic gradient may be generated by the sudden release of groundwater due to thawing, slope stability also can be reduced and fail eventually.

References

Wang NQ, Yao Y (2008) Characteristics and mechanism of landslides in loess during freezing and thawing periods in seasonally frozen ground regions. J Dissaster Prev Mitig Eng 28(2):163–166 (In Chinese)

Wu WJ (1997) Slide accelerated by water entrapment due to seasonal freezing. J Glaciol Geocryol 19(4):359–365 (In Chinese)

Zhang MS (2013) Formation mechanism as well as prevention and controlling techniques of loess geo-hazards in irrigated areas: the yellow river. Geol Bull China 32(6):833–839 (In Chinese)

Zhang MS, Chen XJ, Dong Y, Yu GQ, Zhu LF, Pei Y (2013) The effect of frozen stagnant water and its impact on slope stability: a case study of Heifangtai, Gansu Province. Geol Bull China 32(6):852–860 (In Chinese)

Velocity Changes of Rock Glaciers and Induced Hazards

42

P. Schoeneich, X. Bodin, T. Echelard, V. Kaufmann, A. Kellerer-Pirklbauer, J.-M. Krysiecki and G.K. Lieb

Abstract
Recent observations and geodetic measurements in the European Alps show that changes are occurring on rock glacier dynamics, ranging from moderate velocity variations to strong acceleration or even total collapse. These changes can be related to the ground temperature and to climate warming. In most cases, rock glaciers do not represent any serious hazard, except the instability of their surface and local rockfalls at the steep front. The surface movements, though moderate, can nevertheless cause damages to sensible infrastructures like cableways or buildings, if these are not designed to adapt to surface movements. The strong accelerations observed on some rock glaciers, however, induce a change of magnitude, and may threaten in some cases downslope areas. Thus, the presence of active or inactive rock glaciers with high ice content must be considered not only with regard to present conditions and dynamics, but with respect to possible evolutions due to climate change.

Keywords
Permafrost • Rock glaciers • Hazards

P. Schoeneich (✉) · T. Echelard
Institut de Géographie Alpine, University of Grenoble Alpes, Grenoble, France
e-mail: Philippe.Schoeneich@ujf-grenoble.fr

T. Echelard
e-mail: Thomas.Echelard@ujf-grenoble.fr

X. Bodin
EDYTEM, CNRS, University of Savoie, Le Bourget-du-Lac, France
e-mail: Xavier.Bodin@univ-savoie.fr

V. Kaufmann
Institute of Remote Sensing and Photogrammetry, Graz University of Technology, Graz, Austria
e-mail: Viktor.Kaufmann@tugraz.at

A. Kellerer-Pirklbauer · G.K. Lieb
Department of Geography and Regional Science, University of Graz, Graz, Austria
e-mail: Andreas.Kellerer@uni-graz.at

G.K. Lieb
e-mail: Gerhard.Lieb@uni-graz.at

J.-M. Krysiecki
SAGE/ADRGT, Gières, France
e-mail: Jeanmichel.Krysiecki@gmail.fr

42.1 Introduction

Rockglaciers are the most prominent features in alpine permafrost. Active rock glaciers are creeping landforms made of debris supersaturated by ice, and moving downslope usually at a rate of a few cm/yr to dm/yr. Some rock glaciers are known to move even faster.

Recent observations in the European Alps show that changes are occurring and that some rock glaciers may experience drastic changes in their dynamic. Thus hazards related to rock glaciers could become more important in the future. It is therefore important to understand how rock glaciers react to changes particularly in air and ground temperature.

42.2 Reaction Typology

The observed changes on rock glacier dynamics are all related to velocity changes, and show in most cases an increase in velocity. Depending on the magnitude of the

G. Lollino et al. (eds.), *Engineering Geology for Society and Territory – Volume 1*,
DOI: 10.1007/978-3-319-09300-0_42,

velocity increase, the following five types of reaction can be distinguished (modified from Schoeneich et al. 2011):

- Type 1: Moderate positive and negative velocity variations, in the range of a few cm/y to more than 2 m/y (Delaloye et al. 2008, 2013; Kellerer-Pirklbauer and Kaufmann 2012). These varitions are reversible.
- Type 2a: Accelerated displacement rate of part or whole of a rock glacier significantly above the velocity range of type 1, with opening of crevasses or scarps on the rock glacier surface (Roer et al. 2008; Lambiel 2011). Annual velocity values can range from a few m/y to more than 10 m/yr.
- Type 2b (type 5 of Schoeneich et al. 2011): Very strong acceleration with end velocity up to more than 80 m/y. The latter extreme value was observed, for example, on the lower half part of the Grabengufer rock glacier where velocities up to 30–50 cm/day were measured between July 2009 and February 2010 (Delaloye et al. 2013).
- Type 3: Dislocation and splitting (rupture) of the lower part of rock glaciers: the lower part of the rock glacier starts to move significantly more than the upper part. This leads to the formation of a scarp separating the two parts. In most cases, the lower part shows a disorganization of the surface topography with perturbations of the initial ridge and furrow pattern and the formation of crevasses, whereas the upper part keeps morphologically undisturbed (Roer et al. 2008). Such changes are not reversible, and the lower part stops after a few years and becomes inactive, whereas the upper part remains active.
- Type 4: Collapse of the lower part of the rock glacier: the lower part of the rock glacier breaks down as a debris flow and is totally removed. A new front develops from the scarp. Only one such case is known so far in the Alps (Krysiecki 2009; Krysiecki et al. (submitted)), but potentially similar cases have been identified in the Chilean Andes (Iribarren Anacona and Bodin 2010).

Types 2–4 are often called "destabilized" or "surging" rockglaciers and were only recently discovered. Type 2b is a gradation of type 2a, with increasing velocity. Type 4 can be seen as an end member of the evolution of type 3. The various possible evolution trajectories of rock glaciers in a warming climate can be summarized in the draft of Fig. 42.1.

42.3 Processes Involved

The movement of rock glaciers is usually explained as a cohesive flow due to the internal deformation of the ice-rock mixture constituting the permafrost body. It is admitted that commonly no basal sliding is occurring at the rock glacier base (few exceptions; e.g. Hausmann et al. 2007), and that the whole movement is explained by the flow deformation (Haeberli et al. 2006). The few existing inclinometer data show that an important part of the deformation occurs above the base of the rock glacier in a shear horizon of limited thickness (Arenson 2002; Arenson et al. 2007). This flow mechanism is in some way similar to that of a cold based glacier. The flow is made possible by the viscosity of the ice, but it supposes that the permafrost body is supersaturated with ice at the depth where the deformation takes place.

Moderate interannual velocity changes (type 1) can be explained by variations of the viscosity of ice, related to temperature and water content. They can be related to variations of the mean annual ground surface temperature (MAGST) with a time lag of one to two years (Fig. 42.2). The running mean of the ground surface temperature (12–24 previous months, depending on the rock glacier) shows a good correspondence with the velocity changes (Delaloye et al. 2008; Bodin et al. 2009; Kellerer-Pirklbauer

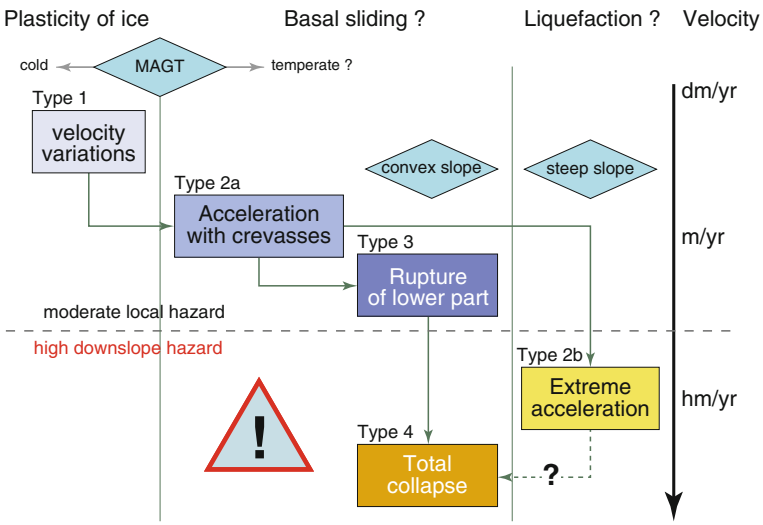

Fig. 42.1 Possible evolution trajectories of rock glaciers (modified from Schoeneich et al. 2011). *Rectangles* indicate types (see text), *diamonds* steering factors

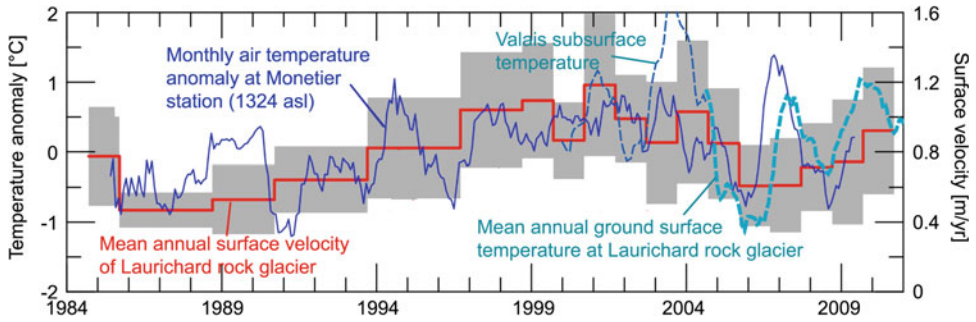

Fig. 42.2 Velocity variations of the Laurichard rock glacier (type 1, France), compared to monthly air temperature anomaly, and with mean annual sub-surface temperature (running mean of 12 previous months, data for Valais 2000–2004 from Delaloye et al. 2008)

and Kaufmann 2012). The match with the mean annual air temperature (MAAT) is not as good (Buck and Kaufmann 2010; Kellerer-Pirklbauer and Kaufmann 2012). This is most probably due to the thermal offset induced between air and ground temperatures by the snow cover.

Stronger accelerations however need a process change. The most probable explanation is the onset of a basal sliding (types 2–3), or in some cases potentially a partial liquefaction of the debris mass due to the increase of melt water content (types 4 and 2b). However, this basal sliding could act only seasonally (increased pore water pressure) or only during certain, warmer years. This might be the case for instance at the Hinteres Langtalkar rock glacier (Figs. 42.3 and 42.4) with sliding/creeping after warmer periods (heat waves 2003/2006) and only creeping during cooler years (Kellerer-Pirklbauer and Kaufmann 2012).

The collapse of the Berard rock glacier occurred by end of summer 2006 (Fig. 42.5). The initiation of its destabilization followed the summer heat wave of 2003, whereas the final collapse was triggered by the heat wave of 2006 (Krysiecki et al. (submitted)).

All these observations show that rock glaciers are sensitive even to short term climate variations (type 1), and that stronger changes in rock glacier behaviour can be regarded as a consequence of permafrost warming and degradation, and thus as an effect of climate change.

42.4 Effect on Hazards Related to Rock Glaciers

In most cases, rock glaciers do not represent any serious hazard, except the instability of their surface and local rockfalls at the steep front. The surface movements, though moderate, can nevertheless cause damages to sensible infrastructures like cableways or buildings, if these are not designed to adapt to surface movements (Bommer et al. 2010a, b). In economic terms the consequences will be either a higher building cost or a reduced lifetime of the investment.

The strong accelerations observed on some rock glaciers however induce a change of magnitude. On such cases, infrastructures can no longer be adapted. Furthermore, the instability of rock glacier fronts may threaten areas situated below. This can occur either directly by rockfalls from the unstable or overhanging rock glacier front like e.g. at Grabengufer rock glacier (Delaloye et al. 2013), or indirectly through an increased debris supply to torrential systems, inducing an increase of frequency and/or magnitude

Fig. 42.3 Lower part of the Hinteres Langtalkar rock glacier in August 2012 (type 3, Austria). The crevasses are clearly visible (photo A. Kellerer-Prklbauer)

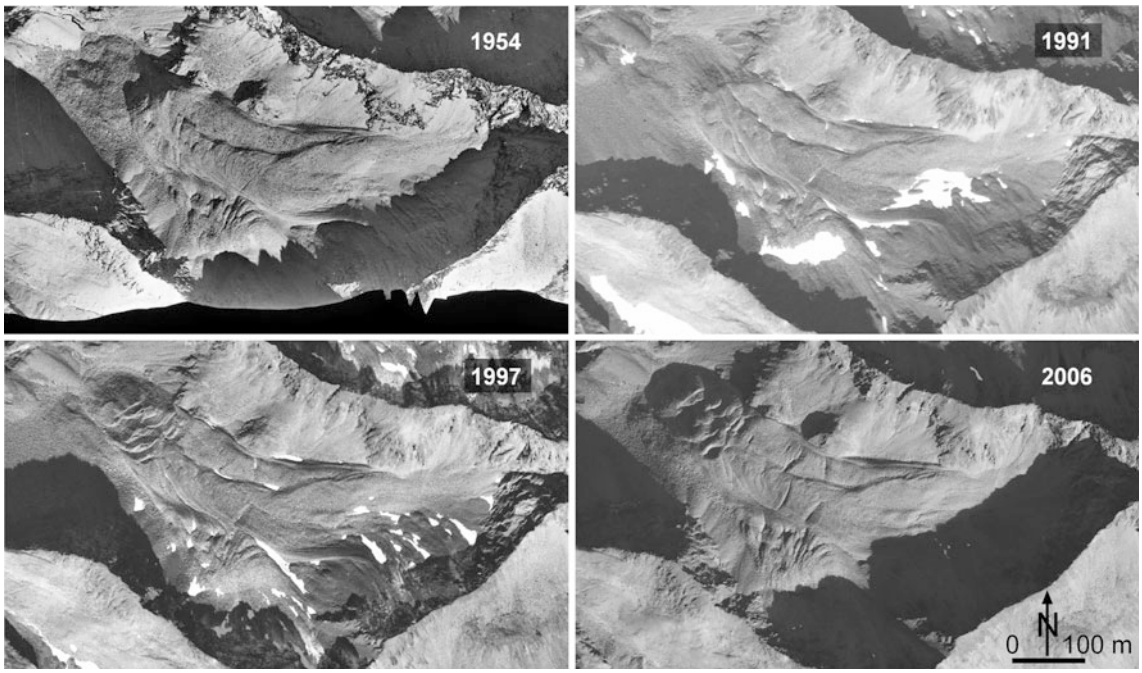

Fig. 42.4 Aerial photographs of the Hinteres Langtalkar Rock Glacier (type 3) between 1954 and 2006 indicating the formation of crevasses and in particular the disintegration through active sliding processes since 1994 at its frontal part, typical of type 3. All aerial photographs were taken by the Austrian Federal Office of Metrology and Surveying, Vienna (BEV) in the month of September

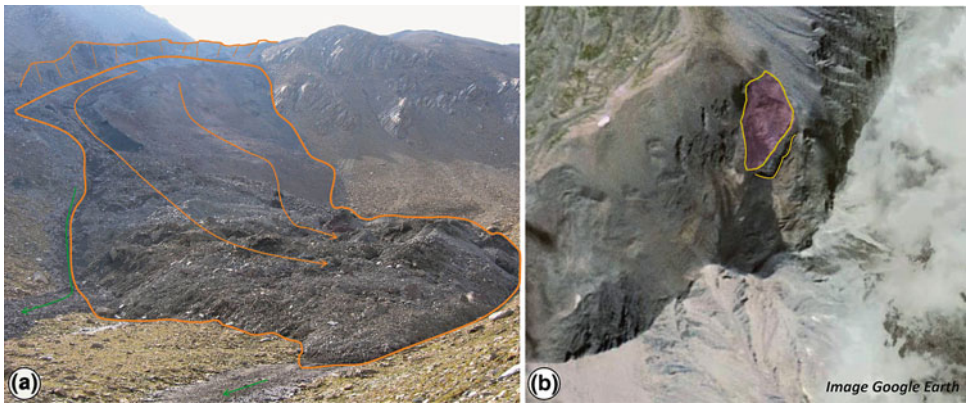

Fig. 42.5 The collapsed Bérard rock glacier (type 4, France). *Left* The collapsed frontal part of the rock glacier end of August 2006 (photo Michel Peyron RTM 04). *Right* Satellite image from July 2006 (image form Google Earth archive). The detachment scar began to form at least since 2004 and is well developed ca one month before the collapse. The collapsing part is outlined. (from Schoeneich et al. 2011)

of debris flows like e.g. at Murfreit (Krainer et al. 2012) and Grabengufer rock glaciers (Graf et al. 2013).

The hazard level will strongly depend on local conditions, such as topography and slope long profile, debris type and grain size, ice content, etc. In all cases of type 3 and 4, the rupture occurred on a slope convexity separating a lower steeper part from the upper gentler part. Strong accelerations of type 2b need a very steep slope. The collapsed Berard rock glacier develops in fine grained schist debris. The parameters controlling the various behaviour types need further investigations.

42.5 Conclusions and Outlook

Based on comprehensive long-term observations of rock glaciers in the European Alps but also at global scale, different types of rock glacier movement behavior have been distinguished. In this study we present an approach to systematically describe possible rock glacier evolution trajectories.

Observed changes in the kinematic behavior of rock glaciers point to a potential increase of hazards both on local scale (infrastructures on or immediately in front of rock glaciers) and in areas situated downslope (rockfall and

debris flows supplied by degrading rock glacier fronts). The presence of active or inactive rock glaciers with high ice content must be considered not only with regard to present conditions and dynamics, but with respect to possible evolutions due to climate change.

Acknowledgments This work was maily done within the PermaNET project, supported by the European Territorial Cooperation through the Alpine Space program. We thank Reynald Delaloye and an anonymous reviewer for valuable comments.

References

Arenson L (2002) Unstable alpine permafrost: a potentially important natural hazard. PhD dissertation, Institute for Geotechnical Engineering Technische Wissenschaften ETH, Zurich.vd/f Hochschulverlag, Zurich, Switzerland

Arenson L, Springman SM, Sego DC (2007) The rheology of frozen soils. Appl Rheol 17(1):12147-1–12147-14

Bodin X, Thibert E, Fabre D, Ribolini A, Schoeneich P, Francou B, Reynaud L, Fort M (2009) Two decades of responses (1986–2006) to climate by the Laurichard rock glacier, French Alps. Permafrost Periglac Process 20:331–344

Bommer C, Phillips M, Arenson LU (2010a) Practical recommendations for planning, constructing and maintaining infrastructure in moutain permafrost. Permafrost Periglac Process 21:97–104

Bommer C, Phillips M, Keusen HR, Teysseire P (2010b) Bauen im Permafrost: ein praxisorientierter Leitfaden/Construire sur le pergélisol: guide pratique. WSL-Institut für Schnee-und Lawinenforschung SLF, Davos

Buck S, Kaufmann V (2010) The influence of air temperature on the creep behaviour of three rockglaciers in the Hohe Tauern. Grazer Schriften der Geographie und Raumforschung, 45. In: Kaufmann V, Sulzer W (eds) Proceedings of the 10th international symposium on high mountain remote sensing cartography (HMRSC-X), Kathmandu, Nepal, September 2008, pp 159–170

Delaloye R, Perruchoud E, Avian M, Kaufmann V, Bodin X, Hausmann H, Ikeda A, Kääb A, Kellerer-Pirklbauer A, Krainer K, Lambiel Ch, Mihajlovic D, Staub B, Roer I, Thibert E (2008) Recent interannual variations of Rock Glacier Creep in the European Alps. In: Proceedings of the ninth international conference on Permafrost, vol 1, University of Alaska, Fairbanks, USA, pp 343–348

Delaloye R, Morard S, Barboux C, Abbet D, Gruber V, Riedo M, Gachet S (2013) Rapidly moving rock glaciers in Mattertal, pp 21–31. Jahrestagung der Schweizerischen Geomorphologischen Gesellschaft, St. Niklaus

Graf C, Deubelbeiss Y, Bühler Y, Meier L., McArdell BW, Christen M, Bartelt P (2013) Gefahrenkartierung Mattertal: Grundlagenbeschaffung und numerische Modellierung von Murgängen. In: Graf C (Red) Mattertal–ein Tal in Bewegung. Publikation zur Jahrestagung der Schweizerischen Geomorphologischen Gesellschaft 29 Juni—1 Juli 2011, St. Niklaus. Birmensdorf, WSL, 85–112

Haeberli W, Hallet B, Arenson L, Elconin R, Humlum O, Kääb A, Kaufmann V, Ladanyi B, Matsuoka N, Springman S, Vonder Mühll D (2006) Permafrost creep and rock glacier dynamics. Permafrost Periglac Process 17:189–214

Hausmann H, Krainer K, Brückl E, Mostler W (2007) Internal structure and ice content of Reichenkar Rock Glacier (Stubai Alps, Austria) assessed by geophysical investigations. Permafrost Periglac Process 18:351–367

Iribarren Anacona P, Bodin X (2010) Geomorphic consequences of two large glacier and rock glacier destabilizations in the Central Chilean Andes. EGU General Assembly 2010. Geophys Res Abstr 12: EGU2010-7162-4

Kellerer-Pirklbauer A, Kaufmann V (2012) About the relationship between rock glacier velocity and climate parameters in central Austria. Austrian J Earth Sci 105(2):94–112

Krainer K, Mussner L, Behm M, Hausmann H (2012) Mulridisciplinary investigation of an active rock glacier in the Stella Group (Dolomites; Northern Italy). Austrian J Earth Sci 105(2):48–62

Krysiecki J-M (2009) Rupture du glacier rocheux du Bérard (Alpes de Haute Provence): analyses géomorphologiques et premiers résultats du suivi mis en place sur le site. Environnements Périglaciaires 16:65–78

Krysiecki J-M, Bodin X, Schoeneich P, Le Roux O, Lorier L, Echelard T, Peyron M, Walpersdorf A (submitted) The collapse of the Bérard rock glacier (Southern French Alps) in 2006 and its post-event evolution: insights from geodetic, thermal and geophysical datasets. Sub. Permafrost Periglac Process

Lambiel C (2011) Le glacier rocheux déstabilisé de Tsaté-Moiry (VS): caractéristiques morphologiques et vitesses de déplacement. Géovisions 36:211–224

Roer I, Haeberli W, Avian M, Kaufmann V, Delaloye R, Lambiel C, Kääb A (2008) Observations and considerations on destabilizing active rockglaciers in the European Alps. In: Proceedings of the ninth international conference on Permafrost, vol 1, University of Alaska, Fairbanks, pp 1505–1510

Schoeneich P, Bodin X, Kellerer-Pirklbauer A, Krysiecki J-M, Lieb GK (2011) Chapter 1: rockglaciers. In: Schoeneich P et al. (eds) Hazards related to permafrost and to permafrost degradation. PermaNET project, state-of-the-art report 6.2. On-line publication ISBN 978-2-903095-59-8, p 1–27

Geocryological Risk: Conception and Estimation Algorithms

43

Sergeev Dmitry and Stanilovskaya Julia

Abstract
The approach of geocryological risk estimation is considered. Depending on the situation, scale and accuracy of investigations the special accent in geocryological situation diagnostics is choosing. These accents are the cryolithology, the ground temperature regime and the geocryological processes' dynamics. The change of geocryological conditions leads to engineering structure damages, loss of the sustainable economic development, loss of natural resources, and the violation of environmental laws. The spatial and temporal factors must be taken into account separately in the risk estimation procedure. The recurrent risk assessment is important at the different stage of the enterprise life cycle.

Keywords:
Geological hazard • Risk • Forecast • Factor

43.1 Basic Approaches

The risk of geological hazard is the product of the frequency of event with determined magnitude and the expectation of damage amount (after Ragozin 1999).

The geocryological risk has some specific components that add difference to analytical algorithm in comparison with common geological risk estimation. The irreversible change of geocryological conditions is the essential meaning and the stochastic component of the geocryological risk. The large amounts of geocryological phenomena are not repeatable, so they have no parameters of frequency as the flooding or the earthquakes.

The principal problem of the geocryological risk estimation is the instability of the agent and subjects of damage. The frequency of estimated events ("hazards") changes considerably with the time and depends on the natural environmental change as well on the human activity (Clarke et al. 2008).

Depending on the situation, scale and accuracy of investigations the special accent in geocryological situation diagnostics is choosing. These accents are the cryolithology, the ground temperature regime and the geocryological processes' dynamics.

The "cryolithology" reflects the ice content and the geocryological history. The paleogeographic studies help understand the spatial distribution of the ground ice in different landscapes and stratigraphic complexes.

The ground temperature regime depends on surface heat exchange as well on the lower temperature condition that keeps the past climate history. The temperature monitoring is important to gathering the data for numerical model calibration (Pavlov 1996; Romanovsky et al. 2010).

The geocryological processes' dynamics reflects the permafrost response on the climate change and human impact. The special monitoring of geocryological processes in disturbed and undisturbed landscape conditions help to understand the period of processes' activation or dying.

The change of geocryological conditions leads to engineering structure damages, loss of the sustainable economic development, loss of natural resources, and the violation of

S. Dmitry (✉) · S. Julia
Institute of Environmental Geoscience RAS, Ulansky per., 13, build. 2, 101000 Moscow, Russia
e-mail: sergeevdo@gmail.com

G. Lollino et al. (eds.), *Engineering Geology for Society and Territory – Volume 1*,
DOI: 10.1007/978-3-319-09300-0_43,

environmental laws. Each of these topics can be used for the damage calculation.

The engineering structure damages are linked with direct effects of geocryological processes (thermokarst, icing, frost heaving, etc.) or with indirect impact with changed landscapes that are located outside of engineering structure allotment (fires, swamping etc.). The economic loss is linked with assurance of technological safety of the engineering structure. E.g. the thermokarst development under the railroad embankment leads to complete reconstruction of the railroad within the distance of the settlement.

The disturbances of sustainable economical development are linked with non-forecasted losses due to abnormal exploitation of engineering structure. E.g. the thermal erosion along the pipeline leads to permanent works on the gullies filling-up by the ground.

The loss or deterioration of natural resources is significant for the society. E.g. the permafrost evolution affects the forest recreation and water resources stability.

The violation of environmental laws leads the surcharges and penalties for the above-standard exposure on the environment or the protected territories.

In all above mentioned cases the charge of the special survey and scientific investigations must be added to general economical losses. These investigations are the base for the revision of geocryological forecast and recurrent risk assessment, like a already developed approach (Kääb 2008).

43.2 Methods of Risk Estimation

Each modification of the environment or the permafrost state needs the separate risk calculation. The human influence is powerful and change more rapidly than climate or landscape conditions. We recommend developing the risk assessment at the stages of the enterprise life cycle: Feasibility study, Prospecting and project management, Constructional engineering, Maintenance, and Restoration. Each stage of structure's life has the specific requirements for the geocryological forecast and the risk estimation procedure. The most complicated stage is the Maintenance because it requires of the long-terms geocryological forecast.

The essential content of the risk assessment is the forecast the temperature regime of the ground. It helps to predict the state of the permafrost. The spatial and temporal factors must be taken into account separately in the risk estimation procedure (Table 43.1).

The spatial factors are:

- Insufficient geological information about location of ice-rich and saline grounds.
- Heterogeneity of ground structure and cryolithological content due the history of landscape evolution.
- Insufficient information about geocryological processes' activity (where and when the geocryological processes accelerate after the climate fluctuation and human impact).
- Uncertainty of future areas of human activity.

Table 43.1 The examples of geocryological risk analysis content for different conditions of uncertainty

"Spatial" Sources of Uncertainties (Spatial statistical analysis of Permafrost State Factors)	"Time" Sources of Uncertainties (Analysis of Time-series of Permafrost Change Factors)			
	Historical Data (Short-time Forecast)		Model Scenarios (Long-term Forecast)	
	Climate statistics and frequency of natural events that affect the permafrost	History of human impact (types and magnitude of forces)	Long-term climate trends and GCM forecasts	Long term forecast for human impact (stages of enterprise life cycle)
1	2	3	4	5
Uncertainties of ice-reach ground site's precise location	Estimation of climate event's critical magnitude probability for the ice-rich grounds	Estimation of the critical human induced event for different permafrost and landscape conditions	Estimation of the permafrost condition statistics shifting due to trend of mean annual climate characteristic	Estimation of geometrical correspondence of territories with typical potential disturbances with ice-rich ground areas
Uncertainties of thermal-physics ground and cover (snow, vegetation, water) variability	Estimation of climate event's influence with different statistics of permafrost state factors (Monte-Carlo method)	Statistical analysis of damage distribution with different landscape conditions	Estimation of natural cover properties' change due the climate shifting	Permafrost condition forecast with variable cover characteristics for the stage of the enterprise life cycle
Uncertainties of human disturbances' precise location	Zoning the variability of permafrost condition as the measure of the risk	Statistical analysis of damage distribution with different ground and permafrost condition	Zoning the expected permafrost dynamics as the measure of the risk	Forecast for typical long-term trends and events of the human influence to permafrost state

- The temporal factors are:
- Anomalous climate events (years and seasons with abnormal characteristics and single weather impact).
- Permanent and repetitive periodic and non-periodic typical human impact that is linked with determined nature management.
- Long-term climate and landscape change.
- Long-term changes of the human impact intensity in the different stages of the engineering structure's life-cycle.

The anomalous climate events and typical human impact demand the statistical analysis of the empirical data. On the contrary the long-term change of climate and human activity need the development of the prognostic scenario for the risk assessment.

The principal task for permafrost professional is the determination of two principal risk factors: the first one is from spatial factors and the second one is from temporal factors. These two factors set the specifications for geocryological forecast. The predicted probability of the irreversible change of geocryological conditions is corresponded to the economic loss during the period of the forecast. The product of mentioned probability and loss is the desired geocryological risk estimation.

The stated approach is valid for different scale and different types of human-nature systems. Particularly it was tested in different permafrost condition with long distance structures (railroads, trunk pipelines) and structures of oil-gaz exploration (Koff et al 2009).

43.3 Conclusion

The geocryological risk contains two principal sources of uncertainty that are different meaning and concernment in stages of the enterprise life cycle. "Spatial sources" are linked with geological history and "temporal sources" due to external human and climate influence on permafrost.

The combination of spatial and temporal types of uncertainty leads to drawing-up the corresponded tasks of the hazard estimation.

The initial stages of human activity and the exploitation stage are the stage that mostly need the geocryological risk estimation.

The ice distribution, the ground temperature regime and the geocryological processes' dynamics are the subject of special prospecting and monitoring survey that must provide the data for geocryological hazards' estimation.

Acknowledgements Thanks' for financial support of RFBR (project 13-05-00462a) and basic RAS scientific program #01201054328. Special thanks to Georgy Perlshtein, Nikolai Romanovski, Alexander Khimenkov, Vladimir Merzlyakov, and Alexey Victorov for a criticism to improving this work.

References

Clarke J, Fenton C, Gens A, Jardine R, Martin C, Nethercot D, Nishimura S, Olivella S, Reifen C, Rutter P, Strasser F, Toumi R (2008) A Multi-Disciplinary Approach to Assess the Impact of Global Climate Change on Infrastructure in Cold Regions. NICOP Proceedings: 279-284.

Kääb A. (2008) Remote sensing of permafrost-related problems and hazards // Permafrost and periglacial processes. Vol.19: 107-136.

Koff GL, Chesnokova IV, Bogomolova TV, Zaigrin IV (2009) Experience in engineering geological typification and mapping of geoenvironmental risk factors (by the example of "East Siberia-Pacific Ocean" oil pipeline route). Geoecology, #2:172-179 (in Russian).

Pavlov AV (1996) Permafrost-Climatic monitoring of Russia: Analysis of Fild Date and Forecast. Polar Geography 20(1):44–64

Ragozin AL (1999) The basic theses of the risk's estimation and management. Geoecology, #5:417-429 (in Russian).

Romanovsky VE, Drozdov DS, Oberman NG, Malkova GV, Kholodov AL, Marchenko SS, Moskalenko NG, Sergeev DO, Ukraintseva NG, Abramov AA, Gilichinsky DA, Vasiliev AA (2010) Thermal state of permafrost in Russia. Permafrost and Periglacial Processes. Volume 21, Issue 2. Special Issue: The International Polar Year:136-155.

Periglacial Geohazard Risks and Ground Temperature Increases

44

Lukas U. Arenson and Matthias Jakob

Abstract

Climate change can impact glacial and periglacial environments, which are likely transforming at unprecedented rates during the Holocene. Progressive increases in air temperature and the associated modification in the ground thermal regime and surface energy balance result in increasing active layer thicknesses, ground warming, changing runoff and alterations in the freeze-thaw cycles. As a consequence to these thermal fluxes and their second order impacts to geomorphological processes the potential for slope instabilities changes accordingly. Active layer detachments, thermokarst or increased mass movement frequency due to frost weathering may result in hitherto unknown, or at least under-appreciated hazards because they may not have led to losses in the past. Where the hazard trajectory intercepts vulnerable infrastructure, geohazard risk may change in response. Quantitative geohazard risk assessments rely on frequency-magnitude relationships constructed from compilation and analyses of proxy data or direct observations. These analyses typically assume data stationarity (i.e., no long-term change in the mean and variance of the reconstructed time series), an assumption that is increasingly questioned considering the observed changes in the periglacial belt. This realization demands alternate approaches in risk assessment. In this paper, we present a general framework for assessing changes in geohazard activity within the periglacial environment heralded by changes in permafrost and ground ice conditions. The proposed framework starts with an examination of the effect of changes in air temperature on the ground thermal regime. Hazard probability and consequences are then assessed. By comparing the risk level under current conditions with the risk associated under a projected change in certain climatic parameters, the sensitivity of the slope stability or strength to climate change can be approximated. Despite considerable uncertainties associated with predictions of a third-order effect of climate change, the general approach outlined in this paper provides at least a tool to identify areas and slopes with high vulnerability to climate change and at best offers a systematic tool to evaluate climate change impacts in the periglacial zone.

Keywords

Global Warming • Permafrost • Geohazard

L.U. Arenson (✉) · M. Jakob
BGC Engineering Inc., Vancouver, BC, Canada
e-mail: larenson@bgcengineering.ca

M. Jakob
e-mail: mjakob@bgcengineering.ca

44.1 Introduction

Global warming continues at unprecedented rates, independent on any inter-annual variability (Marcott et al. 2013; IPCC 2013). The changes in air temperature, combined with

G. Lollino et al. (eds.), *Engineering Geology for Society and Territory – Volume 1*,
DOI: 10.1007/978-3-319-09300-0_44,

changes in precipitation have significant impacts on the naturally very dynamic glacial and periglacial environments (Haeberli and Burn 2002; Huggel et al. 2010). The changes in the surface energy balance and the ground temperatures are responsible for the change the geohazard potential related to slope instabilities in high mountain terrains (Kern et al. 2012; Springman et al. 2013; Gruber et al. 2004; Phillips et al. 2009; Haeberli 2013). The change in the geohazard potential and the associated risks originates mainly from failures of the active layer, thermokarst developments and rock falls (Kenner et al. 2011). Such changes could either be related to more frequent events or to larger events. Both result in a change of the associated risks. A common approach in assessing geohazards is the use of statistical analysis of historical events (Jakob and Hungr 2005; Stoffel and Bollschweiler 2008). However, a statistical analysis of historic event alone is only valid if the conditions are relatively stable during the time when the data are collected. The unprecedented rate at which the periglacial environment is changing requires novel approaches on how to consider risks from geohazards initiated in high mountainous terrain that reach into the permafrost-underlain elevation belt. A framework for assessing changes in risks related to slope instabilities and active layer thickening within the periglacial environment caused by altered permafrost conditions was developed and is presented in this paper.

44.2 Background

After the exceptional rock fall occurrence throughout the Alps during the unusually hot summer of 2003 (Gruber et al. 2004), slope instabilities from the periglacial environment became the focus of various research activities, especially in the highly populated European Alps (Haeberli 2013). Based on the observed clustering of large rock slope failures in high mountain areas around the world in recent years, Huggel et al. (2004; 2013) present approaches that can potentially be used to detect changes in landslide activity in high mountains. The approaches include the analysis of slope failure inventories, case histories and trigger mechanisms, and Huggel et al. (2013) concluded that these are promising avenues for detection studies. Gruber (2013) notes the difficulties of understanding low-frequency and high-magnitude events, such as landslide hazards in cold regions that may be intensified by progressive and nonlinear changes in the periglacial environment.

Geohazard trigger mechanism from permafrost-underlain terrain, such as rock fall and debris flow, usually include some effect of water. Slope instabilities leading to a debris flow may be initiated by the reduction in effective stress at the permafrost table in combination with seepage pressure. Figure 44.1 shows an example of a debris flow scar with exposed ground ice at the frontal area of a rock glacier in the south-eastern Rocky Mountains of Alberta, Canada. Rock fall is often related to the formation of hydrostatic pressures or expansion pressures from the freezing of water in unfavourably oriented joint sets.

Two key meteorological parameters can affect these triggering mechanisms due to climate warming: (i) increase in air temperatures; and (ii) increase in precipitation type, intensity and duration. Higher air temperatures result in a thickening of the active layer and likely changes in the frequency and intensity of freeze-thaw cycles. Changes in precipitation regime can alter seepage pressures in the active layer or the hydrostatic pressure within a fractured bedrock system. For example, a change towards higher rainfall intensities may lead to accelerated transient pore water pressure increases and subsequent slope failure. The combination of such changes may influence the geohazard potential. When evaluating these parameters it is important to not just consider changes in average values but take into account projected extremes, since risk assessments need to account for the full range of possible geohazard scenarios.

44.3 Methodology

A geohazard risk can be expressed as the product of the hazard probability and the associated consequences. The risk can further be expressed as loss of life, economic or environmental losses. A change in the frequency of the triggering mechanism, hence, affects the hazard probability, whereas a change in the event magnitude and the associated intensity may affect the hazard's consequences. When assessing the change in geohazard risk due to climate change it is therefore important to estimate their variation in probability and potential consequences.

For a specific consultation zone (or study area) the total geohazard probability may change if either a single hazard occurs more frequently along a single trajectory and/or if more spatially independent geohazards occur within the consultation zone. For example, the total hazard for a road below a steep slope increases if a single zone of instability produces more frequent debris flows, or if more debris avalanches are occur along the road length under investigation.

The total risk also changes if the magnitude and associated intensity of the event changes and the consequences increase, e.g., more fatalities, higher repair costs or more frequent road closures and associated indirect economic losses. As an example, the changes in the active layer thickness or ground temperature increase can change the potential volume of a glacier lake outburst flood if the lake is dammed by an ice cored moraine. Active layer thickening

Fig. 44.1 Debris flow scar at frontal area of a rock glacier near Canmore, Canada. *Photo* M. Jakob, July 2013

and ground ice warming increases the potential for seepage and piping through the dam. In addition, an unfrozen moraine will likely result in higher peak flows and larger volumes due to greater breach rates in case of overtopping or piping failure. This will likely raise the consequences for such event to occur.

For the evaluation of these changes an understanding of the potential physical changes in the periglacial environment is critical. This includes an evaluation of the current conditions, such as climate parameters, ground ice distribution and geothermal regimes as well as an assessment of impacts of projected changes downslope. The updated hazard scenario needs to be evaluated by assessing the change in temperature and precipitation, that changes the active layer or pore pressure conditions. The major steps in evaluating changes in geohazard risks from the periglacial environment due to climate change are therefore:

1. Evaluation of current risk, i.e., hazard probability, element vulnerability and consequences.
2. Determination of changes in key climate parameters, such as air temperature, snow cover, precipitation, and delineation of design values.
3. Calculation of changes in active layer thickness, ground water flow regimes and ground temperature dependent frozen soil strength, typically by using geothermal modelling.
4. Evaluation of the new hazard potential based on the estimated change in soil strength and active layer thicknesses.
5. Calculation of new hazard probability, magnitude and any potential changes in consequences due to differences in impacts.
6. Identifying new hazards (risks) that may have emerged as a consequence of any loss in soil strength or changes in active layer and hydrological regimes.

44.4 Examples

The suggested approach is illustrated using a simple example of an ice cored moraine dam. Based on current conditions the active layer thickness is approximately 3.0 m, using a mean annual air temperature of −5.3 °C and a standard, frozen till. Geothermal modelling was used (TEMP/W 2012, Geo-Slope International Ltd.) to evaluate the change in the active layer based on changes in the mean annual air temperature (Fig. 44.2). These changes are insignificant, mainly because of the latent heat effect. For example, a change in mean annual air temperature of +2 °C results in an increase in active layer of 0.5 m (+17 %). Assuming that the lake has an area of 10 ha, 50,000 m^3 of additional water may be available in a flood event. In addition, peak discharge is controlled by the breach rate. Since thermal erosion of an ice core is slower than the mechanical erosion of the unfrozen material an increase in active layer likely increases the dam breach rate and the associated peak flow, for example after rock fall or an avalanche that triggered a tsunami in the glacier lake. The consequences of this updated release scenario has to be evaluated. The new flood volume and associated peak flow may exceed current stream capacity or it may trigger debris flows where none had been observed prior. Further, the flood scenario can be used to identify new potential zones of impact and changes in the consequences, hence the risk.

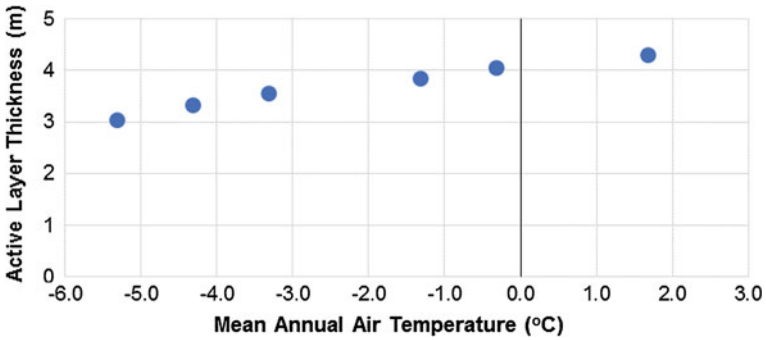

Fig. 44.2 Change in active layer thickness for a standard colluvial soil as a function of mean annual air temperature

65 years of daily temperature data are available for the study site and this information can be used to assess the change in the frequency of active layer thickening caused by a 2 °C air temperature increase. Currently, an average temperature of −5.3 °C occurs, on average, every three years, and a summer that is 2 °C warmer occurs, on average, every 20 years. Assuming that the variability in annual temperatures continues in a similar pattern, one can calculate that a 2 °C warming in average temperature results in −5.3 °C to occur every year and −3.3 °C every three years, on average. Hence, the probability of an additional 50,000 m^3 of water to be available as a consequence of active layer thickening that could change breach rate and peak discharge has therefore increased from an annual probability of 5–33 %.

Rock fall hazards can be evaluated similarly. Calculated changes in the active layer thickness and the rock mass characterization allow for estimating changes in the magnitude of rock slope failures. Because the moisture content is generally much lower in a rock mass, compared to a till, latent heat effects can be ignored and a change in air temperature of +2 °C may result in a change in the active layer of more than 1.5 m, i.e., triple the change expected in an ice-rich frozen soil. If the active layer is currently 4 m and joint spacing of critical discontinuities exceeds 5 m, changes in hazard and risk may be negligible due to ground ice melt for the projected time horizon. However, the new temperature conditions will allow warming and thawing of frozen joints, potential build-up of hydrostatic pressures and rock fall that had not been observed in the past may occur resulting in a new geohazard related risk. As demonstrated by Davis et al. (2003), warm ice is already sufficient to significantly reduce the shear strength of an ice filled joint.

Assessing changes in debris yield and frequency is slightly more complex and the page restriction of this paper does not allow to present the approach herein. However, the method is similar in that the changes in the active layer need to be determined and on that basis, changes in debris volumes and debris channel recharge evaluated.

In the long-term changes in the periglacial belt may also decrease hazard potential. In the example of a moraine-dammed lake, once failed, it will not be a re-occurring hazard. In August of 2012, an ice avalanche occurred on the northwest flanks of Mount Edith Cavell, Jasper National Park (BGC 2012), which impacted a pro-glacial lake leading to a debris flood downstream that impacted park facilities. Fortunately, the event occurred at night; had it occurred during the day time, several fatalities would have been likely as the area is one of the most popular tourist destination in Jasper National Park. This failure involved the entire volume of Ghost Glacier. Given projected temperature changes of 3–4 °C by the end of the century for this region (PCIC 2013), it is likely that this hanging glacier will not reform. Consequently, the hazard potential from this specific event would no longer prevail.

The examples were used to illustrate how assessing potential changes in the physical conditions (e.g., active layer thickness) can be used to evaluate changes in risk. Similarly, new hazards may be identified or known hazards can disappear once released. It is important to first understand the basics, in particular the climate conditions that are used in order to evaluate current hazards. Various climate scenarios may then be utilized to make projection on potential changes that may consequently yield in an update in the risk.

44.5 Conclusions

A systematic approach is outlined that may improve the assessment geohazard risks due to climate change, such as moraine dam failures, debris flows or rock fall, occurring within the periglacial belt. Even though the high complexity of identifying changes in the stability of presently frozen slopes due to global warming is appreciated, the proposed approach can assist in quantifying changes in hazard frequency and/or magnitude. Applying a systematic methodology that incorporates changes in the physical environment is preferable over reliance on historic data in a rapidly changing environment. Additional research will improve the uncertainties in projecting physical changes and associated risks in mountainous permafrost environments around the world.

References

BGC Engineering Inc. (2012) Mount Edith Cavell risk zones map. Report prepared for Parks Canada, Document No. 0829-002-01

Davies MCR, Hamza O, Harris C (2003) Physical modelling of permafrost warming in rock slopes. In: 8th international conference on permafrost, pp 169–174

Geotechnical Engineering Office (GEO) (1998) Landslides and boulder falls from natural terrain: interim risk guidelines. Hong Kong Government, GEO Report No. 75

Gruber S, Hoelzle M, Haeberli W (2004) Permafrost thaw and destabilization of Alpine rock walls in the hot summer of 2003. Geophys Res Lett 31:L13504

Gruber S (2013) Landsides in cold regions: making a science that can be put into practice. In: Margottini C, Canuti P, Sassa K (eds) Landslides science and practice, vol 4. Springer, Berlin, Heidelberg, pp 329–333

Haeberli W (2013) Mountain permafrost—research frontiers and a special long-term challenge. Cold Reg Sci Technol 96:71–76

Haeberli W, Burn CR (2002) Natural hazards in forests: glacier and permafrost effects as related to climate change. In: Environmental change and geomorphic hazards in forests. CABI Publishing, Wallingford, pp 167–202

Huggel C, Haeberli W, Kääb A, Bieri D (2004) An assessment procedure for glacial hazards in the Swiss Alps. Can Geotech J 4:1068–1083

Huggel C, Salzmann N, Allen S, Caplan-Auerbach J, Fischer L, Haeberli W, Larsen C, Schneider D, Wessels R (2010) Recent and future warm extreme events and high-mountain slope stability. Philos Trans Ser A Math Phys Eng Sci 368:2435–2459

Huggel C, Allen S, Clague JJ, Fischer L, Korup O (2013) Detecting potential climate signals in large slope failures in cold mountain regions. In: Margottini C, Canuti P, Sassa K (eds) Landslides science and practice, vol 4. Springer, Berlin, Heidelberg, pp 361–367

Intergovernmental Panel on Climate Change (IPCC) (2013) Working group I contribution to the IPCC fifth assessment report climate change 2013: the physical science basis—summary for policy-makers, Sept. 2013

Jakob M, Hungr O (2005) Debris-flow hazards and related phenomena. Springer, Berlin, Heidelberg

Kenner R, Phillips M, Danioth C, Denier C, Thee P, Zgraggen A (2011) Investigation of rock and ice loss in a recently deglaciated mountain rock wall using terrestrial laser scanning: Gemsstock, Swiss Alps. Cold Reg Sci Technol 67:157–164

Kern K, Lieb GK, Seier G, Kellerer-Pirklbauer A (2012) Modelling geomorphological hazards to assess the vulnerability of alpine infrastructure: the example of the Großglockner-Pasterze area, Austria. Austrian J Earth Sci 105:113–227

Marcott S, Shakun J, Clark P, Mix A (2013) A reconstruction of regional and global temperature for the past 11,300 years. Science 339:1198–1201

Pacific Climate Impacts Consortium (PCIC) (2013) PCIC regional analysis tool (BETA). http://www.pacificclimate.org. Accessed Oct 2013

Phillips M, Mutter EZ, Kern-Luetschg M, Lehning M (2009) Rapid degradation of ground ice in a ventilated talus slope: Flüela pass Swiss Alps. Permafr Periglac Proc 20:1–14

Springman SM, Yamamoto Y, Buchli T, Hertrich M, Maurer H, Merz K, Gärtner-Roer I, Seward L (2013) Rock glacier degradation and instabilities in the European Alps: a characterisation and monitoring experiment in the Turtmanntal, CH. In: Margottini C, Canuti P, Sassa K (eds) Landslides science and practice, vol 4. Springer, Berlin, Heidelberg, pp 5–13

Stoffel M, Bollschweiler M (2008) Tree-ring analysis in natural hazards research—an overview. Nat Hazard Earth Syst Sci 8:187–202

Assessment of Permafrost Distribution in the Mont Blanc Massif Steep Rock Walls by a Combination of Temperature Measurements, Modelling and Geophysics

45

Florence Magnin, Philip Deline, Ludovic Ravanel, Stephan Gruber and Michael Krautblatter

Abstract

Permafrost degradation is thought as an important triggering factor of rockfall affecting the steep rockwalls of the Mont Blanc massif. We investigate permafrost distribution by a combination of rock temperature measurements, statistical modelling and Electrical Resistivity Tomography (ERT). Mean Annual Rock Surface Temperature (MARST) is predicted at regional scale on a 4-m-resolution DEM by implementing a multiple linear regression model with Mean Annual Air Temperature (MAAT) of the 1961–1990 period and Potential Incoming Solar Radiation (PISR) as explanatory variables. Based on recent studies, we assume that fracturation and heterogeneous snow deposit induce a temperature offset between the surface and depth of negligible annual temperature variations that may reach 3 °C. This assumption is supported by temperature measurements in 11-m-deep boreholes at the Aiguille du Midi (AdM, 3842 m a.s.l) and verified with ERT measurements. The underlying hypothesis is that permafrost occurs below MARST ranging up to 3 °C. The preliminary results suggest that permafrost possibly occurs even below warmer MARST than expected.

Keywords

Permafrost distribution • Rock walls • Modelling • ERT • Boreholes

45.1 Introduction

An increase in rock fall activity originating from high-elevation rockwalls has been observed these past decades in the Mont Blanc massif (Ravanel and Deline 2010). Permafrost degradation is thought as a major factor affecting high alpine rockwall stabilities (Gruber and Haeberli 2007). The Chamonix valley is densely populated and lies below a high mountain area strongly frequented by tourists and alpinists. Understanding of geomorphic processes is therefore of interest for risk assessment. We started permafrost investigation by addressing questions on regional permafrost distribution. This study combines rock and air temperature measurements, statistical modelling of Mean Annual Rock Surface Temperature (MARST), a conceptual understanding of temperature offset between the surface and depth of negligible annual temperature variations in steep rock faces and Electrical Resistivity Tomography (ERT) measurements. These approaches and methods are described and preliminary results and interpretations are presented.

F. Magnin (✉) · P. Deline · L. Ravanel
EDYTEM Lab, Université de Savoie, CNRS,
Le Bourget-Du-Lac, France
e-mail: Florence.Magnin@univ-savoie.fr

S. Gruber
Carleton University, Ottawa, Canada

M. Krautblatter
Monitoring, Analysis and Early Warning of Landslides,
Technische Universität München, München, Germany

G. Lollino et al. (eds.), *Engineering Geology for Society and Territory – Volume 1*,
DOI: 10.1007/978-3-319-09300-0_45,

45.2 Methods and Processing

45.2.1 Rock Temperature Measurements

We started our investigations in 2005 by installing a monitoring system at the Aiguille du Midi (AdM), a set of three granite peaks culminating at 3842 m a.s.l (Fig. 45.1). The installation has been lead in collaboration with the ARPA (Valle d'Aosta), the University of Zurich and the Technical University of Munich. About half a million of tourists visit the AdM each year as it is accessible by a cable car and that galleries and terraces allow to move around and inside the peaks. These facilities are an essential asset to maintain installations. Eight surfaces sensors on North, South, East and West (RST_N, RST_S, RST_E and RST_W respectively, Fig. 45.1) aspects have been installed in nearly vertical and snow free rock sections. In September 2009 three 11-m-deep boreholes have been drilled in North, East and South faces (BH_N, BH_E and BH_S, Fig. 45.1). Spatial distribution of MARST is correlated with sun-exposure (Fig. 45.1 bottom left), and is thus suitable for statistical modelling. Temperature-depth (Tz) profiles recorded within the boreholes show that surface temperature is warmer than temperature at 10 m depth (Fig. 45.1 bottom right). BH_N crosses a fracture at about 2.5 m depth that is marked by a cold distortion of the Tz profile and thus appears as one of the possible factor leading to a temperature offset between the surface and depth.

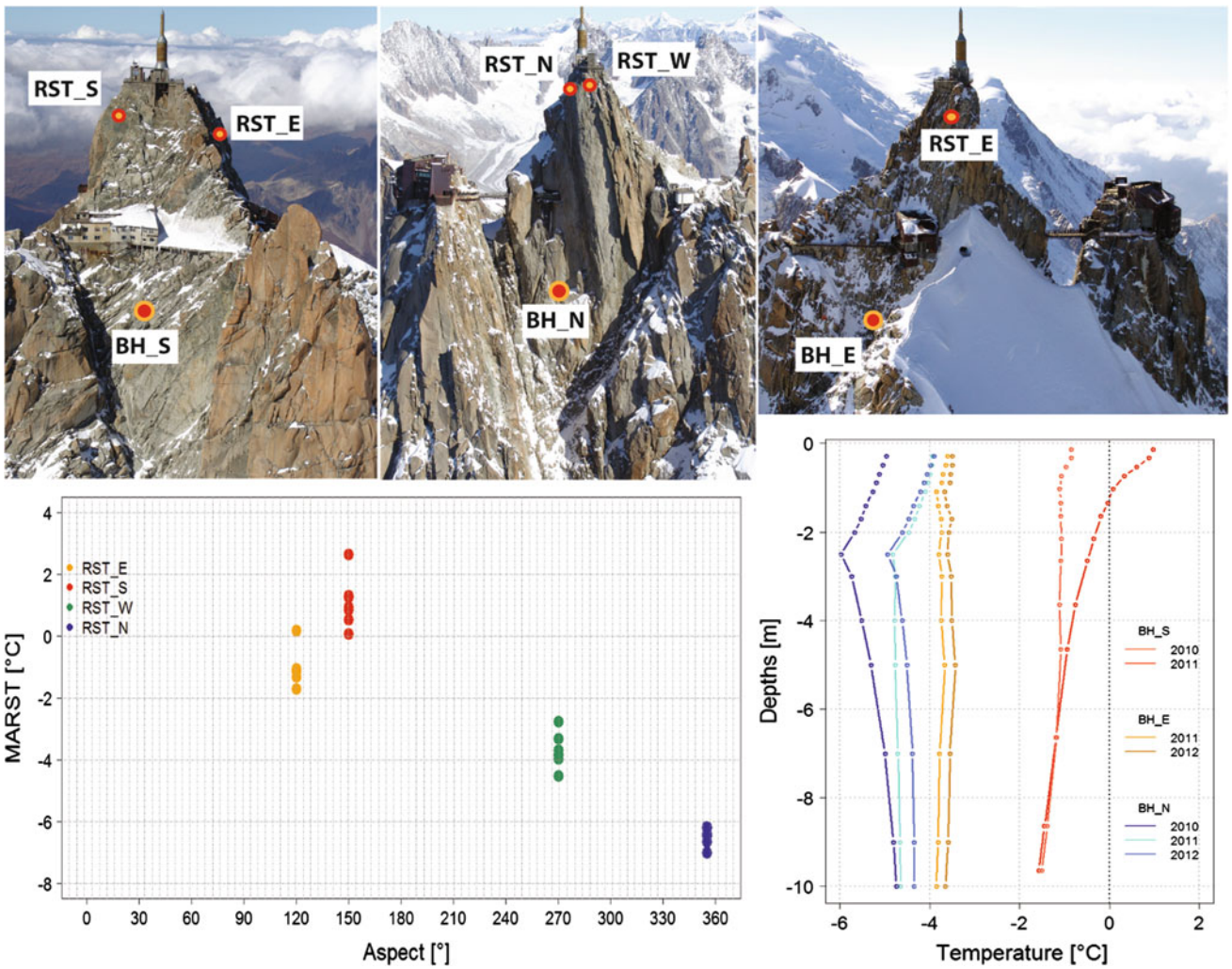

Fig. 45.1 The Aiguille du Midi monitoring system. RST_x show location of rock surface temperature loggers registering temperature every hour at 0.03, 0.3 and 0.55 m depth. BH_x show the borehole locations. *Bottom left* Spatial distribution of the registered MARST (2006–2012) according to aspect. *Bottom right* Temperature-depth (Tz) profiles of the registered mean annual rock temperature in boreholes (2010–2012). The *dots* along the *profile lines* indicate the thermistor depths

45.2.2 Statistical Modelling and Hypothesis

Boeckli et al. (2012) fitted a multiple linear regression model of MARST using Mean Annual Air temperature (MAAT) and Potential Incoming Solar Radiation (PISR) as explanatory variables. More than 50 surface time series spread within the European Alps including the Mont Blanc massif were used for model calibration. We implemented this model on a 4-m-resolution DEM with MAAT calculated from records at Chamonix (Météo France) for the 1961–1990 period, and from the AdM (since 2007) to parameterize the lapse-rate. The PISR is computed with GIS tools. Hasler et al. (2011) have postulated that the combined effects of air ventilation in bedrock fractures, of snow patches and solar radiation at the surface induce a temperature offset that may reach up to 3 °C in steep alpine rock faces. AdM boreholes records are consistent with this statement. Thus, we hypothesize that permafrost occurs below predicted MARST <3 °C (Fig. 45.2). The hypothesis is verified with ERT measurements.

45.2.3 Electrical Resistivity Tomography

Krautblatter and Hauck (2007) showed that ERT is usable for steep bedrock permafrost detection under relevant data acquisition settings. Five sites which simulated MARST ranges from −1 to 3 °C, on various aspects, topographies and surface types from highly fractured bedrock to compact slab have been measured with Wenner array. The survey lines were 160-m-long with 32 electrodes spaced every 5 m which yield a median depth of investigation of about 30-m-deep. Apparent resistivity was inverted with RES2DInv using robust inversion and with 5 iterations in order to avoid overfitted model.

45.3 Results and Preliminary Interpretations

Four of the five measured sites: *"Les Grands Montets", "Le Gros Rognon", "La Pendant"*, and *"Les Petits Charmoz"* are located in the Mont Blanc granite area, while the last one: *"Les Rachasses"* is located in the gneiss area. Locations of the sites are displayed in Fig. 45.2. The four first sites show similar patterns: a high resistivity body at depth (>200 kΩ) with a lower resistivity layer above (Fig. 45.3). According to the values measured on a rock sample from the AdM (Krautblatter M., *pers. com)*, resistivity >200 kΩ indicates frozen rock that we interpret as the permafrost body. The lower resistivity in the shallow layers is interpreted as active layers. Also, for "*Les Petits Charmoz", "Le Gros Rognon"* and *"La Pendant",* a higher resistivity layer is also measured at the surface. These three sites have been measured about 1 week after *"Les Grands Montets"*. Air temperature decreased of nearly 10 °C in between these measurements. Thus, the high resistivity surface layers possibly indicate refreezing of the active layer whereas it was still thawed in *"Les Grands Montets"*. This interpretation is consistent with our observation in active layer dynamics at the AdM boreholes. Even though the lack of temperature-resistivity calibration for *"Les Rachasses"* limits the data interpretation, it is obvious that this site hasn't the same resistivity gradient pattern than the other sites. The resistivity scale is taken from some mineralized

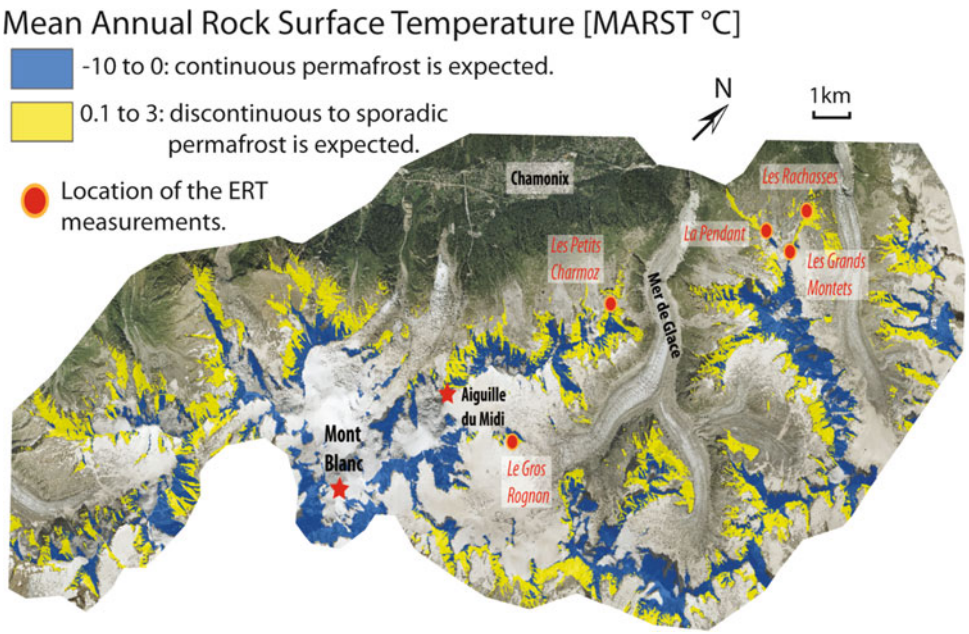

Fig. 45.2 Hypothesis on permafrost distribution in the Mont Blanc massif. *Blue areas* are the simulated MARST ≤0 °C

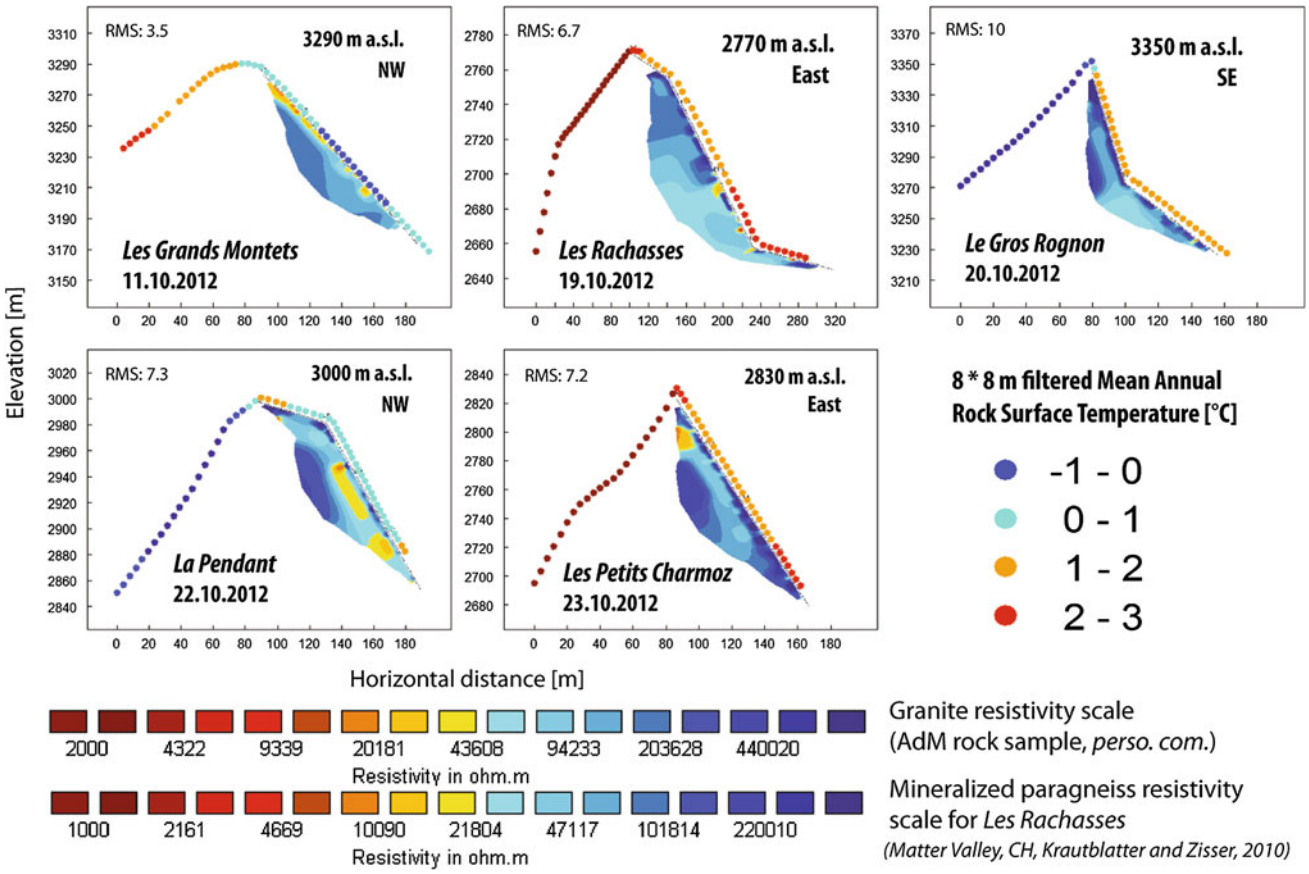

Fig. 45.3 Electrical resistivity tomograms plotted against 8 × 8 m filtered MARST extracted from the statistical model

paragneiss values measured by Krautblatter (2010) but specific calibration is required for further interpretation.

45.4 Conclusion and Perspectives

The Boeckli et al. (2012) model is valuable for estimating MARST in the Mont Blanc massif at high resolution. ERT measurements have been performed for the first time on such steep alpine morphologies and yield promising results. They suggest that permafrost exists below MARST reaching at least 3 °C. By extension, we suspect that permafrost can even occur below warmer temperature and future ERT measurements will aim to verify this hypothesis. The study also encourages at improving our understanding of the parameters and at quantification of the processes that induce a temperature offset between the surface and the depth for a better estimation of permafrost distribution in steep alpine bedrock.

References

Boeckli L, Brenning A, Gruber S, Noetzli J (2012) A statistical approach to modelling permafrost distribution in the European Alps or similar mountain ranges. Cryosphere 6:125–140

Gruber S, Haeberli W (2007) Permafrost in steep bedrock slopes and its temperature related destabilization following climate change. J Geophys Res 112:F02S18

Hasler A, Gruber S, Haeberli W (2011) Temperature variability and offset in steep alpine rock and ice faces. Cryosphere 5:977–988

Krautblatter M, Hauck C (2007) Electrical resistivity tomography monitoring of permafrost in solid rock walls. J Geophys Res 112:1–14

Krautblatter M (2010) Detection and quantification of permafrost change in alpine rock walls and implications for rock instability. PhD thesis, University of Bonn, Bonn, Germany, p 162

Ravanel L, Deline P (2010) Climate influence on rockfalls in high-Alpine steep rockwalls: the north side of the Aiguilles de Chamonix (Mont Blanc massif) since the end of the 'Little Ice Age'. Holocene 7(4):493–501

Freeway Extension Project Island Permafrost Section Foundation Deformation Characteristics

46

Hua Jiang, Wei Shan and Zhaoguang Hu

Abstract

Bei'an to Heihe freeway locates in the China high latitude permafrost region, the permafrost is in the depredating stage, has low altitude and unstable characteristics, and affects the stability and operation safety of freeway. Employed the geological exploration and interior experiment method to obtain the permafrost type and mechanics performances; employed field monitoring method to study the permafrost degrading process and foundation deformation characteristics. Study results show that: the mechanical indexes of soil decrease significantly with frozen soil melted, and water content greater, void ratio higher, the descendant ranges are larger; the permafrost under the widen subgrade degrades from two sides to middle in the frozen period due to the thermal resistance effect of widen subgrade, the upper limit has declined 2.7 m and lower limit has raised 0.7 m; the vertical displacement of subgrade and foundation has obvious accelerating process with the new subgrade filling, the time of vertical displacement reaches a steady state is closely related with the stability of foundation permafrost, under the function of widen subgrade loading and permafrost thawing settlement, the maximum vertical displacement of widen subgrade foundation and original subgrade respectively reach 40.2 and 18.6 cm.

Keywords

Permafrost • Freeway • Foundation deformation • Ground temperature

46.1 Introduction

Permafrost area accounts for about 23 % of the world land area (Wu et al. 2005). China's permafrost is mainly distributed in the Greater and Lesser Khingan Mountains, northern Songnen Plain, western mountains and Tibetan Plateau, accounts for about 22.14 % of land area (Zhou et al. 2000). Permafrost has the special engineering properties which are different from general rock and soil, its particularity is manifested in its physical and mechanical properties are closely related with the temperature (Qi et al. 2005; Wu et al. 2007).

Under the background of global warming, the permafrost universally has degrading trend; constructing subgrade changes the heat exchange relationship between the ground and atmosphere, breaks the heat balance of permafrost, for the permafrost which is under the subgrade, the degrading speed is more quickly (Wu et al. 2001; Wang et al. 2001; Li and Wu 1997). The permafrost occurring degrading phenomenon performs ground temperature elevating, thickness reducing, and melting interlayer forming, the melting interlayer substantially is a soft structure layer of the foundation that has high water content, low strength, and large compressibility, produces serious negative effect on the stability of the subgrade. Bei'an to Heihe Freeway expansion project is located in the Lesser Khingan Mountains island permafrost region, there are many island permafrost distributed along the route. The permafrost of that

H. Jiang (✉) · W. Shan · Z. Hu
Institute of Cold Regions Science and Engineering, Northeast Forestry University, Harbin, 150040 China
e-mail: jianghua3433@163.com

G. Lollino et al. (eds.), *Engineering Geology for Society and Territory – Volume 1*,
DOI: 10.1007/978-3-319-09300-0_46,

area is in a strong degrading process, and has the characteristics of thin thickness, high ground temperature and high ice content (Meng et al. 2001), brings great difficulties for Freeway construction.

46.2 Study Area Climate and Geological Condition

The study area is located in central region of China Lesser Khingan Mountains. Belongs to continental monsoon climate, the spring is short and gets warm quickly, the summer is tepidity and rainy, the autumn is short and cools fast, the winter is long and cold. The annual average temperature is −0.6 °C, the lowest temperature is −48.1 °C, the highest temperature is 35.2 °C, the annual average freezing index is 3000–3300 °C d, the frost-free period is about 96 d. In October the ground begins to freeze every year, in April of following year, the ground begins to melt, the maximum seasonal freezing depth is 2.26–2.67 m, and there are many island permafrost distributed in the cheuch.

The tectonic of study area is in the Wuyun-Jieya new rift zone, the north is Handaqi virgation and the south is Shuhe upwarping zone. Surface exposed stratums contain the upper Cretaceous Nenjiang formation, Tertiary Pliocene series Sunwu formation, Quaternary Holocene series modern river alluvium and stack layer. Permafrost is mainly distributed in the Quaternary Holocene series modern river alluvium and stack layer and the upper Cretaceous Nenjiang formation.

46.3 Study Site Engineering Geological Condition

In order to identify the engineering geology condition, hydrology geology condition, and permafrost upper limit and lower limit of study section, four drilling holes were arranged in the toe of widen subgrade, shoulder of widen subgrade, and shoulders of old subgrade. According to the drilling results, drew the engineering geological profile of study section, as shown in Fig. 46.1.

The lithologies of controlling range are Quaternary loose sediments, Cretaceous pelitic sandstone and mudstone. Subgrade filling: yellow, mainly consist of Tertiary pebbly sandstone, little dense and permeable. Turf soil: brown-black, saturated, soft plastic, including incompletely decomposed grass root; layered and porphyritic frozen soil formation. Silty clay: black, wet, hard plastic, with gloss, dry strength and toughness is larger; layered and porphyritic frozen soil formation. Pelitic sandstone: gray-black, wet, hard plastic, part has fine sandstone lens, weakly cemented, mud structure, layered formation; micro layered and layered frozen soil formation. Mudstone: gray-black, wet, hard plastic, weakly cemented, mud structure, layered formation; layered frozen soil formation.

For the permafrost under the old subgrade, upper limit is 15.8–16.8 m, lower limit is 19.0–21.0 m, and thickness is 2.2–5.2 m. For the permafrost under the original ground, upper limit is 1.5–2.3 m, lower limit is 9.2–10.3 m, and thickness is 7.7–8.0 m. Affected by the old subgrade, the

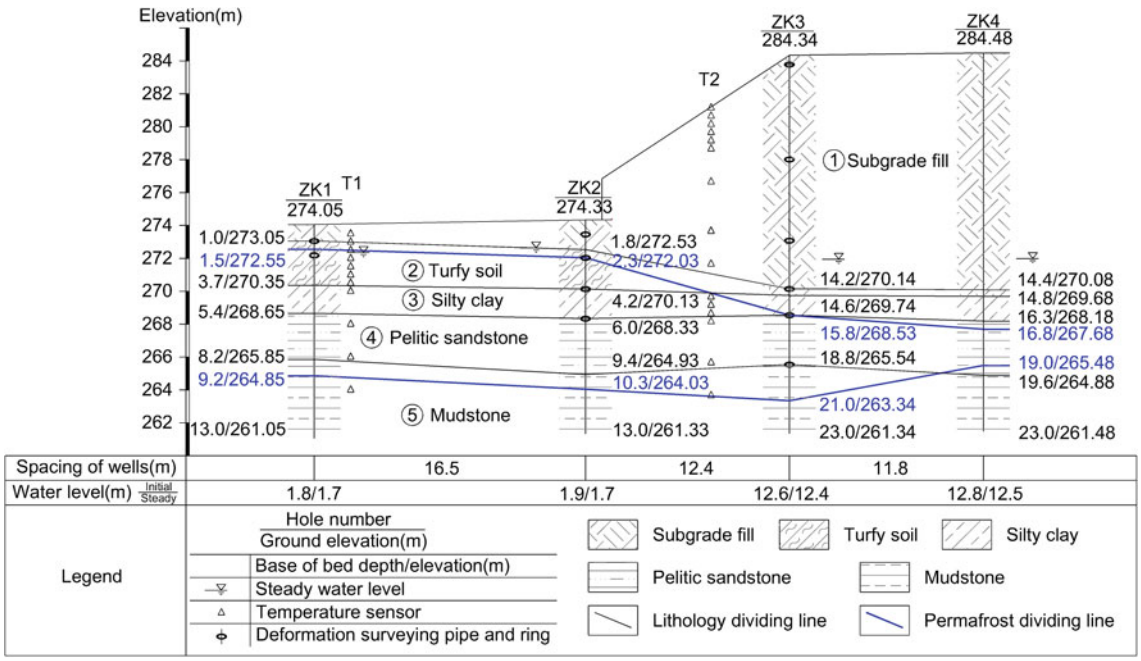

Fig. 46.1 Study section engineering geological profile

permafrost under the old subgrade had occurred obvious degradation.

The permafrost of study section are micro layered, layered, porphyritic frozen soil formation, belong to much ice, rich ice, full ice frozen soil, weak thawing settlement, thawing settlement, strong thawing settlement, the engineering geological condition is poor, foundation is instability.

46.4 Permafrost Mechanical Properties

Got permafrost from ZK1 position, then tested its physical and mechanical indexes. Though indoor test, the natural water content of turf soil is 79.3–95.8 %, the average void ratio is 2.19; the natural water content of silty clay is 31.1–32.5 %, the average void ratio is 1.07; the natural water content of pelitic sandstone is 22.9–26.2 %, the average void ratio is 0.83; the natural water content of mudstone is 40.9–48.3 %, the average void ratio is 1.34. Measured the elastic modulus and shear strength of original frozen soil, original melted soil and 300 kPa consolidated melted soil by triaxial test, the result as shown in Fig. 46.2.

Elastic modulus of rock and soil decreases significantly with the frozen soil melted, and has a certain degree of rebound with the melted soil consolidated; water content greater and void ratio higher, the elastic modulus descendant range is larger; for the maximum water content and highest void ratio turf soil, the elastic modulus of original frozen soil is 25.69 MPa, but the elastic modulus of original melted soil is only 0.44 MPa, the descendant range reaches 98.3 %. Shear strength indexes of rock and soil also decrease significantly with the frozen soil melted, cohesion has a larger rebound and internal friction angle has a smaller rebound with the melted soil consolidated; water content greater and void ratio higher, the shear strength indexes descendant range are larger; for the maximum water content and highest void ratio turf soil, the cohesion and internal friction angle of original frozen soil are respectively 66.1 kPa and 19.83°, but the cohesion and internal friction angle of original melted soil are respectively 8.57 kPa and 1.02°, the descendant ranges reach respectively 87.0 and 94.9 %.

From above analysis, with the foundation permafrost degrading, elastic modulus and shear strength indexes of soil and rock produce substantially decline, under the function of self weight, subgrade load and other loads, the foundation will produce large deformation, seriously affects the stability of widen subgrade.

46.5 Permafrost Degrading Process and Foundation Deformation Characteristics

At the same time of geological exploration, deformation monitoring equipments were buried in the drilling holes (see Fig. 46.1), and began to collect the deformation data.

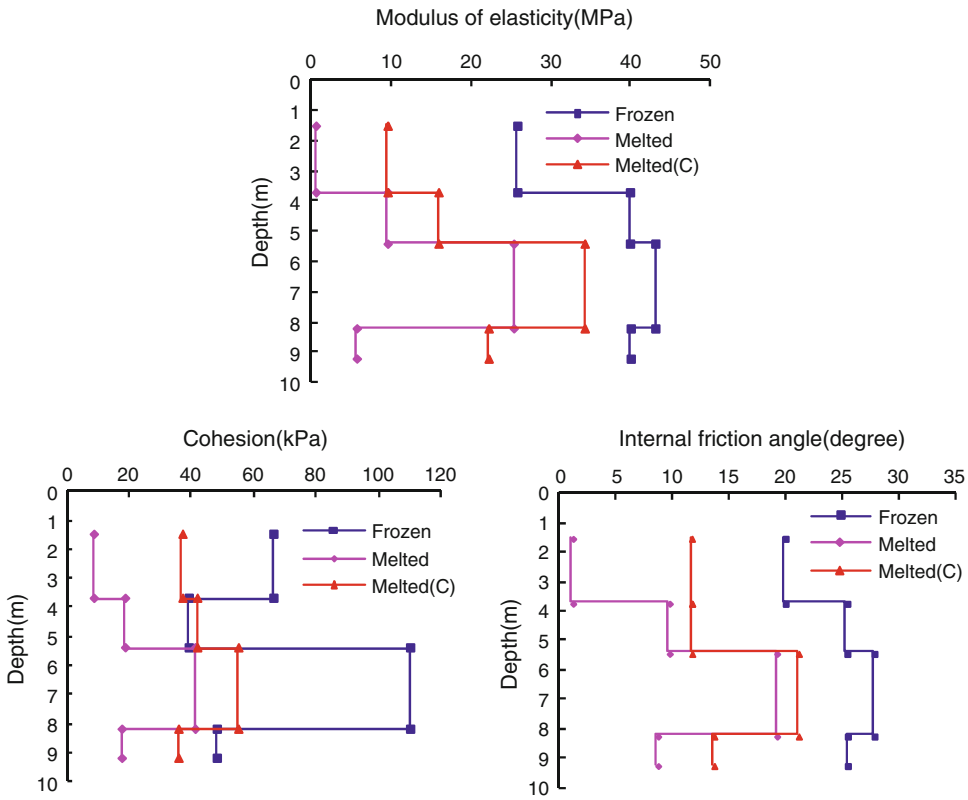

Fig. 46.2 Curve of permafrost mechanical indexes change with temperature

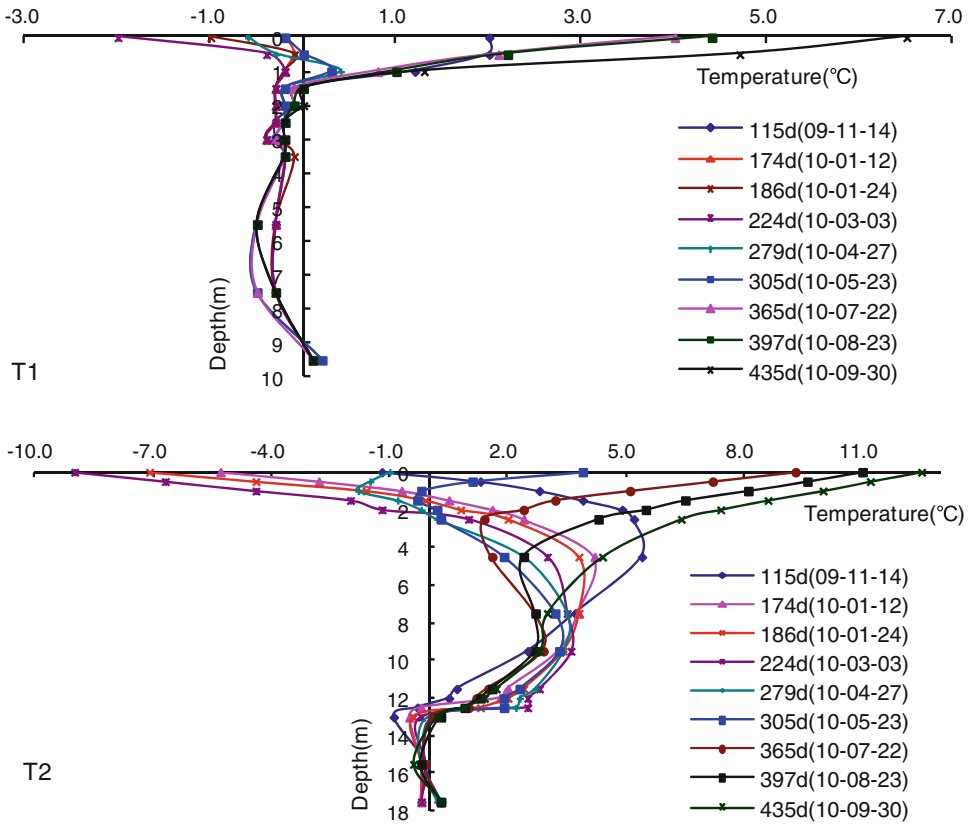

Fig. 46.3 Curve of ground temperature change with temperature

115 d later, the widen subgrade filling height was 7.4 m, temperature sensors were buried in the T1 and T2 position (see Fig. 46.1), and began to monitor the permafrost degrading condition. Curve of T1 and T2 ground temperature changes with time as shown in Fig. 46.3, curve of ZK2 and ZK3 vertical displacement changes with time as shown in Fig. 46.4.

The Fig. 46.3 shows, the temperature of regional island permafrost is 0−0.6 °C, belongs to high temperature permafrost, vulnerable to degrade. In the T1 position, due to no filling, the permafrost hasn't occurred degrading. In the T2 position, when buried the temperature sensors, namely on the 115th day, upper limit of the permafrost had declined 0.8 m, and lower limit hadn't raised; on the 186th day, upper limit of the permafrost had declined 1.4 m, and lower hadn't raised; on the 305th day, upper limit of the permafrost had declined 2.7 m, and lower limit had raised 0.7 m; the upper and lower limit of permafrost hasn't occurred obvious change in the following days. The degrading period of permafrost is during the regional freezing period, subgrade filling blocks soil releasing heat, results in permafrost degrading; the permafrost degrades from two sides to middle, the range of upper limit declined is significantly bigger than the lower limit raised.

The Fig. 46.4 shows, vertical displacement in every position has an obvious accelerating process with subgrade filling, namely the vertical displacement increases with the subgrade load increasing, under the same load, closer to upper, the corresponding displacement is bigger. After the first stage subgrade filling, foundation permafrost gradually degraded, strength of the foundation decreased, vertical displacement reached stability after a longer period; but after the second stage subgrade filling, foundation permafrost was stable, vertical displacement reached stability after a relatively shorter period. The vertical deformation of the new subgrade shoulder (ZK2) is significantly bigger than the old subgrade left shoulder (ZK3). Under the function of new subgrade loading and permafrost thawing settlement, the maximum vertical displacement of new subgrade foundation and old subgrade respectively reach 40.2 and 18.6 cm.

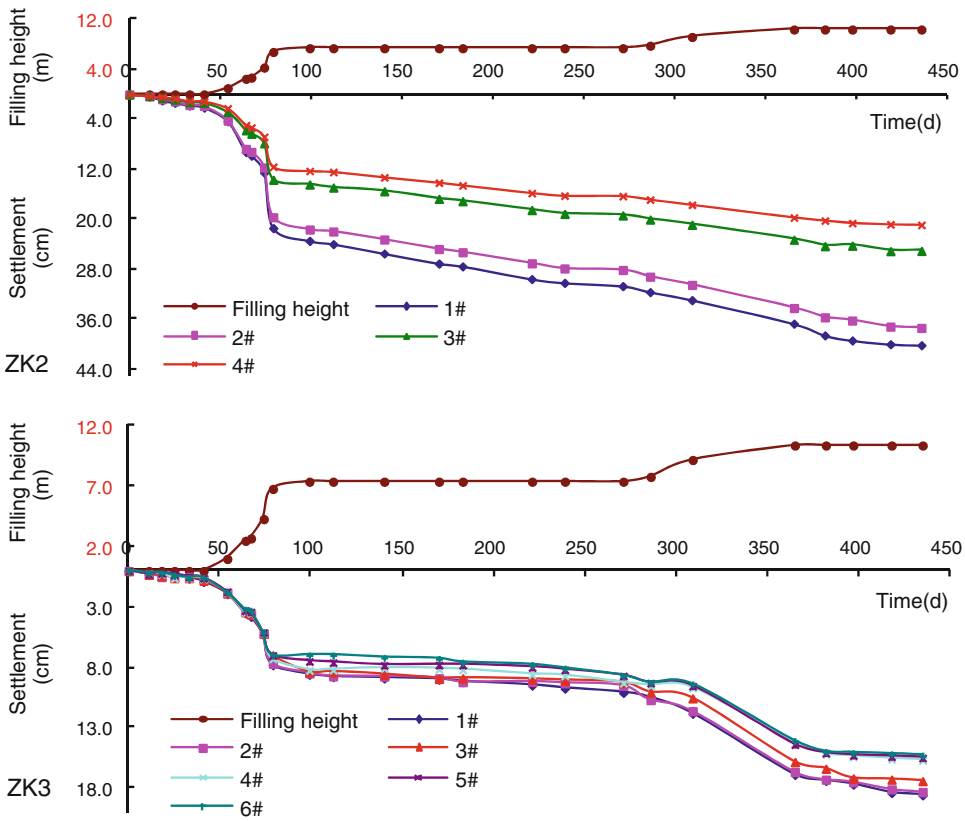

Fig. 46.4 Curve of vertical displacement change with temperature

46.6 Conclusions

The mechanical indexes of soil decrease significantly with frozen soil melted, and water content greater, void ratio higher, the descendant ranges are larger.

The temperature of regional island permafrost is 0–0.6 °C, belongs to high temperature permafrost, is vulnerable to degrade. The permafrost under the new subgrade degrades from two sides to middle in the frozen period due to the thermal resistance effect of subgrade filling, the upper limit has declined 2.7 m and lower limit has raised 0.7 m.

The vertical displacement of subgrade and foundation has obvious accelerating process with the new subgrade filling. The time of vertical displacement reaches a steady state is closely related with the stability of foundation permafrost. Under the function of new subgrade loading and permafrost thawing settlement, the maximum vertical displacement of new subgrade foundation and old subgrade respectively reach 40.2 and 18.6 cm.

Acknowledgements This work was financially supported by the key science and technology project of Heilongjiang Communications Department "Study on Subgrade Stability Controlling Technology of Expressway Expansion Project Permafrost Melt and Landslides Sections" (2011318223630).

References

Li SX, Wu ZW (1997) The change of thaw bulb under asphalt pavement in the region of permafrost on the Qinghai-Tibet Plateau. J Glaciol Geocryol 19(2):133–140

Meng FS, Liu JP, Liu YZ (2001) Design principles and frost damage characteristics of frozen soil roadbed along the Heihe-Bei'an highway. J Glaciol Geocryol 23(3):307–311

Qi CQ, Wu QB, Shi B et al (2005) Stochastic finite element analysis for the temperature field of frozen soil roadbed of Qinhai-Tibet railway. J Eng Geol 13(3):330–335

Wang SL, Zhao L, Li SX et al (2001) Study on thermal balance of asphalt pavement and roadbed stability in permafrost regions of the Qinghai-Tibet highway. J Glaciol Geocryol 23(2):111–118

Wu QB, Zhu YL, Shi B (2001) Study of frozen soil environment relating to engineering activities. J Glaciol Geocryol 23(2): 200–207

Wu JM, Wang SJ, Zhang JZ (2005) The highway engineering on permafrost regions. China Communication Press, Beijing

Wu ZJ, Zhang LX, Ma W et al (2007) Influence of soil's cryogenic course on deformation of roadbed in permafrost region of Qinghai-Tibet railway. Rock Soil Mech 28(7):1477–1483

Zhou YW, Guo DX, Qiu GQ et al (2000) Permafrost in China. Science Press, Beijing

The Bellecombes Rock Glacier Case Study, 2 Alpes, France

47

Héloïse Cadet and Ombeline Brenguier

Abstract

Permafrost is soil or rock that is frozen for at least two successive years. Permafrost is composed by an active layer that thaws during the summer and freezes again during the winter. Temperature changes (2 °C increase of minimum temperatures during the 20th century in the Alps) imply changes in mechanical properties of permafrost that reach a disequilibrium point, enhancing gravitational hazards. As these property changes cannot be detected from outside, the risk assessment is not straightforward. In order to detect and anticipate this increasing hazard, geophysical approach was performed to investigate the permafrost body of the Bellecombes rock glacier. Rock glacier is a kind of permafrost composed of rock debris and ice. The Bellecombes site is located in the French Alps, at the "2 Alpes" winter ski resort. The rock glacier affects a ski lift. This work aims at finding methodology to determine (i) the thickness of the permafrost and the bedrock depth which is important to resolve geotechnical problems; and (ii) the thickness of the active layer which is highly instable. In this paper, investigations were composed of borehole, electrical and seismic tomography, ambient noise measurements and georadar measurements. Results show that geophysical investigations improve knowledge of internal structure of rock glacier when they are combined with preliminary geomorphological study and boreholes.

Keywords

Permafrost • Geophysical survey • Gravitational hazard • Climate change

47.1 Introduction

Permafrost is a thermic definition. It concerns soil or rock that is frozen for at least two successive years (PermaNet, synthesis report). In France, permafrost covers 4–5 % of the Alps surface and may exist above 2,300 m a.s.l.. This is shown by the estimated likelihood of permafrost occurrence for the entire Alps (Fig. 47.1).

A permafrost area generally contains a superficial active layer that thaws during the summer and freezes again during the winter. Permafrost includes steep rock cliffs as well as soft soils, with a very different ice content. Rock glacier is one of the different kinds of permafrost occurrence. Rock glaciers are composed of a mixture of ice and rock debris. This study is focalized on the Bellecombes rock glacier, located in the French Alps, at the *2 Alpes* winter ski resort.

In the Alps, global warming has been characterized by a 2 °C increase of mini-mum temperatures during the 20th century. Temperature changes imply changes in mechanical properties of glacier and permafrost that reach a disequilibrium point. Indeed, the ice contained in the permafrost can either melt, creating a loose of cohesion, or reach a critical temperature around 0 °C that increased drastically the plasticity of the material. These pronounced disequilibria increase gravitational hazards to infrastructure and individuals in Alpine environments. In comparison to the melting of the glaciers, the degradation of permafrost can

H. Cadet (✉) · O. Brenguier
ADRGT, 2 rue de la Condamine, BP 17, 38610 Gières, France
e-mail: h.cadet@adrgt.org

G. Lollino et al. (eds.), *Engineering Geology for Society and Territory – Volume 1*,
DOI: 10.1007/978-3-319-09300-0_47,

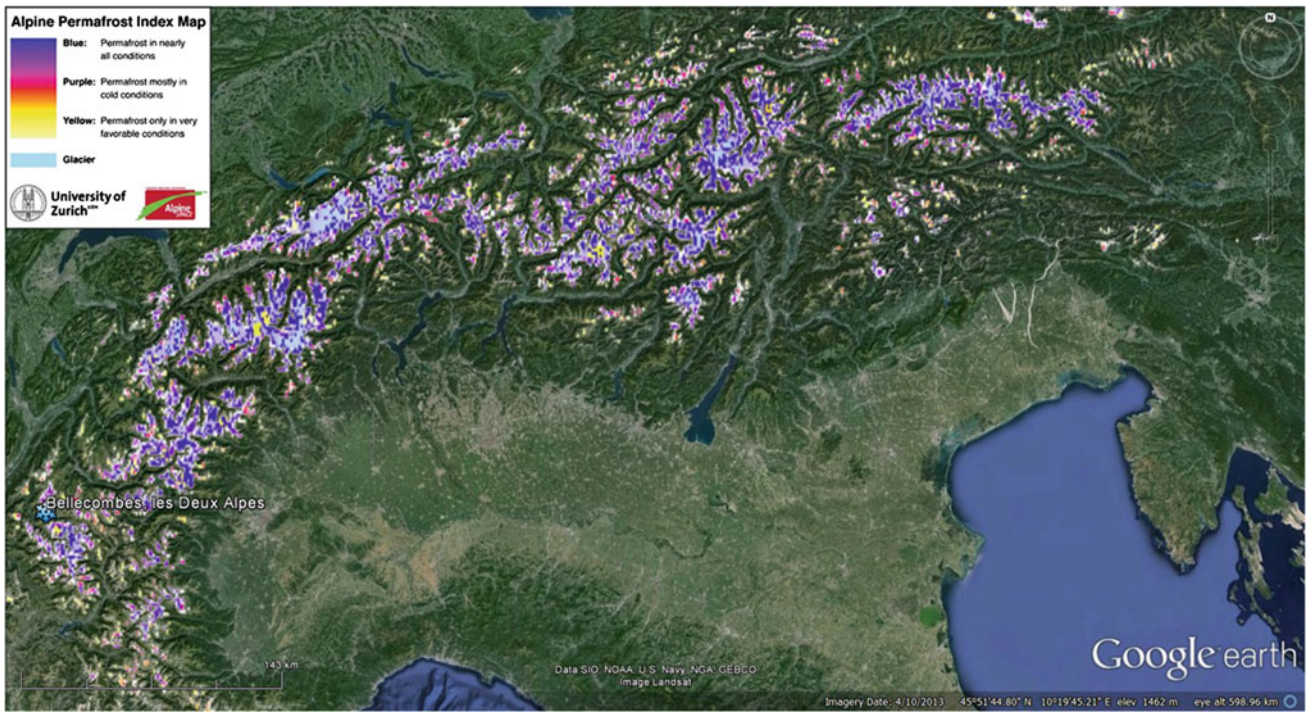

Fig. 47.1 Alpine Permafrost Index Map (Boeckli et al. 2011, APIM) showing a potential permafrost distribution modeling. South-west the Bellecombes rock glacier

hardly be detected from outside. Therefore, the permafrost distribution and the estimation of climate change effects to permafrost are subject to greater uncertainties. The active layer is particularly affected by these disequilibria and thus should be well mapped for a specific study. Geophysical measurements can be helpful for providing an estimation of permafrost extension in a specific area. Some of these methods have already been tested in permafrost, such as electrical surveys. Georadar and ambient noise measurements have never been tested in rock glacier area. A geophysical survey—including electrical, seismic, ambient noise and georadar methods—was performed to investigate the permafrost body of the Bellecombes rock glacier.

This work has two objectives. The first one is to estimate the permafrost thickness mainly to resolve geotechnical problems. The second one is to build-up a methodology of survey to determine the thickness of the active layer which is highly instable in case of high precipitations.

47.2 Site and Survey Descriptions

47.2.1 Site Description

The Bellecombes rock glacier is at the east part of the *2 Alpes* ski resort, around 2,700 m high. In Fig. 47.2 the rock glacier morphology is visible, especially in the north of profile P2. The rock glacier movements affect the arrival station of a chairlift (Fig. 47.2). Here, the effects of climate changes on the common practice are underlined. Indeed, building such an infrastructure on rock glacier has not been an issue since few years. Now, there is an evident challenge to solve this issue.

47.2.2 Survey Description and Geophysical Methodology

Since 2007, five geophysical campaigns were performed along four main profiles from P1 to P4, and five secondary profiles from P5 to P9 (Fig. 47.2). Two destructives borehole were performed inside the rock glacier on P3 profile (SD1 and SD2, Fig. 47.2).

47.2.2.1 Electrical Tomography PE

In 2007 and 2009 profiles P1–P4 were acquired. In 2010 a monitoring (5 measurements) was performed along P4 to evaluate the snowmelt influence.

Electrical tomography provides, after an inversion process, models of the distribution of the ground's electrical resistivity directly under the survey line. The final deduced solution must not be considered as unique. In the following, all profiles were performed with Wenner array.

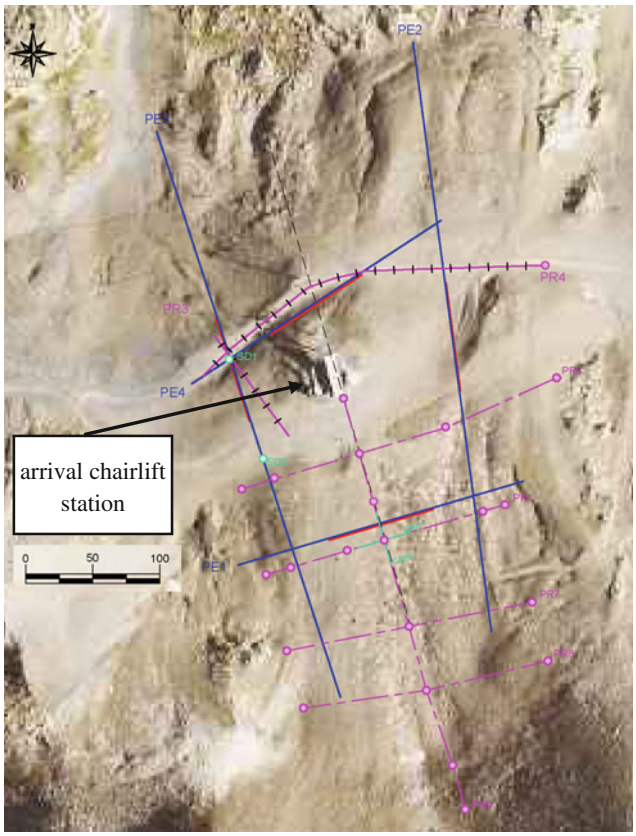

Fig. 47.2 Bellecombes rock glacier, arrival station and geophysical measurements

47.2.2.2 Horizontal Over Vertical, H/V, Method

Noise measurements for H/V analysis were done along profiles P3 and 4.

The H/V method computes the spectral ratio between the horizontal and vertical components of the seismic noise recorded simultaneously at a given location with a 3D seismometer placed at the ground surface. Nogoshi and Igarashi (1971) first proposed the use of the H/V method as a tool for the estimate of the seismic response of the surface layers. In the case of a stratified soil profile composed of a soft layer on top of a stiff bedrock, the amplified frequency f0 may be estimated using the equation f0 = Vs/4Hs (Haskell 1960), where Hs is the thickness and Vs the shear wave velocity of the topmost layer, respectively, provided that the S-wave contrast is sufficiently large (Bonnefoy-Claudet 2004). As outlined by the equation linking f0 to Hs, knowing the shear wave velocity Vs of the upper layer is fundamental to deduce the thickness of this layer.

47.2.2.3 Seismic Surveys

Compressional waves (Vp) and shear waves (Vs) velocities were both measured. Vp was estimated on P1, 2, 3 and 4 profiles. Vs was estimated only on P4 but with two different methods: refraction method using a shear source and surface waves method including an inversion process (using either active or passive sources). To reduce the number of good fitter models of the inversion results, the H/V resonance frequency of the central station was added as an additional constrain during the inversion process.

47.2.2.4 Ground Penetrating Radar, GPR

GPR profiles were developed along PR1, PR4, PR6, PR7, PR8 and PR9 during winter time.

GPR is a geophysical method that uses electromagnetic waves to image the subsurface. The principles involved are similar to reflection seismology. Common midpoint (CMP) determined wave velocity in depth at one point whereas reflection profiles produce 2D image of subsurface. GPR is well adapted to study permafrost because the ice conductivity is very low.

47.3 Data Analysis and Results

47.3.1 Destructive Boreholes

The two boreholes reach the substratum composed by marly limestone through rock glacier. They show the active layer limit at almost 2.2 m deep and the substratum depth is about 9.6 m. The permafrost body thickness is about 7.4 m. On SD1 we found compact ice between 4.8 and 9.6 m.

47.3.2 Active Seismic

The inversion of the dispersion curve of surface wave velocity acquired on PS4 shows S-wave velocity about 200 m/s in the topmost layer, with a well-defined thickness between 2 and 3 m. These results are consistent with S-wave. However the S-wave velocity in the second layer is difficult to resolve. The P-waves show the interface of the active layer with the rock glacier (black dot points in Fig. 47.3).

47.3.3 H/V Results

On profile P3 and P4, a clearly distinguishable dominant frequency can be easily picked on most point measurements. This dominant frequency varies smoothly from 12 to 30 Hz (Fig. 47.3). The thickness (from 1.6 to 4 m) was computed using the formula Hs = Vs/4fo with a constant shear velocity Vs = 200 m/s. It is consistent with the results of other techniques. This method allows following the variations of the depth of the active layer along the profile.

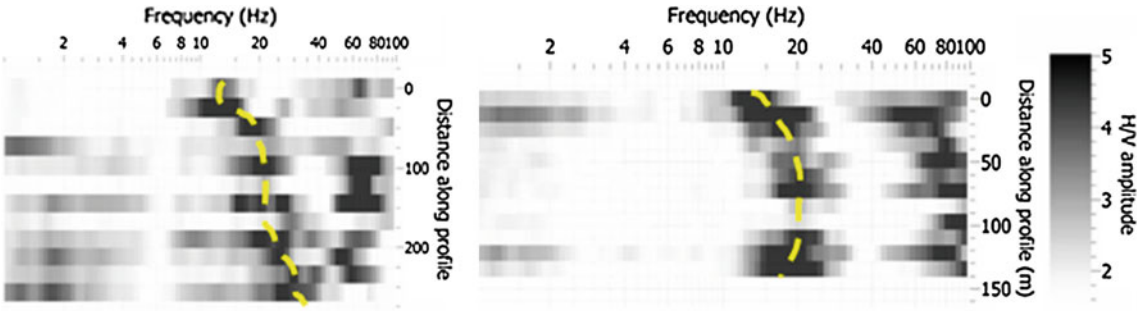

Fig. 47.3 H/V curves of seismic noise obtained along profiles P3 and P4

47.3.4 Electric Tomography

Only PE3 and PE4 respectively transversally and longitudinally to the rock glacier, were presented in this paper (Fig. 47.4). PE4 show clearly the presence of ice (resistivity > 32 KΩ) on each side of the substratum (resistivity $<$ 4 KΩ). Ice seams to flow on each side. Thickness could not be estimated with this profile due to very high resistivity and consequently numerous of equivalent models. This problem is similar on profile PE3 which seems to image an ice thickness of 30–55 m although boreholes detected the substratum at 9.6 m. Moreover no significant differences were found on inversion of 2007 and 2009 on the four profiles. Temperature and water content variations make difficult to monitor the evolution of the permafrost with this technique.

47.3.5 Georadar

GPR profiles acquired during winter have a deep investigation larger than in summer probably due to higher liquid water content in summer. PR3 and PR4 profiles show the ice roof nearby 10 m which is consistent with boreholes. On PR9 the contact between mixture of ice and debris and pure ice is well imaged at around 3–5 m deep (Fig. 47.5). Substratum is well identified at 22 m deep. This is consistent with profiles PR7 and PR8.

47.4 Discussions and Conclusion

To model the melting of permafrost due to global warming, estimation of the thickness of the glaciated area is essential. To forecast and prevent catastrophic event, it is also

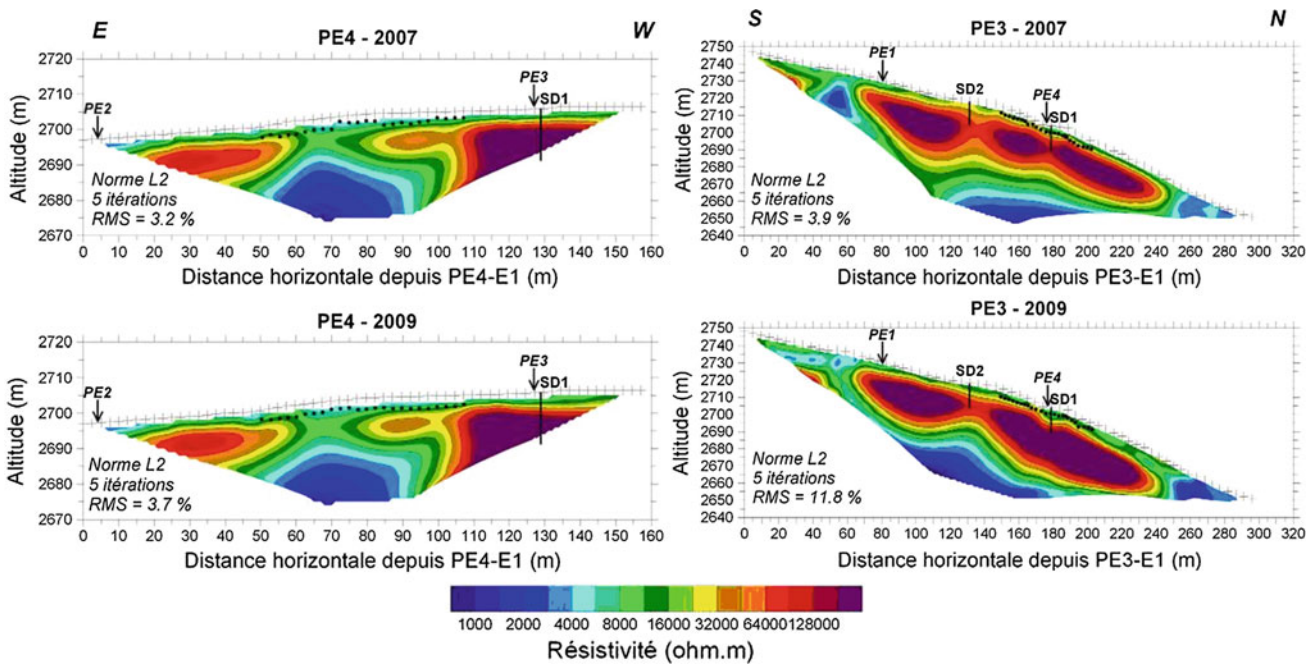

Fig. 47.4 Electrical tomography images PE4 and PE3 in 2007 and 2009

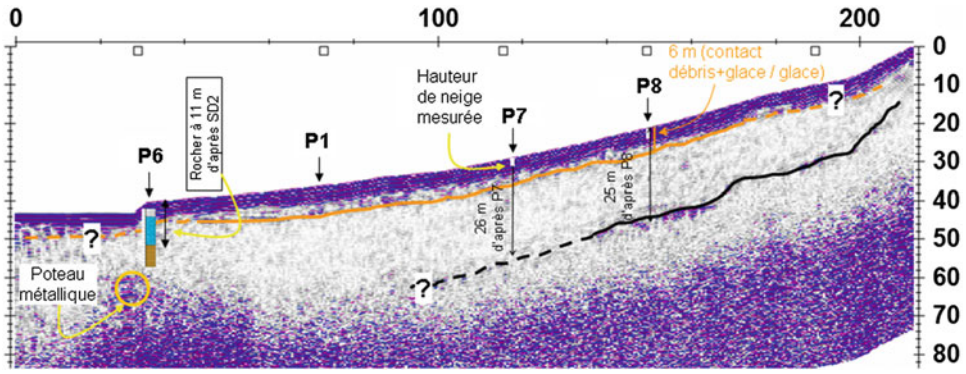

Fig. 47.5 GPR along profile 9

important to estimate thickness of the active layer. Actually this layer is the less stable in case of very bad weather.

This active layer is well characterized by H/V method combined to local Vs estimation. Vs could be determined by seismic refraction or by surface wave velocity inversion. Because of its low-cost and fast deployment, H/V method is very useful to characterize active layer thickness unlike classical seismic refraction method. GPR characterizes also well the active layer.

Electrical tomography detects very well the presence of ice but could not estimate permafrost depth due to equivalence principle. The permafrost thickness is difficult to image with electrical tomography or seismic methods whereas GPR with 100 MHz antenna shows clearly permafrost body.

Finally boreholes are essential to calibrate geophysical results. Combined with preliminary geomorphological study and boreholes, geophysical investigations improve knowledge of internal structure of permafrost. These studies enhance understanding of permafrost evolution and modelling of their degradation.

The methodology to characterize such rock glacier is:

1. Geomorphological study to determine the potential surface limits of the rock glacier
2. Electrical and seismic profiles to confirm and precise the ice occurrence
3. Temperature measurements to cross—check the results with steps 1 and 2
4. Boreholes to fix the rock glacier thickness locally
5. GPR investigation to define the thickness of the rock glacier globally

This study was financed by the MAIF project "Analyse des risques induits par la dégradation du permafrost alpin", Permanet, the PARN 2010 project and the 2 Alpes ski resort. All these studies enhance understanding of permafrost characterization, evolution and modeling of its degradation.

References

Alpine Permafrost Index Map (APIM) http://www.geo.uzh.ch/microsite/cryodata/PF_map_explanation.html

Boeckli L, Brenning A, Gruber S, Noetzli J (2011) A statistical permafrost distribution model for the European Alps. Cryosphere Discuss 5:1419–1459

Bonnefoy-Claudet S (2004) Nature du bruit de fond sismique: implications pour les études des effets de site. PhD thesis, Grenoble University, France, 241 p

Haskell NA (1960) Crustal reflection of plane SH waves. J Geophys. Res 65:4147–4150

Nogoshi M, Igarashi T (1971) On the amplitude characteristics of microtremor (part 2). J Seismol Soc Jpn 24:26–40

PermaNET Permafrost Monitoring Network, Permafrost Long-term Monitoring Network, synthesis report. http://www.permanet-alpinespace.eu/archive/pdf/PermaNETsynthesisreport.pdf

Permafrost-Related Mass Movements: Implications from a Rock Slide at the Kitzsteinhorn, Austria

48

Markus Keuschnig, Ingo Hartmeyer, Giorgio Höfer-Öllinger, Andreas Schober, Michael Krautblatter and Lothar Schrott

Abstract

Rock instability in high mountain areas poses an important risk for man and infrastructure. At 3 p.m. on 18 August 2012 a rock slide event was documented at the Kitzsteinhorn, Austria. The release zone was detected on a north-exposed rock face below the cable car summit station (3.029 m). Analysis of terrestrial laser scanning (TLS) data delivered an accurate identification of the release zone yielding a rock fall volume of approximately 500 m^3. Cubic Blocks with lengths of up to 4 m and block masses of up to 125 t were released during the event. The failure plane is located in a depth of approximately 3–4 m and runs parallel to the former rock surface (mean inclination 47°). Comparison with borehole data located less than 50 m from the release zone shows that failure plane depth is consistent with active layer depth. The event documentation is supplemented with observations of rock and air temperature, data on precipitation and snow depth, electrical resistivity tomography data, observed active layer depth and geological/geotechnical background data. The comprehensive ambient data suggests the influence of high temperatures and water availability for the triggering of the rock slide.

Keywords

Rock permafrost • Rock slide • Rock fall • Monitoring

48.1 Introduction

Numerous rock fall events in the European Alps suggest an increasing occurrence of mass movements due to rising temperatures. In recent years particularly during extensive hot periods large numbers of rock fall events have been reported (e.g., hot summers of 2003 and 2005). However, in most cases reconstruction of triggering mechanisms is problematic due to a lack of information at and before the event. Preparatory factors of subsurface (e.g., geological setting, permafrost conditions), surface (e.g., topography, snow cover) and atmospheric conditions (e.g., climatic and meteorological conditions) and their complex relationships must be taken into account.

The presented activities have been carried out within the research project MOREXPERT ('Developing a Monitoring Expert System for Hazardous Rock Walls') funded by Competence Centers for Excellent Technologies (COMET). MOREXPERT, which was started in September 2010, has

M. Keuschnig (✉) · I. Hartmeyer
alpS—Centre for Climate Change Adaptation, Grabenweg 68, 6020 Innsbruck, Austria
e-mail: markus.keuschnig@sbg.ac.at

I. Hartmeyer
e-mail: ingo.hartmeyer@sbg.ac.at

M. Keuschnig · I. Hartmeyer
University of Salzburg, Hellbrunner Strasse 34, 5020 Salzburg, Austria

G. Höfer-Öllinger · A. Schober
Geoconsult, Hölzlstrasse 5, 5071 Wals bei Salzburg, Austria

M. Keuschnig · M. Krautblatter
Technical University of Munich, Arcisstrasse 21, 80333 Munich, Germany

L. Schrott
University of Bonn, Meckenheimer Allee 166, 53115 Bonn, Germany

G. Lollino et al. (eds.), *Engineering Geology for Society and Territory – Volume 1*,
DOI: 10.1007/978-3-319-09300-0_48,

initiated a new long-term monitoring site focusing on permafrost and rock fall interaction in steep bedrock in the Austrian Alps (Keuschnig et al. 2011; Hartmeyer et al. 2012).

48.2 Study Site

The study site is located at the Kitzsteinhorn (3.203 m, Hohe Tauern Range, Austria), a particularly interesting site for the investigation of glacier retreat and potential permafrost degradation and their respective consequences for the stability of alpine rock faces. The Kitzsteinhorn is constituted of rock of the Bündner schist formation and belongs to the Glockner Nappe, specifically the Glockner Facies, which consists of calcareous mica schist, prasinite, amphibolite, phyllite and serpentinite (Schober et al. 2012). The affected slope is a north-facing back wall of a glacial cirque with a mean inclination of 47°. It extends from the cable car summit station (3.029 m) down to the upper margin of the Schmiedingerkees glacier (2.950 m). The rock face is underlain by permafrost, over the last decades it has been affected by intense glacier retreat at the base and the complete loss of its ice cover.

48.3 Localization and Quantification of the Rock Slide Event

The blockslide occurred on 18 August 2012 at 3 p.m. Touristic visitors and employees, who were present at the cable car summit station at the time of the event, registered the blockslide acoustically and/or visually. Therefore, the exact time and location of the event is known.

The release zone is situated approximately 50 m below the summit station (3.029 m, see Fig. 48.1) at the base of the rock slope, directly above the glacier. At the failure plane ice was visible immediately after the event. The release zone and blockslide volume of 500 m^3 was quantified with TLS. Cubic blocks with lengths of up to 4 m and block volumes of up to 125 t were released during the event. The failure plane is located in a depth of approximately 3–4 m and runs parallel to the terrain surface. During the event several of these joint-bordered rock bodies were detached resulting in a blockslide. After detachment the blocks slid over the glacier surface for more than 200 m. The entire material was deposited on the glacier surface allowing easy identification of movement path and location of deposition.

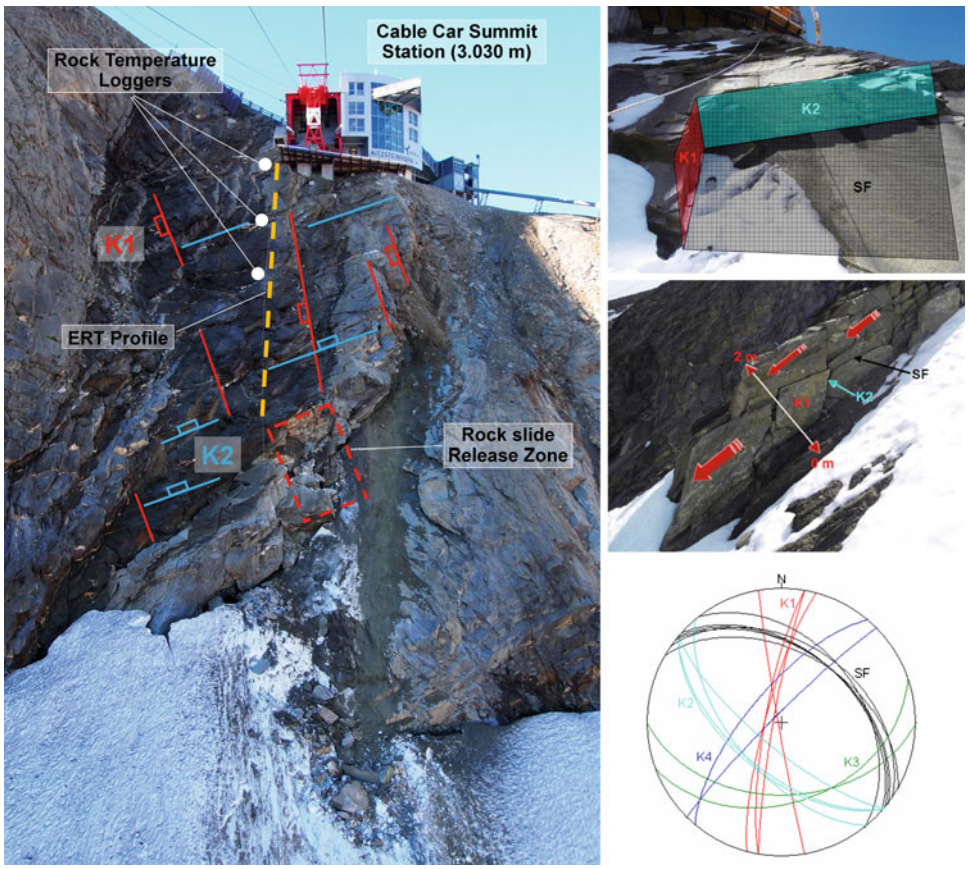

Fig. 48.1 On the *left* side: frontal view of the affected rock face with position of permanently installed monitoring instruments (ERT, rock temperature loggers). On the *left* and *right* side: geotechnical setting and orientation of discontinuities

48.4 Disposition and Type of Movement

The north face has an inclination of 23–67° and a mean value of 47°. The rock mass (calcareous mica schist) at the affected slope shows distinct schistosity (SF). The schistosity dips parallel to the slope, flat to medium steeply in direction NNE-NE and acts as an open interface structure. In addition to the schistosity, the joint sets K1 and K2 represent the main interface sets. K1 dips steeply to W and K2 dips medium-steeply to steeply to SW. The joint sets K3 and K4 are less frequent. The former dips medium-steeply to flat to S–SSE, the latter steeply to NW. K1 and K2 are oriented approximately orthogonal to the schistosity and constitute cubic to rhomboidal rock bodies (see Fig. 48.1). During the event several of these joint-bordered rock bodies were detached resulting in a blockslide.

48.5 Destabilizing Factors

48.5.1 Preparatory Factors

Rising temperatures have led to a substantial glacier retreat that has been particularly pronounced since the 1980s. Due to intense ablation the surface of the Schmiedingerkees glacier has been lowered by approximately 30 m over the last 40 years (see Fig. 48.2). Glacial debuttressing represents a major long-term destabilizing factor for the discussed rock face. In combination with the loss of the ice cover these processes have led to the exposure of oversteepened rock to atmospheric influences and intensified mechanical weathering. Geological discontinuities have become subject to a different thermal regime which includes the development of an active layer and convective heat transport in unfrozen clefts.

Despite the close proximity of the release zone to the upper glacier margin and the seasonal minimum of the snow height at the glacier at the time of the event, the triggering of the event cannot be explained by glacial debuttressing alone: The initial fracture seems to have occurred clearly above the current glacier surface (see Fig. 48.3).

48.5.2 Preparatory Factors

According to Krautblatter et al. (2013) the destabilization mechanism can be discussed using driving and resisting forces. Rock temperature (Davies et al. 2001) and the availability of water are important for slope stability in permafrost-affected rock. For example subsurface temperature variations affect ice pressures (driving force) and the strength of ice and rock (resisting force).

Meteorological data from a weather station (see) located less than 500 m from the release zone shows that air temperatures had not fallen below 0 °C for more than 2 weeks (1 August 2012–18 August 2012) prior to the event (mean 5.5 °C). Rock temperature measurements (sensor depth 0.8 m) which were performed less than 50 m from the release zone also delivered values well above 0 °C for the same time period (mean 4.5 °C, see Fig. 48.4).

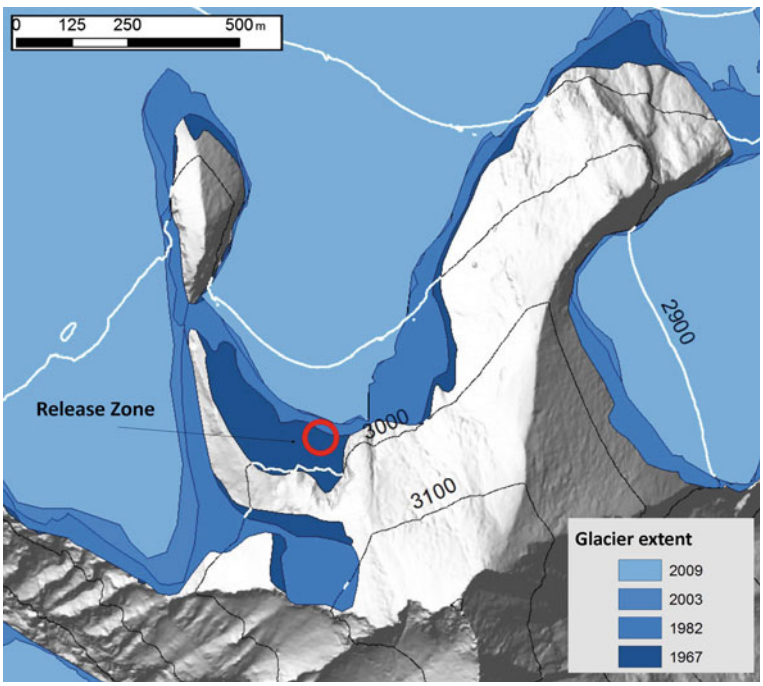

Fig. 48.2 Decreasing glacier extent and ice cover in the area of the release zone during the last decades

Fig. 48.3 Detachment of the blockslide: 18 August 2011 (*left*)—intact rock, 17 August 2012—crack visible in the tensile zone (*middle*), 19 August 2012—situation after the release (*right*)

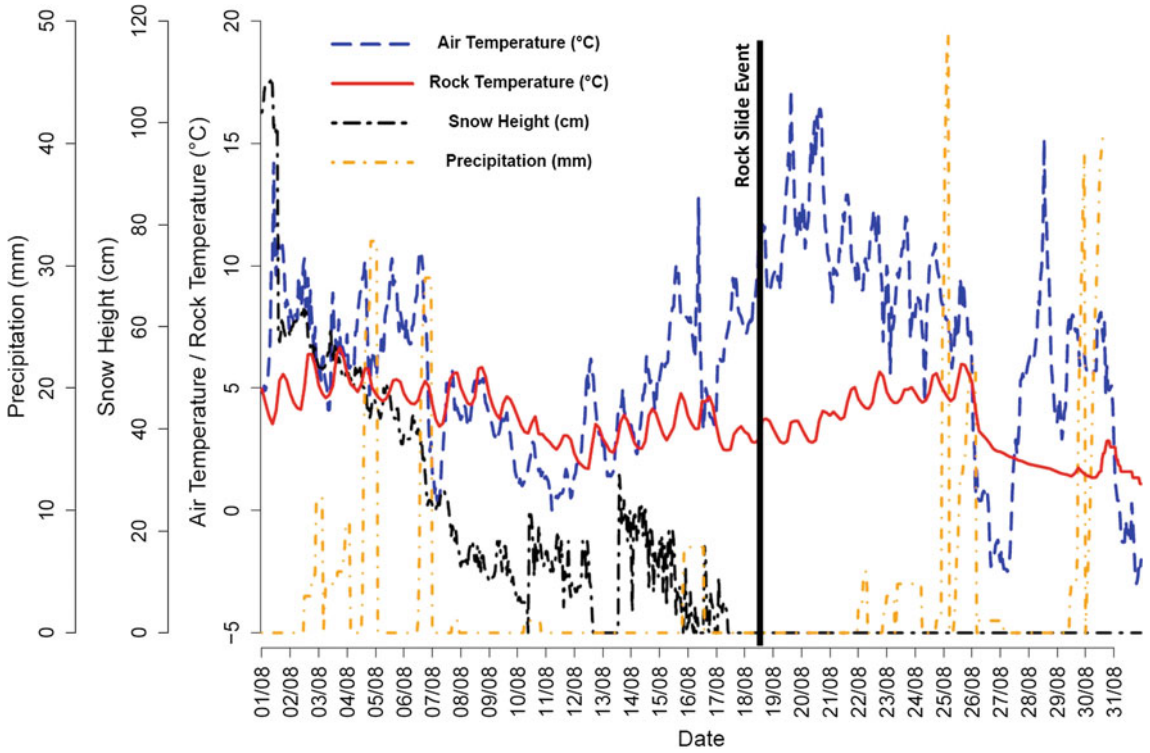

Fig. 48.4 Trends of air temperature, near-surface rock temperature, precipitation and snow height for August 2012. The rock slide event occurred on 18 August at 3 p.m

Comparison with visible ice in boreholes located less than 50 m from the release zone shows that failure plane depth is consistent with active layer depth (approx. 3 m).

Data from a permanently installed Electrical Resistivity Tomography (ERT) profile installed in close proximity to the release zone indicate an increase of electrical conductivity less than 30 m from the release zone (see). The increased conductivity could be the result of higher temperatures and/or increased availability of rain and melt water. Near surface rock temperatures show no

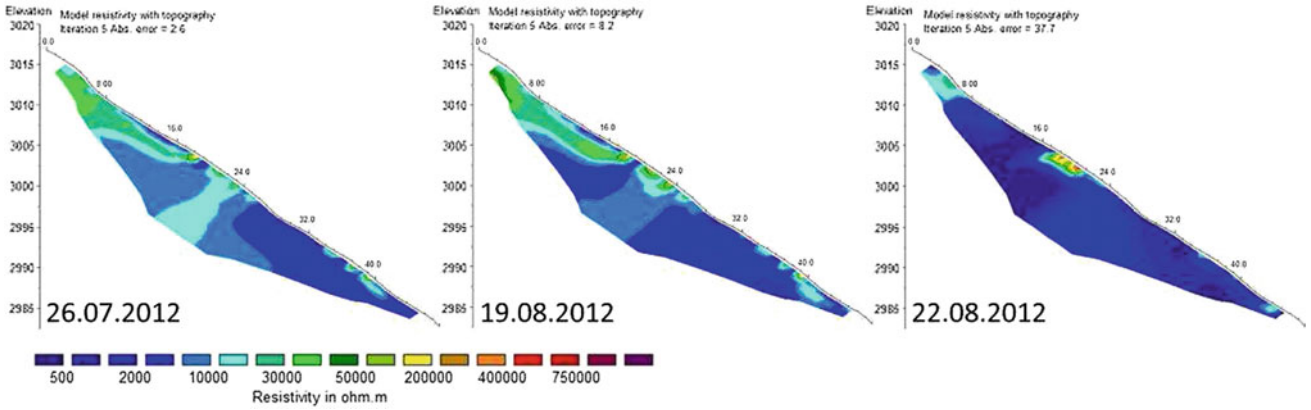

Fig. 48.5 ERT data; decreasing resistivity indicates higher temperatures and/or higher water content

positive or negative temperature trend prior to the event (see Fig. 48.4). Thus, decreasing resistivity has to correlate with an increased availability of (cleft) water (Fig. 48.5).

48.6 Conclusion

High air temperatures led to intensified snow and ice melt and to an increase of active layer thickness (see Fig. 48.4). After the event ice was visible in parts of the release zone. Combined analysis of rock temperature and ERT data is indicative of an increase of (cleft) water availability during the period leading up to the rock slide event. It can be concluded that increased water pressures in combination with decreased rock and ice strength caused by warming were the main trigger factors.

Acknowledgments The research project MOREXPERT ('Monitoring Expert System for Hazardous Rock Walls') is supported by numerous companies and scientific partners. The authors want to particularly thank Gletscherbahnen Kaprun AG, Geoconsult ZT GmbH, Geodata GmbH, Geolog 2000 Fuss/Hepp GdbR, University of Salzburg, University of Bonn, Technische Universität München (TUM), Z_GIS—Centre for Geoinformatics and the Salzburg Research GmbH for financial, material and intellectual support.

References

Davies MCR, Hamza O, Harris C (2001) The Effect of rise in mean annual temperature on the stability of rock slopes containing ice-filled discontinuities. Permafrost Periglac Process 12:137–144

Hartmeyer I, Keuschnig M, Schrott L (2012) Long-term monitoring of permafrost-affected rock faces—a scale-oriented approach for the investigation of ground thermal conditions in alpine terrain, Kitzsteinhorn, Austria. Austrian J Earth Sci 105/2: 128–139

Keuschnig M, Hartmeyer I, Otto J-C, Schrott L (2011) A new permafrost and mass movement monitoring test site in the Eastern Alps—concept and first results of the MOREXPERT project. In: Borsdorf A, Stötter J, Veulliet E (eds) Managing Alpine future II—inspire and drive sustainable mountain regions. Proceedings of the Innsbruck Conference, 21–23 November 2011. (=IGF-Forschungsberichte 4). Verlag der Österreichischen Akademie der Wissenschaften: Wien

Krautblatter M, Funk D, Günzel FK (2013) Why permafrost rocks become unstable: a rock-ice-mechanical model in time and space. Earth Surf Proc Land 38:876–887. doi: 10.1002/esp.3374

Schober A, Bannwart C, Keuschnig M (2012) Rockfall modelling in high alpine terrain—validation and limitations. Geomech Tunn 5(4):368–378

Landslide Mechanism and Shallow Soil Moisture of Soil Cut Slopes in Seasonally Frozen Regions

49

Ying Guo, Wei Shan, Chengcheng Zhang and Hua Jiang

Abstract

In seasonally frozen regions, landslides caused by repeated freeze-thaw cycles often occur on soil cut slopes during spring. In this study, an area along the highway from Tongjiang to Harbin in China was studied to understand landslide mechanisms. This study was done using two methods: one was regular monitoring of soil temperature and moisture by sensors buried in the slope, and the other was comprehensive analysis of the monitored data combination with soil physics theory and heat transfer theory. The results show that when air temperature values are positive, soil moisture is mainly affected by precipitation and evaporation. When air temperature values are negative, soil water migrates and accumulates in the frozen area and results in uneven moisture distribution. During the spring, the frozen water that changes into thaw water when the soil temperature rises to above 0 °C is prevented from infiltrating into the underlying layers by the frozen layer underneath, and its quantity rapidly rises in the layer above the frozen layer. The soil here reaches a saturated or over-saturated state, following which, the effective stress within the slope is reduced and, under gravity, part or the entire shallow slope slides down the "water saturation layer." After data analysis, this landslide process was divided into several temperature dependent stages, and soil pore water migration was also studied in the negative temperature stage. Our results can provide a criterion for early warning and forecast of landslides.

Keywords

Highway cut slope • Seasonal frozen soil • Temperature • Water content

49.1 Introduction

In the seasonal frozen regions of the Heilongjiang Province in Northeast China, soil cut slopes along the highway often experience instability, which significantly affects the safety of highway operations.

Descriptions of permafrost slopes have been made as early as 1897 (Tarr 1897). Soviet scholar Emelyanova (1986) described in detail the phenomena of mudflows on thawing slopes. Subsequently, many countries, including Russia, the United States, Canada, and Norway have conducted research into frozen slopes. In China, over nearly four decades and with the construction of the Qinghai-Tibet Highway, Qinghai-Tibet Railway, Western Route of the South to North Water Diversion Project, and the western development infrastructure projects, as well as other projects, studies into frozen soil engineering properties have increased. Zhou Youwu in 1980 described thaw slumping in periglacial landforms, Wang Wenbao in 1989 studied embankment slope slumping and its remediation, Wang Shaoling in 1990 studied thaw slumping in frozen soil slopes, Zhang Changqi and Zhu Linnan in 1993 studied slope excavation and thawing stability, Guo Dongxin in 1993 studied the terrace of a thawing mud stream. These studies provide useful results and practical experience in

Y. Guo (✉) · W. Shan · C. Zhang · H. Jiang
Institute of Cold Regions Science and Engineering, Northeast Forestry University, Harbin, 150040 China
e-mail: samesongs@163.com

G. Lollino et al. (eds.), *Engineering Geology for Society and Territory – Volume 1*,
DOI: 10.1007/978-3-319-09300-0_49,

understanding slope instability and its prevention in frozen regions, but most of them focused on high-altitude permafrost regions (Dewu 2004; Fujun et al. 2004). Currently, slope freeze-thaw instability and its prevention has become a unique field in science, occurring at the borders of landslide studies and geocryology.

In order to study the role of freeze-thaw on the stability of soil cuts, we selected a study area on the highway expansion project of the Tongsan Highway, from Fangzheng to Harbin. The average annual precipitation in the study area is 569.1 mm, the concentrated rainfall period is from July to August, and the concentrated snow period is from November to January. The annual average temperature is 3.6 °C, the average temperature in coldest in January (−13.2 to −24.8 °C), and hottest in July (18.1–22.8 °C). The maximum freezing depth is 1.8–2.2 m. Along the highway, the uncovered layer is mostly composed of quaternary alluvium, and there is geological stability. The upper region is yellow silty clay, loam, sandy loam, silt loam, with a thickness of 3–20 m, and it is mostly middle or low compressibility soil. The lower region is a yellow, gray gravel layer, with a thickness of 5–15 m, and contains clay lenses.

The study section is on the side of the widening from K560+090 to K565+690. The soil is sandy clay and the natural density is 1.8–2.1 g /cm^3. The height of the cut slope along the highway is 5–15 m, and the slope ratio is 1:1.5–1.75.

49.2 Impact of Freeze-thaw on Shear Strength of Soil in the Slope

Soil samples from the dug holes were sent for laboratory tests to obtain their physical and mechanical properties, such as soil natural density, soil moisture, and other physical indicators (Table 49.1). Remodeling of the soil specimens were done according to the conditions in the survey, triaxial tests were conducted, and shear strength indicators in non-frozen and different freeze-thaw cycles were measured (shown in Figs. 49.1 and 49.2).

In Fig. 49.1, soil cohesion always increases with increase in soil moisture regardless of the number of times the freeze-thaw cycles have occurred. Cohesion reaches peak value when soil moisture is around 13 % (optimum moisture), following which, soil cohesion decreases with increasing soil moisture. Dry density (DD) is also a significant factor, and the soil cohesion increases significantly with increase in soil dry density, especially when the soil moisture content is lower. The soil cohesion decreases with increase in the number of freeze-thaw cycles, and especially after the first freeze-thaw cycle.

Table 49.1 Basic physical properties of silty clay

Liquid limit (%)	Plastic limit (%)	Plasticity index	Maximum dry density (g/cm^3)	Optimum water content (%)
32.5	18.7	13.8	1.90	13

In Fig. 49.2a, the soil internal friction angle (IFA) always declines with increase in soil moisture. The greater the amount of soil moisture, the faster is the decline in the soil (IFA). This is because greater soil moisture means that the soil is closer to its saturation state, and this can cause greater lubrication by soil pore water. With respect to the soil dry density, when the amount of soil moisture is less than 18 %, the (IFA) of soil with dry density of 1.520 g/cm^3 is small. When the amount of soil moisture is greater than 18 %, the soil (IFA) increases with increase in the soil dry density. Figure 49.2b shows the curve of the contrast test for different freeze-thaw cycles. Soil dry density of the soil sample here is 1.615 g/cm^3. There are two points to be noted here. First, regardless of whether the soil undergoes a freeze-thaw cycle or not, the soil (IFA) decreases with increasing soil moisture. Second, the soil (IFA) varies between freeze-thaw cycles. After the first freeze-thaw cycle, (IFA) shows large increases when the soil moisture is less than 17 %. After five freeze-thaw cycles, (IFA) returns to a state corresponding to zero freeze-thaw cycles.

49.3 Moisture Migration During Freeze-thaw and Soil Moisture Monitoring

Site monitoring was performed at different locations of the slope (top of the slope and foot of the slope). Temperature and moisture sensors were buried at different depths (0.6, 1.4, and 2.2 m) of the slope from which a variation curve between soil temperature and soil moisture was obtained. Compared to unfrozen soil, seasonal frozen soil shows obvious distinct features in its physical properties after the freeze-thaw process. Moisture migration and phase change are major factors that occur during this process. Figure 49.3 shows the temperature and moisture curve of a soil body for one and a half years. Figure 49.3 shows the temperature and moisture curves of the top and foot of the slope at three depths (0.6, 1.4, and 2.2 m). Combining these curves, the freeze-thaw process of the soil can be divided into five stages: non-frozen, early-freezing, frozen, early-thawing, and ongoing-thawing. Soil water migration mechanisms as well as soil temperature and moisture in these five stages are discussed in the following section.

The first stage is the early-freezing stage, in which the soil temperature drops from 0 to −1 °C. During the freezing process, the temperature of soil particles first decreases because the different thermal conductivity of solids and gases causes the soil particles to absorb the heat of the pore water and pore air through conduction, which subsequently

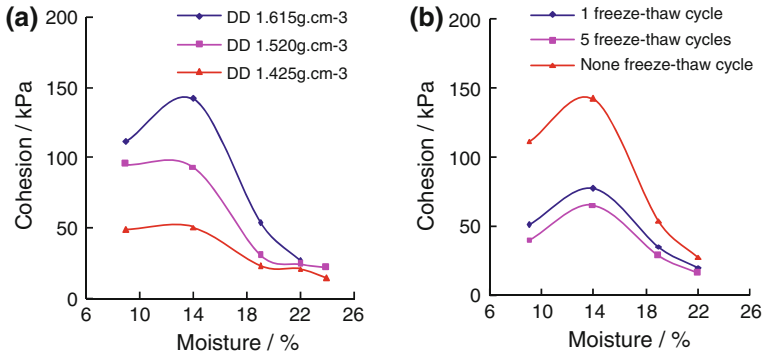

Fig. 49.1 The relationship curve between soil cohesion and soil moisture. **a** Non-freeze-thaw with different dry density (DD). **b** Freeze-thaw with dry density 1.615 g/cm^3

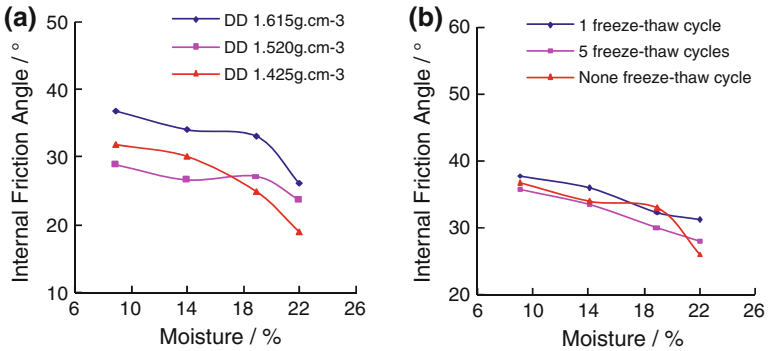

Fig. 49.2 The curve between soil internal friction angle and moisture. **a** Non-freeze-thaw with different dry density. **b** Freeze-thaw with dry density 1.615 g/cm^3

causes all three mediums to attain heat balance. This heat balance persists for a period of time until the pore water near the soil particles crystallize after releasing hydration heat. From then on, this heat balance is broken and the soil temperature decreases continually. A sign of this process occurring is a big drop in the measured moisture curve. The time period for early freezing varies by location, some lasted till January 10, 2010 or so. In Fig. 49.3a, b, the soil moisture continues to decrease except at some locations where the moisture content first drops and then rises higher than before. This phenomenon is due to ice segregation and water migration during the freezing process.

The second stage is the stable frozen stage, in which the soil temperature is lower than −1 °C. With a further decline in soil temperature, the soil moisture curve decreases further, but slightly. This is because small amounts of unfrozen water near the freezing front migrate to the freezing front. With a relatively stable negative soil temperature, the soil moisture content also remains in a stable state for some time. This is because the stable temperature could cause a temporary balance between frozen water and unfrozen water.

The third is the early-thawing stage, in which the soil temperature rises from a negative temperature to −1 °C. With the stable ascent of soil temperature, the soil moisture curve rises slowly and even has an uplift step. Then the soil moisture keeps constant, even as the soil temperature continues to rise. This is because the crystals in the soil voids begin to thaw. Crystal thawing requires sufficient hydration heat, so the soil moisture will be constant until the energy gathered from the soil particles is larger than the heat of hydration.

The ongoing-thawing stage refers to the period during which the soil temperature rises from −1 to 0 °C. During this period, soil temperature lingers near 0 °C but the soil moisture shows a steep rise at a certain moment. After the steep rise in soil moisture, the soil temperature rises rapidly to 5–10 °C. Next, the soil moisture starts rising slowly again, and then the soil temperature also rises slowly. For example, in Fig. 49.3, soil moisture rises from 9.58 % (09.4.23) to 28.09 % (09.5.5), but soil temperature only rises from 0 to 2 °C. At the same time, in the non-frozen soil layer (below the frozen layer), the soil temperature maintains a certain lower temperature, has a slight decline for a short time just before the steep rise in soil moisture in the frozen soil, following which, the soil moisture rises again. The reason is the complete thawing of the crystals in the soil voids which causes the soil moisture to rise rapidly. Heat of hydration and heat of crystallization comes from two directions: one is from the upper soil body which receives solar radiation, and the other is from under the soil body, which receives it from non-frozen soil. Therefore, during the accumulation period of the hydration heat energy, the soil temperature in both frozen and non-frozen soil remains relatively constant. At the same time, because there was an ice thawing layer over the non-frozen soil

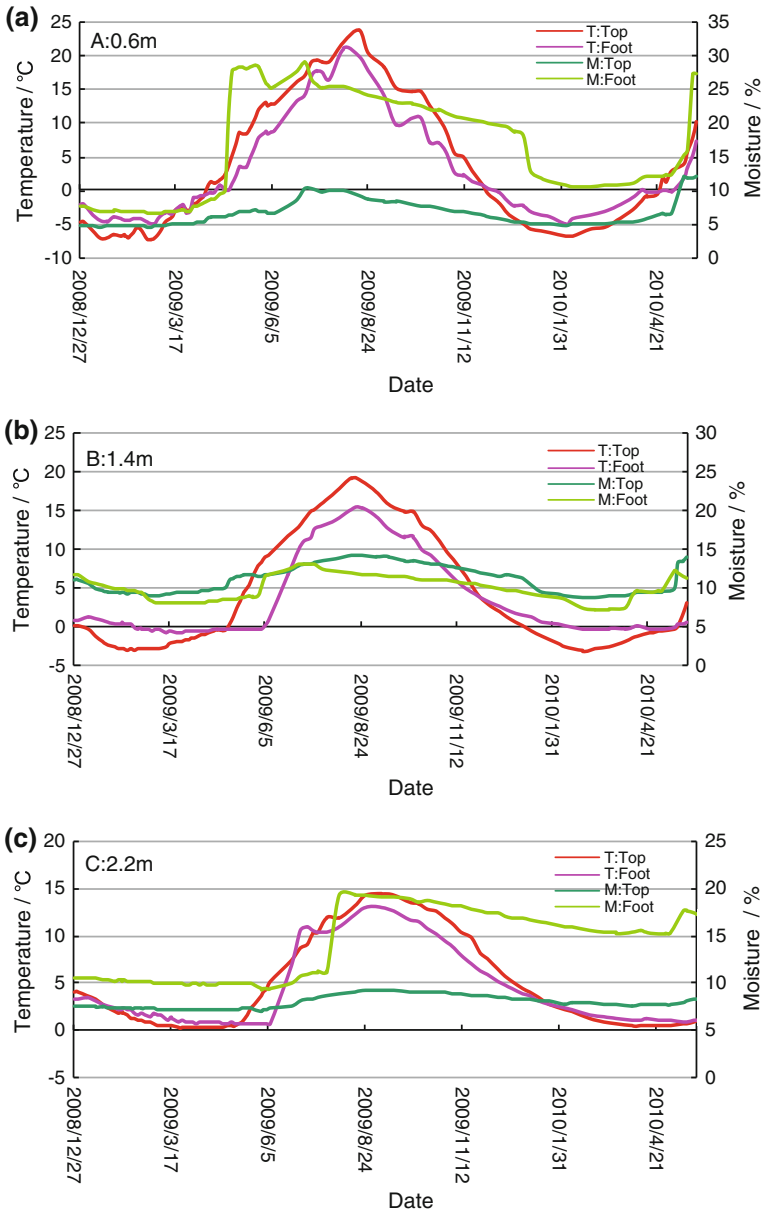

Fig. 49.3 The temperature (T) and moisture (M) curves in K560+700 section. **a** 0.6 m depth; **b** 1.4 m depth; **c** 2.2 m depth

body, which caused the moisture in the non-frozen soil to migrate to the ice thawing interface, the soil moisture in the non-frozen soil declines slightly. When the crystals in the soil voids thaw completely, and the ice interface disappears, the upper soil moisture permeates into the non-frozen soil layer, and the soil moisture of the non-frozen soil rises rapidly again.

The final stage is the non-frozen stage, during which the soil temperature value is always positive. Soil temperature varies with air temperature, and soil moisture is mainly affected by rainfall, evapo-transpiration, and penetration.

49.4 Change in Slope Soil Water Conditions and Its Impact on Slope Stability

In seasonal frozen areas, in addition to seasonal variations of air temperature near the surface and precipitation conditions, the soil moisture and phase state in the shallow layer also go through dramatic changes, which affects the stability of soil cut slopes.

In Fig. 49.3, soil moisture distribution and variation at different locations are overall quite similar, but there are large differences in magnitude and extent. For example, in

the K560+700 section, at the bottom of the slope at 40–120 cm deep, the soil moisture rises from 18.7 % (2009.05.2) to 26 % (2009.5.26), and shows a declining trend till July 26, 2009. At a depth of 200 cm, the soil moisture is also more than the plastic limit of 18.7 % (2009.8.17–2009.11.3), and comes back to 18.7 % on December 2, 2009. In 2010, the soil moisture is again more than 18.7 % (2010.5.10) at the 40–120 cm depth, rises to 24 % (2010.5.22), following which, there was a landslide on May 24, 2010.

Site investigation and measurement confirmed the main reason for shallow landslides. This is the fact that the water in the soil is transferred to the freezing front during the freezing period, resulting in greatly increased water content in shallow slopes. During the spring thawing period, the thaw water is prevented from infiltrating into the lower layers by the frozen layer underneath, resulting in a rapidly increasing water content in the layer above the frozen layer, which causes the effective stress within the slope to reduce. Combining monitoring and laboratory data with finite element analysis, a slope stability factor of 1.069 was obtained, which is in good agreement with the actual site.

49.5 Conclusion

The results of the physical and mechanical indicator tests for soil show that: soil cohesion increases with increase in the soil dry density, and decreases with increasing freeze-thaw cycles. Soil cohesion reaches the peak value when the soil moisture is around 13 % (optimum moisture), following which, the soil cohesion decreases with increasing soil moisture. The soil internal friction angle decreases with increasing soil moisture. After the first freeze-thaw cycle, the internal friction angle largely improves, and after several freeze-thaw cycles, returns to the level corresponding to zero freeze-thaw cycles.

The results of monitoring in the cut slope show that: soil moisture is affected by atmospheric precipitation, soil temperature, permeability coefficient, and permeability conditions, and has cyclical changes that vary with the seasons. When the soil temperature is above 0 °C, soil moisture in the shallow layer is affected by atmospheric precipitation, evaporation, transpiration, and permeability. When soil temperature is less than 0 °C, the water in the shallow layer causes water migration due to phase change and ice segregation, and causes spot or strip crystallization in the soil body. In the spring thawing period, when the soil temperature rises to 0 °C, the frozen water begins to thaw, and the soil moisture curve shows slight fluctuations. When the soil temperature is above 0 °C, the phase transition of frozen water is complete and the soil moisture curve rises rapidly.

The results of our comprehensive analyses show that: in soil cut slopes in seasonal frozen regions, within the seasonal freezing depth, the water in the soil causes ice segregation and migration during the freezing period. During the spring thawing period, the thaw water that is prevented from infiltrating into the underlying layers by the frozen layer underneath, rapidly increases in amount in the layer above the frozen layer, causing the effective stress within the slope to reduce, following which, under gravity, all or part or the shallow slope slides down the "water saturation layer."

Acknowledgments The authors would like to thank the financial supports provided by the research project of Heilongjiang provincial Science and Technology Department (GZ07 C401), and the Key project of Heilongjiang provincial Transportation Department "Highway Slope Stability and Greening by Vegetation in Cold Regions".

References

Dewu J (2004) Slope stability study on permafrost area of Qinghai-Tibet Platean. Chang'an University, Xi'an (in Chinese)

Emelyanova E (1986) The basic rule of landslide action. Chongqing Press, Chongqing (in Chinese)

Niu F, Cheng G., Lai Y et al (2004) Instability study on thaw slumping in permafrost regions of Qinghai-Tibet Plateau. Chin J Geotech Eng Chin Edn 26:402–406 (in Chinese)

Tarr RS (1897) Rapidity of weathering and stream erosion in the arctic latitudes. Am Geol 19(2):131–136

Implementation of Remote Sensing and Mathematical Modeling for Study of Risk Assessment to Linear Engineering Structures Due to Thermokarst Processes

50

Kapralova Veronika

Abstract

The paper presents a new approach for risk assessment of thermokarst impact on engineering structures. The way to estimate the risk of engineering structures damaging due to thermokarst processes with the help methods of mathematical morphology of landscape and remote sensing data was suggested. The suppositions, which were used as a basis for territories models with thermokarst processes, were presented and then theoretical assumptions were applied and the simulation results were compared with empirical data to prove convergence. A number of areas with thermokarst lakes were digitized and correspondence between theoretical suppositions of mathematical analysis and experimental data was verified. The obtained results shows general correspondence of calculated and empirical data.

Keywords

Risk assessment • Remote sensing • Landscape analysis • Mathematical morphology of landscape

50.1 Introduction

More than 25 % of Earth is within a permafrost zone. Accordingly studies of permafrost and related exogenous geological processes are very important.

As a rule, frozen ground processes including those in a stage of stabilization or attenuation become more active under technogenic intervention and climatic changes, receiving a new impulse. And even more, they can reach higher degrees of intensity in their development. Besides other processes arise, which were not developed earlier at this territory. Risk estimation under the conditions of hazardous geological processes development is one of the most challenging problems of geology. It is especially important in rapidly changing natural conditions of the Northern regions. One of the important problems is to find principles of distribution and dynamics of thermokarst development with the purpose of forecasting environmental changes.

Many researches are dedicated to risk estimation of engineering structures damaging (Elkin 2004; Natural risks estimation 2003a, b). With statistic approach to risk estimation, a researcher faces certain problems due to the fact that statistics gathering requires significant time, which often the structure's functioning time. Methods of mathematical morphology of landscape were suggested as another approach to avoid aforementioned problems (Viktorov 1998).

Mathematical morphology of landscape is a branch of landscape science investigating quantitative principles of mosaic patterns formed by nature units on the Earth's surface as well as mathematical analysis methods of these mosaics.

This work aims at developing and substantiating the quantitative risk estimation procedure for linear structures using remote sensing and methods of mathematical morphology of landscape.

K. Veronika (✉)
Sergeev Institute of Environmental Geoscience, Russian Academy of Sciences, Ulansky pereulok 13, building 2, Moscow, Russia 101000,
e-mail: vkapralova@gmail.com

G. Lollino et al. (eds.), *Engineering Geology for Society and Territory – Volume 1*,
DOI: 10.1007/978-3-319-09300-0_50,

The theoretical basis of mathematical morphology of a landscape is formed by mathematical models of morphological patterns—the quantitative dependences describing the basic properties of morphological patterns.

Mathematical models of thermokarst lakes are based on the following assumptions (Viktorov 1998, 2006):

- The process of origination of new depressions is probabilistic and proceeds independently on disjoint areas.
- The probability of origination of depressions within a sample area depends only on area size and on time interval. Also, probability of origination of one depression is much greater than the probability of origination of several depressions.
- Growth rate of depressions due to thermal abrasion occurs independently from each other, it is directly proportional to the heat stocks in a lake and inversely proportional to the area of a lateral surface of the lake basin under water level.

These suppositions result in equations for data analysis and prediction schemes for the territories with thermokarst processes (Viktorov 1998). The obtained equations include:

- probability distribution of the thermokrast lakes number (k) emerged in the given district during the given time (Poisson process)

$$P(k,t) = \frac{(\lambda ts)^k}{k!} e^{-\lambda ts}, \tag{50.1}$$

where λ is the average number of reductions occurring in the area unit during the time unit; s—test area size; t—time;

- probability distribution of thermokarst lakes radius change (Wiener random process with regard to diameters logarithms)

$$f_r(x) = \frac{1}{\sqrt{2\pi}\sigma x\sqrt{t}} e^{-\frac{(\ln x - at)^2}{2\sigma^2 t}}, \tag{50.2}$$

where α, σ—distribution parameters, t—age of lake.

50.2 Implementation of Thermokarst Lake Plain Mathematical Model

We performed the model approval in several test districts in Russia (West and East Siberian planes) and USA (Alaska), which are characterized with quite different geological, climatic, and cryological conditions. We selected the districts based on morphological homogeneity and availability of remote sensing data. The districts must be similar in terms of microstructure and background phototone as well as lakes location and shape. In Fig. 50.1 satellite images of the tested districts are given.

The model shows that at a particular moment of time lakes areas should be lognormally distributed. The studied parcels were analyzed using the specially developed software Vektorizator (by Viktorov A.A). The water surface of lakes contrasts with their surroundings and is clearly identifiable visually. So the Vektorizator reduces it to binary form without losing lake geometry data. After that, on an enlarged section of the image, the operator can outline the lake border in semi-automatic mode. Then the program will automatically calculate with a high degree of accuracy the diameter, area, perimeter, centre of gravity and other parameters of the lake outline. Then via the "Statistic" software we obtained the ratio between theoretical and empirical data. We found good conformity between theoretical and experimental data (Fig. 50.2).

This implies that a lognormal distribution of lake areas is acceptable for the selected parcels. Modeling shows also that the location of lakes should follow a Poisson distribution at a specific moment of time. On the same reference parcels the distribution of hermokarst lakes centers was analyzed. For each parcel several experiments were made. Distribution graphs were plotted, their parameters were obtained and conformity to a Poisson distribution was determined. Here too, we found good conformity between theoretical and experimental data. Thus a number of deductions from the proposed mathematical model for thermokarst lake plains are in general corroborated by empirical data.

50.3 Risk Estimation for a Linear Structure Damage

The created mathematical models allow us to solve the problem of a linear object damaging by a particular hazardous process in homogeneous physical and geographical conditions. Since distribution of thermokarst depressions comply with Poisson distribution and each thermokarst depression development is independent, the damages number distribution for a linear object damaging by the process will be also the Poisson distribution (Viktorov 2006).

$$P(k,t) = \frac{[2\gamma(t)L\bar{r}(t)]^k}{k!} e^{-2\gamma(t)L\bar{r}(t)}, \tag{50.3}$$

where $\bar{r}(t)$ is an average thermokarst depression radius at a certain moment of time t, $\gamma(t)$—average density of thermokarst depression location, L—object length.

For a number of districts the obtained theoretical conclusions verification was carried out (Viktorov and Kapralova 2012).

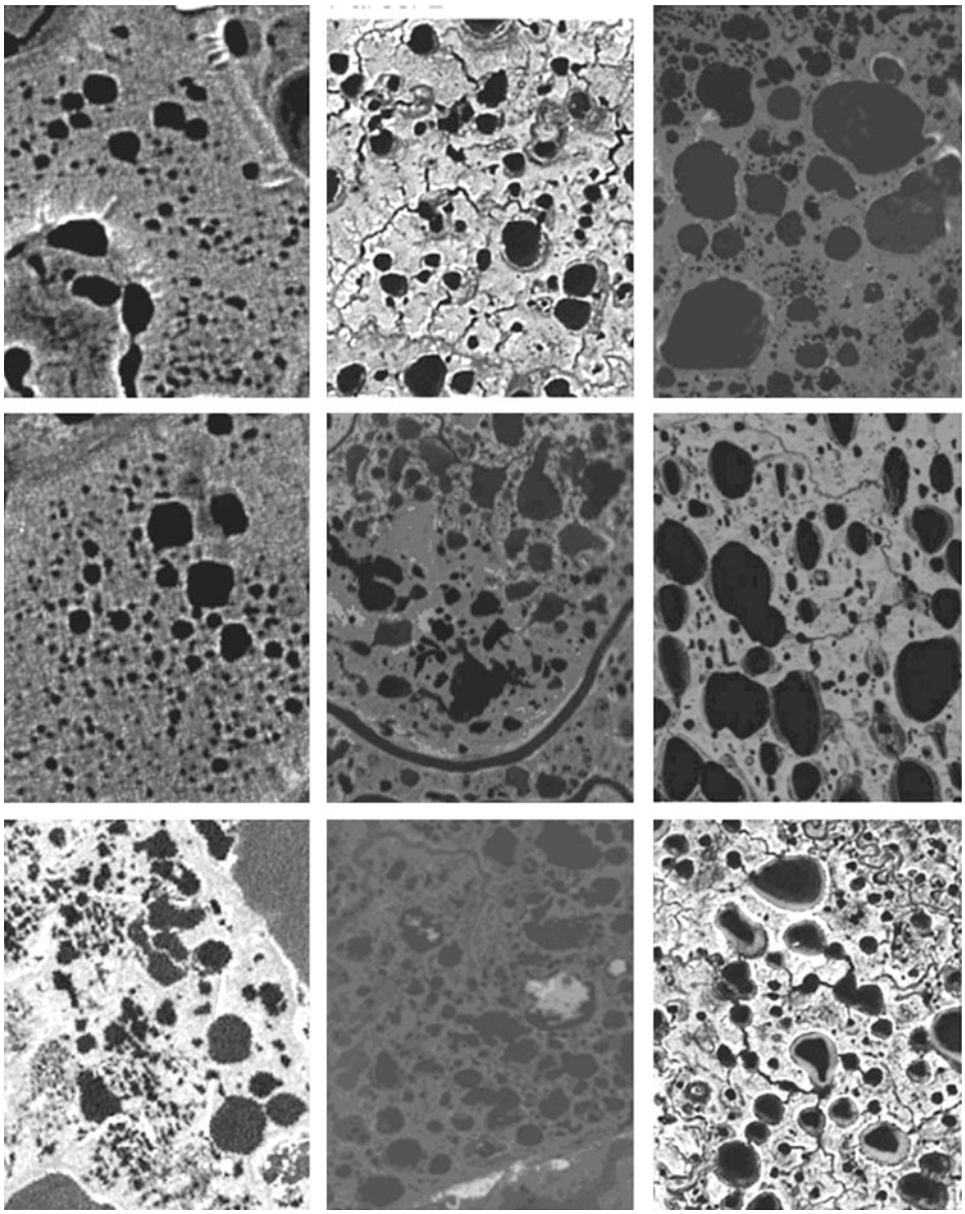

Fig. 50.1 Satellite images fragments of tested districts

Equation for the estimation of a linear object damage probability was verified based on the following reasoning. Suppose, we are in the studied district before the thermokarst process begins. Due to the fact that the district is homogeneous we have no reason to select any special location to place the linear object and it may be placed at any point of the district with equal probability. The thermokarst depressions which develops later and which we currently observe in the image could damage or not the linear structure. Due to the mentioned above, the real situation development may be modeled as follows—in the software with the help of a random-number generator we randomly place the linear object (of various lengths) within the selected district (with already existing lakes) and then count the number of lines not damaged by the process. A particular procedure for the formula verification was implemented as follows: with the help of a random-number generator sets of random projections of parallel sections of various lengths were made on the square-shaped district with lakes digitized on it. These lines modeled the linear structure location. Then the number of lines crossing thermokarst lakes was calculated. The percentage values of sections not damaged by the process from the total amount of the projected sections with the given length were obtained and compared to the calculated ones, which were determined according to the formula.

During calculation some problems occurred caused by the fact that lakes could merge due to their growth, and the calculation was obtained for the case when there were no junctions. These problems are supposed to be solved in the future.

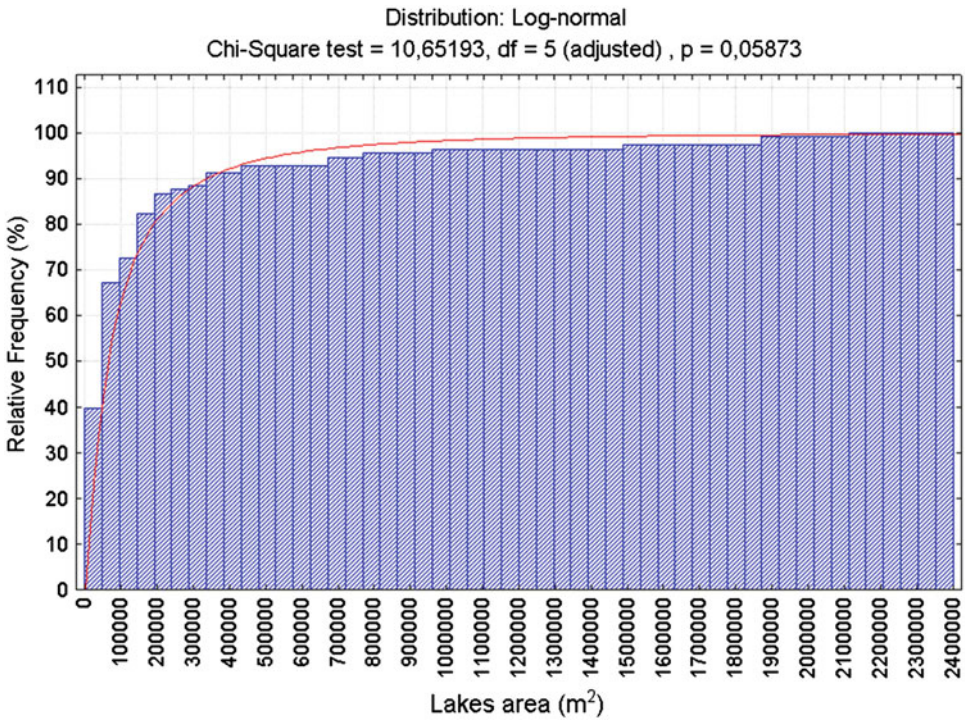

Fig. 50.2 Relationship of theoretical (*red line*) and empirical distributions of areas of thermokarst lakes in parcel 1

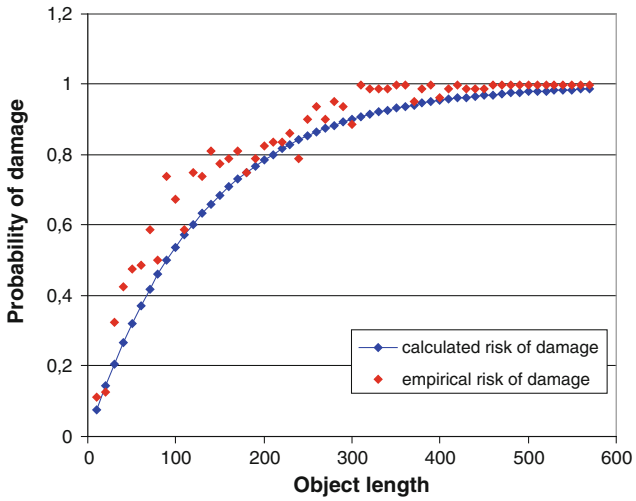

Fig. 50.3 Comparison of theoretical and empirical values of risk of damage from thermokarst processes for linear objects of various lengths after lakes junction consideration

The obtained results analysis shows a general correspondence of calculated and empirical data (Fig. 50.3).

50.4 Conclusions

The obtained results allow us to suggest the method to estimate damage risk for engineering structures due to hazardous exogenous geological processes.

The result of the studies performed is as follows:

1. Mathematic risk estimation models for linear engineering structures damaging by hazardous exogenous geological processes was validated based on mathematical morphology of landscape.
2. Models were experimentally tested for the territories where thermokarst processes developed.
3. The possibility of calculation of linear engineering structures damaging risk by hazardous exogenous geological processes with the help of repeated satellite images was shown.

References

Elkin VA (2004) Regional estimation of karst hazard and risk (Case of the Republic of Tatarstan). Dissertation abstract for PhD in geolmin, science. Moscow: IGE RAN, 24 p

Natural risks estimation and management (2003) All-Russian conference "Risk-2003" materials, vol 1. Izd. Ros. univer. druzh. narodov, Moscow, 412 p

Natural risks estimation and management (2003) Thematic volume/ Edit. A.L. Ragozin. Izd. firma "KRUK", Moscow, 320 p.

Viktorov AS (1998) Mathematical morphology of landscapes. TRATEK, Moscow, 180 p

Viktorov AS (2006) Main problems in mathematical morphology of landscapes. Nauka, Moscow, p 252 p

Viktorov AS, Kapralova VN (2012) Application of methods of mathematical landscape morphology to assessing the risk of damage to linear engineering structures resulting from hazardous exogenous geological processes. Water Res 39(7):790–797

Environmental and Engineering Geology of the Bei'an to Heihe Expressway in China with a Focus on Climate Change

51

Wei Shan, Zhaoguang Hu, Hua Jiang, Ying Guo and Chunjiao Wang

Abstract

The Bei'an to Heihe Expressway in China is located in southern boundary of high latitude permafrost, and intersects the north section of the geologically complex Lesser Khin-gan Mountains. In recent years, this expressway has experienced increasing roadbed settlement, salutatory flow ice and cut slope landslides in the road area, which threaten the stability of the subgrade and highway operational safety. The morphological characteristics and evolution of the above phenomenon are related to permafrost distribution and degradation as well as seasonal freeze-thaw. The relationship between the annual average temperature change and the permafrost distribution are analyzed based on the annual average temperature from 1954 to 2011 in Sunwu County, which was published by "China National Science and Technology Infrastructure Platform," and the cumulative monthly average air temperature, ground temperature, precipitation, and maximum frozen soil thickness in Sunwu County from 1971 to 2000. Uneven settlement of the roadbed and salutatory flow ice caused by freeze-thaw, as well as landslide mechanisms and motion characteristics were analyzed. The analysis used ground temperature, moisture, surface and landslide deformation monitoring data from 2009 to 2012 in the Bei'an to Heihe Expressway sections K161+440, K161+860, and K178+530, which traverses the north section of the Lesser Khingan Mountain. The results of this study demonstrates that in the past 50 years, the annual average temperature in the Sunwu region had an upward trend, and after 1995, when the annual average temperature in the region rose to above 0 °C, the permafrost degradation process accelerated. Landslides, roadbed settlement, and salutatory flow ice in the road area are often influenced by atmospheric precipitation, melting permafrost, seepage water, air temperature, geological condition, and human activity. These geological problems are affected by seasonal temperature changes, slope water content change, and other related geological conditions, and have the characteristics of being low angle, intermittent, and creeping.

Keywords

Climate change • Permafrost • Creeping

51.1 Introduction

Globally, much attention has been focused on climate change and its impacts. The fourth Intergovernmental Panel on Climate Change (IPCC) assessment report (Solomon 2007) states, that the global average surface temperature has increased, showing a consistent warming trend. The warming rate averaged over the last 50 years is twice that

W. Shan (✉) · Z. Hu · H. Jiang · Y. Guo · C. Wang
Institute of Cold Regions Science and Engineering, Northeast Forestry University, Harbin, 150040 China
e-mail: shanwei456@163.com

G. Lollino et al. (eds.), *Engineering Geology for Society and Territory – Volume 1*,
DOI: 10.1007/978-3-319-09300-0_51,

for the last 100 years. Numerous studies show that climate change in China is consistent with the global trend (Chen et al. 2004; Lin et al. 1995; Shi et al. 1995; Zuo et al. 2004; Ren et al. 2005; Ding et al. 2006; Wang et al. 1998; Wang 1994). China's warming rate has been approximately 0.25 °C/10a in the past 54 years, which is higher than the global or hemispherical average temperature increase rate over the same period, with Northeast China showing some of the most significant temperature increases (Cheng 2003). In recent years, permafrost degradation and its impact on ecological environments caused by climate change has become a popular research area.

Permafrost is the result of energy exchange between the lithosphere and the atmosphere and is an important part of the earth's cryosphere system. The presence, distribution, moisture, temperature, nature, and state of permafrost are affected by many factors, and display distinct spatio-temporal variations. At the global and continental scale, permafrost is determined by latitudinal climate (Solomon 2007; Chen et al. 2004). However, at the regional scale, the effect of altitude and longitude is distinct. While, on the local scale, various factors affecting the water and heat balance, such as snow, vegetation, slope, exposure, lithology, and water, which in turn affect the distribution and other characteristics of permafrost is critical (Lin et al. 1995; Ren et al. 2005; Ding et al. 2006).

Permafrost is widely distributed in the Greater and Lesser Khingan Mountain located in northeastern China and the Baikal region in Russia. Northeast China is the second largest and the only high latitude permafrost region of China. In this region, snow, vegetation, water, topography, temperature inversion, and other local factors significantly lower temperature, thus forming the Khingan-Baikal type permafrost, which is very different from permafrost in polar and high altitude regions (He et al. 2013). Affected by climate change, the southern boundary of the high latitude permafrost in Northeast China with its island shaped distribution has moved northward in recent years due to accelerated degradation.

The northeast area is the cradle of Chinese cryopedology and one of the first areas to be studied intensively, beginning some three decades ago. It became clear that climate warming in this area would lead to permafrost degradation and in turn impact infrastructure such as airports, roads, and pipelines. However, there is no current system to study the climate change influence on permafrost change in the northeast high latitude permafrost regions (Chang et al. 2013).

Frozen soil, when ice-rich can be extremely sensitive to temperature changes, giving it rheological properties and long-term strength; this is much lower than its frozen strength. Infrastructure in permafrost areas is at risk of frost heave and thaw settlement, uneven roadbed settlement and deformation, or even bank failures because of these characteristics.

The Bei'an to Heihe Expressway in China, which traverses the Lesser Khingan Mountains, is the study area. In particular, we focus on roadbed settlement, salutatory flow ice in cut slopes, and landslides in the road at sections K161+450, K162+870 and K178+530. Finally, we analyze weather data from Sunwu County's meteorological station, terrain surveys, and slope monitoring data, to analyze causal mechanisms and movement of roadbed settlement, salutatory flow ice, and landslides.

51.2 Study Area Physical Conditions

The study area (K153+440–K184+100) is located in the northwest section of the Lesser Khingan Mountains at the geographical position, N49°27′–N49°45′ and E127°12′–E127°33′, at 210–330 masl. The terrain is undulating with occasional steep slopes and lush vegetation.

Underlying geological strata substrate includes the upper Jurassic Shenshu formation, volcanic lower Cretaceous Guanghua formation, and late Indosinian granite. These are overlain by the upper Cretaceous Nenjiang formation, Tertiary Pliocene series Sunwu Formation River, and Lake Facies deposits. The latest tectonic movement in this area is mainly vertical, and the new rift zone increases then decreases, while the overlying Tertiary Pliocene series Sunwu formation, which mainly consist of coarse sand or sand conglomerate has no cementation, and is mostly unconsolidated. The upper Cretaceous Nenjiang formation in the lower part of the mountains or hills, and its lithology is mudstone, sandy fine sandstone and fine sandstone. It is weakly cemented, and deeply weathered, especially near the surface. Holocene to modern river alluvium is distributed in the valley bottom.

The study area has a continental monsoon climate. In the spring, temperatures rise quickly and it is generally windy and dry. Summer is influenced by the southeast monsoon, and is characterized by more easterly and southerly wind, mild temperatures and rain. In autumn, temperatures fall rapidly, and there is danger of early frost. Winter is affected by Siberian and Mongolian high pressure, and is characterized by more west-northerly and northerly wind, and cold, and dry conditions. Standard seasonal frost depth is 2.3–2.5 m, and maximum seasonal frozen depth is 2.85 m. Figure 51.1 is the 30 year accumulative total month average air temperature, ground temperature (40 cm under the ground), precipitation, maxim unfrozen soil thickness curve from 1971 to 2000 in Sunwu County meteorological station.

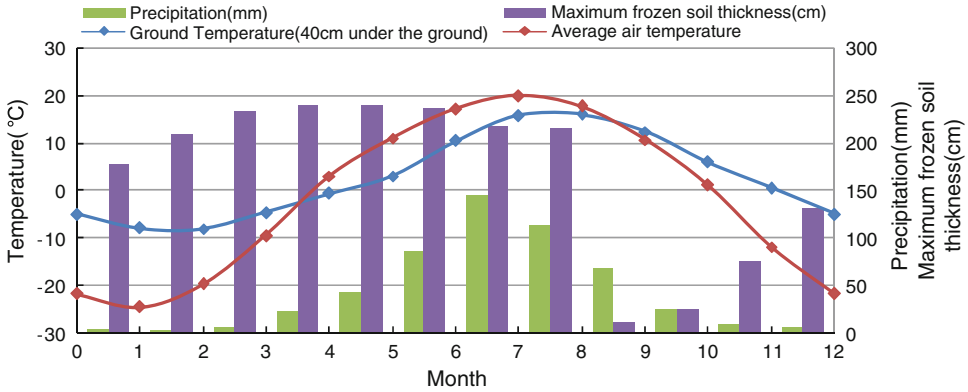

Fig. 51.1 Monthly average temperature/soil temperature in the depth of 40 cm /precipitation/ maximum frozen depth (1971–2000, Sunwu)

51.3 Climate Change and Permafrost Degradation

China's north-northeast area is located in the southern margin of the Eurasian permafrost zone, where the Greater and Lesser Khingan Mountains are oriented in a north east, north-west trend, with the Nenjiang River Valley in the between them. The climate is affected by continental and oceanic high and low pressure systems and alternating monsoonal systems. The Siberian and Mongolian high pressure, and a widely distributed inversion layer influence the cold winters. In turn, the Pacific high enhances the southeast monsoon in summer, which leads to warm air from the south intersecting cold air from the north in this area, resulting in rainy weather. An asymmetrical mountain distribution, slope direction, and hilly area, as well as the wide and stable existence of the inversion layer in winter, play an important role on permafrost distribution development. Vegetative cover, which is composed of forest, shrub, grass, and moss, plays an important role in the development and protection of permafrost. The degree of permafrost distribution and development of geomorphological position in this region varies due to the effects of the inversion phenomenon, surface material type and thickness, vegetation, slope direction, surface water, geological structure, and other natural factors. In this region, "Khingan-Baikal type" permafrost is predominant. It is an especially abundant and thickest in relatively low-lying areas. Degradation advances in descending order, first on slopes with high solar radiation, high areas and mountains, and last on shady slopes, low areas, and valley bottoms (Zhou et al. 2000; Guo et al. 1998).

Figure 51.2 shows the result of our permafrost mapping. We fused the May 3, 2011 and October 10, 2011 Landsat ETM+ images, with extracted thermal infrared band data, and overlaid the June 15, 2004 satellite photo of the study area, which was intercepted from Google earth, to obtain the high upper limit permafrost distribution map of the study area. It has a good agreement with our survey results. The inversion results show that in the study area, permafrost distribution has obvious "Khingan-Baikal type" permafrost characteristics.

In the past 100 years (1906–2005), the global surface temperature has increased 0.74 °C. The most significant temperature increases in the past half century occurred in north China, east Inner Mongolia, and northeast China, with the highest increases reaching 0.8 °C/10a. Our study area is located in the Sun Wu-Heihe district, which has among the highest warming rate sin nearly 50 years. According to the meteorological data from Sun Wu weather station during the period 1954–2011, annual average temperature rose 2.8 °C from −1.6 °C in 1954 to 1.2 °C in 2011 (see Fig. 51.3).

In this study, the effect of climate change is reflected in the annual average temperature increase and in the changing extreme maximum and minimum temperatures. Data was obtained from the 1954–2011 monthly extreme maximum temperature, mini-mum temperature, and average air temperature data from the Sun Wu weather station. We used this data to plot a distribution chart (see Fig. 51.4), which shows a general upward trend in this area. The extreme minimum temperature rose most rapidly, except for September, while, the extreme minimum temperature increase is twice the extreme maximum temperature increase, and Fig. 51.1 shows that September is the month when the seasonal frozen soil thawing depth is the largest in this region. The chart also demonstrates the relationship between permafrost degradation and distribution, and climate change.

Over the past 10 years, permafrost in northeast China high latitude permafrost areas has become more vulnerable due to climate and environment change. This has led to accelerated permafrost degradation, with the southern permafrost boundary moving northwards, reduction in permafrost thickness, and increase in the permafrost temperature. Investigations show that the Bei'an to Heihe Expressway permafrost segments lost permafrost over a ten year period. We identified 17 permafrost sections in 2000, but only 5

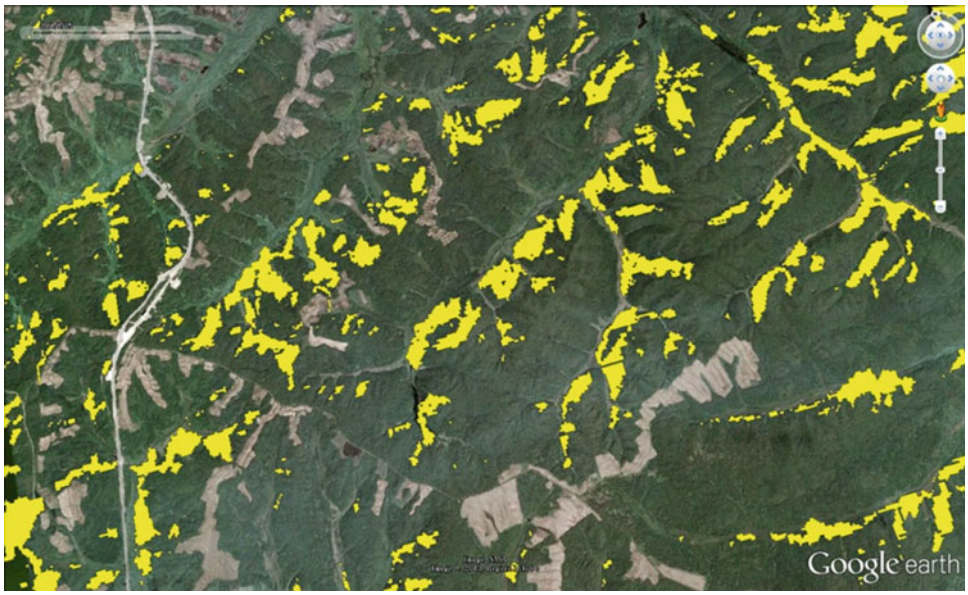

Fig. 51.2 The distribution map of high upper limit of permafrost (Based on Landsat ETM+ images)

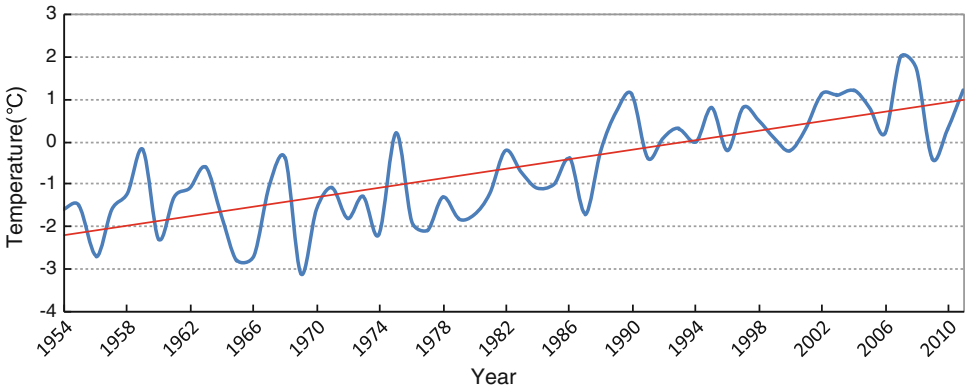

Fig. 51.3 Annual average temperature curve (1954–2011, Sunwu)

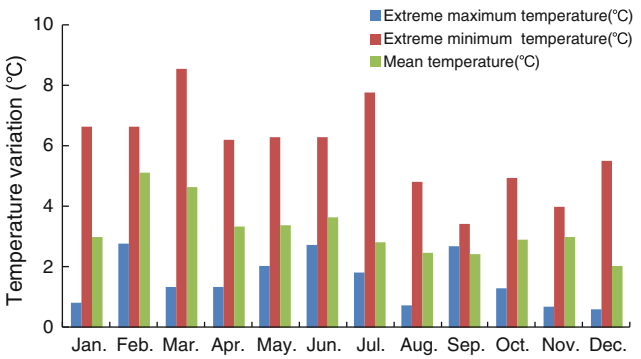

Fig. 51.4 Varies radio of monthly temperature (1954–2011, Sunwu)

sections in 2009 and the length of the sections and the thickness of permafrost, both decreased. In the road area, traversing the Lesser Khingan Mountains, the phenomenon of roadbed settlement, salutatory flow ice in winter and spring, and small-scale and slides have increased significantly.

51.4 The Impact of Seasonal Freeze-Thaw and Permafrost Degradation on the Geological Environment

In the study area, 80 % of the surface is covered by larch, oak, poplar, linden, birch, coniferous, and broad-leaved mixed forest. Hill slopes with gradients between 10–35° are subject to landslides and creep. Carextato, fish-scale pine, drunken forests, sabre trees, and permafrost geomorphic features are distributed on the platform (see Fig. 51.5).

Figure 51.5 is the June 15, 2004 satellite photo of the study area, which was intercepted from Google Earth; there are local surface folds and multi-level platforms distributed in the area. In the photo, the red line marked the geologically unstable region judged from geomorphology and the blue line marked the surface region exposed to water from permafrost thaw. C1 represents west-facing slopes and permafrost melting areas, with is meltwater flow into the

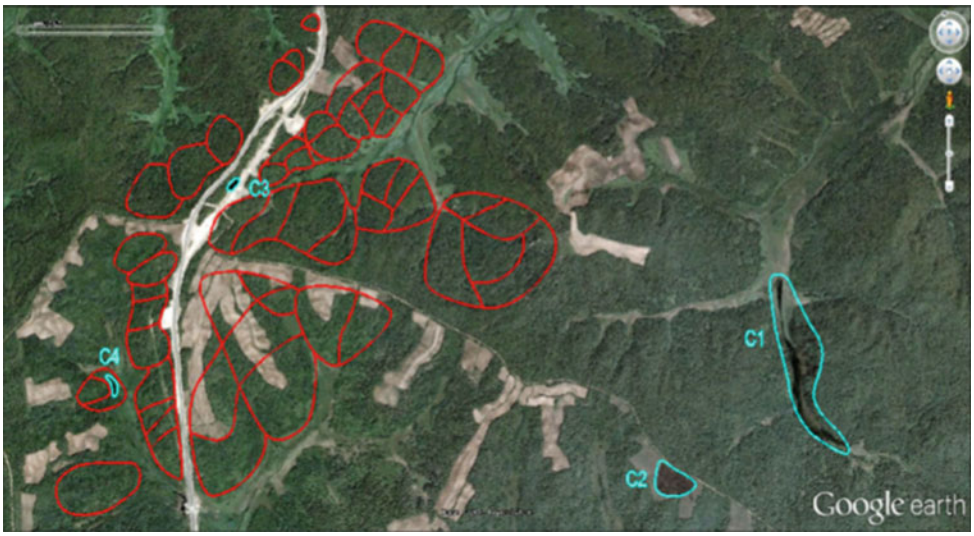

Fig. 51.5 Creeping platform and the distribution of melting permafrost in study area

seasonal river. C2 is the cultivated land surface with shallow permafrost melting areas. C3 is ridge permafrost with meltwater-exposed areas. On the right side of C3 is the abandoned road where, a landslide occurred during the subgrade construction process in 2000 and on the left side of C3 is the changed ridge section. C4 is the landslide creeping platform margin and the area exposed to permafrost-meltwater. Combined with Fig. 51.2, the permafrost distribution map of high upper limit, it could be seen that, permafrost distribution has a good agreement with unstable geological condition regions, so that the multi-level platform in the study area is the result of ongoing permafrost degrading and surface creeping. With the climate change evolution, low-lying areas and deep permafrost will gradually degrade as well. Repeated freeze-thaw, and rain, will melt permafrost and further reduce the strength of shallow soil bodies, and promote the development of surface creep, leading to increased landslide risk.

51.5 Mechanism and Evolution Process of Roadbed Uneven Settlement, Seasonal Salivary Flow Ice, and Landslides in Road Domain

Soil moisture plays an important role in the soil's physical and mechanical properties. In permafrost regions that are affected by air temperature changes, the soil experiences freeze-thaw cycles and has an alternating three-phase and four–phase system, which drastically changes the engineering properties of the soil. The change between soil engineering properties indicators and soil temperature are not linear relationships, so in permafrost regions, engineering geological conditions change as environmental conditions change.

The Bei'an to Heihe Expressway has been widened from the original secondary road; subgrade earthwork was completed in early November 2009. In the engineering exploration, island permafrost was discovered underlying the K161+350–K161+800 sections, with an upper limit of 0.8 m depth and a lower limit of 8.05 m depth. The construction design method adopted to deal with permafrost problems was is to melt permafrost in the roadbed. A gravel compaction pile of 15 m depth is inserted after clearing 120 cm of the original ground surface and filling 200 cm of gravel at the surface of the gravel layer, in order to accelerate the permafrost melting and water discharge.

Figure 51.6 shows the relationship curve between soil temperature at different depths and times at the foot of the slope in the K161+440 section. In Fig. 51.6, the foundation settlement caused by the embankment of the additional load was completed in early July 2010, after a freeze-thaw cycle. From August 2010 to January 2011, the foundation settlement accelerated with an increase in soil temperature until

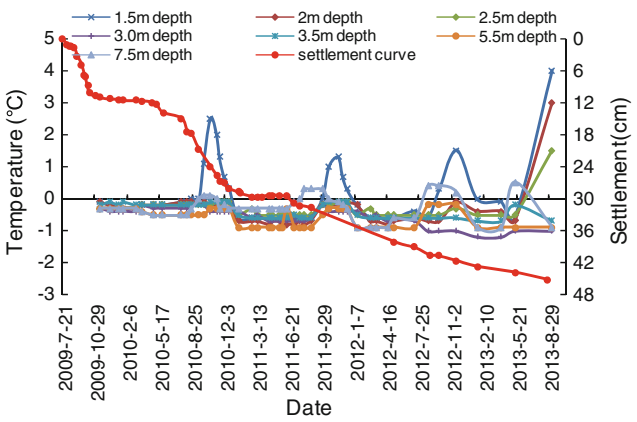

Fig. 51.6 Subsidence and relationship curve between soil temperature and time in K161+440 section

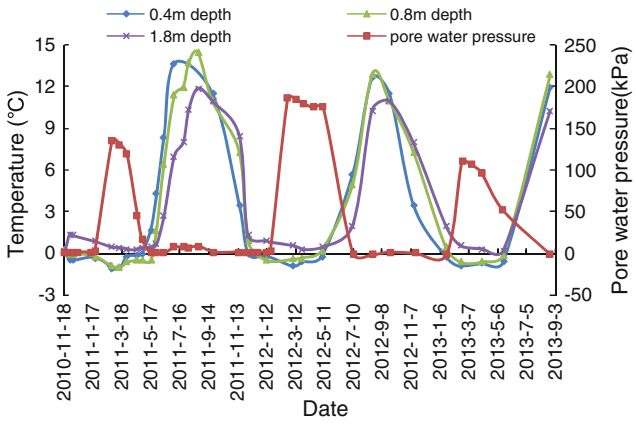

Fig. 51.7 Relationship curve between soil temperature, soil pore water pressure and time in K161+860 section

February 2011, when the foundation soil refroze and the settlement rate was reduced to zero. In May 2011, the soil temperature near the permafrost bottom began to rise, and the roadbed settlement happened again. It was not stabilized until the time of writing. However, from early July 2012, there were significant temperature differences among measuring points in the roadbed, owing to the different heat transfer at different positions during melting, i.e., the permafrost degradation in this measuring point.

Seasonal salutatory flow is a unique geological phenomenon in very cold regions. Its occurrence is related to slope position and topography, vegetation distribution and coverage conditions, moisture and temperature in the slope shallow layer, as well as the impact of engineering structures, they also have seasonal, occasional, and positional uncertainty characteristics. Repeated occurrence of salutatory flow ice could change moisture and temperature in shallow layers of the slope, weaken soil strength, and increase the risk of shallow landslides.

Figure 51.7 is the relationship curve between soil temperatures, pore-water pressure at different depths and times (the second step of cut slope in K161+860 section, 1.5 m depth). Figure 51.7 shows groundwater frozen from surface. The ground water in the shallow layer experiences pressure caused by the upper freezing front moving down and the lower impermeable layer. This pressurizes the interlayer water gradually, leading to rapid increase in the soil pore water pressure, and reaches its peak value in early February. Soil pore water pressure would decrease rapidly, if, there were a weak point on the slope that allows the outflow of unfrozen confined water; otherwise, soil pore water pressure will be near the peak value until the frozen layer melts in spring, when it will decrease rapidly. Landslide risk increases in summer, when the moisture of the position salutatory flow ice is still saturated or near saturation.

Because there is unfrozen water in winter, the salutatory flow ice often takes place at shallower freezing depths, less than average freezing depths, and there must be permafrost under those shallow groundwater layers.

In permafrost areas, due to the freeze-thaw role and permafrost impact, the mechanism and movement law for landslides is also distinctive. Figure 51.8 shows the geological profiles of the K178+530 section. Figure 51.9 is the relationship curve between soil temperature, surface displacement, and time in ZK1(from road shoulder 131 m), ZK2(from road shoulder 33 m), ZK3(road shoulder) of the K178+530 section. In Figs. 51.8 and 51.9, the slope angle of the K178+530 section is 8°. Rain and the shallow groundwater outcrop provide adequate water to the slope shallow layer, hampered by the lower confining layer. When water content in the shallow layer is too high, soil movement occurs along the top surface of the impermeable layer. The slides begin during the spring thawing period and stop after the autumn rainfall period. The slip rate in the rear

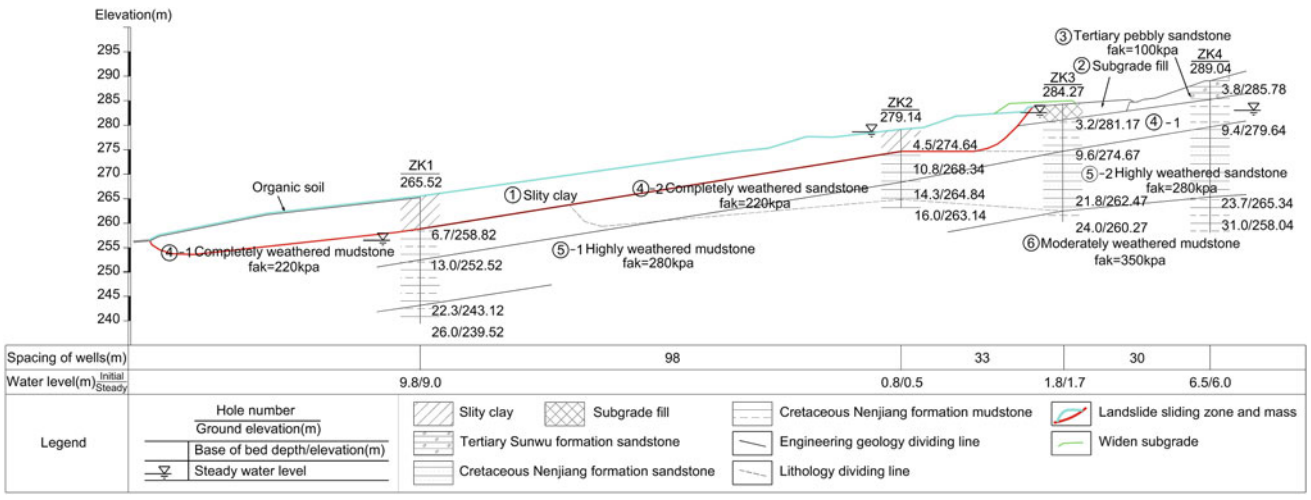

Fig. 51.8 Landslide geological profile and arrangement diagram of monitoring equipment (K178+530 section)

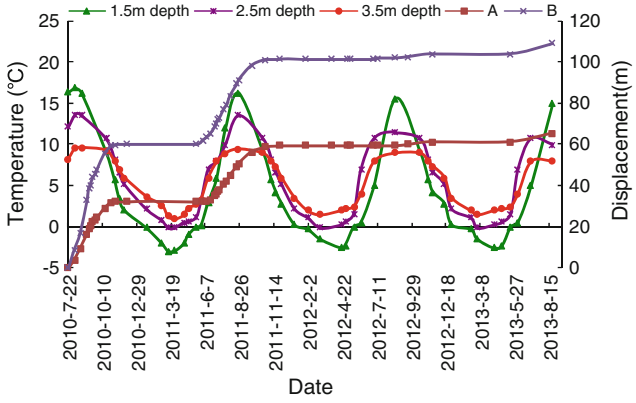

Fig. 51.9 Relationship curve between soil temperature, surface displacement and time in K178+530 section

is much higher than the front. These intermittent landslides have low gradients.

51.6 Conclusions

Topography in high latitude permafrost regions of Northeast China plays an important role in permafrost distribution. With the accelerated process of global climate change, the road area of the Bei'an to Heihe Expressway through Lesser Khingan Mountain has experienced a warming trend. The annual average temperature in the region is rising, not only resulting in permafrost degradation, but also as a result of permafrost degradation.

Permafrost degradation in high-latitude permafrost regions of Northeast China has profound impacts on the regional geological environment, while changes in the engineering geological conditions lead to engineering geological disasters.

Uneven settlement of the roadbed, seasonal salutatory flow ice in the road area, and shallow landslides in the Bei'an to Heihe Expressway through the Lesser Khingan Mountain are not only influenced by geological structure in this region, but also by the changes in the geological conditions. Therefore, changes in the geological environment are the main reason for engineering geological problems.

Acknowledgement This work was financially supported by the key science and technology project of Heilongjiang Communications Department "Study on Subgrade Stability Controlling Technology of Expressway Expansion Project Permafrost Melt and Landslides Sections" (2011318223630).

References

Chang XL, Jin HJ, He RX (2013) Review of permafrost monitoring in the northern Da Hinggan Mountains, Northeast China. J Glaciol Geocryol 35(1):93–100

Chen LX, Zhou XJ, Li WL et al (2004) Characteristics of the climate change and its formation mechanism in China in last 80 years. Acta Meteorologica Sinica 62(5):634–646

Cheng GD (2003) The effects of local factors on permafrost distribution and its revealing of Qinghai-Tibetan railroad design. Sci China, Ser D 33(6):602–607

Ding YH, Ren GY, Shi GY et al (2006) China's national assessment report of climate change (I): climate change in China and the future trend. Adv Clim Change Res 2(1):3–8

Guo DX, Liu TL, Zhang WX (1998) Permafrost Institute, Siberian branch. USSR Academy of Sciences. General geocryology. Science Press, Beijing

He W, Bu RC, Xiong ZP et al (2013) Characteristics of temperature and precipitation in Northeastern China from 1961 to 2005. Acta Ecologist Sinica 33(2):519–531

Lin XC, Yu SQ, Tang GL (1995) Series of average air temperature over China for the last 100-years period. Chin J Atmos Sci 19(5):525–534

Ren GY, Guo J, Xu MZ et al (2005) Climate changes of China's mainland over the past half century. Acta Meteorologica Sinica 63(6):942–956

Shi N, Chen JQ, Tu QP (1995) 4-phase climate change features in the last 100 years over China. Acta Meteorologica Sinica 53(4):431–439

Solomon S (2007) Climate Change 2007: the scientific basis/Contribution of Working Group I to the forth assessment report of the intergovernmental panel on climate change. Cambridge University Press, Cambridge

Wang SW (1994) Diagnostic studies on the climate change and variability for the period of 1880–1990. Acta Meteorologica Sinica 52(3):261–273

Wang SW, Ye JL, Gong DY et al (1998) Construction of mean annual temperature series for the last one hundred years in China. Q J Appl Meteorol 9(4):392–401

Zhou YW, Guo DX, Qiu GQ (2000) Geocryology in China. Science Press, Beijing

Zuo HC, Lü SH, Hu YQ (2004) Variations trend of yearly mean air temperature and precipitation in China in the last 50 years. Plateau Meteorol 23(2):238–244

The Deformation Monitoring of Superficial Layer Landslide in the Northern Part of Lesser Khingan Mountains of China

52

Zhaoguang Hu, Wei Shan and Hua Jiang

Abstract

In recent years, permafrost in the northeast of China is being severely degraded. Bei'an-Heihe Expressway crosses northwest part of the Lesser Khingan Range region. The landslide is located in an area of the island's permafrost. Due to atmospheric precipitation, the presence of permafrost, regional climate conditions, and special geological conditions, landslides occur annually from late May to early November. The area is in a relatively stable state during winter. These seasonal landslides have seasonal, gradual, low angle characteristics. By November 2012, the studied landslide had moved a distance of up to 104.15 m (in the rear), and 24.8 m (at the leading edge). With cumulose soil at rear of landslide decreasing, and the recorded movement of the landslide over time, the landslide deformation appears to show an apparent attenuation trend. This article combines a geological survey and over 2 years of monitoring surface deformation and soil geothermal changes. Research results show that: water infiltration of rainfall, melting snow and permafrost melting is stopped by frozen soil and impermeable barriers, leading to local moisture content rapidly rising, water erosion along interface between the permeable layer and water-resisting layer forms the sliding surface. Sliding velocity of the landslide is large different in different seasons. Within the same cross section of landslide, the sliding displacement of center is largest, and near landslide flank is smallest.

Keywords

High latitude permafrost • Landslide • Deformation monitoring • Freeze-thaw action

52.1 Foreword

Landslides are natural phenomena; the rock and soil on slopes are affected by river scour, groundwater activity, earthquakes, artificial cutting of the slope, and other factors, under the action of gravity (He 1991; Qiao 2002; Gu et al. 2009). Landslides are common along highways constructed in mountain areas due to their geology, geomorphology, hydrology, and climatic conditions. Landslides frequently interrupt the flow of traffic along mountainous expressways (Li et al. 2003; Ma et al. 2006; Liu et al. 2007).

At present, research on the characteristics of the formation of mountainous landslides at high latitudes in the Lesser Khingan Range of Heilongjiang province is in its infancy (Shan et al. 2008). This article combines the results of a geological survey over 2 years that monitored surface deformation, slope soil geothermal changes with the effects of the landslide itself. Large scene surveys such as this can provide precious information on the landslides that occur at high latitudes in permafrost areas; aiding disaster control and evaluating the optimal artificial slope required to prevent landslides in prone areas along highways.

Z. Hu (✉) · W. Shan · H. Jiang
Institute of Cold Regions Science and Engineering, Northeast Forestry University, Harbin, 150040 China
e-mail: huzhaoguang008@163.com

G. Lollino et al. (eds.), *Engineering Geology for Society and Territory – Volume 1*,
DOI: 10.1007/978-3-319-09300-0_52,

52.2 Regional Natural Geographical Conditions

The geographic position of the study area is shown in Fig. 52.1. The landslide of interest is located in the central region of the Lesser Khingan Range, China. Spring in the study area is brief, warming quickly followed by summer, which is hot and rainy. With the onset of autumn, temperature fall rapidly and the short season leads into, winters that are cold and long. The annual average temperature in the area is −0.8 °C. The average annual precipitation is 510–572 mm. Rainfall is concentrated in the months of July to September, and accounts for about 60 % of total annual precipitation. The first snow is generally in the last third of October; the last snow is generally at the end of March or early April. During winter, the maximum seasonal frozen depth is 2.30–2.50 m below the ground. The geomorphology of the study area is mainly dominated by low mountains and hills; topographic relief is large in the high latitude permafrost region (Hu and shan 2011).

K178+530 is located on the left-hand side of the road embankment. Road abandon soil and subgrade filling soil slide along the gully. The 178+530 landslide presents a tongue shape, and its width is 20–30 m, its acreage is about 5,000 m^2, the distance from toe to rear edge is about 200 m, the elevation of toe is 254 m, and the elevation of rear edge is 285 m. The leading edge of the landslide pushes up humus soil of the original ground surface, which consequently slides forward. The arcuate dislocation in the rear edge was in the range of the wider subgrade. There, the trees tilt at the leading edge of the landslide. The landslide scene photos are shown in Fig. 52.2.

52.2.1 Geology of the Study Area

In order to gain insight into the subsurface character of the landslide, we conducted a drilling exploration, drilling four holes, the depths of these drill holes ranged from 14 to 26 m, and their arrangement is shown in Fig. 52.3.

In the research section, the soil distribution is listed as follows: Quaternary loose sediment, Tertiary pebbly sandstone, Cretaceous mudstone, and sandstone (Fig. 52.3). Subgrade filling soil or road construction waste is yellow and waterlogged; it comprises mainly loose material including Tertiary pebbly sandstone, Cretaceous mudstone, and sandy mudstone. Clay in the soil is yellow, soft, and plastic when saturated, and tough and strong when it is dry. Silty clay is located at depths of 1.5–3.8 m in upper section of the landslide, and at depths of 0–6.7 m in the middle to lower sections. More than one intercalated sand layers exist within the silty clay layer; the thickness of a single sand

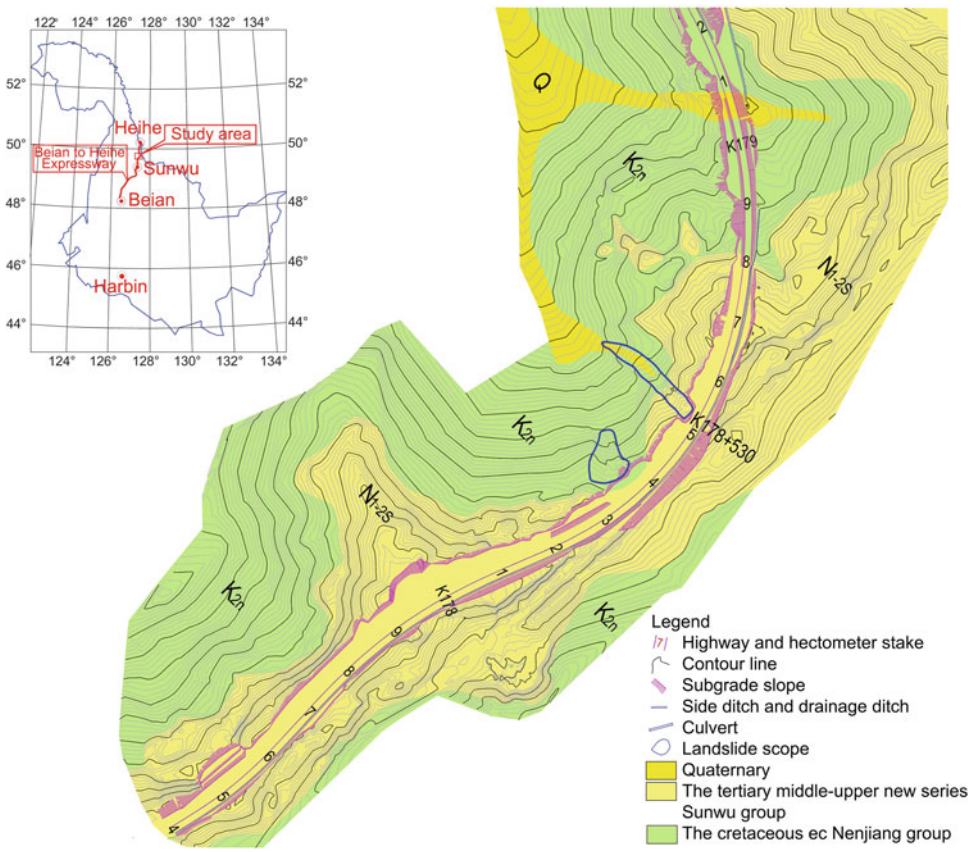

Fig. 52.1 Geographical position of the K178+530 landslide shown on a topographic and geological composite map

Fig. 52.2 Landslide scene photos: (*1*) Panoramic view of landslide; (*2*) The trailing edge of landslide; (*3*) The leading edge of landslide

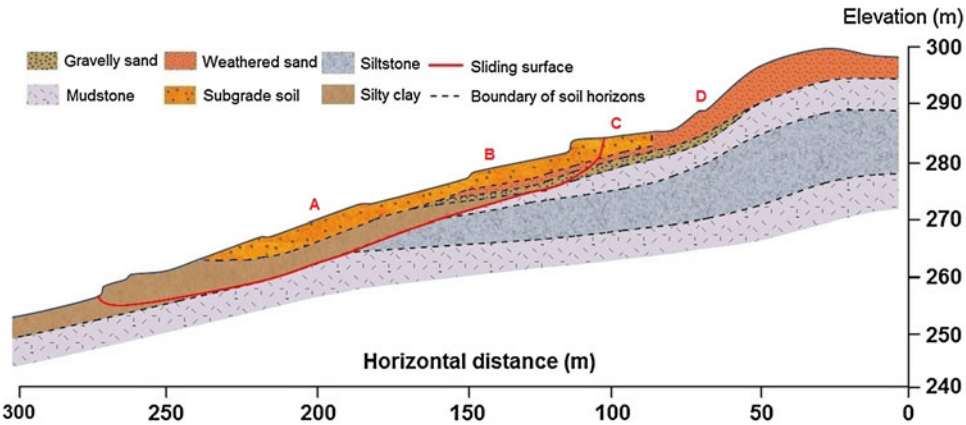

Fig. 52.3 Geological cross section of K178+530

layer is ranges from 1–10 cm. The presence of these sand layers greatly increases the permeability of the soil. Tertiary pebbly sandstone is located at depths of 3.8–4.5 m on the upper sector of the landslide. The components of the pebbly sandstone include large clasts and sand minerals. The layer is weathered, slightly wet, and unconsolidated with loose sand and good gradation, with good water permeability. The weathered siltstone is yellow in colour and is located at depths of 4.5–14.3 m at the upper sector of the landslide. The siltstone has a sandy structure with bedding and poor water permeability. The weathered mudstone is yellow or black-grey and it has a muddy and layered structure, poor water resistance, and poor water permeability. The strongly weathered mudstone is unconsolidated, black-grey with a layered and muddy structure. The moderately weathered mudstone is brown and black-grey with a muddy and layered structure.

52.2.2 Factors Influencing the Formation of Landslides

The formation and development of the K178+530 landslide is mainly influenced by topography, geology, hydrology, climate, specific geography, intense freeze-thaw erosion, and human engineering activities.

During the rainy season and the thawing period in spring, landslides are particularly feasible. Tympanites cracks on the landslide are beneficial to permeate and stockpile. Highly permeable surface soil, grit, and silty clay provide

passage for water infiltration. The infiltration capacity of the lower mudstone and siltstone is very small, forming an impermeable layer. The infiltration of rainfall, snowmelt water, fissure water, and thawed frozen soil are cut off by frozen soil and the lower impervious layer in the process of infiltration. This impedance to the flow of groundwater is the main cause of landslides in the area. The landslide first began moving in late July 2010.

Freezing and thawing have far-reaching consequences for the movement of the landslide; they induce intermittent sliding resulting in drumlins.

52.3 GPS Monitoring Deformation of the Landslide

On September 13, 2010, two deformation monitoring pipes and sensors on the landslide body were bored at respective depths of 4.2 and 6.5 m. We employed GPS to monitor movement of the landslide by arranging nearly 49 GPS gauge piles at different positions on the landslide (Fig. 52.4).

From the rear edge of landslide to the leading edge, we arranged 11 rows of gauge piles on both sides of the outside of the landslide, as well as at the centre of the top and close to the rear edge of the landslide. The distance from the first row to the rear edge of the landslide is 15 m and gauge numbers run from 1–3 (left to right). The distance from the second row to the rear edge of landslide is 30 m, and from the third row to the seventh row to the rear edge of landslide is 50, 70, 93, 119, and 134 m, respectively. The rest of the gauge piles are distributed along the leading edge of the landslide. These GPS monitoring piles can monitor the sliding conditions at the proximal, middle, and distal sections of the landslide, as well as laterally across it. Data collection was conducted from September 13, 2010 to November 16, 2012, a total of 793 days in total.

Figure 52.5 shows the first row of gauge piles to slide in the study area. From September 13, 2010 to November 2010, 1#, 2#, and 3# gauge piles were displaced by 6.90, 8.05, and 4.12 m, respectively. In early June 2011, the landslide began to activate again, and by July 1, 2012, sliding displacements of 1#, 2# and 3 gauge piles was 48.03, 68.08, and 24.63 m, respectively (in 658 days of monitoring). In the middle of the landslide body, the slip rate in a central location (2# gauge pile) exhibited a higher slip rate than nearer to the edge (1# and 3# gauge piles).

From the longitudinal section in the centre of the landslide (Fig. 52.6) we observed that from September 13, 2010 to September 25, 2011, the gauge pile displacement from the first row to the seventh row, respectively, are 65.01, 71.31, 64.20, 54.23, 46.37, and 39.43 m. This slide displacement is different for the different gauge pile positions at the same time. Sliding displacement of the middle and upper sections is the greatest.

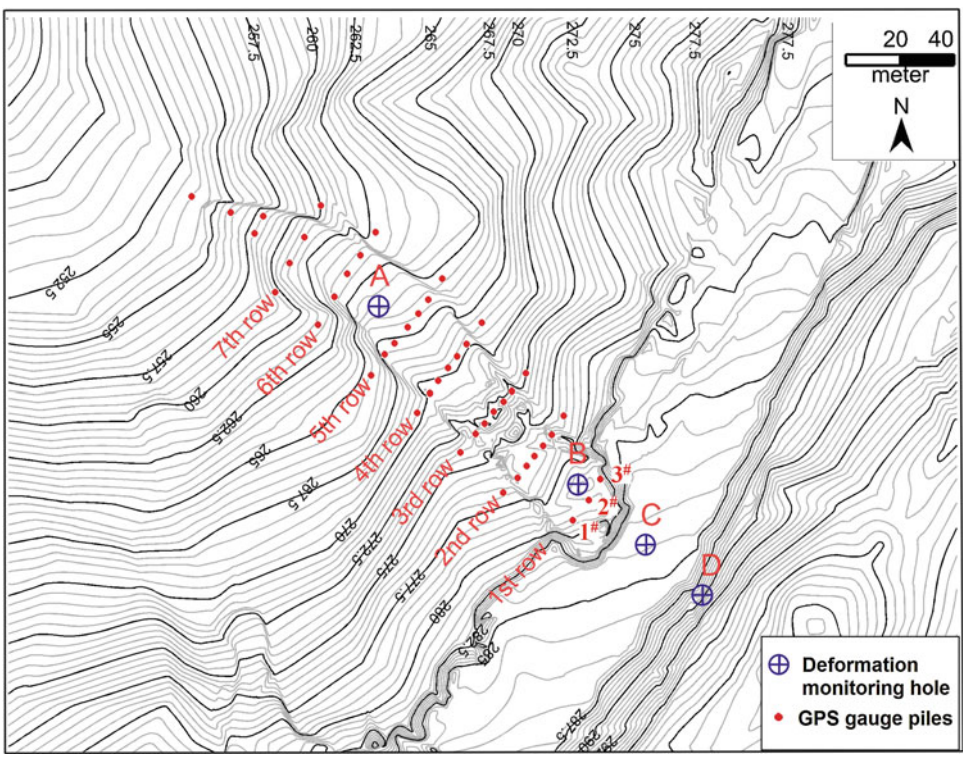

Fig. 52.4 The layout of GPS gauge piles along the landside

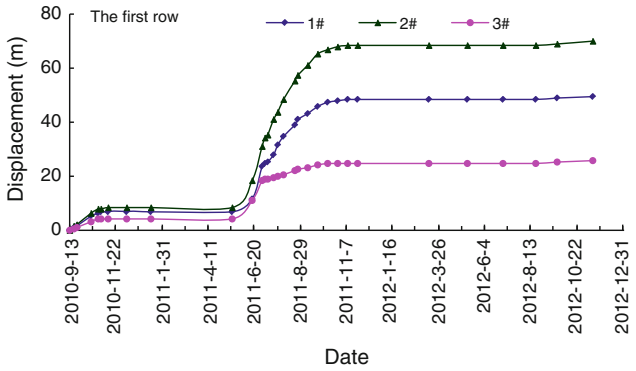

Fig. 52.5 The first row of gauge piles to slide are shown on this displacement graph

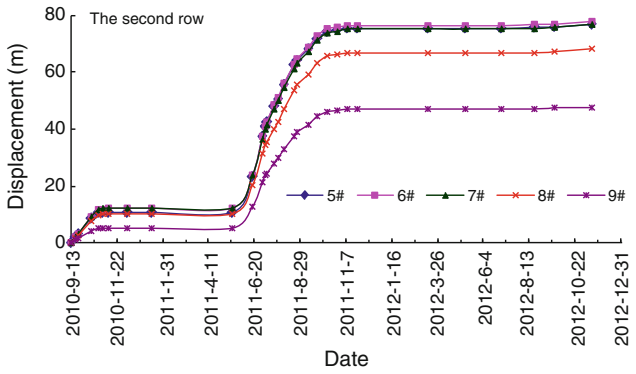

Fig. 52.6 Sliding-displacement graph showing the second row of gauge piles to start moving

52.4 Conclusions

(1) The landslide is superficial, occurring parallel to bedding. water infiltration of rainfall, melting snow and permafrost melting is stopped by frozen soil and impermeable barriers, leading to local moisture content rapidly rising, water erosion along interface between the permeable layer and water-resisting layer froms the sliding surface.

(2) The landslide is located in an area of the island permafrost. Due to atmospheric precipitation, the presence of permafrost, regional climate conditions, and special geological conditions, landslides occur annually from late May to early November. The area is in a relatively stable state during winter. These seasonal landslides have seasonal, gradual, low angle characteristics.

(3) Landslide displacement occurs at different rates in different sections, as shown by bedding plane displacement. Within the same cross section of the landslide, the sliding displacement in the centre is largest and the sliding displacement near the flanks is smallest. The trailing edge of the landslide creeps continuously towards the road, increasing the hazard that this erosional feature poses to commuters.

Acknowledgments This work was financially supported by Heilongjiang Communications Department project, and it is a subtopic of the western communication science and technology project "Study on Subgrade Stability Controlling Technology of Expressway Expansion Project Permafrost Melt and Landslides Sections" (2011318223630).

References

Gu TF, Wang JD, Lu X et al (2009) Characteristics and stability analysis of accumulations landslide No. 3 in Tuoba of Southeast Tibet. J Nat Disasters 18(1):33–38

He YX (1991) Application of D.C. electric sounding for the permafrost exploration along Xinjiang-Xizang highway. J Glaciol Geocryol 13(3):255–260

Hu ZG, Shan W (2011) Application of geological drilling combined with high-density resistance in island structure permafrost survey. In: The International conference on electronics, communications, and control, ICECC2011-proceedings: 1898–1904

Li TL, Zhao JL, Li P (2003) Analysis on the characteristics and stability of the No. 2 landslide of 102 landslide group on Sichuan-Tibet highway. J Catastrophol 18(4):40–45

Liu LH, Zhu DY, Liu DF (2007) Discussion on multiple solutions of safety factor of a slope. Rock Soil Mech 28(8):1661–1664

Ma LF, Niu FJ, Yang NF (2006) Analysis on ground temperature changes and landslide process of thaw slumping in permafrost regions. Hydrogeol Eng Geol 3:53–56

Qiao JP (2002) Structure and shape of landside. Chinese J Rock Mech Eng 21(9):1355–1358

Shan W, Liu HJ, Yang L et al (2008) Study of regularity of variation of water content in shallow layer of soil road cutting slopes in seasonally frozen-ground region. Rock Soil Mech 29(sup.):335–340

Permafrost Distribution Research Based on Remote Sensing Technology in Northwest Section of Lesser Khingan Range in China

53

Chunjiao Wang, Wei Shan, Ying Guo, Zhaoguang Hu and Hua Jiang

Abstract

Lesser Khingan mountain, located in China, whose northwest section range is near the southern permafrost boundary. In order to study regional surface temperature change, permafrost degradation law and conduct in-depth study of its impact mechanism, using Landsat ETM+imagery as data sources, applying the method of remote sensing thermal infrared, two surface temperature maps have been obtained in study area, the initial permafrost distribution map is formed through ArcGIS software. By analysis of elevation, aspect and slope distribution, the initial permafrost distribution map accordant with on-site investigations and geophysical survey results, which show a clear "Khingan–Baikal type" permafrost features. The research shows that the permafrost distribution maps generation from the Landsat ETM+data by ground temperature inversion in study area can assist permafrost degradation mechanisms research and relative disaster research.

Keywords

Permafrost distribution • Remote sensing technology • Lesser khingan

53.1 Introduction

On a global scale, China northeast permafrost zone is one of the most significant impact zone affected by climate warming and human activities in the world. In recent decades, regional permafrost degradation is significant, and its main natural causes are due to global warming, especially winter warming, precipitation, snow periods, thickness and other factors related to climate change (He and Jin 2009). Permafrost degradation exacerbation also poses a threat to the safety of human structures, landslides, thaw settlement and other disasters often happened. Local permafrost distribution study has a great significance to the study of permafrost degradation rule and early warning of induced geological disasters.

Northeast permafrost area terrain are mainly with hills and mountains, they are not high altitude but high latitude, and with the Siberian High pressure impact, the area become the coldest natural areas in China (Zhou and Guo 1982). In the northeast of China, high latitude permafrost zone mainly develops "Khingan–Baikal type", the permafrost is more development and with greater thickness in low-lying areas. Their degradation process is begin with the sunny slope, high area and the hill top, then to shady slope, low area and the hill bottom (Shan and Jiang 2013).

LST is a good indicator of the energy balance at the Earth's surface and the so-called greenhouse effect because it is one of the key parameters in the physics of land-surface processes on a regional as well as global scale. It combines the results of surface-atmosphere interactions and energy fluxes between the atmosphere and the ground (Mannstein 1987).

C. Wang (✉) · W. Shan · Y. Guo · Z. Hu · H. Jiang
Institute of Cold Regions Science and Engineering, Northeast Forestry University, Harbin, 150040 China
e-mail: zlj_832008@126.com

W. Shan
e-mail: shanwei456@163.com

G. Lollino et al. (eds.), *Engineering Geology for Society and Territory – Volume 1*,
DOI: 10.1007/978-3-319-09300-0_53,

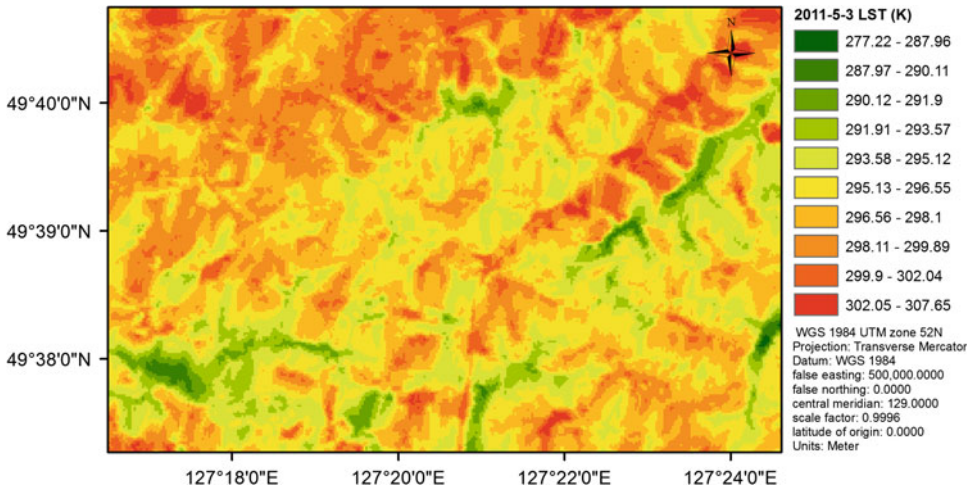

Fig. 53.1 May 3, 2011 Temperature inversion results

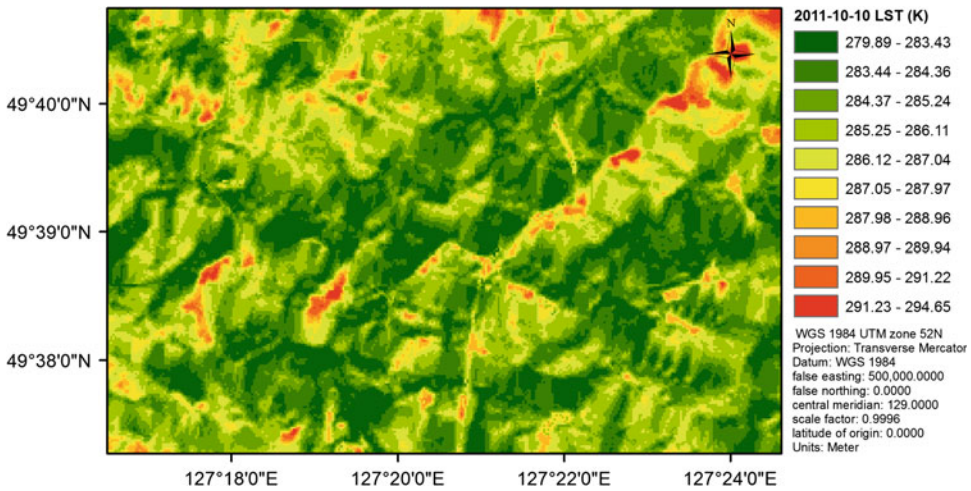

Fig. 53.2 October 10th, 2011 Temperature inversion results

With the development of satellite detection system, different types of sensors can obtain a variety of information related to the Earth's surface and remote sensing as an important method of earth observation make it possible to use thermal infrared remote sensing technology to inverse the surface temperature data. Thermal infrared remote sensing is closely related to the thermal condition of the earth's surface and the entire system. Surface heat status information is associated with many important phenomena and processes (Zhang 2009).

In this paper, May 3, 2011 and October 10, 2011 of two LANDSAT ETM+Remote Sensing Imageries are used, according to radiative transfer equation method to inverse regional surface temperature. ENVI software is used to read data, and conducting radiometric calibration, regional cropping, calculating ground surface emissivity and blackbody radiation brightness values in the thermal infrared band, using Planck equation inverse the surface temperature distribution. Two scenes are calculated through ArcGIS data. The initial formation of permafrost distribution map in study area classified by ground temperature.

53.2 Method

Surface temperature inversion are conducted with Radative Transfer Eqation (RTE) method: using two Landsat ETM+imageries to conduct land surface temperature inversion, data acquisition date is 20110503, 20111010.

Vegetation coverage F_v is obtained by the use of mixed pixels decomposition method, the entire imagery was divided into water, vegetation and buildings. According to the experience of the previous research, the remote sensing image is divided into three types: water, towns and natural surface, water emissivity is 0.995, the estimation of Natural surface and town's emissivity can be calculated respectively.

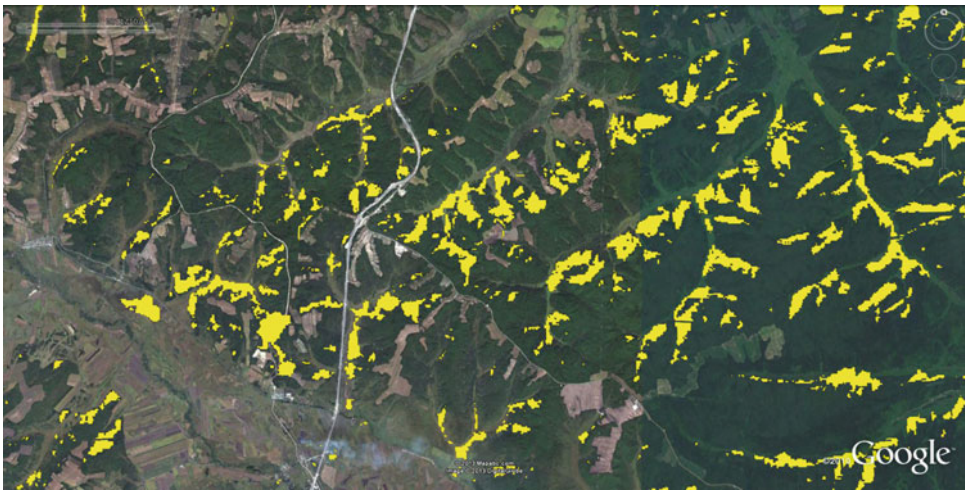

Fig. 53.3 The distribution map of high upper limit of permafrost

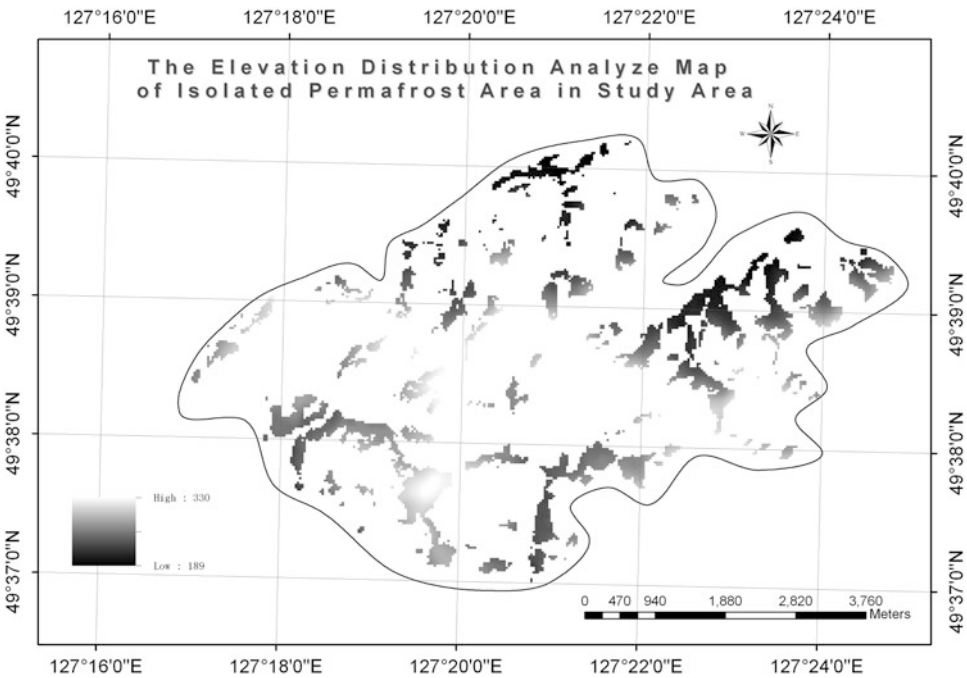

Fig. 53.4 The elevation distribution analysis map of isolated permafrost area in study area

The thermal infrared radiation brightness value L_λ received by Satellite sensor consists of three parts: the atmospheric upwards radiation brightness $L\uparrow$energy received from the ground radiation brightness after pass the atmosphere, the energy when atmospheric radiated downward and reflected after reaching the ground. Thermal infrared radiation brightness value received by satellite sensor can be written as (radiative transfer equation):

$$L_\lambda = [\varepsilon \cdot B(T_s) + (1-\varepsilon)L\downarrow] \cdot \tau + L\uparrow \tag{53.1}$$

ε is the surface emissivity, T_s is the ground surface temperature, $B(T_s)$ is the blackbody thermal brightness value under T_s, τ is atmospheric transmittance in thermal infrared band. Radiation brightness $B(T_s)$ of blackbody in thermal infrared band is:

$$B(T_s) = [L_\lambda - L\uparrow - \tau \cdot (1-\varepsilon)L\downarrow]/\tau \cdot \varepsilon \tag{53.2}$$

After get the Radiation brightness of blackbody in thermal infrared band, according to inverse function of Planck formula, calculated the ground surface temperature T_s:

$$T_s = K_2/\ln(K_1/B(T_s) + 1) \tag{53.3}$$

Temperature inversion results displayed in ArcGIS shown in Figs. 53.1 and 53.2.

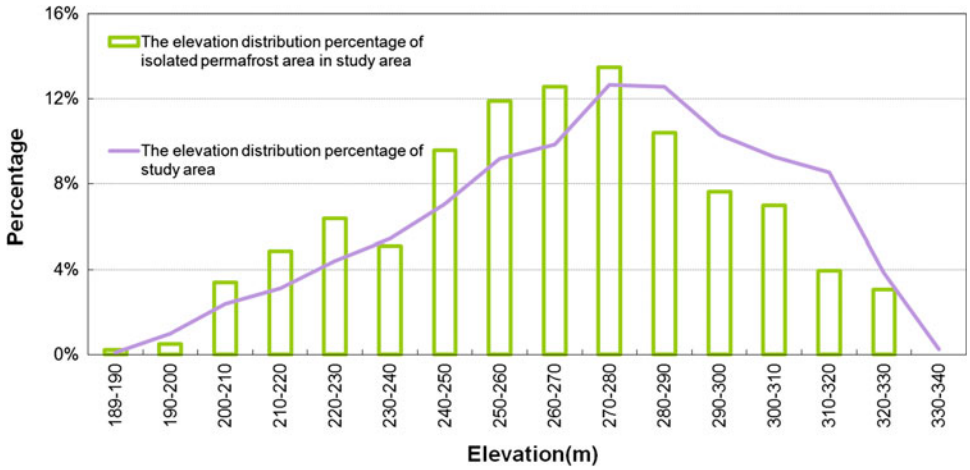

Fig. 53.5 The elevation distribution contrast map of study area and isolated permafrost area in study area

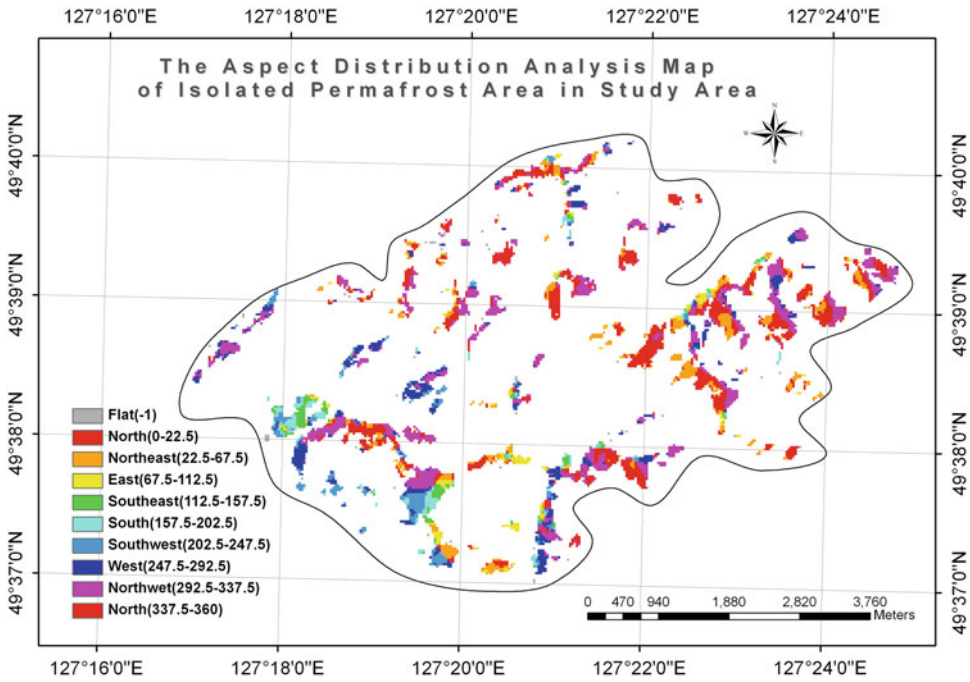

Fig. 53.6 The aspect distribution map of study area and isolated permafrost area in study area

53.3 Results and Discussion

The results of the temperature inversions were putted into ArcGIS to classify the results, through human-computer interaction style in order to find the coldest area in both two maps, and overlay the results on satellite imagery for June 15, 2004. As shown in Fig. 53.3. This map shows the upper limits of permafrost distribution which are consistent with field survey results.

Choosing the permafrost intensive distribution areas, analyzing the distribution rule of height, aspect and slope in research area and isolated permafrost area among research area, classification analysis are conducted between DEM in research area and DEM of isolated permafrost area in study area (Fig. 53.4), obtaining the elevation distribution contrast map of study area and isolated permafrost area in study area (Fig. 53.5). According to analyzing: the study area elevation range is 189–335 m, average value is 273.37 m, the permafrost area in study area elevation range is 189–330 m, average value is 265.57 m, the differs of average height is 7.8 m.

Based on DEM, the aspect and slope distribution map are compared (Figs. 53.6 and 53.7), the aspect distribution contrast analysis map of study area and isolated permafrost area in study area (Fig. 53.8) shows that: permafrost in the study area distributed significantly in north and northwest

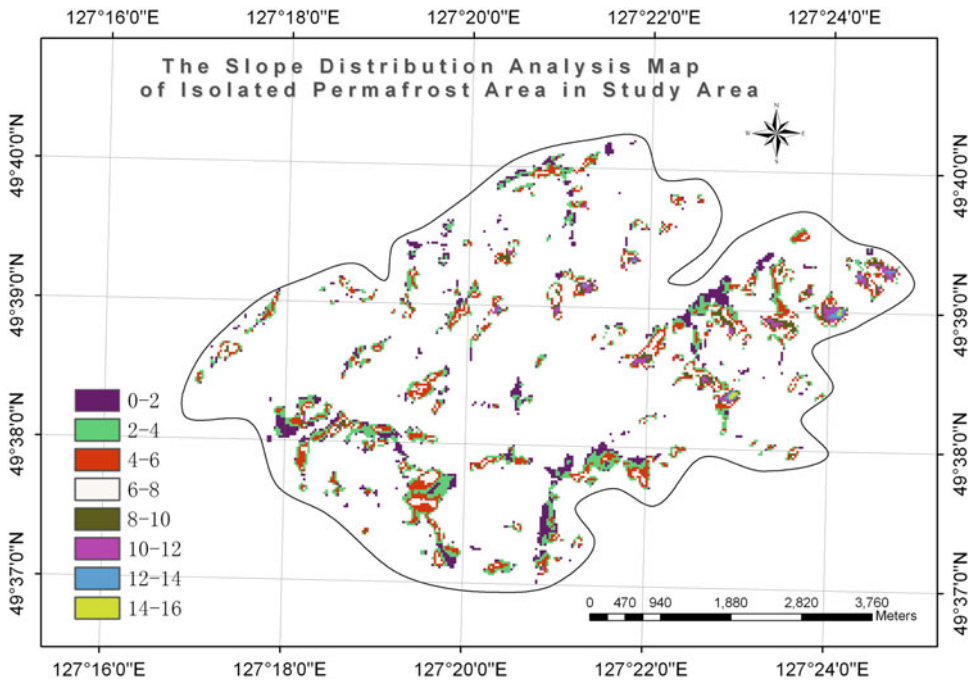

Fig. 53.7 The slope distribution map of study area and isolated permafrost area

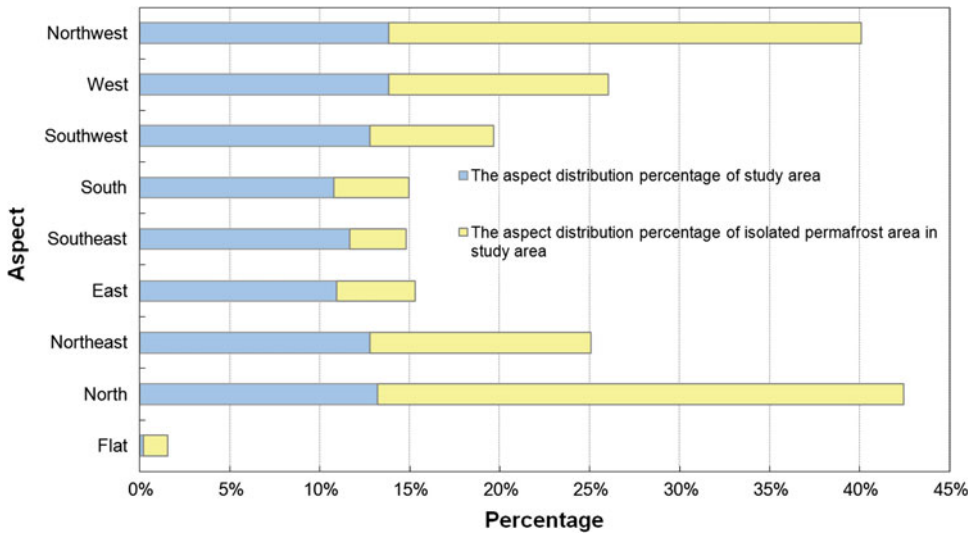

Fig. 53.8 The aspect distribution contrast analysis map

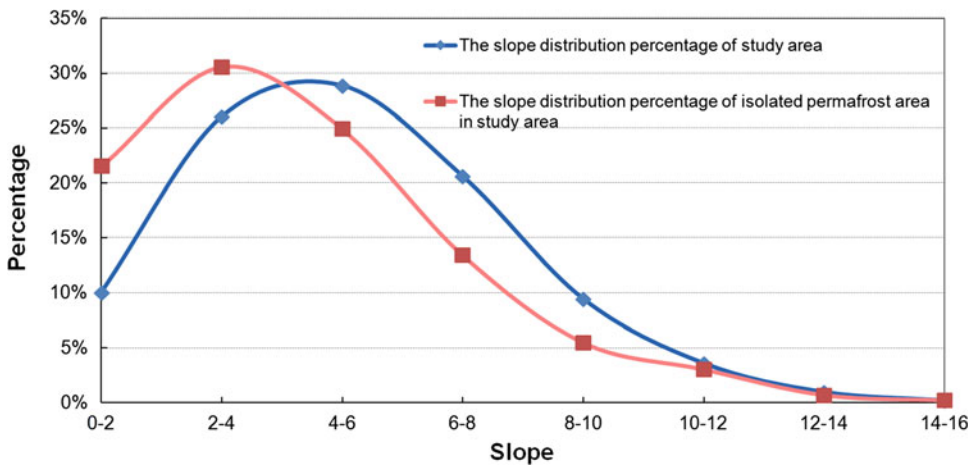

Fig. 53.9 The slope distribution contrast analysis map

aspect, accounting for an area of 29.2 and 26.3 %, totally accounting for 55.5 % of the study area, this confirmed the fact that regional permafrost distribution in shady slope is greater than sunny slope. From the slope distribution contrast analysis map of study area and isolated permafrost area in study area (Fig. 53.9). In the interval 0–2°, permafrost distribution is significantly greater than the distribution proportion of the study area, In the interval 2–4° permafrost distribution ratio is slightly larger than the study area, which in consistence with the characteristic that is permafrost are always located in low-lying and toe position. The data analysis results show that the permafrost distribution presents a clear permafrost feature of "Khingan–Baikal type". It confirmed the reliability of permafrost distribution map.

53.4 Conclusion

Based on LANDSET ETM + remote sensing data source, applying the thermal infrared remote sensing methods for surface temperature inversion and further calculating by ArcGIS, combining RS and GIS technology, which can obtain preliminary permafrost distribution in study area. Distribution map is agreeable with investigation and geophysical survey results, showing a clear "Khingan–Baikal type" permafrost features, which have great significance to the study of permafrost degradation law and early warning for its induced geological disasters. The refinement of initial permafrost distribution map is the future work direction.

References

He R, Jin H (2009) Permafrost degradation and the Cause in northern part of Northeast China. Glaciol Cryopedol 31(5):829–834

Mannstein H (1987) Surface energy budget, surface temperature and thermal inertia, in remote sensing applications in meteorology and climatology. In: Vaughan RA, Reidel D (eds) NATO ASI Ser C: Math Phys Sci, vol 201. A Reidel Publishing Co., Dordrecht, pp 391–410

Shan W, Jiang H (2013) Occurrence Mechanism and Movement Characteristics of Landslides in Bei an to Heihe expressway Area in China under the climate change. Landslide in cold regions in the context of climate change. Springer, Germany, pp 23–37

Zhang R (2009) Quantitative thermal infrared remote sensing model and ground-based experiments. Science, Beijing, p 533

Zhou Y, Guo D (1982) The main features of permafrost in China. Glaciol Cryopedol 4(1):1–19

Engineering-Environmental Problems of Exploration of Mineral Resources Deposits in Conditions of Permafrost and Climate Changing

54

Sergey Tataurov

Abstract

Last decades objectively showed the degree of danger of climate changes, for the environment, as well as for technosphere of the Earth. The cryosphere's territory takes special attention which owing to the specifics is the most vulnerable for changes of climate parameters. As a result we quite often observe a development of engineering-geological processes, accompanied with deconstruction of stability of engineering constructions, which are also used for accumulation and storage of industrial wastes. It leads to pollution of natural ecosystems, including, soil and natural watercourses, infection, deterioration of medical, biological and social situation. Regarding this, the report presents some information on storage of industrial wastes and considers possible ways of solution of this issue. Concretely it proposes the necessity of carrying out of a number of activities such as division into districts of the territories of placement of industrial wastes, elaboration of systems of continuous monitoring of their state, as well as proper use of utilization and neutralization of wastes based on specific features of permafrost.

Keywords

Permafrost • Climate • Tailings storages • Toxic substances • Ecosystem

54.1 Introduction

In these circumstances, the problem of storage and disposal of mining waste becomes more urgent. The reason for this is not only increase in production and processing of mineral resources and high depreciation of engineering and hydro-technical structures—storages of solid and liquid phases of mining and processing industrial wastes (tailings storages, sumps, etc.), but also current the observed global and regional climate change. It should be noted that hazardous geological engineering processes, which could damage these technogeneous facilities, can occur as a result of smooth changes of temperature on the planet, and also due to abrupt climate and weather fluctuations at the regional level—showers, heavy frosts and droughts, snowstorms, etc.

Such example is the flood on the Far East and North-East of Russia in 2013, which reaffirmed the need for a clear program for prevention of civil and industrial facilities from disasters. This applies particularly to the development of extreme weather conditions in a sufficiently short time interval from a few days to 2–3 months. Such scenario was typical for most water facilities of the Amur basin in August–September 2013. According to the Russian Hydrometeorological Center, just in 1 day fell up to 140 mm of rainfall. As a result, the water level in the Amur exceeded the "overall record" of 1913 and rose by more than 8 ft above flood level.

S. Tataurov (✉)
Sergeev Institute of Environmental Geoscience of the Russian Academy of Science, Ulansky Pereulok 13, Building 2, P.O.Box 145, 101000 Moscow, Russian Federation
e-mail: tataurovsb@gmail.com

G. Lollino et al. (eds.), *Engineering Geology for Society and Territory – Volume 1*,
DOI: 10.1007/978-3-319-09300-0_54,

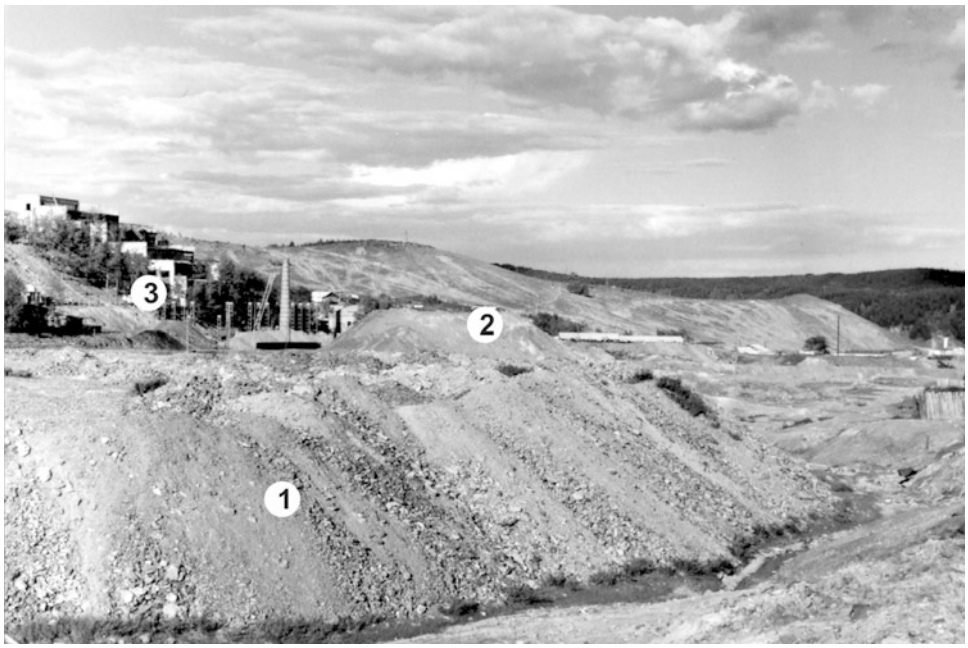

Fig. 54.1 Darasun gold deposit (Eastern Transbaikalia): overburden rocks (*1*)scoria oxidizing roasting (*2*), dressing plant of gold-bearing ores (*3*)

54.2 Mining Waste: As a Source of Increased Danger for the Environment

As a result of natural and technogenic factors consequences of chemical, metallurgical and mining industry waste pollution, can be very extensive and cause long-term chemical and biochemical effects on natural ecosystems, including a man at genetic level. For example, the "Minamata disease", which is inherited. The disease was named after a mass poisoning of people in Japan in the area of the Agano and Minamata Bay due to discharges of mercury compounds by some chemical plants. Similar problems are typical for the areas adjacent to the storages of amalgamation waste generated in the process of gold extraction using mercury, the loss of which was truly colossal (Sukhenko 1995; Tataurov 2008).

Given to the fact that such mining dumps could contain millions of tons of waste with heavy metals, cyanide and other harmful chemicals we can only speculate on the extent of the impact of mining waste on the environment.

Another example of such impact of waste on the environment is the tailings storage of Karamkensky mining and metallurgical complex, located in the North-East of Russia, in the upper basin of the River Hasin. This river flows in the meridional direction from the Okhotsk-Kolyma watershed to the Sea of Okhotsk.

During 1977–1994 this plant used annually about 300 tons of cyanide only for gold leaching and for neutralization of waste it was used: polyacrylamide—120 tons/year, lead nitrate—55 tons/year, thiourea—150 tons/year, liquid chlorine—1,400 tons/year, sulfuric acid—450 tons/year, caustic soda—630 tons/year, quicklime—2,500 tons/year, ion-exchange resins—30 tons/year (Glotov et al. 2004).

As a result, after 15 years of exploration of Karamkensky gold-silver deposits more than 5 million tons of tailings have been accumulated. In 2009, as a result of the flood situation and due to the fact that the tailings storage has been in a disrepair state for a long time, the levee of the tailings storage was destructed and it led to leakage of toxic waste into environment.

Similar situation with the storage of different types of mining waste is usually observed in many cases at large and medium-sized mineral deposits. Development of some of them is still in process.

54.3 Types of Mining Waste and Its Impact on the Environment of Permafrost

Technogeneous rock masses have a complex composition and structure, and their properties are significantly different from the traditional concepts of soil. To the main factors effecting the characteristics of technogeneous rock masses it should have to be reffered: the genesis of mineral deposits, mining technology (underground or open-pit mining), and mineral resources processing (physical, physico-chemical, chemical), permafrost and climate conditions, methods of waste disposal.

In open mining the largest share rave technogeneous masses that formed from stripping or off-balance sheet rock. They represent waste heaps which structure is dominated by the coarse fraction of rock fragments larger than 150–200 mm, and with a height of a few tens of meters (Fig. 54.1).

Fig. 54.2 Sludge storage (Darasun gold deposit, Eastern Transbaikalia)

As a result of the impact of cryogenic factors these masses are able to transform into rock glaciers, which in certain conditions can start moving. The main cause of their movement is a change of conditions of permafrost territory, which influence on physical and mechanical properties of frozen soils, and also a technogeneous load of dumps. All this leads to the natural soil move down the hill under the external pressure of coarse rocks dumps that often causes enormous damage to the environment and human activity as well. An example of this process is the technogeneous dump slide "Post 1" on the mountain "Rudnaya" in the Norilsk industrial region (Malorossiyanov 2001).

The other most dangerous types of waste generated with mining and processing of ores are tailings and sludge storage (Fig. 54.2). Depending on the period of exploration, mining and processing methods, they could contain tens of millions of tons of toxic waste, consisting of rock and sand in the form of dispersed particles, as well as of noxious chemical substances used in extraction of valuable components.

High concentrations of chemicals, dispersion of rock less than 100 microns and specific temperature conditions provide special conditions for the development of chemical processes involved in the formation of new chemical compounds in tailings and sludge storage. As a result they create a sort of "chemical reactors" and there it occures a chemical transformation of mineral ore particles and chemicals brought in from outside.

In particular, it was found that the distribution of the concentration of substances in the sequence of technogenic deposits varies within a wide range. In the upper layers of tailings storage the water-soluble salts are accumulated which presence is explained by migration of the capillary and film water to the surface of tailings storage during cyclic freezing—thawing of tailings.

By this one of the main factors involved in accumulation of chemicals are forming ice lenses, which create a shielding surface in sumps with gravitational settling of solids. Furthermore, during ice formation we can see a process of creation of a layer of non-freezing concentrated solutions and of a solid phase at the same time due to a freezing of highly mineralized solutions with formation of a heterogeneous system "ice–solid phase—the concentrated solution." In this case, the non-freezing concentrated solutions form not only a chemically active environment, but they are also actively involved in transportation of chemicals to the surface of tailings storages. This is also evidenced by the results of studies of the Natalka gold mill tailings storage (Magadan Region, Russia), which has more than 7 million tons of waste (Gashtold et al. 2001). During these studies it was found an increase of the amount of ice in tailings storage. It has increased downward a storage slit from 8 to 18 %, and more to this a purity of ice has increased in the same direction as well.

Usually, the sort of technogeneous structures at working industrial plants in conditions of continuous permafrost form taliks of the "non-through" type, which would later form the cryogenic reservoir of toxic elements that is able to exist preserved for a long time at depths not exceeding the thickness of layer of rocks with annual temperature fluctuations.

At the same time, the changes observed in permafrost conditions within the boundary of the southern permafrost zone of East Siberia tell us about its degradation. As a

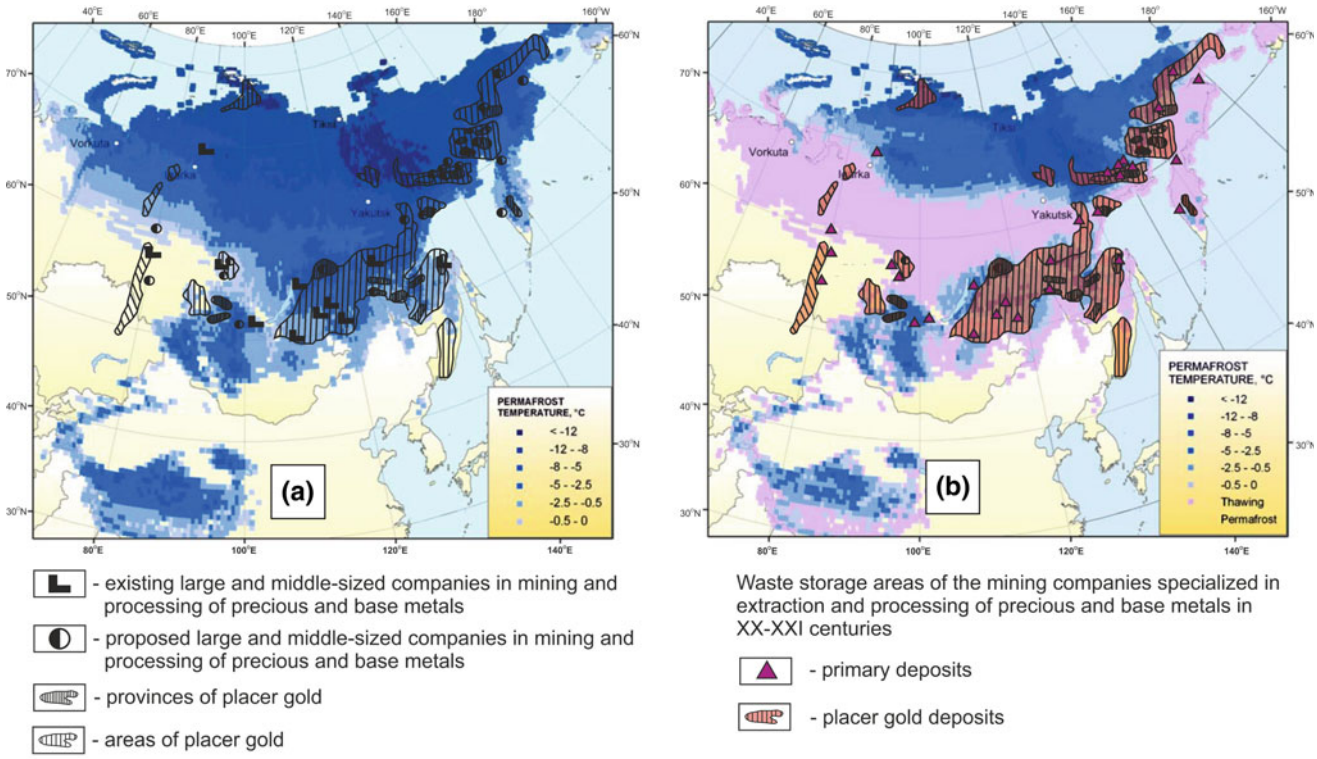

Fig. 54.3 A Schematic map of the existing and proposed tailings of the mining companies in North Eurasia in twenty–twenty first century (based on zoning of Placer Deposits of Russia (Patyk-Kara and Lalerov 1997) and modeled permafrost temperatures in Northern Eurasia) (Romanovsky et al. 2007)

result, within the tailings storages we observe a formation of non-through taliks that after a certain time form a talik "window" due to melting. Consequently, there is a migration of previously conserved hazardous substances for tens of kilometers from the source of infection.

Currently, there are many scenarios of changes in the Earth's climate in the twenty first century (IPCC 2007). Most researchers conclude that in the twenty first century, we can expect a significant increase in growth of global average air and ocean temperatures, as well as in rate of melting glaciers, and global mean sea level. The most warming is expected to occur in high northern latitudes. As a consequence, a map of the thermal state of cryolitosphere will change until the disappearance of a significant part of permafrost zone within southern territories. It is expected that the most significant change in temperature conditions of cryolitozone over the next 100 years will occur in Northern Eurasia (Romanovsky et al. 2007). The result of this will be significant changes in the state of ecosystems through a development of natural and anthropogenic processes including in increase in the cryogenic processes activity accompanied by toxic mine waste releases into the ecosystems of cryolitozone (Fig. 54.3). Experts estimate mining industry waste only in Northern Eurasia in hundreds of millions of tons. Therefore, the scope of environmental pollution can be so severe that it would lead to global consequences for the people of northern and arctic regions.

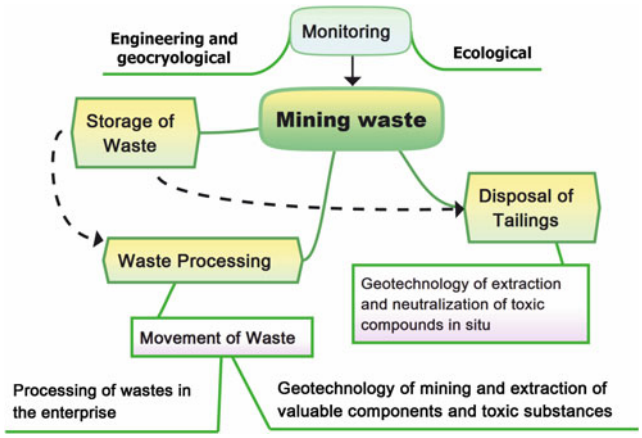

Fig. 54.4 Schematic diagram of the monitoring of mining waste storage and disposal facilities

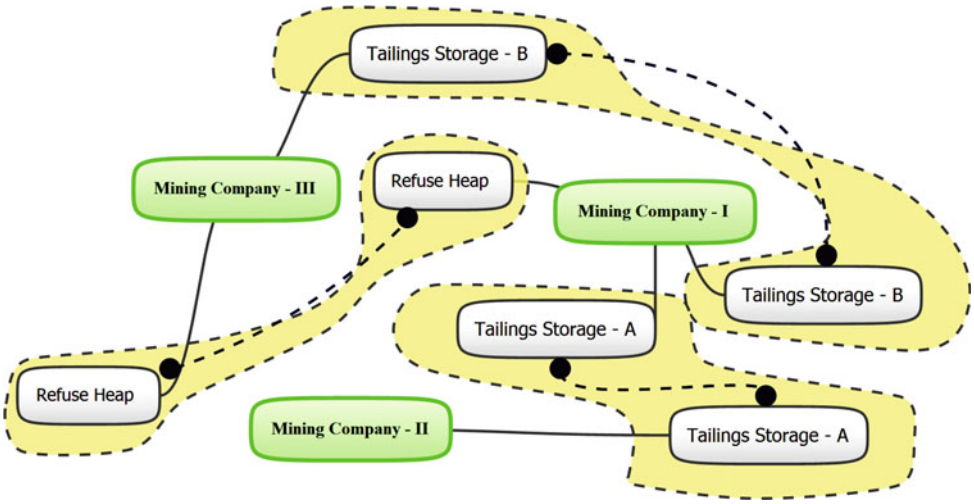

Fig. 54.5 Schematic diagram of a single cluster network for waste disposal facilities

54.4 Conclusion

Solution of engineering and environmental problems in mining industry, namely in accumulation, storage and disposal of mining waste in conditions of permafrost and climate change is one of the most important tasks of environmental protection. This is quite important today, when the accumulated problems of industrial society can pose a serious threat to sustainable development of the post-industrial world. One of the ways out could be a development of an international program on waste which would include monitoring of mining waste storage and disposal facilities (Fig. 54.4). The main tasks on the way out of the problem are the following:

(a) elaboration of new geo-technologies for waste recycling and neutralization based on introduction of environmentally friendly physical, chemical and biochemical processes;
(b) development of unified monitoring system for waste disposal facilities, with a unified classification of danger degree, conditions and methods of storage, disposal and recycling that will help to sort them out into a single cluster network (Fig. 54.5).

These diagrams are an attempt to formulate some main research directions of the state of mining waste and its industrial disposal in permafrost zone and beyond.

References

Gashtold VV, Izoitko VM, Mezhov SV (2001) About the material composition and processing properties of the ore deposits at technogeneous Matrosskaya gold deposit. Miner Process 4:40–43

Glotov VE, Glotova LP, Kobets VI (2004) Geotechnical features and modern geo-environmental conditions of the Karamkensky mining plant tailings storages. Novaya Kolyma 2:10–15

IPCC (2007) Summary for policymakers. In: Solomon S, Qin D, Manning M, Chen Z, Marquis M, Averyt KB, Tignor M, Miller HL (eds) Climate Change (2007) The physical science basis. Contribution of working group I to the fourth assessment report of the intergovernmental panel on climate change. Cambridge University Press, Cambridge, United Kingdom, New York, NY, USA

Malorossiyanov VM (2001) Problems of the transformation of frozen dumps into technogeneous rock glaciers. In: Proceedings of the workshop on the geocryological and geoecological problems of construction in the Far North, Norilsk, p 170

Patyk-Kara NG, Lalerov NP (eds) (1997) Placer deposits of Russia and other CIS countries: mineralogy of placers, geological and commercial types and development of raw material base. Scientific World, Moscow

Romanovsky VE, Sazonova TS, Balobaev VT, Shender NI, Sergueev DO (2007) Past and recent changes in air and permafrost temperatures in Eastern Siberia. Global Planet Change 56:399–413. doi:10.1016/j.gloplacha.2006.07.022

Sukhenko SA (1995) Environmental problems of the use of mercury in the extraction of gold: a review of the World literature. Chem Sustain Dev J 1–2:37–42

Tataurov SB (2008) Transformation and processing of gold-bearing raw materials in conditions of permafrost zone. Gornaya kniga, Moscow

Risk Assessment of Infrastructure Destabilization in Context of Permafrost in the French Alps

55

P.-A. Duvillard, L. Ravanel and P. Deline

Abstract

Due to global warming, high alpine environments are affected by significant changes such as glacial retreat and permafrost degradation. This degradation is thought to be one of the main factors for rock slope instabilities in high mountain areas. Warming permafrost could lead to various risks, including the risk of destabilization of infrastructure (e.g. huts, cable cars, ski-lifts) built on permafrost. In order to assess these risks, an inventory of infrastructure located in permafrost areas in the French Alps has been implemented through a GIS using different layers including a map of potential permafrost distribution. Meanwhile, an index of the risk of infrastructure destabilization has been built to identify and categorize the exposed infrastructure. This risk index allowed 752 infrastructure potentially at risk to be identified among the 1,641 infrastructure located in permafrost areas. Five percent are characterized by a very high risk of destabilization.

Keywords

Risk • Permafrost • Destabilization of infrastructure • French alps

55.1 Introduction

Current permafrost degradation is regarded as one of the main factors of rock slope instabilities in high mountain areas (Ravanel 2010). Warming permafrost affects natural hazards such as boulder falls ($V < 100\ m^3$) and large rockfalls ($V > 100\ m^3$), landslides or debris flows. They can cause three types of risks (Ravanel 2010): snow avalanches or debris flows (cascading effects), (ii) damages to infrastructure (e.g. huts, cable-cars) or people (mountaineers, hikers, tourists) located on the path of a rock mass in movement, (iii) destabilization of infrastructure. This paper focuses on the latter risk with the aim of identifying the exposed sites.

Permafrost is defined as any lithospheric material that permanently remains at or below 0 °C. Permafrost is not directly visible but can be detected by indirect methods such as the study of landforms and geomorphic processes associated with permafrost, or by measuring rock temperature with sensors or geophysical methods. One of the main objectives of the European *PermaNET* program (*Longterm PERMAfrost monitoring NETwork*) was to produce a map of the potential permafrost distribution in the Alps, that resulted in the Alpine Permafrost Index Map (APIM; Boeckli et al. 2012), used for our present inventory. This inventory of infrastructure has been implemented through a Geographic Information System (GIS) with several layers.

In order to classify infrastructure according to their level of risk of destabilization, an index of risk in context of permafrost was built, combining hazard characterization and vulnerability diagnostic.

P.-A. Duvillard · L. Ravanel (✉) · P. Deline
EDYTEM Laboratory, University of Savoie, CNRS, Le Bourget-Du-Lac, France
e-mail: Ludovic.Ravanel@univ-savoie.fr

G. Lollino et al. (eds.), *Engineering Geology for Society and Territory – Volume 1*,
DOI: 10.1007/978-3-319-09300-0_55,

55.2 Methods

55.2.1 Construction of an Index of Risk

Risk analysis in context of permafrost requires a specific approach—generally quantitative—given that an infrastructure has a structural and functional vulnerability. Quantifying the risk makes possible an accurate ranking of the infrastructure according to their vulnerability. Risk can be defined as follow:

$$\textbf{Risk} = \textbf{Hazard} \times (\textbf{Stakes} \times \textbf{Vulnerability})$$

According to the analytical risk definition stated by Canceill (1983), unitary risk **R** assigned to a given value can be obtained by multiplying (i) the potential damaging rate **D** of the element exposed (calculated with the damaging function, ranging from 0 to 1), (ii) the index of the unitary value **V** of this element (economic, strategic and functional value estimated for the owner, between 0 and 1), and (iii) the occurrence probability of destabilization **PI** due to permafrost degradation (from 0 to 1): $\mathbf{R} = \mathbf{D} \times \mathbf{V} \times \mathbf{PI}$.

55.2.2 Hazard Characterization

Hazard refers to the probability of instability in case of permafrost degradation. Hazard value considers four elements:

- the index of permafrost occurrence (APIM); this index informs on the possible permafrost type according to the different field types and conditions;
- the local geomorphology, surveyed from aerial photography, useful to determine favorable and unfavorable permafrost conditions;
- glacial retreat, reconstructed by the observation of landforms and sediments on aerial photographs—glacial retreat can be considered as a triggering factor often in combination with the degradation of permafrost;
- slope angle identified in the *Surface Type* layer of the APIM or estimated by using aerial photographs.

The assessment of the probability of instability is possible through a table of the different possible parameter combinations. Then the use of the occurrence probability that combines qualitative and quantitative dimensions can allow the instability process (0: impossible; 0.2: very unlikely; 0.4: implausible; 0.6: plausible; 0.8: very plausible; 1: sure) to be assessed.

55.2.3 Diagnosis of the Vulnerability

Vulnerability characterization is possible by considering two elements: the potential level of damage (vulnerability *s.s.*), and the economic or financial value of these elements (stakes). The potential damage rate expresses the interaction between a phenomenon and an element at risk in terms of mode and level of damage (Leone 2004). This damage rate (**D**) can be established with a scale of damage intensity (**ID**) by assessing the sensitivity of infrastructure to instability, and its consequences. The potential damage of infrastructure depends on their types. A classification of these types considering their vulnerability to instability is therefore necessary to evaluate a scale of damage intensity, and then a potential damage rate. Types of infrastructure are classified according to their sensitivity to permafrost degradation (Fig. 55.1).

According to this approach, infrastructure at risk are classified on scale of damage intensities (**ID**) from I to IV. The damage modes due to mass movements (Leone et al. 1996) have been adapted (Table 55.1). Quantification of damage modes is based on the damage rate (i.e. the degree of potential loss of infrastructure) with a value ranging from 0 to 1.

In a second step, the vulnerability analysis requires a hierarchy of the elements exposed in terms of financial (cost of acquisition or building) and operating (economic, strategic, functional) values to determine the importance of infrastructure for operators (stakes). An index of unitary value V combines quantitative and qualitative values, in order to estimate the operating value of the infrastructure (not any: $V = 0$; minor: $V = 0.2$; intermediate: $V = 0.4$; considerable: $V = 0.6$; major: $V = 0.8$; indispensable: $V = 1$), in particular by relying on its known financial value or an estimation of its capacity (Table 55.2). The

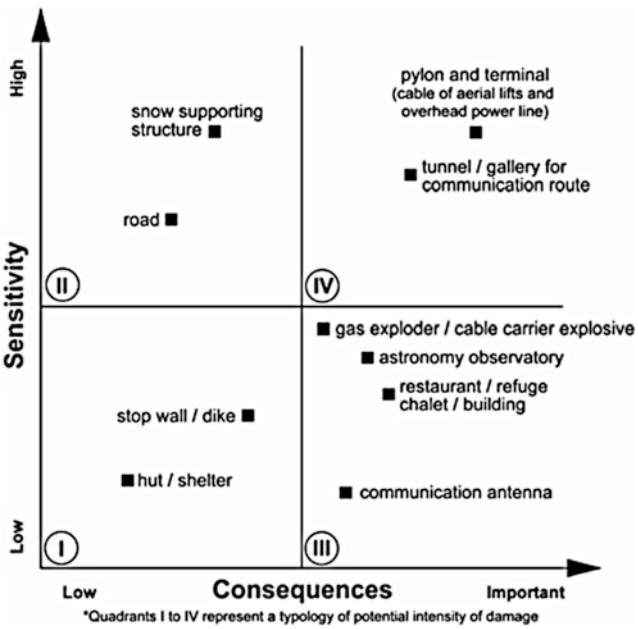

Fig. 55.1 Sensitivity of the infrastructure and consequences in case of destabilization due to permafrost degradation (Bommer et al. 2010, modified)

Table 55.1 Typology of damage modes and potential damage rate of infrastructure (Leone et al. 1996, modified). ID: Scale of damage intensity. D: Damage rate (degree of loss)

ID	Damage modes	D
I	Weak non-structural damage (intact structure) Stability preserved	0.2
II	Cracking Stability preserved—Non-imperative works	0.4
III	Cracking of the structure Stability affected—Partial destabilization	0.6
IV	Fracturing of structure Strong instability	0.8

construction of this index generally results from a subjective appreciation.

55.2.4 Construction of the Risk Index

The assessment of a unitary risk **R** allows an index of the level of risk (Table 55.3) to be built. Indexes of unitary risk **R** are discretized in classes.

55.2.5 Inventory of the Infrastructure with a GIS

The inventory of the infrastructure in context of permafrost with a GIS was needed before employing the risk index. The 7 layers of information were sometimes huge given the extent of the study area (French Alps).

55.3 Results

The study allowed 752 infrastructure « at risk » to be identified among the 1,641 infrastructure documented that are very unequally distributed: the only Savoie encloses 64 % of those infrastructure while the Alpes-de-Haute-Provence only corresponds to 0.1 %. At a regional scale, the Vanoise massif represents 61 % while the Mont-Blanc massif only corresponds to 6 %. Locally, few important ski resorts (Tignes) can contain more than 50 infrastructure at risk. Five percent are characterized by a very high risk and 30 % by a high risk of destabilization. Thirty five percent of the infrastructure in the French Alps could thus be confronted to a important destabilization.

Table 55.2 Determination of the value index V of different infrastructure

Elements exposed		Financial value[a] (k€)	Operating value[b]	V
Skilifts	Detachable chairlift	7,500	Considerable	0.6
	Chairlift	3,000	Minor	0.4
	T bars or rope tow	500	Minor	0.2
	Gondola	8,000	Considerable	0.6
	DMC; Funitel; 3S (big gondola lift)	13,000	Major	0.8
	Cable car—funicular	–	Major	0.8
	Elevator lift	–	Considerable	0.6
Buildings	Hut <30 people dormitory	–	Intermediate	0.4
	Hut >30 people dormitory	–	Considerable	0.6
	Restaurant	–	Intermediate	0.4
	Shelter	–	Minor	0.2
	Chalet/Building	–	Intermediate	0.4
Defense and protection systems	Gas exploder—explosive carrier	80	Intermediate	0.4
	Snow avalanche barrier	0.7/m	Minor	0.2
	Wind structure	0.5/m	Minor	0.2
	Gallery/road tunnel	30 €/m	Considerable	0.6
	Stop wall/dike	0.01/m^3	Minor	0.2
	Brakeman structure for snow avalanche	0.25/m^3	Minor	0.2
Networks	Road—overhead power line pylon	–	Major	0.8
	Communication antenna	–	Considerable	0.6

[a] Average duty-free cost for skilifts in 2012 (*Mountain Leaders*, Jan./Feb. 2012) and equipment and structures against snow avalanche in 2004
[b] Economic, strategic, operational

Table 55.3 Risk index of infrastructure destabilization in permafrost areas (Bommer et al. 2010, modified)

Risk index	Limit R	Definition of risk	Recommendation
Low	[0.008–0.08[	Infrastructure rather stable	No analysis needed
Limited	[0.08–0.128[	Possible weak destabilization	Qualitative analysis recommended[a]
Marked	[0.128–0.256[	Possible partial destabilization	Realization of qualitative analysis[a]: expert opinion, ground reconnaissance and quantitative analysis if no comparable project exist
High	[0.256–0.384]	Possible considerable destabilization	Restricted quantitative analysis[b]: assessment by an engineer, monitoring of the foundations and quantitative analysis if no comparable project exist
Very high	]0.384–0.64]	Possible generalized destabilization	Compulsory monitoring of the structure: detailed quantitative analysis[b] of the foundations on the field and at the lab., independent expert assessment

[a] Qualitative analysis: analytic modelling of impacts of ground instability on the structure
[b] Quantitative analysis: detailed numerical modelling after a detailed field survey on the infrastructure

55.4 Discussion

This work has few limits that future research should solve. The quality of the inventory could be improved. Some very recent infrastructure have probably been unidentified, missing on the documents used. Moreover, the erroneous interpretation of geomorphologic context is possible due to the quality of those documents or to local complexity. Finally, the APIM layer can be criticized.

The risk index could be modified taking into account the possible reinforcement work carried out on instable infrastructure (resilience). For this, systematical surveys should be conducted. The risk index could also be improved by better characterizing hazards (thermal state of the permafrost, remodeling of the ski slopes prone to permafrost degradation, etc.).

55.5 Concluding Remarks

This study has been carried out to prevent infrastructure damages across the French Alps. We recognized 1,641 infrastructure located in areas probably affected by permafrost. The application of a risk index showed 752 infrastructure potentially at risk classified according to their degree of risk of destabilization. Associated geomorphic processes are quite difficult to assess due to the complexity of the geomorphology and of the permafrost distribution in high mountain areas. Only field campaigns would allow the processes which could be involved to be precised, as well as the magnitude and the consequences of the potential destabilizations.

References

Boeckli L, Brenning A, Gruber S, Noetzli J (2012) Permafrost distribution in the European Alps: calculation and evaluation of an index map and summary statistics. Cryosphere 6:807–820

Bommer C, Philips M, Keusen H (2010) Construire sur le pergélisol—Guide pratique. Institut fédéral de recherches sur la forêt, la neige et le paysage WSL, Birmensdorf, p 126

Canceill M (1983) Risque naturels et théorie mathématique du risque. Hydrogéologie, géologie de l'ingénieur 2:137–146

Leone F (2004) Une approche quantitative de la cartographie des risques naturels : application expérimentale au patrimoine bâti de la Martinique (Antilles françaises). Géomorphologie 10:117–126

Leone F, Aste J-P, Leroi E (1996) L'évaluation de la vulnérabilité aux mouvements de terrains pour une meilleure quantification du risque. Revue de Géographie Alpine 84:35–46

Ravanel L (2010) Caractérisations, facteurs et dynamiques des écroulements rocheux dans les parois à permafrost du massif du Mont-Blanc. PhD thesis, Université de Savoie, p 322

Climate Change Impacts on High Alpine Infrastructures: An Example from the Kitzsteinhorn (3200 m), Salzburg, Austria

56

Giorgio Höfer-Öllinger, Markus Keuschnig, Michael Krautblatter and Andreas Schober

Abstract

Numerous rock fall events in the European Alps suggest an increasing occurrence of mass movements due to rising temperatures. In recent years particularly during extensive hot periods large numbers of rock fall events have been reported (e.g. hot summers of 2003, 2005 and 2012). Governed by climate change two major changes can be observed at the summit region of the Kitzsteinhorn, Austria: Intensive glacier retreat and changes of permafrost conditions. The combination of these two major changes leads to an increasing exposure of potentially hazardous areas and higher risks for man and infrastructure. Close to the summit, infrastructure was built in the 1960s, including a cable car station at 3029 m on a north exposed rock face w under permafrost conditions. Due to the decreasing surface area of the glacier and the deepening of the annual active layer, meter thick slabs of the slope became unstable and started sliding down slope parallel to bedding planes. In order to avoid a continuous and deep-reaching destabilization of the entire slope, an intensive rehabilitation program has been established. This program consists of short-, mid- and long-term measures with technical installations (drainage, rock support, etc.) and an intensive monitoring program (including laser scanning, continuous geophysical, geotechnical and temperature monitoring).

Keywords

Permafrost • Climate change • Slope stability • Slope destabilization • Cable car

56.1 Introduction

The project area is situated within the Kitzsteinhorn glacier skiing site, located in the Hohe Tauern mountain range, Austria. The Kitzsteinhorn mountain range consists of rocks of the Glockner Nappe, primarily carbonatic mica schists and greenstones. The affected slope is a north-facing back wall of a glacial cirque with a mean inclination of 47° and is made of carbonatic mica schists.

It extends from the cable car summit station (3.029 m) down to the upper margin of the Schmiedingerkees glacier (2.950 m). The rock face is underlain by permafrost, over the last decades it has been affected by intense glacier retreat at the base and the complete loss of its ice cover (Fig. 56.1).

G. Höfer-Öllinger (✉) · A. Schober
GEOCONSULT ZT GmbH, Hoelzlstrasse 5, 5071 Wals/Salzburg, Austria
e-mail: giorgio.hoefer-oellinger@geoconsult.eu

M. Keuschnig
alpS – Centre for Climate Change Adaptation, Grabenweg 68, 6020 Innsbruck, Austria

M. Keuschnig · M. Krautblatter
Technical University of Munich, Arcisstrasse 21, 80333 Munich, Germany

M. Keuschnig
University of Salzburg, Hellbrunner Strasse 34, 5020 Salzburg, Austria

G. Lollino et al. (eds.), *Engineering Geology for Society and Territory – Volume 1*,
DOI: 10.1007/978-3-319-09300-0_56,

Fig. 56.1 Overview of the project area on the Kitzsteinhorn (view towards *South*)

56.2 Geotechnical Conditions

The north face has an inclination of 23–67°. The rock mass is characterized by a schistosity that is dipping intermediately steeply to NNE-NE. Additionally there are 4 joint sets: K1 dips steeply to the W; K2 dips intermediately to steeply to the SW; K3 strikes EW and dips flatly to intermediately steep to the S; and K4 dips steeply to NW (Fig. 56.2). The main joint sets K1 and K2 and the schistosity joint allow for the development of mostly cubic to tubular shaped rock wedges with cubatures of dm^3 to m^3. The joints are closed to open with width openings of mm-range to a maximum of 20 cm. The open joints are sometimes filled with ice and soil-like materials (sand and clay). The joint spacing is from a few cm up to 2 m. The joint surface profiles are undulating rough to stepped smooth.

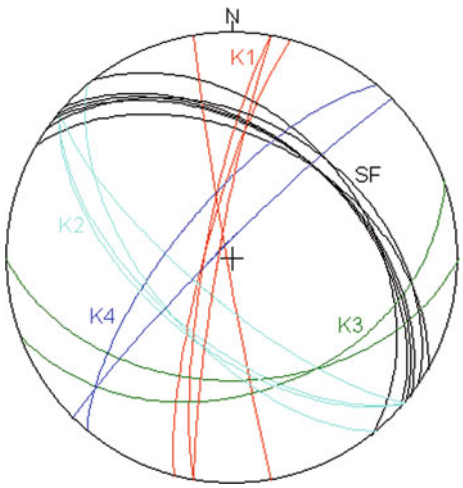

Fig. 56.2 Compilation of the joint sets at the north face (great *circle* diagram, Lambert projection)

56.3 The Emerging Problem

During construction, in the 1960s, the cable car station was constructed on an isolated outcrop of apparently solid and stable rock mass, surrounded by glaciers. Due to continuous degradation of the glaciers the rock slope became exposed. Whilst the western slope is intermediately steep and less vulnerable to instability, the northern slope seems to get steeper with every meter of degrading of the glacier surface. Morphometric analysis of the surface shows inclinations between 23 and 67 degrees, with an average of 47°.

The bedding planes of the carbonate mica schists dip at 35–40° towards NNE-NE. The slope is steeper than the bedding planes and an abutment for the blocks—formerly provided naturally by the glacier—is now missing. Rockfall events (see Keuschnig et al. 2014: same conference) are occurring systematically from the bottom upwards. All sliding planes of the rockfall events have ice on their surfaces.

At this place, the rock mass is underlain by permafrost to a depth of at least 30 m (Keuschnig et al. 2012). Changes in permafrost conditions can lead to slope instabilities, active layer thickening seems to be a major factor for slope instabilities at the investigation area (Hartmeyer et al. 2012).

In addition, surface and melt waters from the roof of the cable car station are contributing to the water infiltration of the rock face.

56.4 Solution to the Problem

Any hazard mitigation measure must consider the role of the permafrost and its development to avoid further destabilization. The principal concept of mitigation is keeping the carbonate mica schists wedges in their current place an altitude as low as possible. The lowermost parts of the rock face are however not accessible anymore. Therefore, from a defined line from about 2970 m asl up towards the station, the wedges are secured by rock bolts. The following requirements for wedge stabilization must be met:

- Possibility to measure the stress on the rock bolts.
- Possibility to tighten initially pre-stressed rock bolts regularly.
- Possibility to monitor the permafrost.
- Possibility to influence the rock mass actively by cooling.

One of the first measures is an additional drainage to stop seepage of surface and melt waters from the roof on the cable car station into the slope was installed.

In order to avoid additional thawing of the permafrost, eight 15 m rock bolts were installed with temperature monitors and injection hoses to carry out injections of liquid nitrogen (rock mass freezing) if required.

The eight monitoring rock bolts are supported by 24 cemented rock anchors of different length. Based on a detailed geological model and failure scenario the design of the bolting was carried out. The bolts are therefore installed +/- horizontally in order to take up any tensional stress. The bolts have to achieve special bending criteria because the wedges are separated from the rock mass by ice prior to installation. After every "melting"—caused by a continuous process triggered by pre-stressing of the bolts—the bolts have to be tightened monthly during the first summer season and twice a year in the following. During installation works, the blocks had to be protected by temporary stabilization measures to avoid mobilization during the drilling works.

56.5 Discussion

Compared to "normal" conditions, rehabilitation of infrastructure and/or rock slopes in permafrost terrain requires considerable effort during the site investigations, geological modeling, assessment of the failure mechanism and interdisciplinary design. In many cases, additional site investigations (i.e. seismic surveying, core drilling) and detailed large-scale geological mapping are hardly possible due to the steepness of the slopes and the dangers of rock and ice fall or avalanches. To carry out drilling works borders on impossible. Under such circumstances, the works have to be carried out in short time periods.

References

Hartmeyer I, Keuschnig M, Schrott L (2012) Long-term monitoring of permafrost-affected rock faces—a scale-oriented approach for the investigation of ground thermal conditions in alpine terrain, Kitzsteinhorn, Austria. Austrian J Earth Sci 105/2:128–139

Keuschnig M, Hartmeyer I, Otto J, Schrott L (2012) A new permafrost and mass movement monitoring test site in the Eastern Alps—concept and first results of the MOREXPERT project. Managing alpine future II—inspire and drive sustainable mountain regions. In: Proceedings of the Innsbruck conference, 21–23 Nov 2011. (= IGF-Forschungsberichte 4). Verlag der Österreichischen Akademie der Wissenschaften: Wien

Keuschnig M, Hartmeyer I, Höfer-Öllinger G, Schober A, Krautblatter M, Schrott L (2014) Permafrost-related mass movements: implications from a rock slide at the Kitzsteinhorn, Austria.In: IAEG XII Congress, Torino (2014, same conference)

Monitoring Rock Wall Temperatures and Microseismic Activity for Slope Stability Investigation at J.A. Carrel Hut, Matterhorn

57

Velio Coviello, Marta Chiarle, Massimo Arattano, Paolo Pogliotti and Umberto Morra di Cella

Abstract

Recent climate changes are increasing the frequency of rock-slope instabilities in the Alpine region. The formation of cracks leading to rockfalls causes a release of energy propagating in form of elastic waves. These latter can be detected by a suitable transducer array together with the vibrations generated by the impact of rockfalls. Geophones are among the most effective monitoring devices to investigate both these phenomena. A monitoring system composed by geophones and thermometers was installed at the J.A. Carrel hut (3829 m a.s.l., Matterhorn, NW Alps) in the framework of the Interreg Alcotra projects PERMAdataROC and MASSA by CNR IRPI and ARPA with the financial and logistic support of the Valle d'Aosta Region. The correlation between temperature trends and microseismic events is presented: cold periods characterized by a rapid temperature decrease present higher concentration of microseismic activity. However, not every drop in temperature is associated to microseismic activity, and the identification of the processes generating microseismic events in occasion of rapid temperature decrease is still uncertain. The objective of the ongoing research activity is to analyze in deep the statistical correlation between the number of microseismic records and the temperatures of air and rock in order to investigate the existence of recurrent patterns in the detected signals.

Keywords

Alpine permafrost • Microseismic monitoring • Rock-slope deformation • Temperature monitoring

57.1 Introduction

The Alpine permafrost degradation due to the ongoing climatic changes is likely causing the increase of high-altitude rock-slope instabilities observed in recent years. In warm periods, the thaw of the ice filling rock discontinuities and the deriving hydro-thermal heat transfer induce a reduction of the rock mass strength; during the cold season, the thermo-mechanical forcing are reinforced by the cryogenic process that freezes the water circulating in rock fractures (Hasler et al. 2012). These processes induce stresses in the rock mass that may lead, in the medium-long term, to rock-falls. Recent climatic changes could also worsen this situation by increasing, in some cases, the frequency of these instabilities, altering the natural cycles of thawing and freezing and modifying the availability of liquid water in the rock fractures (Evans and Clague 1994). In the Mont Blanc massif, the role of permafrost degradation in causing rock-falls is strongly supported by evidence from the

V. Coviello (✉) · M. Chiarle · M. Arattano
Italian National Research Council (CNR), IRPI, Turin, Italy
e-mail: velio.coviello@irpi.cnr.it

P. Pogliotti · U.M. di Cella
Regional Agency for the Environmental Protection (ARPA), Aosta Valley, Italy

G. Lollino et al. (eds.), *Engineering Geology for Society and Territory – Volume 1*,
DOI: 10.1007/978-3-319-09300-0_57,

analysis of documented events occurred since the mid-19th Century and, within the actual context of global warming, high-altitude steep rockwalls instabilities are expected to occur more frequently (Ravanel and Deline 2011).

The formation of cracks, that may eventually lead to rock-falls, is accompanied by a sudden release of energy which propagates in form of elastic waves. These latter can be detected, in laboratory, by an array of acoustic emission sensors and, in the field, by microseismic (MS) transducers (Lockner 1993; Hardy 2003). Therefore, geophones should allow the recording of ground vibrations that precede the rockfall, due to the initiation of cracks and coalescence of existing ones. If AE have been widely investigated at laboratory scale, only in recent years the investigation of MS activity for rock slope stability analysis has been extended to the field (e.g., Amitrano et al. 2005, 2010; Senfaute et al. 2009; Levy et al. 2011). Nowadays, the development of a reliable rock-wall monitoring system for warning purposes is an open challenge. The main difficulty is that rockfall events are frequent and widespread on the alpine slopes and they cannot be easily correlated, before the failure, to specific rupture surfaces. Even if still there are unsolved limitations due to the difficulties of interpreting the recorded signals and to the interference of environmental noises, the MS techniques have started to supply useful insight on the investigated processes. If the use of seismic devices is one of the most effective monitoring systems to investigate eventual precursors of rockfall phenomena, the monitoring of the thermal regime in steep rock walls is of paramount importance to investigate the climatic control on high mountain rock instabilities (Matsuoka and Sakai 1999; Gruber and Haeberli 2007; Hasler et al. 2012).

In the summer 2003, an exceptional heat wave hit central Europe and was accompanied by a large series of rockfall events along the entire alpine chain (Gruber et al. 2004). One of these events was the "Cheminée" rockfall, which occurred on August, 18 along the Italian climbing route to the Matterhorn (North-western Italian Alps) at an elevation of about 3770 m, just below the J.A. Carrel Hut. This event was of particular scientific interest because a large ice lens was observed on the detachment surface but. Other small rock falls occurred on the Matterhorn and surrounding slopes in the same summer and in the following years (Chiarle et al. 2014). To investigate these processes in 2007 an Interreg IIIA Alcotra project, named PERMAdataROC (2007–2008), was funded and within its context a monitoring system composed by geophones and thermometers was installed at the J.A. Carrel hut (3829 m a.s.l.) by the CNR IRPI and ARPA with the support of Guide del Cervino and Valle d'Aosta Region. In 2010, the start of a further Alcotra project (MASSA, 2010–2011) allowed to empower and renovate the MS monitoring system. In this paper MS data recorded since November 2007 are summarized and three months of unpublished recordings are presented. A correlation between temperature variations and MS events occurrence has been evidenced in the whole dataset.

57.2 The Matterhorn Monitoring System

The monitoring system installed at the J. A. Carrel hut, on the South-west ridge of the Matterhorn (Fig. 57.1), is composed by a geophone network and temperature sensors. The first MS recording unit was designed and installed in 2007 by CNR IRPI, with the technical support of the company SolGeo, taking advantage of the previous experience gained in the field of debris flow seismic monitoring (Arattano et al. 2012). The researchers of the CNR IRPI had in fact engaged in the monitoring of this latter type of mass movement since 1989 and continued to test the use of different types of ground vibration detectors, such as seismometers, geophones and underground microphones, till recently (Arattano et al. 2014, Comiti et al. 2014). The monitoring of debris flows provides data for their numerical modeling (Arattano and Franzi 2003; Lin et al. 2005), for rheological studies (Arattano et al. 2006) and for the analysis of the different flow processes that may occur in a mountain torrent (Arattano and Franzi 2004). All these studies permit a broad investigation of the monitoring potentialities of ground vibration detectors like those installed on the Matterhorn.

The instrumentation installed at the Carrel hut in 2007 was renewed in 2010 and currently consists of five triaxial high frequency geophones (100 Hz), three triaxial low frequency geophones (4.5 Hz), a digital 24-channel acquisition system, a GPS receiver for time synchronization, radio data transmission equipment and a solar power supply system. Three high frequency geophones are installed in boreholes and are fixed at the base, the other five sensors (including the low frequency ones) are placed on the rock surface. The system records an event when a threshold value (0.01 mm/s) is exceeded on a selected number of channels (six). The recording has a sampling frequency of 5 kHz covering a time interval from 3 to 5 s, included a pre-trigger of 1 s. See Occhiena et al. (2012) for full details about the MS monitoring instrumentation installed in 2010.

Air and surface rock temperature are monitored since 2006 by ARPA in the surroundings of the J.A. Carrel Hut. The measuring points are located on the rock walls at a distance of some tens of meters from the hut, one on the South rock slope face (South station) and one on the North-west rock slope face (West station). The rock surface temperature is measured every hour at 3 different depths (0.03, 0.30 and 0.55 m) by means of Geoprecision mini-dataloggers. Pogliotti et al. (2008) provide further details on the Matterhorn temperature network and the first thermal

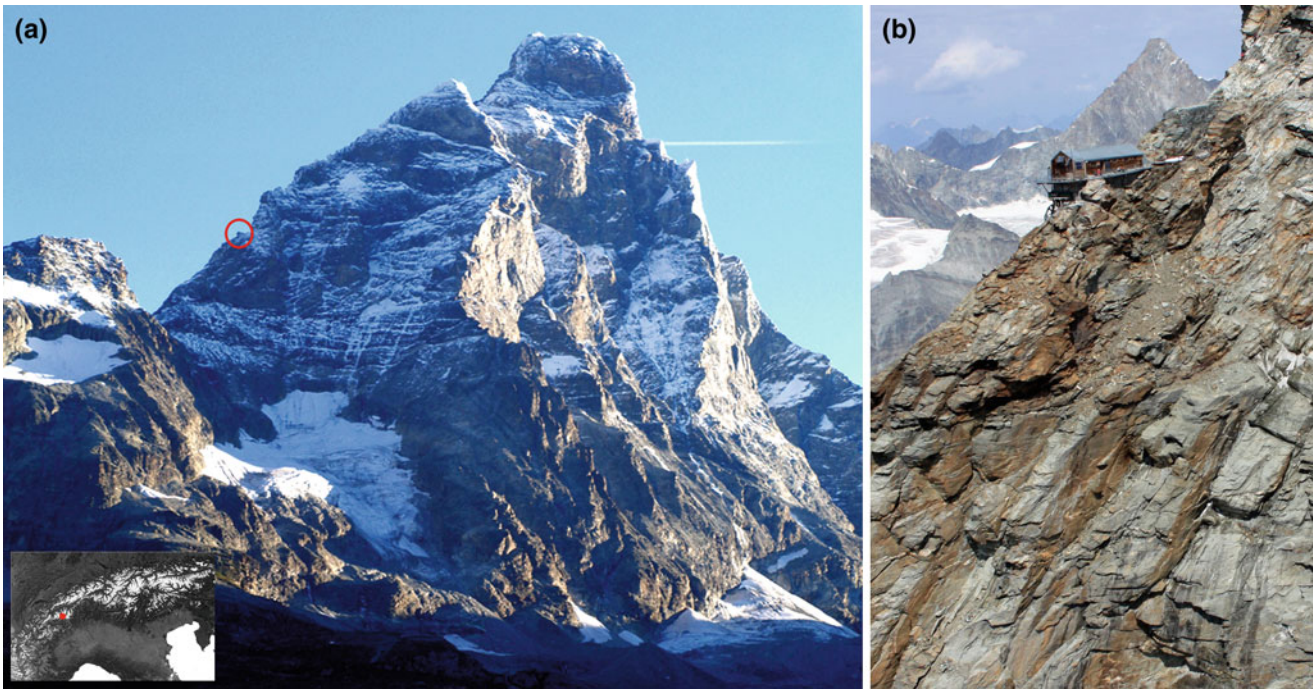

Fig. 57.1 The study site: **a** the Matterhorn South face with the J.A. Carrel hut in the *red* circle (photo: V. Coviello); **b** details of the South-west ridge where the monitoring system is installed (photo: P. Pogliotti)

diffusivity elaboration series inferred from rock temperature data collected. During the summer of 2011, these instruments were replaced by an improved version of the datalogger, equipped with a GPRS module for the data transmission; in that occasion the rock surface temperature sensor (0.03 m) was moved at greater depth (0.10 m), to limit the diurnal solar radiation interference.

57.3 Microseismic and Temperature Data Analysis

In this section two sets of MS data are presented and the correlation is investigated between the daily number of events and the temperature trends. The first dataset is composed by 696 MS events recorded from 1 November 2007 to 30 September 2008 (Fig. 57.2). The system worked properly only until April 2008 and so the summer of 2008 was not continuously covered. An overall number of 652 further events were then obtained during a period of ten months, following the renewal of the system dating 5 October 2010 (Fig 57.3). It must be noticed that during this second recording period the monitoring equipment worked discontinuously. The data processing consists of the classification of the recorded signals, the identification of the most important trace characteristics in time and frequency domain and the analysis of their distribution in space and time. The dataset has been purged by removing events characterized by mute channels and anomalous oscillations and picks due to electrical disturbances. The recorded MS signals are classified in two classes: single events, when the threshold is exceeded only once in the recording; multiple events, if the threshold is exceeded more than once. Some considerations follow about the temporal concentrations of the two classes.

During the first recording period all the temperature sensors worked properly, while between 1 October 2010 and 31 December 2011 the recordings were irregular. Since mid-august 2011 the air sensor went definitely out of order. The South and West stations started their recording from 21 June 2011 to 19 August 2011, respectively. In addition to the available air temperature values, only rock temperature data coming from sensors placed at 0.30 and 0.55 m depth were used in this paper. In fact during the 2011 summer the superficial rock temperature device was relocated at greater depth therefore the temperatures recorded after that moment are not comparable to previous data. Furthermore, data recorded by this latter sensor are too sensitive to solar radiation.

Analyzing the two dataset (Figs. 57.2 and 57.3), the superposition of the number of events per day on the daily temperature trend shows that the most important concentrations of MS activity always occur during cold periods, in both the cold and warm seasons. These observations are in agreement with the mechanisms described in literature through which climate may control slope stability (Gruner 2008). Minor concentrations of MS events occur during the summer months when air and rock temperatures

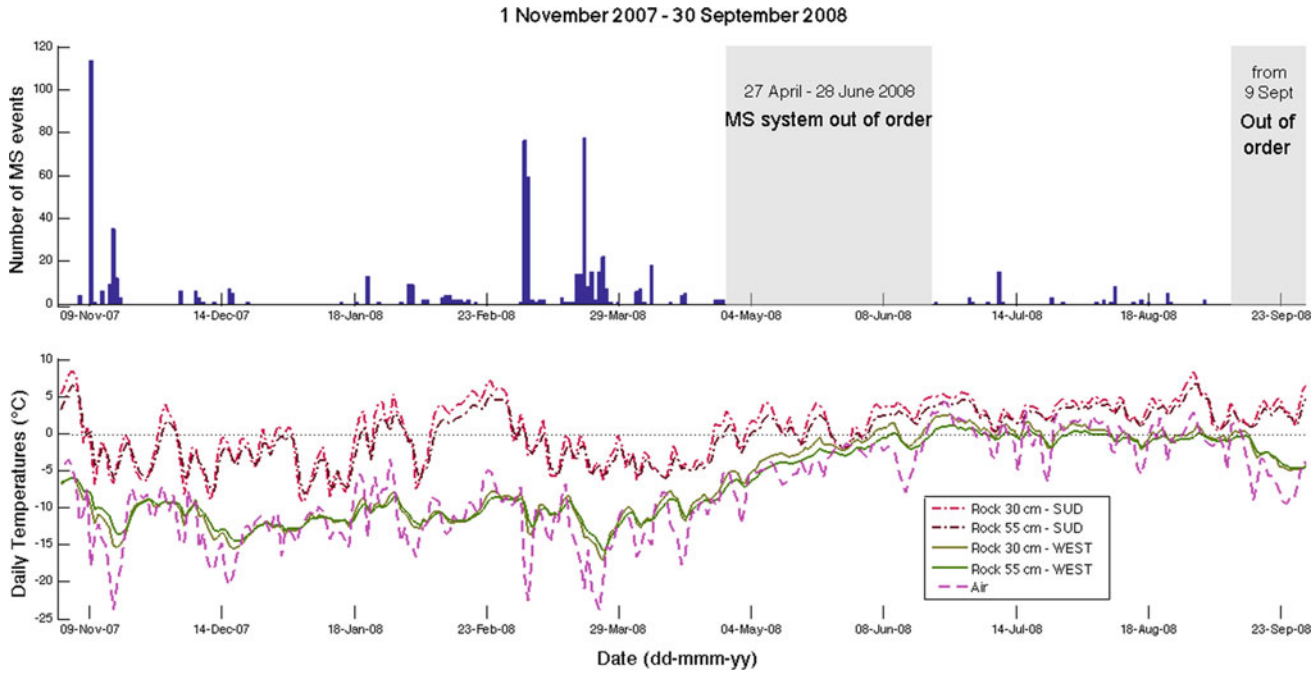

Fig. 57.2 Number of MS events per day (*upper* histogram) and daily temperature trend (*lower* graphs) in the first monitoring period (2007–2008)

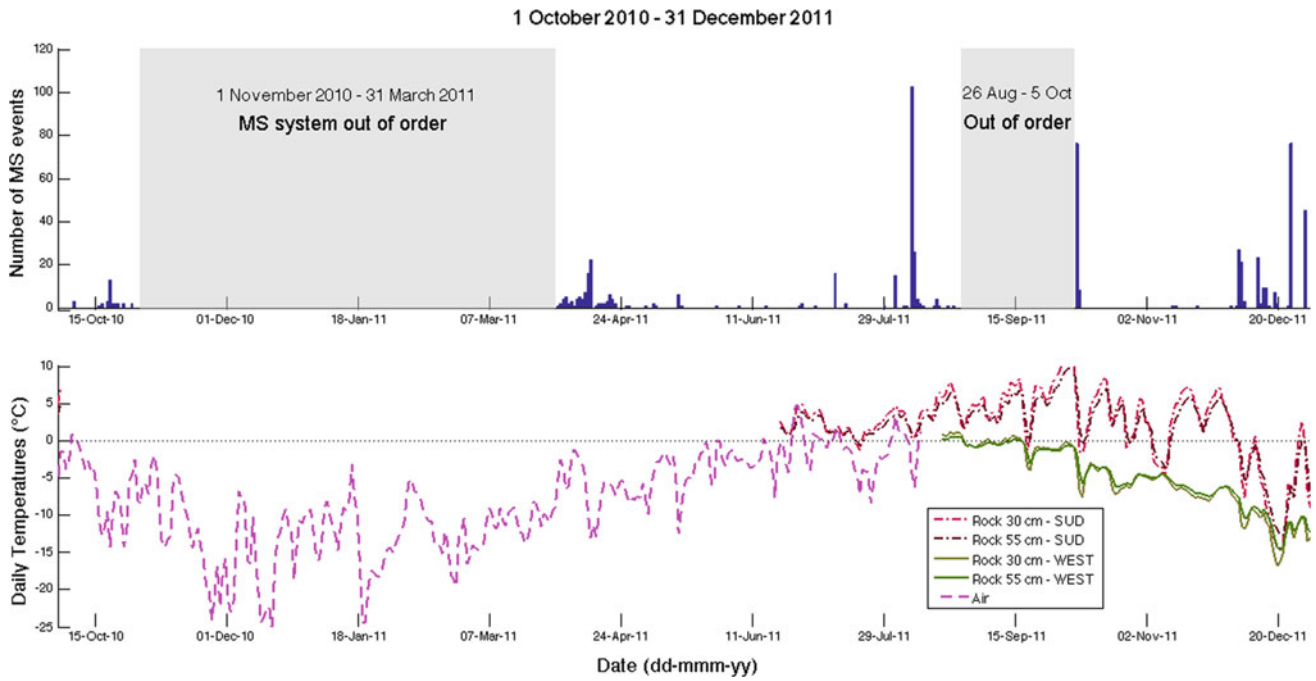

Fig. 57.3 Number of MS events per day (*upper* histogram) and daily temperature trend (*lower* graphs) in the second monitoring period (2010–2011)

temporarily rise above 0 °C. In this sense, recent field observations on the North-eastern ridge of Matterhorn, the Hörnligrat (Hasler et al. 2012), and the Jungfraujoch (Girard et al. 2013) show that: (i) cleft movements during the cold season are caused by thermo-mechanical forcing and are reinforced by cryogenic processes during the freezing period, while, (ii) in summer the main movements originate from hydro-thermally induced strength reduction (increase of water pressure) in rock fractures containing perennial ice.

57.4 Conclusions

The J.A. Carrel hut (3829 m a.s.l.) was selected for installing a MS and rock-wall temperature monitoring system in consideration of his elevation and the documented rock-falls events occurred in the surroundings since summer 2003. The refuge offers the occasion to have a unique logistic base and since 2007 it is the higher research laboratory of the Alpine chain collecting rock-wall MS and temperature monitoring data. The most part of the analyzed MS activity occurs during cold periods and it is likely due to thermo-mechanical forcing produced by cryogenic processes. Minor concentrations of MS events are also observed when the rock temperature temporarily rise above 0 °C. These latter signals were mainly classified as multiple events and can be reasonably ascribed to surface deformation and movements or to block falls. The research is still in progress and the recording is presently restarted. The installation is also planned of two deep thermistors chains, reaching 10 m of depth in the rock mass surroundings the J.A. Carrel hut, respectively on the North and the South side of the ridge. The objective of the future research is to investigate the statistical correlation between the number of MS records and temperatures also at hourly aggregation. The recording of MS events and temperatures is planned for a longer period to better understand the relation between climate, MS activity and rock slope instability. Furthermore, the location of the MS sources is planned and this would supply valuable information to better investigate the nature of these phenomena.

Acknowledgments The authors wish to thank the Regione Autonoma Valle d'Aosta (Dipartimento Difesa del Suolo e Risorse Idriche—Servizio Geologico), for the logistic and financial support; Massimo Signori and Delfino Bani (Solgeo S.r.l.) who assembled and installed the monitoring network; Lucio Trucco (Società delle Guide del Cervino) for the assistance during all the field work phases; Gianni Mortara, senior researcher at CNR IRPI, for his comments and suggestions.

References

Amitrano D, Grasso JR, Senfaute G (2005) Seismic precursory patterns before a cliff collapse and critical point phenomena. Geophys Res Lett 32:L08314

Amitrano D, Arattano M, Chiarle M, Mortara G, Occhiena C, Pirulli M, Scavia C (2010) Microseismic activity analysis for the study of the rupture mechanisms in unstable rock masses. Nat Hazards Earth Syst Sci 10:831–841

Arattano M, Franzi L (2003) On the evaluation of debris flows dynamics by means of mathematical models. Nat Hazards Earth Syst Sci 3(6):539–544

Arattano M, Franzi L (2004) Analysis of different water-sediment flow processes in a mountain torrent. Nat Hazards Earth Syst Sci 4:783–791

Arattano M, Franzi L, Marchi L (2006) Influence of rheology on debris flow simulation. Nat Hazards Earth Syst Sci 6:519–528

Arattano M, Marchi L, Cavalli M (2012) Analysis of debris flow recordings in an instrumented basin: confirmations and new findings. Nat Hazards Earth Syst Sci 12:679–686

Arattano M, Cavalli M, Comiti F, Coviello V, Macconi P, Marchi L (2014) Standardization of methods and procedures for debris flow seismic monitoring. In: Proceedings XII IAEG International Congress, 2014 (in press)

Chiarle M, Coviello V, Arattano M, Silvestri P, Nigrelli G (2014) High elevation rock falls and their climatic control: a case study in the Conca di Cervinia (NW Italian Alps). In: Lollino G et al (eds), Engineering geology for society and territory, Proceedings IAEG XII International Congress, vol 1

Comiti F, Marchi L, Macconi P, Arattano M, Bertoldi G, Borga M, Brardinoni F, Cavalli M, D'Agostino V, Penna D, Theule J (2014) A new monitoring station for debris flows in the European Alps: first observations in the Gadria basin. Nat Hazards 1–24

Evans SG, Clague JJ (1994) Recent climatic change and catastrophic geomorphic processes in mountain environments. Geomorphology 10:107–112

Girard L, Gruber S, Weber S, Beutel J (2013) Environmental controls of frost cracking revealed through in situ acoustic emission measurements in steep bedrock. Geophysical Research Letters 40(9):1748–1753

Gruber S, Haeberli W (2007) Permafrost in steep bedrock slopes and its temperature-related destabilization following climate change. J Geophys Res 112:F02S18

Gruber S, Hoelzle M, Haeberli W (2004) Permafrost thaw and destabilization of Alpine rock walls in the hot summer of 2003. Geophys Res Lett 31:L13504

Gruner U (2008) Climatic and meteorological influences on rockfall and rockslides. In: Proceedings 11th Interpraevent Congress 2008, vol 2, pp 147–158

Hardy HR (2003) Acoustic emission/microseismic activity—principles, techniques and geotechnical applications. A.A. Balkema, Lisse

Hasler A, Gruber S, Beutel J (2012) Kinematics of steep bedrock permafrost. J Geophys Res 117:F01016

Levy C, Jongmans D, Baillet L (2011) Analysis of seismic signals recorded on a prone-to-fall rock column (Vercor Massif, French Alps). Geophys J Int 186:296–310

Lin ML, Wang KL, Huang JJ (2005) Debris flow run off simulation and verification—case study of Chen-You-Lan watershed, Taiwan. Nat Hazards Earth Syst Sci 5(3):439–445

Lockner DA (1993) The role of acoustic emission in the study of rock fracture. Int J Rock Mech Min 30(7):883–899

Matsuoka N, Sakai H (1999) Rockfall activity from an alpine cliff during thawing periods. Geomorphology 28(3–4):309–328

Occhiena C, Coviello V, Arattano M, Chiarle M, Morra di Cella U, Pirulli M, Pogliotti P, Scavia C (2012) Analysis of microseismic signals and temperature recordings for rock slope stability investigations in high mountain areas. Nat Hazards Earth Syst Sci 12:2283–2298

Pogliotti P, Cremonese E, Morra di Cella U, Gruber S, Giardino M (2008) Thermal diffusivity variability in alpine permafrost rock walls. In: Proceedings of the 9th International Conference on Permafrost, vol 2, pp 1427–1432

Ravanel L, Deline P (2011) Climate influence on rockfalls in high-Alpine steep rockwalls: the north side of the Aiguilles de Chamonix (Mont Blanc massif) since the end of the 'Little Ice Age'. The Holocene 21(2):357–365

Senfaute G, Duperret A, Lawrence JA (2009) Micro-seismic precursory cracks prior to rock-fall on coastal chalk cliffs: a case study at Mesnil-Val, Normandie, NW France. Nat Hazards Earth Syst Sci 9:1625–1641

Probabilistic Assessment of Ice Wedge Hazard for Linear Structure

58

Julia Stanilovskaya, Vladimir Merzlyakov and Dmitry Sergeev

Abstract
This paper discusses probabilistic assessment of the potential thermokarst hazard along ice wedge polygonal networks for linear engineering structures. The assessment considers the areas where linear object corridor crosses polygonal networks with the potential risk of ice wedge thawing. The hazard is evaluated in three categories: maximum, minimum, and mean. We calculated the number of danger outbreaks, their dimensions and characteristics for the linear objects. The results are applicable for the construction feasibility study, for the route planning and for the operational robustness assessment.

Keywords
Probability • Linear structure • Polygons • Ice wedges • Random line • Thermokarst

58.1 Introduction

One of the most dangerous cryogenic phenomena are the ice wedges (IW). IW is considered as a cryolithological complex with very high ice content, which is well diagnosed due to the specific polygonal microrelief. Any allocation of the linear structure over or in the vicinity of polygonal areas is considered as hazardous. The degree of danger depends on the type and characteristics of the linear structure. The rule of thumb here is that 2-m upper part of the cross section of a polygonal terrain is the most dangerous one to distort since that violates the thermal and moisture conditions of soils during construction and exploitation of the linear structure. At the same time, polygons may reflect more ancient ice wedges, underlying down the 2 m depth. They can be found during the construction and operation of buried pipelines.

J. Stanilovskaya (✉) · V. Merzlyakov · D. Sergeev
Sergeev Institute of Environmental Geoscience RAS, P.O.Box 145 Ulansky per. 13, 101000 Moscow, Russia
e-mail: stanik85@mail.ru

The aim of the paper is hazard assessment of thermokarst and the probability of its development along linear structures on the polygonal territory.

It is assumed that the number of disturbed spots and their area are characterized by a number of intersections of the engineering object with the polygonal network. Those also depend on the polygon size and the angle of intersection. Therefore, the hazard assessment is necessary here and should be applied on the stage of the corridor planning in order to avoid the dangerous sites with IW. It can be also used when planning the prior stabilization or elimination of the ice. Another application is the assessment of the amount of works on difficult sites (Fig. 58.1). We also assume that such calculations are also necessary at the operational phase for more advanced monitoring and engineering protection.

In that regard, the research had the following tasks:

- the identification of the most dangerous situations that may arise at the lining of linear structures over polygons;
- the calculation of the number of intersections with polygons i.e. dangerous sites;
- the calculation of the probabilities of the number of intersections with polygon;
- the calculation of the square of a possible thermokarst on danger sites for adverse events.

G. Lollino et al. (eds.), *Engineering Geology for Society and Territory – Volume 1*,
DOI: 10.1007/978-3-319-09300-0_58,

Fig. 58.1 Ice wedge polygon in shape of a regular square on the Badami oil pipeline in northern Alaska (Fiscal Year 2007 lease compliance monitoring report)

To meet the objectives the probability analysis was employed. This approach is rarely used in practice of permafrost researches and even less often in the analysis of the thermokarst formation and development along linear structures on the polygons (McIntyre 1953; Khomyakov 2006; Stanilovskaya and Merzlyakov 2013).

The task of the probability finding of a given number of intersections of IW and linear structures is a dividing into two classes (Stanilovskaya and Merzlyakov 2013): (1) a linear structure is located within the polygon and (2) a linear structure extends beyond the polygon.

In the first case, a solution of one of the geometric probability tasks (Kendall and Moran 1972) is solved, which can be called the generalized Buffon's needle problem. The numbers of intersections of the vertical and horizontal lines are interdependent in this task.

In the second case, the number of intersections of vertical and horizontal lines is independent. It is possible then to apply the method based on the solution of the classical problem of a pair of random numbers selected on the unit interval.

58.2 Probabilistic Assessment of Ice Wedge Hazard for Some Linear Structures

The actual data for the two linear structures were used, for the road in Chara Depression, and for the buried pipeline in Chulman Depression (Table 58.1). The data on the size of polygons and linear structures were derived from free available satellite Google Earth images.

Chara site is visible polygonal area with IW thawing on the road. The sizes of polygons vary from 13 to 20 m. It is seen, that IW is thawing along and across the road (the width is 5 m) with formation of settlements and trenches

Fig. 58.2 Polygonal settlements on the road are the result of ice wedges thawing in Chara depression

(up to 2 m wide), filled with water, and distorting the road body (Fig. 58.2). It is assumed that on the average the trench width corresponds to the shape and size of the ice cellar on polygons.

The thermoerosion along and across of oil pipeline "Eastern Siberia–Pacific Ocean-1" (ESPO-1) was recorded during aerial visual and on ground surveys in Chulman area (Fig. 58.3). The ground ice at 1 m depth and of 4 m thickness was recognized as being the ice wedge during drilling.

58.3 Discussion

As the results of the calculations used in the method, the probabilities of some specific events (entering of tilting angle of the segment in a narrow sector, entering in a

Fig. 58.3 Dangerous site with thermoerosion on the polygons with ice wedges along oil pipeline "Eastern Siberia–Pacific Ocean-1" (ESPO-1) in Chulman area

Table 58.1 Probabilistic characteristic of dangerous sites for leaner objects, located on polygons

Site	Structure parameters			Ice wedge parameters		Number of intersections				Square of the				Probability*
	Length of the object	Reduced length of object	Width of object	Characteristic size of the polygon	Width of ice wedges	Mathematical expectation	Min	Max	Number of visible violations on the route	Min	Mean	Max	Maximum, when route lying on the polygon	
	s, m	L	a, m	h, m	b, m	$M\zeta$	ζ_{min}	ζ_{max}	ζ_{field}	S_{min}, m^2	S, m^2	S_{max}, m^2	S_{iw}, m^2	P_{iw}**
Chara – A-B	230	17.7	5	13	2	20.3	14	27	20	140	203	270	460	0.54
Chara – B-C	430	26.9	5	15	2	30.4	21	41	23	210	304	410	860	0.47
Chara – C-D	80	4	5	20	2	5.6	4	8	6	40	56	80	160	0.35
Chara – D-E	800	40	5	20	2	46.1	31	62	No deformations	310	461	620	1600	0.35
Chulman – A-B-10	410	41	1.2	10	1	47.3	32	63	37 gullies	38.4	56.8	75.6	410	0.22

*The unconditional probability of any single event (eg, equality) is low due to the multiplicity of outcomes, so conditional probabilities of imposing a linear object on the edge of the ice axes of polygon (the most dangerous situation) are presented in the "probability" column

**$P_{iw} = (a + b)/h$, where a – width of object, b – width of ice wedge, h – size of polygon

narrow strip of coordinate change, the intersection of a number of lines) are low, but possible. The events have some finite probability and some of them—not so low (the order of 0.1 or higher) in the above-considered cases. Therefore, it can be argued that all of these events may appear not so rare to neglect them.

Should pay attention to a convincing example. A careful study of analogous conditions during the construction of oil pipelines in northern Alaska made possible to substantiate and implement next project (Fiscal Year 2007 Lease Compliance Monitoring Report). The elevated Badami pipeline (40 km length, 0.3 m diameter) was built without road during winter time to avoid the thermokarst formation on polygon territory (Fig. 58.1).

The method presented in the paper allows determining the potential hazard area and the probability of thermokarst development along the route of the line facility. This method can be further developed towards the economical risk assessment.

58.4 Conclusions

1. A method for ice wedge hazard estimation was developed and applied. It is recommended for using in the complex researches to reduce the expenses during the construction and operation of linear structures. It can be used for developing a methodology of optimal route planning on polygonal territories, as well as for total cost calculations.
2. The calculations of the number of the damage centers on the route and their probabilities for linear facilities, located within the polygons, and for linear objects, that intersect the polygons, were used in the method.
3. The danger criterion P_{iw}, was computed and used to evaluate the hazard associated with the relative position of the linear structure and IW (Table 58.1). This quantity is the conditional probability of the most dangerous situations that can appear when planning the route crossings over the polygons imposing a linear structure on the edge of the ice wedge grid.
4. The method application is tested for linear structures (Table 58.1), having the minimum and maximum number of intersections; their mathematical expectation; the maximum, minimum and statistically average square of possible object coverage, the conditional probability of the most dangerous situation were calculated.

Acknowledgments The research was supported by Russian Foundation for Basic Research (number of project is 14-05-31510).

References

Fiscal Year (2007) Lease compliance monitoring report. State pipeline coordinator's office. Alaska Department of Natural Resources, 90 p

Kendall M, Moran P (1972) Geometrical probabilities. Nauka, Moscow, 192 p (in Russian)

Khomyakov PM (2006) The impact of global warming on the gas industry [Electronic resource]. http://www.velesova-sloboda.org/misc/homyakov-gasprom.html (in Russian)

McIntyre GA (1953) Estimation of plant density using line transects. J Ecol 41:320–330

Stanilovskaya JV, Merzlyakov VP (2013) The potential thermokarst hazard assessment of the wedge polygonal ice for the pipelines. Oil and oil products pipeline transportation: science and technologies 3(11):48–54 (in Russian)

An Overview of Some Recent Large Landslide Types in Nahanni National Park, Northwest Territories, Canada

59

Courtney Jermyn and Marten Geertsema

Abstract

Large rock and soil landslides are an important part of the geodiversity in Nahanni National Park in Canada's Northwest Territories. Here we describe five notable events, including two in soil, two in rock, and one involving rock and soil. Three of the events resulted in landslide dams. The Ram Plateau flowslide involved a collapse of a scree slope and fine textured soil over massive ground ice. This complex landslide continues to move in response to permafrost thaw and seasonal moisture. The Wrigley landslide is a large debris slide, involving thick till that dammed Wrigley Creek. The Cathedral Creek rock slide is a dip slope failure which dammed two large creeks. Cliff collapse of limestone on the Ram Plateau transformed into a rock avalanche, which dammed a stream. The Grizzly landslide involved both rock and soil. It is a large rock slide—earth flow in which, we suspect, undrained loading played an important role.

Keywords

Landslides • Northwest territories • Permafrost • Inventory

59.1 Introduction

The South Nahanni watershed has a diverse terrain comprising rolling hills, rugged mountains, plateaus, and steep canyons. The region has been uplifted, folded and faulted, and is subject to earthquake activity. The dynamic environment of the South Nahanni watershed creates favourable conditions for slope failures.

In 2005 and 2006, we mapped landslides over 24,000 km^2 of the watershed using aerial photography and ASTER satellite imagery, and conducted field investigations for validation.

Most large landslides occur in the eastern portion of the study area, generally in Paleozoic limestone and shale lithologies.

59.2 Landslides Observed Within Nahanni

We concentrated our field investigations on Tlogotsho and Ram plateaus, and Cathedral and Wrigley creeks (Fig. 59.1). Landslides in these regions occurred along steep canyon and cliff faces, on steep slopes within the mountains, and on lower terrain. Landslides also occurred on slopes underlain by permafrost. Within the areas visited, there were five notable landslides; a rock slide—earth flow, two rock slides, flowslide, and a debris slide—several of which were found to have impounded streams.

C. Jermyn (✉)
Vlaardingen, Netherlands
e-mail: courtney.jermyn@gmail.com

M. Geertsema (✉)
Ministry of Forests, Lands, and Natural Resource Operations, 1044-5th Avenue, Prince George, BC V2L 5G4, Canada
e-mail: marten.geertsema@gov.bc.ca

G. Lollino et al. (eds.), *Engineering Geology for Society and Territory – Volume 1*,
DOI: 10.1007/978-3-319-09300-0_59,

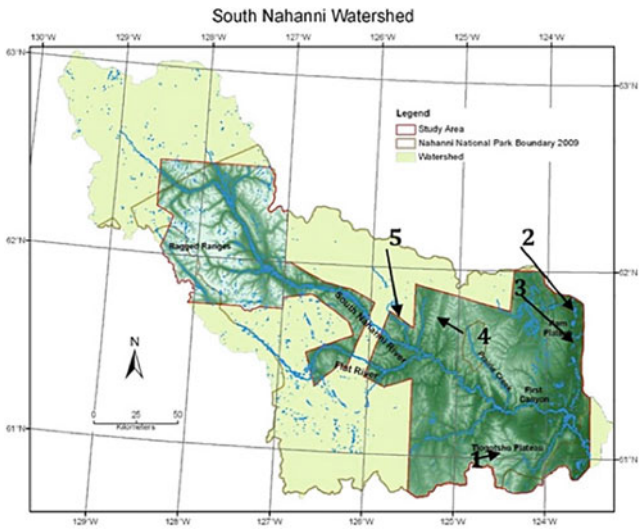

Fig. 59.1 Map of landslide field investigation locations: *1* complex rock slide-earth flow, Tlogotsho Plateau; *2* rock slide, Ram Plateau; *3* complex earth slide-earth flow (flowslide), Ram Plateau; *4* debris slide, Wrigley Creek, *5* Rock slide, Cathedral Creek

59.2.1 Complex Rock Slide: Earth Flow, Tlogotsho Plateau

We identified in the Tlogotsho Plateau, long-runout earth flows on low-gradients (typically less than 7°), mainly on north-facing slopes. The Grizzly landslide covers 7 km^2 and traveled approximately 4 km (Fig. 59.2a–c). The upper portion of the slide displays both rotational and translational movement in jointed sandstone and siltstone along a shale rupture surface (Fig. 59.2d). The middle to lower portions of the landslide involved flowing and minor sliding of cohesive soil on a gradient of 3°. The landslide can thus be classified as a rock slide—earth flow. Based on aerial photos, satellite imagery, and field work observations, this slide was first active prior to 1949 and achieved its current form and extent over 10 years ago (Fig. 59.2a, b). The long runout of this and other similar slides may be caused by undrained loading of cohesive earth material generated by the rock slide. Similar landslides have been described by Geertsema (2006) in northern British Columbia.

59.2.2 Rock Slide, Ram Plateau

This rock slide is located on an unnamed river within a canyon incised in the Ram Plateau. The landslide was likely triggered by a rock fall from the steep, limestone cliff face (Fig. 59.3a). The failed rock rubble moved down slope, entrained lake sediments and ran 20–25 m up the opposite side of the valley (Fig. 59.3b, c). The lake is located on the south side of the landslide deposit and was originally 4 m higher than at present (Fig. 59.3c). We determined the previous highest level of the lake from the presence of a spillway marked by accumulation of woody debris and lateral margins formed in the rock debris. The rock slide was not visible on 1949 air photos indicating that the failure post dates 1949. In addition, the absence of vegetation and

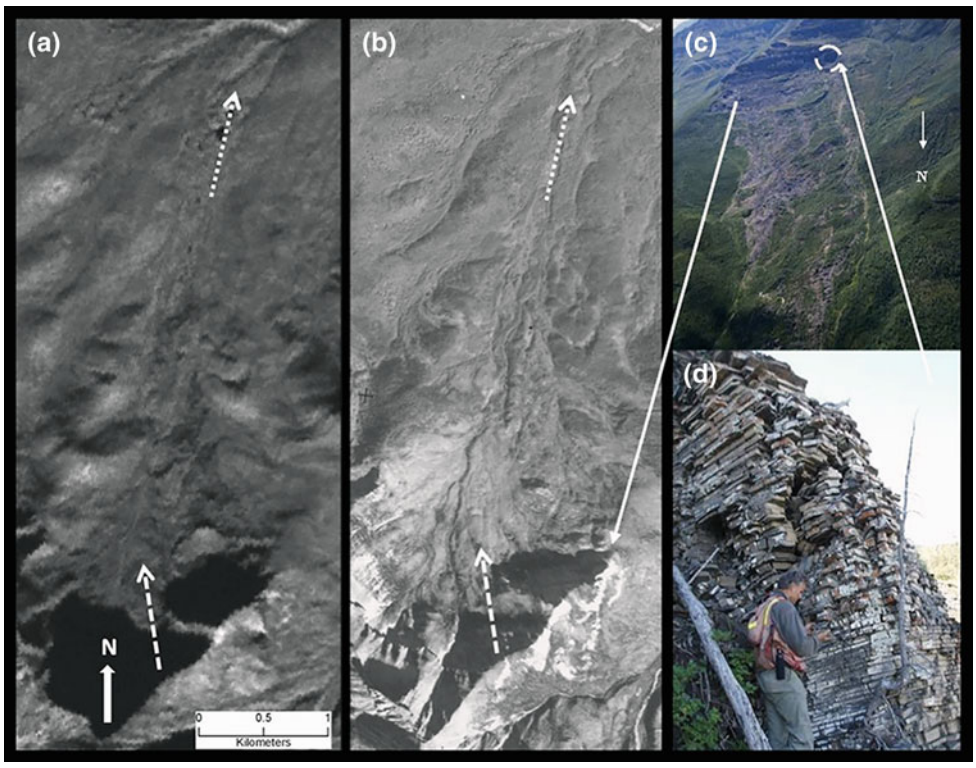

Fig. 59.2 Imagery of the rock slide-earth flow in the Tlogotsho Plateau (photos taken by Dr. Marten Geertsema and Courtney Jermyn). *White dashed lines* represent rock slide movement and *white dotted lines* signify earth flow movement. **a** ASTER ortho-image: *shadows* on north-facing slopes obscure exposed bedrock. **b** 1:40,000 scale, cropped 1949 air photo; A12295-182. **c** Oblique photo illustrating rock slide-earth flow features. **d** Jointed siltstone located at the base of a rotational rock slide (location identified by the circle in photo **c**)

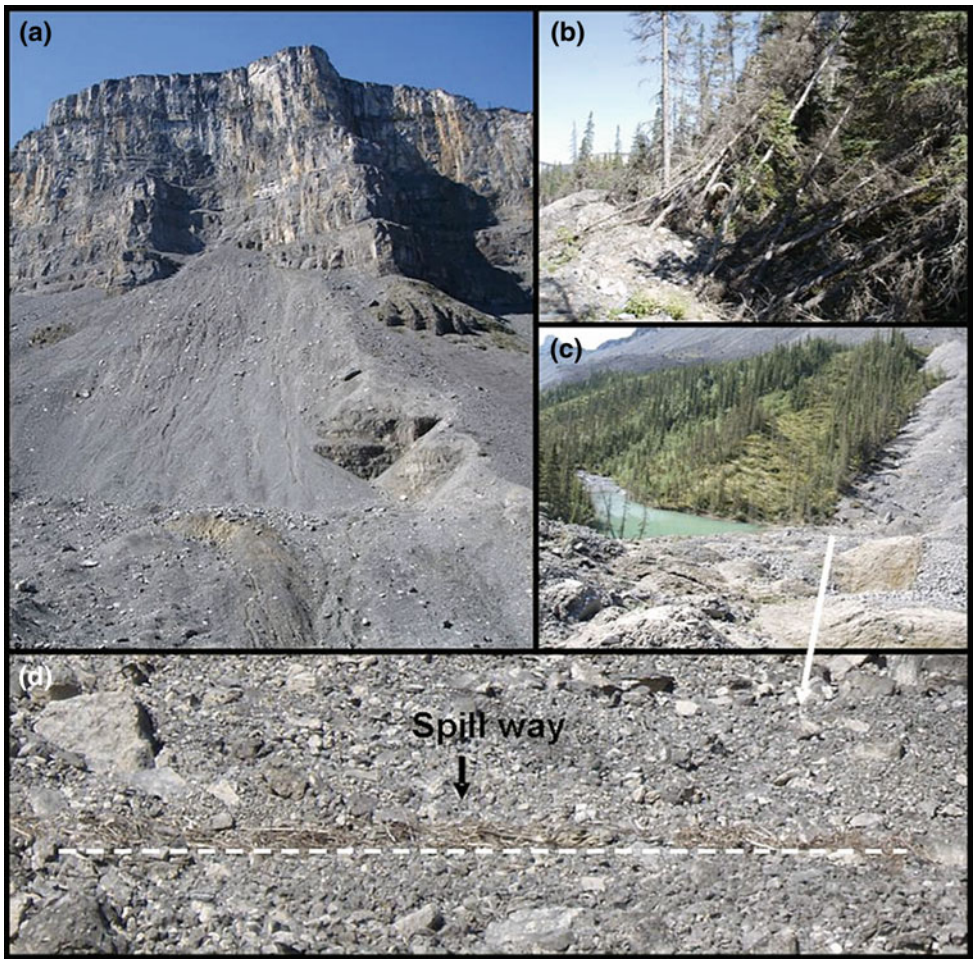

Fig. 59.3 Ram Plateau rock slide 1: **a** rock slide failure surface; **b** uprooted trees caused by run-up of debris during the rock slide event; **c** landslide-dammed lake; **d** spillway (photos taken by Dr. Marten Geertsema and Courtney Jermyn)

disturbance of the landslide deposits and fresh preservation of the spillway (Fig. 59.3d) suggest this failure was recent. Due to cloud cover over the failed region in the image, it was not possible to determine if this rock slide pre- or post-dated the imagery.

59.2.3 Active Complex Earth Slide–Earth Flow (Flowslide), Ram Plateau

We located an active complex landslide south of the rock slide in the canyon on the Ram Plateau (Fig. 59.4a–d). Based on field observations, it appears that riverbank erosion exposed fine-grained glacial lake sediments, causing an earth slide—earth flow that dammed the river (Fig. 59.4a, b, d). The flowslide exposed permafrost (ground ice) and angular rubble in a talus slope (Fig. 59.4c). The exposed permafrost thawed resulting in retrogressive flows. The ASTER scene did not provide additional information about the failure because of strong shadows. Field observations suggest the failure post-dates the ASTER scene acquired in 2000 because retrogressive thaw flow activity was ongoing during our visit.

59.2.4 Debris Slide, Wrigley Creek

During field investigations we identified a translational debris slide (Fig. 59.5a, c, d, and e). The displaced material is matrix-supported diamicton containing sub-rounded to angular clasts (Fig. 59.5d). A landslide-dammed lake was located on the north side of the deposit, and based on strandlines on the shore, the lake was 10 m deeper than at the time of our field visit (Fig. 59.5e).

The slide dates post 1949 as it was not present in the 1949 air photos but was identified in ASTER scenes scanned in the early 2000s. In the field we identified large conical mounds of debris (molards), up to 12 m in height, across the entire deposition zone (Fig. 59.5c). The molards gave the landslide a blocky texture in the ASTER scene.

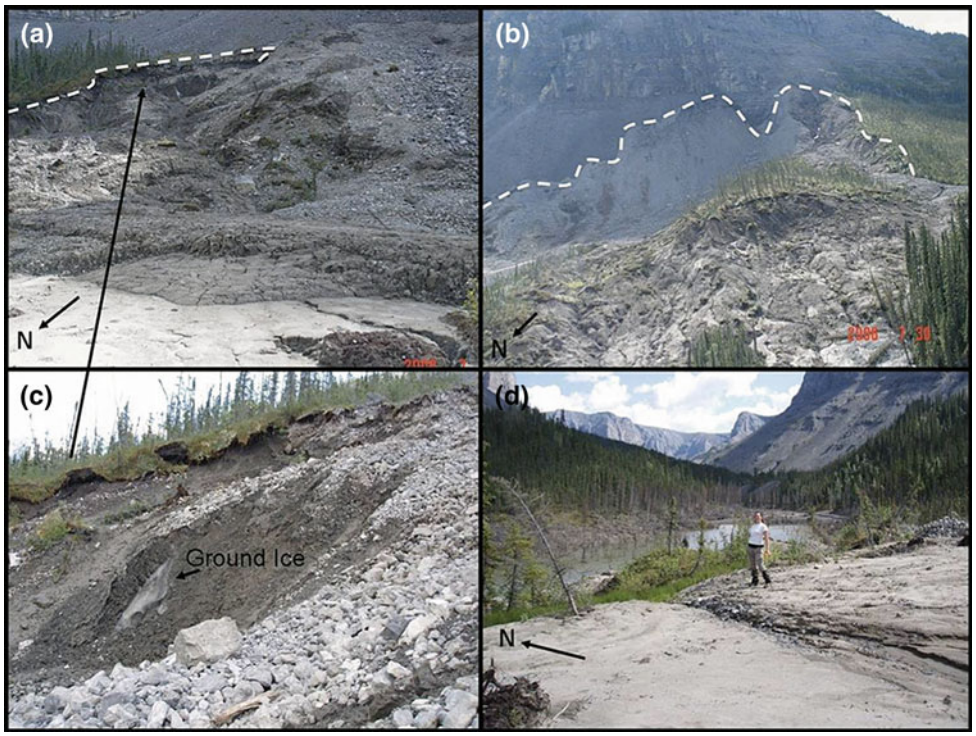

Fig. 59.4 Ram Plateau earth slide-earth flow (flowslide). *Dashed line* delineates headscarp: **a** earth flow movement within a complex landslide; **b** rotational earth slide movement within a complex slide; **c** ground ice exposure; **d** landslide-dammed lake. Photos taken by Dr. Marten Geertsema

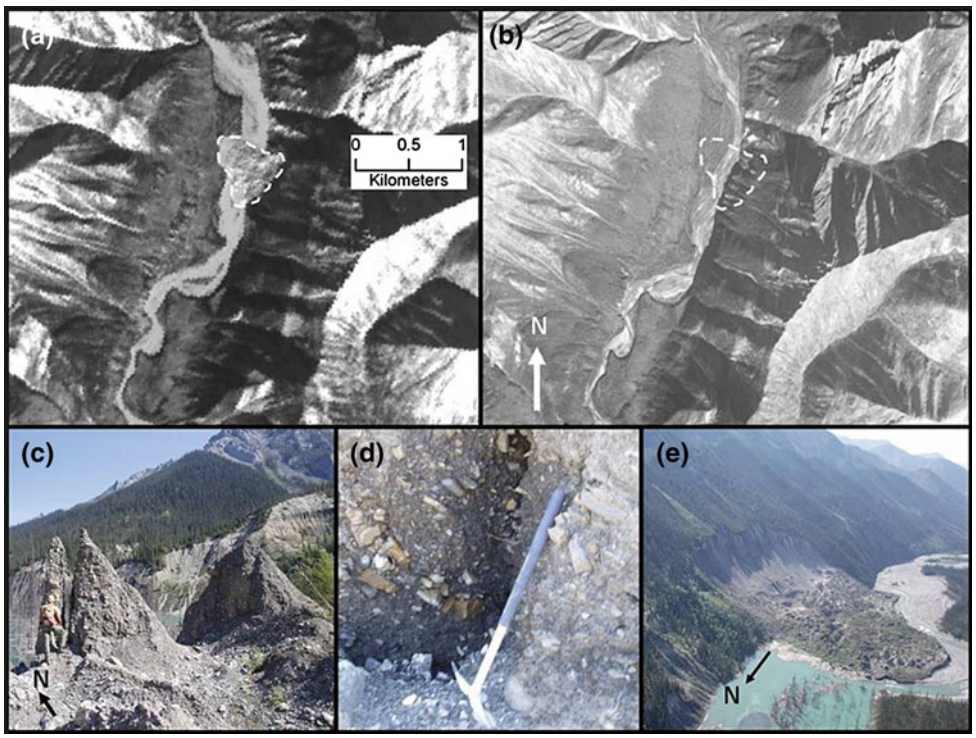

Fig. 59.5 Wrigley Creek debris slide: **a** ASTER scene (*white dashed line* identifies the debris slide); **b** 1949 air photo A12319-230: 1:40,000 scale. The image pre-dates the landslide. The air photo has a higher resolution than the ASTER scene. Geomorphological detail is comparable in the two aerial images. Because the air photo pre-dates the landslide event, gully formation in the headscarp region is visible. The presence of gullies suggest that the material is glacial in origin (*white dashed line* identifies the debris slide); **c** molards; **d** failed diamicton; and **e** view of the landslide-dammed lake. Photos taken by Dr. Marten Geertsema and Courtney Jermyn

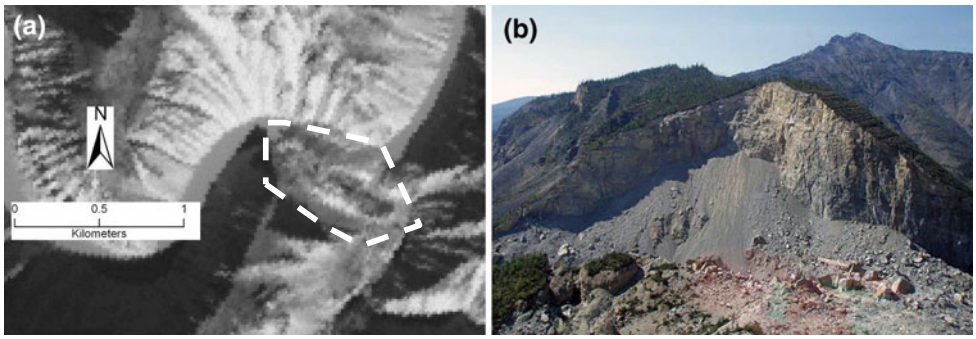

Fig. 59.6 **a** ASTER image of Rock slide, Cathedral Creek, **b** Oblique photo of Rock slide face, Cathedral Creek

59.2.5 Rock Slide, Cathedral Creek

A large rock slide occurred at the confluence of Cathedral and Clearwater creeks (Fig. 59.6a, b). The movement occurred along a dipping bedding plane. The landslide dammed the two creeks forming two lakes. The lake along Clearwater creek was approximately 5 km in length (Parks Canada 2012). Through correspondence with David Murray from Parks Canada in 2005 and reinstated by Parks Canada (2012), the failure occurred in the winter of 1996–1997, which followed a series of earthquake events in the region that year. In the summer of 1997, a portion of the natural dam, caused by the landslide, breached causing an outburst flood that dropped the lake along Clearwater creek 15 m; raising the level of the South Nahanni River in Deadman Valley by more than 4 m. Although no one was injured as a result of the flash flood, groups of canoeists camping downstream had to pack up quickly to avoid the event. The stability of the dam is unknown (Parks Canada 2012).

59.3 Discussion

The observations on large landslides described above, is part of a larger landslide inventory project in the South Nahanni watershed. Results show that many types of failures occur in the watershed. We learned from the landslide inventory and site investigations that in the Ram Plateau and the Ragged Ranges, debris flows and rock falls predominately originate along cliffs in karst gorges and on steep mountain slopes. Rock slide-debris flow failures, also common in these regions, initiate along bedding planes on steep valley walls. Huntley and Duk-Rodkin (2006) identified similar failure mechanisms in the neighbouring Mackenzie Valley. The Tlogotsho Plateau contains many complex rock slide-earth flows, like the Grizzly slide, but also earth flows. Complex slides occur where jointed sandstone and siltstone fail along incompetent shale. Earth flows initiate in shale lower on escarpments. Complex earth slides are found at low elevations within the watershed where glacial deposits are most abundant. They occur predominately along active tributaries and river systems. Morphology of some earth slides in the Ram Plateau area resembles features illustrated by Huntley et al. (2006), suggesting that these failures are active layer detachments or retrogressive-thaw flows caused by permafrost degradation. Landslide activity in the Ragged Ranges of the Mackenzie Mountains is characterized by debris flows and rock slides; the latter appear to slide on bedding planes in agreement with the conclusions of Eisbacher (1977, 1979) and Jackson (1987) who also found that bedrock landslides in this area are controlled by rock structure.

59.4 Conclusion

The landslide inventory identified the Tlogotsho and Ram plateaus, and the creek systems such as Cathedral and Wrigely creeks in the eastern part of the watershed, as especially prone to failure. Based on field studies and the interpretation of remotely sensed imagery, landslide activity in this area is explained by geology (rock type, rock structure, and surficial materials), river undercutting of slopes, and the presence of permafrost.

References

Eisbacher GH (1977) Rockslides in the Mackenzie mountains, District of Mackenzie. Geological Survey of Canada, Paper 77-1A, p. 235–241

Eisbacher GH (1979) Cliff collapse and rock avalanches (sturzstroms) in the Mackenzie mountains, northwestern Canada. Can Geotech J 16:309–334

Geertsema M (2006) Hydrogeomorphic hazards in northern British Columbia. Netherlands Geographical Studies 341, Utrecht, The Netherlands, 185 p

Huntley D, Duk-Rodkin A (2006) Landslide processes in the south-central Mackenzie River valley region, Northwest Territories, Geological Survey of Canada, Current Research, 2006-A9, 7 p

Huntley D, Duk-Rodkin A, Sidwell C (2006) Landslide inventory of the south-central Mackenzie river valley region, Northwest Territories. Geological Survey of Canada, Current Research 2006-A10, 11 p

Jackson LE Jr. (1987) Terrain inventory and Quaternary history of Nahanni map area, Yukon and Northwest Territories. Geological Survey of Canada, Paper 86-18, 23 p

Jermyn C (2011) An approach for remote landslide mapping, South Nahanni Watershed, Northwest Territories Canada. Master of Science thesis, University of Northern British Columbia, Prince George, BC, 135 p

Parks Canada (2012) River Hazards. http://www.pc.gc.ca/pn-np/nt/nahanni/visit/visit6/b.aspx. Accessed 27 Oct 2013

Detection of Permafrost and Foundation Related Problems in High Mountain Ski Resorts

60

Denis Fabre, Héloïse Cadet, Lionel Lorier and Olivier Leroux

Abstract
The ground ice contained in screes with various rock debris ("rock glacier") is the most common form of permafrost currently encountered in the Alps between 2500 and 3200 m asl. This altitudinal range is exactly the one which is concerned with the development of major ski resorts. In the manner of glaciers, rock glaciers will move on the slopes as a result of creep of the ice. However, because of the presence of rocky debris, the internal friction slows the movement. Confirming the presence of ice in the ground can be based at first on ground temperature measurements. But regarding the distribution with depth, in the absence of soundings technically and economically difficult to achieve, the geophysical methods provide good results. In the current context of climatic change, the problem of foundations of structures is increasingly taken into account. The observed warming in the Alps causes a slow melting of permafrost; settlements and collapses are observed. Geotechnical studies to illustrate this behavior are of the two following types: (i) feasibility study upstream projects, in order to define areas of permafrost and to avoid them for optimizing the implementation of the works; (ii) diagnostic studies giving solutions for reinforcement works after disorders due to the evolution of permafrost. Two specific examples are given: (i) the choice to draw a line for a chairlift, and (ii) the reinforcement of a ski-lift station with differential settlements.

Keywords
Permafrost • Rock glacier • Foundations • Geophysical methods

60.1 Introduction

Retreating of glaciers and melting of ice floes are emblematic witnesses of climate change. However, their geotechnical impacts are limited. On the other hand, melting of a soil-ice mixture like permafrost has important consequences for excavation and foundation works in Arctic or high mountain areas. This contribution concerns the occurrence of permafrost in alpine ski resorts where detection of permafrost is an important prerequisite for any development in altitude, especially before deciding the location of pylons or stations of ski-lift installations. Existing foundations on evolutionary ground containing permafrost need also frequently difficult diagnostic and consolidation works. The ground ice contained in screes mixed with various rock debris ("rock glacier") is the most common form of permafrost currently encountered in the Alps between 2500 and 3200 m altitude. This altitudinal range is exactly the one that is concerned with development of the major ski resorts.

Permafrost of rock glacier is always covered with an unfrozen surface layer, at least during the summer season ("active layer"). In the manner of glaciers, permafrost rock glaciers will move on the slopes as a result of creep of the ice. However, because of the presence of rocky debris, the

D. Fabre (✉)
CNAM—Chaire de Géotechnique, 2 rue Conté, 75141 Paris Cédex 03, France
e-mail: denis.fabre@cnam.fr

H. Cadet · L. Lorier · O. Leroux
ADRGT, 2 rue de la Condamine, BP 17, 38610 Gières, France

G. Lollino et al. (eds.), *Engineering Geology for Society and Territory – Volume 1*,
DOI: 10.1007/978-3-319-09300-0_60,

internal friction slows the movement. The topographic measurements at many sites monitored (like in Laurichard near Col du Lautaret, Bodin et al. 2009) show that the speeds are usually between a few centimeters and a few decimeters per year. The rock glacier ends downstream in a steep and unstable front: its gradient is equal to the angle of friction of the rocky debris having lost their ice providing cohesion. Secondary morphological characteristics of rock glaciers are the presence of large blocks on the surface and of transverse ripples and cracks, more or less regular.

Confirming the presence of ice in the ground is based on ground temperature measurement, by means of a sensor recording the temperature in a predetermined time not (Ribolini and Fabre 2006). But regarding the depth distribution, in the absence of soundings technically and economically difficult to achieve, geophysical methods provide good results. Good results are obtained with electrical method, seismic method and, more recently, radar and microgravimetry.

Schematically, the structure of a rock glacier is as follows: (1) surface layer formed of debris without ice (rather loose structure when the rock glacier is moving; (2) more or less ice rich permafrost; (3) bedrock (sometimes a layer of wet debris can be inserted). Electrically, these three levels provide good resistivity contrast: (1) 1–20 kΩ m; (2) a few dozen to several hundred kΩ m (pure ice generally exceeds 1 MΩ·m); (3) a few hundred to a few thousand Ω·m (depending on clay minerals and water contents of the bedrock). In seismic prospecting, the surface layer is loose and provides low speeds. When ice is present, better continuity is established and the speed reaches 3,000 m/ s. This value can be confused with that of a fractured or weathered rock, which often makes hypothetical the distinction with the substrate. The recent contribution of electrical and seismic tomographies is used to specify depth, shape and thickness of glaciated sediments and to qualify their ice content. They clearly show the heterogeneity of distribution of ice in rock glaciers (Ribolini et al. 2010).

In the current context of climatic change, the problem of foundations of structures is increasingly taken into account. The observed warming in the Alps causes a slow melting of permafrost; settlements and collapses are observed…

Geotechnical studies to illustrate this contribution are of two following types:

- Feasibility studies upstream projects, to define areas of permafrost for optimizing the implementation of the works;
- Diagnostic studies, to propose solutions for reinforcement works after disorders due to the evolution of permafrost.

Two examples will be given: the choice to draw a line for a chairlift and the reinforcement of an arrival station with movement and differential settlements.

60.2 Choice of Drawing a Line for a Chairlift

The project of a new Funitel line on station X grows between 2,800 and 3,000 m asl with a horizontal distance of about 750 m (Fig. 60.1). The initial project includes three intermediate pylons (P1 to P3).

In this area, bedrock consists mainly of carboniferous sandstones and shales. In the main part of the line, it is covered with screes and snowfields. There is therefore a risk that the pylons are based on the ice of a glacier residue or on rock glacier permafrost.

Geological observations indicate the likely presence of a rock glacier on the right bank of the future line: surface covered by numerous blocks of all sizes, cracks, steep front. Pylon P1 is projected on the terminal part of that rock glacier. On the other hand, pylons P2 and P3 are planned on a more regular slope near bedrock outcrops (Fig. 60.1).

Two electrical panels where performed near pile P1, one in the direction of the line (PE1: L = 160 m) and the other perpendicular (PE2: L = 80 m). This survey (Fig. 60.2) shows: (i) the presence of a layer of boulders of all sizes with a loose arrangement (5–6 m thick, resistivities below 5,000 Ω·m; (ii) a second layer with resistivities above 10 kΩ·m characteristic of the presence of interstitial ice; (iii) finally, at depth of 20–25 m, a third level with resistivity below 300 Ω·m interpreted as the bedrock resistivity (shale). On the electrical panel made across slope (PE2), the bedrock has a different nature (sandstone with a resistivity of about 2500 Ω·m).

Given the presence of interstitial ice in the ground, with a risk of slow movements affecting this sector, it has been recommended to move the pylon P1 to the north on a small

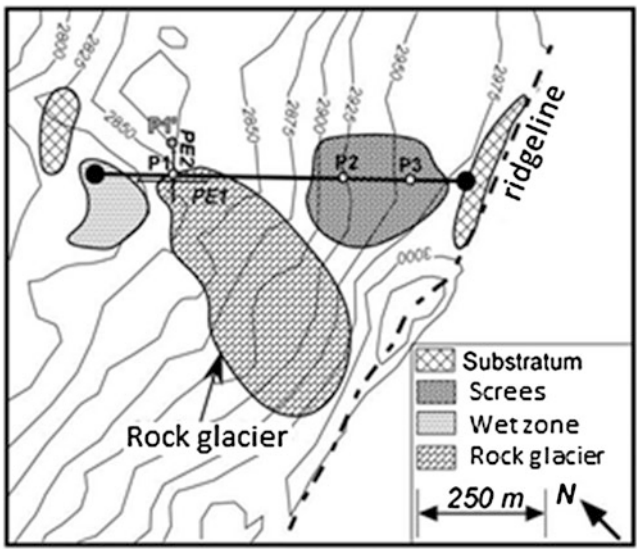

Fig. 60.1 Geomorphological map with the location of the geotechnical investigations

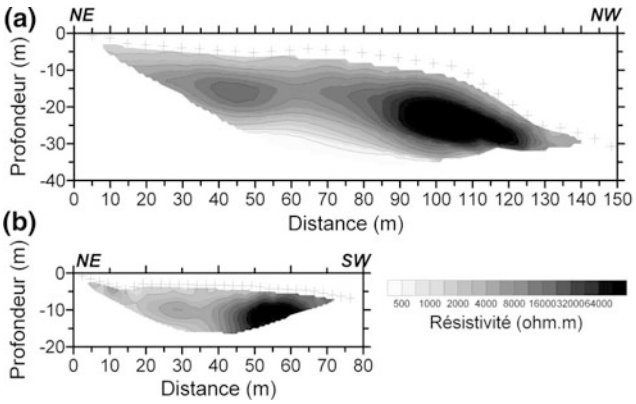

Fig. 60.2 Electrical tomography results: **a** PE1, 5 iterations, RMS = 6.0 %, **b** PE2, 5 iterations, RMS = 3.8 %

hill (location P1′, see Fig. 60.1). This zone corresponds to a thin (less than 3 m) debris layer above a fractured sandstone rock.

60.3 Diagnosis of a Chairlift Station with Significative Disturbances

The top station of the chairlift is located on the edge of a glacier at 3100 m asl. During its operation, the device had to undergo several settings especially after the appearance of some instabilities in the embankments (Fig. 60.3).

The geology corresponds to the ante-permian Briançonnaise area: arkosic sandstone interbedded with shale. Scree covers partially the bedrock behind the station; but some ice is present in the cracks of the visible bedrock. Further downstream, on the west side of the station, the geological map indicates the presence of a rock glacier.

Geotechnical investigations consisted of detailed geological observations, 4 mechanical excavations (TP1 to TP4) and two geophysical profiles (P1 and P2) with both electrical and seismic tomographies (see Fig. 60.3).

Field observations show the following: (1) bedrock outcropping in the berms to the east and west of the station, (2) debris covering the ice surface with a thickness <1 m with a rock glacier like morphology behind the station (direction north), and (3) massive ice at a distance of about 40 m behind the station.

Many signs of movements were also noted: (i) cracks just below the station (west side), related to the melting of the underlying ice; (ii) creep of debris in direction north behind the station; and (iii) a small landslide behind the station.

Four holes were dig around the station. All of them show pure ice or permafrost at shallow depth (<1 m). Fractured bedrock was encountered at TP2, TP3 and TP4 respectively

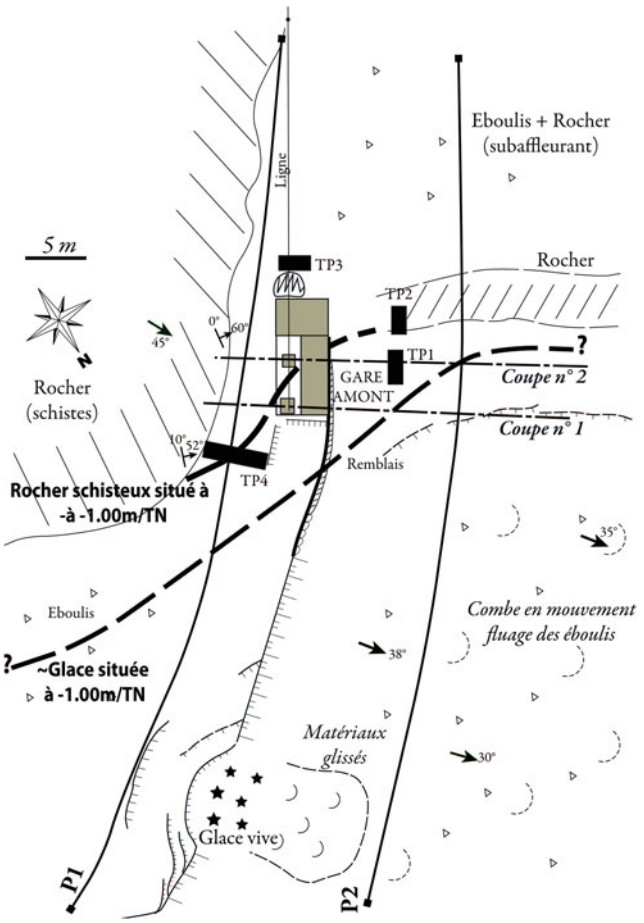

Fig. 60.3 Geomorphological map of the site with the location of the geotechnical investigations

at 1.3, 3, and 1.5 m deep. At TP1, the refusal took place on permafrost at a depth of 1.5 m.

Two profiles of electrical and seismic tomographies (P1 and P2) were performed on both sides of the station. Resistivities (electric tomography) and P wave velocities (seismic tomography) as functions of depth are shown in Fig. 60.4.

Geological formations are identified from their geophysical characteristics: (i) screes, shale (highly fractured and weathered) and shale embankments containing ice are characterized by velocities between 500 and 1,500 m/s and resistivities between 3 and 10 kΩ m; (ii) the fractured shale rock is characterized by velocities between 1500 and 2,500 m/s and resistivities below 3,000 Ω·m; and (iii) the massive ice is characterized by velocity above 3,000 m/s and resistivity greater than 10 kΩ m.

On each of the two profiles, a clear distinction can be made between the northern part and the southern part. Ice is widely present in the northern half of the profile (depths between 0.5 and 4.5 m), while in the southern part the fractured rock is found under 1.5–4 m of scree without ice.

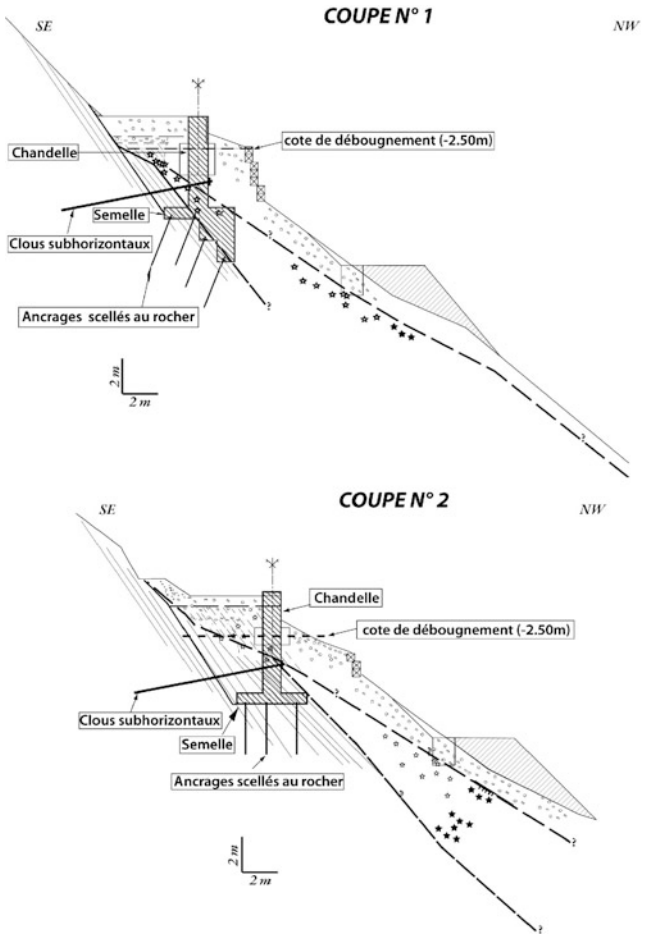

Fig. 60.4 Geotechnical sections 1 and 2 after work (location on Fig. 60.3)

According to the surveys, it appears that the station is on the edge of a glacier, at the transition between the bedrock and the glacier; it seems likely that the front part of the station (south) is anchored on the fractured shale, while the rear part of the foundation (north side) is rooted in permafrost overcoming the glaciated fractured bedrock.

To ensure the sustainability for the long term, a solution of reinforcement of the station) is recommended. It is based on the following features (Fig. 60.4): (i) reshape the arrival of the chairlift with a slight reduction in altitude (the objective is to be almost everywhere on the bedrock); (ii) advance downstream to the south of about 5 m to get away from the glacier; and (iii) anchoring with sub-horizontal nails of the central pylon of the station to seal it deep into the bedrock.

60.4 Conclusion

In a context where the mechanical surveys are the exception (for the first time in France, two destructive mechanical soundings were conducted in 2009 in the permafrost on the Deux-Alpes), morphological analysis and geophysical constitute the main means for detecting the presence of permafrost.

In the Alps, in case of new constructions in altitude, the best solution is obviously to avoid foundations on permafrost in the context of climate change. Because of its high resistivity, the ice can generally well be detected by electrical prospecting; and tomographies have made significant progress on the knowledge of the internal structure of rock glaciers (Ribolini et al. 2009). But other methods are also promising (radar, surface waves…).

Regarding the old facilities in ski resorts, the melting of permafrost may cause subsidence and instability. Consolidation requires significant resources; and purging levels of glaciated screes found in rock glaciers is often the best solution.

References

Bodin X, Thibert E, Fabre D, Ribolini A, Schoeneich P, Francou B, Reynaud L, Fort M (2009) Two decades of responses (1986–2006) to climate by the Laurichard rock glacier, French Alps. Permafrost Periglac Process 20:331–344

Ribolini A and Fabre D (2006) Permafrost existence in the rock glaciers of the Argentera Massif (Maritime Alps, Italy). Permafrost Periglac Process 548–563

Ribolini A, Guglielmin M, Fabre D, Bodin X, Marchisio M, Sartini S, Spagnolo M, Schoeneich P (2010) The internal structure of rock glaciers and recently deglaciated slopes as revealed by geoelectrical tomography: insights on permafrost and recent glacial evolution in the Central and Western Alps (Italy–France). Quat Sci Rev 29:507–521

In-situ Observation on Regularities of Rainfall Infiltration in Cold and Dry Loess Area

61

Ping Li, Tong-lu Li, Xian-li Xing and Hong Wang

Abstract
A monitoring station was set up in Zhengning County, Gansu Province. The changes in soil moisture content within 10.0 m under the condition of natural rainfall infiltration had been observed continuously for a whole year. Combined with the data of precipitation, evaporation and temperature, the rules of water migration in loess were analyzed. The results show that soil moisture within 1.2 m is affected greatly by rainfall and evaporation, changing annually. When the precipitation goes higher than 18 mm/d, soil moisture content within this range will change jumpily on its background trend. In the deep, water moves mainly in the form of vapor, the migrate amount is very small, resulting that soil moisture contents grow not only weakly but also non-annually, the accumulated amount can not be ignored, water will gather around the surface when encountering paleosol layer.

Keywords
Cold and dry loess area • Rainfall infiltration • Water migration • Volumetric moisture content

61.1 Introduction

Naturally, loess slope can maintain stable itself because of the low moisture content and the high strength. However, once rainfall infiltrates, soil saturation will increase, matric suction and shear strength will reduce subsequently within the rainfall affected range, resulting in stability failure at double disadvantages of downslide force growing and anti-slide force dropping. Therefore, study on the regularities of rainfall infiltration is the basis for analyses of loess landslides stability and researches of the failure mechanism.

There is a common belief that large scale loess landslides are caused by the rise of groundwater level that mainly due to rainfall and irrigation (Zhao et al. 2004; Wu and Huang 2011), but groundwater levels are often very deep in loess area, and the permeability of loess is also quite low, surface water infiltration depth is limited in loess area indicated by many field observations (Tu et al. 2009; Li et al. 2005; Liu et al. 2008). Chen et al. (2009) pointed that rainwater can only reach a certain depth. Potential energy between ground and the maximum infiltration depth goes to zero as rainwater reaching a certain depth. He also deduced a formula for the maximum infiltration depth on the basis of energy conservation. Now it is commonly considered that surface water pours into the deep through paths like vertical fissures and sinkholes. However, as can be found from field observations that such paths are generated in unloading areas at the side of loess platforms. Furthermore, these paths often have high hydraulic gradient, water in it is more inclined to run off through exports, so it is unlikely to cause universal rise of groundwater level.

Although there is widespread sentiment believing rainfall infiltration depth is limited currently, final conclusion can not be reached yet due to short monitoring period and shallow monitoring depth. Supposing that rainfall infiltration is really limited, it becomes difficult to explain the

P. Li (✉) · T. Li · X. Xing · H. Wang
Department of Geological Engineering, School of Geological Engineering and Surveying, Chang'an University, Xi'an, 710054 China
e-mail: lp19881028@163.com

G. Lollino et al. (eds.), *Engineering Geology for Society and Territory – Volume 1*,
DOI: 10.1007/978-3-319-09300-0_61,

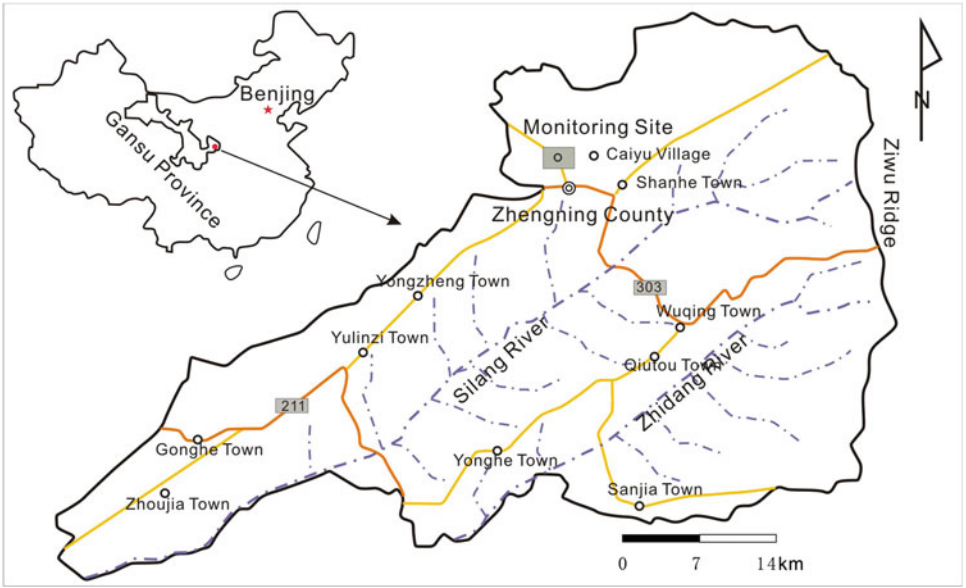

Fig. 61.1 Geographic location of the monitoring site

Table 61.1 Physical and mechanical indexes of loess and paleosol

Physical and mechanical indexes	Loess	Paleosol
Bulk density (g/cm^3)	1.44	1.64
Dry density (g/cm^3)	1.24	1.35
Moisture content (%)	16.3	21.9
Saturated moisture content (%)	43.6	37.2
Specific gravity	2.70	2.71
Void ratio	1.177	1.007
Plastic limit (%)	20.7	21.3
Liquid limit (%)	32.4	31.6
Compressibility coefficient (MPa^{-1})	0.82	0.62
Coefficient of collapsibility	0.079	0.043
Vertical coefficient of permeability (m/s)	2.55×10^{-6}	5.36×10^{-8}
Horizontal coefficient of permeability (m/s)	1.72×10^{-6}	2.12×10^{-8}
Clay content (%)	17.9	29.6

phenomenon that changes of groundwater level in loess area, as well as spring flow at the side of loess platforms, are closely related to rainfall and irrigation. For example, the Southern Tableland of Jingyang County or Heifangtai irrigated area, where a large number of loess landslides have been triggered by the increasing groundwater level due to long-term irrigation (Wu et al. 2011; Wang et al. 2004). In order to reveal the regularities of rainfall infiltration in loess further, a monitoring station was built in Longdong Loess Plateau, soil moisture contents within 10.0 m were observed under the condition of natural rainfall, combined with the data of precipitation, evaporation and temperature, the regularities of water migration in cold and dry loess area were analyzed, then the relationship between groundwater and surface water was attempted to be explained.

61.2 Introduction of Monitoring Area

Monitoring station is located in the former site of Songjiaya primary school in Cai Yu Village, Zhengning County, Gansu Province, the geographic location is shown in Fig. 61.1. Geographic coordinate is 108°19′57″ east longitude, 35°30′47″ north latitude and 1418 m in heights. Zhengning County is in the east of Longdong Loess Plateau, west of Ziwuling Ridge, having typical ravine landform. The average annual precipitation is 623.5 mm, while evaporation can reach more than 1,500 mm. The largest freezing thickness is 58 cm, the depth of groundwater level measured is about 120 m. So study area certainly belongs to typical cold and dry loess area. Tertiary red clay and continuous Quaternary loess stratums were mainly developed.

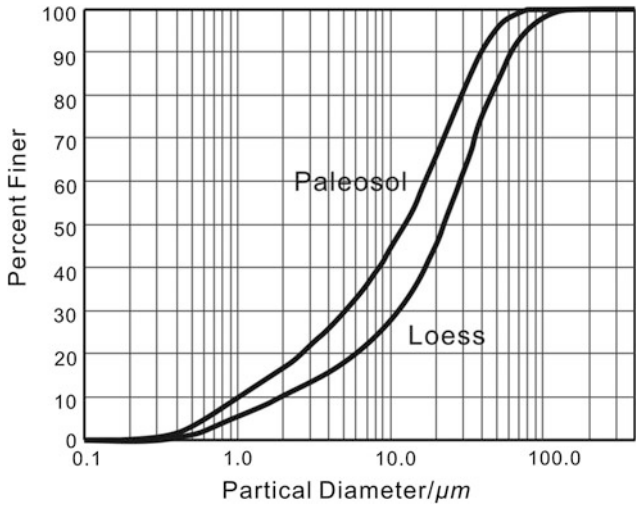

Fig. 61.2 Particle-size distribution curves of loess and paleosol acquired in the monitoring well

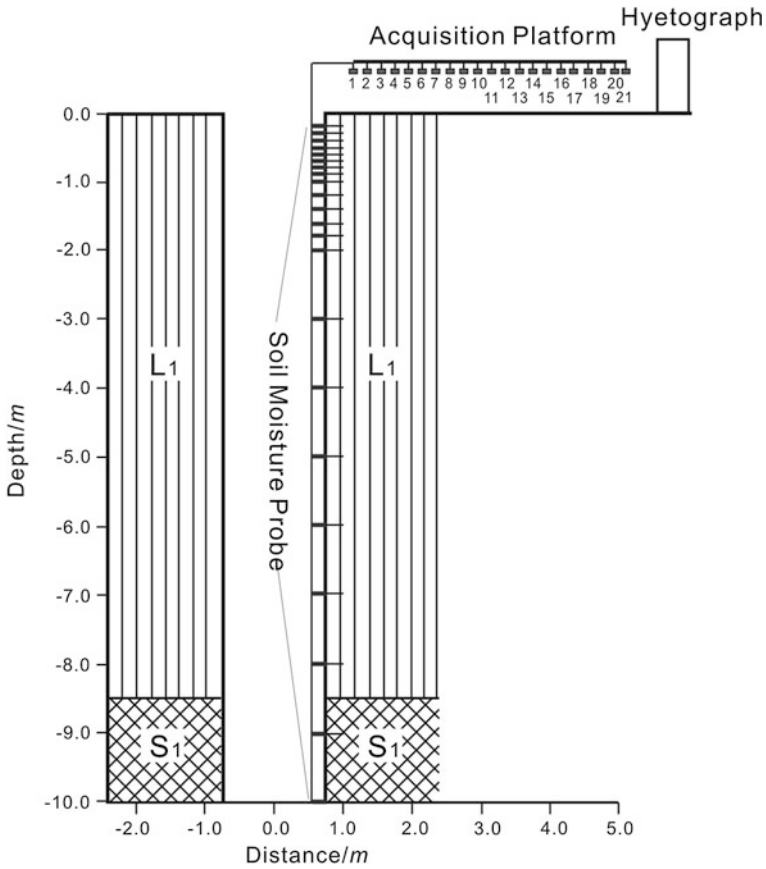

Fig. 61.3 Arrangement of probes and stratigraphic lithology of the site

61.3 Monitoring Site and Instrument Arrangement

An exploratory well with depth of 10 m and diameter of 1 m was excavated in the center of the site, the top Heilu soil had been removed, Malan loess and the first paleosol layer from 8.5 to 10 m were exposed. During the excavation, undisturbed samples of Malan loess and paleosol were taken at the depth of 5 and 9 m respectively. Physical and mechanical indexes were measured in laboratory, showing in Table 61.1, particle-size distribution curves are showed in Fig. 61.2.

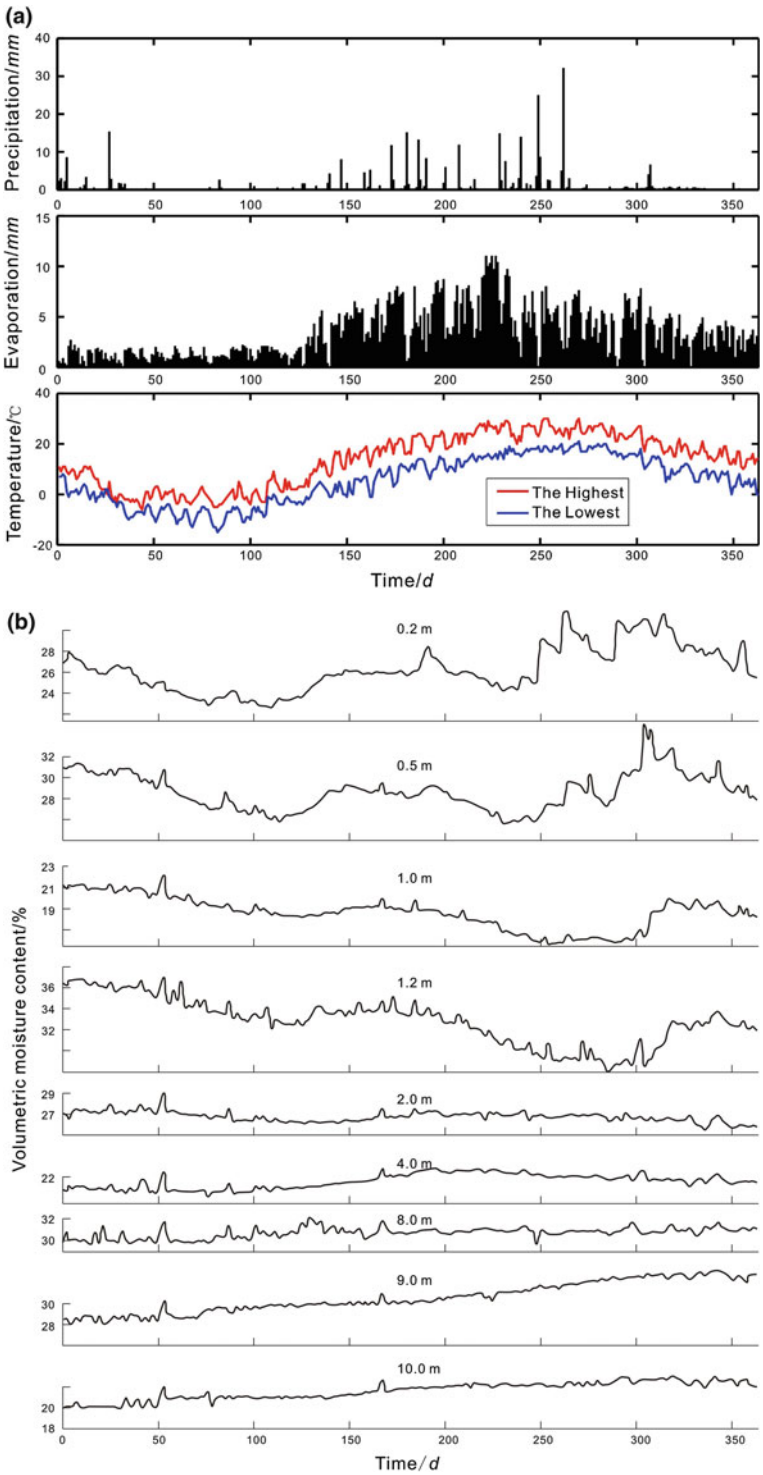

Fig. 61.4 Meteorological data and the changing curves of soil moisture content at parts depth of a whole hydrological year. **a** Meteorological data, **b** The changing curves of soil moisture content at parts depths

Soil moisture meter probes were inserted into the wall of the well. Considering that soil moisture contents in the shallow vary more obviously than that in the deep after infiltration, so the probes installed in the shallow have a small interval than that in the deep. In the first meter below ground, the interval was 0.1 m, in the second meter, 0.2 m, then after, 1.0 m each, 21 probes in total (Fig. 61.3). Afterwards, the wall was painted with straw-reinforced mud, and then cement mortar, finally waterproof coating was outermost to prevent the spread of moisture to the well. The moisture meter has a measurement range of 0–100 % and a resolution of 0.01 %, the applicative temperature

varies from −20 to 80 °C. Soil volumetric moisture content is acquired indirectly by measuring the dielectric constant of soil. Wires connected probes can reach to the data collecting instrument, which is at the surface, so the data can be easily got. A rain gauge with a measurement range of 0.1–9 mm/min and a precision of 0.01 mm, was installed near the well to record the precipitation.

61.4 Analysis of the Monitoring Results

This paper mainly targets at the results of a whole hydrological year from November 2, 2011 to October 30, 2012. Of which moisture contents were measured once a day when it rained, otherwise, twice a day. Evaporation and temperature data during that period were collected from the local weather bureau and China Climatology Network. These data are all shown in Fig. 61.4.

It can be seen from the data of precipitation, evaporation, temperature and soil moisture contents changes of the whole hydrological year, several features can be conclude as follows:

Temperature, precipitation and evaporation present a feature of changing annually. Precipitation increased gradually after March, peaking in July. From August onwards, the average precipitation kept in a quit low level except for several intense rainstorms. Evaporation peaks between May and June, and then it dropped gradually and bottomed out between the next January and February.

Soil moisture contents within 1.2 m were significantly affected by rainfall and evaporation, changing annually either. It can be seen from the overall trend that moisture contents within 1.2 m came to the minimum at the end of January, then rose steadily and reached their maximum on around May 10. In the decreasing process, although precipitation increased continually, the decreasing trend had never changed. This overall trend was consistent with the trend of evaporation, to be more specific, evaporation and soil moisture contents of this range came to the largest/lowest at a similar time.

Moving on to the leaps. All these leaps correspond to high precipitation. It rained 24.9 mm on July 8, 32.1 mm on July 21 and 18.2 mm on August 18. So it can be concluded that the precipitation, which can cause leap in moisture content, is about 18 mm/d. When precipitation goes higher than 18 mm/d, soil moisture content curves will change jumpily. On the contrary, soil moisture contents remain its background trend. However, this abrupt effect can not change the overall trend.

Moisture contents from 5.0 to 8.0 m changed slightly during the whole year, but increased totally, while that from 9.0 to 10.0 m rose significantly. The growth at 9.0 and 10.0 m were about 4 and 2.5 % respectively. The interface between Malan loess and the first paleosol layer appears at 8.5 m. Loess is featured by larger void ratio, higher permeability and worse water-holding ability than paleosol. In the deep, water moves mainly in the forms of unsaturated seepage or vapor form, the migrate amount of vapor is quit small, resulting in soil moisture contents changing not only slightly, but also non-annually. But the accumulated amount can not be ignored, the migrate rate will decrease greatly as encountering paleosol, water will gather around the surface of paleosol layer, which can lead to obvious increase of soil moisture content.

61.5 Conclusions

(1) Soil moisture contents within 1.2 m are sensitive to rainfall and evaporation, changing annually, the trend is consistent with the trend of evaporation.
(2) When precipitation goes higher than 18 mm/d, soil moisture contents in the shallow will change jumpily, otherwise, there are almost no obvious fluctuations on the background trend. This abrupt effect can not change the overall trend.
(3) In the deep, water moves in unsaturated loess mainly in the forms of unsaturated seepage or vapor form, the migrate amount of vapor is quit small, resulting in soil moisture contents changing not only slightly, but non-annually. But the accumulated amount can not be ignored, water will gather around the surface of paleosol layer, leading to obvious increase of soil moisture content.

References

Chen W, Mo H, Chen L (2009) Study on rainfall infiltration process and the biggest infiltration depth for unsaturated soil slope. Min Metall Eng 29(6):13–16

Li AG, Yue AQ, Tham LG, Lee CF et al (2005) Field-monitored variations of soil moisture and matric suction in a saprolite slope. Can Geotech J 42:13–26

Liu H, Ni W, Yang H et al (2008) Site test on infiltration of loess subgrade under rainfall circumstance. J Earth Sci Environ 30(1): 60–63

Tu XB, Kwong AKL, Dai F et al (2009) Field monitoring of rainfall infiltration in a loess slope and analysis of failure mechanism of rainfall-induced landslides. Eng Geol 105:134–150

Wang Z, Wu W, Ziqiang Z (2004) Landslide induced by over-irrigation in loess platform areas in Gansu province. Chin J Geol Hazard Control 15(3):43–46

Wu L, Huang R (2011) A numerical analysis of the infiltration and parameter effects in unsaturated soil. Hydrogeol Eng Geol 38(1):94–98

Wu C, Dai F, Min H et al (2011) Influence of cracks at the platform on hydrologic response of loess slope. J Jilin Univ (Earth Science Edition) 41(5):1512–1519

Zhao H, Dou H, Zhang Y (2004) The distribution law of transient moisture content of slope soil after the rain. Railway Constr 10:46–48

Thermokarst Phenomenon Typification Approaches Near the Southern Border of the Permafrost Zone

62

E.M. Makarycheva

Abstract

The studies of thermokarst phenomena along the oil pipeline in the south of Eastern Siberia and the Far East have been conducted. Thermokarst phenomena were investigated not only in the pipeline-affected zone, but also under natural conditions. Initial data for the research were obtained during the annual aerovisual observations for 2010–2012. The principal goal of the aerovisual observations was the identification of thermokarst phenomena. Thermokarst phenomenon typification near the southern border of the permafrost zone was the results of the following analysis. The differences in the morphology of thermokarst phenomena were identified. It's depends on the landscape-climate, engineering-geological conditions and the type of man-made impact. The analysis of the spatial distribution of thermokarst phenomena was also made. All phenomena were divided into two groups, while the total number of types amounted to 11. Additionally, forms with marks of processes activation due to the human impact on the territory were denoted. The analysis of the allocated types has contributed to finding signs of stadiality of the process. The allocated types of the phenomena were characterized by various time depths and grade of the intensities of a process. This demanded by the development of individual protection measures for each of them. The developed typification can be expanded to other areas of the permafrost zone.

Keywords

Thermokarst phenomenon • Typification • Monitoring • Pipeline

62.1 Introduction

The development of thermokarst processes leads to appearance negative landform. Morphology, vegetation characteristics and filling-up of negative landform depend on geotechnical conditions of building and stages of process development.

Thermokarst phenomenon along more than 2,500 km length of the oil pipeline in the south of the Eastern Siberia and the Far East has been analyzed. The width of the survey area is a 1 km, therefore the phenomenon has been investigated not only in the pipeline affected zone, but also under natural conditions. Invariability construction technology along the investigated object has enabled to estimate the degree of the technogenic bearing on thermokarst processes in different permafrost landscapes and under various climate conditions.

Initial data for the research are spatially determined (coordinate linked) images from helicopter visual survey. We got more than 7,000 images every year within last 3 years.

E.M. Makarycheva (✉)
Sergeev Institute of Environmental Geoscience Russian Academy of Sciences (IEG RAS), Ulansky Pereulok 13, Building 2, P.O.Box 145, Moscow, Russia, 101000,
e-mail: emakarycheva@gmail.com

G. Lollino et al. (eds.), *Engineering Geology for Society and Territory – Volume 1*,
DOI: 10.1007/978-3-319-09300-0_62,

62.2 Thermokarst Phenomenon Identification

The problems of thermokarst phenomenon identification using images were solved (Sergeev et al. 2012). This process has no enough signs for interpretation, and it is difficult to separate it's from the disturbing of natural flow (flooding) or bog formation.

The main identifying features of thermokarst process were considered to be the subsidence, usually accompanied by flooding and continued throughout the period of surveys. The basic condition for the development of thermokarst is the presence of soils with very high ice content or massive ice that were found during geological survey.

The signs of the thermokarst processes development were found only on the part of flooded areas along the pipeline (in disturbed conditions). Thermokarst is identified confidently, if it is located in the unaffected area, for example natural thermokarst lake.

62.3 Special Thermokarst Phenomenon Typification

The thermokarst phenomena whose genesis is connected with human impact belong to the second class. They are haven't confinedness to forms of relief and quaternary deposits complexes. The phenomenon development factor of the second class is the type of human impact. Within the studied territory, groups of the phenomena developed due to the disturbance of the vegetation cover and influence of engineering objects were found (Fig. 62.1). Thus, two types of the phenomena are distinguished in this class: thermokarst on arable land and on sites of the disturbance of the heat exchange (Fig. 62.2).

Each of the eleven distinguished types of the phenomena has been characterized by the description of form, approximate depth, sizes, character of the coastline, water content, type of vegetation within a form, and presence of modifications in vegetation around it. Additionally, forms with activation signs of human impact on the territory were denoted. Thermokarst phenomenon typification near south border of permafrost zone was made on the basis of generalized analysis of typification approaches which were published in Russian and world literature (Kachurin 1961; Koff et al. 2009; Jorgenson et al. 2008; Shur 1988). The regularities of thermokarst process distribution, the dependence of the phenomenon morphology and a morphometry from a structure and a genesis of the territory, and a source of thermal influence underlie this typification.

The distribution regularity analysis of thermokarst phenomena allowed all the phenomena to be divided into two classes by their confinedness to elements of a relief. The first class, i.e. the phenomena having a natural genesis, includes: confinedness to fluvial landforms (rivers valleys, the dead arm of river and drain hollows), or to watersheds (Fig. 62.1).

At the development of thermokarst process on fluvial landforms, morphological and morphometry characteristics of the phenomena have distinctions depending on the form of a relief and landscape type, and as a result, structures of the territory and a source of thermal influence. Within the territory studied, five types of thermokarst phenomena on fluvial landforms were as follows: thermokarst expansions of river arms or drain hollows, thermokarst on drain hollows, thermokarst on dead arms, on mound peat land in valleys of the rivers, saucer-shaped low in river valleys.

At the development of the thermokarst processes on watersheds, obvious dependencies of morphology and morphometry of the phenomena on a type of underground

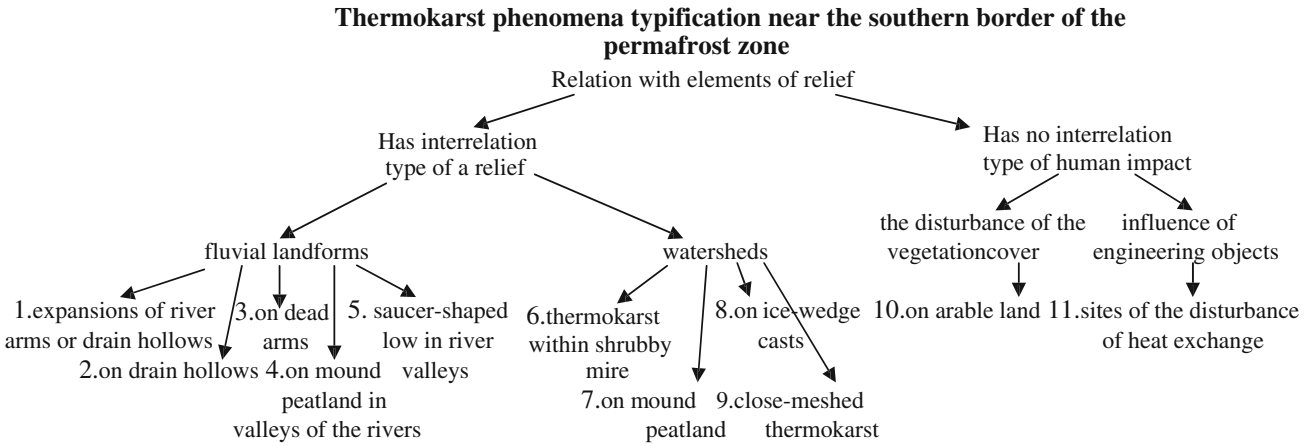

Fig. 62.1 Thermokarst phenomena typification near the southern border of the permafrost zone

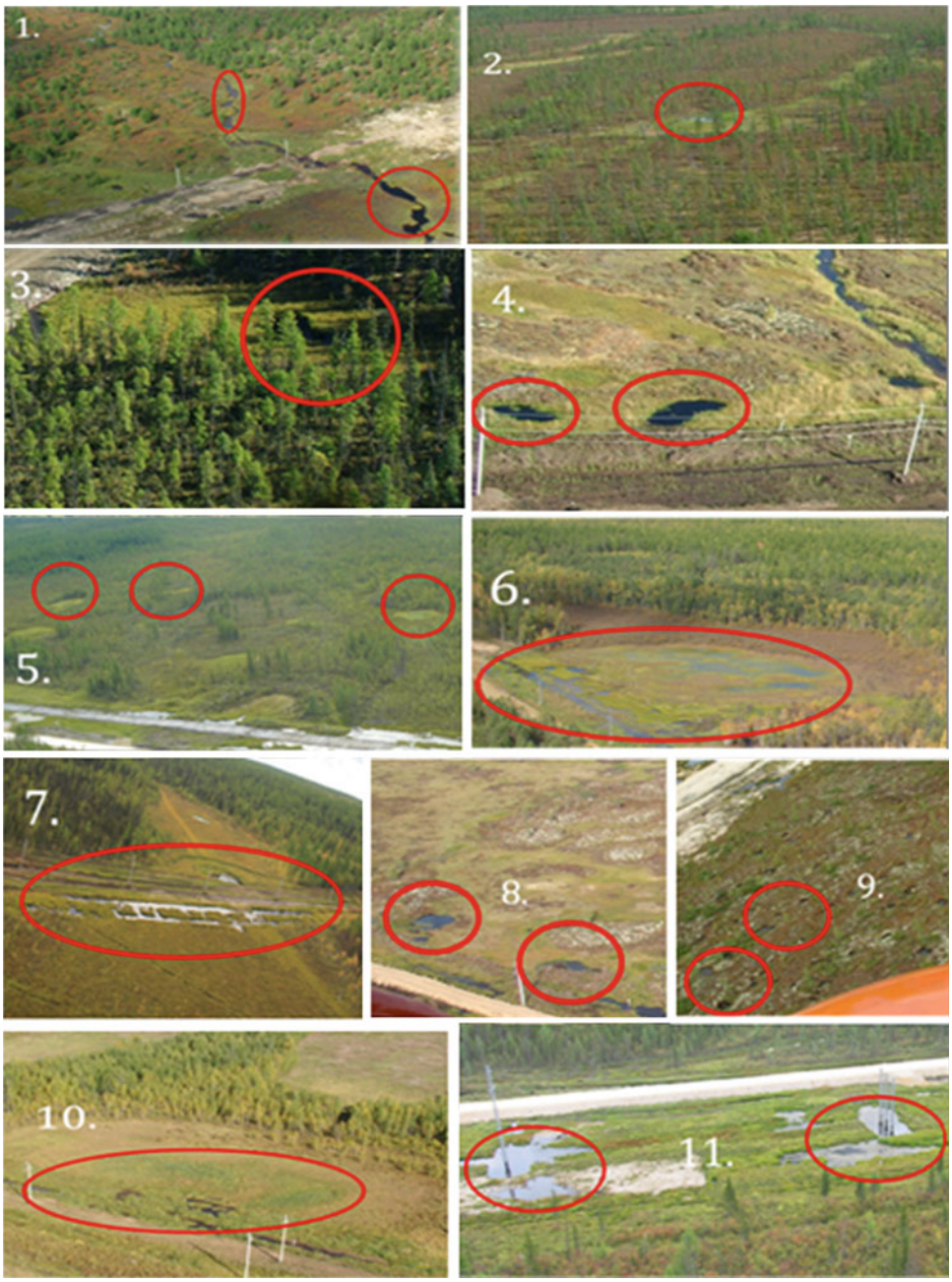

Fig. 62.2 Types of termakarst: *1* thermokarst expansions of river arms or drain hollows; *2* thermokarst on drain hollows; *3* thermokarst on dead arms; *4* thermokarst on mound peatland in valleys of the rivers; *5* saucer-shaped low in river valleys; *6* thermokarst within shrubby mire; *7* thermokarst on mound peat-land; *8* thermokarst on ice-wedge casts; *9* close-meshed thermokarst; *10* thermokarst on arable land; *11* thermokarst on sites of the disturbance of the heat exchange

ices and landscape types are traced. The total amount of the allocated types is leveled to four: thermokarst within shrubby mire, thermokarst on mound peat land, thermokarst on ice-wedge, close-meshed thermokarst on watersheds.

62.4 Conclusion

The allocated type analysis allowed finding a signs of the stadiality of the process inside of the studied territory. The allocated types of the phenomena are characterized by various development times and the intensity of process. That results in the necessity of development of individual protection measures for each of them.

The developed typification can be applied to other areas of the permafrost zone.

References

Jorgenson MT, Shur Y, Osterkamp TE (2008) Thermokarst in Alaska. In: Proceedings of the international conference on permafrost [ICOP], vol. 9, pp. 869–876

Kachurin SP (1961) Thermokarst on the territory of the USSR. Academy of Sciences Press, Moscow: 298 (in Russian)

Koff GL, Chesnokova IV, Bogomolova TV (2009) Experience in engineering geological typification and mapping of geoenviromental risk factor (by the exemple of "East Siberia-Pacific Ocean" oil pipeline route). Geoecology. Engineering geology, Gidrogeology, Geocryology 2:172–179 (in Russian)

Sergeev DO, Khalilova JV, Perlshtein GZ, Khimenkov AN, Ma-karicheva EM, Ugarov AN (2012) Identification, diagnostics and ranking of geocryological hazards for lengthy pipelines and other linear structures. In: Tenth international conference on permafrost: resources and risks of permafrost areas in a changing world, vol. 2. Fort Dialog-Iset, Ekaterinburg, Russia, pp. 382–384

Shur YL (1988) The upper horizon of permafrost and thermokarst, Novo-sibirsk "Nauka": 212 (in Russian)

Part VI

Exploration, Exploitation and Monitoring Geothermal Energy Fields: The Role of Geophysics

Convener: Prof. Luigi Sambuelli—*Co-conveners*: Michele Pipan, Maurizio Fedi, Ettore Cardarelli, Cesare Comina

The target of the session is the state of the art of geophysical developments and applications to geothermal exploration and heat mining. Theoretical works, methodological developments and applications to synthetic and field cases are welcome. A non-exhaustive list of topics include: (a) Theoretical and lab studies on variations of rock physical properties with temperature; (b) Airborne, land and waterborne survey for geothermal exploration; (c) Geophysics for the optimum exploitation of geothermal fields, also in connection with geothermal systems; (d) Modelling and simulation of heat/mass transfer; (e) Applied geophysics to monitor secondary effects of exploitation activities, such as aquifers interactions and microtremors. Contributions showing strong interaction with engineering and structural geology are strongly encouraged.

Physical and Mechanical Properties of Rocks in the Hydrothermal Systems of the Kuril-Kamchatka Island Arc

63

Julia Frolova, Vladimir Ladygin and David Zukhubaya

Abstract
This paper describes engineering geological features of rocks in active hydrothermal systems of the Kuril-Kamchatka island arc. The initial host rocks of studied hydrothermal systems are volcanic complex of Neogene-Quaternary age. Thermal fluids intensely alter them and transform to hydrothermal rocks such as secondary quartzites, propylites, zeolitic rocks, argillic rocks, clays, opalites, and quartz-feldspar metasomatites. Mineralogical alteration of rocks causes the changes in their physical and mechanical properties. The relationship between hydrothermal alterations and properties of rocks is considered. Special attention is given to near-surface alteration zone which affects the selection of sites for geothermal power plants constructions.

Keywords
Hydrothermal system • Alteration • Volcanic rock • Properties • Kuril-Kamchatka arc

63.1 Introduction

Geothermal energy is a renewable, relatively inexpensive, environmentally friendly, and domestic source of heat which is presently used for electricity production in 24 countries. Total worldwide installed capacity from geothermal power plants exceeds 10 GWe. More than 70 countries use geothermal energy for heat supply (Lund and Bertani 2010). Traditionally a complex of different methods is applied to investigate geothermal field among which the geological, geochemical, hydrogeological, and geophysical surveys are most common. This paper focuses on physical and mechanical properties of rocks and their application to identify geothermal targets. Under the action of thermal water properties of rocks change widely. The tendency of properties changes can be different (Sigurdsson et al. 2000; Rigopoulos et al. 2010; Lutz et al. 2011; Wyering et al. 2012). Our previous studies have shown that it depends on a number of factors including parent rocks, PT-conditions, composition of fluid, and duration of fluid-rock interaction (Frolova et al. 2010, 2011). Rock properties and assessment of their variation due to alteration process play an important role in the study of hydrothermal systems and exploitation of geothermal fields including numerical modeling, drilling optimization, assessment of reservoir capacity, geophysical log interpretation etc.

63.2 Geological Setting and Geothermal Conditions

In Russia the richest geothermal heat reserves occur in the Kuril-Kamchatka island arc which is located in the northwestern segment of the Circum-Pacific belt. Geothermal resources in the region are closely associated with active volcanism and its tectonic position above a subduction zone. Tens of low- and high-temperature hydrothermal

J. Frolova (✉) · V. Ladygin · D. Zukhubaya
Faculty of Geology, Lomonosov Moscow State University, Moscow, Russia
e-mail: ju_frolova@mail.ru

G. Lollino et al. (eds.), *Engineering Geology for Society and Territory – Volume 1*,
DOI: 10.1007/978-3-319-09300-0_63,

Table 63.1 Average values of physical and mechanical properties of unaltered rocks

Properties\Rocks	Tuffs, tuffites	Effusive rocks
Bulk density (ρ, g/cm^3)	1.47	2.69
Porosity (n, %)	44	5
Water absorption (W, %)	26	0.8
P-Wave velocity (Vp, km/s)	1.83	4.75
Uniaxial compressive strength (σ_c, MPa)	15	163
Softening coefficient (C_{soft})	0.41	0.76
Number of samples	66	28

systems (HTS) are located in this region. Several geothermal power plants are currently operated in the region for electricity production some fields are used for space heating, recreation and green houses. The host rocks of HTS are volcanic complex of Neogene-Quaternary age. Under the action of thermal fluids volcanic rocks are intensely altered and transformed to hydrothermal rocks (Rychagov et al. 2005). Mineralogical alteration of rocks which can be natural or due to thermal field exploitation changes their physical and mechanical properties. The changes of rocks properties lead to a variety of consequences: a transformation of HTS structure and a change of its hydrodynamic and temperature regimes; a decrease of boreholes production; a promotion of hazard geological processes on the thermal fields such as landslides and hydrothermal explosions.

63.3 Database and Testing Methodology

The database of hydrothermal systems host rocks has been established and processed. It contains data obtained on a number of HTS of the Kuril-Kamchatka island arc: Pauzhetsky, Mutnovsky, Koshelevsky, Paratunsky, Essovsky, North-Paramushir, and Baransky. Description of studied HTS is given in work Frolova et al. (2010). The database consists of three parts: geological description, petrographical characteristics, and rocks properties. It comprises a variety of petrological types among which are basalts, andesites, dacites, tuffs, tuffites, and ignibrites. The intensity of hydrothermal alteration covers the entire spectrum from fresh to totally altered rocks. Rock properties include bulk and grain densities, porosity, gas permeability, hygroscopic moisture, water absorption, velocity of ultrasonic waves, dynamic elastic modulus, uniaxial compressive and tensile strength, magnetic and thermal characteristics. About 750 samples from the different HTS have been collected, studied and processed. Majority of samples were obtained from boreholes (down to 2,500 m) or outcrops; few samples were taken form open pits. Laboratory measurements were applied in accordance with the State Standards (Trophimov and Korolev 1993) which are similar to International Society for Rock Mechanics standards (ISRM, 2007). They were accomplished with geological and petrological examinations (thin sections, X-ray diffraction, electron microscopy with microprobe analysis—Camebax SX-50; LEO 1450VP).

63.4 Results and Discussion

63.4.1 Unaltered Volcanic Rocks

The host rocks of HTS in the Kuril-Kamchatka arc are volcanic types among which effusive and volcaniclastic rocks are the most common. The properties of parent rock to the large extent control the rate, intensity and character of alteration as well as the structure of hydrothermal system. Unaltered effusive and volcaniclastic rocks differ significantly by their properties and the rate of alteration (Table 63.1). Effusive rocks (basalts, andesites, and dacites) have strong crystallization contacts between crystals, which have been formed during lava cooling and solidification. Thus, these rocks are dense with low permeability (0.025 mD) and high values of compressive strength (80–250 MPa), velocity of ultrasonic waves, and elastic modulus (30–70 GPa). Commonly, effusives layers form impermeable horizons in HTS, but occasionally they host fracture-dominated reservoirs. Volcaniclastic rocks (ash, lapilli, and agglomerate tuffs and tuffites) have a cementation type of contacts between grains which have been formed during consolidation of loose pyroclastic deposits. They are characterized by lower values of mechanical properties, higher porosity and permeability. It was noted Neogene tuffs are more lithified and characterized by higher values of properties in comparison with Pleistocene rocks. Tuffs and tuffites are the most common host rocks of HTS. Typically, they form porous or fracture-porous reservoirs, although highly argillized fine ash tuffs define caprock on HTS. Alteration rate appears to be less in the effusive rocks and much more intense in tuffs due to their high permeability.

Table 63.2 Physical and mechanical properties of hydrothermal rocks

Hydrothermal facieses			Density g/m^3	Porosity %	V_p, km/s	σ_c, MPa	C_{soft}	Secondary minerals assemblages
Secondary quartzites			2.4–2.6	10–15	4.0–5.0	>100	0.8–1.0	Quartz, muscovite
Quartz-feldspar metasomatites			2.1–2.4	15–20	3.5–4.5	80–140	0.8–1.0	Quartz, adularia, wairakite
Propylites	High-medium-temperature		2.3–2.6	5–15	3.5–5.0	50–150	0.8–1.0	Chlorite, sericite, actinolite, wairakite, epidote, quartz, albite, Fe oxides
	Low-temperature	Transylvanian	2.0–2.3	15–25	2.5–3.5	25–60	0.6–0.85	Chlorite, illite, calcite
		Zeolitic	1.4–1.8	35–45	0.8–1.2	<10	0.3–0.8	Laumontite, chlorite
		Argillic	1.7–2.0	35–40	1.5–2.5	10–30	0.2–0.6	Mixed-layer clays, calcite, silica minerals
Argillic rocks		Clays	1.0–1.2	50–60	–	–	Soften or soak	Smectite, kaolinite, mixed-layer, silica minerals
		Argillites with zeolites	1.1–1.7	35–50	1.5–2.0	5–20	0.2–0.5	Clinoptilolite, mordenite, heulandite, smectites, opal
Opalites			1.4–1.7	35–40	2.5–3.2	25–50	0.6–1.0	Opal, chalcedony, cristobalite, tridymite, quartz, Fe hydroxides

63.4.2 Hydrothermal Rocks

Under the action of thermal water parent rocks change their composition, pore-space geometry and volume, and properties. The original mineral assemblages of volcanic rocks are dissolved and replaced by secondary minerals, finally transforming into hydrothermal rocks. Commonly, the alterations have pseudomorphic character when original texture is saved but the rocks are almost 100 % altered. Basically the distribution of hydrothermal facies has a zonal character according to fluid composition, pH, and temperature. The following facies are distinguished in geological section of "generalized" HTS (upwards): secondary quartzites, high-medium-temperature propylites, low-temperature propylites, argillized rocks often with high-silica zeolites, hydrothermal clays, and opalites. Quartz-feldspar rocks occur in faults and fractured zones, intersected the entire zoning, and associated with thermal water boiling. Secondary mineralization and average values of rocks properties are shown in Table 63.2.

High-temperature facies (secondary quartzites, high-medium-temperature propylites) are the densest, low porous, with high strength and elastic modulus, resistant to water saturation. This is the result of the development of stiff secondary minerals (quartz, chlorite, epidote, sericite, albite, adularia, prehnite, and calcite), which fill pores and fractures and substitute matrix and phenocrysts. Zeolitic propylites are weak, highly porous and permeable rocks with extremely low values of P-wave velocity and low elastic modulus. The reason of low velocity is the microporous matrix composed of the weakly cemented fine-size crystals of laumontite and leaves of chlorite (or corrensite). Commonly, zeolitic propylites contain thermal water and host porous reservoir. Argillic rocks are distinguished by high porosity but low permeability. They have high hygroscopic moisture (2–6 %) and soften when saturated by water. Smectites significantly reduce rock permeability (0.04–0.65 mD) in spite of their high porosity. They are characterized by ultrasmall pores filled by bound water, which reacts with the rock but doesn't filter through the stratum. The argillized horizon basically forms the impermeable caprock in the HTS. Opalites are formed in near-surface horizons under the action of sulphate acid leaching. Silica minerals developed in this way provide stiff framework to the rocks with relatively high mechanical properties, despite of very high porosity and low density.

The most problematic rocks are low-temperature clayey rocks such as hydrothermal argillites and clays. Hydrothermal clays compose the near-surface horizons on the HTS and are characterized by high heterogeneity, high porosity, plasticity, hygroscopic moisture, and compressibility; commonly they swell or soak in saturated state. Hydrothermal clays were studied in detail in the Koshelevsky, Pauzhetsky and Baransky geothermal fields. In particular, in the Low-Koshelevsky thermal field andesite massif gradually transforms to clays. Alteration starts in fractures network which exposed to thermal water and steam. The walls of fractures are replaced by clay minerals. Gradually the fractures are propagated and expanded, and new blocks of andesite are reworked by argillization. Then only the roundish cores of andesite remain in clayey mass. Relicts of andesite are highly fractured, ferruginizated and argillized. Additional fracturing may propagate due to the swelling pressure in surrounding clay mass. Clay mass is

very heterogeneous, and contains the relict fragments of andesites. The composition of clay is mainly smectites or mixed-layer minerals; silica minerals are also abundant. The transformation of andesites into clays is accompanied by strong reduction in density (from 2.5–2.6 to 1.0–1.1 g/cm^3), an increase in porosity (from 5–8 to 50–60 %) and hygroscopic moisture. The failure character changes from brittle in andesites to ductile in clays. Under the action of water clays soften or soak, swell and acquire plasticity. They form cape-type covers up to several meters thickness in geothermal fields. Slope geological processes (landslides, mud-flows) are developed in hydrothermal clays.

63.5 Conclusion

The hydrothermal systems in the Kuril-Kamchatka region are hosted in volcanic complex of Neogene-Quaternary age. Effusive and volcaniclastic rocks differ significantly by their properties and the rate of alteration. The former are characterized by higher density, strength, and elastic properties, lower porosity and permeability, and lower intensity of alteration. Under the action of thermal fluids the parent rocks are intensely altered and finally transformed to hydrothermal rocks such as secondary quartzites, propylites, argillized rocks, clays, opalites, and quartz-feldspar metasomatites. Hydrothermal facies differ greatly in their properties. Most problematic rocks are hydrothermal clays which compose the near-surface horizons. They are highly heterogeneous and characterized by high porosity, plasticity, hygroscopic moisture, and compressibility; they soften or soak in saturated state, sometimes they swell increasing their volume and forming additional pressure. The changes of rocks properties in geothermal areas lead to gradual transformation of HTS structure and hydrodynamic and temperature regimes; they decrease in borehole production and may trigger hazardous geological processes.

Acknowledgments This research was supported by RFBR (Grant No 13-05-00530). We are grateful to Dr. Rychagov S.N. and the stuff of Geothermic Laboratory, Institute of Volcanology and Seismology, FED RAS for scientific cooperation, discussions, and field works.

References

Frolova Yu, Ladygin V, Rychagov S (2011) Patterns in the transformation of the composition and properties of volcanogenic rocks in hydrothermal–magmatic systems of the Kuril-Kamchatka island arc. Univ Geol Bull 66(6):430–438

Frolova J, Ladygin V, Rychagov S (2010) Petrophysical alteration of volcanic rocks in hydrothermal systems of the Kuril-Kamchatka island arc. In: Proceedings of WGC 2010, Bali, Indonesia. https://www.geothermal-library.org

International Society on Rock Mechanics (2007) In: Ulsay R, Hudson J (eds) The complete ISRM suggested methods for rock characterization, testing and monitoring: 1974–2006. ISRM, Ankara, p. 628

Lund JW, Bertani R (2010) Worldwide geothermal utilization 2010. GRC Trans 34:195–198

Lutz SJ, Zutshi A, Robertson-Tait A, Drakos P, Zemach E (2011) Lithologies, hydro-thermal alteration, and rock mechanical properties in wells 15-12 and BCH-3, Bradys hot springs geothermal field, Nevada. GRC Transactions 35:469–476

Rigopoulos I, Tsikouras B, Pomonis P, Hatzipanagiotou K (2010) The influence of lateration on the engineering properties of dolerites: The examples from the Pindos and Vourinos ophiolites (Northern Greece). Rock Mech Mining Sci 47(1):69–80

Rychagov SN, Korobov AD, Glavatskikh SF et al (2005) Evolution of metasomatic processes in structure of hydrothermal-magmatic systems in island arcs. In: Proceedings of international field Kuril–Kamchatka seminar "geothermal and mineral resources in the regions of recent volcanism" Petropavlovsk-Kamchatskii, pp. 207–216

Sigurdsson O, Gudmundsson A, Fridleifsson GO et al (2000) Database on igneous rock properties in Icelandic geothermal systems. Status and unexpected results. In: Proceedings of the WGC 2000, pp. 2881–2886

Trophimov VT, Korolev VA (1993) Practicum by soil geology. MSU, Moscow 390

Wyering L, Villeneuve M, Wallis I (2012) The effects of hydrothermal alteration on mechanical rock properties of the Andesite Breccia and Tahorakuri Formation from the Ngatamariki geothermal field, New Zealand and empirical relations between rock strength and physical properties. In: Proceedings of New Zealand geothermal workshop, Auckland, New Zealand (34). https://www.geothermal-library.org

Geophysical and Geological Survey to Plan a Low Enthalpy Geothermal System. The Case Study of Borgo Isonzo—Latina Italy

64

E. Cardarelli, C. Alimonti and G. Di Filippo

Abstract
In this study we present a field case in which, through geological and geophysical survey a detailed modelling of the subsurface is defined with the aim to design a geothermal plant. The hydrogeological characteristics were inferred by geological survey and geophysical data collected by electrical resistivity tomography. Model results allowed us to perform a numerical simulation to design a Ground Water Heat Pump plant where particular attention was paid in combining the use of natural resources with environmental protection granting maximum benefit withdrawing.

Keywords
Geothermics • Geophysics • ERT • Environment • GWHP plant

64.1 Introduction

The continued increase in energy demand and the need to control corresponding atmosphere pollution promote the use of renewable energy sources (photovoltaic, solar, geothermal, wind, etc.). Among renewable energy sources, geothermal energy has certainly a reduced environmental impact and is available in most places. With these characteristics, especially Ground Source Heat Pump (GSHP) plants had a remarkable development in the last years. The rapid growth has often not been accompanied by adequate sustainability criteria in plant design.

Low enthalpy geothermal energy plant used for heating and cooling of buildings involves geological structures near the surface, in the first 100 m. In order to ensure sustainability is important to address the problem from a more scientific point of view, defining the geological model and the thermal and hydraulic relationship between layers. Geophysics can be a valid tool to identify possible subsoil structures and its characteristics (cavities, sink-holes, buried geological structures etc.) (Cardarelli et al. 2010), helping in defining the better location of drilling holes. The investigation of the area should be also aimed at identify structures with higher thermal conductivity and evaluate hydrogeological characteristics (such as hydraulic conductivity, and porosity) in order to determine water content and thermal productivity and thus the type of thermal exchange.

It is well known that such studies can be performed through geophysical surveys which, at relatively low cost and short time, provide the necessary parameters for a model that can simulate the thermal responses according to the energy needs of the building (Alimonti et al. 2010). In particular, geoelectric and seismic surveys are the most suitable to characterize and evaluate the main parameters of an aquifer (Böhm et al. 2013; Soupios et al. 2007).

E. Cardarelli (✉) · C. Alimonti
"Sapienza" University of Rome, Via Eudossiana 18, 00184 Rome, Italy
e-mail: ettore.cardarelli@uniroma1.it

G. Di Filippo
Alfa Ambiente Consulting S.r.l, Rome, Italy

G. Lollino et al. (eds.), *Engineering Geology for Society and Territory – Volume 1*,
DOI: 10.1007/978-3-319-09300-0_64,

64.2 The Case Study

The case study is an historical building hosting some laboratories of "Sapienza" University. It is located at Borgo Isonzo, in the south-east of Latina (70 km far from Rome) (Fig. 64.1). In order to renovate the building and to meet energy standards as high as possible, after a redesign of internal space distribution strong attention has been paid in containing energy needs and has been decided to use a GSHP plant for heating and cooling.

To assess the feasibility study of the GSHP, a literature review on geology and hydrogeology of the site was carried out. Then three Electrical Resistivity profiles were performed in the area (Fig. 64.1). The survey was carried out using both pole-dipole and dipole-dipole configurations in order to have the highest resolution and depth of investigation for at relatively small electrode distances. For each profile the acquired data sets were then combined (about 2,000 data points) and inverted using the least square inversion of Loke and Barker (1996). The length of the electrical lines was 141 m with a maximum investigation depth of 37 m. In Fig. 64.2 results of L1 profile are shown, from surface a first layer, almost homogeneous, characterized by low resistivity values (8–20 Ω m), a second layer with a higher value of resistivity (40–60 Ω m), having a thickness of 9–10 m, and a third layer with lower resistivity were identified (15–25 Ω m). These results are in agree with the stratigraphy of a reference well, after an alternation of silty sands, the stratigraphy shows a first aquifer at a depth of about 12 m hosted in sand and gravel layer. The aquifer bed is a clayey layer with a thickness of about 2 m. Only one resistivity section is presented because they are similar.

Successively, was decided to verify the possible use a Ground Water Heat Pump (GWHP) instead of a GSHP to reduce costs. At this purpose numerical simulation was done (Alimonti et al. 2010). A geological model was build up formed by three layers. The first one (T1) corresponds to the ground cover which is unsaturated, the second layer (T2) corresponds to the shallow aquifer interested by the energy plant, the third layer (T3) is the bedding layer of the aquifer formed mostly by silty and clay sands.

To populate the layers properties the Archie formula was used to estimate the porosity from resistivity values. Thus, the 2D resistivity sections were converted into a 2D pseudo-porosity ones by using the following Archie-law parameters: m = 1.3 (non-consolidated sediments) and a = 1, R_t true bulk resistivity, R_w the resistivity of water saturating the formation and Φ the effective porosity:

$$\Phi = \sqrt[1.3]{R_w/R_t} \tag{64.1}$$

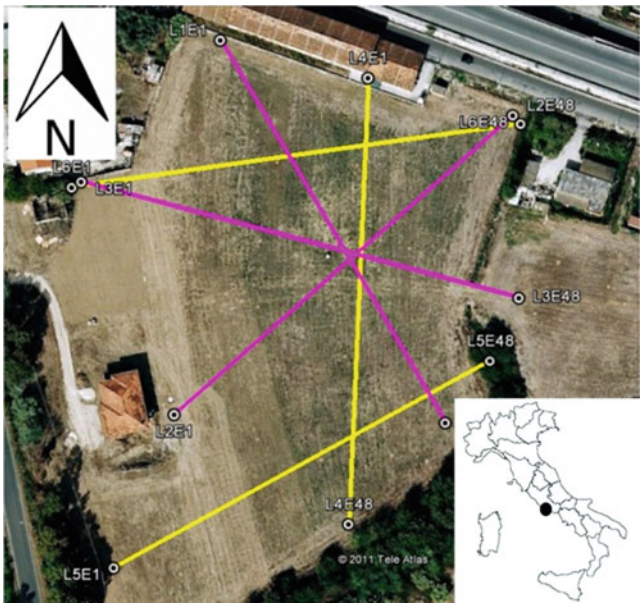

Fig. 64.1 Map of the survey and location of geoelectrical profiles, *Pink* first phase, *Yellow* second phase

The electrical conductivity of groundwater was measured in about 1,200 μS/cm. Thus, its resistivity value was estimated in about 8.3 Ω m. The aquifer layer (T2) shows an average resistivity equal to 50 Ω m; from Eq. (64.1) porosity is 0.25.

The results of the feasibility study highlight the possible use of a GWHP plant. With the aim to improve the knowledge of the site a second geophysical field survey was performed increasing the number of ERT; three profiles were added in order to have a higher coverage of the area and to invert all data set together in 3D mode (Fig. 64.1).

The survey was performed with the same acquisition parameters of the first one. Results confirm the presence of three main layers, with same characteristics. Starting from these considerations to verify the consistency of the results, 2D inversion was repeated by using VERDI algorithm that allows to insert a priori information (Cardarelli and Fishanger 2006); all the profiles were inverted with VERDI, adding the geological model. Data misfit was reduced confirming the goodness of the geophysical model. The results of the model are similar to the ones obtained with Res2Dinv. An example of VERDI inversion is depicted in the Fig. 64.3 where second layer is inferred by Res2Dinv results.

Taking into account the inferred model, a 3D inversion was performed on the whole data set by using ERTlab software. In Fig. 64.4 the resistivity map and a 3D view at 15 m depth is shown. Evident heterogeneities are present in the surveyed volume. Following these results, the

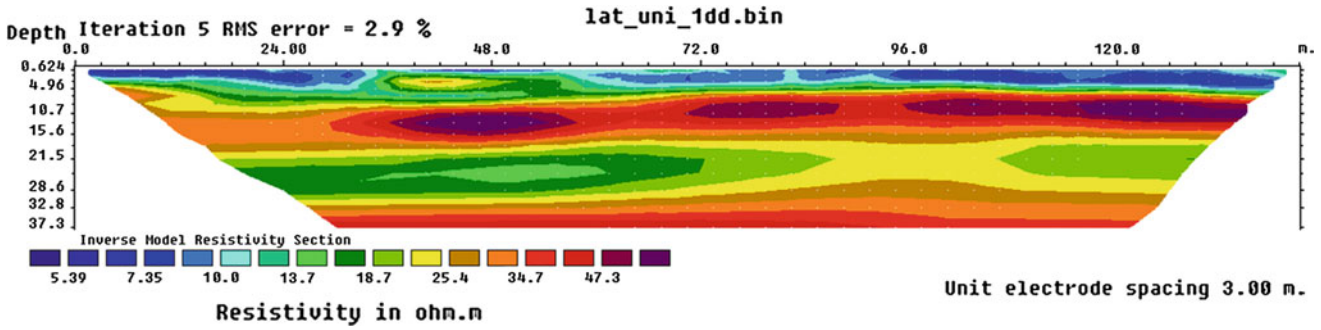

Fig. 64.2 Resistivity profile L1

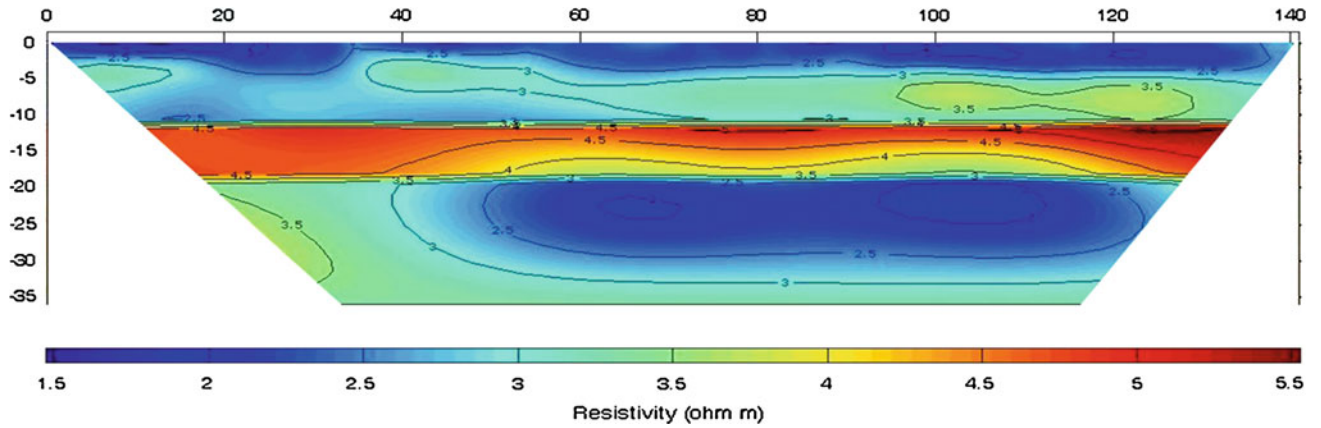

Fig. 64.3 Resistivity profile L4

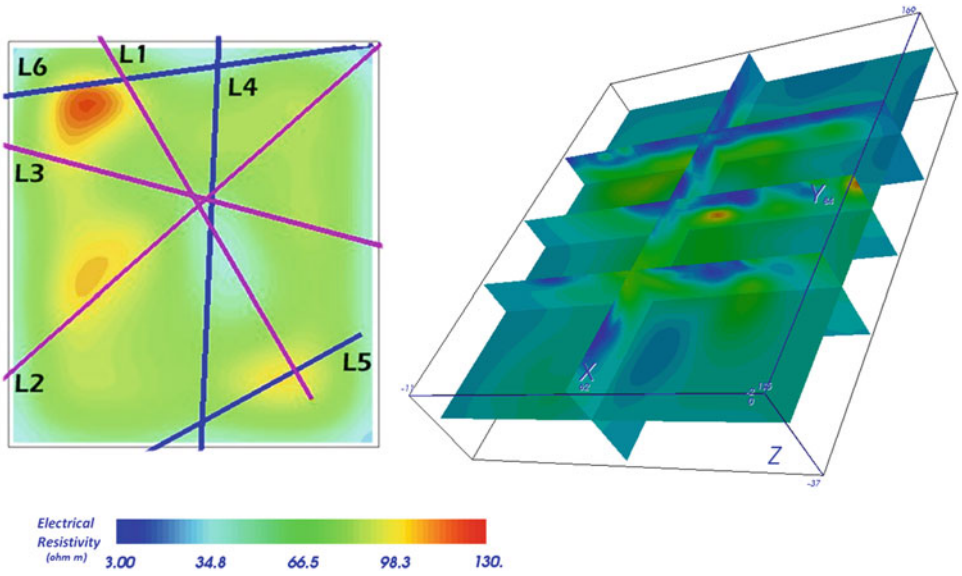

Fig. 64.4 Resistivity map 15 m depth by ERTlab and location of the electrical profiles **a** 3D resistivity view of the investigated area at 15 m depth

geological model has been revised using a larger number of boreholes stratigraphy and a simulation of the underground lithofacies distribution using the software Rockworks was produced. The obtained profile highlights the presence of a sandy layer from the surface down to 20 m. Under it, alternating layers of silty sand or sandy clay are present. The geophysics confirms the reconstructed asset but highlight the presence of heterogeneities.

Table 64.1 Petrophysical and thermal parameters

Layer	Effective porosity	Hydraulic conductivity (m/s)	Thermal conductivity (W/m °C)
T1	0.20	1.0×10^{-4}	1.0
T2	0.15	3.0×10^{-5}	1.5
T3	0.05	3.7×10^{-9}	0.5

To proceed with design of the GWHP plant was decided to simulate the entire volume possibly accounting the heterogeneities. Therefore, to evaluate the spatial distribution of thermo-petrophysical properties in the investigated volume geophysical results were used. The obtained 3D underground model in terms of resistivity is the base to estimate thermal and petrophysical properties. Porosity was calculated by using Archie law for each layer, the hydraulic conductivity of the aquifer was calculated by the Kozeny-Carman-Bear equation (Chapuis and Aubertin 2003). The thermal resistivity was determined by equation of Singh et al. (2001), relating it to the electrical resistivity.

Based on the improved geological model the numerical model has been defined. The simulation region has an extension of 306 × 204 m. The vertical thickness of the region is fixed in 30 m in order to host the entire volume of interest. To compare geophysical results in terms of calculated properties the study region was divided in three layers. The summary of layer data is shown in Table 64.1.

The reported value of porosity is quite different from the first one (0.25). The main reason is in the deeper analysis conducted in order to have a full reconstruction of the volume. The value is obtained by averaging the calculated porosity values and not via an average resistivity value and the Archie formula.

64.3 Conclusions

A thorough knowledge of the subsoil in the design of low enthalpy geothermal plant was the aim of present paper. Thanks to an increased number of electrical profiles the knowledge of underground properties was improved. More important improvements have been obtained for porosities that result more realistic than previous one. By a 3D geophysical survey a complete 3D geological model of the site has been obtained.

Next step is to provide a 3D model of the aquifer improving numerical simulation of heat and mass flow with a more appropriate simulation model considering the heterogeneous media.

Consider that an accurate model in the preliminary design phase of a large building complex can reduce the main cost of about the 20–30 %.

References

Alimonti C, Gnoni A, Marinucci E (2010) Toward a sustainable optimisation of very low enthalpy geothermal plant. configuration efficiency and environmental assesment. In: ASME-ATI-UIT 2010 Conference on thermal and environmental issues in energy systems, 16–19 May, Sorrento, Italy

Böhm G, Brauchler R, Nieto DY, Baradello L, Affatato A, Sauter M (2013) A field assessment of site-specific correlations between hydraulic and geophysical parameters. Near Surf Geophys 11:473–483

Cardarelli E, Fishanger F (2006) 2-D data modelling by electrical resistivity tomography for complex subsurface geology. Geophys Prospect 54(2):121–134

Cardarelli E, Cercato M, Cerreto A, Di Filippo G (2010) Electrical resistivity and seismic refraction tomography to detect buried cavities. Geophys Prospect 58:685–695

Chapuis RP, Aubertin M (2003) On the use of the Kozeny-Carman equation to predict the hydraulic conductivity of soils. Can J Geotech/Rev Can Geotech 40(3):616–628

Loke MH, Barker RD (1996) Rapid least-squares inversion of apparent resistivity pseudosections by a quasi-Newton method. Geophys Prospect 44:131–152

Singh DN, Kuriyan SJ, Manthena KC (2001) A generalised relationship between soil electrical and thermal resistivities. Exp Thermal Fluid Sci 25:175–181

Soupios PM, Kouli M, Valliantos F, Vafidis A, Stavroulakis G (2007) Estimation of aquifer hydraulic parameters from superficial geophysical methods: a case study of Keritis Basin in Chania (Crete-Greece). J Hydrol 338:122–131

Integration of Geological and Geophysical Survey for a Geo-Exchange System Design

65

Sabrina Bonetto, Domenico Antonio De Luca, Cesare Comina and Marco Stringari

Abstract

The design of a geothermal system represents a key moment since the future effective operation of the plant will strictly depend from it. A correct and effective design of a geo-exchange system should not be performed without a precise and accurate knowledge of the subsoil variability and its related thermal properties. The present work shows a case study for the design of a field of borehole heat exchangers for climate control and domestic hot water production in a newly constructed residential area located in the municipality of Tarvisio (NW Italy). It is pointed out the fundamental importance of a correct geological prospection, based on the integration of direct and indirect surveys. Correct investigations were indeed crucial, coupled to a Thermal Response Test, for a proper identification of the thermodynamic characteristics of the subsoil and then for the optimization of the system. Specifically, this case study aims to serve as an example to highlight the importance of variability in the horizontal scale of the thermal conductivity of the subsoil and the potential errors that can be made if no investigation is undertaken.

Keywords

Borehole heat exchangers • Geophysical surveys • Geological investigations • Thermal response test • Low enthalpy geothermal systems

65.1 Introduction

Environmental cleanliness and energetic efficiency of borehole geo-exchange systems are strictly related to the quality with which the plants are designed and built. In this respect a reliable assessment of the in situ thermal properties and their variability with space and depth is an essential starting point for the design in order to reach an optimal coefficient of performance (COP) of the whole system, to exploit the underground heat in a sustainable way and, last, to economize the resource. Indeed the only component of any geothermal system which can not be changed by engineering is the underground (Andersson et al. 1997). However a proper soil characterization is rarely performed in most sites, the design being based only on literature data and prior knowledge on the area. Even when numerical simulations of heat propagation are performed it must be underlined that numerical simulations alone are rarely completely effective if a proper evaluation of the thermal properties is not accomplished. The present paper presents a case study of the integration of geological and geophysical surveys for the determination of the geological variability in an area in which a borehole heat exchanger system is about to be built. Geophysical tests can indeed play an important role in the elucidation of the distribution of subsurface layers by their physical characteristics (Sanner and Abbas 1998).

S. Bonetto (✉) · D.A. De Luca · C. Comina (✉) · M. Stringari
Dipartimento Di Scienze Della Terra, Università Degli Studi Di Torino, Via Valperga Caluso, 35, Torino, Italy
e-mail: sabrina.bonetto@unito.it

C. Comina
e-mail: cesare.comina@unito.it

G. Lollino et al. (eds.), *Engineering Geology for Society and Territory – Volume 1*,
DOI: 10.1007/978-3-319-09300-0_65,

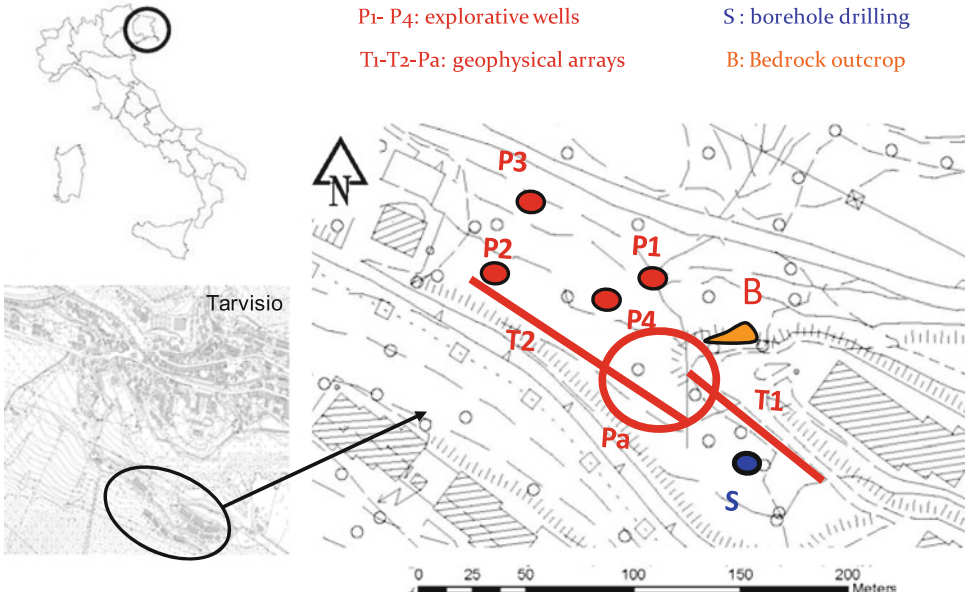

Fig. 65.1 Investigated area and surveys location

For instance depth of bedrock or delineation of aquifers may be estimated using geophysical techniques. These data have been interpreted and integrated with a Thermal Response Test (TRT) to allow for an accurate design of the planned system.

65.2 Geographical and Geological Setting

The study area, 7,000 squares meters wide, is located in the municipality of Tarvisio (NW Italy) along a slope located in the south side of the city between 750 and 790 m.a.s.l (Fig. 65.1).

The area is mainly formed of dolomitic and marly limestone of Triassic age belonging to the Southalpine geological domain (Carulli 2006; Assereto et al. 1968). Outcrops related to the "Bellerophon", Werfen and "Brecce di Ugoviza" formations have been recognized in the surroundings of the area (Kravina 2006).

The quaternary coverage is mainly constituted by glacial and glacio-lacustrine deposits, of variable composition and thickness, but generally represented by sands and gravels in silty-clay matrix (usually lower than 25 %). The variability of this unit above the bedrock is one of the main aspects to be considered in a correct borehole heat exchanger (BHE) design since the thermal properties of these deposits are usually very different from the ones of the consistent substratum. Still the rock fracturing and the presence of water play an important role in thermal properties definition; therefore, this study focused on the reconstruction of the geological model of the area in which BHE are about to be planned.

65.3 Materials and Methods

The only outcrops in the area (Fig. 65.1) shows a calcareous marly bedrock, fractured and altered with local interbedded layers of marls. Underground explorations have been performed consisting of invasive and non invasive methods: one borehole drilling (S), four explorative pits (P1–4) and two different geophysical arrays (T1–2) of both electric and seismic tomography. Along T2 array data have been further elaborated to obtain the surface wave dispersion curve integrated also by a passive seismic array (Pa). The surveys location is reported in Fig. 65.1.

The borehole (S) has been performed up to a depth of 100 m with a percussion drilling using water as circulating fluid, while explorative wells reached a maximum depth of 5 m.

Electric tomographies have been acquired by means of a PASI tomograph along two different arrays of 48 electrodes spaced respectively of 1.5 m along T1 and 1.8 m along T2. A Wenner-Schulumberger measuring sequence has been adopted for both arrays and data have been inverted by the RES2DINV code (Loke 1998).

For seismic tomographies two GEODES sismographs have been used with 48, 4.5 Hz vertical SENSOR SM-6/U-B geophones placed, along the two arrays, in the same position and with the same spacing of the electrodes of the previous surveys. A 5 kg hammer has been used as seismic source. Data have been interpreted with the RAYFRACT (Intelligent Resources Inc.) code. Along T2 array the surface wave dispersion curve has been also extracted, using the same active seismogram of tomographic data, by means of the SWAT (Surface Wave Analysis Tool) program

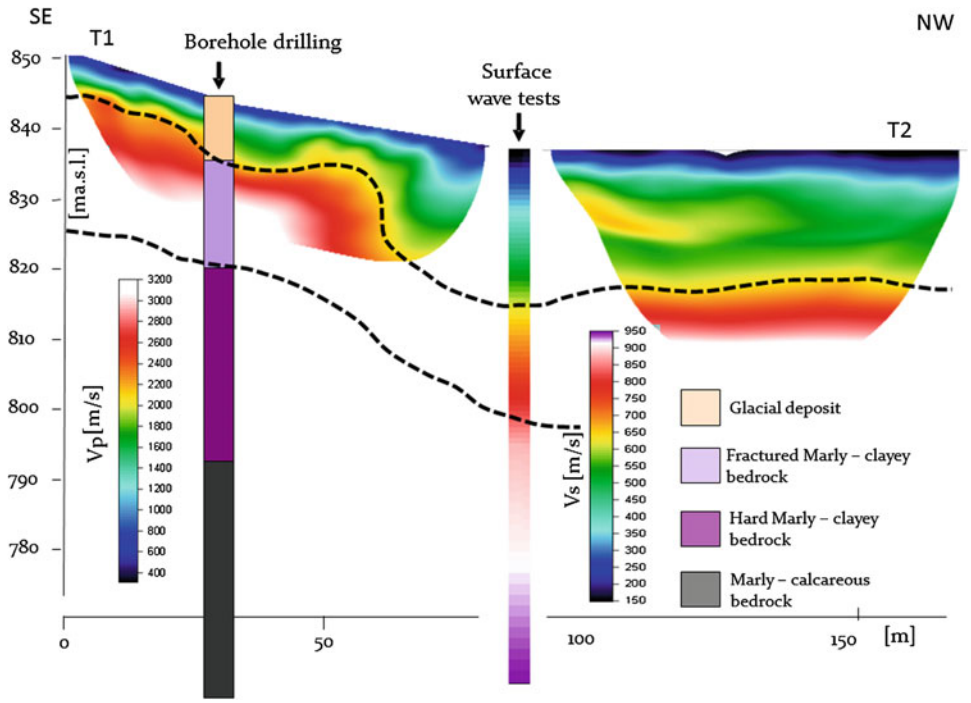

Fig. 65.2 Results of the drilling borehole and of seismic geophysical surveys: seismic tomographies along the T1 and T2 arrays (Vp) and Surface wave tests (Vs)

developed in Matlab environment at Politecnico di Torino. Active data have been further integrated with the record of the passive microtremor in the area performed along a 2D array of 12, 2 Hz vertical GEOSPACE geophones equi-spaced along a circle of 22 m diameter. The ambient noise has been interpreted by means of a frequency domain beamformer technique (Ziwicki 1999). Combined use of passive and active methods has been indeed suggested to improve both resolution and depth of investigation (Foti et al. 2007).

Finally, a TRT has been conducted to allow for the direct determination of thermal properties. This has been performed after the installation of a test geothermal heat exchanger in the drilled hole. The test has been performed for 93 h several days after the installation of the exchanger to allow for complete maturation of the concrete casing. Following ASHRAE recomandation (Ashrae 2007) a constant electric power (70 W each m of exchanger) has been used during the test.

65.4 Results and Discussions

Notwithstanding the limitations related to the drilling technique adopted, an indicative stratigraphy (Fig. 65.2) has been reconstructed from the cutting analysis and the variability of the drilling rate. The depth of the quaternary deposits (mainly represented by pebbles and blocks in a silty-sandy matrix) has been locally estimated at about 9 m from surface; below this depth, a progressively more resistent bedrock has been recognized with a probable transition from clayey marls to marly limestone or limestone. A stable water table has been observed from 52 m but local water inflows have been also encountered particularly around 9 m depth.

In the explorative wells, an high variability in the depth of the interface between quaternary deposits and bedrock has been however observed: P2 and P3 did not intercepted the bedrock within the investigation depth while an highly tectonized substratum has been observed at 2 m depth in P1 and at 4 m depth in P4. This can be preliminary related both to the different elevations of the surface in correspondence of the pits excavation and to the indented topography of the bedrock itself.

Electric tomographies have underlined an overall difference in the resistivity values among the two arrays and a global heterogeneity of shallow deposits related to different water contents and local water inflow. However the limited investigation depth didn't allowed for particularly relevant considerations in respect to the bedrock apart along the T1 array in which an highly altered interface is revealed from about 10 m depth. Seismic tests gave instead more interesting results (Fig. 65.2). Both seismic tomographies underlined a clear interface between shallow loose deposits with medium-low propagation velocity (400–2000 m/s increasing with depth) and a more consistent high velocity material (2500–3500 m/s). Locally, this interface accord with the drilling stratigraphy (Fig. 65.2), but it also shows an high lateral variability: from an average of 9 m depth at the beginning of T1 array to about 20–24 m along T2. An abrupt change in depth is also observed within T1 array (Fig. 65.2).

Surface wave tests allowed to locally extend the investigation depth and confirm the presence of the first seismic interface at a comparable depth with the one observed with the seismic tomography along the T2 array (20–24 m depth); moreover they suggest the presence of a more consistent bedrock in depth due to a further seismic interface at 45 m depth. A Vp/Vs ratio of about 3 is observed for the first seismic interface (red colors in Fig. 65.2). This is in agreement with the fractured marly - clayey bedrock revealed from the sounding, even if possible uncertainties in shear wave velocity determination may arise due to the non ideal mono-dimensionality of the site.

An overall thermal conductivity coefficient of 2.53 W/(mK) has been evaluated from the TRT. It is important to underline that this coefficient is strictly related to the local stratigraphy observed in the drilling borehole. However, a steep variation in depth is observed in the interface between quaternary deposits and bedrock along the seismic tomography sections. Therefore an increased thickness of quaternary deposits can result in an overall global reduction of the thermal conductivity. Indeed, considering the different thermal properties of the quaternary coverage (thermal conductivity of about 0.4–0.5 W/m K) compared to the bedrock (thermal conductivity variable-between 2 and 2.6 W/m K), a significantly different horizontal equivalent thermal conductivity in the area is observed. According to preliminary evaluation, it is estimated that the thermal conductivity of the western sector of the study area would be about 15 % lower compared to that measured by the TRT on the eastern sector.

65.5 Conclusion

This case study intended to offer an appropriate methodological approach for a correct design of a borehole heat exchanger systems in which the detailed knowledge of the thermal properties of the underground is fundamental.

Accessibility and high economic costs for a deep thermal characterization should be responsible of an inaccurate geological reconstruction of the area with unpleasant consequences in the efficiency of the plant. This study focuses on an integrated approach combining economic and rapid direct and indirect survey techniques to identify the thermal underground properties. In the study case, the combination of a limited number of specific surveys (i.e. drillings and TRT test) with indirect surveys allowed to obtain interpretable and coherent results in a consistent and accurate way, also confirming the scarce reliability of a TRT test performed in a single location in case of lateral geological variability. Correct evaluation of this variability allowed to properly estimate the thermal properties and perform a more correct design.

Acknowledgments Authors are indebted with Politecnico di Torino for the permission of using the seismic geophysical instrumentation and related software.

References

Andersson O, Mirza C, Sanner B (1997) Relevance of geology, hydrogeology and geotechnique for UTES. In: Proceedings of MEGASTOCK 97, Sapporo, pp 241–246

Ashrae (2007) ASHRAE handbook on HVAC applications (Chapter 32). American Society of Heating, Refrigerating and Air-Conditioning Engineers, Atlanta

Assereto R, Desio A, DI Colbeltrando D, Passeri LD (1968) Note illustrative della carta geologica d'Italia alla scala 1:100.000. Foglio 14A—Tarvisio. Servizio Geologico Italiano, Roma

Carulli GB (2006) Carta geologica del friuli venezia giulia alla scala 1:150.000. Regione Autonoma Friuli Venezia giulia—Direzione centrale Ambiente e Lavori Pubblici, Servizio Geologico

Foti S, Comina C, Boiero D (2007) Reliability of combined active and passive surface wave methods. RIG 41(2):39–47

Kravina C (2006) Relazione geologica. Variante generale al piano regolatore comunale di tarvisio di reiterazione dei vincoli urbanistici e di adeguamento alla L.R 52/91, Revisione 1. Regione autonoma Friuli—Venezia Giulia, Provincia di Udine, Comune di Tarvisio

Loke MH (1998) Rapid 2D resistivity and IP inversion, Geotomo Software

Sanner B, Abbas MA (1998) How can geophysical exploration help to determine gshp ground properties? In: Proceedings of the 2nd stockton international geothermal conference, 16 and 17 Mar 1998

Zywicki DJ (1999) Advanced signal processing methods applied to engineering analysis of seismic surface waves. Ph.D. dissertation. Georgia Institute of Technology, Atlanta, USA

Groundwater Thermal Trends Analysis in Support to Sustainable Use of Low-Enthalpy Resources: A Preliminary Monitoring Approach in Vicenza (Northern Italy)

66

Bertoldo Silvia, Mion Filippo, Passadore Giulia, Pedron Roberto and Sottani Andrea

Abstract

In the province of Vicenza, a study that takes into account the experimental data to verify the geothermal potential of the area is in progress. The studied area corresponds to the high plains where the processes of recharge of the aquifer system of the entire province and the surrounding area are active. It is a sensitive area as a source of water supply for most of the region. The study is useful for the purposes of developing a plan for geothermal use and for the protection of aquifers. The investigations involving temperature data that are acquired continuously at a limited number of wells and data that are measured at certain times of the year at a considerable wells network. In this way it is possible to verify the temperature distribution and identify areas with similar behavior and, in the same context, the trend of temperature in areas not yet affected by geothermal plants are analyzed.

Keywords

Geothermal surveys • Temperature • Groundwater • Monitoring

66.1 Introduction

Low-enthalpy geothermal energy produced by heat pumps and used for buildings, recently raised a scientific interest and an increased number of applications in Italy. Long term plans are crucial for energy-related aspects as well as for quality groundwater protection. These premises are more important than ever in the context of Veneto region aquifers, where massive drinkable water pumping and distribution occur. Over the last few years, a study of the thermal characteristics of the subsoil has been performed with the aim to support a sustainable use of geothermal heat pumps. This study takes inspiration from previous researches commissioned by the public waterworks administration (Passadore et al. 2012). Studies described in this paper refer specifically to province of Vicenza, where several groundwater monitoring networks have been active for years (Fig. 66.1) for both open and closed loop heat pumps systems (Bertoldo et al. 2010). The current analysis aims at mapping similar areas in terms of geothermal parameters. The criteria examined can correlate the requirements for protection of groundwater resources with the need for technological development and use of energy. Due to the complexity of structural and geological conditions of the examined area, a detailed characterization has been necessary. This assessment highlights much different areas not only related to aquifer structure and groundwater table depth but also connected to seasonal variability of water levels and, most importantly, thermal regimes. These

B. Silvia (✉) · P. Roberto · S. Andrea
Sinergeo, Contrà Del Pozzetto, 4, 36100 Vicenza, Italy
e-mail: info@sinergeo.it; sbertoldo@sinergeo.it

M. Filippo
ARPAV—Agenzia Regionale Per La Prevenzione E Protezione Ambientale Del Veneto, Direzione Tecnica, Servizio Osservatorio Acque Interne, Via Matteotti, 27, 35137 Padua, Italy

P. Giulia
Dipartimento Di Ingegneria Civile Edile Ed Ambientale (DICEA), Università Di Padova, Via Loredan, 20, Padua, Italy

G. Lollino et al. (eds.), *Engineering Geology for Society and Territory – Volume 1*,
DOI: 10.1007/978-3-319-09300-0_66,

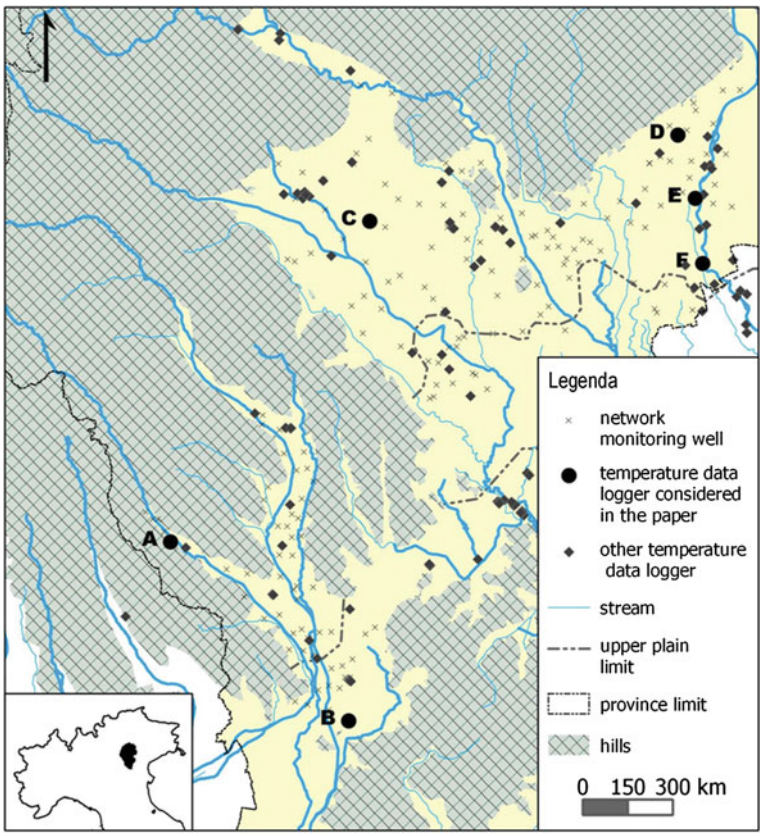

Fig. 66.1 Monitoring well network

features depend on aquifer recharge and physiography of the area, more and more subject to change and to anthropic modifications. Integrated knowledge of these elements and their complex relations represents a basic stage of study for designing a proper geothermal heat pump system. This is because these elements can deeply influence energy efficiency of plants to the extent that at times the whole system results could be deemed not recommendable. The identification of representative control points among similar areas will give the possibility to constantly monitor ongoing trends in terms of dynamic aquifer protection.

66.2 Methodology

The monitoring took place mainly over unconfined aquifer located the in upper plain area but, because this system is in connection with the confined systems of the middle plain, also some wells in there were monitored. Considering a network counting more than 150 wells, some surveys have been conducted with the aim of defining the spatial distribution of temperature in groundwater and to assess the influence of climatic and recharge factors. The data were acquired by means of a water level meter, capable of measuring both the depth of groundwater and the water temperature. These surveys were performed in different periods of the year to try to understand how the boundary conditions affect the temperature of groundwater, particularly focusing on the variations in groundwater level, the temperature of the atmosphere and the recharge factors (e.g. river recharge). Furthermore, systematic recordings of the water depth and temperature of groundwater have been ongoing for some years at some of these wells. Data recording is performed with data-logger placed below the groundwater level; they are periodically calibrated by manual measurements. In all cases the measurements were performed by placing the sensor at the greatest possible depth, depending on the characteristics of the well and the data-logger measuring range. The temperature trend in the surface portion is in fact influenced by irradiation of solar energy, while the contribution of endogenous geothermal heat flow prevails at greater depths.

66.3 Results

Through the use of automatic data-logger, we can reconstruct the aquifer level and the temperature trends at the monitored well. In particular, the trends were analyzed over a period of several years, thus allowing the evaluation of the seasonal cycles. In the following, we present some cases considered significant for the water temperature at key points in the area investigated (see Fig. 66.1). The first case refers to a comparison between an upper and a middle plain

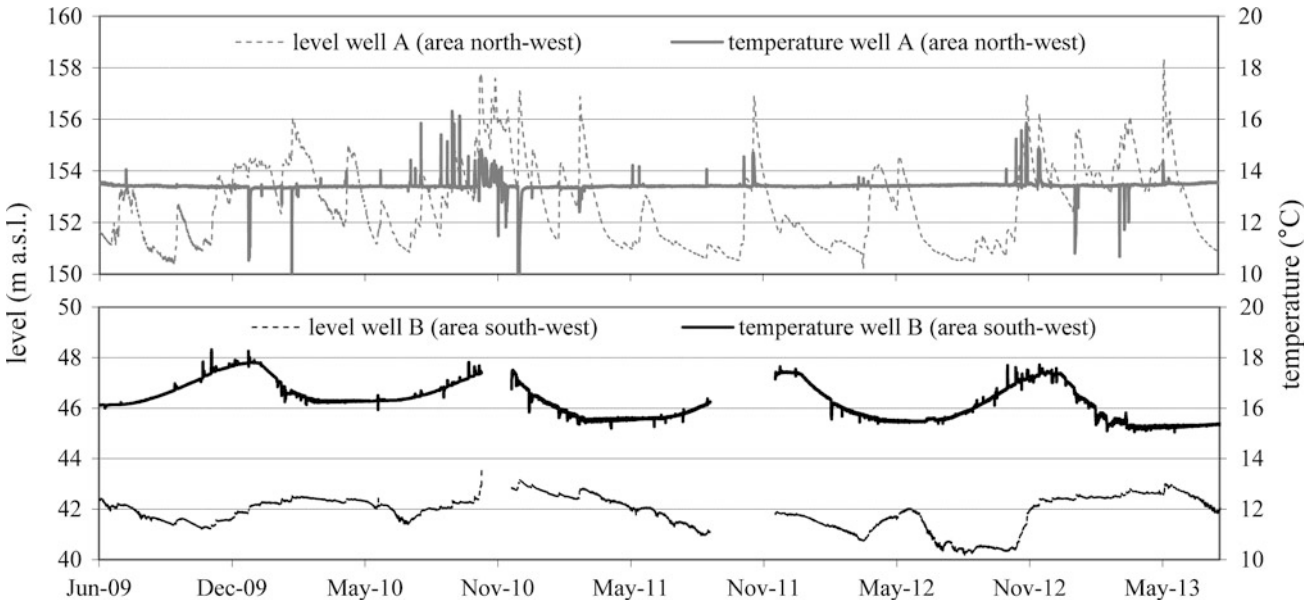

Fig. 66.2 Level and temperature of wells A and B, located in the western part

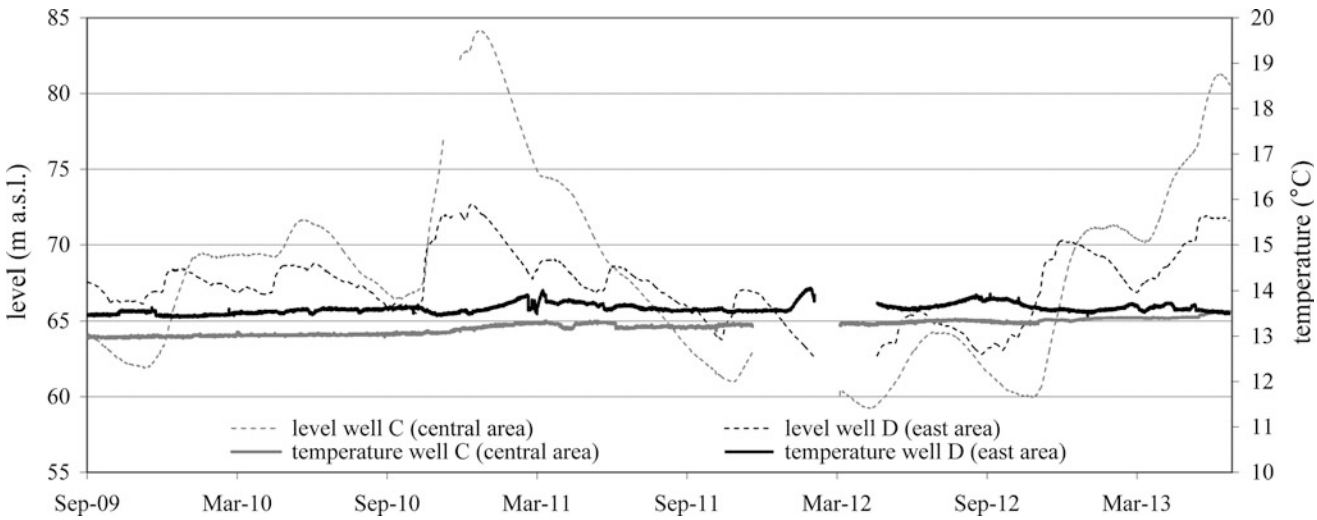

Fig. 66.3 Level and temperature of wells C and D, located in upper plain

sites both located in the western part of the province (Fig. 66.2). At the northern point the temperature tends to stay constant throughout the year while the southern point shows seasonal temperature changes related to external conditions.

In the second case (see Fig. 66.3) the measured temperatures of two wells both located in the high plane are compared. The two points are structurally different (C site in the central sector and site D in the eastern sector). Although, the oscillations of the groundwater level highlight the differences between the two recharge basins, the temperature value is similar and stayed almost constant under varying boundary conditions. Finally, we show the trend of two piezometers located close to the Brenta riverbed (see Fig. 66.4). Both aquifer levels and temperature at the northern point (well E) are significantly influenced by the river with variations of 14 °C, while a few kilometers downstream such variations is reduced to 1 °C (well F). This impact is connected to the recharge capacity caused by the river in the northern section, where the river recharge rate is between 1.3 and 3.6 m^3/s per kilometer; while in the southern point the relationship between river and groundwater tend to reverse and the impact of the river is less prominent.

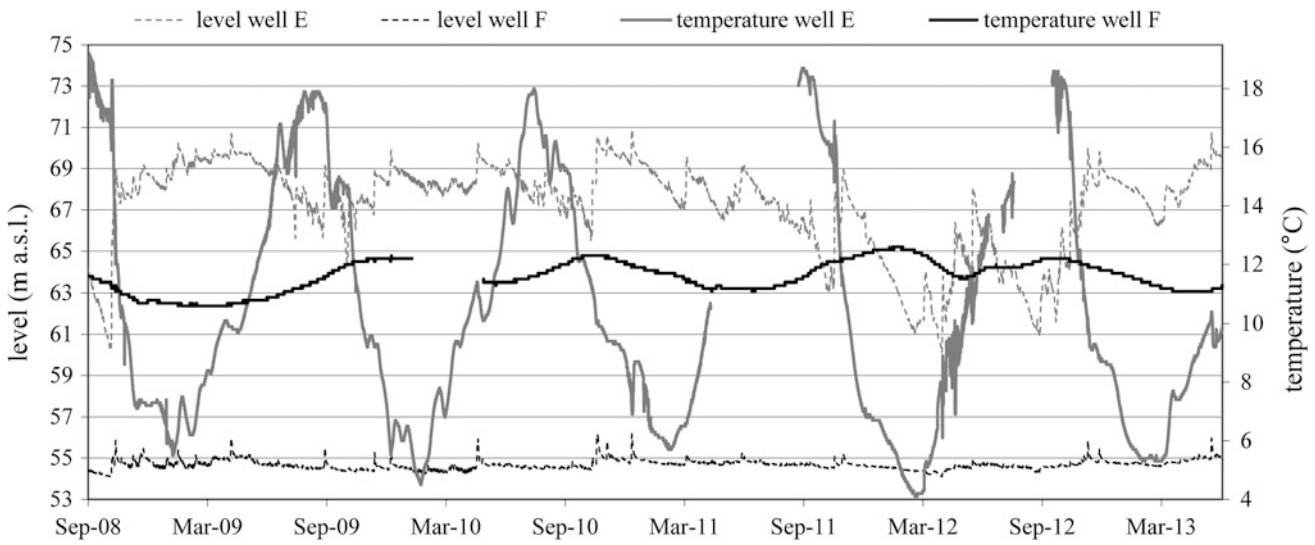

Fig. 66.4 Level and temperature of wells E and F (along River Brenta)

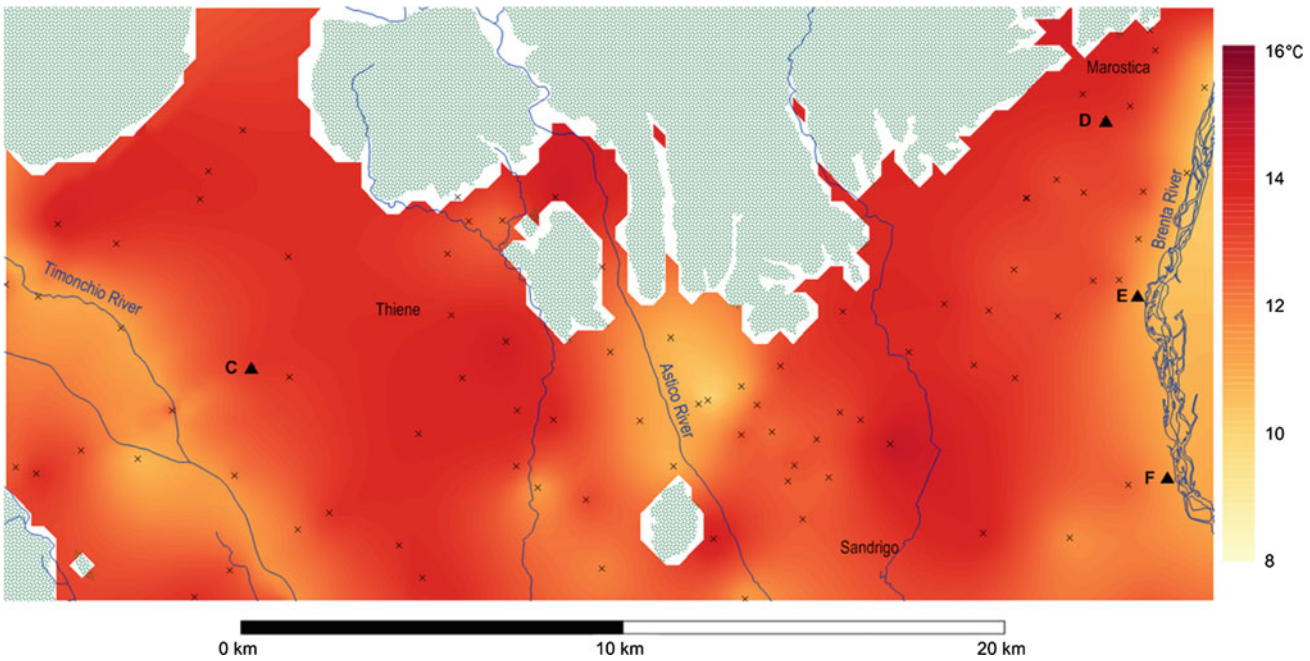

Fig. 66.5 Temperature preliminary distribution (upper Vicenza plain)

The monitoring points discussed above are located inside the area considered for the mapping of temperatures (a portion in the Fig. 66.5). The temperature data, periodically monitored by using a water temperature meters on the several points in the area, have been interpolated with contouring algorithms for the reconstruction of the temperature distribution. The desired result is a map of temperatures in the upper and middle plain throughout the changing external conditions. The still ongoing mapping has already shown some areas with homogeneous behavior. Results show that, although between domains considered similar under hydrogeological values (hydraulic conductivity, transmissivity, etc.) some significant temperature variations can be traced. In brief:

- Absolute values of groundwater temperatures are considerably variable even within short distances;
- Seasonal thermic regimes with identifiable peculiarities exist and at times they are related to level trends;

- Temperatures in general showed a range between 4 and 18 °C;
- The rivers induce an important change in groundwater temperature due to the aquifer recharge.

66.4 Conclusions

In conclusion, the results of this study allow to determine that design choices and solutions for low-enthalpy geothermic plants must take into account that temperature variability is not only associated to structurally different contexts but sometimes it occurs into very similar geological situations. Designing a geothermic plant powered by aquifer water, other than depending on structural parameters, must also take into account the importance of site's specific data, taken from many different hydro-geological and environmental monitoring. The methodology of these studies must be therefore inspired by the rigorous conservation of natural equilibrium, in order to maintain the characters of sustainability and renewability of geothermal energy as well as the preservation of quality of hydrogeological resources.

References

Bertoldo S, Pedron R, Sottani A (2010) Hydrogeological researches for vertical closed loop heat exchanger system assessment in an experimental pilot site (Vicenza, Northern Italy). In: Proceedings of 18XXXVIII IAH congress groundwater quality sustainability, Krakow, 12–17 Sept 2010

Lo Russo S, Boffa C, Civita M (2009) Low-enthalpy geothermal energy: an opportunity to meet increasing energy needs and reduce CO_2 and atmospheric pollutant emissions in Piemonte, Italy. Geothermics, vol 38. Elsevier, p 9, ISSN: 0375–6505. doi:10.1016/j.geothermics.2008.07.005

Passadore G, Monego M, Altissimo L, Sottani A, Putti M, Rinaldo A (2012) Alternative conceptual models and the robustness of groundwater management scenarios in the multi-aquifer system of the Central Veneto Basin, Italy. Hydrogeol J 20:1–13. doi:10.1007/s10040-011-0818-y

Sustainable Use of Geothermal Resources: Applications and Case Studies in Northern Italy

67

Cerutti Paolo, Lo Russo Stefano, Sottani Andrea and Bertoldo Silvia

Abstract

In recent years, Italy has witnessed an increasing interest in the use of geothermal resources as well as in the key role hydrogeology plays in the study of geothermal systems and in design of installations. For these reasons within the framework of activities aimed at studying current and future exploitation and the related sustainability of geothermal resources and within the Italian Chapter of the International Association of Hydrogeologists, the Working Group IDROGEOTER was set up in 2012 and started operating in 2013. With regard to the work plan of the Working Group, the first step is an analysis of the state of the art in the current use of low-to-high enthalpy geothermal resources in Italy. This will be achieved through an inventory of data, applications and case studies, aimed at determining the relationship between the hydrogeological settings resulting from features such as hydro-stratigraphy, hydraulic and hydrodynamic conditions, hydro-geochemistry, and the availability of the resource and the potential of the systems (Cerutti et al. 2013a, b). Further activities of IDROGEOTER will include the preparation of proposed guidelines for hydro-geothermal studies, specifically focused on sustainability.

Keywords

Enthalpy • Geothermal systems • Groundwater • Monitoring • Temperature

Working Group IDROGEOTER, IAH Italian Chapter—www.iahitaly.it

67.1 Introduction

Increasing interest in the use of geothermal resources in Italy in the last decade, as well as the key role hydrogeology plays in the study of geothermal systems, in the design of installations and in related sustainability, led to the setting up of the Working Group IDROGEOTER (WGI) within the IAH (International Association of Hydrogeologists) Italian Chapter in October 2012. The WGI started operating in February 2013, with an initial analysis of the state of the art in the current use of low-to-high enthalpy geothermal resources in Italy, to be achieved through an inventory of

C. Paolo
ECOTER CPA S.r.l., Via Selvagreca 14H, 26900 Lodi, Italy

L.R. Stefano
Politecnico di Torino, C.so Duca degli Abruzzi 24, 10129 Turin, Italy

S. Andrea · B. Silvia (✉)
SINERGEO S.r.l., Contrà del Pozzetto 4, 36100 Vicenza, Italy
e-mail: sbertoldo@sinergeo.it

G. Lollino et al. (eds.), *Engineering Geology for Society and Territory – Volume 1*,
DOI: 10.1007/978-3-319-09300-0_67,

data, applications and case studies, aimed at determining the relationship between the hydrogeological settings resulting from features such as hydrostratigraphy, hydraulic and hydrodynamic conditions, hydrogeochemistry, and the availability of the resource and the potential of the systems. WGI will then propose guidelines, specifically focused on sustainability, for hydro-geothermal studies. Whatever the type of geothermal system, groundwater plays a key role in the study of geothermal installations. The hydrogeological characteristics, such as the piezometric pattern, the recharge mechanism, hydraulic parameters, hydrodynamic conditions and hydrochemical features, influence the availability of the resource in terms of temperature, amount and quality. Selected hydrogeological studies, carried out in Italy in order to optimize the use of geothermal resources, regarding different enthalpy levels and various geological environments (volcanic, carbonate rock aquifers,…), are described. In the Lombardy Region (N Italy), currently the most populated and industrialized region in Italy and therefore the area where the highest number of Groundwater Heat-Pump (GWHP) plants are installed, a representative sample of both open-loop and closed-loop systems could be selected, considering the need to identify the critical hydrogeological factors contributing to both geothermal potential and sustainable use of the resource in the current trend of urban sprawl. In the Veneto Region (NE Italy), with regard to low enthalpy, other studies are in progress on sites potentially suitable for closed-loop and open-loop systems, and together with data from the automated monitoring of several wells, these could be used for advanced analysis of different geothermal systems, advanced analyses which have already been carried out at the pilot site of Vicenza described in further detail below. The design of the system, combining a heat pump with a ground heat exchanger (closed loop systems), was authorized temporarily, until the results of the monitoring phase become available; these results may be useful for completing hydrogeological and environmental assessment and achieving a more specific knowledge of the local application for heat pump systems.

67.2 Site A: Veneto Region, Treviso, Area "Ex-Appiani"

This is a project for the redevelopment of a former industrial area (P.IR.U.E.A. "Citadel of the institutions"), designed by the architect Mario Botta; the geothermal heat pump installation is now in regular operation; the main features of the site are:

- surface area of the site: 68,000 m^2;
- volume of buildings above ground: 236,000 m^3
- volume of underground parking: 150,000 m^3
- users: Municipality, Police, Chamber of Commerce, Associations
- new housing units: approximately 100 apartments
- total of 10 new buildings: 5 of them, corresponding to approximately 120,000 m^3, have opted for the installation of an open-loop geothermal heat pump system, with ground water returning into the same aquifer.

The technical activities carried out include:
pre-works phase

- geotechnical and hydrogeological investigation
- temperature monitoring (average T = 13 °C)
- groundwater flow and heat transfer mathematical modeling
- completion of required documentation
installations
- drilling and testing of heat exchange wells
- groundwater sampling and analyses
- tests for alternate activating of wells
- hydrogeological and hydro-geothermal monitoring
- chemical/physical on-site and laboratory analytical testing

To date, no adverse effect on the aquifer has been noted due to the operation of the heat exchange wells (no change in either the piezometric levels or the flow directions of the aquifer). Similarly, no correlation (cause-effect) between withdrawals from the heat exchange wells and temperature variations in groundwater at the piezometers has been found. The chemical-analytical data do not highlight any differences between extracted ground water and "waste" water returned to the aquifer, so there has been no qualitative impact on the aquifer due to the initiative. All qualitative and quantitative controls are in place in accordance with a monitoring plan that provides for the periodic transmission of the results obtained to the relative authorities.

67.3 Site B: Veneto Region, Vicenza, Palladian Basilica

The case study is based on the need to optimize the operating costs of the heating/cooling of the Palladian Basilica, located in the central square of Vicenza. The use of renewable energy sources was preceded by verification of hydrogeological and environmental sustainability. The geothermal system is a ground water heat pump (open loop) and consists of one extraction well and one injection well. The scientific value added of the case concerns the local hydro-geological context of a system of confined aquifers (upper aquifer) for which there is a lack of specific information (e.g. piezometric levels, groundwater flow, relationships with other aquifers, chemistry, etc.) and for which pumping and reinjection pose additional technical problems, including subsidence and building stability.

The technical activities carried out include:
pre-works phase
- pre-feasibility study of legal requirements
- carrying out of geotechnical tests to a depth of up to 50 m
- completion of pilot plant piezometer and thermometric monitoring
- preliminary parameter identification of aquifer intercepted between depths of 30 and 50 m below ground level

installations
- drilling of heat exchange wells to a max. depth of 50 m
- pumping test and water re-injection tests
- implementation of mathematical model of flow and heat transport
- calculation of forecast scenarios
- definition of monitoring program for medium-term verification

The case of the Palladian Basilica reveals interesting potential applications, especially in relation to the thermal effects in a confined-type hydrogeological system, where the outflow velocities of the water are quite low. All technical activities were carried out in compliance with the regulations imposed by the authority responsible for the protection of the artistic and architectural heritage; in particular, further study of geotechnical issues was carried out for the structural protection of the Palladian Basilica.

67.4 Site C: Lombardy Region, Milan, School and Facilities

The case study refers to the redevelopment of an existing complex of schools (nursery and primary), financed by local bodies. The geothermal heat pump installation is based on an open-loop system, including two extraction wells, and is now in full operation; water is discharged as surface water, rather than underground. The main features of the hydrogeological setting are the alluvial system underlying the installation, typical of the central Po Plain, and the very shallow water table (2–3 m below ground level). The intervention is of limited size, the supply wells designed to provide a total flow rate of 6 l/s. The local area is characterized by a high density of civil and industrial settlements and by several land planning and environmental restrictions.

The technical activities carried out include:
pre–works phase
- geological and hydrogeological data collection
- technical feasibility and environmental sustainability analyses
- pilot well drilling and hydraulic testing
- final design of wells

installations
- drilling of two wells (depth 22 m, yield 3 l/s each),
- pumping tests and physical-chemical laboratory analyses
- installation of heat-pump and general testing

Systems of this type and size represent the majority of intervention carried out nowadays in Lombardy. In a situation of this kind, environmental context and land use influence the choice of intervention criteria and works design more than the hydrogeological conditions; groundwater resources are abundant compared to the rather limited output required. The reduced overall impact of the intervention does not render particularly stringent limitations and requirements necessary on the part of the regulators, does not require monitoring measures over time and does not contribute to the production of useful data (amount and quality) for ex-post efficiency evaluation of the management of the system and its long-term impact.

67.5 Site D: Lombardy Region, Brescia, Industrial Estate

This last case study regards activities supporting the design of a system to provide the refrigeration necessary for a food industry storage plant. The designed geothermal system (open loop) includes a ground water heat pump and 4 extraction wells (5 including the reserve); studies and analyses included comparative analyses of different configurations regarding the layout of the wells, water flow rates, discharge (ground water/surface water).

Installations have yet to be completed; the technical activities carried out so far include:
- geological, geotechnical and hydrogeological studies
- technical feasibility and social and legal sustainability analyses
- comparative economic analysis of different design solutions
- field surveys (monitoring wells, hydraulic testing)
- detailed hydrological data analysis,
- preliminary aquifer parameter identification and environmental assessment
- groundwater flow and heat transfer simulation (numerical modeling)
- final design of number and layout of wells, flow rates, water discharge.

A large amount of water (200 l/s) was initially requested by the designers of the refrigeration plant; studies and surveys, together with a careful analysis of the feasibility of the various alternatives in terms of cost, permitted optimization of the use of groundwater, reducing by more than 50 % the volume of water to be drawn from wells, with a corresponding reduction in the volume of water to be discharged.

67.6 Final Considerations

These case studies relate to plant designed and/or completed in accordance with local national and regional laws, supported by appropriate hydrogeological studies based on scientifically-validated criteria.

The case studies presented here have been chosen specifically considering only open-loop systems in alluvial (both confined and unconfined) groundwater settings. Instrumental direct measurements were taken over the short-, medium- and long-term (i.e. monitoring plans were drawn up, including post-works), by means of manual or automatic measurement, as deemed necessary considering the system to be designed and/or as required by the control bodies. Direct measurement is essential both in the short-term for plant inspection and authorization, and also in the medium- and long-term, both for energy performance checks and for the necessary tests of environmental compatibility of the use of groundwater for low enthalpy geothermal purposes. These measurements, sometimes required to maintain authorization for plant use, permit the certification of the quality of its installation and operation, and from time to time may include checks on the air conditioning plant, sampling and periodic laboratory analysis of water extracted and/or returned and chemical-physical vertical logging in the well itself.

The promotion of scientific criterion of technical analysis is one of the strong points of the program of the Italian WG IDROGEOTER and in this sense the experiences cited are case studies representative of the national context, whose analysis will support the development of guidelines, methodological protocols and operating procedures. It is believed that analysis of research and planning experiences relating to different local situations can make a technical contribution useful for guiding both local authorities in the definition of more coherent rules and local laws than those existing today, and workers in the sector in the adoption of suitable planning and work protocols, standardized and of recognized efficacy and efficiency.

References

Cerutti P, Ducci D, Fabbri P, Fidelibus MD, La Vigna F, Lo Russo S, Mazza R, Polemio M, Sottani A (2013) Hydrogeological features and sustainable use of geothermal resources: selected case studies in Italy. European Geothermal Congress, Pisa, 3–7 June 2013

Cerutti P, Ducci D, Fabbri P, Fidelibus MD, La Vigna F, Lo Russo S, Manzella A, Mazza R, Polemio M, Sottani A (2013) Sustainable Use of Geothermal Resources in Italy: first inventory of data, applications and case studies. In: IAH Central European Groundwater Conference 2013. Mórahalom, 8–10 May 2013

G.TES: Pilot Plant for Seasonal Ground Energy Storage in Italy

68

Cesare Comina, Nicolò Giordano, Andrea Giuliani and Giuseppe Mandrone

Abstract

Ground heat storage is considered a powerful solution for supplying thermal energy for heating and cooling (H&C) demand in buildings, covering the energy demand using the ground as a heat reservoir. The Turin University set up a test site at the Campus of Grugliasco in which this method is being tested at a real scale. Apart from direct temperature measurements in the ground and in different part of the hydraulic circuit, a laboratory scale modeling and a numerical simulation are being carried out as well as some direct measurements on the involved geological materials. All the measurements are targeted to the determination of physical parameters of soil, to the quantification of storable heat but also to the evaluation of environmental impact of the whole system. This experiment will allow in the near future a better design of seasonal ground storage facility in northern Italy.

Keywords

Heat storage • Thermal properties • Numerical modeling

68.1 Introduction

Buildings are globally responsible for approximately 40 % of the total world annual energy consumption. Most of this energy is for provision of lighting, heating, cooling, and air conditioning. Reducing the impact of building energy consumption would be therefore one of the best options for a global reduction of dangerous emissions in atmosphere. One way of achieving this result is to design buildings that are more economical in their use of energy. Passive measures can dramatically reduce primary energy consumption and exploitation of renewable energies can also significantly contribute to lower the fossil fuel dependency.

Energy sources are nevertheless important and in the recent years the energy production from renewable sources has grown exponentially, being rising further in the near future in Italy. Most of the renewable sources (solar and wind in particular) are intermittent and non-programmable, owing to their nature, and their generation is often not contemporary with consumption. Thermal energy storage can play consequently an important role towards a green revolution and it can lead to save economical and environmental impacts. The storage systems offer interesting technological perspectives for the control and the stability of this type of energy, by allowing to adapt the consumption to the production in a smart grid view. Several applications of boreholes thermal energy storage (BTES) all over the world are showing the feasibility and efficiency of this kind of systems (Table 68.1). More information can be taken from (Bauer et al. 2010; Fisch et al. 1998).

C. Comina (✉) · N. Giordano · G. Mandrone
Dept. Earth Science, Turin University, Via Valperga Caluso 35, 10125 Turin, Italy
e-mail: cesare.comina@unito.it

A. Giuliani · G. Mandrone
AG3 S.R.L. – Progetto Lagrange – Fondazione C.R.T, Turin, Italy
e-mail: andrea.giuliani@unito.it

G. Lollino et al. (eds.), *Engineering Geology for Society and Territory – Volume 1*,
DOI: 10.1007/978-3-319-09300-0_68,

Table 68.1 Some examples of central solar heating plants with seasonal storage (CSHPSS) from Germany (DE), Sweden (SE) and Canada (CA)

CSHPSS with BTES storage	Total heat demand	Solar collectors	Storage volume	Solar fraction	Max design temperature
	[GJ/y]	[m^2]	[m^3]	[%]	[°C]
Neckarsulm (DE)	1,663	5,000	63,400	50	85
Crailsheim (DE)	14,760	7,300	37,500	50	85
Anneberg (SE)	3,888	3,000	60,000	60	45
Okotoks (CA)	1,900	2,293	34,000	90	80
Attendorn (DE)	205	488	13,500	55	80

The present paper shows an experimental site built in the Grugliasco Campus of the Turin University in the summer 2013. The main purpose of the study is that to describe the behavior of the ground subjected to a heat injection, in order to evaluate the feasibility of a ground heat storage system and to assess the possible environmental impacts of the plant. The test site follows several laboratory experiments performed during the last years, aimed at understanding the heat storage capability of a sandy-gravelly porous media (Giordano et al. 2013), very common geological units in Northern Italy.

68.2 State of the Art on the Heat Storage

The thermal energy storage applications are divided in three different mechanisms which are: sensible heat storage, latent heat storage and chemical reaction/thermo-chemical heat storage. The first cited is considered to be a simple, low-cost, more reliable and acceptable technology compared to other alternatives, even if the latter methods have much higher energy storage densities than sensible heat (Sanner et al. 2003; Xu et al. 2013). The seasonal thermal energy storage (STES) systems fall back into the first category and could also be called "long-term" heat storage, thanks to their capability of guaranteeing a seasonal energy storage: this consists in collecting and storing the heat in the hot seasons and extracting and using it in the winter period, when the heat demand is bigger. The STES systems include several methodologies for storing the heat: these can exploit the groundwater (ATES—aquifer thermal energy storage) (Dickinson et al. 2009; Paksoy et al. 2000; Rosen 1999), hot water confined in steel tanks (Bauer et al. 2010; Novo et al. 2010) or the ground itself, being it constituted by rocks or dry or wet quaternary sediments; in this last case the connection with the ground is provided by a series of boreholes (BTES) (Fisch et al. 1998). Focusing on the last type of seasonal storage, the behavior of the ground exposed to a thermal treatment is a fundamental concept. The amount of heat stored in the selected material is determined by the specific heat capacity of the material (and its density) and the temperature increase. In this respect, a wide knowledge of the thermal properties of the ground, whether porous media or crystalline rocks, and their influencing factors is needed towards a reliable design of a BTES system, which should be efficient, cost-effective and environmentally sustainable.

68.3 Case Study at Laboratory Scale

The distribution of thermal flows in porous media plays an important role in many geological and engineering applications. Moreover, in regard to the design of the borehole heat exchangers of a STES application, the soil characteristics, such as moisture content, particle size and shape, and the heat transfer coefficients, greatly control the power output or determine the amount of heat which potentially could be stored in the ground and then extracted at a later stage (Casasso and Sethi 2013; Diao et al. 2004). For these reasons we built a laboratory device as a necessary characterization tool for predicting the ground's behavior. The proposed procedure is useful for a first order quali-quantitative understanding of the thermal behavior of the investigated medium. A plastic box, sized 1.0 × 0.4 × 0.4 m, was used to simulate the heat transfer within a selected porous medium. It was equipped with an electrical resistance as heat source, continuously controlled by a thermometer and a rheostat during the tests in order to assure the desired constant temperature. Along the major axis of the box, four thermo-resistances Pt100 were placed, located at definite distances from the source, in different positions depending on the test; four Watermark soil moisture sensors, previously properly calibrated, were placed to check simultaneously the moisture conditions. Several tests were carried out and they differ in: time of heat up; static or dynamic hydraulic conditions; number, position, temperature and geometric configuration of the heat sources; position of the T-sensors; grain size distribution of the medium

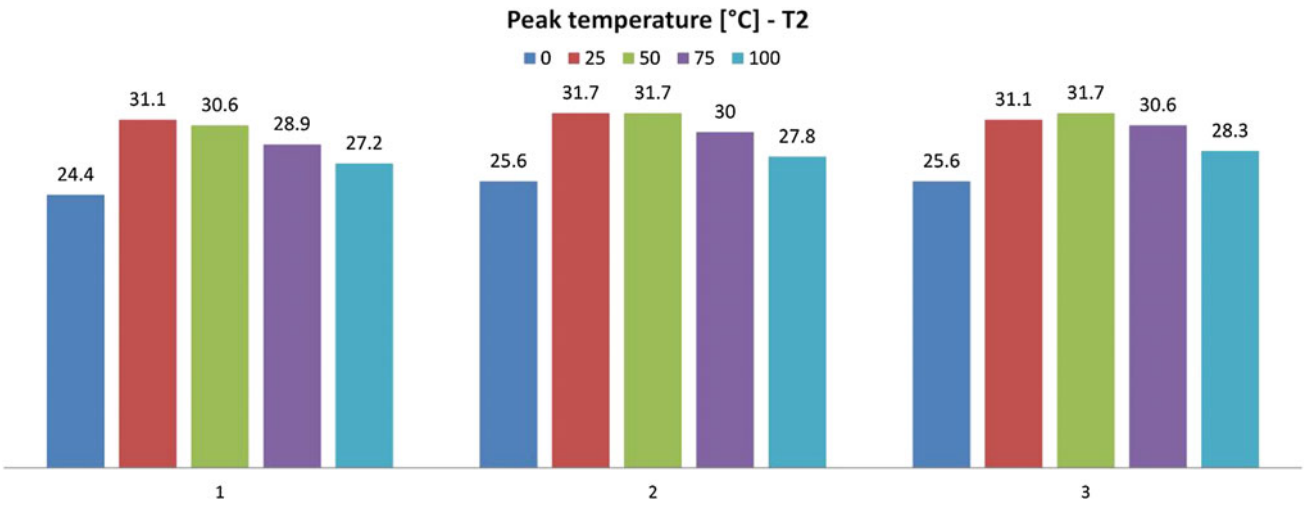

Fig. 68.1 Temperature values registered at 10 cm from the source during a test performed on a fine sand. The three data series show the consecutive testing days; in each series 0 and 100 % of water content are the end members

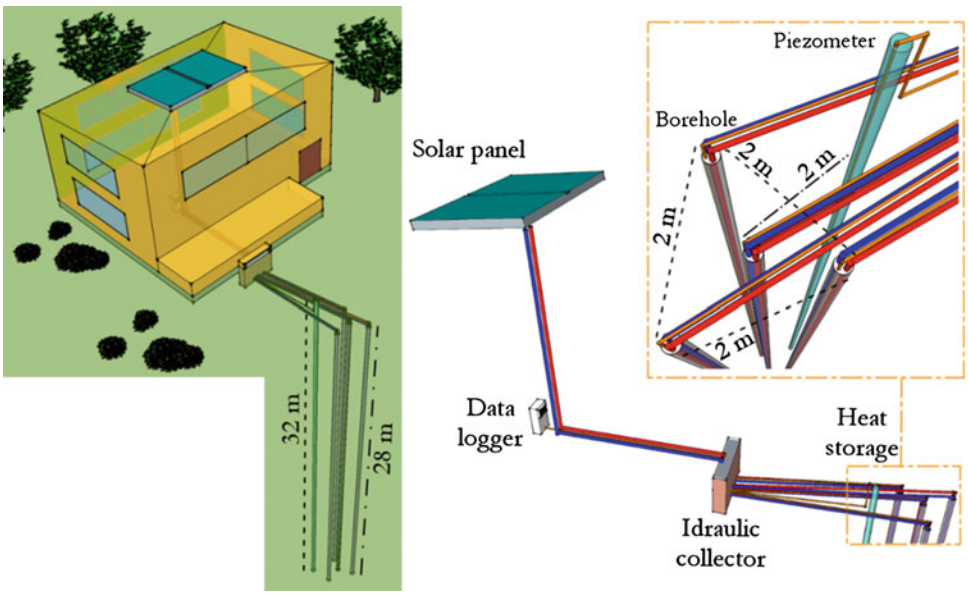

Fig. 68.2 Sketch of the experimental site built in Grugliasco (TO)

and its moisture content. The lab device allowed to simulate different real cases and to understand the behavior of the ground by changing the boundary conditions and the position of the heat exchangers.

A numerical simulation was also carried out to check and validate the analogical modeling. Figure 68.1 compares the temperature values registered in three consecutive days at different moisture content of the tested porous medium. It can be easily noted that the presence of water strongly controls the heat propagation but the less water amount produces a best distribution of the thermal flows within the medium (Giordano et al. 2013).

68.4 Living Lab at Field Scale: The Grugliasco Test Site

The system here presented consists in two solar thermal panels coupled with four borehole heat exchangers (BHEs) drilled in gravelly sandy alluvial deposits (Fig. 68.2).

The BHEs assume a triangular (side 2 m) shape in plan view, with one borehole located at the center of the configuration and equipped by a double-U tube; in the three external BHEs a single-U tube is placed. A piezometer is located 2 m far from the central borehole, in the direction of the groundwater regional flow, even if the bottom of the BHEs (28 m) stands at least 3 m above the medium level of the local groundwater table. The whole circuit, 3 BHEs and the piezometer are equipped with temperature sensors which are continuously recording data.

Analogical and numerical modeling, as well as direct measurements of the ground thermal properties, will be carried out together with the progress of the temperature recording data. The planned monitoring activity will assure a reliable understanding of the ground's behavior. This will be useful to describe the propagation of the thermal plume within the ground, the storage capacity of the ground itself and the potential effect on the surrounding environment (both bio-sphere and hydro-sphere). The amount of heat losses will be moreover monitored in order to evaluate some technical expedients to improve the system's efficiency.

68.5 Expected Results and Future Outlooks

Dealing with the relatively new use of mature technologies, only a real case study is able to demonstrate that similar plants can be useful from the environmental and economic point of views. To do that, a simple but noticeable system has been built to understand the potential of the heat storage within a dry sandy porous medium. At the end of a significant testing period, several parameters (geometrical disposition of the BHEs, working temperatures, insulation methods) will be known in order to assess the optimal working condition of the system. A fundamental step will also be that of showing to both technical and non-technical listeners the real working principles of the heat storage applications.

The G.TES plant will be used as a living laboratory where many activities will be held by students from high school and university. Events and workshops will be planned to share with people all the parts of the plant, from the technical to the geological topic. Our purpose is to create an output showing that the seasonal ground heat storage is a technology easily reproducible, with a minor technical adjustment in similar environmental context.

The added value of the G.TES plant will be that to make a real trial school and to allow stakeholders to assess whether or not this type of system satisfies their needs. According to these scientific and technical issues, the overall expected results of this project will be that to provide a high level of building performance from the energy consumption point of view, which can reflect to indoor and outdoor environmental quality and energy cost efficiency. Moreover secondary, but not less important, the expected results will be that to promote the use of renewable energies at a wider level in respect to what is done nowadays.

Acknowledgments This study is related to a project funded by ALCOTRA Innovation and it was selected in the POR F.E.S.R. 2007/2013 Activity I.1.3—Innovation. This project aims at pilot actions on both lab and field testing of heat storage applications, and at a knowledge spreading with living lab approach. The authors would like also to acknowledge a grant from the Lagrange Project—C.R.T. Foundation.

References

Bauer D, Marx R, Nuβbicker-Lux J, Ochs F, Heidemann W, Müller-Steinhagen H (2010) German central solar heating plants with seasonal heat storage. Sol Energy 84:612–623

Casasso A, Sethi R (2013) Efficiency of closed loop geothermal heat pumps: a sensitivity analysis. http://dx.doi.org/10.1016/j.renene.2013.08.019

Diao N, Li Q, Fang Z (2004) Heat transfer in ground heat exchangers with groundwater advection. Int J Thermal Sci 43:1203–1211

Dickinson JS, Buik N, Matthews MC, Snijders A (2009) Aquifer thermal energy storage: theoretical and operational analysis. Geotechnique 59:249–260

Fisch MN, Guigas M, Dalenbäck JO (1998) A review of large-scale solar heating systems in Europe. Sol Energy 63(6):355–366

Giordano N, Bima E, Caviglia C, Comina C, Mandrone G, Passarella M (2013) Modellizzazione analogica e numerica di un flusso termico in un mezzo poroso in laboratorio attraverso scatola termica. GEAM Anno XLX 1:23–32

Novo AV, Bayon JR, Castro-Fresno D, Rodriguez-Hernandez J (2010) Review of seasonal heat storage in large basins: Water tanks and gravel-water pits. Appl Energy 87:390–397

Paksoy HO, Andersson O, Abaci S, Evliya H, Turgut B (2000) Heating and cooling of a hospital using solar energy coupled with seasonal thermal energy storage in an aquifer. Renew Energy 19:117–122

Rosen MA (1999) Second-law analysis of aquifer thermal energy storage systems. Energy 24:167–182

Sanner B, Karytsas C, Mendrinos D, Rybach L (2003) Current status of ground source heat pumps and underground thermal energy storage in Europe. Geothermics 32:579–588

Xu J, Wang RZ, Li Y (2013) A review of available technologies for seasonal thermal energy storage. Sol Energy. http://dx.doi.org/10.1016/j.solener.2013.06.006

Shallow Geothermal Exploration by Means of SkyTEM Electrical Resistivity Data: An Application in Sicily (Italy)

69

A. Santilano, A. Manzella, A. Donato, D. Montanari, G. Gola, E. Di Sipio, E. Destro, A. Giaretta, A. Galgaro, G. Teza, A. Viezzoli and A. Menghini

Abstract

A novel procedure for estimating the geothermal energy exchanged by a unit volume was tested in northern Sicily (Italy), where public well data for depicting the complex geological setting were insufficient. An airborne electromagnetic survey was carried out in 2011, providing a 3D cell distribution of resistivity values. The integrated analysis of geological and resistivity data was used to identify six Litho-Electrical Units and to build a 3D geological model. This model was integrated with laboratory thermal conductivity measurements on rock samples, and was used to characterize the heat exchange at depths of up to 200 m, which in turn can be exploited for planning and designing geothermal heating and cooling plants using GSHP (Ground Source Heat Pump).

Keywords

Geothermal energy • 3D modelling • Heat exchange • Airborne electromagnetic • GSHP

69.1 Introduction

Geophysical data are powerful for determining underground conditions and providing useful information for planning geothermal exploitation. Ground source heat pump systems (GSHPs) coupled with the ground by means of borehole heat exchangers (BHEs) have gained increasing consensus in Europe as they are an efficient and environmentally friendly technology for heating and cooling purposes. Designing and installing these systems entails assessing the thermal and hydraulic properties of the underground, down to a depth of a few hundred meters. The exchange capacity analysis is defined on the basis of the thermal properties of the rocks and the presence of fluid circulation. When thermal and hydraulic conditions at depth are not known in advance, the geo-exchange is estimated on the basis of thermal properties assuming that outcropping units extend to the maximum depth of BHEs. This hypothesis is seldom fulfilled in regions of complex geology, such as most of those in Italy. Within the framework of the VIGOR Project (Manzella 2013), aimed at assessing geothermal potential in four regions of southern Italy, we tested the possible use of electrical resistivity data to establish geothermal features in the underground of Sicily, a region characterized by the presence of strong physical property changes also within short distances and at shallow depths. A geophysical airborne electromagnetic (AEM) survey provided a wide 3D distribution of electrical resistivity. The same areas were

A. Santilano (✉) · A. Manzella · A. Donato · D. Montanari · G. Gola
C.N.R. (National Research Council) Institute of Geosciences and Earth Resources, Via G. Moruzzi 1, 56124, Pisa, Italy
e-mail: alessandro.santilano@igg.cnr.it

E. Di Sipio · E. Destro · A. Giaretta
C.N.R. (National Research Council) Institute of Geosciences and Earth Resources, Via G. Gradenigo 6, 35122, Padua, Italy

A. Galgaro · G. Teza
Earth Sciences Department, Padova University, Via G. Gradenigo, 6, 35122, Padua, Italy

A. Viezzoli · A. Menghini
Aarhus Geophysics, C.F.Møllers Allé 4, 8000, Aarhus C, Denmark

G. Lollino et al. (eds.), *Engineering Geology for Society and Territory – Volume 1*,
DOI: 10.1007/978-3-319-09300-0_69,

also investigated in order to establish the thermal energy exchange capacity of the underground, based both on outcropping lithological units and on a more detailed geological model constrained by resistivity data.

69.2 AEM Data Acquisition, Processing and Inversion

The AEM survey was acquired using the SkyTEM system (Sørensen and Auken 2004), which, thanks to its dual moment methodology, ensures both near surface resolution and good depth penetration. The first time gate used was at 12 ms after beginning of ramp down, and the last one at 8 ms. The moment of the system was approximately 200.000 Am^2. The data, totalling approximately 2,000 line km (equivalent to 60,000 soundings), were acquired, QC (Quality Control), preprocessed and quickly inverted in the field. The final detailed processing and modelling was carried out at the lab, adopting the workflow (Auken et al. 2009) for quantitative hydro-geological mapping, which had proved successful in the Danish groundwater mapping campaign. The data were edited to remove different sources of noise, then inverted using the "spatially constrained inversion" (SCI, Viezzoli et al. 2008). We produced both blocky (few layers) and smooth (multilayers) models. In both cases the inversion was started with homogeneous half space, and no a priori information. The inversion provided a wide 3D distribution of electrical resistivity with a maximum investigation depth up to a few hundred meters. The geophysical results are made up of 3D cell distribution of resistivity (X, Y, Z, ρ) from which resistivity slice maps and resistivity cross-sections were drawn.

69.3 3D Geological Modelling

The target area is 300 km^2 wide and is located in north-central Sicily, south of the spa town Termini Imerese in the province of Palermo. The area belongs to the "collisional" complex of Sicily, developed along the European-African plate boundary (Catalano et al. 2000), and shows a very complex structural setting. The outcropping rocks belong to different Stratigraphic Structural Units, which constitute the tectonic edifice, unconformely overlaid by sedimentary syn-tectonic basins later involved in the deformation (Catalano et al. 2011). An integrated approach was used for the 3D geological modelling. We analysed geological cartographic data and electrical resistivity data distribution in order to constrain the 3D geological model. Initially we performed an integrated analysis of geological maps and surface AEM data, to identify the resistivity values of outcropping geological units. These units were grouped into Litho-Electrical (LE) Units based on stratigraphic and electrical evidences. The geological cross-sections were then built, by interpreting the resistivity profiles and considering the proposed LE classification.

The integrated analysis of geological maps and surface resistivity map (mean values from 0 to 5 m b.g.l.), allowed us to recognize six LE units, from bottom upward:

- **Imerese LE Unit** (80–1,000 Ω/m): corresponding to Triassic-Oligocene pelagic carbonate of the "Imerese Domain".
- **Numidian Flysch, Portella Colla LE Unit** (5–30 Ω/m): mainly made up of pelites alternating with quartz-arenitic layers representing the lower Member of the Numidian Flysch.
- **Numidian Flysch, Geraci Siculo LE Unit** (10–50 Ω/m): corresponding to the higher Member of Numidian Flysch mainly composed of turbiditic quartz-arenites with interbedded pelites.
- **Tavernola LE Unit** (mainly <10 Ω/m): belonging to the Numidian Basin, consisting of marls and pelites with interbedded quartz-arenites.
- **Sicilide LE Unit** (mainly <10 Ω/m): corresponding mainly to the Varicoloured Shales Fm.
- **Syn-tectonic basins LE Unit** (variable from 7 to >100 Ω/m): including a wide range of lithologies belonging to Neogene basins.

Each LE unit can be identified by an average electrical behaviour, but for "Numidian" and "syn-tectonic basins" Units the ranges of resistivity values are wider due to heterogeneous lithological features. The Quaternary deposits were not considered in the 3D model, because they are mainly characterized by alluvial-colluvial thin deposits with a scattered distribution in the area analysed.

The dataset consisted of topographic DEM, seven geological maps, 21 geological cross-sections, resistivity distribution maps (every 10 m in depth) and 48 resistivity profiles. This dataset was the basis of the 3D geological modelling of LE units.

The modelling workflow was typical of PETREL software (Schlumberger), and consisted of three main processes: "Fault Modelling Framework", "Horizon Modelling" and "Structural Gridding". The faults inserted in the modelling were those dislocating LE units, and were modelled considering geological data and 3D geophysical data, where high electrical contrasts between hanging wall and footwall were identified (Fig. 69.1). All the control points needed to depict the tops of the six LE Units were then defined from the interpretation of geological data constrained by resistivity data. Faults and interpretation points were the input data for the modelling of "Horizons" that represent the tops of units built following stratigraphic and structural rules.

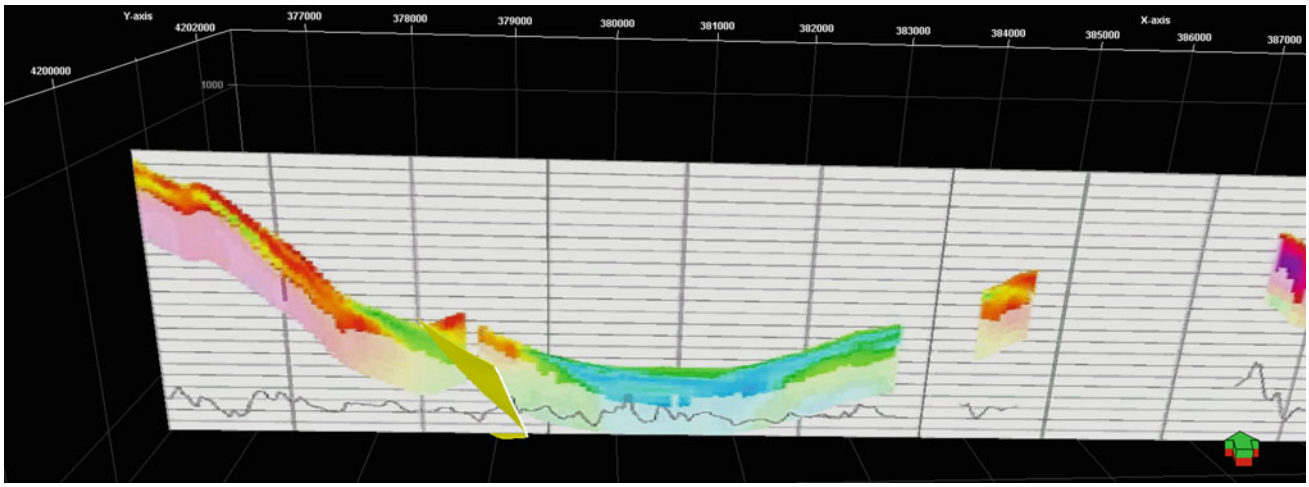

Fig. 69.1 Fault (*yellow plane*) depicted by AEM data interpretation (West-East No. 6 resistivity profile)

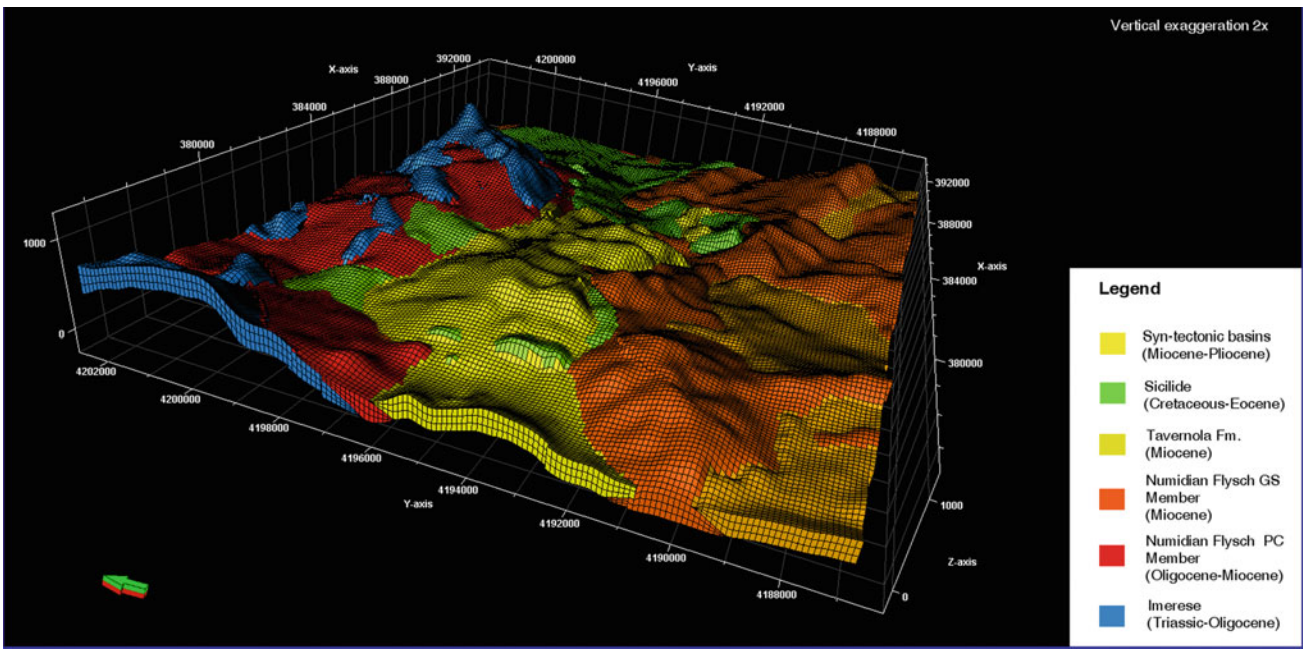

Fig. 69.2 Three-dimensional geological model of the Termini area

Finally, the "Fault framework" and the "Horizons" were used to build the 3D geological model of the area, where the depth of investigation was 250 m b.g.l. and a regular cell grid with 100 m horizontal spacing (Fig. 69.2).

69.4 Thermophysical Parameters Modelling

The geo-exchange map was calculated using a specific algorithm, implemented in the frame of VIGOR Project, able to combine ground and GSHP parameters in order to obtain the energy exchanged ability in a closed-loop geothermal system. In order to define the thermal conductivity of rocks and sediments that were representative of the main lithological units, several samples were collected and analysed in the laboratory, both in dry and wet conditions, using a thermal analyser system (C-Therm TCi) following the Modified Transient Plane Source method (Di Sipio et al. 2013). This non-invasive, highly accurate and rapid technique provides a detailed overview of the thermal nature of the sample material from the thermal conductivity and effusivity measured from the slope of the voltage drop plot (Cha et al. 2012).

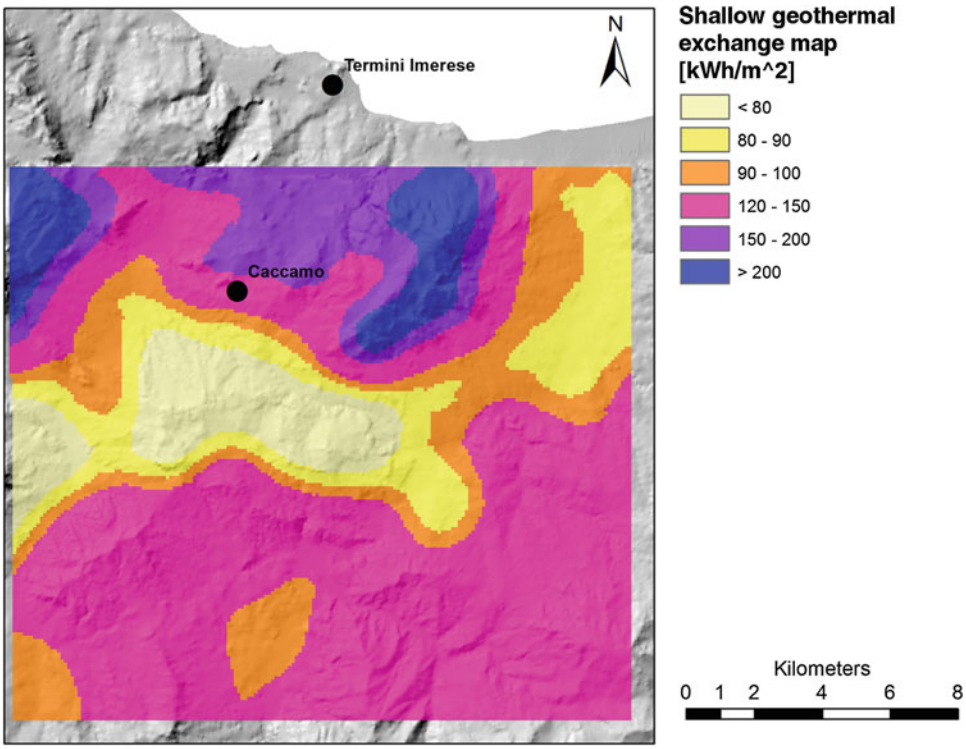

Fig. 69.3 Shallow geothermal exchange map of Termini area

The heat conductivity values were assigned to the LE units, described in Sect. 69.3, by computing mean values of the lithologies belonging to the same unit. To assign the thermal conductivity values, a pseudo-stratigraphic model of the underground was obtained with Modalstrata, a specific MATLAB toolbox developed to improve the correlation of the stratigraphic succession (Cultrera et al. 2012). The new regularized model defined on a 1-km-side regular grid has 5 m vertical, regular steps, where for each grid node the geological unit, provided by the 3D geological model, was associated with its mean thermal conductivity. A weighted average thermal conductivity value was computed for each 1-km-side prism of the 3D grid. These data were then used to calculate the corresponding shallow geo-exchange map (Fig. 69.3).

69.5 Conclusions

The geo-exchange map provides a clear picture of the areas where heat exchange is favoured by geological conditions. Three main sectors can be identified. The most favourable sector is located in the northern part, with values usually higher than 150 kWh/m^2. Here, in spite of the outcrops of pelitic "Numidian" deposits, the buried carbonate "Imerese" Unit, having much higher thermal conductivity, enhances the potential of exchanged thermal energy.

The central sector is the least favourable, with values mainly lower than 100 kWh/m^2, due to the presence of low thermal conductivity Neogene syn-tectonic basins and clayey "Sicilide" Unit.

The third and southernmost sector has good potential, with values up to 150 kWh/m^2, due to the widespread presence of a quartz-arenite "Numidian" Member, characterized by a high thermal conductivity.

The geophysical data we used were very useful in constraining the 3D model, thereby producing a geo-exchange map with higher level of detail than standard ones which tend to be based on geological maps alone. The best example is in the first sector, where the standard approach of using just the outcropping units would have resulted in a much lower exchange energy than what was obtained in this study.

We believe that it could be exploited by policy makers for decisions concerning the promotion and use of GSHP technology.

References

Auken E, Christiansen AV, Westergaard JA, Kirkegaard C, Forged N, Viezzoli A (2009) An integrated processing scheme for high-resolution airborne electromagnetic surveys, the SkyTEM system. Explor Geophys 40:184–192. doi:10.1071/EG08128

Catalano R, Franchino A, Merlini S, Sulli A (2000) Central western Sicily structural setting interpreted from seismic reflection profiles. Mem Soc Geol It 55:5–16

Catalano R, Avellone G, Basilone L, Contino A (2011) Note illustrative della Carta Geologica d'Italia alla scala 1:50.000 foglio 609-596 Termini Imerese—Capo Plaia. (I.S.P.R.A., Servizio Geologico d'Italia e Progetto CARG, 2011) http://www.isprambiente.gov.it/Media/carg/note_illustrative/596_609_CapoPlaia_Termini.pdf. Accessed June 2012

Cha J, Seo J, Kim S (2012) Building materials thermal conductivity measurement and correlation with heat flow meter, laser flash analysis and TCi. J Therm Anal Calorim 109:295–300. doi:10.1007/s10973-011-1760-x

Cultrera M, Antonelli R, Teza G, Castellaro S (2012) A new hydrostratigraphic model of Venice area (Italy). Environ Earth Sci 66:1021–1030

Di Sipio E, Chiesa S, Destro E, Galgaro A, Giaretta A, Gola G, Manzella A (2013) Thermal conductivity as key parameter for geothermal numerical models. Energy Procedia 40:87–94. doi:10.1016/j.egypro.2013.08.011

Manzella A (2013) Geothermal development in southern Italy and the contribution of VIGOR Project. In: Proceedings of European Geothermal Conference, Pisa, 2013

Sørensen KI, Auken E (2004) SkyTEM—a new high-resolution helicopter transient electromagnetic system. Explor Geophys 35:191–199

Viezzoli A, Christiansen AV, Auken E, Sørensen KI (2008) Quasi-3D modeling of airborne TEM data by spatially constrained inversion. Geophysics 73:F105–F113. doi:10.1190/1.2895521

Geothermal Investigations of Active Volcanoes: The Example of Ischia Island and Campi Flegrei Caldera (Southern Italy)

70

S. Carlino, R. Somma, A. Troiano, M.G. Di Giuseppe, C. Troise and G. De Natale

Abstract

The active volcanic zone of Ischia Island and Campi Flegrei caldera (Campania) have been the site of many geothermal investigations, since the early 20th century. These areas are characterized by very high geothermal gradient and heat flow as consequence of upward migration of magmatic sources coupled with vigorous hydrothermal circulation. After the increment of installed geothermal power in Larderello (Tuscany), the extensive geothermal exploration of Campania was not followed by exploitation projects. In recent time, the attention on the possibility to exploit electric energy has been drawn by the new Italian regulation for exploitation leases. The larger geothermal potential of Campi Flegrei caldera and Ischia Island, located west to the Bay of Naples, makes these areas as possible sites of new geothermal plants installation. We present here the results of recent geothermal researches of Campi Flegrei caldera and Ischia Island, which integrate and improve the information obtained during the exploration performed by SAFEN and AGIP-ENEL companies from the earlier 1940 to 1985. These data are useful to characterize the geothermal reservoirs of this active volcanoes and also to increase the knowledge of volcanic processes and related risk.

Keywords

Geothermal exploration • Geothermal exploitation • Campi flegrei caldera • Ischia island

70.1 Introduction

The most obvious geological features for identifying geothermal targets areas are, of course, active volcanoes. They are, in many cases, associated with geothermal circulation systems, energized by magma chambers that reside in the shallow crust, generally from a few to few tens of kilometers. Volcano dynamic at Campi Flegrei caldera and Ischia island is related to extensional tectonics due to the spreading of Tyrrhenian Basin, which was active at least since Pleistocene. The extension produced the upward migration of the Moho to a depth of less than 20 km, and the propagation of magma towards the brittle crust, forming large reservoirs. The occurrence of these large reservoirs is inferred from geological, volcanological, geochemical and geophysical surveys (Zollo et al. 2008) and is highlighted at the surface by the high heat flow (Fig. 70.1).

Large caldera-forming eruptions occurred both at Campi Flegrei and Ischia, such as the Campania Ignimbrite (39ky B.P.) and Neapolitan Yellow Tuff (15ky B.P.) (Campi Flegrei) and Mount Epomeo Green Tuff (55Ky B.P.) (Ischia). The amount of emitted magma during these events ranges from few tens to more than 200 km^3 of dense rocks equivalent (DRE). The location of both residual shallow magma chambers (2–4 km) and deeper magmatic systems

S. Carlino (✉) · R. Somma · A. Troiano · M.G. Di Giuseppe · C. Troise · G. De Natale
Istituto Nazionale di Geofisica e Vulcanologia, Sezione di Napoli Osservatorio Vesuviano, Napoli, Italy
e-mail: stefano.carlino@ov.ingv.it

G. Lollino et al. (eds.), *Engineering Geology for Society and Territory – Volume 1*,
DOI: 10.1007/978-3-319-09300-0_70,

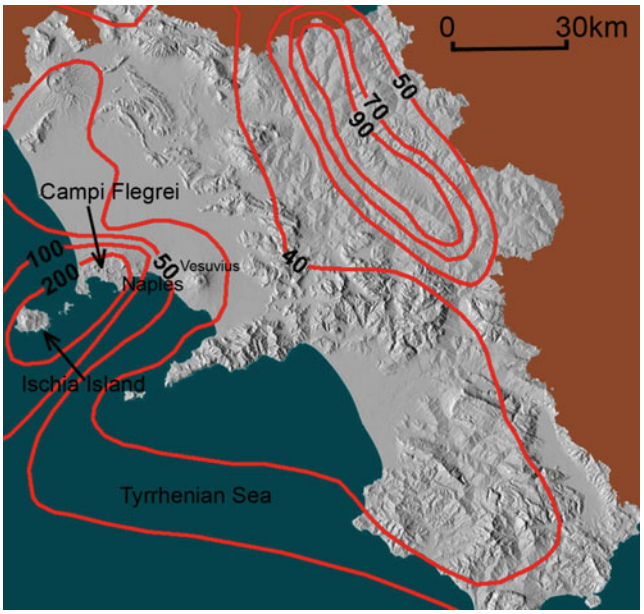

Fig. 70.1 The Campania region with indication of heat flow isolines (mW/m^2) (after Della Vedova et al. 2001). The western margin of the region is characterized by the presence of two important active volcanic districts: Campi Flegrei caldera and Ischia Island, west to Naples, and Vesuvius, east to Naples. The larger heat flow values are concentrated within the former district with value above 200 m Wm^2. This area is the most interesting from geothermal exploitation point of view

(7–10 km) have been inferred from seismic tomography, gravity and geochemical data, but is still matter of debated (Carlino and Somma 2010, and references therein).

The formation of both the caldera structures, has been followed by the occurrence of vigorous hydrothermal systems, which transport a larger part of heat by advection processes, forming a diffuse systems of fumaroles fields and hot springs at the surface. These features were an appeal for people living in Southern Italy, since Roman Empire age. The first systematic study of hot springs was performed at Ischia by Giulio Iasolino (1588), who introduced them into medical practice and boost Ischia's fame. Otherwise, the interest in Ischia also grown due to the eruption of the nearby Campi Flegrei, in 1538 A.D., which made the more popular thermal baths of Pozzuoli and Baia impracticable. The attention for the extensive geothermal fields at Ischia and Campi Flegrei, turns from a merely spa use to a geothermal exploitation during the early 20th century. An extensive campaign for geothermal investigation started in 1939 with many drillings performed at Ischia and Campi Flegrei, by the SAFEN Company. The researches continued later, in the framework of the Joint Venture AGIP-ENEL companies, and were focused in the Campi Flegrei area, starting from 1979 (AGIP 1987). Several wells reached few kilometers of depth, with a maximum depth of 3 km at Campi Flegrei. The geothermal researches involved also the Vesuvius area, starting from 1952, but the temperature gradient measured in the 2 km depth well ($\sim$30 °C km^{-1}), southernmost to the volcano, was not of interest for geothermal exploitation. On the contrary the results obtained by drillings at Ischia and Campi Flegrei, encouraged the planning of a project of exploitation for electric energy production. Nevertheless, at the end of 80'years the project was abandoned. In recent time, thanks to a new Italian regulation, which favors and incentivizes innovative pilot power plants with zero emission, a number of exploitation leases have been submitted to the Ministry for Economic Development. This require to assess the geothermal potential of reservoirs and the sustainability of the resource. We report here a summary of preliminary results which the INGV obtained in the framework of geothermal projects for electric exploitation at Campi Flegrei and Ischia.

70.2 Historical Data from Geothermal Exploration

The data obtained from SAFEN and AGIP-ENEL geothermal exploitation and drillings, from 1939 to 1985, allow us to infer a number of important parameters which are useful for electric energy exploitation (AGIP 1987; Carlino et al. 2012 and references therein). The average geothermal gradient is about 150 up to 220 °C km^{-1} for Campi Flegrei and Ischia respectively. The maximum heat flow recorded at Ischia, is $\sim$500 m Wm^2, while at Campi Flegrei is about $\sim$120 m Wm^2. Saline content of fluids ranges in a wide interval (from 20.000 to more than 300.000 ppm TDS) due to different temperature and pressure condition of the reservoir and interaction with sea water. At Campi Flegrei, during the productive tests, it was also possible to evaluate the potential production for each well, at Mofete site (eastern caldera). These wells were characterize by a vapor–water mixture with a well head temperature of 180–230 °C, TDS of 30–70 g l^{-1}, 10 % in weight of non-condensable gases. The flow rate of the shallower aquifer was 200th^{-1} with maximum pressure of 0.8 MPa (8 bar). The intermediate aquifer was characterized by a lower flow rate of 70th^{-1} but an higher content in weight of vapor (40 %), thus the resulting enthalpy was 1,100 kJ kg^{-1} for the shallower aquifer and 1,600 kJ kg^{-1} for the intermediate one. This allow to obtain an electric production of 1–1.5 MWe for a single productive well.

Finally, it is worth mentioning that the first experimental binary-cycle plant worldwide for electric production was installed at Ischia, in 1939, on the beach of Citara, with an

actual power of 250 kWe (500 kWe nominal). This small power plant was fed by a shallow well, with flow rate of 19 kg s^{-1} of water and 28 kg s^{-1} of vapor, temperature of 176 °C at the well bottom and 130 °C at the well head. The plant operated in 1942 for about one year, after that the production was interrupted when Italy was enrolled in the World War II.

70.3 Recent Geothermal Projects in Campania

Nowadays, the interest towards the geothermal-electric exploitation at Ischia and Campi Flegrei is largely increasing, since a number of exploitation leases have been submitted to the Ministry for Economic Development of Italy and to the Campania Region, by several Companies. This represents an important step, since the exploitation of geothermal energy in Italy, despite the very high potential, is still limited to the district of Larderello and Mt. Amiata, with total electric power of about 800 MWe.

Following the new Italian regulations which favor and incentivize innovative pilot power plants with zero emission, several geothermal projects have started in the Campania Region, thanks to the cooperation among large to small industries, Universities and public Research Centers. INGV Sezione di Napoli (Sezione di Napoli, Osservatorio Vesuviano) has the technical/scientific leadership of such initiatives. Most of such projects are coordinated in the framework of the Regional District for Energy, in which a large part is represented by geothermal resource. Leading geothermal projects in the area include "FORIO" pilot plant project, aimed to build two small (5 MWe each one) power plants in the Ischia Island and two projects aimed to build pilot power plants in the Agnano-Fuorigrotta area, in the city of Naples, at the easternmost part of Campi Flegrei caldera. One of the Campi Flegrei projects is named "SCARFOGLIO" and is devoted to build a 5 MWe geothermal power plant located in the Agnano area, whereas the "START" project has the goal to build a tri-generation power plant in the Fuorigrotta area, fed mainly by geothermal source improved by solar termodynamic and biomass. Such projects have not yet entered in the field work operational phase, and are partially approved ("FORIO" and "SCARFOGLIO") by the Ministry for Economic Development. As concerned the "FORIO" project, a study related to the possible interaction between geothermal exploitation and thermal spring activities has to be developed. To this aim, it is also analyzed the possible changes of temperature and pressure in the shallow geothermal reservoir of Ischia western sector, due to the heat withdrawal for

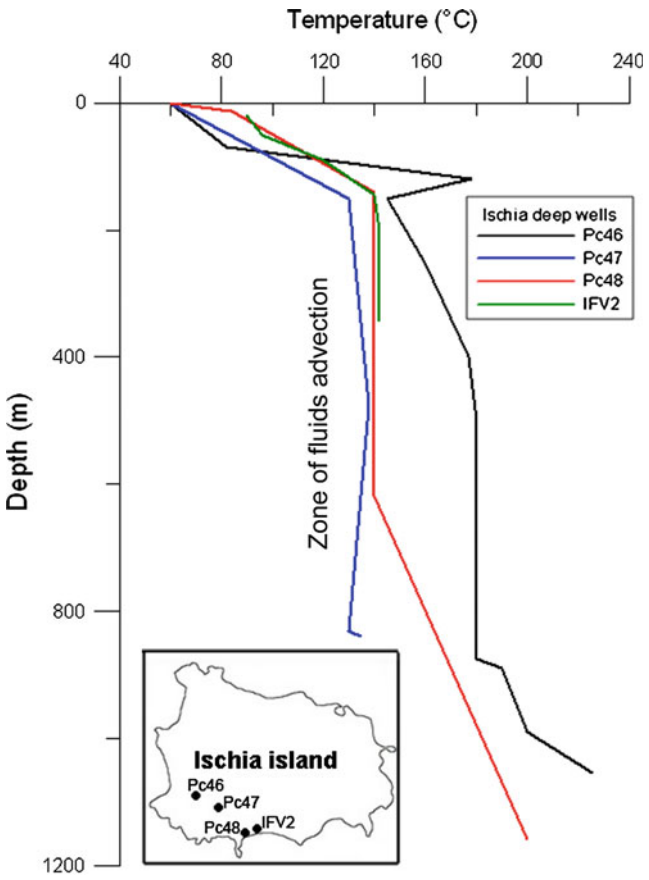

Fig. 70.2 Temperature profiles measured in the deeper wells of the hottest sector of Ischia Island (down to about 1 km). The depth range from 200 m to about 800 m represents the shallow geothermal reservoir where advection of fluids occurs. A possible target of well for electric production is 600–700 m (after Carlino et al. 2012)

electric production related to small power plant size (1–5 MWe). The potential occurrence of shallow geothermal resource is inferred from the observation of temperature trend vs. depth, which evidenced the presence of an advection zone from about 200 m to about 800 m of depth (Fig. 70.2). Our analysis has been performed by using numerical simulations based on a well-known thermofluid-dynamical code (TOUGH2®). Obtained results show that geothermal exploitation (after 30 years of exploitation) can be made compatible with thermal spring exploitation (Carlino et al. 2014) and that the most significant perturbation of the geothermal systems in terms of temperature and pressure is confined along a radial distance of about 500 m from the well axis (Fig. 70.3).

Furthermore, in recent time a pilot hole drilling in the framework the Campi Flegrei Deep Drilling Project "CFDDP" (ICDP) has completed, and represents an important experience for several operational aspects, which should constitute an example to be followed by the next

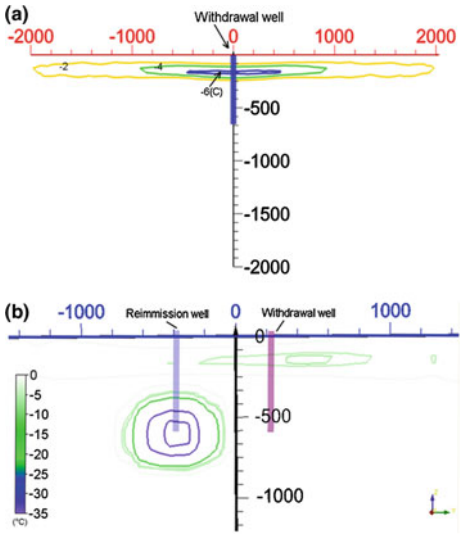

Fig. 70.3 Example of simulation (using TOUGH2®) of the thermal perturbation due to extraction (**a**) and both extraction and reinjection (**b**) of the fluid (flow rate = 22 l s^{-1}) at a temperature of 180 °C (well head, 40 % vapor phase), for electric production (1–1.5 MWe for each well), after 30 years of exploitation (after Carlino et al. 2014). Simulation is performed assuming heat transport by both convective flow in a porous media (Darcy law) and conduction; the supposed temperature reservoir for Ischia Island is T ~ 240 °C at depth 500–900 m (inferred from SAFEN drillings data) (AGIP 1987); it is also assumed the following value of permeability vs. depth: 10^{-15} m^2 for shallow layer, 10^{-16} m^2 for intermediate layer; 10^{-18} m^2 for deeper layer. The depth of the boreholes is 600 m

geothermal activities in the area. This project, which consists of two drillings (the first one, a 500 m pilot hole, concluded in December 2012, the second one, a planned deeper drilling, 3.5 km depth) despite is aimed to pure volcanological items, provided important data related to the geothermal system of the western sector of Campi Flegrei caldera. The drilling site was equipped with dense and multidisciplinary continuous monitoring systems, an example to follow anyway to assure the minimum impact on such densely urbanized areas. Furthermore, innovative leak-off experiments mainly aimed to permeability and strength/stress measurements have been developed and tested. Such tests put also in evidence a significant local increase of permeability, about one order of magnitude, obtained at the end of the injection experiment.

70.4 Conclusions

The recent regulation of geothermal exploitation in Italy, through innovative and zero emissions power plants, has permitted to give a new impulse to the development of highly performing technological power plants in terms of either efficiency than mitigation of environmental impact. In this framework, the recent developments of scientific and technological studies of the geothermal exploitation in the Campania Region seems to suggest a good expectation in terms of development of this alternative energy in the next future. This is well shown by the recent studies in the framework of "FORIO" and "SCARFOGLIO" exploration leases at Ischia Island and Campi Flegrei respectively. Power plants size between 1MWe and 5Mwe represent a good compromise given the high urbanization of the area where projects have been applied. Furthermore, the CFDDP will provide important knowledge from one side of the historical volcanological reconstruction of the Campi Flegrei Caldera and from the other side a new definition of the important parameters such us formation permeability and stress configuration of the area.

References

AGIP (1987) Geologia e geofisica del sistema geotermico dei Campi Flegrei, Technical report. Settore Esplor e Ric Geoterm-Metodol per l'Esplor Geotermica, San Donato Milanese Italy 1987(1–2):3

Carlino S, Somma R (2010) Eruptive versus non-eriptive behaviour of large calderas: the example of Campi Flegrei caldera (southern Italy). Bull Volcanol 2010. doi:10.1007/s00445-010-0370-y

Carlino S, Somma R, Troise C, De Natale G (2012) The geothermal exploration of Campanian volcanoes: Historical review and future development. Renew Sustain Energy Rev 16(1):1004–1030

Carlino S, Somma R, Troiano A, Di Giuseppe MG, Troise C, De Natale G (2014) The geothermal system of Ischia Island (southern Italy): critical review and sustainability analysis of geothermal resource for electricity generation. Renew Energy 62:177–196

Della Vedova B, Bellani S, Pellis G, Squarci P (2001) Deep temperatures and surface heat flow distribution. In: Vai GB, Martini IP (eds) Anatpmy of an orogen: the apennines and adjacent mediterranean basins. Kluwer Academic Publishers, Dordrecht, pp 65–76

Zollo A, Maercklin N, Vassallo M, Dello ID, Virieux J, Gasparini P (2008) Seismic reflections reveal a massive melt layer feeling Campi Flegrei caldera. Geophys Res Lett 2008(35):L12306. doi:10.1029/2008GL034242

Wells Declivity Temperature Geothermal Field Bora-Sigi, Central Sulawesi, Indonesia

71

Suparman, Murni Sulastri and Suci Sarah Andriany

Abstract

Indonesia is a rich source of geothermal energy. This island is located on the "Ring of Fire" volcanic belt, accounting for 40 % of the world's geothermal reserves. Geothermal energy is needed as one of the alternative power generation to satisfy electricity demand in Indonesia. Some Geothermal field in Indonesia is a non-volcanic, unfortunately utilization of Geothermal energy in the field of non-volcanic Geothermal has not been developed for use not directly into electrical energy. One field of non-volcanic Geothermal potential as a powerhouse, namely Geothermal Field Bora-Sigi Central Sulawesi. The research method is a three step process: method studios are obtained by examining the regional area of volcanic Geothermal field area, field methods is obtained by measuring the temperature (Temperature Logging) on wellbore BRA-1 and BRA-2 at a certain depth, and laboratory methods by calculating the data well BRA-1 and BRA-2 by using the Horner plot method. Temperature slope drilling BRA-1 and BRA-2 in the geothermal field Bora-Sigi, Central Sulawesi was conducted to determine the temperature gradient and prove the results of previous investigations. Temperature gradients in the temperature slope wells BRA-1 and BRA-2, respectively 29.72° and 28.51° per 100 m depth. The results are good and in accordance with the results of an integrated investigation and potential to be developed as energy power plants for the region.

Keywords

Geothermal • Temperature declivity • Temperature • Non-volcanic

71.1 Introduction

Indonesia needs new alternative energy to fulfill electricity demand more efficiently and in accordance with the rich natural resources in Indonesia. Geothermal is a perfect solution because it is supported by Indonesia's strategic location in the development of this potential. There are two types of geothermal resources: Non-volcanic geothermal resources and Magmatic-volcanic geothermal resources.

Bora geothermal area, Central Sulawesi, Non-volcanic geothermal field. Non-volcanic Geothermal field has not been developed for use not directly into electrical energy. The purposes of this research to obtain subsurface data and the objective is to determine the slope of the temperature (temperature gradient), so that the area is known to be developed or not.

71.2 Literature Review

Geothermal energy is the heat energy derived from the earth. Geothermal energy is an alternative that has unique characteristics because of the geothermal fluid form can

Suparman
Center of Geological Resources, Jl. Soekarno Hatta no. 444
Bandung, 40254 Jawa Barat, Indonesia

M. Sulastri (✉) · S.S. Andriany
Padjadjaran University, Jl. Raya Bandung Sumedang KM 21
Jatinangor, 45363 Jawa Barat, Indonesia
e-mail: naomi_murni@yahoo.com

G. Lollino et al. (eds.), *Engineering Geology for Society and Territory – Volume 1*,
DOI: 10.1007/978-3-319-09300-0_71,

only be used as an energy close to the source. If geothermal energy is transported then the economic value of it will be lost (Permana 2008).

At certain geological conditions, geothermal energy can be stored in reservoirs in sedimentary basins or along the fault zone is where water circulation occurs, either from rain water, surface water, and water from the magmatic system. There are two types of geothermal resources: Non-volcanic geothermal resources and Magmatic-volcanic geothermal resources. Natural impacts associated with geothermal areas include dissolving primary minerals and formation of secondary minerals are quite stable in the hydrothermal environment generated; reservoir rock permeability changes primarily by argillic alteration, silicification, and desification, and the formation of surface manifestations such as fumarola, springs heat, and steam surface (Nugraha and Yuniarto 2008).

Bora geothermal area, Central Sulawesi, A non-volcanic Geothermal field. Establishment of geothermal systems in areas closely related to Bora estimated tectonic activity that causes the formation of zones and trigger depression Bora breakthrough igneous (intrusive) old young Quaternary who still keep the residual heat from the magma chamber. The residual heat acts as a heat source that heats the water below the surface which then rises through the cracks/fractures and trapped in a geothermal reservoir (Geological Survey 2010) (Fig. 71.1).

Geothermal gradient is the rate of increase of temperature (°C) if down/enter into the earth every 100 m. Under the constant-temperature zone layer contained geothermal zones, is areas of high temperature heat from the earth itself. With reference to the geothermic degree 33 m for lithosphere layers, the temperature at a depth of 33 km is 1.000 °C and at a depth 66 meter it will reach 2.000 °C. At this highest temperature, the rocks below lithosphere will melt, but in depth of the high pressure (11,000–14,000 atmosphere), causing rocks or substances in the solid state is a plastic (Mulyo 2004).

Logging temperature gradient based on the geometric parameters where each increment depth of 100 meter will be an increase in temperature of 3 °C. If the addition of a depth of 100 m over 100 m, then it shows the depth of the temperature anomalies associated with geothermal fluid contained beneath (Menzeis et al. 1979).

71.3 Methodology

The research method is in a three step process: Method studio obtained by examining the volcanic region Geothermal field area, field methods is obtained by measuring the temperature (Temperature Logging) on wellbore BRA-1 and BRA-2 at a certain depth, and laboratory methods to calculate the temperature data drilling (Temperature Logging) on wellbore BRA-1 and BRA-2 at a certain depth by using the Horner plot method. The uses data is "conductive" temperature data not "convective" temperature data, so that the formation temperature at that depth can be calculated.

71.4 Results and Discussion

Measurement results in BRA-1 well was at a depth of 100 and 160 m. On measurements at a depth of 100 m measured temperature of 37.7 °C, after about 20 h of soaking instruments, temperature changed to 44.4 °C. Measurements at a depth of 160 m measured temperature of 53.7 °C, after about 8 h of soaking instruments, temperature changed to 53.9 °C (Fig. 71.2).

Measurement results in BRA-2 performed well at a depth of 66, 110 and 250 m. On measurements at a depth of 66 m measured temperature of 38.1 °C, after the soaked for 11 h and 10 min, the temperature changed to 44.1 °C. Measurements at a depth of 110 m measured temperature of 46.8 °C, after 10 h 18 min, of soaking instruments, the temperature turn to 53.9 °C. Measurements at a depth of 250 m measured temperature of 64.5 °C, after 18 h 35 min of soaking instruments, the temperature changed to 73.5 °C (Fig. 71.3).

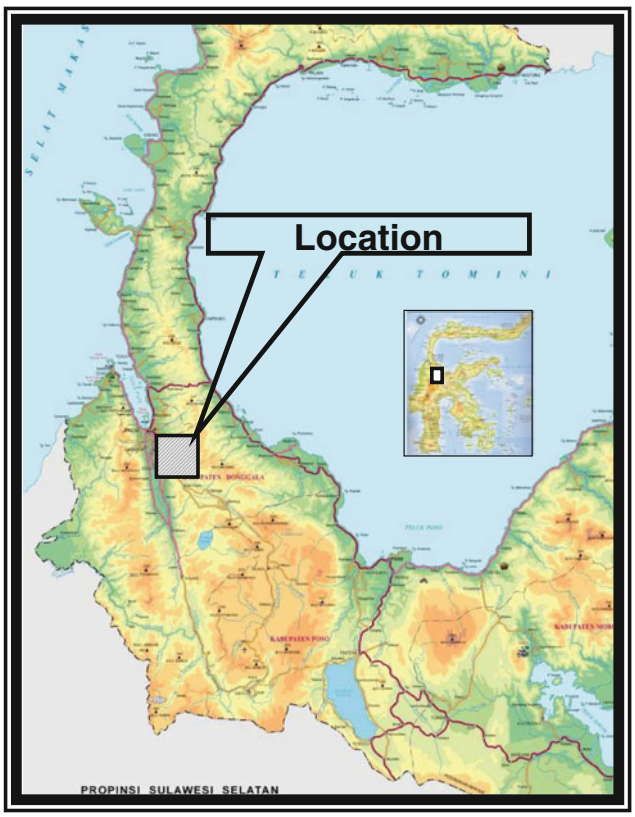

Fig. 71.1 Map location of Bora geothermal areas

Fig. 71.2 Temperature well logging activities in BRA-1

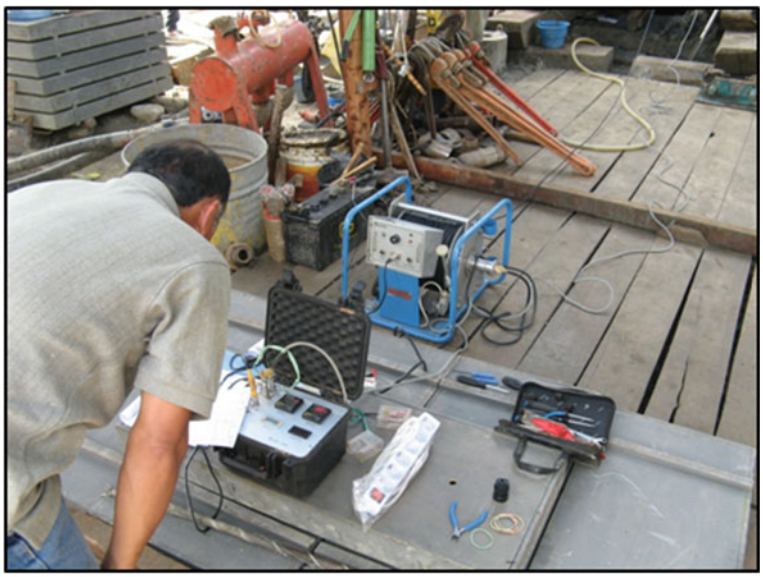

Fig. 71.3 Temperature well logging activities in BRA-2

The results of calculations BRA-1 well data in a depth of 100 m using the Horner plot obtained the slope of the temperature rates (gradient temperature) of 29.7 °C per 100 m (more than nine times the average gradient).

While data from 160 m depth can not be calculated because of the well out of hot water (in flux) temperature 44.2 °C with a flow of 12 lpm (Fig. 71.4).

The results of calculations BRA-2 well data using the Horner plot method at the depth of 66, 100 and 250 m obtained temperature gradients, respectively 27.27 °C/100 m, 29.77 °C/100 dan 28.5 °C/100 (average 27.51 °C/100 m) or more than 9 times the average gradient of the earth (±3 °C per 100 m) (Figs. 71.5 and 71.6).

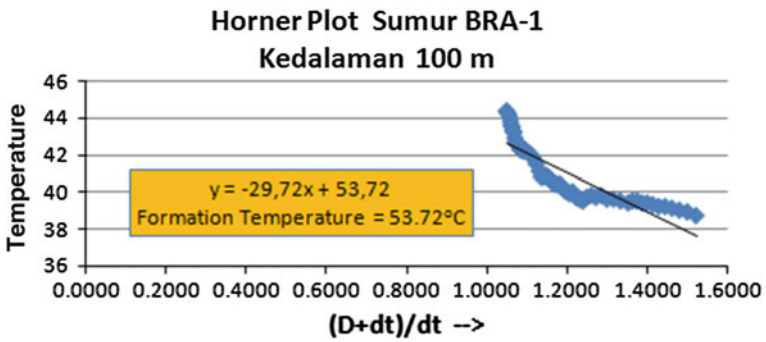

Fig. 71.4 Horner Plot BRA-1 well at 100 m Depth

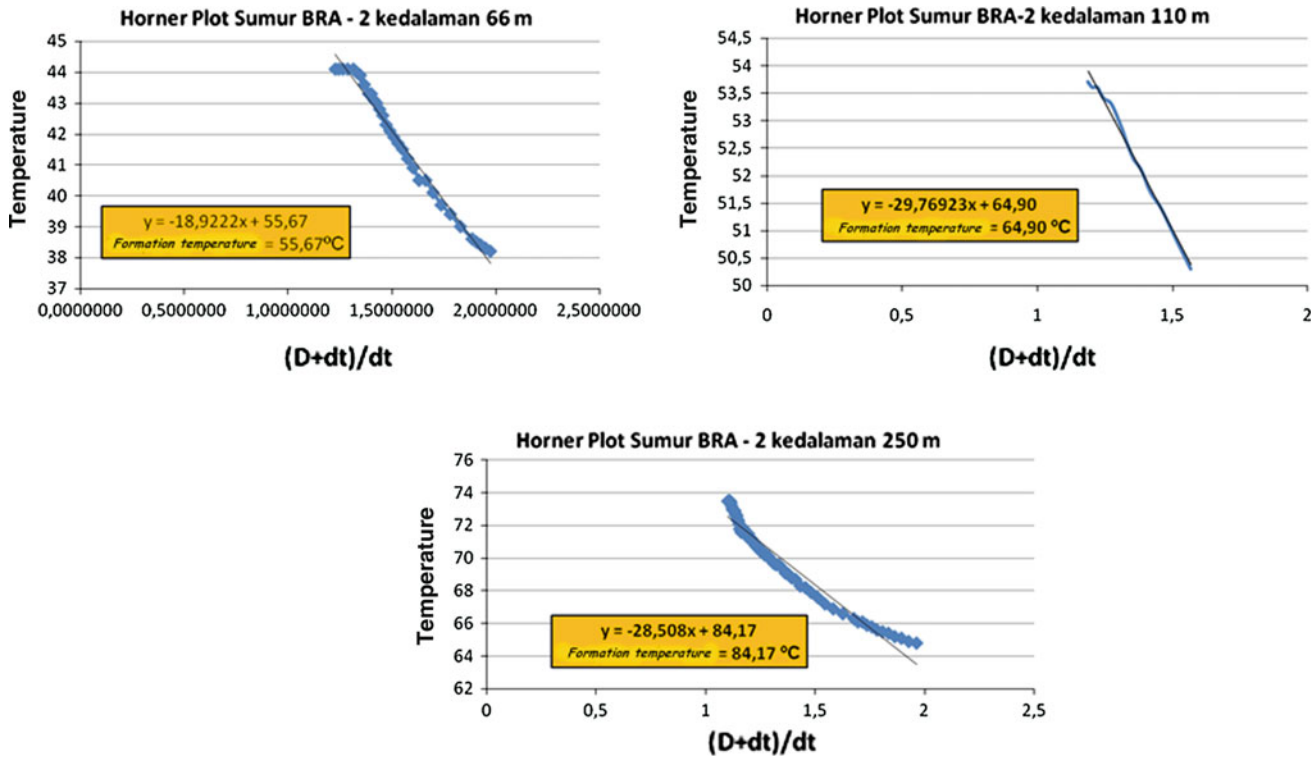

Fig. 71.5 Horner Plot BRA-2 well at 66, 110, and 250 m depth

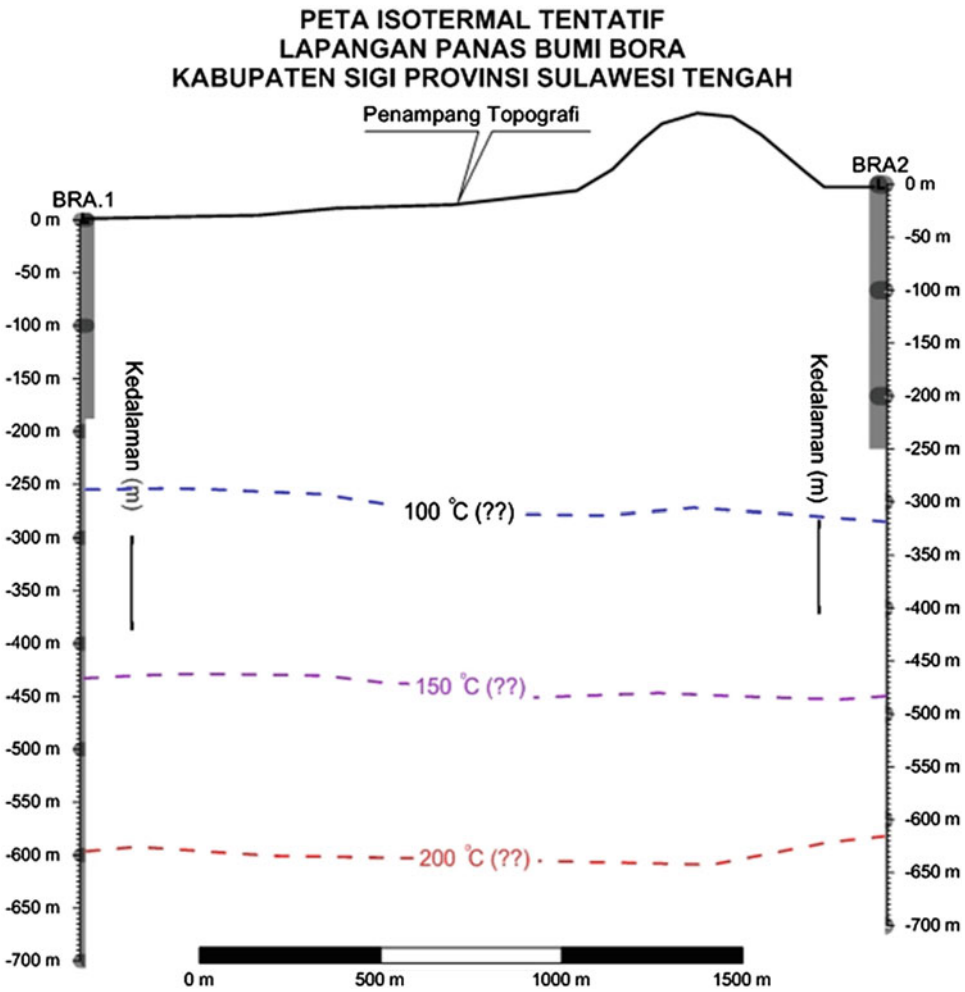

Fig. 71.6 Isothermal tentative map of Bora geothermal field, Sigi—South Sulawesi

71.5 Conclusion

Geothermal research in Bora, Central Sulawesi conducted to determine the gradient temperature and prove the results of previous investigations. Gradient temperatures on the temperature slope wells BRA-1 and BRA-2, respectively 29.72° dan 28.51° per depth of 100 m. The results are good and in accordance with the results of an integrated investigation and the potential to be developed as an energy power plants to the area.

Acknowledgments On this occasion, the author would like to thank the Head of Geological Resources and editors.

References

Alam AL Understanding Of Geological Geothermal (Introduction to Geothermal Exploration Technician Training)

Geologi B (2010) Status Potensi Panas Bumi Indonesia Tahun 2010

van Bemmelen RW (1949) The geology of Indonesia, vol I. A. The Hague, Netherlands

D Suhanto, E Kasbani (2008) Prospect of geothermal resource development in Indonesia. Center for Geological Resources, Geological Survey

K Morrison (1997) Important hydrothermal minerals and their significance, Architects Engineers Planners Scientists, P134205 Mineral Services

Lawless J (1995) Guidebook: an introduction to geothermal system. Short Course. Unocal Ltd., Jakarta

Arif dkk M (2009a) Joint study on non volcanic hosted geothermal system in central part of Sulawesi. Pusat Sumber Daya Geologi, Bandung

Arif dkk M (2009b) Proposal Pemboran Landaian Suhu BJL-1. Daerah Panas Bumi Bonjol, Kabupaten Pasaman—Sumatera Barat

Nugraha HS, dan Yuniarto (2008) Geothermal concession in Indonesia. Directorate Geothermal Exploitation Concession and Ground Water Management, Directorate General of Mineral, Coal and Geothermal

Simanjuntak TO, Surono dan Supandjono JB (1997) Peta Geologi Lembar Poso, Sulawesi, Skala 1:250.000. Pusat Penelitian dan Pengembangan Geologi, Bandung

Stuwe K (2007) Geodinamics of the lithosphere, 2nd edn. Springer, Berlin

Sukido, Sukarna D, dan Sutisna K (1993) Peta Geologi Lembar Pasangkayu, Sulawesi Skala 1:250.000, Pusat Penelitian dan Pengembangan Geologi, Bandung

Sumadirdja H, Suptandar T, Hardjoprawiro S, dan Sudana D (1973) Peta Geologi Tinjau Lembar Palu, Sulawesi, Skala 1:250.000, Pusat Penelitian dan Pengembangan Geologi, Bandung

Tim Survei Terpadu (2010a) Survei Panas Bumi Terpadu Geologi dan Geokimia Daerah Bora, Kabupaten Sigi, Provinsi Sulawesi Tengah. Pusat Sumber Daya Geologi, Badan Geologi, Bandung

Tim Survei Terpadu (2010b) Survei Panas Bumi Terpadu Geofisika (Geomagnet, Gaya berat dan Geolistrik) Daerah Bora, Kabupaten Sigi, Provinsi Sulawesi Tengah. Pusat Sumber Daya Geologi, Badan Geologi, Bandung

Tim Survei Terpadu (2010c) Survei Magnetotellurik Daerah Panas Bumi Bora, Kabupaten Sigi, Provinsi Sulawesi Tengah. Pusat Sumber Daya Geologi, Badan Geologi, Bandung

Part VII

Impact of Climatological Changes on the Hydro Geomorphological Process in the Coast Areas

Convener: Prof. Bardhyl Avdyli—*Co-conveners*: Niko Pano, Fatos Hoxhaj, Erald Silo

There are many scientific issues or problems regarding session title that contributors may consult and analyse in this session description, such as the following: The air temperature and precipitation trends over the multi-annual period; Implications of climate changes on the water potential in the river system; Correlation between solid river discharge and water river discharge; Climate change impact on erosion processes in the river catchment area sediment contributions; Coastal erosion phenomen; Sediment discharge by river system; The bottom morphology; Transformation and evolution of coastline; Sediments granulometric structure; Riverbed deformation; Coastline migration; Wave refraction in coast area; Sea water masses circulation in coast area, sea current; Littoral transport and coastal sedimentation; Marin deep erosion in accumulative littorial; Marine erosion coast.

Impact of the Climate Change on Adriatic Sea Hydrology

72

Pano Niko, Frashęri Alfred, Avdyli Bardhyl and Hoxhaj Fatos

Abstract

In the paper there are presented the impact of the climate change on Adriatic Sea hydrology. The study is based on the results of inversion of 6 thermologs data for the ground surface temperature history in Albania, and climate change according to the meteorological data from different regions of Albania. The wells and the meteorological stations are located at the field region in the west of Central Albania and in the mountainous region of the northeast Albania. Ground Surface Temperature history presents a gradual cooling before a middle of the nineteenth century, followed by 0.6 K warming. This warming mainly after the second half of the twentieth century is presented also by meteorological data. The warming has caused its impact on country climate, inland and coastal water systems and ecosystems of the Albania, and to the Adriatic Sea hydrology.

Keywords

Ground temperature • Climate changes • Hydrology • Hydrographic system • Adriatic sea • Environmental impact

72.1 Introduction

Water discharge from the Albanian Hydrographic System into Adriatic Sea is one of the main factors, which determined processes of the forming and circulation of the Adriatic Sea water mass. Analyze of the factors that conditioned water discharge and their impact on Adriatic Sea Hydrology are presented in the paper.

P. Niko (✉) · A. Bardhyl · H. Fatos
Institute of Geosciences, Energy, Water, Environment, Polytechnic University of Tirana, Tirana, Albania
e-mail: evispano@hotmail.com

F. Alfred
Faculty of Geology and Mining, Polytechnic University of Tirana, Tirana, Albania
e-mail: alfred.frasheri@yahoo.com

In the first part of the paper is presented detailed analyzes of the climate in Albania, the ground surface history (GSH) and paleoclimate change according to the temperature measurements in the different wells in Albania. Climate changes during the last half of the twentieth century has been analyzed also based on the meteorological data. In paper is estimated continental water flow, created by atmospheric rainfalls and its impact on processes of the forming and circulation of the Adriatic Sea water mass has been analyzed.

According to the complicated nature of the Albanian Hydrographic System, in the second part of the paper, is presented the analytical methodic for estimation of the total continental water flow in this system.

72.2 Materials and Methods

Climate change are analyzed in two directions: firstly by temperature record in the deep wells and shallow boreholes, and secondly by the meteorological observations data. The

G. Lollino et al. (eds.), *Engineering Geology for Society and Territory – Volume 1*,
DOI: 10.1007/978-3-319-09300-0_72,

ground surface temperature reconstruction for long period, about 5 centuries, has been performed by estimation of the ground surface temperature changes at the past, according to the present-day distribution of the temperature at the depth, recorded in the borehole (Frashëri 1995; Frashëri and Pano 2002; Frashëri et al. 2008). Six thermoplots were used for inversion of the ground surface temperature history. Wellsare located at the plane region in the west of Central Albania, and in the mountainous region of the northeast of the Albania.

Air and ground temperatures, total annual rainfall quantity, wind speed and wetness, which are analyzed by records in Meteorological Stations. These stations are located in different plane regions (Shkodra, Tirana, Kugova and Fier) and in mountainous region of Albania (Kukes), where the investigated wells are situated (Albanian Climate 1978; Boriçi and Demiraj 1990; Gjoka 1990; Mici et al. 1975, the data for 1985–2000 after Mustaqi V).

Water potential of the Albanian Rivers System have been evaluated by a specific way, because this System is very complicated (Pano 1974, 1984, 2008). Albanian River System represents in general a mountainous hydrographic network, with an average altitude 785 m above the sea level. Part of Albanian Hydrographic Network are lake system, Prespa-Ohri, and Scutary. A karstic phenomenon is very intensive in the limestone formation, which is extended in great surface of the country. The monitoring network has more than 22 meteorological and hydrometric stations, during the observed period 20–100 years.

Estimation of run-off discharge (Qi) are performed for two categories of river basins, with different hydrographical and hydraulical natural conditions:

1. Water system: Scutary Lake-Drini River-Buna River, where the run-off discharge Q_i is computed by $Q_i = F(H_i,Q_l)$, where Q_l represent the discharge of the lateral source.
2. Drini, Mati, Ishmi, Semani, Vjosa River systems, etc., where the run-off discharge Qi is computed by Qi-f(Hi), where Hi- level in the river Qi = f(Hi), where Hi is altitude of the water level river (i) section.

The hydrographical complex Scutary Lake-Drini River-Buna Riveris is very complicated and unique for its hydraulic regime, this particularity has made necessity of the estimation of the water flow of Buna River, based on hydraulic conditions:

The discharge of the Buna River, when it flows away from the Scutary Lake Q2 depends not only from the level of the water H2, but also on the level H2 and the Drini River discharge into the Buna River Q4. So, the only possibility to calculate the discharge of the Buna River Q2 is to find the connection Q2 = f(H2, Q4). The Q2 = f(H2, Q4) correspond to the results obtained through the hydraulic calculations the dependence Q3 = f(H3), topomorphometric data, and the hydraulic parameters of the rivers discharge are the basic dependence of this calculation. Giving standard values to the discharge Q_4 equal to 50, 100, 300, 1500 m^3/s and salving the dependence of Q_2 as an explicit function from the Scutary Lake level H_2 and the Drini discharge Q_4, it was made possible to from a single family of the countable curves of the Buna discharge in the Scutary Lake.

The phenomenon of dry and wet years has always had a significant role and great interest. All modeling and calculations have been performed for the model of dry and wet characteristic years, to analyze the climate impact on Albanian Hydro-graphic System.

Processes of the forming and circulation of the Adriatic Sea water mass have analyzed based on hydrographic data and Results of Albanian Marine Expeditions "Saranda 1963", "Patosi 1964" for the wet years (Pano 1974), and Italian—Albanian Expeditions "Italica I and II, 2000 and 2001" for dry years (Pano 2008).

72.3 Results and Discussion

The ground surface temperature (GST) history, yielded by tighter inversion of Ko- 10, at coastal plane region of western Albania, presents a gradual cooling of 0.6 K, before a middle of the nineteenth century (Fig. 72.1). Later followed by 0.6 K warming, with a gradient 5.4 mK/years, that seems quite reasonable and is consistent with generally accepted ideas about the climate of the last 2–3 centuries. GST history of boreholes, which are located in the mountainous regions of Northeast Albania, presents some changes, which are observed in these regions as to the cooling of 0.2 K during the nineteenth century. Later, was observed the warming trend of 0.6 K during the twentieth century, by a gradient 6.7 mK/year. Warming gradient increasing at

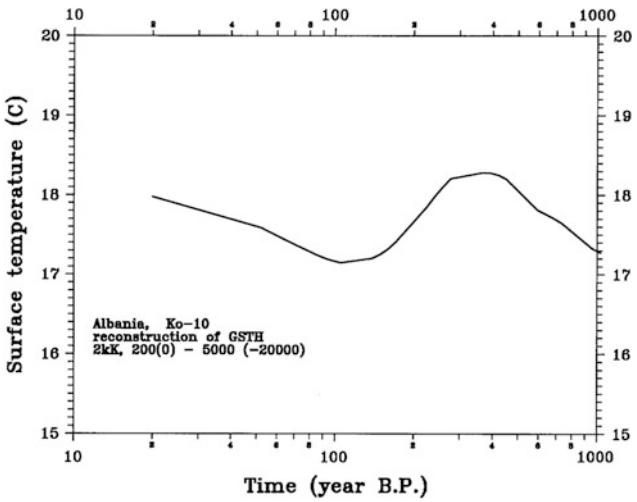

Fig. 72.1 Ground surface temperature history according to thermoplot of Ko-10 and Arza-31 wells

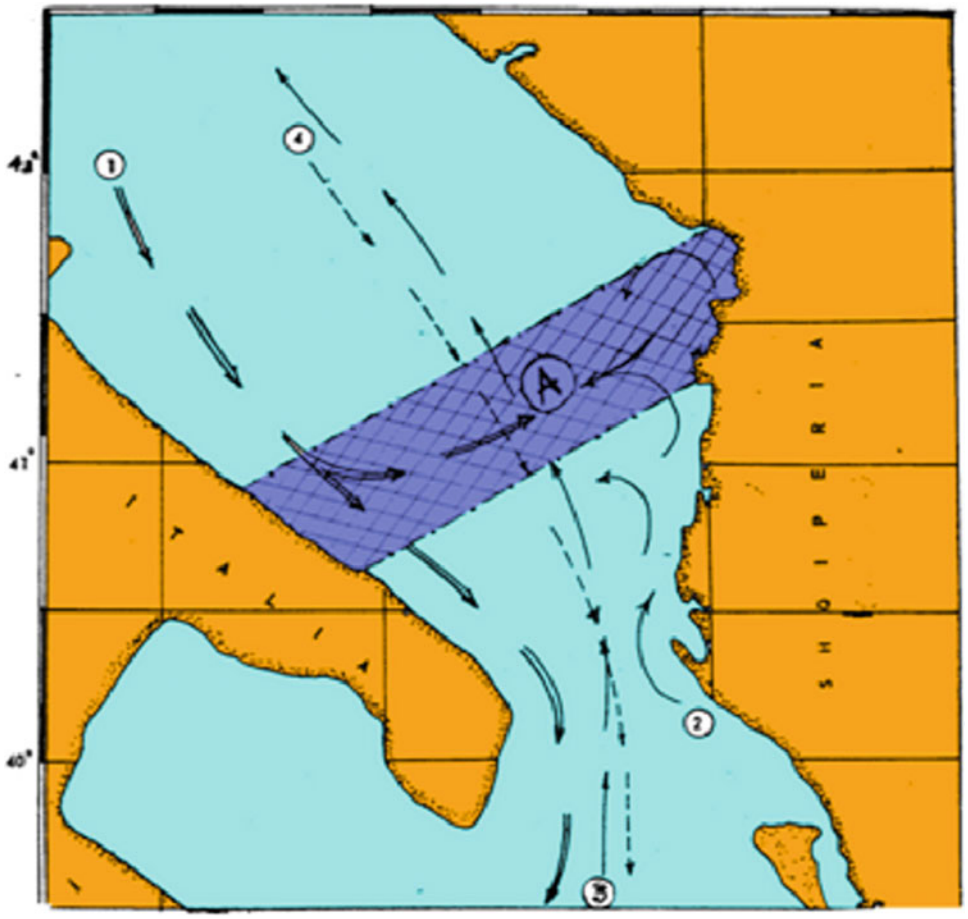

Fig. 72.2 "The Bridge" of continental water in the Adriatic Sea. 1. Adriatic deep water mass, 2. Eastern adriatic superficial water mass, 3. Intermediate levantine water mass, 4. Northern adriatic water mass

mountainous regions, in comparison with coastal areas, is caused by intensive deforestation during the last half of twentieth century.

Climate changes in Albania are observed also by the meteorological studies. Thirty quarter of twentieth century is characterized by a cooling of 0.6 °C, and later, up to present a warming of 1.2 °C. The warming trend is not a monotone one, in short intervals are observed cooling and warming (Boriçi and Demiraj 1990; Demiraj et al. 1996). Warming trend of maximum 1.2 °C, in particular after 70 years, is observed in all Albanian territory. Warming of the soil is more intensive than air warming.

The warming period in Albania is accompanied with changes of the rainfall regime, wind speed and wetness. There are observed a decreasing of the total year rainfall quantity, for about 200–400 mm. In the dependence of the geographical location of the areas changes the cross correlation of the rainfall quantity: Tirana area with Shkodra area $C_c = 0.62$, with Korga $C_c = 0.81$, Kugova $C_c = 0.66$, Kukesi $C_c = 0.88$, Gjirokaster $C_c = 0.88$, Vlora $C_c = 0.53$, during the period of 1930–1970. The warming have accompanied with decreasing of the wind speed about 1.5 m/s and 5 % increasing of the wetness, during the period of 1950–1994.

This warming is part of the global Earth warming during the second half of twentieth century. Its impact has been observed also on water systems and water resources. Inland water resources change has its impact on the hydrographic regime of the Adriatic Sea. These processes, in the particularly intensity of the penetration of the Levantine hot and saline waters in the Adriatic Sea through Otranto Strait, for long time period have been explained by the external phenomena from this sea. Has been supposed that Adriatic Sea doesn't participate in this penetration.

Based on two Albanian Oceanographic Expeditions have been collected data related to the mechanism of the forming and circulation of the Adriatic Sea water (Pano 1974, 2008).

The water potentials of Albanian rivers system is $Wo = 41.249.10^9$ m^3 that correspond to a mean annual discharge of $Qo = 1306$ m^3/s. So, Albania is one of high specific water potential in Mediterranean. The multi annual data have arguments that the total discharge of the Albanian rivers system in the Adriatic and Ionian Seas varies in very wide limits. Minimal discharge is 700–800 m^3/s for the hydrological dry years of low precipitation, up to maximal values 1900–2200 m^3/s for the hydrological wet years of high precipitation. Buna River is one of the most important rivers of the Mediterranean Basin. This river, together with

Po River in Italy, are determinant in the water balance of the Adriatic Sea.

The oceanographically situation of the wet years 1963–1964 has been characterized by formation of "The Bridge" with continental water in the Adriatic sea (Fig. 72.2). "The Bridge" is closely linked with the intensity of the river flow (Pano 1974). The eastern water mass are formed in SE Adriatic Sea area by the discharge of the Albanian rivers, and the Adriatic North water masses are formed by the discharge of Po River, Italy. This "Bridge", includes not only the surface layer, but also the Levant Intermediate Water (LIW) up to 600 m. depth. Low salt content and density of the seawaters are observed over "the bridge". This phenomenon has a complex and an important influence on many dynamics aspects of the formation Adriatic Deep Water (ADW), the deportation Levant Intermediate Water (LIW), and the monitoring mechanism of water into Otranto Street.

72.4 Conclusions

1. The climate at coastal plane region of Western of Albania was cooled of .6 K before of middle of nineteenth century. Later a warming of 0.6 K occurred, from last quarter of 19th until present-day. In northwestern mountainous region of Albania confirmed also a climate warming of 0.6 K during twentieth century.
2. The rainfall regime changes have their consequences in the fresh water resources of the country, of surface's and underground waters.
3. Warming has caused its impact on country climate and ecosystems. There is observed a decreasing of the water resources of the country, and thermal stress in the wetlands, lagoons and lakes.
4. The oceanographically situation in the Adriatic Sea is characterized from the formation of "The bridge" with continental water in the Adriatic Sea. "The bridge" is closely linked with the intensity of the river flow.

Acknowledgments Authors gratefully acknowledge the geothermal team colleagues of Geophysical Section in Faculty of Geology and Mining, Polytechnic University of Tirana, Geophysical Institute of Academy of Sciences in Prague. Many thank to Institute of Geosciences, Energy, Water, Environment, Tirana, Albania, Polytechnic University of Tirana, and in particularly to the Vangjel Mustaqi for calculation of the annual average value of the meteorological data for the period 1985–2000.

References

Albanian Climate (1978) Tables, vol 1. Hydrometeorological Institute of Academy of Sciences, Tirana, Albania (in Albanian)

Boriçi M, Demiraj E (1990) The air temperature and precipitation trends in Albania over the period 1888–1990 and 1931–1990. Hydrometeorological Institute of Academy of Sciences, Tirana (in Albanian)

Demiraj E et al. (1996) Implications of climate changes for the Albanian coast. MAP technical reports series no. 98. United Nations Environment Programme, Athens

Frashëri A (1995) Bore-holes temperature and climate changes in Albania. In: Proceedings of the international union of geology and geophysics, XXI general assembly (IASPEI meeting), Colorado, USA, 2–14 July

Frashëri A, Pano N (2002) Outlook on paleoclimate changes in Albania. In: Proceedings of the international conference on the earth thermal field and related research methods, Moscow, May 2002

Frashëri A, Pano N, Bushati S, Frashëri N (2011) Outlook on seawaters dynamics and geological setting factors for the Albanian Adriatic coastline developments. In: Proceedings of the European geosciences union, general assembly, Vienna, Austria, 03–08 April 2011

Gjoka L (1990) Ground temperature features in Albania. Ph.D. thesis, Hydrometeorological Institute of Academy of Sciences, Tirana, Albania (in Albanian)

Meteorological Bulletin for the 1931–2001 Years: Hydrometeorological Institute of Academy of Sciences, Tirana, Albania (in Albanian)

Mici A, Boriçi M, Mukeli R, Nafi R, Jaho S (1975) Albanian climate. Hydrometeorological Institute of Academy of Sciences, Tirana, Albania (in Albanian)

Pano N (1974) Sur les lois de penetration des eauz Ionienne dans l'Adriatique. Institute of Hydrometeorology, Academy of Sciences, Tirana (in French)

Pano N (1984) Hydrology of the Albania. Institute of Hydrometeorology, Academy of Sciences, Tirana (in Albanian)

Pano N (2008) Water Resources of Albania. Academy of Sciences of Albania, Albania (in Albanian)

Outlook on Seawaters Dynamics Factors for the Albanian Adriatic Coastline Developments

73

Pano Niko, Frashëri Alfred, Avdyli Bardhyl and Hoxhaj Fatos

Abstract

Results of integrated offshore and onshore hydrographical studies in Albanian Adriatic Littoral are presented in this paper. According to the geophysical and geological marine and onshore surveys, geodesic and bathy metric mapping has study different geomorphology and setting of Albanian Adriatic Shelf and coastline. Accumulative coastlines are extended at plain areas. Beautiful sandy beaches and dunes are main elements of these areas. Marine Quaternary deposits from plain sea floor up to some kilometres in the land have e thickness from some to hundred meters. Narta, Karavasta and Kune-Vaini Lagoons are located in plain area of the littoral. These lagoons are formed in some sea bays, which are closed by solid sediments transported by rivers to the sea. Erosive coastlines are extended in the hilly base of some capes. Sandstone banc are extended in the sea floor. Neotectonics development at the present has caused submergence of two sectors to the accumulative areas.

73.1 Introduction

The Albanian coastal area has its environmental individuality, and a perfect ecological balance. River mouths and deltas, lagoons system, abandoned riverbeds, inland, marsh labyrinths, sandy beaches, dunes covered with vegetation, dense forests represent an important and particular natural area of great international values.

Albanian littoral represent continuation of coastlines of two major paleogeographic zones: Erosion Coastline of Ionian tectonic zone in the southwestern part of Albania, and Adriatic Coastline of Peri-Adriatic Depression in the central and northwestern part of Albania. There are three different segments: Accumulative segments, erosive segments, and submerged areas, where is observed marine transgression toward the mainland.

The Adriatic coastline geomorphology and dynamics are conditioned by geological setting of the western side of Albanides, the neotectonic developments. Very important role has the dynamics of the seawaters and solid material solid discharge from Albanian River network to the Adriatic Sea, and their deposition along the coastal zone.

73.2 Material and Methods

Albanian Adriatic Coastline developments study is based on integrated marine and onshore surveys results.

73.2.1 Hydrological and Hydro-Geomorphological

Studies represent the interpretation of the information of Albanian hydrometric network during the observed period of 20–100 years.

P. Niko (✉) · A. Bardhyl · H. Fatos
Institute of Geosciences, Energy, Water, Environment, Polytechnic University of Tirana, Tirana, Albania
e-mail: evispano@hotmail.com

A. Bardhyl
e-mail: bavdyli@icc-al.org

F. Alfred
Faculty of Geology and Mining, Polytechnic University of Tirana, Tirana, Albania
e-mail: alfred.frasheri@yahoo.com

G. Lollino et al. (eds.), *Engineering Geology for Society and Territory – Volume 1*,
DOI: 10.1007/978-3-319-09300-0_73,

73.2.1.1 Hydrological Studies

Temperatures, water levels and discharge into the Adriatic Sea, suspended material discharge; alluvial granulometric composition, chemical composition etc. were observed in main Albanian rivers. Estimation of run-off discharge (Qi) are performed for river basins with different hydrographical and hydraulic natural conditions.

73.2.1.2 Hydrogeomorphological Studies

Hydrogeomorphological studies were performed to evaluate the geomorphologic characteristics, evolution and migration of Albanian Adriatic coastline, The geomorphological regime of the Adriatic. Limnological observation on the Albanian lagoon system were performed in hydrometric stations in Butrinti, Karavasta, and Narta lagoons, by periodical expeditions.

73.2.1.3 Oceanographic Studies

Oceanographic studies have been carried out in 59 hydrometric stations. Oceanographic expedition were organized in the Southern Adriatic and Northern Ionian.

73.2.1.4 The Integrated Geological-Geophysical

Marine geological mapping and integrated offshore geophysical surveys have been performed using reflection seismic, electrical soundings and profiling, magnetic radiometric surveys.

73.2.1.5 Climate Change

Climate change was analyzed by ground surface temperature history, using the temperature record in the wells, and by the meteorological observations data.

73.3 Regional Hydrographic Outlook on the Albanian Littoral

The Albanian coastal area lies on the east side of the Southern Adriatic Sea, from Shengjini to Vlora bays and Northern Ionian Sea, from Vlora to Saranda bays at the south (Fig. 73.1). The coastal line length is 447 km. The water basin of this network is 43,305 km^2, from which 28,550 km^2 is inside of the Albanian state territory. Albanian River System represents in general a mountainous hydrographic network, with an average altitude 785 m above the sea level. The hydric resources of Albania are 41,249 $\times$ 10^9 m^3 water, which correspond to a module of 30 liter/s.1 km^2.

73.3.1 Adriatic Coastline

Adriatic coastline is lies over the Neogene Peri-Adriatic Depression, covered by Quaternary deposits, in western plain areas. Flattened accumulative coast is general characteristic of this coastline. There are also some marine caps with cliffed coast. The caps are located in the sectors where the Neogene molassic structures are abrupt by coastline and continues in the Adriatic Sea.

73.3.2 Outlook on Albanian Littoral Hydrology

The water flow of the hydrographic network of the Albanian rivers to the sea varies in wide limits. The discharge of the Albanian rivers into the Mediterranean Basin varies in very wide limits, from Q_o = 700–850 m^3/s for the hydrological years of a lower precipitation up to Q_o = 1850, 2150 m^3/s for the years of a higher precipitation. The volume of suspended material, which is transported through river network, is 65,7 $\times$ 10^6 ton/year, while the turbidity Q_o = 1,260 gr/m^3. The flow module of the suspended matter on the catchment surface of the Albanian rivers is R = 1,260 ton/km year. (Pano 1984). The river suspended matter deposits itself the river mouth in the Adriatic Sea. This process is very dynamic, making river's mouths very active. The period with the wave height of H_1 = (0,1–0,2)m represents about 80 % of the general cases, while the height of H = (0.2–4.5)m about 20 % of them for the average multi annual year. The highest waves have a direction from Northwest to West and a maximum wave height about h = 3.5–4.5 m near shore. Sea level has an average daily amplitude 0,30–0,40 meters and a multi annual maximal amplitude h = 1,14–1,53 m. Intensive winds with their maximal speed of 40–45 m/s. The average annual temperature of the water varies from t = 17,7–19,2°C.

73.4 Analyze and Results

73.4.1 Albanian Adriatic Coastal Areas

Adriatic coastal line has the marine accumulation flattened coast, the marine erosion coast, and the submerged areas.

73.4.1.1 Accumulative Areas Represents Main Part of the Coastline

Accumulative areas represents main part of the coastline are extended over the edge of western Albanian plains. This littoral is characterized by presence of the different genetic types Quaternary (Q) (Frasheri et al 1996, 1994; Thereska 1981). Sandy littoral belt along the accumulative littoral have a width up to 5 km. Sand dunes are situated along this belt. Sand dunes belts have a length of 25 km and an average width more of 50–100 m. Generally, the granulometry of quartzite sand deposits represented by fine sand. Very beautiful sandy beaches are extended in accumulative

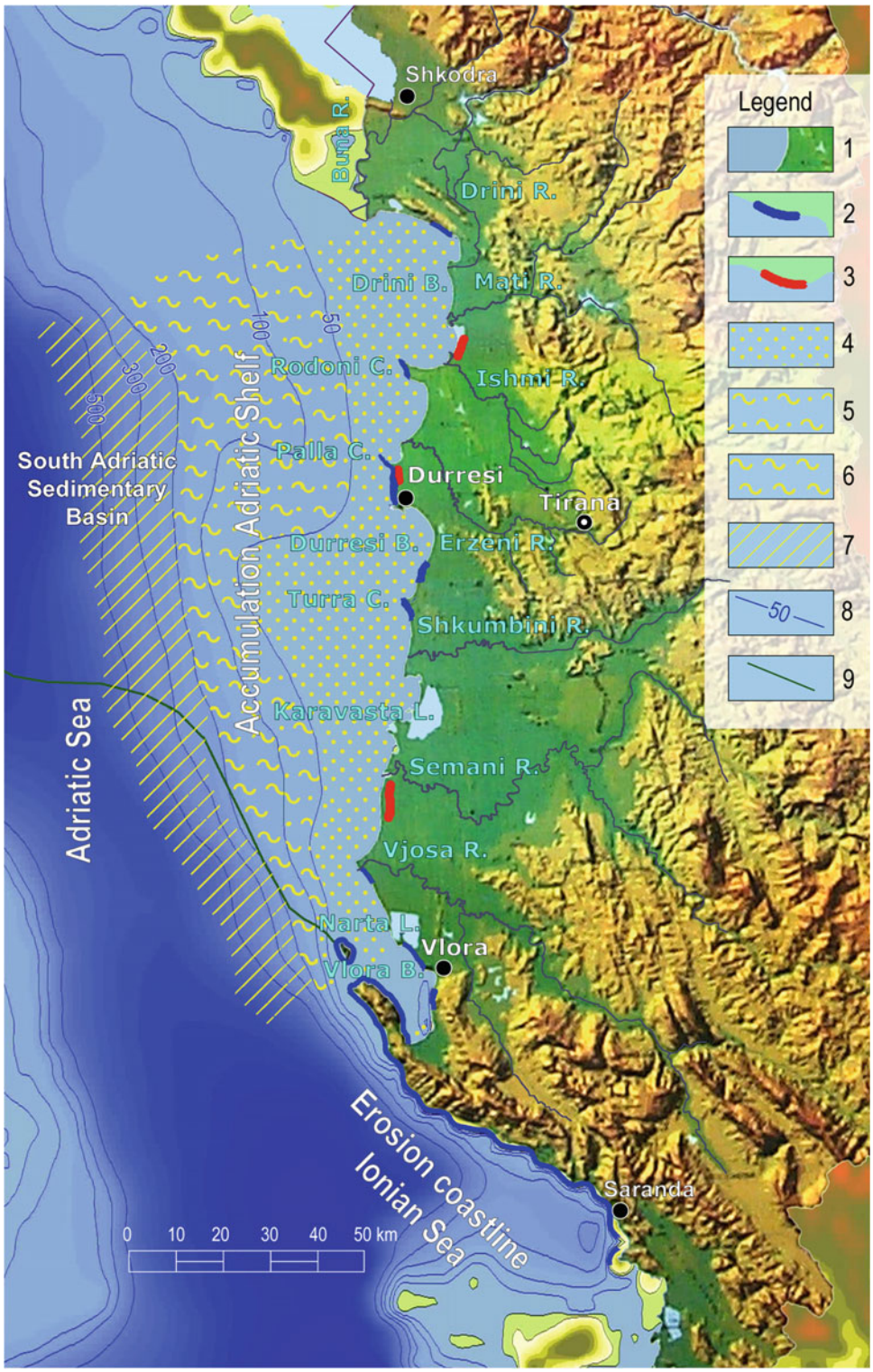

Fig. 73.1 Geomorphological Scheme of Albanian Adriatic and Ionian Seas coastline. (Digital Terrain Model, National Geophysical Data Center (NGDC), Geodas database, 2005. *1* Accumulative coastline; *2* Erosion coastline; *3* Submerged littoral zone; *4* Shoal shelf area with sand deposits; *5* Flat shelf area with sandy-silt deposits; *6* Inclined shelf area with muddy silt and deposits; *7* Continental slope with argillaceous sediments; *8* Isobaths; *9* Western flank of the South Adriatic Sedimentary Basin.1

coastal areas. In the accumulation coast the flat shelf sinks gradually up to the depth 100 m. Over there, the majority of deposits represents by sand and silt.

73.4.1.2 Erosive Zones

Erosive zones were developed in accumulation littoral of Adriatic shoal. In the erosion coast, usually, the sea bottom is sandy. Durrësi–Kepi Pallës area is one most typical erosive segment. Durrës-Kepi Pallës coastline is extended along the western flank of the Neogene molasses anticline. Western fold flank are lies under the Adriatic Sea waters. (Aliaj 1989; Frashëri et al. 1996). Zvërneci hilly zone is located at northwestern direction of Vlora Bay. The Tortonian molasse Zvërneci hills chain from the isle separated Narta lagoon from the Adriatic Sea.

73.4.1.3 Submerged Areas, Where is Observed Marine Transgression Toward the Mainland

Semani beach at western Albanian region and Patoku beach in the southern side of the Shwngjini Bay represent submerged areas within accumulative coastline. Submerged process is caused by the neotectonics activity, consequently there are observed a marine transgression (Aliaj 1989). In Semani beach coastal water line has a ingression of 305 m toward the mainland, with a gradient 9.4–8.1 m/year.

Second submerged area is observed at the Patoku beach, between Ishmi River Mouth at the south and Mati River Mouth at the north. During the period 1972–2012 coastal water line has a ingression of 175 m toward the mainland.

73.4.1.4 Lagoon Area

Lagoon area has a total surface of about 150 $km^{2,}$ while the volume over 350-million m^3 water. The most important lagoons are those of Karavasta, Narta, Butrinti, Viluni etc. Albanian lagoons represent crypto-depressions, with the floor under the level of the sea's bottom. The lagoons represent the new lakes. Its creation started during Pliocene Period, some 4–5 million years ago, and its creation lasted during the Quaternary Era till our days.

73.4.2 Impact of the Climate Change on Adriatic Sea Hydrology

Ground Surface Temperature history according to the geothermal studies presents a climate change influence. Generally, during the first half of twentieth century, the climate worming for about 1°C is observed. Thirty quart of this century has been characterized by a cooling for 0.6 °C. Later, up to present a worming for 1.2 °C is observed (Frasheri et al. 2004; Pano et al. 2001). Climate changes in Albania are observed also by the hydrometeorological studies (Albanian Climate 1978; Demiraj et al. 1996). The warming period in Albania is accompanied with changes of the rainfall regime., wind speed and wetness. There are observed a decreasing of the total year rainfall quantity, for about 200–400 mm. Inland water resources change has its impact on the hydrographic regime of the Adriatic Sea (Pano 2008).

Based on two Albanian Oceanographic Expeditions has been proposed a mechanism of the forming and circulation of the Adriatic Sea water (Pano 1975, 1984, 2008). The multi annual data have arguments that the total discharge of the Albanian rivers system in the Adriatic and Ionian Seas varies in very wide limits. Minimal discharge is 700–800 m^3/s for the hydrological dry years of low precipitation, up to maximal values 1900–2200 m^3/s for the hydrological wet years of high precipitation. Buna River is one of the most important rivers of the Mediterranean Basin. This river, together with Po River in Italy, are determinant in the water balance of the Adriatic Sea.

73.5 Conclusions

- Albanian Adriatic coastline has an intensive change and continuously modifying its shape.
- Submerged process, caused by neotectonic activity, is observed in some sectors within accumulative Adriatic coastline.
- The climate at coastal plain region of Western of Albania has a warming of 0.6 K occurred, from last quarter of nineteenth until present-day. These climate changes have their impact on country water system, on and water resources, on the erosion processes, and on the hydrographic regime of the Adriatic Sea.

References

Albanian Climate (1978) Tables, Vol.1 (In Albanian); Hydrometeorological Institute of Academy of Sciences, Tirana, Albania

Aliaj Sh. (1989) Present geodynamic location of the convergence between the Albanids orogen and the Adriatic Plate. (In Albanian, abstract in English), Seismological Studies, III, No. 10, pp. 15–38, Seismological Center, Academy of Sciences, Tirana

Demiraj E. et al (1996) Implications of climate changes for the Albanian coast. MAP Technical Reports Series No. 98. United Nations Environment Programme, Athens

Frasheri A, Papa A, Lubonja L, Leci V, Hyseni A, Kokobobo A (1991) The geology of Adriatic Sea Shelf. National Symposium, Academy of Science of Republic of Albania, Tirana

Frasheri A, Pano N (2003) Impact of the climate change on Adriatic Sea hydrology. Elseiver, Amsterdam

Frasheri A, CermakV, Doracaj M, Lico R, Safanda J, Bakalli F, Kresl M, Kapedani N, Stulc P, Malasi E, Çanga B, Vokopola E, Halimi H, Kucerova L, Jareci E (2004) Atlas of geothermal resources in Albania. Facylty of Geology and Mining, Polytechnic University of Tirana, Tirana

Pano N (1975) A propos des lois qui regissent la penetration des eaux Ionienne dans l'Adriatique. Hydrometeorological Institute, Academy of Sciences, Tirana

Pano N (1976). Hydrology of the Seman river. Monograph. (In Albanian), Hydrometeorological Institute, Academy of Sciences, Tirana

Pano N (1984) Hydrology of the Albania. Monograph. (In Albanian). Institute of Hydrometeorology, Academy of Sciences, Tirana

Pano N (1994) Dinamica del littorali Albanese. (In Italian). Atti del 10 Congresso A.I.O.L., Genova, Italy

Pano N, Frasheri A, Avdyli B (2001) The impact of climate change in the erosion processes in the Albanian hydrographic rivers network

Pano N (2008) Water resources of Albania. Academy of Sciences of Albania, Tirana

Papa A (1985) Geology and geomorphology of Albanian Sedimentary Basin and Adriatic Shelf. (In Albanian, resume in French), Geographical Studies, Academy of Sciences, No 1, pp 96–116

Thereska J (1981) Study of natural radioactivity in some Albanian Adriatic shoal shelf. (In Albanian), M.Sc. Thesis, Institute of Nuclear Physics, Academy of Science, Tirana

Climate Change Impact on Buna River Delta in Adriatic Sea

74

Pano Niko, Frasheri Alfred, Bushati Salvatore and Frasheri Neki

Abstract
In the paper are analyzed impact of climate change, and hydrologic characteristic of the river and sea: Buna River runoff discharge, water mass circulation in Drini bay, wave refraction, sea level and incursion of the high tide waves, coastal accumulation and erosion processes et al that are conditioned hydro-geomorphologic development of the delta of Buna River. The morphology and hydro-geomorphologic development dynamics of the Buna River Delta are conditioned by hydrological regime of the river, thalassographic regime of the Adriatic Sea, and climate change impact.

Keywords
Delta • Ground temperature • Climate changes • Hydrographic system • Adriatic sea

74.1 Introduction

Albania is a subtropical zone. To the east, in the mountain areas, the climate is Mediterranean mountainous. The climate in Albania varies from a region to the other. The climate change studies are based on geothermal inversion results and meteorological observation data. There is analyzed the ground surface history (GSH) and paleoclimate change according to the temperature recorded in the different wells in Albania. Climate changes during the last half of the twentieth century has been analyzed also based on the meteorological data. There are estimated continental water flow, created by atmospheric rainfalls and its impact on processes of the forming and circulation of the Adriatic Sea water mass has been analyzed. In the second part of the paper, is presented the analysis of climate change impact on Buna River Delta in Adriatic Sea.

P. Niko (✉)
Institute of Geosciences, Energy, Water, Environment, Polytechnic University of Tirana, Tirana, Albania
e-mail: evispano@hotmail.co

F. Alfred
Faculty of Geology and Mining, Polytechnic University of Tirana, Tirana, Albania
e-mail: alfred.frasheri@yahoo.com

B. Salvatore
Academy of Sciences of, Tirana, Albania
e-mail: sbushati@yahoo.com

F. Neki
Information Technology Center, Polytechnic University of Tirana, Tirana, Albania
e-mail: neki.frasheri@gmail.com

74.2 Materials and Methods

Climate changes are analyzed in two directions: firstly by temperature record in the deep wells and shallow boreholes, and secondly by the meteorological observations data. The ground surface temperature reconstruction for long period, about 5 centuries, has been performed by estimation of the ground surface temperature changes at the past, according to the present-day distribution of the temperature at the depth, recorded in six boreholes, which are located at the plain and mountain regions. The study of geothermal field of Albania has been carried out based on the temperature logging in the wells and boreholes (Cermak et al. 1996;

G. Lollino et al. (eds.), *Engineering Geology for Society and Territory – Volume 1*,
DOI: 10.1007/978-3-319-09300-0_74,

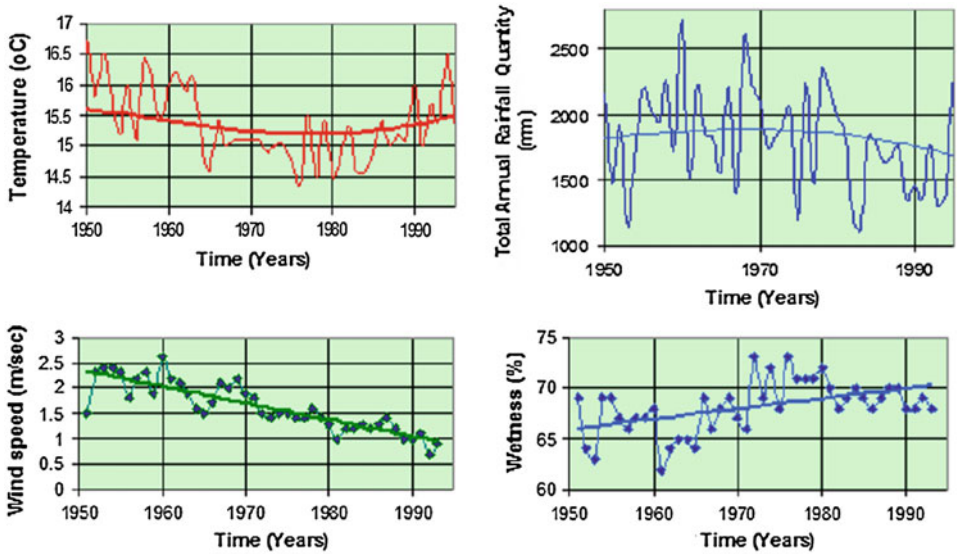

Fig. 74.1 Air average annual temperature, total year rainfall quantity, wind speed and wetness variations, at Shkodra meteorological stations (Period 1950–1994)

Frasheri et al. 1995, 2004). Air and ground temperatures, total annual rainfall quantity, wind speed and wetness, which are analyzed by records in Meteorological Stations (Fig. 74.1) (Albanian Climate 1978; Borifi and Demiraj 1990; Gjoka 1990; Mici et al. 1975, the data for 1985–2000 after Mustaqi V.).

Water potential of the Albanian Rivers System have been evaluated by a specific way (Pano 1967, 1995, 1998), based on the multi annual archival data (Hydrometeorological Institute of the Academy of Sciences of Albania) have calculated the annual runoff discharge of the Scutary Lake-Buna River-Drini River System, according to the corresponded types of the water supply, structure of the annual discharge distribution. All modeling and calculations have been performed for the model of dry and wet characteristic years, to analyze the climate impact on Albanian Hydrographic System. Processes of the forming and circulation of the Adriatic Sea water mass have analyzed based on hydrographic data and Results of Albanian Marine Expeditions "Saranda in 1963", "Patosi in 1964" (Pano 1967), and Italian-Albanian Expeditions "Italica I and II, 2000 and 2001" (Pano 2008).

74.3 Results and Discussion

Buna River is important part of the hydrographic complex "Scutary Lake-Buna River-Drini River". Delta of the Buna Rives is located in Drin Bay at Adriatic Sea. This delta presents one of more active and interesting area of the Mediterranean Sea.

The ground surface temperature reconstructions of the thermoplots of Kolonja-10 deep wells, which are located at coastal plain region of western Albania presents a gradual cooling of 0.6 K, before a middle of the nineteenth century. Later followed by 0.6 K warming, with a gradient 5.4 mK/years, that seems quite reasonable and is consistent with generally accepted ideas about the climate of the last 2–3 centuries. GST history shows that warming gradient increasing is observed also at mountainous regions.

Climate changes in Albania are observed also by the hydrometeorological studies. Figure 74.1 present graphics of yearly average temperature of the air in Shkodra Meteorological Stations, for the period from 1931 to 2004. In general, the end of first observes half twentieth century, a warming of climate, about 10 °C (Borifi and Demiraj 1990).

Thirty quarter of twentieth century is characterized by a cooling of 0.6 °C, and later, up to present a warming of 1.2 °C. The same climate changes are observed also at Shkodra City. The cross correlation coefficient is Cc = 0.78 between variation curves of the average annual temperatures of both of these stations. Warming trend of maximum 1.2 °C, in particular after 70 years, is observed in all Albanian territory. The warming have accompanied with decreasing of the wind speed about 1.5 m/s and 5 % increasing of the wetness, during the period of 1950–1994.

This warming is part of the global Earth warming during the second half of twentieth century. Its impact has been observed on water systems and water resources. Inland water resources change has its impact also on the hydrographic regime of the Adriatic Sea (Pano 1984, 1994, 2008). There are great impacts of the specific natural conditions of the Albanian Hydrographic System catchment in particular of the Scutary Lake-Buna River-Drini River System.

Buna River maximal flow (respectively discharge (QM p%) and volume (WMp%) for different probabilities (p = 0,01; 0,1; 1; 2; 5; 10, 20 %) is presented in Fig. 74.2. Maximal flow with a probability p = 1 % (one in

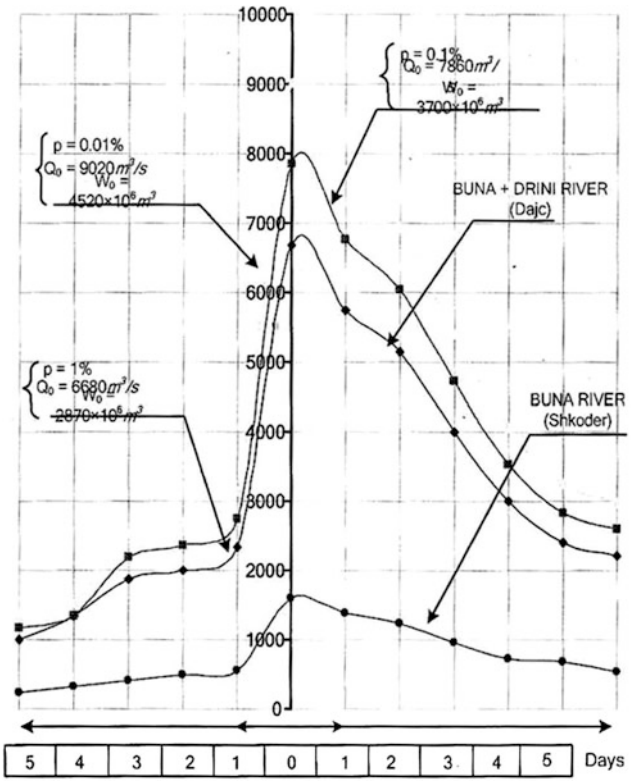

Fig. 74.2 Maximal flow, Buna + Drini River-Dajg

100 years) has the discharge QMp = 1 % = 6680 m2/s and a volume WMp = 1 % = 2870.106 m3.

The average annual sea level is H = 0,12 m on the 0" absolute level. In the multi annual period the maximal level with the probability of p = 1 % on the Albanian offshore is Hmax = 1,2 m on the 0" absolute level, while the minimal level is Hmin = −0,5 m Abs. as the results the maximal amplitude of the sea level during the multiannual period is AH = (Hmax-Hmin) = 1,62 m. The most eventual waves observed during the year in the Drini Bay are h = 0,6–1 m (33 % of the cases). Same important ones are also the following: h = 1,6–3,1 m (20 % of the cases). The one of the h = 3,5 m have are not observed very often, about 0,3 %. Their principal directions are S, SW, NW, and S. The maximal waves in marine shelf: height h = 5,10 m, length L = 80,6 m, velocity C = m/s and period T = 7,2 s. Minimal discharge is 700–800 m^3/s for the hydrological dry years of low precipitation, up to maximal values 1900–2200 m^3/s for the hydrological wet years of high precipitation.

Buna River is one of the most important rivers of the Mediterranean Basin. This river, together with Po River in Italy, is determinant in the water balance of the Adriatic Sea.

Climate change and variation of the discharges have its impact on the marine water mass flows and solid material transport in the time, velocity and locations, and also on the wave regime. Consequently, in the Buna delta during the short period for about 37 years (1972–2009) are developed intensive erosion, and in the both side of the coastline an accumulation process. In the Buna River Delta actually is formed a marine spit.

Ecosystems, and biodiversity, in the particularly in the water's flora and fauna have an important influence from climate change. Temperature augmenting has caused increasing of the evaporation in the water systems. Consequently in the river system, reservoirs, wetlands, lakes and lagoon system has been observed thermal stress. In very beautiful ecosystems of Albanian lagoon as Kune-Vaini in Lezha region etc. thermal stress has its impact, first of all on the biodiversity. This stress is extended also in the shallow coastal waters; consequently there are observed diminution of the fish quantity.

74.4 Conclusions

1. The climate at coastal plain region of Western of Albania was cooled of 6 K before of middle of nineteenth century. Later a warming of 0.6 K occurred, from last quarter of 19th until present-day. Temperature records in northwestern mountainous region of Albania confirmed also a climate warming of 0.6 K during twentieth century. Warming, mainly during the last quarter of the twentieth century, is demonstrated also by meteorological data.
2. Warming has caused its impact on country climate and ecosystems. There is observed a decreasing of the water resources of the country, and thermal stress in the wetlands, lagoons and lakes of Albania. Impact it is observed first of all on the biodiversity.
3. The rainfall regime changes have their consequences in the fresh water re-sources of the country, of surface's and underground waters.

   In the Buna delta during the short period for about 37 years (1972–2009) are developed intensive erosion and in the both side of the coastline an accumulation process.
4. Geomorphologic change of the coastline it is necessary to evaluate during the urban planning of the coastline.

Acknowledgments Authors gratefully acknowledge the geothermal team colleagues of Geo-physical Section in Faculty of Geology and Mining, Polytechnic University of Tirana, Geophysical Institute of Academy of Sciences in Prague, Well logging Enterprise in Patosi for the temperature logging. We express cordially thanks to the Frasheri et al. (1999) for the paleoclimate reconstruction of thermolots. Many thank to Institute of Meteorology of Academy of Sciences of Albania, and in particularly to the Dr. Vangjel Mustaqi for calculation of the annual average value of the meteorological data for the period 1985–2000.

References

Borifi M, Demiraj E (1990) The air temperature and precipitation trends in Albania over the period 1888–1990 and 1931–1990; (in Albanian). Hydrometeorological Institute of Academy of Sciences, Tirana

Frasheri A, Cermak V, Kapedani N, Li^o R, £anga B, Jareci E, Kresl M, Safanda J, Kucerova L, Shtulc P (1995) Geothermal Atlas of Albania. Faculty of Geology and Mining, Polytechnic University of Tirana, Tirana

Frasheri A, Cermak V, Safanda J (1999) Outlook on paleoclimate changes in Albania. Workshop "Past climate changes inferred from the analysis of the underground temperature field » . Sinaia, Romania, 14–17 March

Frasheri A, Pano N (2002) Outlook on paleoclimate changes in Albania. In: International conference the earth thermal field and related research methods. Moscow

Gjoka L (1990) Ground temperature features in Albania; PhD thesis, (In Albanian) Hydrometeorological Institute of Academy of Sciences, Tirana, Albania

Hydrometeorological Institute of Academy of Sciences, Meteorological Bulletin for the 1931–2001 Years; (In Albanian), Tirana, Albania

Mici A, Borifi M, Mukeli R, Na^i R, Jaho S (1975) Albanian climate (In Albanian). Hydrometeorological Institute of Academy of Sciences, Tirana, Albania

Pano N (1967). Southern Adriatic and Northern Ionian Seas hydrology during the summer of 1863 year (In Albanian). Hydrometeorological studies, Nr. 4. Institute of Hydrometeorology, Academy of Sciences, Tirana

Pano N (1984) Hydrology of the Albania. Monograph (In Albanian). Institute of Hydrometeorology, Academy of Sciences, Tirana

Pano N (1994) Dinamica del littorali Albanese (In Italian). Atti del 10 Congresso A.I.O.L., Genova, Italy

Pano N (1995) A way to calculate the discharge of Buna River. International Center for Theoretical Physics, Trieste

Pano N (2008) Water resources of Albania. Monograph (In Albanian). Academy of Sciences of Albania

Simeoni U, Pano N, Ciavola P (1997) The coastline of Albania: morphology, evolution and coastal management issues. CIESM Science Series No. 3, transformation and evolution of the Mediterranean coastline. Bulletin de l'Institut Oceanographique, Monaco, No. Special 18, 1987

Effects of Climate Change on Coastal Evolution

75

Diez J. Javier, Efren M. Veiga and Vicent Esteban

Abstract
Climate determines coastal morphology through sea level and coastal processes, which are mainly steered by wind waves except in tidal inlets. They manage to erode coasts and transport their sediments if available. Coastal morphodynamic is so the result of its dialectic answers and it witness of wave direction and the whole climate through cyclone latitudes. This paper tries to approach the long term coastal processes and the trends of sedimentary coasts answer.

Keywords
Climate changes • Coastal morphodynamic • Thermal machine • Windwaves

75.1 Introduction: About Climate Changes

The planet is suffering a global warming since the Little Ice Age that is leading to current sea level rise. The tendency has likely suffered intensity changes being mostly assumed to be progressively increasing since the last quarter of the 19th century. "Human factor" was never before able of current influence on Climate. Some of assessments on this significant warming are often questionable. The explanation of the anthropogenic factor by Arrhenius (1896) had first consequences much later because of sea level rise. Among relevant discussions, Fairbridge discerned (1983) eustatic changes from other attendant causes, and Mörner (1976) stressed the effects of geoid changes and rescued Milankovitch's "forgotten" theory, itself a thorough consequence of the Arrhenius "doctrine".

Milankovitch's (1930) accepted the meaning role of solar activity and, through modulating effects of the planet movement, explained with surprising accuracy the four main quaternary glacial cycles and other minor oscillations within them. It cannot explain however many of the stoppages and reversals of their associated processes. As the history of the planet was finely tuned, however, other types of changes in sea levels became apparent, resulting from vertical movements of the crust, modifications of sea basins due to continents drifting, or different types of climate patterns. Current warming (EPA 2012) and the previous Little Ice Age cold wave have precedents, always linked with changes in sea level. Therefore the data of ancient sea levels always were indicators for past climates (Fig. 3 in Diez 2001).

75.2 Climate and Its Effects: Coastal Morphodynamics

Climate must be thought as the outcome of an Atmospheric-Oceanic Thermal Machine: The atmosphere and oceans as a whole comprise a double system of interactive fluids in which great thermal and pressure gradients are established by solar radiation, being atmospheric warming just a consequent surface radiation effect; gradients lead to winds motion, only conditioned by Earth's rotation (Coriolis) and continents. Winds drive all the ocean movements, which in

D.J. Javier (✉) · E.M. Veiga
Universidad Politécnica, Madrid, Spain
e-mail: josejavier.diez@upm.es

E.M. Veiga
e-mail: efrenmartin@gmail.com

V. Esteban
Universidad Politecnica, Valencia, Spain
e-mail: vesteban@tra.upv.es

G. Lollino et al. (eds.), *Engineering Geology for Society and Territory – Volume 1*,
DOI: 10.1007/978-3-319-09300-0_75,

turn are conditioned by their thermo-saline gradients as well and feed back through its radiation to the Atmosphere. So they both together dictate the climate, whose pattern is, then, intrinsically changeable, because of the intrinsically variable character of those interactive phenomena.

Coastal processes are mainly steered by wind waves, which produce the littoral currents able to transport littoral sediments. If sediments are not available waves erode rocks with the assistance of tides (and tidal currents on outlets) and other concomitant phenomena as biological activity, rock weathering, mineral dissolution and other chemical and physical actions. The coastal answer to fluid-dynamic actions is the origin of the morphodynamic changes, which so depends of climate changes: (a) wind waves are ruled by cyclone displacements, whose latitude and size follow the climate changes so affecting to the incidence obliquity of waves on the coastline; (b) the accompanying changes of temperature largely affect the speed of both rock weathering and cliff dissolution processes. If the coastal stretch "answering inertia" is small enough (barrier islands, pocket beaches,…) it can changes both in plant and orientation, becoming more perpendicular to the climatic average wind wave direction (Diez and Esteban 1994); or if rainfall conditions change enough they can affect rates of sediments that reach the shore.

Thus, shoreline erosions and accretions are due to climate as to climate changes. It may shift landward or seaward as result of sea level changes (Leathermann et al. 1982; Pilkey et al. 1998) as to littoral fluid-dynamics. This well-known influence of maritime climate on coastal morphodynamics does not appear to have been fully considered until recently; erosive and sedimentary processes, alongshore and onshore-offshore transports and genesis and migration of barrier islands and other forms of deposits have been thoroughly studied, though only in relation to current environmental impacts; however, other longer term morphodynamics and pattern changes were no so extensively considered. Plant changes of both structural and sedimentary coasts so depend on the climatic factors that unleash littoral processes, as on the coast nature and morphology that affect the local littoral transport patterns (Williams 1982). Structural shoreline is mainly determined by erosive processes and its nature determines the resulting forms and sediments, the last feeding other coastal stretches; sedimentary shores are modified also by transport and deposit processes (Bores 1978; Diez 1996). Bores Genetic Classification of Coasts is a conceptual systemic instrument to understand processes, foresee changes, and diagnostic changes in plant to approach protection designs.

Finally, there are historic examples of climate affecting coastal settlements through its morphodynamic impacts, as the amazingly delayed process of settlement on the Atlantic coast of North America, especially considering how early the explorations began (Diez 2001). A time-correlation across history was found between different post-Würm orientations of a restricted shoreline stretch and the contemporary average latitudes of the paths of extra-tropical cyclones (Diez and Esteban 1994). That correlation implies an "immediate response" of those short enough coastal stretches to the average wave direction.

75.3 Observable Changes Under Different Climates Along Time

Shoreline dynamically answers to wave direction along the year as the hyper-annual cycles. It also can answer to trends in maritime climate if it has the appropriate dimension in relation with the climatic term scale. Climatic changes run with some changes in hydrology (case B) as in the latitude of the atmospheric perturbations. In North Atlantic Ocean, the most important atmospheric factor is constituted by nature and paths of extra-tropical cyclones (part of the NAO) (case A). These cyclones move eastwards and penetrate Europe or North Africa, and some of them keep active on Western Mediterranean Sea. Depending on both their deepness and latitude they can establish either on Liguria Gulf or on North of Africa. Littoral dynamic depends on them (case C).

75.3.1 Short Term: The Evolution of Long Beach Island (NJ, USA)

This study was based (Diez and Esteban 1994) on the figures brought to the Shore Protection Manual (Figs. 4.7–4.9 in C.E.R.C. 1984, vol. I) to show the barrier island landward migration under current S L R process. Long Beach Island extends between Barnegat and Egg inlets and closing Manahawkin Bay and Little Egg Harbor. The Manual presents its evolution between 1839 and 1924 near Ship Bottom, (Fig. 75.1) trying to show its landward migration due to sea level rise. But an additional rotation of the barrier is also relevant, at least since 1838–1872. Though more information could be required the 19th century stable point of the barrier island can established around 39° 36′ latitude, 74° 12′ longitude, and the rotation angle must have been over 2°, with stretch local variations depending on the stretch nature, morphology and size: the longer stretch length the greater inertia to changes accommodation.

75.3.2 Medium Term: The Example of Spanish Alboran Coast

Almería port facilities were carried out since 10th century, becoming first port in the Muslim Mediterranean area for

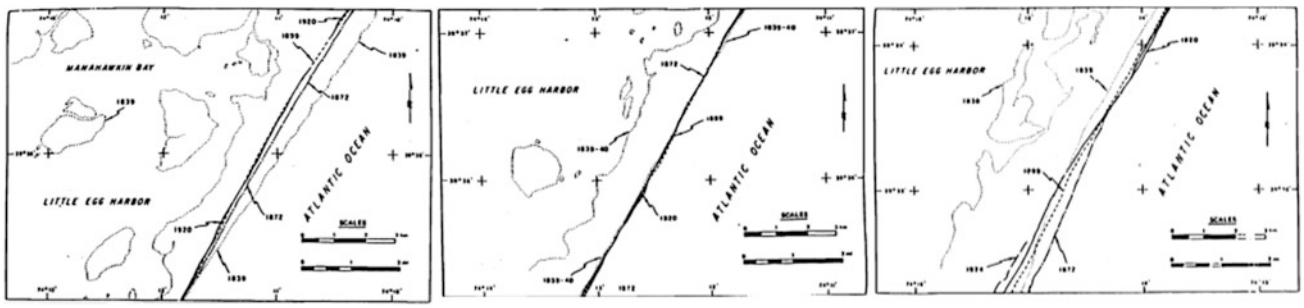

Fig. 75.1 Shoreline evolution on Long Beach Island. N.J. (from CERC 1984)

Fig. 75.2 Almeria/Adaratx basin maps: Cantelli's, Lopez's and current situation

12th century (Esteban et al. 2006). It was then located at 6 miles upstream from estuary river mouth, the river being navigable (Fig. 3.2). Arsenal and most facilities had to be moved to the estuary after 14th c. due to river siltation, but no delta form appeared before XVIII c. (Cantelli map 1696). A relevant delta was formed later in that century looking at Thomas Lopez's map (1795) and the port had to move out seawards. Similar sequences may be observed in the Malaga port and most of Alboran Spanish coast, likely linked to final LIA hydrological events. And it is congruent with the tremendous growth of the Almeria Gulf coastal plain if compared both maps, although delta acquired later a larger dimension. The congruence extends to other meaning differences between both maps (Diez 1996):

- Both maps show the *Llanos de Almería* "rasa", with Roquetas on the coast, but only Lopez draw the coastal plain beside the delta. Besides, Cantelli ignores Carchuna plains a little eastwards, no doubt a product of intense alluvial activity.
- All river-mouths are shown estuary-shaped and structural by Cantelli, versus Lopez's deltas and coastal plains. That could correspond to lower erosion and lesser exploitation of major rivers, under more humidity and regular rainy regime.
- The evolution of Ebro delta (Fig. 75.3) is also congruent in time with the anterior observations.

75.3.3 Longer Term: The Case of Javea Bay, Alicante, Spain

Javea bay, between *San Antonio* and *San Martin/La Nao* capes, east Iberian Peninsula, borders a natural depression filled by Quaternary deposits as a littoral barrier. Sub-aerial beach materials are mostly calcareous gravel but in the only current sandy *El Arenal* pocket beach, generated by e fluvial flood drag during the Holocene breaking the relict barrier. Present morphology was conformed at the end of Middle Pleistocene after several marine transgression/regressions (Diez and Esteban 1994). The beach-barrier-lagoon system formed during the upper Pleistocene and became relict during the significant regression of the last glacier period. Littoral dynamics were strong enough since Pleistocene to carve successive chains of barriers which determined the continental advance.

Main climatic factor in the North Atlantic-Mediterranean area featuring hydrodynamic actions on the coast is the system of extra-tropical cyclones and its path. Few of them keep still active over the western Mediterranean Sea. Warmer climates lead to lower latitude of the cyclone paths and reciprocally. Relict barrier so responded to lower cyclones than El Arenal beach (Fig. 75.4). The average wave resultant in the bay always was remarkably perpendicular to the shoreline. The cross-shore transport is thus more significant than alongshore transport in El Arenal as in

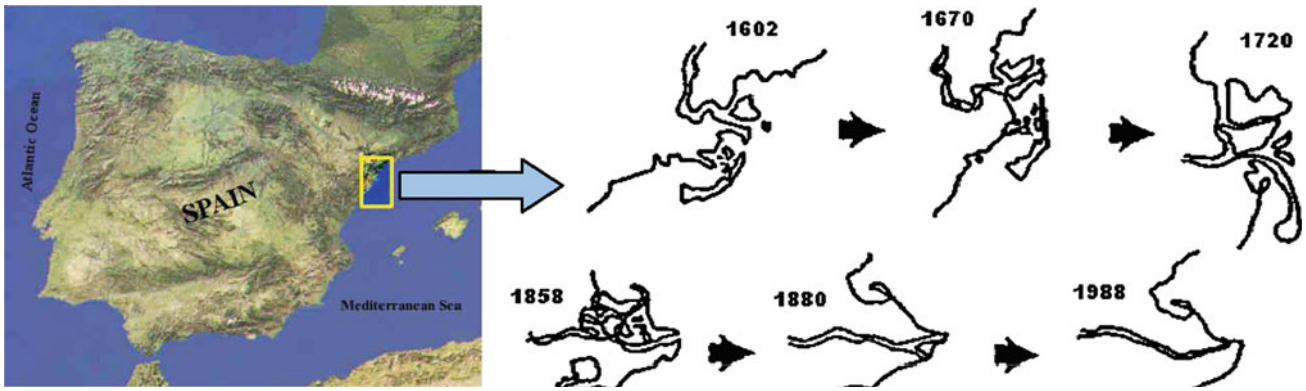

Fig. 75.3 The Ebro delta evolution

Fig. 75.4 Situation and schemes of Javea bay and *El Arenal* beach

ancient relict beaches, although a certain obliquity with respect to the last relict barrier exists now.

75.4 Conclusions

- Climate determines the morphology of the coast, through its determination of average and current sea level as by generating littoral fluid-dynamics and processes. And Climate Change of course determines sea levels, but also other fluid-dynamic processes that affect coastal morpho-dynamics.
- Time is determinant in the witness permanence of coastal forms, permitting or not their fossilization, depending on nature of cliffs and sediments.
- Human activities and settlements have also influenced the morphology of the coast but, further than through anthropogenic climate change, interfering littoral processes. And a lack of a holistic understanding of the whole nature of the fluid-dynamic and morpho-dynamic processes is still perceivable.

References

Arrhenius S (1896) On the influence of carbonic acid in the air upon the temperature of the ground. Philos Mag J Sci S. 5 41:251

Bores PS (1978) Shore classification-simple forms with prevailing wind wave action. III IAEG international congress proceedings, Madrid, pp 150–169

C.E.R.C. (1984) Shore Protection manual. Department of the Army, Waterway Experiment Station, Vicksburg. Mississippi, 2 Vols

Diez JJ, Esteban V (1994) Large scale answer in plan of open sandy shorelines to climate changes. Proceedings of international. coastal. symposium, Hofn, pp 485–492

Diez JJ (1996) Guía Física de España: Las Costas, pp 62–76. Alianza ed., Madrid

Diez JJ (2001) Climatic versus geomorphologic changes: influence on landing processes in Eastern Coasts of North America. J C R 17(3):553–562

EPA (2012) Climate change indicators in United States. EPA, Washington

Esteban V, Diez JJ, Fernandez P (2006) Evolution of the Iberian Peninsula Coast and recent climatic changes: port facilities and coastal defense in the Muslim Domain. J Coast Res SI 39:1839–1842

Fairbridge RW (1983) Isostasy and eustasy. In: Smith DE et al. (eds) Shoreline and isostasy. Institute of British Geographer. Academic Press, London

Leathermann HL, Rice TH, Goldsmith V (1982) Virginia barrier island configuration. A reappraisal. Science 215:285–287

Milankovitch M (1930) Mathematische Klimalehre und Astronomische. Theorie der Klimaschwankungen, Handbuch der Klimalogie B.1. T. A Borntrager. Berlin

Mörner NA (1976) Eustasy and geoid changes. J Geol 84(2):123–151

Pilkey OH et al (1998) The North Carolina shore and its barrier islands. Duke University Press, Durham

Williams SJ (1982) Barrier island shorelines: assessment of their genesis and evolution. Florida Shore and Beach Association, Proceedings, 26th Annual Meeting, Tallahassee, pp 188–199

The Plumes Influence on the General Circulation Along the Albanian Adriatic Region

76

Monika Burba, Bardhyl Avdyli and Fatos Hoxhaj

Abstract
The plume structure is considered on the basis of simulations with a primitive equations model. In this scope, a σ-coordinate numerical model for the South-Eastern Adriatic Coast was configured to examine the dynamical properties under the winter wind, river, tidal, and atmospheric pressure forcing. The complex picture of the circulation is conjectured to be a balance between conventional forcing (tides, atmosphere and buoyancy) and the hitherto unknown effect of plumes as surface signatures of small scales instabilities in the sea regions of strong horizontal convergence. By using the plume as a new forcing mechanism, we obtain a general circulation pattern affected strongly by enhanced horizontal mixing.

Keywords
Plume structure • Spiral eddy • General circulation

76.1 Introduction

There are a number of considerations to weigh when choosing a numerical method to apply to a set of partial differential equations (Chu and Fan 1997 and Yang and Przekwas 2012). The governing equations of ocean models together with their boundary conditions are solved by finite difference techniques (Bryan 1969 and Stelling and Van Kester 1994). Some sort of hybrid scheme which handles different pieces of the discretized equation in different ways are used.

In connection with the numerical tool there is an intention of improving the numerical parts of the code to investigate nonlinear effects. Some ideal bottom matrixes are used to test the numerical code and a real matrix is based on the topography of the Coastal Area. This model use so-called the flow relaxation scheme in the boundary zones (Martinsen and Engedahl 1987) and the numerical code is adjusted for the computation of the relaxation parameters in different dimensions.

An important driving force in the coastal area is due to freshwater discharge. Implemented in the model is a procedure of modelling river runoff. Modeling of a freshwater source (i.e. a river) is done by adjusting the boundary conditions at the position of the source into the model domain. Instabilities of the geophysical fluids are revealed in a coastal area with strong gradients of the water density. In order to treat them numerically a new numerical method is employed in advection terms and is incorporated into the Numerical Code. This is a numerical reflection of theoretical aspects on nonlinear instability at the seawater-freshwater interface (Hoxhaj preprint). A numerical investigation is meant to focus attention on the coastal zone in the southeastern Adriatic Sea in order to touch on the instabilities and their influence on the plumes. The region is within the quadrant where latitude varies from 40.5 to 41.5 N and longitude varies from 19.3 to 19.55 E. Spiraling short wave instabilities can be studied and knowledge of how are

M. Burba (✉) · B. Avdyli · F. Hoxhaj
Faculty of Geology and Mines, Polytechnic University, Tirana, Albania
e-mail: burba.monika@gmail.com

G. Lollino et al. (eds.), *Engineering Geology for Society and Territory – Volume 1*,
DOI: 10.1007/978-3-319-09300-0_76,

generated spiral eddies can be improved. Owing to the effects of spiral eddies a deformation of the plume structure can occur. This effect is more intense under the influence of an other plume and all this can be interpreted as a interaction among plumes.

There is not any previous modelling work for plumes on this region. For the south–western Adriatic Sea, on the other hand, the publications of the Italian researchers could be found. Besides this, the present paper belongs to the studies for an open problem; the numerical discussion of spiral eddies at the interface freshwater-seawater and their influence on the general circulation pattern.

76.2 The Model

The 3-D modesplit σ-coordinate model for this work is being developed basing on POM (Princeton Ocean Model) which was developed by A. Blumberg and G. Mellor at Princeton University and is described in detail in the paper by Blumberg and Mellor (1987). The basic computer code is adapted and changed concerning to.

The centered differencing scheme both in space and in time used in the POM will be unable to calculate a correct advection of this physical phenomenon since the different Fourier components (waves) are travelling at different phase speeds. This numerical dispersion is problematic everywhere where fronts and sharp gradients occur. So, Blumberg (1991) modified the POM codes with the following features: a Euler forward scheme in time and a semi-implicit numerical scheme for the shallow water equations, which removes the constraint of the CFL (Courant—Friedrichs—Levy) criterion on time step. But it is found that this version is not suitable for modelling the small and mesoscale eddies in the sea. The reason is that the Euler forward scheme in time together with an explicit scheme for the Coriolis terms, which were proved to be an unstable scheme for the case of weak dissipation. Under the circumstances, the predictor/corrector numerical scheme is employed in (Wang and Ikeda 1997). Furthermore, in future versions it would be desirable to include more sophisticated numerical techniques into advection terms in connection with simulations involving large gradients (Kliem and Pietrzak 1999).

The first version applies implicit methods to solve the depth integrated shallow water equations. This facilitates the use of the same time step for both the 2-D and 3-D steps, but accuracy may be lost in the 2-D steps due to Courant numbers larger than unity. A time-split version was therefore implemented recently and a new numerical method is provided as a convenient numerical scheme in order to increase the accuracy to $0(\Delta t^2)$ for the non-linear part of the system of equations (Florez 2011).

By analogy with the advection/diffusion equation, we can use some sort of hybrid numerical scheme which handles different pieces of the discretised equation in different ways. In order to investigate numerically spiral eddies and their influence on the plume structure a second-order numerical method for the non-linear terms is developed (Hoxhaj preprint) and employed in the code which is an improved version of the formula given by Bell et al. (1989).

Because of there are some changes on the code, the model output of test run is compared with the output produced by the GFDL at Princeton. Outputs are consistent with each other and there are only minor differences due to different computer arithmetic on different machines.

76.3 Numerical Simulations

It is, however, one thing to know the dynamics of the plumes of rivers, quite another to know how to correlate them with one another and with instability. In the Albanian Adriatic Coast discharge eight rivers (along a distance of 140 km) which gave us a good chance to study instabilities in the coastal zone.

Since freshwater discharge consists of different subprocesses on many time and length scales, the numerical simulations are concentrated on a subset of these processes. This investigation would require high horizontal and vertical resolutions. The model has a number of parameter settings to make that can influence your results. In this manner, you have the possibility to tune the mixing and sub-grid scale processes in the model by different settings. To do this as correctly as possible, a study of the model's sensitivity to different settings is realised (Hoxhaj preprint).

Our model domain is a rectangular basin with a realistic coastline and 32-layers vertically focused on towards the surface layer in order to touch upon the surface phenomena. The model resolutions were (250 × 250 m), (500 × 500 m) and (1 × 1 km). The seawater temperature was 8 °C and salinity was 32.0 everywhere, denoting the ambient water in the winter. There were only a coastline on the eastern side and three open boundaries elsewhere. No normal flow was set at the coast. On lateral open boundaries are used FRS zones for the water levels, Dirichlet conditions for the velocities and a zero-gradient boundary condition for heat and salt fluxes. The flow in the sea area is forced in a realistic topography with the following mechanisms:

- Four components of the tide—M_2, S_2, N_2, K_2
- Wind forcing 8 m/s from north
- Forcing strength of rivers (with buoyancy influx $\Delta S = 15.0$)
- Coriolis force $f = 14.6 \times 0^{-5} \sin \varphi$ [s^{-1}]
- The effect of spiral eddies

The physical parameters were as follows.

- Bottom friction coefficient $C_D = 0.00125$ and vertical mixing $K_h = 4 \times 10^{-5}$ [m^2/s]
- Horizontal mixing $C = 0.015$ and temperature of freshwater discharges $t_r = 10$ °C.

The data for seawater parameters, tides, winds, rivers and topography on the Albanian Coastal Area are taken from the Academy of Sciences in Tirana.

76.4 Summary and Concluding Remarks

A lot of numerical simulations in the Southern Adriatic were undertaken to understand the dynamics of the coastal zone. Our code is able to reproduce not only the plume physics well known up to now but to reveal the spiral eddies (small-scale eddies) at the seawater-freshwater interface.

This instability is caused by the density gradient and from the physical point of view, the unstable configuration of Fig. 76.1 is a superposition of disturbances on the value of parameters ρ and $\vec{u}$ for both fluids: freshwater and seawater. A horizontal view of density field in the depth 2 m is given in Fig. 76.2. If the plumes are not considered as a forcing mechanism, it is obtained a classic general circulation pattern (Fig. 76.3).

The strong influence of plumes in the general circulation pattern is clearly revealed by the comparison of the respective views.

Because of complex mechanisms nobody expect to be able to reproduce all aspects of nonlinearity. On this background, we have started to develop the ideas for the interaction among plumes, the role of spiral eddies on the structure of plumes and the instability concerning to.

There is a striking difference in the pattern of the river plume dependent on whether spiral eddies are considered or not. The role of spiral eddies can be dominant and can not be neglected in reality because it results in strong horizontal mixing which retards the moving speed and destroys the leading edge of the plumes. This significant contribution of spiral eddies to horizontal mixing is not completely studied yet. The result does not necessarily represent the best reproduction of what nature looks like, but it will be suitable as a base for investigation

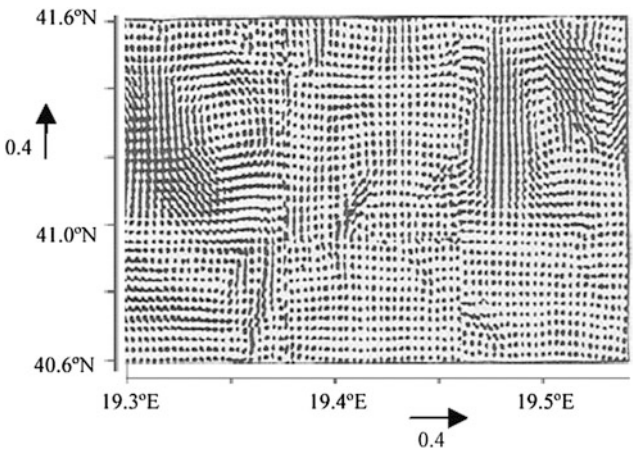

Fig. 76.1 General circulation

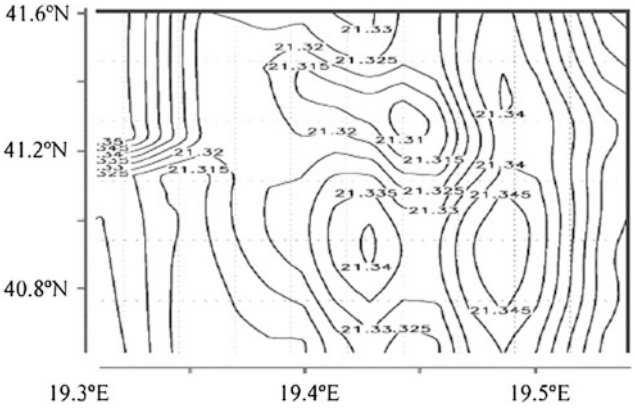

Fig. 76.2 Field of density

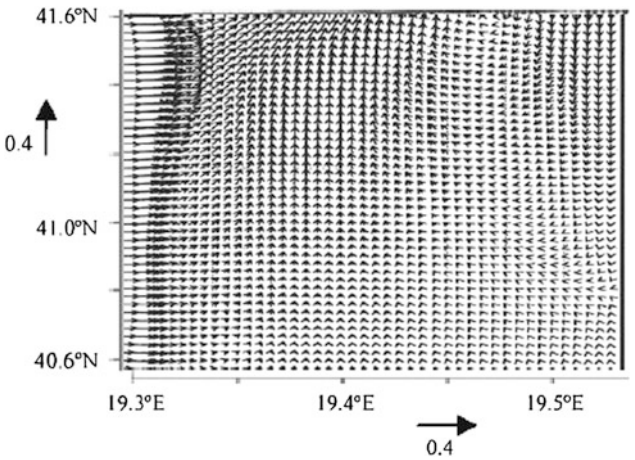

Fig. 76.3 General circulation without plumes influence

Acknowledgments This research was funded by the International Center of Theoretical Physics (ICTP). We have greatly valued and are immensely grateful for the help and technical support of Roberto Purini, Alan Blumberg, Jarle Berntsen and Patric Tallec.

References

Bell JB, Colella P, Glaz HM (1989) A second-order projection method for the incompressible Navier-Stokes equations. J Comput Phys 85:257–283

Blumberg AF (1991) A prime for ECOM –si. Technical Report for Hydroqual, Inc., Mahwah, pp 66

Blumberg AF, Mellor GL (1987) A description of a three-dimensional coastal ocean circulation model. Am Geophys Union 1–16

Bryan K (1969) A numerical method for the study of the circulation of the world ocean. J Comput Phys 4:347–376

Chu PC, Fan C (1997) Sixth-order difference scheme for sigma coordinate ocean models. J Phys Oceanogr 27:2064–2071

Florez W (2011) Nonlinear flow using dual reciprocity. Topics in engineering, London

Hoxhaj F (2009) An improved second-order numerical method for the non-linear terms of geofluid equations. ICTP Pub., Bull. 4

Kliem N, Pietrzak JD (1999) On the pressure gradient error in sigma co-ordinate ocean models: a comparison with a laboratory experiment. Accepted by J Geophys Res

Martinsen EA, Engedahl H (1987) Implementation and testing of a lateral boundary scheme as an open boundary condition for a barotropic model. Coast Eng 11:603–637

Stelling GS, Van Kester JATM (1994) On the approximation of horizontal gradients in sigma coordinates for bathymetry with steep bottom slopes. Int J Numer Meth Fluids 18:915–935

Wang J, Ikeda M (1997) Inertial stability and phase error of time integration schemes in ocean general circulation models. Mon Wea Rev 125:2316–2327

Yang HQ, Przekwas AJ (2012) A comparative study of advanced shock-capturing schemes applied to burgers equation. J Comp Phys 102:139–159

The Seasonal Deformations of the Coastal Slopes in the Permafrost Zone

77

Oksana Maslikova, Debolskaya Elena, Vladimir Debolsky and Ilja Gritsuk

Abstract
With the recent global warming, especially in the northern hemisphere, requires expansion of research on the modeling and prediction of the destructive processes of coastal water bodies located in the permafrost. We have considered a set of interrelated factors that have a significant impact on deformations of the coastal slopes in the permafrost zone under conditions of seasonal changes in the environment. The model consists of several blocks: the thawing of frozen soil and the occurrence of melt flow, the division of the precipitation on the infiltration and the catchment (surface fluxes) and the seasonal melting of snow as a type of the incoming rainfall, the impact of surface runoff erosion on the coastal slope.

Keywords
Permafrost • Coastal deformations • Melting • Ice content of soils • Solar radiation

77.1 Introduction

According to modern concepts, the natural environment in the mid-and high latitudes of the Northern Hemisphere is most sensitive to the observed global climate change. The threshold temperature of 0 °C associated with the phase transitions of water-ice and ice-water is critical for the northern regions. In conditions of significant climate warming, one should expect accelerated sharp degradation of permafrost that has already been observed nowadays. It can lead to significant erosion and settling of the soil. However, the effect of climate change on permafrost is usually mitigated by vegetation and seasonal snow cover. The total changes in air temperature, precipitation, vegetation properties and phenomena associated with these factors, determine the complex change in the thermal balance of the ground surface which is difficult to predict.

To simplify the modeling of thermodynamic processes taking place on coastal slopes of water bodies in permafrost conditions, consider the coastal slope as a formation consisting of three layers: annual thawed layer, permafrost rock layer and talik. Each layer is described by its own system of thermodynamic and hydrodynamic equations properly reflecting the state changes of the soil as well as environmental conditions (temperature changes and flow velocity changes). The upper annual thawed layer is exposed to most severe (thermal and mechanical) impacts. Its looseness and mobility is explained not only by the wind wave effects on the water basin surface but also by the influence of intra-slope, infiltration and seasonal precipitation. The permafrost rock layer is destroyed much slower due to its high consolidation and characterized by time intervals of a different scale (tenths and thousands of years). The talik layer often remains intact to erosion owing to small near-bottom velocities.

O. Maslikova (✉) · D. Elena · V. Debolsky · I. Gritsuk
Institute for Water Problems of the Russian Academy of Sciences, Gubkina Street 3, 117971 Moscow, Russia
e-mail: oksana68@mail.ru

D. Elena
e-mail: e_debolskaya@yahoo.com

G. Lollino et al. (eds.), *Engineering Geology for Society and Territory – Volume 1*,
DOI: 10.1007/978-3-319-09300-0_77,

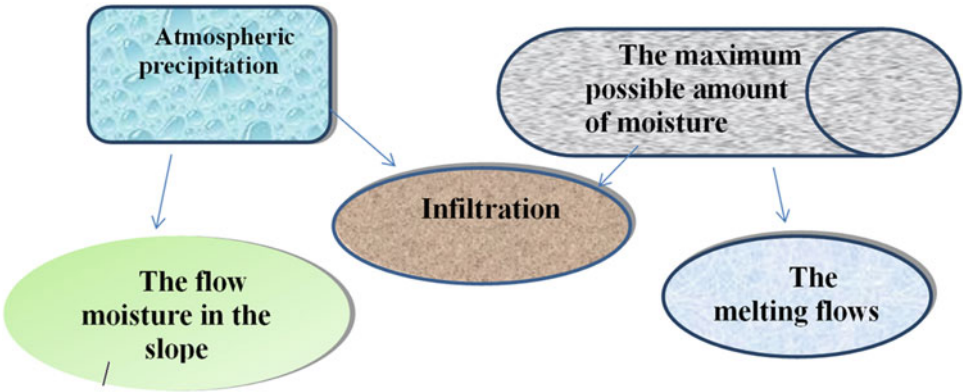

Fig. 77.1 Distribution of fluid flows in annual thawed layer of water body coast

77.2 Washout Model for Annual Thawed Layer of Water Basin in Permafrost Rock Conditions

The Fig. 77.1 illustrates a distribution of liquid flows in the annual thawed layer located in the permafrost zone. It is obvious that during the process of thawing the fluid is redistributed in each block: the part of the melting flow is increased, the soil conductivity is changing and, accordingly,—the maximum possible amount of moisture for this type of soil is changing also. As a result, possible infiltration changes and, as a consequence, the proportion of slope flows changes over time. At the end of the thawing process the movement of the soil moisture in the slope is stabilized, and the proportion of slope flows will depend on rainfall, which, in turn, is a function of the seasonal and diurnal temperatures and solar radiation.

77.2.1 Atmospheric Precipitation

Atmospheric precipitation arriving at the soil surface while the soil is thawing consists of melting snow and/or rain. The rainfall intensity is the amount of precipitation produced per one time unit. Snow melting (Shmakin et al. 2009) occurs when the temperature at the snow surface becomes equal to 0 °C. The melting rate M is expressed in kg/(m^{2}s) or mm/s for a water-equivalent layer depth, and defined as:

$$M = E_{melt}/L_i \tag{77.1}$$

where L_i is the specific heat of melting (freezing) in J/kg; E_{melt} is the heat energy demands for melting, in W/m^2.

Snow melting is classified as either convectional (thermal) melting, or radiation melting. The convectional snow melting occurs in dreary weather conditions, and is caused by the inflow of warm air masses. The radiation melting implies that the sun rays penetrating into the snow cause its melting both on the surface, and within a top layer 20–40 cm thick. Using the law which states that the intensity of incoming solar radiation decreases with the depth (the Burger-Lambert Law), taking into account the snow albedo change during the melting, and considering Eq. (77.1) as an integral sum of flows spreading over the snow cover depth, the following formula may be obtained:

$$M = \frac{I}{L_i(1 - e^{-\beta z})(1 - A(t))} \tag{77.2}$$

Here $A(t)$ is the albedo change over time, β is the radiation extinction (attenuation) factor, m^{-1}, at a depth of z m below the snow surface.

77.2.2 Flow Transporting Capacity on Slope

Using the sediment transportation formula (Debolsky et al. 1994) and the Darcy-Weissbach formula for the flow on the slope allowing for iciness, the washaway of solids by the surface runoff is expressed as:

$$S = \frac{6 \times 10^{-9}\sqrt{[3]}gq_{sl}}{w(i^2 + 10^{-6})\lambda^{4/3}} tg\left(\alpha^{4/3}\right) \tag{77.3}$$

where S is the flow transporting capacity; q_{sl} is the specific rate of the slope flow; w is the hydraulic size of non-frozen matter; i is the iciness due to glacial inclusions, in fractional units; λ is the resistance factor, or the energy losses over length, to be determined experimentally; α is the coastal slope tangent.

77.2.3 Infiltration into Soil

Atmospheric precipitation falling on a frozen or thawed soil is subdivided into filtration precipitation (the one that the

soil is capable of passing through itself depending on its structure, the maximum moisture-holding capacity of the soil) and slope precipitation of an intensity equal to the difference between the rainfall intensity and the filtration capacity of a given soil type:

$$q_{atm} = q_f + q_{sl} \tag{77.4}$$

where q_{atm} is the flow rate of atmospheric flows (pertaining to rain or snow melting), q_f, of filtration flows, and q_{sl}, of slope flows.

The maximum moisture-holding capacity of the soil may be derived from the filtration factor. The soil will be fed from inside by thawed flows completed from outside by a part of rain (infiltration) flows. This means that the difference between the limiting saturation volume and the generated thawed flows is completed by the very part of rain flows that is soaked by the soil:

$$q_f = q_n - q_t \tag{77.5}$$

where q_n is the limiting soil saturation volume.

77.2.4 Contribution of Thawed Flows

The flow velocity of thawed flows is determined basing on the flow rate of melt water or the melted ice volume per cross-section area unit. The melted ice volume is evaluated basing on the iciness change i (Gritsuk et al. 2012):

$$q_t = 1.1\Delta i V/(1 + \Delta i) \tag{77.6}$$

where V is the initial frozen soil volume. The cross-section area of the section F under consideration changes with the soil thawing rate. The thawing rate is determined as per [2]:

$$\frac{dx}{dt} = \frac{1}{F\rho L_c}\left(\lambda_a \frac{d\theta}{du}\Big|_+ - \lambda_n \frac{d\theta}{du}\Big|_-\right) \tag{77.7}$$

where $L_c = 33.3 \times 10^4$ J/kg is the melting or crystallization heat; $\lambda_т$ and $\lambda_м$ are the heat conductance factors of thawed and frozen mass, respectively; $\frac{d\theta}{du}\Big|_+$ and $\frac{d\theta}{du}\Big|_-$ are the heat dissipation intensity of thawed and frozen soil; ρ is the rock density; F is the non-frozen water content in frozen soils.

Alongside with that, the filtration rate governed by the Darcy law is $V = k_f J$, where J is the hydraulic gradient.

The factor of 0.6 has been proposed by Armand (1983) to reduce the water permeability in summer seasons to the one of the frozen soil. If the iciness changes are slow (linear, in our case), the filtration factor will gradually change in time from $0{,}6k_f$ for iciness equal to 1, to k_f under complete thawing. The same law will apply to changes of the limiting filtration flow, and to the fraction thereof:

$$\begin{aligned} q_n &= \left(\frac{0.4t}{T} + 0.6\right)k_f F \quad at\ t < T \\ q_n &= k_f F \qquad\qquad\qquad at\ t > T \end{aligned} \tag{77.8}$$

where T is the time of complete soil thawing (Kotlyakov et al. 2011).

77.2.5 Contribution of Slope Flow

If the intensity of atmospheric precipitation, namely, of seasonal rainfalls or of melting snow (or, in many cases, of both) does not exceed the infiltration rate, then all moisture is spent for soil saturation, and no surface washaway occurs.

If the intensity of melting exceeds the infiltration rate, then the excess thawed water goes to runoff. The slope flow at the very top is equal to the difference between the rainfall intensity and the infiltration rate: $q_{скл} = q_m$-$q_{инф}$. However, since each slope section has its own vertical of atmospheric water, these flows are joined down the slope with the upper ones, and the flow rate at each slope point will be equal to:

$$q_{sl} = (q_m - q_{\inf})l \tag{77.9}$$

where l is the distance from the slope top to the point being considered. Thus, the slope runoff will increase linearly as the height decreases, the washout formula will depend on the distance from the slope top, and the washout itself will tend to increase from the top to bottom.

If the lower border of the snow cover is a frozen rock (the most common case), then the Armand correction 0,6 at the lower border (the initial condition) is introduced for the infiltration rate. The flow rate at each slope point will be $(q_m - 0.6q_{\inf})l$ where l is the distance from the slope top. As the thawing (77.7) continues, the area where the factor of 0.6 is applicable will extend down inside the soil, with the changes from 0.6 to 1 in each particular point (Gritsuk et al. 2012). In this way the resulting slope flow for Eq. (77.9) is evaluated.

In the laboratory for testing of some blocks we used the mechanism for the simulating of the rain with varying intensity that can measure the rate of flow during infiltration of the thawing soil and the amount of lateral flow. The effect of solar radiation (ultraviolet and infrared parts of the spectrum) was investigated also.

77.3 Conclusions

The presented mathematical model completely describes the washaway of the annual thawed layer of coastal water bodies located in the permafrost zone, in conditions where the seasonal changes of environmental temperatures occur, and under exposure to atmospheric precipitation.

References

Armand DL (1983) Geograficheskaya sreda I racional'noe ispolzovanie priridnyh resursov. Nauka, Moskva (in russian)

Debolsky VK, Massel SP, Zaidler R (1994) Dynamika ruslovyh potokov I litodynamika pribrezhnoy zony moray. Moskva, Nauka, 303 s. (in russian)

Gritsuk II, Debolsky VK, Maslikova OJ, Ponomarev NK (2012) Vliyanie osadkov v vide dozhdya na deformacii beregovogo sklona rusel rek v usloviyah mnogoletnemerzlyh porod, Led I Sneg, vol 3(119), pp S73–S78 (in russian)

Kotlyakov AV, Ponomarev NK, Maslikova OJ (2011) Eksperimental'noe issledovanie vliyaniya l'distosti gruntov, slagayuschih ruslo rek, na dinamiku beregovogo sklona, Led I Sneg, vol 2(114), pp S92–S98 (in russian)

Shmakin AB, Turkov DV, Mikhailov AJ (2009) Model snezhnogo pokrova s uchetom sloistoi struktury I ee sezonnoy evolyucii, Kriosfera Zemli, T. XII vol 4, pp S69–S79 (in russian)

Part VIII

Landslides, Climate and Global Change

Convener: Dr. Huggel Christian—*Co-conveners*: John Clague, Oliver Korup

Economic losses from landslides have been rising over the past decades, mainly because of increasing development and investment in landslide-prone areas. Yet concern is growing that effects of climate change could exacerbate landslide impacts. Current projections indicate an increase of extreme precipitation events in the near future. Effective risk reduction and adaptation measures require an improved understanding of climate and global change effects and observed and projected impacts on society. This session seeks to attract interest across a wide range of subjects on landslides, and climate and global change, including observed changes in landslide occurrence and possible attribution to climate change, or analysis of factors influencing changes in landslide damage. We particularly encourage contributions on various aspects of climate-related mass-wasting processes such as slope failures in rock and ice, shallow and deep-seated landslides and debris flows.

Climate Change and Landslide Hazard and Risk in Scotland

78

M.G. Winter and B. Shearer

Abstract
Although the UK is a relatively low-risk environment where landslides are concerned such events do have important socio-economic impacts and fatalities do occur. This report considers the potential for landslide events in Scotland in the light of future climate change. In particular, the UKCIP02 (deterministic) and UKCP09 (probabilistic) climate change forecasts, current climate data and historic trends in Scotland's climate are discussed to obtain a clear picture of recent, current and likely future trends. The outcomes from this analysis are then reconciled with a view of likely future landslide hazard trends and a picture of potential future landslide risk in Scotland is presented.

Keywords
Landslides • Debris flow • Climate change • Rainfall

78.1 Introduction

The causal link between anthropogenic emissions of greenhouse gases, increases in the global temperature anomaly and climate change, which may or may not manifest as higher temperatures at any given location, are now well-established and have become part of the body of mainstream thinking (Stocker et al. 2013). Climate change is thus increasingly seen as a scientific fact; occasionally a dissenting voice may be heard but such disputes are increasingly focused upon the scale of such changes and on the most appropriate actions to be taken in terms of mitigation and adaptation.

M.G. Winter (✉) · B. Shearer
Transport Research Laboratory (TRL), 13/109 Swanston Road, Edinburgh, EH10 7DS, UK
e-mail: mwinter@trl.co.uk

B. Shearer
e-mail: bshearer@trl.co.uk

There is perhaps a tendency to focus upon the future climate change issues at the expense of the wealth of information captured within current weather patterns and recent climate trends. In this paper these three closely related threads of information—recent trends/current climate, historical trends and future change (UKCIP02 and UKCP09)—are brought together to provide a more holistic view of climate patterns as they relate to landslides. A more extensive treatment of the available data is given by Winter and Shearer (2013) as part of the SafeLand project.

78.2 Scotland's Rainfall Climate: Past Trends and Current Position

The climate of Scotland in terms of its rainfall broadly divides into the relatively dry east and the relatively wet west (Fig. 78.1, left), where the average annual rainfall is almost twice as high. The trend towards greater rainfall in the west is broadly maintained throughout the UK. While rainfall peaks in the summer months of July and August in the east, the monthly average rainfall data for Edinburgh (Fig. 78.1, right), which is broadly representative of the east

G. Lollino et al. (eds.), *Engineering Geology for Society and Territory – Volume 1*,
DOI: 10.1007/978-3-319-09300-0_78,

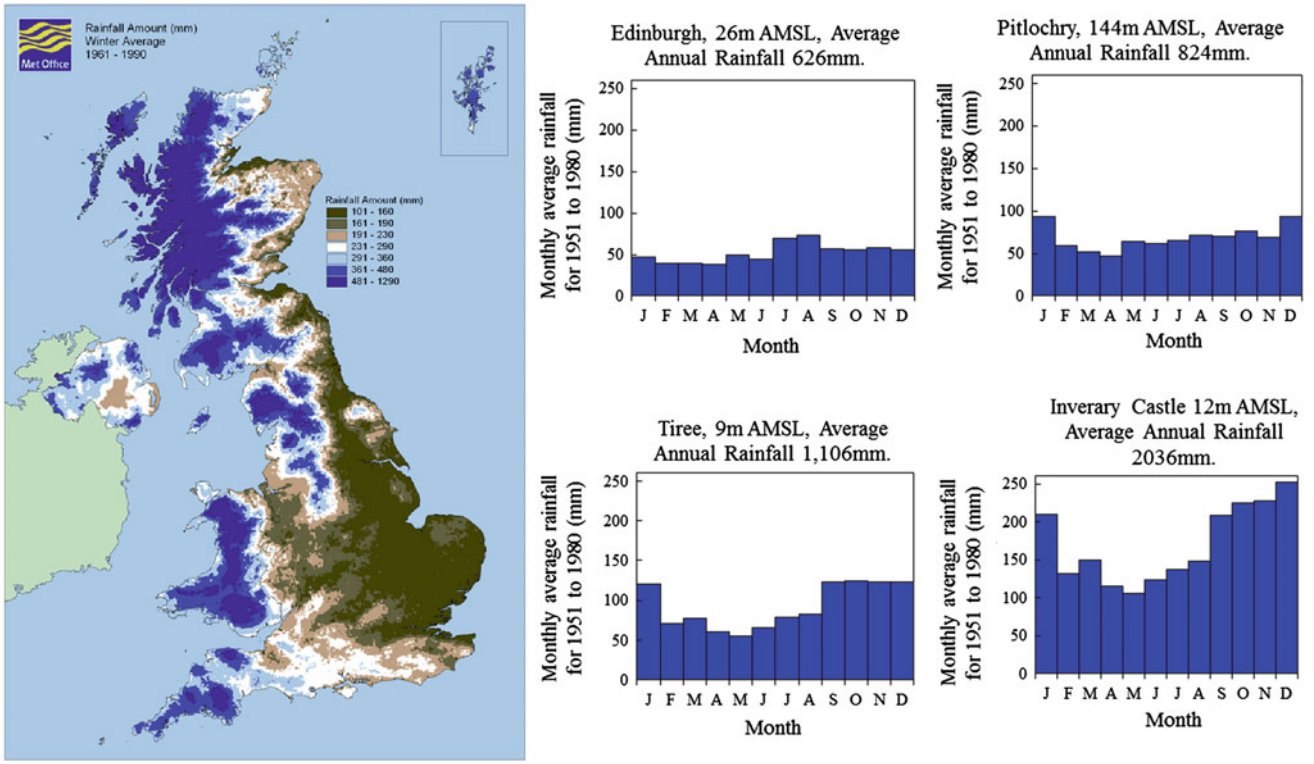

Fig. 78.1 Rainfall patterns. *Left* UK Met Office 30-year monthly average rainfall data (1961–1990) for winter; *blue* indicates high and *brown* low rainfall (images courtesy of the Met Office). *Right* Average rainfall patterns for selected locations in Scotland, based upon 30-year 1951–1980 averages from Anon (Anon 1989)

and one of the driest locations in Scotland, indicates that the monthly variations in rainfall are relatively small.

In the wetter west, maximum rainfall levels are reached between September and January (e.g. Tiree, Fig. 78.1, right). The variation in the monthly averages with the driest month of May receiving around half of the rainfall experienced in the wettest month of October. Although rainfall in the west is relatively low in August, levels increase from a low point in May. While Tiree shows rainfall levels significantly in excess of those for Edinburgh and Pitlochry (1,106 mm per annum compared to 626 and 824 mm respectively) in other parts of the west rainfall is greater: (e.g. Inverary Castle 2,036 mm of rainfall per annum: Fig. 78.1). The central area (e.g. Pitlochry: Fig. 78.1), has rainfall characteristics of the 'east' and the 'west'. Barnett et al. (2006) indicate that the annual average rainfall for the west of Scotland is between 1,200 mm and 2,100 mm (1914–2004) and for the east it is between 770 and 1,450 mm.

Data for both the west and the east indicate that the soil may be undergoing a transition from a dry to a wetter state at or around August and that in the period October/November to January the soil is likely to be in a wet, if not saturated, state and that rainfall continues to be at relatively high levels. This indicates an increased potential for debris flow and other forms of landslide activity during these periods. Barnett et al. (2006) describe historical trends in Scotland's climate for 1914–2004 and show a broad, but small, increase in the running annual average rainfall for the north and, particularly, the west of Scotland; figures for the east of Scotland are broadly stable. The statistical certainty inherent in the data is poor and only two clear trends are apparent: a reduction in summer precipitation in the east and an increase in spring precipitation in the west. However, the data more generally point to greater increases in precipitation in the winter and in annual precipitation levels, particularly in the north and west. Changes in summer precipitation show a likely reduction, particularly in the north and east.

78.3 Potential Climate Change: UKCIP02 and UKCP09

The deterministic UKCIP02 (Hulme et al. 2002) gave scenarios for Scotland that showed little predicted change in annual mean precipitation over the next few decades, with change being within the range attributable to natural variability. However, Galbraith et al. (2005) discerned a distinct seasonal pattern by the 2020s and in the low emissions

scenario, with changes found to be likely for the winter and summer. Winter precipitation increases were between 10 and 15 % for the Low and High emissions scenarios in the eastern regions, with changes elsewhere being within the range of that which can be accounted for by natural variability.

Decreases in the summer average precipitation are predicted to be widespread with only the far northwest seeing little change. By the 2020s Galbraith et al. (2005) indicate that the high emissions scenario implies that decreases of as much as 20 % are likely in the south east of Scotland. Year-on-year, or inter-annual, variability in precipitation is also predicted to change (Galbraith et al. 2005).

The probabilistic UKCP09 (Jenkins et al. 2009) was usefully simplified by Anon. (2011a) designated the 2050s as the central point and structured the relationship between emissions scenarios and predicted climate change as follows:

- Lower limit: 10 % probability with low emissions scenario.
- Central estimate: 50 % probability with medium emissions scenario.
- Upper limit: 90 % probability with high emissions scenario.

The data presented by both Anon (2011a, b) broadly confirm the likelihood of decreased summer precipitation and increased winter precipitation. Additionally, the data suggests approximately unchanged annual precipitation.

Precipitation intensity is considered by the proxy of wettest day in winter and summer (Anon 2011b). In the winter for the lower limit and central estimate the change is less than ±10 % across most of the country. However, for the upper limit the increase is of the order of 30–40 % in coastal areas. In the summer the change could range from 10 to 20 % less in the lower limit prediction to 10–20 % greater in the upper limit prediction.

The various data sets present a consistent picture and a number of clear themes emerge:

- Annual, spring and autumn rainfall is broadly unchanged or slightly less.
- Winter precipitation increases while summer precipitation decreases.
- Storm rainfall events may become more frequent/more intense (Although climate models are less well-suited to determining this).
- Winter temperatures will increase.

78.4 Changing Hazard and Risk

The soils that form the slopes subject to debris flow comprise a wide range of materials, albeit that periglacial, glacial, and post-glacial (including paraglacial) processes dominate their formation and subsequent modification. The particle size composition of debris flow materials includes sizes ranging from coarse granular (including boulders) to fine cohesive with most sizes between potentially represented (e.g. Winter et al. 2009). Both Winter et al. (2010) and Milne et al. (2009) acknowledge the importance of water-bearing soils, particularly peat, located on high, relatively flat ground as trigger materials for gulley-constrained debris flows. The materials that are later eroded, entrained and transported in the body of the flow may be of entirely different characteristics; often coarser-grained materials from morainic and related features are critical to the development of such flows.

Increased rainfall during the winter months seems likely to increase the prevalence of landslides. This is particularly so when the likelihood of more intense rainfall events is considered. The reduced soil moisture, as a result of both predicted temperature increases and rainfall decreases, during the summer and autumn may mean that the short-term stability of some slopes, particularly those formed from granular materials, may be enhanced by the suction pressures that may develop in such conditions. However, the available evidence for climate change does point to an increase in short duration, high intensity rainfall events, including in summer. Soils under high levels of suction are vulnerable to rapid inundation (Toll 2001), and a consequent reduction in the stabilising suction pressures.

Increased winter temperatures seem likely to reduce the, already very low, effect of snow and associated snow melt on landslide hazard in Scotland, although it is acknowledged that this is a potentially complex issue.

In addition, non-granular soils may form low permeability crusts during extended dry periods as a result of desiccation. If these do not experience excessive cracking due to shrinkage, then runoff to areas of vulnerable granular deposits may be increased. However, the formation of drying cracks could lead to the rapid development of instabilities in soil deposits, potentially creating conditions for the formation of debris flows. It is thus clear that there is a number of potential failure mechanisms that may lead to the initiation of a debris flow.

Extended dry periods leading to wildfires and associated debris flow seem less likely to be a major factor in the relatively wet climate of Scotland. An extension to the growing season seems more likely—a factor that may well have a positive effect upon instability. However, the possibility of vegetation desiccation cannot be dismissed during prolonged summer dry spells.

The available climate change forecasts thus present a picture that tends to suggest that landslide hazard frequency and magnitude may well increase in Scotland, at least in the winter months. A rather more complex picture emerges for the summer months but one possible outcome is that the

frequency of events may decrease but that the magnitude of those that do occur may increase.

The primary landslide risks relate to transport infrastructure, albeit not exclusively. Increases in the elements at risk and the associated vulnerability (both the infrastructure and road traffic/users) seem likely in line with road traffic and rail passenger growth. Set against this are major activities such as the planned upgrade of the A9 strategic road to dual-carriageway and major studies to identify and examine options to reduce landslide risk. Indeed, it is worth considering that should traffic levels grow substantially then the infrastructure will cease to be viable in its current form. If limits on access to the network are not to be introduced, then major upgrades will become necessary affording the opportunity to address landslide hazards and risks from the outset.

However, the approach of infrastructure upgrade does seem to be unlikely to be viable across the network and certainly is unlikely to be so much beyond the strategic road network for example. In such cases localised hazard mitigation schemes and route-based exposure management schemes will be necessary.

In addition the complex interplay between changing land use and the effects of emerging technology on work patterns will change the way in which society addresses such infrastructure and may also introduce new infrastructure that may itself be at risk from landslide hazards (Winter and Shearer 2013).

78.5 Conclusions

Rainfall-induced debris flow events are a relatively common occurrence in Scotland. In broad terms the available climate change forecasts present a picture that suggests that landslide hazard frequency and magnitude will increase in Scotland in the future, at least in the winter months. The picture for the summer months is considerably more complex, but one likely outcome is that while the frequency of events may decrease their magnitude, when they do occur, may increase.

The primary landslide risks relate to transport infrastructure, albeit by no means exclusively. It seems clear that the effects of climate change is most likely to increase the hazard and also that increases in the elements at risk and their vulnerability are likely to increase in line with traffic growth. Landslide risk is thus likely to increase as a result of these factors.

Planned network upgrades may minimize such hazards and risks at the outset, albeit this will not be a universal panacea and exposure management and hazard mitigation schemes will be necessary. The complex interplay between changing land use and the effects of emerging technology on work patterns will change the way in which society addresses such infrastructure and may also introduce new infrastructure that may itself be at risk from landslide hazards.

References

Anon (1989) The climate of Scotland—some facts and figures. The Stationery Office, London

Anon (2011a) Paths and climate change—an investigation into the potential impacts of climate change on the planning, design, construction and management of paths in Scotland. Commissioned Rep 436 by Walking-the-Talk. SNH, Inverness

Anon (2011b) Scottish road network climate change study: UKCP09 update. Report by Jacobs for Transport Scotland. http://www.transportscotland.gov.uk/

Barnett C, Perry M, Hossell J, Hughes G, Procter C (2006) Patterns of climate change across Scotland, Technical report, Project CC03. Sniffer, Edinburgh, p 102

Galbraith RM, Price DJ, Shackman L (eds) (2005) Scottish road network climate change study. Scottish Executive, Edinburgh, p 100

Hulme M, Jenkins GJ, Lu X et al (2002) Climate changes scenarios for the UK: the UKCIP02 scientific report. Tyndall centre for climate change research. University of East Anglia, Norwich, p 120

Jenkins GJ, Perry MC, Prior MJO (2009) The climate of the United Kingdom and recent trends. Met Office Hadley Centre, Exeter

Milne FD, Werritty A, Davies MCR, Browne MJ (2009) A recent debris flow event and implications for hazard management. Q J Eng GeolHydrogeol 42(1):51–60

Stocker TF, Qin, D, Plattner, G-K et al (2013) Climate change 2013, the physical basis: summary for policymakers. IPCC http://www.climatechange2013.org/

Toll DG (2001) Rainfall-induced landslides in Singapore. Proc Inst Civil Eng (Geotech Eng) 149(4):211–216

Winter MG, Shearer B (2013) Climate change and landslide hazard and risk—a Scottish perspective. Published project report PPR 650. Transport Research Laboratory, Wokingham

Winter MG, Macgregor F, Shackman L (eds) (2009) Scottish road network landslides study: implementation. Transport Scotland, Edinburgh, p 278

Winter MG, Dent J, Macgregor F, Dempsey P, Motion A, Shackman L (2010) Debris flow, rainfall and climate change in Scotland. Q J Eng GeolHydrogeol 43(4):429–446

Climate Change, Sea Level Rise and Coastal Landslides

79

Max Barton

Abstract
A long term rise in sea level due to thermal expansion as warm surface water conducts its heat to lower levels is now inevitable. To this can be added an additional rise from melting ice with the quantity dependent on the economic scenario. The paper outlines the consequences of this rise over the next few hundred years for different categories of coastal landslides.

Keywords
Sea level rise • Landslides • Slope stability • Coastal recession

79.1 Long Term Sea Level Rise

This paper is concerned with the potential response of large, complex coastal landslides to global warming induced sea level rise. We will start with the latter and focus on the potential long term rise. We note that the nearly the whole of the IPCC Assessment Reports and the bulk of the vast literature on this subject, concentrate on the current century leading up to the year 2100. However, we need to be aware that global warming by virtue of heating the oceans, has set a long term sea level rise in operation: as the warm surface waters transmit their heat downwards, so the thermal expansion will continue for many centuries (Meehl et al. 2012). The rise from the melting of small glaciers and changes in the mass balance of the ice sheets will continue and be an additional source of rise, with perhaps some additional rise from dynamic thinning of the ice sheets (Bromwich and Nicholas 2010; Pritchard et al. 2012) which will make the predicted values conservative. Although the further we look forward, so the errors will increase, nevertheless we cannot escape from the inevitability that a long term rise has been set in motion. Predicted values for the long term rise up to 2300 given by Meehl et al. (2012) are shown in Fig. 79.1, similar values for this period and economic scenarios are given in the 5th Assessment Report (IPCC 2013).

A major source of uncertainty resides in the economic scenarios. Figure 79.1 uses a simplified scheme which makes use of "representative concentration pathways", RCP (van Vuuen 2011; IPCC 2013) in preference to the multitude of economic scenarios used in the early IPCC Assessment Reports. Figure 79.1 shows the predicted sea level rise for two of these pathways. RCP 4.5 represents a moderate level of emissions producing an increased radiative forcing level of 4.5 W/m^2 by 2100 while RCP 8.5 reflects the failure of international agreement to reduce emissions resulting in an increased radiative forcing level of 8.5 W/m^2 by 2100. RCP 4.5 shows sea level rise levelling out by 2300 but RCP 8.5 shows the rise still increasing well beyond the catastrophic level already reached by 2300.

Our concern is with the sea conditions which will lead to increased rates of cliff toe erosion. Crucial to this concern is the possibility that the increased energy in the atmosphere will increase the frequency and/or intensity of storms (Tebaldi et al. 2012) and the associated surge height built up above the normal tidal level. We can treat the curves of Fig. 79.1 as a baseline above which future meteorological surges will become higher. Higher mean sea levels can significantly decrease the return period for exceeding a given threshold (IPCC 2013).

M. Barton (✉)
Faculty of Engineering & the Environment,
University of Southampton, Southampton, UK
e-mail: M.E.Barton@soton.ac.uk

G. Lollino et al. (eds.), *Engineering Geology for Society and Territory – Volume 1*,
DOI: 10.1007/978-3-319-09300-0_79,

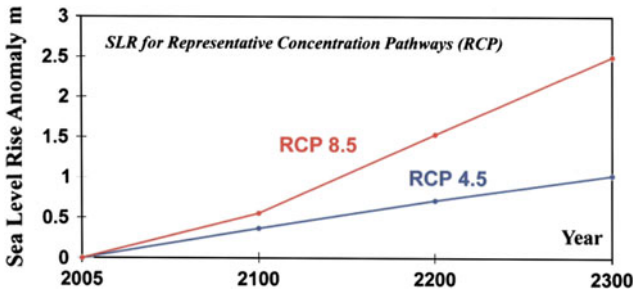

Fig. 79.1 Predicted increased sea level rise from 2005 to the year 2300 for two representative concentration pathways (RCP) using data from Meehl et al. (2012)

79.2 Coastal Landslides

The rate of cliff toe erosion, the frequency of landsliding and cliff top recession in response to sea level rise will depend on geology, cliff height, morphology, landslide mass and volume. We can make use of a visual model devised by Cosgrove et al. (1998) to illustrate the interaction of these factors for soft rocks but include an additional category to give three categories of coastal landslide (Fig. 79.2). We can summarise the response of the three categories of soft rock coasts as follows.

79.2.1 Category A: Low Cliffs Fronted by a Single Steep Slope, Recession Occurring by Isolated Falls from the Cliff Face

The cliff recession rate can be readily predicted by numerical models such as the *SCAPE* model (Walkden and Dickson 2008) as applied to the low London Clay cliffs on the Essex (UK) coastline. The basis of the model is to use coastal hydrodynamics to assess beach profiles and shore platform erosion with the recession of the cliff line being directly linked to the latter. No input is required in respect of the morphology or geotechnical response of the cliffs on the assumption that the low clay cliffs will continue to conform to a single angle of repose whatever the rate of marine erosion.

79.2.2 Category B: Medium Height Cliffs Undergoing Cyclic Failure in the Form of Periodic Large Slumps

The slump masses produced by the initial failure provide passive pressure support to the intact cliff and also reduce the rate of marine erosion at the toe. However, they undergo steady decay mainly by lobate mudsliding over the cyclic period and their eventual removal leads to the initiation of a new cliff slump. These types of landslides were described by Hutchinson (1973) as those where the rate of marine erosion exceeds the rate of supply of colluvial material by weathering. Examples were given for London Clay cliffs on the North Kent Coast where the cyclic period was estimated as being in the order of 30 to 40 years, but longer in the case of less severely eroded localities. It is clear that an increase in the rate of erosion, consequent upon sea level rise, will reduce the cyclic period. A numerical model can be set up but forecasting the changes taking place in the slope morphology, as well as the characteristic changes in overall slope angle from cliff toe to cliff crest, requires geotechnical input and not just the hydrodynamic treatment as used by the SCAPE model.

79.2.3 Category C: Large Complex Landslides Covering a Variable Lithostratigraphy Which May Including Two or More Slide Prone Horizons

These are of episodic frequency with the time lapse between major sliding events extending to hundreds or even thousands of years. The event and conditions which initiated the landslide may not be known but the concern is that sea level rise will lead to a reactivation and since these landslides are

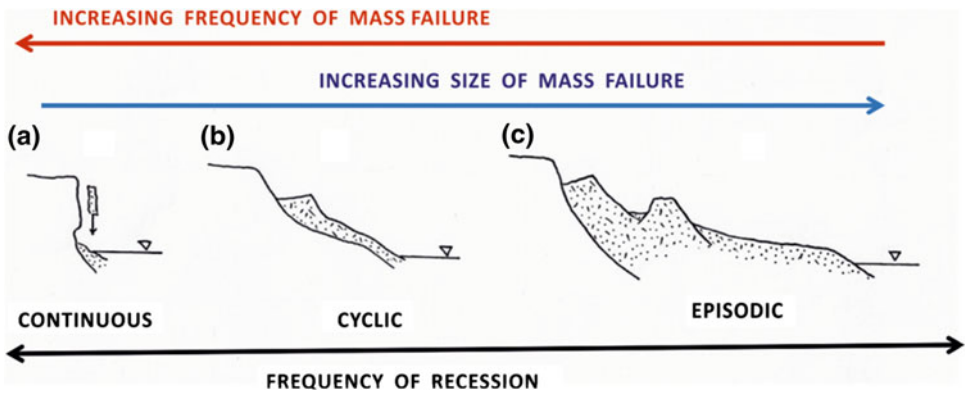

Fig. 79.2 Visual model to show the relationship between rate of erosion and the size, frequency and type of cliff failure in soft rock cliffs. Model based on an original by Cosgrove et al. (1998) with an additional type to give three categories of failure

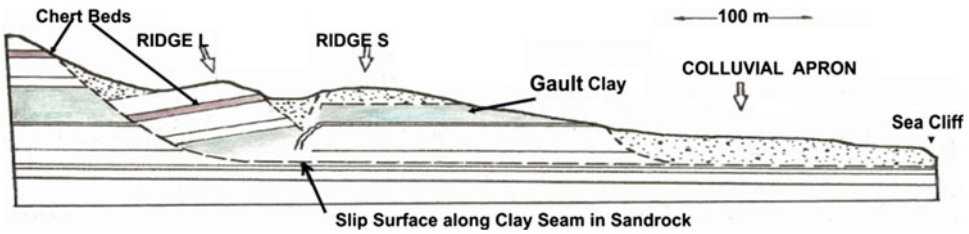

Fig. 79.3 Geological section of the St. Catherine's Point landslide showing the two slump blocks L (for landward) and S (for seaward) and the colluvial apron seaward of the buried cliff. Section based on Bromhead et al. (1988)

very large features, the consequences will be very dramatic. Their extent, stratigraphic range and varied geomorphology precludes generalisations about their likely response to sea level rise: each landslide requiring individual study. Therefore we will examine a well known landslide of this type to demonstrate the problems which arise and the difficulty they create for making generalisations about the future response over the time length we are considering. The example chosen for study will be the St. Catherine's Landslide in the Isle of Wight (UK).

79.3 The St. Catherine's Point Landslide

This landslide is located at the western end of the famous undercliff of the Isle of Wight. It is formed within Cretaceous sediments and is considered to be the result of a series of events during the mid to late Holocene (Hutchinson et al. 1991). The main features are two slump blocks (S and L on Fig. 79.3) and a large apron of colluvium seaward of a buried cliff line. Two shear surfaces can be identified, the earliest one is within the Gault Clay seen in Block S. The latest and deepest one uses a clay seam within the Sandrock Formation as the basal, translational surface. Figure 79.4 shows the wide colluvial apron upon which the lighthouse is built. The large colluvial apron contains much rock debris derived from the Chert Beds, including chert nodules and well cemented sandstone fragments with a size ranging from boulders to masses the size of a small shed. The accumulation of this material on the beach acts as a kind of natural rock armouring, dissipating the wave energy and slowing toe erosion, increases in marine erosion having a negative feedback by increasing the amount of rock armouring on the beach. Thus the rate of cliff recession is relatively slow, although owing to its proximity to the cliff edge, the lighthouse is likely to be an early casualty.

A currently active lobate mudslide is generated by seepage from Ridge S and leads down to the western margin of the landslide complex. Although it causes back sapping of Ridge S, its small size in comparison to the extent of the colluvial apron does not suggest an imminent serious risk to the stability of the apron. Both the erosion of the sea cliff and the activity of the lobate mudslide are components of the natural processes which lead to the slow degradation of a landslide: their activity will continue irrespective of global warming induced sea level rise, albeit with some acceleration.

A serious problem induced by sea level rise is the effect on the tail water level of the groundwater outflow from the cliff and hence raising the piezometric level within the colluvial apron. Slow creep occurs in the apron as shown by movements which have damaged the lighthouse and adjacent buildings (Bromhead et al. 1988) so a further rise in groundwater levels beyond that already experienced in wet winters could lead to a loss of stability. Calculations showing how a relatively small rise in pore pressure will result in loss of stability are given in Barton (2007). Seaward movement of the apron will in turn lead to movement of Ridge L which provides passive support to the intact cliff, such movement will inevitably lead to fresh slumping and recession of the back scarp thus reactivating the whole landslide complex.

79.4 Discussion

The three fold classification of soft rock coastal landslides given in Sect. 79.3 is open to criticism in that there will be many transitional types and also that Category C will verge into the hard rock category with geologically older sediments. Nevertheless it is put forward as a basis for discussing landslide response to sea level changes. A key factor indicated by this classification is the dual role of colluvial mass; namely in providing passive support to the in situ cliff and secondly acting as a protective barrier during wave attack. Its resistance to both wave attack and sub-aerial weathering is a vital aspect of the geotechnical evolution of the coastal slope.

Fig. 79.4 Oblique aerial view of the *cliff line* and wide expanse of the colluvial apron upon which stands the St. Catherine's Point lighthouse. Photograph taken from the Future coast project

The IPCC prediction of long term sea level rise has undergone a revolution. A forecast for the next millennium was given in the Third Assessment Report (summarised in Barton 2006) but the 4th Assessment Report was more cautious stating that there was too much uncertainty in respect of ice sheet dynamics to make long term predictions. The 5th Assessment Report (IPCC 2013) has now provided a series of predictions in respect three ranges of economic scenarios up to the year 2500: the highest range predicting a world very different from that with which we are familiar.

79.5 Conclusions

- The predicted values for long term sea level rise should be more widely known especially in view of the disparity shown between the low and high emissions scenarios. The high values shown for RCP 8.5 (Fig. 79.1) should have a greater effect upon the conscience of those make decisions regarding emissions control than the much smaller values predicted for the end of the current century.
- The largest source of error for long term predictions is in respect of potential dynamic thinning of the ice sheets. The high values predicted even without this source of error should provide much incentive for ice sheet monitoring as a matter of urgency for the benefit of future generations.
- We can confidently predict that coastal landsliding will be accelerated but the rate of change and recession for particular coasts needs much further research. Apart from the mudslides, the properties of the colluvium is often neglected which is a pity because it plays a key role in the evolution of the landslides.

References

Barton ME (2006) Do coastal cities have a sustainable long-term future ? Engineering geology for tomorrow's cities. In: Culshaw M, Reeves H, Spink T, Jefferson I (eds) Proceedings 10th IAEG, Nottingham, UK, Paper 263, CD ROM. Geological Society, London

Barton ME (2007) Sleeping demons and terrified horses: determining the onset of instability. In: McInnes R, Jakeways J, Fairbank H, Mathie E (eds) Landslides and climate change: challenges and solutions. Taylor and Francis Group, London, pp 475–480

Bromhead EN, Curtiss RD, Schofield W (1988) Observation and adjustment of a geodetic survey network for measurement of landslide movement. In: Proceedings of 5th international symposium on landslides, vol 3. Lausanne, pp 383–386

Bromwich DH, Nicolas JP (2010) Ice-sheet uncertainty. Nat Geosci 3:596–597

Cosgrove ARP, Bennett MR, Doyle P (1998) The rate and distribution of coastal cliff erosion in England: a cause for concern ? In: Bennett D (ed) Issues in environmental geology: a british perspective. Geological Society of London, UK

Hutchinson JN (1973) The response of London Clay cliffs to differing rates of toe erosion. Estratto da geologia applicata e idrogeologia, vol 8, Part 1. Bari, Italy

Hutchinson JN, Bromhead EN, Chandler MP (1991) Investigations of the Landslides at St. Catherine's point, Isle of wight. In: Chandler RJ (ed) Slope stability engineering: developments and applications. Thomas Telford, London, pp 169–180

IPCC 5th Assessment Report (2013) Chap. 13, Sea level change

Meehl GA et al (2012) Relative outcomes of climate change mitigation related to global temperature versus sea-level rise. Nat Clim Change 2:576–580

Pritchard HD et al (2012) Antarctic ice-sheet loss driven by basal melting of ice shelves. Nature 484:502–505

Tebaldi C, Strauss BH, Zervas CE (2012) Modelling sea level rise impacts on storm surges along US coasts. Environ Res Lett 7(014032) 1–11

van Vuuen DP et al (2011) The representative concentration pathways: an overview. Clim Change 109:5–31

Walkden M, Dickson M (2008) Equilibrium erosion of soft rock shores with a shallow or absent beach under increased sea level rise. Mar Geol 251:75–84

Realizing, Monitoring and Evaluating of Georisks in a Changing Climate

80

Martin Scherbeck and Michael Alber

Abstract

We employ an interdisciplinary approach to realize, monitor and evaluate landslides and related slope movements caused by changing climate. The stability of natural slopes and existing earth structures, such as dams and road cuts, will be affected by changing precipitation and groundwater conditions. The study was conducted at three sites in southwestern of Germany along the A8 motorway on the northern edge of the Swabian Alb. These included a dam, a cut slope and natural rock towers. The results so far seem to indicate climate-related slope movements could increase in the future. Monitoring verifies that deformations occurring and correlations between climate data and geodata have been found. Previously published results indicate an increase in extreme rainfall events. Changes in water content of the exposed mud- and siltstones lead to irreversible weakening of material structure, as expected by changing precipitation and groundwater conditions.

Keywords

Georisks • Landslides • Climate change • Geomonitoring

80.1 Introduction

Heavy precipitation, floods and other exceptional hydrological events have likely increased globally in the past decade as a result of climate change. Medium and long-term trends indicate a further intensification of these phenomena (IPCC 2012). In the case of southern Germany, there will likely be an increase in heavy precipitation events during the winter (Kliwa 2006).

The stability of natural slopes and existing earth structures, such as dams and road cuts will be affected by changing precipitation and groundwater conditions. We conducted an interdisciplinary research project involving the disciplines of engineering geology, hydrogeology and climatology to realize, evaluate and monitor georisks (i.e. landslides and related slope movements) in the context of climatic change. The research area is in southwest Germany, on the northern edge of the Swabian Alb. The aim of the project is to validate the interdisciplinary approach.

80.2 Research Areas

Our research project was conducted at three sites (Fig. 80.1). "Rock Fill Dam" and "Cut Slope" (≈475 m asl) are located along the A8 motorway, near the Aichelberg exit, and are part of the 16-km-long Albaufstieg. The Albaufstieg is a vertical rise of the motorway of approximately 400 m

M. Scherbeck (✉) · M. Alber
Engineering Geology, Ruhr-University, Universitätsstraße 150, 44801 Bochum, Germany
e-mail: martin.scherbeck@rub.de

M. Alber
e-mail: michael.alber@rub.de

G. Lollino et al. (eds.), *Engineering Geology for Society and Territory – Volume 1*,
DOI: 10.1007/978-3-319-09300-0_80,

Fig. 80.1 Geological overview and location of the research sites (Bayerisches Landesamt für Umwelt 1996)

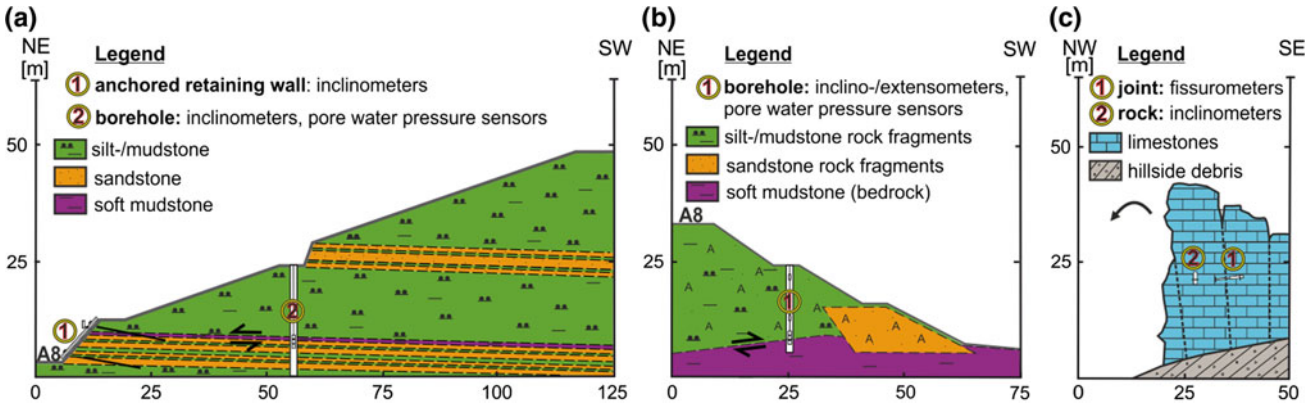

Fig. 80.2 Schematic cross-sections of the three research sites: Cut Slope (**a**), Rock Fill Dam (**b**) and Upper Jurassic Cliff (**c**)

over a distance of 16 km and leads through the Middle and Upper Jurassic Rocks of the Swabian Alb. This section of the motorway was modernized in 1986/1990 with the construction of a rock fill dam and a deep cut slope. The research site "Upper Jurassic Cliff" (≈750 m asl) consist of natural rock towers and is situated 13 km southeast of the other areas.

80.2.1 Rock Fill Dam

The research site is a part of an up to 30-m-high, 150-m-wide and about 700-m-long rock fill dam of the A8 motorway. The dam consists of fragments of mud-/silt- and sandstones of the Middle Jurassic age (Fig. 80.2b). It was constructed with layers of mud-/silt-/sandstones with a maximum edge length of 40 cm, compacted to a specified proctor density. Geotechnical monitoring up to 2004 include inclinometer and surface measurements, which show that vertical and horizontal deformations are still happening after more than 18 years of settlement, although rates are decreasing. With anticipated climatic change, i.e. rising natural water availability, continuing or increasing deformation rates are expected.

80.2.2 Cut Slope

The second research site is located about 800 m southeast of the "Rock Fill Dam" site along the A8 motorway. It is a rock slope with a height up to 50 m. The exposed rock is Middle Jurassic in age and consists of layered mud-/siltstones with a few sandstone layers (Fig. 80.2a). The lower part of the slope is stabilized by a deep-anchored retaining wall. Geotechnical monitoring up to 2005 include inclino-/extensometer and anchor-loads, which show that horizontal deformations are still occurring after 16 years. The deformation, which is highly variable in rate, is localized mainly within a thin plastic mud layer directly above a sandstone layer (LfS 2002). Due to slope relaxations and the sensitivity of the mud-/siltstones to changes in water content, an increase in deformation due to future climatic change is expected.

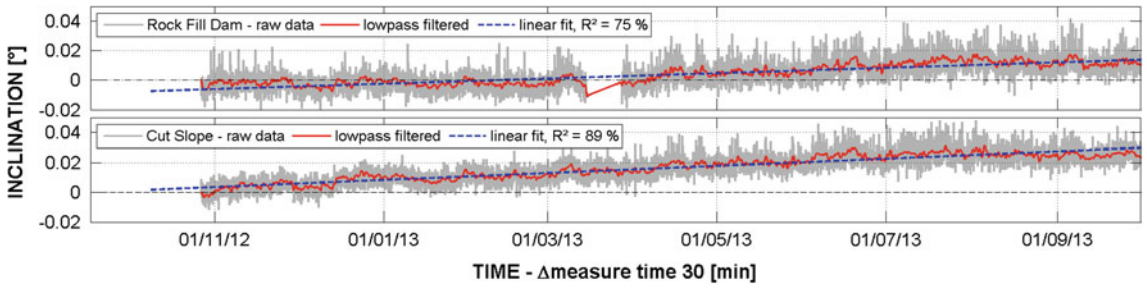

Fig. 80.3 Horizontal deformations of the rock fill dam and cut slope. Measured in boreholes by inclinometers at depths of 16.3 m (Rock Fill Dam) and 9.5 m (Cut Slope)

80.2.3 Upper Jurassic Cliff

The third research site is the north-west-facing cliff of the Swabian Alb, near the village of Drackenstein. Karstified and jointed massive limestones of Upper Jurassic age form rock towers on this steep terrain. The massive limestone rock towers are up to 20 m high. Limestones and marlstones underlay these massive limestones. Rising ground water levels following heavy precipitation events are expected and may lead to high erosion rates and high water pressures in joints. Especially high erosion rates can destabilize the marlstones. An increase of rock fall events with a rising water table is expected.

80.3 Methods

80.3.1 Common Approach and Achievements

Regional forecasts of precipitation over the next several decades are used to estimate groundwater recharge rates, which in turn are used to estimate future changes in groundwater levels. Three geosensor networks were installed in 2012 to provide geodata (deformation, groundwater level) and climate data (precipitation, air temperature). The geosensors include extensometers and inclinometers, pore water pressure and rock temperature sensors (Fig. 80.2a, b), fissurometers (Fig. 80.2c), precipitation gauges and air temperature sensors. Geodata are acquired by three automatic data acquisition units with independent power supply and GPRS data transmission. Climate data are acquired with a simple data logger. Details of the geosensor networks are given in Plinninger et al. (2013).

Data gathered in the different subprojects indicate that the risks from mass movements at the study sites may increase. Geotechnical-geological tests of the exposed mud- and siltstones at "Rock Fill Dam" and "Cut slope" confirm their limited strengths. Under experimental conditions (i.e. samples were immersed in water), an increase in water content led to irreversible weakening of the material structure. Similar changes in water content are expected from changes groundwater conditions. Evaluation of historical regional climate data verifies that extreme precipitation events are becoming more frequent. Details concerning laboratory and field test of the exposed rocks and the evaluation of climate data were published in Scherbeck et al. (2013). Groundwater modeling of the research sites is almost complete. Recent data from the geosensor networks indicate that deformations are continuing.

80.3.2 Approach for Evaluating Data from Geosensor Networks

Data from 77 sensors are collected and stored every 30 min. The data processing includes the following steps:

Data preparation

- remove outliers and erroneous values, interpolate gaps and correct data,
- transform data to spectral representation by means of Fast Fourier Transformation (frequency analysis),
- low-pass filtering (cut-off frequency of 9.9 μHz/period of 28 h), minimizing measured noise and the impact of daily temperature variation,
- calculation of daily sums, relative changes and difference quotients.

Analysis of measured values

- estimate trend of time series by means of least-square curve-fittings,
- perform correlation and cross-correlation analysis to identify linear correlations between measured values of different sensors; calculate Pearson correlation coefficients,
- visually evaluate of the essential interface between climate data (precipitation, air temperature) and geodata (porewater pressure, deformation),
- check on geological and geotechnical plausibility of the correlations.

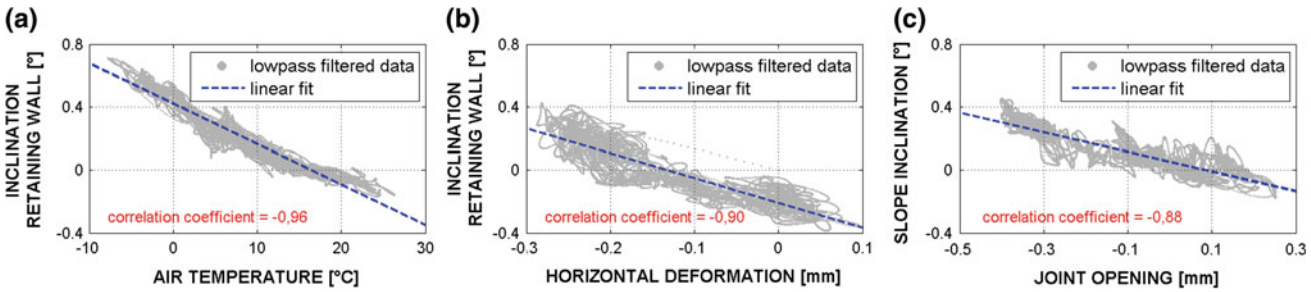

Fig. 80.4 Correlation of the Cut Slope **a** Rock Fill Dam, **b** and Upper Jurassic Cliff, **c** between inclination, deformation and air temperature

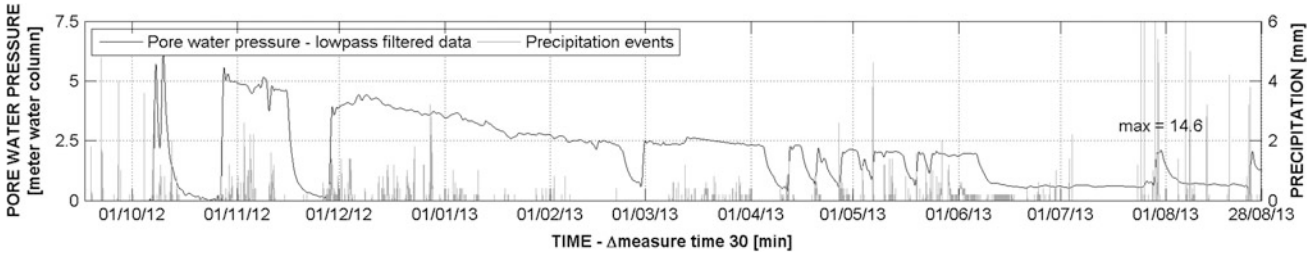

Fig. 80.5 Pore water pressure caused by precipitation events at Rock Fill Dam

80.4 Results and Discussion of Geomonitoring

Recent data from the Rock Fill Dam and Cut Slope sites demonstrate a nearly linear increase in horizontal deformation of up to 0.03° inclination (≈0.5 mm) in about 1 year (Fig. 80.3). At Rock Fill Dam, the zone of deformation is located at the base of the structure, where it is in contact with the underlying Lower Jurassic bedrock (Fig. 80.2b). The main deformation of the Cut Slope occurs in or close to the thin plastic mud layer (Fig. 80.2a). The other data, including temperature, pore water pressure, vertical deformation, slope inclination and joint opening, do not yet show a significant trend. However, data acquired for monitoring periods less than 1 year indicate a trend related to air temperature. This relationship affects geosensors near the surface, particularly those that measure inclination of the retaining wall, slope inclination and joint opening. The calculated correlation coefficients show a high linear correlation between air temperature and deformation. Deformation caused by air temperature, i.e. thermal expansion of rock, have a correlation coefficient up to |1| (Fig. 80.4a). In some cases, changes in deformation correlate to one another. For example, at Cut Slope between horizontal deformation and inclination of the retaining wall and at Upper Jurassic Cliff between joint opening and slope inclination (Fig. 80.4b, c). However, the coefficients are not proof of a causal link between the measured values. It is obvious that the correlation evident in Fig. 80.4c is caused by air temperature, but in Fig. 80.4b, the correlation is unaffected by air temperature because horizontal deformation is measured at a depth of 5–12 m. We also found correlations between climate data (precipitation) and geodata (pore water pressure). In the areas Rock Fill Dam and Cut Slope, the correlation coefficients are low, but a correlation between precipitation and changes in pore water pressure can be detected in Fig. 80.5. Some precipitation events do not cause an increase in pore water pressure. To understand these effects, we will perform an analysis of precipitation in the future.

80.5 Conclusion

We found correlations between climate data and geodata at our study sites. Monitoring verifies that deformations occurring. Previously published results (Scherbeck et al. 2013) indicate that the sites have experienced an increase in extreme rainfall events. Changes in water content of the exposed mud-/siltstones lead to weakening of material structure, as expected by changes in rainfall and groundwater conditions. The results to date seem to indicate climate-related slope movements could increase at the "Rock Fill Dam" and "Cut Slope" sites in the future.

Acknowledgments This research is sponsored by the Federal Ministry of Education and Research of Germany under contract No. 16V0114— VIP0087.

References

Bayerisches Landesamt für Umwelt (1996) Geol. Karte Bayern, 1:500.000

Intergovernmental Panel on Climate Change—IPCC (2012) Managing the risks of extreme events and disasters to advance climate change adaptation. A special report of working groups I and II of the intergovernmental panel on climate change. Cambridge University Press, Cambridge

Kliwa (2006) Regionale Klimaszenarien für Süddeutschland. KLIWA-Berichte, Heft , München, p 9

Landesamt für Straßenwesen Badenwürttemberg—LfS (2002) Geotechnische Überwachung Aichelberg—A8 (unpublished)

Plinninger R, Alber M, Brodbeck M, Singer J, Scherbeck M (2013) BMBF-Forschungsprojekt GeoKlimB—Teil 2: Einrichtung und Betrieb dreier Geosensor-Felder am Albaufstieg der BAB A8. Tagung für Ingenieurgeologie, München, p 19

Scherbeck M, Alber M, Steinrücke M, Brodbeck M, Plinninger R (2013) BMBF-Forschungsprojekt GeoKlimB—Teil 1: Erfassen, Bewerten und Verfolgen von Georisiken als Folge des sich verändernden Klimas. Tagung für Ingenieurgeologie, München, p 19

Rockfall Hazard in the Mont Blanc Massif Increased by the Current Atmospheric Warming

81

Ludovic Ravanel and Philip Deline

Abstract

The study of rockfall (volume >100 m^3) in high mountains is essential to understand landscape evolution and to evaluate natural hazard. The number of rockfalls seems actually to rise in the European Alps, while exposure is increasing from high elevation areas (e.g. cable cars, huts) to valley floors (e.g. urbanization, transport). Recent rockfalls from high-Alpine steep rockwalls are hypothesized to be a consequence of the climate change through the warming of the permafrost. Given the lack of systematic data on rockfall, this relationship has however remained difficult to assess despite few evidences including laboratory tests and temperature measurements indicating permafrost degradation, while the increase of rockfall frequency and magnitude remained conjectural. Here we analyze several inventories of rockfalls acquired in the Mont Blanc massif by innovative methods in order to characterize the rockfall triggering conditions and to emphasize the role of permafrost.

Keywords

High alpine infrastructure • Landslides • Permafrost • Glacier shrinkage • Hazards

81.1 Introduction

In the last two decades, numerous rockfalls and rock avalanches occurred in permafrost-affected rockwalls worldwide (Huggel 2008). Part of them involved rock and ice, with volume exceeding 2×10^6 m^3. Due to their steep topography, mountains are indeed affected by significant gravity-related transfers of material, in particular by rockfall in supraglacial areas (Deline et al. 2008). Rockfall is the detachment of a rock mass (volume exceeding 100 m^3) from a steep rockwall, according to the sets of discontinuities affecting the rock mass, which travels down slope to a variable distance. It is one of the most hazardous geomorphological processes because of its high speed and the related risks for infrastructure (Harris et al. 2001; Ravanel et al. 2013) and population up to valley floors through cascading effects (Haeberli et al. 2004). Three major factors possibly combined can trigger rockfalls in high mountains: seismic activity, glacial debuttressing due to glacier retreat (Oppikofer et al. 2008) and permafrost degradation (Gruber and Haeberli 2007; Allen and Huggel 2013) i.e. the warming of bedrock whose temperature remains at or below 0 °C for at least 2 years. It generates physical changes of the potential interstitial ice (Gruber and Haeberli 2007) and increases the hydraulic permeability of the rock mass.

The characterization of the rockfall dynamics is a prerequisite for risk reduction. However, data on rockfall at high elevation are rare and discontinuous, thus non-representative. In order to investigate the possible correlation between global warming and rockfall, and the permafrost role, we collected and analyzed a dataset of 486 recent and present rockfalls in the Mont Blanc massif (Fig. 81.1),

L. Ravanel (✉) · P. Deline
EDYTEM Lab, University of Savoie, CNRS, Le Bourget-du-Lac, France
e-mail: ludovic.ravanel@univ-savoie.fr

G. Lollino et al. (eds.), *Engineering Geology for Society and Territory – Volume 1*,
DOI: 10.1007/978-3-319-09300-0_81,

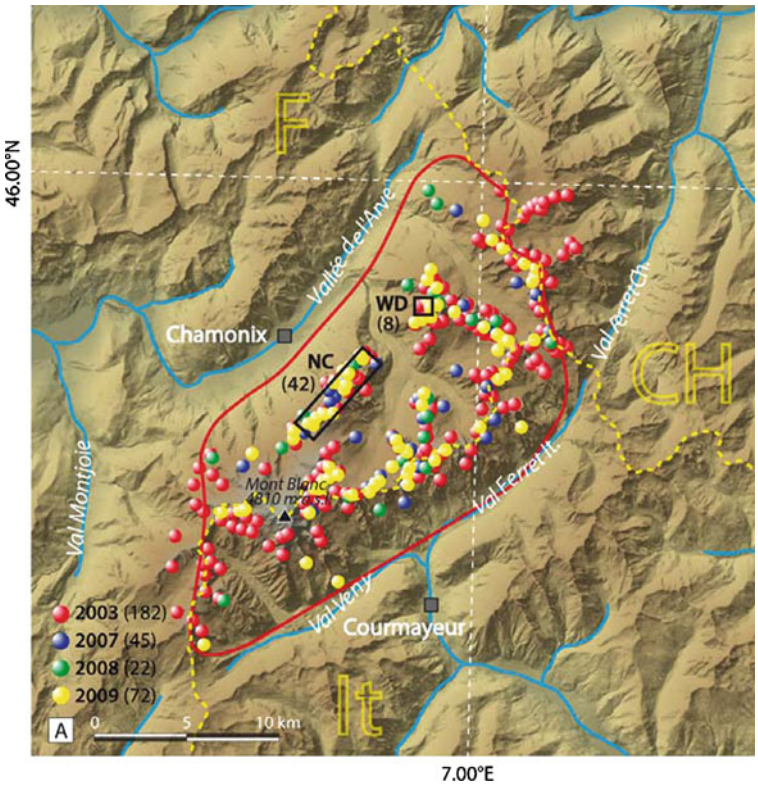

Fig. 81.1 The Mont Blanc massif and the surveyed rockfalls (DEM ESRI). *Rectangles* sectors with a morphological reconstruction since the end of the Little Ice Age; *WD* West face of the Drus, *NC* North Side of the Aiguilles de Chamonix. *Red line* area covered by the network of observers

a 550 km^2, granitic, widely glacierized and permafrost-affected massif, where fracturing and slope steepness make it prone to rockfall.

81.2 Methods

We photo-interpreted a series of photographs of two areas of the Mont Blanc massif selected because of their rich existing documentation since the end of the LIA. The oldest document is a daguerreotype of 1854 (Ravanel and Deline 2008, 2011). Nearly 400 photographs have been gathered from many sources. Photographs were compared and analyzed to determine limits of scars and time of rockfalls on the basis of morphological and color changes. In the two study areas, it was often necessary to diversify and cross-check information sources to date the collapses. Comprehensive recognition of rockfalls was supplemented by estimates of the collapsed volumes.

A network of rockfall observers in the Mont Blanc massif was set up in 2005 (Ravanel et al. 2010). It consists in mountaineers sensitized to rockfall observation. Fully operational since 2007 and regularly reactivated, it focuses on the central part of the massif (Fig. 81.1). Observers fill a reporting form, indicating the main characteristics of the rockfall and the rockwall conditions. To ensure a higher completeness of the inventory, fieldwork is conducted every fall. Summer 2003 rockfalls in the whole massif were identified from their supraglacial deposits through the analysis of the 051/257 SPOT-5 image taken on the 23rd of August, at the end of the heatwave (Ravanel et al. 2011). Elevation of the scars, slope and orientation of affected rockwalls, and area of the deposits were calculated in a GIS. Possible presence of permafrost was determined from the TEBAL model (Gruber et al. 2004a) of the distribution of the mean annual ground surface temperature.

81.3 Results

8 rockfalls affected the WD between 1905 and 2009, mainly related to the retrogressive erosion of the SW Pillar (Pilier Bonatti) which finally collapsed in 2005 (Ravanel and Deline 2008). On the NC, 42 rockfalls occurred between 1947 (largest rockfall: 65,000 m^3) and 2009, mostly recently: the 1990s and the 2000s were characterized by an increasing frequency of rockfalls involving larger volumes.

Since 2007, a network of observers surveys the occurrence of rockfall (Ravanel et al. 2010) in the central area of the massif, with volume in the range 100–60,000 m^3. In 2007, 45 rockfalls occurred with only three out of the modeled permafrost area (MPA). In 2008, 22 rockfalls were reported (Deline et al. 2008); only one occurred out of the MPA. In 2009, 72 rockfalls were recorded with small volumes

(up to 7,000 m^3); only two occurred out of the MPA. Identified by their deposit onto glacier, 182 rockfalls occurred during the summer 2003 heatwave throughout the whole massif (Ravanel et al. 2011).

81.4 Discussion

To deal with the relationships between global warming and rockfalls, we crossed the occurrence of the WD and NC documented rockfalls with local air temperature data (Fig. 81.2). More than 70 % of these rockfalls occurred during the past two decades characterized by an acceleration of the atmospheric warming. These rockfalls mainly occurred during the hottest periods.

There is also a close relationship between the 2003 and 2007–2009 rockfalls and the air temperature of those years. 48 % of the rockfalls of the period 2007–2009 have been precisely dated. Among them, 95 % occurred between June and September, i.e. during the hottest months of the year. It is also striking to note that the cool months that have characterized certain summers have resulted in a delay of rockfall (2009). With 152 rockfalls in the central part of the massif surveyed by the observation network, the rockfall frequency of 2003 has been exceptional (Gruber et al. 2004b; Ravanel et al. 2011), as was the temperature of that summer.

The strong correlation between rockfall occurrence and hottest periods at the time scale of the century strengthens the hypothesis of the relationship between permafrost degradation and rockfall. But permafrost degradation is a long-term process and it is hard to directly link rockfall and permafrost degradation at the time scale of the year. However, modeling suggests the presence of permafrost in nearly all of the affected rockwalls, and massive ice was observed in many scars. Exceptional penetration into the rockfaces of warm temperatures (as in 2003) leading to a deepening of the active layer can be seen as a first mode of permafrost degradation (short-term effect). Strong snowmelt and infiltrating water into rock clefts can enhance rock fall activity by lowering shear strength (Hasler et al. 2012). In the same way, no significant seismic activity was measured during the Summer 2003 and only 14 % of the 2003 affected rockwalls were formerly glaciated at their foot (during the Little Ice Age in particular). Several other elements support permafrost degradation as main triggering factor of rockfall. The mean elevation of 2003 and 2007–2009 scars is much higher than the mean rockwall elevation (2,880 m a.s.l.), while very few detachments occur below 3,000 m a.s.l., which suggests that the main triggering factor is not ubiquitous. The most affected altitudinal belt is 3200–3600 m a.s.l. (55 % of the total number of rockfalls in 24 % of the rockwalls located between 2,000 and 4,800 m a.s.l.), with warm permafrost. Moreover, the

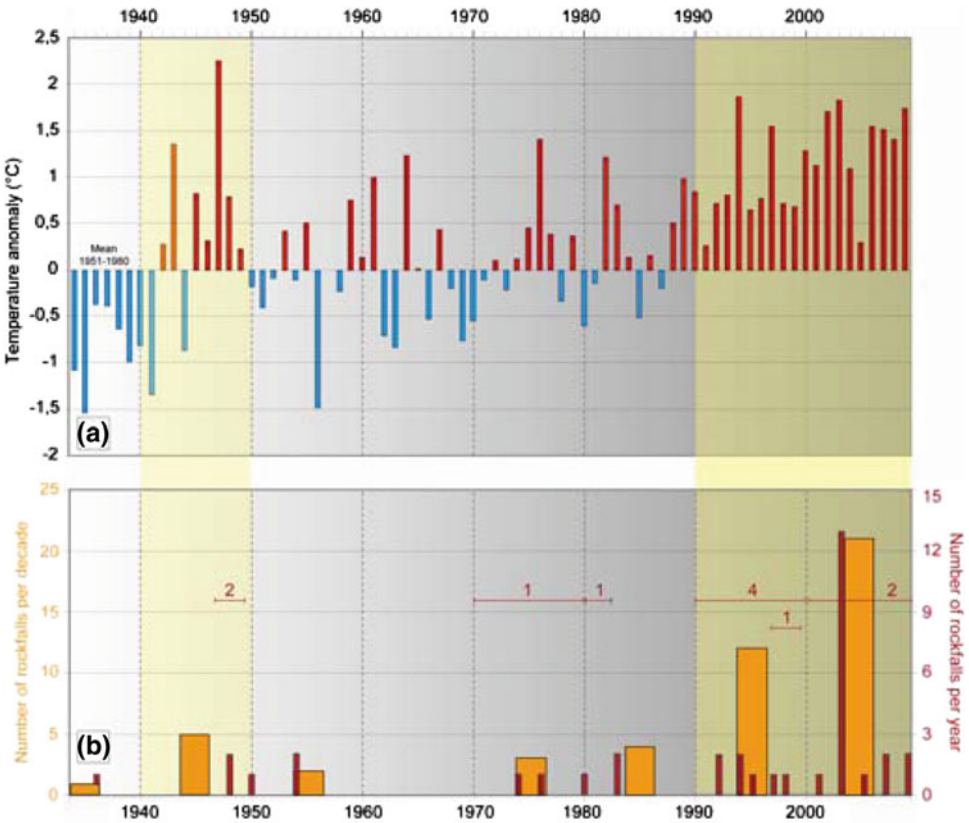

Fig. 81.2 Comparative evolution of climate in Chamonix-Le Bouchet (1,040 m a.s.l.) and rockfalls in the WD and on the NC. **a** MAAT anomaly compared to the mean 1951–1980; **b** number of rockfalls per decade and per year. Wide bars with number in B: rockfalls not precisely dated

hotter the summer is, the higher the scar elevation. The sharp contrast in scar elevation between north and south faces is also consistent with permafrost distribution (Noetzli et al. 2007; Noetzli and Gruber 2009). Finally, rockfall especially affects topography prone to permafrost degradation such as pillars, spurs and ridges (Noetzli et al. 2007).

81.5 Conclusion

Permafrost-induced rockfalls differ in space (volume) and time according to three main types of permafrost degradation: (i) vanishing of ice/snow cover generates very superficial rockfalls, due to the formation of an active layer; (ii) several meter thick detachments result from the deepening of the active layer; (iii) several decameter thick detachments may result from the permafrost degradation at depth by the slow rising rock temperature or the quick formation of thaw corridors.

The climatic control on rockfall in high mountain rockwalls, which involves the current permafrost degradation, means that this hazard should significantly grow during the twenty first century (see Huggel et al. 2010).

References

Allen S, Huggel C (2013) Extremely warm temperatures as a potential cause of recent high mountain rockfall. Global Planet Change 107:59–69

Deline P, Kirkbride M, Ravanel L, Ravello M (2008) The Tré-la-Tête rockfall onto the Lex Blanche Glacier, Mont Blanc massif, Italy, in September 2008. Geografia Fisica e Dinamica Quaternaria 31:251–254

Gruber S, Haeberli W (2007) Permafrost in steep bedrock slopes and its temperature-related destabilization following climate change. J Geophys Res 112:F02S18

Gruber S, Hoelzle M, Haeberli W (2004a) Rock-wall temperatures in the Alps: modeling their topographic distribution and regional differences. Permafrost Periglac Process 15:299–307

Gruber S, Hölzle M, Haeberli W (2004b) Permafrost thaw and destabilization of Alpine rock walls in the hot summer of 2003. Geophys Res Lett 31:L13504

Haeberli W, Huggel C, Kääb A, Zgraggen-Oswald S, Polkvoi A, Galushkin I, Zotikov I, Osokin N (2004) The Kolka-Karmadon rock/ice slide of 20 September 2002: an extraordinary event of historical dimensions in North Ossetia, Russian Caucasus. J Glaciol 50:533–546

Harris C, Davies MCR, Etzelmüller B (2001) The assessment of potential geotechnical hazards associated with mountain permafrost in a warming global climate. Permafrost Periglac Process 12:145–156

Hasler A, Gruber S, Beutel J (2012) Kinematics of steep bedrock permafrost. J Geophys Res 117:F01016

Huggel C (2008) Recent extreme slope failures in glacial environments: effects of thermal perturbation. Quatern Sci Rev 28:1119–1130

Huggel C, Salzmann N, Allen SK, Caplan-Auerbach J, Fischer L, Haeberli W, Larsen C, Schneider D, Wessels R (2010) Recent and future warm extreme events and high-mountain slope stability. Phil Trans R Soc A 368:2435–2459

Noetzli J, Gruber S (2009) Transient thermal effects in Alpine permafrost. Cryosphere 3:85–99

Noetzli J, Gruber S, Kohl T, Salzmann N, Haeberli W (2007) Three-dimensional distribution and evolution of permafrost temperatures in idealized high-mountain topography. J Geophys Res 112:F02S13

Oppikofer T, Jaboyedoff M, Keusen HR (2008) Collapse at the eastern Eiger flank in the Swiss Alps. Nat Geosci 1:531–535

Ravanel L, Deline P (2008) La face ouest des Drus (massif du Mont-Blanc): évolution de l'instabilité d'une paroi rocheuse dans la haute montagne alpine depuis la fin du Petit Age Glaciaire. Géomorphologie 4:261–272

Ravanel L, Deline P (2011) Climate influence on rockfalls in high-Alpine steep rockwalls: the North side of the Aiguilles de Chamonix (Mont Blanc massif) since the end of the Little Ice Age. Holocene 21:357–365

Ravanel L, Allignol F, Deline P, Gruber S, Ravello M (2010) Rock falls in the Mont Blanc Massif in 2007 and 2008. Landslides 7:493–501

Ravanel L, Allignol F, Deline P, Bruno G (2011) Les écroulements rocheux dans le massif du Mont-Blanc pendant l'été caniculaire de 2003. Géovisions 36:245–261

Ravanel L, Deline P, Lambiel L, Vincent C (2013) Instability of a highly vulnerable high alpine rock ridge: the lower arête des Cosmiques (Mont Blanc massif. Geografiska Annaler A, France). doi:10.1111/geoa.12000

Climate Change Impact for Spatial Landslide Susceptibility

82

Christine Gassner, Catrin Promper, Santiago Beguería and Thomas Glade

Abstract

Climate change is influencing future precipitation patterns. Especially the short intense rainfalls are expected to increase. Intense precipitation is regarded as one of the main landslide triggering factors. In order to investigate the likely impacts of precipitation change on spatial and temporal patterns of landslide susceptibility it is important to distinguish which type of rainfall has a major influence. Therefore, this study analyses the influence of precipitation maxima and antecedent rainfall conditions on landslide susceptibility. Other dynamic factors such as land cover change are excluded from the analysis. Logistic regression was applied to derive landslide susceptibility maps based on different climate change scenarios. Independent variables were several precipitation indices, current land cover maps and DTM derivatives (e.g. the slope gradient, aspect and curvature). The dependent variable was an inventory of shallow landslides for the period 1962–2007. The extrapolation of landslide susceptibility to the future was performed by applying the coefficients determined from past precipitation indices to those computed from future climate scenarios. The assumption herein is that conditions of the future that are similar to the past result in the same consequences. The study area Waidhofen/Ybbs is located in the alpine foreland in the province of Lower Austria. The predominant lithology is composed of calcareous rocks and Flysch. The land cover is mainly grassland and forest. The results show distinct changes in landslide susceptibility for some regions of the study area. Altered precipitation patterns intensify landslide susceptibility as well as enlarge susceptible areas.

Keywords

Climate change • Susceptibility • Landslides • Statistical modelling

82.1 Introduction

Landslides cause tremendous economic and human loss worldwide. Landslide susceptibility maps as powerful instruments have been established in many communities, as well as a base for hazard analysis. Main triggers of landslides are extreme precipitation, snowmelt and seismic activity (e.g. Tatard et al. 2010; Wieczorek and Glade 2005). Usually susceptibility maps are elaborated based on data from past events, serving as key to the future (Carrara et al. 1991). It is assumed that the same conditions of the past (regarding land use, climate, etc.) will prevail in the future. Therefore developing landslide susceptibility maps

C. Gassner (✉) · C. Promper · T. Glade
University of Vienna, 1010, Wien, Austria
e-mail: christine.gassner@univie.ac.at

C. Promper
e-mail: catrin.promper@univie.ac.at

S. Beguería
Consejo Superior de Investigaciones Científicas,
50059 Zaragoza, Spain

G. Lollino et al. (eds.), *Engineering Geology for Society and Territory – Volume 1*,
DOI: 10.1007/978-3-319-09300-0_82,

for different climate change scenarios is a challenging task. For this purpose precipitation is taken as an important proxy (Tatard et al. 2010), since heavy rainfall events have been recognized as a major triggering factor in the study area (Remaître et al. 2013; Schwenk 1992). Also damage reports in the building ground register (BGR) of the Geological Survey of Lower Austria refer to rainfall as a predominant triggering factor in that region (Petschko et al. 2010). The main objective of this study is to assess how landslide susceptibility may change as a consequence of changes in precipitation rates.

82.2 Study Area

The study area is located in the alpine foreland in Lower Austria. The district of Waidhofen/Ybbs covers an area of 130 km^2. Due to data availability the study area itself is approx. 112 km^2. The main land cover classes are grassland in the northern part and forest in the southern part. The building area is concentrated in the valley bottoms as well as dispersed farm houses and small settlements on the hilltops. The lithology is mainly comprised of Flysch and calcareous rocks. The smooth hills underlayed by the Flysch in the northern part are prone to slides. However, landslides also occur on the steep slopes in the southern part. The total distribution of different types of landslides in Waidhofen/Ybbs is described in Petschko et al. (2010).

Regarding the climate in Waidhofen/Ybbs, temperature as well as precipitation changes will be expected within the next hundred years. For this region Loibl et al. (2007) mentioned generally, that the change of the mean annual air temperature in the scenarios applied is around +2.2 °C. A stronger warming in autumn is expected while the warming in winter is estimated to be weaker. Precipitation is projected to decrease in summer and autumn for wide areas. In winter the region shows a more or less strong increase. The overall reduction of precipitation amount of around −11 %, the decreasing number of precipitation events with less than 10 mm/day, as well as the constant number of events exceeding 20, 30, 40 and 50 mm/day, indicates that the mean intensity is increasing while the frequency is decreasing. Consequently heavy rainfall conditions can be expected in the future (Loibl et al. 2007).

82.3 Data

Several datasets are considered in this research. Since the focus of this study is mainly on precipitation data and the landslide inventory, these will be explored in more detail.

82.3.1 Precipitation Data

The climate simulations for Europe were conducted with the Climate Local Model (CLM) based on the local model (LM) developed by the German Meteorological Service (DWD). The grid size is 18 km and rotating spherical coordinates are used. The model was driven in time steps of 75 s and the input from ECHAM/MPIOM was induced every 6 h. The timeframe is 1950–2100. Observed greenhouse gases were used until 2000 and then the SREX scenarios A1B and B1 were applied. For modelling at regional scale the grid size was downscaled to 1 km. The signal of the CLM and the LM were combined with dynamic, as well as with statistical methods (Loibl et al. 2007). The output of this meteorological model, the daily precipitation sum from 1.1.1948 to 31.12.2100 was integrated in our susceptibility model.

82.3.2 Landslide Inventory

The inventory was compiled by mapping landslides on orthophotos. The inventory is based on the years 1962, 1979, 1988 and a combination of 2005 and 2007. A total number of 133 events were mapped as polygons. As described in Petschko et al. (2010) there are several landslide inventories available for the study area. To get an approximate overview about the landslide occurrence in time, the inventory mentioned above was chosen. However this incorporates also clear limitations, as not all landslides can be seen due to e.g. land cover (forest).

82.4 Methods

The susceptibility modelling is based on a statistical logistic regression analysis (Atkinson and Massari 1998; Bell 2007; Van Den Eeckhaut et al. 2006). First the current susceptibility was investigated. Afterwards the computed model parameters were transferred to the parameters of future and past time periods.

82.4.1 Data Preparation

Particularly the climate data had to be prepared as model input. Originally the precipitation is based on precipitation sums in mm per day. In the study area most landslides are triggered by heavy rainfall events. In rare instances the triggering conditions relate also to high snow melt rates in spring or thunderstorms during summer (Schwenk 1992).

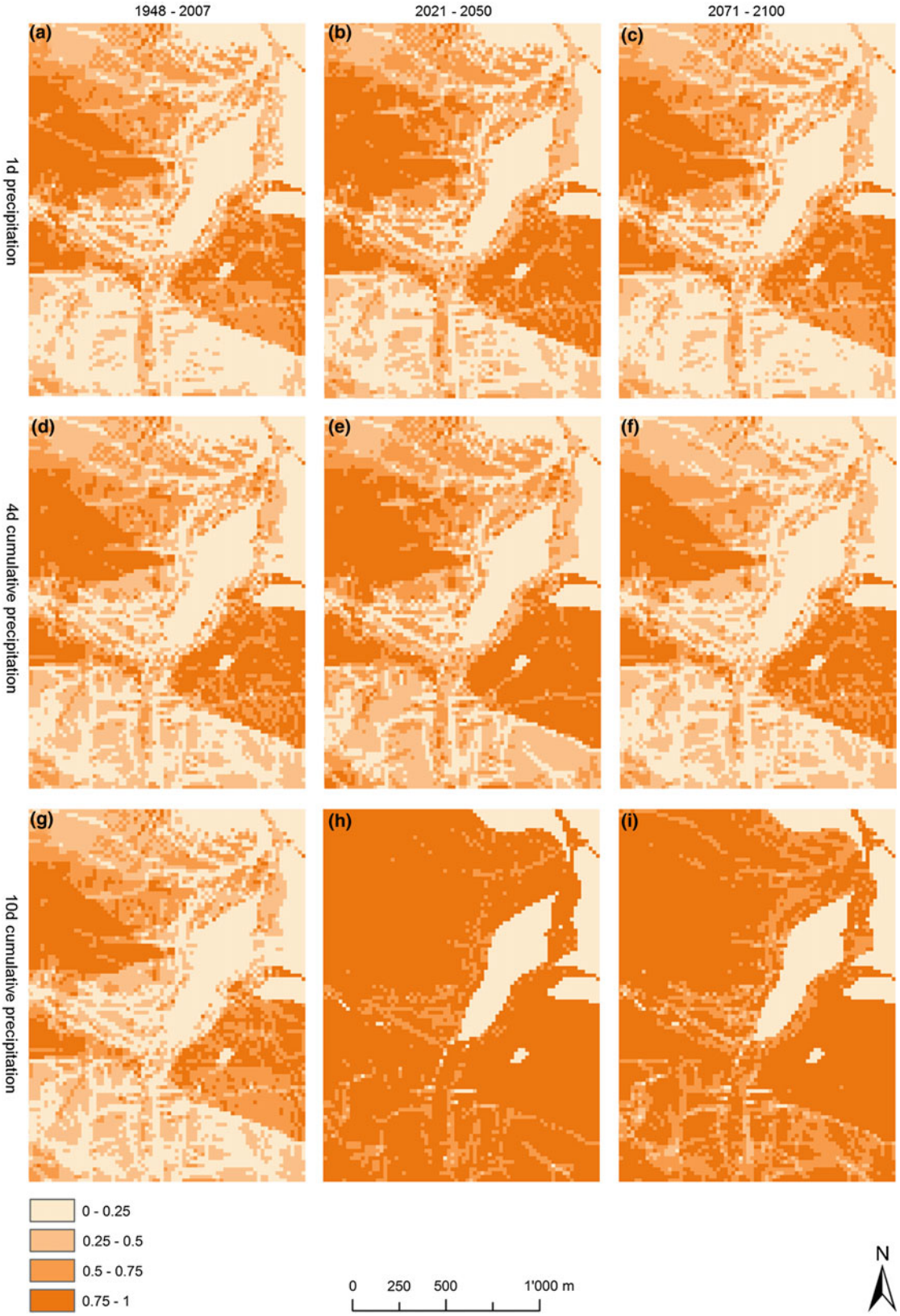

Fig. 82.1 Matrix with susceptibility maps at a small scale for modelled scenarios

Based on this and complemented by the analysis of Remaître et al. (2013) the focus of this study is on summer precipitation (June to August). For the current (1948–2007) and future (2021–2050 and 2071–2100) climate data the 90th percentile of the n-days summer precipitation is taken, where "n" defines a range between 1 and 10 days cumulative rainfall. All databases were aggregated to the land cover grid size of 20 m. Finally the input datasets for the models are the derivates of the DEM: slope gradient, aspect and plan curvature. Further the DEM, lithology, topographic wetness index, land cover (2005/2007) and the cumulative precipitation value (1, 4 and 10 days) were taken as explanatory variables. The landslides from the inventory of Riedler (unpublished project report 2013) represent the dependent variables.

82.4.2 Regression Modelling

For the modelling in R, a random sample is taken (n = 606). The sampling of slides and non-slides is equally distributed. The statistical modelling of present input parameters was conducted by stepwise backward variable selection in R, based on the Akaike's Information Criterion (Akaike 1974). The Area Under ROC curve is provided as validation criterion which will be calculated by a training and test dataset (Beguería 2006; Brenning 2005). The extrapolation of the landslide susceptibility to the future was performed by applying the regression coefficients for precipitation (time period 1988–2005) to the future scenarios. The static parameters (i.e. lithology, slope, etc.) remain the same. Precipitation data are replaced for each time step. For visualization and comparison the values in the susceptibility maps were divided into quartiles. A second validation marked the true positives of each scenario of the classified maps.

82.5 Results and Discussion

The output of the stepwise variable selection calculated for the best fitted models has always the same variable setting (lithology, land cover, plan curvature, wetness index, slope angle and precipitation data). The 7-, 8- and 9-day cumulative precipitation models have no precipitation data in their output setting. Further these models have smaller AUROC values. However the AUROC values of the test data differs slightly at a high level from 0.80 to 0.82. The extrapolation of landslide susceptibility to the future was performed by applying the regression coefficients to synthetic datasets with the original precipitation values replaced with those obtained from future climate scenarios. Figure 82.1 shows a matrix of the resulting susceptibility maps at a small scale. The maps aligned horizontally represent a precipitation scenario (1, 4 and 10 days cumulative precipitation). In vertical direction the maps show the time period (1948–2007, 2021–2050, 2071–2100). Generally the maps of the period 2021–2050 show the highest susceptibility whereas the period 2071–2100 are closer to the past period (1948–2007). The highest susceptibility classes rise in the second period significantly. Despite a small change in the pixel distribution, there is a significant increase in the landslide susceptibility. In the 10 day scenario (Fig. 82.1g–i) a surpassing susceptibility rise can be seen especially in the two highest classes. The interpretation of this increase in susceptible areas is dichotomous. Either the data set is biased or the extrapolation thresholds take effect on the visualisation or it indicate a tendency of high susceptibility for long term precipitation periods, such as 10 day cumulative precipitation periods. This and the 4 day scenario are the statistically best fitted models.

82.6 Conclusion

This study focuses on summer precipitation. It can be seen that the long term precipitation data show significantly different results. Hence the next step of analysis is to test the models for winter and spring respectively, to measure the influence of snowmelt processes on landslide susceptibility. Climate change driven changes in precipitation do influence landslide susceptibility. However more proxy data e.g. and cover, land cover change or other anthropogenic proxy indices can contribute to improve the significance of susceptibility models.

References

Akaike H (1974) A new look at the statistical model identification. IEEE T Automat Contr 19:716–723

Atkinson PM, Massari R (1998) Generalized Linear Modelling of susceptibility to landsliding in the Central Apennines, Italy. Comput Geosci 24:373–385

Beguería S (2006) Validation and evaluation of predictive models in hazard assessment and risk management. Nat Hazards 37:315–329

Bell R (2007) Lokale und regionale Gefahren- und Risikoanalyse gravitativer Massenbewegungen an der Schwäbischen Alb (Dissertation). Universität Bonn

Brenning A (2005) Spatial prediction models for landslide hazards: review, comparison and evaluation. Nat Hazards Earth Syst Sci 5:853–862

Carrara A, Cardinali M, Detti R, Guzzetti F, Pasqui V, Reichenbach P (1991) GIS techniques and statistical models in evaluating landslide hazard. Earth Surf Proc Land 16:427–445

Loibl W, Beck A, Dorninger H, Formayer H, Gobiet A, Schöner W (2007) Kwiss-Programm reclip: more research for climate protection: model run evaluation. Final report

Petschko H, Glade T, Bell R, Schweigl J, Pomaroli G (2010) Landslide inventories for regional early warning systems. In: Malet

JP, Glade T, Casagli N (eds) International conference 'Mountain Risks: Bringing Science to Society', 2010, Strasbourg, CERG Editions

Remaitre A, Wallner S, Promper C, Glade T, Malet JP (2013) Rainfall characteristics associated to the triggering of fast- and slow-moving landslides—a comparison between the South French Alps and Lower Austria. In: European Geoscience Union General Assembly, 2013, Vienna

Schwenk H (1992) Massenbewegungen in Niederösterreich 1953–1990. Jahrbuch der Geologischen Bundesanstalt 135:597–660

Tatard L, Grasso JR, Helmstetter A, Garambois S (2010) Characterization and comparison of landslide triggering in different tectonic and climatic settings. J Geophys Res: Earth Surf 115:F04040

Van Den Eeckhaut M, Vanwalleghem T, Poesen J, Govers G, Verstraeten G, Vandekerckhove L (2006) Prediction of landslide susceptibility using rare events logistic regression: a case-study in the Flemish Ardennes (Belgium). Geomorphology 76:392–410

Wieczorek G, Glade T (2005) Climatic factors influencing triggering of debris flows. In: Jakob M, Hungr O (eds) Debris flow hazards and related phenomena. Springer, Heidelberg

Analysis of Factors Controlling Landslide Susceptibility in the Aosta Valley (NW Italy): Relationship to Climatic and Environmental Changes

83

Mauro Palomba, Marco Giardino, Sara Ratto and Paolo Pogliotti

Abstract

Recent climate changes are evident, especially in alpine environments, and have implications for natural hazards. Geomorphological studies have been performed at a regional scale in the Aosta Valley to better understand the spatial distribution and frequency of landslides and to investigate their controlling factors. A comparison between areas with permafrost and the rest of the territory has also carried out. Landslides inventories, permafrost distribution and geothematic maps have been produced and integrated into a GIS system. The lowest values of landslides density have been observed within the permafrost areas with respect to the whole region. The frequency of landslides has increased slightly during the last few decades in high mountains areas, possibly due to climate warming.

Keywords

Slope instability • Permafrost • Controlling factors • GIS • Alps

83.1 Introduction

Recent changes in global climate are affecting both polar and alpine environments. The observed effects have significant implications for natural hazards and risks: reduced duration of snow cover, glaciers thinning and retreat, permafrost degradation and increased slope instability in high mountain areas.

Landslides are among the most hazardous geomorphic processes occurring in mountain areas, especially due to their unique geomorphic context: high relief, steep slope gradient and strong climatic variations over small areas. Improving knowledge of past and present slope instability is essential for better understanding their dynamics and developing reliable forecasts of slope performance under future climatic conditions.

We have carried out geomorphological studies in the Aosta Valley, a small alpine watershed in NW Italy, to better understand the spatial distribution and frequency of landslides and to investigate the main factors controlling instability. A comparison between high mountain areas, which are more affected by climate change, and the rest of the territory has been also performed.

83.2 Geological and Geomorphological Setting

The Aosta Valley is a major alpine valley drained by the Dora Baltea river. Elevations range from 400 m a.s.l., at the valley mouth on the Po Plain, to 4,810 m at Mont Blanc, the highest peak in the European Alps.

M. Palomba (✉) · M. Giardino
Earth Sciences Department, University of Torino, Torino, Italy
e-mail: mauro.palomba@unito.it

M. Palomba · M. Giardino
NatRisk, Interdepartmental Center for Natural Risks, University of Torino, Torino, Italy

S. Ratto
Centro Funzionale, Regione Autonoma Valle d'Aosta, Valle d'Aosta, Italy

P. Pogliotti
Arpa Valle d'Aosta, Valle d'Aosta, Italy

G. Lollino et al. (eds.), *Engineering Geology for Society and Territory – Volume 1*,
DOI: 10.1007/978-3-319-09300-0_83,

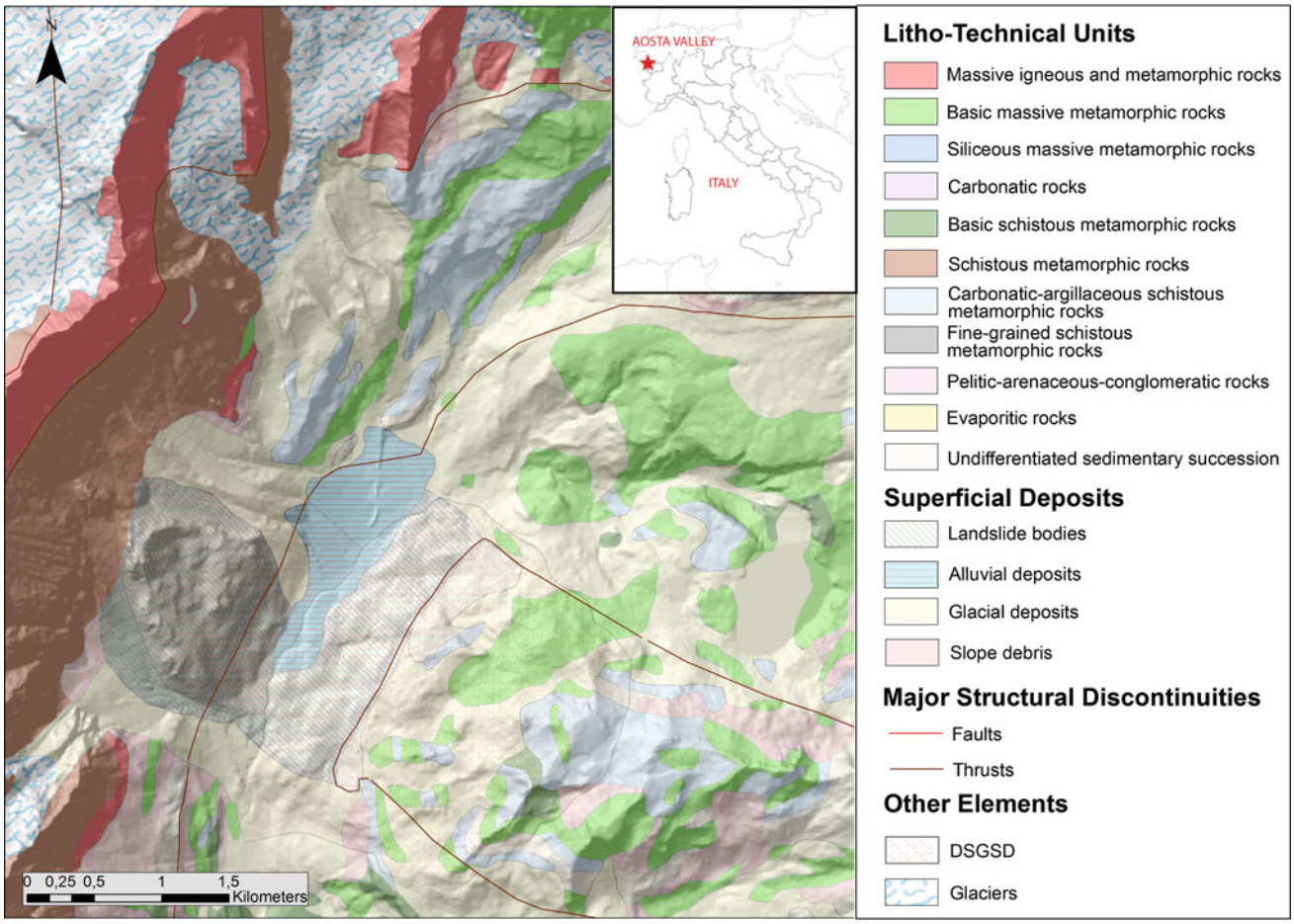

Fig. 83.1 A portion of the litho-technical map of the Aosta Valley in the Valtournenche district area

The Aosta Valley is located within the axial zone of the Western Alps, which consists of a tectonic stack of continental and oceanic metamorphic units.

Glaciers have played an important role both in eroding the landscape and leaving thick deposits of drift on valley floors. They also have indirectly influenced past and present-day slope dynamics.

Rivers have gradually deepened valleys in the Aosta watershed. Alluvial and alluvial and debris flow fans are widespread and many of them are active, as shown during recent heavy rainstorms (i.e. 13–16 October 2000).

A fundamental role in shaping the geomorphology of the region is played by gravitational phenomena, which range from simple shallow landslide to large slope instabilities. At least 18 % (580 km^2) of the watershed area has been affected by landsliding (Ratto et al. 2007).

83.3 Methods

The methodology used in this research is as follow:

- production of geo-thematic maps for the study of factors controlling instability;
- data collection and incorporation in a GIS system;
- data processing and statistical analysis.

First, slope and aspect maps, derived from a Digital Elevation Model, were produced to analyze topographic factors. Litho-structural data were incorporated by producing a new simplified litho-technical map, derived from regional geological maps (Carta Geotettonica della Valle d'Aosta; De Giusti et al. 2003). (Fig. 83.1). It is a map wherein rock masses originally classified according to their affinity towards the alpine tectonic units have been assembled depending on their litho-technical properties.

Table 83.1 Comparison between the landslide spatial distribution in permafrost areas and in the rest of the region

	Area	No. of landslides	Total landslide area	Landslide index (LI)	Percentage landslide affected areas
Permafrost areas	534.11 km^2	255	58.60 km^2	0.48	10.97 %
Rest of the region	3,261 km^2	3849	635.64 km^2	1.18	19.50 %

In addition to geo-thematic maps, we collected data on slope instabilities derived from landslides inventories (IFFI Project National Database, Regional "Catasto Dissesti") and added a potential permafrost distribution map layer (Permaclim model, Guglielmin et al. 2003; Alpine Permafrost Map, Boeckli et al. 2012).

The permafrost spatial distribution allowed us to identify two distinct sectors: one with permafrost and the other without permafrost. For each of these two areas, landslide spatial analysis was carried out, which allowed us to consider differences in the frequency, areal extent and types of landslide.

While processing the data, we calculated a "landslide index" (LI), represented by landslide density per parameter class (events/km^2), for each factors controlling slope instability taken in account; in particular, we considered topographic (slope and aspect) and litho-structural factors (lithology, spatial distribution of structural discontinuities and rock masses geomechanical conditions).

83.4 Analysis and Results

83.4.1 Spatial Landslide Distribution

The data analysis showed that there is less slope instability within permafrost areas than in the rest of the region, both in terms of LI and of the percentage of the total area affected by landslides: 0.5 events/km^2 and 11% versus 1.2 events/km^2 and 19 % (Table 83.1). Lower values of LI were observed also for almost all classes of the beforementioned factors of instability (slope, aspect, lithology).

The most common landslide typologies in permafrost areas are rock falls, followed by deep-seated gravitational slope deformations (DSGSD); in contrast, slides and flows are very rare. In terms of the mean areal extent of landslides, the calculated values in permafrost areas are higher for almost all landslide types; e.g. the mean areal extent of rock falls in permafrost areas is considerably greater, more than 40 % over that observed in the rest of the watershed.

83.4.2 Topographic and Litho-Structural Factors

There is a progressive decrease in LI values with increasing elevation. In contrast, slope gradient analysis showed a progressive increase in the LI values with increasing slope.

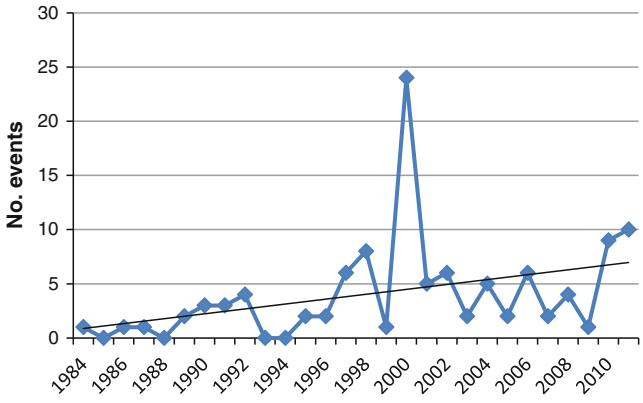

Fig. 83.2 Landslides temporal frequency above 2,000 m a.s.l. (1984–2011)

Examination of lithological factors reveals that, in permafrost areas, LI values are generally higher for competent lithological units, with the maximum values associated with "carbonatic/evaporitic" rocks. No appreciable variations in LI values were detected with distance from the main structural discontinuities.

83.4.3 Temporal Landslide Distribution

Our analysis of the temporal distribution of landslides yielded the following conclusions:

- Landslides frequency has increased in recent years, but this increase may be due to improved reporting of events, especially since 2000, following the establishment of extensive observation and monitoring networks and more widespread use of the new communication technologies.
- Only 16 % of the recorded events occurred above 2,000 m a.s.l., where rock falls and debris flows dominate, making it difficult to correctly assess landslide frequency in high mountain areas.
- A slight increase in landslides is evident during the past few decades above 2,000 m a.s.l., albeit with a large interannual variability (Fig. 83.2).

83.5 Discussions

Permafrost areas in the Aosta Valley have fewer landslides than the rest of the watershed. There are two possible explanations for this difference: (1) There is more awareness of slope processes at lower elevations, as a consequence of

the greater human presence there; (2) Permafrost increases the stability of rock and soil, resulting in fewer landslides at high elevations.

Both high LI on steep slopes and in areas of competent lithological units is expressed mainly in frequent rock falls, which occur on steep bedrock valley slopes.

Higher LI on north-facing slopes may indicate more efficient permafrost degradation, resulting in a greater number of landslides involving larger slopes' sectors.

The lack of data for high mountain areas prevent us from exactly quantifying the role of climate in the observed recent increase in landslides frequency in these areas. Nevertheless, this role has already been established in the Alps, as in the case of rock falls on the Mont Blanc Massif, where a good correlation between slope instability and warming in the past several decades has been established (Ravanel and Deline 2011). According to climatic model scenarios (IPCC 2013) a further increase of rock falls activity on steep high rock slopes can be expected in coming decades.

83.6 Conclusions

A better understanding of the spatial distribution of landslides and of the main factors controlling slope instabilities, both in permafrost areas and in the rest of the Aosta Valley watershed, has been achieved by this study. Increased landslides frequency and a complex response to climatic forcing have been observed at a regional scale; still, further data on landslides occurrence and improved knowledge on failure mechanisms are needed for high mountain sectors.

References

Boeckli L, Brenning A, Gruber S, Noetzli J (2012) A statistical approach to modelling permafrost distribution in the European Alps or similar mountain ranges. Cryosphere 6:125–140

De Giusti F, Dal Piaz GV, Massironi M, Schiavo A (2003) Carta geotettonica della Valle d'Aosta. Mem Sci Geol 55:129–149

Guglielmin M, Aldighieri B, Testa B (2003) Permaclim: a model for the distribution of mountain permafrost based on climatic observations. Geomorphology 51(4):245–257

IPCC (2013) Climate change 2013: the physical science basis. contribution of working group i to the fifth assessment report of the intergovernmental panel on climate change. Cambridge University Press, Cambridge (in press)

Ratto S, Giardino M, Giordan D, Alberto W, Armand M (2007) Carta dei fenomeni franosi della Valle d'Aosta, scala 1:100.000. Regione Autonoma Valle d'Aosta Assessorato Territorio, Ambiente e Opere Pubbliche. Aosta, Tipografia Valdostana

Ravanel L, Deline P (2011) Climate influence on rockfalls in high-Alpine steep rockwalls: the north side of the Aiguilles de Chamonix (Mont Blanc massif) since the end of the 'Little Ice Age'. Holocene 21:357–365

High Elevation Rock Falls and Their Climatic Control: a Case Study in the Conca di Cervinia (NW Italian Alps)

84

Marta Chiarle, Velio Coviello, Massimo Arattano, Paolo Silvestri and Guido Nigrelli

Abstract

One of the impacts of climate warming in recent years is the evident increase of the number of rock fall occurrences at high elevations. With few exceptions, these events have small magnitudes and thus are rarely reported and documented, even less so in the past. Therefore it is difficult to use a statistical approach to analyze of the relationships between climate warming and rock slope instability. On the other hand, it is often difficult to carry out a time analysis of meteorological conditions responsible for rock fall triggering, considering that very few automatic weather stations (AWS) are located in the areas and in the altitudinal range that are affected by cryosphere degradation (i.e. above c.a. 3,000 m elevation in the Alps), and that climatic conditions in high elevation environments are spatially and temporally variable. The present study addresses the above-mentioned issues through analysis of a series of small rock falls that occurred in the last 10 years on the Matterhorn and surrounding rock slopes. A specific focus is temperature: we present a preliminary analysis of the spatial and seasonal variability of the vertical temperature gradient in the Conca di Cervinia, where the Matterhorn is located, to illustrate the uncertainty in estimates of the thermometric conditions at high elevation rock fall sites.

Keywords

High-elevation rock walls • Stability • Climate • Italian Alps

84.1 Introduction

Rock slope stability at high elevations has been affected by climate warming, and the effects have become more evident in the past ten years (Gruber et al. 2004; Tamburini et al. 2013), even though the exact role of climatic factors (precipitation and especially temperature) is not easily assessed. In fact, it commonly is difficult to carry out a punctual analysis of meteorological conditions responsible for rock fall triggering, considering that very few automatic weather stations (AWS) are located in the areas and in the altitudinal range that are affected by cryosphere degradation (i.e. above about 3,000 m elevation in the Alps). The distance of the nearest AWS from the rock fall source, as well as the specific geographic setting (e.g. slope aspect), may introduce important differences between data registered by the AWS and the actual conditions that triggered the event.

M. Chiarle (✉) · V. Coviello · M. Arattano · P. Silvestri · G. Nigrelli
Consiglio Nazionale delle Ricerche, Istituto di Ricerca per la Protezione Idrogeologica, Strada delle Cacce, 73, 10135 Torino, Italy
e-mail: marta.chiarle@irpi.cnr.it

P. Silvestri
e-mail: paolosilves@gmail.com

G. Nigrelli
e-mail: guido.nigrelli@irpi.cnr.it

P. Silvestri
Dipartimento di Scienze della Terra, Università di Torino, Via Valperga Caluso, 35, Torino, Italy

G. Lollino et al. (eds.), *Engineering Geology for Society and Territory – Volume 1*,
DOI: 10.1007/978-3-319-09300-0_84,

Fig. 84.1 The Grandes Murailles ridge, on the *left*, and the Matterhorn south face, on the *right* (*Photo* Guido Nigrelli, June 26, 2013)

In addition, mountain environments are well known for their complex climatic patterns, which result in a high spatial and temporal variability of the actual values of climatic parameters (Beniston 2006).

The present contribution addresses this issue by presenting as a case study the Conca del Breuil-Cervinia in the Italian Alps.

84.2 Description of the Site

The Conca del Breuil-Cervinia is located at the head of the Valtournanche Valley (Aosta Valley, NW Italy). The most prominent peak is the Matterhorn (4,478 m), one of the highest peaks in the Alps, at the border between Switzerland and Italy. The two flanks of the Conca del Breuil-Cervinia have different morphologies due to the different geological units in which are carved. The right side (including the Matterhorn) of the Conca is formed mainly of gneisses and metagabbros, which give rise to high peaks and steep slopes (Fig. 84.1), while the left flank of the Conca is formed by the ophiolitic rocks, mainly calcshists. These slopes have been affected in recent years by several small rock falls.

In order to study the relationships between climatic parameters and rock slope stability, a monitoring system consisting of geophones and thermometers was installed in 2007 near the Carrel Hut (3,829 m) along the Italian climbing route to the Matterhorn, taking advantage of the previous experience gained in the field of the seismic monitoring of debris flows (Arattano et al. 2012; Occhiena et al. 2012; Coviello et al. 2014).

84.2.1 Documented Rock Fall Events

Rock falls are considered an important process in the geomorphological evolution of high mountains, yet they are rarely reported and documented, and they were even less reported in the past. Nevertheless, after the hot summer in the European Alps in 2003, awareness of the phenomena was raised, due to instabilities that have affected world-famous sites.

One of these events was the "Cheminée" rock fall, which occurred on August 18, 2003 along the Italian climbing route to the Matterhorn, just below the Carrel Hut, at an elevation of about 3,770 m. No one was injured but the route was blocked to climbers for a long period. This event was of particular scientific interest because a large ice lens was observed on the detachment surface. Other rock falls occurred on the Matterhorn Peak in the same summer: on August 4 a few tens of cubic meters fell along the same climbing route, but just above the Carrel Hut at an elevation of about 3,850 m. Earlier in the summer, on July 15 and 16, 1,000–2,000 m^3 of rock fell in two separate events on the Swiss side of the peak, at the base of the northeastern ridge known as the Hörnligrat, at an approximate elevation of 3,400 m; 84 climbers had to be evacuated (Hasler et al. 2012). Ice was observed along the failure plane shortly after the second rock fall. All these events occurred without significant precipitations. Finally, on October 8, 2003, a few hundreds m^3 of rock fell from the base of the Cresta De Amicis, on the eastern side of the Lower Tyndall Glacier (Pogliotti 2006).

The instability of these slopes continued in the following years (Coviello 2009). A rock fall occurred during heavy rain on July 18, 2005 on the Testa del Leone ridge, at an elevation of 3,715 m, impacting the Italian route to the Matterhorn. On July 25, 2006, a failure occurred on the west side of the Italian route to the Matterhorn at about 3,750 m of elevation forcing the evacuation of 24 climbers from the Carrel Hut. Finally, on August 28, 2009, several climbers were rescued because of slope instability along the Italian route to the peak, at an elevation of about 3,900 m (Fig. 84.2).

Fig. 84.2 **a** Rock fall on the Matterhorn in 1862 ("A cannonade on the Matterhorn"); **b** scar of the 2003 "Cheminée" rock fall, where ice was exposed; **c** rock fall in 2006 (*black circle*); the arrow points to the Carrel Hut (*Photos* courtesy of Lucio Trucco, Guide del Cervino)

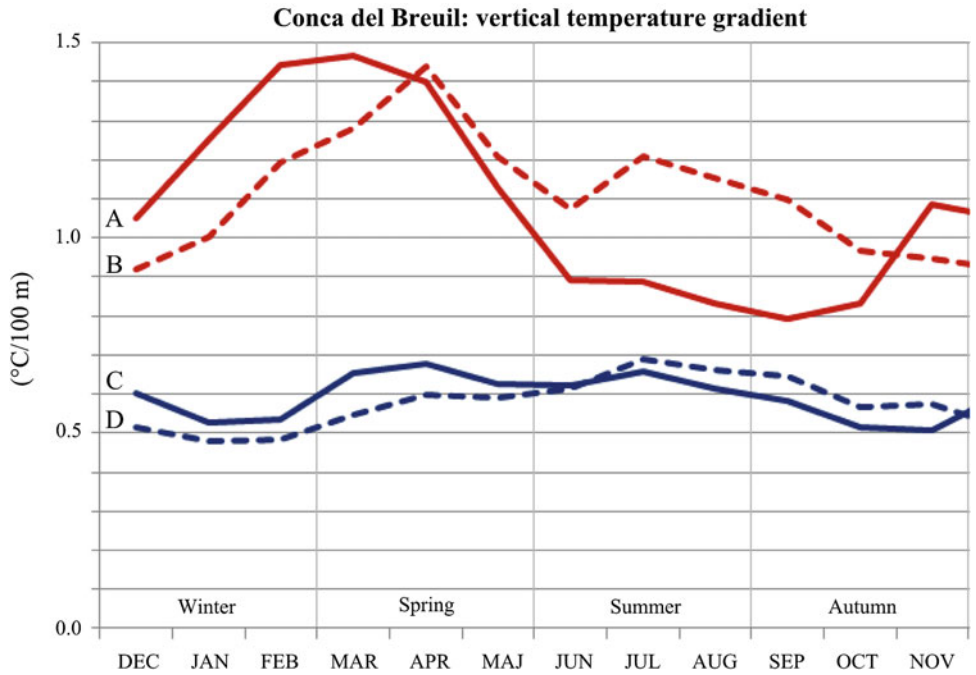

Fig. 84.3 Mean monthly vertical temperature gradient (*VTG*) in the Conca del Breuil, calculated using four pairwise comparisons. **A** daily maximum temperature VG (AWS 3,100 m a.s.l. vs. AWS 2,566 m); **B** daily maximum temperature VG (AWS 3,100 m vs. AWS 2,541 m); **C** daily minimum temperature VG (AWS 3,100 m vs. AWS 2,566 m); **D** daily minimum temperature VG (AWS 3,100 m vs. AWS 2,541 m). *Red* and *blue lines* identify, respectively, daily maximum and minimum temperature VG. *Continuous* and *dotted lines* indicate, respectively, the comparisons AWS 3,100 m vs. AWS 2,566 m and the comparisons AWS 3,100 m vs. AWS 2,541 m

84.3 Variability of the Vertical Temperature Gradient

In the case of most of the above-mentioned events, precipitation did not play a significant role in triggering the instability. Rather, the main trigger was warm temperatures. In order to assess the role of temperature in landslide initiation, series of data of rock temperature would be needed. Unfortunately, very few rock slopes are instrumented with temperature sensors. As a consequence, in most cases thermal conditions at the times of rock falls must be inferred from air temperature measures registered at meteorological stations. Usually, a standard vertical temperature gradient (VTG) is used to extrapolate temperatures

Table 84.1 Main characteristics of the automatic weather stations (AWS) at high elevation sites in the Conca del Breuil

	A	B	C	D
Temperature	Maximum	Maximum	Minimum	Minimum
Aggregation	daily	daily	daily	daily
Obs. period	2007–2012	2003–2012	2007–2012	2003–2012
Highest AWS	3,100 m a.s.l.	3,100 m a.s.l.	3,100 m a.s.l.	3,100 m a.s.l.
Lowest AWS	2,566 m a.s.l.	2,541 m a.s.l.	2,566 m a.s.l.	2,541 m a.s.l.
Distance	6.9 km	2.7 km	6.9 km	2.7 km

Data from these AWS were used to calculate the four mean monthly vertical temperature gradients (A, B, C and D; results are shown in Fig. 84.3)

at meteorological stations to rock fall sites. We quantified the errors that can be made by using a standard VTG instead of the actual temperature gradient by carrying out a detailed analysis of the VTG and of its variability in the Conca del Breuil over a short period. We calculated VTG values by comparing daily maximum and minimum temperatures at three weather stations located at elevations between 2,541 and 3,100 m (Table 84.1). Each comparison was based on data from two stations (Fig. 84.3). In addition, daily and monthly mean VTG values and seasonal means were calculated. Three main trends with increasing elevation are evident: (1) an increase in the mean VTG value, (2) an increase in the irregularity of seasonal cycles, and (3) a decrease in variability. The mean VTG is 0,51 ± 0,24 °C/hm, averaged between two elevation levels; the seasonal fluctuations are greatest in April, July and December.

84.4 Concluding Remarks

Although the relation between climate warming and increased high-altitude rock slope instability is now widely recognized, as is apparent from the series of rock falls documented at the Matterhorn in the past ten years, in many cases this relationship is difficult to prove. In fact, in most cases, thermal conditions at times of slope failures must be inferred from air temperatures measured at meteorological stations that are located at elevations and in topographical contexts that are different from those of the failure zone. The analysis presented here shows that the use of a standard vertical temperature gradient may be misleading; while minimum temperatures show a gradient very close to standard VTG and are stable during the year, maximum temperatures follow much higher VTG values that are highly dependent on the season and on the range of altitude that has been considered.

The study is still in progress. Future developments include the use of resulting VTG to extrapolate temperature conditions at failures sites, and the comparison of extrapolated values with rock temperatures that have been monitored in the vicinity of the Carrel Hut since 2005 (Pogliotti et al. 2008).

Acknowledgments The authors thank the Centro Funzionale della Regione Autonoma Valle d'Aosta, for the temperature data that have been processed for this work. The VTG analysis was carried out in the framework of a curricular stage of the University of Turin tutored by dott. G.Mandrone.

References

Arattano M, Marchi L, Cavalli M (2012) Analysis of debris flow recordings in an instrumented basin: confirmations and new findings. Nat Hazards Earth Syst Sci 12:679–686. doi:10.5194/nhess-12-679-2012

Beniston M (2006) Mountain weather and climate: a general overview and a focus on climatic change in the Alps. Hydrobiologia 562:3–16. doi:10.1007/s10750-005-1802-0

Coviello V (2009) Monitoraggio di emissioni acustiche in roccia nell'ambito di indagini relative agli effetti dei cambiamenti climatici sulla degradazione del permafrost alpino. Applicazione al sito della Capanna Carrel (3835 m), M. Cervino. Master thesis, Politecnico di Torino, p 209

Coviello V, Chiarle M, Arattano M, Pogliotti P, Morra di Cella U (2014) Monitoring rock wall temperatures and microseismic activity for slope stability investigation at J.A. Carrel hut, Matterhorn. In: Lollino G, et al (eds) Engineering geology for society and territory - Volume 1, Proceedings IAEG XII international congress. doi:10.1007/978-3-319-09300-0_57

Gruber S, Hoelzle M, Haeberli W (2004) Permafrost thaw and destabilization of Alpine rock walls in the hot summer of 2003. Geophys Res Lett 31:L13504. doi:10.1029/2004GL020051

Hasler A, Gruber S, Beutel J (2012) Kinematics of steep bedrock permafrost. J Geophys Res 117:F01016. doi:10.1029/2011JF001981

Occhiena C, Coviello V, Arattano M, Chiarle M, Morra di Cella U, Pirulli M, Pogliotti P, Scavia C (2012) Analysis of microseismic signals and temperature recordings for rock slope stability investigations in high mountain areas. Nat Hazards Earth Syst Sci 12:2283–2298. doi:10.5194/nhess-12-2283-2012

Pogliotti P (2006) Analisi morfostrutturale e caratterizzazione termica di ammassi rocciosi recentemente deglaciati. Master tesi, Università degli studi di Torino, p 191

Pogliotti P, Cremonese E, Morra di Cella U, Gruber S, Giardino M (2008) Thermal diffusivity variability in alpine permafrost rock walls. Proceedings of the 9th international conference on Permafrost. Fairbanks, 30 June–3 July, vol 2, pp 1427–1432

Tamburini A, Villa F, Fischer L, Hungr O, Chiarle M, Mortara G (2013) Slope instabilities in high-mountain rock walls. Recent events on the Monte Rosa East Face (Macugnaga, NW Italy). In: Margottini et al. (eds) Landslide science and practice, vol 3. doi:10.1007/978-3-642-31310-3_44

Landslides as Climate Indicators in Argentinean Central Andes (32° S)

85

Stella M. Moreiras

Abstract

Landslide occurrence in the Arid Central Andes of Argentina (~32°L) is strongly related to topography and climate conditions. In middle-low mountains and valleys, landslides are linked to summer rainfall, while in highest Andean areas, instability conditions are mainly caused by water saturation due to snow thawing in spring sessions. Besides, climate phenomena forced precipitation and slope instability in these mountain ranges. Warm phases of ENSO episodes are linked to more landslides activity in Frontal Cordillera, and a delayed signal of this phenomenon was found for Main Cordillera in the following warm session. Besides, no influence of ENSO is found for eastern Precordillera responding to Atlantic Anticyclone behavior.

Keywords

Mendoza river valley • International road to Chile • Triggering mechanisms • Slope instability

85.1 Introduction

Natural hazards and their socio-economic impact are strongly influenced by precipitation regime and climate phenomena in the Arid Central Andes. Summer rainstorms are a major forcing of landslide occurrence in the central Andes of Argentina; still many landslides have been also triggered by historical earthquakes (Ms >3.9). In the past century, at least 500 rainfall-induced events have affected the international road No 7 connecting Mendoza (Argentina) with Santiago (Chile) that runs along the valleys of Las Cuevas—Mendoza rivers (32°S) (Moreiras 2005, 2006). On summer 2013, intense summer storms triggered a large number of debris flows in the Andes of central Chile and Argentina. The main flows occurred along the Mendoza River valley (Argentina), where at least 50 debris flows caused serious disruption to the international road infrastructure and high impact to the population, mainly due to potable water supply cut offs to major cities (Moreiras and Sepúlveda 2013) (Fig. 85.1).

Over long-term periods, warm phase of ENSO has been linked to major landslides activity and above-normal river streamflows (Moreiras 2005; Sepúlveda et al. 2006; Araneo and Compagnucci 2008). However, the influence of the Pacific Anticyclone seems to be limited to high mountain areas of Main and Frontal Cordillera, while hill slope instability in eastern Precordillera is forced by humid periods of the Atlantic Anticyclone (Moreiras 2006). Analysis of synoptic situations for summer and winter precipitation events have recently been documented (Viale and Nuñez 2011; Viale and Garreaud 2013); however, the extreme precipitation processes leading to debris-flow is still lacking in the study area, and need investigations.

This paper updated previous published and new unpublished data about rain-induced landslides, climate phenomena influence and variability of this landslide links along the central Andes.

S.M. Moreiras (✉)
Consejo Nacional de Investigaciones Científicas y Tecnológicas (CONICET), Instituto Argentino de Nivología, Glaciología y Ciencias Ambientales (IANIGLA) – CCT Mendoza, Av. Dr Ruiz Leal s/n Parque, 5500 Mendoza, Argentina
e-mail: moreiras@mendoza-conicet.gob.ar

G. Lollino et al. (eds.), *Engineering Geology for Society and Territory – Volume 1*,
DOI: 10.1007/978-3-319-09300-0_85,

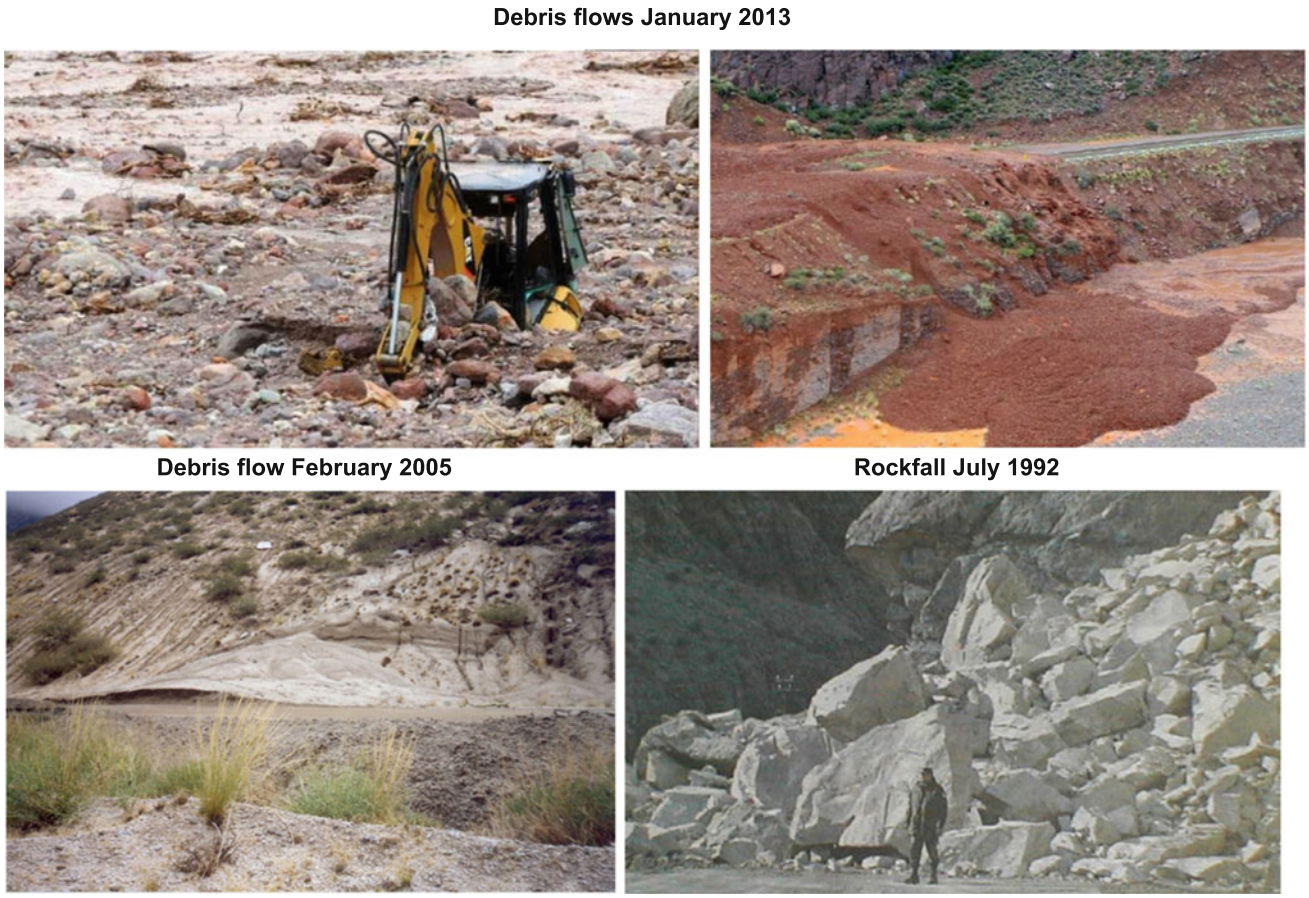

Fig. 85.1 Recent damaging events recorded along the Mendoza River valley induced by rainfall

85.2 Study Area

A high topography reaching up 7 km in altitude (eg. Aconcagua mount 6,958 m asl) and an arid climate characterized this portion of Arid Central Andes. However both parameters vary gradually longitudinal wise from west to east (Fig. 85.1). Topography of this mountain landscape decreases toward the eastern piedmont (700 m a.sl.) forcing precipitation behavior. While solid winter precipitation predominates in highest mountain areas, summer rainfall does in lower areas and valleys. Likewise, an average annual precipitation of 500 mm is measured in highest areas of the Andes diminishing until 200 mm in the Andes foothill where Mendoza city is established (Fig. 85.2).

At the latitude of study area, Central Andes are comprised by three different geological provinces in argentine territory: Main Cordillera, Frontal Cordillera and Precordillera, from west to east. The Main Cordillera, comprising highest peak such as Aconcagua, involves Cretaceous- Jurassic marine rocks and vulcanites. Permo-Triassic volcanic Choiyoi Group outcrops mainly in the Frontal Cordillera; while Paleozoic sedimentary rocks with Permian intrusives do in Precordillera range (Fig. 85.2). Even though, lithology and slope are main conditioning factors for landslide distribution, this link is not analyzed in this work.

85.3 Precipitation Threshold Value

Daily precipitation records suggest a relative low rainfall threshold for landslide occurrence in middle elevations ranging 1,500–2,700 m asl. during South Hemisphere summer (Dec–Feb). A daily precipitation range of 6.5–12.9 mm has been determined for landsliding in those locations not farer than 10 km of meteorological stations. This low threshold could be partially explained by the reduced amount of annual precipitation (200 mm) and the abundant generation of debris in these mountain areas. Errors in determination could have resulted from impossibility of determine intensity of rainfall. Mountain meteorological stations measure 24 h precipitation. Likewise, meteorological records are scarce in the region limiting a precise determination of the threshold values. Meteorological stations are located along

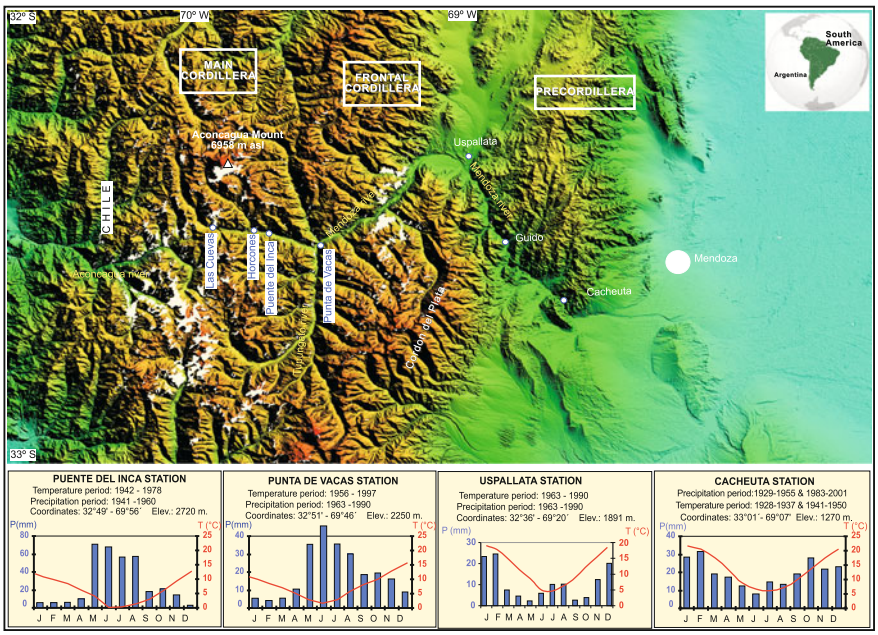

Fig. 85.2 *Above* Location of study area indicating localities and meteorological stations along the Mendoza River valley on a SRTM image. *Below* Meteorological records: mean monthly precipitation in blue bars and mean monthly precipitation temperatures in *red line*

the Mendoza river valley, but no data exists for remote highest areas where events have been reported as well.

Antecedent precipitation plays an important role. Mean values of accumulated rainfall reach to 28 mm whether a 5-day precipitation window previous to the landslide events is taken in account. In fact, 50 debris flows induced by rainfall during 2013 rainfall were associated to 29 days of weather anomalies in the Central Andes (Moreiras and Sepúlveda 2013) (Fig. 85.1).

Landslides are also associated to snowfall precipitation taking place during South Hemisphere winter in higher topography (See Fig. 85.2). Greater slope instability is recorded in the following spring period associated to snow thawing (Moreiras et al. 2012a, b).

Herein, landslide triggering factors (rain /snow thawing) and temporal distribution (summer/spring) varies in the different ranges of the Argentinean Central Andes. Whereas debris flows and rockfall induced by rainfall are clustered in summer periods (December–February) along the valleys and lowest areas; debris flows and debris avalanches are consequence of snowmelt in highest areas of Main and Frontal cordilleras during spring (September–November).

85.4 Climatic Anomalies Forcing

Temporal variations in landslide occurrence are related to climatic anomalies linked to the Pacific Anticyclone (ENSO). Humidity coming from western Pacific Ocean falls as snow in highest Andes areas and as rain in lowlands in winter season. During warm-phase of ENSO (El Niño) this precipitation is above mean annual records, while a precipitation below mean annual precipitation is recorded during cold phase (La Niña). As a consequence, landslides induced by rainfall are more common during El Niño years in the lower areas of the Frontal Cordillera, decreasing in number during La Niña events (Moreiras 2006). Likewise, severity of debris flows generated by snow melting in the Main Cordillera is greater in the following year of above mean annual precipitation linked to the warm phase of ENSO phenomena (Moreiras et al. 2012a, b).

The Precordillera range, located east of the Frontal Cordillera, does not seem to be sensible to Pacific Anticyclone. Not significant differences were recorded between cold-warm ENSO events in this range (Moreiras 2005, 2006). In contrast, slope instability in the Precordillera rises during wet periods induced by the incursion of wet air masses from the Atlantic Anticyclone during summer.

Uspallata valley looks like a natural limit of influence of Pacific and Atlantic Oceans. Rain induced landslides are associated to behavior of both Atlantic and Pacific anticyclones in surrounding areas of this valley. Instability on eastern hill slope of the Cordon del Plata range, just toward the South of Uspallata, does not reflect any increase during warm phase anomaly of the El Niño. However, impacts and damages of historical events occurred during this anomaly resulted significantly more severe (Páez et al. 2013).

85.5 Future Scenarios

Climate change might affect the timing, phase and variability of precipitation, along with the resulting damaging events. General circulation model simulations predict a

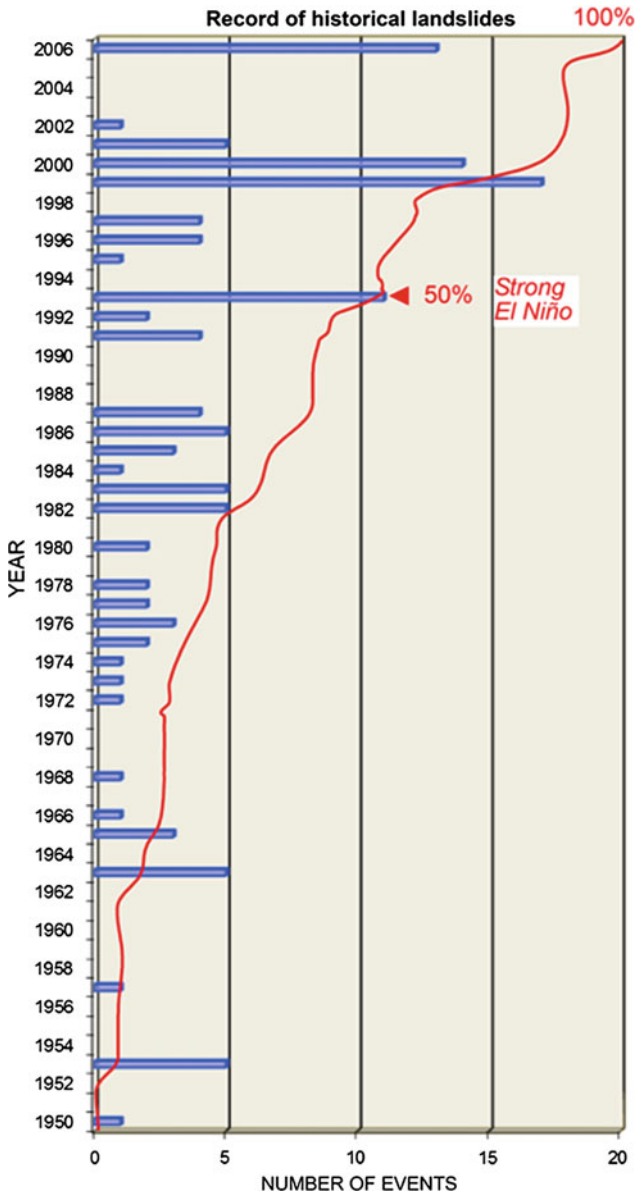

Fig. 85.3 Records of landslides induced by rainfall along the Mendoza River valley from 1950 to 2006. *Red line* indicates the percentage of total events

significant decrease in precipitation over the highest Andean region for the next decades (Cubasch et al. 2001), and an overall negative trend (Quintana 2004) has been observed in annual and winter rainfall over Central Chile. However rainfall anomalies took place in last decades, like in summer of 2013 triggering exceptional volume of material and summer of 2014.

Besides, a greater landslide activity is predicted as El Niño climate phenomenon may become more frequent and severe in the future (Diaz and Kiladis 1992; Yamaguchi and Noda 2006) suggesting a higher landslide hazard in the highest Central Andes involving Main and Frontal cordilleras. As well a positive trend for summer rainfall linked to Atlantic Anticyclone predicts more debris flows and rockfall in lower areas and valleys where main infrastructures and cities are established.

Elevation of the 0 °C isotherm as a response to global warming is forcing slope instability. Areas below 0 °C isotherm will be water–saturated and prone to mobilize. Rockfall and debris-flow records have increased during the last three decades due to both precipitation and temperature increases in the middle altitudes (Fig. 85.3).

These changes could significantly impact facilities, agriculture, water resources and natural ecosystems. In particular, the mountain areas of Central Chile and Argentina were affected by damaging debris-flows associated with extreme summertime and wintertime precipitation events (e.g. Sepúlveda and Padilla 2008; Moreiras and Sepúlveda 2013). Analysis of synoptic situations for summer and winter precipitation events have recently been documented (Viale and Nuñez 2011; Viale and Garreaud 2013); however, the extreme precipitation processes leading to debris-flow is still lacking in the study area.

However, the relationships between landslide occurrence in Main Cordillera, Frontal Cordillera, and Precordillera with climatic anomalies induced by the Pacific and Atlantic oceans respectively, suggest the possibility of using the landslide chronologies in the Central Andes as a geo-indicator of global climate change.

References

Araneo D, Compagnucci R (2008) Atmospheric circulation features associated to Argentinean Andean rivers discharge variability. Geophys Res Lett 35(L01805):1–6. ISSN: 0094-8276, doi:10.1029/2007GL032427

Moreiras SM (2005) Climatic effect of ENSO associated with landslide occurrence in the Central Andes, Mendoza province, Argentina. Landslides 2(1):53–59. doi:10.007/s10346-005-0046-4

Moreiras SM (2006) Frequency of debris flows and rockfall along the Mendoza river valley (Central Andes), Argentina. Special Issue Holocene Environmental Catastrophes in South America. Quat Int 158:110–121

Moreiras SM, Lauro C, Mastrantonio L (2012a) Stability analysis and morphometric characterization of palaeo-lakes of the Benjamin Matienzo Basin- Las Cuevas River, Argentina. Nat Hazards 62(2):593–611. doi:10.1007/s11069-012-0095-7

Moreiras SM, Lisboa S, Mastrantonio L (2012) The role of snow melting upon landslides in the central Argentinean Andes. Earth Surface and Processes Landforms. Special issue on Historical Range of Variability. Guest editors: Ellen Wohl and Sara Rathburn. doi:10.1002/esp.3239

Moreiras SM, Sepúlveda SA (2013) The high social and economic impact 2013 summer debris flow events in central Chile and Argentina. Bollettino di Geofisica Teorica ed Applicata 54(Supp. 2):181–184

Páez MS, Moreiras SM, Brenning A, Giambiagi LB (2013) Flujos de detritos-aluviones históricos en la cuenca del Río Blanco (32°55′-33°10′ Y 69°10′-69°25′), Mendoza. Revista de la Asociación Geológica Argentina 70(4):488–498

Sepúlveda SA, Rebolledo S, Vargas G (2006) Recent catastrophic debris flows in Chile: geological hazard. climatic relationships and human response. Quat Int 158:83–95

Viale M, Garreaud R (2013) Summer precipitation events over the western slopes of the subtropical Andes. Mon Wea Rev accepted

Viale M, Nuñez MN (2011) Climatology of Winter Orographic Precipitation over the Subtropical Central Andes and associated synoptic and regional characteristics. J Hydrometeorol 12(4): 481–507

Active Layer Detachment Slides and Retrogressive Thaw Slumps Susceptibility Mapping for Current and Future Permafrost Distribution, Yukon Alaska Highway Corridor

86

Andrée Blais-Stevens, Marian Kremer, Philip P. Bonnaventure, Sharon L. Smith, Panya Lipovsky and Antoni G. Lewkowicz

Abstract

The Yukon portion of the Alaska Highway Corridor traverses the discontinuous permafrost zone. Air-photos and high resolution satellite imagery were used to produce an updated landslide inventory (2013) that identified 1,600 landslides in the corridor. Landslide susceptibility models were developed for the corridor for two types of landslides triggered in permafrost, active layer detachment slides (ALD) and retrogressive thaw slumps (RTS), which comprise about 3 % of the inventory. A qualitative heuristic approach was used to combine data layers for slope, vegetation, surficial geology unit, slope aspect, and permafrost distribution. ALD and RTS susceptibility maps were produced for present day permafrost distribution and also equilibrium permafrost distribution resulting from air temperature increases of 1–5 °C. The resulting susceptibility maps indicate that with warming and reduced permafrost extent, there will be fewer zones of high susceptibility. The maps for warmer conditions give a "snapshot" of a potential decrease in zones of high landslide susceptibility, but they do not show the potential landslide occurrence as permafrost warms and thaws. It is expected that as permafrost warms and thaws, ALD and RTS activity will increase until conditions stabilize as permafrost disappears.

Keywords

Landslide susceptibility • Active layer detachment slides • Retrogressive thaw slumps • Permafrost • Climate change in the North

86.1 Introduction

A collaborative landslide inventory and susceptibility mapping project was conducted along the Yukon Alaska Highway Corridor (YAHC) to support risk assessments and decision making regarding linear infrastructure, including a proposed pipeline (Fig. 86.1). Portions of the pipeline route intersect critical geological regions and areas prone to geological hazards, such as landslides, earthquakes due to active faults, subsidence from thermo-karstic erosion, and permafrost degradation.

An earlier paper (Blais-Stevens et al. 2012a) presented derived results from a landslide inventory and qualitative heuristic landslide susceptibility models to create susceptibility maps for debris flows and rock falls/rock slides. This paper focuses on landslide susceptibility models developed

A. Blais-Stevens (✉) · M. Kremer · S.L. Smith
Geological Survey of Canada, 601 Booth Street, Ottawa, ON K1A 0E8, Canada
e-mail: ablais@nrcan.gc.ca

P.P. Bonnaventure
Department of Geography, Queen's University, Kingston, ON K7L 3N6, Canada

P. Lipovsky
Yukon Geological Survey, 300 Main Street, Whitehorse, YT Y1A 6E7, Canada

A.G. Lewkowicz
Department of Geography, University of Ottawa, Ottawa, ON K1A 0E8, Canada

G. Lollino et al. (eds.), *Engineering Geology for Society and Territory – Volume 1*,
DOI: 10.1007/978-3-319-09300-0_86,

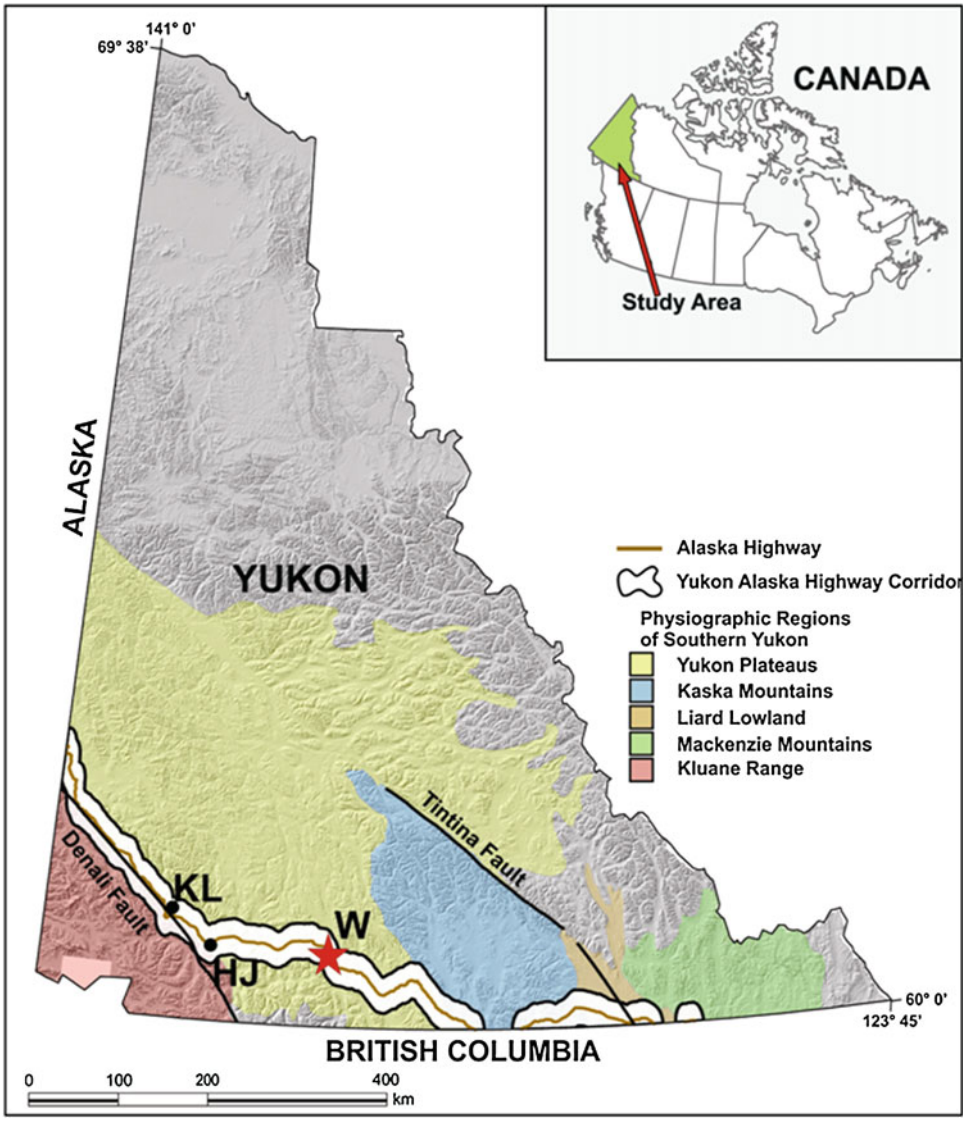

Fig. 86.1 Location map of the Yukon Alaska Highway Corridor. Also shown are the physiographic regions of southern Yukon. Inset map of Canada shows location of the study area in Yukon Territory. *W* Whitehorse, *KL* Kluane Lake, *HJ* Haines Junction

for landslides triggered in permafrost, such as active layer detachment slides (ALD) and retrogressive thaw slumps (RTS), using a high resolution permafrost probability model developed by Bonnaventure et al. (2012). The potential impact of climate warming was also investigated.

86.1.1 Physiographic Setting and Present-Day Climate

The YAHC crosses Shakwak Valley, Yukon Plateau, Kaska Mountains, Liard Lowlands, and Mackenzie Mountains (Fig. 86.1). Parts of the area are seismically active near the Tintina, Duke River and Denali faults (Huscroft et al. 2004; Seitz et al. 2009; Blais-Stevens et al. 2013). Elevation in the study area ranges from 527 m near Haines Junction to 2,799 m to the southeast of Kluane Lake. The minimum elevation of 527 m occurs about 15 km west of Haines Junction (Fig. 86.1). The YAHC is located east of the St. Elias Mountains, which contain icefields and Canada's highest mountains. Moreover, the corridor traverses the discontinuous permafrost zone (Heginbottom et al. 1995).

The study area is defined by a 40 km wide corridor along the Yukon Alaska Highway (Fig. 86.1). The total distance is approximately 873 km, which equals an area of approximately 22,000 km^2 excluding portions extending into British Columbia. The YAHC is a vital transportation route that encompasses about 85 % of Yukon's population and a pipeline route has been proposed to run roughly parallel to the highway.

The study area has a sub-arctic continental climate with long cold winters and short mild summers with relatively low humidity and low to moderate precipitation (Huscroft et al. 2004).

Table 86.1 Susceptibility index equation parameters and their assigned weights for active layer detachment slides (ALD) and retrogressive thaw slumps (RTS)

Parameters	ALD		RTS	
	Code	Weight (%)	Code	Weight (%)
Permafrost	P	25	P	25
Slope angle	S1	25	S1	20
Slope aspect	S2	10	S2	5
Surficial Geol.	G	25	G	25
Vegetation	V	15	V	15
Dist.to drainage		–	DD	10
Total		100		100

86.2 Methods

An updated landslide inventory was compiled from airphotos captured in the 1970s to mid-1990s (Blais-Stevens et al. 2010b) and high resolution satellite imagery (WorldView 2010). All data compilation related to creating thematic maps was carried out using ArcGIS V10.0 with Yukon digital topographic data (Environment Yukon Geomatics 2010). A qualitative heuristic approach modified from Soeters and van Westen (1996) and Blais-Stevens et al. (2012a, b) was used for each separate type of landslide.

The data layers that served as variables for ALD and RTS susceptibility models were assigned weights based on expert knowledge (modified from Lyle 2006 and compiled from six academic experts) as outlined in Table 86.1. Classes within each layer were rated based on the potential contribution to slope failure. The sum of the weighted variables represents a Susceptibility Index (SI) ranging between 0 and 1 for each pixel (30 × 30 m). SI units were subsequently divided into four (low to high) categories using even breaks. Development of the equations for the SI values was carried out independently from the landslide inventory.

The active layer detachment slide equation for the susceptibility model was:

$$SI = 0.25S1 + 0.1S2 + 0.25P + 0.15V + 0.25G \quad (86.1)$$

The equation for the retrogressive thaw slump susceptibility model was:

$$SI = 0.25P + 0.2S1 + 0.05S2 + 0.15V + 0.25G + 0.1DD \quad (86.2)$$

Parameters are defined in Table 86.1. Distance to drainage is a parameter included in the RTS model because they are initiated close to water bodies.

To investigate the potential impact of future permafrost conditions resulting from climate warming, susceptibility models were also developed using equilibrium permafrost distribution corresponding to air temperature increases of 1, 2, and 5 °C (Bonnaventure and Lewkowicz 2013).

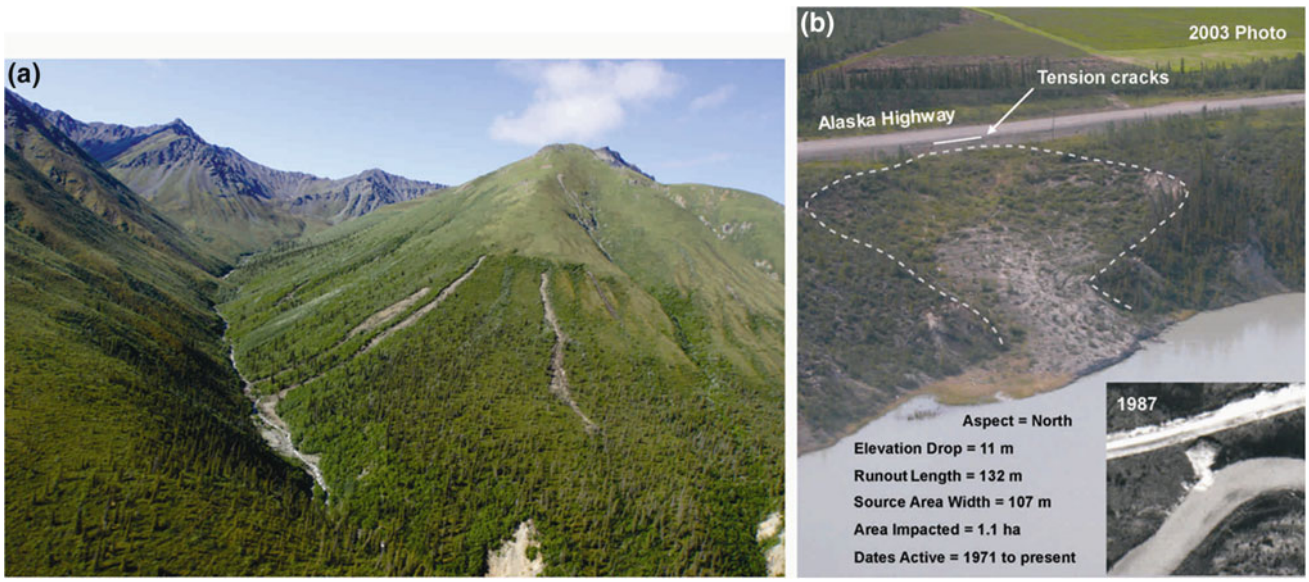

Fig. 86.2 **a** Active layer detachment slides (*ALD*) located north of Kluane Lake, on east south-southeast facing slope. **b** Retrogressive thaw slump (*RTS*) along the Alaska Highway near the Takhini River

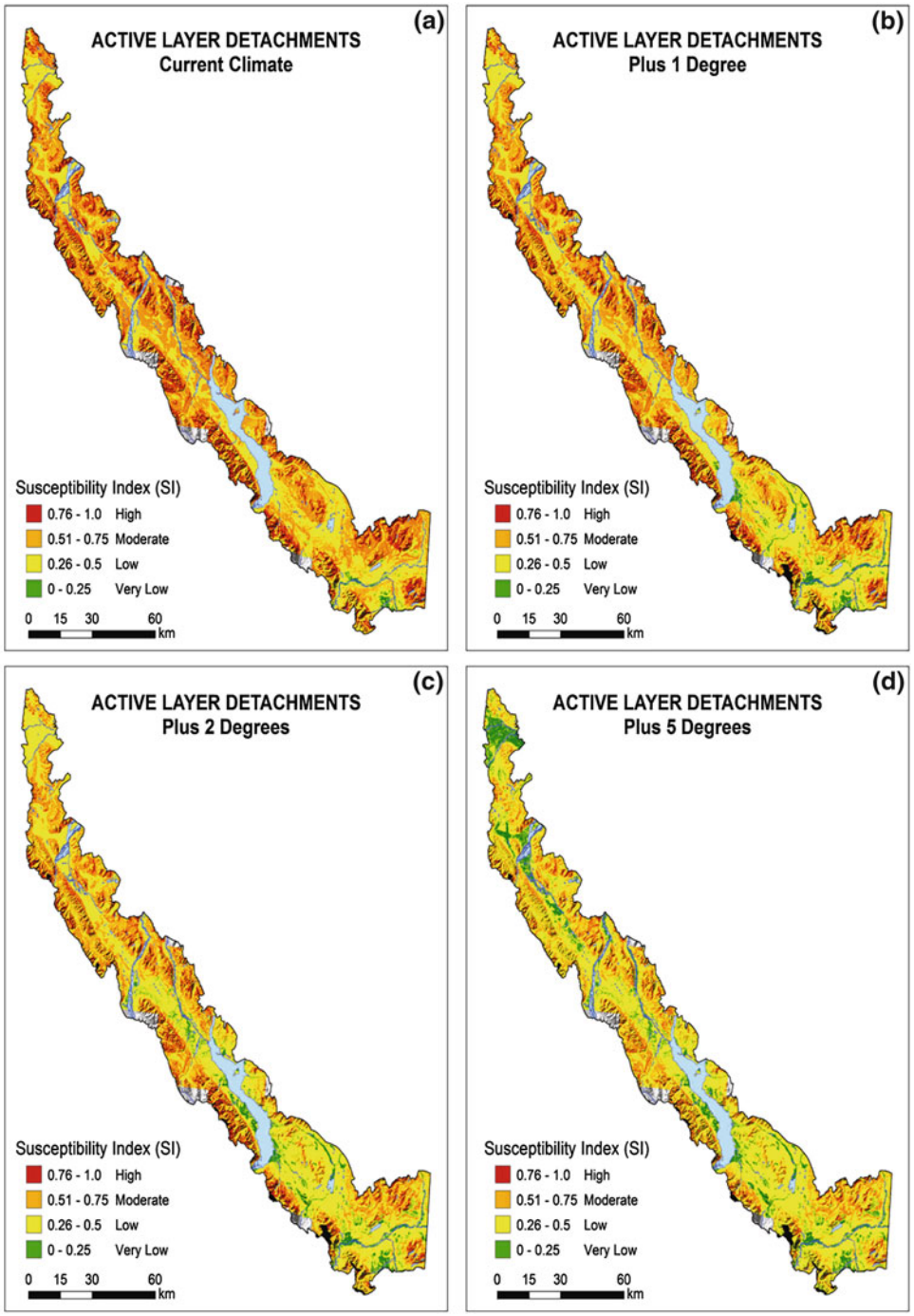

Fig. 86.3 ALD susceptibility maps of the northern section of the YAHC for present-day permafrost conditions (**a**) and for permafrost distribution associated with air temperature increases of 1 °C (**b**), 2 °C (**c**), and 5 °C (**d**)

86.3 Results and Discussion

86.3.1 Landslide Inventory and Susceptibility Models

The updated inventory from Blais-Stevens et al. (2010b) identified a total of 1,600 landslides, approximately 1 landslide per 16 km^2. Three percent of these are ALD and RTS (Fig. 86.2a, b, respectively) (Table 86.1).

ALD and RTS susceptibility maps were produced for present-day permafrost conditions. The ALD susceptibility map is shown in Fig. 86.3a. Validation of the ALD and RTS models is ongoing and has proven more difficult than with the debris flow and rock fall/rock slide susceptibility models (Blais-Stevens et al. 2012a) because there are fewer ALD and RTS in the inventory and they are often smaller therefore harder to detect in lower resolution imagery. This may also be partly due to the relatively short lifespan of

these features. ALD and RTS commonly occur in fine-grained sediments that can rapidly be vegetated, masking the slope disturbance. If permafrost has completely thawed and a state of equilibrium has been reached, there is no longer a potential for these types of landslides. The presence of the White River ash layer may also play a role in triggering of this type of landslide as it is almost always present at the initiation zone.

The ALD susceptibility associated with future permafrost distribution is shown in Fig. 86.3b, c and d. A similar pattern is projected for the RTS susceptibility. These demonstrate that with a warming climate and decrease in permafrost occurrence, there will be fewer zones of high susceptibility (red) and an increase in zones of low susceptibility (green). The maps give a "snapshot" indicating decreased landslide susceptibility under warmer climate conditions, but they do not include the preceding slope processes that will likely take place as permafrost warms and thaws. It is expected that during an increase in temperature, there will be more ALD and RTS activity as permafrost warms and thaws, until permafrost disappears and ground temperature conditions reach equilibrium.

86.4 Conclusion

An updated inventory along the YAHC revealed about 1,600 landslides were compiled of which, 3 % are ALD and RTS, triggered in permafrost. Landslide susceptibility models were created for ALD and RTS and susceptibility maps were produced considering present day permafrost conditions. Validation of the models was difficult due to the relatively small number of ALD and RTS in the inventory.

Using equilibrium permafrost distribution maps associated with air temperature increases of 1–5 °C, ALD and RTS susceptibility maps were created to project the potential impact of climate change on ALD and RTS activity. With a warming climate, there will be a decrease in zones of high susceptibility. However, areas that will likely be the most unstable are the ones transitioning from high to lower susceptibility, until equilibrium is reached.

Acknowledgments This research was supported by Natural Resources Canada, the Program for Energy Research and Development, University of Ottawa and the Yukon Geological Survey. Réjean Couture (Geological Survey of Canada) and an anonymous critical reviewer are thanked for their invaluable comments. Most points made will be addressed in a journal article.

References

Blais-Stevens A, Couture R, Page A, Koch J, Clague JJ, Lipovsky P (2010a) Landslide susceptibility, hazard and risk assessments along pipeline corridors in Canada. In Proc 63rd Can Geot Conf & 6th Can Perm Conf, Calgary, pp 878–885.

Blais-Stevens A, Couture R, Page A (2010b) Landslide inventory along the Alaska Highway Corridor, Geological Survey of Canada Open File 6654, DVD, Yukon

Blais-Stevens A, Lipovsky P, Kremer M, Couture R, Smith S (2012a) Landslide inventory and susceptibility mapping for the Yukon Alaska Highway Corridor. Proceedings of the 11th international and 2nd North American symposium on landslides and engineered slopes, Banff, vol 1, pp 777–782

Blais-Stevens A, Behnia P, Kremer M, Page A, Kung R, Bonham-Carter G (2012b) Landslide susceptibility mapping of the Sea to Sky transportation corridor, British Columbia, Canada- Comparison of two methods. Bull Eng Geol Env 71:447–466

Blais-Stevens A, Smith SL, Kremer M, Bonnaventure P, Lewkowicz AG, Lipovsky P, Duguay M, Ednie M, KochJ (2013) Geohazard information and permafrost characterization surveys along the Yukon Alaska Highway corridor. Geological Survey of Canada Scientific Presentation SP16

Bonnaventure PP, Lewkowicz AG, Kremer M, Sawada MC (2012) A permafrost probability model for the southern Yukon and northern British Columbia, Canada. Perm Per Proc 23:52–68

Bonnaventure PP, Lewkowicz AG (2013) Impacts of mean annual air temperature change on a regional permafrost probability model for the southern Yukon and Northern British Columbia, Canada. Cryosphere 7:935–946

Huscroft CA, LipovskyPS, Bond JD (2004) A regional characterization of landslides in the Alaska Highway corridor, Yukon. Yukon Geol. Surv. OF and CD-ROM 2004-18, p 65

Environment Yukon Geomatics (2010) http://www.geomaticsyukon.ca/data/datasets

Heginbottom JA, Dubreuil M-A, Harker PA (1995) Canada—Permafrost; National Atlas of Canada, 5th edn, Geomatics Canada, National Atlas Information Service, and Geological Survey of Canada, Ottawa Plate 2.1, (MCR 4177)

Lyle RR (2006) Landslide susceptibility mapping in discontinuous permafrost: Little Salmon Lake, central Yukon., Unpublished M.Sc. Thesis, Queen's University, Kingston

Seitz GJ, Haeussler PJ, Crone AJ, Lipovsky P, Schwartz DP (2009) Eastern Denali fault slip rate and paleoseismic history, Kluane Lake Area, Yukon Territory, Canada. AGU Fall Meeting, San Francisco, CA, Dec 15–19, 2008, poster T53B-1947

Soeters R, van Westen CJ (1996) Slope instability recognition, analysis, and zonation, Landslides. Investigation and mitigation. In: Turner AK, Schuster RL (eds)Transp. Res. Board, spec. rep. 247, Washington, D.C, pp 129–177

World-View (2010) https://www.digitalglobe.com/about-us/content-collection

Part IX

Role of Geosciences in Climate Change and Energy Security

Convener: Prof. T. N. Singh—*Co-convener*: V. Vishal

Climate change and energy security is an alarming question of the day where scientists from all domains are addressing the same to save the planet earth. Carbon sequestration is one of the promising solutions to the outstanding questions for mitigating the release of greenhouse gas emissions in the atmosphere. The target sink spaces may be deep saline aquifers, basaltic formations, depleted oil and gas reservoirs and coal seams. Detail investigation of these target spaces is vital for estimation of the storage capacity of reservoirs as well as to ensure long-term safe and stable disposal of gases for geologically significant periods of time. Papers are invited in this section for geotechnical investigation, engineering geology applications, cap rock integrity, permeability characteristics, rock response to stress and related areas.

Rainfall, A Major Cause for Rockfall Hazard along the Roadways, Highways and Railways on Hilly Terrains in India

87

M.K. Ansari, M. Ahmed, T.N. Rajesh Singh and I. Ghalayani

Abstract

Rock-falls are well-known phenomena, all over the world and every part of the hilly and mountainous regions suffered from rock-fall. Rockfall is a type of landslide in which a single rock or boulder or a small groups of independently moving rocks become dislodged from an exposed face or slope and move downward by means of some combination of sliding, rolling, bouncing or free-fall under the action of gravity. If the rock-falls occur in a remote area, they will be of scientific interest only. However, if they occur, along highways, roadways and railways then they are more than a spectacular natural process. Moreover depending upon where and when rock-falls occur, they have potentially serious consequences. The major cause of rockfall is heavy rainfall, though there are also other causes but rainfall shares the majority of the percentage directly or indirectly. There are too many reported rock-falls from India that have triggered exclusively by rainfall. Landslide along Jammu-Srinagar National Highway, caused by heavy rainfalls, triggered rock-fall at Bailey bridge across Panthal Nala and completely destroyed the bridge. The Malpa rock-fall tragedy of 18th August 1998 instantly killed 220 people and wiped out the entire village of Malpa on the right bank of river Kali with the tracking route, in the Kumaun Himalaya of the state of Uttarakhand. The most recent devastating accident related to rockfall along the railway occurred on 19th July 2012, when Chhatrapati Shivaji Terminus bound Kasara local, derailed from the tracks due to boulder on the track after the minor landslide caused by heavy rainfall for almost a week and was rammed by speeding Vaidarbha Express causing one death and 14 others injured.

Keywords

Rainfall • Rock-fall • Hazard

87.1 Introduction

Rockfall is a sub-type of the phenomena related to as landslide in which a single rock or boulder or a small groups of independently moving rocks become dislodged from an exposed face or slope and move downward by means of some combination of sliding, rolling, bouncing or free-fall under the action of gravity (Varnes 1978). In some cases rockfall refers to quantitative measure, describing small phenomena ranging from few m^3 up to 10,000 m^3 events,

M.K. Ansari (✉) · M. Ahmed · T.N. Rajesh Singh
Indian Institute of Technology Bombay, Powai, Mumbai 400076 Maharashtra, India
e-mail: mkhalidgly97iitk@gmail.com

M.K. Ansari · I. Ghalayani
Dar Al Handasah (Shair and Partners), Hadapsar, Pune 411003 Maharashtra, India

G. Lollino et al. (eds.), *Engineering Geology for Society and Territory – Volume 1*,
DOI: 10.1007/978-3-319-09300-0_87,

whereas rockslide is used to describe more than 1,00,000 m^3 and rock-avalanches can reach several millions m^3 (Dussauge-Peisser et al. 2002).

Keefer (2002) studied 40 worldwide historical landslides induced by earthquakes and found rockfalls to be the most abundant of all type of landslides, along with disrupted soil slides and rockslides. According to World Bank data, 95 % of the deaths occurred in developing and under-developing countries due to natural disasters i.e. earthquakes, landslides, floods and rock-falls etc. (Kremier and Arnould 2000).

87.2 Causes of Rockfalls in India

There are 14 causes of rockfall. Out of 14 causes, 6 are directly related to water, namely rain, freeze-thaw, snowmelt, channeled runoff, differential erosion, and springs and seeps. Also growth of tree roots in cracks is indirectly related to rainfall that can open the cracks and loosen the rock blocks. These seven causes of rock-fall together account for 68 % of the total falls (Hoek and Bray 1981) (Fig. 87.1).

India, due to its unique climatic conditions and its closeness to geodynamical active areas, has always been vulnerable to large number of landslides due to rainfall. The Himalayas, including Jammu and Kashmir, Himachal Pradesh, Gharwal, Kumaon, Sikkim, the Darjeeling Hills, Arunachal, and the Northeast hill, are where the rate of incidence of landslides/rock-falls range from high to very high whereas the Western Ghat, Nilgris hills have high to moderate landslides/rock-falls incidences and the Eastern Ghats, Vindhyan ranges show low landslides/rock-falls incidences (Kumar et al. 2008).

About 90 % of the landslides/rock-falls takes place during monsoon or winter rains in the Northwestern Himalayas. Moreover rains play a vital role in triggering most of the landslides in the Himalayan region. From south to north, the Indian Himalayas can be divided into different climatic zones, i.e. the tropical, sub-tropical, sub-temperate, semi-arid and arid zones. Precipitation also varies across these climatic zones. Monsoon precipitation is largely received south of the Higher Himalayas as compare to north Himalayas. Snow brought by winter rains at higher altitudes is more pronounced in the western region as compare to eastern region of Himalayas.

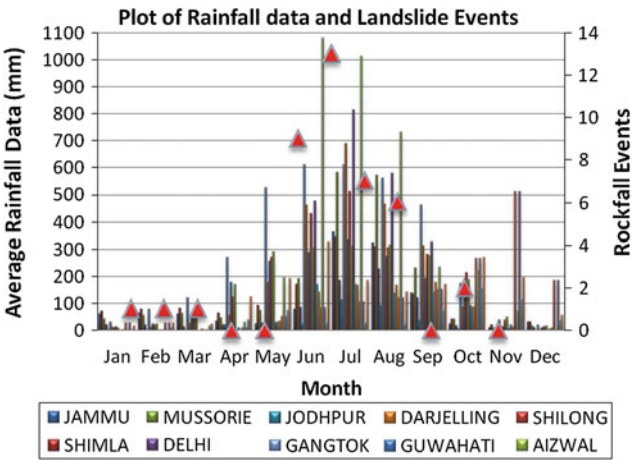

Fig. 87.2 Rainfall distributions for different states of India since 1901–2010. Also showing events of landslides/rock-falls (*Source* www.imd.gov.in)

The rainfall data plotted against the landslides/rock-falls events since 1901–2010 indicates that most of the landslides/rock-falls are associated to monsoon time during June-September (Fig. 87.2). However some of the landslides/rock-falls do occurs in the month of Dec–March (Table 87.1). Also Table 87.1 demonstrates some notable landslides/rock-falls events happened in the past in India.

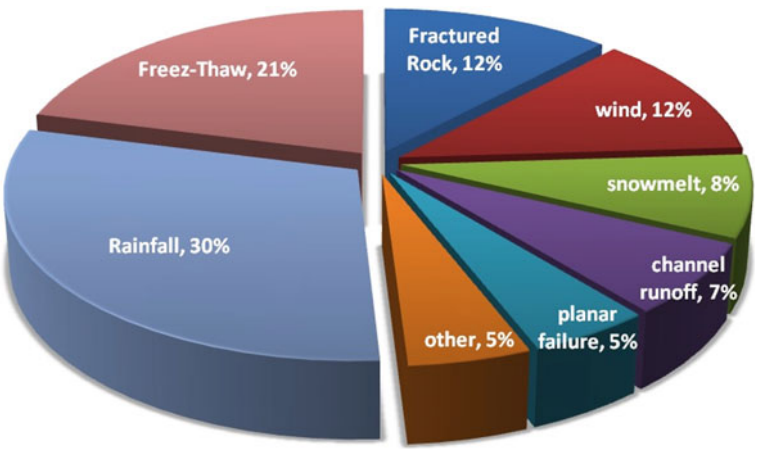

Fig. 87.1 Pie chart showing causes of rock-falls (modified after Hoek and Bray 1981)

Table 87.1 Summary of landslide and rock-fall events occurred in India (*Sources* GSI reports and newspaper)

Date	Location	Description
18th Sep. 1880	Sher ka Danda Hill, Nainital	Killed 143 people, closes route for over a week
14th Nov. 1893	Gona Slide of Birehi valley, Garhwal	Damming Birehi Ganges stream
Jul-67	Along Jammu-Srinagar N.H. (1A), J&K	Bailey Bridge across the Panthal Nala collapsed
20th July 1970	Hemlet of Belakuchi. Garhwal	Landslide: Killing 55 persons and flooding downstream up to the town of Srinagar
1st Aug. 1978	Naina Devi	143 structures, portion of the road, steps of the temple carried down slope over a distance of 150 m
19th Sep. 1989	Kaliasur landslide in Alaknanda valley	Landslide: route block more than a week
June-July 1983	Nashri Landslide, 131 Km from Jammu	Road Blockade lasting for 13 days
1st July 1993	Itanagar, Arunachal Pradesh	Landslide: 25 lives were lost
5th Aug. 1993	Kalimpong, West Bengal	Landslide: 40 lives were lost
18th Aug. 1998	43 km north of Dharchula, Malpa	221 people died
19th Aug. 1998	Okhimath tehsil, Haridwar-Badrinath road	101 life's perished, loss of valuable properties
01st Nov. 2001	Amboori Landslide, Kerala	Landslide: caused blockage of the route
23rd June 2003	Vaibhavwadi Train Crash, Sindhudrug	52 people killed in crash and over 1,000 injured
24th Sept. 2003	Bhagirathi valley, Dist. Uttarkashi	Damage to residential area, infrastructures
16th June 2004	Matsyagandha Express Train Crash	14 people killed and 62 injured
23rd Jan. 2008	Near Nathpa Jhakri Dam, H.P	Two persons were killed and one got injured
17th Mar. 2008	Nehru Kund Landslide, Kullu, H.P	5–6 persons. Size of falling block $\sim$400 m^3
18th July 2008	Saptashrungi Temple, Nashik, Maharashtra	Some damage caused to Temple. No casualty
11th June 2010	Haati Surey (NH 31A, Siliguri-Gangtok)	Rock-fall closes route for over a week
18th Sep. 2011	Jorethang-Rishi section (along River Rangit)	One person killed, one car damaged
27th June 2011	Dharasu, Chilyasan	1 child die, NH-108 block for 18 h
28th June 2011	Nalupani along National highway 108	3 cars damage and blockage of the routes
9th July 2011	Thrang	NH-108 closed for 8 h and 200 pilgrims struck
22nd July 2011	Vasuti taal	8 mountaineers died
22nd July 2011	Thrang along National Highway 108	More than 200 vehicles struck
12th Aug. 2011	Sainj	Road block for days, resulted in food scarcity
18th July 2012	Kasara Local Train Crash	One killed, 14 injured
10th June 2013	Devram Chawl, Wadala, Mumbai Maharashtra	People stuck in debris. No casualty reported
16th,17th July 2013	Uttarakhand (Rudrapyarag District Town)	Thousands of Pilgrims, local person buried under debris
25th July 2013	Malshej Ghat along NH-222, Maharashtra	Two men died, one vegetable carrier van trapped and highway blocked for more than a week

87.3 Rainfall and Landslides in India

Indian highways, roadways and railways in mountainous and hilly areas have been experiencing horrific landslide incidences that caused rockfalls. According to Sharda (2007), 15 % of the land area is affected by landslides. Every year during the monsoon period, several region of India is affected by landslides/rock-falls. Landslide along Jammu-Srinagar National Highway in July, 1967, caused by heavy rainfall, triggered rock-fall at Bailey bridge across Panthal Nala and completely destroyed the bridge. The Malpa rock-fall tragedy of 18th August 1998 instantly killed 220 people and wiped-out the entire village of Malpa on the right bank of river Kali with the tracking route, in the Kumaun Himalaya of the state of Uttarakhand.

A few notable examples of the recent rock-falls caused by rainfall are as follows;

The recent most casualty caused by landslide, induced by heavy rainfall, occurred on 16th and 17th June 2013 at Uttarakhand. According to Indian Meteorological Department (IMD), Uttarakhand received rainfall greater than 400 % from normal rainfall. These heavy rainfalls triggered

the landslide and the town of Rambara was totally washed away. Also thousands of pilgrims and local at Kedarnath town were buried under debris or flowed away by the flood caused by heavy rain.

On 25th July 2013, in the western part of India on NH-222 near Malshej Ghat, Maharashtra, rockfall triggered after the preceding day one week heavy rainfall. Giant boulders almost of two truck size, fell on two men, killing them and blocked the highway for almost a week. In a similar situation, rockfall occurred at Wadala area, Mumbai, Maharashtra. The rock-fall destroyed the house and buried it. However no causality was caused. This event too happened after very heavy rainfall.

Heavy rainfall on August 2012 in Uttarkashi was the source of flash flood and landslide that took the life of 31 peoples. Also thousands of pilgrims were trapped there due to wiped out roads. Not only has the Himalayan region suffered from casualties due to rainfall induced landslide but also northeastern part has been the witness of such type of casualties. In June 2012, the landslide triggered by heavy monsoon in Ri-Bhoi district, Meghalaya, blocked the NH-40. Also at the same district, on 26th July 2012, landslide killed two members of the family when the house was buried in the landslide. Rock-fall occurred after 18th September 2011 earthquake in Sikkim caused death to person and damage a car at Baluwakhani area.

Highways and roadways were not only affected by landslides and rockfalls in India, but railways too have history of landslides and rock-falls that caused loss of life's and property as well as economy. The most recent devastating accident related to rock-fall along the railway occurred on 19th July 2012, when Chhatrapati Shivaji Terminus bound Kasara local, derailed from the track due to boulder on the track after the minor landslide and was rammed by speeding Vaidarbha Express causing one death and 14 others injured. This is not only the case of railway accidents due to falling blocks/boulders on the railway tracks but also we have few more in the past viz. Vaibhavwadi train crash in June, 2003 (ExpressIndia 2003) and Karanjadi train crash in June, 2004 (People's Daily 2004).

87.4 Conclusion

The primary concern is to save the lives of the people living and/or travelling in rockfall prone areas. The number of death due to rock-falls is much smaller than the number of people died in stream and river and certainly much smaller than the number of people died in traffic accidents. However one big rockfall in wrong place at a wrong time, could cause dramatically increase in the number of death as describe in this article. At present, rockfall is a new filed in India and it needs more research for handling the problem related to rockfall. Due to this reason we are focusing on learning everything we can about rockfall using laser scanning, computer modeling, and monitoring of slope/cliff faces. Also efforts are being made to develop a relationship between rainfall and triggering mechanisms for rock-falls.

References

Dussauge-Peisser C, Helmstetter A, Grasso J-R, Hantz D, Desvarreux P, Giraud A (2002) Probabilistic approach to rockfall hazard assessment: potential of historical data analysis. Nat Hazards Earth Syst Sci 2:15–26

ExpressIndia (2013) http://www.expressindia.com/news/fullstory.php?newsid=22451

People's Daily (2004) http://english.people.com.cn/200406/17/eng20040617_146644.html.

Geological Survey of India (1992) The October 21, 1991 Uttarkashi Earthquake. In geological Survey of India. Special Publication No. 30, 212

Keefer DK (2002) Investigating Landslides caused by earthquakes—a historical review. Surv Geophys 23(6):473–510

Kremier A, Arnould M (2000) World Bank'srole in reducing impacts of disasters. Nat Hazards Rev 1(1):37–42

Kumar VK, Lakhera RC, Martha TR, Chatterjee RS, Bhattacharya A (2008) Analysis of the 2003 Varunawati Landslide, Uttrakashi, India using earth observation data. Environ Geol 17:247–255

Sharda YP (2007) Landslide studies in India, glimpses of geosciences research in India 99–101

Varnes DJ (1978) Slope movement types and processes. In: Schuster RL, Krizek RJ (eds) Landslide, analysis and control. Transportation Research Board, National Research Council, Washington, D.C., pp 11–13

A Preliminary Cost Estimation for Short Tunnels Construction Using Parametric Method

88

Ahmad Reza Sayadi, Jafar Khademi Hamidi, Masoud Monjezi and Meysam Najafzadeh

Abstract
Cost estimation is one of the most critical tasks in pre-feasibility studies and planning of tunnel construction projects. This paper presented a cost estimation model for excavation and support of short tunnels using uni-variate (UVR) and multi-variate regression (MVR) techniques. Hence, a database consisting of two explanatory variables including RMR and tunnel depth along with tunnel support and excavation costs was compiled from 12 tunnel sections in the North-West of Iran. Mean absolute error rates of 13 and 11 %, respectively obtained from UVR and MVR analyses provide promising initial results of relation between rock mass characterization and construction costs in the phase of pre-feasibility study. However, an extended database is required to extend the finding of this study to develop a universal model.

Keywords
Short tunnels • Cost estimation • Regression analysis • Drilling and blasting

88.1 Introduction

Rock tunnels as the most appropriate underground structures for traffic works in mountainous areas are generally constructed by using two conventional (drilling and blasting) and mechanized excavation methods. Feasibility studies, design and selection of tunneling method and finally project completion are a function of several factors but above all, of construction costs. Several models have been developed in this field. One of the first systematic studies is that of California department of water resources in which the diameter and geological conditions of the tunnel are used as cost effective parameters (Lamb 1971). This model presented in 1961 is only applicable to limited areas of the United States and only for water transfer tunnels which are constructed by conventional method. In 1971, a computer model was developed based on previous models (Bledsoe 1970). In 1976, a tunnel cost model (TCM), as a computer simulation system for estimating the cost and time of building stone tunnels was proposed (Moavenzadeh and Markow 1976). In 1999, a time and cost estimation model was developed for both mechanized and conventional methods on the basis of construction data of 250 km of road tunnels in Norway and some other countries (Bruland 2000). In another study in 2006, a model was presented on the basis of 149 cases of 23 sections of 42 km of dug tunnels in Greece between 1988 and 2004 (Petroutsatou et al. 2006). Another cost estimation model of urban subway system in Turkey was presented in 2009 (Sonmez and Ontepeli 2009). Gunduz et al. (2011) estimated the costs of light rail transport systems (LRT) and metro using parametric method. Most recently, Rostami et al. (2013) estimated the costs of tunneling based on multivariate

A.R. Sayadi (✉) · J.K. Hamidi · M. Monjezi
Academic Member, Tarbiat Modares University, Tehran, Iran
e-mail: sayadi@modares.ac.ir

M. Najafzadeh
Msc Student, Tarbiat Modares University, Tehran, Iran

G. Lollino et al. (eds.), *Engineering Geology for Society and Territory – Volume 1*,
DOI: 10.1007/978-3-319-09300-0_88,

Table 88.1 Descriptive statistics of gathered data

	Overburden height (m)	Length (m)	RMR	Excavation unit cost (million IRR/m)	Rock support unit cost (million IRR/m)	Total unit costs (million IRR/m)
Minimum	24	111	35	22.34	24.06	51.97
Mean	54	325	46	23.7	26.21	54.98
Maximum	92	540	61	23.9	28.95	58.82
Standard deviation	25	74	9	0.56	0.16	0.23

statistical analysis of data from 272 tunneling projects in the U.S. and Canada.

The effective factors on tunnel cost depending on the type of tunnel and circumstances may be classified as follows:

1. Geomechanical parameters, geology and geological hazards within the tunnel path: compressive and tensile strength of rock material, the height of overburden, rock mass classification systems such as the rock quality index (RQD), rock mass rating (RMR), rock mass quality (Q) and geological strength index (GSI), weathering of rocks, fault areas, groundwater, the percent of abrasive minerals such as quartz, the in situ stress, wall strain and tunnel roof (Bledsoe 1970; Bruland 2000; Petroutsatou et al. 2006);
2. Technical parameters of tunnel: tunnel shape, length and size, cross-section, slope and curve (Lamb, 1971; Moavenzadeh and Markow 1976; Rostami et al. 2013);
3. Economic parameters: methods of financing, exchange rate, inflation rate (Bledsoe, 1970; Rostami et al. 2013);
4. Management parameters: executive experience of managers, human resource skills, support and logistics.

In this research, the main purpose is to provide a reliable early cost estimating model for short tunnels which are constructed by drilling and blasting method. This model is developed by using univariate (UVR) and multivariate regression (MVR) techniques.

88.2 Data Structure

The dataset consists of 12 records from 12 tunnel sections along the main path of Shahriar dam in Eastern Azerbaijan province of Iran, including tunnel length and depth, RMR value for each section, excavation and support costs. These tunnels have been constructed using conventional drill and blast method. The cross section of each tunnel is horseshoe-shaped. The tunnels vary in length from 111 to 540 m. This range of tunnel length is mainly associated with short tunnels. Costs are based on prices of fourth quarter of 2009 in Iranian Rial (IRR) currency. At this period, one US dollar equal to about IRR 10,000. Descriptive statistics of variables in the database and input parameters for generated models is summarized in Table 88.1.

As seen in the Table, the RMR changes from 35 to 61, indicating that the tunnels are mostly excavated in fair rock masses. The height of overburden has a range from 24 to 92 m, showing that the tunnels are shallow.

88.3 Methodology

Various methods have been proposed for cost estimation models in construction practices in mining and civil engineering. In the pre-feasibility and feasibility levels, parametric methods are commonly used. In this method, the correlation between actual costs and other system variables which have technical or economic nature have been studied, and one or more cost estimation relationship (CER) has been presented (Evans et al. 2006). Various approaches can be used in this context, but preceding research shows that the regression technique because of strong mathematical basis and ease of use of the obtained cost function, is very common (Mason and Smith 1997; Sayadi et al. 2011, 2012).

The structure of the proposed model is dependent on previous experiences in cost modeling as well as statistical considerations of data and the results of validation functions. In this study, a variety of cost functions as indicated in Eq. (88.1), because of its widespread use in the other models of cost estimate, have been evaluated. Here, Y represents the cost and x is the explanatory variable.

$$\begin{aligned} Y &= ax^b \\ Y &= ae^{bx} \\ Y &= ax + b \end{aligned} \tag{88.1}$$

The general form of the multivariable regression function is linear polynomial as shown in Eq. (88.2). In this equation, Y and x denote the cost and independent variable, respectively, c_0 is intercept, c_1 to c_n are coefficients of each independent variable, and ε_0 is residual error. However, other functions including logarithmic and exponential ones used for modeling resulted in unacceptable estimates compared to linear polynomial equation. The statistical software package Statistica Release was used for making multivariate models.

$$Y_i = c_0 + c_1x_1 + c_2x_2 + \cdots c_nx_n + \varepsilon_i \tag{88.2}$$

Table 88.2 Specification of univariate regression results

	Function $Y = ax + b$		Function $Y = ax^b$		Function $Y = ae^{bx}$	
	Support	Excavation	Support	Excavation	Support	Excavation
R^2	0.66	0.65	0.69	0.67	0.73	0.7
RMSE	$10^5 \times 7.15$	$10^5 \times 3.11$	$10^5 \times 3.26$	$10^5 \times 3.25$	$10^5 \times 3.02$	$10^5 \times 1.25$
a	$-10^5 \times 1.61$	$10^4 \times 5.18$	$10^7 \times 1.87$	$10^7 \times 1.57$	$10^7 \times 2.46$	$10^7 \times 2.07$
b	$10^7 \times 3.26$	$10^7 \times 2.07$	0.14017	0.1018	−0.00617	0.00218

To evaluate the overall significance of the model, F-test method, t and p values are applied. In the F-test, the hypothesis of being zero of all regression coefficients is evaluated. Accordingly, significance of each explanatory variable is analyzed with t-test. In the t and F tests, basis is numerical comparisons which are defined in the significance level and considering degrees of freedom, desire regression is obtained from relevant table. But the simplest and fastest way to accept or reject the premise of the studied hypothesis is the p value.

For validation of the developed models, two methods have been applied. In first step, each function's performance is measured by the mean absolute error rate (MAER) [18]. In this method, the mean difference between actual and estimated costs is assessed based on a percentage of the actual costs. This value can be calculated using Eq. (88.3) (Kim et al. 2004), in which *Ce* is the estimated tunnel costs, C_a is the actual tunnel costs (from the database) and n is the number of data used in regression model.

$$MAER = \frac{\sum\left(\frac{Ce-Ca}{Ca}\right) * 100}{n} \tag{88.3}$$

In the second method, the suitability of MVR is evaluated using the residual analysis.

88.4 Regression Analysis for Unit Cost Estimation

88.4.1 Explanatory Variables

Since in planning phase of a tunneling project, access to all parameters affecting the costs is very difficult and sometimes impossible, the parameters with the most influence and easily accessible are selected. These parameters include RMR classification system and the height of overburden. Since all the tunnel sections have similar cross section, the parameter of tunnel diameter was excluded from the independent variables set.

88.4.2 Univariate Regression

Different mathematical functions, as indicated in Eq. (88.1), have been examined by using RMR as the explanatory variable for unit cost estimation of support installation and excavation (Table 88.2). Among all the functions tested, the function in the form of cost = (ae^{bx}) showed more consistency with the data, given to the high R^2 and low RMSE. Here, constants a and b are obtained by regression analysis.

Finally, the relation of tunnel excavation (C_{EXC}) and support unit costs (C_{SUP}) with RMR are obtained as given in Eqs. (88.4) and (88.5). Costs are in million IRR per meter of the tunnel length.

$$C_{EXC} = 20.7 \times e^{(0.002RMR)} \tag{88.4}$$

$$C_{SUP} = 24.6 \times e^{(-0.006RMR)} \tag{88.5}$$

88.4.3 Multivariate Regression

Tables 88.3 and 88.4 show the results obtained from the MVR in which two independent variables including RMR and overburden height (H) were used for unit cost estimation of tunnel excavation and wall support. Tables include coefficients for each independent variable, intercepts, t- and F-test and p values.

As seen in the Tables, in generated equations, low p values and high t- and F-test values under the hypothesis H_0 validate the regression results.

Finally, multivariate unit cost functions for tunnel excavation (C_{EXC}) and wall support (C_{SUP}) using RMR and overburden height (H) are obtained as Eqs. (88.6) and (88.7), respectively. Costs are in million IRR per meter of the tunnel length.

$$C_{EXC} = 20.577 + 0.0584RMR - 0.0005H \tag{88.6}$$

$$C_{SUP} = 32.707 - 0.119RMR - 0.0008H \tag{88.7}$$

Table 88.3 Obtained results for tunnel excavation unit cost

	Coefficient B	t-test	p-level	Total F-test	Total p-level
Intercept	20.57	14.95	0.0001	92.4	0.0001
RMR	0.058	2.16	0.0009		
Height of overburden	0.0055	2.71	0.0002		

Table 88.4 Results for tunnel support unit cost

	Coefficient B	t-test	p-level	Total F-test	Total p-level
Intercept	23.70	74.52	0.0001	145.8	0.00011
RMR	−0.119	8.89	0.0008		
Height of overburden	0.0007	5.17	0.0008		

Table 88.5 Mean absolute error rate (in percent)

Function	Excavation cost	Support cost	Total costs
$Y = ax^b$	14.56	14.45	14.23
$Y = ae^{bx}$	13.25	12.86	12.85
$Y = ax + b$	14.43	14.25	14.10
$Y = ax_1 + bx_2$	11.04	11.12	11.37

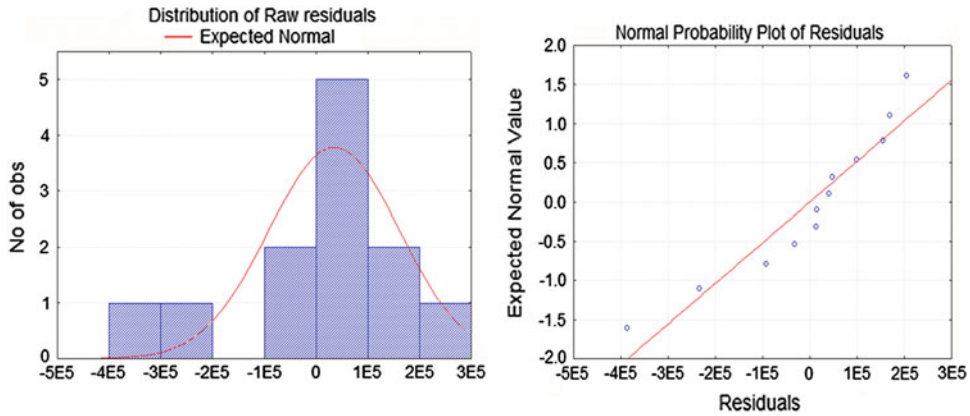

Fig. 88.1 Residual analysis for cost model of excavation

88.4.4 Model Validation

The accuracy of the results obtained from the developed equations were evaluated by the mean absolute error rate (MAER) values as shown in Table 88.5. It can be noted that this rate for the selected cost function ($Y = ae^{bx}$(is less than 14 %, meaning that the newly developed formulas have the required estimation validity and capability for tunneling costs.

In this study, the model adequacy is also checked through analyzing the residual. The analysis is made to check the distribution of residuals using histogram and normal probability plot as illustrated in Figs. 88.1 and 88.2. As can be followed from the figures, the residuals have nearly a normal distribution with zero mean, indicating that the developed estimation model is almost unbiased.

88.5 Discussion

In previous researches on cost estimation models, the parameter of diameter has been used. However, the tunnels studied in this research have similar cross section and the same diameter, and hence this parameter can be excluded. The tunnel length parameter is another effective parameter. The length of tunnels varied from 111 to 540 m showed a negligible effect on tunnel excavation and support costs. On the contrary, the RMR and overburden height demonstrated strong correlations to tunneling costs, consequently were

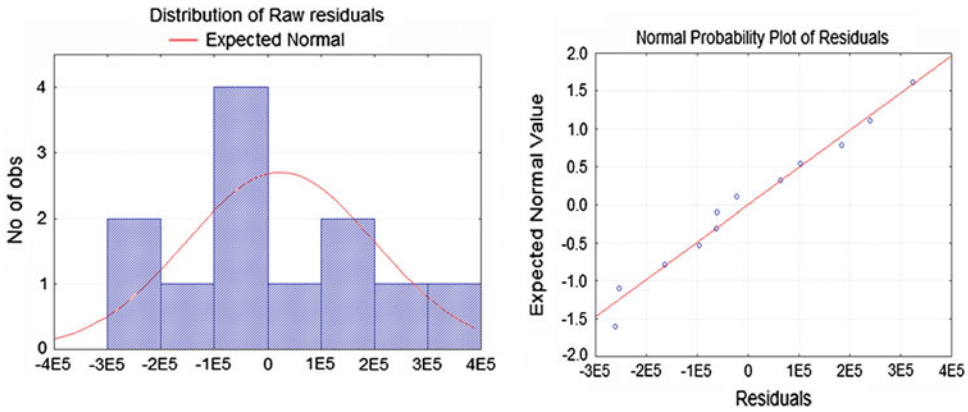

Fig. 88.2 Residual analysis for cost model of support

taken into account as explanatory variables. Based on the obtained results, among the three possible univariate functions, the form of $Y = ae^{bx}$, with a mean absolute error rate of 13 % is better than others for estimation of the tunneling cost. The results showed that the costs of excavation increase with RMR. Also, the cost of tunnel excavation showed a reverse relation with RMR. The reason for this is that, with increasing rock mass quality, the less and lighter support system with less installation expenditure is required. Linear, logarithmic and exponential regression techniques were applied for multivariate modeling and it was concluded that only the linear regression model is significant. Validation of the model using MAER method indicated that the error changed in 11–13 % provides an acceptable range in pre-feasibility study phase.

88.6 Conclusion

The aim of this paper was to provide a reliable cost estimation model for short tunnels which are constructed using conventional method in Iran. For this, both uni- and multivariable regression techniques were implemented because of their mathematical background and their wide applications in cost estimation using RMR and tunnel depth. Low error of provided models which have been tested with respect to mean criteria of absolute error rate and other statistical tools, confirms the adequacy of the results. This model provides the possibility of a fast and acceptable estimation of the excavation as well as support cost of tunnels at the phase of pre-feasibility study in tunnel projects.

References

Bledsoe JD (1970) The development of a tunnel system model. Massachusetts Institute of Technology, Massachusetts

Bruland A (2000) Hard rock tunnel boring advance rate and cutter wear, doctoral thesis. Norwegian institute of technology, Trondheim

Evans D, Lanham J, Marsh R (2006) Cost estimation method selection: matching user requirements and knowledge availability to methods. University of the West of England, Bristol

Gunduz M, Ugur LO, Ozturk E (2011) Parametric cost estimation system for light rail transit and metro trackworks. Expert Syst Appl 38(3):2873–2877

Kim GH, An SH, Kang KI (2004) Comparison of construction cost estimating models based on regression analysis, neural networks, and case-based reasoning. Build Environ 39:1235–1242

Lamb TJ (1971) A computer model for tunneling costs. Massachusetts Institute of Technology, Massachusetts

Mason AK, Smith AE (1997) Cost estimation predictive modeling: regression versus neural network. Eng Eco 42(2):137–162

Moavenzadeh F, Markow MJ (1976) Simulation model for tunnel construction costs. J Constr Div ASCE (CO1):51–66

Petroutsatou C, Lambropoulos S, Pantouvakis JP (2006) Road tunnel early cost estimates using multiple regression analysis. Oper Res Int J 6(3):311–322

Rostami J, Sepehrmanesh M, Alavi E, Mojtabai N (2013) Planning level tunnel cost estimation based on statistical analysis of historical data. Tunn Undergr Space Technol 33:22–33

Sayadi AR, Lashgari A, Paraszczak JJ (2011) Hard-rock LHD cost estimation using single and multiple regressions based on principal component analysis. Tunn Undergr Space Technol 27:133–140

Sayadi AR, Lashgari A, Fouladgar MM, Skibniewski MJ (2012) Estimating capital and operational costs of backhoe shovels. J Civil Eng Manag 18(3):378–385

Sonmez R, Ontepeli B (2009) Predesign cost estimation of urban railway projects with parametric modeling. J Civil Eng Manag 15(4):405–409

Impact of Anthropocene Vis-à-vis Holocene Climatic Changes on Central Indian Himalayan Glaciers

89

Rameshwar Bali, S. Nawaz Ali, S.K. Bera, S.K. Patil, K.K. Agarwal and C.M. Nautiyal

Abstract

Systematic palaeoclimatic study of the glacio-lacustrine sediments using multiproxy data in Pindari glacier area, Central Himalaya has helped in better understanding of the climatic fluctuations since the last 7 Ka. The palynological data supported by the environmental magnetic parameters suggests that the climate of the Pindar valley was cold and dry during 7 ka BP followed by five different vegetational shifts. The studies further suggest that since the last 300 yr BP, the climate has been warm and moist. It has to be ascertained weather the present phase of warming as inferred from the current phase of deglaciation is anthropogenic or is the continuation of the warm period that was initiated prior to the anthropocene time around 300 years B.P.

Keywords

Holocene • Palaeoclimate • Central Himalayan glaciers • Anthropogenic

89.1 Introduction

The Himalaya and Tibet, the most glaciated regions outside the poles, have influenced the regional and global environmental change. In spite of the importance of Himalayan glaciation, the nature of late Pleistocene and Holocene glaciation in the region is poorly understood. The geomorphological setup of the Higher Himalayan region suggests that these areas have experienced phases of glaciations as well as deglaciation in the recent geological past (Sharma and Owen 1996; Pant et al. 2006; Nainwal et al. 2007; Bali et al. 2013). The process of deglaciation, similar to the present one, is believed to have taken place a number of times in the past as well. Although most of the studies indicate multiple events of glaciations in the Himalaya, however, the quantitative estimate on their timing is lacking due to scarcity of organic material that precludes the use of standards radiocarbon-dating techniques (Owen 2009; Owen et al. 2002).

The present work is based on the studies carried out along the upper reaches of Pindari glacier basin, central Himalayan region. The basin located in the upper reaches of Bageshwar District of Uttarakhand, has an area of 632.67 km^2 (Fig. 89.1). The Pindari basin is constituted of the Central Crystalline rocks of the Higher Himalaya. Geomorphologically, the area is constituted of a number of erosional and depositional landforms that seem to have been influenced by neotectonic activity (Bali et al. 2012).

R. Bali (✉) · K.K. Agarwal
Centre of Advanced Study in Geology, University of Lucknow, Lucknow, India
e-mail: rameshbali@rediffmail.comrameshbali@gmail.com

S. Nawaz Ali · S.K. Bera · C.M. Nautiyal
Birbal Sahni Institute of Palaeobotany, Lucknow, India

S.K. Patil
Dr. K.S.Krishnan Geomagnetic Research Laboratory, Jhunsi, Allahabad, India

G. Lollino et al. (eds.), *Engineering Geology for Society and Territory – Volume 1*,
DOI: 10.1007/978-3-319-09300-0_89,

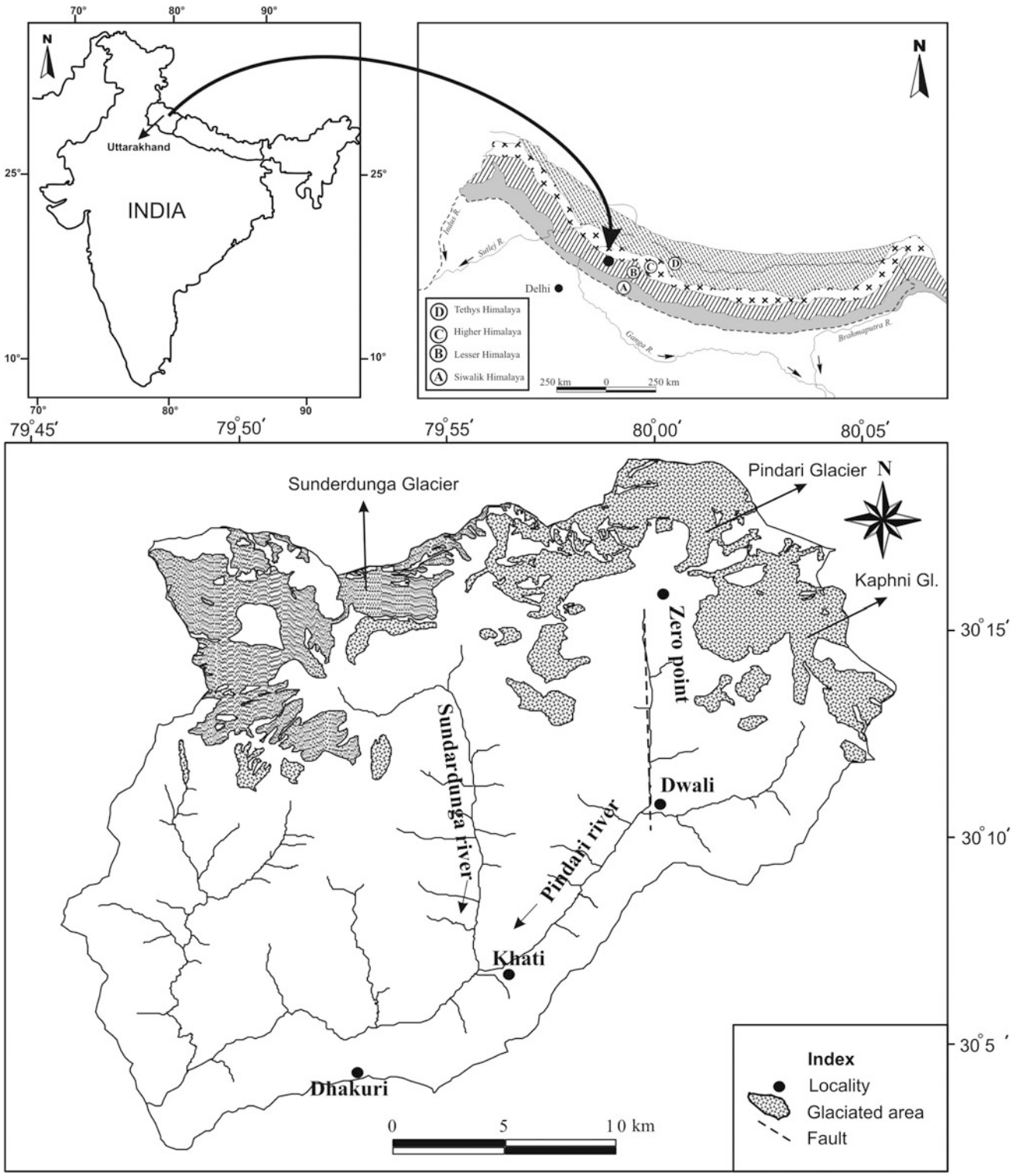

Fig. 89.1 Location of the study area

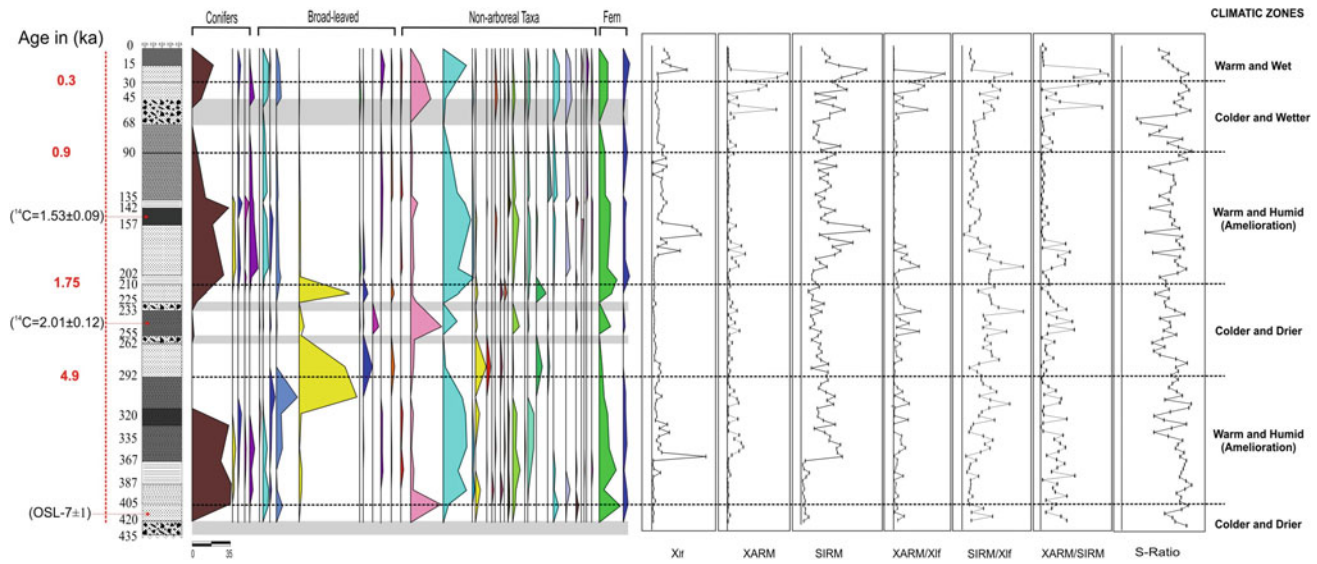

Fig. 89.2 Climatic zones as deduced from the pollen and magnetic data. Both the parameters show a good correlation

89.2 Palaeoclimatic Reconstruction

In order to have a better understanding of the Holocene climate changes, multi proxy studies including establishing the moraine stratigraphy using geomorphological studies, carrying out palynological, environmental magnetic, remote sensing and GIS studies and geochronology using optical dating has been carried out. Samples for Palynological and mineral magnetic studies have been collected from the 435 cm pit excavated within a kame deposit located in between the depression of two left lateral moraines (30° 15′ 36″ N and 79° 59′ 52″ E). The area lies about 4 km above the present day tree line and the vegetation around the area is of alpine meadow type. A total of 16 samples throughout the vertical extent of the 435 cm pit profile have been analysed for palynological analysis.

89.2.1 Mineral Magnetic Studies

Magnetic measurements of the samples have been carried out using Bartington MS-2B Susceptibility meter at Dr. K. S. Krishnan Geomagnetic Research Laboratory, Jhunsi, Allahabad. A total of 118 samples throughout the vertical extent of the pit profile were taken in 2 × 2 × 2 cm cubical non-magnetic samplers for environmental magnetic studies. The environmental magnetic measurements including low field magnetic susceptibility, Anhysteretic Remanent Magnetization (ARM), Isothermal Ramanent Magnetization (IRM) and hysteresis parameters have been determined using the standard procedure (Dekkers 1997; Evans and Heller 2003; Peters and Dekkers 2003).

Anhysteretic **(ARM)** and isothermal **(IRM)** remanent magnetization mostly reflect changes in magnetic concentration within the sediment. The Low frequency magnetic susceptibility **(χ_{lf})** shows peaks of high χ_{lf} and troughs of low χ_{lf} throughout the pit profile. All along the vertical extent of the 435 cm deep pit, the low frequency magnetic susceptibility **(χ_{lf})** shows three major peaks and four troughs (Fig. 89.2). The fluctuations in the χ_{lf} in the glacio-lacustrine deposit are modulated by climate (Verosub and Roberts 1995).

The three peaks in the χ_{lf} graph are indicative of relatively higher concentrations of ferromagnetic minerals. These peak values may be due to warmer climatic conditions prevailing during that period. Warmer periods provide higher weathering conditions of the country rocks and deposition of good amount of sediments resulting in the higher concentration of iron minerals.

The anhysteretic susceptibility **(χ_{ARM})** and Saturation Isothermal Remanent Magnetization **(SIRM)** indicate higher concentration of Stable Single Domain **(SSD)/** Pseudo Single Domain **(PSD)** type ferromagnetic minerals thereby indicating deposition to have taken place during warmer climatic conditions.

89.2.2 Palynological Studies

In the present investigation the interpretation of the climate is based on the fluctuation in the representation of pollen assemblage comprising conifers, broad-leaved taxa and alpine-subalpine non-arboreal complex (Fig. 89.2). The pollen inferred vegetation scenario together with

comparison with the magnetic susceptibility results of the pit profile has been divided into six distinct zones (PG-I, PG-II, PG-III, PG-IV, PG-V and PG-VI). The pollen zones have been prefixed with 'PG' after the name of the site of investigation (Pindari Glacier). The study is aided with two ^{14}C and one OSL dates indicating that the sedimentation of this Glacio-lacustrine deposit has initiated prior to 7 ka BP.

The climate for the region has been worked out to be cold and dry during 7 ka BP followed by five different vegetational shifts. The vegetation complex as marked by high conifers associated with broad leaved as well as herbaceous taxa and high magnetic susceptibility suggests the amelioration of climate during 7–4.9 ka BP. Thereafter, during 4.9–1.75 ka BP, the climate once again shows cold and drier condition as evidenced by acceleration of alpine herbaceous taxa with gradual decrement of conifers and broad leaved taxa. However, during 1.75–0.9 ka BP, the climate seems to have become relatively warm and moist (~Medieval Warm Period) as evidenced by the presence of both conifers and broad leaved taxa along with fair amount of *Rhododendron*. During 0.9–0.2 ka BP, a drastic climatic change has been witnessed (~Little Ice Age) as evidenced by the relative decline in conifers and broad leaved taxa except *Quercus* and *Rhododendron*. The sediments of this zone also show lower values of the magnetic susceptibility. Since the last 300 yr BP onwards, the vegetation complex including conifers, broad leaved taxa along with herbaceous elements along with high magnetic susceptibility indicates warm and moist climatic regime. The presence of cereals (>60 μm) along with culture pollen like Tubuliflorae, Acanthaceae, Caryophyllaceae and Polygonaceae also support the high pastoral activity during this phase. Further, the steady presence of both monolete and trilete fern spores suggest an overall warm and moist climatic condition as prevailing presently in and around the study area.

89.3 Discussion and Conclusions

Holocene climatic data as recorded from the palynological and environmental magnetic proxies from the Pindari glacier valley located in the higher central Himalayan region, suggests that this region has experienced at least six major climatic shifts during the last 7,000 years. The study further suggests that in the (central) Himalayan region, the present phase of warming started almost 300 years BP and seems to have been continuing since then, prior to the beginning of the time of industrial revolution i.e. Anthropocene.

There seems to be a general view, that of late, the Himalayan glaciers have been showing alarmingly high rate of melting and recession. Such an activity is suggested to have been caused due to the anthropogenically induced climatic changes. Systematic field observations taken during the last several decades for few selected glaciers in the central Himalayan region shows that although the glaciers have been receding, the rate of recession has in fact been reducing. Field observations for the Pindari glacier located in the Kumaun Himalaya reveals that the rate of recession for this glacier has come down from 26.50 m/yr recorded during 1845–1906 AD to 6.5 m/yr during 1966–2007. However, the later observations show a sudden rise in the rate of recession between 2007 and 2010 (Bali et al. 2013). On the other hand, the rate of recession for the Gangotri glacier (largest in the central Himalayan region) recorded between 1935–1971 AD has also come down to around 12 m/yr during 2004–05 AD (Bali et al. 2011).

Thus the present phase of warming that started almost 300 B.P. is a natural cycle of warming or has resulted due to anthropogenic activity has yet to be ascertained. It is believed that more such scientific inputs and proxies including geochemistry of lacustrine deposits, ice core studies, dendrochronology etc. are required from different parts of the Himalaya to have better understanding of the Holocene climatic changes vis-à-vis impact of anthropogenic activity on the current climate change.

Acknowledgements Authors are thankful to the Head of Department, Centre of Advanced Study in Geology, University of Lucknow, Lucknow and Director, BSIP Lucknow, for providing working facilities. Thanks are also due to Department of Science and Technology, Government of India, New Delhi, for funding the project vide project no.ESS/91/29/2004.

References

Bali R, Agarwal KK, Nawaz Ali S, Srivastava P (2011) Is the recessional pattern of Himalayan glaciers suggestive of anthropogenically induced global warming? Arab J Ear Sci 4:1087–1093

Bali R, Agarwal KK, Nawaz Ali S, Rastogi SK, Krishna K (2012) Drainage morphometry of Himalayan Glacio-fluvial basin, India: hydrologic and neotectonic implications Environ. Earth Sci 66:1163–1174

Bali R, Agarwal KK, Nawaz Ali S, Rastogi SK, Krishna K, Srivastava P (2013) Chronology of late quaternary glaciation in the Pindar valley, Alaknanda Basin, central Himalaya (India). J Asian Earth Sci 66:221–233

Dekkers MJ (1997) Environmental magnetism: an introduction. Geol Mijnbouw 76:163–182

Evans ME, Heller F (2003) Environmental magnetism: principles and applications of enviromagnetism. Internat geophy series, vol 86. Acad Press, New York, p 293

Nainwal HC, Chaudhary M, Rana N, Negi BDS, Negi RS, Juyal N, Singhvi AK (2007) Chronology of the late quaternary glaciation around Badrinath (upper Alaknanda basin): preliminary observations. Curr Sci 93:90–96

Owen LA (2009) Latest pleistocene and holocene glacier fluctuations in the Himalaya and Tibet Quat. Sci Rev 28:2150–2164

Owen LA, Finkel RC, Caffee MW (2002) A note on the extent of glaciations throughout the Himalaya during the global last glacial maximum. Quat Sci Rev 21:147–157

Peters C, Dekkers MJ (2003) Selected room temperature magnetic parameters as a function of mineralogy, concentration and grainsize. Phys Chem Earth 28:659–667

Pant RK, Juyal N, Basavaiah N, Singhvi AK (2006) Late quaternary glaciation and seismicity in the higher central Himalaya: evidence from Shalang basin (Goriganga). Uttaranchal Curr Sci 90:1500–1505

Sharma MC, Owen LA (1996) Quaternary glacial history of NW Garhwal, central Himalayas. Quat Sci Rev 15:335–365

Verosub KL, Roberts AP (1995) Environmental magnetism: past, present. Future J Geophys Res 100(82):2175–2192

Design of Ultimate Pit Slope for a Proposed Opencast Limestone Mine in the Hilly Region of Northern India

90

Jagdish C. Jhanwar and A. Swarup

Abstract

This paper presents the investigation conducted for the design of ultimate pit slope of a proposed limestone opencast mine in the hilly region of the state of Himachal Pradesh in northern India. The limestone rock mass at this project-site was classified as good with Bieniawski's basic RMR varying from 60 to 72. The intact rock was weak to medium weak with uni-axial compressive strength in the range of 16–37 MPa. The kinematic analysis suggested plane and wedge types of failure conditions. Based on the stability analysis, the overall slope angles of 43° and 35° were suggested for ultimate pit depths of 100 and 150 m respectively. The bench height and bench slope angle were suggested at 10 m and 80° respectively. In addition to above, it was suggested that a minimum distance of 150 m be maintained between the cliff bottom and the crest of ultimate pit slope. Further, it was suggested that the above slope designs could be used as an initial estimate and after the mining was actually started the slope design could be revised, if required based on the actual geotechnical exposures and the response of rock mass.

Keywords

Limestone mine • Rock mass • Kinematic analysis • Stability analysis • Slope design

90.1 Introduction

The stability assessment of opencast mine slopes can be made through stability analysis using limit equilibrium based methods and through rock mass classification using empirical methods. Slope Mass Rating (SMR) is one of the widely used empirical methods for classification of rock mass vis-à-vis slope stability (Romana 1985). SMR was used effectively to evaluate the stability of an opencast coal mine slope in India (Pradhan et al. 2011).

J.C. Jhanwar (✉) · A. Swarup
CSIR-Central Institute of Mining and Fuel Research,
Dhanbad 826015, India
e-mail: jcjhanwar@yahoo.com

The case study presented in this paper pertains to a limestone deposit situated in the Himalayan region of Northern India, which was proposed to be developed as an opencast mine to feed limestone to the nearby proposed cement plant. The lease area of this limestone deposit is situated in the state of Himachal Pradesh in India. The lease area forms a part of the lesser Himalayan ranges characterized by an extremely rugged topography comprising high peaks, steep slopes and deeply incised valleys. No flat plain land occurs in and immediately around the lease area. The mountain that hosts the limestone deposit rises from the banks of river Sutlej that meanders within the inter-mountainous valleys. A surface plan showing the general topography of lease area is shown in Fig. 90.1. A scientific study was conducted to design ultimate pit slopes through stability analysis by a software using limit equilibrium based method for the proposed opencast limestone mine in this deposit.

G. Lollino et al. (eds.), *Engineering Geology for Society and Territory – Volume 1*,
DOI: 10.1007/978-3-319-09300-0_90,

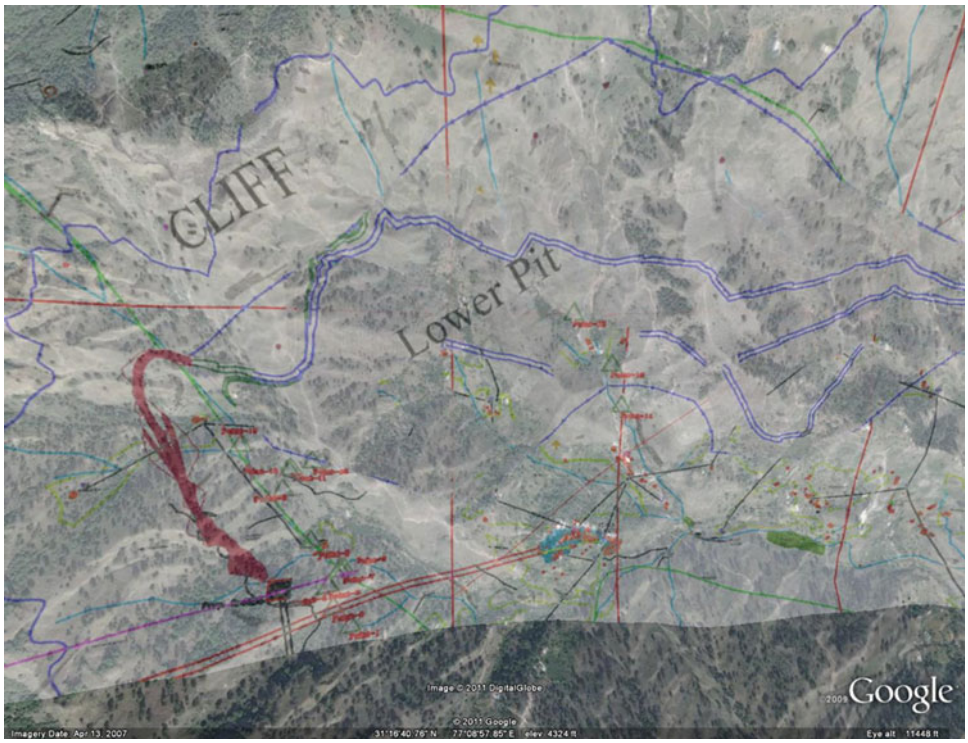

Fig. 90.1 A satellite view of the plan of mine lease area

90.2 Geology

90.2.1 Regional Geology

Regionally, the area forms part of the Shali structural belt in the Mandi district of Himachal Pradesh, which consists of two distinct belts viz. the main Shali structural belt and the Shali subsidiary belt of Bandia range. The Shali structural belt comprises the older (Palaeoproterozoic) Sundernagar group followed by the younger (Mesoproterozoic) Shali group.

90.2.2 Local Geology

The rocks in this region belong to the Shali formations, which are predominantly carbonate rocks in association with orthoquartzite. The Shali group is subdivided, litho-stratigraphically into eight formations with an aggregate average thickness of over 3,000 m. It represent a typical shallow stable platform type sedimentation, which is amply testified by the presence of stromatolites, sedimentary structures like mud cracks, oscillation ripple marks and the occurrence of salt beds in the sequence. Dolomite is more dominant than limestone in the sequence. Locally, the rocks of the Khatpul, Sorgharwari and Tattapani formations (three of the eight formations) of the Shali group are exposed in the lease area. The limestone of Sorgharwari member is underlain by Khatpul dolomite and overlain again by Tattapani dolomite.

90.2.3 Structure of the Deposit

The limestone appears to occur in the core of an overturned antiform, whose limbs are represented by the dolomite. The axial plane as well as the limbs of the fold are likely to have steep to moderately steep dips due NE. This is yet to be proved by detailed exploration. As per the outcrops, the general strike of bedding in the rocks is NW-SE with dips at 23–72° towards NE. The rocks in this area seems to be folded resulting in an increase of the apparent thickness of the limestone beds. Owing to location between two major thrusts, the rocks in the area exhibit effect of deformation manifested in moderate to steep dips and broad anti-formal folds. Loose soil over-burden of fine clay with cobbles and boulders of limestone and dolomite generally occupy the depression in the area.

90.3 Geotechnical Investigation

90.3.1 Structural Mapping

Field studies were conducted in the mining lease area to carry out structural mapping of the rock mass exposures (Fig. 90.2). The area is essentially a hilly terrain and the

Fig. 90.2 Structural mapping of rock mass in the mining area

rock masses are covered with grass and bushes. The rock mass is jointed with the presence of three joint sets, which include a bedding joint and two other joint sets. The joints are very closely to closely spaced. The kinematic analysis indicates the formation of wedges, which remain stable considering the friction angle of 35°. However, these wedges may become unstable if the friction angle becomes lower than the dip of the plane of intersection. The plane failure is also unlikely as indicated by the kinematic analysis. However, the plane failure may occur at some places as and when the dip of the plane/joint becomes more than the friction angle. This analysis is based on the limited amount of structural data and is therefore indicative only. It is expected that the bench level slope failure as and when occurs will be controlled mainly by structures. The slope failure completely through intact rock is unlikely, however, in the event of a large scale slope instability the failure surface may partly pass through the weathered and very weak rock and through the structures. A structurally controlled large scale slope failure is possible only when the persistence of a structure meets the requirement. A total of 28 data sets of orientation were recorded at different locations. The great circles of the identified joint sets along with the bench and pit slopes are shown in Fig. 90.3. The likely modes of slope failures in different sides of the mine are shown in Table 90.1. The slopes are identified both on the bench and overall scales with dip amounts of around 80 and 45° respectively (CIMFR Report 2011).

90.3.2 Determination of Physico-Mechanical Properties

Rock samples were tested in the laboratory for different physico-mechanical properties. The uni-axial compressive strength as obtained from laboratory testing varied from

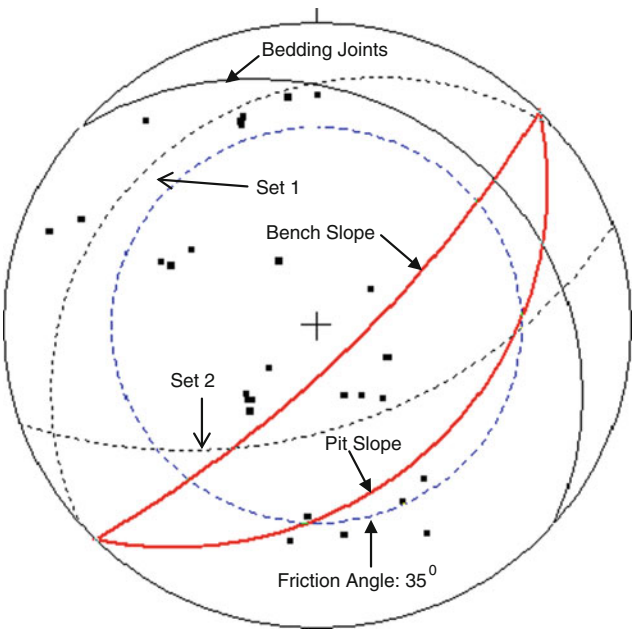

Fig. 90.3 Great circles of joint sets and slopes

Table 90.1 Likely modes of slope failures at different slope locations and orientations

Slope direction	Slope type	Dip/direction	Likely mode of failure
South	Pit slope	45°/180°	Wedge
	Bench slope	80°/180°	Wedge
South west	Pit slope	45°/225°	Wedge
	Bench slope	80°/225°	Wedge
West	Pit slope	45°/270°	Wedge
	Bench slope	80°/270°	Wedge
North west	Pit slope	45°/315°	Plane
	Bench slope	80°/315°	Plane/Wedge
North	Pit slope	45°/360°	Wedge
	Bench slope	80°/360°	Wedge
North east	Pit slope	45°/45°	Plane
	Bench slope	80°/45°	Plane
East	Pit slope	45°90°	Wedge
	Bench Slope	80°/90°	Wedge
South east	Pit slope	45°/135°	Wedge
	Bench slope	80°/135°	Wedge

16.64 to 37.87 MPa, which indicated weak to medium weak rock types as per the ISRM classification (ISRM 1981). The cohesion and angle of internal friction varied from 4.75 to 6.1 MPa and from 43 to 48 degree respectively. The rock mass at this mine area was classified as good with Rock Mass Rating (RMR) varying from 60 to 72 (Bieniawski 1989).

90.4 Evaluation of Pit Slope Design

Slope Stability analysis was performed using the Slope Stability Analysis Software, GALENA (v 4.0) to evaluate the pit slope design. The unit weight, cohesion and friction angles for limestone rock mass were considered at 26.0 KN/m^3, 300–400 kPa and 35–40° respectively. The following parameters were considered in stability analysis:

i. Height of the cliff: 620 m
ii. Overall slope angle of the cliff: 44° (from horizontal)
iii. Height of excavated pit slope (below cliff): 280 m
iv. Height of excavated ultimate pit slope (other sides): 100–110 m

A typical output of the stability analyses is shown in Fig. 90.4. The proposed pit area falls under the seismic zone and therefore peak ground acceleration of 0.36 g was considered in the stability analysis. The stability analysis results indicated that mining near the cliff could induce instability in the cliff especially under seismic effects (peak ground acceleration) of more than 0.2 g. However, if the cliff side pit slope crest was maintained at a distance of 150 m from the cliff, the stability improved considerably. Based on the stability analysis, the following slope designs were suggested for ultimate pit depths of 100 and 150 m.

Slope Design for an Ultimate Pit Depth of 150 m (*Cliff side*)

i. The overall slope angle: 35°
ii. Bench width: 12.5–13.5 m
iii. Bench height: 10.0 m
iv. Bench slope angle: 75–80°

In addition to above, it was suggested that a minimum distance of 150 m be maintained between the cliff bottom and the slope crest of the cliff side slope.

Slope Design for an Ultimate Slope Height of 100 m (*Other slopes*)

i. The overall slope angle: 43°
ii. Bench width: 5.0–6.0 m
iii. Bench height: 10.0 m
iv. Bench slope angle: 75–80°

These slope designs could thus be used as an initial estimate and after the mining was actually started the slope design could be revised, if required based on the actual geotechnical exposures and response of the rock mass.

90.5 Conclusions

The rock mass at proposed mine area was classified as good with RMR varying from 60 to 72. The intact rock/limestone was weak to medium weak with its uni-axial compressive strength in the range of 16–37 MPa. The rock mass was jointed with the presence of three joint sets, which included a bedding joint and two other joint sets. The joints were

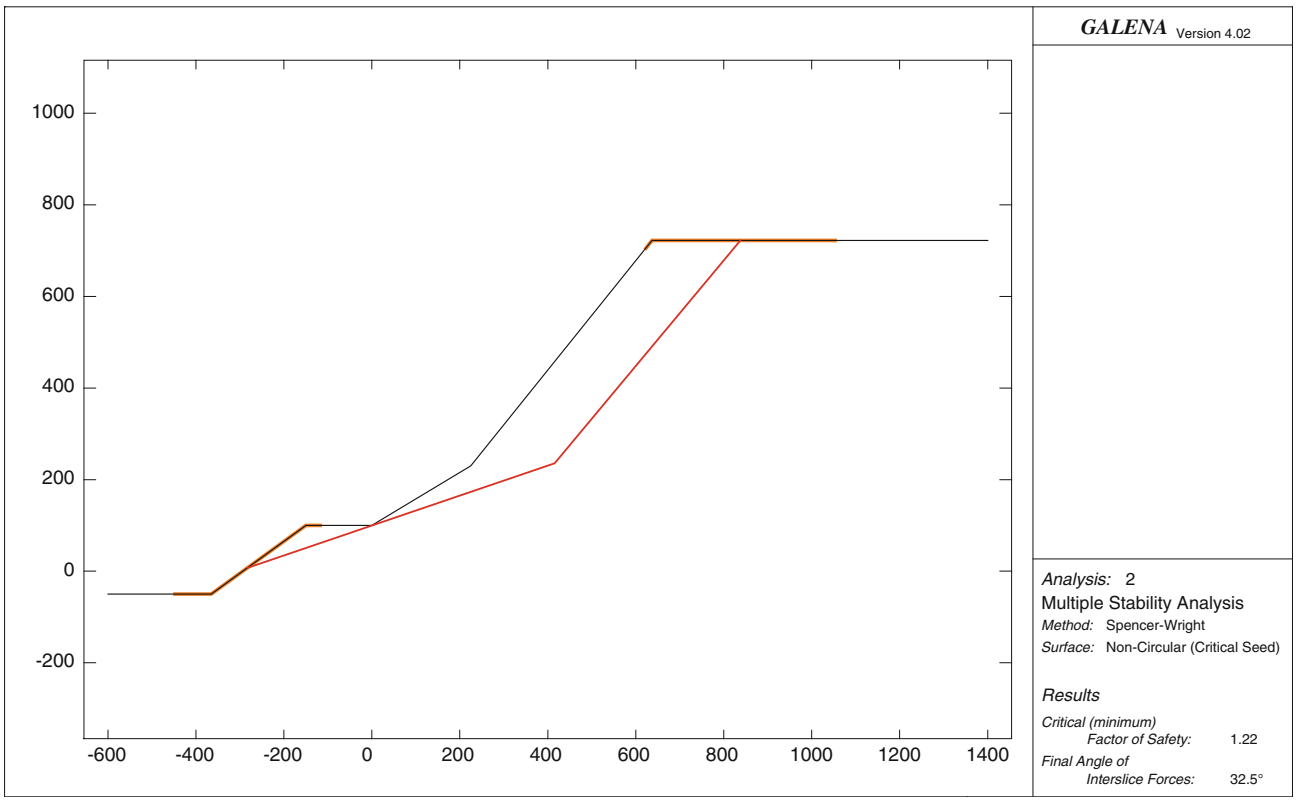

Fig. 90.4 Stability analysis of cliff slope without seismic load

very closely to closely spaced. The kinematic analysis indicated the formation of wedges, which remained stable considering the friction angle of 35°. However, these wedges could become unstable if the friction angle was lower than the dip of the plane of intersection. The plane failure was also unlikely as indicated by the kinematic analysis. However, the plane failure could occur at some places as and when the dip of discontinuity/joint was more than the friction angle. This analysis was based on the limited amount of structural data and was therefore indicative only.

It was expected that the bench level slope failure as and when occurred will be controlled mainly by structures. The failure completely through intact rock was unlikely, however, in the event of a large scale slope instability the failure surface could partly pass through the weathered and very weak rock and through the structures. Based on the results of stability analysis, it was indicated that the slope stability was significantly influenced by the seismic effect. Overall slope angles of 43 and 35° were suggested for ultimate pit depths of 100 m and 150 m respectively. These slope designs could be used as an initial estimate and after the mining was actually started the slope design could be revised, if required based on the actual geotechnical exposures and response of the rock mass.

Acknowledgments The authors are thankful to Dr. A. Sinha, Director, CSIR-Central Institute of Mining & Fuel Research for his kind permission to carry out this study. Sincere thanks are also due to their colleagues, who were associated in this study. The first author sincerely thanks Prof. T. N. Singh and Dr. V. Vishal, Dept. of Earth Sciences, Indian Institute of Technology, Mumbai, India for kindly providing the reprint of their paper.

References

Bieniawski ZT (1989) Engineering rock mass classifications. Wiley, New York, p 251

Pradhan SP, Vishal V, Singh TN (2011) Slope mass rating for evaluation of health of slopes in an opencast mine in Jharia coalfield, India. Min Eng J 12(10):36–40

Romana M (1985) New adjustment ratings for application of Bieniawski classification to slopes. Proceedings of the international symposium on role of rock mechanics. Zacatecas, Mexico, pp 49–53

Slope Stability Analysis System GALENA (V.4.0) User Guide (2003) Clover Associates Pty. Limited Australia

International Society for Rock Mechanics (ISRM) (1981) Suggested methods for the quantitative description of discontinuities in rock masses. In: Brown ET Pergamon Press, Oxford, UK, p 211

CIMFR Report of Investigations (2011) Geotechnical study to evaluate slope stability for proposed pit layout (lower pit) of Alsindi limestone deposit—Himachal Pradesh. Project No. CNP/N/2782/2010-11, Dhanbad, India, p 53

Effect of Brine Saturation on Carbonation of Coal Fly Ash for Mineral Sequestration of CO_2

91

Ukwattage Nadeesha Lakmali and Pathegama Gamage Ranjith

Abstract

Mineral sequestration with alkaline waste materials is being studied extensively for its application as a way of reducing the increased level of CO_2 in the atmosphere. Coal combustion fly ash has the potential to react with CO_2 to form minerals which are stable over geological times. For industrial level application of this concept, the mineralization reaction is required to enhance. The acceleration of the reaction is done through ex situ carbonation inside the reactors. The mineral carbonation reaction can be made more efficient through mixing the alkaline material with brine. Therefore the objective of the present study was to evaluate the effect of brine saturation of coal fly ash on the rate and the efficiency of CO_2 sequestration. Three types of Australian fly ashes (Loy Yang, Yallourn and Hazel Wood) were saturated with brine and then carbonated inside a pressure vessel at 3 MPa CO_2 pressure and 40 °C. Then the weight gain after carbonation was measured to estimate the sequestration potential. As a control another set of carbonation tests were performed replacing brine with water. Results showed a positive effect from brine on the rate and the efficiency of carbonation of coal fly ash.

Keywords

Mineral sequestration • Fly ash • Brine saturation

91.1 Introduction

Mineral sequestration of certain rapidly accumulating waste materials provides a promising method for CO_2 sequestration due to its potential to be introduced as a finishing step in industries those produce CO_2 and alkaline solid by products (Huijgen and Comans 2003). Coal combustion by products (fly ash and bottom ash), municipal solid waste incineration by products (fly ash, bottom ash and air pollution control residues) and steel slag are some of the common residues which are being evaluated for their potential for CO_2 sequestration. In mineral sequestration, atmospheric CO_2 is taken up by alkaline oxides and hydroxides present in the candidate materials to form thermodynamically stable forms of carbonates (Huijgen and Comans 2003; Baciocchi et al. 2006). Mineral carbonation is basically an acid base reaction where an acid formed by dissolution of CO_2 in water (H_2CO_3) is neutralised by a solid base (alkaline mineral). Mineralization of Ca and Mg-bearing silicates to form to form Ca and Mg carbonates can occur under ambient conditions, but at extremely slow rates. Therefore, for the applications in industrial level CO_2 sequestration, the natural reaction should be enhanced by many folds through accelerated and aqueous mineral carbonation. In this, the carbonation reaction is accelerated by manipulation of the reaction parameters such as temperature, CO_2 pressure, moisture content and mixing to overcome the slow reaction kinetics.

U.N. Lakmali (✉) · P.G. Ranjith
Deep Earth Energy Laboratory, Bld 60, Monash University, Vic 3800 Melbourne, Australia
e-mail: nadeesha.ukwattage@monash.edu.au

G. Lollino et al. (eds.), *Engineering Geology for Society and Territory – Volume 1*,
DOI: 10.1007/978-3-319-09300-0_91,

Coal combustion fly ash is a solid waste material contains oxides such as CaO and MgO that can be converted to carbonates in the presence of CO_2. Each year a large mass of fly ash is collected in storage ponds without getting any beneficial use of it. This emphasizes the need for the investigation of large-scale applications for this waste product. Over the last few decades fly ash has attracted attention as a potential source in the mineral sequestration process, which involves the capture and storage of atmospheric C in alkaline materials. In addition, as the carbonation process helps to alter the chemical stability of the fly ash, the leachability of heavy metals such as Pb, Zn tends to reduce after carbonation (van Gerven et al. 2005). This allows the safe disposal of carbonated fly ash into landfills or dumpsites.

However the mineral carbonation of coal fly ash for CO_2 sequestration is still not implemented in industrial level due to several drawbacks in the process which needs to be solved through further research on the discipline. Especially to achieve increased efficiency of carbonation, different processing methodologies are being experimented including fractionation of fly ash. In addition to that the saturation of fly ash with brine is being considered to increase the sequestration efficiency. However, not much research evidence is available in the literature about the effect of brine on carbon sequestration. Therefore, the objective of the present study is to evaluate the effect of brine saturation on the mineral carbonation for CO_2 sequestration.

91.2 Materials and Method

The fly ash samples for the study were collected from three power plants (Hazelwood, Loy Yang and Yallourn) located in Latrobe valley, Victoria, Australia. Victorian brown coal is the parental material for all three of these ashes. The morphology of the Latrobe valley ash particles is generally irregular and ranges from sub-angular through to rounded, sometimes spherical. The powder used in the study came from the collection ponds and initially contained large clods of ash which needed to be broken into individual particles for testing. Fly ash samples were then sieved with 1.18 mm sieves to get the uniform sized particles for test-ing. After that the samples were oven dried at 105 °C for 24 h to remove all moisture. From the dried material 300 g of ash samples were taken for each test. For the tests with water, 300 g of water was added to the 300 g of dried ash samples to get 100 % moisture. For the tests with Brine 300 g of brine solution was added to the 300 g of dried ash. The brine used in the study was a solution mainly consisting of NaSO4. In addition it contained a significant amount of Ca, K, Mg and Cl. The prepared samples were then carbonated inside a pressure chamber shown in Fig. 91.1.

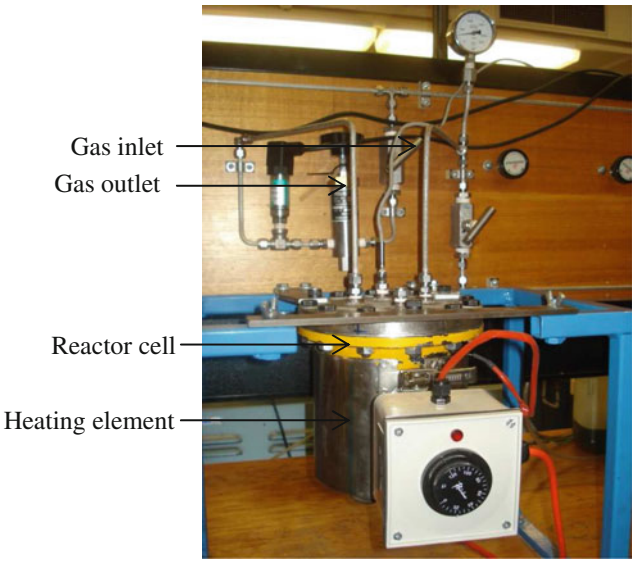

Fig. 91.1 The experimental apparatus used for the carbonation tests

After placing the fly ash slurry, the rector cell was heated up to 40 °C temperature and CO_2 gas was charged into the cell until the cell inside pressure becomes 3 MPa. Thereafter, the reactor cell was isolated and the ash was allowed to react with gas for 24 h. At the end of 24 h's period the container with the fly ash slurry was taken out of the chamber and dried in an oven until a constant weight. The weight gain due to carbonation with water and brine was calculated and compared for each fly ash type.

91.3 Results and Discussion

The alkaline oxide present in coal fly ash is converted to carbonates at the presence of CO_2 and moisture through a series of chemical and mineralogical transformations as shown in Eqs. (91.1)–(91.4)

$$H_2O + CO_2 \rightarrow H_2CO_3 \tag{91.1}$$

$$H_2CO_3 \rightarrow H^+ + HCO_3^- \rightarrow 2H^+ + CO_3^{2-} \tag{91.2}$$

$$CaO + H_2O \rightarrow Ca(OH)_2 \rightarrow Ca^{2+} + 2OH^- \tag{91.3}$$

$$Ca^{2+} + CO_3^{2-} \rightarrow CaCO_3 \tag{91.4}$$

Therefore, after 24 h of carbonation reaction, the dry weight of fly ash is in-creased due to increased carbonates content. The percentage weight gain at the presence of water and brine for each type of fly ash tested is shown in Fig. 91.2.

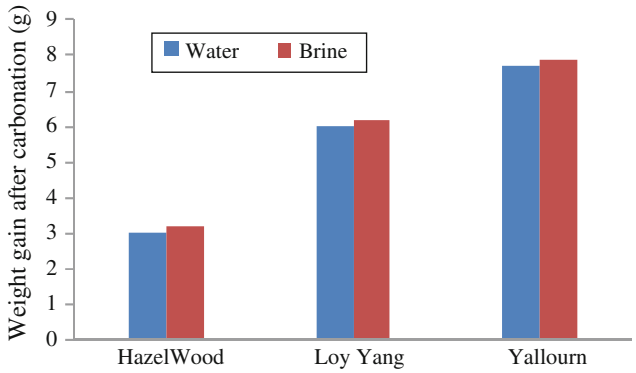

Fig. 91.2 The carbonation weight gain of fly ash in different saturation media

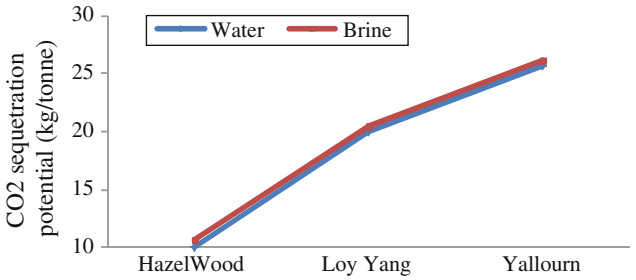

Fig. 91.3 CO_2 sequestration of coal fly ash in different saturation media

Fig. 91.4 SEM images of carbonated and non-carbonated fly ash

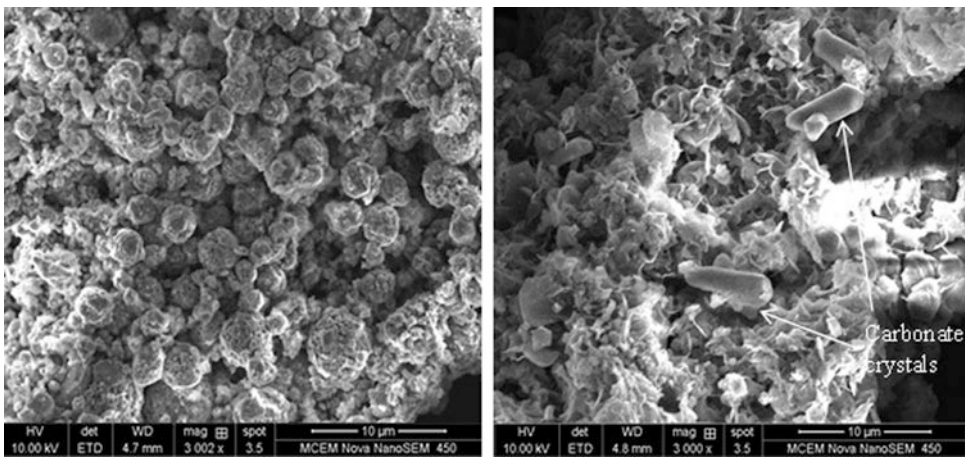

According to the results, the carbonation weight gain of three fly ash types was considerably different to each other. Hazelwood fly ash showed the least weight gain in both water and brine saturation media whereas Yallourn showed the highest. The X-Ray diffraction analysis for the mineralogy of Latrobe valley fly ashes showed that Hazelwood has the least potential to sequester CO_2 in terms of the available oxides for the carbonation. According to the analysis, Hazelwood, Loy Yang and Yallourn fly ashes contains 12.5, 18.5 and 24.8 % of CaO respectively. The potential of fly ash for mineral carbonation depends directly on the proportion of alkaline (Ca, Mg) oxides and/or hydroxides present in the fly ash matrix (Montes-Hernandez et al. 2009). Therefore the difference in the weight gain can be mainly attributed to the content of alkaline oxides present in each fly ash type.

Across each fly ash type, there is a slight increase in weight gain observed with the replacement of brine solution instead water. Although the difference is not much significant there is a positive effect on carbonation weight gain created by brine saturation compared to water. This can be due to the contribution of extra Ca^{2+} cations from brine solution for the carbonation reaction (Nyambura et al. 2011). The results from the study were used in estimation of the CO_2 sequestration of three fly ashes under test conditions. Figure 91.3 shows the sequestration potential in Kg of CO_2 per tonne of fly ash.

According to the figure Hazelwood fly ash shows the least sequestration potential due to its mineralogical composition. Yallourn ash showed the highest potential sequestration. The sequestration of Kg of CO_2 per tonne of fly ash for Hazelwood, Loy Yang and Yallourn was 10.03, 19.93 and 25.66 respectively for the water saturation. For brine saturation it was 10.60, 20.50 and 26.23 kg of CO_2 per tonne of ash respectively. Therefore there was a positive gain in sequestration with brine saturation compared to water saturation. Similar results are reported by Nyambura et al. (2011) for their experiment with brine saturated and fractionated coal fly ash. In order to confirm the carbonation in fly ash during the experiment, Scanning Electron

Microscopic (SEM) imaging was done for carbonated and none carbonated fly ash samples. Figure 91.4 compares the SEM images of two samples.

In carbonated ash samples the hexagonal rod shaped carbonate crystals were abundantly visible compared to none carbonated ash sample. Therefore the weight gains of samples due to carbonation were confirmed.

91.4 Conclusions

The study revealed the potential of using coal combustion fly ash for CO_2 sequestration. Latrobe valley fly ashes can store up to 23 kg of CO_2 per tonne of fly ash, The use of brine solution to saturate ash brings positive effects on CO_2 sequestration compared to water saturation.

References

Baciocchi R, Polettini A, Pomi R, Prigiobbe V, Nikulshina V, Zedwitz V, Steinfeld A (2006) CO_2 sequestration by direct gas solid carbonation of air pollution control (APC) residues. Energy Fuels 20:1933–1940

Huijgen WJJ, Comans RNJ (2003) Carbon dioxide sequestration by mineral carbonation: literature review. Energy Research Centre of the Netherlands ECN, The Netherland

Montes-Hernandez G, Perez-Lopez R, Renard F, Nieto JM, Charlet L (2009) Mineral sequestration of CO_2 by aqueous carbonation of coal combustion fly-ash. J Hazard Mater 161(2–3):1347–1354

Nyambura MG, Mugera WG, Felicia PL, Gathura NP (2011) Carbonation o brine impacted fractionated coal fly ash: implications for CO_2 sequestration. J Environ Manage 92:655–664

van Gerven T, Van Keer E, Arickx S, Jaspers M, Wauters G, Vandecasteele C (2005) Carbonation of MSWI bottom ash to decrease heavy metal leaching, in view of recycling. Waste Manage 25:291–300

Blasting Operation Management Using Mathematical Methods

92

M. Yari, M. Monjezi, R. Bagherpour and A.R. Sayadi

Abstract
Blasting is one of the most important operations in the mining projects. Inappropriate blasting pattern may lead to unwanted events such as poor fragmentation, back break, fly rock etc. and affect the whole operation physically and economically. In fact selecting of the most suitable pattern among previously performed patterns can be considered as a Multi Attribute Decision Making (MADM) problem. In this paper, firstly, from various already performed patterns, efficient and inefficient patterns were differentiated using Data Envelopment Analysis (DEA). In the second step numerical Taxonomy method was used for ranking the remaining efficient patterns and recognizing the most suitable pattern in the Sungun copper mine, Iran. According to the obtained results, blasting pattern with burden of 3 m, spacing of 4 m and stemming of 3.2 m was selected as the best pattern and suggested to be considered for the future operation.

Keywords
Numerical taxonomy • Data envelopment analysis (DEA) • Blasting pattern • Sungun copper mine

92.1 Introduction

Blasting process plays significant role in the civil and mining projects. Incorrect blasting pattern can result in many technical, economical and safety problems (Hudaverdi 2012; Monjezi and Rezaei 2011; Kecojevic and Radomsky 2005). In the mining activities, the prime aim of blasting operation is to achieve a suitable rock fragmentation necessary for subsequent processes such as transportation, crushing, etc. (Chakraborty et al. 2004; Crum and Crum 1990; Latham et al. 2006; Morin and Ficarazzo 2006; Ozkahraman 2006; Shim et al. 2009). In other hand, the explosive energy is not fully used for rock breakage and only 20–30 % of the energy is practically consumed for the assigned purpose and the rest of the energy is exhausted in the form of unwanted phenomena such as ground vibration, air blast, flyrock, backbreak, etc. (Singh and Singh 2005). Also, environmentalists are increasingly concerned about mining activities; hence, there should be much effort to control and eliminate the unwanted blast-induced environmental problems.

Conventional models can only provide an approximation to the solution for approaching perfect result of blasting considering technical, environmental and safety parameters and the final applicable design can be identified using a trial-error process (Inanloo Arabi Shad and Ahangari 2012). Available experimental methods of designing blasting pattern are not accurate enough since they are site specific and therefore cannot be implemented in all the situations

M. Yari (✉)
Isfahan University of Technology, Isfahan, Iran
e-mail: mojtaba.yari@yahoo.com

M. Monjezi · R. Bagherpour · A.R. Sayadi
Faculty of Engineering, Tarbiat Modares University, Tehran, Iran
e-mail: monjezi@modares.ac.ir

R. Bagherpour
e-mail: bagherpour@cc.iut.ac.ir

A.R. Sayadi
e-mail: sayadi@modares.ac.ir

G. Lollino et al. (eds.), *Engineering Geology for Society and Territory – Volume 1*,
DOI: 10.1007/978-3-319-09300-0_92,

(Inanloo Arabi Shad and Ahangari 2012). For finalizing a proposed initial pattern, an analysis of the obtained results would lead to adaptation of the design parameters (Jimeno 1995). However, this approach is time consuming and imposes extra costs on the operation.

Given the existence of different parameters and multiple alternatives, it is relatively difficult to select the most suitable pattern among several patterns. So, it is necessary to employ a mechanism to optimize the design. The selected pattern should be reasonable from both technical and economical point of view. Safety and environment are the other important issues to be considered in the blasting operation (Hudaverdi 2012; Kecojevic and Radomsky 2005).

The main goal of the blasting is obtaining a proper fragmentation of materials while decreasing the unfavourable effects such as ground vibration, back break and flyrock (Monjezi and Rezaei 2011). In the previous studies, fragmentation is regarded as the most important goal of the blasting (Ghasemi et al. 2012b; Sanchidrián et al. 2006; Michaux and Djordjevic 2005; Kulatilake et al. 2010; Morin and Ficarazzo 2006) and Blasting experts have not paid enough attention to other effective parameters such as back break, flyrock, ground vibration and air blasting for evaluation of blasting patterns.

So far, great efforts have took place in order to management, prediction and control of blasting operation. Case in point, researchers portrayed some careful investigations noticing flyrock and presented causative components for the occasion to propose preventive measures (Stojadinović et al. 2011; Kecojevic and Radomsky 2005; Amini et al. 2011; Bajpayee et al. 2002, 2003, 2004a, b; Ghasemi et al. 2012a, b; Little and Blair 2010; Monjezi et al. 2012; Monjezi et al. 2011a; Ning 1999; Rehak et al. 2001; Rezaei et al. 2011; Tota et al. 2001). Wherever back break has been the blasting problem in a new bench, the lower amount of back break is considered as the blasting pattern evaluation factor (Rezaei et al. 2011; Gate et al. 2005; Khandelwal and Monjezi 2012; Monjezi et al. 2012; Monjezi and Dehghani 2008; Monjezi et al. 2010b). In addition, a few endeavours have been made to diminish ground vibration (Erarslan et al. 2008; Ak et al. 2009; Hudaverdi 2012; Shuran and Shujin 2011; Bakhshandeh Amnieh et al. 2012; Dehghani and Ataee-Pour 2011; Monjezi et al. 2010a; Guosheng et al. 2011; Ak and Konuk 2008; Iphar et al. 2008; Monjezi et al. 2011b). The essential issue of these examinations is to recognize stand out of the impact criteria in the blasting operation enhancement.

DEA is a non-parametric method used for evaluating the relative efficiency of decision-making units (DMUs) according to multiple inputs and outputs (Cooper et al. 2007). It can also be employed to generate local weights of alternatives from pair-wise comparison judgment matrixes in the analytic hierarchy process (AHP) (Ramanathan 2006). This method has been applied in different fields of science and engineering (Athanassopoulos et al. 1999; Hermans et al. 2009; Kao and Liu 2009).

In order to achieve a global evaluation of blasting patterns, some aspects (criteria) such as fragmentation, back break, flyrock and blasting costs must be considered (Jimeno 1995). Hence, due to the presence of various blasting effects (consequences), it is not easy to select the best applied alternative. For this reason, rather new mathematical based methods such as numerical Taxonomy, a branch of multi attribute decision making (MADM), can be employed. However, in cases where the number of alternatives is too high, it is better to limit the search space by omitting inefficient alternatives and considering only efficient ones. The work can be performed using methods such as data envelopment analysis (Li et al. 2007). In this study, the most efficient applied blast patterns of mine were selected by DEA method. After that, among the selected patterns, the most suitable pattern was chosen using numerical Taxonomy method for Sungun Copper Mine (Fig. 92.1).

92.2 Data Envelopment Analysis (DEA)

Data envelopment analysis (DEA), was presented by Charnes et al in 1978 emphasizing researches of Farrel (1957). DEA systems are passed on a linear or non-linear programming model. This model is implemented in order to evaluation of comparable decision making units (DMUs) efficiency considering multiple inputs and outputs (Sowlati et al. 2005). DEA and TOPSIS combined technique, can be practical for evaluating service operations using a ranking mechanism (Cooper et al. 2005). Generally, DEA models can be categorized into two main branches, i.e. input-orientated and output-orientated. Input oriented methods consists of the models in which input quantities can be regularly decreased without altering the outputs amounts produced, while in the second group, the output quantities can be proportionally increased by keeping the input quantities unchanged. Selection of the method depends on the nature of problem to be solved (Allen and Thanassoulis 2004; Bal et al. 2010).

The efficiency is a ratio of the weighted sum of outputs to the weighted sum of inputs. The relative efficiency (w_o) of particular DMUs is obtained by solving the following fractional programming problem, $w_o = 1$, It means that DMU_0 is efficient while $w_o < 1$ shows the inefficiency of the DMU under evaluation.

Fig. 92.1 Geological map of Sungun copper mine (http://www.mobinco.com/en/projects/sungun, 2012)

$$w_0 = Max \frac{\sum_{r=1}^{s} u_r y_{ro}}{\sum_{i=1}^{m} v_i x_{io}}$$

$$\frac{\sum_{r=1}^{s} u_r y_{rj}}{\sum_{i=1}^{m} v_i x_{ij}} \leq 1 \qquad (92.1)$$

$$j = 1, 2, \ldots, n$$
$$u_r \geq 0,\ r = 1, 2, \ldots, s$$
$$v_i \geq 0,\ i = 1, 2, \ldots, m$$

where
j is the DMU index, j=1, …,n;
r is the output index, r=1,…,s;
i is the input index, i = 1,…,m;
yrj is the value of the r-th output for the j-th DMU;
xij is the value of the i-th input for the j-th DMU;
ur is the weight given to the r-th output;
vi is the weight given to the i-th input.

The fractional program (92.1) can be converted into a linear programming problem (92.2) by forcing the weighted sum of the inputs to 1. This model, which is the first applicable type of DEA models, is called Charnes, Cooper and Rhodes (CCR) model. In this technique, all probable combinations are proportionally scaled up or down. Solution of the problem can be found with constant return to scale (CRS).

$$w_0 = Max \sum_{r=1}^{s} u_r y_{r0}$$

$$\sum_{i=1}^{m} v_i x_{i0} = 1$$

$$\sum_{r=1}^{s} u_r y_{rj} - \sum_{i=1}^{m} v_i x_{ij} \leq 0 \qquad (92.2)$$

$$j = 1, 2, \ldots, n$$
$$u_r \geq 0,\ r = 1, 2, \ldots, s$$
$$v_i \geq 0,\ i = 1, 2, \ldots, m$$

The second type of DEA models refers to Banker, Charnes and Cooper (BCC) model. Unlike CCR model, in the BCC approach, the solution comes with variable return to scale (VRS). The BCC model can be as follows:

$$w_0 = Max \sum_{r=1}^{s} u_r y_{r0} + c_0$$

$$\sum_{i=1}^{m} v_i x_{i0} = 1$$

$$\sum_{r=1}^{s} u_r y_{rj} - \sum_{i=1}^{m} v_i x_{ij} + c_0 \le 0 \qquad (92.3)$$
$$j = 1, 2, \ldots, n$$
$$u_r \ge 0,\ r = 1, 2, \ldots, s$$
$$v_i \ge 0,\ i = 1, 2, \ldots, m$$

where C0 indicates returns to scale (RS) and is free in sign

When there is more than one efficient DMU, a complementary concept has to be employed to recognize the most efficient alternative. One of the applicable concepts is numerical Taxonomy technique, which can identify the most efficient DMU using a ranking mechanism.

92.3 Numerical Taxonomy

Taxonomy analysis method is one of the most applicable methods of ranking the zones in terms of development which has been widely used in geography. This method was posed by Adneson for the first time in 1763 and expanded by some mathematicians in 1950. In 1968, it was posed by Holling in UNESCO as an important way for classification of development degree of the different countries and has been posed in different fields of sciences at present. Taxonomy analysis is applied for different classifications in sciences of which special type is numerical taxonomy. In this method, a set is divided into relatively homogenous sets and gives the planners an acceptable scale for studying and measuring development rate of the zones. Taxonomy has been based on analysis of a series of predetermined indices which is used in prioritization of a series of alternatives and gives a full ranking for evaluation of alternatives (Mohammadi et al. 2011; Eghbali et al. 2007). Different stages of taxonomy analysis are given in 9 steps as follows(Eghbali et al. 2007; Mohammadi et al. 2011):

Stage 1: specifying alternatives and determining attributes. Indices can be selected by analyst or experts group (by forming panel or Delphi method). In this stage, i alternative is considered which will be evaluated by j attributes.

Stage 2: Forming Data Matrix and Calculating Mean and Standard Deviation. i alternatives and j attributes are ordered as the Table 92.1.

In this matrix, r_{ij} is Compliance of i-th alternative from each index view point, qualitatively or quantitatively. In this stage, one should note that the negative indices should be reversed or its negativity should be considered in other ways.

Stage 3: Normalizing the Obtained Matrix Data

In data matrix, alternatives have been expressed in terms of the indices which have different units (scales) and in this stage; attempt is made to remove its different units. For this purpose, standard normal method is used that calculates as (92.4).

$$Z_{ij} = (x_{ij} - \bar{x}_j)/\sigma_j \qquad (92.4)$$

where

x_j mean indices or each one of the columns of matrix

S_j standard deviation of each column of matrix

In this stage, matrix of the standard (normalized matrix) data is specified.

Stage 4: Determining Compound Distance between Alternatives

One can obtain distance (difference) of each alternative from other alternatives and determine distance between two alternatives using the (92.5).

$$D_{ab} = \sqrt{\sum_{j=1}^{m} \left(Z_{aj} - Z_{bj}\right)^2} \qquad (92.5)$$

where, a and b are the evaluated alternatives.

Table 92.1 Data matrix

Attributes alternatives	C_1	C_2	C_3	.	.	.	.	C_j
A_1	r_{11}	r_{12}	r_{13}	.	.	.	.	r_{1j}
A_2	r_{21}	r_{22}	r_{23}	.	.	.	.	r_{2j}
.	.	.	.	.	.	.	.	.
.	.	.	.	.	.	.	.	.
.	.	.	.	.	.	.	.	.
A_i	r_{i1}	r_{i2}	r_{i3}	.	.	.	.	r_{ij}
Mean	$\bar{x}_1$	$\bar{x}_2$	.	.	.	.	.	$\bar{x}_J$
Standard deviation	σ_1	σ_2	.	.	.	.	.	σ_J

Distance of alternatives a and b is equal to distance of alternatives b and a. Considering the above cases, one can form matrix of compound distances between alternatives of which main diameter indicates difference (distance) of each alternative from itself which equals to zero.

Stage 5: Determining the Shortest Distance

In this stage, the shortest distance of each row of matrix is determined after calculating compound distances. Then, mean distance of the alternatives and their standard deviation are obtained and this is done for the shortest distance as well.

Stage 6: Delimiting the Alternatives (Homogenizing Alternatives)

There may be units which have longer or shorter distances from other alternatives; therefore, heterogeneous alternatives should be excluded from the set. In order to do so, upper and lower limits are obtained from (92.6), (92.7) and (92.8).

$$O_r = \bar{d}_r \pm 2\sigma_{dr} \tag{92.6}$$

$$O_r(+) = \bar{d}_r + 2\sigma_{dr} \quad \text{Upper limit} \tag{92.7}$$

$$O_r(-) = \bar{d}_r - 2\sigma_{dr} \quad \text{Lower limit} \tag{92.8}$$

In this case, d_r between upper and lower limits is coordinated and the alternatives which are out of this determined limit should be excluded.

Stage 7: Determining distance between alternatives and ideal value (Cio)

In this stage, distance between each one of the alternatives and ideal value (specified in stage 4) is obtained as (92.9).short distance from ideal value indicates development (and its suitable condition) and long distance indicates that the alternative has not been developed.

$$Cio = \sqrt{\sum_{j=1}^{M} \left(Z_{ij} - Z_{bj}\right)^2} \tag{92.9}$$

Stage 8: Ranking of Alternatives Development Rate (Fi)

In this stage, ranking of development and condition of the alternatives are studied. Equation (92.10) indicates how to calculate alternatives development rate.

$$F_i = C_{io}/C_o \tag{92.10}$$

where

F_i alternatives development rate

C_{io} development model of each alternative

C_o upper limit of development

In order to calculate C_o, one should specify mean and deviation of C_{io} and this is done at the end of stage 7 and it is calculated as (92.11):

$$C_o = \overline{C_{io}} + 2\sigma_{C_{io}} \tag{92.11}$$

F_i is between 0 and 1 and the closer alternative to zero, indicates the better development of that alternative and the closer the alternative to 1, the worse development of that alternative (no development). In this case, taxonomy problem is ended and rank of its alternatives is specified.

92.4 Model of Rock Blasting Patterns Evaluation for Sungun Copper Mine Using DEA-Taxonomy Method

Use For selecting the most economical, efficient and appropriate blasting pattern in terms of technical concepts using numerical Taxonomy method, in first stage all alternatives should be determined.

Each pattern has been evaluated by considering 5 attributes:

Authors should consider the following points:

(1) Powder factor: This parameter has been shown with PF. It should be noted that since the cost of explosive should be minimized, it is considered a negative attribute. It means that blasting system should be inclined to decrease it.

(2) Specific drilling: It is marked with SD. This attribute is a negative index like PF. Although increasing specific drilling improves fragmentation, drilling expenses are increased to a great extent.

(3) Fly rock: This index has been marked with F. The smaller number indicates the suitable arrangement of the pattern.

(4) Back break: Back break is the maximum distance of crack propagation at the back of the last blast row. It is regarded as a negative attribute and shown with BB.

(5) Fragmentation: It is the last index shown with letter K. This index is a negative parameter because the goal is to decrease fragmentation dimensions.

For filtering inefficient blasting patterns output-oriented BCC has been used for 50 alternatives.

Sungun copper deposit is a Porphyry resource that involves numerous dikes with near—vertical slope and North–North West and North–West directions. The body of this porphyry deposit includes the mineralization of Monzonite to Quartz Monzonite. Along mining design process, final slope of 37° for final walls, bench height of 12.5 m, bench Width of 9.6 m, bench incline of 65° and road width

of 24 m is considered. To achieve the most proper blasting pattern in Sungun copper mine, different geometric patterns are implemented Table 92.2. In this table A, B, C, D and E represents Hole diameter, Hole length, Spacing, Burden and Stemming, respectively.

Relative comparison of different attributes calculated by DEA and more efficient patterns are mentioned in Table 92.3 with details. As a result, 27 patterns have been selected as more efficient alternatives using DEA system.

In order to solve Multi Attribute Decision Making problem, it is necessary to form decision making matrix. This matrix consists of six columns and 28 rows. All attributes expressed as a real numeric value that has been measured in the mine (Table 92.2). The first column is the pattern numbers while the other columns relate to the attributes including powder factor (column 2), specific drilling (column 3), flyrock (column 4), back break (column 5) and mean fragmentation size (column 6).

Table 92.2 Data matrix

	A	B	C	D	E
P1	5.5	12.1	4.5	3.5	3.8
P2	6.0	11.5	4.5	3.5	3.0
P3	5.5	12.5	4.5	3.5	3.6
P4	6.0	12.3	4.5	3.5	3.6
P5	5.0	13.0	5.0	4.0	3.8
P6	6.0	11.8	4.5	3.5	3.8
P7	5.5	12.0	4.0	3.0	3.2
P8	6.0	12.8	5.0	4.0	4.1
P9	5.0	13.5	5.5	5.0	4.5
P10	5.5	11.5	4.0	3.0	3.2
P11	5.5	11.5	4.5	3.5	3.6
P12	5.0	13.5	5.0	4.0	4.1
P13	6.0	13.2	5.0	4.0	3.5
P14	5.0	11.0	4.5	3.5	3.8
P15	5.5	13.0	4.5	3.5	4.1
P16	5.5	12.0	4.5	3.5	3.8
P17	5.5	13.0	5.0	4.0	3.0
P18	5.0	13.2	5.5	4.5	3.8
P19	6.0	12.0	5.0	4.0	4.1
P20	5.5	12.5	5.0	4.0	4.3
P21	5.0	13.2	5.0	4.0	4.0
P22	5	11	3.5	3	3
P23	5	12.8	4.5	3.5	4.1
P24	5	11.5	4	3	3
P25	6	12.9	5	4	4.1
P26	5.5	12.5	4.5	4	4
P27	5	11.8	4	3	3.2

27 blasting performed patterns in Sungun Copper Mine have been measured with the 5 indices. These 27 patterns have been evaluated with Numerical Taxonomy analyze in 8 stages.

Stage 1: specifying alternatives and determining attributes

All impressive parameters on most appropriate blasting pattern selection are indicated in Table. 92.2.

Stage 2: forming data matrix and calculating mean and standard deviation

27 operated blasting patterns and 5 indices as blasting evaluation factors are arranged in Table 92.4.

Stage 3: data matrix normalization

Stage 4: Determining Compound Distance between Alternatives

It has been calculated in a matrix of 27 × 27. After determining shortest distance for each row in paired distances matrix, Mean and standard deviation of short distances should be obtained that mentioned in Table 92.5.

Stage 5: Determining the Shortest Distance

After calculating normalized matrix, the negative ideal alternative (DOj) in terms of factors is evident in Table 92.3. In this stage distance of each alternative from DOj is calculated. Results are given in Table 92.5.

Stage 6: Homogenizing alternatives

Table 92.3 Matrix of values, mean and standard deviation

Pattern	PF	SD	F	BB	K
Pattern 1	0.36	0.05	72	2.5	31
Pattern 2	0.34	0.05	75	2	31.5
Pattern 3	0.42	0.05	76	3	30
Pattern 4	0.43	0.05	76	3	31
Pattern 5	0.4	0.05	75	3	32
Pattern 6	0.41	0.05	76	3	29
Pattern 7	0.38	0.05	75	2	30.1
Pattern 8	0.59	0.07	80	5	24.7
Pattern 9	0.85	0.09	85	9	20.8
Pattern 10	0.37	0.05	74	2	30.2
Pattern 11	0.4	0.05	76	3	31
Pattern 12	0.59	0.06	78	5.5	24.7
Pattern 13	0.59	0.07	81	5.5	24.6
Pattern 14	0.4	0.05	76	3	30
Pattern 15	0.59	0.07	80	5.5	24.7
Pattern 16	0.4	0.05	75	3	30
Pattern 17	0.59	0.06	80	5	24.7
Pattern 18	0.59	0.07	80	5	24.6
Pattern 19	0.59	0.07	82	5.5	24.9
Pattern 20	0.52	0.06	79	5	26.3
Pattern 21	0.54	0.06	79	5	25.7
Pattern 22	0.34	0.05	73	2	31
Pattern 23	0.52	0.06	78	5	26.7
Pattern 24	0.34	0.05	73	2	31.6
Pattern 25	0.52	0.06	79	5	26.8
Pattern 26	0.46	0.06	75	4	28.2
Pattern 27	0.37	0.05	74	2	30
Average	0.478	0.0578	77.11	3.907	27.99
STEV	0.12	0.0101	3.13	1.687	3.057

Table 92.4 Shortest distances in each row of paired distances matrix (d_r) and mean and standard deviation values of them

Pattern	d_r	Pattern	d_r	Pattern	d_r
Pattern 1	0.467	Pattern 11	0.250	Pattern 21	0.258
Pattern 2	0.566	Pattern 12	0.686	Pattern 22	0.196
Pattern 3	0.167	Pattern 13	0.321	Pattern 23	0.321
Pattern 4	0.250	Pattern 14	0.167	Pattern 24	0.196
Pattern 5	0.457	Pattern 15	0.296	Pattern 25	0.164
Pattern 6	0.338	Pattern 16	0.320	Pattern 26	1.292
Pattern 7	0.332	Pattern 17	0.619	Pattern 27	0.065
Pattern 8	0.033	Pattern 18	0.033	$\bar{d}_r$	0.456
Pattern 9	3.952	Pattern 19	0.334	σ_{dr}	0.744
Pattern 10	0.065	Pattern 20	0.164		

Table 92.5 C_{io} calculation matrix

	PF	SD	F	BB	K	
DOj Pattern	−1.15	−0.768	−1.63	−1.13	−2.35	Cio
Pattern 1	0.028	0	0	0.088	11.13	3.354
Pattern 2	0	0	0.919	0	12.25	3.629
Pattern 3	0.445	0	1.634	0.351	9.058	3.389
Pattern 4	0.563	0	1.634	0.351	11.13	3.699
Pattern 5	0.25	0	0.919	0.351	13.42	3.866
Pattern 6	0.34	0	1.634	0.351	7.196	3.086
Pattern 7	0.111	0	0.919	0	9.256	3.207
Pattern 8	4.342	3.9	6.534	3.161	1.628	4.423
Pattern 9	18.07	15.6	17.25	17.21	0	8.254
Pattern 10	0.063	0	0.408	0	9.457	3.151
Pattern 11	0.25	0	1.634	0.351	11.13	3.656
Pattern 12	4.342	0.975	3.675	4.303	1.628	3.863
Pattern 13	4.342	3.9	8.27	4.303	1.545	4.729
Pattern 14	0.25	0	1.634	0.351	9.058	3.361
Pattern 15	4.342	3.9	6.534	4.303	1.628	4.55
Pattern 16	0.25	0	0.919	0.351	9.058	3.252
Pattern 17	4.342	0.975	6.534	3.161	1.628	4.079
Pattern 18	4.342	3.9	6.534	3.161	1.545	4.414
Pattern 19	4.342	3.900	10.21	4.303	1.799	4.955
Pattern 20	2.251	0.975	5.003	3.161	3.237	3.825
Pattern 21	2.779	0.975	5.003	3.161	2.570	3.806
Pattern 22	0.000	0.000	0.102	0.000	11.13	3.352
Pattern 23	2.251	0.975	3.675	3.161	3.725	3.713
Pattern 24	0.000	0.000	0.102	0.000	12.48	3.548
Pattern 25	2.251	0.975	5.003	3.161	3.853	3.904
Pattern 26	1.000	0.975	0.919	1.405	5.861	3.187
Pattern 27	0.063	0.000	0.408	0.000	9.058	3.087
$\overline{C_{io}}$						3.902
σ_{Cio}						1.01

Table 92.6 C_{io} and F_{io} calculation and final raking

Pattern No.	Cio	Fio =Cio/co	Rank
Pattern 1	3.354	0.5664	8
Pattern 2	3.629	0.6128	12
Pattern 3	3.389	0.5723	10
Pattern 4	3.699	0.6246	14
Pattern 5	3.866	0.6528	19
Pattern 6	3.086	0.5210	1
Pattern 7	3.207	0.5415	5
Pattern 8	4.423	0.7469	23
Pattern 9	8.254	1.3938	27
Pattern 10	3.151	0.5320	3
Pattern 11	3.656	0.6174	13
Pattern 12	3.863	0.6523	18
Pattern 13	4.729	0.7984	25
Pattern 14	3.361	0.5674	9
Pattern 15	4.550	0.7683	24
Pattern 16	3.252	0.5492	6
Pattern 17	4.079	0.6888	21
Pattern 18	4.414	0.7453	22
Pattern 19	4.955	0.8367	26
Pattern 20	3.825	0.6458	17
Pattern 21	3.806	0.6427	16
Pattern 22	3.352	0.5660	7
Pattern 23	3.713	0.6270	15
Pattern 24	3.548	0.5990	11
Pattern 25	3.904	0.6592	20
Pattern 26	3.187	0.5382	4
Pattern 27	3.087	0.5212	2

Upper and lower boundaries are calculated as follow.

$O_r(+) = +2\sigma_{dr} = 1.94$

$O_r(-) = -2\sigma_{dr} = -1.03$

d_r between upper and lower limits is homogenous and the alternatives which are out of this interval should be excluded.

Stage 7: Determining model and alternatives (C_{io})

Values of C_{io} are calculated and mentioned for each alternative in Table 92.6.

Stage 8: Ranking of Alternatives Development Rate (Fi)

Fi is calculated and Final ranking based on Fi is evident in Table 92.6. These results indicates that after assessment of 27 blasting patterns, pattern A6 with burden of 3.5 m, spacing of 4.5 m, stemming of 3.8 m and hole length of 12.1 m has been evaluated as most appropriate blasting pattern for Sungun copper mine.

92.5 Conclusion

Blasting operation in mines is one of the most important operations when considering technical, economic and safety effects. Blasting is a very important operation in all next mining stages. Safety in blasting operations is very important due to irreparable damages which inflict on people, equipment and environment in mine. Suitable management and the design of blasting patterns are all effective factors. MADM methods are useful methods for evaluating blasting patterns because it is very difficult to make decision about the most suitable blasting pattern. This complexity is due to the variety of the operated blasting patterns and the plurality of attributes which significantly influence the evaluation of blasting patterns. Among different patterns, TOPSIS model is one of the most applicable methods of MADM used to evaluate and rank blasting patterns in Sungun copper mine. Through this method, pattern 27 was selected as the most appropriate blasting pattern and alternative 9 was known as the most unsuitable blasting pattern. Based on the results, the selected pattern with burden of 3 m, spacing of 4 m and stemming rate of 3.2 m was selected as the most suitable blasting pattern for Sungun copper mine.

References

Ak H, Iphar M, Yavuz M, Konuk A (2009) Evaluation of ground vibration effect of blasting operations in a magnesite mine. Soil Dyn Earthq Eng 29:669–676

Ak H, Konuk A (2008) The effect of discontinuity frequency on ground vibrations produced from bench blasting: a case study. Soil Dyn Earthq Eng 28:686–694

Allen R, Thanassoulis E (2004) Improving envelopment in data envelopment analysis. Eur J Oper Res 154:363–379

Amini H, Gholami R, Monjezi M, Torabi SR, Zadhesh J (2011) Evaluation of flyrock phenomenon due to blasting operation by support vector machine. Neural Comput. Appl. 1–9

Athanassopoulos AD, Lambroukos N, Seiford L (1999) Data envelopment scenario analysis for setting targets to electricity generating plants. Eur J Oper Res 115:413–428

Bajpayee T, Bhatt SK, Rehak TR, Engineer G, Mowrey GL, Ingram DK (2003) Fatal accidents due to flyrock and lack of blast area security and working practices in mining. J Mines Metals Fuels 51:344–349

Bajpayee T, Rehak T, Mowrey G, Ingram D (2002) A summary of fatal accidents due to flyrock and lack of blast area security in

surface mining, 1989–1999. In: Proceedings Of The Annual Conference On Explosives And Blasting Technique, ISEE; 1999, pp 105–118

Bajpayee T, Rehak T, Mowrey G, Ingram D (2004a) Blasting injuries in surface mining with emphasis on flyrock and blast area security. J Saf Res 35:47–57

Bajpayee T, Verakis H, Lobb T (2004b) An analysis and prevention of flyrock accidents in surface blasting operations. In: Proceedings Of The Annual Conference On Explosives And Blasting Technique, ISEE; 1999, pp 401–410

Bakhshandeh Amnieh H, Siamaki A, Soltani S (2012) Design of blasting pattern in proportion to the peak particle velocity (PPV): artificial neural networks approach. Saf. Sci. 50:1913–1916

Bal H, Örkcü HH, Çelebioğlu S (2010) Improving the discrimination power and weights dispersion in the data envelopment analysis. Comput Oper Res 37:99–107

Chakraborty A, Raina A, Ramulu M, Choudhury P, Haldar A, Sahu P, Bandopadhyay C (2004) Parametric study to develop guidelines for blast fragmentation improvement in jointed and massive formations. Eng Geol 73:105–116

Cooper WW, Seiford LM, Tone K (2005) Introduction to data envelopment analysis and its uses: with DEA-solver software and references

Cooper WW, Seiford LM, Tone K (2007). Data envelopment analysis: a comprehensive text with models, applications, references and DEA-solver software, Springer

Crum S, Crum S (1990) Fractal concepts applied to bench-blast fragmentation. Proc. Rock Mech. Contrib. Challenges 919

Dehghani H, Ataee-Pour M (2011) Development of a model to predict peak particle velocity in a blasting operation. Int J Rock Mech Min Sci 48:51–58

Eghbali AR, Zamarri AA, Gaskari R (2007) The ranking iran's banks by taxonomy numerical analysis. J Int Res Publ Econ Bus

Erarslan K, Uysal Ö, Arpaz E, Cebi MA (2008) Barrier holes and trench application to reduce blast induced vibration in Seyitomer coal mine. Environ Geol 54:1325–1331

Gate W, Ortiz B, Florez R (2005) Analysis of rockfall and blasting backbreak problems. In: Paper ARMA/USRMS, proceedings of the American rock mechanics conference, pp 671–680

Ghasemi E, Amini H, Ataei M, Khalokakaei R (2012a) Application of artificial intelligence techniques for predicting the flyrock distance caused by blasting operation. Arab J Geosci 1–10

Ghasemi E, Sari M, Ataei M (2012b) Development of an empirical model for predicting the effects of controllable blasting parameters on flyrock distance in surface mines. Int J Rock Mech Min Sci 52:163–170

Guosheng Z, Jiang L, Kui Z (2011) Structural safety criteria for blasting vibration based on wavelet packet energy spectra. Min Sci Technol 21:35–40

Hermans E, Brijs T, Wets G, Vanhoof K (2009) Benchmarking road safety: lessons to learn from a data envelopment analysis. Accid Anal Prev 41:174–182

Hudaverdi T (2012) Application of multivariate analysis for prediction of blast-induced ground vibrations. Soil Dyn Earthq Eng 43:300–308

Inanloo Arabi Shad H, Ahangari K (2012) An empirical relation to calculate the proper burden in blast design of open pit mines based on modification of the Konya relation. Int J Rock Mech Min Sci 56:121–126

Iphar M, Yavuz M, Ak H (2008) Prediction of ground vibrations resulting from the blasting operations in an open-pit mine by adaptive neuro-fuzzy inference system. Environ Geol 56:97–107

Jimeno C (1995) Rock drilling and blasting. AA Balkema, Rotterdam, Brookfield

Kao C, Liu S-T (2009) Stochastic data envelopment analysis in measuring the efficiency of Taiwan commercial banks. Eur J Oper Res 196:312–322

Kecojevic V, Radomsky M (2005) Flyrock phenomena and area security in blasting-related accidents. Saf Sci 43:739–750

Khandelwal M, Monjezi M (2012) Prediction of backbreak in open-pit blasting operations using the machine learning method. Rock Mech Rock Eng, 1–8

Kulatilake P, Qiong W, Hudaverdi T, Kuzu C (2010) Mean particle size prediction in rock blast fragmentation using neural networks. Eng Geol 114:298–311

Latham J-P, van Meulen J, Dupray S (2006) Prediction of fragmentation and yield curves with reference to armourstone production. Eng Geol 87:60–74

Li S, Jahanshahloo GR, Khodabakhshi M (2007) A super-efficiency model for ranking efficient units in data envelopment analysis. Appl Math Comput 184:638–648

Little T, Blair D (2010) Mechanistic Monte Carlo models for analysis of flyrock risk. Rock Fragmentation Blasting, 641–47

Michaux S, Djordjevic N (2005) Influence of explosive energy on the strength of the rock fragments and SAG mill throughput. Min Eng 18:439–448

Mohammadi A, Shohani J, Borzooei R (2011) Numerical taxonomy analysis with trapezoidal fuzzy data. J Math Comput Sci 2:100–110

Monjezi M, Ahmadi M, Sheikhan M, Bahrami A, Salimi A (2010a) Predicting blast-induced ground vibration using various types of neural networks. Soil Dyn Earthq Eng 30:1233–1236

Monjezi M, Amini Khoshalan H, Yazdian Varjani A (2012). Prediction of flyrock and backbreak in open pit blasting operation: a neuro-genetic approach. Arab J Geosci 5: 441

Monjezi M, Bahrami A, Varjani AY, Sayadi AR (2011a) Prediction and controlling of flyrock in blasting operation using artificial neural network. Arab J Geosci 4:421–425

Monjezi M, Dehghani H (2008) Evaluation of effect of blasting pattern parameters on back break using neural networks. Int J Rock Mech Min Sci 45:1446–1453

Monjezi M, Ghafurikalajahi M, Bahrami A (2011b) Prediction of blast-induced ground vibration using artificial neural networks. Tunn Undergr Space Technol 26:46–50

Monjezi M, Rezaei M (2011) Developing a new fuzzy model to predict burden from rock geomechanical properties. Expert Syst Appl 38:9266–9273

Monjezi M, Rezaei M, Yazdian A (2010b) Prediction of backbreak in open-pit blasting using fuzzy set theory. Expert Syst Appl 37:2637–2643

Morin MA, Ficarazzo F (2006) Monte Carlo simulation as a tool to predict blasting fragmentation based on the Kuz-Ram model. Comput Geosci 32:352–359

Ning K (1999). Prevention measures for controlling flyrock in engineering blasting. Blasting

Ozkahraman H (2006) Fragmentation assessment and design of blast pattern at Goltas Limestone Quarry, Turkey. Int J Rock Mech Min Sci 43:628–633

Ramanathan R (2006) Data envelopment analysis for weight derivation and aggregation in the analytic hierarchy process. Comput Oper Res 33:1289–1307

Rehak T, Bajpayee T, Mowrey G, Ingram D (2001) Flyrock issues in blasting. In: Proceedings Of The Annual Conference On Explosives And Blasting Technique, ISEE 1999:165–176

Rezaei M, Monjezi M, Yazdian Varjani A (2011). Development of a fuzzy model to predict flyrock in surface mining. Saf Sci 49: 298–305

Sanchidrián J, Segarra P, López L (2006) A practical procedure for the measurement of fragmentation by blasting by image analysis. Rock Mech Rock Eng 39:359–382

Shim H-J, Ryu D-W, Chung S-K, Synn J-H, Song J-J (2009) Optimized blasting design for large-scale quarrying based on a 3-D spatial distribution of rock factor. Int J Rock Mech Min Sci 46:326–332

Shuran L, Shujin L (2011) Applying BP neural network model to forecast peak velocity of blasting ground vibration. Procedia Eng 26:257–263

Singh T, Singh V (2005) An intelligent approach to prediction and control ground vibration in mines. Geotech Geol Eng 23:249–262

Sowlati T, Paradi JC, Suld C (2005) Information systems project prioritization using data envelopment analysis. Math Comput Model 41:1279–1298

Stojadinović S, Pantović R, Žikić M (2011) Prediction of flyrock trajectories for forensic applications using ballistic flight equations. Int J Rock Mech Min Sci 48:1086–1094

Tota EW, Mudge K, Branson JW, Georgiou PN, Gavrilovic M, Watson JD (2001) Method and apparatus for flyrock control in small charge blasting. Google Patents

Tectonic Consideration for Location of the Kishau Dam Site on Tons River in Lesser Himalaya, India

93

Vaibhava Srivastava, Pradeep Srivastava, Hari B. Srivastava and Yogesh Ray

Abstract

A 236 m high concrete gravity dam named Kishau dam is proposed on Tons river in Lesser Himalayan region of Uttarakhand state of India. The possible site for this upcoming dam on Tons river lies in the close proximity of Tons thrust which makes a tectonic boundary between allochthonous rocks of Krol nappe and the autochthonous Simla Group rocks. The Tons thrust lies in the close vicinity of the proposed dam site. Many geomorphic and geological evidences have been observed around the dam site which indicate that active tectonics is prevalent in the region. The present study examines the geological structures of the region in order to understand the tectonic conditions that the area has experienced and finds that the southward movement of the Krol nappe is responsible for active tectonics in the region. Due to mass transfer by the movement of Krol nappe from over the autochthonous zone, the autochthonous zone is getting uplifted at an average rate of 9.7 mm/per year. In light of these active movements, the Kishau village, which lies in the southwards moving allochthonous zone, cannot be good site of Kishau dam and the dam location should preferably be placed across the Tons thrust in the autochthonous zone.

Keywords

Kishau dam • Himalaya • Active tectonics • Tons thrust

93.1 Introduction

The Himalayan region being the active fold mountain is still undergoing the tectonic movements. Progressive northward movement of the Indian plate and its collision with the Eurasian plate has led to the formation of various geological structures and recent seismicity (Molnar and Tapponier 1975; Bilham and Gaur 2000). After the collision of the Indian and the Tibetan landmasses resulting in the development of the Himalaya, tectonic activity has been witnessed in the form of intracontinental deformation along major faults and thrusts (Nakata et al. 1990; Valdiya 1986, 2001). The convergence is also accommodated by active thrusts and faults and is expressed in associated geomorphic features. Though the tectonic movement of the plate is geologically a continuous phenomenon, its impacts may be both of sudden and continuous in nature. The effects may be of regional and local levels too. The Kishau dam, a proposed dam on the Tons river lies in the Lesser Himalayan regions of India, falls in the active tectonic regions of the Himalaya. Named after the village Kishau in Dehradun district of Uttarakhand state of India, the proposed dam will be a 236 m high concrete gravity dam for 660 MW hydropower

V. Srivastava (✉) · H.B. Srivastava
Department of Geology, Banaras Hindu University, Varanasi, India
e-mail: vaibhavasri9@yahoo.co.in

P. Srivastava
Wadia Institute of Himalayan Geology, Dehradun, India

Y. Ray
National Centre for Antarctic and Ocean Research, Vasco, India

G. Lollino et al. (eds.), *Engineering Geology for Society and Territory – Volume 1*,
DOI: 10.1007/978-3-319-09300-0_93,

generation. The present study examines the structure and tectonic conditions of the rocks around the proposed Kishau dam site for the suitability of the dam site location.

93.2 Engineering Considerations

The 1824 MCM Gross Storage capacity (with 1324 MCM live storage capacity) Kishau Dam Project would utilize the water of river Tons which is a major tributary of river Yamuna and forms boundary between Himachal Pradesh and Uttarakhand in most of its reaches in this region. This multipurpose project with a proposed installation of 660 MW (165 MW × 4 vertical Francis turbine) is envisaged to generate an annual energy generation of 181.51 MU is expected to be completed in 2023 (UJVN 2014). The length of this concrete dam would be 680 with 236 m maximum height above foundation and maximum water level at 864 m. The dam would have chute type spillway with 6 radial spillway gates each of 5 m diameter (NRSC 2012). The water stored in the Kishau reservoir shall be utilized for irrigation, power generation and to augment drinking water supply for National Capital Delhi.

93.3 Geological Setting

The area under investigation forms a part of Precambrian rocks of Lesser Garhwal Himalaya covering the Autochthonous zone and Krol Nappe (Fig. 93.1) tectonic divisions of Auden (1937). The Tons thrust demarcates boundary between allochthonous Krol nappe and autochthonous Simla Group rocks. The Tons thrust is exposed by and large parallel to Tons river but it cuts across it at north of Kishau village in the study area. Auden (1937) is of the opinion that the Krol Nappe rocks—represented by Chandpur, Nagthat, Blaini, Infra Krol, Krol Tal and Subathu Formations, have been translated for about 8 kms southwards along the Krol Thrust over the Simla slates. The Quaternary sediments comprising of semi-consolidated to unconsolidated pebbles, cobbles, boulders, sand, silt and clay occur either as fluvial deposits in the area along the river beds and streams. These materials are also seen at higher elevation than the present river course (Fig. 93.2).

93.4 Structure and Tectonics

The detailed structural analyses (Srivastava 2011; Srivastava and Lakhera 2007) carried out in the Tons valley region recognize multiple phases of deformation in these Precambrian rocks. As a result there exists much complexity in the geology of the area. However, the intensity and style of deformation of Krol Nappe zone and the Autochthonous zones are not same. These deformational phases have brought about the development of many pervasive or non pervasive planes of weakness such as foliations, axial planes of the folds, faults, thrusts joints and lineaments on varying scales of local and regional dimensions.

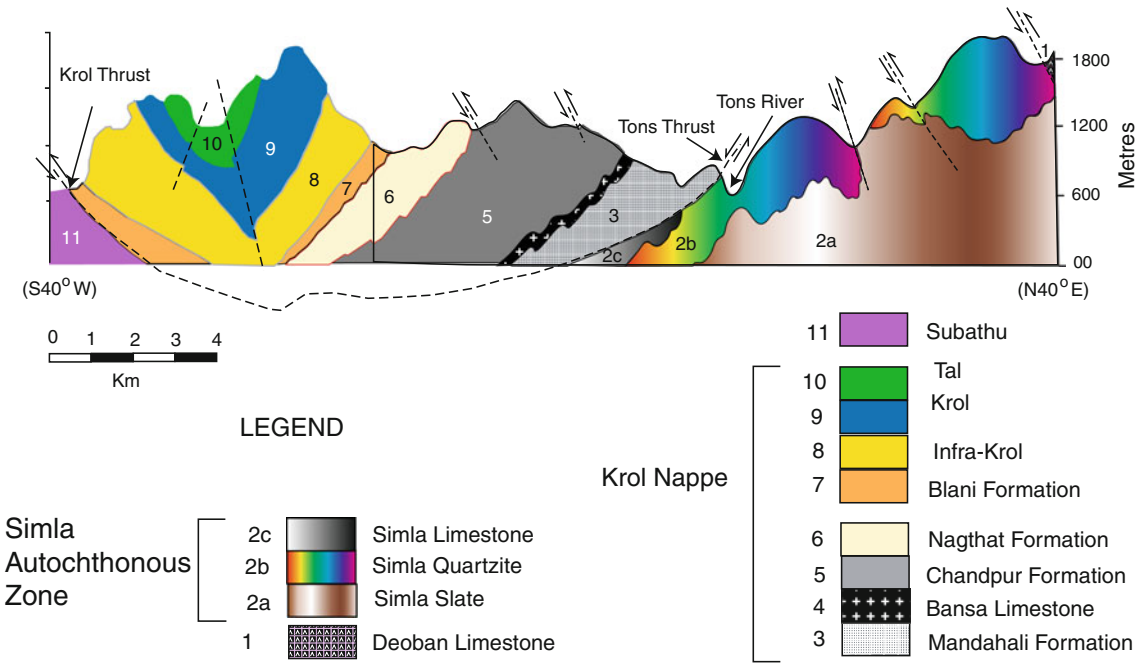

Fig. 93.1 A schematic geological section across the Kishau dam area showing the tectonic conditions of Simla autochthonous zone and Krol Nappe. Kishau dam will be placed on Tons river which is near the Tons thrust

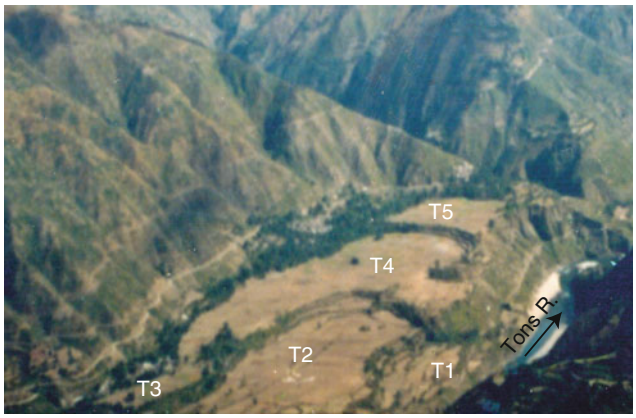

Fig. 93.2 Field photograph showing five levels of Quaternary river terrace formed by Tons river on its left bank in the vicinity of Kishau dam site near Kwanu village

Orientations of the planar fabrics, linear fabrics and folds have their due impact on the strength of the rocks. The orientation of the reconstructed stress conditions using the orientation of shear joints (one of the latest developed structures) reveals maximum principal stress direction towards SSW-NNE, a stress direction matching with the principal stress direction of collision of Indian and Tibetan plates.

93.4.1 Active Tectonics

The area under study is traversed by numerous faults some of them are still active. The faults of the study area are classified as transverse and longitudinal (Srivastava and Lakhera 2007). In the study area, faults that strike parallel or sub-parallel to the strike direction of axial plane of macroscopic F_3 folds are termed as longitudinal faults. Many of these faults which strike NW-SE, have controlled the flow direction of Tons river to a large extent. The longitudinal faults occurring along the Tons river, have the upthrown side towards the left bank of the river due to its reactivation which is evidenced by the river bed material (fluvial deposits) on the elevated portions. Such fluvial material can be observed at many places along the Tons river banks and most of them occur only one (left) side of these faults (Fig. 93.2).

Many of the other faults of present area belong to the categories of transverse fault. The transverse faults seem to be younger than longitudinal faults in their geological history because they have displaced many other structures, such as longitudinal faults, lineaments, Deoban Fault, Tons Thrust and Krol thrusts. They are responsible for sudden change in the course of drainage along fault line. They have shown both sinistral and dextral strike-slip movements along the fault traces. Reactivation of these faults adds up a vertical component along them. The reactivations of these longitudinal and transverse faults are very well reflected in the upliftment and displacement patterns of the river terraces as an exhibition of the neotectonic activities.

There are a number of fluvial terraces mapped in the study area that range in dimensions from 600 to 11,200 sq. m. These terraces are made up of sediments brought by Tons river. All these terraces occur outside the Krol nappe zone and lay over the autochthonous rocks of Simla Group and Deoban Group. Kwanu terrace is one of the most eye catching plain-like geomorphological features in the rugged mountainous terrains of the study area. The terrace shows five levels (T_1–T_5) with a gradual semi circular stair wise lowering towards north and west directions (Fig. 93.2). The terrace lies in the left bank of Tons river and it can be easily seen on satellite images and aerial photographs. The uplifting of the terrace has occurred in five impulse evidenced by the five arc shaped stair casing on it (Fig. 93.2).

The upliftment of recent sediments definitely indicates for ongoing active tectonics in the region. Five tectonic impulses have been recognized in the form of five terrace levels (T1–T5) in Quaternary sediments along Tons river in the autochthonous zone. The oldest of these terraces (T5) has been dated as 12.9 ± 1.1 ka, while the youngest one (T1) gave average OSL dating of 0.244 ± 0.037 ka. The average rate of upliftment has been calculated as 9.7 mm/year for the autochthonous rocks as a whole.

93.5 Discussion and Conclusion

The prevalent active tectonics around the dam site need studies in a broader region than that confined around the dam site. Auden (1937) has already recognized that the Krol napped has moved 8 km southward from its root zone and now resting over the autochthonous rocks of the Simla Group. With the dating of the uplifted terrace sediments, it has been recognized in present study that movement of the Krol allochthon over the Simla Group autochthonous zone along Tons Thrust is still on. The southward movement of hanging wall block of Krol allochthon along the Tons Thrust crops up as Krol thurst in the southern part of the Krol nappe (Fig. 93.1) where numerous features of active tectonics are visible. The progressive movements of the Krol allochthon along Tons Thrust towards SSW, is responsible for mass transfer and thus releasing loads from the autochthonous zone of Simla Group. The release of weight is responsible for upliftment of the Simla Group autochthonous zone that lies north of the Tons Thrust

causing the development of many morphotectonic features such as terrace upliftment, reactivation of some of the preexisting fault planes and triggering of landslides in the area. Five tectonic impulses that have been recognized in the form of five terrace levels (T1–T5) in Quaternary sediments along Tons river in the autochthonous zone gave the average rate of upliftment as 9.7 mm/year for the autochthonous rocks as a whole.

This kind of continued movement has many engineering geological and tectonic implication regarding the location of the actual site of Kishau dam, such as: (1) The zones occurring in the vicinity of Tons thrust have been found as the most active tectonically. It is also manifested by distribution of majority of active landslides in its vicinity. Thus the Kishau dam site should not at all be close to Tons thrust. (2) The Kishau dam location should also not be put in the allochthonous part, and hence, the Kishau village which lies in this part cannot be good site because a dam here will not remain stable but move away along with the nappe sheet. The decision of shifting of the dam site location from Kishau village to further upstream of Tons river in Samberkhera village appears to be better because the Samberkhera village lies in the autochthnous zone. (3) The autochthonous part (northern side of the Tons Thrust) of the area though getting uplifted may be better than other areas in the region. Moreover, the additional weight of impounded water in the reservoir will try to retard the vertical movements of the autochthonous zone. However, the water level in reservoir should never touch the Tons thrust as the water will now act as lubricant or facilitator of the movements along the thrust which may be disastrous.

References

Auden JB (1937) Structure of the Himalaya in Garhwal. Rec Geol Surv India 71(4):407–433

Bilham R, Gaur VK (2000) Geodetic contribution of the study of seismotectonics in India. Curr Sci 79:1259–1269

Molnar P, Tapponier P (1975) Cenozoic tectonics of Asia: effect of collision. Science 189:419–426

Nakata T, Otsuki K, Khan SH (1990) Active faults, stress field and plate motion along the Indo-Eurasian plate boundary. Tectonophysics 181:83–95

NRSC (2012) http://india-wris.nrsc.gov.in/wrpinfo/index.php?title=KishauDamProject_D00717

Srivastava V (2011) Structural control of Lead and Zinc mineralization in a part of Tons River valley, Uttarakhand- Himachal Lesser Himalaya. J Sci Res 55(1&2):1–10

Srivastava V, Lakhera RC (2007) Geology, structure and tectonics of the Kwanu-Shillai area, Uttaranchal- Himachal Pradesh, using remote sensing techniques. In: Saklani PS (ed) Himalaya (Geological Aspects), vol 5. Satish Serial Publishing House, New Delhi, pp 229–264

UJVN (2014) http://www.uttarakhandjalvidyut.com/kaisu.php

Valdiya KS (1986) Neotectonic activities in the Himalayan belt. In: International symposium on Neotectonics in South Asia, Survey of India, Dehradun, pp 241–267

Valdiya KS (2001) Reactivation of terrain-defining boundary thrusts in central sector of the Himalaya: implications. Curr Sci 81:1418–1430

Numerical Simulation of High Level Radioactive Waste for Disposal in Deep Underground Tunnel

94

Amit Kumar Verma, Pradeep Gautam, T.N. Singh and R.K. Bajpai

Abstract

It is necessary to isolate the long-lived high level radioactive waste from environment for the protection of ecosystem. One of the methods suggested to isolate the nuclear waste from ecosystem is its burial in deep underground repository. In this paper, a discrete element method approach is used to simulate the effect of heat generated after buried of radioactive waste on stability of underground space and its surrounding rock strata. Effect of temperature increment on stresses-strains and temperature variation of surrounding rockmass due to heat generated by nuclear waste is studied and discussed. Simulation was performed on both strong and weak granite rock in which tunnel is excavated. Clay is used as buffer because of its high sorptivity, longevity, and low permeability. The simulation is carried out for 16 years at constant heat flux generated by canisters containing nuclear waste to study the maximum possible effect on tunnel and surrounding rockmass for a period of time.

Keywords

Nuclear waste • Deep geological repository • THM • Discrete element • PFC

94.1 Introduction

Nuclear power is an important and vast source of energy. The major technical drawback of nuclear power is that it produces high-level radioactive waste (HLW) which can be in gaseous, liquid, solid or a composite forms and their radiation strength vary over a large scale (Giusti 2009). These are hazardous radiations which greatly affects its surrounding environment so there is need of its isolation from the ecosystem. Although radioactivity of waste depletes with time, but it remains highly dangerous for long period such is essential to be isolated from the living environment, until it has decayed to levels that cause no significant risk to health and contamination. Long lived radioactive element are Strontium (^{90}Sr), and Caesium (^{137}Cs), found in nuclear waste whose half-lives are approximately of 30 years. Radioactive waste is generated by a wide range of industrial, medical and military activities, each having its own specific inventory of radio nuclides.

There are various possible methods adopted for safe disposal of nuclear waste like recycling, transmutation (Chwaszczewski 2003; Vladimir et al. 2005), space disposal (Ehricke 1983), ocean disposal, ground burial (Kwon 2005) etc. Whatever is the method of disposal, measurement and understanding of radiation affect on surrounding environment is utter importance. Out of these methods disposal of highly hazardous radioactive waste in deep underground

A.K. Verma (✉) · P. Gautam
Department of Mining Engineering, Indian School of Mines, Dhanbad, Jharkhand-76, India
e-mail: neurogeneticamit@gmail.com

T.N. Singh
Department of Earth Science, Indian Institute of Technology, Powai, Mumbai-76, India

R.K. Bajpai
Technology Development Division, Nuclear Recycle Group, BARC, Mumbai-76, India

G. Lollino et al. (eds.), *Engineering Geology for Society and Territory – Volume 1*,
DOI: 10.1007/978-3-319-09300-0_94,

Table 94.1 Parameters that define a contact-bonded material (Hard and Jointed Granite)

Parameters	Hard granite	Jointed granite
Height (m)	25	25
Width (m)	25	25
Minimum ball radius (m)	0.006	0.006
Ball size ratio, uniform distribution	1.66	1.66
Wall normal stiffness multiplier	1.1	1.1
Ball density (Kg/m^3)	2660.0	2660.0
Ball-ball contact modulus (GPa)	88.0	10.0
Ball stiffness ratio	1.0	1.0
Ball friction coefficient	0.50	0.50
Contact bond normal strength mean (MPa)	200	20
Contact bond normal strength standard deviation (MPa)	50	0.5
Contact bond shear strength mean (MPa)	200	20
Contact bond shear strength standard deviation (MPa)	50	0.5
Specific heat (J/Kg K)	1,576	1,576
Thermal expansion coefficient	1.92×10^{-5}	1.92×10^{-5}
Conductivity (W/mK)	2.523	2.523

repositories/tunnels has been chosen as solution by several developed and developing countries. In order to ground burial of radioactive wastes several factors must be taken into account concerning the safety of the site where a nuclear waste repository's (NWR) construction is planned. Among them are the depth of the burial, the tectonic stability, the geo- hydrological properties of the host rock and the properties of the rock for proper radioactive attenuation. In the process of ground disposal, a suitable site is located which can able to tolerate the effect of radiation on it. The site is then excavated with required dimensions and bore holes are created in it. In these bore holes, clay material is filled with canister, mainly made up of high strength and non corrosive metal is placed in it. Radioactive waste is sealed in the canister. The second layer of protection has been provided by clay. These layers will also provide protection not only migration of heat but also prevent any kind of migration and contamination in surrounding medium. Applied and basic sciences of clay mineralogy have played a significant role in radioactive waste disposal practices. Clay material is used because its high sorptivity, longevity, and low permeability make it promising candidate for retaining most natural and anthropogenic long-lived radio nuclides within the contaminated and engineered disposal sites (Allard 2009). In this paper, two numerical models have been simulated in PFC 2D (Itasca 1999) to demonstrate the effect of nuclear radiations on the underground disposal tunnel in strong and weak granite rock. It is a commercial code based on DEM (discrete element method). A physical problem that is concerned with the movement and interaction of circular particles may be modelled directly by PFC2D (Cundall and Strack 1979; Potyondy et al. 1996). This study aimed to demonstrate the feasibility of PFC2D to excavate an underground tunnel and examine its behaviour by simulating the thermal effect of nuclear waste disposal. In this approach, initially, an assembly of particles is constructed with required micro parameters like Elastic modulus, Poisson's ratio, Friction, Density etc. In assembly a tunnel is excavated as per geometry. Then, the effect of ground water and heat generated by nuclear waste is examined on the assembly.

94.2 Numerical Modelling

94.2.1 Validation

Inverse modelling for intact rock properties: Particle flow model simulates the mechanical behaviour (both static and dynamic) of a material by representing it as an assembly of circular particles that can be bonded to one another. Contact bonded material is used for simulation of rock. To obtain desired micro-properties which can match the laboratory results of rock there is need for inverse modelling which can simulate laboratory tests. For this purpose inbuilt Fish functions for biaxial and tensile (brazilian) tests are used. Micro-properties obtained by this procedure are listed in Table 94.1. The macro and micro-properties of canister and clay used in the model are given in Table 94.2.

Table 94.2 Parameters that define clay and canister material

Parametres	Clay	Canister
Ball density (Kg/m^3)	2,670	3,500
Contact bond normal strength mean (MPa)	250	2,500
Contact bond shear strength mean (MPa)	250	2,500
Specific heat (J/Kg K)	888	424
Thermal expansion coefficient	3.1×10^{-4}	1.2×10^{-5}
Conductivity (W/mK)	1.74	43

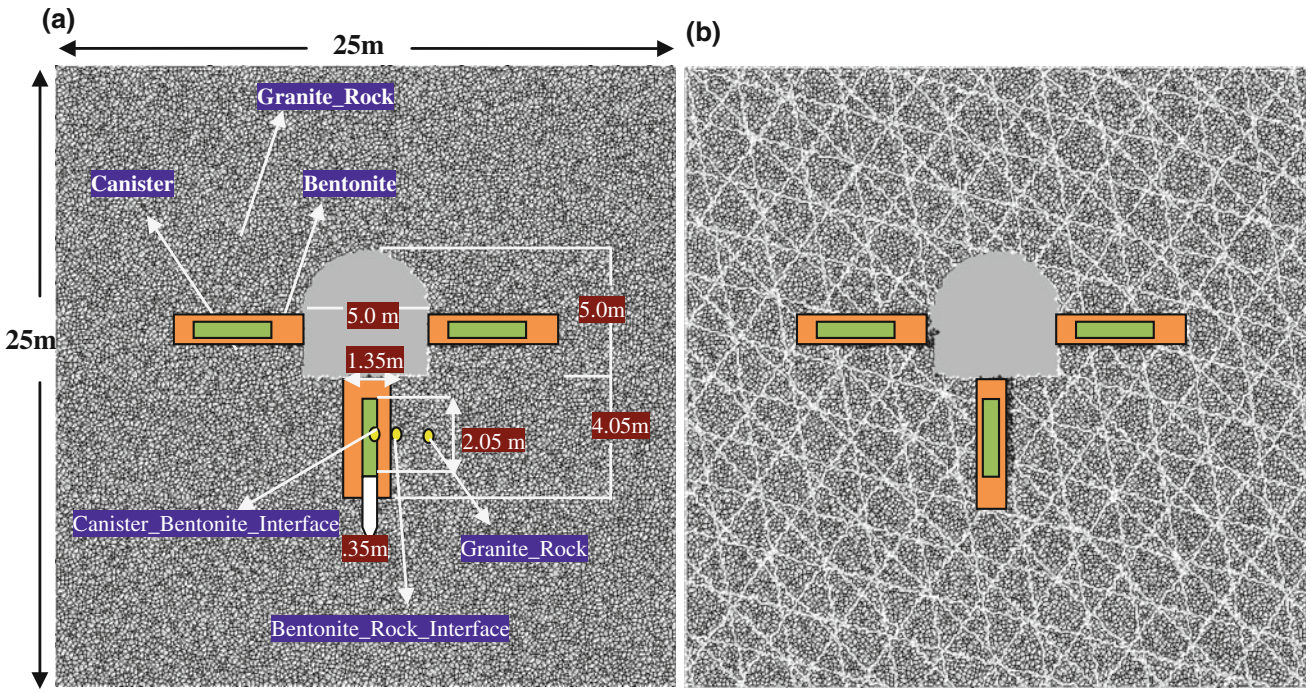

Fig. 94.1 Mechanically stable model of excavated tunnel in **a** Hard granite rockmass and **b** Jointed granite rockmass, and disposal holes with canisters

94.3 Case Study

Two models that is each intact and joint rock consist of 26,242 particles or balls having radius of range 0.06–0.0996 m are generated by radius expansion method. In each case, contact bonded assembly in square shape of dimension 25 × 25 m is generated. To create a model of jointed granite, there joints sets were incorporated at different angles shown in Fig. 94.1b. Insitu stress is applied to these models to create the insitu stress environment. These stresses are applied using built-in FISH function. Now, the whole assembly is solved to reach the equilibrium. After reaching at equilibrium a horseshoe shape tunnel is excavated in the square space and properties of buffer (bentonite) and canister are given in disposal area (Fig. 94.1a, b). In this model, canisters have dimension of 2.05 × 0.35 (length x diameter) and are used for containing the nuclear waste. After the excavation, models are solved for stability by applying gravity loading. Displacements, stresses and velocities of 10 vunerable positions were recorded at an interval of 5 steps.

94.3.1 Applying Heat Flux

A constant heat flux of 50 W/m^2 is applied to the all canisters. Hence canisters behave as a source of heat. Initial temperature of the model is taken as 21 °C. In these models, constant heat flux is applied to canisters to analyse the thermal effect for one year. Effect of heat flux generated by nuclear waste can also be analysed for hundreds years by varying heat flux with time but it takes much computational time so effect of constant heat flux for one year is analysed to

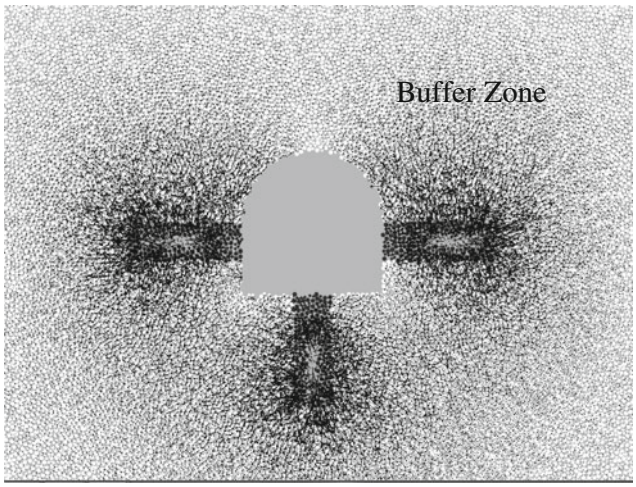

Fig. 94.2 Thermal heat distribution in particles

understand the behaviour of heat migration and subsequent effect in surrounding rockmass. Models are solved by coupled thermo-mechanical mode to study the both thermal and mechanical effects with time. Due to thermal expansion of particles, stresses and strains will develop in the system. So, all three stress components, displacement in x and y-direction, velocity in x and y-direction and temperature at 10 different vulnerable locations were recorded at every 5 steps. Strain energy, frictional work and kinetic energy of whole model were also calculated at an interval of 5 steps.

94.4 Results and Discussion

In each step heat released by canister models are solved for reduction in unbalanced force to simulate the real sequence of tunnel excavation. Effect on temperature, stresses and strains of selected locations is observed for 16 years.

Heat power distribution and displacement of particles: Thermal heat distribution in canister particles is occurred with a magnitude proportional to their radii. Conduction of heat power occurs through contact bonds between particles. As power is dissipated by the radioactive waste as exponentially decay so its effect would be observed for long time but because of the computational time required for solving numerical model, a constant heat flux (maximum heat generated by nuclear waste) for one year is applied to the canisters to analyse the maximum possible effect of heat generated and dissipated by waste. Most of the heat power is accumulated in buffer due to its low thermal conductivity. Roof of the tunnel experiences less heat migration as its distance from the heat source (canisters) is more than other locations. Figure 94.2 shows the closer view of tunnel, it can be seen that most of the heat source is present in buffer material in floor of the tunnel and low heat energy is present at roof of tunnel. In the floor heat power decreases towards the corners but bentonite particles (buffer material) also experience low power because of its buffer material properties.

94.4.1 Temperature Effect

For the thermal analysis, initial temperature of each particle is kept 21 °C. As the model dimensions are small so effect of thermal gradient of earth is neglected. Figure 94.3a demonstrates temperature variation in every region with reference to the canisters. Temperature is maximum in buffer material and minimum at roof of the tunnel. Because of constant heat generated by canisters, temperature of canisters shall rise at very high rate. It can be seen that maximum temperature reached in 16 year in canister is about 90 °C as compared to base temperature equilibrium i.e. 21 °C. Temperature at different points of floor and boundaries of tunnel is different. It is maximum in the middle of floor and decreases towards boundaries and again increases in the middle section of boundaries of tunnel where canister is disposed and again decreases with height. It is because; thermal energy is absorbed by buffer and granitic rock. It is observed that temperature increment in roof of tunnel is minimum (1 °C). It is maximum in the floor of tunnel because floor particles experience combined effect of thermal heat radiation of all three canisters but in roof, particles are affected by two canisters (as the canister disposed in floor of tunnel has negligible effect on roof). It is also observed that the rate of temperature increment is maximum in canister and minimum in buffer material. It is because material of canister is more thermally conductive than buffer and surrounding rock. At initial stage of applying heat flux, temperature increment in the particles near wall of tunnel was zero but with time it increases at high rate than buffer particles because of the higher conductivity of granitic material than bentonite. In both models, temperature increment observed similar.

94.4.2 Effect on Stresses

Among all selected 4 monitoring points, σ_{xx} is accumulated mostly in the location near to the canisters. Stresses acting on particles increase with increase in temperature (Fig. 94.4b). This may be due to the increment in temperature resulted from thermal expansion of particles and also due to the increased contact forces between particles. Stress accumulation is maximum at the centre of the floor of the tunnel and decreases with distance from centre point. At the roof of tunnel, there is very little variation in temperature, so, change in σ_{xx} is very less.

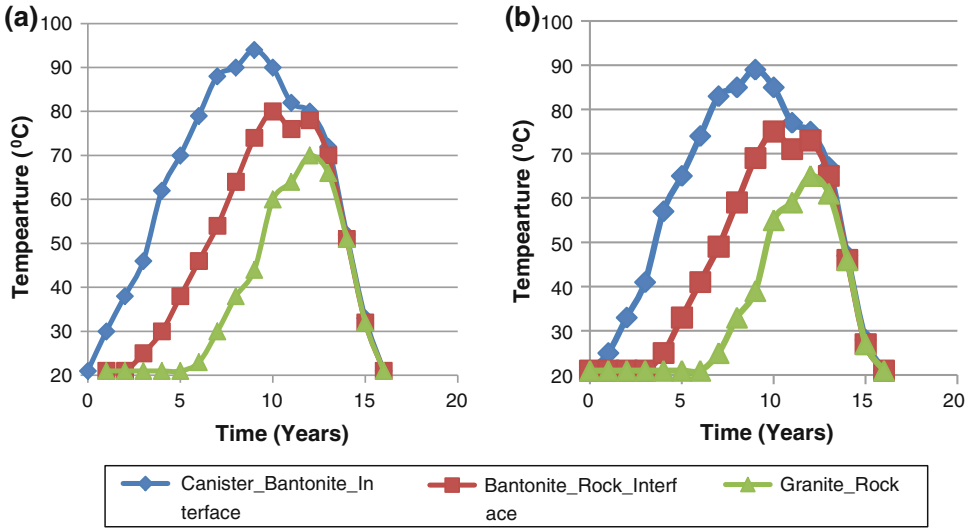

Fig. 94.3 **a** Temperature variation of DGR without joint at different monitoring points. **b** Temperature variation of DGR with joint at different monitoring points

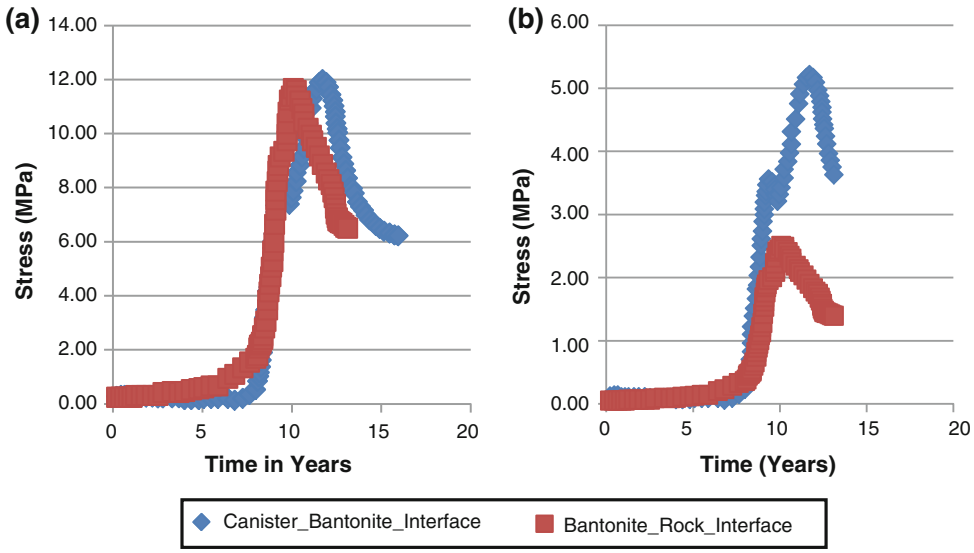

Fig. 94.4 **a** Stress variation of DGR without joint at different monitoring points. **b** Stress variation of DGR with joint at different monitoring points

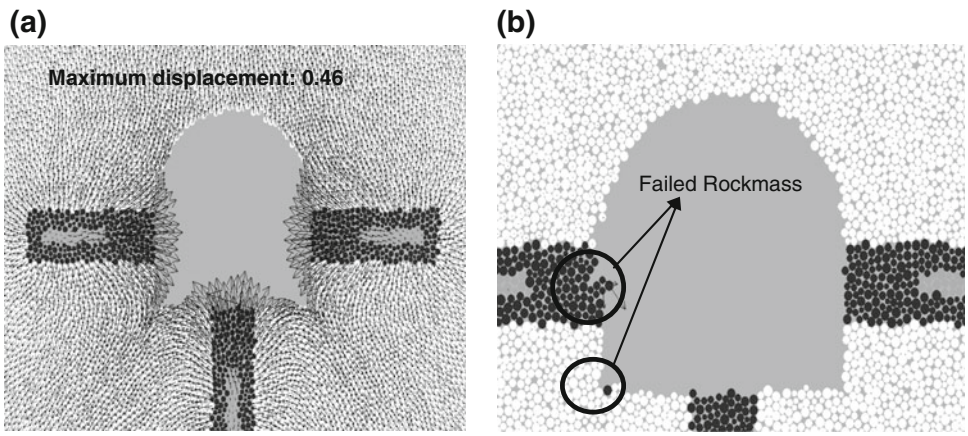

Fig. 94.5 **a** Displacement of particles in the tunnel in hard granite after 16 year **b** Falling of particles in tunnel in jointed granite rock mass

94.4.3 Effect on Strain

Displacement of particles nearest to the tunnel floor, sides and buffer is maximum due to more increment in temperature hence more thermal expansion (Fig. 94.5a). At the roof of the tunnel displacement of particles are negligible because there is very small increment in the temperature. Figure 94.5b shows the falling of particles from boundary.

94.5 Conclusion

In this paper a numerical simulation based on discrete element method of a new approach to dispose the nuclear fuel waste is presented here. Numerical models of a tunnel in hard and jointed granitic rock mass with disposal hole densely filled with buffer (bentonite) and canisters (containing nuclear waste) at the centre of tunnel floor and sides were prepared. Because of computational time required to simulate this model effect of constant heat flux for 16 year is studied. Change in stress, strain and temperature was studied at the selected locations. It was observed that displacement of particles is maximum near the canisters. Buffer experiences compression and canister is in tension zone. Temperature increment at the centre of floor is maximum and minimum at roof. Maximum temperature increment over 16 year time is observed 94 and 90 °C without and with joint cases. There is some rockmass failure in case of jointed granite which suggests that radioactive waste should be disposed in tunnel with high strength and least fractured rock strata.

References

Allard Th (2009) Radiation effects on clay mineral properties. Appl Clay Sci 43:143–149

Chwaszczewski S (2003) Transmutation of radioactive waste. Appl Energy 75(1–2):87–96

Cundall PA, Strack ODL (1979) A discrete numerical model for granular assemblies. Geotechnique 29:47–65

Ehricke KA (1983) A practical approach to the disposal of highly toxic and long-lived spent nuclear fuel waste between Venus and Earth. Acta Astronaut 10(11):719–737

Giusti L (2009) A review of waste management practices and their impact on human health. Waste Manag 29(8):2227–2230

Itasca Consulting Group (1999) PFC2D users' guide, command reference, FISH reference, and theory and background, minneapolis, Itasca Consulting Group Inc., Minnesota

Kwon (2005) Concept development of an underground research tunnel for validating the Korean reference HLW disposal system. Tunn Undergr Space Technol 2:203–217

Potyondy DO, Cundall PA, Lee CA (1996) Modeling rock using bonded assemblies of circular particles. In: Rock mechanics tools and techniques (Proceedings of the second North American rock mechanics symposium NARMS96), Rotterdam, Balkema, pp 1937–1944

Vladimir A, Saito Masaki, Stankovsky Alexey (2005) Challenge of transmutation of long-lived nuclides. Prog Nucl Energy 47(1–4):327–338

The Model and Experiments of Solubility of CO_2 in Saline with Complex Ions

95

Wang Lu and Yu Qingchun

Abstract

Geological storage of CO_2 is recognized as an effective way in reducing the greenhouse effect, and saline aquifers hold the greatest potential for CO_2 storage. CO_2 solubility in saline groundwater is a key parameter for assessing storage capacity in saline aquifer and CO_2 leakage risk. Establishing models to predict CO_2 solubility accurately with coexisting mixed ions is still a difficult problem. Based on the equations of state, this paper proposes a semi-empirical model to calculate CO_2 solubility according to experimental CO_2 solubility data. The solubility of CO_2 in aqueous $MgCl_2$ and $CaCl_2$ solution was measured. New experimental apparatus was established specifically for the CO_2 solubility measuring at the *T-P-m* range according to the geological reservoirs. The predicted values are proposed at a comprehensive combination of *T-P-m*. The average absolute deviation of CO_2 solubility between the model and experimental results is 2.37 %, and the maximum absolute deviation is less than 5.146 %. The proposed model therefore possesses high accuracy and better adaptability to saline groundwater with mixed ions.

Keywords

Geological carbon storage • Saline groundwater • CO_2 solubility

95.1 Introduction

As a consequence of the high-use fossil fuels, the emissions of CO_2 increase so rapidly that they bring evident greenhouse effect. Climate change, consequently, has caused a series of environmental problems, such as melting glaciers, rising sea levels, extreme weather events and damage to ecosystems. In order to alleviate these problems, carbon capture and storage (CCS) technology should be attended as a potential option for large scale mitigation of anthropogenic CO_2 (Vishal et al. 2013a). In terms of carbon storage, geological formation is a currently accepted option to reduce CO_2 emissions into the atmosphere (IPCC 2005; Bachu et al. 2007; Darwish and Hilal 2010). In general, offshore saline sedimentary basins, depleted oil and gas fields, basalt formations and unmineable coal seams are potentially targeted for geological storage of CO_2 (Vishal et al. 2013b). Among all the geological formations, deep saline aquifers potentially have the largest storage capacity (Bachu et al. 2007; Darwish and Hilal 2010).

CO_2 solubility is crucial not only for the solubility trapping in saline aquifers, but also for modeling the reaction of CO_2 with minerals in the aqueous phase (Yan et al. 2011). Obtaining the accurate CO_2 solubility is indispensable for the CO_2 storage estimate, carbonate precipitation, risk assessment of supercritical CO_2 leakage and fluid inclusions (Spycher and Pruess 2003).

Previous researches have mainly focused on the solubility of CO_2 in pure water and aqueous NaCl solutions (Yan et al. 2011) as the coexistence of different ions makes it hard to model the solubility of CO_2 (Duan et al. 1992).

W. Lu · Y. Qingchun (✉)
School of Water Resources and Environment, China University of Geosciences (Beijing), Beijing 10083, China
e-mail: yuqch@cugb.edu.cn

G. Lollino et al. (eds.), *Engineering Geology for Society and Territory – Volume 1*,
DOI: 10.1007/978-3-319-09300-0_95,

Therefore, data for CO_2 solubility in important alkaline-earth halides at reservoir conditions are relative scarce, although they have non-negligible effect on the solubility of CO_2 (Tong et al. 2013). So this model is proposed for calculating the solubility in an easier way with satisfied precision by quantifying the extents of different cations.

95.2 The Model

The CO_2 solubility model has been established based on the solubility data of CO_2 in pure water. A semi-empirical equation derived from Setschenov formula (Darwish and Hilal 2010) is added and modified by the experimental measurements in this work.

The CO_2 solubility is obtained in this study by determining the ratio of CO_2 solubility in pure water (calculated) and aqueous solutions. The fundamental equation is referred to as Eq. (95.1), where m is the concentration of Na^+, c_{g0} is CO_2 solubility in pure water, c_{gs} is CO_2 solubility in aqueous NaCl solutions and k_{gs} represents the Setschenov constant.

The calculated results will fit better to the experimental measurements if Eq. (95.1) is modified to Eq. (95.2) at the conditions in this study, where m is a function of the mixed ions.

$$\log\left(\frac{c_{g0}}{c_{gs}}\right) = k_{gs}m \tag{95.1}$$

$$\lg\left(\frac{c_{g0}}{c_{gs}}\right) = f(p,T) \times m \tag{95.2}$$

$$\begin{aligned} f(p,T) = (0.342 \times p_r^{\frac{8}{9}} \times \left(\frac{318}{T}\right)^{\frac{7}{9}} - \lg\left(\frac{p}{5000}\right)^{1.47} - 0.1187) \\ \times [(-8.772) \times \alpha + 0.076 \\ \times (T - 273.16)^{0.98} + 13.260] \end{aligned} \tag{95.3}$$

$$\alpha = 0.215 \times p_r^{1.04} T_r^{0.58} \times 0.057 e^{1813 \times \left(\frac{1}{7} - \frac{1}{318}\right)} \tag{95.4}$$

As Eq. (95.5) shows, different coefficients are distributed to different ionic species. Solubility of hydrophobic molecules decreases with increasing ionic strength (Xie et al. 1997), and the hydrated radius of cations will also affect the solubility (Erten et al. 2008). So taking both the characteristic into consideration, these coefficients are determined based on ionic potentials and the experimental data, where ionic potential is denoted as the ratio of the electric charge and the hydrated radius of the cation.

$$M = 1.064[Na^+] + [K^+] + 2.136[Ca^{2+}] + 2.232[Mg^{2+}] \tag{95.5}$$

$$m = 0.0347 \times M \tag{95.6}$$

95.3 The Experiment

The core part of the experimental setup is a steel autoclave with the volume of 500.00 mL (shown as Fig. 95.1). The precision pressure gauge is connected to the top of the autoclave and the setup is seated in a heated water bath.

The saltwater of V_2 was injected into the autoclave at the beginning of the experiment, and the water bath was applied to adjust the temperature. When the temperature of the system was constant, high-pressure pump was applied to inject certain amount of CO_2 into the autoclave to reach the preset pressure. When the system of CO_2–H_2O was in equilibrium (this period lasted about 12 h), CO_2 existed in two different phase state: supercritical state with the moles denoted as N_1 and dissolved CO_2 with the moles of N_2.

To begin with the measurement, the temperature and the pressure were recorded, respectively. Then the valve of the autoclave was turned on and CO_2 displaced H_2O out of the measuring cylinder at 1 atm, the volume of which was denoted as V_3. After the drainage, the water bath was used

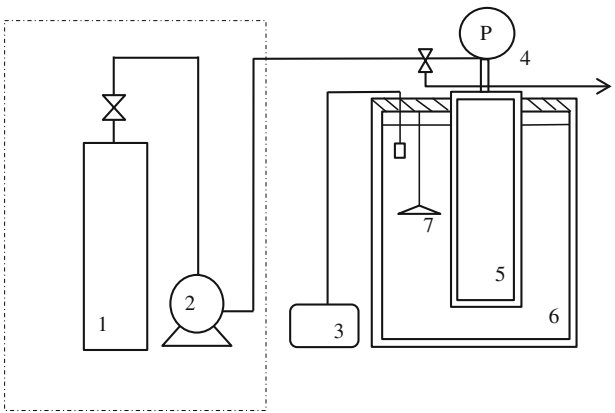

1.CO_2 storage tank 2. Booster pump 3.Temperature controller
4. Precision pressure gauge 5. High pressure autoclave.
6. Heated water bath 7. Stirrer

Fig. 95.1 Schematic diagram showing the experimental set-up of CO_2 solubility experiment. *1* CO_2 Storage tank *2*. Booster pump *3*. Temperature controller *4*. Precision pressure gauge *5*. High pressure autoclave *6*. Heated water bath *7*. Stirrer

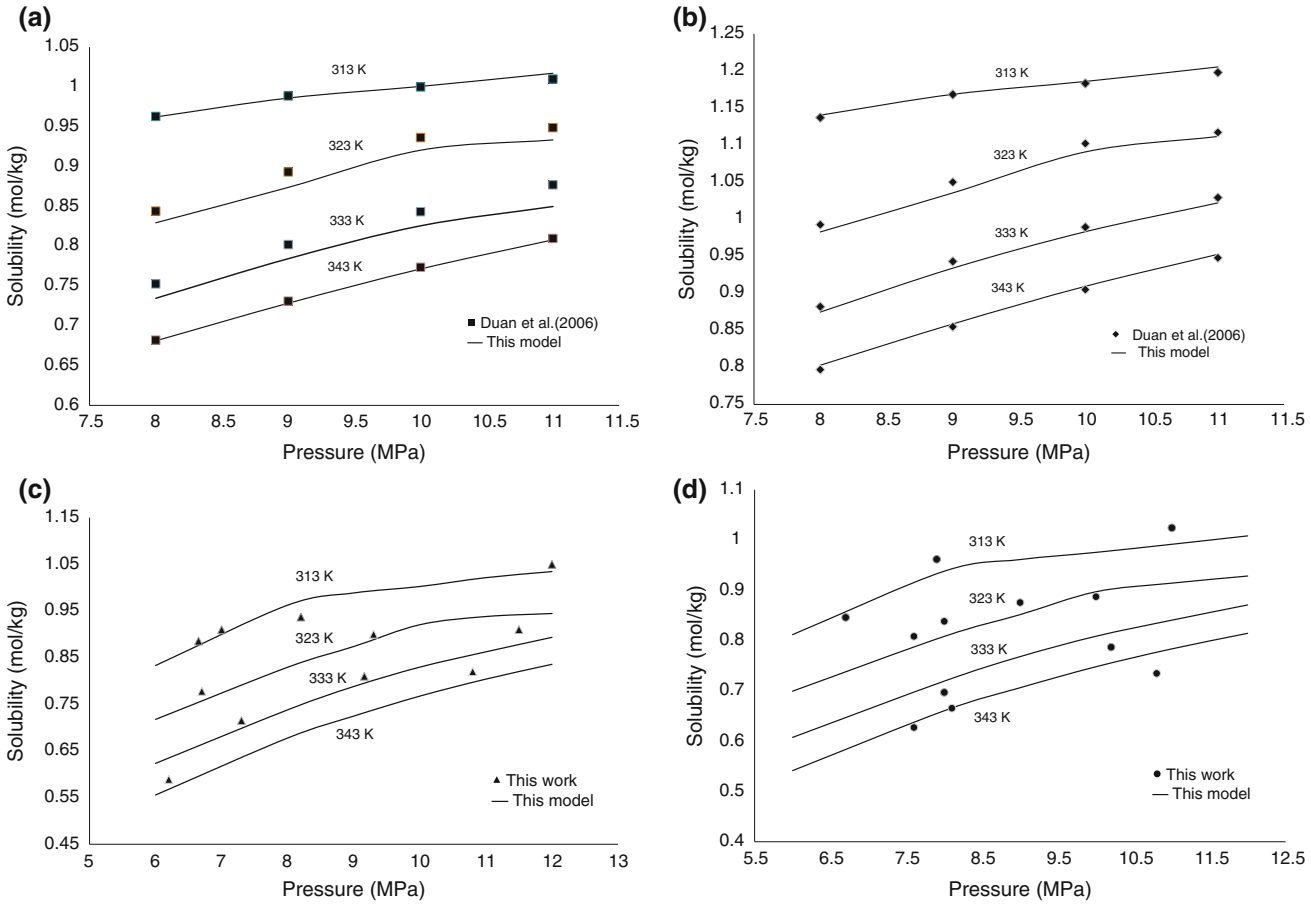

Fig. 95.2 Comparison of predicted values of CO_2 solubility with Duan's model and the experimental measurements. **a** comparison of model predictions in aqueous NaCl solution. **b** comparison of model predictions in aqueous KCl solution. **c** comparison between model predictions and experimental data in aqueous $CaCl_2$ solution. **d** comparison between model predictions and experimental data in aqueous $MgCl_2$ solution

to control the autoclave to room temperature. 10 mL solution with unsaturated CO_2 was sampled and the concentration of CO_2 was obtained by titrating with the indicator of phenolphthalein and methyl orange, sequentially. CO_2 concentration is converted to moles and denoted as N_4. By combining N_1, N_3 and N_4, the solubility of CO_2 can be calculated.

$$N_1 + N_2 = N_3 + N_4 \tag{95.7}$$

N_1 is the function of temperature and pressure of the system, and is obtained by Peng-Robinson equation of state shown as Eqs. (95.9)–(13) (Peng and Robinson 1976). V_1 is the volume of CO_2 in the autoclave. In this study, V_1 is 3.70 mL.

$$N_1 = \frac{V_1}{V} \tag{95.8}$$

$$P = \frac{RT}{V-b} - \frac{a(T)}{V(V+b)+b(V-b)} \tag{95.9}$$

$$a(T) = 0.45724R^2\beta(T)\frac{T_c^2}{P_c} \tag{95.10}$$

$$b = 0.07780R\frac{T_c}{P_c} \tag{95.11}$$

$$\beta(T) = [1 + k(1 - Tr^{0.5})]^2 \tag{95.12}$$

$$k = 0.3746 + 1.54226\omega - 0.26992\omega^2 \tag{95.13}$$

Based on the balance of pressure, the volume of CO_2 in the autoclave can be obtained under atmospheric pressure by the drainage volume of V_3. The amount of CO_2 is

denoted as N_3. As the molar volume of the gas varies with temperature, N_3 is calculated by Eqs. (95.14)–(95.15):

$$N_3 = \frac{V_3}{V'} \tag{95.14}$$

$$V' = \frac{22.4T}{273} \tag{95.15}$$

N_4 was denoted as the moles of dissolved CO_2 in the water samples after the drainage. HCl solution of 0.01 mol/L was applied as titrant to titrate 10 mL samples. Phenolphthalein and methyl orange were used as indicators. 0.01 mol/L NaOH was added until the phenolphthalein indicator changed from colorless to pink indicating that only HCO_3^- remained in the solution and the pH was about 8.0. Then the methyl orange reagent was added to the solution. After continuing the titration, the second end point was obtained when the pH reached 4.3, when methyl orange turned to orange from yellow. Only carbonic acid remained in the solution at this point. The volume of HCl consumed was denoted as V_5. The number of moles of dissolved CO_2 was obtained by Eqs. (95.16)–(95.17), where V_4 is the sampling volume of sample, in this study, V_4 was 10 mL and V_2 is the total volume of the solution.

$$N_4 = C \times V_2 \tag{95.16}$$

$$C = \frac{V_5 \times 0.01}{V_4} \tag{95.17}$$

95.4 Results and Discussion

The model results for CO_2 solubility are shown in Fig. 95.2a–d together with the calculated values and the experimental values in this work. Figure 95.2a, b illustrate that this model is in excellent agreement with the Duan's model (Duan et al. 2006) in aqueous NaCl solution (1 mol/kg) and KCl solution (0.2 mol/kg). Curve fitting is better when the pressure is higher than 10,000 kPa, indicating that our method is reliable for CO_2 solubility modeling under the conditions GCS requires.

Figure 95.2c–d indicate that this model is in satisfied agreement with experimental values presented in this work. From the figures we can see that the solubility of CO_2 in aqueous $MgCl_2$ solution (0.5 mol/kg) is less than that in the aqueous $CaCl_2$ solution (0.5 mol/kg). This may be attributed to the fact that $MgCl_2$ is a stronger electrolyte which has a stronger ionic potential. The polarization effect is more evident when the stronger electrolyte is added into the water, which makes the difference of polarities of H_2O and CO_2 increases, leading to the release of CO_2.

However, the model results tend to under-predict CO_2 solubility at 338 K, whereas the maximum absolute deviation between the two results is less than 5.14 %, which is within the acceptable range of experimental error. The fluctuation of the errors could be explained by the fact that the polarization effects of ions, which may affect the solubility, varies with temperature, but the model deals with such effects based on unified weighted processing.

95.5 Conclusions

In this study, both the modeling calculations and experimental measurements have been performed to acquire accurate CO_2 solubility data, which is important for estimating CO_2 sequestration in saline aquifers.

(1) In this paper, our mixed ions model and the models proposed by Duan et al. (2006) are compared in calculating CO_2 solubility in aqueous solutions containing NaCl and KCl solution. The comparison is also made between the results of this model and the experimentally measured values in this work. The average absolute deviation between our predicted values and literature model results is 2.77 %.

(2) Experiments measuring CO_2 solubility were conducted with the solutions containing Ca^{2+} and Mg^{2+}. The method of measuring the volume of CO_2 at atmospheric pressure was applied in the experiment, and double indicator titration was used to measure the amount of residual CO_2 in the solutions, which is found to provide good accuracy.

(3) The average absolute deviation between the model results and experimental measurements of CO_2 solubility is 2.37 % and the maximum absolute deviation is 5.146 % in the range of 313–343 K. The average absolute deviation at 313 K is 2.43 %, and this fluctuates with increase temperature to 2.35 % at 343 K. Average absolute deviations between the model results and experimental measurements also show a decreasing trend with increasing pressure, that is, the deviation decreases from 2.48 to 2.15 % as the pressure rises from 6,000 to 12,000 kPa.

Comparative analysis of our mixed ions model, the experimental values and the calculated results from other scholars show that the model proposed in this paper has a satisfactory adaptability for the solubility calculation of CO_2 in saline groundwater.

References

Bachu S, Bonijoly D, Bradshaw J, Burrussd R, Hollowaye S, Christensenf RP, Mathiasseng OM (2007) CO_2 storage capacity estimation: methodology and gaps. Int J Greenhouse Gas Control 1:430–443

Darwish NA, Hilal N (2010) A simple model for the prediction of CO_2 solubility in H_2O–NaCl system at geological sequestration conditions. Desalination 260:114–118

Duan ZH, Miller N, Weare JH (1992) An equation of state for the CH_4-CO_2-H_2O system: I. Pure systems from 0 to 1,000 °C and 0 to 8000 bar. Geochem Cosmochim Acta 56:2605–2617

Duan ZH, Sun R, Chen Z, Chouc IM (2006) An improved model for the calculation of CO_2 solubility in aqueous solutions containing Na^+, K^+, Ca^{2+}, Mg^{2+}, Cl^-, and SO_4^{2-}. Mar Chem 98:131–139

Erten Y, Güneş-Yerkesikli A, Çetin AE, Çakıcıoğlu-Özkan F (2008) CO_2 adsorption and dehydration behavior of LiNaX, KNaX, CaNaX and CeNaX zeolites. J Therm Anal Calorim 94:715–718

IPCC (2005) Special Report on CO_2 Capture and Storage. Cambridge University Press, Cambridge, United Kingdom and New York, USA

Peng DY, Robinson DB (1976) A new two-constant equation of state. Ind Eng Chem Fundam 15:59–64

Spycher N, Pruess K (2003) CO_2–H_2O mixtures in the geological sequestration of CO_2. II. Partitioning in chloride brines at 12–100 °C and up to 600 bar. Geochim Cosmochim Acta: J Geochem Soc Meteoritical Soc 69:3309–3320

Tong DL, Trusler JPM, Vega-Maza D (2013) Solubility of CO2 in aqueous solutions of CaCl2 or MgCl2 and in a synthetic formation brine at temperatures up to 423 K and pressures up to 40 MPa. J Chem Eng Data 58:2116–2124

Vishal V, Singh L, Pradhan SP, Singh TN, Ranjith PG (2013a) Numerical modeling of gondwana coal seams in India as coalbed methane reservoirs substituted for carbon dioxide sequestration. Energy 49:384–394

Vishal V, Ranjith PG, Pradhan SP, Singh TN (2013b) Permeability of sub-critical carbon dioxide in naturally fractured Indian bituminous coal at a range of down-hole stress conditions. Eng Geol 167:148–156

Xie WH, Shiu WY, Mackay D (1997) A review of the effect of salts on the solubility of organic compounds in seawater. Mar Environ Res 44:429–444

Yan W, Huang SL, Stenby EH (2011) Measurement and modeling of CO_2 solubility in NaCl brine and CO_2–saturated NaCl brine density. Int J Greenhouse Gas Control 5:1460–1477

Analysis of Stability of Slopes in Himalayan Terrane Along National Highway: 109, India

96

V. Vishal, S.P. Pradhan and T.N. Singh

Abstract

Morpho-dynamic terrane of Himalaya is continually facing challenges in stability of rock cut slopes, aggravated due to increased disturbance levels in rock/soil mass due to human intervention. Increased civil constructions, exploitation of resources, deforestation, changing pattern of river-flows and increase in population are among the key reasons for such disturbances leading to increased susceptibility of these slopes. Huge loss of property and lives has been reported every year from the Himalayan regions and therefore, must be attended on a priority basis. The lithological and structural variations, orientation and pattern of different water bodies and vegetation are varied along the slopes indicate site-specific studies of landslide prone areas for assessing the health of slopes and providing early warning, wherever necessary. Highly jointed rock mass along the slopes between Rudraprayag and Agasthyamuni along NH109, which connects to Indo-China border, the hilly population to the plains and runs parallel to River Alakananda, were studied. A detailed field study was carried out in the landslide area and the relevant geological data were recorded. The area constituted of mainly weak phyllitic and schistose rock at most of the places with some jointed and weathered quartzitic rock mass at a few locations. Stability of slope was investigated using two dimensional finite element methods. Slope geometry and rock parameters were incorporated in the models that were analysed for factor of safety. The changes in geomorphology as a consequence of surface and sub-surface deformations were also premeditated. At places, formation of weak tensile zones towards the rear end of the slopes as well as coalescence of schistose rock due to loading, indicate possible subsidence in weak areas, and may lead to changes in landforms. It is indicated that a stable slope in dry season may become hazardous in the wet season and remedial measures may be applied in advance to prevent any major damage to the ongoing traffic and other operations.

Keywords

Slope stability • NH-109 • Finite element method

96.1 Introduction

The National Highway (NH109) witnesses considerably high density traffic especially when the gates for the holy Badrinath and Kedarnath are opened around the end of April. The traffic and tourist density increases manifolds during the months of March to July. Along these two

V. Vishal (✉)
Department of Earth Sciences, Indian Institute of Technology Roorkee, Roorkee, Uttarakhand 247667, India
e-mail: vikram12july@gmail.com

S.P. Pradhan · T.N. Singh
Department of Earth Sciences, Indian Institute of Technology Bombay, Mumbai 400076, India
e-mail: tnsingh@iitb.ac.in

G. Lollino et al. (eds.), *Engineering Geology for Society and Territory – Volume 1*,
DOI: 10.1007/978-3-319-09300-0_96,

highways are exposed nearly vertical road cut sections of the Lesser Himalayan rocks. Quaternary River Sediments as well as the soil cover pose serious problems for road slope stability. In the past, a number of landslides have been reported and the frequency has been increasing due to the development work in this area. In fact the area is rated as high risk in most of the landslide classification maps in India. The famous Kaliasur landslide occurred in the nearby area along NH 58 en route to Badrinath.

The present study was done to characterize the slopes in the area with regards to landslide vulnerability. The stress was on the slope failure of the harder, stronger quartzites, epidiorites and observing why and how these rock with extremely high c and φ values show prominent slope failures even in the dry season. Landslides in the area are no longer a monsoon phenomenon. blasting induces an effect equivalent reduction in φ and c and brings these values down to the level to weaker rocks for all practical purposes. This is what the finite element models were made to stress upon. Characterization of the movements of element inside the generated mesh upon reduction of strength parameters, inducing failure is what the present study is essentially aimed at.

96.2 Field Works and Rock Characterization

The aim of the field study was to study the geo-technical aspects of the slope along the road cut sections, measure joint, bedding, schistosity, and other discontinuity orientations and collect samples of the different rock types to conduct laboratory tests aimed at characterizing the physico-mechanical properties (Vishal et al. 2011; Pradhan et al. 2011; Gupte et al. 2013). The determined rock parameters were useful for prediction of other geomechanical characteristics as well (Singh et al. 2012a, b). The road cut slopes are almost vertical and the slope height varies from 5–30 m. There are exposures of Proterozoic rocks, Quaternary sediments as well as soil. At some locations having massive quartzites, even negative slopes are found to be stable (Fig. 96.1). As mentioned above there is a lot of variation in the road cut sections from the hard quartzites to the soil as well. Different slope failures were observed in almost all the rock types as well in case of the soil. Many of the slope failures have been extremely localized showing that blasting is the main contributor to these slope failures. Natural slope failures are usually on a larger scale. Salient rock parameters were determined in the laboratory. The average UCS of epidorite was obtained as 71.24 MPa while the average tensile strength of this section was found to be 9.56 MPa. The Young's modulus was equal to 23.7 GPa while the Poison's ratio was found to be 0.26. Density was found to be 2.68 g/cc while its porosity was 4.3 %. Cohesion was obtained to be 17 MPa while the angle of internal friction was 33°.

96.3 Numerical Modeling

To create a model of slope in PLAXIS, the user has to create a finite element model and specify the material property and boundary conditions. To emulate the field conditions the user has to create a two dimensional geometry model composed of geometry lines and geometry points (Singh et al. 2013; Vishal et al. 2010; Sarkar et al. 2012). The generation of an appropriate customizable finite element mesh and the generation of properties and boundary conditions on an element level are automatically performed by the PLAXIS mesh generator, based on the input of the geometry model. The final part of the input comprises the generation of water pressures and initial effective stresses to set the initial state. For the present purpose a Mohr-Coulomb model was used, following its simplicity and the common knowledge that most failures take place in the shear mode. Hence the Mohr-Coulomb model would be the closest to real conditions.

For the calculations of the present study as first phase of calculations was a consolidation analysis, leading to minimum pore pressure. This would model the behaviour of the hard rocks, which have undergone this strain so millions of years to consolidate to a theoretical minimum pore pressure. After the consolidation analysis a Phi-C reduction is carried out. This calculation is the safety analysis to model the effect of a gradual loss of strength parameters of the rock mass. To model the jointing behaviour, loss in cohesion due to water percolation and the most importantly the effect of blast induced vibrations the strength parameters, i.e., c and φ are gradually reduced to model the field conditions and thus a best suited factor of safety is obtained. It is to be noted that this is an average global factor of safety for a given slope. The aspects of numerical modelling are shown in Figs. 96.2, 96.3, 96.4 and 96.5. The salient observations of the slope investigation may be summarised as:

1. The slope has got a very steep geometry, even negative slope, but is still standing due to the high cohesion of the rocks, the lower degree of weathering and lesser height of the slope.

Fig. 96.1 View of the epidorites road cut along NH109

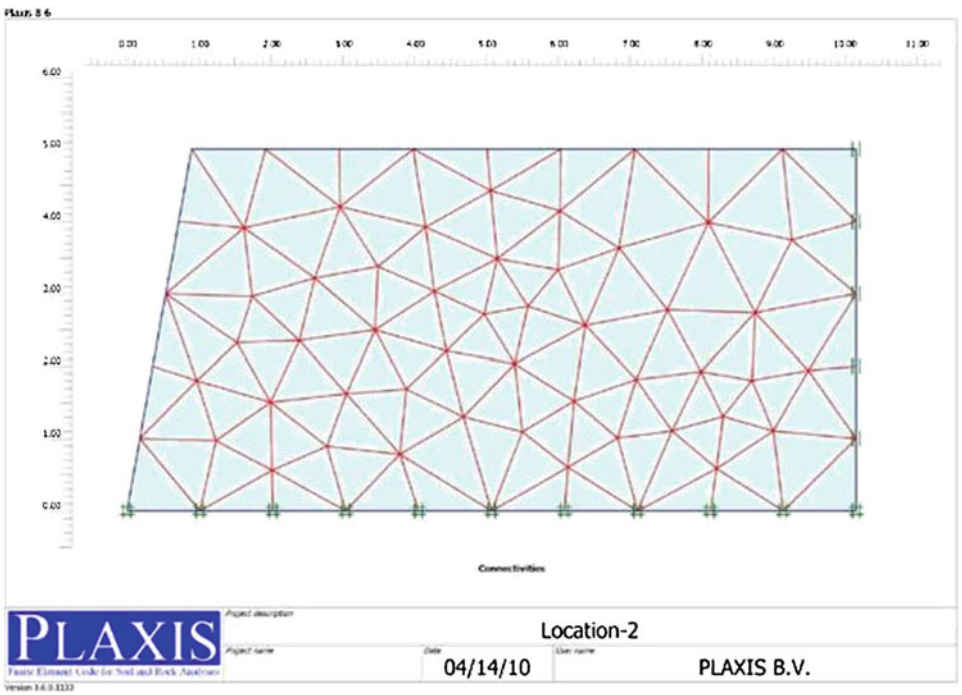

Fig. 96.2 Initial mesh generated for the location

2. Horizontal displacements are maximum near the base of the slope and decrease towards the top.
3. Vertical displacements are maximum near the top of the slopes and decrease towards the base.
4. Shear stresses and shear strains are concentrated near the base of the slope.
5. There has been development of very few tension cut-off points, indicating lesser permanent deformation.
6. With a factor of safety of about 1.476 the slope is just about stable, the influx of water during monsoon may accelerate the horizontal movements at base and vertical movements at the top causing a circular like failure movement.

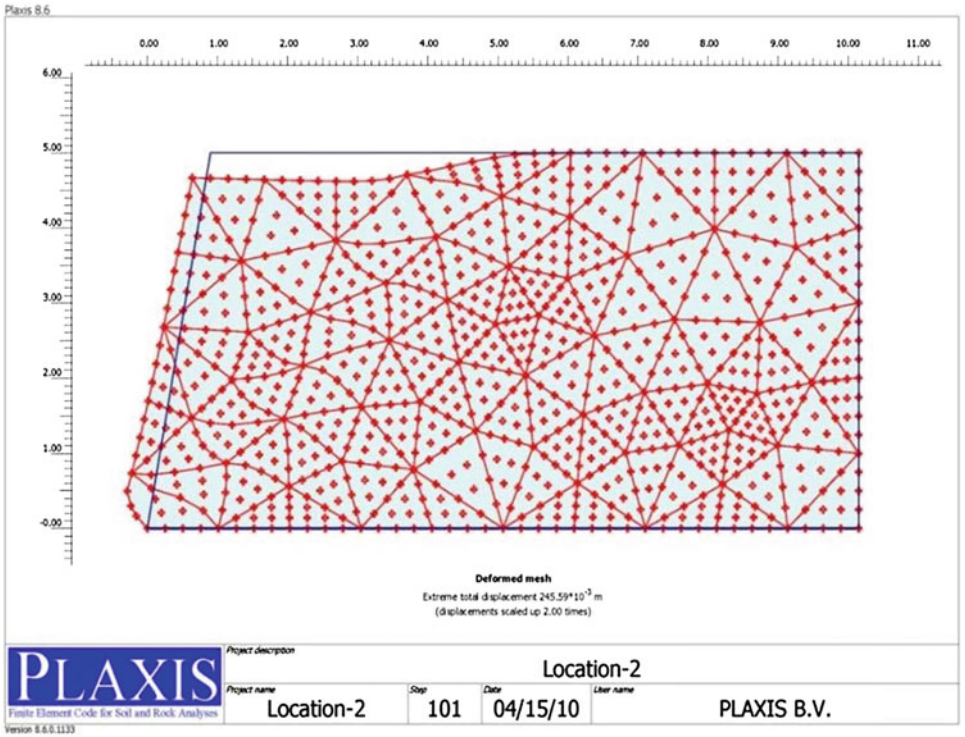

Fig. 96.3 Deformed mesh with nodes

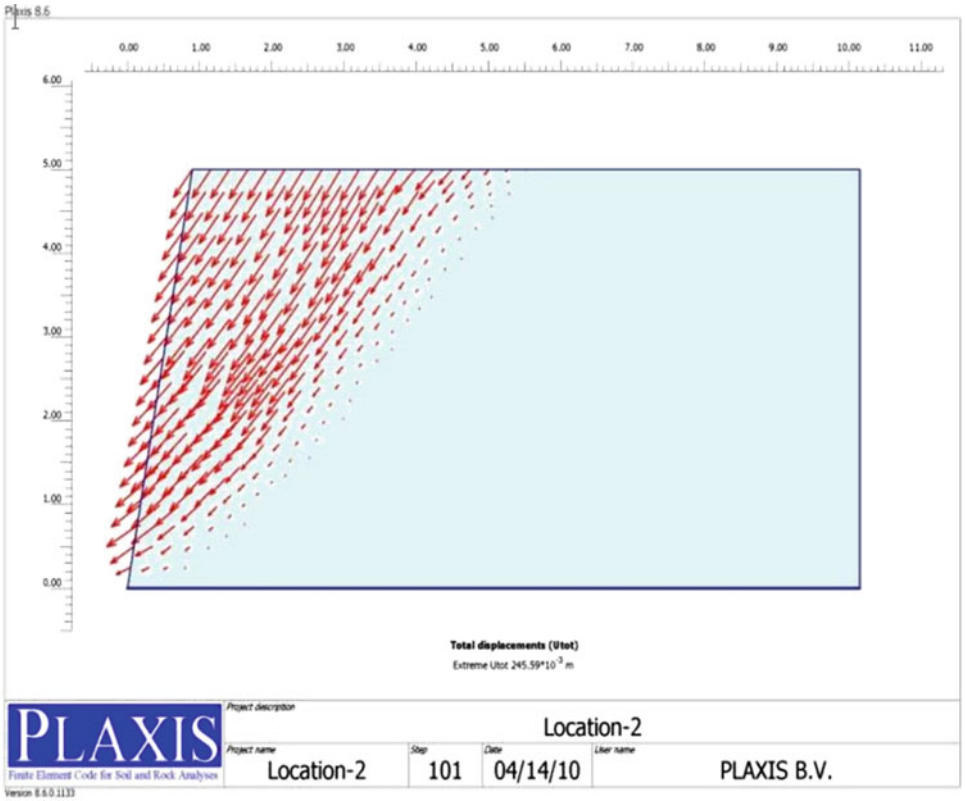

Fig. 96.4 Overall displacement vectors

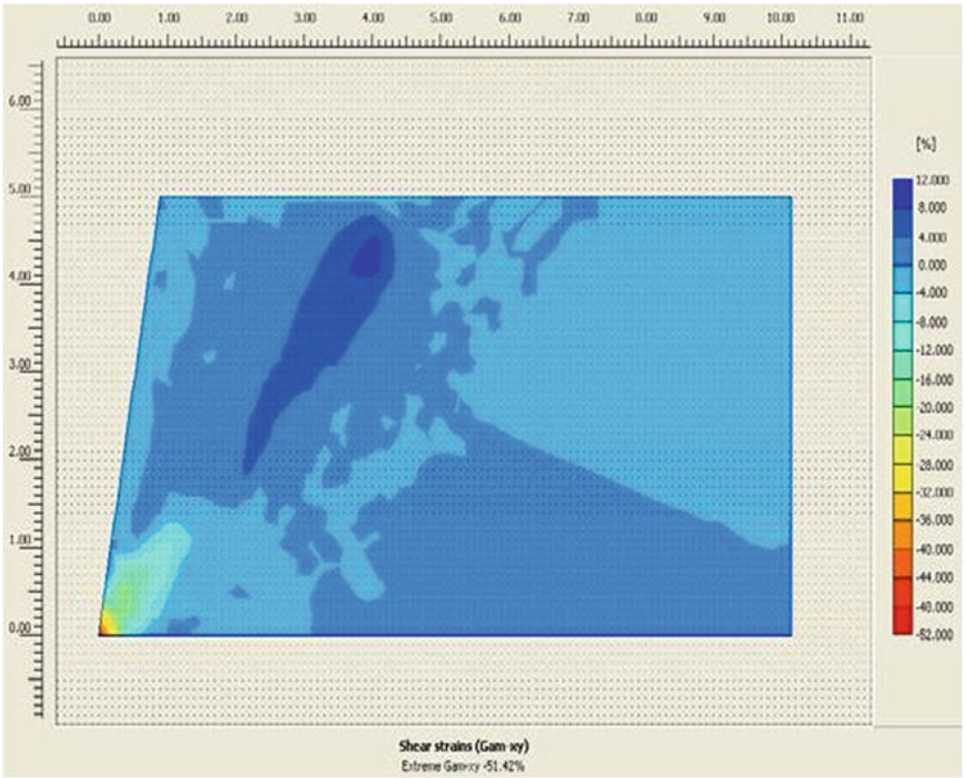

Fig. 96.5 Shadings showing the shear strain in different parts

96.4 Conclusions

Detailed investigation was carried out to understand the health of the slopes. The results indicate that despite high slope angle, the hill cut stands still due to its material characteristics. However, blasting activities nearby or widening of roads may induce failures in rocks. The Factor of Safety although above unity, is not very high and weakening of materials during monsoons may also lead to failure. Care should be taken in advance to avoid mishaps in future.

References

Gupte SS, Singh R, Vishal V, Singh TN (2013) Detail investigation of stability of in-pit dump slope and its capacity optimization. Int J Earth Sci Eng 6(2):146–159

Pradhan SP, Vishal V, Singh TN (2011) Stability of slope in an open cast mine in Jharia coalfield, India—a slope mass rating approach. Min Eng J 12(10):36–40

Sarkar K, Vishal V, Singh TN (2012) An empirical correlation of index geomechanical parameters with the compressional wave velocity. Geotech Geol Eng 30:469–479

Singh R, Vishal V, Singh TN (2012a) Soft computing method for assessment of compressional wave velocity. Sc Iranica Trans Civ Eng (Elsevier)19(4):1018–1024

Singh R, Vishal V, Singh TN, Ranjith PG (2012b) A comparative study of generalized regression neural network approach and adaptive neuro-fuzzy inference systems for prediction of unconfined compressive strength of rocks. Neural Comput Appl 23:499–506

Singh TN, Pradhan SP, Vishal V (2013) Stability of slopes in a fire-prone mine in Jharia Coalfield. India, Arab J Geosci 6:419–421

Vishal V, Pradhan SP, Singh TN (2010) Instability assessment of mine slope—a finite element approach. Int J Earth Sci Eng 3:11–23

Vishal V, Pradhan SP, Singh TN (2011) Tensile strength of rock under elevated temperatures. Geotech Geol Eng 29:1127–1133

Study of Slopes Along River Teesta in Darjeeling Himalayan Region

97

S.P. Pradhan, V. Vishal and T.N. Singh

Abstract

Landslides of different magnitudes are frequent in different regions of the morpho-dynamically active Himalayan regions. Geologically, the presence of young active fold mountains, some rejuvenated faults along with the anthropogenic factors such as unplanned urbanization in risk areas, widening of roads along cut slopes, environmental degradation and population expansion play a significant role in the occurrence of such geohazards. The landslide zones have been identified for Indian scenario to demarcate the locales susceptible to landslides and various studies are being carried out in the high risk areas to mitigate the probability of occurrence of hazards. Assessment of stability of such areas by developing models can act as early warning systems and help to implement preventive and mitigative measures to minimize the damage level. The present work focuses a similar study in a landslide prone area with evidences of recent and paleo landslides in Darjeeling—Himalayan area of India. The Birrik fault cuts across the River Teesta in the foothills of the Darjeeling Himalayan fold and thrust belt and in the close vicinity lies the National Highway No. 31A. This area has a hilly topography and some high angle slopes are further aggravated by the presence of active thrust. Evidences of landslides were observed in the field and samples were collected from the adjoining areas of slide for determination of their geomechanical properties. There are many methods to analyze the slope conditions like Slope Mass Rating, limit equilibrium method, kinematic tools, numerical simulations etc. These approaches are good to see the disturbances within the rock mass due to change in its dynamics. In this study, slope mass rating was used to evaluate the health of slopes based on various rock parameters, as determined in the laboratory. This study will be helpful to monitor the slope conditions in this area and to design the

S.P. Pradhan · T.N. Singh
Department of Earth Sciences, Indian Institute of Technology
Bombay, Mumbai 400076, India
e-mail: saradaiitb@gmail.com

T.N. Singh
e-mail: tnsingh@iitb.ac.in

V. Vishal (✉)
Department of Earth Sciences, Indian Institute of Technology
Roorkee, Roorkee 247667, Uttarakhand, India
e-mail: vikram12july@gmail.com

G. Lollino et al. (eds.), *Engineering Geology for Society and Territory – Volume 1*,
DOI: 10.1007/978-3-319-09300-0_97,

preventive measures to minimize the chances of failure, which is required for smooth transportation through highway NH 31A. It can also be set an example for regions with similar geological and geotechnical conditions, especially in the Lower Himalayan regions.

Keywords
Slope mass rating • Slope stability • NH-31A • India

97.1 Introduction

Slope Stability Analysis deals with the application of rock mass and structural geology principles in stabilising the slope of rock/slope (Gupte et al. 2013; Singh et al. 2013). Slope stability investigation, analysis, design and mitigation need to be understood with detailed understanding of the characteristics of the rocks comprising the slope (Sarkar et al. 2012; Vishal et al. 2011; Singh et al. 2012a, b). Slope stability can be defined as the resistance of a structure or slope or embankment to failure by sliding or collapsing under normal condition (Pradhan et al. 2011; Vishal et al. 2010). Landslides due to slope stability failure have always been a major concern for the Sikkim-Darjeeling Himalayas especially during the monsoon season. The present investigation deals with the study of the general geology, geotechnical parameters and the structural aspects of the landslide along the Birrik Fault Zone located in the Eastern Himalayas. The first stage involved a detailed investigation of the rock type with major emphasis given on the joint types and their orientation. The second stage involved determination of the various geotechnical parameters for calculating RMR which will be the main input for calculating SMR. The landslide being dominated by joints and fractures is mainly governed by tectonic factors with monsoon, construction of dams and movement of heavy vehicle contributing to trigger it. Hard rock like quartzites also presence of minor fractures thereby decreasing the strength the rock mass.

97.2 Field Observations

The field is located on the Eastern Himalayas which comprises the domain of Darjeeling, Sikkim, Bhutan and Arunachal Pradesh and is similar to the overall Himalayan Belt. The area is very prone to landslides and has evidences of both palaoe-landslides and active landslides affecting both life and property. The landslides are enhanced by man-made causes such as construction of dam, cutting of roads on unsuitable areas and heavy road trafficking. The slide zone belongs to the Daling Group of rocks (Proterozoic) and comprises of weathered quartzites at some places enriched with iron and shaly slates. The argility content of the area increases as we approach closer towards the landslide area with more Fe enriched quartzites. The Birrik Fault is an out-of sequence active fault in between the Ramgarh and the Main Boundary thrust in the Sikkim-Darjeeling Himalayas giving rise to landslides. The fault dips 70° northerly near the field area and forms a landslide zone of 8–10 kms but the fault related deformation is visible for much larger areas. The rocks in the hanging wall and the footwall have been cataclasized to form the landslide zone which is the main area of interest. The area was prominently active in the 1980s and is still active. The construction of a dam on the Teesta River to support the Lower Teesta Hydel Power Project by NHPC has made the fault more active causing new landslides and disturbing the stabilised slopes.

The slopes of the road cuts are very steep with being almost vertical in most areas. The lithology is mainly quartzite with minor occurrences of slates and phyllites in some areas. Two sets of joints are observed in quartzite with one set being parallel to the bedding dipping north-west and the other set perpendicular to the bedding dipping south east. Tilting of the trees is observed in some cases indicating the movement of soil particles down the slope of the road cuts. Evidences of structural deformation are very prominent in the area. The tectonics is so active that minor fractures have propagated through almost all the quartz rocks making the rock mass very weak. Minor fault evidences are also seen in the form of slickenslides. Multiple joint sets are observed in the area. The area being neo- tectonically active joint sets are present in all the areas. The major type of failures in the area is related to joint orientations. Wedge failure, block failure and toppling failure are observed in the area at different locations (Fig. 97.1).

97.3 Slope Mass Rating

Slope Mass Rating is a system of classification developed by Romana (1985) as an application of Bieniawski (1979) Rock Mass Rating (RMR).The SMR is useful instrument for the evaluation of slope risk (Table 97.1).

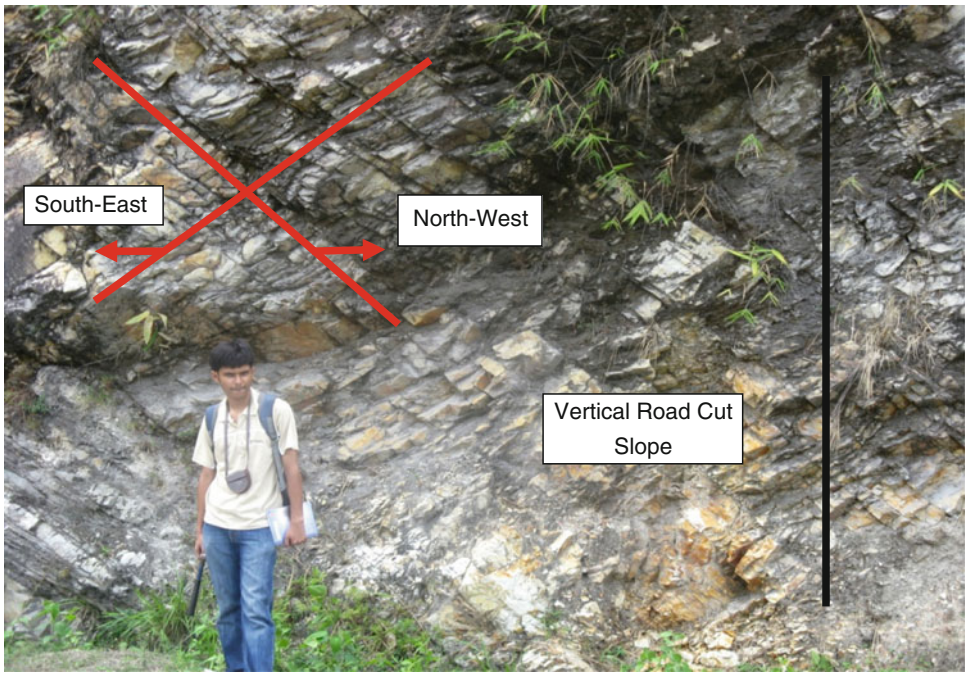

Fig. 97.1 Cross joints observed in quartzites

Table 97.1 Adjustment factor for different joint condition, Location 1

No	Condition consideration	F1	F2	F3	F1 * F2 * F3
1	J_1 and slope	0.70	1	−6	−4.2
2	J_2 and slope	0.70	1	−6	−4.2
3	J_3 and slope	0.15	0.15	0	0

From above it is clear that J_1 and J_2 are critical joints and should be taken into consideration for SMR
F4 value is 0 because normal blasting and mechanical excavation
RMR for the dominant rock type (quartzite) in this area is 47.06
SMR = 43.33 – 4.2 + 0 = 39.13
SMR Class is IV, Bad Rock Mass leading to Planar or big wedge failures in an unstable domain

The proposed Slope Mass Rating is obtained from RMR by subtracting a factorial adjustment factor depending on the joint slope relationship (F1, F2, F3) and adding a factor depending on the method of excavation (F4). SMR = RMR_{basic} − (F1.F2.F3) + F4.

97.4 Conclusion

The strength of the rocks near the landslide zone is very high, but the overall rock mass is weak. The formation of landslide is directly related to the thrusting along the Birrik fault zone. The construction of NHPC dam on the banks of the Teesta river can reactivate the Main Boundary Fault lying beneath the river causing more severe landslides. The presence of minor fractures and multiple sets of joints all along the area are strong evidences for the structure-related causes of the landslides. The major types of failure in the area are wedge, toppling and block failure. The main landslide zone may also be a major wedge failure, where the two planes of failure meet along a curvilinear line resulting for the concave up surface of the slide. The NH-31A being the only major means of connection between Sikkim and the rest of the India, high movement of traffic may further accelerate the process of landslides.

From the slope stability analysis using SMR, it is established that the affected area is quite unstable and the SMR Class 4 indicates unfavourable slope conditions adjacent to the thrust zone where large wedge failures take place. Landslides have been one of the most hazardous natural disaster in the Sikkim-Darjeeling Himalayas causing huge loss of life and property. The landslides occur mostly during the monsoons as this area receives very high amount of rainfall and the sliding is aggravated. Several government and non-governmental organisations are working towards the mitigation of landslides. The government should step forward and actively participate in preventing the landslides to enhance the safe and unhindered thoroughfare in this region.

References

Bieniawski ZT (1979) The geomechanics classification in rock engineering applications. In: Proceedings of the 4th international congress on rock mechanics, vol 2, pp 41–48. ISRM, Montreaux

Gupte SS, Singh R, Vishal V, Singh TN (2013) Detail investigation of stability of in-pit dump slope and its capacity optimization. Int J Earth Sci Eng 6(2):146–159

Pradhan SP, Vishal V, Singh TN (2011) Stability of slope in an open cast mine in Jharia coalfield, India—a slope mass rating approach. Min Eng J 12(10):36–40

Romana M (1985) New adjustment ratings for application of Bieniawski classification to slopes. In: proceedings of the international symposium on the role of rock mechanics, pp 49–53

Sarkar K, Vishal V, Singh TN (2012) An empirical correlation of index geomechanical parameters with the compressional wave velocity. Geotech Geol Eng 30:469–479

Singh R, Vishal V, Singh TN (2012a) Soft computing method for assessment of compressional wave velocity. Sci Iranica Trans Civ Eng (Elsevier) 19(4):1018–1024

Singh R, Vishal V, Singh TN, Ranjith PG (2012b) A comparative study of generalized regression neural network approach and adaptive neuro-fuzzy inference systems for prediction of unconfined compressive strength of rocks. Neural Comput Appl 23:499–506

Singh TN, Pradhan SP, Vishal V (2013) Stability of slope in a fire prone opencast mine in Jharia coalfield. India, Arab J Geosci 6:419–427

Vishal V, Pradhan SP, Singh TN (2010) Instability analysis of mine slope by finite element method approach. Int J Earth Sci Eng 3(06):11–23

Vishal V, Pradhan SP, Singh TN (2011) Tensile strength of rock under elevated temperatures. Geotech Geol Eng 29:1127–1133

Climate Change—Present Scenario in Parts of India; Needed Preventive Measures and Role of Earth System Scientists

98

D. Venkat Reddy and P.R. Reddy

Abstract

It is now evident, from glacier receding in Himalaya, ice melting in Arctic and Green Land, significant fluctuations in day and night temperatures, unprecedented monsoon vagaries that Climate change is a reality and Man needs to take urgent measures to contain its impact and save himself and Fauna-Fauna. The expected sea water rise, due to ice melting of Polar Regions, is bound to affect the long coastal corridors flanking the eastern and western parts of India. Unfortunately, in spite of many warnings by the Nature in the form of unprecedented spells of cloud bursts during non monsoon seasons of 2012 and 2013 no steps have been initiated to safe guard erosion of our coasts that are inhabited by millions of people. Since both the administrative channels and the political mind set are not tuned to take preventive measures it is essential for the earth system scientists to prepare land erosion, land subsidence, saline water ingression details in space and time using remote sensing and GIS techniques .In this exercise the earth scientists and space scientists should evolve strategies that can convincingly produce models showing how the coastal corridor can be affected with varied intensity and magnitude of sea water rise, in time and space. Specific details of the expected ill effects on the coastal segments of Andhra Pradesh and parts of Tamilnadu will be discussed along with proposed remedial measures to strengthen the wind and tide barriers in these areas.

Keywords

Coastal ecosystem • Climate change • GIS techniques • Integrated environmental management • Sea rise • Ocean acidity • Bio-diversity

98.1 Introduction

Coastal eco system is fragile and threatened by human action. The solutions demand the practical application of coordinated and integrated environmental management. To safe guard the coastal ecosystem a holistic vision, better scientific data, better management models and the recognition/realization in the part of administrators that the reconstruction of local communities environmental management is as vital as rebuilding of biophysical environment. Coastal ecosystem management demands top-down integration as well as grass-roots coordination. It is paramount to realize that already considerable damage has been

D. Venkat Reddy (✉)
Department of Civil Engineering, National Institute of Technology Karnataka, Surathkal, Srinivasnagar, Mangalore 575025, India
e-mail: dvr1952@gmail.com

P.R. Reddy
Scientist (Retd), National Geophysical Research Institute, Hyderabad 500007, India
e-mail: paravatarreddy@gmail.com

G. Lollino et al. (eds.), *Engineering Geology for Society and Territory – Volume 1*,
DOI: 10.1007/978-3-319-09300-0_98,

done to our vulnerable coastal corridor, due to irrational and improper management policies, based on short term gains and natural calamities. To control or at least decelerate the damage multi-disciplinary team work of committed professionals has to be put in order. There is a need for new strategies. For that we need new data and better access and utilization of existing data. Since ecosystem processes are non-linear, strategies should be oriented more to practice than theoretical nicety. Reconstruction activities must give priority to local community, its socio-economic condition, cultural context, and capacity for self-management. It is often the society and economy of the local community, as much as the physical environment that is in need of reconstruction. The problems include shortage of scientific and technical expertise; land use conflicts that pit local against national priorities; weak local economic system and rural depopulation. Another account that has become all too evident these recent years is that the environment may react unexpectedly when its fragile equilibrium is disrupted by human activities and/or natural events, and that poor land management can increase the frequency of natural disasters and the severity of their affliction on the population. Some strategies to better manage our coastal ecosystem are detailed. The suggested strategies assume importance, seeing the large scale destruction in Uttarakhand and Assam due to 2013 monsoon abnormalities and coastal ecosystem degeneration, post 2004 Tsunami, super cyclone of 1999 Orissa, 2012 Nilam cyclone that devastated the coastal corridor of Andhra Pradesh and significant damage and threat to entire Kona seema of Andhra Pradesh due to unprecedented Godavari River floods in July, 2013. In addition, the 2005 Mumbai cloud burst and 2009 Krishna River floods that crossed the maximum flood levels of the reservoirs and dams have taught us the impact of cloud bursta, monsoon extremes, super floods on the drainage system and pollution of the coastal corridor. The recent developments cited above have motivated us to bring out this presentation .We opine that a concerted effort has to be made by technical and scientific experts to understand the mechanism associated with unusual hydrological catastrophes.

Coastal corridor is the nerve centre of any country, as it is rich, dynamic and vibrant. Due to various natural and manmade activities, these corridors are exposed to different types of hazards, and as such one has to address this problem by developing area specific environment up gradation models. The coastal zone represents that part of the land affected by its proximity to the sea, and that part of the ocean affected by its proximity to the land; from 200 m above to 200 m below sea levels. According to one principle of classification, an emergent coastline is a coastline which has experienced a fall in sea level, because of either a global sea level change, or local uplift. If one wants to achieve lasting impact of coastal ecosystem management, he has to ensure both preservation and conservation of natural resources. Preservation means maintaining natural resources by not using them and preventing human interference as much as possible. Alternatively, conservation allows a controlled usage of natural resources while maintaining the sustainability of those resources for future generations. The preservation of nature, without regard to human needs, may lead to societal disasters such as economic collapse, rising health issues, and overall chaos. Natural regulation ties in with preservation. Conservation, if carried out methodically can help both the Man and Environment. It is necessary for the Man to choose any of the two approaches, analyzing the existing scenario at a location at a specific time. The ecosystems, including coastal corridor, are an intricate part of the human lifecycle as they provide us with our water, food and energy. Ecosystem preservation is the continued, uninterrupted natural cycle of a particular ecosystem by mankind. When an ecosystem is encroached by mankind the slightest disturbance could disrupt the entire system bringing an end to any particular flora or fauna that may solely thrive within that ecosystem. It is essential to know that any ecosystem, including coastal, get affected by pollution and excessive use of the resources. Most pollution in India arises from land-based sources-industrial and domestic wastes and agricultural run-off. Shipping and associated ship-building, breaking and port activities are becoming increasingly significant. The crop of recently started coastally located industries uses sea-water as a resource and the coastal domain as a sink of altered sea-water (temperature and density). These pose newer, more direct threats to sensitive eco areas. In addition exploration and exploitation of Oil and Gas has introduced number of problems to the health of coastal ecosystem. The data, collected a decade back by NIO, indicate that the Indian coasts have well circulated oxygenated waters, and that hot-spots remain contained within reasonable limits. However, the uncontrolled exploitation of coastal corridor and continued pollution of marine environment through land originated pollution have made the coastal ecosystem prone for significant degradation. Some segments of our coastal corridor have become vulnerable and sea waters relatively acidic and turbid. As such we need to give due weightage to various facets of coastal dynamics and take appropriate measures in time and space, using a holistic approach involving apt technological interventions and implementable administrative mechanisms.

Climate-alarmists claim that rising atmospheric CO_2 concentrations tend to acidify seawater (reduce its pH), which in turn leads to catastrophic decreases in the calcification rates of numerous marine organisms. Caldeira and Wickett (2003) calculated that earth's atmospheric CO_2 concentration could approach 2,000 ppm around the year

2300, leading to a concomitant surface seawater pH reduction of 0.7 unit, a change they describe as being much more rapid and considerably catastrophic. "ocean acidification" phenomenon will negatively impact the process of calcification in corals and other marine life. Feely et al. (2009) suggested that atmospheric CO_2 levels could approach 800 ppm near the end of the century, and as a result, "the skeletal growth rates of calcium-secreting organisms will be reduced leading to direct and profound impacts on our living marine ecosystems". However, NOAA's Pieter Tans presents a much different take on the subject. His analysis begins by indicating that the anthropogenic-induced component of the air's CO_2 concentration "depends primarily on the total amount emitted and in about 200 years the air's CO_2 concentration actually drops back to about what it is today. Irrespective of these contradictory scientific results, one can state without any subjectivity that ocean acidification is enhancing, as evidenced from large scale destruction of coral reefs along the East Coast of India and Lakshadweep islands. The high rate of turbidity of shallow sea waters and bleaching of coral reefs in these coastal sea corridors, especially since the last 10–15 years clearly warn us that both natural and anthropogenic factors have profoundly altered the marine ecosystem.

98.2 Steps to Protect the Coastal Ecosystem

Tides often determine the range over which sediment is deposited or eroded. Today riverine deposition at the coast is often blocked by dams and other human regulatory devices, which remove the sediment from the stream by causing it to be deposited inland. The Earth's natural processes, particularly sea level rises, waves and various weather phenomena, have resulted in the erosion, accretion and reshaping of coasts as well as flooding and creation of continental shelves and drowned river valleys. It is clearly noticed in the coastal corridor stretching from southern parts of Tamilnadu to segments beyond Visakhapatnam of Andhra Pradesh that coastal erosion has increased considerably and the geomorphology of coastal corridor has changed significantly, in the recent past. Estuaries, especially those along Tamilnadu coast have been affected post 2004 tsunami and the changes have significantly altered the biodiversity in this part of the country. In addition, climate change is likely to accelerate the historical rise in sea level through warming of oceans and melting of ice, which in turn will affect coastal development, wetland resources, and recreation along different coasts including Indian. The impacts of sea-level rise will occur in coastal areas that are continually evolving and already face a wide range of natural and human-induced stresses, including erosion, storms, land subsidence, wetland loss, and environmental degradation from recreation and development pressures. Responses to sea-level rise at the national, state, and local level must therefore reflect an understanding of the complex interactions of human and ecological systems in coastal areas. Impact assessment for sea-level rise requires careful assessment of local conditions, the magnitude and uncertainties of global sea-level rise, and the costs and feasibility of response options. Important local conditions include coastal topography, geology, and economic and demographic factors. Existing threats to coasts that may be increased by climate change include: gradual sea-level rise, catastrophic sea-level rise (i.e., Arctic and Antarctic ice sheet melt), and changes in storm frequency or intensity. Sea level rise will not be consistent globally, but will be affected by coastal bathymetry (the depth of the water offshore), local topography, and tides. There will also be secondary impacts of sea level rise, such as the displacement of human populations and agricultural activities and the salinization of aquifers, which could have additional consequences for wetland and biodiversity loss. The primary impacts of sea-level rise are physical changes to the environment. These changes, in turn, affect human uses of the coast such as tourism, settlement, shipping, commercial and recreational fishing, agriculture, and wildlife viewing. The most serious physical impacts of gradual sea-level rise on coastal lowlands are (1) inundation and displacement of wetlands and lowlands; (2) coastal erosion; (3) increased vulnerability to coastal storm damage and flooding; and (4) salinization of surface water and groundwater. It is well established that coastal corridor in the East Godavari district of Andhra Pradesh, including Konasema (Rice Bowl of the state) has been affected considerably due to the above cited 4 impacts. Industrial segments of the long coast of India and major coastal cities will have to upgrade flood defenses and drainage systems or risk adverse consequences. The studies in India suggest there will be adverse impact on cities along East Coast, especially Visakhapatnam, Kolkata, and Chennai.

Three options have been proposed to respond to coastal threats: planned retreat, accommodation, and protection. Impact and adaptation assessments evaluate where these responses might be implemented and then calculate the costs of implementation and the damages to resources that are not protected. Though the cumulative costs are a relatively small percentage of total property values in the coastal zone, one has to explicitly evaluate potentially large effects on coastal wetlands. Depending on the policy options chosen to respond to sea-level rise, the impact of rising seas could fall disproportionately on a small number of people or communities in the most vulnerable areas. This is clearly witnessed in the Konaseema area of north coastal Andhra Pradesh and Tamilnadu.

98.3 Strategies for Coastal Ecosystem Management in India

The strategies include institutional strengthening, capacity building, policy plan, management plans for areas highly degraded, education and awareness; all these issues are crucial for India's costal management. However, post 2004 Tsunami resultant vulnerabilities it has been felt prudent to integrate local, regional and global aspects in developing sustainable strategies. Integrated coastal management and planning are processes through which rational decisions are made concerning the conservation and sustainable use of coastal and ocean resources and space. The principles of Integrated Coastal Management (ICM) are well-known and widely accepted throughout the world, employing a suite of tools including marine protected areas (MPAs), land-use control, marine zoning and permit systems, conflict resolution, planning and fisheries management. The above mentioned strategies/principles, as part of integrated long term responses, can be of use to Indian environment. Well-formulated and implemented ICM plans can significantly reduce the loss of lives and physical assets from tsunami, storm surges, cyclones, frequent monsoon vagaries and large scale geo-morphological changes due to sea level rise and ocean acidification. The processes of short-term action require integration with the disaster response practitioners and activities.

98.4 What Needs to Be Done?

(1) Coastal spaces are where nutrients are recycled often (with a positive benefit for fisheries) before sequestering or export. Dissolved and partialate carbon find their way to the sea. This is slowly turning into source of CO_2 to the atmosphere. As such we need to understand the processes of carbon and nutrient cycling and the global significance of the coastal seas to the carbon cycle. Also we need to be able to predict the evolution of the coastal ecosystems for different global change scenarios and the effects of these changing coastal systems on social and economic activities and how we can improvise strategies for the sustainable management of coastal resources, as the coastal seas undergo cumulative changes which though localized have global impact.

(2) The other major problem is the complexity of biological systems. Even in a localized environment, the species are numerous, the numbers are large, and there are different metabolic rates, life styles and life expectancies. Environmental changes will affect species differently and thus their effect on the biogeochemical cycles will alter. Biological systems have a slowness of response to chronic low levels of external forcing, and this buffering capacity delays or in some cases masks the eco-system response. Indian coasts have a large variety of sensitive eco-systems. Sand dunes, coral reefs, mangroves, sea-grass beds and wet lands are some that deserve special mention. A critical feature of these ecosystems is the variety of bioactive molecules that they host. And as such a systematic scientific appraisal of complex biological systems of the coastal corridor, in time and space, is essential.

(3) Sand dunes seem to be ecosystems that are most often destroyed, probably because their place in the scheme of dynamic coastal morphology is not obvious. It is essential to provide needed changes to strengthen sand dunes at strategic locales that are identified as vulnerable segments of the corridor; evidenced by 2004 tsunami effect.

(4) A systematic long-term study of pollutants, in a regional context, and their effects on biota is necessary.

(5) Synoptic monitoring tools of moored buoys and remote sensing by satellites and by acoustics, should be used where possible. Geographic Information System, various data bases, rapid communication of alarms are other tools for successful monitoring, along with risk analysis and disaster management plans.

(6) A geocentric view of global change sees humans as driving forces of global change. We need to get various models right, to achieve sustainable development(Refer Dr. E. Desa presentation on NIO, Goa for more details).

We present below some additional strategies to sustain coastal ecology.

(A) In emerging technology paradigm, "Geographical Information System (GIS)" coupled with Remote Sensing has emerged as powerful tool which has potential to organize complex spatial environment with tabular relationships. Real Time GPS investigations should be taken up in a systematic way to monitor coastal corridor morphological changes, including subsidence due to oil and gas extraction(especially in Krishna- Godavari Basin of Andhra coast).

(B) Mangroves, admittedly, are not only important but crucial for the coastal areas. Since estuarine areas are highly populated areas, the slightest ecological imbalance will take a heavy toll. They play a vital role in stabilizing these areas. No engineering and technological solutions can be sought for stabilizing these areas. Even if we negate all benefits of mangroves as forests, their value as "protector of shore-line" is enough to convince us for conserving them. The distribution of mangrove ecosystem on Indian coastlines indicates that the Sundarban mangroves occupy very large area followed by Andaman-Nicobar Islands and

Gulf of Kutch in Gujarat. Rest of the mangrove ecosystems is comparatively smaller. We need to strengthen mangrove raring, in a big way to save Indian coastal segments.

98.5 The Goal

Our target should be

- To improve the quality of life of human communities who depend on coastal resources, while maintaining the biological diversity and productivity of coastal ecosystems.
- To provide resources and long-term funding GOALS that inspires the people of the place to assiduously strive to save the coastal corridor and Land-Marine Life.
- To encourage a culture of self-assessment, peer review and adaptive management.

Acknowledgments We thank Prof. Giorgio Lollino, Congress Chair, XII IAEG Congress-Torino 2014 for accepting our abstract and extending an invitation to write this article. We also thank Prof. T.N. Singh for his support.

References

Caldeira K, Wickett ME (2003) Anthropogenic carbon and ocean pH. Nature 425:365

Feely RA, Doney SC, Cooley SR (2009) Ocean acidification: present conditions and future changes in a high-CO_2 world. Oceanography 22:36–47

Tans P (2009) An accounting of the observed increase in oceanic and atmospheric CO2 and an outlook for the future. Oceanography 22:26–35

Part X

Slope Dynamics and its Control in a Climate Change Scenario

Convener: Dr. Mauro Rossi—*Co-conveners*: Dino Torri, Jean Poesen

Mass movements, gully erosion and diffuse soil loss are controlled by vegetation, soil management and intense rain events. Climatic changes worldwide seem to evolve towards more intense events larger in intensity, duration and frequency. Not only croplands are exposed to increased hazard, as even grasslands and forests are under increasing threats due to positive feedbacks of increased air temperatures on pests (exotic species can reduce and destabilize the functional diversity of plant communities having adverse effects on slope dynamics). Plant communities and their dynamics regulate soil formation and characteristics (i.e. erosion resistance, soil porosity, water infiltration and redistribution). Models dealing with the complex system characterizing slope dynamics, where all the components can vary according to climate change, can be useful to prepare strategies to adapt to new climatic situations. We hereby invite all contributions dealing with these issues.

Co-evolution of Soils and Vegetation Under Changing Climatic Conditions at a Desert Fringe

99

Aaron Yair and Ram Almog

99.1 Introduction

Dry land areas are often regarded as highly sensitive to climate change. Many researchers assume a positive relationship between average annual rainfall, water resources, vegetation cover, species diversity, etc. Such an approach disregards the fact that with decreasing average annual rainfall the number of rainstorms; storm rain amounts and water availability may be highly dependent on the relationship between rainfall and surface properties. Later properties influence greatly the degree to which rainwater will percolate or will be transformed into runoff, thereby significantly affecting the spatial redistribution of water resources. The northern Negev desert offers unique conditions for the study of the possible effects of climate change along a rainfall gradient under changing surface conditions. Two case studies are considered (Fig. 99.1). The first deals with the environmental effects of loess penetration into the area, during a wet climatic phase. The second considers the differential effects of biological topsoil crusts, in a sandy area, on the water regime along a rainfall gradient under present day rainfall conditions,

99.2 Environmental Effects of Loess Penetration

Aeolian loess was deposited in the semi-arid northern Negev desert, under wet climatic conditions, during the last Würm glacial episode. Dead Sea level, at that time, was −180 m below the general sea level (as compared to the present day level of ∼420). The loess mantle was deposited directly on rocky hillslopes devoid of any soil cover (Fig. 99.2). The loess buried the pre-existing drainage network (Yair and Enzel 1987). A comparative study of the environmental characteristics of a rocky desert area, that had not be covered by the loess, with a wetter loess covered area allows us to describe and analyze the environmental effects of loess deposition.

The comparative sites selected are the Sede Boqer area, representative of a rocky arid area, and the Hovav Plateau area, representative of the loess covered area. Average annual rainfall at Sede Boqer is ∼90 mm; and at Hovav Plateau ∼170 mm. The study compares two north facing slopes. In both areas the hillslopes are divided into two units: an upper rocky area and a colluvial area at the lower slope section. Table 99.1 compares floristic data from both sites. The drier Sede Boqer site clearly reflects a better environment, for both rocky and colluvial slope sections, than the wetter Hovav Plateau site (Kadmon et al. 1989). The explanation proposed for the drier ecosystem in the wetter area is the spatial variability in runoff generation and water concentration in dry-land areas. Bare rocky areas are characterized by a high frequency, and magnitude of runoff events (Yair and Raz-Yassif 2004). The quick response to rainfall of rocky areas results in the concentration of runoff water from extensive rocky contributing areas into limited adjoining collecting soil covered areas. The process of water concentration leads to deep water penetration and preservation at a depth little influenced by evaporation. An opposite situation exists in areas with extensive soil cover. Due to the high water absorption capacity of the loess mantle, rich in fine-grained particles, runoff frequency and magnitude are low; and the positive effect of water concentration is inhibited. In addition, rainfalls from most rainstorms are low, resulting in shallow water penetration (20–40 cm). Infiltrated waters are afterwards lost by evaporation during the lengthy intervals between successive storms, contributing to salt accumulation at shallow depth. The overall result of loess penetration, during a wet climatic phase, may therefore be regarded as a desertification process.

A. Yair (✉) · R. Almog
Department of Geography, Hebrew University of Jerusalem, Jerusalem, Israel
e-mail: aaron.yair@mail.huji.ac.il

G. Lollino et al. (eds.), *Engineering Geology for Society and Territory – Volume 1*,
DOI: 10.1007/978-3-319-09300-0_99,

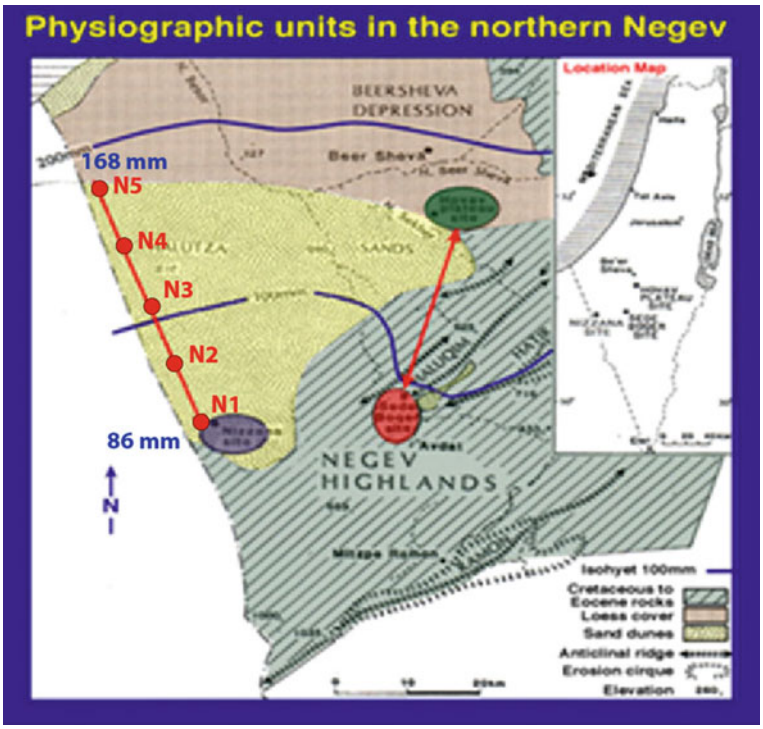

Fig. 99.1 Location of rainfall transects

99.3 Environmental Effects of Biological Topsoil Crusts Along a Rainfall Gradient in a Sandy Arid Area

The north-western Negev sand field (Fig. 99.1) offers unique conditions for the analysis of the possible effects of a climatic change on a sandy ecosystem, characterized by semi-stable dunes. The whole area is composed of uniform quartzitic sand. The rainfall gradient is very sharp: ~168 mm in the north and ~86 mm in the south, over a short distance of ~35 km. In view of sand properties (limited water absorption and high porosity) one would expect deeper water penetration and water preservation with increasing average annual rainfall; resulting in a positive relationship between average annual rainfall and environmental variables; such as species diversity, vegetal cover etc., However, field observations reveal a non-uniform vegetation cover. Vegetation cover is limited at the dune crests (5–19 %), very dense at the dune base (up to 100 %) and sparse in the interdune corridors (20–30 %). The view regarding a positive relationship between average annual rainfall and water availability in sandy areas may be valid in the case of unconsolidated sand, but it is questionable for sandy areas stabilized by biological topsoil crusts. Early studies conducted in the southern part of the sandy area (Yair 1990; Kidron and Yair 1997) had shown

Fig. 99.2 Sharp contact between the loess mantle and the underlying bedrock

that the biological crust plays an important role in the local water regime, strongly affecting rainwater infiltration, runoff generation and the spatial redistribution of water resources. However, field observations show a differential development of the topsoil crust along the rainfall gradient, pointing to differences in surface properties. The aim of the study was to answer the simple question: are the differences in surface properties; along the rainfall gradient; significant enough to

Table 99.1 Floristic data: sede boqer and hovav plateau

Variable	Rocky slope section		Colluvial slope section	
	Sede boqer	Hovav plateau	Sede boqer	Hovav plateau
C	30	10	10	0
SP	27	11	12	2
Smd	22	18	7	0
Ssa	33	55	42	100

C Cover of perennial vegetation (%)
SP Number of perennial species
Smd Percentage of Mediterranean and Irano-Turanian species
Ssa Percentage of perennial Saharo-Arabian species

Table 99.2 Rainfall-runoff relationships

Rainfall year	Plot	Annual rainfall (mm)	Annual runoff (mm)
2001–2002	N5	146.5	0.55
	N3	76.2	0.93
	N1	57.7	1.80
2002–2003	N5	82.7	0.12
	N3	95.1	1.06
	N1	99.3	3.60

exercise a strong effect on infiltration, runoff; soil moisture regime as to inhibit, or even eliminate, the expected positive effect with increasing annual rainfall.

The study was based on five monitoring sites located along the rainfall gradient (Fig. 99.1). Runoff plots were established at the base of north facing dune slopes where runoff frequency and magnitude are high. Data collected cover the following variables: rainfall, runoff, infiltration depth and characteristics of the biological topsoil crusts (for more details see Yair 2008). Data cover the rainfall years 2001–2003. Rainfall-runoff data, collected at three of the sites equipped with rain and runoff recorders, are presented in Table 99.2.

Runoff depth collected, in both years decreased with increasing annual rainfall. So did the frequency and magnitude of runoff events. This may indicate two opposing processes. The first is an increase in percolation with increasing annual rainfall. The second is that significant differences in the properties of the biological crusts not only limit runoff generation with increasing annual rainfall, but at the same time limit the depth of rainwater percolation and water availability for perennial plants (Table 99.3).

In both years depth of water percolation was higher in the southern than in the northern area (see Yair 2008). Data obtained are ascribed to substantial differences in the properties of the topsoil crusts along the rainfall gradient. Organic matter content, percent of silt and clay, crust thickness and field capacity increase with increasing annual rainfall. Such trends explain the significant increase in field capacity from the southern area to the wetter area. An additional factor contributes to the increase in water absorption with increasing annual rainfall. The biological crust in the drier areas is predominantly composed of a thin and smooth microbial crust. This crust absorbs a limited amount of water, seals quickly and generates runoff frequently. The northern crust is predominantly composed of mosses known for their high absorption capacity. Such crusts act as sponge. In summary; the better developed crusts in the wetter area are able to absorb all rainwater from most rainstorms, strongly limiting the depth of water percolation, runoff generation and consequently water availability for perennial plants. At the same time, the thinner crust in the drier area absorbs less water and allows a higher frequency and magnitude of runoff generation.

Table 99.3 Properties of the topsoil crusts along the rainfall gradient (n = 20)

Location	Silt and clay (%)	Crust thickness (mm)	Organic matter Content (%)	Field capacity (% by weight)
N1	26.7	5.3	2.7	6.1
N3	37.8	7.1	4.2	11.9
N5	49.2	11.2	7.6	19.5

Runoff generated over the dune slope infiltrates at the dune base, and at local concavities, where the amount of infiltrated water is beyond that allowed by the direst rainfall.

References

Kadmon R, Yair A, Danin A (1989) Relationships between soil properties, soil moisture and vegetation along loess covered hillslopes, Northern Negev, Israel. Catena Suppl 14:43–57

Kidron GJ, Yair A (1997) Rainfall-runoff relationships over encrusted dune surfaces, Nizzana, Western Negev, Israel. Eatth Surf Processes Land 22:1167–1184

Yair A, Enzel Y (1987) The relationship between annual rainfall and sediment yield in arid and semi-arid areas. Catena Suppl 10:121–301

Yair A (2008) Effects of surface runoff and subsurface flow on the spatial variability of water resources in longitudinal dunes. In: Breckle SW, Yair A, Veste M (eds). Arid dune ecosystems. Ecological studies, vol 200 p 251–272. Springer, Berlin

Yair A, Raz-Yassif N (2004) Hydrological processes in a small arid catchment: scale effects of rainfall and slope length. Geomorphology 42:43–57

Yair A (1990) Runoff generation in a sandy arid area, Nizzana Sand Dunes, Israel. Earth Surface Proceeses and Landforms 15:597–609

Integrated Approach to the Evaluation of Denudation Rates in an Experimental Catchment of the Northern Italian Apennines

100

Francesca Vergari, Marta Della Seta, Maurizio Del Monte, Linda Pieri and Francesca Ventura

Abstract

This paper presents the main results of a multidisciplinary study, aimed at the quantitative direct and indirect evaluation of erosion rates. The investigation was carried out in the small semi-agricultural Centonara catchment, in the Northern Italian Apennines, within the Mediterranean climate region. The Centonara catchment is heterogeneous from the point of view of lithology, geology, slope angle, vegetation and land cover. 20 % of the entire area is occupied by badlands (*calanchi*), characterized by bare soil and slope gradient over 40 % and affected by rapid morphogenesis mainly due to rill and gully erosion. For this study, 21-years monitoring data of sediment rate were compared with the results of the grid analysis of the "*Tu* Denudation index". Direct monitoring of sediment transport showed the high variability of rainfall, flow and erosion rates. Moreover, during a single year a few very intense rainfall events determine peak flow of the Centonara stream and exceptional sediment transport, influencing the overall erosion rates. The zonation of the estimated erosion rates highlighted that more than 40 % of the sediment rate derived from the *calanchi* badlands, while the arable lands and the areas occupied by natural vegetation (both herbaceous and woody) contributed only minimally to the generation of surface runoff and erosion.

Keywords

Soil erosion • Badlands • Northern apennines • Quantitative geomorphic analysis • Fluvial monitoring station

100.1 Introduction

Water erosion may cause significant landscape modifications during the time scale of a human life and, in particular, badlands denudation "hot spots" are able to influence the overall erosion rates on the catchment scale (Della Seta et al. 2009). Information on properties of eroded sediment is important because biological, chemical and physical properties of soil may change as a result of soil erosion and, in some cases, they may lead to reduced crop productivity (Vergari et al. 2013a, b). Thus, understanding and monitoring the processes involved in badlands dynamics is of crucial importance, especially with regard to distinguishing between the on- and off-site effects of denudation, in terms of water erosion and sediment production.

In Italy the seasonality of the Mediterranean climate, as well as the variability of vegetation cover and land use, induce marked yearly variations in the hydrological response of the watersheds (Soler et al. 2008).

F. Vergari (✉) · M. Della Seta · M. Del Monte
Dipartimento Di Scienze Della Terra, Università Degli Studi Di Roma "La Sapienza", P.Le Aldo Moro 5, 00185 Rome, Italy
e-mail: francesca.vergari@uniroma1.it

L. Pieri · F. Ventura
Dipartimento Di Scienze Agrarie, Università Di Bologna, Viale Fanin 44, 40127 Bologna, Italy

G. Lollino et al. (eds.), *Engineering Geology for Society and Territory – Volume 1*,
DOI: 10.1007/978-3-319-09300-0_100,

Though providing detailed understanding of the erosion processes, field studies have limitations because of the complexity of interacting local factors and the difficulty of regionalizing the local results. Cost-efficient methods for estimating erosion over whole catchments are required as ways of predicting erosion scenarios given certain disturbances or erosion management strategies. Nonetheless, direct monitoring is essential in validating indirect estimation.

This paper presents the main results of a series of multidisciplinary studies, aimed at the quantitative direct and indirect evaluation of denudation processes in a small catchment of the Northern Italian Apennines, by investigating the complex cause/effect relationships among different factors influencing both the morphodynamics and the erosion rates of the study area.

100.2 Study Area

The study was carried out in the small semi-agricultural Centonara catchment (44° 28′N, 11° 28′E), in the Northern Italian Apennines (Fig. 100.1a), about 20 km far from Bologna. It comprehends an area of 273 ha, with an altitude ranging between 84 and 350 m a.s.l. The watershed is characterized by a Mediterranean climate (Köppen-Geiger classification), where the maximum and minimum temperature occur in July–August and December–January respectively, while rainfall is concentrated in spring and autumn. The mean air temperature is 15 °C and the total annual rainfall is 749 mm y^{-1} (mean of the period 2000–2010). The hydrological response of the Centonara stream is highly seasonal, with discontinuous discharge values over the year.

The watershed is heterogeneous in terms of geology (Farabegoli et al. 1994), slope, and vegetation and land cover. About 20 % of the total area is represented by badlands (*calanchi*). These areas, characterized by bare soil and slope gradient over 40 %, are affected by rapid morphogenesis mainly due to rill and gully erosion, associated to pipe development and shallow and deep mass movements, such as slides, slumps, mudflows and slope collapses. The rest of the catchment is occupied by arable lands (25 %), spontaneous vegetation (herbaceous, shrubs and trees) and riparian strips (55 %). Slope gradient values of the entire

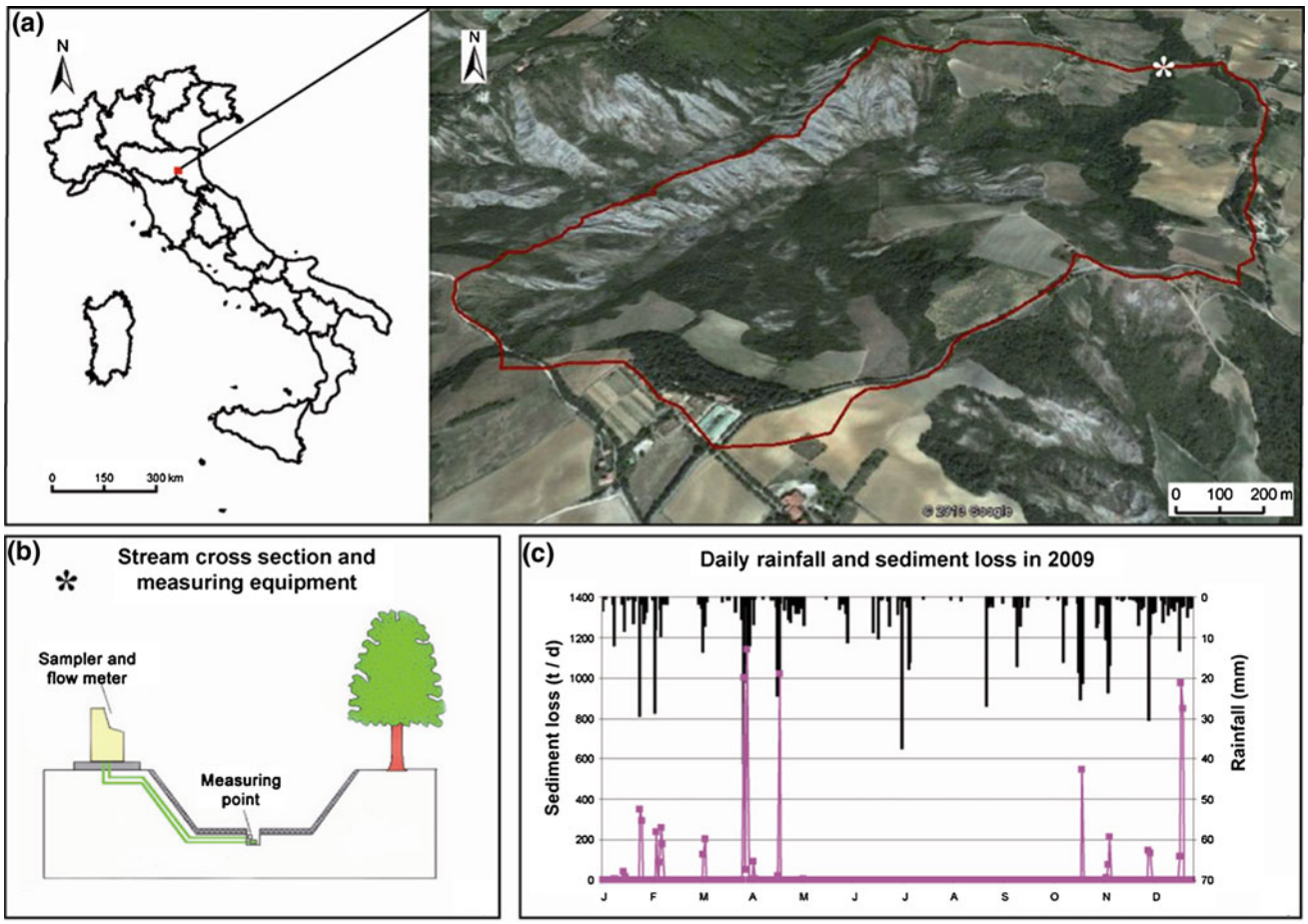

Fig. 100.1 **a** Location of the study area, **b** stream cross section and measuring equipment, **c** graph showing the daily rainfall (*black* mars) and sediment loss data (*violet solid lines*) in 2009

catchment range from less than 10 % (more than 13 % of area) to more than 50 % (almost 14 % of area), with the intermediate classes, 20–30 % and 30–35 %, as predominant. As a consequence of the lithological variability, the soil texture varies with the area: it is loam in the flat area, while in the hilly part and the badlands area the textural classes are silty-clay-loam and silty-clay.

Since 1990 the Centonara catchment has been an important experimental site for researches on runoff and erosion processes, some specifically regarding: (i) efficiency of soil conservation techniques; (ii) use of cover crops (Ventura et al. 2004); (iii) dynamics of erosion processes (Pieri et al. 2007); (iv) landslides (Bittelli et al. 2012); (v) efficiency of buffer stripes in preventing worsening of the water stream quality due to agricultural activity (Pieri et al. 2011).

The variety of studies performed over the years has lead to a detailed characterization of the catchment as well as to the installation of a variety of devices and facilities.

100.3 Materials and Methods

To consider the combined action of ongoing climate changes and human activities on the catchment morpho-evolution, direct monitoring was performed since 1992 by means of an automatic hydrological station (ISCO, 6700), installed to measure the water discharge of the Centonara stream and collect water samples to determine soil loss (Fig. 100.1b). Its data logger has a control for collecting both in time and volume: the sampler collects one sample every 24 h and one every 3000 m^3 of flow, to avoid losing large events that could occur within a 24 h-intervals, which transport the majority of sediments. To determine the sediment rate, runoff samples were dried in the oven at 105 °C for 24 h and then weighted. Due to the sampling method, for intense events, we had more sediment concentration measures for each event, while, for small events, the single sediment concentration was assumed to be uniform throughout the runoff period.

The catchment was also equipped with an automatic meteorological station, which records rainfall, air temperature, relative air humidity, wind speed and direction, and solar radiation, every 10 min.

21 years monitoring data were then compared with the results of the grid analysis of the "*Tu* Denudation index".

To predict catchment scale erosion rates, Ciccacci et al. (1981, 1986) obtained empirical equations for the *Tu* index, by statistically correlating the values of measured suspended sediment yield at the outlets of several Italian catchments to some geomorphic and climatic parameters (such as drainage density, pluviometric regime indices, mean annual discharge and other parameters expressing the hierarchical structure of the drainage network). In fact, the suspended sediment yield (*Tu*, t km^{-2} y^{-1}) seems to be the most suitable expression of erosion rate, because it is easily measured and represents approximately 50 % (arid and semi-arid climates) to 90 % (humid climates) of total sediment yield by rivers (Cooke and Doornkamp 1974).

Given these encouraging results, during the last years some attempts have been made to perform more detailed zonations of the predicted denudation rates (Aucelli et al. 2010; Maerker et al. 2012), in order to better zoning the negative ground level changes on badland sites within the catchment area (cm y^{-1}). To this aim, the Eqs. (100.1) and (100.2) were used, which were derived by Ciccacci et al. (1981) considering as independent variable the only drainage density (D) of 14 Italian sample drainage basins:

$$\log Tu = 0.35312\ D + 1.43225 \quad R^2 = 0.96221 \quad (\text{with } D < 6) \tag{100.1}$$

$$\log Tu = 2.93936 \log D + 1.13430 \quad R^2 = 0.94987 \quad (\text{with } D > 6) \tag{100.2}$$

In this study, in order to evaluate the *Tu* index for unit areas, the Centonara catchment was divided using a grid of 0.25 km^2 cells. The grid was then eight times spatially shifted by 125 m, in order to increase the number of cells for *Tu* computation and thus the analytical detail (one value for each unit area of 0.0156 km^2). For each cell, the D value was calculated from drainage network digitized from 1:25,000 topographic maps. The *Tu* index value (in t km^2 y^{-1}) was estimated for each cell, corresponding to the estimated sediment output from the same cell. The *Tu* value was then converted into the average negative ground level change of the cell (cm y^{-1}), assuming a mean bulk density of outcropping clays equal to 2 t m^{-3}. These estimated erosion rates were assigned to the cells' centroids, to get a point cloud to be used for geostatistical interpolations, thus obtaining the estimated erosion rate map of Centonara catchment. The spline interpolation method was applied, since the interpolated surface can exceed the known value range, but must pass through all of the sample points. The smoothing effect of the interpolator was in this case applied, since the input data do not represent point values measured in the field but values over unit areas.

100.4 Results

The study area experienced significant variation in annual precipitation, typical of Mediterranean climate. Considering the period 2000–2010, annual rainfall ranged from 584.5 mm in 2007 to 1115.2 in 2002, with a mean value of 749 mm.

The Centonara stream discharge had seasonal trends more pronounced than those of the precipitation: it was prevalently dry (with no flow) during the driest period (the summer and the first weeks of fall), except for a few small peaks due to summer storms. The annual field-observed stream discharge ranged between 210000 m^3 in 2000 and 767351 m^3 in 2002, with peaks of single events reaching also 100000 m^3. Indeed, these peaks were occasional (not more than one per year) and occurred as a result of exceptionally long or intense rainfall events, prevalently during the rainy seasons (spring and autumn).

Also the annual amount of eroded sediments had a marked inter-annual variability (Fig. 100.1c): the mean measured annual sediment yield was about 23 t ha^{-1}, with maximum value of 42.2 t ha^{-1}. This value may somehow underestimate the real solid transport, due to the non-continuous measurement of the sediment load. Actually, in the majority of cases (80–90 %) the sampled water was limpid, while a few rain events determined peaks in the Centonara discharge with a variable solid transport.

In Fig. 100.2, the estimated erosion rate map of Centonara catchment is shown. The highest erosion rates are estimated for the eastern portion of the area, where hillslope characterized by *calanchi* badlands are widespread. Here, the estimated rates were compared with the rates measured by erosion pins in other Italian *calanchi* badlands (Della Seta et al. 2009; Vergari et al. 2013b), which correspond to average values that range between 1 and 4 cm y^{-1}, to verify the reliability of the results. For the area, the estimated denudation rates in calanchi badlands reach more than 3 cm y^{-1}, underlining the good estimation performance.

100.5 Discussion and Conclusions

During the monitoring period, field-measured data of the study area highlighted the high inter-annual variability of rainfall, but especially of discharge and erosion rates (Fig. 100.1c). There is not a linear relationship between annual rainfall and discharge and erosion rate. The discharge and, consequently, the rate of erosion depend on few rain events which, for their erosivity, cause the runoff, the erosion process and the peak flow. In fact, only about 15 % of the daily samples of water from the Centonara stream contains sediment and very few of these have high concentrations (up to 60 g l^{-1}). These results are consistent with the findings of many previous studies (Della Seta et al.

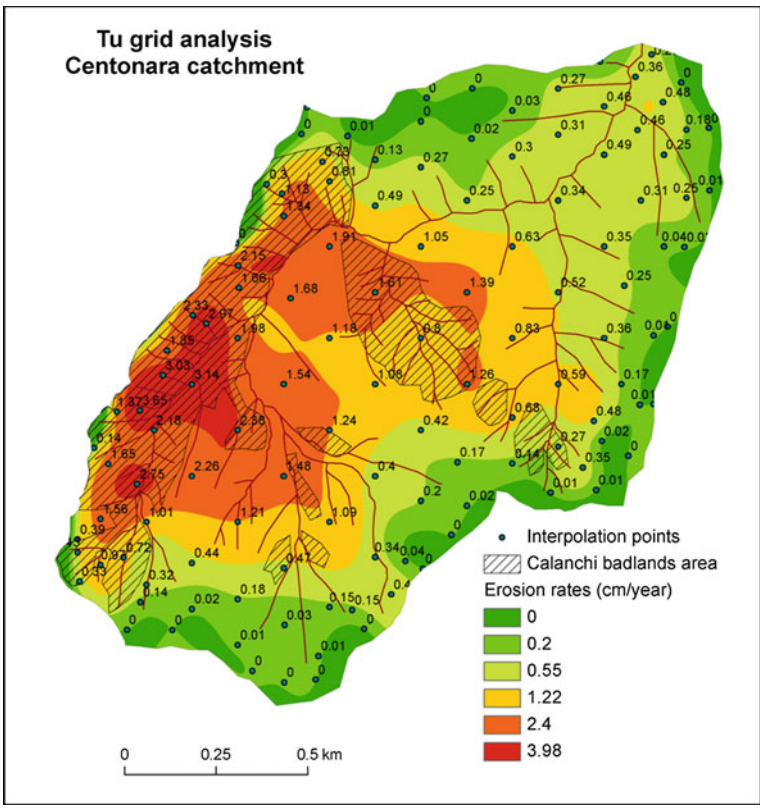

Fig. 100.2 Zonation of sediment source areas by means of *Tu* grid analysis

2007, 2009). Moreover, the rain-runoff-sediment relationship is very complex, since many factors are involved: an intense rain does not always determine a peak of outflow, since the surrounding conditions of the area strongly affect the hydrological response.

The *Tu* grid analysis method is a very simple but at the same time an efficient estimator of the denudation rates in areas characterized by rapid slope erosion processes, as shown in previous works. The zonation of the estimated erosion rates for the Centonara catchment allowed deepening the contribution of the different subareas of the watershed to the total sediment loss, showing that the *calanchi* badlands, that occupy about 20 % of the whole basin, contribute for more than 40 % of the Centonara catchment sediment delivery. Arable lands or the areas occupied by natural vegetation (both herbaceous and woody) contribute only minimally to the generation of surface runoff and erosion. In fact, as previously reported (Pieri et al. 2013), plants act with a dual role in preventing from erosion: on one hand they intercept the rain drops decreasing their erosivity, while on the other hand they hold the soil particles with the roots. In any case, the analysis of the impact of land use changes showed that there was a correlation between the agricultural land use (expressed as percentage of the land cultivated with different crops) and soil losses, underlining the importance of the differentiation of cropping systems in the watershed to reduce soil losses.

References

Aucelli PPC, Baldassarre MA, Conforti M, Della Seta M, Rosskopf CM, Scarciglia F, Vergari F (2010) Assessment of present morphodynamics and related erosion rates by means of direct erosion monitoring and digital photogrammetric analysis: the case study of the Upper Orcia Valley (Tuscany, Italy). In: Proceedings of the 1st Italian-Russian workshop on water erosion "slope processes and matter movement", Moscow 2010, Faculty of Geography of the MSU, p 96

Bittelli M, Valentino R, Salvatorelli F, Rossi Pisa P (2012) Monitoring soil-water and displacement conditions leading to landslide occurrence in partially saturated clays. Geomorphology 173–174:161–173

Ciccacci S, Fredi P, Lupia Palmieri E, Pugliese F (1981) Contributo della analisi geomorfica quantitativa alla valutazione dell'entità dell'erosione nei bacini fluviali. Boll Soc Geol Ital 99:455–516

Ciccacci S, Fredi P, Lupia Palmieri E, Pugliese F (1986) Indirect evaluation of erosion entity in drainage basins through geomorphic, climatic and hydrological parameters. In: Gardiner V (ed) International geomorphology part II. Wiley, Chichester, pp 33–48

Cooke RU, Doornkamp JC (1974) Geomorphology in environmental management. Clarendon Press, Oxford, p 413

Della Seta M, Del Monte M, Fredi P, Lupia Palmieri E (2007) Direct and indirect evaluation of denudation rates in Central Italy. Catena 71:21–30

Della Seta M, Del Monte M, Fredi P, Lupia Palmieri E (2009) Space-time variability of denudation rates at the catchment and hillslope scales on the Tyrrhenian side of Central Italy. Geomorphology 107(3–4):161–177

Farabegoli E, Rossi Pisa P, Costantini B, Gardi C (1994) Thematic cartography for the study of the erosion at the catchment scale. Ital J Agron 28:356–363

Maerker M, Della Seta M, Vergari F, Del Monte M (2012) Process-based assessment of erosion dynamics in the Upper Orcia Valley (Southern Tuscany, Italy): a new semi-quantitative integrated approach. Rend Online Soc Geol It 21:1208–1211

Pieri L, Ventura F, Gaspari N, Salvatorelli F, Vitali G, Rossi P (2013) Runoff in cultivated hilly areas as influenced by crops and land management. Ital J Agrometeorol XVIII(1):23–32

Pieri L, Bittelli M, Wu JQ, Dun S, Flanagan DC, Rossi Pisa P, Ventura F, Salvatorelli F (2007) Using Water Erosion Prediction Project (WEPP) model to simulate field-observed runoff and erosion in the Apennines mountain range Italy. J Hydrol 336:77–84

Pieri L, Ventura F, Vignudelli M, Rossi Pisa P (2011) Nitrogen balance in a hilly semi-agricultural catchment in Northern Italy. Ital J Agron 6(e12):67–75

Soler M, Latron J, Gallart F (2008) Relationships between suspended sediment concentrations and discharge in two small research basins in a mountainous Mediterranean area (Vallcebre, Eastern Pyrennes). Geomorphology 98:143–152

Ventura F, Rossi Pisa P, Vicari A (2004) Effect of land use on soil erosion in a small catchment in Emilia—Romagna Region. Ital J Agron 8:29–36

Vergari F, Della Seta M, Del Monte M, Barbieri M (2013a) Badlands denudation "hot spots": the role of parent material properties on geomorphic processes in 20-years monitored sites of Southern Tuscany (Italy). Catena 106:31–41. doi:10.1016/j.catena.2012.02.007

Vergari F, Della Seta M, Del Monte M, Fredi P, Lupia Palmieri E (2013b) Long- and short-term evolution of several mediterranean denudation hot spots: the role of rainfall variations and human impact. Geomorphology 183:14–27. doi:10.1016/j.geomorph.2012.08.002

Susceptibility and Vulnerability to Landslides—Case Study: Basin of River Bengalas—City of Nova Friburgo—Brazil

101

L.T. Silva, E.P.F.F.M. Sampaio, J.A.M. Corte-Real, D.A. Rodriguez, F. Carnauba Medeiros, B.E. Moraes and D.G.M. França

Abstract

Landslides have frequently occurred in last years, due to the disorderly growth of the cities and the occupation of risk areas by the poor population, causing social, environmental and economic impacts. Urban areas in expansion move to geologically unstable areas and topographically inclined, such as the River Bengalas Basin, located in the city of Nova Friburgo, mountainous region of the State of Rio de Janeiro, Brazil. This article aims to present the model developed and used to evaluate the susceptibility and vulnerability of the River Bengalas Basin to landslides, which in January 2011, with the occurrence of heavy rains, caused landslides that impacted in the death of 429 people in city of Nova Friburgo. For the case study, several investigations have been made related to the areas of the basin, such as slope, soil conditions, lithology, land use and cover, vertical curvature (Very Convex, Convex, Flat, Concave, Very Concave), horizontal curvature (Very Divergent, Divergent, Flat, Convergent, Very Convergent), and precipitation data. With this study it was possible to understand how the natural and anthropics elements of the basin are related to the local dynamics of the disasters regarding to their interferences in the induction of landslides; evaluate the effectiveness of the guidelines of the Plano Diretor Participativo of the city of Nova Friburgo regarding the landslides; identify the susceptible and vulnerable areas to landslides and assess the rates of susceptibility and vulnerability to landslides from new calculation model proposed.

Keywords

Index • Susceptibility • Vulnerability • Landslides

L.T. Silva (✉) · D.A. Rodriguez · B.E. Moraes · D.G.M. França
National Institute for Space Research, Rodovia Pres. Dutra, Km. 40, 12630-970, Cachoeira Paulista, SP, Brazil
e-mail: luiz.tadeu@cptec.inpe.br

D.A. Rodriguez
e-mail: daniel.andres@inpe.br

B.E. Moraes
e-mail: brunofloyd@gmail.com

D.G.M. França
e-mail: david.franca@cptec.inpe.br

E.P.F.F.M. Sampaio · J.A.M. Corte-Real · F.C. Medeiros
ICAAM and University of Évora, Largo dos Colegiais 2, 7004-516, Évora, Portugal
e-mail: ems@uevora.pt

J.A.M. Corte-Real
e-mail: jmcr@uevora.ptjoao.cortereal@ulusofona.pt

F.C. Medeiros
e-mail: carnauba.fabiana@gmail.com

J.A.M. Corte-Real
ULHT - Departamento de Aeronáutica e Transportes, Campo Grande, 376, 1749-024, Lisbon, Portugal

G. Lollino et al. (eds.), *Engineering Geology for Society and Territory – Volume 1*,
DOI: 10.1007/978-3-319-09300-0_101,

101.1 Introduction

Humankind has been challenged by the occurrence of extreme natural events, responsible for large amounts of material damage and for innumerous fatalities. Since 1970, with the increasing frequency and intensity of disasters, the scientific community and international institutions like the United Nations (UN), were mobilized to worry about this issue. In Brazil, this concern is due to the increase in the number of fatalities in the 1960s, 1970s and 1980s, associated with rapid urban growth and the disordered occupation of unsuitable areas for urbanization in the country. Year after year natural disasters result in a large number of dead and wounded, besides the costly economic losses. According to UNDP report (2004), 75 % of the world population lives in areas that were affected at least once by cyclones, floods, droughts and earthquakes between the years 1980 and 2000, causing numerous deaths, impacts on agriculture, on water resources, in health, in economy etc. (Braga et al. 2006).

101.2 Objective

In this paper we attempt to create indexes of susceptibility and vulnerability to landslides, from the survey of environmental data and the precipitation occurred on January 12, 2011 in the River Bengalas Basin, city of Nova Friburgo, State of Rio de Janeiro, Brazil. These indexes and the methodology here created taking into account the conditions of environmental variables and the precipitation of the area of study, can be used universally for research centers and other active institutions in the prevention, monitoring and forecasting of landslides.

101.3 Methodology

For each variable (morphology, pedology, lithology, use and cover of land, vertical and horizontal curvature) were adopted weights which were proportionally calculated to the number of landslides occurred for each class of each variable, ranging from 0.00 to 1.00, while those closer to 0.00 indicate classes of low relationship with the susceptibility to landslides, while those closer to 1.00 indicate classes of high relationship. The interaction of information plans of these variables are based on studies of Tricart (1977), following the principles of ecodynamics that establishes a gradation between the morphogenesis, prevailing the modifiers erosive processes of the soil's forms, and the pedogenesis, where the forming processes of soils prevail. Several studies have been conducted, such as:

- Survey of all the points of landslides which triggered the disasters in the River Bengalas Basin, in January 2011;
- Analysis to understand how the natural and man-made elements of the study area are related to the local activities, regarding to their interference in the induction of landslides;
- Compilation of georeferenced data of the study area to treat them through Geographic Information System (GIS) so that the spatial information represents the best way possible its susceptibility/vulnerability to landslides;
- Calculation and analysis of the group of indicators of physical environmental susceptibility of the study area, based on the characteristics of the physical environmental of morphology, pedology, lithology, use and land cover. It is emphasized that on this new model, the geomorphometrics variables "vertical curvature" and "horizontal curvature" were included in the calculations and analysis, besides the calculation of the susceptibility areas 'of the basin were done according to the proportion of 183 landslides;
- Survey and evaluation of precipitation data; and
- Development of equation to the new methodology of calculating the vulnerability to landslides from data of the indicators of susceptibility and of the precipitations occurred in the Basin.

The method adopted in this work is based on the study of the Empirical Analysis of the Fragility of Natural and Anthropogenic Environments proposed by Tricart (1977), that systemizes a nominal hierarchy of fragility represented by values or weights (very low, low, medium, high and very high) with adaptations of the Authors, which systematizing a nominal hierarchy of weakness represented by nominal values or weights, named in this work as "Classes of Susceptibility /Vulnerability and their Indexes", adapted by the Author. They are: very low (0.00–0.19), low (0.20, 0.39), medium (0.40–0.59), high (0.60–0.69) and very high ($\geq$0.70). Those classes with "very low" or "low" susceptibility /vulnerability are the areas that present lower risks to landslides, while "medium", "high" and "very high" are the areas that have, respectively, medium, high and very high susceptibility /vulnerability to landslides.

101.4 Results

The weights assigned to the classes of the variables, as shown in Table 101.1, were introduced into the Eq. 101.1 (Silva 2014) below, created specifically in this work to calculate the indexes of susceptibility (S) of the River Bengalas Basin to landslides.

Table 101.1 Classes of susceptibility/vulnerability to landslides and its weights

Variables	Indexes used	Variables	Indexes used
Morphology (%)		*Pedology*	
<5	0.02	Argisols	0.00
5 a 12	0.03	Neosols	0.00
12 a 30	0.38	Rocky Outcrops	0.00
30 a 47	0.41	Cambisols	0.13
> 47	0.16	Urban Area	0.20
Lithology		Latosols	0.68
Igneous Rock		*Use and cover of the soil*	
Gabbro	0.00	Lakes	0.00
Gneiss	0.00	Rocky outcrops	0.00
Granite, diorite and granodiorites; and Metadiorite, metatonalite, metagabbro and gneiss granulitico	0.65	Agriculture	0.01
		Degraded areas	0.01
Quartzite	0.00	Eucalyptus and Pines	0.01
Granitic composition of orthogneiss	0.14	Forest (Atlantic Forest)	0.04
Metamorphic rock		Pastures and forages	0.19
Amphibole gneiss	0.00	Forest home and media	0.26
Biotitic gneiss	0.04		
Sedimentary rock		Urban area	0.48
Colluvial; and alluvial and colluvial sediments	0.17		
Vertical curvature		*Horizontal curvature*	
Very convex	0.03	Very divergent	0.10
Convex	0.08	Divergent	0.10
Flat	0.27	Flat	0.19
Concave	0.39	Convergent	0.33
Very concave	0.23	Very convergent	0.28

Source Tricart (1977) and Ross (1994), adapted by the Author

$$S = \left(\frac{\sqrt{Vdc} + \sqrt{Vpd} + \sqrt{Vli} + \sqrt{Vus} + \sqrt{Vcv} + \sqrt{Vch}}{NVA} \right) \quad (101.1)$$

where S is the susceptibility varying from 0.00 to 1.00; $\sqrt{Vdc}$ is the square root of the morphology variable; $\sqrt{Vpd}$ square root of the pedology variable; $\sqrt{Vli}$ square root of the lithology variable; $\sqrt{Vus}$ square root of the use and cover of the soil; $\sqrt{Vcv}$ square root of the vertical curvature; $\sqrt{Vch}$ square root of the horizontal curvature; and NVA is the number of variables (6). So, from the calculation of the susceptibility of the River Bengalas Basin, its own map was generated. Weights ranging from "0.00" to "1.00", calculated proportionally to the number of landslides occurred in the Basin, were assigned to classes of the studied variables to calculate the susceptibility of it and are shown in Table 101.1.

The generated map (Fig. 101.1) shows that from the areas of the Basin, 114.22 Km^2 are classified as medium susceptibility, 52.72 Km^2 of low susceptibility and 22.73 Km^2 of high susceptibility to landslides. Imperceptible on the map, 1.15 Km^2 of the Basin are areas of very low susceptibility and 0.19 Km^2 of very high susceptibility to these types of disasters. The methodology created to calculate the vulnerability to landslides of the Basin was developed from the calculation of the susceptibility (S), in other words, we calculate the susceptibility and then, with the inclusion of calculation involving several indicators related to the "precipitation of rains", according to the Eq. 101.2 (Silva 2014) below, the vulnerability was calculated.

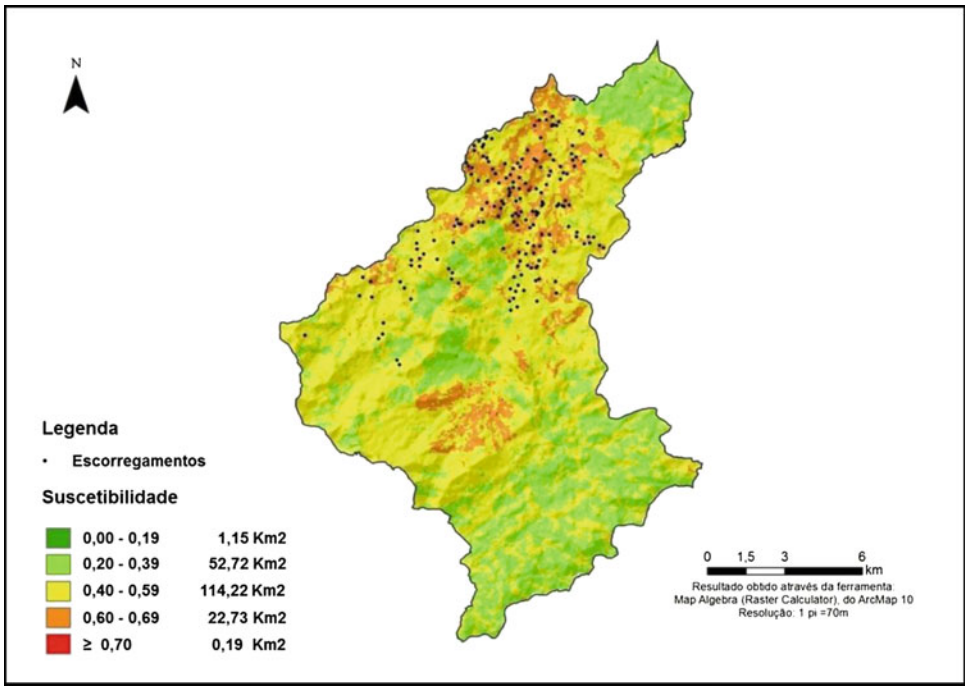

Fig. 101.1 Map of susceptibility of the river Bengalas Basin to landslides

$$V = \frac{\left(\frac{\sqrt{Vdc}+\sqrt{Vpd}+\sqrt{Vli}+\sqrt{Vus}+\sqrt{Vcv}+\sqrt{Vch}}{NVA}\right) + \sqrt{\left[\frac{\left(\frac{PD}{CPC}\right)+\left(\frac{PA5}{MAXPA5}\right)}{2}\right]}}{2} \quad (101.2)$$

This equation was developed specifically in a PhD thesis, as the susceptibility. It was tested in 4 events of heavy precipitation occurred on 19/01/2005, 04/01/2007, 12/01/2011 and 18/03/2013. The letter V is vulnerability; $\sqrt{Vdc}$ is the square root of the morphology variable; $\sqrt{Vpd}$ square root of the pedology variable; $\sqrt{Vli}$ square root of the lithology variable; $\sqrt{Vus}$ square root of the use and cover of the soil; $\sqrt{Vcv}$ square root of the vertical curvature; $\sqrt{Vch}$ square root of the horizontal curvature; NVA is the number of variables (6); PD is the daily precipitation; CPC is the coefficient of critical precipitation (70 mm/24 h); PA5 is the cumulative precipitation for 5 days; MAXPA5 is the maximum cumulative precipitation for 5 days in the historical series 01/01/1995 to 03/19/2013. Combining the susceptibility with the precipitation, it's obtained the vulnerability. From this historical series, four dates (01/19/2005, 01/04/2007, 01/12/2011, and 03/18/2013), here called a "day of the event" had their data separated for analysis, because these were recorded in the city of Nova Friburgo a daily precipitation exceeding 80 mm (Table 101.2).

It was observed that the events occurred on 01/04/2007 and on 01/12/2011, there were respectively 350 and 183 landslides, due to the rain precipitation started 1 day before (01/03/2007 and 01/11/2011) to the days of the events, with its elevation and continuity in the days events. However the events of 01/04/2007 and 03/18/2013, the high rain precipitation occurred only on these dates, insufficient for the occurrence of the landslides. Hence the importance of analyzing the PA5, in case of prediction of landslides, always for a minimum of 2 days. The vulnerability maps of the Basin were generated by the software ArcGIS ® 10,

Table 101.2 Analysis of events in the city of Nova Friburgo with a daily precipitation exceeding 80 mm

Accumulated precipitation (mm)	Day before the event (mm/dd/yyyy)	Day of the event (mm/dd/yyyy)	Number of landslides occurred
	01/18/2005	01/19/2005	
	32.8	117.5	0
	01/03/2007	01/04/2007	
	88.6	176.3	350
	01/11/2011	01/12/2011	
	85.0	219.9	183
	03/17/2013	03/18/2013	
	26.8	131.6	0

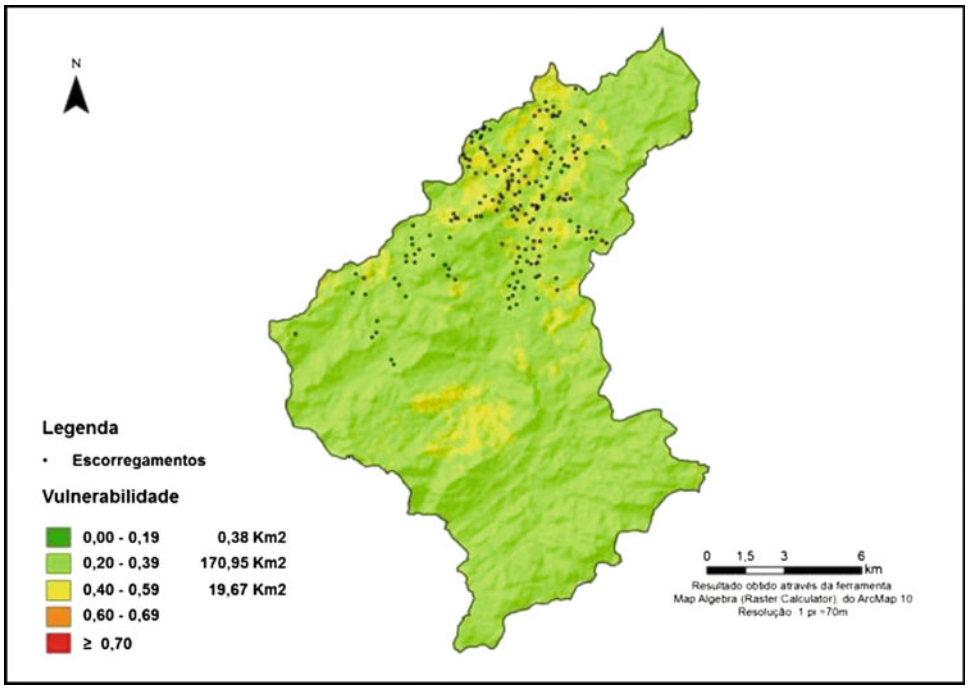

Fig. 101.2 Vulnerability Map of the river Bengalas Basin to landsides for the days 7, 8 and 9 January, 2011, respectively the 5th, 4th and 3rd day before the day event

with the overlay of the map's variables "morphology, pedology, lithology, use and cover of land, vertical and horizontal curvature", with their related information, including the vulnerability indexes of the Basin calculated from Eq. 101.2. The map generated for the vulnerability of the River Bengalas Basin to landslides (Fig. 101.2) is identical to the 5th, 4th and 3rd preceding day of the day event, respectively the days 7, 8 and 9 January, 2011. The Fig. 101.3 presents the map of vulnerability of the Basin generated for the day January 10, 2012 (2 days before the day of the event). The vulnerability map generated for 1 day prior to the event (01/11/2011), as well as for the event day (01/12/2011), when there were 183 landslides in the Basin, also was identical. It was observed in this map that the applied methodology indicated two major classes of vulnerability—very high and high—which correspond respectively to 136.18 Km^2 and 54.63 Km^2 of the River Bengalas Basin. However, the indexes adopted for the

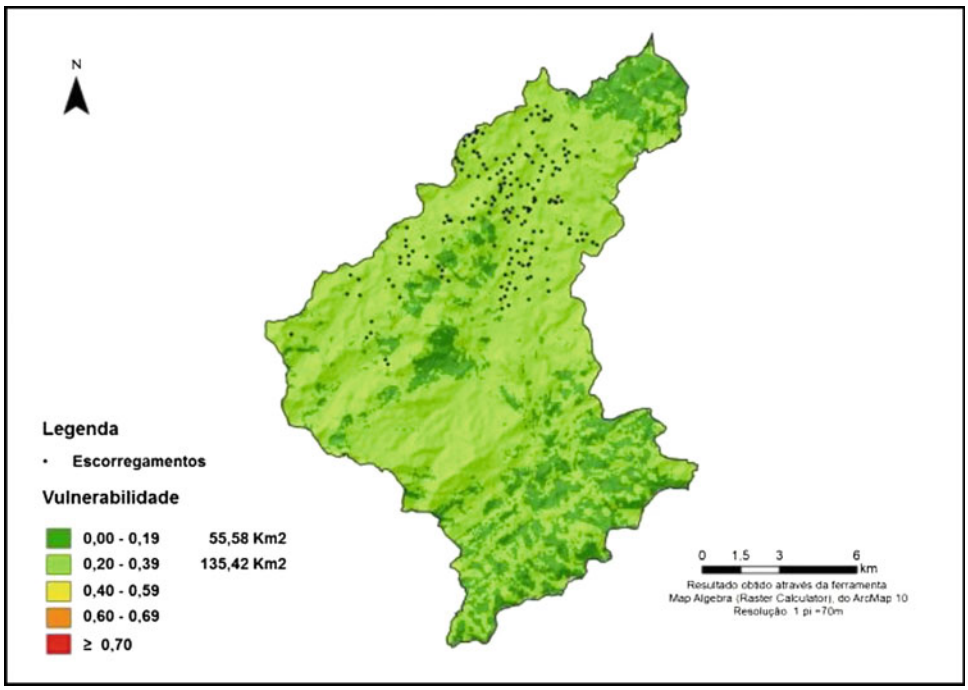

Fig. 101.3 Vulnerability map of the river Bengalas Basin to landslides for the day 10 January, 2011, 2nd before the day event

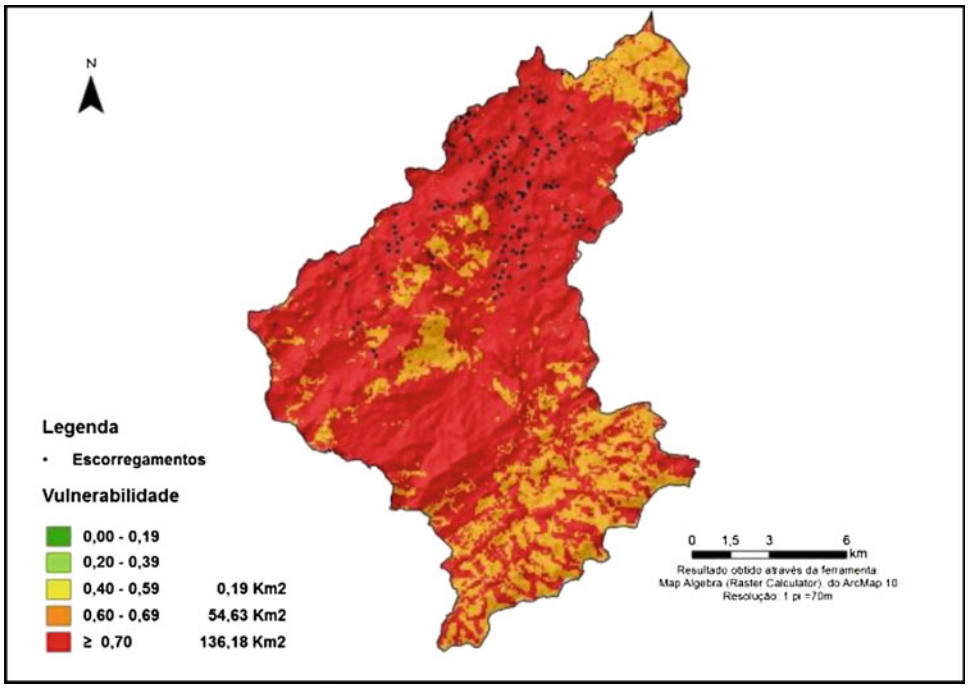

Fig. 101.4 Vulnerability map of the river Bengalas Basin to landslides for the days 11 and 12 January, 2011 respectively the 1st day before the day event and the day event

classes of vulnerability standardized in this study (Table 101.1) do not allow for a more detailed observation and analysis of which areas of the River Bengalas Basin are more vulnerable to landslides. The first impression is that the entire study area has the same characteristic. Therefore, the technique of algebra maps applied from the weighting of all the thematic maps results in continuous numeric values that allow other ways to categorize the vulnerability, if it is necessary to assess the areas more or less critical of the Basin. Thus, it was decided to reclassify the vulnerability indexes to landslides calculated for the days 11 and 12 January, 2011, from the slicing of these indexes so the analysis could be more detailed (Fig. 101.4).

Figure 101.5 shows the alternative to the case, which deals with the division of vulnerability classes from percentages found in the resulting histogram of algebra maps for the days 11 and 12 January 2011. This type of classification is done for various phenomena of the nature, which seeks to define a critical threshold that, from this, there is the occurrence of extreme/rare considered events (spatial and temporarily). This occurs, for example, in the precipitation data analysis. In this case, the temporal distribution of the rains over a given period (annual or decadal) is statistically evaluated, so the rains that corresponds to the 99 % percentile are called as very extreme events. In other words, they are rains that don't occur 99 % of the times in a region during a determined period. For the vulnerability case to landslides, aimed to draw such percentages in order to define the areas of River Bengalas Basin that represents a very critical situation, that is, very high vulnerability to these types of disasters. In the literature, there are several validated studies that indicate that the most critical vulnerability class, normally, occupies between 3.5 and 8.0 % of the analyzed basins (Kayastha et al. 2013; Bai et al. 2009; Ayalew et al. 2004; Akinci et al. 2011). So, the limit for the vulnerability class "very high" was traced to the 95 % percentile, as option of viewing of the results shown on the vulnerability map of the River Bengalas Basin to landslides (Fig. 101.5). This means that the vulnerability class "too high" is over 95 % from the values found within the River Bengalas Basin, representing the 5 % more critical from the Basin in relation to landslides. It is noteworthy that other classes of vulnerability—very low, low, medium, and high - were also traced based on the values found in the literature, so the less critical class represents 10 % and the other classes were placed equidistant each other, according to the result presented in Fig. 101.5. It was counted 35,318 pixels on the vulnerability map of the River Bengalas Basin to landslides. Given that the class "very high" represents the most critical 5 % from the Basin, such class has 5 % of the total pixels, that is, has 1,766 pixels. Sarkar and Kanungo (2004), in a study conducted in Darjeeling, a mountainous region of the Himalayas, India, the frequency of landslides per Km^2 and from calculated classes by them were "very low: 0.00", "low: 0.16", "moderate: 0.50" and "high: 1.79".

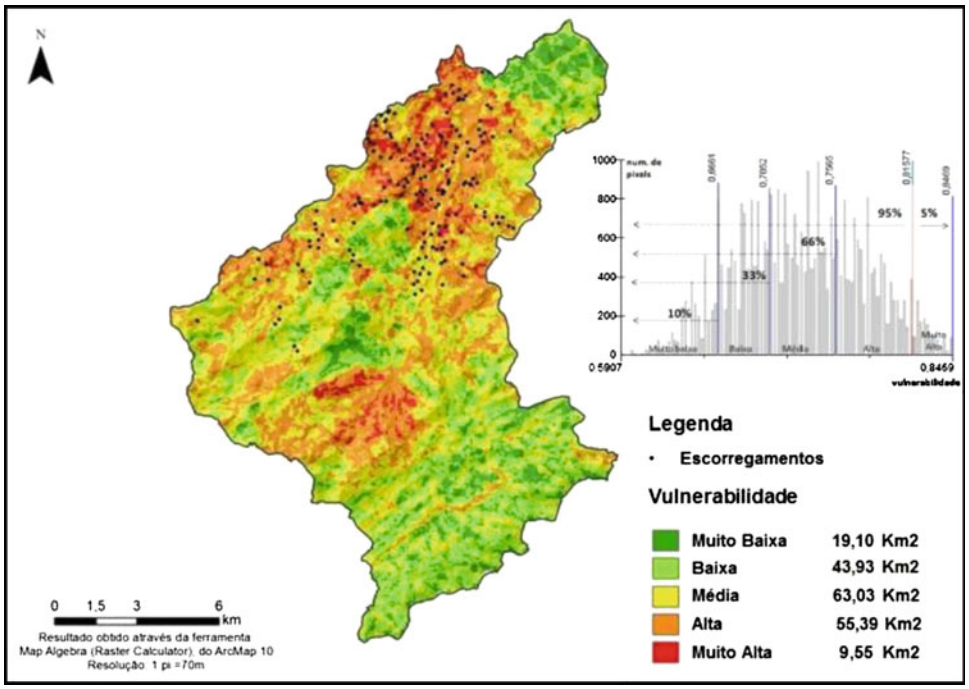

Fig. 101.5 Vulnerability map of the river Bengalas Basin to landslides for the days 11 and 12 January, 2011, representing the more critical 5 % of the Basin

101.5 Conclusion

With the development of this work, it was possible to create a specific methodology capable of creating indexes of susceptibility and vulnerability to landslides, probably it regards about a methodology that can be potentially applied in other areas of study for research centers and other institutions active in the prevention, monitoring and forecasting of landslides. Also, it proved effective regarding the concepts, tools, techniques, and applicability, having been applied to four (4) events of high rain precipitation that occurred in the city of Nova Friburgo, being efficient in the four (4) situations and proving that it is a methodology that can be used universally for research centers and other institutions active in the prevention, monitoring and forecasting of landslides. It was observed that when the vulnerability index to landslides is greater than or equal to 0.70 (critical threshold) for 2 days in a row, as proposed in this study, the incidence of these types of disasters is "very high". Moreover, it is highlighted the importance of analyzing the 5-day Accumulated Precipitation (PA5) of at least 2 days. From the analysis of pixels of the vulnerability map to landslides, if the frequency of these disasters per Km^2 calculated in this work for the class "high: 2.57", is compared to the frequency obtained from the class "high: 1.79" from the work validated by Sarkar and Kanungo (2004), it is concluded that the results found here is above compared to the found by the authors, so that this type of classification by the percentiles is able to represent well the critical situation which corresponds to landslides.

References

Akinci H, Doğan S, Kiliçoğlu C Temiz MS (2011) Production of landslide susceptibility map of Samsun (Turkey) City center by using frequency ratio method. Geomatics Engineering, Ondokuz Mayis University, 55139, Kurupelit/Samsun, Turkey. Kavak Vocational School, Ondokuz Mayis University, Kavak/Samsun, Turkey. Int J Phys Sci 6(5):1015–1025. doi: 10.5897/IJPS11.133. (Acad J)

Ayalew L, Yamagishi H, Ugawa N (2004) Landslide susceptibility mapping using GIS-based weighted linear combination, the case in Tsugawa area of Agano River, Niigata Prefecture, Japan. School of Natural Resources. University of Arizona. doi 10.1007/s10346-003-0006-9

Bai S-B, Wang J, Lü G-N, Zhou P-G, Hou S-S, Xu S-N (2009) GIS-based and data-driven bivariate landslide-susceptibility mapping in the three Gorges area, China. College of Geography Science, Nanjing Normal University, Nanjing 210097 (China). China Institute of Geo-Environment Monitoring, Beijing 100081 (China). Elsevier 19(1):14–20

Braga TM, Oliveira EL, Givisiez GHN (2006) Avaliação de metodologias de mensuração de risco e vulnerabilidade social a desastres naturais associados à mudança climática. São Paulo em Perspectiva, São Paulo, Fundação Seade 20(1):81–95

Kayastha P, Dhital MR, Smedt F (2013) Evaluation and comparison of GIS based landslide susceptibility mapping procedures in Kulekhani watershed, Nepal. Department of Hydrology and Hydraulic Engineering, Vrije Universiteit Brussel, Brussels, Belgium. Mountain

Risk Engineering Unit, Tribhuvan University, Kirtipur, Kathmandu, Nepal. J Geol Soc India 81:219–231

Ross JLS (1994) Análise empírica da fragilidade dos ambientes naturais e antropizados. Revista do Departamento de Geografia, n. 8, São Paulo: FFLCH/USP

Sarkar S, Kanungo DP (2004) An integrated approach for landslide susceptibility mapping using remote sensing and gis. American society for photogrammetry and remote sensing. Photogram Eng Remote Sens 70(5):617–625

Silva LT (2014) Vulnerability to landslides: case study: Basin of the River Bengalas (2011). Ph.D thesis. University of Évora. Évora, Portugal (2014)

Tricart J (1977) Ecodinâmica, Rio de Janeiro: IBGE-SUPREN, (Recursos Naturais e Meio Ambiente), p 91

UNDP (2004) Reducing disaster risk: a challenge for development, a global report. UNDP bureau for crisis prevention and recovery. UNDP, New York

Slope Stability Scaling Laws Within Physically Based Models and Their Modifications Under Varying Triggering Conditions

102

Massimiliano Alvioli, Mauro Rossi and Fausto Guzzetti

Abstract

The appearance of scaling phenomena in rainfall-induced landslides has been observed by several authors, and discussed within various theoretical models. A few properties of landslides are known to exhibit a power-law functional dependence, as shown by a number of world-wide datasets, which is often interpreted as a signature of the occurrence of self-organized criticality. We show that the adoption of a complex, physically motivated model for rainfall infiltration and slope stability can reproduce fairly well the observations over a wide range of rainfall durations and intensities, accounting for most of the features exhibited by the datasets in a natural way. Namely, we reproduce within our approach the observed functional dependencies and the slope of the scaling laws of intensity–duration triggering thresholds for shallow landslides, and the observed distribution of landslide sizes. We applied the model over a very large study area partitioned in many sub-basins characterized by different geological, hydrological and morphological conditions. In such a way we assess the risk associated with the stability of slopes subject to substantial rainfall activity. In particular, focusing on the intensity/duration dependence of rainfall thresholds for triggering shallow landslides, we estimate the response of the various sub-basins under different triggering conditions, and analyze the dynamics of the systems under different climatic scenarios, examining the scaling properties of slope responses.

Keywords

Landslide • Numerical modeling • Rainfall thresholds • Frequency–size statistics • Upper Tiber river basin • Italy

There is accumulating evidence that natural landslides exhibit scaling properties including the area and volume of the slope failures and the amount of rainfall required for the initiation of landslides in a region (Caine 1980; Innes 1983; Aleotti 2004; Guzzetti et al. 2007, 2008a). The scaling properties of landslides are revealed by power law dependencies, and are considered evidence of the critical state of landscape systems dominated by slope wasting phenomena.

Rainfall is a recognized trigger of landslides, and early investigators have recognized that empirical rainfall thresholds can be established to determine the amount of rainfall required to initiate landslides in a region (Caine 1980; Innes 1983). With a few exceptions, all the empirical rainfall thresholds are represented by power law models. Despite the abundant empirical evidence, the reasons for the scaling behaviors of landslide phenomena are poorly known; in a recent paper (Alvioli et al. 2014), we have shown that a relatively simple, physically based model that describes the stability conditions of slopes forced by rainfall, when applied to a sufficiently large geographical area

M. Alvioli (✉) · M. Rossi · F. Guzzetti
Consiglio Nazionale delle Ricerche, Istituto di Ricerca per la Protezione Idrogeologica, via Madonna Alta 126, I-06128 Perugia, Italy
e-mail: alvioli@pg.infn.it

M. Rossi
Dipartimento di Scienze della Terra, Università degli Studi di Perugia, Piazza Università, I-06123 Perugia, Italy

G. Lollino et al. (eds.), *Engineering Geology for Society and Territory – Volume 1*,
DOI: 10.1007/978-3-319-09300-0_102,

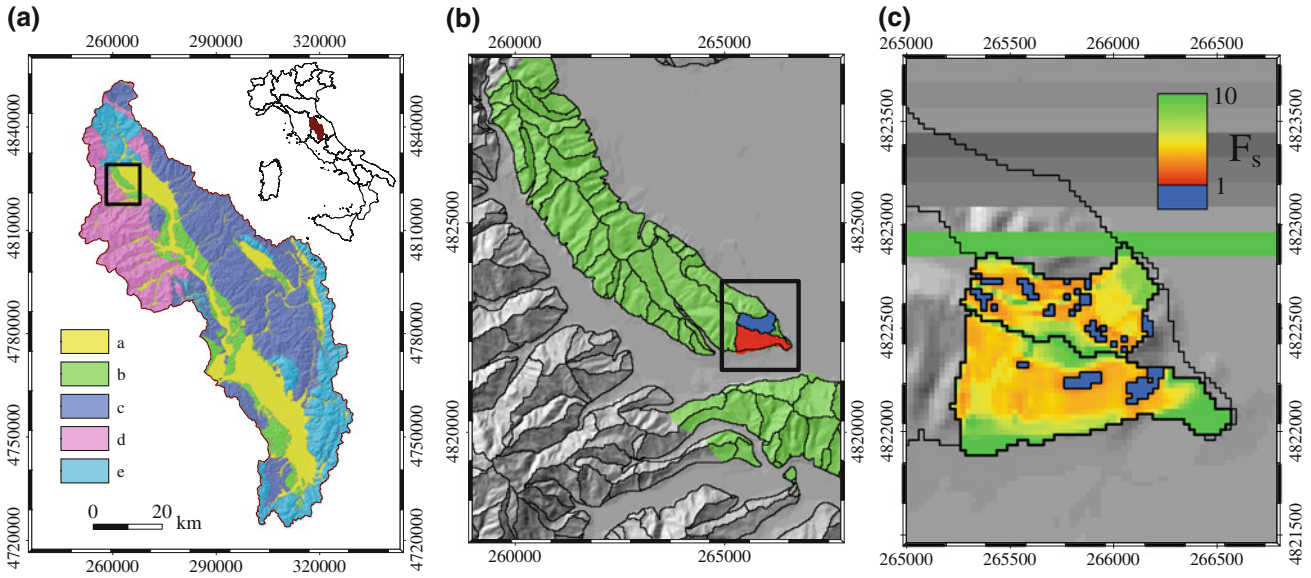

Fig. 102.1 The Upper Tiber River Basin (UTRB), in Central Italy. Colours show five lithological complexes (Cardinali et al. 2001; Guzzetti 2008b): *a* Fluvial and lake deposits, recent in age. *b* Continental, post-orogenic sediments, Pliocene to Pleistocene in age. *c* Allochthonous rocks, lower to middle Miocene in age. *d* Tuscany and Umbria turbidites sequences, Eocene to Miocene in age. *e* Umbria-Marche sedimentary sequence, Lias to lower Miocene in age. *Black box* in (**a**) shows location of enlargement portrayed in (**b**) where *black lines* show hydrological sub-basins derived automatically from a 25 × 25 m DEM; the only lithological area shown in colour is (**b**), and two sample sub-basins are shown in *red* and *blue*. *Black box* in (**b**) shows location **c**, which shows the result of the TRIGRS numerical modeling for two sub-basins. Values for the factor of safety F_S are shown with a color ramp ranging from large values (*green*) to small values (*red*). F_S values smaller than unity (shown in *blue*) represent cells predicted unstable by the model

produces results that are in agreement with two known scaling properties of landslides, namely: (i) the rainfall conditions that result in unstable slopes, which match regional empirical Intensity–Duration (*I–D*) thresholds for possible landslide occurrence (Guzzetti et al. 2007, 2008a), and (ii) the frequency distribution of the area of the patches of terrain predicted as unstable by the model, which matches the statistics of landslide area for event landslides (see, e.g., Malamud et al. 2004).

We adopted TRIGRS version 2.0 (Baum et al. 2008). The software implements a grid-based, spatially distributed slope stability model coupled with an infiltration model capable of simulating the infiltration of rainfall in the terrain, modulating the stability/instability conditions of the individual grid cells (Iverson 2000; Baum et al. 2008; Godt and McKenna 2008; Godt et al. 2008).

We performed our analysis in the Upper Tiber River Basin (UTRB), in central Italy, shown in Fig. 102.1a. The landscape is hilly or mountainous, with open valleys and intra-mountain basins and climate is Mediterranean. For the numerical experiments we selected the area in the UTRB where unconsolidated and poorly consolidated continental sediments crop out (green area in Fig. 102.1). This is the lithological complex where shallow landslides are more frequent in the study area (Cardinali et al. 2000; Guzzetti et al. 2008b), and where the TRIGRS conceptual landslide scheme is best suited to model the stability/instability

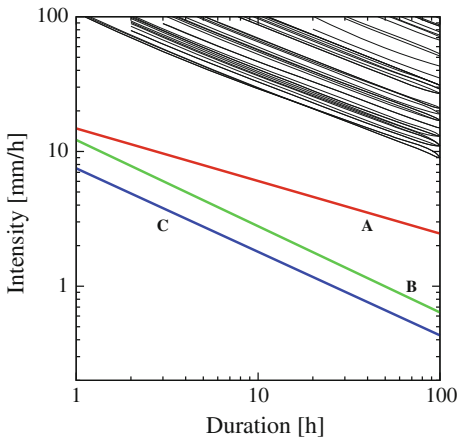

Fig. 102.2 Colored lines are rainfall intensity–duration (*ID*) thresholds applicable to the UTRB, taken from: *A* (*red*) $I = 14.82\ D^{-0.39}$ (Caine 1980), *B* (*green*) $I = 12.17\ D^{-0.64}$ (Brunetti et al. 2010), and *C* (*blue*) $I = 7.5\ D^{-0.62}$ (Peruccacci et al. 2012). Exponents for the *black lines* are in the range -0.54 ± 0.09, obtained fitting each threshold line with a power law, averaging the exponents, and combining in quadrature the uncertainties given by the fits

conditions of slopes forced by rainfall. The geotechnical properties for the soils in this lithological complex used for the numerical modeling are listed in Alvioli et al. (2014).

The TRIGRS model adopts a grid-based representation of a real landscape based on a DEM, and uses local terrain

characteristics as an input for the solution of a system of equations whose output is the factor of safety F_S i.e., a positive number representing the balance of the driving and the resisting forces acting in each grid cell. For unstable conditions, where driving forces exceed the resisting forces, $F_S < 1.0$, and the slope cell fails.

To investigate the relationship between the magnitude of the rainfall trigger (i.e., I and D) we first partitioned the study area into sub-basins i.e., hydrological ensembles of slope units, where a slope unit is a hydrological region bounded by drainage and divide lines. Next, we forced the individual sub-basins in the study area with a uniform rainfall of a given intensity I, for a given period of time D. We then studied the rainfall conditions that have resulted in unstable cells in the sub-basins. For simplicity, we considered only (nearly) mono-lithological sub-basins i.e., sub-basins for which at least 50 % of the area is covered by unconsolidated and poorly consolidated continental sediments. We further considered unstable the sub-basins with at least 10 % of the grid-cells with $F_S < 1.0$. We have chosen the 10 % threshold for the following reasons. We are interested in distinguishing those hillsides that become critical under a given I–D rainfall trigger. Setting a threshold in terms of failing grid cells is needed to give an objective measure of such critical state. The threshold must be a small one, since the adopted stability model is strictly well-defined on a cell-by-cell basis, so any method of clustering neighboring cells is in principle arbitrary. This means that a small fraction of failing cells must be considered as potentially altering the stability of a significant portion of the hillside. We have checked that our conclusions are unchanged if a different threshold is chosen, as long as it stays small enough. In other words, a slightly different threshold would not affect the sensitivity of the model to the most important input features and parameters, namely the local slope, cohesion, friction angle and infiltration rate. For each sub-basin, we started with a given (reasonable e.g., Guzzetti et al. 2007, 2008a) set of D and mean I conditions, and we checked if these conditions resulted in landslides. Next, we increased I maintaining D constant, and we checked if the new rainfall conditions had resulted in landslides. The procedure was repeated for different, increasing rainfall durations. For the modeling, we used (i) $I = 1$ mm h^{-1} to $I = 200$ mm h^{-1} with steps of 2 mm h^{-1}, and (ii) $D = 1$ h to $D = 100$ h, with steps of 1 h for the 1–10 h range, and steps of 10 h for the 10–100 h range. At the end of the procedure, for each of the considered sub-basins we obtained a set of rainfall (D, I) conditions that had resulted in (predicted) slope instabilities (10 % or more of the grid-cells with $F_S < 1.0$). We plotted these rainfall conditions in a D, I plot, in log-log coordinates. A representation of typical output of the code for F_S for two sample sub-basins is shown in Fig. 102.1c. The result of the simulations is shown in Fig. 102.2, where each black line represent the threshold above which a single sub-basin in the study area is unstable, and known rainfall thresholds obtained on global and regional scales are shown for comparison. Visual inspection of Fig. 102.2 reveals that the rainfall (D, I) conditions that have resulted in unstable conditions in each sub-basin follow power laws that represent rainfall thresholds for slope instability in the sub-basins. Fig. 102.2 reveals that the threshold lines are well defined, and obey distinct power law trends for a significant range of rainfall durations ($1 \leq D \leq 100$ hours) known to initiate landslides (Guzzetti et al. 2007, 2008a). Significantly, the slope of the threshold curves is in agreement with the slope of empirical rainfall thresholds for possible landslide occurrence established for central Italy (Peruccacci et al. 2012) and for Italy (Brunetti et al. 2010).

The position of the threshold curves in the D, I plane depends on the location and geomorphological characteristics of the individual sub-basins, but all of the threshold curves lay above the empirical thresholds proposed in the literature and applicable to the study area (e.g., Caine 1980; Brunetti et al. 2010; Peruccacci et al. 2012), which are defined as lower ID boundary conditions in a large area, while in our case each curve corresponds to a specific (local) morpho-lithological setting. We stress that the result was obtained using reasonable values for the model parameters, without any attempt to fine-tune the parameters or to use a probabilistic-inspired approaches (Raia et al. 2014). We maintain that this indicates that the scaling behavior of the rainfall conditions responsible for shallow landslides in the UTRB emerged from the physical modeling, and is dependent on the local geomorphological setting and the rainfall trigger.

We conclude that the scaling exponent of the power-law curves describing the mean rainfall intensity versus rainfall duration conditions that produced slope instability in (quasi) mono-lithological sub-basins where unconsolidated and poorly consolidated sediments crop out in the study area was almost identical to the scaling exponent of empirical ID rainfall thresholds for possible landslide occurrence defined for Central Italy (Peruccacci et al. 2012), and for Italy (Brunetti et al. 2010). The finding is important because it reconciles the physically-based and the statistically-based approaches to the prediction of rainfall induced landslides (Crosta and Frattini 2003; Aleotti 2004; Guzzetti et al. 2007, 2008a). This is relevant for landslide warning systems based on rainfall thresholds (Chleborad 2003; Aleotti 2004; Guzzetti et al. 2008a; Brunetti et al. 2009; Kirschbaum et al. 2012). Moreover, the results of this work in our opinion can be considered as a starting point for investigating the underlying mechanisms giving rise to the scaling properties of landslide phenomena.

We would like to stress that we used, for the simulations reported in Alvioli et al. (2014), synthetic rainfall thresholds, with fictitious rainfall durations and intensities. We

also used reasonable values for the cell-by-cell geotechnical parameters controlling the stability of the slopes. Using the flexibility of the TRIGRS code it is possible to run realistic scenarios, in which actual climatic conditions and soil properties can be simulated. The fact that rainfall thresholds can actually be observed from simulations, even if they were not keyed in the model equations, makes us confident that actual climatic conditions would reproduce the local thresholds with great detail, and climate change scenarios can be effectively described within our approach.

Acknowledgments MA was supported by grants provided by the Regione Umbria, under contract *POR-FESR Umbria 2007–2013, asse ii, attività a1, azione 5*, and by the *Dipartimento della Protezione Civile*, Italy.

References

Aleotti P (2004) A warning system for rainfall-induced shallow failures. Engineering Geology 7:247–265

Alvioli M, Guzzetti F, Rossi M (2014) Scaling properties of rainfall induced landslides predicted by a physically based model. Geomorphology 213: 38–47. doi: 10.1016/j.geomorph.2013.12.039

Baum R, Savage W, Godt JW (2008) TRIGRS—a fortran program for transient rainfall infiltration and grid-based regional slope-stability analysis, version 2.0. U.S. Geological Survey Open-File Report 2008-1159, p 75

Brunetti MT, Peruccacci S, Rossi M, Guzzetti F, Reichenbach P, Ardizzone F, Cardinali M, Mondini AC, Salvati P, Tonelli G, Valigi D, Luciani S (2009) A prototype system to forecast rainfall induced landslides in Italy. In: Proceedings of the first Italian workshop on landslides, Naples, 8–10 June 2009, vol. 1, pp 157–161

Brunetti MT, Peruccacci S, Rossi M, Luciani S, Valigi D, Guzzetti F (2010) Rainfall thresholds for the possible occurrence of landslides in Italy. Nat Hazards Earth Syst Sci 10:447–458. doi:10.5194/nhess-10-447-2010

Caine N (1980) The rainfall intensity-duration control of shallow landslides and debris flow. Geogr Ann A62:23–27

Cardinali M, Antonini G, Reichenbach P, Guzzetti F (2001) Photogeological and landslide inventory map for the Upper Tiber river basin. CNR, Gruppo Nazionale per la Difesa dalle Catastrofi Idrogeologiche, Publication n. 2154, scale 1:100,000

Cardinali M, Ardizzone F, Galli M, Guzzetti F, Reichenbach P, (2000) Landslides triggered by rapid snow melting: the December 1996–January 1997 event in Central Italy. In: Proceedings of the EGS Plinius Conference on Mediterranean Storms, Maratea, Italy, pp 439–448

Chleborad AF (2003) Preliminary evaluation of a precipitation threshold for anticipating the occurrence of landslides in the Seattle, Washington, Area. US Geological Survey Open-File Report 03-463

Crosta GB, Frattini P (2003) Distributed modelling of shallow landslides triggered by intense rainfall. Nat Hazards Earth Syst Sci 3:407–422

Godt JW, McKenna P (2008) Numerical modeling of rainfall conditions for shallow landsliding in Seattle, Washington. Rev Eng Geol 20:121

Godt JW, Schulz WH, Baum RL, Savage WZ (2008) Modeling rainfall conditions for shallow landsliding in Seattle, Washington. Rev Eng Geol 20:137

Guzzetti F, Peruccacci S, Rossi M, Stark CP (2007) Rainfall thresholds for the initiation of landslides in central and southern Europe. Meteorol Atmos Phys 98:239–267. doi:10.1007/s00703-007-0262-7

Guzzetti F, Peruccacci S, Rossi M, Stark CP (2008a) The rainfall intensity-duration control of shallow landslides and debris flows: an update. Landslides 5:3. doi:10.1007/s10346-007-0112-1

Guzzetti F, Ardizzone F, Cardinali M, Galli M, Reichenbach P, Rossi M (2008b) Distribution of landslides in the Upper Tiber river basin, central Italy. Geomorphology 96:105–122. doi:10.1016/j.geomorph.2007.07.015

Innes JL (1983) Debris flows. Prog Phys Geogr 7:469–501

Iverson RM (2000) Landslide triggering by rain infiltration. Water Resour Res 36(7):1897–1910

Kirschbaum BD, Adler RF, Hong Y, Kumar S, Peters-Lidard C, Lerner-Lam A (2012) Advances in landslide nowcasting: evaluation of a global and regional modeling approach. Environ Earth Sci 66:1683–1696. doi:10.1007/s12665-011-0990-3

Malamud BD, Turcotte DL, Guzzetti F, Reichenbach P (2004) Landslide inventories and their statistical properties. Earth Surf Proc Land 29:687–711. doi:10.1002/esp.1064

Peruccacci S, Brunetti MT, Luciani S, Vennari C, Guzzetti F (2012) Lithological and seasonal control on rainfall thresholds for the possible initiation of landslides in central Italy. Geomorphology 139–140:79–90. doi:10.1016/j.geomorph.2011.10.005

Raia S, Alvioli M, Rossi M, Baum RL, Godt JW, Guzzetti F (2014) Improving predictive power of physically based rainfall induced shallow landslides models: a probabilistic approach. Geoscientific Model Dev 7:495–514. doi:10.5194/gmd-7-495-2014

Slope Dynamics and Climatic Change Through Indirect Interactions

103

Mauro Rossi, Dino Torri, Elisa Santi, Giovanni Bacaro, Ivan Marchesini, Alessandro Cesare Mondini and Giulia Felicioni

Abstract

The rapid variation of climate can cause direct changes in slope dynamics due to a modified rainfall regime. Variations in evapotranspiration regime determines changes in soil moisture, modifies shrinking-swelling cycles, creeping, surface mass movement, and soil erosion, including gully erosion. All these effects can be considered as direct consequences of any climate modification. Besides them, other indirect effects should be considered to fully determine climate change impact on slope dynamics. This is the case of the effects of climate change on vegetation, that strongly controls slope instability phenomena. Here we will concentrate on the effect of increased danger due to forest fire, and in particular we discuss the changes in the hydrogeological hazard linked to the effect of drought on wild fires in a case-study in Umbria (Italy), mainly considering field observations and simulations with LANDPLANER (LANDscape, Plant, LANdslide and ERosion) model. This study shows that when discussing of climate changes particular emphasis must be put on side effects that can influence slope dynamics and basin behavior. In particular the understanding of where threats can come, requires the identification of complex framework describing the dynamic interaction of all the elements coexisting in a slope.

Keywords

Erosion • Climatic change • Curve number • Land use • Fire • Satellite image • Vegetation

103.1 Introduction

Analyses of climate changes are usually focused on the evaluation of the effects of variations of meteorological factors (e.g. rainfall, temperature, droughts). In this study emphasis is given to some side effects that can strongly influence the slope and consequently the basin behavior. In particular we present a framework to evaluate the effects of different scenarios on erosion rate in a burned area, based on the land use description. Forest fires, increased in frequency in Mediterranean areas over the last few decades and extreme weather conditions intensify the erosion and land degradation processes. An example of this situation was experienced in Umbria (Central Italy), where, the decreasing trend of fire-affected acreage, which characterized the last 20 years, due to a national and local efficient system of

M. Rossi (✉) · D. Torri · E. Santi · G. Bacaro · I. Marchesini · A.C. Mondini
Consiglio Nazionale Delle Ricerche, Istituto Di Ricerca Per La Protezione Idrogeologica, Via Madonna Alta 126, 06128 Perugia, Italy
e-mail: mauro.rossi@irpi.cnr.it

M. Rossi
Dipartimento Di Scienze Della Terra, Università Degli Studi Di Perugia, Piazza Università, 06123 Perugia, Italy

G. Felicioni
Regione Umbria, Servizio Geologico E Sismico, Corso Vannucci, 96, 06121 Perugia, Italy

G. Lollino et al. (eds.), *Engineering Geology for Society and Territory – Volume 1*,
DOI: 10.1007/978-3-319-09300-0_103,

firefighting and prevention, was interrupted in the recent past few years.

103.2 Case Study

An unusual prolonged dry period in the Umbria region in 2012 (Fig. 103.1), coupled with high temperatures, favored the condition for the fire to burn an area larger than in the previous years as shown by the fire statistics relative to the period 1985–2012 (data from the Umbria regional fire inventory and from the European Forest Fire Information System).

A fire event occurred in July 2012 closed to the SS3 "Flaminia" national road (Terni province). It burned an area of approximately 5 km^2 characterized by Mediterranean forest (specifically, *Quercus ilex* dominated evergreen forest with other sclerophyllous species as *Arbutus unedo* and *Viburnum tinus*) (Fig. 103.2c–d).

In September/October 2012 the first two rainy events deposited along the main road almost 1000 Mg of material, originated from the burned area shown in Fig. 103.2d. Very high resolution satellite images were acquired to show the slope condition before and after the fire.

The land cover maps derived from the satellite images classification, and field surveys carried out in 2012–2013, allowed the identification of four different situations: (i) before the fire (Pre-Fire scenario, June 2012), (ii) immediately after the fire (Post-Fire Pre-Event scenario, August 2012), (iii) two months after the erosion events (Post-Fire Post-Event, December 2012), and (iv) 1 year after the fire (Post-Fire Post-Event Summer, August 2013). To analyze the changes in the possible erosion triggering conditions we exploited the LANDPLANER (Rossi et al. 2012) model.

LANDPLANER is a modeling tool mainly designed to describe the dynamic response of slopes (or basins) under different changing scenarios including: (i) changes of meteorological factors, (ii) changes of vegetation or land-use, (iii) and changes of slope morphology. The model is raster-based and distributed and it is able to estimate the effects of a given rainfall on the triggering of landslide and erosion processes.

LANDPLANER was applied to the different scenarios allowing a first test of the model and an evaluation of its ability to deal with scenarios. The model is based on the Runoff Curve Number model (NRCS 2013), modified to work in spatially distributed environment. Land use, its management and hydrological conditions are consequently represented by maps of curve number (CN) values from which storage, infiltration and erosion resistance can be derived.

Curve number maps (Fig. 103.3a–d) showing the ground conditions for the different scenarios were derived from the satellite images classification, field survey data collected in 2012–2013 and other ancillary data.

A twofold modeling schema was adopted to analyze the critical erosion triggering condition. The first modelling approach exploits an empirical topographic threshold equation (Torri and Poesen in press), based on the analysis of the morphological conditions and on soil/vegetation/land use characteristics existing along a slope.

$$\sin(s)A^{0.38} \geq c \cdot e^{1.3RCF} \cdot (0.00124S_{0.05} - 0.037) \quad (103.1)$$

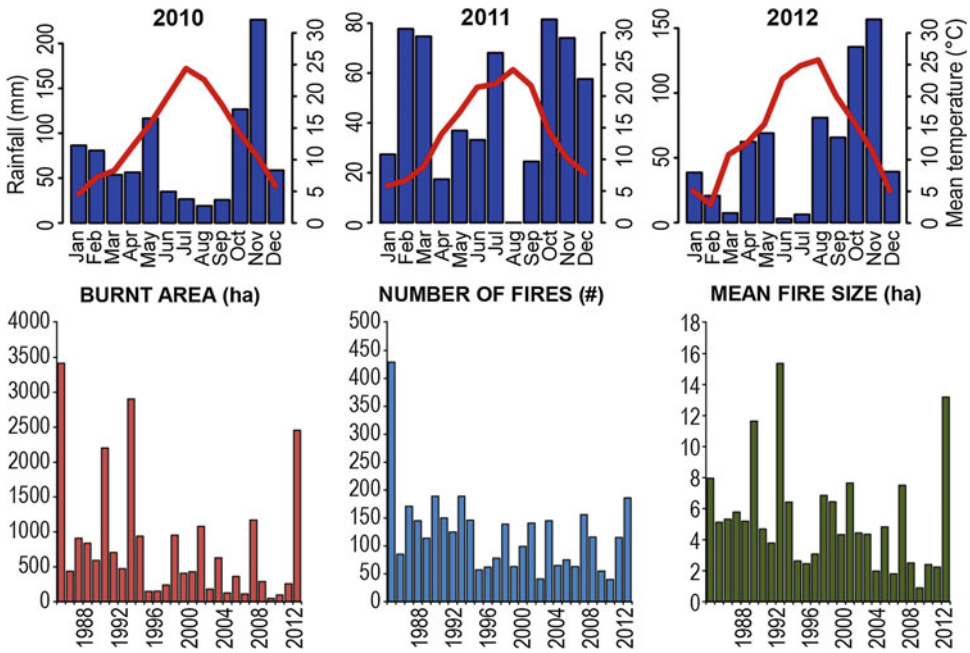

Fig. 103.1 *Upper* Temperature (*red line*) and precipitation (*blue bars*) in the study area from 2010 to 2012. *Lower* Fire statistics (from *left* to *right*: Total burnt area, number of fires, average fire size) in the Umbria region for the period 1985–2012

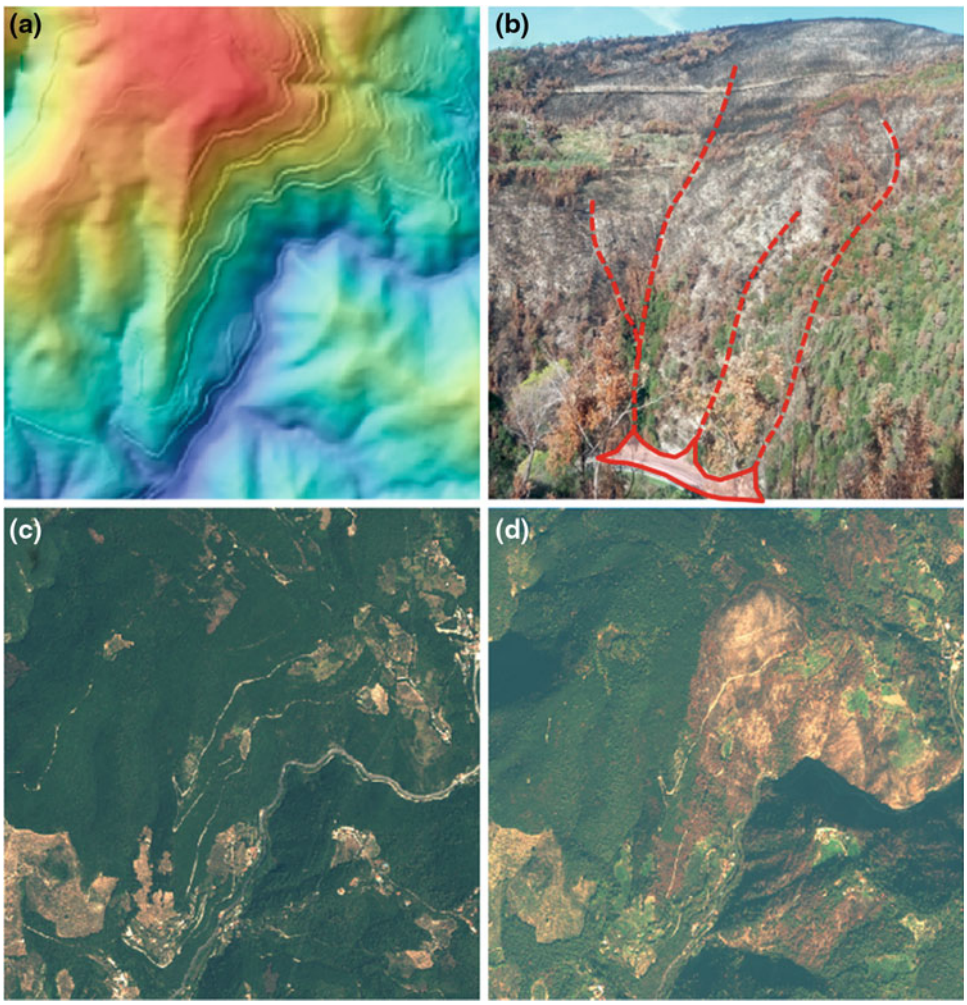

Fig. 103.2 **a** Digital terrain model; **b** Erosional events that occurred in october 2012; **c** Pre-fire satellite image (July 2011); **d** Post-fire satellite image (August 2012)

where s is the slope angle, c is a constant (assumed equal to 1), RCF is the percentage of rock fragments, A is the upslope contributing area in hectares, and S in $S_{0.05}$ is a storage index in mm derived from CN maps (NRCS 2013). When the threshold condition is exceeded, erosion is possible and areas prone to gully erosion (GHPA) can be identified. Erosion channels are identified starting from the uppermost upslope erosion points and following flow paths (recognized exploiting drainage directions). Potential erosion and deposition/transportation location along the channels are identified by places where the topographic threshold is exceeded (erosion) or not (deposition/transportation).

The second model is based on an erosion index calculated as follows:

$$E = \frac{Q_{off} \sin(s)}{S_{0.05}} \tag{103.2}$$

where Q_{off} is the overland flow exiting a given cell.

To calculate Q_{off} LANDPLANER integrates spatially distributed (pixel based) runoff valued calculated on the base of the Curve Number method and the accumulation and drainage direction maps derived from a DEM (flow accumulation).

The results of the gully head threshold model and of the erosion index calculated for a daily rainfall of 100 mm are shown in Fig. 103.3.

103.3 Discussion and Conclusion

High CN values (in blue in Fig. 103.3a–d) correspond to low permeability conditions, with a higher runoff and hence where erosion processes can preferentially occur. Our results agree with other studies showing that fires increase runoff rate and soil erosion (Giovannini and Lucchesi 1991; Andreu et al. 1994; Inbar et al. 1998; Pierson et al. 2002; De Luis et al. 2003). Immediately after the fire (Fig. 103.3b, f, j) both the gully head threshold approach and the soil erosion index show larger areas prone to erosion (compared to the pre-fire conditions shown in the first column). This is mostly due to the presence of a slight hydrophobic layer in the soil (highest CN values), but is also related to the strong reduction of soil litter and foliage after burning which cause

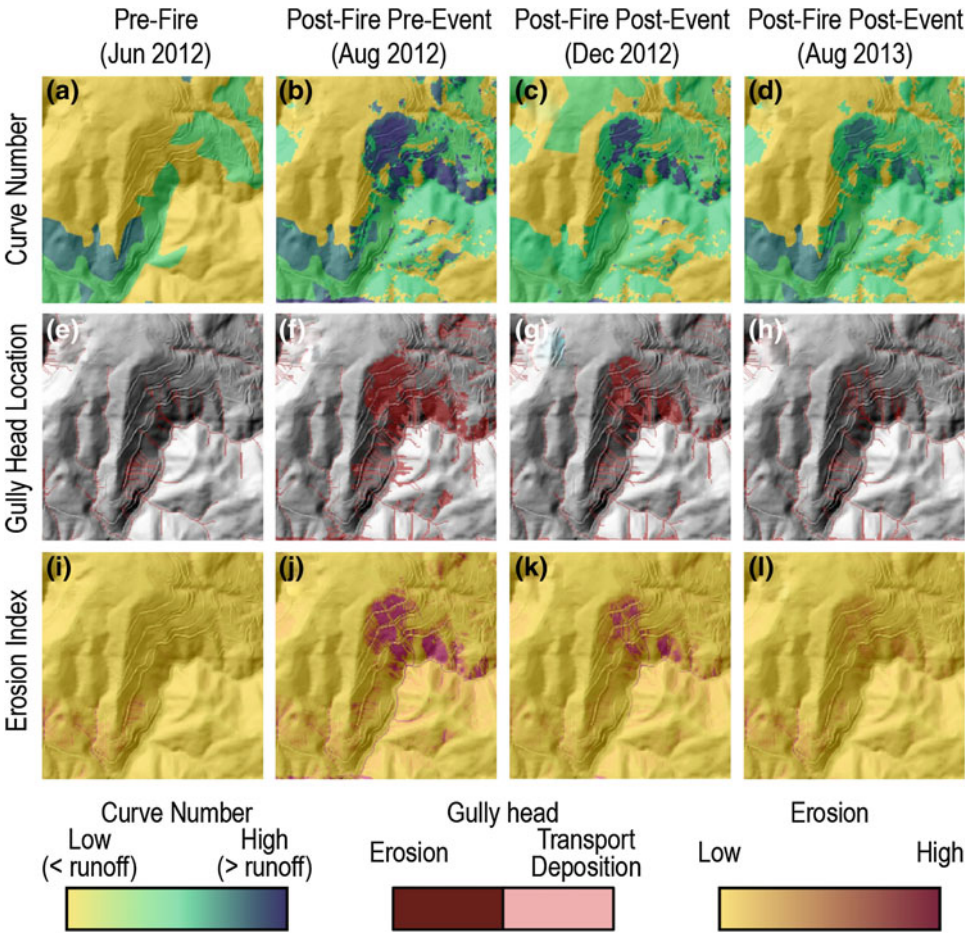

Fig. 103.3 LANDPLANER simulations results. Curve number maps in the *upper* part show four different simulated scenarios: **a** before the fire (June 2012), **b** immediately after the fire (August 2012), **c** 2 months after the erosion events (December 2012), and **d** 1 year after the fire (August 2013). Maps **e–h** show results of the gully head threshold model. Maps **i–l** show values of the erosion index calculated for a 100 mm daily rainfall

both a decrease in infiltration capacity (Elwell and Stocking 1976; Martin and Moody 2001) and an increase of vulnerability to erosion agents (Inbar et al. 1998).

Erosion is more intense where the higher fire intensity is observed (darker blue colors, Fig. 103.3a–d). After the fire, the hydrophobicity behavior reduces and then disappear, while herbaceous species (belonging to *Leguminosae* and *Graminaceae* families), and resprouting from burned trees (mainly pyrophyte species as *Q. ilex*, *Fraxinus ornus* and *A. unedo*) rapidly and progressively reinstate vegetation protection. Hence, CN values decrease and the erosion susceptibility gradually approaches the pre-fire conditions, even if slightly higher erosion susceptibility still persists and will possibly disappear during the next growing season.

This model description (Fig. 103.3) corresponds to field observations and confirms similar descriptions found in other studies (Soler et al. 1994; Rubio et al. 1997; Inbar et al. 1998; Robichaud 2000; Pierson et al. 2001, 2002). The gully erosion prone areas (GHPA) in the four different scenario conditions are shown in Fig. 103.3f–h. An additional erosion index *E*, estimated by Eq. (103.2), with runoff corresponding to a 100 mm daily rainfall, is shown in Fig. 103.3i–l. GHPA vary significantly in the four scenarios. The most critical conditions occurred immediately after the fire (August 2012, Fig. 103.3f) when the runoff potential was maximum (highest CN values). The GHPA gradually decrease with the regeneration of vegetation cover and the disappearance of hydrophobicity (from December 2012 to August 2013, Fig. 103.3g–h). Erosion index results show smaller GHPA, and prove more efficient in characterizing their spatial distribution. Both results are in accordance with the rills and gullies observed in the field in the three situations after the fire. In particular results obtained for the August 2013 scenario significantly correspond with the field observations which witness active gullies and rills to have abandoned large part of the area previously affected, as shown by the results in terms of E index (Fig. 103.3l). The overestimation of the eroded area obtained using Eq. (103.1) is actually apparent because the threshold suggests that is possible to observe a gully erosion but this does not imply that it must necessarily be formed or reactivated. Gully erosion can be certainty reached only when the threshold is largely overcome.

Acknowledgments The LANDPLANER model was developed mainly to evaluate flow connectivity within the EC BIO_SOS project (FP7/2007-2013, SPA.2010.1.1-04, GA263435) (www.biosos.eu).

References

Andreu V, Rubio JL, Forteza J, Cerní R (1994) Long term effects of forest fires on soil erosion and nutrient losses. In: Sala M, Rubio JL (eds.) Soil erosion as a consequence of forest fires. Geoforma Ediciones, Logroño, pp 79–90

De Luis M, Raventós J, González-Hidalgo JC (2003) Effects of fire and torrential rainfall on erosion in a Mediterranean gorse community. Land Degrad Dev 14:203–213

Elwell H, Stoking M (1976) Vegetal cover to estimate soil erosion hazard in Rhodesia. Geoderma 15:61–70

Giovannini G, Lucchesi S (1991) Is the vegetation cover the primary factor controlling erosion in burned soils? Sala M, Rubio JL (eds.) Proceedings of E.S.S.C. conference on soil erosion and degradation as a consequence of forest fires, Barcelona and Valencia, Spain, p 16, Sept 1991

Inbar M, Tamir M, Wittenberg L (1998) Runoff and erosion processes after a forest fire in Mount Carmel, a Mediterranean area. Geomorphology 24:17–33

Martin DA, Moody JA (2001) Comparison of soil infiltration rates in burned and unburned mountainous watersheds. Hydrol Process 15:2893–2903

NRCS (2013) National engineering handbook hydrology chapters, part 630. http://www.nrcs.usda.gov/wps/portal/nrcs/detailfull/national/water/?cid=stelprdb1043063. Last visited Oct 24 2013

Pierson FB, Robichaud PR, Spaeth KE (2001) Spatial and temporal effects of wildfire on the hydrology of a steep rangeland watershed. Hydrol Process 15:2905–2916

Pierson FB, Carlson DH, Spaeth KE (2002) Impacts of wildfire on soil hydrological properties of steep sagebrush-steppe rangeland. Int J Wildland Fire 11:145–151

Rossi M, Torri D, Diele F, Marangi C, Ragni S, Blonda P, Nagendra H, Marchesini I, Santi E (2012) Report on habitat state and ecosystem status assessment. Deliverable. 6.5, BIO_SOS. http://www.biosos.eu/deliverables/D6-5.pdf

Robichaud PR (2000) Fire effects on infiltration rates after prescribed fire in Northern Rocky Mountain forests, USA. J Hydrol 231:220–229

Rubio JL, Forteza J, Andreu V, Cerni R (1997) Soil profile characteristics influencing runoff and soil erosion after forest fire: a case study (Valencia, Spain). Soil Technol 11(1):67–78

Soler M, Sala M, Gallart F (1994) Post fire evolution of runoff and erosion during an eighteen month period. In: Sala M, Rubio JL (eds.) Soil erosion and degradation as a consequence of forest fires. Geoforma Ediciones, Logroño, pp 149–161

Torri D, Poesen J (in press) A review of topographic threshold conditions for gullyhead development in different environments. Earth Sci Rev

Land Use Change Scenarios and Landslide Susceptibility Zonation: The Briga Catchment Test Area (Messina, Italy)

104

Paola Reichenbach, Claudia Busca, Alessandro Cesare Mondini and Mauro Rossi

Abstract

Landslides spatial distribution and frequency are the consequence of different meteorological and environmental conditions including morphological, hydrological, lithology the land use settings. In this work we have attempted to evaluate the influence of land use change on landslide spatial distribution occurrence (susceptibility) for a portion of the Briga catchment, located along the Ionian coast of Sicily, Italy. On 1 October 2009, the area was hit by a high intensity rainfall event that triggered abundant slope failures, and resulted in widespread erosion and deposition of debris along ephemeral drainage channels. After the storm, an accurate event landslide inventory map was made for the catchment and a pre-event landslide map was prepared using aerial photographs. Moreover two different land use maps were realized, the first was obtained through a semi-automatic classification of digitized aerial photographs acquired in 1954, the second through the combination of supervised classifications of two QuickBird images acquired in 2006 and 2009. Using the available thematic data, we have prepared susceptibility zonation through multivariate statistical models exploiting the 2009 event landslides as grouping variable and simple morphological and 2009 land use data as explanatory variables. To evaluate the influence of land use change on the susceptibility zonation, the same discriminant models were applied to different land use distribution including the 1954 land use map. Differences in the landslide susceptibility maps were analysed to understand how land use change affects the landslide occurrence.

Keywords

Landslide • Susceptibility zonation • Land-use change • Satellite image

104.1 Introduction

Land use together with other environmental factors (including morphology, hydrology and lithology) influences the landslides spatial distribution and occurrence. Land use pattern can change after climatic modifications, natural events or can be modified by human actions. Studies focusing on the effect of human-induced land use changes on slope stability have shown that, in populated regions, the impact of anthropic actions contributes significantly to the initiation and reactivation of landslides (e.g. Vanacker et al. 2003; Van Den Eeckhaut et al. 2009).

P. Reichenbach (✉) · A.C. Mondini · M. Rossi
Consiglio Nazionale delle Ricerche, Istituto di Ricerca per la Protezione Idrogeologica, Via della Madonna Alta 126, 06128 Perugia, Italy
e-mail: paola.reichenbach@irpi.cnr.it

C. Busca
Dipartimento di Scienze della Vita e dell'Ambiente, Università Politecnica delle Marche, Piazza Roma 22, 60121 Ancona, Italy

G. Lollino et al. (eds.), *Engineering Geology for Society and Territory – Volume 1*,
DOI: 10.1007/978-3-319-09300-0_104,

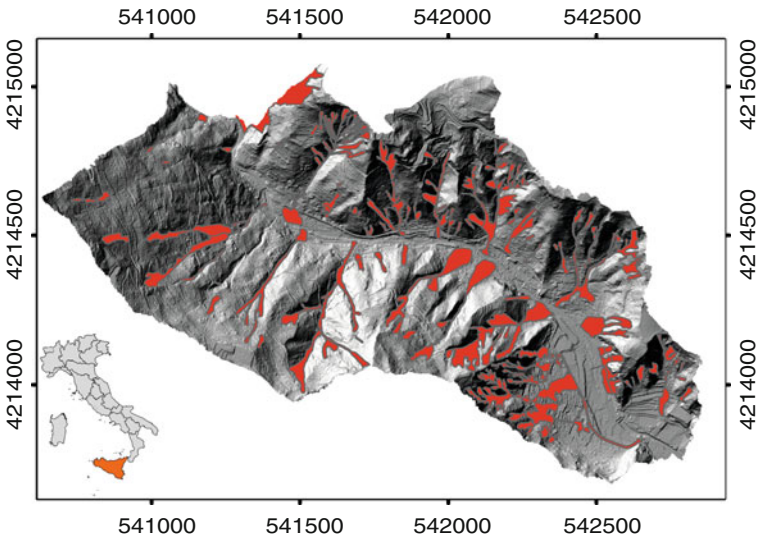

Fig. 104.1 *Shaded* relief of the test area located at the outlet of the Briga catchment, along the Ionian coast of the Messina province (Sicily, Italy). *Red areas* show landslides triggered by the rainfall event

In this work we have attempted to evaluate the influence of land use change on landslide spatial occurrence (susceptibility) for a test area located in the Briga catchment (Southern Italy). We define the landslide susceptibility (LS) as the likelihood of a landslide occurring in an area on the basis of local terrain conditions (Brabb 1984). To evaluate how the susceptibility zonation is influenced by the land use pattern and distribution, we have prepared different maps applying four multivariate statistical classification techniques. In the multivariate modelling an event landslide inventory was selected as grouping variable and simple morphological and land-use classes as explanatory variables.

104.2 Study Area and Available Data

The study area (1.7 km^2) is the lower part of the Briga catchment (Fig. 104.1) located in the Messina province, along the Ionian coast of Sicily (Italy). On 1 October 2009, the area was hit by a high intensity storm with more than 220 mm of rain in 7 h measured at the St. Stefano di Briga rain gauge (Maugeri and Motta 2011). The rainfall event triggered more than 1,000 shallow landslides, mainly shallow soil slides and debris flows, in an area of about 60 km^2. Landslides and inundation caused 37 fatalities, numerous injured people and severe damages in the affected villages and along the transportation network.

After the event, for the test area the following thematic data have been prepared: (i) a detailed and accurate landslide inventory map at 1:10,000; (ii) two land-use maps and (iii) a Very High-Resolution DEM (1 m × 1 m).

The landslide inventory map was completed through a combination of field surveys and visual interpretation of pre-event and post-event stereoscopic and pseudo-stereoscopic aerial photographs (Ardizzone et al. 2012). The map shows the distribution and types of the landslides triggered by the 1 October 2009 rainfall event (Fig. 104.1) and the distribution and types of pre-existing landslides.

Two land use maps were prepared exploiting available aerial photographs (1954 land use map) and Very High Resolution satellite images (land use just before the event). The 1954 map was derived from the analysis of stereoscopic, black and white aerial photographs taken in 1954 by the Geographic Military Institute, at about 1:33,000 scale. The 2009 map was obtained through the combination of supervised classifications of two QuickBird images acquired on 2 September 2006 and on 8 October 2009.

The VHR-DEM was obtained using airborne Lidar sensor. Exploiting the DEM and using a standard WPS tools based on GRASS GIS 7 (grass.osgeo.org/grass70/), R (www.r-project.org/), and Python Web Processing Service (PyWPS), we have partitioned the test area into slope-units (SU), hydrological terrain subdivision bounded by drainage and divide lines (Marchesini et al. 2012). For each slope-unit, we calculated descriptive statistics of elevation and slope that were used as explanatory variables to analyse the spatial distribution of landslides (Carrara et al. 1991).

104.3 Susceptibility Models

To evaluate the influence of land use change on landslide spatial occurrence we prepared three single models and one combined susceptibility zonation through different multivariate statistical analysis (Rossi et al. 2010). For the single models we applied different multivariate classification techniques, including a linear discriminant analysis, a quadratic discriminant analysis and a logistic regression (Reichenbach et al. 2014), exploiting the 2009 event landslides as grouping

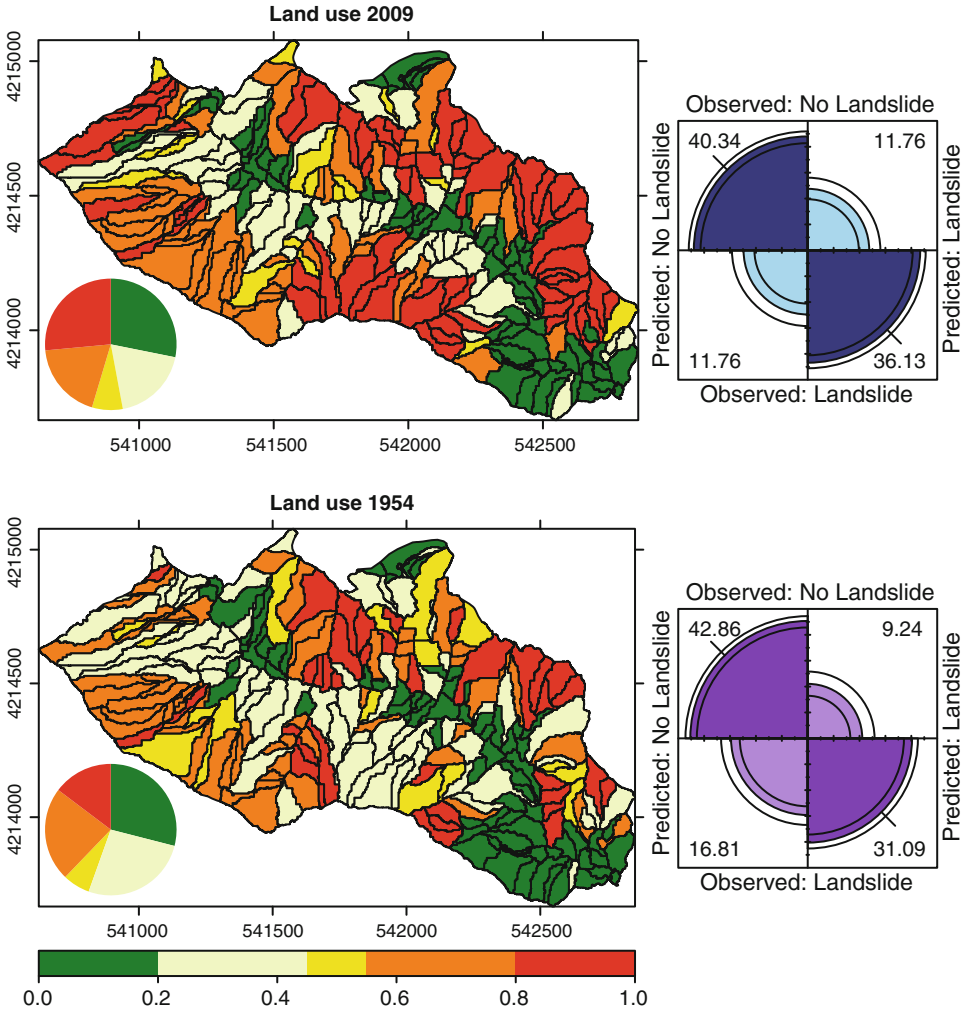

Fig. 104.2 Susceptibility maps (CFM) classified in five classes, prepared using the 2009 land use map (*on the top*) and the 1954 land use map (*on the bottom*). For each model the figure shows a four-fold plot and a pie chart with the distribution of slope-units in the five susceptibility classes

variable and the morphological and the land-use classes as explanatory variables. For the combined susceptibility model (CFM) we adopted a regression approach where the presence or absence of landslides in each slope unit was taken as the dependent variable and the results of the three single models were the independent, explanatory variables.

To evaluate the influence of land use change on landslide susceptibility zonation, single models obtained using the 2009 land use map were applied using the 1945 land use distribution. Figure 104.2 portrays in the upper part, the combined landslide susceptibility model (CFM) realized combining single models prepared using the 2009 land use map, and on the lower part the zonation obtained applying the single model results but considering the 1954 data. The figure shows: (i) the map of the predicted LS in five classes, (ii) a pie chart showing the distribution of slope-units in the same classes and (iii) a four-fold plot summarizing the number of true positives, true negatives, false positives and false negatives.

To better evaluate the influence of land use changes on landslide susceptibility we have designed different land use scenarios obtained changing, at slope unit scale, the 2009 land use distribution. Assuming an increase in the forested areas, we have considered the following scenario: (i) 75 % decrease in the pasture extent (Scenario 1); (ii) 75 % reduction of both pasture and cultivated areas (Scenario 2) and (iii) 75 % decrease in bare soil with SU mean angle greater than 15° and 75 % decrease in pasture areas (Scenario 3).

Results are shown in Fig. 104.3 where maps of the predicted LS and pie charts of the SU distribution are reported. The analysis of the scenarios allows confirming how land use changes affect significantly the distribution of unstable/stable slope. Moreover, inspection of Table 104.1 reveals that the increase in stable SU is highly dependent of the land use arrangement and distribution. The more optimistic scenario (Scenario 3) is related to an enlargement of forest and a reduction of bare soil.

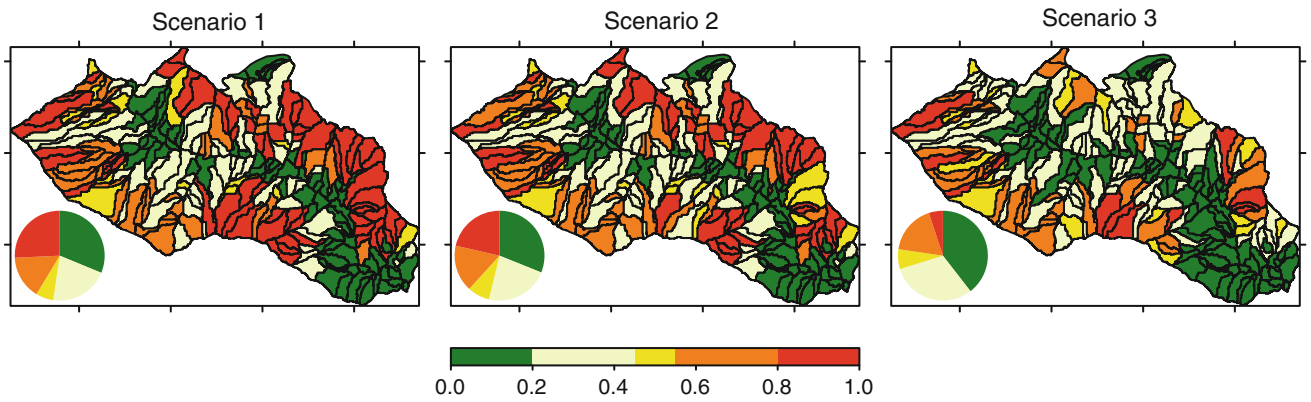

Fig. 104.3 Susceptibility maps (CFM) obtained assuming three possible land use change scenarios

Table 104.1 Percentage of slope-units in the susceptibility classes computed for the different susceptibility zonation (see maps and pie charts of Figs. 104.2 and 104.3)

	<0.20 (%)	0.20–0.45 (%)	0.45–0.55 (%)	0.55–0.80 (%)	>0.80 (%)
Land use 2009	28.2	18.9	7.6	18.9	26.5
Land use 1954	29.0	26.5	6.7	23.1	14.7
Scenario 1	31.1	21.4	6.3	15.5	25.5
Scenario 2	31.1	22.7	8.0	16.8	21.4
Scenario 3	39.5	30.7	7.1	17.6	5.0

104.4 Discussion and Conclusion

This work proposes to analyse the effect of different land use scenarios on the landslide susceptibility zonation in a small test area located at the outlet of the Briga catchment (Messina, Italy). The area was affected by a severe rainfall event that caused fatalities and serious damages to structures and infrastructures. After the event two land use maps were realized exploiting 1954 aerial photographs and QuickBird images (acquired 2006 and 2009). The comparison of the two maps reveals that in about 60 years the spatial extension of the forest decreased of nearly 15 %, bare areas increase of about 9 %, cultivated zones of 3 % and urban areas of about 3 %.

We have evaluated the influence of land use change on landslide spatial occurrence preparing different susceptibility zonation through different multivariate statistical analysis. Models results show an overall variation in the susceptibility distribution. In particular the increase in bare soils to the detriment of forested areas seems to favour the terrain instability. Possible land use change scenarios have been investigated assuming different distribution of the land use classes, always considering an increase in forested areas. In the analysed scenarios the enlargement of forested areas tends to stabilize slopes, but this consequence is variable and depends on the type and percentage of land use changes.

This information can be exploited to evaluate the consequences of land use change on landslide vulnerability and risk. Moreover the proposed approach could be helpful to analyse the potential effects of land use planning and management on slope instability.

References

Ardizzone F, Basile G, Cardinali M, Casagli N, Del Conte S, Del Ventisette C, Fiorucci F, Garfagnoli F, Gigli G, Guzzetti F, Iovine G, Mondini AC, Moretti S, Panebianco M, Raspini F, Reichenbach P, Rossi M, Tanteri L, Terranova O (2012) Landslide inventory map for the Briga and the Giampilieri catchments, NE Sicily, Italy. J Maps 8(2):176–180

Brabb EE (1984) Innovative approaches to landslide hazard mapping. Proceedings of the 4th international symposium on landslides, Toronto

Carrara A, Cardinali M, Detti R, Guzzetti F, Pasqui V, Reichenbach P (1991) GIS Techniques and statistical models in evaluating landslide hazard. Earth Surf Proc Land 16(5):427–445

Marchesini I, Alvioli M, Rossi M, Santangelo M, Cardinali M, Reichenbach P, Ardizzone F, Fiorucci F, Balducci V, Mondini AC, Guzzetti F (2012) WPS tools to support geological and geomorphological mapping. OGRS 2012—Open source geospatial research and education symposium, Yverdon-les-Bains, Switzerland, 24–26 Oct 2012. http://ogrs2012.org/index.php/ogrs2012/ogrs2012/paper/view/34

Maugeri M, Motta E (2011) Effects of heavy rainfalls on slope behaviour: the October 1, 2009 disaster of Messina (Italy). Geotechnics and earthquake geotechnics towards global

sustainability, Susumu Iai eds. Geotechnical, geological and earthquake engineering, vol 15 (Springer Science + Business Media B.V)

Reichenbach P, Busca C, Mondini AC, Rossi M (2014) The influence of land use change on landslide susceptibility zonation: the Briga catchment test site (Messina, Italy). Submitted to Environ Manage (2014)

Rossi M, Guzzetti F, Reichenbach P, Mondini AC, Peruccacci S (2010) Optimal landslide susceptibility zonation based on multiple forecasts. Geomorphology 114:129–142

Vanacker V, Vanderschaeghe M, Govers G, Willems E, Poesen J, Deckers J, De Bievre B (2003) Linking hydrological, infinite slope stability and land-use change models through GIS for assessing the impact of deforestation on slope stability in high Andean watersheds. Geomorphology 52:299–315

van den Eeckhaut M, Poesen J, van Gils M, van Rompaey A, Vandekerckhove L (2009) How do humans interact with their environment in residential areas prone to landsliding? A case-study from the Flemish Ardennes. In: Malet JP, Remaître A, Bogaard T (eds) Landslide processes: from geomorphologic mapping to dynamic modelling. Proceedings of the International Conference 'Landslide Processes', Strasbourg, France, 6–7 February 2009, pp 19–24

Multi-method Evaluation of Denudation Rates in Small Mediterranean Catchments

105

Maurizio Del Monte, Francesca Vergari, Pierluigi Brandolini, Domenico Capolongo, Andrea Cevasco, Sirio Ciccacci, Christian Conoscenti, Paola Fredi, Laura Melelli, Edoardo Rotigliano and Francesco Zucca

Abstract

The paper presents the results of the research tasks of the Quantitative Geomorphology Working Group (of the Italian Association of Physical Geography and Geomorphology) focused on multi-method evaluation of denudation rates in small catchments of Italy. Several study areas are compared with the goal of quantifying the morphodynamic evolution in different response times and with traditional and innovative techniques. The final aims are the direct erosion monitoring, the geomorphic analysis for the comprehension of drainage basin morphodynamics, up to the geomorphological hazard evaluation. The catchments are key Mediterranean areas particularly sensitive to climatic and anthropic modifications. The efforts of the Working Group are finalized to favour scientific collaboration activities among members with the aim of strengthen the potential of Quantitative Gomorphology in morphodynamic studies.

Keywords

Quantitative geomorphology • Denudation rates evaluation • Italy • Geomorphological hazard

M. Del Monte · F. Vergari (✉) · S. Ciccacci · P. Fredi
Dipartimento di Scienze della Terra, Università degli Studi di Roma "La Sapienza", P.le Aldo Moro 5, 00185 Rome, Italy
e-mail: francesca.vergari@uniroma1.it

P. Brandolini · A. Cevasco
Dipartimento di Scienze della Terra, dell'Ambiente e della Vita (DISTAV), Corso Europa 26, 16132 Genoa, Italy

D. Capolongo
Dipartimento di Scienze della Terra e Geoambientali, Università degli Studi di Bari - Aldo Moro, via Orabona 4, Bari, Italy

C. Conoscenti · E. Rotigliano
Dipartimento di Scienze della Terra e del Mare (DiSTeM), Università degli Studi di Palermo, via Archirafi 22, 90123 Palermo, Italy

L. Melelli
Dipartimento di Fisica e Geologia, Università degli Studi di Perugia, P.za dell'Università, 1, Perugia, Italy

F. Zucca
Dipartimento di Scienze della Terra e dell'Ambiente, Università degli Studi Pavia, via a. Ferrata 1, 27100 Pavia, Italy

105.1 Introduction

Denudation processes are well widespread in different areas of Italy producing loss and depletion of soil, landsliding, economic damages and hazardous conditions. The aim of this paper is the study of denudation phenomena in representative catchments located in seven Italian Regions (Piedmont, Liguria, Tuscany, Umbria, Latium, Basilicata and Sicily), characterized by different climate and geological conditions, orographic and tectonic settings (Fig. 105.1).

This paper shows the multiple contribution of the Quantitative Geomorphology (QG) to the quantification of the morpho-evolution rates, through: (i) investigation on the causal factors predisposing denudational processes; (ii) direct measurement of denudation intensity by traditional and innovative technologies; (iii) implementation of indirect models for erosion rate estimation and geomorphological hazard prediction.

G. Lollino et al. (eds.), *Engineering Geology for Society and Territory – Volume 1*,
DOI: 10.1007/978-3-319-09300-0_105,

Fig. 105.1 Location of the study areas

The methods examine both the immediate response and the longer term evolution of drainage basin systems to the denudation processes.

105.2 Short-Term Evolution of Erosion Processes Effects

Given the fragmentation of the national (or local) networks of monitoring stations for fluvial sediment transport, some attempts have been undertaken for quantifying sediment delivery at catchment scale.

In Piedmont region, a small instrumented basin of Valle del Gallina Stream (1.08 km^2), tributary of the Marchiazza stream and of the Cervo River, has been equipped since 1982 by a sedimentary and hydrometric station at its closure (Anselmo et al. 2011). The basin is a key area between the Alps and the upper Po plain for understanding the dynamic interactions between erosion and vegetation, also in a climate change perspective. Continuous records of hydrological data for the period 1982–2008 showed an annual average precipitation of 1279 mm, with the rainy seasons mainly corresponding to spring and autumn. The maximum specific year runoff is 1,341 mm (2002) and the minimum is 375 mm (2007). Summer rainstorms are frequent and can generate soil erosion on the local bare slopes and sediment transport in the channel network, so feeding the sediment supply at the hydro-sedimentary station.

In order to deepen the hillslope contribution to catchment sediment transport, geomorphological studies have been conducted over the past two decades in specific key areas of central Italy affected by badlands and strong denudation rates, at the catchment scale (erosion "hot spots" in Tuscany, Umbria and Latium regions; Della Seta et al. 2009). Thus, understanding and monitoring the processes involved in their development is of crucial importance, especially in regard to distinguishing between on- and off-site effects of water erosion. The goal was achieved by setting up a series of monitoring stations, some of which have been working continuously since 1993 (Vergari et al. 2013), while others have been active for shorter periods between 1993 and 2011. These studies examine areas within the drainage basins of the Tevere River and the Ombrone River, characterized by widespread outcropping of clayey deposits. Geomorphological survey, monitoring with erosion pins and differential GPS are used to detect local modifications of the topographic surface with time and, thus, to quantify local water erosion rates.

Volumetric estimations of the material removed by denudation processes can support geomorphological study in quantifying the velocity of denudation processes. Even so, the size of the study area, the observed time span, and the quality of the required data are perhaps the most critical issues to be considered when looking for the most appropriate technique. DGPS survey can be appropriate when a single hillslope of less than few hectares is being monitored, as the time and effort required would be acceptable. For larger areas or wider time interval, high resolution photogrammetric analysis could be more appropriate. However, all these methods are affected by many error sources, such as those linked to instrument resolution and sensitivity or the difficulty of removing vegetation influence on bedrock remote sensing, that limit their use to very specific time and spatial ranges.

When considering the effect of a single extreme rainfall event, LiDAR data can represent the correct data source for volumetric evaluation. The Vernazza catchment (Cinque Terre, eastern Liguria) was chosen as test area for evaluating the response, in terms of denudation processes, of a small coastal catchment to a single extreme rainfall event. This catchment has a small area (5.7 km^2), very steep slopes and short rectilinear streams with high erosive power. About 50 % of the slopes were terraced for vineyard and olive grove cultivations during the last millennium, and progressively abandoned in the last century, with increasing erosion and geomorphological instability (Cevasco et al. 2013a). On October 25, 2011 after an extreme rainfall event, the Vernazza catchment was affected by more than 500 shallow landslides and erosional processes, with an unusual amount of mud and debris, transported along steep channels and causing the obstruction of the final, urbanized, reach of the Vernazza stream. The centre of Vernazza village was affected by flooding, with mud and debris reaching heights up to 5–6 m (Cevasco et al. 2013b; Galve et al. 2014). The LiDAR data allowed to identify the source areas of denudation processes by analyzing the topographic attribute as slope or plan and radial curvature and then the removed volumetric amount.

105.3 Medium and Long-Term Contribution of Erosion in Morphodynamic Evolution of Drainage Basins: The Quantitative Geomorphic Analysis

During the last decades, quantitative geomorphic analysis has proved to be a suitable tool for an objective characterization of the river basins. In particular, several works showed that some parameters can quantify the spatial geometry of the drainage network (such as extent and hierarchization degree) that strongly affect denudation intensity (Strahler 1957; Dramis and Gentili 1977; Tokunaga 2000; Del Monte et al. 1996).

Ciccacci et al. (1981) suggested the "denudation index" (Tu) for indirectly estimating denudation rates, based on statistical correlations among quantitative geomorphic parameters and suspended sediment yield data. The highest Tu values indicate erosion "hot spots", represented by small sub-catchments affected by badlands developed on uplifted Plio-Pleistocene marine clays (Della Seta et al. 2009).

As well known, the hypsometric integral (Strahler 1957) depicts the evolutionary stage of basins and the intensity of denudation processes (Del Monte 1996). The hypsometric analysis, achieved by Digital Elevation Model analysis in GIS environment (Pérez-Peña et al. 2009), was applied to Rio Torbido basin (Latium region), characterized by a volcanic reference surface dated 300 ka and located at the top of clayey marine deposits affected by badland erosion. The calculated average denudation rate ranges between 0.1 and 0.2 mm y^{-1}. In the same area, erosion monitoring showed that active geomorphic processes are much more intense, with centimetric annual water erosion rates.

Moreover, volumetric analysis can be used for medium- to long-term erosion rate evaluation, once specific geomorphic markers (i.e. dated surfaces) are available.

To this end, DGPS survey was performed for the evaluation of erosion rates due to human impact and rainfall variations of the last 30 years for a sample hillslope, focused on a badland area and named Bargiano, located in Latium region (Vergari et al. 2013). DGPS surveys on both remnants of a 1980 cropland surface and presently eroded surface, with a 2-year monitoring with erosion pins, permitted comparisons between long- and short-term average erosion rates.

Volumetric analysis have been performed also in Basilicata (Piccarreta et al. 2012), where during the last century agricultural soils underwent continuous degradation, due to the highly erodible nature of outcropping terrains and to the anthropic pressure. An attempt to quantify the contribution of gully erosion to overall soil loss and sediment production, by adopting a consolidate procedure in GIS to determine medium-term sediment production and deposition rates in a large gully of Fossa Bradanica, was based on the subtraction of multi-date elevation values from DEMs, including sediment produced by different processes.

The same technique allowed to estimate the volume removed in the Rio Torbido catchment area (Latium), where the top of the subhorizontal 300 ka volcanic caprock (Peccerillo 2012; Gregori and Melelli 2012) of the clayey hillslope was reconstructed with spatial interpolation methods. The calculated mean erosion rate was comparable with that obtained through the hypsometric analysis (Del Monte et al. 2014).

105.4 Assessment of Geomorphological Hazard

QG has also contributed to the development of statistical methods aimed at the assessment of the geomorphological hazard, synthesizing geomorphic processes and predisposing factors as numerical variables. A statistical method was applied to a small (9 km^2) agricultural catchment of western Sicily (sub-basin of the Belice River Basin), investigating functional relationships between spatial distribution of gullies and variability of a set of environmental attributes. The relationships were explored by means of forward stepwise logistic regression analysis that allowed to calculate the probability of cells to host a gully (Conoscenti et al. 2014). The performance of the models was evaluated by drawing Receiving Operating Characteristic (ROC) curves and by calculating the Area Under the ROC Curve (AUC). The results of the experiment allowed to identify driving factors of gully erosion within the studied agricultural catchment and to prepare a susceptibility map that reliably classifies the territory according to its proneness to gullying.

The conditional multivariate analysis was applied to evaluate landslide susceptibility in the Upper Orcia River Basin (Tuscany), where widespread denudation processes and agricultural practices have a mutual impact. An unbiased procedure for causal factor selection was propose, based on some intuitive statistical indices (Vergari et al. 2011). This procedure is aimed at detecting among different potential factors the most discriminant ones in a given study area. Moreover, this step avoids generating too small and statistically insignificant spatial units by intersecting the factor maps. The multitemporal landslide database allowed the validation of the obtained susceptibility model, giving rise to encouraging results.

105.5 Conclusions

Even if using different approaches, each one suitable for evaluating denudation intensity at different spatial scales, for different time intervals and with different resolutions, as synthetically described in the previous paragraphs, the numerous investigations of the Italian QG Working Group have allowed to compare the denudation rates of small Mediterranean catchments, highlighting and confirming that: (a) the maximum off-site effects of denudation "hot spots" are concentrated during occasional but extreme rainfall events, that can produce, in few days, the total annual sediment yield estimated for a single catchment; and (b) human land management can provoke an intensification of erosion rates, especially when cropland are abandoned

and land maintenance activities are not programmed; (c) a multi-method approach allows to reconstruct the short-term evolution of representative catchments that can be compared to the long-term evolution in order to better understand the morpho-evolution of larger areas.

The Working Group has prospects of favouring scientific collaboration activities within members with the aim of strengthen the potentiality of QG in the morphodynamic studies.

References

Anselmo V, Caroni E, Maraga F, Pelissero C (2011) Tendencies in the hydrological budget of a pre-alpine small basin. Die Bodenkultur 9(62):9–15

Cevasco A, Brandolini P, Scopesi C, Rellini I (2013a) Relationships between geo-hydrological processes induced by heavy rainfall and land-use: the case of 25 October 2011 in the Vernazza catchment (Cinque Terre, NW Italy). J Maps. doi:10.1080/17445647.2013.780188

Cevasco A, Pepe G, Brandolini P (2013b) The influences of geological and land-use settings on shallow landslides triggered by an intense rainfall event in a coastal terraced environment. Bull Eng Geol Environ. doi:10.1007/s10064-013-0544-x

Conoscenti C, Angileri S, Cappadonia C, Rotigliano E, Agnesi V, Märker M (2014) Gully erosion susceptibility assessment by means of GIS-based logistic regression: a case of Sicily (Italy). Geomorphology 204:399–411

Ciccacci S, Fredi P, Lupia Palmieri E, Pugliese F (1981) Contributo della analisi geomorfica quantitativa alla valutazione dell'entità dell'erosione nei bacini fluviali. Bollettino della Società Geologica Italiana 99:455–516

Della Seta M, Del Monte M, Fredi P, Lupia Palmieri E (2009) Space-time variability of denudation rates at the catchment and hillslope scales on the Tyrrhenian side of Central Italy. Geomorphology 107(3–4):161–177

Del Monte M (1996) Rapporti tra caratteristiche morfometriche e processi di denudazione nel bacino idrografico del Torrente Salandrella (Basilicata). Geol Romana 32:151–165

Del Monte M, Della Seta M, Melelli L, Vergari F, Ciccacci S (2014) Intensità dell'erosione nel bacino idrografico del Rio Torbido (Bagnoregio, VT). Atti del Convegno "Dialogo intorno al Paesaggio", Perugia, 19-22 febbraio 2013. In: Culture, Territori Linguaggi 4(I), 119–128

Dramis F, Gentili B (1977) I parametri F (Frequenza di drenaggio) e D (Densità di drenaggio) e le loro variazioni in funzione della scala di rappresentazione cartografica. Boll Soc Geol Ital 96:637–651

Galve JP, Cevasco A, Brandolini P, Soldati M (2014) Assessment of shallow landslide risk mitigation measures based on land use planning through probabilistic modelling. Landslides. doi:10.1007/s10346-014-0478-9

Gregori L, Melelli L (2012) Di fuoco e di acqua: forme e paesaggi delle "Città del Tufo". In: Peccerillo A (ed) "L'ignimbrite di Orvieto-Bagnoregio", Nuova Phromos Ed. Città di Castello, 113–134, 156 pp. ISBN 978-88-97900-29-0

Peccerillo A (2012) L'ignimbrite di Orvieto-Bagnoregio, Nuova Phromos Ed. Città di Castello, 156 pp. ISBN 978-88-97900-29-0

Pérez-Peña JV, Azañón JM, Azor A (2009) CalHypso: An ArcGIS extension to calculate hypsometric curves and their statistical moments. Applications to drainage basin analysis in SE Spain. In: Proceedings of computers and geosciences 2009, pp. 1214–1223

Piccarreta M, Capolongo D, Miccoli MN, Bentivenga M (2012) Global change and long-term gully sediment production dynamics in Basilicata, southern Italy. Environ Earth Sci 67:1619–1630

Strahler AN (1957) Quantitative analysis of watershed geomorphology. Am Geophys Union Trans 38:913–920

Tokunaga E (2000) Dimension of a channel network and space-filling properties of its basin. Trans Jpn Geomorphol Union 21:431–499

Vergari F, Della Seta M, Del Monte M, Fredi P, Lupia Palmieri E (2011) Landslide susceptibility assessment in the upper Orcia Valley (Southern Tuscany, Italy) through conditional analysis: a contribution to the unbiased selection of causal factors. Nat Hazards Earth Syst Sci 11:1475–1497

Vergari F, Della Seta M, Del Monte M, Fredi P, Lupia Palmieri E (2013) Long- and short-term evolution of several Mediterranean denudation hot spots: The role of rainfall variations and human impact. Geomorphology 183:14–27. doi:doi.org/10.1016/j.geomorph.2012.08.002

Author Index

G. Lollino et al. (eds.), *Engineering Geology for Society and Territory – Volume 1*,
DOI: 10.1007/978-3-319-09300-0,